AD-A182 954   ADVANCED INSTRUMENTATION FOR AERO ENGINE COMPONENTS: 1/6
                CONFERENCE PROCEEDIN..(U) ADVISORY GROUP FOR AEROSPACE
                RESEARCH AND DEVELOPMENT NEUILLY..   NOV 86 AGARD-CP-399

UNCLASSIFIED   F/G 14/2   NL

MICROCOPY RESOLUTION TEST CHART

AGARD

ADVISORY GROUP FOR AEROSPACE RESEARCH & DEVELOPMENT

AGARD CONFERENCE PROCEEDINGS No.399

Advanced Instrumentation
for Aero Engine Components

DTIC
ELECTE
MAR 0 9 1987
S D

NORTH ATLANTIC TREATY ORGANIZATION

COMPONENT PART NOTICE

THIS PAPER IS A COMPONENT PART OF THE FOLLOWING COMPILATION REPORT:

TITLE:___Advanced Instrumentation for Aero Engine Components: Conference Proceedings

of the Propulsion and Energetics Panel Symposium (67th) Held in Philadelphia,

Pennsylvania on 19-23 May 1985.

TO ORDER THE COMPLETE COMPILATION REPORT, USE __AD-A182 954_____.

THE COMPONENT PART IS PROVIDED HERE TO ALLOW USERS ACCESS TO INDIVIDUALLY
AUTHORED SECTIONS OF PROCEEDING, ANNALS, SYMPOSIA, ETC. HOWEVER, THE COMPONENT
SHOULD BE CONSIDERED WITHIN THE CONTEXT OF THE OVERALL COMPILATION REPORT AND
NOT AS A STAND-ALONE TECHNICAL REPORT.

THE FOLLOWING COMPONENT PART NUMBERS COMPRISE THE COMPILATION REPORT:

AD#:__P005 524 thru P005 553_____ AD#:_____

AD#:_____ AD#:_____

AD#:_____ AD#:_____

DTIC
SELECTED
AUG 1 2 1987
A

DTIC FORM 463
MAR 85

OPI: DTIC-TID

AGARD-CP-399

NORTH ATLANTIC TREATY ORGANIZATION

ADVISORY GROUP FOR AEROSPACE RESEARCH AND DEVELOPMENT

(ORGANISATION DU TRAITE DE L'ATLANTIQUE NORD)

AGARD Conference Proceedings No.399

ADVANCED INSTRUMENTATION

FOR AERO ENGINE COMPONENTS

Papers presented at the Propulsion and Energetics Panel 67th Symposium, held in Philadelphia, Pennsylvania, USA, 19—23 May 1986.

THE MISSION OF AGARD

The mission of AGARD is to bring together the leading personalities of the NATO nations in the fields of science and technology relating to aerospace for the following purposes:

— Exchanging of scientific and technical information;

— Continuously stimulating advances in the aerospace sciences relevant to strengthening the common defence posture;

— Improving the co-operation among member nations in aerospace research and development;

— Providing scientific and technical advice and assistance to the Military Committee in the field of aerospace research and development (with particular regard to its military application);

— Rendering scientific and technical assistance, as requested, to other NATO bodies and to member nations in connection with research and development problems in the aerospace field;

— Providing assistance to member nations for the purpose of increasing their scientific and technical potential;

— Recommending effective ways for the member nations to use their research and development capabilities for the common benefit of the NATO community.

The highest authority within AGARD is the National Delegates Board consisting of officially appointed senior representatives from each member nation. The mission of AGARD is carried out through the Panels which are composed of experts appointed by the National Delegates, the Consultant and Exchange Programme and the Aerospace Applications Studies Programme. The results of AGARD work are reported to the member nations and the NATO Authorities through the AGARD series of publications of which this is one.

Participation in AGARD activities is by invitation only and is normally limited to citizens of the NATO nations.

RECENT PUBLICATIONS OF THE PROPULSION AND ENERGETICS PANEL

Conference Proceedings

Testing and Measurement Techniques in Heat Transfer and Combustion
AGARD Conference Proceedings No.281, 55th *A* Meeting, May 1980

Centrifugal Compressors, Flow Phenomena and Performance
AGARD Conference Proceedings No.282, 56th *B* Meeting, May 1980

Turbine Engine Testing
AGARD Conference Proceedings No.293, 56th Meeting, Sep/October 1980

Helicopter Propulsion Systems
AGARD Conference Proceedings No.302, 57th Meeting, May 1981

Ramjets and Ramrockets for Military Applications
AGARD Conference Proceedings No.307, 58th Meeting, October 1981

Problems in Bearings and Lubrication
AGARD Conference Proceedings No.323, 59th Meeting, May/June 1982

Engine Handling
AGARD Conference Proceedings No.324, 60th Meeting, October 1982

Viscous Effects in Turbomachines
AGARD Conference Proceedings No.351, 61st *A* Meeting, June 1983

Auxiliary Power Systems
AGARD Conference Proceedings 352. 61st *B* Meeting, May 1983

Combustion Problems in Turbine Engines
AGARD Conference Proceedings 353, 62nd Meeting, October 1983

Hazard Studies for Solid Propellant Rocket Motors
AGARD Conference Proceedings 367, 63rd *A* Meeting, May/June 1984

Engine Cyclic Durability by Analysis and Testing
AGARD Conference Proceedings No.368, 63rd *B* Meeting, May/June 1984

Gears and Power Transmission Systems for Helicopters and Turboprops
AGARD Conference Proceedings No.369, 64th Meeting October 1984

Heat Transfer and Cooling in Gas Turbines
AGARD Conference Proceedings No.390, 65th Meeting, May 1985

Smokeless Propellants
AGARD Conference Proceedings No.391, 66th *A* Meeting, September 1985

Interior Ballistics of Guns
AGARD Conference Proceedings No.392, 66th *B* Meeting, September 1985

Working Group Reports

Aircraft Fire Safety
AGARD Advisory Report 132, Vol.1 and Vol.2. Results of WG11 (September and November 1979)

Turbulent Transport Phenomena (in English and French)
AGARD Advisory Report 150. Results of WG 09 (February 1980)

Through Flow Calculations in Axial Turbomachines
AGARD Advisory Report 175. Results of WG 12 (October 1981)

Alternative Jet Engine Fuels
AGARD Advisory Report 181. Vol.1 and Vol.2. Results of WG 13 (July 1982)

Suitable Averaging Techniques in Non-Uniform Internal Flows
AGARD Advisory Report 182 (in English and French). Results of WG 14 (June/August 1983)

Producibility and Cost Studies of Aviation Kerosines
AGARD Advisory Report 227. Results of WG 16 (June 1985)

Lecture Series

Non-Destructive Inspection Methods for Propulsion Systems and Components
AGARD LS 103 (April 1979)

The Application of Design to Cost and Life Cycle Cost to Aircraft Engines
AGARD LS 107 (May 1980)

Microcomputer Applications in Power and Propulsion Systems
AGARD LS 113 (April 1981)

Aircraft Fire Safety
AGARD LS 123 (June 1982)

Operation and Performance Measurement of Engines in Sea Level Test Facilities
AGARD LS 132 (April 1984)

Ramjet and Ramrocket Propulsion Systems for Missiles
AGARD LS 136 (September 1984)

3-D Computation Techniques Applied to Internal Flows in Propulsion Systems
AGARD LS 140 (June 1985)

Engine Airframe Integration for Rotorcraft
AGARD LS 148 (June 1986)

Other Publications

Airbreathing Engine Test Facility Register
AGARD AG 269 (July 1981)

THEME

The Symposium was addressed to research scientists and development engineers for aero engines in order discuss the state-of-the-art and to be informed on new measurement possibilities. The scope included CARS, laser anemometry, pyrometry, clearance measurement including X-ray, high speed data acquisition and processing, stress measurement and vibration and thin layer technique, unsteady and transient phenomena, and future prospects. The Symposium was organized in six sessions mostly followed by discussion periods in order to exchange experience in detail. For each session, a 'Rapporteur' prepared a technical evaluation report and edited the discussions for inclusion in the Conference Proceedings. After most of the sessions, there was a short verbal evaluation by the Rapporteur.

* * *

Ce Symposium s'adressait aux chercheurs et ingénieurs de développement concernés par les moteurs d'aeronefs: son but était d'examiner l'état de l'art et de donner des informations sur les nouvelles possibilités de mesure. Le programme englobait la SRAC[1], l'anémométrie laser, la pyrométrie, la mesure des jeux (en particulier par rayons-X), l'acquisition et le traitement à haute rapidité des données, la mesure des contraintes et les techniques relatives aux vibrations et pelliculaires, les phénomènes instationnaires et transitoires, ainsi que les perspectives d'avenir. Le Symposium comportait six sessions, l'accent étant mis sur les temps de discussion qui permettent aux participants d'échanger en détail leur expérience. Pour chaque session, un 'Rapporteur' a préparé un rapport d'évaluation technique et a fait paraître le texte des discussions qui est inclus dans les Actes du Symposium (Conference Proceedings). La Rapporteur a fait une brève évaluation verbale après la plupart des sessions.

(1)SRAC: Spectroscopie Raman Anti-Stockes Cohérente.
    L'expression française est DRASC: Diffusion Raman-Anti-Stokes Cohérent.

PROPULSION AND ENERGETICS PANEL

Chairman: Prof. H.Wittenberg
Delft University of Technology
Dept. of Aerospace Engineering
Kluyverweg 1, 2629 HS Delft
Netherlands

Deputy Chairman: Dr W.L.Macmillan
National Defence Headquarters
CRAD/DRDA
101 Colonel By Drive
Ottawa, Ontario K1A 0K2
Canada

PROGRAMME COMMITTEE

Mr M.Pianko (Chairman)
Institut de Mécanique des Fluides
5 Boulevard Paul Painlevé
59000 Lille, France

Professor F.Breugelmans
Von Kármán Institute for
 Fluid Dynamics
72 Chaussée de Waterloo
1640 Rhode Saint-Genèse
Belgium

Mr A.Cruttenden
Royal Ordnance, Explosives Div.
Westcott, Aylesbury
Bucks HP18 0NZ, UK

Professor R.S.Fletcher
School of Mechanical Engineering
Cranfield Institute of Technology
Cranfield, Bedford MK43 0AL, UK

Major M.Metochianakis
Hellenic Air Force, KETA
Terpsithea Post Office
16501 Glyfada, Greece

Professor M.N.R.Nina
Instituto Superior Tecnico
Avenida Rovisco Pais
1096 Lisboa Codex, Portugal

Professor G.C.Oates
Dept. of Aeronautics & Astronautics
University of Washington
Seattle, Washington 98105, US

Dr R.Rosen
Office of Aeronautics & Space Technology
NASA Headquarters
Washington DC 20546, US

Professor G.Winterfeld
DFVLR
Postfach 90 60 58
5000 Köln 90, Germany

HOST NATION COORDINATORS

Professor A.M.Mellor
Drexel University
Department of Mechanical Engineering
Philadelphia, Pennsylvania 19104
US

Mr A.A.Martino
Manager, Systems Development and
 Evaluation Group — Code PE 2
Naval Air Propulsion Center
P.O. Box 7176
Trenton, New Jersey 08628, US

PANEL EXECUTIVE

Dr E.Riester
AGARD-NATO
7 rue Ancelle
92200 Neuilly sur Seine
France

ACKNOWLEDGEMENT

CONTENTS

TECHNICAL EVALUATION REPORT
SESSION I — COHERENT ANTI STOKES RAMAN SPECTROSCOPY (CARS)

by

R.B.Price
Rolls Royce plc
P.O. Box 32
Derby DE2 8BJ, UK

SUMMARY

The session on CARS at the 67th PEP meeting successfully achieved the objectives of reviewing the present status of its development as a diagnostic method and enabling its capability and applicability to be assessed. The main conclusions may be summarised as follows:

CARS is a powerful diagnostic method for both basic combustion studies and flows of practical importance. It has demonstrated applicability to a wide range of practical devices. Temperature measurement by CARS is at an advanced stage of development. Measurement accuracy capability has been established at $< \pm 1.5\%$ for time averaged measurements and $\pm 3-6\%$ for instantaneous measurements over a wide range of temperatures and pressures in nitrogen. Improvement in spectral quality and, possibly, refined analysis techniques are required to improve the precision of instantaneous measurements. CARS measurement of species concentration is at a less advanced state and sensitivity is currently limited to $> 1-5\%$ in practical systems. Most major species of interest in combustion can be measured. with the notable exception of hydrocarbons. Spectroscopic data needs to be refined and better "in-situ" referencing schemes developed to improve the measurement accuracy.

For practical applications CARS still has some severe limitations at present, particularly its low data acquisition rate. Other problems, such as beam steering or beam attenuation, could also limit its range of applicability in practical flows.

1. INTRODUCTION

Coherent Anti-Stokes Raman Spectroscopy (CARS) has aroused considerable interest over the last decade or so because of its capability for making non-intrusive "in-situ" measurements of temperature and major species concentrations with good spatial and temporal resolution in flow systems. It has particular attraction for making such measurements in the hostile and demanding environments presented by practical combustion systems. For these, CARS has distinct advantages either in signal strength or background rejection capability compared with competing techniques such as spontaneous Raman or Rayleigh scattering.

This continuing strong interest in CARS and its growing stature and maturity was reflected in the decision to have a whole day session at the 67th PEP meeting devoted to the subject. It was fitting that two scientists who have been largely responsible for bringing CARS to its present state of prominence should be co-chairmen for the session. Dr A.C.Eckbreth, from United Technologies Research Centre, took the chair for the morning session and Dr J.P.Taran from ONERA, whose pioneering work in the mid-seventies inspired much of the subsequent interest in the subject, chaired the afternoon session.

Five formal papers by eminent workers in the field (Refs.1—5) were presented. In addition each co-chairman gave a brief information presentation (Refs.6—7). Finally, a round table discussion (Ref.8) was held, with Dr Taran as Chairman, at which members of the audience were invited to pose questions and comments to a panel consisting of his co-chairman and the five speakers at the formal session.

Four of the formal papers (Refs.1—4) were concerned almost exclusively with the use of CARS for thermometry. Species concentration measurements were only discussed in Ref.5 although Dr Eckbreth in his informal presentation also described some interesting recent work relating to such measurements carried out by himself and co-workers at UTRC. This bias towards thermometry in the presentations fairly reflects the activity and state of the art in the two measurement areas. Thermometry is at a more advanced stage of development than species concentration measurement, a situation possibly dictated by the priority needs of the engineering community but also largely governed by the relative difficulties of making the two measurements.

It is not the intention in this report to summarise and evaluate each paper separately. Instead, the presentations and the post paper and round table discussions are considered collectively. On this basis, current CARS practice and recent developments are assessed, and outstanding limitations and problems are highlighted. Finally, the conclusions drawn and recommendations made for further work are summarised.

2. BASIC CARS METHOD AND CURRENT PRACTICE

In CARS, laser beams at two frequencies w_1 (pump laser) and w_2 (Stokes laser) undergo optical wave-mixing and interact via the third order non linear susceptibility of the medium to produce a coherent laser-like signal beam at the higher anti-Stokes frequency $w_{as} = 2w_1 - w_2$. This signal is resonantly enhanced when the frequency difference between the two beams coincides with that of a Raman-active molecular transition of a constituent species of the medium. By varying this frequency difference various transitions in a given spectral band can be accessed and the CARS spectrum generated.

For phase method monochromatic input beams, the CARS spectral signal intensity I_{as} is given by

$$I_{as} \propto I_p^2 . I_s . L^2 . |3 \, \chi^{(3)}|^2$$

where I_p and I_s represent the pump and Stokes laser beam intensities in their region of interaction of length L where the CARS beam is generated. x is the third order non-linear susceptibility of the medium and determines the shape of the CARS spectrum. It is the sum of a resonant contribution and a non-resonant contribution. The non resonant component is frequency independent and is the sum of the contributions of distant Raman and electronic transitions. The resonant component is strongly temperature dependent and is proportional to the molecular number density of the resonant species.

For strong resonances and when the concentration of the resonant species is high, the effect of the non resonant term on the spectral shape is small and can often be neglected. Temperature may then be derived by fitting synthesised CARS spectra to experimental spectra with temperature as the main variable. As the concentration of the resonant species is reduced, the two terms become progressively of comparable magnitude. Over a limited range of concentrations, which is dependent on species, the spectral shape is then concentration sensitive as well. Within this range (typically 0.5—20%) species concentration can also be determined by matching experimental and synthesised spectra with concentration and temperature as the main matching variables. Fortunately, the concentrations of major species, other than N_2, of interest in practical combustion systems generally fall within this range. Species concentrations can alternatively be derived from measurements of signal strength. It is generally necessary to use referencing techniques because variations in signal strength can occur for non-concentration dependent reasons. One well tested method is to normalise the measured CARS signal by a non resonant signal, generated by the same laser-beams, from a suitable gas held at known conditions in an "in-line" reference cell. This method however can be subject to large errors due to non-correlated laser beam overlap characteristics in the two CARS generation volumes. For this reason, concentration measurement from spectral shape is normally preferred where possible.

An "in-situ" referencing technique which shows considerable promise and is more sensitive and precise than the above methods has recently been developed (Ref.5). In this method, the resonant and non-resonant background components of the CARS signal from the sampled gas are separated by polarisation techniques and measured simultaneously. Concentration and temperature may then be inferred by fitting theoretical background normalised spectra to experimental spectra.

In practice, the pump laser beam is normally at a fixed frequency. Frequency-double Nd/YAG pulsed lasers are normally used in modern CARS systems. They combine the necessary features for diagnostic use of high power (since $I_{as} \propto I_p^2$), short pulse duration (10^{-8}s), narrow linewidth, and reasonable pulse repetition rates (10—20 Hz). They can also conveniently be matched with optically pumped dye-lasers to produce the Stokes beam.

Various pump and Stokes laser beam focussing arrangements can be employed to satisfy the phase-matching requirements for optimum CARS signal. BOXCARS arrangements give the best spatial resolution (typically a few mm by 50—110 μm). A two-beam 3D variant termed USED CARS (Ref.6) which is more tolerant to beam misalignment has proved useful for practical applications. Where optical access is restricted, carefully configured colinear pump and Stokes beams can sometimes give acceptable spatial resolution (Ref.2).

CARS spectra can be generated in two ways. One method is to build the spectrum in piecemeal fashion by scanning a narrow band Stokes laser through the frequency range of interest. Alternatively, use of a broad band Stokes laser permits the complete spectrum in a given band region to be captured simultaneously using an appropriate spectrograph/optical multichannel detector; intensified linear diode array detectors are now used in most systems. The two methods are referred to as "scanning and broadband" CARS respectively. The use of scanning CARS is restricted to steady-state flow. Broad-band CARS must be used for measurements in randomly time-varying flows such as those in turbulent flames. As usually implemented, only one dye laser is used and only one species can be interrogated at a time. However, a recently demonstrated "dual-broad band" technique which uses two dye lasers (Ref.6) is capable of measuring all the major species in fuel-air combustion simultaneously but is not yet developed for engineering use.

3. ACCURACY AND PRECISION OF CARS MEASUREMENTS

3.1 Governing Factors

The accuracy and precision of CARS measurements are governed by the accuracy of the computer model used to generate the synthesised "observed" CARS spectra, the quality and integrity of the experimental signals, and the data processing techniques used to match the experimental and calculated spectra. Each of these aspects is considered separately.

(a) *Computer Modelling*

Models which are spectrally correct and accurately model the physics of the beam interaction process in the CARS generation volume are required. They must also correctly allow for the laser linewidth, spectrograph and detector characteristics in calculating the synthesised "observed" spectra to compare with the experimental spectra. Thus the CARS spectral intensities calculated for monochromatic laser beams must be convolved with the spectral profiles of the pump and Stokes beams and with an instrumental "slit" function. For broad band CARS it is not necessary to convolve with the Stokes laser profile provided the experimental spectrum is ratioed to a non-resonant CARS spectrum.

The importance of correctly accounting for collisional line narrowing and cross-coherence effects in the model is now widely recognised. Earlier "isolated-line" models ignored the collisional-narrowing effects and have been shown (Ref 1,5) to be reasonably successful in modelling CARS spectra in atmospheric pressure flames, provided the Raman linewidth variations are accurately modelled. However, even at atmospheric pressure there is evidence (Ref.2,3) that collisional narrowing effects cannot be ignored and, at high pressure, their inclusion can be vitally important. Cross-coherence terms arise in the convolution of the calculated spectral intensities with the pump laser profile and are especially important when the Raman linewidth is comparable with the pump laser linewidth. Ignoring them can lead to large errors (Ref.2). Finally, calculated spectra have been demonstrated to be highly sensitive to the form of the instrumental "slit" function and care must be taken to define this function accurately. In most CARS systems it is well represented by a Voight profile with the Gaussian and Lorentzian contributions suitably adjusted.

Efficient computational models which account for these effects are now available for N_2 (see Refs.2,3 for details). They have also been developed for several other species of interest in combustion but for some of these refinement of the spectroscopic data is required.

(b) *Quality and Integrity of Measured CARS Spectra*

Factors which govern the quality and integrity of the experimental spectra include noise, non linear detector response, medium perturbation effects and biasing effects.

Detector "shot-noise" and CARS signal noise (Refs.2,3) are both important contributors to the noise in measured single-shot CARS spectra and must be minimised. Careful design of the Stokes dye laser can significantly reduce the CARS signal noise (Ref.2). The possibility of further reducing this noise by using a single-mode instead of a multi mode pump laser is currently the subject of controversy. Data presented in Reference 3 indicate that broad band resonant CARS signal noise in N_2 Q branch spectra measured in flames is actually higher with a single mode pump laser. This finding is in marked contrast to the reverse result found for non resonant spectra (Ref.3) and narrow-band scanned data (Ref.5). Clearly, further work is required to investigate more fully the relative merits of single and multi-mode pump lasers for CARS work.

Detector shot-noise most seriously affects the low intensity parts of the recorded spectrum. For accurate measurements, especially when the analysis method gives a high weighting to these parts, it is important that only spectra with count levels above an acceptable minimum are analysed. On the other hand, care must also be exercised to ensure that the count level in the high intensity parts of the spectrum remain below saturation level for the detector. In some circumstances, such as turbulent combustion flows for example, the CARS signal can fluctuate over a range considerably greater than the dynamic range of the detector and meeting both the above requirements simultaneously can be difficult. However, data acquisition schemes such as that described in Ref.4 which record both unattenuated and attenuated signals can overcome this problem.

Medium perturbation effects can be caused by excessively high pump laser beam intensity in the CARS generation volume. Gas breakdown must obviously be avoided. Ref.5 shows that pump laser intensity must also be restricted to avoid Stark splitting effects, although these effects are not likely to be too important for Q branch spectra which are generally employed in practical CARS experiments.

Biasing errors can occur if the gas contained in the CARS generation volume is non-homogeneous. The measured spectra will be biased to the cooler gas within the volume because cf the squared dependence of CARS signal on the molecular number density. This problem is likely to be most acute in studies of turbulent combustion where high temperature gradients can occur over very small distances, down to the Kolmogoroff turbulence scale (Ref.8). More work is required to understand better the effect of such biasing on the statistics of the measured parameter.

(c) *Data Processing Methods*

Multi-parameter least-squares fitting routines are generally employed to fit theoretical CARS spectra to the experimental data. For best accuracy, the whole of the measured spectrum in a spectral region must be fitted. Efficient methods for doing this are now available and published (See Ref.2 for examples). Current so called "quick-fit" methods are prone to large errors (Refs.2,4) but can be useful for providing on-line monitors of the measured parameters. More work is required to refine the accuracy of such methods, which can be particularly useful when a large volume of spectra has to be analysed.

Even under nominally steady state conditions, single pulse CARS spectra exhibit a substantial shot to shot variation in the measured parameters, mainly because of the noise effects discussed above. Weighted least-squares fitting routines show promise in increasing the precision of such measurements. For example, Ref.3 shows that by correctly accounting for the noise variance and using the inverse of this as the weighting parameter in the least-square

fitting routine, a very significant improvement in precision of single-shot CARS temperature measurements in a steady-state flame occurred. However, this was accompanied by a shift in the mean temperature determined compared to a non-weighted fit for reasons that are not yet fully understood. Such weighted fitting techniques clearly need to be investigated further.

3.2 Current CARS Capability

In assessing the current accuracy and precision capability of CARS for temperature and species measurements due note must be taken of the above considerations. Most of the reported CARS temperature measurements, r rticularly for broad-band CARS, have used the N_2 Q branch spectrum as the probe. This is mainly because N_2 is generally the most abundant species in fuel-air combustion systems and consequently gives a strong resonant signal. Detailed assessments of the accuracy of such measurement have recently been made (Refs.2,7) over a wide range of temperature and pressure (300—3500°K at 1 bar and 300—800°K up to 20 bar) in N_2 under known and constant homogeneous gas conditions. The mean or average temperature measurement accuracy is estimated to be of the order of $\pm$ 1—1.5% over all conditions. Single-shot temperature accuracy is estimated at $\pm$ 3—6%.

Measurements of temperature and species concentration in flames have successfully been carried out for several other major species of interest in combustion e.g. CO_2, CO, H_2O and O_2. For broadband CARS, species concentration sensitivity is currently estimated to be > 1—5% for time averaged measurements. Where scanning CARS can be applied, the background normalisation method (Ref.5) has been shown capable of improving sensitivity by a factor of 5. Unfortunately its use in broad band CARS has not been demonstrated and seems likely to be possible only at high pressures. The accuracy of concentration measurements is largely limited by the lack of accurate spectroscopic data and the complicating effects of varying non-resonant backgrounds. As better quality spectroscopic data is becoming available, so the measurement accuracy is improving but more work is required to overcome the problems with varying backgrounds.

Concentration measurements of hydrocarbons pose particular problems because of their spectroscopic complexity, especially the larger polyatomic molecules. Spectral models are not currently available for hydrocarbons, apart from acetylene, and there is a general dearth of good quality spectroscopic information for these species. Pending the availability of accurate models, the generation of a library of CARS spectra for known samples and the use of these to fit experimental spectra could be considered as an interim method of making hydrocarbon concentration measurements.

4. APPLICABILITY OF CARS

Demonstrated Applications

CARS is being used increasingly for a wide range of applications ranging from basic kinetic (Ref.6) and spectroscopic (Ref.5) studies to measurements in flows of practical interest (Refs.2,4,7).

Many of the basic studies are carried out under steady-state conditions, e.g. in laminar flames where either broad-band or scanning CARS systems can be applied. For spectroscopic measurements the higher resolution offered by scanning CARS systems is often essential. Very high resolution CARS, made possible by the advent of single mode lasers and pulse amplification techniques, offers the prospect of generating very accurate Raman linewidth and other spectroscopic measurements. Much of the data generated in this way will be used to refine the models used in the application of CARS to practical systems.

Over the last decade or so, CARS has been demonstrated successfully in several practical flow environments including jet engine exhausts, IC and diesel engines, gas turbine combustion simulators, furnaces, propellent flames. Recently, its application to supersonic combustion has also been demonstrated successfully. It is now moving out of the development and demonstration phase and is being used more and more as a routine research and development tool. Mobile, hardened and flexible CARS systems (see Ref.7 for example) which facilitate use of the technique for field applications are being built.

In many of these applications, CARS is used in conjunction with other non-intrusive diagnostic techniques such as LDA. The data generated can be used both to better the understanding of complex turbulent flow-combustion interaction processes and to develop and validate computational models.

Despite the very notable success that has been achieved to date, CARS still has some severe limitations and applications problems which are likely to restrict its use in flows of practical interest in the future unless they can be overcome. These are discussed briefly below. Some are common to most optical techniques but other are peculiar to CARS.

Optical Access Requirements

CARS requires "double-sided" optical access to the measurement volume. Geometrical constraints might make this difficult to achieve for some applications e.g. annular combustors.

Beam Steering/Attenuation Problems

In some practical flow environments serious reduction, or even total loss, of the measured CARS signal may be caused by beam steering due to density gradients in the flow normal to the direction of beam propagation. High pressure conditions

and long optical path lengths will accentuate this problem. As a rough guide, (Ref.8) measurements in a gas turbine primary zone combustion region for instance could become very difficult at pressures above 3 atmospheres and beam path lengths through the medium greater than ~1 5 cm.

In particle or droplet laden flows further signal loss can occur due to beam attenuation, particularly of the input beams. Measurements in high density sprays with low voidage fractions are therefore precluded but, where the voidage fraction is reasonable, CARS measurements can be successfully conducted provided the recorded spectra are selectively filtered for analysis.

In liquid fuelled combustors, beam steering and attenuation problems will clearly be compounded.

Low Data Acquisition Rate

CARS is a single-point measurement technique. Moreover, spectra acquisition rate is currently limited to 10—20 Hz by the pulse-repetition rate capability of available Nd—YAG pulsed lasers. Since, for the turbulent flows of practical interest, a large number (typically a few hundred) of individual measurements is required to define adequately the measured parameter statistics at each point, the time required to map the flow conditions can be exorbitant for some applications. Newer lasers e.g. excimer or copper-vapour, offer hope of increasing data acquisition rate by orders of magnitude in the future if they can be developed to combine high pulse power with their existing high repetition rate capability.

The "dual broad band" CARS technique which allows several species to be measured simultaneously could with development also significantly increase the data acquisition rate for species concentration measurements in practical flows.

Data Handling/Storage Problems

Clearly a very large amount of data can be generated in a practical CARS experiment. Handling and storage of this data may prove a problem unless some on-line processing of data is carried out. The development of rapid but accurate on-line processing techniques would be a major step forward in the application of CARS to practical systems.

High Cost and Complexity

The high hardware capital costs (~$100 K) and complexity of the techniques mitigate against its widespread adoption and will continue to limit the number of deployable CARS systems available. A "Knock-on" effect is that the number of experienced and skilled exploiters of CARS is also limited. Transfer of the technology to non-expert users may therefore present problems, especially in the short term. However, the concensus view of the experts at the session was that these problems are surmountable and successful transfer has already been achieved in some instances. A possible alternative solution is to have centres of excellence in CARS which would provide a consultancy service to customers.

5. SUMMARY OF CONCLUSIONS AND RECOMMENDATIONS FOR FURTHER WORK

The following were the main points to emerge from the presentations and discussions at the session:

1. CARS is at an advanced stage of its development and is increasingly being used for routine R & D studies. It has demonstrated applicability both to basic flames and to a wide range of practical devices.

2. The general theory is now reasonably well established. Efficient and accurate computational models are now available for N_2. Several other major species of interest in combustion can also be modelled although the spectroscopy for some still needs to be further refined. Hydrocarbons are a notable exception and work is urgently required on the spectroscopy and modelling of these species.

3. For broad band CARS, temperature measurement accuracy has been established at $< \pm 1.5\%$ for mean measurements and $\pm 3—6\%$ for single shot measurements in N_2 over a wide range of temperature and pressure. Species concentration measurement sensitivity is rather low at present ($> 1—5\%$ time averaged) but accuracy is improving as the spectroscopy is being refined.

4. Further work is required to overcome varying non-resonant background effects on species concentration measurements and "in-situ" referencing schemes require further development.

5. Singe-shot temperature measurement accuracy is currently limited by dye laser noise. Further work is required to determine the relative merits of single and multimode pump lasers in reducing the shot to shot variation in CARS signal.

6. Data processing schemes can have a marked effect on the measurement accuracy. Further work is needed to determine the improvements attainable by using "weighting" schemes.

7. Use of CARS for routine R & D in practical devices could be restricted by its low data acquisition rate.

8. Beam steering in large scale devices at high pressure and beam attenuation in high density sprays or particle laden streams may cause problems which limit the range of applicability of CARS.

6. REFERENCES

1. Stricker, W., Kreutner, W., and Just, Th. Simultaneous Temperature Measurements with Raman and CARS in

Laminar Flames. Paper and Discussion.

2. Greenhalgh, D.A. CARS Thermometry for Low and High Pressure Combustion Systems. Paper and Discussion.

3. Snelling, D.R., Smallwood, G.J., Sawchuck, R.A. and Parameswaran, T. Nonlinearity and Single Shot Noise Problems in CARS Spectroscopy. Paper and Discussion.

4. Magre, P., Moreau, P., Collin, G. and Pealat, M. Application de la Méthode DRACS à la Mesure de la Température dans une Flamme Turbulente. Paper and Discussion.

5. Farrow, R.L. Accurate Measurements of Combustion Species Concentrations Using CARS. Paper and Discussion.

6. Eckbreth, A.C. Informal Presentation. See also — Eckbreth A.C. The Application of Spatially-Precise Laser Diagnostics to Fundamental and Applied Combustion Research. AIAA-86-0138.

7. Taran, J.P. Informal Presentation. See also — Pealat, M., Bouchardy, P., Latebvre, M. and Taran, J.P. Precision of Multiple CARS Temperature Measurements. Appl. Opt. Vol.24, (1985) pp.1012—22.

8. Round Table Discussion.

SIMULTANEOUS TEMPERATURE MEASUREMENTS WITH RAMAN AND CARS
IN LAMINAR FLAMES

W. Stricker, W. Kreutner, Th. Just
DFVLR - Institut für Physikalische Chemie der Verbrennung
Pfaffenwaldring 38-40
D-7000 Stuttgart 80
West Germany

SUMMARY

Spatially resolved temperature measurements in laminar premixed flames were made using Coherent Antistokes Raman Scattering (CARS) and spontaneous Raman spectroscopy. In the case of narrowband (scanning) CARS, the experimental arrangement allows the performance of simultaneous temperature measurements with both techniques. For broadband (multiplex) CARS the measurements have to be made successively. Three different Raman linewidth models were used for CARS data evaluation. The results were compared with the independently recorded rotational Raman temperatures. Temperature differences up to 10 % were observed, depending on the linewidth model used. For two, more complicated linewidth models the CARS and Raman temperatures are in good agreement.

1. INTRODUCTION

One aim in modern combustion research is the development of theoretical computer flame models, in order to predict the desired properties and the behaviour of flames (in a final stage also of technical flames like in furnaces, combustors, and internal combustion engines). Laser diagnostic techniques offer the possibility for in-situ, non-intrusive, spatially resolved measurements of temperature and species concentrations in combustion processes. Experimentally determined temperature and concentration data are used to examine, improve and further develop the chemical kinetics of flames and the theoretical flame models. As an example, the temperature profile assumed in such calculations is a very sensitive parameter for the resulting calculated hydroxyl radical concentration.
Both CARS and spontaneous Raman spectroscopy are well suited for temperature measurements. In the past, several research groups have demonstrated the applicability of CARS for temperature measurements in laboratory flames /1-7/, in combustors /8-11/, and in internal combustion engines /12-15/. Due to the coherent nature of the process and the high signal intensities CARS offers some unique advantages for the diagnosis of technical combustion situations. Unlike CARS spontaneous Raman spectroscopy is limited to weakly luminous, non-sooting flames, because of its inherently low signal intensity and its incoherent character.
For both techniques the accuracy of the deduced temperature values depends on the quality of the experimental data and the reliability of the theoretical models used to analyze the recorded spectra. The theory of spontaneous Raman scattering is well developed, and the data reduction is straightforward, whereas for the reduction of CARS data some points remain to be clarified.
In order to establish the accuracy of temperature measurements with CARS, in the past comparisons have been made between CARS and other techniques: Thermocouple measurements /16-19/, sodium line reversal spectroscopy /4, 17, 20, 21/, and heat balance and thermo-dynamic equilibrium calculations /4, 17/.
The disadvantages of thermocouple measurements in hot reacting flows are well known. The unavoidable perturbation of the flowfield may change the chemical kinetic reactions in the flame. The temperature measured has to be corrected for radiation and conductive heat losses of the thermocouple, and care has to be taken to minimize catalytic reactions on the surface of the thermocouple. Coating the tip of the thermocouple with quartz may lower the influence, but can not prevent it completely depending on the flame composition. The sodium line reversal technique may suffer from the fact that the probed volume is not identical to the volume from which the CARS information is taken, and that seeding the flame with sodium can be difficult. Heat balance calculations which require an accurate measurement of the heat flux to the burner used to stabilize the flame, lead to results without any spatial resolution.
In this work we report a comparison of the temperature determination in laminar flames between CARS and spontaneous Raman scattering. Both spectroscopic techniques offer the potential for non-intrusive, spatially resolved temperature measurements in laboratory flames. In the case of narrowband CARS really simultaneous temperature measurements with both techniques are possible, whereas in the case of broadband excitation the experiments have been performed in two consecutive runs. One of the advantages of the technique described in this paper is that the same laser is used to excite the CARS as well as the Raman process, and the probed volume for both measurements is well controlled.

2. SPONTANEOUS RAMAN SCATTERING

For thermometry in flames, preferably on N_2 as indicator molecule, the vibrational Stokes transition /22-27/, the ratio of Stokes/Antistokes vibrational bands /28,29/ and the pure rotational Raman spectrum /23, 30-32/ have been utilized. In our special case the pure rotational Raman spectrum is used for temperature determination (Fig. 1).

The Raman scattered intensity I_R is given in eq. (1)

$$I_R = I_o \cdot N(v,J) \cdot \frac{d\sigma}{d\Omega} \cdot \Omega \cdot 1 \cdot \varepsilon \qquad (1)$$

where I_o is the intensity of the exciting laser radiation; $N(v,J)$ is the number density in the particular quantum state of the species under consideration. In thermal equilibrium the population of the states is given by the Maxwell-Boltzmann distribution. $\frac{d\sigma}{d\Omega}$ is the differential Raman scattering cross section; Ω is the solid angle from which Raman scattered radiation is collected; 1 is the length of the probed volume, and ε describes an efficiency factor including the throughput of the monochromator and the quantum efficiency of the detector.

For temperature measurements only the relative intensity distribution of the pure rotational Raman spectrum has to be considered.

$$I_R(J) \sim \left[\omega_o - (4J+6) \cdot B \right]^4 \cdot g(J) \cdot f(J) \cdot \exp \left[-hcB \cdot J(J+1)/kT \right] \qquad (2)$$

ω_o is the frequency (in cm^{-1}) of the exciting laser; B is the rotational constant of the indicator molecule; J is the rotational quantum number; the factor $g(J)$ takes into account the nuclear spin degeneracy of homonuclear molecules; $f(J)$ is a line strength factor containing the Placzek-Teller coefficient $b_{J',J''}$.

$$f(J) = (2J+1) \cdot b_{J',J''} = \frac{3}{2} \cdot \frac{(J+1) \cdot (J+2)}{2J+3} \qquad (3)$$

The constants h, c, and k have their usual meaning: Planck's constant, speed of light, and Boltzmann's constant.

For a more accurate treatment of the pure rotational Raman spectrum the influence of centrifugal distortion has to be taken into consideration by a multiplicative correction factor /33/.

$$f'(J) = f(J) \cdot (1+4r_e\beta_e'/\beta_e) \cdot (\frac{B_e}{\omega_e})^2 \cdot (J^2+3J+3)^2 \qquad (4)$$

β_e' is the derivative of the molecular polarizability anisotropy with respect to internuclear distance r_e. A value of $r_e\beta_e'/\beta_e = 2.2$ for N_2 is taken from the literature /32/ and used in this work.

To evaluate the temperature from the pure rotational Raman spectrum the (log intensities) of the rotational lines are plotted as a function of the term values of the rotational states. From the slope of the resulting straight line fitted by a least squares procedure the temperature is deduced.

3. COHERENT ANTISTOKES RAMAN SCATTERING (CARS)

CARS is a coherent, nonlinear Raman process. It is for this reason that temperature measurements with this technique require the comparison of the experimentally measured CARS spectrum and a theoretical, calculated spectrum.

A detailed description of the CARS theory can be found in the literature /34/. In this paper only a short summary of the theory is given. By the interaction of two incident laser beams of frequency ω_1 (pump laser) and ω_2 (probe laser) with the third order dielectric susceptibility $\chi^{(3)}$ of the molecule a polarisation field is induced which generates the CARS signal at frequency $\omega_3 = 2\omega_1 - \omega_2$. The CARS signal intensity is given by

$$I_{CARS} \sim \left| \chi^{(3)} \right|^2 \cdot I_1^2 \cdot I_2 \cdot L^2 \cdot (\frac{\sin(\Delta kL/2)}{\Delta kL/2})^2 \qquad (5)$$

In eq. (5), I_1 and I_2 are the intensities of the pump laser and the probe laser, respectively. L defines an interaction length where the CARS signal is generated. The expresssion in brackets gives the phase matching condition and depends on experimental parameters. For high signal generation the phase-mismatch Δk should be zero, i.e. $(\frac{\sin\Delta kl/2}{\Delta kL/2})^2 = 1$.

The spectral shape of the CARS spectrum is given by the third order dielectric susceptibility $\chi^{(3)}$ according to eq. (6)

$$\chi^{(3)} \sim \sum_{v,J} \Delta N \cdot \frac{\omega_R}{\omega_R^2 - (\omega_1 - \omega_2)^2 - i \cdot \Gamma_R \cdot (\omega_1 - \omega_2)} + \chi_{NR}^{(3)} \qquad (6)$$

where ΔN is the population difference between the states involved in the observed CARS spectrum; ω_R is the Raman frequency; ω_1 and ω_2 are the frequencies of the pump and probe laser, respectively; Γ_R is the homogeneous Raman linewidth. In addition, there is an non-resonant part of the susceptibility, $\chi_{NR}^{(3)}$, which is frequency independent and summarizes the contributions arising from distant Raman and electronic transitions. In the case of measurements on N_2 in high concentration the influence of $\chi_{NR}^{(3)}$ on the spectral structure of the CARS signal is negligible and, therefore, can be omitted in the data reduction.

As can be seen from eq. (6) the CARS signal is resonantly enhanced, if the frequency difference between the two exciting laser frequencies ω_1 and ω_2 is nearly to or equal a Raman transition frequency ω_R. A further important feature of CARS spectroscopy - in contrast to other spectroscopic techniques - is the dependence of the signal on the homogeneous Raman linewidth Γ_R.

In this work three different models of the homogeneous Raman linewidth Γ_R have been used and compared for data evaluation.

1. As the simplest assumption a constant linewidth is used in the calculation, independent of p and J. Today there are better models for Γ_R, if N_2 is used as indicator molecule. But for other molecules than N_2 reliable linewidth models scarcely exist, and mostly a constant linewidth is the only possible choice.

2. In the model proposed by Hall /35/ the self-broadened N_2 linewidths have been calculated using the linewidth theory of Robert and Bonamy /36/. As a result, experimental line-width data /37/ can be fitted very well with a relatively simple expression, which describes the Raman linewidths as a function of temperature T and the rotational quantum number J. The pressure dependence is linear. The analytical form is shown in Table 1, valid for the temperature range 900 K - 2400 K.

3. Farrow et al. /16/ used the low pressure flame linewidth data measured with stimulated Raman scattering /37/ and fitted them to a polynomial expression up to the fourth order in the rotational quantum number J. The dependence on pressure is linear, too, but the temperature scales as $T^{-1/2}$. For temperatures below 600 K the formula reduces to only one term, linear in J. (Table 1)

Hall	$\Gamma_R(T,p,J) = 8 \cdot T^{-0.71} - 18.6 \cdot T^{-1.45} \cdot J$
	$900\ K \leq T \leq 2400\ K$
Farrow et al. high temperature T > 600 K	$\Gamma_R(J) = A - B \cdot J + C \cdot J^2 - D \cdot J^3 + E \cdot J^4$ $A = 1.79534 \cdot 10^{-2}$ $\qquad$ $B = 6.3087 \cdot 10^{-4}$ $C = 4.7995 \cdot 10^{-5}$ $\qquad$ $D = 1.5139 \cdot 10^{-6}$ $E = 1.50467 \cdot 10^{-8}$
low temperature T < 600 K	$\Gamma_R(J) = A_1 - B_1 \cdot J$ $A_1 = 1.99 \cdot 10^{-2}$ $\qquad$ $B = 4.575 \cdot 10^{-4}$

Table 1 Analytical expressions of linewidth models proposed by Hall /35/ and Farrow et al. /16/

4. EVALUATION PROCEDURE

For the evaluation of temperature data from CARS spectra a computer code has been developed which fits the theoretical CARS spectrum to an experimental one. The evaluation scheme is shown in Tab. 2. The program calculates the squared modulus of the dielectric suscepti-bility of the rotation - vibrational CARS spectrum of N_2 (Q-branch). In order to achieve the best agreement between experimental and theoretical spectra in the region of the hot band (overlapping rotational lines originating from the fundamental vibrational transition $v = 0 \to 1$ and the first excited vibrational transition $v = 1 \to 2$) the molecular constants for N_2 given by Gilson et al. /38/ are used. Different linewidth models can be employed. The influence of the laser bandwidths for narrowband (scanning) CARS is taken into con-sideration by a convolution procedure with Gaussian profiles. For broadband (multiplex) CARS the monochromator/detector influence is treated by a convolution with a Voigt profile containing equal Gaussian and Lorentzian contributions. A non-linear least-squares algorithm is utilized. Three parameters are varied simultaneously: the temperature, a dispersion factor which describes the increment size on the frequency axis, and the absolute fre-quency of the first data point of the experimental spectrum. To avoid additional numerical errors analytical derivatives are employed. The spectra are fitted on a linear scale, nor-malized to the area under the spectral shape, and all data points are weighted equally. Depending on the quality of the initial guess of the input parameters, our program usually needs 3 - 6 iterations to find the best fit.

```
┌─────────────────────────────┐      ┌─────────────────────────────┐
│  experimental spectrum      │      │  theoretical spectrum       │
│                             │      │                             │
│    noise sources:           │      │     dependence on:          │
│                             │      │                             │
│    alignment drift          │      │     temperature             │
│    laser intensities        │      │     molecular constants     │
│    spatial jitter           │      │     Raman linewidth          │
│    frequency drift          │      │                             │
│    electronic noise         │      │                             │
└─────────────────────────────┘      └─────────────────────────────┘
                                      ┌─────────────────────────────┐
                                      │  experimental influences    │
                                      │     laser bandwidth         │
                                      │     slit/detector profile   │
                                      │  convolution procedure      │
                                      └─────────────────────────────┘
                                      ┌─────────────────────────────┐
                                      │  synthesized spectrum       │
                                      └─────────────────────────────┘
            ┌────────────────────────────┐
            │  normalisation             │
            └────────────────────────────┘
┌──────────────────────────────────────────────────────────┐
│                    comparison                            │
│  experimental data      ◄──►      simulated spectrum     │
│        non-linear least-squares algorithm                │
│                   fit parameter:                         │
│                   temperature                            │
│                   dispersion factor                      │
│                   absolute frequency                     │
│         (equal weighting of data points)                 │
└──────────────────────────────────────────────────────────┘
            ┌────────────────────────────┐
            │  best fit                  │
            └────────────────────────────┘
            ┌────────────────────────────┐
            │  temperature               │
            └────────────────────────────┘
```

Table 2   Evaluation of temperature data from CARS spectra

5. EXPERIMENTAL

The experimental setup, capable of measuring simultaneously narrowband CARS and spontaneous Raman spectra, is shown in Fig. 2. The two frequencies ω_1 and ω_2, necessary for the excitation of the CARS process, are delivered by a pulsed, frequency-doubled Nd:YAG laser (JK Hyper YAG 750) and a dye laser. The available energies are about 50 mJ/pulse in the pump beam (532 nm) with a smooth beam profile and about 5 mJ/ pulse in the probe beam from the dye laser ($\sim$ 607 nm). The bandwidth of the dye laser amounts about $0.25 - 0.30$ cm^{-1}. To achieve a suitable spatial resolution a crossed beam BOXCARS configuration /39/ is used. The geometry of the laser beams is shown in Fig. 3. By this means the spatial resolution can be matched to the experimental requirements of laboratory flames and can be adapted to the volume probed with the Raman technique. After recollimation (L2) the CARS signal is separated from the exciting laser beam by a dense flint prism (P) and recorded by the photomultiplier (PMT 2) and a boxcar integrator. The wavelength scan of the dye laser and the data acquisition is controlled by a DEC (MINC) laboratory computer.

As can be seen from Fig. 1 different Raman processes are excited simultaneously by the laser beams needed for the CARS process, both by the pump laser (ω_1) and the probe laser (ω_2). More or less unaffected by other scattering processes the pure rotational Raman spectrum excited by the most powerful pump laser beam at frequency ω_1 can be observed in an optical path under 90° to the incoming laser beams. The Raman scattered light is collected by lens L3 and a backreflecting mirror CM and imaged onto the entrance slit of the monochromator (SPEX 14018). The Raman signal is recorded by a gated, microchannel plate intensified diode array (PAR OMA-II/1420). The data are transferred to the laboratory computer for further processing. A second photo multiplier (PMT 1) allows the registration of pure rotational Raman spectra in a scanning mode where the resolution is higher than with the diode array.

In the case of broadband CARS directly simultaneous measurements are not possible, because the recording of both the broadband CARS spectra and the pure rotational Raman spectra requires the frequency dispersing monochromator. However, the imaging optics are designed in such a way to allow a quick change from recording broadband CARS spectra to rotational Raman spectra. To measure broadband CARS spectra the radiation of the dye laser as probe laser has to be generated spectrally broad. This is achieved by replacing the grating in the dye cavity by a high reflecting broadband mirror yielding a bandwidth of the dye laser emission of about 130 cm^{-1} FWHM. This bandwidth is broad enough to cover

the entire CARS spectrum at every laser pulse, even at flame temperatures, where the
the spectrum spreads out.

Both broadband CARS and spontaneous Raman data measured with the diode array are
corrected for the thermal and electronic background, non-uniform sensitivity across
the target, and the wavelength dependent transmission characteristics of the optics
in the signal path. The spectral distribution of the radiation of the broadband dye
laser is accounted for by measuring the nonresonant CARS signal of oxygen (5 bar)
at the same spectral position and with the same optical configuration used for the re-
sonant N_2 CARS measurements. Thus, the effects influencing the intensity distribution
of the spectra can be treated by one correction.

6. RESULTS AND DISCUSSION

The results reported in this paper were obtained in a premixed laminar propane/air
flame at atmospheric pressure and an equivalence ratio of ϕ = 1.1. The low luminosity
flame is stabilized on a multicapillary burner 28 mm in diameter. The burner is on a
constant temperature of 330 K to prevent condensation of water. The measurements have
been made 10 mm above the burner surface in the flame axis where a flat temperature
profile can be expected.

During our investigations of CARS temperature measurements in flames we found that the
application of a rotational quantum number and temperature dependent model for the
homogenous Raman linewidth included in the evaluation procedure of CARS data considerably
improves the theoretical fit of experimental narrowband CARS spectra /40/. Especially
in the region of the band head of the N_2 Q-branch the deviations between experimental
and calculated data are reduced, in agreement with the observations by Hall /35/. How-
ever , as can be seen in Fig. 4, it is possible to estimate a constant value of the Raman
linewidth, in our example Γ_R = 0.033 cm^{-1}, which also leads to an excellent theory-
experiment fit. Compared to a theoretical fit with Hall's linewidth model exploiting
the same experimental data the error curves in Fig. 4 do not show remarkable differences.
However, the residual error is slightly reduced, and the evaluated temperature by both
fitting procedures changes by about 10 % from 2174 K to 1954 K.

To look for a decision, which temperature is the correct one, and to get an impression
how accurate CARS temperatures can be measured a more systematic investigation has been
started. A selected set of experimental CARS data was used for evaluation with the above
mentioned different linewidth models. In our opinion, temperatures deduced from Raman
spectra, measured under special flame conditions (laminar, non-luminous) can reliably be
used for comparison. Raman spectroscopy is an optical non-intrusive method based upon a
well developed theory.

Fig. 5 shows a part of the pure rotational Raman spectrum recorded in the flame center,
ranging from J = 22 to J = 41. In the lower part the least-squares straight line, fitting
the (log intensities) according to eq. (2), is plotted. To reduce the influence on the N_2
rotational lines, which are used for temperature analysis, by underlaying lines of the
combustion products like CO, CO_2, H_2O and unburnt hydrocarbons, the monochromator wave-
length setting is 258 cm^{-1} apart from the exciting laser line at 18797 cm^{-1} (532 nm). At
flame temperatures the population of the rotational states peaks at higher quantum numbers
(for 2000 K at J = 19). Therefore, only N_2 rotational lines with highest possible inten-
sities occur in the oberved spectrum. The resolution of our optical detection system is
sufficient to separate the lines originating from vibrational states v = 0 and v = 1.
Lines with their initial states v = 2 merge into the wings of the preceding lines of
v = 0. As the population of the N_2 vibrational state v = 2 amounts only about 3.5 % at
2000 K the perturbation of the intensity distribution of the v = 0 rotational lines may
be considered negligible.

As already mentioned the Raman scattered intensities are extremely low. In order to reach
a good signal-to-noise ratio in the spectrum and, hence, a statistically reliable accuracy
30,000 signal pulses at 10 Hz repetition rate have been accumulated. The resulting
temperature is 2039 ± 56 K (± 2.8 %, one standard deviation). Fairly long accumulation
times are required to achieve this or better accuracy. A spectrum taken with doubled
exciting laser energies shows reduced scatter in the intensity distribution of the
rotational lines and indicates a temperature of 2043 ± 28 K. However, if the Raman signal
from the same flame position is accumulated for only 3,000 pulses, the measured tempera-
tures differ from each other much more. The mean and standard deviation of 10 successive
measurements is 2072 ± 86 K.
We conclude, provided that the flame itself fullfills the necessary stability, spontaneous
Raman spectroscopy is an independent technique to measure reliable flame temperatures
in an environment of low luminosity.

Assuming the rotational Raman temperature in our experiment as reference temperature CARS
spectra have been evaluated using different models for the homogeneous Raman linewidth
and fitting different parts of the spectrum, e.g. only the vibrational ground state of
the N_2 Q-branch (v = 0 → 1) or the vibrational ground state and the hot band (v = 0 → 1
and v = 1 → 2). A typical broadband CARS spectrum from the flame center is shown in Fig. 6,
together with the residual error curve for the best fit. Some of the results of our com-
parative investigation are summarized in Tab. 3.

Line Model for Γ_R	Evaluated Part of the Spectrum			
	$v = 0 \to 1$		$v = 0 \to 1$ and $v = 1 \to 2$	
	NB CARS	BB CARS	NB CARS	BB CARS
Γ_R = constant	2174 K	2181 K	2142 K	2080 K
residual error	0.97	0.78	0.94	1.00
Γ_R Hall	1954 K	1989 K	2065 K	2001 K
residual error	1.00	1.00	1.00	0.87
Γ_R Farrow	2008 K	2037 K	2065 K	2014 K
residual error	0.86	0.62	0.88	0.60

Raman pure rotational spectrum	
long time	(2039 ± 56) K
10 x short time	(2072 ± 86) K

Table 3 Summary of CARS (narrowband and broadband) and Raman temperatures, measured in the center of a propane/air flame, 10 mm about the burner surface; data evaluation with different linewidth models and different parts of the spectrum; for a better understanding the residual errors were normalized.

The approach to restrict the data evaluation to the region of the vibrational ground state transition $v = 0 \to 1$ is of some practical interest. By excluding the hot band ($v = 1 \to 2$) in the data analysis the cpu computer time needed by our evaluation program can be reduced considerably. It has to be examined in a practical situation whether the uncertainty in the temperature values coming in by the evaluated reduced spectrum is tolerable or not.

Comparing the three linewidth models used in the evaluation program the constant linewidth assumption always yields temperatures which are higher than those resulting from the other two linewidth models and from spontaneous Raman data. It should be mentioned that Hall's linewidth model is restricted to temperatures above 900 K. The result will be a too high temperature. When Hall's and Farrow's linewidth models are compared the result is that the temperatures from Hall's model are always slightly lower. The CARS temperatures derived with Hall's and Farrow's model are in good agreement with the Raman temperatures, if long time Raman spectra are considered. Raman spectra with shorter exposure times show enhanced scatter of the intensities of the rotational lines and, therefore, yield less accurate temperature.

The CARS temperatures are usually slightly lowered, if the hot band is included in the data analysis. If only the vibrational ground state is evaluated, the differences between constant linewidth and J-dependent linewidths become more pronounced.

The theory-experiment fit is pretty good for all three models considering the spectral shape, but it turns out that this fact alone is not a sufficient criterion for accurate temperature measurements. Considering the residual error as the sum of the squared deviations between the best fit and the experimental data Farrow's model performs best, whereas in the case of a constant linewidth and Hall's model less significant differences are observed.(For a better understanding the residual errors have been normalized in Tab. 3).

For further illustration a radial temperature profile of the investigated propane/air flame is plotted in Fig. 7. The results of the temperature evaluation with and without including the hot band in the CARS data analysis are shown separately. Different symbols indicate the temperatures derived with different assumptions for the homogeneous Raman linewidth and the Raman values. The Raman data contain measurements with variable exposure times. The scatter of the data points on the flame edge becomes larger, where steep temperature gradients ($\geq$ 200 K/mm) are found. Flame flickering is the most probable explanation for the observed scatter.
In conclusion, the two linewidth models of Hall and Farrow et al. yield temperatures, which coincide within $\pm 1.5\%$. The temperatures are in good agreement with those derived from spontaneous rotational Raman spectra. Provided that a practical application requires still more accurate temperature values, both, a more precise reference technique and still further improvements in the linewidth models are necessary.

7. REFERENCES

/ 1/ A.C. Eckbreth, R.J. Hall. CARS Thermometry in a Sooting Flame
Comb. Flame 36, 87 (1979)

/ 2/ K.A. Marko, L. Rimai. Coherent Antistokes Raman Spectroscopic Probe of Combustion
SAE-Paper 800138 (1980)

/ 3/ R. L. Farrow, P.L. Mattern, L.A. Rahn. Comparison between CARS and Corrected Thermo-
couple Temperature Measurements in a Diffusion Flame
Appl. Opt. 21, 3119 (1982)

/ 4/ K. Müller-Dethlefs, M. Pealat, J.P. Taran. Temperature and Hydrogen Concentration
Measurements by CARS in an Ethylene-Air Bunsen Flame
Ber. Bunsenges. Phys. Chem. 85, 803 (1981)

/ 5/ M. Aldén, H. Edner, S. Svanberg. Coherent Antistokes Raman Spectroscopy (CARS)
Applied in Combustion Probing
Phys. Scr. 27, 29 (1983)

/ 6/ J.A. Vanderhoff, A.J. Kotlar. Application of CARS to Obtain Temperature in Flame
Environments
Techn. Rep. ARBRL-TR-02417 (1982)

/ 7/ S. Furuno, K. Akihama, M. Hanabusa, S. Iguchi, T. Inoue. Nitrogen CARS Thermometry
for a Study of Temperature Profiles through Flame Fronts
Comb. Flame 54, 149 (1983)

/ 8/ A.C. Eckbreth, G.M. Dobbs, J.H. Stufflebeam, P.A. Tellex. CARS Temperature and
Species Measurements in Augmented Jet Engine Exhausts
AIAA-Paper 83-1294 (1983)

/ 9/ D.A. Greenhalgh, F.M. Porter, W.A. England. The Application of Coherent Anti-
Stokes Raman Scattering to Turbulent Combustion Thermometry
Comb. Flame 49, 171 (1983)

/10/ G.L. Switzer, D.D. Trump, L.P. Goss, W.M. Roquemore, R.P. Bradley, J.S. Stutrud,
C.M. Reeves. Simultaneous CARS and Luminosity Measurements in a Bluff-Body Combustor
AIAA-Paper 83-1481 (1983)

/11/ R. Bédué, P. Gastebois, R. Bailey, M. Péalat, J.P. Taran. CARS Measurements in a
Simulated Turbomachine Combustor
Comb. Flame 57, 141 (1984)

/12/ L.A. Rahn, S.C. Johnston, R.L. Farrow, P.L. Mattern. CARS Thermometry in an Internal
Combustion Engine
in: Temperature, its Measurement and Control in Science and Industry, Vol.V,
J.F. Schooley, Ed. (American Institute of Physics, New York), p. 609 (1982)

/13/ K. Kajiyama, K. Sajiki, H. Kataoka, S. Maede, C. Hirose. N_2 CARS Thermometry in
Diesel Engine
SAE-Paper 821036 (1982)

/14/ G.C. Alessandretti, P. Violino. Thermometry by CARS in an Automobile Engine
J. Phys. D: Appl. Phys. 16, 1583 (1983)

/15/ D. Klick, K.A. Marko, L.Rimai. Optical Multichannel Analysis with Rapid Mass Storage
of Spectra: Application to CARS Measurements of Temperature Fluctuations
Appl. Opt. 23, 1347 (1984)

/16/ R.L. Farrow, P.L. Mattern, L.A. Rahn. Comparison between CARS and Corrected Thermo-
couple Temperature Measurements in a Diffusion Flame
Appl. Opt. 21, 3119 (1982)

/17/ R.R. Antcliff, O. Jarrett. Comparison of CARS Combustion Temperatures with
Standard Techniques.
AIAA-Paper 83-1482 (1983)

/18/ R.L. Farrow, R.P. Lucht, W.L. Flower, R.E. Palmer. Coherent Anti-Stokes Raman
Spectroscopic Measurements of Temperature and Acetylene Spectra in a Sooting
Diffusion Flame
20th Symp. (Int.) Comb., p. 1307, The Combustion Institute (1984)

/19/ M. Péalat, P. Bouchardy, M. Lefebvre, J.P. Taran. Precision of Multiplex CARS
Temperature Measurements
Appl. Opt. 24, 1012 (1985)

/20/ L.P. Goss, G.L. Switzer, P.W. Schreiber. Flame Studies with the Coherent Anti-
Stokes Raman Spectroscopy Technique
AIAA-Paper 80-1543 (1980)

I-8

/21/ L.E. Harris, M.E. McIlwain. Coherent Anti-Stokes Raman (CARS) Temperature
      Measurements in a Propellant Flame
      Comb. Flame 48, 97 (1982)

/22/ W. Stricker. Local Temperature Measurements in Flames by Laser Raman Spectroscopy
      Comb. Flame 27, 133 (1976)

/23/ D.P. Aeschliman, J.C. Cummings, R.A. Hill. Raman Spectroscopic Study of a Laminar
      Hydrogen Diffusion Flame in Air
      J. Quant. Spectrosc. Radiat. Transfer 21, 293 (1979)

/24/ J.H. Bechtel. Temperature Measurements of the Hydroxyl Radical and Molecular
      Nitrogen in Premixed, Laminar Flames by Laser Techniques
      Appl. Opt. 18, 2100 (1979)

/25/ G. Alessandretti. Some Results on the Measurement of Temperature and Density in
      a Flame by Raman Spectroscopy
      Optica Acta 27, 1095 (1980)

/26/ M.C. Drake, M. Lapp, C.M. Penney. Use of the Vibrational Raman Effect for Gas
      Temperature Measurements
      in: Temperature, its Measurement and Control in Science and Industry, Vol. V,
      J.F. Schooley, Ed. (American Institute of Physics, New York), p. 631 (1982)

/27/ J. Haumann, A. Leipertz, M. Fiebig. Flame Temperature and Concentration Measu-
      rements from the Oxygen Stokes Vibrational Q-branch
      Proc. IXth Int. Conf. Raman Spectrosc., Tokyo, p. 248 (1984)

/28/ A.C. Eckbreth. Laser Raman Thermometry Experiments in Simulated Combustor
      Environments
      AIAA-Paper 76-27 (1976)

/29/ M.C. Drake, M. Lapp, C.M. Penney, S. Warshaw, B.W. Gerhold. Measurements of
      Temperature and Concentration Fluctuations in Turbulent Diffusion Flames Using
      Pulsed Raman Spectroscopy. 18th Symp. (Int.) Comb., p. 1521, The Comb. Inst. (1981)

/30/ W. Stricker, Th. Just. Lokale Temperaturmessung in Flammen mit Laser-Raman-Verfahren
      VDI-Berichte Nr. 346, S. 111 (1979)

/31/ B.S. Samyal, R.S. Hickmann. Temperature and Concentration Measurements in H_2-Air
      Flames Using Rotational Raman Scattering
      AIAA-Paper 80-1360 (1980)

/32/ M.C. Drake, C. Asawaroengchai, D.L. Drapcho, K.D. Veirs, G.M. Rosenblatt. The
      Use of Rotational Raman Scattering for Measurements of Gas Temperature
      in: Temperature, its Measurement and Control in Science and Industry, Vol. V,
      J.F. Schooley, Ed. (American Institute of Physics, New York), P. 621 (1982)

/33/ T.C. James, W. Klemperer. Line Intensities in the Raman Effect of Σ Diatomic
      Molecules
      J. Chem. Phys. 31, 130 (1959)

/34/ J.W. Nibler, G.V. Knighten. Coherent Anti-Stokes Raman Scattering
      in: Raman Spectroscopy of Gases and Liquids, A. Weber, Ed. (Springer, Berlin),
      p. 253 (1979)

/35/ R.J. Hall. Pressure-broadened Linewidths for N_2 Coherent Anti-Stokes Raman
      Spectroscopy Thermometry
      App. Spectrosc. 34, 700 (1980)

/36/ D. Robert, J. Bonamy. Short Range Force Effects in Semiclassical Molecular
      Line Broadening Calculations
      J. Physique 40, 923 (1979)

/37/ L.A. Rahn, A.Owyoung, M.E. Coltrin, M.L. Koszykowski. The J Dependence of Nitrogen
      "Q"Branch Linewidths
      Proc. VIIth Int. Conf. Raman Spectrosc., Ottawa, p. 694 (1980)

/38/ T.R. Gilson, I.R. Beattie, J.D. Black, D.A. Greenhalgh, S.N. Jenny.
      Redetermination of Some of the Spectroscopic Constants of the Electronic Ground
      State of Di-Nitrogen $^{14}N_2$, $^{14}N^{15}N$, and $^{15}N_2$ Using Coherent Anti-Stokes Raman
      Spectroscopy
      J. Raman Spectrosc. 9, 361 (1980)

/39/ A.C. Eckbreth. BOXCARS: Crossed-beam Phase-matched CARS Generation in Gases
      Appl. Phys. Lett. 32, 421 (1978)

/40/ W. Kreutner, W. Stricker, T. Just. Temperature Measurements in Flames by Laser
      Raman Techniques
      Ber. Bunsenges. Phys. Chem. 87, 1045 (1983)
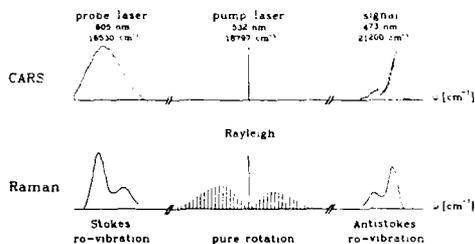
Fig. 1 Schematic plot of the frequency regions of the exciting lasers and the CARS signal, and the Raman spectra excited by the pump laser at 532 nm
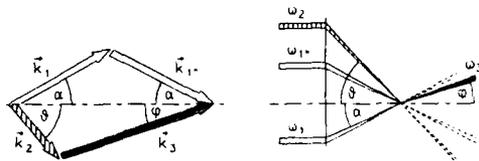
Fig. 3 BOXCARS geometry for improved spatial resolution
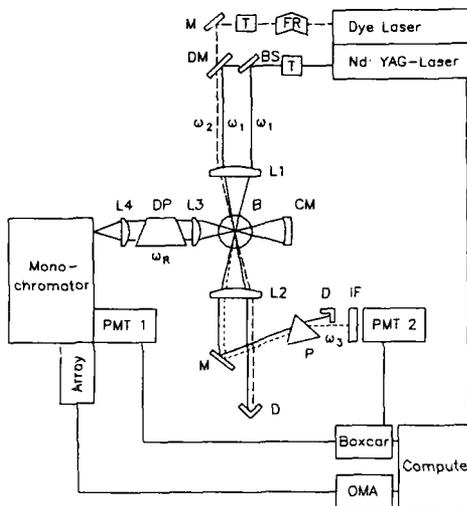
Fig. 2 Experimental setup used for simultaneous CARS and Raman measurements
B burner   BS beam splitter   CM concave mirror
D laser dump   DM dichroic mirror   DP Dove prism
FR Fresnel rhomb   IF interference filter
L1-L4 lense   M dielectric mirror   P dense flint prism   T telescope
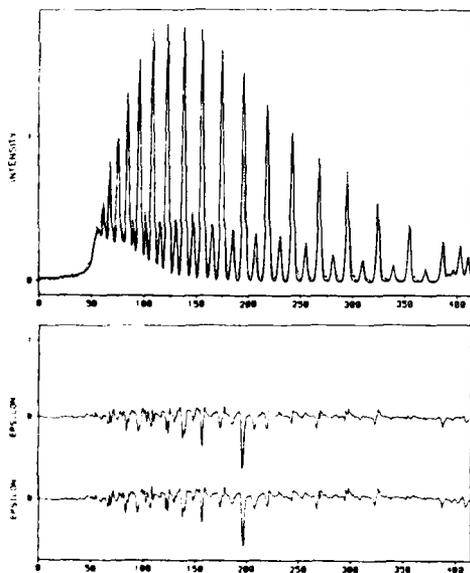
Fig. 4 Top: Theory-experiment fit of a narrowband CARS spectrum using a constant linewidth
Bottom: Residual error curves
Upper trace: Theory-experiment fit using a constant Raman linewidth; T=2174K
Lower trace: Theory-experiment fit of the same experimental data, but using Hall's linewidth model; T=1954K
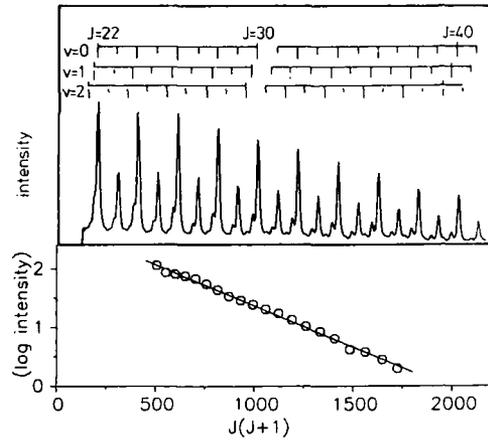
Fig. 5 Part of the pure rotational Raman
spectrum, recorded in the premixed propane/
air flame; the N_2 lines belong to vibratio-
nal states v=0,1,and 2.
The least-squares fitted straight line in-
dicates T=(2043±28)K
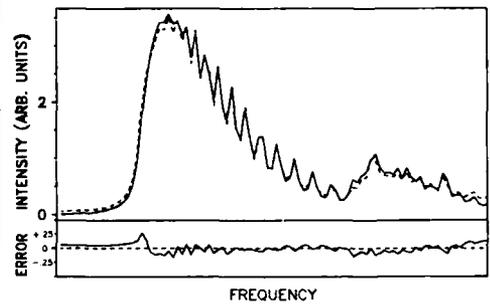
Fig. 6 Theory-experiment fit of a typical
broadband CARS spectrum (several hundred
laser pulses averaged) in the premixed pro-
pane/air flame; Farrow's linewidth model was
used; T=2014K
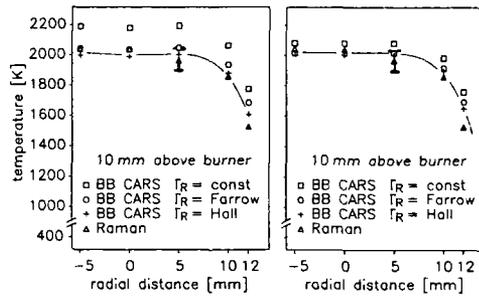
Fig. 7 Radial temperature profile in the atmospheric, laminar
propane/air flame; CARS temperature values evaluated with dif-
ferent linewidth models and spontaneous Raman data are shown.
The full triangles represent Raman measurements with shorter
exposure time and therefore lower accuracy as indicated by the
error bars.
left: evaluation of vibrational ground state only
right: hot band included in data evaluation

DISCUSSION

A.Eckbreth, US

What value of constant linewidth did you use?

What values of constant linewidth gave "correct" temperatures even if the fit was not the best least squares?

Author's Reply

For the best fit spectrum shown we used a linewidth of .033 cm⁻¹.

Other linewidths lead to bad theory-experiment fits, especially in the region of the band head, and have not been evaluated.

R.Farrow, US

Comment

Both models are now dated in comparison with current work. Polynomial exponential gap (D.Greenhalgh et al) models and other exponential gap models (Koszykowski et al, Rodsasco et al, and others) should give more accurate linewidth over a broader temperature range.

R.B.Price, UK

In the paper the assumption of equal contributions from Lorentzian and Gaussia ources is made.

(a) What is the basis for this assumption?

(b) If you allow the ratios to vary, does this make a difference to the conclusions drawn?

Author's Reply

In broadband CARS thermometry the influence of the combined slit/detector profile has to be taken into account in the spectrum calculation. We do this by fitting a suitable spectral line which we record with our detection system. In most cases equal amounts of Gaussian and Lorentzian contributions give a good fit. With these evaluated parameters a CARS spectrum of known temperature is calculated and fitted. However, sometimes it is necessary to change the contributions somewhat to improve the theory-experiment fit (temperature influences on the monochromator/detector system?). But this should have no remarkable influence on the conclusions drawn in the paper.

CARS THERMOMETRY FOR LOW AND HIGH PRESSURE COMBUSTION SYSTEMS*

by

Douglas A. Greenhalgh

Harwell Combustion Centre
Building 10.4,
Harwell Laboratories
Oxfordshire
OX11 ORA, U.K.

SUMMARY

This paper discusses the theory and application of broadband CARS spectroscopy for ambient (low) and high pressure combustion thermometry. The accuracy of broadband CARS is assessed from 300-3500 Kelvin for pressures around 1 bar, and from 300-700 Kelvin for pressures from 1-20 bar. The use of CARS thermometry for both "average" and "instantaneous" measurements is discussed. Systematic accuracy strongly depends on the quality of the spectral model used in the CARS data analysis step. CARS spectral modelling methods are discussed with particular reference to important recent developments. Instantaneous CARS accuracy is importantly influenced by noise arising in both the broadband dye laser and the multichannel detector. Both of these factors, and their relative influences are assessed. The application of CARS thermometry is illustrated by application to both in-cylinder studies of an operating production i.c. petrol engine and to turbulent combustion in an oil-fired 30 kilowatt furnace.

1. INTRODUCTION

Coherent Anti-Stokes Raman Spectroscopy (CARS) is a laser spectroscopic technique for probing gaseous systems. CARS has been widely used for 'in-situ' probing of temperature and species concentration in a wide variety of research[1-5] development[6-10], and industrial[11-14] devices. Current application areas include combustion[1-3, 5-14], chemical engineering[4, 15], steam thermometry for nuclear systems application[16] and micro-electronics[17]. To date its greatest usage has been for probing hostile combustion systems, normally for thermometry but increasingly for species concentrations. For combustion diagnostics and heat transfer studies it offers certain significant advantages over conventional mechanical probes.

(i) it is non-invasive (apart from windowing when required)

(ii) it is spatially precise

(iii) measurements are typically made in a single 10 nano-second laser pulse - thus flow fluctuation (turbulence) are frozen

(iv) it is insensitive to background luminosity or fluorescence emissions

(v) it is durable - laser beams are not irreparably damaged by violent flow transients or particles.

For these reasons CARS is rapidly becoming an important diagnostic technique for research and practical combustion studies. In this paper we discuss and analyse the accuracy of broadband CARS nitrogen thermometry. The analysis of CARS spectra requires an accurate computer model of the nitrogen CARS spectrum. Firstly, a descriptive overview is presented. Secondly, a detailed mathematical presentation of the latest CARS computer model is given. Thirdly the accuracy of both "average" and "instantaneous" thermometry is presented; in particular dye laser and detector noise problems are discussed. Application of the technique is illustrated from recent studies of a production petrol i.c. engine[13,14] and 30 kW oil-fired furnace [2].

2. CARS SPECTROSCOPY OVERVIEW

Both the theory and application of CARS spectroscopy have received wide attention in a number of reviews (18-20). These reviews provide an additional indepth treatment to which the interested reader is referred. The essentials of the CARS process are illustrated in Figure 1. Two lasers provide beams of frequencies ω_1 and ω_2, which are used to generate a signal beam at a frequency ω_{as}. To generate the

signal efficiently the beams must be geometrically combined in the medium to achieve phase or momentum matching. The resultant signal is a coherent 'laser-like' beam at a frequency $\omega_{as} = 2\omega_1 - \omega_s$. The laser at ω_1 is termed the pump laser and is usually spectrally narrow. The laser at ω_s, usually broadband, is termed the "Stokes" laser due to its 'red shift' with respect to the pump laser. The generated CARS signal beam at ω_{as} is termed "anti-Stokes" due to the its 'blue shift' from the pump wavelength. In this paper only broadband CARS where ω_s is broad will be discussed. Narrow band CARS is not usually suitable for studying practical or turbulent combustion devices.

One conceptual model of the CARS process is presented below. The interaction of a pump laser beam (ω_1) and a Stokes laser beam (ω_s) will result in an interference pattern where the laser beams cross. Interaction of the lasers with the medium will result in a complex optical density modulation of the medium which mimics the interference pattern, thus the induced "pattern" is in effect a transmission grating. Because the two lasers are of different frequencies the induced grating will be apparently moving across the intersection volume at great speed. Also the finite interaction length of the lasers will cause the grating to be three dimensional. Therefore a second incoming component, of the pump laser (ω_1) must be specifically vectored onto this grating to optimise diffraction from the grating. A small portion of this second laser beam will interact with this induced transmission grating and will be both diffracted through an appropriate angle and frequency up shifted (by an amount $\omega_1 - \omega_s$). Using this conceptual model most of the important effects of CARS can be accounted for. The accurate vectoring of the laser beams is usually known as phase-matching. In Figure 1 the three beam phase-matching geometry, well known as folded BOXCARS is illustrated [21-23]. BOXCARS can also be realised using a two beam geometry [24,11]. However, another very common geometry is colinear CARS. In colinear CARS all beams co-propagate and the induced grating may be thought of as possessing a one dimensional structure which lies along the propagation axis of the laser beams. In this case the generated CARS signal appears frequency shifted, but is not deflected.

CARS
(COHERENT ANTI-STOKES RAMAN SPECTROSCOPY)

— METHOD —

— ENERGY LEVEL DIAGRAM —

— SPECTRUM —

$\lambda = 606\,nm$ $\lambda = 532\,nm$ $\lambda = 474\,nm$
(NITROGEN SPECTRUM)
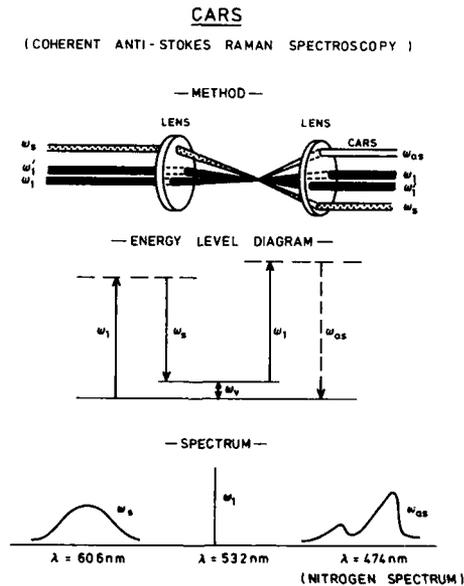
FIG. 1. Schematic of CARS Process

The efficiency of the grating will depend on the interaction of the two laser beams with the medium. The principal coupling coefficient between the lasers and the medium is termed the third order bulk susceptibility ($\chi^{(3)}$). To generate a signal at $\omega_{as} = 2\omega_1 - \omega_s$ the medium must have a response at either ($\omega_1 - \omega_s$) or $2\omega_1$. The first of these ($\omega_1 - \omega_s$) normally corresponds to a Raman active vibrational transition of a gas molecule, the second ($2\omega_1$) is normally a two photon sum electronic transition. In

the second case ($2\omega_1$) the grating would of course be formed from the two pump laser beams. Usually $2\omega_1$ is not resonant with an electronic transition and the two photon electronic effects is weak, thus this process gives rise only to a weak, spectrally flat, term known as the non-resonant background. However, ($\omega_1 - \omega_s$) may be readily tuned to strong Raman transitions such as the nitrogen Q-branch. Q-branch transitions occur for vibrational quantum state changes of one ($\Delta V = \pm 1$) and rotational state changes of zero ($\Delta J = 0$). For nitrogen this band is at 2330 cm^{-1} and is easily matched by the frequency difference between a doubled Nd:YAG laser and an optically pumped dye laser. The grating induced by the frequency difference ($\omega_1 - \omega_s$) is a two photon transition and will contain contributions both from the imaginary part of $\chi^{(3)}$(equivalent to absorption or optical density for a one photon transition)and the real part of $\chi^{(3)}$ (equivalent to refractive index for a one photon transition). Thus the final CARS spectrum also contains contributions from both terms.

To enable a temperature to be recorded in a single laser pulse the whole of the nitrogen Q-branch spectrum must be generated in a single laser pulse. This is achieved by using a broadband dye laser for the Stokes laser; spectrally this is illustrated in the lower part of Figure 1. The main problems with single-pulse broadband CARS are noise in the spectrum of the dye laser and Poisson noise arising in the multichannel detector. These problems are fully discussed in a later section. CARS nitrogen Q-branch spectra are strongly temperature dependent. Typical spectra (theoretical) from 500K to 2000K are shown in Figure 2. At low temperatures the spectrum arises from transitions between the vibrational levels V=0 and V=1 for many rotational levels (Quantum number J). Each rotational "side-band" is shifted by approximately α_e J(J+1) from the J=0 level, α_e is the vibrational-rotational coupling constant and is of order 0.02 cm^{-1}. A typical broadband CARS system has a resolution of only 1-2 cm^{-1} so many of these rotational "side-bands" are not fully resolved. However, at high temperatures where high J states are populated the splitting between lines is just sufficient to observe some structure in the spectrum. Generally the effect of increasing temperature is to broaden the V=1+V=0 Q-branch. At high temperatures, normally above 1000K a new band appears at lower Raman shift, these correspond to V=2+V=1, V=3+V=2 etc transitions. The pronounced features on the V=2+V=1 band arise due to accidental coincidence of rotational side-bands of both V=2+V=1 and V=1+V=0 transitions. In CARS, the intensity depends on the modulus squared of the bulk molecular susceptibility and hence such coincidences give rise to a non-linear increase in intensity.
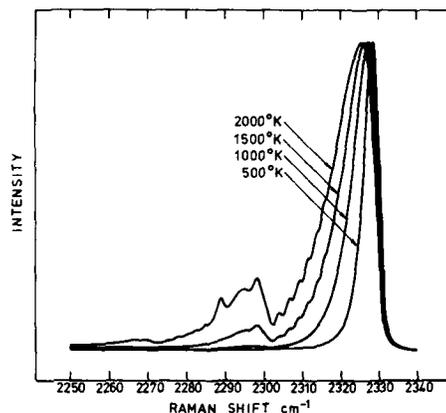
FIG. 2 Plots of CAPS Spectra of Nitrogen as a Function of Temperature (intensities normalised)

Temperature analysis of a CARS spectrum is performed by analysing its overall shape. There are several methods. In the most widely used, a model spectrum is least squares fitted to an experimental spectrum with temperature as the principal variable[1,2,7,14,20]. Alternatively, simple algorithms, based on the areas, widths or height of specific spectral features may be employed[11]. Temperature analysis is also facilitated if the spectral operation of the dye laser is modified to specifically select certain features of the spectrum[25]. Lastly, for the pure rotational CARS S-branch spectrum of nitrogen[26], which is occasionally chosen as an alternative to the vibrational Q-branch spectrum[27], Fourier analysis may be employed[28]. At Harwell we have found the least square method to be both the most reliable and the most general for broadband CARS thermometry[29] and that Q-branch spectra are easier to generate. Comparison of the first two analysis techniques, on the same CARS data obtained in an isothermal tube furnace, has shown that some simple algorithms may lead to systematic errors of up to 8%[29]. The latter two methods are relatively new, and as yet, have not been extensively tested. Extensive testing for least squares analysis has shown the method to be completely reliable[29-31] for the region 300-1500K. For temperatures in excess of 2000K a new method for determining CARS temperature accuracy has recently been proposed [32,33] and accuracies of order 1% have been found for the region 2000K to 3500K using least squares analysis[32,33]. Further, for thermometry measurements in turbulent diffusion flames the apparent nitrogen concentration may change in an unpredictable manner. Concentration changes can markedly affect CARS temperature analysis if not accounted for. By using least squares analysis concentration changes can be readily accounted for with only a minimal

effect on temperature accuracy[29,34]. For the above reasons this paper will concentrate on temperature analysis of broadband CARS spectra of nitrogen Q-branches using least squares analysis.

3. THEORY OF CARS SPECTROSCOPY

In the preceding section an overview description of the CARS process was given. In this section a theoretical basis for the interpretation of CARS spectra of nitrogen Q-branches will be given. Physically, the origin of CARS lies in macroscopic polarization induced by the incident electric fields. This induced polarization acts as a source term in Maxwell's equations applied to coherent CARS signal generation. It is the third order nonlinear electric susceptibility ($\chi^{(3)}$) which relates macroscopic polarization to the cube of the incident electric field, consequently the analysis of $\chi^{(3)}$ is central to the analysis of CARS spectra. A fuller review of the basic theory may be found in references 18, 19 and 35.

The nonlinear polarization of matter is given by

$$P = \chi^{(1)}E + \chi^{(2)}E^2 + \chi^{(3)}E^3 + \ldots \quad (1)$$

Unless the electric field power is high the first term dominates and accounts for most simple optical phenomena (e.g. absorption, refraction, dispersion etc). At high field strength the second and third terms become important. $\chi^{(2)}$ is associated with processes such as frequency doubling, this process is commonly used to up convert laser frequencies as in the frequency doubled Nd:YAG laser. The lowest order nonlinearity in isotropic media such as gases is $\chi^{(3)}$. As well as CARS this term is responsible for a whole variety of effects including third harmonic generation, optical Kerr effects and inverse or stimulated Raman. The CARS polarization component is given by[35]

$$P^{(3)}(\omega_{as}) = \chi^{(3)}_{ijkl}(-\omega_{as}; \omega_1,\omega_1', -\omega_s) \, E(\omega_1)E(\omega_1')E^*(\omega_s) + c.c.; \quad \omega_{as} = \omega_1 + \omega_1' - \omega_s \quad (2)$$

$\chi^{(3)}_{ijkl}$ is a fourth rank tensor and is characterised by four polarizations (i,j,k,l) and four frequencies ($\omega_1,\omega_1',\omega_s$ and ω_{as}), Assuming plane waves defined as

$$E(\omega_j) = \tfrac{1}{2} A_j e^{i(k_j z - \omega_j t)} + c.c. \quad (3)$$

where z is the propagation axis, and by using equation (2) as a source term in Maxwell's wave equation it can be shown that[18-20,35] the CARS signal intensity is

$$I_{as} = \frac{4\pi^2\omega_{as}}{c^2 n_{as}} \, I_1^2 \, I_s \, |3\chi^{(3)}|^2 \, L^2 \quad (4)$$

where both perfect phase matching and monochromatic laser sources are assumed. In equation (4) c is the speed of light, ω_{as} is the CARS signal frequency, n is the refractive index at ω_{as}, L is the laser beam interaction length and I_1 and I_s are the intensities of the pump and Stokes lasers respectively. The effects of finite laser widths are discussed later. $\chi^{(3)}$ is the third order bulk electric susceptibility of the medium and, assuming isolated lines is given by

$$\chi^{(3)} = \chi_{NR} + \frac{4\pi N c^4}{h \omega_s^4} \, \sum_j \left(\frac{d\sigma}{d\Omega}\right)_j \, \Delta\rho_j \, \left[(\omega_j - \omega_1 + \omega_s) - i\,\Gamma_j\right]^{-1} \quad (5)$$

where $(d\sigma/d\Omega)_j$ is the so-called Raman cross section of the jth line of the probed species, h is Planck's constant, N is the number density, $\Delta\rho$ the population differences between upper and lower states of the jth resonance of the probed species. Note the line shape term [....] is a complex Lorentzian, for high pressures this function is replaced by the reciprocal of the eigenvalues of the complex G matrix together with associated complex weights[36,37]. This point is discussed later. χ_{NR} is a spectrally flat contribution from all the constituents of the medium. For strong resonances χ_{NR} produces only a slight modification to the spectrum. For a single resonance $(\chi^{(3)})^2$ becomes

$$\chi_j^{(3)2} = (Imag\chi_j)^2 + (Real\chi_j)^2 + 2\,Real\chi_j\,\chi_{NR} + \chi_{NR}^2 \quad (6)$$

As the concentration decreases the contribution to the CARS signal from the species resonance χ_j will approach χ_{NR}. Thus the last two terms in equation (3) become important. Imaginary χ_j has a simple Lorentzian shape but Real χ_j has a dispersive shape. Therefore as species concentration changes, the spectrum shape changes; this is illustrated in Figure 3 for the Q-branch of CO.

30

20

Intensity

10

0

——5%

——10%
——15%
——20%
——30%
——50%
——100%

477·3 477·4 477·5 477·6 477·7 477·8

Anti-Stokes Wavelength
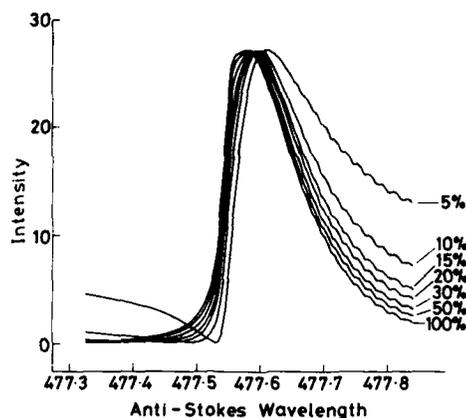
FIG. 3. Calculated Spectra of CO as a Function of Concentration at 703K (intensities normalised)

Species concentrations may, in principle, be derived directly from the signal intensity; however, uncertainties in laser intensity and the complex form of equations 3-6 can lead to serious error. Most practical analysis is based on equation 6 and uses the shape of the spectrum[20,11]. This has the advantage that both temperature and species concentration are simultaneously determined[29,2,34] and this enables spectra from turbulent diffusion flames to be correctly analysed.

The central problem in calculating CARS spectra is to determine an "observed" $\chi^{(3)}$ such that all medium, laser, spectrograph and detector parameters are properly accounted for. Certain advances in CARS theory have, at first, appeared to significantly complicate the problem and considerable increase computing times. One factor is the so-called "cross-coherence" effect which properly accounts for partial coherences in the CARS signal, these partial coherences arise when finite bandwidth pump lasers are used[38,39]. Another factor is motional narrowing[40-42,14,16]. Both these factors are important even for ambient temperature and pressure nitrogen. Recently a simple approach which properly accounts for both these effects has been published[43]. The model used for analysis of the data presented in this paper is based on this approach and, excluding detector and spectrograph convolutions is defined by[43].

$$I_{as}(\omega_{as}) = I_s \left(2 \omega^{(o)} - \omega_{as}\right) \left[\chi_{NR}^2 + \frac{1}{\Gamma_1} \frac{2}{\tilde{\omega}} \sqrt{\pi} \chi_{NR} \Sigma a_j w_j^2 + c.c.\right.$$

$$\left. + \frac{1}{2} \frac{\sqrt{\pi}}{\Gamma_1} \Sigma U_j a_j w_j^2 + c.c. + \frac{\pi}{2 \Gamma_1^2} (\Sigma a_j w_j)(\Sigma a_j w_j)^* \right] \tag{7a}$$

where

$$U_j = \Sigma a_k^2 \left[\lambda_k' - \lambda_j' - i \lambda_j'' - i \lambda_k''\right]^{-1} \tag{7b}$$

and w_j is the well known complex error function, namely

$$w_j = w(z_j) = \frac{i}{\pi} \int_{-\infty}^{\infty} \frac{e^{-t^2}}{z_j - t} dt \quad (Im \ z_j > 0) \tag{7c}$$

with

$$z_j = -\frac{(\lambda_j' - (\omega_{as} - \omega_1(p))) - i \lambda_j''}{\tilde{\Gamma}_1} \tag{7d}$$

Here λ_j' and λ_j'' are the complex eigenvalues of the so-called G-matrix and the a_j are complex weights formed from the complex eigenvectors of the G-matrix, Raman scattering cross sections,, and quantum state population factors. For most situations, where $\Gamma_1 >> \Gamma_D$ (Γ_D is the Doppler width) simultaneous $(\Gamma_D^2 + \Gamma_1^2)^{\frac{1}{2}}$ and the factor $\left[\lambda_k' - \lambda_j' - i(\lambda_k'' + \lambda_j'')\right]^{-1}$ is replaced by

$$(- 1 \sqrt{\pi}/\sqrt{2}\Gamma_D) \ W\left(\frac{\lambda_k' - \lambda_j' - i \ (\lambda_j'' + \lambda_k'')}{\sqrt{2} \ \Gamma_D}\right) \tag{7e}$$

Following references 34 and 35 mathematically this gives:

$$\underline{\underline{A}} \cdot \underline{\underline{A}}^{-1} \cdot \underline{\underline{G}}^{(o)} \cdot \underline{\underline{A}} \cdot \underline{\underline{A}}^{-1} = \underline{\underline{A}} \ \underline{\underline{\lambda}} \ \underline{\underline{A}}^{-1} \tag{8a}$$

so that

$$\underline{a} = (\underline{\alpha} \cdot \underline{\underline{A}}) \cdot (\underline{\underline{A}}^{-1} \cdot \underline{\underline{\Delta\rho}} \cdot \underline{\alpha}) \tag{8b}$$

with

$$\underline{\underline{G}}(\omega) = \underline{\underline{I}}(\omega) + \underline{\underline{G}}^{(o)} \tag{8c}$$

Thus the simplistic scalars and Lorentzian function of equation (5) are replaced by equations (7) and (8) together with the following further definitions. Neglecting polarization effects, we have

$$\alpha_j^2 = \frac{4\pi \ N \ c^4}{h \ \omega_s^4} \quad \frac{d\sigma}{d\Omega}_{V,J} \tag{9a}$$

where

$$\frac{d\sigma}{d\Omega}_{V,J} = \frac{d\sigma}{d\Omega}_{0,0} \cdot C_J \cdot C_V \tag{9b}$$

and C_J and C_V are given by (42)

$$C_J = 1 - 1.5 \ (a_1+1) \ J(J+1) \ a_2^2 \tag{9c}$$

also

$$C_V = [1 - 1.5 \ Vb_1 + (11/4) \ Vb_2^2]/[1 - 1.5 \ b_1 + (11/4)b_2^2]^2 \tag{9d}$$

with

$$a_1 = \frac{1 - \alpha_e\omega_e}{6B_e^2} \tag{9e}$$

$$a_2 = \frac{2B_e}{\omega_e} \tag{9f}$$

$$b_1 = \frac{a_1\sqrt{a_2}}{2} \tag{9g}$$

$$b_2 = 1/6 \ [2\omega_e x_e/B_e(15/4)a_2^2] \tag{9h}$$

The population difference matrix $\underline{\underline{\Delta\rho}}$ in equation 8 is diagonal and is defined as

$$\Delta\rho_{jk} = \delta_{jk}(\rho_{ji} - \rho_{jf}) \tag{10a}$$

where ρ_{ji} and ρ_{jf} are the initial and final state populations of the jth transition, δ_{jk} is the Kronecker delta function ($\delta_{jk} = \delta(j-k)$).

$$\rho_{ii} = \frac{g_J(2J+1)V}{Q_V, \ Q_{R,(V)}} \ (e^{-(E_V+E_J)/kT}) \tag{10b}$$

where Q_V and $Q_R(V)$ are the vibrational and rotational partition functions and i represents quantum states J and V. The crucial element for calculating spectra as a function of pressure is the G-matrix. This is given by

$$G_{jk}^o = [-\omega_j - \omega_o - \Delta_j - i\Gamma_j]\delta_{jk} + i\gamma_{jk}(1-\delta_{jk}) \tag{11a}$$

where ω_j is the line transition frequency, ω_0 is an arbitrary constant, Γ_j the transition half widths at half maximum and Δ_j are the transition frequency pressure shifts. The latter are normally independent of J and constitute only an overall frequency shift of the spectrum. This is easily handled in the data processing and the Δ_j's are consequently ignored. Note that the diagonal of the G-matrix is just the inverse of a complex Lorentzian vector. The key factors in motional narrowing are the γ_{jk}'s. There are two important constraints on the γ_{jk}'s. Firstly, Γ_j is related to γ_{jk} by the unitary principle which is

$$\Gamma_j = \phi_v + \sum_k - \gamma_{jk} \tag{11b}$$

where ϕ_v is a small vibration dephasing contribution to the molecular linewidth, typically ϕ_v is less than 5% of Γ_j for nitrogen. Secondly detailed balance requires that

$$\gamma_{jk} \, \rho_k = \gamma_{kj} \rho_j \tag{11c}$$

Equations 7-11 form the basis for calculating CARS spectra fully including the effects of laser cross-coherence, motional narrowing, and anharmonic and centrifugal corrections. The latter two factors are small other than at high temperatures (e.g. above 2000K). The two most important effects are laser cross-coherence and motional narrowing. Cross-coherence effects arise since the pump laser has a finite bandwidth. Consider two discrete components of ω_1, namely ω_1' and ω_1''. In this case the equations

$$(\omega_1' - \omega_s) + \omega_1'' = \omega_{as} \tag{12a}$$

$$(\omega_1'' - \omega_s) + \omega_1' = \omega_{as} \tag{12b}$$

give exactly equal anti-Stokes frequencies but for different Raman shifts (component in parenthesis) and consequently corresponds to different values of $\chi^{(3)}$. Further, it is easy to see if ϕ is substituted for ω in equations 12a and 12b both of the generated waves at ω_{as} are in-phase and will consequently add coherently. Simultaneously the two components (ω_1' and ω_1'') give rise to spectral separate, randomly phased contributions at

$$(\omega' - \omega_s) + \omega_1' = \omega_{as}' \tag{12c}$$

and

$$(\omega_s'' - \omega_s) + \omega_1'' = \omega_{as}'' \tag{12d}$$

Processes arising from 12a and 12b can be thought of as "cross-coherent terms" and those from 12c and 12d as incoherent or "normal stoichastic contributions". These two types of contributions correspond directly to the 4th and 3rd terms in equation (7a). In equation (7a) a full integration over an assumed Gaussian distribution of laser mode intensities is included.
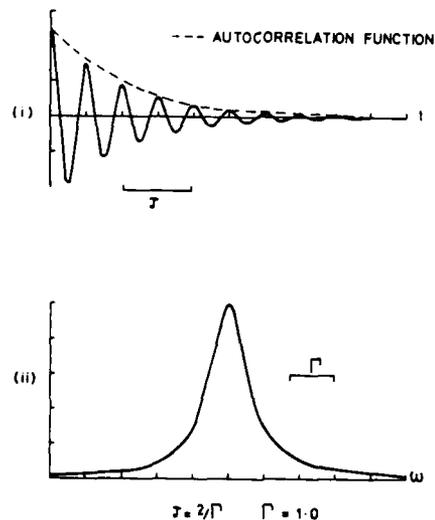
FIG. 4. Fourier Pair of an Exponentially Decaying Sine Wave and a Lorentzian Line Shape

The effects of motional narrowing may be illustrated by considering a Q-branch of a hypothetical molecule with two vibrational transitions arising from only two rotational levels, say J_1 and J_2. Consider one of the two states and its associated transition or spectral line. Inelastic collisions will restrict the lifetime of any molecule in this state in a random way. Thus an ensemble of molecules may be thought of as having a "characteristic" or "average" lifetime in the state τ. Increasing pressure will increase collision rate and correspondingly linearly decrease τ. The emitted CARS signal, from this ensemble of molecules, will then correspond to a randomly interrupted ensemble of sine waves. This process is properly represented by an exponentially decaying sine wave where the characteristic of the exponent is $-\tau$. The above situation and its equivalent Fourier transform pair in the frequency domain, is illustrated in Figure 4. Note that the spectral lineshape is a Lorentzian, at low pressures its half width will increase linearly with gas pressure as τ decreases. This is the classical picture of pressure broadening of spectral lines; because it treats each transition separately it is referred to as the "isolated lines model". However, the isolated lines model does not take account of what happens to a molecule after an inelastic collision. If it merely "jumps" into the other state (e.g. $J_1 \rightarrow J_2$) and the apparent vibrational motion is essentially unperturbed then the molecule will have appeared to have changed frequency but with no interruption in its vibrational phase. Such a situation will significantly complicate the isolated lines picture. Just such a situation is schematically illustrated in Figure 5. For clarity, the time domain in Figure 5 shows the specific behaviour of the spectral emission from an "average" molecule undergoing collisions at intervals of τ. This is obviously hypothetical since in practice an ensemble of molecules will be experiencing collisions after random time intervals where τ is the characteristic time interval. The frequency domain does represent the real situation of a molecular ensemble. At low pressure, molecular lifetimes are long and the transitions narrow. As pressure increases, τ decreases and the transitions broaden in a linear fashion. However, when τ is small the molecule switches rapidly between its two quantum states (J_1 and J_2) and the spectrum collapses to a single, sharp, line. Under these circumstances, the switching time, or mean time between collisions, is, in effect, comparable to the inverse of the frequency difference between the spectral lines. Nitrogen behaves in this fashion at high pressure, but in this case the calculation is very complex because, depending on the temperature, up to 50 rotational states and 4 vibrational Q-branches may be involved.
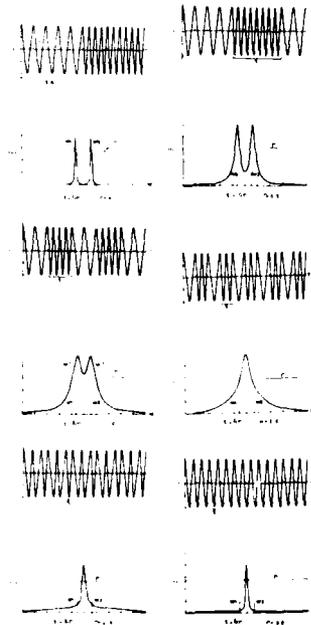
FIG. 5. A Schematic Illustration of Motional Narrowing for a Hypothetical "Two State" Molecule. Pseudo Fourier Pairs - see text.

In practice, the problem is to define the individual relaxation rates between individual states; for nitrogen, up to 2,500 rates may be required to compute a spectrum by inverting the G-matrix. The first attempt at an efficient formulation which solved both problems was found by Hall and Greenhalgh[41] and is based on the Gordon rotational diffusion model. However, recent experimental data, particularly from Sandia National Labs[37,45], but also in-cylinder i.c. engine measurements at Harwell[13,14], have shown that this model is inadequate. Therefore calculations have to be based on the full G-matrix approach equations 7-11 and a model for describing the rates, γ_{jk}'s, in equation 11 is required. Such a model needs to properly accounted for the constraints of unitary (equation 11b) and detailed balance (equation 11c). Initial approaches[42] fitted simple models, usually called scaling laws[46], to known or predicted experimental linewidths.

More convenient are models which are accurately self consistent with known linewidths and equations 11b and 11c. Such a model has been formulated and is known as the Polynomial Energy Gap or PEG law[47]. However, this model also underestimates narrowing in known N_2 spectral dated[13,14,37,45]. This has led to impro'-d models based on the exponent of the energy defect between the states involved in the rotationally inelastic collisions. A model which is self consistent with early experimental linewidth data, equations (11b) and (11c), and known CARS spectra up to 1000K is the Differential Energy Gap (DEG) scaling law[31,14]. Such a model has been employed for a wide range of CARS data and has been found to give excellent results up to 1000K and 2C bar (detailed results are shown later). The full parameterised model, fitted to known data[48-50], gives

$$\gamma_{jk} = P \cdot T^{-a} \cdot K \cdot \rho_j^{-b} \rho_k^{+c} \qquad (13)$$

where $a = 1.2807$, $K = 33.3226$, $b = 1.63$, $c = 1.4$, P is pressure and T is temperature.

Very recently an alternative model has been formulated[45,51] from a full range of accurate inverse Raman linewidth measurements[51]. The DEG model as stated in equation (13) gives very good accuracy for CARS thermometry. Essentially the DEG model is a conventional exponential scaling law[37,38,40] with the inclusion of a term ρ_k^{b-c} where $b-c = 0.23$. This factor behaves in a similar fashion to the perturbation correction factor employed in the Energy Corrected Sudden (ECS) extension of Impact Order Sudden Theory (IOS)[46,52]. The perturbation correction factor which accounts for partial rotation of the molecules during the molecular collision, was first investigated for nitrogen CARS applications by Hall[52]. A similar factor is also employed in alternative models. The DEG model, equation (13), accurately reproduces the functional form of the rotational or "J" dependence of even the most recent linewidth data[51], however its overall scaling of linewidths is slightly out (circa 10% maximum). This small error does not significantly affect CARS thermometry accuracy for a wide range of temperatures and pressures and, as is shown in the results section, excellent accuracy may be achieved using equation 13. Small errors in linewidth scaling are in any case unimportant for low and medium resolution CARS[29]; however, errors in the form of the J dependence are not[29,53]. This clearly points to the fact that the overall linewidth scaling of the DEG model is not properly described by the T^{-a} factor. A model which, for practical purposes, rectifies this situation is proposd below and is termed P-DEG or Polynomial-Differential Energy Gap.

$$\gamma_{jk} = P(\sum_1^n K_i T^{-i}) \rho_j^{-b} \rho_k^{+c} \qquad (14)$$

Comparison of predicted and known linewidths[48,51] is shown in Figure 6. The overall agreement is excellent. All these scaling laws are however approximations and there is, as yet, no overriding physical basis for preference of a given model, indeed recently both the Gordon model and the PEG model have been extensively revised and used to obtain much improved agreement with experimental data[54,55].
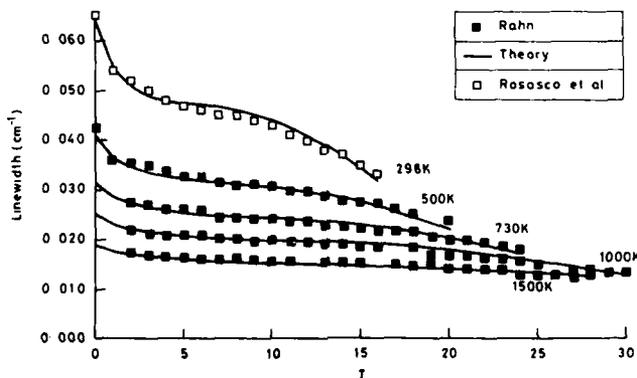
Modified DEG Scaling Law

FIG. 6. Comparison of Linewidth Measurements (refs. 48 & 51) with the P-DEG Scaling Law Model

In forming a computer code for prediction and temperature analysis of CARS spectra, it is vital to include appropriate convolutions for the "instrument function". This arbitrary function arises from the finite resolving power of the analysing spectrograph and from cross-talk in the intensified detector. For many instruments this function is well represented by a Voight function[29,53]. Typically most of the CARS spectrometers at Harwell have instrument functions indistinguishable from Voight profiles. Thus the "observed" CARS spectrum is given by

$$I^0_{as}(\omega_{as}) = \int V(\Gamma_L\Gamma_G, \Delta)d\Delta \ I_{as}(\omega_{as}) \qquad (15)$$

where $I_{as}(\omega_{as})$ is given by equation 7-11 and 13 or 14, Δ is detuning from ω_{as} and Γ_L and Γ_G are the H.W. Lorentzian and 1/e H.W. Gaussian components of the instrument function. Such a convolution may be readily computed by a single Simpsons rule integration. However, after a little thought, an essentially fully analytic solution for equation 15, following the integral methods used in equation (7), is possible and will be published shortly[56]. Occasionally, as in the case of one of our Harwell instruments, a slightly asymmetric instrument function is found. This has been accounted for by post convoluting equation 15 by a "one-sided" exponential function, this is physically somewhat analogous to a time constant of a chart recorder. This process is mathematically trivial and is not given explicitly.

4.   DATA ANALYSIS THERMOMETRY ACCURACY AND INSTRUMENTAL NOISE

In this section the data processing method employed is discussed. Secondly the accuracy of CARS "averaged" temperatures is assessed. Thirdly, factors affecting instrumental noise for instantaneous or single pulse CARS are discussed. Finally, the combined effect of instrument noise (lasers and detector) are examined and an analysis presented.

All results published here are based on the above model. These equations have been formed into a sophisticated computer code which includes facilities for a least-squares processing of large quantities of experimental data. The computer model is known as CARP-2[57]. For very large quantities of single shot data an alternative method is employed. This is based on a library of spectral curves representing essentially terms 2 and (3+4) of equation (7a), after convolution by a suitable instrument function. Libraries are generated using CARP-2 and, subsequently, very rapid least-squares fitting, can be achieved using the codes QUICK[57] or QUICK-2D[57]. The QUICK codes have been developed to utilise Libraries for processing data from such as an isobaric turbulent flame where temperatures may change by up to 2000K from shot to shot (QUICK) or for processing i.c. engine data where both temperature and pressure (on average) tend to change modestly from laser shot to laser shot for a given measurement location at a given engine crank angle (QUICK-2D).

CARS "average" thermometry accuracy at atmospheric pressure has been carefully studied by two groups for the region 300-1700K[30] and 300-1050K[29,31]; excellent agreement with standard thermocouples has been found. Examples of this will not be reproduced here. The accuracies of the Harwell CARS systems are typically 1-1.5% for the range 300-1000K[29,31]. However, the accuracy of CARS in the temperature range 300-1000K at 1 bar does crucially require the cross-coherence effect [29] to be accounted for. If cross-coherence is neglected, CARS temperatures may be in error by up to 50 or 60K[29]. Also at the lower temperatures motional narrowing is important. The improved accuracy of Harwell data around 300K[29,31] over data obtained elsewhere [30] is most likely due to the inclusion of motional narrowing effects. Above 2000K it is very much more difficult to compare CARS temperatures to recognised temperature standards. However, by measuring CARS nitrogen gas temperatures inside a specially designed incandescent lamp filament[32,33] it has been possible to relate CARS temperature measurements to two-colour pyrometer measurements[33,58,2]. Care has to be taken to ensure that gas and filament temperatures are in equilibrium, if this is achieved excellent agreement (of order 1%) is found between filament (pyrometer) and gas (CARS) temperatures. To illustrate this a CARS spectrum at 3500K is shown in Figure 7. In conclusion, for atmospheric pressure, CARS "average" thermometry
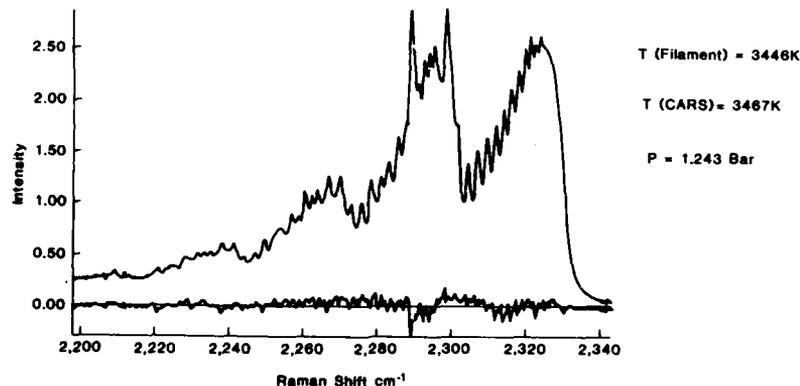
FIG. 7. CARS Spectrum from inside a Tungsten Filament. Upper Trace Experiment, Lower Trace Theory-Experiment

accuracy is of order 1-1.5% from 300K to 3500K, the worst region for accuracy lies between 700 and
1100K where the vibrational hot bands are almost absent and the overall rate of change of spectral
shape with temperature is a minimum[29].

At high pressures, typical of gas turbine primary zones or i.c. engines, (e.g. 0-40 bar) the
effects of motional narrowing are vitally important. Its effect on accuracy may be dramatically judged
from Figures 8 and 9. In both these figures the same "conditionally averaged" i.c. engine CARS
spectrum, taken in the compressed charge prior to ignition, has been analysed using CARS models with
and without motional narrowing effects. The error, 190K in 876K, is considerable. In these CARS
experiments the term "conditionally averaged" means that many CARS spectra (say 50+) are summed
together for the same conditions of engine crank angle and in-cylinder pressure. Comparison of theory
and experimental data of this type are certainly useful in excluding CARS models and rotational
relaxation models that do not work. A better test of accuracy comes from comparison with measurements
of nitrogen gas under known conditions. Recently, measurements of CARS in isobaric, isothermal N_2 for
the range 300 to 800K and from 1 to 20 bar have been made. In order to ensure that the test gas was
perfectly homogeneous the complete test cell was heated. The cell and surrounding oven are shown in
the photograph in Figure 10. The principal problem with this approach is to maintain an effective seal
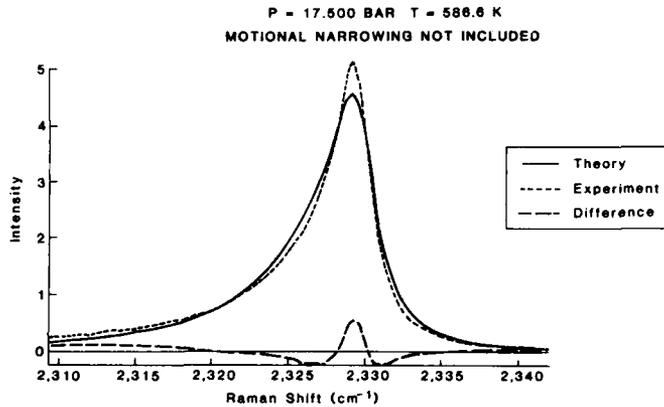
FIG. 8. Pre-Combustion I.C. Engine CARS Spectrum, Fitted using an Isolated lines Model
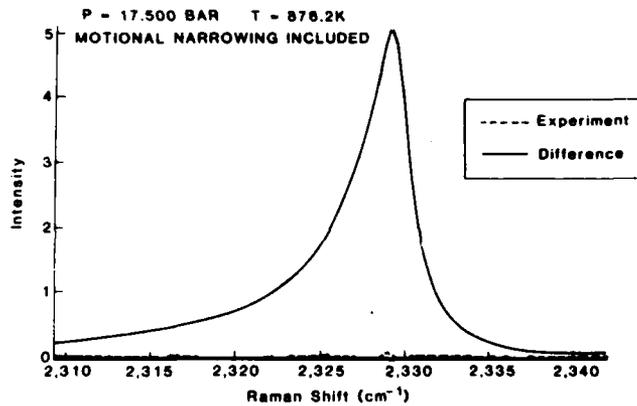
FIG. 9. Pre-Combustion I.C. Engine CARS Spectrum (as Fig. 8), Fitted Using CARP-2 (ref. 57)
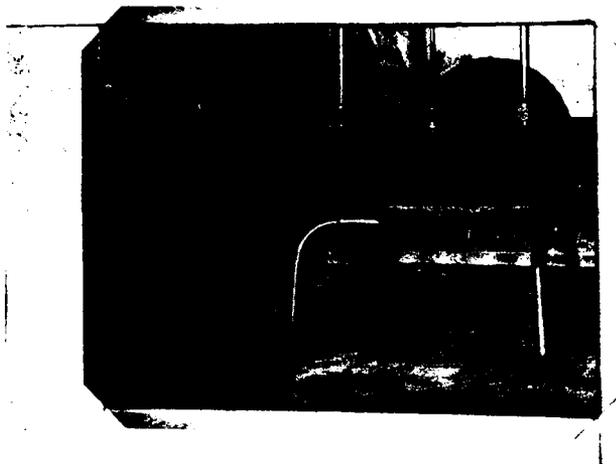
FIG. 10. Photograph of The Farwell Isothermal High Pressure, High Temperature Test Cell

between the windows and the high pressure stainless steel test cell. This has been achieved by using a differentially expanding sealing system where a high expansion packing washer is included. By this means stable isobaric, isothermal gas is created inside a 300 mm long cylinder. Excellent agreement between experimental and theoretical CARS spectra has been obtained for all temperatures and pressures. However, the accuracy of the CARS technique may be judged from Figure 11 where some preliminary data is presented. At the time of writing the data available from the test cell was only for a preliminary study where the sapphire windows employed were not properly "c" cut; consequently the windows exhibited a slight time and temperature dependent birefringence. This resulted in some small random distortions to the experimental CARS spectra. Therefore the present results are only preliminary. The problem has now been rectified and an improved set of data will shortly be published[59]. Nevertheless, Figure 11 shows that there are no specific systematic errors for the complete region up to 700K and 20 bar. The scatter on the data primarily results from the slight random birefringence.

PRELIMINARY CARS MEASUREMENTS
in the high temperature/high pressure cell
(Horizontal lines indicate thermocouple temperatures)
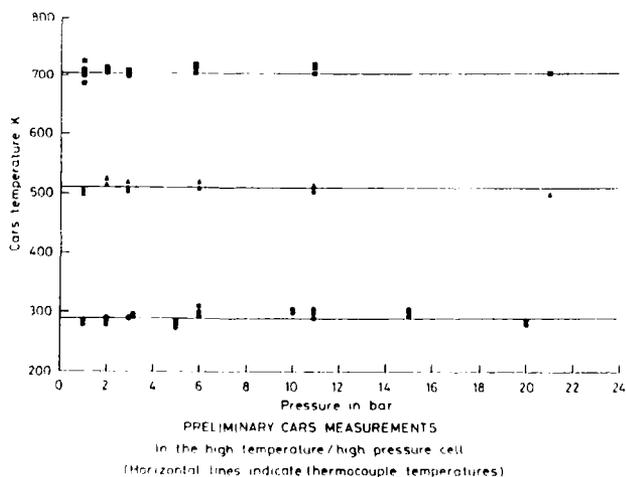
FIG. 11. Comparison of CARS and Thermocouple Temperatures 0-700K, 0-20 bar

These tests establish CARS accuracy from 300-3500K at 1 bar and from 300-800K up to 20 bar. For very high temperatures and pressures the testing of CARS accuracy awaits development of an appropriate test device. However, as will be shown later, for typical post i.c. engine combustion CARS data of circa 2300K and 30 bar, the choice of relaxation rate model is far less critical than that for temperature and pressures up to 1000K and 20 bar.

A major feature of the CARS technique is its capability to make instantaneous measurements. Unfortunately such CARS data is subject to additional noise, typically 8%[1] but sometimes larger. A principal source of the noise lies in the broadband dye laser used in the CARS instrument. Typical broadband dye lasers produce spectral profiles which possess an observed r.m.s. noise of order 8-10%. The source of this noise has been studied both experimentally[11,60-62] and theoretically[60,63]. Attempts have been made to account for the noise on a purely schematic basis[11,61,63] however a detailed theoretical model[60,63] which shows excellent agreement with measurements[60] and accounts for reported experiments[60] now exists. This published theoretical model[60,63] is used as the basis for the discussion that follows.

Essentially a broadband dye laser consists of a spectral 'comb' of individual frequencies. The 'comb' is formed from the longitudinal modes of the Fabry-Periot cavity of the laser where individual modes are separations are on the order of 0.01 cm^{-1}. Over the whole spectral profile, of 150 cm^{-1} there may be upwards of 10^4 modes. The phase and intensity of each mode is determined by the thermal or spontaneous emission processes, at the start of the laser pulse with the exited gain medium of the dye laser. Such thermal processes have exponential statistics and may be considered to possess 100% noise. As a consequence, the observed noise for a broadband laser, measured using a multichannel/spectrograph detector with a resolution of say 1 cm^{-1}, is approximately 8-10%[1,60]. Essentially the observed noise on a pixel is inversely proportional to the square root of effective modes sampled (e.g. sampling 50% of 1 mode and 100% of another gives 1.5 effective modes). Figure 12 shows an example of dye laser noise as it appears in the CARS spectrum for a purely non-resonant signal. The appearance of this noise in the final CARS spectrum has been postulated to nearly follow that of the input Stokes[60] laser[60]. This postulate is substantially supported by recent theoretical work[63]. This theoretical work clearly shows that, for certain conditions, additional noise will arise in the CARS signal. The most important case arises when the pump length of the pure laser becomes short compared to the round trip time of the broadband dye laser. When this arises essentially a restricted sub set of modes of the dye or Stokes laser are sampled in the CARS process, this reduces the effective number of modes and results in increased noise in the CARS signal.

Wavelength
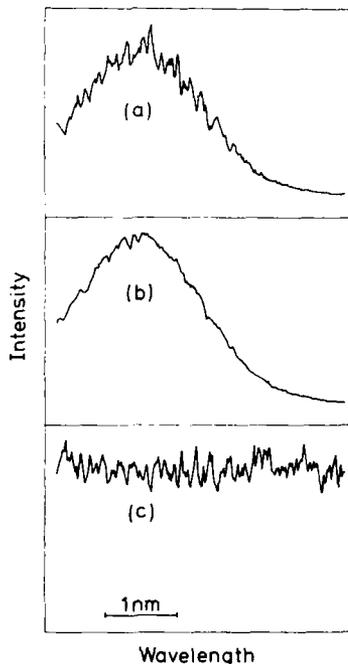
FIG. 12. Examples of Single Pulse CARS Noise: (a) Single Pulse CARS Spectrum of X_{NR}, (b) 100-Pulse Average CARS Spectrum of X_{NR}, (c) a divide by b.

The effect of dye laser cavity length on noise is illustrated in Figures 13 and 14. In Figure 13 purely broadband dye laser noise for two simple laser cavities is compared with theory[64]. Note the excellent agreement for the plane-plane cavity case. Comparison of theory and experiment for the stable cavity case is not very good, principally because it was not possible to accurately estimate the number of transverse modes and their relative intensities as a function of cavity length. However, note that measured noise for this laser asympotically approaches the Amplified Spontaneous Emission (ASE) points which correspond to the total number of modes being restrocted by the laser pulse length according to the uncertainty principle. In Figure 14 observed CARS noise is compared with theory. Note, in particular, that the biggest discrepancy between theory and experiment is at the longest cavity lengths where the criterion for pump laser pulse being much greater than rount trip time is only marginally valid. The noise experiments reported in Ref. 60 correspond to a "phase delayed" BOXCARS experiment where the two pump components do not arrive at exactly the same instant in the control volume. For colinear or non-phase delayed experiments temporal reinforcement of the pump laser fluctuations is likely to lead to an effective shortening of the observed CARS pulse. Consequently anti-Stokes noise from such experiments may be higher. At Harwell colinear CARS experiments have been found to be generally noisier than phase delayed BOXCARS using equivalent lasers.
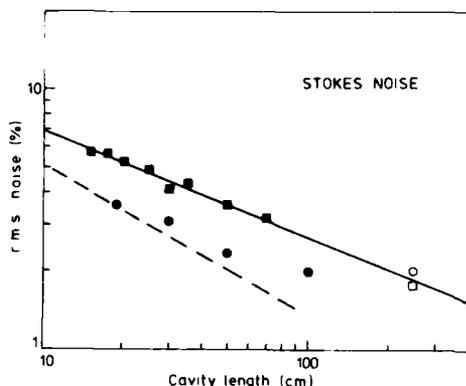
FIG. 13. Stokes Laser Noise Versus Cavity Length. Squares and Continuous Line Experiment and Theory for a Simple Plane-Plane Laser Cavity. Dashes and Dots are the Same for a Stable Laser Cavity. Open Symbols are ASE Measurements.
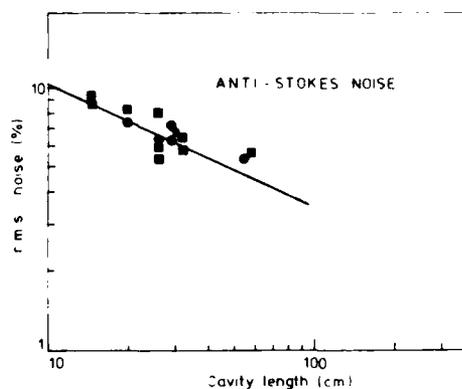
FIG. 14. Theory (ref. 60) Continuous Line, Squares and Dots CARS Noise as per Cavities for Fig. 13.

Fortunately careful choice of dye laser design can reduce this noise[60] and such a noise reducing design has been employed throughout this work. Clearly there is also a need to choose multimode lasers with long, rather than short, pulse lengths. Alternatively, single mode Nd:YAG lasers can be employed [30,62], if in future satisfactory rugged and cost effective designs may become available[64] then this may become the preferred option. However, the accuracies reported below, using a multimode CARS pump laser, are essentially identical to those using a single mode laser[30], thus the gain in using a single mode laser may not be substantial. Also, for practical measurements, detector noise may be as least as important; this is discussed next.

A second source of noise, in instantaneous CARS, lies in the ccunting statistics of the detector (65,66). A typical CARS signal contains a peak of say 10^3-10^5 photons per detector channel. Typically 1/10 of these photons are detected by the multichannel detector. The observed uncertainty will, according to well known Poisson statistics for photons, be $\sqrt{N}$ where N is the number of observed photons. A simple minded analysis may assume that such noise appears independently on individual channels; however, in practice, cross talk in the detector cause correlations of order 2-4 channels. Therefore the Poisson or shot noise will be weighted to the lower spatial frequencies of the multichannel detector. Interpreting this effect, together with the complex shape and temperature dependence of a CARS spectrum, does not lead to a straightforward analysis. Consequently, we have experimentally investigated the combined effect of dye laser and detector noise using instantaneous CARS data from an isothermal tube furnace[29,31]. In these experiments 100 instantaneous CARS spectra were recorded for various known temperatures between 300 and 1000K and for various average 'peak' detector counts. All CARS spectra were then processed using QUICK[57] and the 1σ CARS temperature uncertainty determined: these results are summarised in Figure 15. Two points are clear. Firstly the detector Poisson noise contributes a major part of the temperature measurement uncertainty for signal levels below 2500 counts (our maximum detector range is 16,383 counts). Secondly, dye laser noise, described above, dominates only for very strong CARS signals. The marked contributon of detector noise to temperature uncertainty might appear to be surprising, however as already pointed out, careful consideration must be given to the correlation properties of the noise which arises from the 3-4 channel detector cross-talk, together with the large range of intensity and temperature sensitivity of the the various parts of a CARS spectrum.

TEMPERATURE σ vs $1/COUNT**0.5$
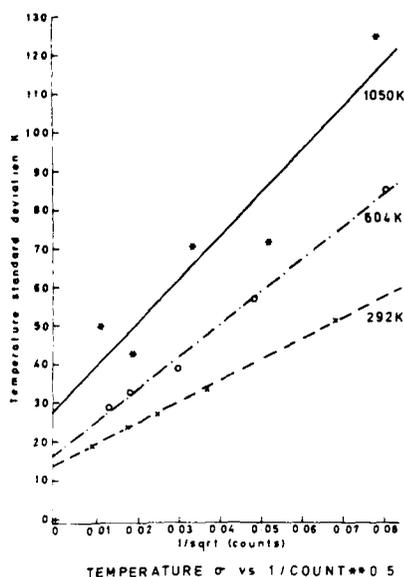
FIG. 15. CARS Instantaneous Thermometry Uncertainty for Various Temperatures

Detector noise will be particularly devastating on an analysis method which places undue weight on the lower intensity portions of a spectrum. Undoubtedly, this explains our success with least squares analysis of the full spectrum and the unreliability of simpler analysis algorithms[29]. The potential overall accuracy for instantaneous CARS is seen to be of order 4%, based on extrapolations of Figure 15 to infinite detector counts. This is based on a least-squares analysis method and the multimode pump laser. However, typical accuracies are closer to 6-7% with detector noise contributing approximately 50% of this uncertainty (assumes 1000 to 2000 counts on a 16000 count range detector). It is therefore clear that dye laser noise is by no means the sole factor in current instantaneous CARS thermometry. Schemes designed to limit the use of low intensity CARS signals[67-69] will be vital for optimum accuracy in the study of turbulent combustion.

5. APPLICATIONS OF CARS THERMOMETRY

5.1 Production Petrol I.C. Engines

CARS thermometry has been successfully applied to the study of combustion processes in a production two-litre petrol engine for a range of conditions of speed and load which are realistic of all conceivable drive conditions. These experiments have been supported by an industrial consortia[70]. The CARS experiment is illustrated in the photograph in Figure 16. CARS experiments on such an engine must access the combustion space through two small (typically 4 mm dia) windows. In order to optimise signal strength through the limited optical access colinear CARS is used. Colinear CARS spatial resolution can be controlled by choosing the correct beam size combinations[65]. In these experiments care is taken to ensure (1) that the Stokes laser beam diameter is made much smaller say $1/3$ of the pump laser prior to the field lens (typically 10 cm focal length) which focuses both beams to the measurement point, and (2) the pump laser is essentially TEM_{oo}. This procedure ensures phase matching and thus efficient signal generation is effective only over 3-4 mm length around the focus. Recent theoretical work[71] supports this experimental finding. Typical for a homogeneous environment the effective interaction length is closer to 1 mm. By careful testing we have found that in the worst creditable situation, 2400K nitrogen at the measurement point and 700K say 10 mm away we induce errors of less than 1%.

FIG. 16. Photograph of 2-Litre Production Petrol Engine with CARS Thermometry Instrument
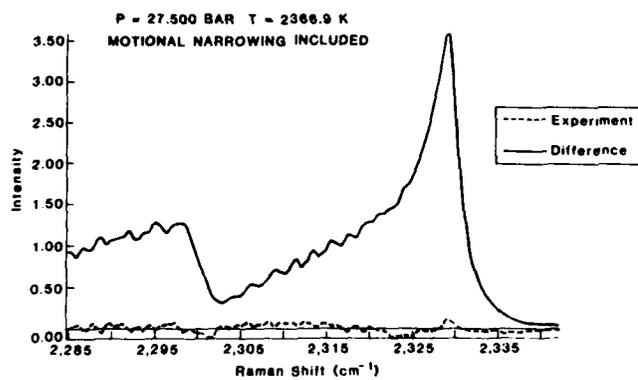
FIG. 17. Post COmbustion CARS Spectrum from a Production Petrol Engine.

Examples of the high quality data obtained from the operating engine, both for a precombustion (824K and 17.5 bar) and post combustion (2317K and 27.5 bar) spectra are shown in Figure 9 and Figure 17 respectively. The calculation for Figure 17 also employed the same parameterisation of equation 13. However fractionally better agreement was obtained using values of b = c of 3.5 with associated small changes to K and a to maintain agreement with known linewidth data. These increases in b and c produce a superficially better agreement to the experimental engine data but the 'fitted' temperature only differs by approximately 30K from that obtained using the original values for b and c. Since this experimental CARS data was taken from a real engine, one cannot conclude that these adjustments are physically real. The engine data has been 'conditionally averaged' for some 50 engine cycles with the condition that crank angle and in-cylinder pressure are constant. The in-cylinder gas is almost certainly not exactly equivalent from cycle to cycle for the post combustion gases and some small biasing of the experimental data may have occurred. However, recent theoretical work of Hall[52] using the Energy Corrected Sudden theory, supports the idea that b and c should slightly increase with increasing temperature. We are currently seeking a satisfactory source of isothermal nitrogen at 1500K - 2500K for pressures greater than 15 bar to complete the testing of our computer model and to resolve this small uncertainty.

5.2 30K watt Oil Fired Furnace
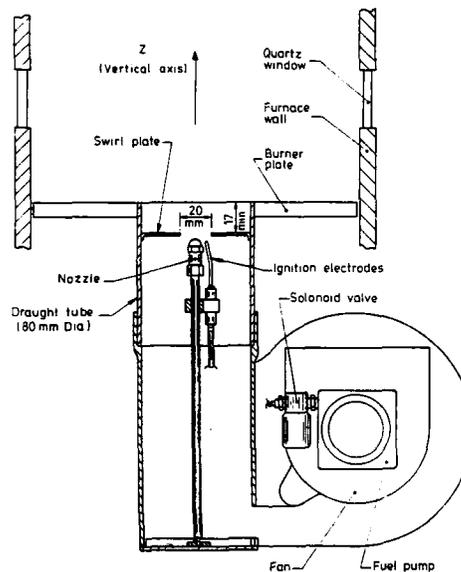
FIG. 18. Schematic Diagram of Burner Assembly of 30KW Oil-Spray Furnace

The essentials of the furnace are shown diagrammatically in Figure 18. Briefly it consists of a hollow 0.3 m diameter water cooled cylinder fitted with an opposing pair of quartz windows; this allows optical access across a diameter for various heights. The burner consists of an oil-jet atomiser centred in a swirl vane. The latter supplied with air at nominally S.T.P. by a blower. The furnace was mounted on an x, y traverse, and the burner on a vertically (z axis) adjustable platform. This allows the CARS measurement volume to be positioned within a radial plane covering the central 50% of the furnace tube diameter and from 4 cm to 40 cm above the burner plate. The fuel was kerosene and was supplied at a pressure of 690 kPa (100 psi) and at a flow rate of 2.8×10^{-3} m^3/hr and air was supplied at 1.1 m^3/min.

The results of CARS thermometry are shown in Figures 19 to 22. The map of average temperatures in degrees Kelvin, Figure 19, shows a slight asymmetry which is consistent with a known velocity asymmetry in the furnace[72]. These temperatures have been used to compare computer models of droplet behaviour in combustion; comparisons with this CARS data have been published elsewhere[73].
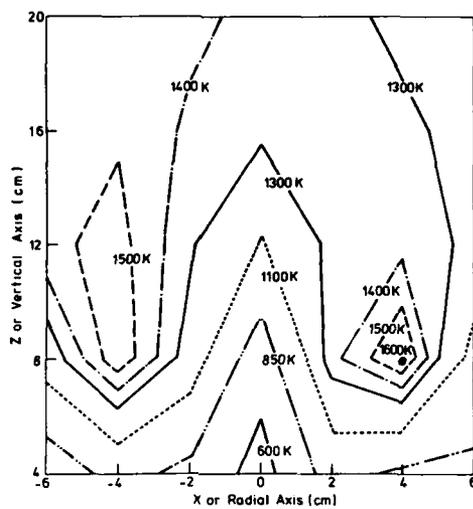
FIG. 19. Map of Average CARS Temperature Across a Diameter of the 30KW Oil-Spray Furnace
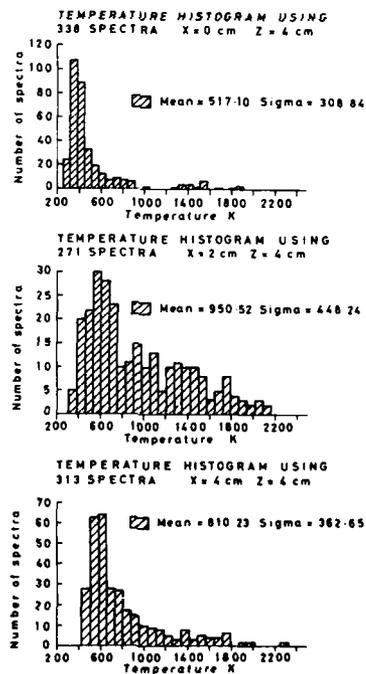
FIG. 20. P.d.f's from Instantaneous CARS Temperatures at a Height of z = 4 cm Above the Burner Plate
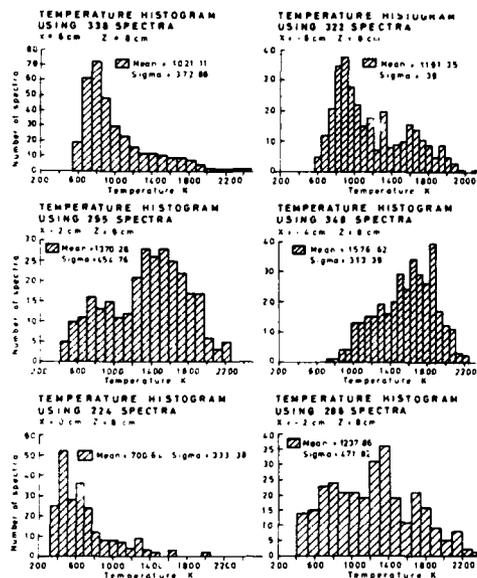
FIG. 21. P.d.f's from Instantaneous CARS Temperatures at a Height of z = 8 cm Above the Burner Plate
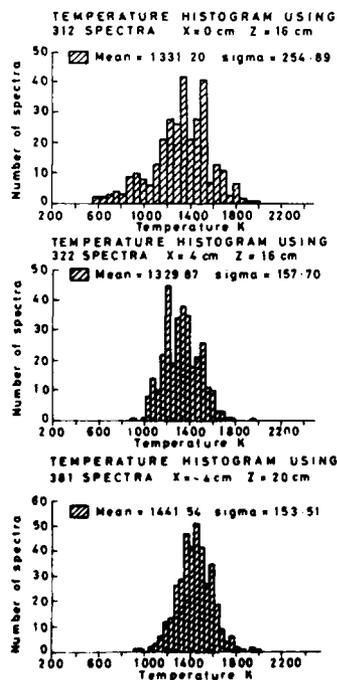
FIG. 22. P.d.f's from Instantaneous CARS Temperatures at a Height of z = 16 cm and z = 20 cm Above the Burner Plate
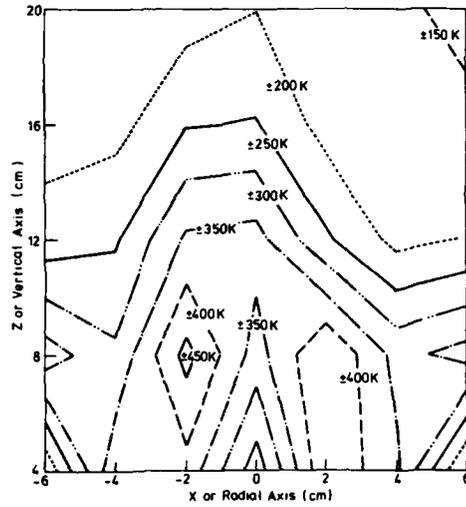
FIG. 23. Map of 1σ Temperature Variance Corrected for CARS Instrument Contributions in the 30 kW Oil-Spray Furnace
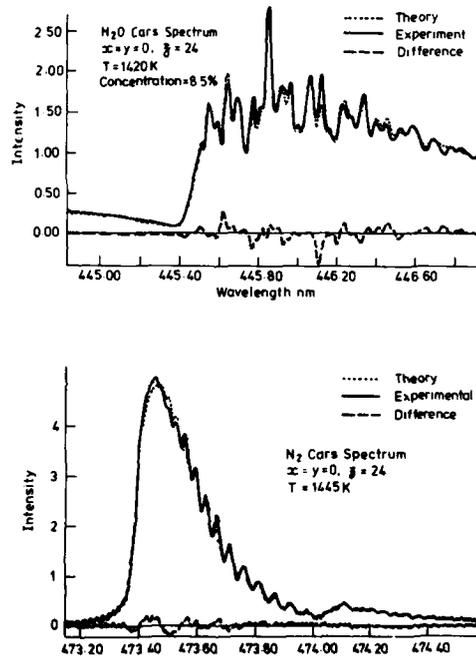
FIG. 24. Average CARS Spectra of Water Vapour and Nitrogen Measured at the Same Point in the Post-Flame Zone of the 30 kW Oil-Spray Furnace

The form of the temperature fluctuations for two radial heights ($z = 4$ cm and $z = 8$ cm) are shown in Figures 20 and 21. Note that for temperature measurements near the flame sheet ($x = 2$ at $z = 4$ and $x = 2$ or 6 at $z = 8$) bimodal temperature distributions are observed, this is intuitively expected if pockets of burnt and unburnt gases randomly pass through the measurement point. In general we found that the p.d.f's of temperature were markedly non-Gaussian in and around the burning fuel spray. Maximum temperature turbulence levels of ± 80% around the mean (measured near the centre of the fuel spray at $z = 4$ cm) drop to ± 10% in the post-flame zone. In the post-flame zone the p.d.f's are close to normal Gaussians, Figure 22. However, these levels of turbulence are significantly larger than our instantaneous measurement uncertainty of approximately ± 5% in the post-flame to say ± 10% at worst actually in the oil spray. A plot of temperature variance is shown in Figure 23. The variances shown are corrected for the instrument uncertainty. Peaks in the turbulence level are seen in the centre of the fuel spray and around its edges, where we assume the burning front is located.

We have successfully measured CARS spectra of H_2O, CO_2 and O_2 as well as N_2 in this oil spray furnace. To date we have processed some of the H_2O data. Figure 24 shows CARS spectra of nitrogen and water from the same point in the post-flame zone. Note that (i) the independent measurements of temperature agree within 20K and (ii) the concentration of water is found to be 8.5%. This concentration is consistent with the known approximately 75% excess air and assumes full mixing of the post-flame gases (Kerosene is a C_{12}-C_{16} paraffin thus perfect stoichiometry would yield 15% H_2O). Further confidence in concentration measurements of water vapour await improved spectra data, particuarly linewidths. Some recent work in this area has recently been completed[74] and further is planned, improved accuracy should then be forthcoming. This example importantly illustrates that thermometry and species concentration measurements are simultaneously possible.

6. CONCLUSIONS

The theory and application of CARS thermometry has been discussed and the need for high quality, accurate spectral models is shown. Important aspects affecting accuracy include:- motional narrowing, finite laser bandwidth effects, accurate spectral modelling, dye laser noise and detector noise. The average accuracy of CARS thermometry is generally found to be of order 1-1.5%. Instantaneous thermometry is shown to have a practical accuracy of 6-7%. The generality of CARS thermometry has been established with examples of application to two industrial combustion systems, (1) a two-litre production petrol (gasoline) engine and (2) a 30 kilowatt oil fired furnace.

7. ACKNOWLEDGEMENTS

REFERENCES

(1) GREENHALGH, D.A., ENGLAND, W.A. and PORTER, F.M. "The Application of CARS to Turbulent Combustion Thermometry." Combustion and Flame, Vol.49, (1983) p.171.

(2) GREENHALGH, D.A. and PORTER, F.M. "CARS Temperature Measurements in a 30 kW Oil-Fired Furnace". Harwell Report AERE-R12221 (1986).

(3) STENHOUSE, I.A., WILLIAMS, D.R., COLE, J.B. and SWORDS, M.D. "CARS on an Internal Combustion Engine". Appl. Opt., Vol.18, (1979) pp.3819-3825.

(4) ENGLAND, W.A., MILNE, J.M., JENNY, S.N. and GREENHALGH, D.A. (1984) "Application of CARS to an Operating Chemical Reactor". Appl. Spectrosc., Vol.38, p.867-875.

(5) PEALAT, M., TARAN, J-P.E. and MOYA, F. (1980) "CARS Spectrometer for Gases and Flames". Opt. Laser Technol., Vol.12, p.21.

(6) KLICK, D., MARKO, K.A. and RIMAI, L. (1981) "Broadband Single-Pulse CARS Spectra in a Fired Internal Combustion Engine". Appl. Opt., Vol.20, p.1178.

(7) KAJIYAMA, K., SAJIKI, K., KATAOKA, H., MAEDA, S. and HIROSE, C. "N_2 CARS Thermometry in a Diesel Engine". (1982) SAE Technical Paper, 821036.

(8) FERRARIO, A. and MALVICINI, C. "Real Time Temperature and Concentration Measurements in a Semi-Induced Furnace with CARS Spectroscopy". NATO ASI Ser., Ser. B; Vol.19, (1985) pp.89-105.

(9) HARTFORD, A., CREMERS, D.A., LOREE, T.R., QUIGLES, G.P., RADZIEMSKI, L.J. and TAYLOR, D.J. "Optical Instrumentation for On-Line Analysis of Chemical Processes" Proc. SAE - Inf. Soc. Opt. Eng., Vol.411, (1983) pp.92-6.

(10) MURPHREE, D., COOK, R.L., BAUMAN, L.E., BEITING, E.J., STICKEL, R.E., DAUBACH, R.O. and ALI, M.F. (1982), AIAA Paper 85-0377.

(11) ECKBRETH, A.C., DOBBS, G.M., STUFFLEBEAM, J.H. and TELLEX, P.A. "CARS Temperature and Species Measurements Augmented Jet Engine Exhaust". Appl. Opt., Vol.23, (1984) pp.1328-1339.

(12) ALDEN, M. and WALLIN, S. "CARS Experiments in a Full-Scale (10x10) Industrial Coal Furnace". Appl. Optics, Vol.24, (1985) pp.3434-3437.

(13) GREENHALGH, D.A., WILLIAMS, D.R. and BAKER, C.A. "CARS Thermometry in a Firing Production Petrol Engine". Proc. 'Autotech' Conference, I.Mech.E., Birmingham (1985).

(14) GREENHALGH, D.A. and WILLIAMS, D.R. "Modelling of CARS N_2 Spectra for In-cylinder Engine Research" Harwell Report AERE-R12222 (1986).

(15) ENGLAND, W.A., GLASS, D.H.W., BRENNAN, G. and GREENHALGH, D.A. "Study of a Tube Wall Methanation Reaction using CARS Spectroscopy". J. Catalysis, accepted for publication (1986).

(16) GREENHALGH, D.A., HALL, R.J., PORTER, F.M. and ENGLAND, W.A. "Application of the Rotational Diffusion Model to the CARS Spectra of High Temperature, High-Pressure Water Vapour". J. Raman Spectrosc., Vol.15, (1984) pp.71-79.

(17) HATA, N., MATSUDA, A. and TANAKA, K.I. "Neutral Radical Detection in Silane Glow-Discharge Plasma Using Anti-Stokes Raman Spectroscopy". J. Non-Cryst. Solids. Vol.59-60, (1983) pp.667-670.

(18) DRUET, S. and TARAN, J-P.E. "Coherent Anti-Stokes Raman Spectroscopy". In Lasers (Moore, C.B., Ed.) (1979) Academic, New York.

(19) NIBLER, J.W. and KNIGHTEN, G.V. "Coherent Anti-Stokes Raman Spectroscopy". In Raman Spectroscopy of Gases and Liquids. (Weber, A., Ed.) (1979) Springer, Berlin.

(20) HALL, R.J. and ECKBRETH, A.C. "Coherent Anti-Stokes Raman Spectroscopy (CARS) : Applictions to Combustion Diagnostics". In Laser Applications, Vol.5, (1984) (Erf, R.K., Ed.) Academic, New York.

(21) ECKBRETH, A.C. "BOXCARS : Crossed Beam Phase-Matched CARS Generation in Gases". Appl. Phys. Lett., Vol.32, (1978) pp.421-423.

(22) SHIRLEY, J.A., HALL, R.J., ECKBRETH, A.C. "Folded BOXCARS for Rotational Raman Studies". Opt. Lett. Vol.5, (1980) pp.380.

(23) GREENHALGH, D.A. "Comments on the Use of BOXCARS for Gas-Phase CARS Spectroscopy". J. Raman. Spec., Vol.14, (1983) pp.150-153.

(24) DAVIS, L.C., MARKO, K.A. and RIMAI, L. "Angular Distribution of Coherent Raman Emission in Degenerate Four-Wave Mixing with Pumping by a Single Diffraction Coupled Laser Beam : Configurations for High Spatial Resolution". Appl. Opt. Vol.20, (1981) p.1685.

(25) ALDEN, M., FREDRIKSON, K.A. and WALLIN, S. "Application of a Two-Colour Dye Laser in CARS Experiments for Fast Determination of Temperatures". Appl. Opt. Vol.23, p.2053 (1984)

(26) BEATTIE, I.R., GILSON, T.R. and GREENHALGH, D.A. "Low Frequency Coherent ti-Stokes Raman Spectroscopy of Air". Nature, 276, (1978) pp.378-379.

(27) ZHENG, J., SNOW, J.B., MURPHY, D.V., LEIPERTZ, A., CHANG, R.K. and FARROW, R.L. "Experimental Comparison of Broadband Rotational Coherent Anti-Stokes Raman Scattering (CARS) and Broadband Vibrational CARS in a Flame". Opt. Lett, Vol. 9, (1984) pp.341-343.

(28) LASSER, Th., MAGENS, E. and LEIPERTZ, A. "Gas Thermometry by Fourier Analysis of Rotational Coherent Anti-Stokes Raman Scattering". Opt. Lett. Vol.10, (1985) pp.535-537.

(29) PORTER, F.M. "A Study of Temperature Measurements Using Coherent Anti-Stokes Raman Spectroscopy". PhD Thesis, (1985) University of Surrey, U.K.

(30) PEALAT, M., BOUCHARDY, P., LETEBVRE, M. and TARAN, J-P. "Precision of Multiplex CARS Temperature Measurements". Appl. Opt. Vol.24, (1985) pp.1012-22.

(31) GREENHALGH, D.A. and PORTER, F.M. "CARS Applications in Chemical Reactors, Combustion and Heat Transfer". Proc. 1st Int. Laser Sci. Conf. Dallas, Texas, November (1985).

(32) GREENHALGH, D.A., DRING, I., DEVONSHIRE, R., BOYSON, F. and WARMBY, E.O., patent applied for.

(33) GREENHALGH, D.A., DRING, I. and DEVONSHIRE, R. "The Accuracy of CARS Thermometry at Ultra High Temperatures", (1986) to be published. Also see reference 58.

(34) HALL, R.J. and BOEDEKER, L.R. (1984) "CARS Thermometry in Fuel-Rich Combustion Zones". Appl. Opt., Vol.23, pp.1340-1346.

(35) DEWITT, R.W., HARVEY, A.B. and TOLLES, W.M. "Theoretical Development of Third-Order Susceptibility as Related to Coherent Anti-Stokes Raman Spectroscopy". NRL Memo. Rep. (1976) NRL-MR-3260.

(36) GORDON, R.G. and MCGINNIS, R.P. J. Chem. Phys. "Line Shapes in Molecular Spectra". Vol.49, (1968) p.2455.

(37) KOSZYKOWSKI, M.L., FARROW, R.L. and PALMER, R.E. "Calculation of Collisionally Narrowed Coherent Anti-Stokes Raman Spectra". Opt. Lett. Vol.10, (1985) p.478.

(38) KATAOKA, H., MAEDA, S, HIROSE, C. and KAJIYAMA, K. "A Study for Diatomic Nitrogen Coherent Anti-Stokes Raman Spectroscopy Thermometry at High Pressure". Appl. Spectrosc., Vol.37, (1983) pp.565-512.

(39) TEETS, R.E. "Accurate Convolutions of Coherent Anti-Stokes Raman Spectra". Opt. Lett., Vol.19, (1984) p.226.

(40) HALL, R.J., VERDIECK, J.F. and ECKBRETH, A.C. "Collisional Narrowing of the High Pressure CARS Spectrum of Diatomic Nitrogen". Opt. Comm., Vol.35, (1980) p.69.

(41) HALL, R.J. and GREENHALGH, D.A. "Application of the Rotational Diffusion Model to Gaseous N_2 CARS Spectra". Opt. Comm., Vol.35, (1980) p.69.

(42) HALL, R.J. "Coherent Anti-Stokes Raman Spectroscopic Modelling for Combustion Diagnostics". Opt. Eng. Vol.22, (1983) pp.322-329.

(43) GREENHALGH, D.A. and HALL, R.J. "A Closed Form Solution for the CARS Intensity Convolution". Opt. Comm., Vol.57, (1986) pp.125-128.

(44) BOVANICH, J.P. and BRODBECK, C. "Vibration Rotation Matrix Elemens for Diatomic Molecules; Vibration Rotation Interaction Functions $F_\nu^{\nu'}$ (m) For CO. J. Quant. Spectrosc. Radiat. Transfer Vol.16,(1976) p.153.

(45) KOSZYKOWSKI, M.L., RAHN, L.A. and PALMER, R.E. "Theoretical and Experimental Studies of High-Resolution Inverse Raman Spectra of N_2 at 1-10 atm". Submitted for publication to J. Phys. Chem. (1986).

(46) BRUNER, T.A. and PRITCHARDS, D.E. "Fitting Laws for Rotationally Inelastic Collisions". In Advances in Chemical Physics, Dynamics of the Excited Sate, (K.P. Lawley, Ed.) Wiley, New York (1982) pp.589-641.

(47) GREENHALGH, D.A., PORTER, F.M. and BARTON, S.A. "A Polynomial Energy-Gap Model for Molecular Linewidths". J.Quant. Spectrosc. Radiat. Transfer. Vol.34, (1985) pp.95-99.

(48) ROSASCO, G.J., LEMPERT, W. and HURST, W.S. "Line Interference Effects in the Vibrational Q-Branch Spectra of N_2 and CO". Chem. Phys. Lett. Vol.97 (1985) p.435.

(49) RAHN, L.A., OWYOUNG, A., COTTON, M.E. and KOSZKOWSKI, M.L. Proc. 7th Int. Raman Conference, (Murphy, W.F., Ed.), North Holland, Amsterdam, (1980) p.694.

(50) RAHN, L.A. Private communication of preliminary inverse Raman linewidth data of nitrogen at 1280K.

(51) RAHN, L.A. and PALMER, R.E. "N_2 Raman Linewidth for CARS measurements of Temperature and Major Species Concentrations in Flames". Submitted to J. Opt. Soc. Am. (B) (1986)

(52) HALL, R.J. (1985) "Rotationally Inelastic Rate Calculations using the Energy Corrected-Sudden (ECS) Scaling Law". (1985) Harwell Report AERE-R 11888.

(53) KREUTNER, W., STRICKER, W. and JUST, T. "Temperature Measurements in Flames by Laser Raman Techniques". Ber. Bunsenges, Phys. Chem. Vol.87, (1983) pp.1045-1048.

(54) LAVOREL, B., MILLOT, G., SAINT-LOUP, R., WENGER, C., BERGER, H., SALA, J.P., BONAMY, J. and ROBERT, D. "Rotational Collisional Line Broadening at High Temperatures in N_2 Fundamental Q-Branch Studied with Stimulated Raman Spectroscopy" J. Physque 47, (1986) to be published.

(55) SALA, J.P., BONAMY, J., ROBERT, D., LAVOREL, B., MILLOT, G. and BERGER, H. "A Rotational Thermalisation Model for the Calculation of Collisionally Narrowed Isotropic Raman Scattering Spectra - Application to the S.R.S. N_2 Q-Branch" to be published (1986).

(56) HALL, R.J. and GREENHALGH, D.A. Results to be published (1986).

(57) CARP2, QUICK and QUICK2D are UKAEA copywright computer codes for the analysis of CARS spectra and have been developed at Harwell. Sub-licences for these codes are available from Epsilon Research Limited, Paynes Lane, Rugby, U.K.

(58) GREENHALGH, D.A., DRING, I. and DEVONSHIRE, R. "CARS Thermometry at Ultra High-Temperatures", submitted to the 10th Int. Raman Conference, Oregon, (1986).

(59) GREENHALGH, D.A., WILLIAMS, D.R. and BAKER, C.A. "CARS Thermometry for Production I.C. Engines; Its Accuracy and Application", to be published (1986).

(60) GREENHALGH, D.A. and WHITTLEY, S.T. "Mode Noise in Broadband CARS Spectroscopy". Appl. Optics. Vol.24 (1985) pp.907-913.

(61) ECKBRETH, A.C. and STUFFLEBEAM, J.H. "Considerations for the Application of CARS to Turbulent Reacting Flows". Expt. in Fluids, Vol.3 (1985) p.301.

(62) SNELLING, D.R., SAWCHUK, R.A. and MUELLER, R.E. "Single Pulse CARS Noise : A Comparison Between Single-Mode and Multimode Pump Lasers". Appl. Opt. Vol.24, (1985) pp.2771-2778.

(63) HALL, R.J. and GREENHALGH, D.A. "The Noise Properties of Single Pulse CARS Spectroscopy with Multimode Pump Sources". Submitted to J. Opt. Soc. Am. (B) (1986).

(64) RAHN, L.A. "Feedback Stabilization of an Injection Seeded Nd:YAG Laser". Appl. Opt. Vol.24 (1985) pp.940-942.

(65) SNELLING, D.R., SAWCHUK, R.A. and SMALLWOOD, G.J. "Multichannel Light Detectors and the use for CARS Spectroscopy". Appl. Opt. Vol.23 (1984) pp.4083-4089.

(66) ANTCLIFF, R.R., HILLARD, M.E. and JARRETT Jr. 0. "Intensified Silicon Photodiode Array Linearity : Application to Coherent Anti-Stokes Raman Spectroscopy". Appl. Opt. Vol.23, pp.2369-2375.

(67) GOSS, L.P., SWITZER, G.L., TRUMP, D.D. and SCHREIBER, P.W. "Temperature and Species - Concentration Measurements in Turbulent Diffusion Flames by the CARS Technique". AIAA Paper No. 82-0240 (1982).

(68) ECKBRETH, A.C. "Optical Splitter for Dynamic Range Enhancement of Optical Multichannel Detectors". Appl. Opt. Vol.22 (1983) pp.2118-2123.

(69) MAGRE, P., PELAT, M. and COLLIN, G. "Mesures par DRASC de Températures et de Concentration dans les Flammes". (1986) ibid.

(70) The Petrol Engine Working Party (PEWP) is a principally industrial consortia concerned with the application of advanced diagnostic techniques to petrol fuelled i.c. engines and currently consists of B.P. UK Dept of Trade and Industry, Ford UK., Jaguar and Lucas.

(71) TEETS, R.E. "CARS Signals : Phase Matching Traverse Modes, and Optical Damage Effects". Appl. Opt. Vol.25 (1986) pp.855-862.

(72) BOSLEY, R.B. and NEGUS, C.R. "Determination of Flow Characteristics in a Model Furnace using the LDA Technique". Harwell Report AERE-R11814 (1985).

(73) STOPFORD, P.J. and LEVER, D.A. "Oil-Spray Modelling". Harwell Report AERE-R12134 (1985).

(74) RAHN, L.A. and GREENHALGH, D.A. "High-Resolution Inverse Raman Spectroscopy of the V_1 Bond of Water Vapour". J. Mol. Phys. to be published (1986).

DISCUSSION

A.L.Buggele, US

Can you comment on the data rate limitation of your CARS measurement process — for example, can we achieve a 5000 per second sample rate for future engine work.

Author's Reply

For 1 atmosphere flows, and slightly less, we need 200—300 milliJoules of laser energy per pulse to generate satisfactory signals. At 5 kHz this gives a mean power of 1 KWatt. Such high power would require an enormous laser. Also such lasers are certainly not commercially available. Current data rates are also limited to 100—200 Hz for broadband CARS with multiplex detection. For high pressures > 20 bar much lower powers are required. For these systems large copper vapour lasers may ultimately allow the potential but this is probably at least 2 to 3 years in the future.

P.Stewart, UK

The internal combustion engine is an unsteady state system. The spatial resolution has been described — what is the temporal resolution, i.e. — how long does it take to make a measurement and has the temperature changed significantly during the course of the measurement?

Author's Reply

For single pulse measurements the measurement time is typically 10-15 nanoseconds. This is very short compared with the timescale of fluid flow variations which are likely of order milliseconds. For "steady-state" systems we use 10—20 Hz sampling and determine the statistics of temperature. For "non-stationary" systems such as I C engines the above approach could be used but interpretation of the data would require considerable thought. Typically in the engine all our CARS data is "conditionally sampled". With each spectrum we simultaneously recorded full cylinder pressure histories plus many other timing details such as crank angle and ignition timing. For most data prior to combustion we can then determine average parameters (such as temperature) for a chosen scenario of conditions. For instance, prior to combustion for a given crank angle and for a given pressure we can average together all spectra and reduce data processing needs. However for less well determined conditions (e.g. post combustion) it is still important to process CARS data single shot so that both mean and r.m.s. etc., quantities may be examined as a function of condition.

M.N.R.Nina, PO

With limited optical access to the petrol I C engine, I would like to know more about the spatial resolution in your system: In the paper you mention 3—4 mm effective length around the focus which is still very large in terms of the turbulent reacting structures existing in the flow.

Author's Reply

Spatial resolution is primarily limited by the need for adequate signal strength. Potentially smaller sampling volumes may be generated, however higher laser intensity could stress the medium and lead to inaccuracies in the measurement. Certainly for single pulse CARS it would be most difficult to decrease this figure given that CARS signals scale as the control volume length squared. These spatial resolutions can be achieved for both BOXCARS and colinear CARS. In the latter case the lasers must have very pure TEMoo transfer mode characteristics and the Stokes beam should be reduced to be say 1/3 the diameter of the pump beam prior to the input field lens. Then for short focal length lasers (say 10 cm) phase matching will not be well satisfied before the focus. This technique minimises the possibility of extraneous signals from possible high density, cold gases surrounding the desired measurement point.

H.May, GE

I think that the shown application of CARS technique to a real Otto-engine is a very great success and I would like to congratulate Dr Greenhalgh for this. The knowledge of the temperature distribution within the engine cylinder during compression and combustion stroke is very important with respect to knocking phenomena and the mechanism of NO-formation. Direct temperature measurements in the cylinder are only possible by spectroscopic methods. My question is in as far it is intended to continue the reseach work in this direction.

Author's Reply

Much of this work is now continuing, funded by the petrol engine working party group which is described in one of my references.

R.B.Price, UK

You quote mean temperature accuracies of the order ± 15°K as being possible over the full temperature range of interest in turbulent combustion. To achieve this

(a) How many single shot spectra have to be recorded?

(b) What is the method of processing? Do "quick fitters" give this accuracy?

Author's Reply

(a) Single pulse noise is typically *at worst* ± *100 K*, thus at least 100 spectra are required to potentially reduce uncertainty to ± 10 K. We commonly use 500 spectra however 50 spectra for many circumstances are perfectly adequate.

(b) We do not use "quick fitters" for two reasons:

(i) We have yet to find a satisfactory method with "quick fitters" that allows for unpredictable changes in nitrogen concentration (eg turbulent diffusion flame). This could be avoided by Background Suppression. We find that background suppression is expensive in signal (typical 30 fold) and for many practical conditions we would not wish to use higher laser powers.

(ii) Even on near perfect (high intensity high detector count) single pulse real data we have found that typical "quick fitters" can lead to unpredictable apparently systematic errors of ± 50 K or worse. On the same data least-squares gives ± 15 K. We speculate that part of this reason arises from the Poisson Detector noise that markedly affects weaker parts of the spectrum. Quick fitters only use part of the spectral data and may be much more susceptible to noise in certain parts of the spectrum. The particular effect of this noise, combined with dye laser noise is clearly shown in Figure 15. It should also be noted that Poisson multichannel detector noise is pink noise. i.e. it is white noise and its has a cutoff in detector spatial frequency of order 3—4 channels (eg the same as detector cross-talk). This cut off is most important since it means that there is no averaging at Poisson noise in any signal analysis as would be the case if Poisson was truly independent per channel.

ACCURATE MEASUREMENTS OF COMBUSTION SPECIES
CONCENTRATIONS USING CARS

R. L. Farrow
Combustion Research Facility
Sandia National Laboratories
Livermore, California 94550

SUMMARY

We present results of research at the Combustion Research Facility, Sandia National Laboratories, on improving the capabilities of coherent anti-Stokes Raman spectroscopy (CARS) for species concentration measurements in combustion gases. Scanning CARS experiments based on single- and multi-mode Nd:YAG lasers, and on pulse-amplified and conventional pulsed dye lasers have been used to evaluate an *in situ* normalization technique, to measure Raman linewidths in flames, and to determine nonresonant electronic susceptibilities. We discuss experimental and theoretical considerations affecting concentration measurement accuracy.

I. INTRODUCTION

Coherent anti-Stokes Raman Spectroscopy (CARS) is one of the most widely applied optical techniques for measuring temperature and species concentrations in combusting gases. Measurements have been reported for a variety of combustion systems, ranging from laboratory flames[1-4] to jet engine exhausts.[5] However, in comparison with its thermometric capabilities, the development of CARS for quantitative density or concentration determinations is less mature. Concentration measurements are more difficult because the nonlinear nature of CARS signal generation can give rise to intensity variations not correlated to sample density. Short-term fluctuations, associated with pulse-to-pulse laser pulse variations, and long-term changes, associated with beam alignment drift, are typically observed. Thus, referencing schemes are usually required to normalize signals for density measurements.

Most referencing schemes that have been used to measure concentrations with CARS can be classed among the following: (1) measuring a ro-vibrationally resonant signal from the species of interest and normalizing its intensity by nonresonant signals generated with the same laser pulses from external media,[3,6] (2) normalizing resonant signals by nonresonant signals generated from the sample itself,[7,8] and (3) inferring concentrations from the spectral shapes of CARS measurements containing significant nonresonant intensity.[9-11] The first method is capable of yielding densities from the normalized signal intensities, but is sometimes limited by incomplete correlation between the reference and sample signals. The third technique provides mole fractions by indirectly comparing resonant to nonresonant susceptibilities, but lacks sensitivity and accuracy for very low or high concentrations.[10,11] The second method is capable of higher sensitivity than either (1) or (3) and can provide significantly better signal reproducibility.

In this paper, we present an investigation of the nonresonant susceptibility normalization technique for high-pressure, room- temperature measurements and for minor species measurements in atmospheric-pressure flames. We also report high-resolution CARS measurements of Raman transition linewidths in flames and a measurement of the nonresonant susceptibility of H_2O, both using a single-mode Nd:YAG laser.

Methods (2) and (3) above are based on inferring concentrations by comparisons of resonant with nonresonant electronic susceptibilities. [In the case of (3) the ratio of these quantities affects the observed spectral profile.] A quantitative determination of the mole fraction of the resonant species requires knowledge of the nonresonant susceptibility of the total mixture, which must be measured independently or modeled. In addition, a means of calculating the resonant susceptibility spectrum for a given concentration is necessary. These susceptibilities are usually used to generate a theoretical CARS spectrum that is varied for best fit to the observed spectrum. The computed spectrum must also take into account the spectral profiles of the lasers and, for multiplex CARS, the instrument function of the detection system.

In many instances, the accuracy of the resulting concentration measurement is not limited by experimental noise but by uncertainties in spectroscopic parameters used in calculating the susceptibilities. For most combustion-related species, the accuracy of theoretical resonant susceptibilities is primarily limited by the accuracy of Raman linewidths used in the calculations. (At elevated pressures, collisional narrowing processes have a significant effect on resonant spectra, and theoretical predictions are quite model-dependent.[12]) As these linewidths are not resolved in most CARS experiments, linewidth models[13] based on flame observations by

high-resolution inverse Raman spectroscopy[14] (IRS) are typically used. However, the scope of such data is currently limited with respect to species, collision partners, and gas temperature. The recent availability of commercial single-axial mode Nd:YAG lasers, and development of pulse-amplification techniques providing near-transform-limited tunable radiation permit high-resolution CARS experiments[15] capable of measuring these linewidths directly. We have used a scanning CARS system with a resolution better than 0.005 cm^{-1} to measure spectra of CO and N_2 in a methane/air flame. Raman linewidths derived from these me..surements are compared to infrared linewidths measured in similar flames by Varghese and Hanson.[16]

In the absence of independent knowledge of the background susceptibility, nonresonant electronic susceptibilities of combustion species are needed for inferring concentrations with methods (2) and (3). As in the case of Raman linewidths, limited data exists for combustion-related species. Early measurements by Rado,[17] with scale factor corrections suggested by Eckbreth and Hall,[10] Lundeen et al.,[18] and Rosasco et al.,[19] are typically used for important species such as N_2, CO_2, CH_4, etc. Recently, techniques based on CARS[18] and field-induced second-harmonic generation[20] have provided nonresonant susceptibilities for gases at room temperature. We report a method using CARS that is applicable in flames as well as in sample cells. Measurements of N_2 and Ar using this technique compared well with previously reported results;[19] new investigations of the nonresonant susceptibility of H_2O are described.

II. NONRESONANT BACKGROUND NORMALIZATION

For this technique the anti-Stokes beam is divided with a beamsplitter, and the resulting beams are directed to separate polarization analyzers and detectors. One polarizer is oriented to reject the nonresonant background and transmit the Raman (ro-vibrationally resonant) components of the signal. The other polarizer is set to reject the dominant Raman components and transmit primarily the nonresonant background signal. The resonant signal is then divided by the nonresonant background signal for each laser pulse. This ratio is concentration- and temperature-sensitive, while being relatively insensitive to overall CARS signal fluctuations and drift. The sample can be said to provide its own normalization signal for concentration calibration because the nonresonant susceptibility is, in many cases, insensitive to gas composition. The method represents an improvement on a similar approach suggested by Oudar et al.[7] that uses a single polarizer.

The capabilities of the background normalization technique are illustrated in two experiments. The first demonstrates that high-precision, narrowband measurements using a single laser pulse are possible in low-temperature or high-pressure media. The second experiment includes time-averaged species concentration and temperature measurements obtained in an atmospheric methane/air flat flame. The latter results illustrate the analytical capabilities of background-normalized CARS for steady-state or reproducible combustion processes.

A crossed-beam, three-dimensional phase matching geometry was used to obtain a probe volume diameter of ~80 μm by 4 mm in length. The CARS pump beam was provided by the frequency-doubled output of a Molectron MY-32 Nd:YAG laser, which had a bandwidth of 0.1 cm^{-1} (FWHM). Part of the 532-nm radiation pumped a scannable dye laser (Molectron DL-18), which had a bandwidth of 0.1 cm^{-1}. As shown in Fig. 1, a beamsplitter was inserted into the anti-Stokes beam path to reflect 30% of the signal to one polarizer (nonresonant channel) while transmitting the remainder to a second polarizer (resonant channel).
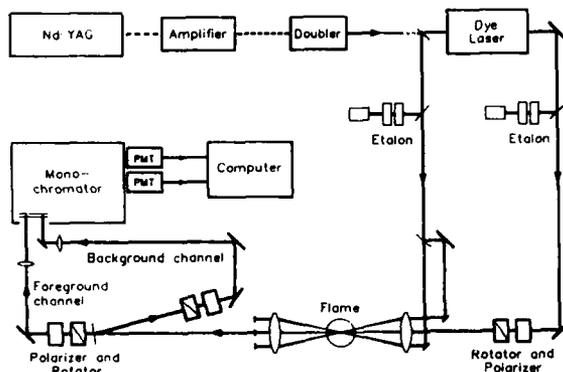
1. Experimental diagram of two-channel, background-normalized CARS experiment.

The two polarizers were adjusted to produce a background-free (resonant) spectrum and a spectrum with the Raman contributions mostly suppressed (background). The resonant spectrum was obtained by rotating one polarizer to an angle 60 degrees from the vertically polarized pump laser. With the probe laser polarization at -60 degrees from the vertical, this orientation results in rejection of the nonresonant background and in partial transmission of isotropic and anisotropic Raman components. This background-subtraction technique has been shown to improve scanning CARS species detectivity.[21] The second polarizer was oriented to reject one Raman symmetry component, while transmitting the nonresonant background (along with part of the other Raman component). Both spectra, as well as the spectrum formed from their pulse-by-pulse ratio, were recorded.

Half-wave retarders were used to rotate polarizations of the analyzed signal beams to the same angle in order to maintain equivalent transmission through a filter monochromator (SPEX 1870). The two signals were separately measured using photomultiplier tubes (RCA C-31034A) wired for amplification with six dynodes, charge integrators, and digitizers. Relative detection channel sensitivity was determined by measuring the relative response to a nonresonant CARS signal with both polarizers rotated to the same angle. The data were acquired and stored using a PDP 11/34 computer.

Studies of the pulse-to-pulse reproducibility of normalized CARS signals were performed in a mixture of CO and Ar gases with respective mole fractions of 0.04 and 0.96, and at a temperature of 297 K. A pressure of 10 atm was chosen so that the collisionally broadened Raman linewidths overlapped to form an envelope that was fully resolved by the combined laser linewidths.

The ratio of resonant to nonresonant CARS signals was found to have a reproducibility approaching the shot-noise limit in single-pulse measurements on the 10-atm CO/Ar mixture. At the peak of the CO Q-branch bandhead, the RMS standard deviation of the ratio was measured to be 2%. The corresponding distribution of measurements was symmetric and nearly Gaussian. In contrast, the standard deviation of the individual, non-normalized signals exceeded 12%. Shot noise was calculated to be 1.2% based on detecting 19,000 and 10,000 photo-electrons in the two respective channels. Fig. 2 shows the resonant, nonresonant, and ratio spectra of the CO Q-branch obtained by stepping the probe laser frequency after each laser pulse (note that the square root of intensity is plotted, so that peak heights are proportional to density). The relatively high noise in the non-normalized data is characteristic of CARS signals generated with multi-mode lasers, and results from pulse-to-pulse temporal and spatial variations in the laser fields. This noise is greatly reduced in the ratio because fluctuations in the two signals are highly correlated.
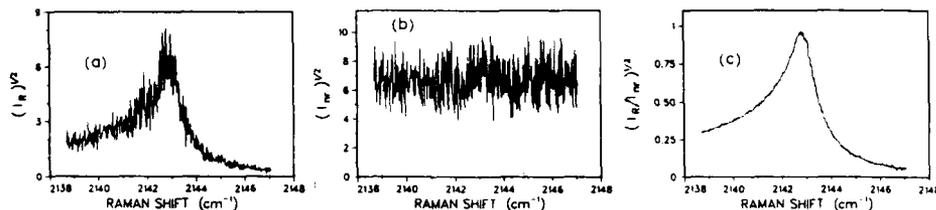
2. Resonant foreground (a), nonresonant background (b), and background-normalized (c) CARS spectra of the collisionally narrowed Q-branch of 0.04 mole fraction CO in Ar at 10 atm, obtained by stepping the probe laser frequency. Signals were measured after each step using a single laser pulse. Reproducibility at the peak was ±2%. The square root of the intensity is plotted.

The remaining noise in the ratio arises primarily from shot noise, from different detection channel responses to the fluctuating spatial profiles of the two anti-Stokes beams, and from noise induced by frequency fluctuations in the lasers. The nonresonant signal is much less sensitive to these fluctuations, in comparison to the resonant signal, because the nonresonant susceptibility is nearly independent of frequency. Thus, stable lasers with bandwidths smaller than the Raman linewidths of interest are required for highest repeatability in the signal ratio.

III. CARS SPECTRAL ANALYSIS

For analytic measurements, we developed a CARS analysis computer code to interpret normalized, scanned spectra. The code yields temperature and relative species concentrations by calculating foreground and background spectra, forming the ratio, and fitting the result to a background-normalized experimental spectrum. Species concentrations expressed in mole fractions of the total gases can be determined, provided the in situ nonresonant susceptibility is known. If desired, absolute densities can be computed from the fitted temperature and an independent pressure measurement.

Calculation of the theoretical resonant susceptibility has been described previously.[4,11,22] A significant improvement for the present analysis is that the contributions to the CARS spectrum of up to four species can be included simultaneously. This is accomplished by summing the contributions of the species to the total susceptibility amplitude over all transitions that fall within the desired frequency range. The wing of the N_2 Q-branch, which can be significant, is also included if the N_2 Q-branch lies outside the desired range, as is the case for the CO Q-branch. The temperature and relative concentrations of all species are specified or varied for best fit. We included contributions from N_2, CO, and H_2 for analyzing spectra in the region of the CO Q-branch.

The temperature and J-dependence of CO Raman linewidths were modeled according to high-resolution infrared (IR) P- and R-branch measurements of extracted methane/air post-flame gases by Varghese and Hanson.[16] (Rosasco et al.[23] have reported good agreement between Raman Q-branch and IR P- and R-branch linewidths of pure CO.) Best straight line fits to the J-dependent IR linewidths at 300 K and 1850 K were used to derive a temperature-dependent model given by:

$$\gamma(J,P,T) = (AT^{-0.77} - JBT^{-1.31})P, \qquad (1)$$

where $A = 6.89$, $B = 2.026$, P is the pressure in atm, and $\gamma(J,P,T)$ is the HWHM in cm^{-1}.

Linewidths of H_2 and N_2 were based on high-resolution inverse Raman measurements by Rahn et al.[14,24] The linewidths of individual nitrogen Q-branch transitions observed in a methane/air flame were fit by a fifth-order polynomial[4] and scaled according to $PT^{-0.5}$. Nitrogen O-branch linewidths were approximated by Q-branch values multiplied by 1.15, according to O-branch investigations by Rahn.[25] The linewidth of a single pure rotational S(9) H_2 transition was similarly based on direct observation by Rahn.[25]

Due to lack of sufficient collisional broadening data, linewidths were not adjusted according to gas composition. This approximation is reasonable here because of the predominance of N_2 throughout the flame. Collisional narrowing effects associated with line overlap were also neglected. However, perturbations introduced by these effects are expected to be small in an atmospheric-pressure flame.

Transition frequency accuracy exceeding 0.03 cm^{-1} was required due to numerous overlapping lines among these species. We used molecular rotational and vibrational constants of CO and H_2 reported by Guelachvili[26] and by Jennings et al.,[27] respectively. N_2 constants are from unpublished results of Rahn and Owyoung.[14] These constants are in good agreement with those reported by Gilson et al.[28]

Based on recent new investigations,[18,19,29] values used for theoretical nonresonant susceptibilities were derived from the data of Rado[17] using a multiplicative factor[30] of 6.25. The flame nonresonant susceptibility was measured relative to that of nitrogen in a manner described below. This ratio was then multiplied by the theoretical nitrogen value and used as input for the flame nonresonant background calculations. Raman cross-sections for N_2 and CO compiled by Schrotter and Klockner[31] were used in the calculation of resonant susceptibilities. The polarizability anisotropy reported by Bridge and Buckingham[32] for H_2 was used for the pure rotational S(9) line.

To analyze each background-normalized spectrum, two theoretical spectra were calculated according to the experimental analyzer angles for the respective foreground and background channels. To account for the linewidths of the lasers, which were in all cases larger than the Raman linewidths, these spectra were convolved using the formula described in Ref. 29. This new convolution was proposed by Kataoka et al.[33] and by Teets.[34] It can differ significantly from the widely used Yuratich expression[35] in predicting the ratio of resonant to nonresonant intensities when the pump linewidth is broad relative to Raman lines. A normalized spectrum was then computed from the point-by-point ratio of the convolved spectra for comparison with the data.

IV. FLAME MEASUREMENTS

Normalized CARS measurements in atmospheric combustion environments do not exhibit the high pulse-to-pulse repeatability observed for the 10-atm CO/Ar mixture. The primary reason is an increase in shot noise in the weak nonresonant intensities from high-temperature gases. For example, we typically observe ~100 counts per laser pulse in nonresonant signals from post-flame gases. In addition, frequency-jitter-induced noise occurs in the resonant signals, since our multi-mode lasers did not resolve Raman linewidths in flames. Thus, we acquired flame spectra by averaging 30-

60 laser pulses per probe frequency step, resulting in up to 40-minute scan times. The signal-to-noise ratio of the background-normalized measurements was nevertheless approximately a factor of two better than for the raw signals in the separate resonant and nonresonant channels.

The burner used for the flame measurements consisted of a stainless-steel honeycomb plug 50 mm in diameter, surrounded by a 75-mm-o.d. coflow annulus. A methane/air flame with a stoichiometry of 1.32 ± 0.13 and a dry air coflow was stabilized on the burner. With this stoichiometry the flame front was located 2.0 mm above the burner surface, as indicated by the measured temperature profile. Enclosures shielded the flame from room drafts. CARS measurements were made at points along the centerline extending from 1.1 mm to 20 mm above the burner.

Measurements on extracted post-flame gases were performed using a low-pressure gas sampling system. We used a quartz probe with a water-cooled jacket. The probe was inserted into the post-flame gases at a height 10 mm above the burner. The outlet of the probe was connected to a windowed sample cell and the system was operated with a continuous flow of gas at a cell pressure of 25 torr.

Absorption spectra of CO were measured using two passes through the sample cell, for a total path length of 80 cm. The IR source was a single-mode F-center laser, Burleigh model FCL-20. This laser was scanned by tuning an intra-cavity etalon, resulting in discrete frequency steps at the cavity mode spacing of 0.01 cm^{-1}. The linewidth of the laser was <0.001 cm^{-1}.

A rich methane/air flat flame was chosen to test the utility of the ratio technique as a probe of steady-state combusting flows. The rich flame was investigated for several reasons, including the presence of appreciable quantities of CO and H$_2$, and the ability to accurately predict the post-flame concentrations of these species via thermodynamic equilibrium models. The relatively large distance between the burner surface and the flame front allowed probing of the preheat region and the flame zone.

Background-normalized spectra of isolated N$_2$ O-branch transitions and of the CO ground-state and first hot-band Q-branch were measured at various heights on the centerline above the burner. The N$_2$ O-branch spectra were analyzed for temperature and N$_2$ concentration through least-squares fitting. These transitions were chosen because they occur in the vicinity of the CO bandhead and are easily and efficiently analyzed. Also, it is possible to completely suppress the relatively weak N$_2$ O-branch intensities in the background channel, providing a flat reference spectrum. (Intense N$_2$ Q-branch signals could not be suppressed entirely.)

CO concentrations were determined from the CO Q-branch spectra using the temperatures obtained from the N$_2$ O-branch spectra. Due to the extensive time required to compute CO Q-branch spectra (involving over 200 transitions) we did not perform least-squares fitting. However, because of the normalization method and the use of background subtraction, varying the theoretical CO concentration primarily amounted to adjusting the vertical scale factor. Thus, we judged that a visual fit was accurate to ~5%.

To minimize uncertainty in deduced mole fractions, which are normalized to the flame nonresonant background, a method was devised for measuring the latter directly. Using one channel, the polarizer was rotated to 87.8 degrees to reject the N$_2$ Q-branch susceptibility. With the probe laser tuned far from resonance with any O-branch transition (near 2182 cm^{-1}), the resulting signal was predominantly due to the nonresonant electronic susceptibility. This signal was measured at various flame positions and compared to that of the room-temperature air coflow. Using measured flame temperatures, these ratios were corrected to yield flame nonresonant susceptibilities relative to N$_2$ at the same densities.

The measured nonresonant susceptibilities at various heights in the flame, together with temperatures measured at the same positions from O-branch spectra, are shown in Fig. 3. We see that the relative susceptibilities are all greater than unity, i.e., greater than that of N$_2$. This result is consistent with the fact that many flame species, including CH$_4$ and CO$_2$, have nonresonant susceptibilities[17] larger than N$_2$. A mixture-weighted calculation using the input CH$_4$, N$_2$, and O$_2$ fractions is indicated by an X on the ordinate of Fig. 3, and is slightly lower but in reasonable agreement with the susceptibility measured closest to the burner. Since the background measurements in the flame and in the room-temperature air coflow were both non-normalized measurements, the accuracy is probably limited by such systematic effects as slight beam steering in the flame.

In many cases, the flame nonresonant susceptibility can be estimated rather than actually measured. Accurate predictions require knowledge of relative concentrations and nonresonant susceptibility values for all major species, which are not always available. However, as previously noted,[36] in near-stochiometric, air-fed combustors, the nonresonant susceptibility (molecular basis) will not vary greatly

with combustion. This expectation is in agreement with Fig. 3, where the susceptiblity changes by only 15% from reactants to products.
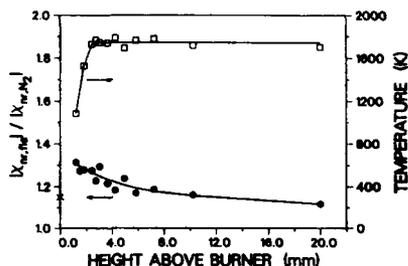
3. Measurements of temperature (squares) and nonresonant susceptibility (circles) measured along the centerline of a rich (φ = 1.32) methane/air flat flame. The nonresonant susceptibility magnitude is relative to that of N_2. An X symbol on the left ordinate indicates the susceptibility calculated from reported values[17-19] for the input gases. Solid lines are smooth curves drawn through the data points.

The concentration of N_2 was measured from background-free spectra of O(19) (v=0→1) and O(16) (v=1→2) near 2177 cm^{-1}, normalized by the nonresonant background spectrum. A polarizer angle of 37.6 degrees from the vertical was used for the latter. The resulting background-normalized spectra were analyzed using the CARS computer code described previously. Parameters varied for best fit included N_2 concentration, temperature, pump linewidth, and vertical offset (foreground spectrum only, to account for small zero errors). The inclusion of both v=0→1 and v=1→2 transitions in the measured spectra provided temperature information from the relative peak heights. Concentration sensitivity derived mostly from the ratio of peak to background intensity.

In the course of these measurements, we investigated the effects of two factors on concentration accuracy: laser field intensity and choice of model for convolution over pump laser linewidth. Both factors can result in underestimation of concentration. In particular, we examined under what conditions excessive laser power can lead to Stark broadening effects.[37,38] We also tested the significance of using the Yuratich convolution theory[35] rather than the results of Kataoka et al.[33] and Teets.[34] These latter equivalent models account for the finite linewidths of the pump and probe lasers, which are significant when Raman linewidths are not fully resolved. The Yuratich model does not properly account for the pump laser linewidth,[29,34] but requires considerably less computation time.

The initial N_2 concentration profile, measured with the pump laser focused to an intensity of 140±30 GW/cm^2, is shown by the square symbols in Fig. 4. A cross symbol on the abscissa indicates the input N_2 mole fraction. The measured concentrations are observed to decrease rapidly as temperature increases (Fig. 3), falling to nearly one-half the input value. From equilibrium calculations of the post-flame composition, this reduction of N_2 mole fraction appeared excessive. Further investigation revealed that the ratio of peak-to-background intensities, and hence the inferred concentration, was dependent on the pump laser intensity, with higher powers resulting in lower concentrations. This result is illustrated in Fig. 5, which shows that at minimum usable power levels the concentration was nearly constant, but at a relatively modest 70 GW/cm^2 intensity, the measured concentration was reduced by ~15%. Since higher pump intensities had been used for the data marked by squares in Fig. 4, the effect would have been even more pronounced. Temperature measurements were not significantly perturbed, as both v=0→1 and v=1→2 transition intensities were similarly affected (typical temperature uncertainty was 50 K).
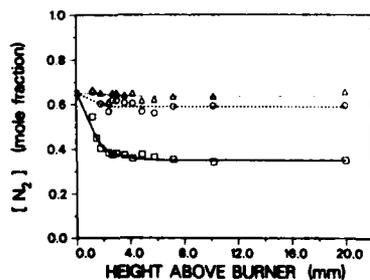
4. Measurements of N_2 concentrations along the centerline of the flame, based on background-normalized CARS spectra of O-branch transitions. Triangles indicate measurements obtained using total pump intensity <30 GW/cm^2. Squares show data measured with excessive pump intensity, 45 mJ energy, resulting in 140 GW/cm^2, and illustrate the effects of Stark broadening. Circles represent data analyzed using a more efficient but less rigorous convolution theory[35] to account for the pump laser lineshape. The theory of Kataoka et al.[33] and of Teets[34] was used to analyze the other data. Lines are smooth curves drawn through the data points.

| 18 GW/cm² | 35 GW/cm² | 70 GW/cm² |
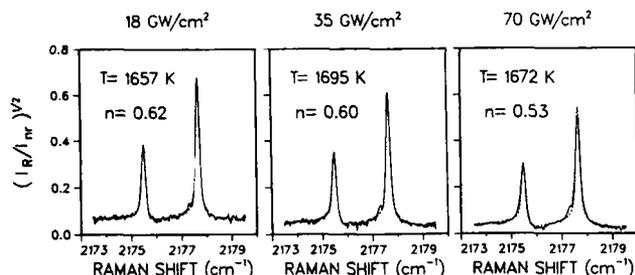
5. Illustration of Stark broadening of N_2 O-branch transitions and its effect on inferred mole fraction concentrations (denoted by "n"). Spectra are background-normalized to the nonresonant CARS signal, so peak intensities should be independent of pump laser power. The square root of the signal ratio is plotted.

Several possible explanations for the dependence of peak-to-background ratio on pump intensity were examined. Detector linearity was checked over the appropriate range of signal strengths. We verified concentration calibration at room temperature by measuring the ambient concentration of N_2, with resulting accuracy better than 5%. The possibility of significant saturation by stimulated Raman pumping was eliminated by the observation that the effect was not dependent on the pr(: intensity (typically much lower than that of the pump), and by theoretical estimates of pumping rates.

Instead we attribute these results to Raman linewidth broadening resulting from dynamic Stark splitting of the rotational transition.[37] The apparent temperature dependence of the effect results from the fact that smaller linewidths occurring at higher temperatures are more effectively broadened by the splitting, whose magnitude is independent of temperature. This hypothesis was supported by calculations based on a classical polarizability-derivative model for the Stark splitting. The calculations predicted a linewidth broadening effect of 0.012 cm^{-1}/100 GW/cm^2, compared with a broadening of 0.016±0.003 cm^{-1}/100 GW/cm^2 inferred from our observations. This was considered consistent in view of the approximations of the model (e.g., the laser fields were assumed spatially uniform).

Following this study we substituted a beam-focusing lens with a longer focal length (42 cm instead of 30 cm) and reduced the pump intensity to a level where broadening effects were not observed, i.e., below 30 GW/cm^2. (Note that similar Stark splitting effects are expected to be less important for Q-branch transitions because splittings occur only for depolarized spectra.[37-40])

The N_2 concentration measurements obtained with reduced pump intensity displayed little temperature dependence, and agreed closely with the input N_2 mole fraction. Represented by the triangle symbols plotted in Fig. 4, the concentration profile shows relatively little variation as a func.ion of temperature or height in the flame.

We also investigated the error introduced by using the computationally efficient Yuratich convolution[35] to account for the laser linewidths. The circles in Fig. 4 show the results of analyzing the same data as above, but using the Yuratich formula rather than the more rigorous Kataoka[33] or Teets[34] results. For all but the lowest measured temperature, the former method gave a concentration ~10% lower than the correct one. The fact that the difference was not larger is probably due to the use of an etalon in the Nd:YAG pump laser, resulting in a FWHM linewidth of 0.1 cm^{-1} at 532 nm. In previous investigations of this effect,[34,29] Nd:YAG lasers with bandwidths of 1.0 cm^{-1} and 0.7 cm^{-1}, respectively, have been used. We observed no significant differences between temperatures measured using the two convolution methods.

CO concentration measurements were obtained from normalized, background-free Q-branch spectra of the CO ground-state and first hot-band. This spectral region contains contributions from three species, allowing CO, N_2, and H_2 concentrations to be monitored. A typical foreground spectrum measured 20 mm above the burner is shown in Fig. 6a. The prominent lines near 2153 and 2143 cm^{-1} and between several CO Q-branch lines are N_2 O-branch transitions. An N_2 O(22) transition at 2124.78 cm^{-1} coincides with the CO Q(32) frequency and results in destructive interference. A pure rotational S(9) transition of H_2 is observed at 2130.1 cm^{-1}.
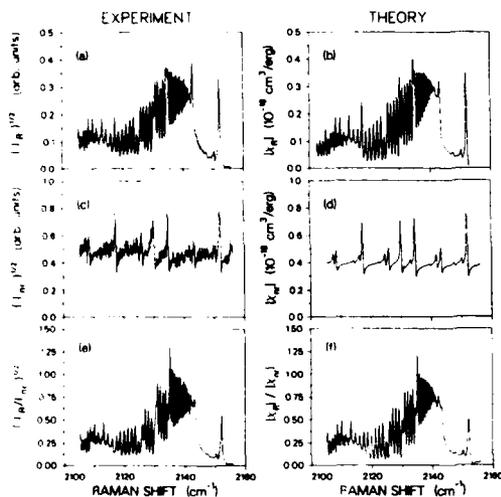
6. Experimental CARS foreground (a), background (c), and ratio (e) spectra of the CO Q-branch region measured 20 mm above the burner surface. (Ratio is the foreground divided by the background.) Calculated CARS foreground (b), background (d), and ratio (f) spectra. Temperature (obtained from separate N_2 spectra) was 1750 K in the calculations. We used CO, H_2, and N_2 mole fractions of 0.062, 0.03, and 0.66, respectively, for the calculations. The etalon was removed from the dye laser, resulting in a linewidth of 0.35 cm^{-1}, to permit long scans.

A resonant spectrum was calculated using the temperature and N_2 concentration measured previously, and CO concentration as described below. The result is shown in Fig. 6b. The agreement with experiment is good except for small discrepancies involving intensities of interspersed N_2 O-branch lines, which are typically overestimated. As high-resolution measurements revealed later, these differences partly resulted from slightly inaccurate N_2 O-branch transition frequencies and linewidths. In addition, the laser field intensity was ~70 GW/cm^2, which probably caused Stark broadening of the N_2 O-branch, but not the CO Q-branch, transitions. In one case, the intensity of the O(23) N_2 transition, which coincides closely with the CO bandhead frequency, is underestimated. However, other researchers have reported similar difficulty in modeling the bandhead region of neat CO.[41] Thus, some of the discrepancy may stem from the CO spectral model rather than its interaction with N_2 O-branch lines. Stufflebeam et al.[41] have suggested that the spike may result from the effects of correlated mode amplitudes in the pump beam fields.

The nonresonant background spectrum for these data was measured with the polarizer oriented 86.2 degrees from the vertical to reject Q-branch components. N_2 and H_2 rotational transitions, having anisotropic symmetry, were not rejected and appear as relatively weak peaks interfering with the background. Figure 6c shows the background spectrum measured 20 mm above the burner surface. Except for the S(9) H_2 transition, all features are due to N_2 O-branch transitions. Since this spectrum is later divided into the foreground data, these features will affect the ratio spectrum and thus must be included in calculations. The corresponding theoretical background is shown in Fig. 6d. An H_2 mole fraction of 0.03 gave the best qualitative agreement with the data.

As shown in Figs. 6e and 6f, the normalized experimental and theoretical spectra are in good agreement when a CO mole fraction of 0.059 is used. Note that the normalization permits a direct comparison between the normalized theoretical and experimental intensities. Varying the theoretical concentration essentially varies the CO peak amplitudes.

Varying the theoretical CO concentration for best agreement with the data resulted in the profile indicated by circles in Fig. 7. The CO concentration is seen to follow the temperature profile, reproduced from Fig. 2 and indicated by squares. Above 3 mm the concentration maintained a constant value of 0.060±0.003. We also made measurements along a flame radius to establish the minimum observable CO concentration for our system. A CO mole fraction of 0.0035 was easily detected at a temperature of 1900 K. From these data we estimate a minimum detectable CO mole fraction of 0.001 for a 20-minute measurement time.

For comparison with the CARS concentration results, IR absorption measurements of CO were performed on post-flame gases extracted with the sampling probe. After being drawn from the flame at a height 10 mm above the burner, the gases were measured at room temperature and 25 torr. This low pressure prevented condensation of H_2O and inhibited conversion of CO to CO_2. Using similar flow systems, good agreement has been reported among CO concentrations analyzed in gases from rich

flames, in situ flame absorption results,[42] and flame calculations assuming chemical equilibrium.[42,43]
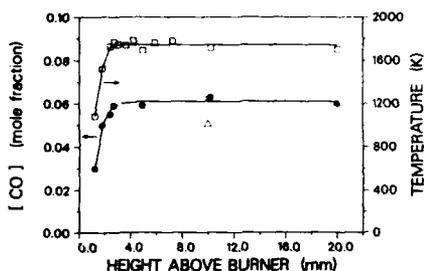
7. CO concentration profile (circles) obtained from data such as those shown in Fig. 6. Squares are temperatures reproduced from Fig. 3. The triangle symbol indicates the CO concentration measured by IR laser absorption in flame gases extracted at this height. The cross symbol shows the result of a thermodynamic equilibrium calculation for the post-flame gases.

Spectra of the CO overtone $(v=0\rightarrow2)$ R(18) transition were measured in the equilibrated flame gases and compared with spectra from an assayed gas sample of 0.110 ± 0.001 mole fraction CO in N_2 at the same pressure and temperature. A comparison of spectrally integrated line strengths indicated a CO mole fraction of 0.05 ± 0.01 in the flame gases. The estimated error arises primarily from uncertainty in the baseline for determining absorbed laser power (there was approximately 50% absorption at line center in the flame gas).

This result is in reasonable agreement with the CARS result of 0.062 ± 0.015 for the mole fraction of CO measured at the same flame position. The 25% uncertainty for the concentration of CO determined from CARS is largely systematic. An experimental precision of ±0.003, or $\pm5\%$, is due to random noise and fitting errors. Systematic errors result mainly from uncertainties in theoretical nonresonant susceptibilities, Raman and laser linewidths, and Raman cross-sections, which govern the predicted ratio of resonant to nonresonant CARS intensities. For CO these factors are estimated to contribute 20% to the concentration uncertainty. For N_2, this uncertainty is smaller, approximately $\pm10\%$ due to more accurate Raman linewidth and cross-section data. Other possible error sources are uncertainty in determining the flame nonresonant susceptibility ($\pm10\%$) and the relative detection channel gain ($\pm5\%$). Thus, the total N_2 concentration uncertainty is estimated to be $\pm20\%$.

To obtain maximum species detectivity, all CARS measurements were performed using nearly equal pump beam path lengths. This geometry maximizes signal strength but can lead to anomalous enhancement of nonresonant compared to resonant intensities, and thus subsequent underestimation of concentrations.[29] The relative enhancement occurs only when the CARS pump laser is broader than transition linewidths, and when the two pump beams are mutually coherent.[29,44] This effect is associated with random fluctuations of the field within a single laser pulse.

From measurements in gas cells at various pressures, we estimated the resulting concentration underestimation to be ≤5% for the isolated N_2 O-branch lines, and probably negligible for the CO Q-branch.[45] This result, as well as the simplified convolution requirements, points out the value of using narrowband pump lasers for CARS measurements. Because of the dominance of other systematic errors, we did not apply any correction to the N_2 concentration results.

A calculation of relative species concentrations based on metered input flow rates and measured flame temperatures was also in good agreement with the CARS results for CO and N_2. To make the calculation, we used the DEQUIL computer code,[46] which assumes thermodynamic equilibrium. The result for CO was a mole fraction of 0.062 ± 0.020, with error limits due to uncertainty in temperature (±50 K) and equivalence ratio ($\pm10\%$). This value compares well with the average post-flame CARS result of 0.061 ± 0.015 molar. For H_2 the calculated mole fraction was 0.055 ± 0.025, whereas the CARS result was 0.030 ± 0.015. The latter had a relatively large uncertainty because the measurement was based on a single line which could only be clearly observed in the relatively noisy background spectrum, and any residual Stark splitting would have been enhanced by the low J number (J≈9 compared to J>20 for the N_2 transitions). More accurate results could be obtained by measuring the H_2 Q-branch near 4192 cm^{-1}, but this approach would provide little information on other species. Finally, the calculated molar concentration of 0.640 ± 0.025 for N_2 is in excellent agreement with the average post-flame CARS measurement of 0.641.

V. HIGH-RESOLUTION MEASUREMENTS

The experimental configuration of the high-resolution scanning CARS experiment is similar to that previously described, except that the laser sources are different. A VAX 11/730 computer acquired the digitized anti-Stokes signal and normalized the signal strength for each laser pulse by the measured Stokes energy and the square of the pump energy; 5-8 pulses were averaged for each Stokes frequency step.

The pump radiation was provided by the frequency-doubled output of a modified Molectron MY-34 Nd:YAG laser equipped with a MY-SAM single-axial-mode option. During data acquisition, the 532-nm frequency of the laser was monitored for single-mode operation with a 3-Ghz free-spectral-range Fizeau interferometer. We estimate the pulse-averaged linewidth (HWHM) of the laser to be less than 25 MHz at 532 nm, based on measurements of other single-mode Molectron Nd:YAG lasers.[47] For the Stokes radiation, 60 mJ of the total 90 mJ 532-nm output was used to pulse-amplify the cw beam from a Coherent 699-29 actively stabilized ring-dye laser. The linewidth (HWHM) of this laser after three dye amplifier stages was measured to be 35 MHz. The Stokes frequency was stepped in increments of $(3-5) \times 10^{-4}$ cm^{-1} via an externally applied programming voltage. The frequency scan was calibrated by measuring fringe spacings from a 750-MHz monitor etalon.

Each Raman linewidth was determined by least-squares fitting a restricted spectral region containing the transition of interest. For each fit, a fitting parameter was used to simultaneously vary all the transition linewidths by a multiplicative factor; this technique minimized fitting time, yet provided essentially independent transition linewidths because the wings of neighboring transitions depend only weakly on linewidth.

The same methane/air flame used previously was operated with a total flow rate of 6.0±0.24 SLPM and an equivalence ratio of 1.4±0.1. Measurements were performed 10 mm above the flame zone, which was ~3mm above the surface of the honeycomb burner. An air sheath flow was used to stabilize the flame. A flame temperature of 1690±40 K was measured from least-squares fits of the v=0→1 and v=1→2 Q-branch bands of N$_2$, obtained with a conventional pulsed dye laser (HWHM linewidth of 0.015 cm^{-1}).

The use of narrowband lasers to measure relatively small linewidths requires that precautions be taken to avoid broadening by two-photon Raman saturation.[48] Stark-broadening can also be significant. The lasers were focused using a 400-mm-focal-length lens and f-numbers >70 to obtain large focal diameters (80-100 μm) and low power densities (pump: 18±6 GW/cm^2, probe: 6±2 GW/cm^2). We checked for saturation effects by measuring the dependence of peak signal intensities on Stokes laser power; the dependence was found to be linear. Stark effects were estimated[38] to contribute no more than 10^{-3} cm^{-1} to the linewidths.

To further verify the absence of saturation in the spectra and to check the fitting methods used to extract linewidths, measurements of Q-branch linewidths of N$_2$ in a buffer of Ar at 250 torr were compared with recent values reported from IRS experiments.[29] The measured CARS linewidths were found to be, on the average, 5% lower than the 250-torr collisional widths computed from the IRS broadening coefficients. (Doppler contributions to the linewidth at this pressure are negligible.) These differences are well within the uncertainties of ±10% quoted for the IRS measurements[29] and ±10% estimated for the CARS linewidths.

Observations with IRS of N$_2$ O-branch transitions in a flame have not been attempted because of low signal strength. The data points in Fig. 8 show a CARS spectrum of the O(22) transition of N$_2$ at 2151.97 cm^{-1}, measured in the flame. The solid curve is a calculation, with the Raman linewidth varied for best fit. The average of two such measurements gave a linewidth (HWHM) of 0.017±0.0017 cm^{-1} at 760 torr. This result is 20% smaller than estimated above, based on room-temperature O-
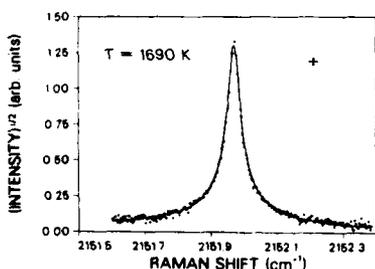
8. Experimental spectrum of the O(22) transition of N$_2$ in a methane/air flat flame at 742 torr, indicated by data points. The flame gas temperature was measured to be 1690 K from analysis of N$_2$ Q-branch spectra. The solid curve is a theoretical spectrum with the Raman linewidth varied for best fit.

branch linewidths measured with IRS. The other J-dependent N_2 O-branch linewidths in the CO spectral region were not measured because of their proximity to CO transitions; instead, they were adjusted for agreement with the O(22) value using the same J-dependence as for the N_2 Q-branch.[24]

Since absolute transition frequencies of CO are accurately known ($\sim 10^{-4}$ cm^{-1}) from high-resolution infrared measurements,[26] the analysis of small CO-N_2 splittings can provide accurate N_2 O-branch frequencies. A near coincidence between the O(25) transition of N_2 and the Q(31) transition of CO is shown in the spectrum indicated by the data points in Fig. 9. Varying the frequency of the former for best agreement gave a value of 2126.020±0.003 cm^{-1} for the theoretical spectrum shown by the solid curve in the figure. This result, combined with new high-resolution measurements of N_2 Q-branch frequencies,[26] were used to refine the molecular constants of N_2 employed in our CARS fitting code. The new constants will be reported elsewhere. We found it necessary to include in the calculated spectrum off-resonant contributions from the S(9) transition of H_2 at 2130.10 cm^{-1} to reproduce intensities in the wings of the lines correctly.
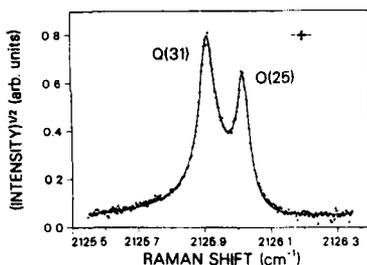
9. Experimental spectrum of the O(25) transition of N_2 and the Q(31) transition of CO in the flame, indicated by data points. Varying the N_2 transition frequency for best fit (2126.020±0.003 cm^{-1}) resulted in the theoretical spectrum shown by the solid curve.

The increased accuracy in these O-branch linewidths and frequencies resulted in improved modeling of the CO bandhead compared to the low-resolution measurements described previously. An experimental measurement of the CO bandhead region is shown by the data points in Fig. 10; the prominent peak at 2143.35 cm^{-1} is the O(23) transition of N_2. The underestimation of this peak seen in previous calculations (Fig. 6a,d) partly resulted from the use of too large a linewidth and a 0.015-cm^{-1} frequency error to the low side. (An additional contribution to the discrepancy may result from the effects of laser field statistics.[41,44]) The solid line in Fig. 10 is a theoretical spectrum obtained by varying the linewidth scaling factor for the CO linewidths and the concentration relative to N_2 for best fit. The resulting concentration, while subject to large error due to the presence of only one N_2 transition, was nevertheless in reasonable agreement with the prediction[46] of equilibrium chemistry calculations: CO mole fraction of 0.064±0.02 compared to a calculated value of 0.073±0.012 based on the measured temperature and input gas flows. We consider the small differences between experimental and theoretical spectra to be within the noise of the measurement.
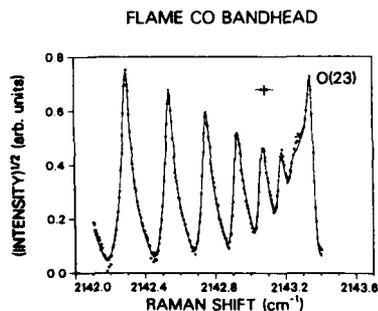
FLAME CO BANDHEAD

10. Experimental spectrum of the CO bandhead region in the flame. The labeled peak is an O-branch transition of N_2, and the solid curve is a theoretical spectrum with CO Raman·linewidths and relative concentrations varied for best fit.

CO Q-branch linewidths were measured for J=2 to 17 by fitting individual transitions as discussed above. The results, normalized to 760 torr, are given by the data points in Fig. 11. The solid curve is a straight-line fit to the data. The error bars shown in the figure indicate uncertainties, principally due to random errors such as statistical noise, baseline errors, and fit errors. Over this range of rotational quantum number, we did not observe a significant dependence of the linewidths on J. The results also show that the approximation of using N_2 linewidths for CO in this flame results in linewidths up to 14% too small, compared to collisional widths for N_2 in a flame from Ref. 24.
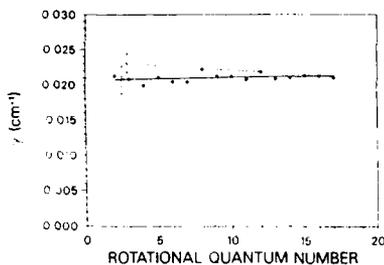
11. Raman HWHM linewidths of Q(J) transitions of CO in the flame, indicated by data points and referenced to 760 torr. The solid curve is a straight-line fit to the data: $\gamma(J) = 0.02074 + 3.72 \times 10^{-5}J$ cm^{-1}. (From regression analysis, the data are also consistent with a horizontal line.) The broken curve is a fit to the infrared linewidths reported by Varghese and Hanson,[16] corrected for our flame temperature (1690 K) and including an estimated Doppler width of 0.001 cm^{-1}.

The CO Raman linewidths were found to be comparable to the infrared P- and R-branch collisional widths reported by Varghese and Hanson,[16] which formed the basis for Eq. 1 above. A straight-line fit[16] to the infrared collisional widths was corrected for our flame temperature of 1690 K using J-dependent temperature exponents reported in the same reference. Since full linewidths were not reported, an additional 0.001 cm^{-1} was added to each width to account for Doppler contributions. (This additional width was deduced from a Voigt analysis, which had been used to correct the original observations.) The results are indicated by a broken line in Fig. 11. The infrared linewidths appear to be somewhat larger, at least for low J, than the corresponding Raman linewidths. This result is not unreasonable since the infrared transitions are subject to additional broadening by pure rotational dephasing. However, given the uncertainties in both sets of measurements, the differences are not significant.

VI. NONRESONANT SUSCEPTIBILITY MEASUREMENTS

Nonresonant susceptibilities were measured indirectly by measuring the spectrum of a gas containing the species of interest plus a smaller, known fraction of a resonant species used as a reference. We used polarization background suppression and chose the resonant species concentration to obtain comparable resonant and nonresonant intensities in the spectrum. The nonresonant susceptibility (χ_{nr}) was extracted by fitting the spectrum with the concentration fixed at the known value and allowing χ_{nr} to vary. For accurate results it is important to have accurate collisonal broadening coefficients for the resonant species by the nonresonant species. In addition, the use of a single-mode pump laser reduces uncertainties due to pump field fluctuation statistics and spectral convolution calculations. This technique was previously demonstrated for N_2 and Ar,[29] resulting in estimated uncertainties of ±10%.
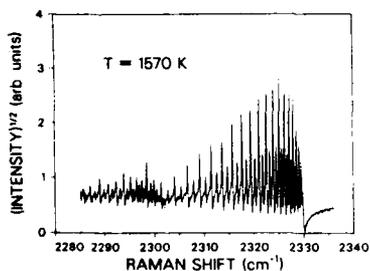
12. Experimental spectrum of the Q-branch of N_2 in the post-flame gases of a stochiometric $H_2/O_2/N_2$ premixed flame, indicated by the solid curve. A pulsed dye laser with a HWHM linewidth of 0.045 cm^{-1} was used as the Stokes laser. The broken curve is a spectrum calculated using a value for $\chi_{nr}(H_2O)$ that was varied for best fit (see text).

The nonresonant susceptibility (χ_{nr}) of H_2O vapor was measured in such a way from a CARS spectrum of N_2 in flame gases containing 67 mole % H_2O and 33 mole % N_2 (see Fig. 12). A conventional pulsed dye laser with etalon (HWHM linewidth of 0.015 cm^{-1}) was used to obtain a large frequency scan. A preliminary analysis of these data gives an STP value for $\chi_{nr}(H_2O)$ of $18.5\pm1.8 \times 10^{-18}$ cm^3/erg, or 2.18 ± 0.22 times that of N_2. High-resolution spectra of N_2/butane and N_2/propane mixtures have also been measured, and are being analyzed to determine nonresonant susceptibilities and collisional broadening coefficients.

VII. CONCLUSIONS AND SUMMARY

The two-channel, background normalization technique has been shown to be a powerful tool for analytic CARS spectroscopy. With the capability of nearly shot-noise-limited signal reproducibility, very precise single-pulse intensity measurements are possible in high-density media. We were able to achieve ±2% reproducibility of normalized CARS signals from a gas sample at 10 atm and 300 K. Depending on the nature of the sample, such data could provide time-resolved concentration, temperature, or even pressure measurements. With the addition of a second probe laser and detectors to simultaneously monitor another Raman line, temperature could be obtained.

For atmospheric-pressure combustion studies, the background-normalization technique provides precise concentrations with high sensitivity. For the CO measurements reported here, sensitivity apparently surpasses (by a factor of ~5) that of CARS experiments not using background-suppression.[10] This improvement results from the combined factors of background-suppression, narrowband excitation, and photon-limited detection. Useful information provided by the background intensity is not lost but is separately detected. The resulting normalized signal is relatively insensitive to beam alignment and, assuming similar detectors, is automatically corrected for system spectral response. Signal-to-noise ratio is also improved, though not to the extent observed for cold gases because of shot noise.

The normalization also permits precise CARS intensity measurements: we observed better than 5% long-term repeatability in our flame data. This reproducibility is due in part to inherent corrections for laser power and alignment drift provided by the normalization. Since the reference signal is generated by the sample rather than an external medium, corrections for minor beam steering, defocusing, and attenuation induced by the combustion environment are also automatically included. However, as shown by our results, the accuracy of the technique is currently determined more by systematic errors rather than experimental precision. That is, concentration accuracy is largely determined by that of the resonant and nonresonant susceptibility models, since no adjustable parameters were used. Accuracy approaching 5% of the measured concentration can probably be achieved through refinements of the spectral models or through experimental calibration in well-characterized samples.

The background normalization method has two main limitations. Since the use of narrowband lasers requires scanning of spectra, measurements are restricted to steady-state or highly reproducible combustion processes. Broadband implementations are not practical with this technique because of signal loss accompanying the use of polarization analysis. (An exception may be measurements in high-density gases.) Second, because concentrations are based on knowledge of the nonresonant susceptibility, uncertainty is introduced when this parameter is not accurately known. However, the same is true of concentration measurements based on CARS spectral shapes. One solution is to measure independently the nonresonant susceptibility, as in this work. Or, if major species are known, this susceptibility can be calculated from mixture-weighted theoretical values. For single-pulse measurements in fluctuating systems, neither approach may be practical. In this case, less accurate normalization by externally generated signals may be the only recourse.

Our results obtained with single-mode lasers demonstrate that high-resolution CARS is a viable technique for spectroscopic investigations of many species important in combustion. Raman linewidth measurements of CO in a flame were found to be consistent with infrared linewidths reported by others. N_2 O-branch linewidths and frequencies were also measured and found to produce improved agreement between experimental and theoretical spectra of CO in flames. It appears that high-resolution CARS can provide greater accuracy in concentration measurements, compared to conventional CARS experiments, due to a reduced uncertainty in the Raman linewidths.

As a spectroscopic tool, CARS offers some advantages over IRS: sensitivity appears to be higher, and nonresonant susceptibilities can be measured directly. However, interferences among transitions and coherent backgrounds in CARS spectra tend to complicate the analysis of linewidths and transition frequencies. In addition, CARS requires two pulsed high-resolution lasers rather than one pulsed and one cw laser. We are currently working to extend the continous scanning range of this experiment and are planning further investigations of CO and other combustion-related species.

REFERENCES

1. A. C. Eckbreth and R. J. Hall, "CARS Thermometry in a Sooting Flame," Combust. Flame 36, 87 (1979).

2. R. E. Teets and J. H. Bechtel, "CARS Spectra of Oxygen Atoms in Flames," Opt. Lett. 6, 458 (1981).

3. L. P. Goss, G. L. Switzer, and D. D. Trump, "Temperature and Species Concentration in Turbulent Flames by the CARS Technique," J. Energy 7, 403 (1983).

4. R. L. Farrow, P. L. Mattern, and L. A. Rahn, "Comparison between CARS and Corrected Thermocouple Temperature Measurements in a Diffusion Flame," Appl. Opt. 21, 3119 (1982).

5. A. C. Eckbreth, G. M. Dobbs, and J. H. Stufflebeam, "CARS Temperature and Species Measurements in Augmented Jet Engine Exhausts," AIAA-83-1294, 1983.

6. B. Attal, M. Pealat, and J. P. Taran, "CARS Diagnostics of Combustion," AIAA-80-0282, 1980.

7. J.-L. Oudar, R. W. Smith, and Y. R. Shen, "Polarization-Sensitive CARS," Appl. Phys. Lett. 34, 758 (1979).

8. R. L. Farrow, R. E. Mitchell, L. A. Rahn, and P. L. Mattern, "Crossed-beam, Background-Free CARS Measurements in a Methane Diffusion Flame," AIAA-81-0182, 1981.

9. F. S. Moya, S. Druet, M. Péalat, and J.-P. Taran, "Flame Investigation by CARS," Prog. Astronaut. Aeronaut. 53, 549 (1977).

10. A. C. Eckbreth and R. J. Hall, "CARS Concentration Sensitivity with and without Nonresonant Background Suppression," Combust. Sci. Technol. 25, 175 (1981).

11. R. J. Hall, "CARS Spectra of Combustion Gases," Combust. Flame 35, 47 (1979).

12. See, for example, M. L. Koszykowski, R. L. Farrow, and R. E. Palmer, "Calculation of Collisionally Narrowed CARS Spectra," Opt. Lett. 10, 478 (1985), and references therein.

13. R. J. Hall, "Pressure-broadened Linewidths for CARS Thermometry," Appl. Spectrosc. 34, 700 (1980).

14. L. A. Rahn, A. Owyoung, M. E. Coltrin, and M. L. Koszykowski, "The J-dependence of Nitrogen Q-branch Linewidths," in Proceedings of the VII International Conference on Raman Spectroscopy, ed. W. F. Murphy (North-Holland, New York, 1980), pp. 694-95.

15. See, for example, S. Yu. Volkov, D. N. Kozlov, M. R. Malikov, E. A. Otlivanchik, and V. V. Smirnov, "High-Sensitivity High-resolution Pulsed CARS Spectrometer," Sov. J. Quantum Electron. 14, 1240 (1984).

16. P. L. Varghese and R. K. Hanson, "Collision Width Measurements of CO in Combustion Gases Using a Tunable Diode Laser," J. Quant. Spectrosc. Radiat. Transfer 26, 339 (1981).

17. W. G. Rado, "The Nonlinear Third Order Dielectric Susceptibility Coefficients of Gases and Optical Third Harmonic Generation," Appl. Phys. Lett. 11, 123 (1967).

18. T. Lundeen, S.-Y. Hou, and J. W. Nibler, "Nonresonant Third Order Susceptibilities for Various Gases," J. Chem. Phys. 79, 6301 (1983).

19. G. J. Rosasco and W. S. Hurst, "Measurement of Resonant and Nonresonant Third Order Nonlinear Susceptibilities by Coherent Raman Spectroscopy," Phys. Rev. A. 32, 281 (1985).

20. D. P. Shelton and A. D. Buckingham, "Optical Second-Harmonic Generation in Gases with a Low Power Laser" Phys. Rev. A. 26, 2787 (1982).

21. L. A. Rahn, L. J. Zych, and P. L. Mattern, "Background-Free CARS Studies of Carbon Monoxide in a Flame," Opt. Commun. 30, 249 (1979).

22. S. A. J. Druet and J.-P. E. Taran, "CARS Spectroscopy," Prog. Quant. Electron. 7, 1 (1981).

23. G. J. Rosasco, W. Lempert, and W. S. Hurst, "Line Interference Effects in the Vibrational Q-branch Spectra of N_2 and CO," Chem. Phys. Lett. 97, 435 (1983).

24. L. A. Rahn, R. L. Farrow, and P. L. Mattern, in Raman Spectroscopy: Linear and Nonlinear, eds. J. Lascombe and P. V. Huong, (Wiley, New York, 1982), pp. 143-152.

25. L. A. Rahn, private communication.

26. G. Guelachvili, "Absolute Wavenumbers and Molecular Constants of the Fundamental Bands of $^{12}C^{16}O$, $^{12}C^{17}O$, $^{12}C^{18}O$, $^{13}C^{16}O$, $^{13}C^{17}O$, $^{13}C^{18}O$, and of the 2-1 Bands of $^{12}C^{16}O$ and $^{13}C^{16}O$, Around 5 μm, by Fourier Spectroscopy Under Vacuum," J. Mol. Spectrosc. 75, 251 (1979).

27. D. E. Jennings, L. A. Rahn and A. Owyoung, "Laboratory Measurement of the S(9) Pure Rotational Frequency in H_2," Astrophys. J. 291, L15 (1985).

28. T. R. Gilson, I. R. Beattie, J. D. Black, D. A. Greenhalgh, and S. N. Jenny, "Redetermination of Some of the Spectroscopic Constants of the Electronic Ground State of di-Nitrogen $^{14}N_2$, $^{14}N^{15}N$, and $^{15}N_2$ Using CARS," J. Raman Spectrosc. 9, 361 (1980).

29. R. L. Farrow and L. A. Rahn, "Interpreting CARS Spectra Measured with Multi-mode Nd:YAG Pump Lasers," J. Opt. Soc. Am. B 2, 903 (1985).

30. See the discussion in Refs. 18 and 19. This correction factor includes a factor of 3 due to different definitions of the nonresonant susceptibility (we are using the notation of Ref. 10).

31. H. W. Schrötter and H. W. Klockner, in "Raman Spectroscopy of Gases and Liquids," ed. A. Weber (Springer-Verlag, New York, 1979), pp. 123-201.

32. N. J. Bridge and A. D. Buckingham, "Polarization of Laser Light Scattered by Gases," Proc. Roy. Soc. 295A, 334 (1966).

33. H. Kataoka, S. Maeda, and C. Hirose, "Effects of Laser Linewidth on the CARS Spectral Profile," Appl. Spectrosc. 36, 565 (1982).

34. R. E. Teets, "Accurate Convolutions of CARS Spectra," Opt. Lett. 9, 226 (1984).

35. Y. A. Yuratich, "Effects of Laser Linewidth on CARS," Mol. Phys. 39, 625 (1979).

36. R. J. Hall and A. C. Eckbreth, "CARS: Application to Combustion Diagnostics," in Laser Applications, Vol. 5, eds. J. F. Ready and R. K. Erf (Academic Press, New York, 1984), pp. 213-309.

37. R. L. Farrow and L. A. Rahn, "Optical Stark Splitting of Rotational Raman Transitions," Phys. Rev. Lett. 48, 395 (1982).

38. L. A. Rahn, R. L. Farrow, .I. L. Koszkowski, and P. L. Mattern, "Observation of an Optical Stark Effect on Vibrational and Rotational Transitions," Phys. Rev. Lett. 45, 620 (1980).

39. R. L. Farrow and L. A. Rahn, "Optical Stark Effects in Nonlinear Raman Spectroscopy," in Raman Spectroscopy: Linear and Nonlinear, eds. J. Lascombe and P. V. Huong (Wiley, New York, 1982), pp. 159-60.

40. R. A. Hill, P. Esherick, and A. Owyoung, "High-resolution Stimulated Raman Spectroscopy of O_2," J. Mol. Spectrosc. 100, 119 (1983).

41. J. H. Stufflebeam, R. J. Hall, and A. C. Eckbreth, "Investigation of the CARS Spectrum of Carbon Monoxide at High Pressure and Temperature," Air Force Rocket Propulsion Laboratory Technical Report No. TR-84-042, 1984.

42. S. M. Schoenung and R. K. Hanson, "CO and Temperature Measurements in a Flat Flame by Laser Absorption Spectroscopy and Probe Techniques," Comb. Sci. and Tech. 24, 227 (1981).

43. P. C. Malte and J. C. Kramlich, "Further Observations of the Effect of Sample Probes on Pollutant Gases Drawn from Flame Zones," Comb. Sci. and Tech. 22, 263 (1980).

44. L. A. Rahn, R. L. Farrow, and R. P. Lucht, "Effects of Laser Field Statistics on CARS Intensities," Opt. Lett. 9, 223 (1984).

45. R. L. Farrow, L. A. Rahn, and R. P. Lucht, in Proceedings of the IX International Conference on Raman Spectroscopy, ed. M. Tsuboi (Chemical Society of Japan, Tokyo, 1984), pp. 340-41. These results show that the effect of field statistics appears to be less pronounced for overlapping Q-branch transitions in comparison to isolated lines.

46. The DEQUIL program was modified by R. J. Kee, Sandia National Laboratories, from the program STANJAN, developed by W. C. Reynolds, Stanford University.

47. R. L. Schmitt and L. A. Rahn, "Diode-Laser-Pumped Nd:YAG Laser Injection Seeding System," Appl. Opt., accepted for publication, 1986.

48. A. D. Wilson-Gordon, R. Klimovsky-Barid, and H. Friedmann, "Saturation Effects in CARS," Phys. Rev. A 25, 1580 (1982).

DISCUSSION

R.B.Price, UK

Does the use of the "in-situ" normalisation technique you have discussed become feasible for broadband CARS at high pressures representative of gas turbine combustors or I C engines?

Author's Reply

Yes, in fact we have applied the *in-situ* referencing technique to an I C engine at Sandia. The largest obstacle to overcome is insufficient signal from the sample nonresonant background. Depending on the conditions of the application, i.e. pressure and temperature, enough signal might be obtained to permit broadband measurements.

D.A.Greenhalgh, UK

What strategies would you recommend for measuring

(i)   CO concentration

and

(ii)   hydrocarbon concentrations?

Are there any particular problems to be overcome?

Author's Reply

CO concentration measurements have been demonstrated using a number of different CARS techniques. The selection of technique depends on experimental conditions and the measurement requirements (e.g. spatial and temporal resolution required, signal strengths expected).

Hydrocarbon species measurements pose special problems due to the spectroscopic complexity associated with large polyatomic molecules. Assuming lack of existing CARS spectral models, an initial approach might be to use library spectra measured in controlled samples. The use of a low-spectral resolution experiment might be considered in order to simplify data fitting. Another consideration arises from the large nonresonant susceptibilities of hydrocarbon species. When measuring concentrations by referencing to the sample nonresonant background, the larger background contribution of the resonant species may not be negligible.

NONLINEARITY AND SINGLE SHOT NOISE PROBLEMS IN CARS SPECTROSCOPY

by

D.R. SNELLING, G.J. SMALLWOOD and R.A. SAWCHUK
Defence Research Establishment Ottawa
Ottawa, Ontario K1A 0Z4

and

T. PARAMESWARAN
Roy Ball Associates

1.0   SUMMARY

In this paper we describe the design and operation of a CARS spectrometer and its use to perform accurate temperature measurements in a simple laboratory flat-flame burner. Instrumental sources of systematic error and noise in CARS temperature measurements are discussed. An analysis of the system noise is presented and the use of the measured noise to perform weighted least mean squares fits of experimental and theoretical CARS spectra is discussed. The use of a weighted fit is shown to markedly improve the precision of single pulse CARS temperature measurements. Finally, the incorporation of some recent advances in CARS theory which have resulted in more computationally efficient algorithms for calculating theoretical CARS spectra and their effect on the accuracy of temperature measurements are discussed.

2.0   INTRODUCTION

A program was initiated at the Defence Research Establishment Ottawa (DREO) to develop optical diagnostics that could be applied to diesel engine combustion research. As part of this program a coherent anti-Stokes Raman spectroscopy (CARS) system was constructed. This program has very recently been transferred to the National Research Council's Gas Dynamics Laboratory with a shift in emphasis to continuous combustion research related to gas turbines.

The theory and application of CARS are described in a number of recent review articles[1-4]. CARS is a technique which is receiving much attention because of its capability for providing remote, in-situ measurements of major species concentration and temperature with good spatial and temporal resolution in practical combustion environments. Single pulse CARS measurements are possible[5] if a broadband dye laser is used to generate the Stokes laser frequencies. Temperature measurements can be derived from the spectral shape of CARS signals (e.g., nitrogen spectra) by fitting them to calculated theoretical spectra whose temperatures are systematically varied in order to obtain a best fit.

Although CARS temperature measurements have successfully been demonstrated in simulated gas turbine environments[6-9], and afterburning jet engines[10], further work is required to improve the accuracy and precision of CARS thermometry. It is important to improve the single shot precision in order to reduce the instrumental contribution to measured histograms such as those reported in reference 9.

The sources of error and noise can be broadly classified as: instrumental, theoretical, or a result from perturbations due to the medium being probed. Since most of our CARS temperature measurements have been performed in a flat-flame burner the effects of the medium in, for example, deflecting or defocusing the laser beams are negligible. In this paper we discuss various instrumental and theoretical sources of error and noise we have encountered and techniques for their amelioration.

We discuss instrumental effects such as detector nonlinearity[11] and the effect of single-mode or multimode operation of the pump laser on the CARS spectral noise[12]. Measurements of detector noise and noise due to the pulse-to-pulse variability of the CARS signal are presented. The use of these measured noise variances as weighting parameters in a weighted least mean squares fit of experimental and theoretical CARS spectra is described. The noise and precision of single pulse CARS measurements is examined using both nonresonant CARS spectra and resonant N_2 spectra recorded in a flat-flame burner which was previously calibrated using the Na line reversal technique.

Recent advances in CARS theory have modified the original approach which was based on isolated spectral lines and a convolution integral[13] which neglected "cross-coherence" terms in the pump laser convolution[14,15]. At higher pressures it is necessary to account for collisional effects which result in the initial broadening and overlap of individual lines and eventually to line mixing and collisional narrowing. Under these conditions a knowledge of the state-to-state relaxation rates and the inversion of the "G-matrix" is required[16].

We have included the coherence effect due to a finite Gaussian pump laser spectral bandwidth[17] and the collisional narrowing approach of Koszykowski et al[18] in our code, and compare the temperatures derived with and without these modifications.

3.0   CARS Spectrometer and Data Acquisition System

A scale diagram of the CARS layout is shown in Fig. 1. The pump laser is a frequency-doubled Nd:YAG (Quanta Ray DCR 1A) operating at 10 Hz with the electronic line narrowing (ELN-2) option. After the main doubler, the pump beam (ωp) is split off from the residual 1.06 μm radiation, which is sent to a second frequency doubler. The output of this second doubler is used to pump the dye laser oscillator (ω_s). The amplifier portion of the dye laser is pumped by a portion (30%) of the main ω_p beam split off by a beam splitter.

The oscillator dye cell is an AR-coated quartz cuvette (10 mm wide by 17.5 mm high) which is rotated 10° to avoid optical feedback. The pump beam is focused into the dye cell by a 750 mm focal length lens with the dye cell ~ 170 mm from the focus. The pump beam size in the dye cell is ~ 1.5 mm and pump beam axis is 7° from the dye oscillator lasing axis. A quartz plate at the Brewster angle or a calcite polarizer in the dye oscillator cavity ensures that the dye output is suitably polarized.

Originally the centre wavelength of the dye laser was tuned by varying the dye concentration which is typically 2.6×10^{-4} M rhodamine 640. A more convenient method was to insert a bandpass filter in the dye cavity [centred at 610 nm with a width (*FWHM*) of 9.5 nm]. The filter is typically set at 20° to obtain a centre wavelength of 606 nm for N_2 CARS. The filter reduces the dye laser bandwidth from 150 to 70 cm^{-1} (*FWHM*).

The pumping geometry of the dye amplifier is essentially identical to that of the oscillator. The dye amplifier cuvette is 17 mm wide and 21 mm high and a rhodamine 640 concentration of 1.06×10^{-4} M is used. The dye solutions are circulated with linear flow rates of 10 cm/sec (oscillator) and 4.5 cm/sec (amplifier).

Galilean telescopes are incorporated into the pump and Stokes beams to control beam diameter and focal spot location. The telescopes provide beam magnification of 1.9. The two beams were combined collinearly with a dichroic mirror and focused with a 203 mm focal length lens. Typically 30-40 mJ of pump radiation and 10 mJ of Stokes radiation were used. The 3-D phase matching technique[19] employed, called USED CARS[10], involves passing the ω_s Stokes beam coaxially through the annular ω_p pump beam. The ω_p and ω_s beams and the resulting CARS (ω_{as}) beam are recollimated and low pass filters are used to reflect the now unwanted pump and Stokes radiation. A beam splitter directs part of the CARS signal to a photomultiplier tube connected to an EG&G model 162 boxcar integrator. The boxcar signal gives a time-averaged measure (time constant 5 sec) of the undispersed CARS signal. The remaining CARS radiation is focused on the entrance slit of a spectrometer utilizing a single concave holographic diffraction grating (American Holographics). This grating disperses the CARS radiation across the face of a Tracor Northern 1024-element intensified diode array rapid scan detector (IDARSS TN-6132). The 1.6 m spectrometer has a reciprocal linear dispersion of 2.24 Å/mm corresponding to 0.25 cm^{-1}/diode.

Nonresonant CARS spectra were recorded by placing a carbon dioxide filled cell at the focal volume. In order to provide sufficient CARS signal to overcome the shot noise of the detector, it was sometimes necessary to pressurize the cell to 3 atm[11].

It is necessary to correct the CARS signals by subtracting a background which results from detector dark current, detector fixed pattern noise, and a small signal due to scattered 532 nm radiation. This background signal is obtained by acquiring spectra while blocking the Stokes laser.

Single longitudinal mode operation of the Quanta Ray DCR 1A is achieved using the electronic line narrowing (ELN-2) device. The ELN-2 controls the oscillator to maintain a low gain for a time sufficient to achieve narrow linewidth. The laser is then rapidly Q-switched to provide maximum gain producing a pulse of high spectral purity. With careful adjustment of the Q-switch bias and the intracavity etalon, ~50% of the pulses are single-mode and exhibit the smooth temporal profile indicative of the absence of mode beating. In normal operation without the ELN-2, the stated bandwidth of the pump laser is <0.4 cm^{-1}.

Single longitudinal mode (single-mode) data were obtained by using the "smooth" output signal from the ELN-2 as the spectrometer trigger input on the Tracor Northern TN1710 optical multichannel analyzer (OMA). Multiple longitudinal mode (multimode) data were obtained by triggering the OMA from the external timing circuits.

The spectral width of the pump laser was measured with two Fabry-Perot etalons with 0.27 cm^{-1} and 1.7 cm^{-1} free spectral range, respectively. An unintensified photodiode array was used to display the interference fringes from a single laser pulse. The measured average spectral widths (FWHM) when operating the laser single-mode, multimode (etalon in YAG cavity), and multimode (no etalon in YAG cavity) were $0.016 \pm .001$ cm^{-1}, $.10 \pm .01$ cm^{-1}, and $.69 \pm .03$ cm^{-1} respectively. The single-mode width probably represents the resolution of the 0.27 cm^{-1} etalon.

In order to remove the small residual signals remaining on the detector due to image lag, it was necessary to perform two "cleansing scans" of the detector between each laser pulse[20]. When the detector was read 60 ms after exposure (see Fig. 2), the residual signal (as registered by the first "cleansing scan") was determined to be 0.25% of the original signal. No residual signal was detected by the second "cleansing scan". The "cleansing scans" were initiated by the external read signal from the external

timing circuits triggering the OMA to read but not store the diode intensities. The laser pulse and signal integration began immediately after completion of the "cleansing scans". The entire cycle was completed within 100 ms for 10 Hz operation.

The acquisition and storage of 1,24-element spectra at a 10 Hz rate was accomplished through a complex hardware and software interfacing procedure, shown conceptually in Fig. 3. As each spectrum was collected by the OMA, a previous one was transferred to the DEC VAX 11/730 via the parallel long-line drivers, where it was checked for saturation or transmission errors. The data was transmitted and temporarily stored in binary form in order to increase speed and reduce storage. Upon completion of a collection run, the data was treated by post-processing software on the VAX. This included multiplication by 8 (to retain accuracy during later manipulation of the data), subtraction of the background spectrum, division by the nonresonant spectrum (to correct for diode to diode sensitivity variations and the spectral variations due to the dye laser, spectrometer, etc.), calculation of the average spectrum for the collection, and permanent storage of these treated spectra in binary form (2k bytes per spectrum). A typical multimode unreferenced hot flame spectrum and the associated nonresonant reference are shown in Fig. 4. The effect of division by the nonresonant reference on an averaged hot flame spectrum is illustrated in Fig. 5, showing the resultant calibrated spectrum. Averaged (100 to 400 pulses) background and nonresonant reference spectra were recorded at the beginning and end of each data acquisition period.

The burner in Fig. 6 was designed to have a premixed, well controlled, constant temperature, stabilized flat-flame[21,22]. The flame front established itself in a equilibrium position a short distance from the burner surface, where the heat loss to the water-cooled burner reduced the flame speed to the mixture stream velocity. The region probed was the flame from the inner combustion zone. The outer combustion zone protects the flame from large temperature gradients. The sheath of inert gas further protects the flame from atmospheric effects. Temperature calibration of the burner was performed using the sodium line-reversal technique[22]. The burner was operated with a hydrogen/air flame at an equivalence ratio of 0.574 and CO_2 as the sheath gas. The linear flow velocity was approximately 30 cm/s. The burner was also run with a stoichiometric methane/air flame. It was calibrated at 1600 K and 2000 K.

4.0   Theory and CARS Data Reduction

The theory of CARS has been dealt with extensively[1-4,23-25]. In brief, CARS is a nonlinear optical phenomenon involving three wave mixing. When two laser beams of frequencies ω_p and ω_s interact in a medium, three wave mixing produces a resultant coherent beam with frequency ω_{as} and this is the CARS beam. The mixing occurs for all samples but the CARS signal is greatly enhanced when $\omega_p - \omega_s$ approaches a Raman frequency of the medium.

The interaction of the laser radiation with the medium occurs through the third order nonlinear electric susceptibility denoted by $\chi^{(3)}$. This gives rise to an induced polarization field which acts as the source term in Maxwell's wave equation. On solving the wave equation one gets, for monochromatic input waves, the intensity of the CARS signal as

$$I(\omega_{as}) \sim I_p^2\, I_s\, |\chi^{(3)}|^2 \tag{1}$$

where I_p, I_s, and $I(\omega_{as})$ represent the pump, Stokes, and CARS intensities respectively. $\chi^{(3)}$ has resonant χ^R and nonresonant χ^{NR} contributions:

$$\chi^{(3)} = \chi^{NR} + \chi^R \tag{2}$$

The nonresonant susceptibility χ^{NR} is real and proportional to the number density. Raman active modes involved in the CARS spectra of combustion processes are strongly polarized vibration rotation transitions. It is considered sufficiently accurate to restrict calculations to the Q-branch. The widths of these Raman lines are functions of pressure, temperature and rotational quantum number[26]. When pressure increases the lines broaden and may overlap; at higher pressures, when there is sufficient interference between adjacent transitions, collisional narrowing occurs[27,28] and the system relaxes according to the density matrix equation. Hall has applied the density matrix formalism to the CARS process and arrived at the following expression for the resonant susceptibility[29].

$$\chi^R = \frac{12\,N}{h}\, \sum_t\, \alpha_t\, \sum_s\, \alpha_s\, \Delta\rho_{ss}(G)^{-1}_{ts} \tag{3}$$

where N is the number density, α_t and α_s are the polarizability matrix elements, $\Delta\rho$ is the population factor, and t,s denote the combined vibration and rotation quantum numbers. The elements of the G-matrix in equation 3 are given by

$$G_{ts} = i(\omega_p - \omega_s - \omega_t)\, \delta_{ts} + \Gamma_t/2\, \delta_{ts} + \gamma_{ts}\,(1-\delta_{ts}) \tag{4}$$

where ω_p, ω_s, and ω_t denote the pump, Stokes and Raman frequencies respectively, Γ_t is the isolated line width and γ_{ts} are the off diagonal matrix elements of the relaxation rate matrix G. In equation 4, γ_{ts} are assumed to be real and line shifts are neglected. Koszykowski et al[18] have shown that by using an efficient algorithm equation 3 may be reduced to

$$\chi^R(\delta) = \int \frac{a_j}{\lambda_j' - \delta + i\lambda_j''} \tag{5}$$

where $\lambda_j = \lambda_j' + \lambda_j''$ is the complex eigenvalue of the G-matrix, δ is the detuning, and a_j is in general a complex weight factor. At low pressures one may neglect the overlap between lines and set γ_{ts} to 0; then λ_j' approaches the Raman frequency ω_j; λ_j'' approaches Γ_j, the Raman line width; and χ^R reduces to

$$\chi^R(\delta) = \frac{4\pi Nc^4}{h \ \omega_s^4} \int \frac{\Delta\rho_{jj} \left| d\sigma/d\Omega \right|_j}{2\delta - i\Gamma_j} \tag{6}$$

This is the isolated line approximation. The Raman cross-section can be expressed as follows for the Q-branch:

$$\left| \frac{d\sigma}{d\Omega} \right|_j = \frac{\omega_s^4}{c^4} \ \frac{h}{4\pi M\omega_0} \ [\ \alpha^2 + \frac{7}{45} \ b_j^2 \ \gamma^2] \ [v + 1] \tag{7}$$

where M is the reduced mass, ω_0 is the angular frequency of the molecular oscillator, b_j are the Placzek-Teller coefficients, α is the derivative of the mean molecular polarizability with respect to inter-nuclear distance, γ is the similar derivative of anisotropy and v is the vibrational quantum number of the initial level.

Knowing χ^R and χ^{NR}, equation 1 can be directly used to get the CARS spectrum for monochromatic laser beams. The effect of laser bandwidths on theoretical CARS spectra is treated extensively by Yuratich[13]. In a "standard" method widely used in CARS theory, the final CARS intensities are obtained by a simple convolution of $|\chi^{(3)}|^2$ with the pump and Stokes spectral profiles[20,30,31]. This approach ignores the cross terms that arise from the coherence between the polarization components in which the roles of the driving and scattered pump photons are exchanged. In this approximation, when the pump width is very small and the Stokes width is much greater, the CARS intensity may be expressed as

$$I(\omega_{as}) \sim I_p \int I_s(\omega_p^{(0)} - \delta) \ I_p \ (\omega_{as} - \delta) |\chi^{(3)}(\delta)|^2 \ d\delta \tag{8}$$

where $\omega_p^{(0)}$ is the centre frequency of the pump.

A computer program based on equation 8 and the isolated line approximation[32] was kindly provided by the United Technologies Research Centre, USA (UTRC). Theoretical spectra were generated with a modified version of this program. Since the experimental spectra were ratioed with a nonresonant CARS spectrum, the convolution over dye profile was eliminated. Storing the pump exponents once calculated and reusing them helped reduce the convolution cpu time. All the computations were done with the DEC VAX 11/730 computer.

The CARS spectrum thus generated was then convolved with a Voigt instrumental (slit) function. Since an exact Voigt is rather too complicated, an approximate expression due to Whiting[33] was used. This approximation (eqn. 5 of Ref. 33) is expressed in terms of a Voigt width w_V and a Lorentz width w_L related to the Gaussian width w_G as follows:

$$w_V = \frac{w_L}{2} + [\frac{w_L^2}{4} + w_G^2]^{1/2} \tag{9}$$

An asymmetric Voigt with different values of w_V and w_L on the higher and lower cm^{-1} sides was found to be suitable.

Initially the Voigt parameters were obtained from room temperature (RT) CARS spectra of N_2. Theoretical RT spectra of N_2 were convolved with a Voigt of trial parameters and compared with experimental spectra. Best fit values of w_V and w_L were obtained with a nonlinear least mean squares fitting program based on the well known Gauss-Newton algorithm as adapted by Kim[34].

The Voigt function determined from several RT N_2 spectra was used for convolution with theoretical spectra at temperatures ranging from 300 K to 2700 K. A fitting program similar to the one used for the slit function calculation was then employed to fit hot theoretical spectra with experimental spectra and best fit values of temperatures were determined. In this procedure, temperature and frequency shift between theory and experiment were used as fit parameters. It is too time consuming to generate the theoretical spectra for each iteration and therefore a library of spectra calculated at 50 K intervals was used. These spectra were interpolated for intermediate temperatures.

The flame temperatures thus determined were somewhat sensitive to the Voigt slit parameters. Hence attempts were made to obtain the four Voigt parameters, as well as temperature and frequency with a six parameter fitting scheme. The results of these fits are presented in a later section.

Input Variables

The variables that determine the theoretical CARS spectrum of a molecule are: the spectroscopic constants, the Raman line width Γ_i, the concentration, temperature T, pressure P, nonresonant susceptibility χ^{NR}, the Raman cross-section $d\sigma/d\Omega$, the pump laser frequency $\omega_p^{(0)}$ and bandwidth $\Delta\omega_p$, and the statistical weight factors. The term $d\sigma/d\Omega$ was calculated for every level from the molecular polarizability parameters. The constants α and γ were calculated from Penney[35]. Corrections to χ^R due to anharmonicity and centrifugal distortions were computed with the results of Bouanich and Brodbeck[36]. The spectroscopic constants were from Sandia[37]. For the isolated lines the width was calculated according to Hall[38]. There has been considerable uncertainty in the scaling of the χ^{NR} of diatomic molecules. Rosasco et al[39] and Lundeen[40] review the various measurements. For N_2 we have used the value of 8.31 x 10^{-18} cm^3/erg, which is the average of that quoted by Rosasco and that reported by Farrow[41]. The χ^{NR} values for O_2 and Ar that are needed for the H_2/air flame were also from ref. 39. For H_2O the χ^{NR} used was 18.29 x 10^{-18} cm^3/erg[41]. Further details of CARS input variables are described in ref. 42. All the theoretical spectra were generated at one atmosphere pressure.

Collisional Narrowing

It is now accepted that[18], while collisional narrowing of Raman lines cannot be neglected for CARS spectra at high pressures, it can become significant even at atmospheric pressures. To test this effect a library of theoretical spectra with collisional narrowing was also generated. These calculations were based on eqns. 5 and 8. The off diagonal line matrix elements γ_{ts} of the relaxation rate matrix were obtained with an exponential gap law[18] model.

Cross-Coherence Effects

Teets[15] and Kataoka[14] have observed that neglecting the cross-coherence terms that arise in the laser convolution of CARS intensities can lead to temperature errors, especially when the pump bandwidth is comparable to the Raman line width and the nonresonant contribution competes with the resonant signal. Including this effect the CARS intensity may be written (not including dye convolution) as

$$I_{as}(\omega_{as}) = \chi_{NR}^2 \langle 1 \rangle + 2\chi_{NR}\langle \mathrm{Re}\,\chi_R(\omega_{as}-\omega') \rangle$$
$$+ \frac{1}{2}\langle |\chi_R(\omega_{as}-\omega')|^2 \rangle + \frac{1}{2}\langle \chi_R(\omega_{as}-\omega')\chi_R(\omega_{as}-\omega'') \rangle \tag{10}$$

where

$$\langle F \rangle = \int d\omega' I_p(\omega') \int d\omega'' I_p(\omega'') F(\omega',\omega'') \tag{11}$$

Normally the fourth term in equation 10 is difficult to evaluate because of the double integral. However analytical closed form expressions for this problem have been derived by Teets[15] for Lorentzian pump profile and by Greenhalgh and Hall[17] for Gaussian pumps. For the latter case the fourth term $I^{(cc)}$ may be given in terms of an error function $W(Z_j)$.

$$I_{as}^{(cc)}(\omega_{as}) = \frac{\Pi}{2\Delta\tilde{\omega}_p^2}\left| \sum_j a_j W_j(Z_j) \right|^2 \tag{12}$$

where cc refers to cross-coherence, $\Delta\tilde{\omega}_p$ is the pump width and Z_j is a complex argument given below:

$$Z_j = \frac{(\lambda_j - (\omega_{as}-\omega_p^{(0)})) - i\lambda_j''}{\Delta\tilde{\omega}_p} \tag{13}$$

Presently we have included this term in the CARS program with the collisional narrowing corrections. The complex error functions were generated with an efficient algorithm by Hui et al[43]. With this technique the cross coherence terms required very little additional computer time.

Results obtained from the three theoretical models viz: isolated line approximation collisional narrowing, and the latter with accurate laser convolution including cross-coherence effects will be compared with experimental CARS spectra in a later section.

5.0 Detector Nonlinearities

The problem of detector nonlinearity[11,20,44] was encountered in making temperature measurements in a flat-flame burner. The burner was fueled with a 10.5% CH_4 in air mixture, at a linear (cold) flow velocity of 28.5 cm/sec, and the Na line-reversal temperature 10 mm above the burner centre was 2060 K. CARS temperatures in this burner ranged from 2050 to 2500 K. Since some of these temperatures were significantly higher than even the adiabatic flame temperature (2195 K) it was clear that a source of error existed in the CARS measurements.

The main source of error was identified as nonlinearity in the intensified optical multichannel detector. Provided the output of the individual detector diodes was confined to the lower third of the A-D converter (i.e., 1500 counts out of a maximum 4096 counts per diode), the temperatures obtained were in the 2050-2200 K range. As the signals approached the maximum allowed by the A-D converter, increasingly higher temperatures were obtained.

The detector nonlinearity was evaluated, using resonant room temperature N_2 CARS spectra, by placing calibrated neutral density filters in the CARS beam. The boxcar signal was also attenuated by the neutral density filters and thus provided an additional signal against which the IDARSS output could be evaluated.

The large shot-to-shot variability of CARS signals (a standard deviation of ±30% is typical) required that data averaging be used to establish the linearity. Thus for each measurement 100 single pulse nitrogen spectra were accumulated to reduce this variability. To quantify the linearity, the intensity had to be varied from zero to the maximum output of the detector. To have an average signal which approached this maximum output (4096 counts/diode) some of the spectra included in the average had intensity levels that exceeded the maximum capability of the A-D converter. To correct for this effect, 100 room temperature nitrogen CARS spectra were recorded at low intensity (<1000 counts). The distribution of peak counts was scaled by a fixed multiplier and distribution averages were calculated with and without a 4096 count limit. The difference between these two averages then represents the correction due to A-D cutoff and this was used to correct the observed data.

An example of the data, including this correction, is shown in Fig. 7 where the observed counts/diode (for the peak of the room temperature N_2 spectra) is plotted against filter transmission and boxcar signal. The curves representing the best fit to the corrected data are described below.

If a significant nonlinearity exists, a fit of the data to an equation of the form $C = aX + bX^2$ (where C is the number of counts and X is the relative intensity, i.e. filter transmission or boxcar signal) should produce a significant nonlinear b term. A linear regression line for C/X against X was calculated for each set of data and values of the a and b coefficients and their standard deviation were obtained. (A similar linear regression analysis of the boxcar signal against the filter transmission was linear, i.e., no statistically significant value of b was obtained as expected.) The only exception to this was when the CARS intensity drifted during the course of the experiment as evidenced by a change in the signal level with no filter in place before and after the experiment.

Since the boxcar signal was in arbitrary units and since the CARS intensity changed from day to day, it was necessary to normalize all the data so that they could be presented on a common plot. It was decided to use the a and b parameters obtained from the linear regression analysis to calculate a value (X_0) of the dependent variable X corresponding to 1500 counts (in the linear range of the detector). The equation then takes the form

$$C = a'(X/X_0) + b'(X/X_0)^2 \qquad (14)$$

where $a = a'/X_0$ and $b = b'/X_0^2$. This normalization permits the coefficients (a',b') to be expressed in normalized coordinates and allows all the data to be presented on a common plot against a normalized signal level (X/X_0). Such a composite plot is shown in Fig. 8 for the TN-1223-4GI detector. The plots are for a CARS image height (see below) of 0.275 mm.

A final estimate of the nonlinearity was then obtained either by fitting the data in the composite plot or by averaging the a',b' coefficients obtained from individual plots. The results of these two procedures were essentially identical and the values listed in Table I were obtained by the first method.

TABLE I

SUMMARY OF BEST-FIT VALUES FOR THE COEFFICIENTS IN
THE DETECTOR RESPONSE EQUATION $C = a'I + b'I^2$

Expt. no.	Image height mm[a]	b'	σb'	a'	σa'	Detector
1	0.203	-235.4	10.9	1735.0	23.4	TN-1223-4GI
2	0.275	-151.7	8.8	1650.2	19.5	TN-1223-4GI
3	0.521	+2.3	21.8	1495.2	29.5	TN-1223-4GI
4	0.275	+2.8	21.9	1496.2	27.7	TN-6132

[a] See Fig. 9

The image heights listed in Table I were obtained by rotating the detector through 90° about the optical axis of the spectrometer. The heights represent the equivalent width of the image and the exact profiles are shown in Fig. 9.

In our spectrometer the CARS image height can be varied by adjusting the grating to detector spacing. The aberrations inherent in a concave diffraction grating result, at optimum resolution, in an image of the circular CARS input spot which is greatly elongated in the direction of the long axis of the diodes. The pixel size of the diode array is 25 μm by 2.5 mm. The image height at optimum resolution (0.275 mm) can be increased to 0.521 mm or decreased to 0.203 mm by moving the detector ~ 13 mm toward or away from the grating. The effect of moving from the point of optimum resolution is such as to increase the apparent width (FWHM) of room temperature N_2 CARS spectra from twelve to sixteen diodes.

The data in Table I show that the TN-1223-4GI detector exhibits marked saturation behavior for the two smaller image heights in that the nonlinear term, b', is negative and statistically significant. For the largest image height the TN-1223-4GI exhibits no such saturation since the nonlinear term is positive and is not statistically significant.

The saturation effect is clearly dependent on radiation density in that, as the height of the CARS image (hence the detector area illuminated) is increased, the nonlinear term decreases. Thus the nonlinearity can be avoided by paying appropriate attention to image size. This is consistent with the observation [4] that nonlinear behavior of a CARS spectrometer, incorporating an EG&G PARC model 1420 intensified diode array detector, could be eliminated by interposing a cylindrical lens between the grating and the detector in order to selectively defocus the radiation along the height of the diodes.

The data in Table I show that for an image height of 0.275 mm the TN-6132 behaved linearly, in marked contrast to the TN-1223-4GI. The difference in behavior can be attributed to the reduced sensitivity and reduced microchannel plate gain of the TN-6132 (see discussion below).

Because of astigmatism many grating spectrometers, at optimum resolution, produce an image which is elongated in the direction orthogonal to the dispersion plane. By suitably selecting the image plane this effect can be used to increase the CARS image size although some loss of resolution will result. The astigmatism decreases with increasing f-number and the inherent low angular divergence of the CARS signal can lead to very tight imaging. Thus it may also be beneficial to fill the field of view of the spectrometer.

For the two experiments showing no significant saturation (Table I, expts. 3 and 4) the effect of nonlinearity was estimated as follows. The maximum negative slope (at 90% confidence limit) was obtained and used to calculate a theoretical worst case saturation. A comparison of this curve with a best linear fit of the saturation curve then yields the error involved in, incorrectly, assuming linearity. For the last two entries in Table I the maximum error involved in assuming linearity is <2% over the range of 0 to 3500 counts (i.e., from 0 to 85% of full scale). To put this in perspective a 2% error in the ratio of the 2-1 and 1-0 peaks of N_2 (see Fig. 7) corresponds to an error in the assigned temperature of 13 K at 2100 K.

A similar analysis for the first two entries in Table I, taking b' values as a measure of the nonlinearity, yields errors of ±15% (Table I, expt. 2 for a range of 0 to 3500 counts) and ±25% (Table I, expt. 1, for a range of 0 to 3000 counts). Reducing the range to 0 to 1500 counts produces errors of ±7% and ±4.5%, respectively.

The nonlinear effects observed with the TN-1223-4GI detector were constant over a 60-fold change in the microchannel plate intensifier setting (light level was varied to maintain a constant output signal). This suggests that the saturation is in the microchannel plate intensifier or in the diode array rather than the photocathode. The most likely explanation appears to be saturation in the microchannel plate intensifier.

The nonlinear effects observed with CARS signals from the TN-1223-4GI detector were not duplicated when direct continuous illumination or scattered doubled Nd:YAG radiation at 532 nm, which fills the detector, was substituted for the CARS radiation.

Thus, in summary, it is important to evaluate the detector nonlinearity at the appropriate signal level, pulse duration, and CARS spectrometer f-number. The nonlinearity can be made negligible by increasing the image height on the detector and thus illuminating more of the 2.5 mm height of the detector pixel size.

6.0   Detector Noise and Absolute Sensitivity

To compare detector performance at constant sensitivity we measured the absolute sensitivity of three Tracor Northern intensified diode array detectors (IDARSS), an older TN-1223-4GI and two newer TN-6132's. A calibrated irradiance standard was used to illuminate the diodes directly. The radiation was isolated to a 60 nm band centred at 507 nm and the IDARSS exposure was calculated by integrating the product of the lamp spectral irradiance and the filter transmission over the bandpass of the filter. Neutral density filters were used to further limit the exposure to 1.02 X 10^{-3} μW/cm^2, which, for a 0.02 sec exposure, corresponds to 1.3 X 10^{-4} J/diode or 3.2 X 10^4 photons/diode at 507 nm.

The absolute sensitivities obtained were: for the two TN-6132 detectors, 2.9 and 3.5 photons/count at a video amplifier setting of x4 and 9.5 and 11.5 photons/count at a video amplifier setting of x1; and for the TN-1223-4GI detector, 1.3 photons/count. (We consistently observed the video amplifiers of the TN-6132 detectors to have a gain of ~ 3.4.)

Detector noise was measured in two ways. First, under conditions of constant illumination, a set of (typically 100) spectra were acquired and the mean and standard deviation calculated diode by diode. An average of these diode by diode standard deviations then gave a single noise figure for the detector. Second, the acquired spectra were sequentially added to and subtracted from memory and the statistics calculated, as above, on the residuals.

The noise (standard deviation) was $\sqrt{2}$ higher using the second method as would be expected from two statistically uncorrelated processes. The second method was preferred for measuring detector noise as a function of light level since it placed fewer demands on the constancy of the light source.

The noise (a single standard deviation expressed as a percentage of the signal counts) is shown in Fig. 10 as a function of light level for two different detectors. The Tracor Northern 1710 provides a front panel control of intensifier gain over a range of approximately 100 and this was used to vary the overall sensitivity of the detector.

The detector shot noise shows the $E^{-1/2}$ dependence expected of a process which obeys Poisson statistics. At very high intensities, the noise falls off less rapidly than this as dark current noise and fixed pattern diode read noise become important. For an ideal detector exposed to a signal of E quanta the standard deviation associated with the signal is $E^{1/2}$. The "ideal detector" curve is shown in Fig. 10 where the $\sqrt{2}$ factor results from using the second method to obtain the noise statistics. The measured noise of the two detectors is between 1.5 and 2.0 times this quantum limit.

The data in Fig. 10 were recorded over a range of intensifier settings. The measured signal variance as a function of signal counts at a fixed intensifier setting is shown in Fig. 11. The measured variance was linear in signal counts as expected and the intercept corresponded to the measured detector dark noise. The noise was measured in this way for a range of intensifier settings in order to obtain the coefficients σ_0 and k in the expression:

$$\sigma^2 = \sigma_0^2 + kC \tag{15}$$

σ_0 was largely independent of intensifier setting but k increased with increasing sensitivity. These parameters were used to calculate the weighting coefficients used in the least mean squares fitting routines described below.

7.0 Noise in CARS Spectra

Temperatures are derived from the shape of CARS spectra, thus one source of noise is the pulse to pulse variability in the spectral energy profile of the dye laser.

Nonresonant CARS spectra can provide a measure of system noise. These spectra are convenient to record and, since the nonresonant susceptibility is essentially independent of wavelength, they have a spectral shape which is largely determined by the broadband dye laser. In addition, the noise in the Stokes laser and the nonresonant CARS signal can be readily compared. The analysis procedure described below can be applied to both resonant and nonresonant spectra.

A set of CARS spectra can be represented by S_{ij} where

$$S_{ij} = I_{ij}K_i$$

$$i = 1...N \text{ diodes}$$

$$j = 1...M \text{ pulses} \tag{16}$$

with i representing the diode number of the diode array detector and j the spectrum index. I_{ij} is the CARS intensity associated with the diode number i and spectrum number j and K_i is the sensitivity of diode i. The averaged CARS signal ($\bar{S}_i$) is given by

$$\bar{S}_i = (\sum_j I_{ij}K_i)/M \tag{17}$$

In the first stage of the analysis the individual spectra are divided by an average spectrum to produce a ratioed CARS signal X_{ij} where

$$X_{ij} = (S_{ij}/\bar{S}_i) = (I_{ij}/\sum_j I_{ij})M \tag{18}$$

The ratioed CARS signal is now independent of diode sensitivity and represents the shot-to-shot variation of the CARS spectral profile from an averaged spectrum.

Since it is only the spectral profile of the N_2 CARS signal that is used to deduce temperatures, the absolute magnitude of the CARS signal is not important. Thus, for comparison purposes, we can normalize the CARS spectra such that they have the same integrated X value over the spectral region of interest. If N_L and N_U are the lower and upper diode limits for the spectral region of interest, the normalized CARS signal, Y_{ij}, is given by

$$Y_{ij} = X_{ij} / \sum_{i=N_L}^{N_U} X_{ij} \qquad (19)$$

These normalized CARS signals, Y_{ij}, are used to calculate the noise due to pulse-to-pulse variation in the spectral profile of the CARS signal.

The standard deviation of each spectrum about the mean yields a percentage noise, N_j, which, when averaged over the M spectra, gives an average noise $\bar{N}$ and a standard deviation σ, which represents the shot-to-shot variability of the noise. Finally, the experiments are repeated to assess the day-to-day variability. The average noise, standard deviation, and the 95% confidence limits (using t-test) were calculated for the set of experiments. Thus, there are two measures of variability, one representing the variation within a set of spectra and the other representing the set-to-set variability. In general we have found these two estimates to be very similar, indicating that there is little systematic day-to-day variation in the noise.

The averaged signal, S_i, for a set of sixty-four multimode nonresonant CARS spectra is shown in Fig. 12 along with a single normalized CARS spectrum, Y_{ij}. Much of the structure observed in S_i is not real but is due to periodic variations in diode sensitivity, K_i. The noise (single standard deviation) for the single shot spectrum of Fig. 12 is 8.37% and the average percentage noise for the set of sixty-four spectra is 9.56 ± 0.43 (single standard deviation of the mean).

From a detailed analysis of nonresonant CARS spectra we have shown previously[12] that when a single-mode pump laser is used the CARS noise is reduced to a level exhibited by the Stokes laser itself (~5% noise at 2.0 cm^{-1} resolution for our broadband dye laser). The increased CARS (but not Stokes) noise observed using multimode lasers was attributed to a spectral dependence of the Stokes temporal profile and its consequent effect on the temporal overlap of the CARS beams.

We have repeated the earlier nonresonant analysis and have also included the analysis of resonant flame spectra recorded in the flat-flame burner. The spectra were recorded at 0.25 cm^{-1} resolution and a 15 cm^{-1} spectral analysis width was used. The nonresonant spectra were recorded at a low detector sensitivity where the effect of detector shot noise is negligible. The resonant noise can be corrected for the residual detector shot noise by assuming that the detector shot noise σ_D and the noise in signal σ_C are uncorrelated giving a net noise σ_N:

$$\sigma_N^2 = \sigma_C^2 + \sigma_D^2 \qquad (20)$$

This corrected noise σ_C, attributable to pulse-to-pulse variations in the spectral profile of the CARS signal, is shown in parentheses in Table 2.

The results confirm the earlier conclusion[12] that the nonresonant spectra recorded with a single-mode pump laser exhibit less noise than those recorded with a multimode pump laser. The actual noise values are somewhat higher than we observed previously and we speculate on the cause of this below. For the resonant spectra the reverse is true and the single-mode spectra exhibit greater noise.

This noise, expressed as a percentage, was largely constant and thus represents a fixed fraction of the total signal. Thus the total noise (σ_T) associated with a particular diode count C can be expressed as:

$$\sigma_T^2 = \sigma_0^2 + kC + mC^2 \qquad (21)$$

where σ_0^2 is the "dark noise" or noise in the absence of a signal, kC is the shot noise component and mC^2 represents the component associated with the shot-to-shot variation in the CARS signals. The mC^2 term is an approximation in that it is difficult to measure and the percentage noise in signal probably increases at very low signal levels.

In a weighted least squares fit the parameters are determined by minimizing the weighted sum of squares where the reciprocal of the variance is used as the weighting coefficient. The above expression for σ_T has been used to perform a weighted least squares fit of experimental CARS data, as is described below.

TABLE 2

NOISE STATISTICS: STANDARD DEVIATION σ EXPRESSED AS %

SPECTRUM TYPE	PUMP LASER CONFIGURATION	
	SINGLE-MODE	MULTIMODE
CO_2 Nonresonant spectra	6.6	8.4
N_2 Flame spectra		
T = 1580 K	22.4(22.0)	16.1(15.6)

8.0 **Single shot CARS temperature measurements**

Single shot CARS temperature measurements were performed in the hydrogen/air fueled flat-flame burner with single-mode and multimode pump laser operation. Typically sets of 100 spectra were recorded and the spectra analysed individually. The data collection system automatically averages the individual spectra and these average spectra were also analysed. The mean temperature and the standard deviation were calculated for each set of individual spectra and the results averaged.

One aim of these experiments was to examine whether the greater noise of single-mode resonant spectra, shown in Table 2, would be reflected in a bigger temperature spread in the single shot data. Typical results are shown in Fig. 13. The widths of histograms in Fig. 13 represent the instrumental resolution since no temperature variations are expected in the premixed flame. It can be seen that, as expected, the single-mode histograms are significantly wider than the multimode ones. This confirms the conclusion that resonant CARS spectra, unlike nonresonant spectra, exhibit greater noise with a single-mode pump laser than with a multimode pump laser.

We also performed a weighted least mean squares fit of theoretical (T) and experimental (E) CARS spectra where the quantity minimised was:

$$\sum_i w_i \, (T_i - E_i)^2 \tag{22}$$

where i is the diode index and the weighting parameter w_i is $1/\sigma^2$. σ_i was calculated from equation 21 using experimentally determined values of σ_0 and k and an estimated value of m corresponding to 4% shot-to-shot CARS noise, approximately the noise observed in the Stokes laser[12].

The effect of weighting the data is to greatly reduce the width of the histograms. The two fold reduction in the width of single-mode temperature histograms is particularly dramatic. Thus taking proper account of signal variance can greatly increase the precision of single pulse CARS measurements.

The histograms in Fig. 13 were calculated using the isolated line CARS theory code. More recently we have included collisional narrowing and cross-coherence effects in the CARS theory code and repeated the earlier isolated line analysis. Essentially the same reductions in standard deviation were obtained when these effects were included, as demonstrated in Tables 3 and 4. The effect of the choices of weighting coefficients on the average temperatures and average standard deviations obtained from all of the single pulse data is also shown in Tables 3 and 4. The standard deviations are largely insensitive to the amount of CARS noise included in the weighting coefficients. However, a larger CARS noise contribution resulted in a greater temperature bias.

TABLE 3

EFFECT OF WEIGHTING COEFFICIENTS ON ANALYSIS OF SINGLE PULSE
SINGLE-MODE DATA WITH COLLISIONAL NARROWING INCLUDED IN CARS CODE

AV. TEMP $\bar{T}_{AV}$ (K)	ST. DEVIATION $\bar{\sigma}_T$ (K)	WEIGHTING
1563	131 ± 17	NONE
1551	71 ± 5	DETECTOR SHOT NOISE ONLY
1531	59 ± 6	DETECTOR SHOT NOISE + 4% CARS NOISE
1492	61 ± 7	DETECTOR SHOT NOISE + 20% CARS NOISE

ERROR LIMITS ARE 95% CONFIDENCE INTERVALS

TABLE 4

EFFECT OF WEIGHTING COEFFICIENTS ON ANALYSIS OF SINGLE PULSE
MULTIMODE DATA WITH COLLISIONAL NARROWING AND CROSS-COHERENCE
INCLUDED IN CARS CODE

AV. TEMP $\bar{T}_{AV}$ (K)	ST. DEVIATION $\bar{\sigma}_T$ (K)	WEIGHTING
1586	88 ± 5	NONE
1554	51 ± 3	DETECTOR SHOT NOISE ONLY
1526	45 ± 2	DETECTOR SHOT NOISE + 4% CARS NOISE

ERROR LIMITS ARE 95% CONFIDENCE INTERVALS

The cause of the systematic temperature shifts with weighting is not clear. However, it should be noted that the weighted fits are more sensitive to the value of the nonresonant susceptibility (χ^{NR}) used in the calculation of the theoretical spectra. We have examined the effect of changing χ^{NR} by 10% on the best fit temperatures with weighting (4% CARS noise) and without. The fit to the single-mode data (including collisional narrowing in the code) produced temperature changes of 9 K (unweighted fit) and 18 K (weighted fit). The corresponding numbers for the multimode data (with the effect of cross-coherence included) were 13 K and 24 K. A decrease in χ^{NR} leads to an increase in the fitted temperatures. Thus a 20% decrease in the value of χ^{NR} used would eliminate about 1/2 of the single pulse temperature shifts observed in Tables 3 and 4 and would entirely eliminate the similar but smaller shifts observed in fitting the multipulse averaged data discussed below.

The selection of weighting coefficients appears to be a compromise between reducing the standard deviation and avoiding temperature shifts. Weighting places emphasis on the lower intensity parts of the CARS spectrum and thus the need, for example, to know χ^{NR} (and hence composition) accurately. The nonresonant background can be eliminated[45] (with an accompanying 16 fold reduction in CARS signal), however temperature biasing has been observed in fitting background free spectra[46].

The use of a multimode laser clearly confers an advantage in reducing the single shot CARS noise and thus reducing the temperature spreads observed with repeated single shot temperature measurements. With this advantage comes the greater complexity of the CARS theory calculations, although the recently developed analytic solutions[15,17] of the cross-coherence effects minimize this difficulty. The possible effect of pump laser field statistics on the ratio of the resonant to nonresonant CARS signal[47,48] is a problem which can be avoided by using a single-mode pump laser. Providing this latter problem can be resolved, the use of a multimode pump laser is indicated because of the reduced noise.

9.0   Multipulse Avera,ₑ CARS Temperature Measurements

The question of the accuracy of the flat-flame burner CARS temperature measurements and their dependence on including collisional narrowing and cross-coherence effects in the CARS theory code is more readily addressed by analysing multipulse averaged CARS spectra.

A 100 pulse average single-mode CARS flame spectrum and a best-fit theory spectrum calculated with collisional narrowing effects included in the CARS code is shown in Fig. 14. The spectrum was recorded 10 mm above the burner surface on the centre line. The estimated sodium line reversal temperature 10 mm a ove the burner surface was 1593 ± 18 K. CARS temperature measurements taken along the Na line reversal axis showed that the centre line temperature was some 18 K hotter than the average temperature observed over the Na seeded region of the flame. Thus the observed sodium line reversal temperature of 1575 K was increased by this amount to give the estimated centre line value of 1593 ± 18 K.

Over a period of six months we have recorded a series of multimode (0.10 cm⁻¹ spectral width) and single-mode 100-400 pulse average CARS spectra 10 mm above burner centre. The data was initially analysed using the isolated line computer code and then analysed by including the effects of collisional narrowing and cross-coherence as these codes became available. We have also examined the consistency of the instrumental (slit) function by determining the four Voigt parameters from both room temperature and flame spectra. The room temperature instrument function was routinely used to obtain the temperatures reported here. The average temperatures so obtained are summarized in Table 5. Including collisional narrowing in the code increases the best-fit temperatures of single-mode and multimode pump laser data by 20-25 K. With collisional narrowing included in the CARS code the instrument (slit) functions determined either from single-mode room temperature or from flame N_2 spectra were essentially identical. With the isolated line code the room temperature slit function was 10-15% narrower than that derived from hot spectra. With collisional narrowing included in the code the final temperature derived from the single-mode data is in excellent agreement with the Na line reversal temperature.

TABLE 5

**SUMMARY OF CARS TEMPERATURE MEASUREMENTS
10 mm ABOVE BURNER CENTRE**

SINGLE-MODE PUMP LASER

TEMP (K)	COMPUTER CODE
1577 ± 17	ISOLATED LINE
1599 ± 19	COLLISIONAL NARROWING

MULTIMODE (0.10 cm⁻¹) PUMP LASER

TEMP (K)	COMPUTER CODE
1588 ± 10	ISOLATED LINE
1611 ± 11	COLLISIONAL NARROWING
1569 ± 11	COLLISIONAL NARROWING + CROSS-COHERENCE

ERROR LIMITS ARE 95% CONFIDENCE INTERVALS

With multimode data cross-coherence must also be included in the code and as shown in Table 5 the effect is to lower the best fit temperatures ~40 K. Collisional narrowing and cross-coherence have opposing effects on best-fit temperatures and the final temperature is only 19 K less than the isolated line temperature. This cancellation is a function of the assumed pump bandwidth since a fit to the data with a 0.4 cm⁻¹ pump laser bandwidth (the laser manufacturer's specification produced a final best fit temperature of 1531 K, some 57 K lower than the isolated line temperature and 62 K lower than the Na line reversal temperature. The 0.1 cm⁻¹ pump laser result of 1569 ± 11 K is in satisfactory agreement with the Na line reversal temperature of 1593 ± 18 K. The instrument function was very similar to that derived from the single-mode data.

Reducing χ^{NR} by 20% gives approximate best fit temperatures of 1617 ± 19 K (single-mode) and 1595 ± 11 K (multimode) in equally good agreement with the line reversal temperature of 1593 ± 18 K.

In summary we conclude that it is necessary to include the effects of collisional narrowing and cross-coherence to correctly predict CARS temperatures in atmospheric pressure flames. With these effects included the calculated temperatures are within 25 K of the Na line reversal temperatures for both multimode and single-mode pump laser data.

10.0   Stokes laser noise

With the large number of modes excited in the Stokes laser there is the possibility of selective focusing of these modes whereby the lower-order modes may focus more tightly and thus more efficiently wave mix with the pump laser field. In our earlier work we saw no evidence of this but the astigmatism produced by a tilted CARS focusing lens may have masked any effect.

As noted above the observed nonresonant noise of 8.0% (70 cm^{-1} analysis bandwidth) with a single-mode pump laser was higher than that observed previously[12] (5.7%). We therefore investigated the effect of adding a beam expansion telescope with a magnification of 1.0, with lenses chosen to deliberately induce some spherical abberation. With this arrangement the CARS intensity dropped a factor of ~2 and the observed nonresonant noise was 5.5%. When the telescope was removed the noise returned to the previous 8.0%.

The 5.5% noise is approximately equal to the 5% noise previously observed in the Stokes laser itself[12]. A plausible explanation of this observation is that the spherical aberration introduced in the Stokes laser "blurred" any tendency for selective focusing of various modes. Thus the pump laser wave mixed with a Stokes laser whose modes were effectively averaged.

Acknowledgement

T. Parameswaran would like to thank R.J. Hall of UTRC, for his continued help and advice on the development of the computer programs needed for generating the theoretical CARS spectra.

The authors would like to acknowledge the help of Dr. F.D. Findlay for his participation in the sodium line reversal measurements and his contributions to the development of CARS spectroscopy at DREO.

References

1. S.A.J. Druet and J.P.E. Taran, "CARS Spectroscopy", Prog. Quantum Electron. 7, 1 (1981).

2. R.J. Hall and A.C. Eckbreth, "Coherent Anti-Stokes Raman Spectroscopy (CARS): Application to Combustion Diagnostics", in Laser Applications, Vol. 5, J.F. Ready and R.K. Erf, Eds. (Academic, New York, 1984), pp. 213-309.

3. A.B. Harvey, Ed., Chemical Applications of Nonlinear Raman Spectroscopy (Academic, New York, 1981).

4. J.W. Nibler and G.V. Knighten, "Coherent Anti-Stokes Raman Spectroscopy", in Raman Spectroscopy of Gases and Liquids, A. Weber, Ed. (Springer, Berlin, 1979), pp. 253-299.

5. W.B. Roh, P.W. Schreiber and J.P.E. Taran, "Single-Pulse Coherent Anti-Stokes Raman Scattering", Appl. Phys. Lett. 29, 174 (1976).

6. G.L. Switzer, L.P. Goss, W.M. Roquemore, R.P. Bradley, P.W. Schreiber and W.B. Rob, "Application of CARS to Simulated Practical Combustion Systems", J. Energy 4, 209 (1980).

7. J.P. Taran and M. Pealat, "Practical CARS Temperature Measurements", Temperature, Its Measurement and Control in Science and Industry, American Institute of Physics 5, 575 (1982).

8. D.A. Greenhalgh, F.M. Porter and W.A. England, "The Application of Coherent Anti-Stokes Raman Scattering to Turbulent Combustion Thermometry", Combustion and Flame 49, 171 (1983).

9. A.C. Eckbreth, "CARS Thermometry in Practical Combustors", Combust. Flame 39, 133 (1980).

10. A.C. Eckbreth, G.M. Dobbs, J.H. Stufflebeam and P.A. Tellex, "CARS Temperature and Species Measurements in Augmented Jet Engine Exhausts", Appl. Opt. 23, 1328 (1984).

11. T. Snelling, R.A. Sawchuk, and G.J. Smallwood, "Multichannel Light Detectors and Their Use for CARS Spectroscopy", Appl. Opt. 23, 4083 (1984).

12. T. Snelling, P.A. Sawchuk, and R.E. Mueller, "Single pulse CARS noise: a comparison between singlemode and multimode pump lasers", Appl. Opt. 24, 2771 (1985).

13. M.A. Yuratich, "Effect of Laser Line Width on Coherent Anti-Stokes Raman Spectroscopy", Mol. Phys. **38**, 625 (1979).

14. H. Kataoka, S. Maeda, and C. Hirose, "Effects of Laser Line Width on the Coherent Anti-Stokes Raman Spectroscopy Spectral Profile", Appl. Spectro. **36**, 565 (1982).

15. R.E. Teets, "Accurate convolutions of coherent anti-Stokes Raman spectra", Opt. Lett. **9**, 226 (1984).

16. R.J. Hall, J.F. Verdieck, and A.C. Eckbreth, "Pressure-Induced Narrowing of the CARS Spectrum of N_2", Opt. Commun. **35**, 69 (1980).

17. D.A. Greenhalgh and R.J. Hall, "A Closed Form Solution for the CARS Intensity Convolution", Opt. Commun. **57**, 125 (1986).

18. M.L. Koszykowski, R.L. Farrow, and R.E. Palmer, "Calculation of Collisionally Narrowed Coherent Anti-Stokes Raman Spectroscopy Spectra", Opt. Lett. **10**, 478 (1985).

19. K.A. Marko and L. Rimai, "Space-and Time-Resolved Coherent Anti-Stokes Raman Spectroscopy for Combustion Diagnostics", Opt. Lett. **4**, 211 (1979).

20. L.P. Goss, D.D. Trump, B.G. MacDonald, and G.L. Switzer, "10 Hz Coherent Anti-Stokes Raman Spectroscopy Aparatus for Turbulent Combustion Studies", Rev. Sci. Instrum. **54**, 563 (1983).

21. Botha, J.P., and Spalding, D.B., "The laminar flame speed of propane/air mixtures with heat extraction from the flame", Proc. Royal Soc. **225A**, 71, (1954).

22. Snelling, D.R., and Fischer, M., "Design and Calibration of a Flat-Flame Burner using Line-Reversal Techniques", DREO Technical Note 85-4 (1985).

23. Andersen, H.C. and Hudson, B.S., "Coherent Anti-Stokes Raman Scattering", Molecular Spectroscopy (Chemical Society, London) **5**, 142 (1978).

24. R.N. Dewitt, A.B. Harvey and W.M. Tolles, NRL Memorandum Report 3260, Apr. 1976.

25. S.A.J. Druet, and J.P. Taran, "Coherent Anti-Stokes Raman Spectroscopy" in Chemical and Biochemical Applications of Lasers, C.B. Moore, Editor, Academic Press 1979.

26. F. Printer, "Dependence of the width of the rotational Raman lines of N_2 and CO_2 on the quantum number j", Opt. and Spectry. **17**(5), 428 (1964).

27. A.D. May, J.C. Stryland and G. Varghese, "Collisional narrowing of the vibrational Raman band of nitrogen and carbon monoxide", Can. J. Phys. **48**, 2331 (1970).

28. J. Bonamy and L. Bonamy, and D. Robert, "Overlapping effects and motional narrowing in molecular band shapes: application to the Q branch of HD", J. Chem. Phys. **67**, 4441 (1977).

29. R.J. Hall, "Coherent Anti-Stokes modelling for combustion diagnostics", Opt. Engg. **22**, 322 (1983).

30. R.J. Hall, "CARS spectra of combustion gases", Combust. Flame **35**, 77 (1979).

31. R.L. Farrow, P.L. Mattern and L.A. Rahn, "Comparison between CARS and corrected thermo couple temperature measurements in a diffusion flame", Appl. Opt. **21**, 3119 (1982).

32. R.J. Hall, United Technologies Research Centre, East Hartford, Connecticut, USA (private communication).

33. E.E. Whiting, "An empirical approximation to the Voigt function", JQSRT **8**, 1379 (1968).

34. H. Kim, "Computer Programming in Physical Chemistry Laboratory", J. Chem Education **2**, 120 (1970).

35. C.M. Penney, R.L. St. Peters and M. Lapp, "Absolute Rotational Raman Cross-sections for N_2, O_2 and CO_2", J. Opt. Soc. Am. **64**, 712 (1974).

36. J.P. Bouanich and C. Brodbeck, "Vibrational matrix elements for diatomic molecules", JQSRT **15**, 873 (1975).

37. L.A. Rahn, Sandia National Laboratories, published results.

38. R.J. Hall, "Pressure broadened line widths for CARS thermometry", App. Spectrosc. **34**, 780 (1980).

39.   G.J. Rosasco and W.S. Hurst, "Measurement of resonant and non-resolant third order nonlinear susceptibilities by Coherent Raman Spectroscopy", Phys. Rev. A **32**, 281 (1985).

40.   T. Lundeen, S.Y. Hou, J.W. Nibler, "Nonresonant third order susceptibilities of various gases", J. Chem. Phys. **79**, 6301 (1983).

41.   R.L. Farrow, Sandia Laboratories, Livermore, California (private communication).

42.   T. Parameswaran and D.R. Snelling, "A computer program to generate Coherent Anti-Stokes Raman Spectra", Technical note 81-18, Defence Research Establishment Ottawa, Canada, 1982.

43.   A.K. Hui, B.H. Armstrong and A.A. Wray, "Rapid computation of the Voigt and Complex Error functions", JQSRT **19**, 509 (1978).

44.   R.R. Antcliff, M.E. Hillard and O. Jarrett, Jr., "Intensified Silicon Photodiode Array Detector Linearity: application to Coherent anti-Stokes Raman Spectroscopy", Appl. Opt. **14**, 2369, 1984.

45.   L.A. Rahn, L.J. Zych, and P.L. Mattern, "Background-free CARS Studies of Carbon Monoxide in a Flame", Opt. Commun. **30**, 249 (1979).

46.   M. Pealat, P. Bouchardy, M. Lefebvre, and J.P. Taran, "Precision of Multiplex CARS Temperature Measurements" Appl. Opt. **24**, 1012, (1985).

47.   L.A. Rahn, R.L. Farrow, and R.P. Lucht, "Effects of Laser Field Statistics on Coherent Anti-Stokes Raman Spectroscopy Intensities", Opt. Lett. **9**, 223 (1984).

48.   R.L. Farrow, L.A. Rahn, and R.P. Lucht, "Effect of Non-Gaussian Pump Field Statistics on Unresolved CARS Spectra", in Proceedings of the Ninth International Conference on Raman Spectroscopy (Chemical Society of Japan, Tokyo, 1984), pp. 340-341.

BS - BEAM SPLITTER
CG - COLOR GLASS FILTER
C×2 - DOUBLING CRYSTAL
D - DIODE ARRAY DETECTOR
DC - DYE CELL
DM - DICHROIC MIRROR
G - GRATING
GF - GEOMETRIC FILTER

GT - GALILEAN TELESCOPE
I - IRIS
IF - INTERFERENCE FILTER
K - KG3 GLASS
L - LENSE
M - MIRROR
NF - NEUTRAL DENSITY FILTER
P - PRISM

PBS - POLARIZING BEAM SPLITTER
PMT - PHOTOMULTIPLIER TUBE
PR - PARTIAL REFLECTOR
PT - PHOTOTUBE
QP - QUARTZ PLATE
S - SLIT
T - TRAP
TR - TOTAL REFLECTOR
WP - WAVE PLATE

ω_1 - PUMP FREQUENCY
ω_2 - STOKES FREQUENCY
ω_3 - CARS FREQUENCY

Fig. 1: Optical Arrangement of the CARS Spectrometer
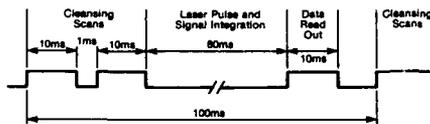
Fig. 2: Optical Multichannel Detector
         Read Sequence
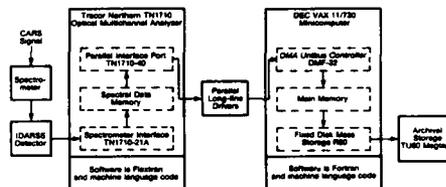
Fig. 3: Diagram of Detector/Computer
         Interface
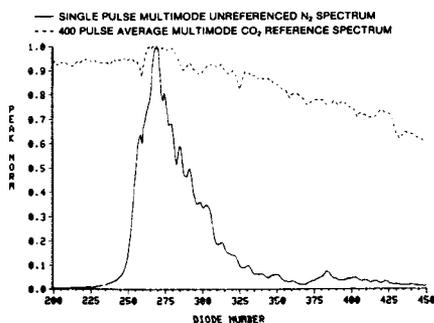
'g. 4: Individual N_2 Spectrum with
        Average Nonresonant Spectrum
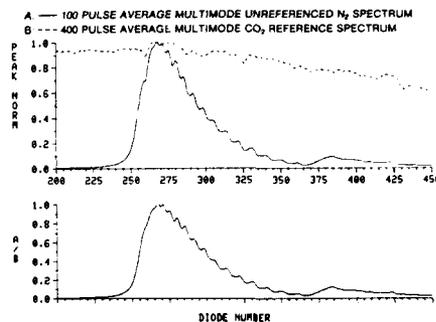
Fig. 5: Average N_2 Spectrum with Average
         Nonresonant Reference Above and
         Referenced Spectrum Below
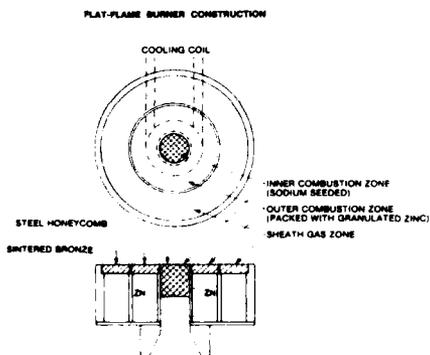
Fig. 6: Flat-Flame Burner Construction
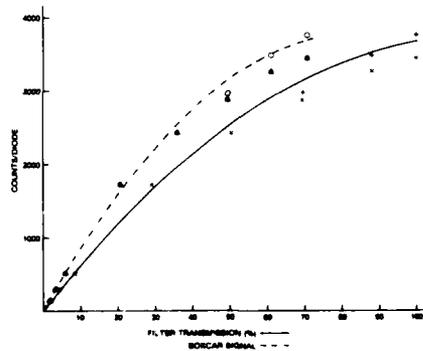
Fig. 7: Detector Output Versus Filter
         Transmission (%) or Versus
         Boxcar Signal (Arbitrary Units)
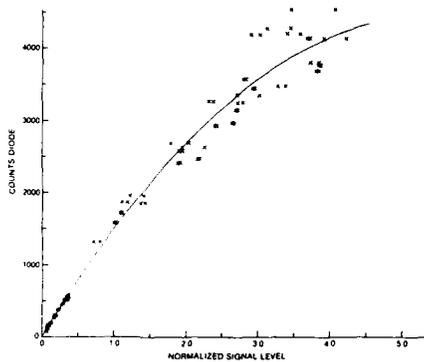
Fig. 8: Detector Output Versus Normalized Signal Level
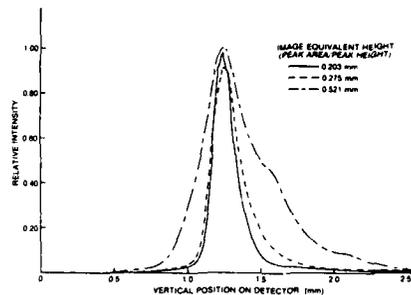
Fig. 9: CARS Image Height Intensity Profiles
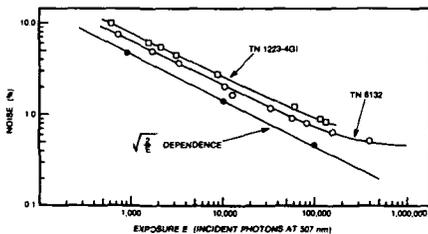
Fig. 10: Detector Shot Noise as a Function of Incident Light Intensity

$\sigma^2 = 4.60 + 0.511C$
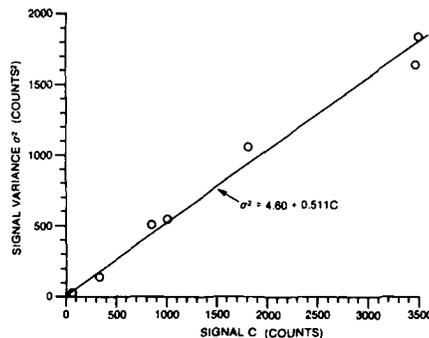
Fig. 11: Detector Shot Noise as a Function of Signal Counts For a Fixed Intensifier Setting

NON-RESONANT CARS SIGNAL (MULTI-PULSE AVERAGE)

SINGLE SHOT NOISE

1 DATA POINT = 8.8 cm⁻¹
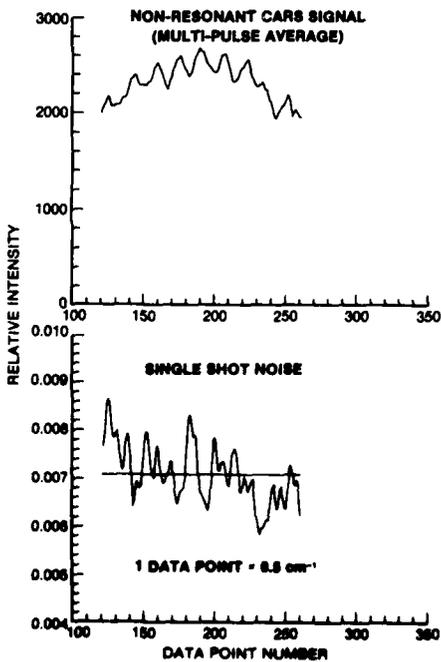
Fig. 12: Average Nonresonant CARS Spectrum (Si) and a Normalized Single Shot
(left) CARS Spectrum (Y_{11}) for Typical Multimode Operation. Analysis Bandwidth 70 cm⁻¹

CARS TEMPERATURE HISTOGRAMS

SINGLE MODE PUMP LASER - UNWEIGHTED LMS FIT

MEAN TEMP = 1543 K
STAN DEV = 126 K

SINGLE MODE PUMP LASER - WEIGHTED LMS FIT

MEAN TEMP = 1527 K
STAN DEV = 57 K

MULTIMODE PUMP LASER - UNWEIGHTED LMS FIT

MEAN TEMP = 1597 K
STAN DEV = 80 K

MULTIMODE PUMP LASER - WEIGHTED LMS FIT

MEAN TEMP = 1559 K
STAN DEV = 43 K
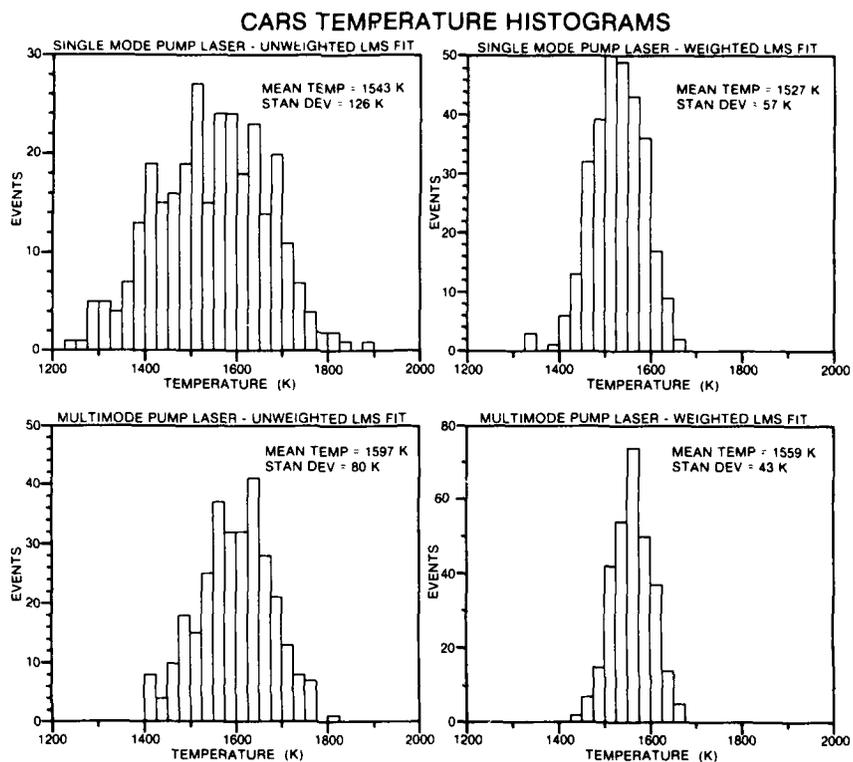
Fig. 13:   Temperature Histograms Calculated for Single-Mode and
Multimode Pump Operation with Weighted and Unweighted
Least Mean Squares Fits Using Isolated Line CARS Code

- - EXPERIMENTAL N₂ CARS SPECTRUM
H₂ AIR FLAT FLAME φ · 0.575
— THEORETICAL LMS FIT T · 1584 K
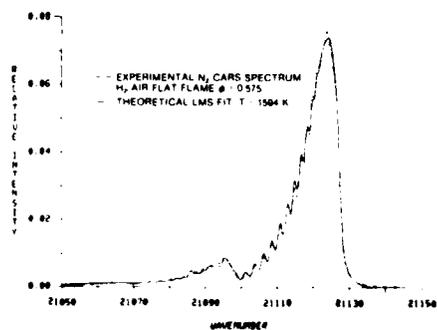
Fig. 14:   Experimental N_2 CARS Flame Spectrum
Compared with a Best Fit Theory
(above)   Spectrum Calculated Using Collisional
Narrowing

DISCUSSION

D.A.Greenhalgh, UK

Have you compared your dye laser noise data with published theories?

Comment

The difference between single-mode and multimode 1 σ temperature, for low/modest pressure high temperature spectra may be due to the multimode laser causing better (smoother) excitation of the Raman spectrum.

Author's Reply

We have deliberately avoided any discussion of the emerging theories of CARS noise and we have concentrated instead on empirical observations of CARS noise. We have not characterised our dye laser in a way that would allow us to apply existing theories of dye laser noise.

It is clear that the various pump laser modes will mix with a different set of Stokes modes thus leading to smoother excitation of the polarization. At higher pressures and lower temperatures we might expect the differences we have observed between single-mode and multimode behaviour to decrease as the larger Raman linewidth involves a greater number of Stokes modes. In effect we are progressing towards the non-resonant limit as the Raman linewidth increases.

J.P.Taran, FR

The difference in behaviour of the single mode and multimode arrangements (with regard to standard deviation) may result from changes in beam shape of the YAG laser. Have you observed any such changes?

Unless stabilized, single mode lasers may experience frequency jitters as large as 1 cm^{-1}. These would translate the CARS spectra along the frequency axis in a random manner, and might affect the result of the computer processing. Do you track these frequency jitters?

Author's Reply

The focal spot sizes are indistinguishable for single-mode and multimode pump operation. (Approximately 60% of the radiation is contained within a 50 μm spot size.)

With regard to the second question we do allow for a frequency shift between theoretical and experimental spectra. This is a fitting parameter, along with temperature, in our least mean squares analysis. The typical short term frequency jitter with our single mode laser is 0.03 cm^{-1} (single standard deviation).

R.Farrow, US

Your results comparing CARS signal statistics for single and multi-mode pump lasers contrast with our investigations. Do you attribute this difference to your use of a broadband Stokes laser compared to our use of a narrowband (0.1 cm^{-1}) laser?

Author's Reply

In measuring temperature histograms or spectral profiles we are looking at the shot-to-shot variation in spectral shapes rather than the variation in total signal level. Because of that I think we are measuring different quantities. We do observe that the shot-to-shot variability in the spectrally integrated CARS signals is greater for a multimode laser. The latter variation is of secondary important in CARS thermometry compared to the variation in spectral shapes.

APPLICATION DE LA METHODE DRASC A LA MESURE DE LA TEMPERATURE DANS UNE FLAMME TURBULENTE

par

Philippe Magre, Pierre Moreau, Gérard Collin et Michel Pealat
ONERA
29 Avenue de la Division Leclerc
92322 Châtillon Cedex
France

RESUME

Une flamme prémélangée à grande vitesse a été étudiée par la Diffusion Raman Anti-Stokes Cohérente (DRASC).

La bonne résolution spatiale et temporelle du montage DRASC en large bande conveient parfaitement pour l'étude des écoulements turbulents et permet des mesures instantanées de température dans une zone de réaction. A partir de ces valeurs instantanées, sont construits des fonctions de densité de probabilité de température (PDF).

La combustion d'un mélange air-méthane u ≃ 55 m/s, T ≃ 560 K, φ = 0,8 est entretenue et stabilisée par un écoulement parallèle de gaz chauds (u ≃ 110 m/s, T ≃ 2000 K). Le mélange de ces 2 écoulements est aussi étudié lorsque la possibilité d'inflammation est supprimée φ = 0.

Ces résultats sont comparés à ceux obtenue avec stabilisation par une zone de recirculation.

ABSTRACT

The good spatial and temporal resolution of broad-band CARS diagnostic is suitable for turbulent flows and allows instantaneous temperature measurements in the reaction zone. From these instantaneous values, temperature probability density functions (PDF) are built.

Coherent Anti-Stokes Raman Scattering (CARS) thermometry is applied to a high velocity premixed flame. The combustion of an air-methane flow (u ≃ 55 m/s, T ≃ 560 K, equivalence ratio φ = 0,8) in the combustor is ignited and stabilized by a parallel flow of hot gases (u ≃ 110 m/s, T ≃ 2000 K). The mixing of the two flows without combustion (φ = 0) is also studied as well as combustion stabilized by a step replacing the hot gases.

1 – INTRODUCTION

La Diffusion Raman Anti-Stokes Cohérence (DRASC) est une méthode de mesure ponctuelle et résolue dans le temps de la température et de la composition [1] dans les milieux fluctuants. Sa grande luminosité la rend particulièrement attrayante dans l'étude de milieux réactifs tels que les flammes, qui produisent généralement un fort rayonnement parasite. Les caractéristiques standards de ces mesures sont les suivantes:

résolution spatiale	: diamètre 50 μm × longueur 2 mm
temps de mesure	: 10 ns
cadence de répétition	: quelques Hertz
domaine de mesure	: 300–2500 K
seuil de détectivité	: ∼ 1% en fraction molaire
précision de mesure	: 3–5% [2].

Ces caractéristiques font de la DRASC une méthode de choix pour l'étude des milieux fluctuants tels que les explosions ou les flammes turbulentes. L'étude présentée ici est celle d'une flamme turbulente stabilisée:

– soit par un écoulement pilote à haute température et relativement grande vitesse.

– soit par un décrochement de paroi derrière lequel s'établit une zone de fluide mort à la température de fin de combustion.

Les essais ont été effectues dans des conditions d'écoulement différentes de celles régnant d'habitude dans les installations utilisant la DRASC

Dans les deux cas, dans un large domaine de l'écoulement situé de part et d'autre de la zone de réaction, les expériences antérieures (visualisation par strioscopie, vélocimétrie laser, mesure pyrométrique de température) ont toutes mis en évidence le passage de paquets de fluides alternativement chauds ou froids, rapides ou lents suivant qu'il s'agissait de gaz déjà brûlés ou de gaz encore frais.

Il n'est pas possible dans ce cas d'utiliser les techniques classiques de dépouillement des histogrammes, comme il est décrit ci-dessous.

2 – DESCRIPTION SOMMAIRE DU MONTAGE ET DU BANC DRASC UTILISE

2.1 – Montage d'étude de la flamme turbulente

Le montage expérimental utilisé [3] restitue dans un laboratoire les conditions usuelles régnant dans la zone primaire d'une chambre de combustion, qu'il s'agisse de chambre primaire de turboréacteur, de chambre de rechauffe ou de chambre de statoréacteur.

Le montage (fig.1) de section carrée 100 mm × 100 mm dans la zone d'essais et de longeuer supérieure à 1000 mm est de dimensions industrielles.

De l'air, dont la température est portée à 575 K par un échangeur, est mélangé avec du méthane à température ambiante, l'ensemble constituant un écoulement sensiblement homogène à la température de 550 K. Cet écoulement ou "flux primaire" est injecté dans une partie de la section d'entrée du foyer.

Pour le reste de celle-ci deux configurations doivent être envisagées;

— flamme pilote: sur environ 20% de la hauteur de la veine, soit 20 mm, on injecte des gaz issus d'une combustion stoechiométrique dans un foyer auxilaire. Ces gaz, à une température de l'ordre de 2000 K, assurent l'inflammation du flux primaire et la stabilité de la flamme dans un large domain de richesse et de vitesse; ils constituent le "flux auxiliaire";

— décrochement de paroi: une fraction de la section d'entrée, soit ici 35%, comporte une marche descendante derrière laquelle s'établit une zone de recirculation comportant initialement des gaz précarburés provenant de l'écoulement primaire; après allumage classique par bougie, un noyau chaud et stable s'établit dans cette zone et assure encore l'inflammation et la stabilisation de la flamme.

Les parois du foyer ne sont pas refroidies afin de limiter les gradients thermiques pariéteux. En conséquence la durée des essais ne peut pas dépasser 40 secondes environ, ce qui constitue un inconvénient majeur lorsqu'on désire accumuler plusieurs centaines de mesures avec un appareil dont la cadence d'acquisition est de 1 Hz.

Toutes les grandeurs aérodynamiques et thermiques de l'écoulement, sauf évidemment celles données par la DRASC, sont enregistrées de façon continue. Les principales d'entre elles sont:

— débit
— pression,
— température
— richesse,

Pour chacun des flux, ces grandeurs peuvent être lues en temps réel sur le pupitre de commande.

2.2 – Architecture du système DRASC

Le système DRASC dont dispose actuellement l'ONERA est un système modulaire qui se compose schématiquement des éléments suivants.

2.2.1 – Emission

Le bloc émission se présente sous forme d'une table ' · montage "source" de 1,5 m × 0.5 m sur laquelle sont assemblés les 2 lasers. Une description détaillée de cet ensemble peut être consultée [4—6].

Rappelons brièvement les caractéristiques essentielles des deux faisceaux laser émis:

— le faisceau de fréquence ω_1
λ_1 = 532 nm, énergie — 75 mJ, durée d'impulsion = 10 ns. Il est obtenue par doublage de fréquence du faisceau émis par une chaine laser comportant un oscillateur Nd—YAG suivi de 2 amplificateurs;

— le faisceau de fréquence ω_2
λ_2 = 607 mm (pour N_2), énergie: 3 mJ, durée d'impulsion 10 ns. Il est délivré par un laser à colorant suivi d'un amplificateur excités par une fraction de l'énergie du faisceau ω_1.

Parce que le spectre du laser à colorant présente une modulation et que la puissance du laser YAG n'est pas constante, il est nécessaire de normaliser le spectre signal (S) en le divisant point à point par un spectre référence (R) enregistré simultanément.

2.2.2 — Détection

Le spectromètre à réseau holographique (2100 tr/mm), le détecteur vidicon et différentes optiques associées sont montées sur une table appelée bloc détection.

2.2.3 — Acquisition

Le contrôleur de détecteur vidicon est connecté à un ordinateur PDP 11/23, dont le rôle est de:

— mettre en mémoire les informations en provenance du vidicon. La cible est lue à raison de 1 pt toutes les 80 µs. Trente balayages de la cible sont effectués à chaque tir des lasers. La cadence d'acquisition est ainsi de 1 tir laser par seconde environ;
— donner les ordres de charge et de tir de la chaîne laser Nd—YAG;
— lire les amplitudes des spectres S et R;
— mettre en mémoire sur disque dur ces informations;
— traiter en temps différé les spectres.

3 — SPECIFICITE DES ESSAIS DRASC SUR FLAMME TURBULENTE

Un grand nombre de difficultés rencontrées dans la mesure DRASC de température dans les foyers industriels ont pu être identifiées et résolues au cours des essais de laboratoire sur flamme turbulente.

3.1 — Difficultés expérimentales

Ces difficultés sont liées à l'environnement de la cellule d'essais (bruit, température ambiante, accès optique, etc...). Elles ont été résolues en installant les optiques délicates du banc DRASC et de la détection dans la salle de commande. Des mécaniques de grande stabilité ont également été employées pour soutenir les optiques diverses.

3.2 — Technique d'acquisition des histogrammes

L'intensité du signal DRASC dépend très rapidement de la température. Entre 600 K et 2350 K, qui sont les températures extrêmes qui peuvent être rencontrées, le signal est réduit d'un facteur 100. De plus, à température constante, le signal fluctue par le fait des fluctuations de puissance des lasers et de l'influence des gradients thermiques rencontrés dans le foyer. Globalement le signal change de 1 à 300, ce qui est beaucoup plus que la dynamique permise par le détecteur. Une solution avait été proposée par Switzer et al. [8], mais elle n'est pas compatible avec notre montage expérimental. Une autre solution est proposée. L'histogramme est enregistré en deux temps, le niveau du signal étant ajusté au moyen de verres neutres gris (atténuation optique).

— Une première série de mesure est effectuée avec une forte atténuation. Dans ce cas, la nombre de tirs saturés est négligeable ($N_F \simeq 0$) mais le nombre de tir N_C pour lesquels les spectres sont trop faibles peut être grand.

— Une deuxième série de mesure est effectuée sans atténuation. Les spectres correspondants aux hautes températures sont ainsi enregistrés. Dans ces conditions de mesure $N_C \simeq 0$ mais N_F (le nombre de spectre pour lesquels le détecteur est saturé) peut être grand.

A partir de ces deux séries de mesures, deux histogrammes sont construits de la façon suivante:

(a) les tirs défectueux sont rejetés. Le critère de rejet ne porte que sur le signal de référence. Les causes d'une référence défectueuse n'étant pas corrélées à la température du foyer, ces rejets ne peuvent pas introduire de biais systématiques;

(b) les essais de la première série donnent naissance à l'histogramme $P_1(T)$ avec:

$$P_1(T) = \frac{n_1(T)}{\Sigma_T n_1(T) + N_c}$$

ou $n_1(T)$ est le nombre de mesures pour lesquels la température est située entre T et $T + \Delta T$ où ΔT est la taille d'une classe de température;

(c) de façon identique les essais de la seconde série de mesure donnent naissance à l'histogramme $P_2(T)$:

$$P_2(T) = \frac{n_2(T)}{\Sigma_T n_2(T) + N_F}$$

(d) les deux histogrammes ainsi obtenus se recouvrent partiellement du fait des fluctuations d'intensité induites par les fluctuations de puissance des lasers et par l'effet des gradients thermiques (fig.2).

Dans certaines conditions d'enregistrement et de dépouillement, il peut être montré (cette justification est donnée en [7]) que l'histogramme réel P (T) est formé de la superposition des histogrammes P_1 (T) et P_2 (T):

$$P(T) = P_1(T) + P_2(T)$$

Cette technique donne avec le maximum de sécurité des histogrammes à deux pics dans le cas d'essais effectués dans des domaines à fortes fluctuations de température.

Notons que cette méthode de mise bout à bout d'histogrammes peut poser des problèmes délicats de raccordement du fait des fluctations d'amplitude des signaux résultant des fluctuations diverses, comme celles des lasers. La justification de notre traitement est donnée ailleurs [7].

4 — ANALYSE DES RESULTATS

La position des points de mesure est représentée sur la figure 1 ainsi que les conditions expérimentales qui ont été figées pour l'ensemble des essais (6 heures de combustion proprement dite, 600 rafales au cours desquelles 18000 spectres ont été enregistrés).

4.1 — Flamme pilote sans combustion principale

Dans ces conditions on étudie la coexistence et le mélange d'un jet chaud pariétal de hauteur à l'entrée 20 mm, avec un jet plus froid de hauteur 80 mm.

La figure 3 représente les histogrammes relevés au voisinage de la section de confluence des deux écoulements (x = 42 mm) et dans un second plan de mesure sortie plus en aval (x = 122 mm) [9].

Il apparaît nettement un réchauffement rapide du flux frais et un refroidissement corrélatif du flux chaud. A l'abscisse maximale explorée, une uniformité de l'écoulement n'est pas encore apparue.

Cette constatation explique le fait que même au voisinage du plan d'entrée, où les histogrammes mettent en évidence un prédominance d'un pic chaud (T = 2100 K) dans le jet pariétal et d'un pic frais (T = 600 K) dans l'écoulement principal, les températures intermdiaires ont une probabilité non nulle.

4.2 — Flamme pilote avec combustion dans le flux principal (richesse φ = 0,8)

La figure 4 donne pour les mêmes points d'essais que précédemment, les histogrammes obtenus lorsque l'écoulement primaire est composé d'une mélange air-méthane de richesse φ = 0,8. Celui-ci s'enflamme au contact des gaz chauds de l'écoulement auxiliaire pariétal et l'analyse des histogrammes met en évidence cette inflammation.

Dans le plan de mesure situé à x = 42 mm en aval de la zone de confluence les histogrammes obtenus sont tout à fait semblables à ceux correspondent dans la même section à un mélange à richesse nulle, ce qui vérifie la reproductibilité des essais et des dépouillements. Toutefois dans le sillage immédiat de la plaque séparant les deux écoulements (y = 20 mm), les signes précurseurs de la combustion apparaissent déjà.

Dans le plan de mesure situé à x = 122 mm en aval du plan de confluence des écoulements les histogrammes font apparaître un double effet:

— le maintien de l'écoulement auxiliaire pariétal pratiquement à sa température initiale dans tout le domaine qu'il occupait antérieurement (0 < y < 20 mm) et l'existence de gaz brûlés sur une hauteur de veine assez élevée (20 < y < 40 mm);
— la persistance de gaz frais au voisinage de la limite inférieure de l'écoulement principal, c'est-à-dire dans un domaine où la combustion devrait être logiquement très avancée.

Cette deuxième observation conduit tout naturellement à définir comme "zone de réaction" la partie de la veine où les histogrammes présentent deux pics (même de hauteurs nettement différentes); ces "flammes épaisses" sont bien caractéristiques de la combustion turbulente.

4.3 — Flamme stabilisée par un décrochement de paroi (fig.5)

Des explorations ont été effectuées dans un plan situé à x = 35 mm du plan d'entrée de l'écoulement et permettent encore de mettre en évidence trois zones:

— une zone de gaz de recirculation à une température d'environ 1700 K (correspondant à la combustion à la richesse φ = 0,8) dans la zone de recirculation (0 < y < 20 mm);
— une zone de mélange (20 < y < 35 mm) apparement encore sans combustion et présentant des histogrammes à deux pics;
— une zone de gaz frais à température à peu près uniforme (y > 35 mm).

On remarquera à la suite de cette analyse les précautions qu'il faut prendre pour interpréter les histogrammes, la même configuration à deux pics pouvant représenter des zones à mélange et à réaction chimique ou des zones à mélange seul.

5 — CONCLUSION

Les essais effectués au moyen du système DRASC dans un foyer où se propage une flamme turbulente ont montré que si on prend des précautions particulières pour l'interprétation des histogrammes, et notamment des histogrammes à deux

pics, une description fine de la température instantanée et locale peut être obtenue.

Ces essais ont été effectués dans des conditions très sévères:

— bruit acoustique et électronique éleveés,
— grande distance entre le point de mesure et l'émetteur ou le récepteur,
— température locale élevée avec importantes fluctuations,
— montage d'essais difficilement accessible.

Malgré ces difficultés et bien que le conception du foyer non refroidi n'ait que des tirs de quelques dizaines de secondes, des résultats nombreux et précis ont pu être obtenus mettant en évidence la structure fine de l'écoulement.

Ces essais ont montré que les système DRASC peut maintenant être employé sur des montages industriels.

REFERENCES

[1] —F.Moya, S.Druet, J.P.Taran. Optics Commun 13, 169 (1975).

[2] —M.Pealat, M.Lefebvre, P.Bouchardy, J.P.Taran. Appl. Optics 24, 1012, 1985.

[3] —P.Moreau, RA n° 1974, Tiré n° 3, p.125—135, Inflammation et développement de la combustion turbulente dans un mélange homogène air-méthane.

[4] —M.Pealat, J.P.Taran, F.Moya, Opt. Laser Technology, 21 February 1980.

[5] —S.Druet, J.P.Taran, Progr. Quant. Elect. 7, 1 (1981).

[6] —K.Muller-Dethlefs, M.Pealat, J.P.Taran, Ber. Bunsengesell., Phys. Chem. 5, 803 (1981).

[7] —P. Magre, P.Moreau, F.Dupoirieux, G.Collin, R.Borghi, M.Pealat (article en préparation).

[8] —G.L.Switzer, D.D.Trump, L.P.Goss, W.M.Roquemore, R.B.Bradley, J.S.Stutrud, C.M.Reeves, Simultaneous CARS and luminosity-measurements in a bluff body combustor, in Combustion Diagnostics by Nonintrusive Methods, Progress in Astronautics and Aeronautics, vol.92.

[9] —Vu la nécessité de réduire le nombre d'essais, les points où a priori aucun phénomène intéressant ne peut se produire n'ont pas été explorés.
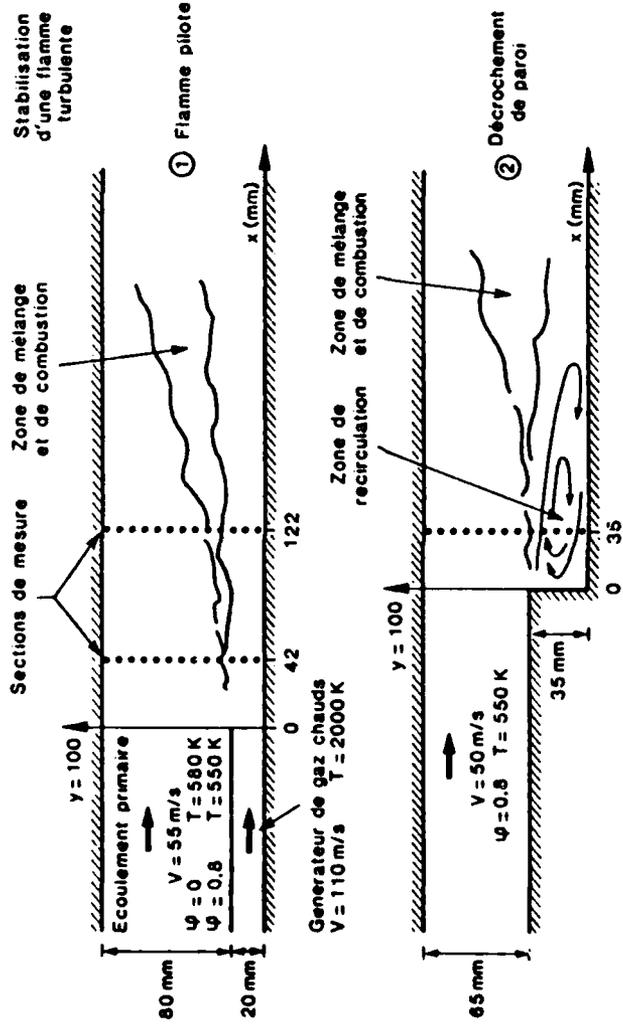
Fig. 1 - Représentation schématique de la veine d'étude de la propagation d'une flamme turbulente

Histogramme obtenu à partir de la série des spectres 'intenses'

Histogramme obtenu à partir de la série des spectres 'faibles'
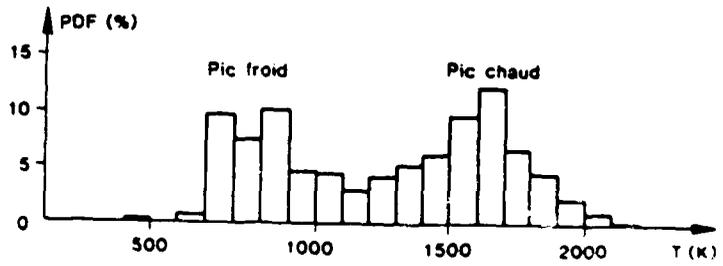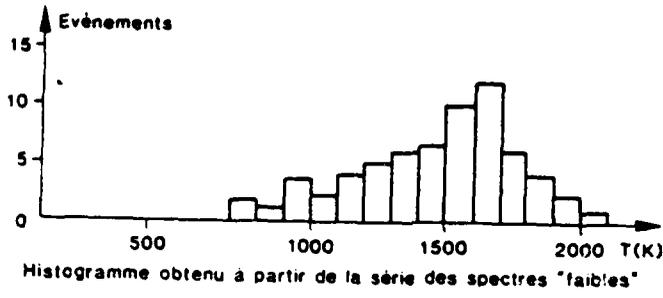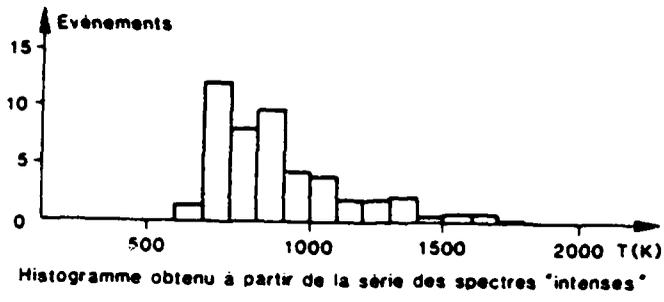
Fig. 2 - Fonction de densité de probabilité (PDF) de températures
construite avec les deux histogrammes "froid" et "chaud"
(Flamme pilote, ψ = 0,8 - x = 42 mm - v = 20 mm)

AD-A182 954   ADVANCED INSTRUMENTATION FOR AERO ENGINE COMPONENTS: 2/6
CONFERENCE PROCEEDIN..(U) ADVISORY GROUP FOR AEROSPACE
RESEARCH AND DEVELOPMENT NEUILLY..   NOV 86 AGARD-CP-399

UNCLASSIFIED   F/G 14/2   NL

MICROCOPY RESOLUTION TEST CHART
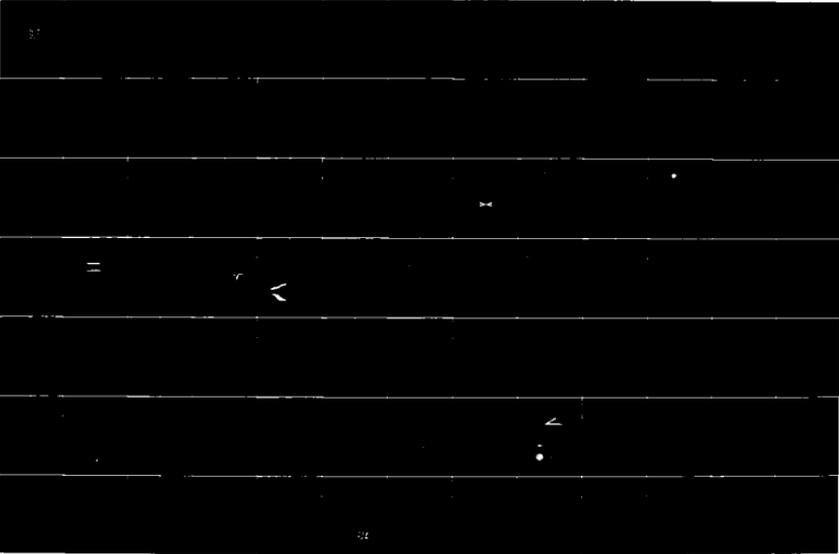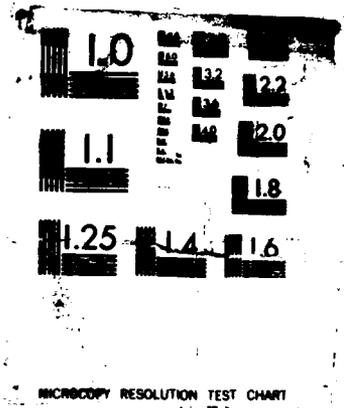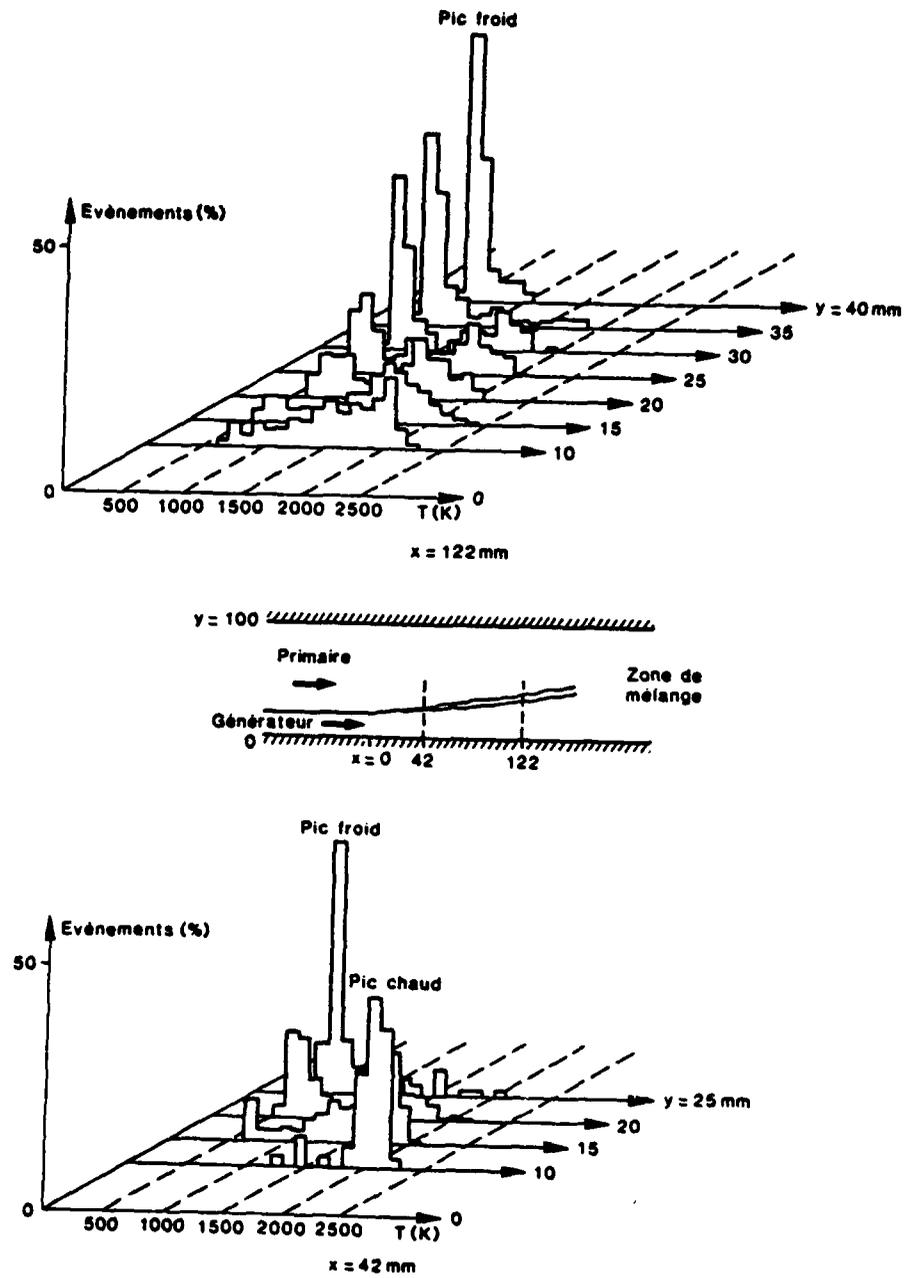
Fig. 3 - Fonction densité de probabilité (PDF) des températures
Montage avec flamme pilote
Générateur stoëchiométrique
Pas de combustion primaire

Histogrammes
à deux pics

Evénements(%)

Pic chaud

y = 50 mm

40

35

30

25

20

15

10

0

500 1000 1500 2000 2500 T(K)

x = 122 mm

y = 100

Primaire

Zone de
reaction

Générateur

0

x = 0   42   122

Pic froid

↓ Evénements(%)

Pic chaud

y = 45 mm

25

20

15

10

0

500 1000 1500 2000 2500 T(K)

x = 42 mm
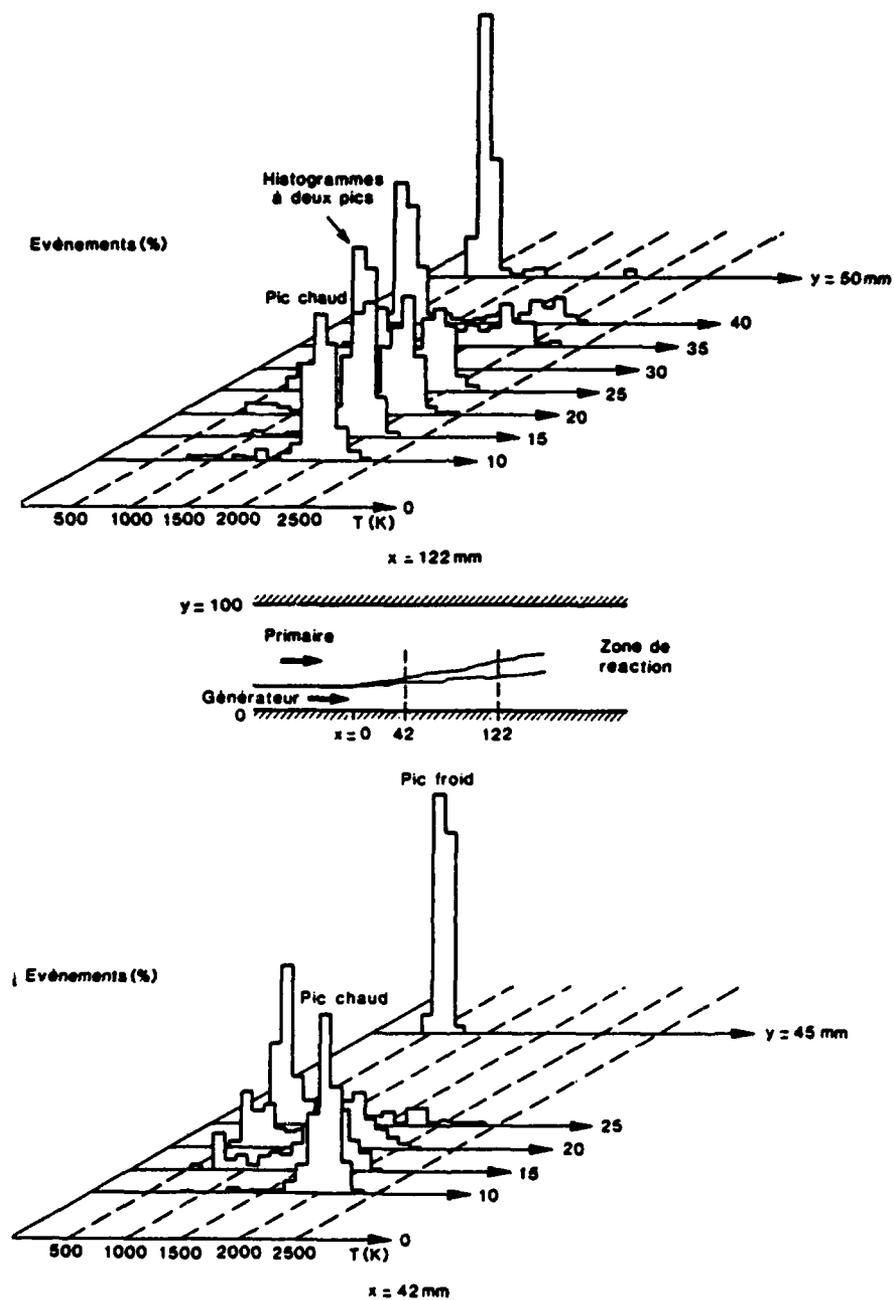
Fig. 4 - Fonction densité de probabilité (PDF) des températures
Montage avec flamme pilote
Générateur stoéchiométrique
Ecoulement principal richesse φ = 0,8
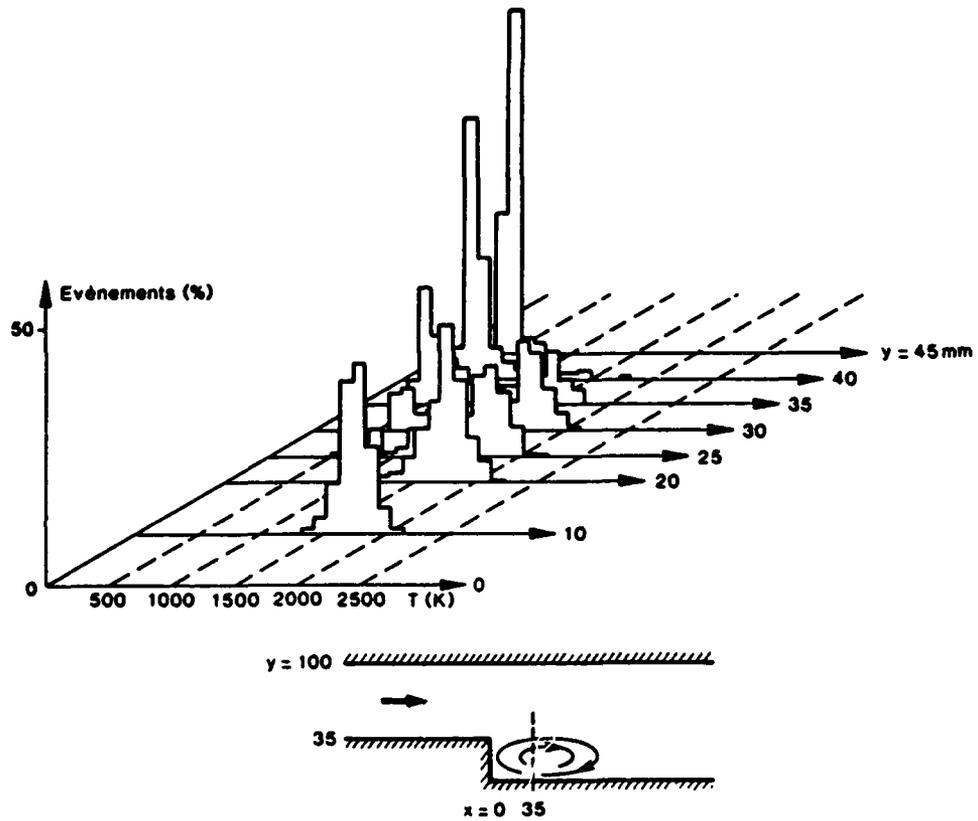
Fig. 5 - Fonction densité de probabilité (PDF) des températures
Montage avec décrochement de paroi
Ecoulement à richesse $\varphi = 0,8 - x = 35$ mm

DISCUSSION

A.Melling, UK

The geometry in Figure 1 Part (1), is of interest in fundamental studies of turbulent combustion with a supersonic primary stream and a subsonic hot gas steam to stabilise the flame. Could you speculate on the additional difficulties which are likely to be encountered if CARS were to be applied to such a supersonic combustion experiment?

Author's Reply

There is not any principle objection for application of CARS in a supersonic combustion environment. However it should be kept in mind that

— high density gradients (and consequently high refractive index gradients) could lead to defocalisations of the laser beams.
— the intensity of the CARS signal is proportional to the square of the number density of the probed molecule. In consequence the CARS signal could be very weak in low density flows.

J.P.Taran, FR

Comment

I think if the size of the flow is not too large there should be no reason why we could not make a measurement under those conditions. However, if the size of the flow and the temperature gradients become too large then the density gradients cause beam defocussing. This effect is well known to those working in CARS. If the problem becomes severe it also becomes difficult to get single shot spectra because the beams are so damaged by the density gradients that there is not enough signal to collect on a single shot basis and you end up having to integrate over a long time and then naturally you start asking questions about what it is you are measuring. What is this average which you get which is certainly biased and may also have a biased PDF?

A.C.Eckbreth, US

Comment

This area of turbulent beam steering strain is often talked about but it is one that is really difficult to quantise in internal combustion engines. There have been experiences where there has been complete loss of signal, during say flame front passage or something like that. Our experience in jet engines is that we use the geometry that I showed you earlier where we put the dye beam inside the annular pump beam. That causes the dye beam to focus not as tightly as the ω_1 beam. So you have a broad intensity profile for the dye laser, you have a more narrow intensity profile in the ω_1 laser, so you can tolerate a certain amount of dithering. At full augmentation at very high acoustic levels we typically experience maybe 25%, perhaps as much as a 50% loss in total signal. We still have enough signal to do single pulse thermometry. We have not in our tests to date definitely ascertained whether we simply have dithering of all our optics causing our beams to shake about or whether it really is due to flow effects. You know, it is a sort of uncertain area of measurement and there are instances where there could be problems. But it seems in the range 1-20 atmospheres, if you look at the body of measurements that have been reported in the literature, people have generally been successful in gathering data under very difficult conditions.

R.B.Price, UK

1. Has the CARS data reduction been carried out using "quick fit" methods?

2. Have you done flow visualisation on the flames in the two flames you have got CARS data for? Are there large coherent structures present?

Author's Reply

1. The "quick fit" CARS data processing has only been used to have a nearly real time first approximation of the temperature. This "quick fit" is based on the slope of the cold vibrational band or on the width of this band.

   For definitive results, given in the paper, the processing of the data was based on a complete fitting between the experimental and theoretical spectra. The routine based on least mean square method needed 5 seconds of computation time on a PDP 11/23 for each spectrum.

2. Visualization of this flow have already been carried out by means of high speed cinematography and shadowgraphy [3]. These pictures have shown large structures in the flow and also turbulence of lower spatial scales. However the large structures, pockets of hot or cold gases, can not be considered as "coherent" structures. For discussion on this last point see Ref.7, to be submitted to Combustion and Flame.

D.Kretschmer, CA

How do you view the possibility of applying CARS in the primary zone of the combustion chamber where the flame isn't transparent?

Author's Reply

The possibilities of CARS have already been demonstrated at the outlet from the main combustion chamber sector of gas turbines, and from inside the primary zone. Temperatures have been measured there (1) without the non-transparency of the environment or the luminosity of the flame presenting a problem. New difficulties, making the

method harder to apply, could arise in a primary zone functioning at high pressure. In this case, above 3 bars, significant variations in density could cause significant de-focussing of the beams for optical traverses of the flame of approximately 30 cm.

(1) R.Bedue, P.Gastelois, R.Bailly, M.Pealat, J.P.Taran. CARS measurements in a simulated turbomachine combustor. **Combustion and Flame**, 57(141), 1984.

J.P.Taran, FR
Comment
We have done some measurements on a simulated turbomachine combustor at SNECMA. We found no problem with optical traversals of ~10—15 cm using kerosene as the fuel and at 1 atmosphere. To establish the connection with this other question we had about extreme temperature and pressure gradients. When we raised the pressure to 3 atmospheres we started running into severe problems of beam steering and signal loss. That is because the gradients can get very large. The beam steering of course changes the positions of the beam foci and also changes the size of the focal spots so the CARS signal is lost. So, as a rule of thumb, ~10 cm beam path length and a pressure of 3 atmospheres is going to be close to the limit for CARS measurements.

A.C.Eckbreth, US
Comment
I would like to comment on Pierre Taran's comment. There have been a number of CARS measurements on primary zones. We made some measurements back in 1979 on a 30" diameter combustion tunnel fuelled with Jet A and 1 atmosphere pressure. The biggest problem we had was that as we increased the equivalence ratio to 1.2 —1.4, we started experiencing fairly severe beam attenuation due to increased soot formation. I am wondering whethering in your particular case as you went up in pressure from 1 to 3 atmospheres whether is was really beam steering or perhaps an increase in soot formation.

J.P.Taran, FR
Comment
I do not think in our case it was soot formation because there did not seem to be any appreciable attenuation of the laser beams going through the combustor. This was more of the beam blurring-type problem that we experienced. I remember that.

D.A.Greenhalgh, UK
Comment
I would support Taran's comment. We have made a lot of measurements in I C engines and there you see a lot of beam steering. When the flame front comes through where you are making the measurement the beam does not come out of the engine at all. It vanishes inside due to very severe deflection which is worse when the beam is traversing parallel to the flame front.

We have also done measurements in an ammonia oxidation reactor at 10 atmospheres and ~2—300°C in which we were traversing through around 1.5 metres of reacting gas. There we saw very large beam steering, more than we anticipated. This flow was clear with no particles of size greater than 0.2 μm in the gas stream. Dithering of 2—5 cm on the laser beams was observed. So beam steering is likely to be a worry at high pressure. It is a function of the product of path length and the density gradient. Large gradients can be tolerated over short path lengths. The particular problems in the ammonia reactor arose because the path length was 1.5 metres which is a long way.

ROUND TABLE DISCUSSION
SESSION 1

J.P.Taran, FR

Dr Price will give a brief introduction of a few minutes on his feelings about the subject. Then we will invite questions. Those questions will be asked to the entire batch of speakers whom you have heard since this morning. So I will ask all the speakers and my session co-chairman, Alan Eckbreth, to stand up and come to the table here and be ready to face your questions.

I suggest to make you more comfortable about questions that we do not write down the questions and the answers because that means doubling or tripling the volume of effort you have to put in. Writing down the questions may inhibit you in asking questions, so I think it better if we do not write down the questions and therefore do not write down the answers. I hope you do not mind. We will have a freer discussion. I believe that this is better in encouraging more exchange of views.

R.B.Price, UK

I hope that like myself you will have drawn some encouragement from what you have heard today as regards the usefulness of CARS as a practical tool, and as regards the understanding that has by now been achieved and the ability to model CARS spectra. I think that as far as applications are concerned we have been given examples of quite notable success, ranging from furnaces through IC engines and moving on through subsonic combustion in gas turbine type environments to supersonic combustion scram-jet type combustors. As far as my own industry is concerned, and there are others in the room who can deal much better than I can with applications to furnaces and IC engines, there are three main applications of CARS that I can foresee. All fall in the general area of combustion modelling. I might add that these are personal views and do not necessarily represent the views of my company.

The first application is in the field of radiation modelling. As we go further towards stoichiometric combustion and higher burnt gas temperatures, radiation to the walls of the combustion can is going to become an increasingly important source of heat transfer. The ability to predict that radiation is going to be an important requirement for the future. As part of the development of the model for doing this and its validation, the ability to make spatially resolved measurements of both mean gas temperature and its pdf, together with corresponding data for major species concentration, within the environment of the primary zone of a gas turbine combustor is going to be very valuable to us. Such data is of course equally valuable in validating 3D models of the combustion process. I can think of no technique other than CARS that is capable of giving this information in that demanding environment. I consider it worthwhile developing the CARS technique for that application alone.

As far as the physics of the combustion process is concerned, many of you will know that there are models which treat a turbulent combustion zone as a composition of laminar flamelets. One of the models whose development we are supporting requires knowledge of the pdf of temperature as input for the calculation of heat release locally by the laminar flamelet. Again, CARS has an important role to play in providing this information.

Thirdly, in the general context of turbulence modelling for combustion flows there is a requirement to measure correlated velocity and scalar quantities. These measurements will help us to assess different turbulent transport models and decide on the most appropriate ones. Some of you may be aware of the work that Larry Goss has been doing in generating this type of data using CARS to measure gas temperature and making near-simultaneous measurements of velocity by laser anemometry.

So these are three examples from my own particular industry where I can foresee CARS being a technique that can produce valuable data that is not going to be available to us by any other method.

J.P.Taran, FR

Now what I think is appropriate is to invite your questions and perhaps also ask those members here to make propositions or suggestions.

G.B.Kretschmer, CA

In gas turbine primary zones, you can easily have temperature gradients in the order of 1000°k per millimetre. That mean that with your 3 mm, 4 mm and 10 mm long measuring volume you can have gas at a lot of different temperatures in that volume. What is the form of the measured mean temperature? I suppose it is ʌot the true mean of the temperatures.

J.P.Taran, FR

I think I can try and answer this question because we have addressed it specifically for the past two years. The problem is the data will be biased in favour of the cold spectra because there is a quadratic dependency on density and they are much stronger. We have conducted computer simmulations of the spectra that you would get by putting side by side in the same volume a hot and a cold gas and you find that if the temperature gradient is not too large you indeed get something which is close to the true mean of the two temperatures, but certainly if you are to increase the gradient then you may get into trouble. Now I cannot quantify this because the data is not finished and furthermore we are working on an experimental programme to verify this. This is part of a one or two year programme to explore the effect of spatial resolution on the data quality in CARS. So basically we only have a partial answer to your question. Perhaps others have more.

A.C.Eckbreth, US

I agree it is a difficult problem. I think in this context you just have to look at the alternatives. If you put in any kind of probe which may have to be water cooled to survive the kind of conditions that you envisage then that probe may have to be many millimetres in diameter. It is unclear what kind of temporal or spatial resolution you are going to get in that situation. Albeit in these situations CARS is not perfect because of averaging over the spatial resolution it may nevertheless be superior to what else is available.

D.A.Greenhalgh, UK

I would like to make a general comment that the spatial resolution that you get with CARS is typically 3 or 4 millimetres long by 100 microns in diameter, or something of that order. It varies slightly from system to system but that is typical of what you get with a lot of point-scanning optical diagnostics and it will be wrong to assume that another optical diagnostic is not going to suffer the same problems that we have with CARS, particularly with beam steering and so on. So I think one of the things to bear in mind is that where CARS does suffer with beam steering you are not going to solve that problems necessarily by turning to another optical method.

J.P.Taran, FR

To just add one comment to the subject I was discussing these problems specifically in connection with the work done and presented by Philip Magre. Given the very high shear in his experiment some people expected the turbulent scale to be of the order of the Kolmogoroff scale, that is largely sub-millimetre in size. So we know in this experiment we are a factor of 10 to 100 away from what you might expect to be necessary for adequate spatial resolution. That doesn't stop me from sleeping for the time being, at least not for a year or two.

A.Buggele, US

I would like you to address the data rate one more time. What I have got in mind is how we can get to 5000 shots per second. Let me pose something to you. The Gatling gun; I don't know whether they have got 10 barrels or 20 barrels. Suppose you use 20 generic lasers all of a standardised design, because we are talking about limitations on costs, and let us say X number of CRAYS or whatever kind of computer you choose, and gang them together. Is it feasible to combine a system with 10 to 20 different lasers so you can get the rate of shots up to 1 or 2 thousand per second because it will be most beneficial if you can do that?

A.C.Eckbreth, US

If you are really interested in going to the extremely high data rates I would suggest that you do not study flames that we find in really practical combustion devices but rather, for example, turbulented premixed flames or hydrogen air diffusion flames where you can isolate say the fundamental turbulent chemistry that you want to study. There are other laser diagnostics, for example, Rayleigh scattering which when properly performed can give you temperature rates up to the order of 15 kilohertz. There are a number of studies like this in the literature where you take a diagnostic technique which has the data rate capability and you match your experiment to it. If you really want to study such problems, say in turbulent soot-forming combustion, you could interleave lasers at 50 Hz, you could interleave those together but I think it would be very difficult to find anyone who would financially support such an experiment. So I would say for these more fundamentally oriented questions the best solution is to define the experiment and then there are existing diagnostic techniques which can have a go at those kind of problems.

D.A.Greenhalgh, UK

I think you posed the same question to me after my paper and I wrote an answer. First of all if you want to do a practical experiment, we can currently have 2—300 millijoules per pulse and I would prefer more signal to mitigate against some of the problems we have now. Quick calculations say I am going to have a kilowatt of output from the frequency doubled source. Now I shudder to think what the electricity supply required to do that is with about 1% wall plug efficiency. That is going to be a hefty amount of current and it is going to be a huge laser. That would represent the facility you are going to drive to do what you are asking for whether you do it like a Gatling gun or you use a big barrel. The alternative, I think, where there is a possibility is the copper vapour laser which does get to the required power. But if you go to the high pressure combustion then you do no need the source of high power I am talking about. We managed with a few millijoules in our engine spectra. So on the laser front I can see a possible match of high pressure systems with an advanced copper vapour laser. Where you get into a snag is if you want to do multiplex CARS and use the detection technology you currently have for the multi channel detector. Even if I crank that thing up I do not think I am going to get beyond 200—300 Hz. However solid state devices are emerging rapidly so may be a year or two from now we might get there.

R.Farrow, US

There is another CARS technique that may have a bearing on this. This is relatively new and uses a narrow band laser to simultaneously probe the different transitions in the nitrogen spectrum. That might alleviate some of the requirements for such a large laser since it would be a narrow band measurement.

D.A.Greenhalgh, UK

That might be a bit more problematic at high pressure.

R.Farrow, US

You could look at the hot band and the ground-state band, and that has been demonstrated.

J.P.Taran, FR

I was going to suggest some other thing and eventually will turn the question back to you in a sense. What exact problem do you want to solve? I think there is another method if you are willing to trade repetition rate for spatial resolution or if you want to trade points in time for points in space. If you have a flow you could either elect to look at one point and take measurements at the same point in an equal succession or you could sample the flow all at one time but in different positions. If you want to do this then maybe you could disguise again, and if you take your positions close together you could indeed resolve some fast moving flows and study fast phenomena with a fine spatial resolution. Now clearly there may be solutions to your problem if the problem is formulated so that we know if we are dealing with high pressure, or low pressure, what kind of dominant species we have in the flow and so on.

Unidentified Questioner

Do you have experience of CARS usage for rocket exhaust jets and what will be the limitation for using CARS for such flows?

D.A.Greenhalgh, UK

I guess the two types of rocket are the solid burning and the liquid burning. In the solid burning I think one of the things you are going to run into is particulates in the system itself and therefore some optical attenuation. Apart from that there are obviously the shock diamonds that you are going to have to cut through and you may be dependent on the stability of those shock diamonds in order to successfully traverse the system to make measurements. I do not think that I know of anyone who has achieved that but some of the other panel members may.

R.Farrow, US

There has been a demonstration by Lee Harris. He made CARS measurements in a solid double based propellant not in the combustion zone but just above it and he made single shot measurements at about 1500°k.

D.A.Greenhalgh, UK

We have also made measurements in similar things and I would prefer not to have to go back to some of the very rich systems where you have a lot of fuel. You can imagine there is always some sort of fuel and oxidant mixture present and if you have got a lot of fuel, so the stoichimetry in effect is greater than one, then it is not easy to make the measurements.

A.C.Eckbreth, US

If you are talking specifically about making measurements in expanded nozzle flows we are currently doing some work for NASA, Marshall looking at diagnostic techniques for example to make measurements in the exhaust of the space shuttle main engine. A lot depends there on the degree of expansion. On some of these highly expanded jets the pressures get extremely low. As you have seen, CARS nominally has a pressure squared scaling dependence. So if you want to use CARS, one of the problems you have in some of these devices, even if they are clean and you do not have to worry about the refractive effects, is that the pressure starts getting quite low and therefore we actually have to relax the spatial resolution to get enough interaction length to get the signal up. Now that might not be a really big constraint and you may be able to tolerate 25 mm or 30 mm resolution if you are looking at a couple of metres diameter exhaust, but that could be a problem. In fact if the flow is clean enough spontaneous Raman scattering may become more sensitive than CARS. So you might not want to use CARS in a situation like that.

T.Jackson, US

I think that Dr Greenhalgh indicated some CARS measurements in a spray. I am interested in measurements in a vapourising liquid fuel spray. I wonder if the panel could comment generally on the problems associated with that measurement, and specifically whether there is a clear limitation in terms of droplet concentration that you have to avoid?

D.A.Greenhalgh, UK

Yes. We are not unique in making spray measurements; Alan Eckbreth has also made spray measurements. When we made those measurements there was certainly a limit and we found that it is when you get down to about 30%--40% attenuation of the pump beam that life starts to hurt. At that stage you tend to get quite a lot of signal drop out and that arises because as a drop passes through the beams themselves it acts like a really weird lens completely deforming the laser beam and I think that is the thing that primarily hurts. One thing going for you, unless you have a very dense spray, is that you get a fairly high voidage there and you can get shots in between the droplets. I think the thing that you really need to think about is that typically in some of the spray regions, you could take 500 shots but only 300 would go through as being appropriate for analysis. Then you should be saying 'can I believe the complete statistics of the flow I have sampled or is there some artefact that has arisen because of the fact that I have got data drop out?' I think actually in the core region of the spray it should not be a problem. You probably have more of a problem at the burning front where you have got the combination of two effects, beam steering and droplet effects.

A.Melling, UK

Bryn Price said he was encouraged by the process that was going on in CARS and the fact that one can have temperature and concentration measurements. I am probably not alone in being a little bit put off by seeing some of the things like third order susceptibilities and four miles of computer magnetic tape full of data. What about other techniques which are probably a lot cheaper and do not give you proportionally less information, for example laser induced fluorescence? Can the panel comment please?

D.A.Greenhalgh, UK

The four miles was an order of magnitude out; it was actually forty miles! That represents the actual data we have collected. However, we do not just collect CARS data, we also collect full cycle pressure data. It is a data logging exercise. I would not be at all surprised if Rolls-Royce or Pratt and Whitney when they run their gas turbines do not wind up with similar quantities of data for some of the tests they do with or without CARS. So that statistic was brought out to try and indicate that we use CARS as an engineering tool on the test bed. It is just another measurement you make on the engine when it is running at a certain condition along with other things. One comment I would make is perhaps a bit provocative but CARS is the only optical technique that I know that has not fallen short when it has got near a practical device, so it really has got that going for it.

J.P.Taran, FR

I would like to add a comment that if you can process your data in real time you do not end up with miles of magnetic tape. I think we are getting close to this point really. For instance in our case at ONERA, the simple addition of a co-processor would enable us to operate at 10 Hz with maximum performance in data processing. So the situation can be improved by just a little more sophisticated computer equipment or data handling. Perhaps Alan Eckbreth would like to comment on laser fluorescence because you raised this point.

A.C.Eckbreth, US

I thought your question was a good one. There are a lot of optical techniques. A lot of us have got into CARS because we tried a lot of other techniques that did not work. In the gas turbine business, the things we are most interested in, in many cases, are temperature and major species concentration measurements in terms of profiling heat release and in measuring efficiencies. Fluorescence techniques are primarily suited to radical species and are commonly used in kinetic studies; if you will, in more fundamental studies of flame chemistry. In many cases there are fluorescence thermometry techniques. Most of them by the time you are finished emerge not being too unlike CARS in that you need optical multichannel detectors, you need Nd/YAG pulsed lasers driving narrow band tuneable dye-lasers which have to be tuned to specific transitions and, in fact in many cases the thermometry is not as well grounded as CARS is. I think CARS is a technology which can be transferred to people who do not know what third order non linear susceptibilities are but it is very good to have some experts in house who can help those people out at a moment's call when they need help. It is a technology I think that is going to be somewhat more difficult to transfer than laser anemometry. Many of you are versed in laser anemometry. You know those systems are commercially available and you know the difficulties involved in doing LDV measurements.

W.A.Stange, US

I believe, Alan, you have done some measurements with CARS in a supersonic combustion facility with hydrogen fault. Have you compared calculated temperatures with your measured temperatures?

A.C.Eckbreth, US

In some internal corporate documents, primarily in proposals, we have used those demonstration measurements and suggested the plausibility of the measurements, but at this point you should take those measurements primarily as demonstrations of the ability of CARS to make measurements in supersonic flows. They have not really been rigorously used for model evaluation at this point, but certainly with activities in hypersonics increasing at the rate they obviously are, I think CARS and other laser diagnostic techniques are very important for model validations particularly in those supersonic regimes where we can experimentally access the flows. The particular experiment you mention is not modelled in detail so the answer to your question is no. We do not have temperatures to compare from say two dimensional CFD calculations of the flows.

P.A.E.Stewart, UK

In transferring the technology, what do you see as the major problems and do you foresee a use for expert systems?

J.P.Taran, FR

In France if I try to start a company that would run the service of CARS because clearly the demand is very high, the chance of failure is also very high, given the difficulty of the experiments. It is obvious that it is much cheaper to rent services for three months than to buy this complex equipment at something like a few hundred thousand dollars and then try to hire the people, which you will not be able to find anyhow, to do the experiments for you, at least not within two or three years. So that is one approach which you can try. The other possibility is that you can try to pull the existing experts into some kind of working force that would provide services here and there locally but not moving. That is one approach we are trying in France without really knowing if it will arrive at some result but we are considering it.

D.A.Greenhalgh, UK

A very good comment was made earlier by Alan that you can transfer the technology and you can do the experiment very successfully without having a detailed knowledge of all factors involved. The snag arises if you run into a problem such that the tougher the application the more the likelihood of that problem occurring. I think what people do need when they get into these applications is some sort of pool of expertise that they can draw on and I think I would support that proposal. There is the problem if you want an expert on CARS that they are not readily available. It takes maybe three or four years to train someone who really could be utilised for consultancy type work in a variety of environments and I think that is probably a minimum period for that sort of role. There are not that many worldwide potential consultants and so I would support Jean Pierre and say that what expertise exists does need to be used with care and to best effect.

R.Farrow, US

I might use this opportunity to put in a plug for Sandia Labs and the combustion research facility there. We have a facility worth visiting. Combustion scientists come in and do experiments with the staff. There have been cases of people proposing CARS investigations where the person coming in brings with him the apparatus where the measurements are to be done. That has happened a couple of times.

D.A.Greenhalgh, UK

I agree that is a smart move. It is very easy to see, for instance, working at Harwell, that those people who successfully imported the technology from us are those people who have come to us and worked with us. I think one of the reasons for that is as must as we try to be honest in putting down as everyone else does the way we do our experiments, there is a certain amount of deep knowledge of the tricks that lasers can play on you that perhaps does not always get through and people can pick this up very rapidly from working on a successful experiment. Perhaps the motto is go find yourself a successful CARS experiment and get friendly with it.

M.N.R.Nina, PO

My question is related to interference of the CARS high energy beams with the flow itself. A solid probe interferes with the flow in many ways. To what extent do CARS high energy beams interfere with the flows that one wants to measure?

D.A.Greenhalgh, UK

There are some certain obvious ones. If you turn the lasers up to high intensity levels in just a plain gas you will actually get breakdown and that is to be avoided. Then there are a number of other aspects with regard to saturations and so on and Roger Farrow has told us some of the possibilities there are for distorting the spectrum. You have to take a prudent approach to your experiment so that it is properly designed to mitigate against these effects. However, having done that, there are still circumstances which can cause problems and one of those is particle laden flows. Particles as they pass through the high intensity part of the focus can induce yet further breakdown and you can literally see sparking in the laser, and there is some work by Ed Whiting which addresses that problem. He looked at ash laden flows basically and we have seen similar results in that type of system where you have particles that probably are grey-white. But, if you have particles that are black we see a different type of behaviour which is also important. So in answer to your question I think I would expect that the biggest problem would arise from particles in flows and there is probably quite a bit of work that needs to be done there for such flows to figure out all of these effects.

R.Fletcher, UK

I think it is very worthwhile to take measurements on $\pm 40^\circ$K at some temperatures. At say 2500°K is useful, but not half as useful as measuring at $\pm 4^\circ$K at 2500°K. I would be interested to know whether the panel think that such levels of accuracy can be obtained? If so, how and how soon?

J.P.Taran, FR

There are several aspects to the answer. We at ONERA have tried scanning CARS in media at very high temperatures like discharges where in actual fact the static or rotational temperature is low but the vibrational temperature is very high, above 4000°K. In principle in these situations by scanning CARS again you should be able to get a temperature within a few $^\circ$K. Unfortunately we then run into several problems which are of the following nature. You see the different vibrations respond to the excitation in different manner and roughly speaking the response, that is the squared root of the CARS intensity which is what we get in the end, is proportional to the vibrational quantum state number plus one. This is a rough approximation and in fact there are high order corrections which are not always easy to calculate since they necessitate a deep knowledge of the molecular potential functions which are not always known. Furthermore, the vibrational saturation also becomes important in these high level vibrational states because the saturation is dependent on the vibrational quantum number also and these corrections are sometimes extremely hard to evaluate. If we are talking about flames and single shot spectroscopy then of course the difficulty is that we might not have much signal at the higher temperatures and therefore the temperature measurement precision might not be so good. We also have to spread the laser energy available over many modes and the signal to noise ratio per channel decreases quickly. So, that is to give you a feel but I am not giving you a specific answer.

D.A.Greenhalgh, UK

I tend to support that. I do not think we have enough CARS signal at the moment to intrinsically get that accuracy single shot. So we would certainly have to improve the quantity of the CARS signal we are getting from the system to get towards that. Also, Jean Pierre discussed the point of absolute accuracy. I think the international scale for measurements and relating to that as we move towards 4°K at those very high temperatures may prove to be a significant problem. We made a stab at that with our high temperature lamp and there is an enormous amount of physics in the subtle corrections that can come in when we are talking about 15 or 20°K. If you are going to 4°K I think there is an immense problem there in being able to believe your measurement in an absolute sense.

M.Z.Matteson, US

My question is directed to Alan Eckbreth.
In your UTRC scram jet tests I believe you were running your primary only and you were going through a quartz window with your CARS. With scram jets you are in a high temperature environment and there is another application problem caused by water droplets. Is there any possible way of closely ganging together a couple of CARS systems in parallel close proximity for getting a temperature mean because of your lost signal? You say that you get the water droplets to give distortion and you lose your signal. Is there any way of getting something in close proximity so there will not be that much of a temperature gradient but at least getting a ball park of what the temperature might be in that region.

A.C.Eckbreth, US

I guess I am having trouble following your question on the water droplets.

M.Z.Matteson, US

One of the other gentlemen (Dr Greenhalgh) said that you lose your signal count and go down to maybe 40% counts or something on that line and that you should question whether or not to trust that count as being an accurate statistical profile of what your signal should be. Is there any way of running the CARS in parallel so that you can kind of match that signal to validate whether it is accurate or not, to try and get a new ball park of your temperature when you are having trouble with droplets in the air?

A.C.Eckbreth, US

Where are you getting your water droplets from?

M.Z.Matteson, US

We do some spray cooling occasionally in our effluent gases. Because of water particles, you lose your count on the CARS. Is there any way of saying that the validity of the CARS signal is not that good? Is there anything in parallel to try and get an accurate measurement.

D.A.Greenhalgh, UK

The point I was referring to is this: If you make say about 500 measurements, you can only analyse maybe 300 of those in a dense two-phase flow region where you have got reasonably low voidage and then you certainly do have to ask questions as to exactly whether you sample the flow properly.

If, for instance, the arrival of the particles that pass through the beams is a purely uncorrelated random process compared to the temperature field you are sampling then you probably do not care and you just wait there twice as long until you have got a 1000 points and you are back to the original 500 valid ones. What I was trying to do was to put out a warning that if you do that, if you are losing a lot of data, then that might be happening under a specific circumstance, and one needs to be aware that that is a possibility. In terms of how you can address that statistical problem I do not have anything to offer at the moment other than to say we have got to think about that, but you have to get a pretty low voidage before that is a significant problem.

A.C.Eckbreth, UK

Can I ask you where are you doing this spray cooling? Is this external to the windows or internally?

M.Z.Matteson, US

It would be with a CARS shot on the back end of a nozzle with no quartz windows, and that is the problem, there are no quartz windows. With quartz windows you could move further up your test item and there would be no problem because you could shoot through your quartz windows. But say you want a temperature profile of the exhaust gases you have got to cool down the effluent stream because of the high temperatures you are achieving in the tunnel.

A.C.Eckbreth, US

I see, prior to dumping. What about, say, measuring the effluent stream just upstream of where you are dumping in water to cool it?

M.Z.Matteson, US

Well we might be wanting to cool the test item with some water spray also to lower the temperature. So it is hard to get around.

A.C.Eckbreth, US

Physically I think in a situation like that you start off with something very inexpensive like an helium neon laser and just ascertain what the degree of attenuation is. Also, obviously if you are actually getting films of water on lenses or windows, that distortion is going to destroy feasibility fairly quickly.

J.P.Taran, FR

I was going to say that perhaps windows are not necessary in your case.

W.A.Strange, US

The comment I would like to make is that the sampling rates we are talking about, 10, 20 or maybe 30 Hertz, are really not acceptable to a real experiment, especially in view of the fact that a lot of people are doing simultaneous measurements of a lot of parameters such as temperature, pressure, particle size and velocity and so on and so forth. For example I am an L.D.A. user and a data rate of 10, 20 or even 200 is very much unacceptable in any type of real situation because you get truly different and inadequate answers in the velocities and turbulences and so on and so forth. So with CARS we are a long way away from a real instrument that is useful to engineering. The other thing I want to say is that it seemed that the CARS technique had an inherent characteristic of broadening the temperature that you measure from what I gather. In a real application like in a turbojet combuster where you have dilution jets and you have tremendous mixing and high turbulence, you then really do not know what type of temperature fluctuations you have. That knowledge is a very important aspect to the model requirement and is equally what we are looking for.

J.P.Taran, FR

Shall we fight back?

A.C.Eckbreth, US

I am not going to fight back. I think they are very valid comments. The one thing I would say is perhaps in contrasting CARS with LDV. When we are running at 20 or 30 Hertz in CARS, we know when we are making a measurement and obviously we are statistically sampling the medium. I think in an LDV situation you are waiting for a particle to trigger when you get signal. For very low data rates in LDV of say 20 or 50 Hertz, you are waiting for particles. Maybe there is a greater chance that you are conditionally sampling the flow and maybe the LDV situation at low data rates is a lot worse than the CARS situation at low data rates because there may be greater danger for you to conditionally sample. In terms of the fluctuations, as Doug has mentioned, there are several approaches in the literature. Because of the very large signal change which accompanies a large fluctuation in temperature then, when you get into these situations, to keep the data rate up you have to split the beam and go through varying amounts of attenuation so that you are putting the same spectrum on the optical multi channel detector but with different degrees of attenuation. At least one of those spectra is always within some linear range so that the last problem you threw out is in principle soluble and there are people making measurements with every pulse despite the temperature fluctuations which are occurring.

D.A.Greenhalgh, UK

I think there is an interesting piece of work by Larry Goss in which he initially took some CARS measurements under conditions where CARS gives, if I can use this term, "a true average". It is a fairly slow data rate but it fires at a predetermined point which is very different to LDA where you are waiting for the particle to arrive and probably the measurements you are going to make are Favre averaged. What Larry then did was to make some temperature measurements where he conditionally sampled the field for temperature following the arrival of an LDA particle. He found that he indeed got a temperature shift which was more appropriate for the Favre average expectation of the temperature. So I think you have to be careful about how you address the statistical problems. I think the other comment I would make is that LDA is a technique which has its own set of biasing problems which are all pretty well documented and known. In my judgement there does not seem to be a particular stand point where you would say that CARS is definitely the worse technique in terms of its liabilities. In response to your last point, the temperature broadening that we have seen is inherently instant. The one thing that has amazed us is how small it is compared to the actual flow fluctuations you see, which are abolutely giant by comparison.

TECHNICAL EVALUATION REPORT
SESSION II – LASER ANEMOMETRY

by

A.Boutier
ONERA
BP 72
92322 Châtillon Cedex
France

RESUME

La session II avait pour objectif de traiter les problèmes de mesures de vitesses par vélocimétrie laser dans les turbomachines. Les meilleurs spécialistes mondiaux dans ce domaine étaient réunis et leurs exposés (ainsi que les discussions qui ont suivi) ont permis de faire le point des possibilités techniques actuelles des appareillages utilisés.

Les conclusions essentielles sont les suivantes :

• les turbomachines constituent un environnement hostile pour l'application de la vélocimétrie laser : accès optique limité au travers de petits hublot plans (ou courbes, d'où des problèmes de propagation des rayons lumineux) et par la géométrie parfois complexe d'aubes vrillées ;

• les deux montages optiques de vélocimétrie laser (à franges : LDA, LDV ; deux points : LTA, L2F) doivent être considérés comme complémentaires ; les vélocimètres à franges analysent très bien des écoulements tridimensionnels très turbulents, mais loin des parois que les faisceaux laser heurtent normalement et nécessitent de larges accès optiques. Les vélocimètres deux points ont un meilleur rapport signal sur bruit en présence de forte lumière parasite et mesurent des vitesses très près des parois, mais dans des écoulements dont le taux de turbulence n'excède guère 10 % ;

• les particules servant de traceurs de l'écoulement doivent être générées d'une manière abondante, avec une granulométrie submicronique, loin en amont du point de mesure pour minimiser les perturbations de la canne d'ensemencement. D'une manière générale, les aérosols effectivement utilisés dans le volume de mesure sont mal connus et leur génération reste empirique et constitue un cas d'espèce pour chaque application ;

• l'utilisation de calculateurs performants et travaillant en temps réel est fondamentale pour réduire les temps d'essais et diagnostiquer tout problème de mesure. Une représentation graphique soignée des résultats (éventuellement en perspective) est très importante pour bien comprendre et interpréter les phénomènes complexes existant dans des machines tournantes, surtout celles à multi-étages.

Pour le futur, même si la vélocimétrie deux points est bien adaptée et bien que son extension à la mesure non simultanée de trois composantes soit en cours de développement, les trois sujets suivants semblent devoir mériter des efforts de recherches importants :

• l'ensemencement des écoulements (propriétés de diffusion des aérosols, mode de génération, calibration, etc...) ;

• l'utilisation de fibres optiques (pour rendre les systèmes plus compacts auprès des machines) ;

• le traitement du signal en vélocimétrie à franges par une analyse spectrale des signaux numérisés en sortie des photomultiplicateurs : cette technique doit conduire à un rapport signal sur bruit équivalent à celui d'un vélocimètre deux points près d'une paroi, mais avec tous les avantages de la vélocimétrie à franges pour sonder les écoulements turbulents.

1. INTRODUCTION

Ce rapport essaye de dégager les idées importantes, parfois nouvelles, de chaque exposé, afin que le lecteur puisse accéder plus rapidement à l'information précise qu'il recherche.

Certains textes sont plus orientés vers la vélocimétrie à franges, d'autres vers la vélocimétrie à barrières optiques (2 points, 2 traits) ; mais la comparaison des mérites respectifs des deux techniques est donnée selon différents aspects dans plusieurs papiers. Il en est de même pour l'ensemencement de l'écoulement, pour lequel des idées sont à prendre dans chaque communication, en plus de l'exposé général de A. Melling.

Après cette analyse texte par texte, les conclusions essentielles sont rassemblées et des recommandations pour des recherches futures sont exprimées.

2. INFORMATIONS IMPORTANTES CONTENUES DANS LES DIFFERENTS PAPIERS

2.1 Papier n°6 - Laser fringe anemometry for aero engine components
                 A. Strazisar - NASA Lewis (USA)

   - Un bref rappel de principe de la vélocimétrie à franges est donné : mesure d'une composante, puis de deux, quelques montages tridimensionnels (simultanés ou non). Les formules donnant le degré de confiance dans les valeurs moyennes de vitesse et de taux de turbulence permettent d'estimer le nombre de mesures nécessaires pour obtenir une précision voulue.

   - De nouveaux types de vélocimètres à barrières optiques, remédiant à la faible cadence d'acquisition de données des vélocimètres 2 points (surtout en écoulement turbulent) sont cités en références 8

et 18 (travaux ONERA et NASA Lewis sur des vélocimètres 2 traits ou 2 traits dédoublés).

- La quantité de particules nécessaires à une cadence d'acquisition élevée est calculée et montre la nécessité d'un ensemencement local en amont du volume de mesure ; l'intérêt des particules fluorescentes (Rhodamine 6G dans de l'alcool) utilisées en liaison avec un vélocimètre à franges est expliqué.

- Les différentes causes de difficultés de mesure dans les turbomachines (et éventuellement leurs remèdes) sont décrites : lumière parasite due à des parois proches du volume de mesure, géométrie complexe d'aubes vrillées, glaces de veine plates (mais de petites dimensions) ou courbes (mais déplacement du volume de mesure et modification de sa géométrie théorique). Des références sont données sur des travaux en cours étudiant le trajet des rayons lumineux à travers des hublots de forme complexe et les systèmes compensateurs envisagés (Ref. 20 et 21). Des méthodes pour nettoyer les hublots sans arrêter la machine sont indiquées.

- Une étude détaillée des différentes manières d'acquérir et de traiter les mesures de vitesse, au niveau d'un rotor muni de N aubes, avec un volume de mesure fixe, est fournie ; selon les possibilités du calculateur, certaines informations sont perdues : une hiérarchie est même établie. La meilleure façon de procéder consiste à dater tous les événements et à les replacer a posteriori selon leur date à la position où ils ont été acquis relativement aux aubes. Néanmoins un contrôle en temps réel du nombre de mesures acquises non seulement globalement, mais par classes, est important pour éviter un manque total d'informations à certains endroits de la roue.
La représentation graphique tridimensionnelle des résultats aide à la compréhension des phénomènes mesurés : certains diagrammes sont ainsi présentés, mais beaucoup d'efforts doivent être effectués dans ce domaine.

- Des mesures de turbulence plus fines devront être mises en oeuvre à l'avenir pour séparer les fluctuations aléatoires de vitesse des structures cohérentes. D'autre part, le développement de méthodes optiques permettant de corréler vitesse, densité, pression ou température est vivement souhaité.

2.2 Papier n°7 - Laser two-focus velocimetry
R. Schodl - DFVLR (Allemagne)

- De longs développements mathématiques ont pour but de justifier un traitement des données plus rapide et plus simple pour obtenir la vitesse moyenne ; mais avec cette procédure, les informations sur la turbulence sont tronquées.

- Il est clairement mis en évidence qu'un vélocimètre 2 points est limité à l'étude d'écoulements de turbulence locale inférieure à 10 % car la probabilité de mesure décroît très rapidement ; la réduction de l'intervalle entre les 2 points permet de mesurer des taux de turbulence plus élevés (15 à 20 %) mais au détriment d'une aggravation de l'incertitude de mesure.

- La distance minimale d'une paroi pour obtenir des mesures varie entre 0,1 et 1 mm (ou plus), essentiellement en fonction des possibilités d'ensemencement (et aussi du taux de turbulence).

- Un vélocimètre 2 points capable de mesurer la composante de vitesse selon la direction de propagation des faisceaux laser est clairement décrit ; ce vélocimètre tridimensionnel n'effectue en aucun cas des mesures simultanées ; sa précision de mesure, ainsi que l'exploitation des résultats en vue de mesures de turbulence, demandent encore de longues études.

- Une étude comparative vélocimètre à franges-vélocimètre 2 points est présentée en se basant sur la géométrie des volumes de mesure respectifs des 2 types de vélocimètres ; les résultats essentiels sont :

• les plus petites particules détectables en rétrodiffusion avec un vélocimètre 2 points sont de 0.15 µm environ. Ces résultats ne doivent toutefois être considérés que comme des ordres de grandeur car la taille minimale détectable dépend énormément des caractéristiques de l'optique réceptrice, y compris le photomultiplicateur et le système de traitement du signal ;

• avec le même ensemencement, la cadence d'acquisition d'un vélocimètre à franges atteint 10 kHz contre 500 Hz seulement en moyenne pour un vélocimètre 2 points.

- En référence 73 est décrit un vélocimètre 2 points, chaque point étant dédoublé avec des polarisations orthogonales : cette disposition optique améliore la précision avec laquelle est estimé le maximum de chaque impulsion due au passage d'une particule dans un point.

2.3 Papier n° 8 - Seeding gas flows for laser anemometry. A. Melling, Cranfield Institute of Technology (Angleterre)

- Les lois du mouvement et du traînage des particules sont rappelées.

- Une revue des différents modes de génération des aérosols est fournie : atomiseurs d'huiles, cyclones, lits fluidisés et autres pour particules solides.
Les particules liquides sont généralement sphériques, ce qui n'est absolument pas le cas des particules solides qui se présentent sous forme d'agglomérats polydispersés.

- La mesure de la taille des particules reste un problème difficile ; les différentes méthodes couramment employées sont décrites : microphotographie après prélèvement, réponse à un choc, diffraction, diffusion de Mie, absorption ; mesure de la visibilité des franges ; mesure de déphasages de signaux Doppler recueillis selon différentes directions d'observation.
Le résultat des mesures est toujours la corrélation de la distribution réelle par la probabilité de pouvoir détecter une taille donnée par l'appareillage ; il reste toujours très délicat de qualifier des aérosols submicroniques.

2.4 Papier n° 9 - Comment choisir un vélocimètre laser pour une application donnée ? A. Boutier, ONERA
(France)

- Le rappel de principe des 4 configurations optiques possibles pour des vélocimètres interféren-
tiels conduit, après analyse des inconvénients des nombreux montages optiques possibles pour un véloci-
mètre bi- ou tri-dimensionnel, à la description du vélocimètre tridimensionnel à trois couleurs opéra-
tionnel en soufflerie.

- Une étude détaillée sur les sources d'imprécision dans les mesures avec un vélocimère tridimen-
sionnel mène aux conclusions suivantes :

● l'étalonnage précis et rapide avec un théodolite informatisé donne en une 1/2 heure les inter-
franges des 3 composantes à 1 % près et la matrice de passage des composantes mesurées à un ré-
férentiel lié à la soufflerie, ainsi que divers angles utilesà l'expérimentateur avec une préci-
sion de 0,1° ;

● les angles entre composantes mesurées doivent être les plus grands possibles (voisins de 90° et
au moins 60°) afin de minimiser l'incertitude sur la vitesse moyenne (l'emploi de mélangeurs
électroniques étant peu recommandé car nécessitant des filtrages) et surtout afin de réduire
l'importance de "particules virtuelles" dans la détermination du tenseur de Reynolds ;

● pour obtenir des aérosols submicroniques, il est recommandé de vaporiser des huiles diluées dans
des solvants (alcool, trichloréthylène) et surtout des billes de latex calibrées. Vers les hau-
tes températures (2700 K maximum), une poudre de ZrO_2 fournit une granulométrie polydispersée
inférieure à 1 µm, alors qu'Al_2O_3 donne systématiquement des agglomérats de 2 ou 3 µm.

- L'utilisation de fibres optiques en vélocimétrie laser est en plein essor. Actuellement existent
des têtes optiques de vélocimètres à franges monodimensionnels de la grandeur d'un crayon, mais visant
à 50 mm en rétrodiffusion axiale et n'admettant que des puissances laser limitées (1 W environ).

- Une étude comparative du rapport signal sur bruit lors de l'approche de parois a été menée sur 3
configurations optiques de vélocimètre laser : franges, 2 points, 2 traits ; le vélocimètre 2 traits
apparaît comme une solution de compromis.

- Un tableau synoptique des capacités essentielles des différents types de vélocimètres laser per-
met de choisir le vélocimètre le plus approprié au besoin expérimental.

- Beaucoup d'espoir doit être fondé sur le traitement du signal par analyse spectrale des signaux
numérisés en sortie du photomultiplicateur, car cela donne une valeur du rapport signal sur bruit voi-
sine de celle d'un vélocimètre 2 points, tout en gardant les possibilités de mesure en écoulement très
turbulent (zones de recirculation, etc...) d'un vélocimètre à franges.

2.5 Papier n° 10 - Application of Doppler and transit laser anemometry in small turbomachines. R.L.
Elder, C.P. Forster, M.E. Gill - Cranfield Institute of Technology (Angleterre)

- Des mesures ont été effectuées dans des compresseurs axiaux et centrifuges avec un matériel
Malvern, essentiellement utilisé dans sa version vélocimètre à franges, avec traitement du signal par
corrélateur de photons. Les écoulements analysés sont particulièrement instables.

- Le corrélateur de photons actuel est assez mal adapté pour mesurer des vitesses élevées.

- Pour les températures inférieures à 200°C des aérosols à base d'huile conviennent comme tra-
ceurs ; à température plus élevée, TiO_2 initialement sous forme d'une poudre de 0,2 µm, s'agglomère car
naturellement hygroscopique.

- Les hublots étaient démontés toutes les 40 minutes ; il ne faut pas déposer sur les hublots des
couches anti-reflets car elles se dégradent très rapidement et diffusent les faisceaux laser. Une bonne
solution consiste à déposer un film d'huile au début des essais pour éviter le dépôt de gouttes d'huile
individuelles perturbant les faisceaux laser.

- La validité des résultats est assurée en effectuant des comparaisons avec d'autres mesures, no-
tamment en prenant comme critère le débit massique : même si certains écarts apparaissent, ces compa-
raisons donnent confiance dans les mesures.

2.6 Papier n° 11 - Laser velocimetry study of stator-rotor interactions in a multi-stage gas turbine
compressor. M.C. Williams - Pratt and Whitney (USA)

- Un vélocimètre à franges monodimensionnel (bientôt transformé en bidimensionnel), fonctionnant
en rétrodiffusion axiale, a été mis en oeuvre avec succès sur un compresseur multi-étages aux niveaux
suivants : 6ème stator-7ème rotor, 9ème stator-10ème rotor (surtout) et 13ème stator-14ème rotor. La
particularité du vélocimètre est d'avoir bien isolé la partie réception de tous les reflets parasites
possibles dus à la partie émission, et de travailler avec une très grande ouverture : diamètre de 80 mm
de l'optique collectrice, avec une occultation centrale de 54 mm et une distance de visée de 183 mm.
Des mesures ont été faites sur des particules d'huile jusqu'à 1,5 mm du moyeu; les composantes sont me-
surées à + et - 28° par rapport à la direction principale de l'écoulement, sans cellules de Bragg ; cet
angle inférieur à 45° a été choisi pour diminuer les risques de biais angulaire.

- Si le DOP donne de bonnes particules au niveau 9ème stator-10ème rotor, il n'en est plus de même
au niveau 13ème stator-14ème rotor, car les températures et pression y sont plus élevées. Un mélange de
DOP et de ZrO_2 ne s'est guère avéré satisfaisant ; de plus le hublot se salit très vite.

- L'acquisition de données est beaucoup plus rapide qu'avec un vélocimètre 2 points : une dizaine
de minutes contre 2 h pour la même accumulation d'informations.

- La représentation des histogrammes de vitesse pour une position angulaire de la roue peut mettre en évidence des oscillations périodiques quand l'histogramme est bi-modal.

- Une analyse spectrale par transformée de Fourier des fluctuations du module et de l'angle de la vitesse avec la position angulaire par rapport à la machine montre que plusieurs rotors contribuent aux flucutations enregistrées localement. A partir de cette idée, des traitements de données plus élaborés sont proposés, qui conduisent à une meilleure compréhension de l'écoulement dans une machine aussi complexe.

2.7 Papier n° 12 - Evaluation of L2F measurements in unsteady turbine flow. W. Forster, R. Schodl, H. Kruse - DFVLR (Allemagne)

Les écoulements sont souvent périodiquement instables dans les turbomachines (argument bien développé dans le papier). Le vélocimètre 2 points a donc sondé l'écoulement entre les aubes du rotor, ainsi que légèrement en amont et en aval.

Pendant tous les essais, à une position radiale et axiale, le volume de mesure est fixe ; pour une position des aubes du rotor, la mise en oeuvre de la fonction "multi-fenêtres" du système d'acquisition de données du vélocimètre 2 points permet de connaître l'évolution du champ de vitesse entre 2 aubes du rotor (16 fenêtres) ; puis les aubes du stator sont tournées et une autre série d'essais est reprise (6 positions successives du stator sont ainsi analysées). Ensuite le volume de mesure est déplacé radialement, puis axialement, à différentes positions, avec toujours la même procédure d'acquisition de données. Ces essais permettent de visualiser la déformation des distributions spatiales d'énergie turbulente en fonction du temps dans un canal inter-aube du rotor (film présenté lors du congrès).

Cette application met bien en évidence toutes les possibilités de la vélocimétrie 2 points, en liaison avec un système informatique élaboré.

2.8 Papier n° 13 - Combined fringe and Fabry-Perot laser anemometer for three component velocity measurements in turbine stator cascade facility. R.G. Seasholtz, L.J. Goldman. NASA Lewis (USA)

Un vélocimètre tridimensionnel non simultané a été construit avec, comme objectif, la possibilité de n'utiliser qu'un petit hublot comme accès optique.

Les composantes axiales et transverses sont mesurées successivement avec un vélocimètre à franges (fonctionnant sur des particules fluorescentes) et la composante radiale est obtenue par analyse spectrale avec un Fabry-Pérot des décalages Doppler existant dans la lumière diffusée par les faisceaux laser du vélocimètre à franges. Toutes les caractéristiques techniques, ainsi que les sources d'élargissement instrumental sont bien détaillées. Les parois ne peuvent être approchées à moins de 3 mm ; il faut accumuler les données pendant 20 s environ, avec un fort ensemencement, pour obtenir un résultat alors que le vélocimètre à franges les obtient en moins d'une seconde). Des précautions anti-vibratoires sont nécessaires autour du système optique, notamment pour garder une fréquence laser bien stable.

Il ne s'agit de mesurer que des vitesses moyennes, avec une précision de l'ordre de 1 % et de 1° sur l'orientation.

La mesure de faibles vitesses radiales est délicate, car la raie due à la rotation du moyeu est très intense : la vitesse radiale est obtenue par différence entre les spectres obtenus avec et sans ensemencement.

La possibilité d'utiliser un tel moyen d'essai en turbomachine doit être retenue (bien que ne permettant pas des acquisitions rapides), mais dans toute autre application bénéficiant d'un accès optique plus confortable ce n'est sûrement pas la méthode optimale.

2.9 Papier n° 14 - Velocity and temperature measurements in a can-type gas-turbine combustor. A.F. Bicen, M.V. Heitor, J.H. Whitelaw - Imperial College, Londres (Angleterre)

Dans une chambre de combustion fonctionnant au propane, un vélocimètre laser à franges monodimensionnel (diffusion avant, ensemencement avec des particules d'Al_2O_3 de 1 µm environ) et un thermocouple de 40 µm de diamètre (en Rhodium-platine) ont été mis en oeuvre pour connaître l'importance du rapport air-combustible (AFR) sur les cartes de vitesse et température moyennes et les cartes des fluctuations de ces mêmes quantités.

Une analyse des erreurs statistiques possibles en vélocimétrie laser fait surtout apparaître la nécessité de corriger les fluctuations de vitesse du biais de gradient de vitesse moyenne. Les erreurs sur les mesures de température sont évaluées à 7 %.

L'effet du AFR est faible dans la première partie de la chambre de combustion, mais s'accroît en aval. Les intensités maximales de turbulence (vitesse ou température) sont de l'ordre de 13 %.

2.10 Papier n° 15 - The flow arround a squared obstacle. D.F.G. Durao, M.V. Heitor, J.C.F. Pereira. Instituto Superior Tecnico, Lisbonne (Portugal)

Le papier a été présenté par le professeur Nina et n'a fait l'objet d'aucune question, les auteurs n'ét t pas présents.

Les mesures sont effectuées avec un vélocimètre laser monodimensionnel (source laser He-Ne 15 mW) dans un tunnel hydrodynamique (V ≃ 0,68 m/s) avec un système de comptage fabriqué à l'Institut mais sans avantage particulier par rapport aux compteurs du commerce.

L'analyse spectrale des fluctuations de vitesse, en aval de l'obstacle, fait apparaître une variation linéaire de la position de la fréquence principale avec le nombre de Reynolds (fréquence comprise entre 4,7 et 0,7 Hz pour des nombres de Reynolds entre 14000 et 2200). Le nombre de Strouhal est par contre quasi constant et égal à 0,13.

3. CONCLUSIONS

Les turbomachines constituent un environnement hostile pour utiliser la vélocimétrie laser ; les problèmes essentiels proviennent d'un accès optique difficile au point de mesure, dû à la géométrie de la machine :
- on ne peut installer que de petits hublots plans,
- sinon, avec des hublots courbes (cylindriques) se pose le problème du trajet des rayons lumineux (en cours d'étude),
- géométrie des aubes vrillées.

De plus, les écoulements étant confinés dans des canaux très étroits, la lumière parasite due aux impacts des faiceaux laser sur les parois (moyeu, aube, hublot) est généralement intense.

Deux techniques de vélocimétrie laser ont été largement décrites, avec leurs avantages et inconvénients respectifs : la vélocimétrie à franges et la vélocimétrie 2 points. Ces deux techniques ne doivent pas être mises en concurrence, mais être considérées comme complémentaires.

La vélocimétrie 2 points semble actuellement la plus appropriée pour obtenir des mesures près des parois que les faisceaux laser heurtent perpendiculairement en raison des propriétés suivantes : sensibilité à de très petites particules (jusqu'à 0,2 µm en rétrodiffusion), meilleur rapport signal sur bruit. Des résultats de mesures très élaborés sont obtenus notamment au DFVLR grâce à un traitement du signal optimisé pour accélérer la cadence d'acquisition de données. Enfin, un prototype de vélocimètre 2 points tridimensionnel est en cours d'étude. Une cartographie complète d'un canal interaube dure environ 2 heures. Cette technique de vélocimètre 2 points devient difficilement applicable dès que le taux de turbulence excède 10 % car la probabilité de mesure diminue et si on change la géométrie du volume (réduction de la distance entre points) c'est l'incertitude de mesure qui augmente.

La vélocimétrie à franges doit donc être utilisée quand le rapport signal sur bruit en présence de lumière parasite le permet, car elle constitue un outil très performant pour le sondage des écoulements très turbulents. En aérodynamique, les trois composantes du vecteur vitesse instantanée sont mesurées simultanément, mais cela nécessite pour des mesures précises de larges hublots car les angles entre composantes mesurées doivent être grands (d'où la difficulté de mise en oeuvre en turbomachines). Chez Pratt et Whitney un vélocimètre monodimensionnel (qui sera bientôt bidimensionnel) est mis en oeuvre avec succès dans des machines multi-étages (grâce à un montage optique particulier). A NASA Lewis, des particules fluorescentes sont utilisées pour s'affranchir de la lumière parasite due aux parois (mesure monodimensionnelle) ; il y a été construit aussi un vélocimètre tridimensionnel : il mesure successivement les composantes axiale et tangentielle par un vélocimètre à franges et la vitesse radiale est obtenue par analyse spectrale avec un Fabry-Pérot de la lumière diffusée par les faisceaux laser du vélocimètres à franges ; cette technique ne permet pas d'approcher les parois à moins de 3 mm et nécessite un fort ensemencement, ainsi que des précautions antivibratoires.

Il est important de souligner les deux points suivants apparus lors des conférences et des discussions :
- nécessité d'un traitement de données en temps réel et de représentations graphiques élaborées (visualisation des résultats en perspective tridimensionnelle) pour bien comprendre et interpréter les résultats,
- importance de l'ensemencement en particules "connues" ; généralement ce sont des huiles ou des particules réfractaires qui sont utilisées comme traceurs de l'écoulement. A l'ensemencement de l'écoulement est lié le problème de nettoyage des hublots (parfois automatique, mais technique non généralisable).

4. RECOMMANDATIONS POUR L'AVENIR

Trois axes de recherches importants doivent être particulièrement soutenus :
- Amélioration de l'ensemencement et de la connaissance de la granulométrie des aérosols utilisés au niveau même du volume de mesure du vélocimètre. Une solution proposée consiste à essayer de généraliser l'emploi de billes de latex calibrées ; les difficultés actuelles proviennent de leur mode de génération et de leur coût.
- Utilisation de fibres optiques pour miniaturiser les équipements proches de la machine.
- Développement de nouvelles techniques de traitement du signal en vélocimétrie à franges (numérisation du signal issu du photomultiplicateur, puis traitement par analyse spectrale numérique dans le calculateur) qui doivent théoriquement conduire à un rapport signal sur bruit équivalent à celui des vélocimètres 2 points près des parois, mais avec tous les avantages de la vélocimétrie à franges en écoulement turbulent.

LASER FRINGE ANEMOMETRY FOR AERO ENGINE COMPONENTS

Anthony J. Strazisar
National Aeronautics and Space Administration
Lewis Research Center
Cleveland, Ohio 44135

ABSTRACT

Advances in flow measurement techniques in turbomachinery continue to be paced by the need to obtain detailed data for use in validating numerical predictions of the flowfield and for use in the development of empirical models for those flow features which cannot be readily modelled numerically. The use of laser anemometry in turbomachinery research has grown over the last 14 yr in response to these needs. Based on past applications and current developments, this paper reviews the key issues which are involved when considering the application of laser anemometry to the measurement of turbomachinery flowfields. Aspects of laser fringe anemometer optical design which are applicable to turbomachinery research are briefly reviewed. Application problems which are common to both laser fringe anemometry (LFA) and laser transit anemometry (LTA) such as seed particle injection, optical access to the flowfield, and measurement of rotor rotational position are covered. The efficiency of various data acquisition schemes is analyzed and issues related to data integrity and error estimation are addressed. Real-time data analysis techniques aimed at capturing flow physics in real time are discussed. Finally, data reduction and analysis techniques are discussed and illustrated using examples taken from several LFA turbomachinery applications.

INTRODUCTION

The first application of laser anemometry to the measurement of turbomachinery flow fields was reported by Wisler and Mosey in 1972 (Ref. 1). In the following 14 yr the quality and quantity of data generated by laser anemometer applications in turbomachinery has continued to increase due to advances in optics, electronics, and computer hardware. This data has been used to improve our understanding of the flow physical phenomena in turbomachinery and to validate numerical flow analysis schemes.

Until recent years laser anemometer investigations in turbomachinery have dealt with isolated rotors since flow analysis techniques have until recently been confined to the steady, axisymmetric flow regime which exists in the rotor relative reference frame for isolated rotor configurations. However, several recent experiments have involved the use of laser anemometry in studies of the periodically unsteady flow within the blade rows in single stage machines and between the blade rows in multistage machines.

The application of laser fringe anemometry to measurements in turbomachinery environments is reviewed in this paper. Example results are limited to axial-flow type compressor blading since most laser fringe anemometer experiments have involved flow surveys in fans and compressors rather than turbines. Although radial-type turbomachinery has been surveyed using laser anemometry, the majority of these applications have involved laser transit anemometry due to the generally superior ability of the LTA to make measurements in the narrow exit channels of centrifugal impellers. A recent review of published results obtained in centrifugal compressors has been given by Krain (Ref. 2). Additional LTA applications will be covered in detail in this symposium by Schodl and Elder (Refs. 3 and 4).

FUNDAMENTALS OF LASER FRINGE ANEMOMETRY

Basic Operating Principles

The operating principles of laser fringe anemometers will be briefly reviewed below. In an LFA the laser output beam is divided into two equal power beams which are focussed to a common point in space which is referred to as the measurement or probe volume. The crossing of the beams in the probe volume results in constructive and destructive interference between the train of laser light waves contained in each beam. This interference creates bright planes of light created by constructive interference separated by dark planes caused by destructive interference as shown in Fig. 1. The fringe planes are perpendicular to the plane which contains the laser beams and are parallel to the beam bisector. As shown in Fig. 1 the spacing between bright fringe planes is $s = \lambda/(2 \sin K)$. A particle which crosses the probe volume scatters light at the fringe crossing frequency, f_c. Note that the fringe crossing frequency is determined solely by the component of particle velocity U_x, which is perpendicular to the fringe planes. The U_y and U_z components carry the particle parallel to the fringe planes and do not therefore contribute to the fringe crossing frequency. Also note that while a rotation of the plane containing the laser beams about the beam bisector can be used to measure velocity components in directions between the x- and y-direction, the line of sight velocity component U_z cannot be measured.

Figure 1 illustrates three features which make laser anemometry (or LA) attractive compared to other velocity measurement techniques:

(1) The system output, i.e., the doppler or fringe-crossing frequency, is linearly related to the velocity

(2) The technique is not subject to drift since the proportionality between f_c and U_x is given by the laser light wavelength, λ, and beam crossing angle, K, both of which are constant in time

(3) The technique is only sensitive to one component of velocity

Since each of the incident laser beams is circular in cross-section, the actual probe volume shape is an ellipsoid as shown in Fig. 2. The light intensity distribution across each beam is Gaussian in shape. The beam diameter, $d_{\bar{e}}^2$, defined as the diameter at which the intensity is $1/e^2$ of the peak intensity at the center of the beam, is typically used as a measure of the beam diameter. Using this definition of beam diameter, the probe volume diameter, d_m, and length l_m defined by the $1/e^2$ intensity level can be calculated as shown in Fig. 2. Note that the ratio of probe volume length-to-diameter is given by $L/d = 1/\tan(K)$. Since the beam crossing angle K is usually between 2 and 10°, the value of L/d is on the order of 10 to 20.

Another feature of Gaussian laser beams which impacts laser anemometer optical performance is that of beam divergence which is illustrated in Fig. 3. The two important properties of the beam geometry shown in this figure are:

(1) the laser light wave front radius $R(z)$ is infinite only at the location of the beam waist, $z = 0$

(2) the output beam waist diameter $d_{\bar{e}}^2$ is related to the input beam waist diameter $D_{\bar{e}}^2$ through the formula $d_{\bar{e}}^2 = 4\lambda f/\pi D_{\bar{e}}^2$.

The first beam divergence property implies that the probe volume fringes will not be parallel to one another unless the incident laser beams cross at the beam waist. If the fringe planes are not parallel, false levels of flow fluctuation will be indicated since particles of equal velocity which pass through different parts of the probe volume will generate different fringe crossing frequencies due to the variation in fringe spacing across the probe volume. A laser light collimator or mode matching lenses (see Ref. 5) can be used to insure that the beam waist will be located at the probe volume location.

The second beam divergence property shown in Fig. 3 implies that the probe volume size can be controlled through control of the incident laser beam diameter $D_{\bar{e}}^2$. Beam expanders can be used to increase the beam diameter $D_{\bar{e}}^2$, which in turn reduces the beam diameter at the probe volume, $d_{\bar{e}}^2$. From the relations shown in Figs. 2 and 3 we see that expanding the beam diameter $D_{\bar{e}}^2$ while holding the beam separation d constant results in a reduction in probe volume size and in the number of fringes in the probe volume. This results in an increase in the power density in each fringe. This in turn will result in more photons being scattered from a given particle size or in the ability to generate the same number of scattered photons from smaller size particles.

Optical Design Considerations

The successful design of an LA optical system represents a trade-off between several conflicting factors. This issue can best be addressed by considering an illustrative example.

The minimum variance which one may expect in a single velocity measurement has been shown in Ref. 6 to be

$$\sigma_m^2 = \frac{8}{\sqrt{\pi}} \frac{h \cdot c}{n \cdot \lambda \cdot \sigma_s \cdot \Omega} \frac{\Gamma_0}{P^2} \frac{V^3 W_0^3}{N^2 + \frac{18}{\pi^2}}$$

c   velocity of light
h   Planck's constant
N   number of fringes
P   laser power
V   velocity
W_0 probe volume radius
n   PMT quantum efficiency
Γ_0 background light flux
σ_s particle light-scattering cross-section
Ω solid angle of collection optics

This relation indicates that the measurement accuracy is enhanced by:

(1) reducing flare light and probe volume size

(2) increasing the collection optics solid angle, the laser power, and the number of fringes in the probe volume.

Flare light can be reduced by using antireflective coatings on window surfaces and by optically masking the collection optics. The solid angle of the collection optics can be increased by using large aperture (i.e., small f-number) lenses. However, the lens diameter and price increase for a given focal length as the f-number decreases and lens imperfections become harder to correct.

The probe volume size can be reduced by increasing $D_{\bar{e}}^2$ while the number of fringes in the probe volume can be increased by increasing the beam crossing angle K. However, one may reach a point at which there are not enough fringes in the probe volume or the fringe spacing is too small. Referring to Fig. 2, consider the following example: $d = 22$ mm, $D_{\bar{e}}^2 = 1$ mm, $f = 200$ mm. These parameters yield a probe volume diameter of $d_m = 131$ μm containing 23 fringes with a fringe spacing of $S = 4.68$ μm. Commercially available counter-type signal processors can accurately measure fringe crossing frequencies up to 100 MHz, but start to yield less accurate results for higher frequencies. The velocity which corresponds to a fringe crossing frequency of $f_c = 100$ MHz is therefore a relevant parameter to consider and is equal to $V = f_c \cdot S = 468$ M/sec for the present case. Increasing the input beam diameter $D_{\bar{e}}^2$ by a factor of 2 would reduce the probe volume diameter to 65 μm but would also reduce the number of fringes in

the probe volume to 14. This is close to the eight fringes required by most counters and can lead to angle biassing errors if Bragg shifting is not used. The number of fringes in the probe volume could be increased back to the original value of 28 by doubling the input beam spacing, d. However, this would change the fringe spacing to $S = 2.35$ μm and would decrease the velocity which corresponds to a fringe crossing frequency of 100 Mhz to $V = 235$ M/sec.

Measurement of Multiple Velocity Components

There are many optical configurations which can be constructed for measuring one, two, and three velocity components simultaneously. Reference 7 contains a rather complete description of several one-, two-, and three-component configurations as well as a comparison of the relative merits of the various configurations. This issue will be further addressed in this symposium by Boutier (Ref. 8) and will therefore be only briefly addressed below.

In turbomachinery flowfields the streamwise and circumferential components of velocity V_z and V_θ respectively, are usually much larger in magnitude than the velocity component in the hub-to-shroud direction, V_r. In addition, the radial velocity component generally lies along the optical axis of the LA system and therefore cannot be measured directly. Most LA applications to date have therefore been aimed at measuring the V_z and V_θ velocity components. Increasing emphasis on secondary flow studies is currently generating applications which require measurement of the V_r velocity component as well.

The simplest method of measuring velocity magnitude and flow angle is to acquire measurements with a one-component LA system at two different fringe orientations. Use of a one-component LA system results in two limitations. First, the statistical error in velocity, V, and flow angle, α, measured with a single-component system is greater than that resulting from a two-component system as will be described in the next section. Second, the magnitude of the turbulence components V_z' and V_θ' can only be determined if measurements are taken in the z- and θ-coordinate directions or if measurements are made at three different fringe orientations. If measurements are acquired at two arbitrary fringe orientations, one can only determine upper bounds on V_z' and V_θ'. Despite these limitations single channel LA systems have been used extensively in turbomachinery applications. The advantages of a single channel system are its simplicity and the fact that the available laser power is concentrated into a single fringe system.

Two-component LA systems can be implemented by using two colors to create two separate measurement channels. Measurement channels can also be generated by using polarization separation or by using two Bragg cells to achieve frequency separation. If signal processor logic is used to accept only those events for which a velocity measurement is simultaneously made on both channels, the statistical error in calculating V and α is reduced relative to the error obtained when using a single-component LA system and the magnitude of the turbulence components V_z', V_θ', and $V_z'V_\theta'$ will be directly measured.

Three-component LA systems can be implemented by using three colors or two colors plus frequency separation to create three measurement channels. These systems are quite complex. The accuracy with which such systems measure the radial velocity component is directly related to the off-radial beam separation angle. These systems have transmitted beams which occupy a large solid angle and which therefore require relatively large windows for optical access to the flowfield. In addition, the complex blade geometry found in most turbomachines may prevent such systems from having optical access to large areas of the flowfield.

It should be noted that one does not have to resort to a three-component LA system in order to obtain measurements of the radial velocity component. A technique in which the beams enter the flowfield from a single channel LA system are deflected from the radial direction is described in Ref. 9. This technique uses measurements obtained from two off-radial beam orientations to calculate the radial velocity component. As will be shown in the following section, the statistical error in the radial velocity component, V_r, measured by this method will be greater than if V_r were measured directly since this technique utilizes measurements made at two different times.

A second approach to the measurement of radial velocities is reported in Ref. 10. This approach utilizes the window configuration shown in Fig. 4 to enable direct direct measurement of the radial velocity component when using the window labelled P'. While this approach does not require off-radial deflection of the transmitted beams, it can only be used in regions which are upstream and downstream of the blade row.

A third approach, which can be used to obtain radial velocity component measurements within a blade row, is illustrated in the right half of Fig. 5. The transmitted beams enter the flowpath at the blade stagger angle through an optical access hole located upstream of the blade row. Scattered light is collected in an off-axis direction through a window located over the blade row. This optical arrangement provides measurements of V_r and a combination of V_z and V_θ. The separate V_z and V_θ components are determined using the conventional approach shown on the left in Fig. 5. This approach is applicable only to a single stage machine with no inlet guide vane. Application of this approach to multistage machines would require the use of fiber optics to introduce the transmitted laser beams into the flowfield.

Statistical Measurements Errors

In order to determine accurate estimates of the mean velocity and the turbulence properties of a flow, many individual LA measurements must be acquired and averaged together. The mean and standard deviation estimated from the data are subject to both systematic and statistical uncertainty. An analysis of these uncertainties is given in Refs. 11 and 12. As shown in Ref. 11, the number of measurements required to establish a given level of confidence in the mean velocity is given by

$$\frac{V_m - V}{V} = C_v = \frac{Z}{\sqrt{N}}\left(\frac{V'}{V}\right)$$

where V is the true mean velocity, V_m is the measured mean velocity, (V'/V) is the true turbulence intensity, Z is the confidence level, and N is the number of measurements used to calculate V_m. A value of $Z = 1.97$ corresponds to a 95 percent probability that the measured mean velocity lies within the range $V(1 - C_v) < V_m < V(1 + C_v)$. The expression for the confidence level for the rms velocity estimate is

$$\frac{V'_m - V'}{V'} = C_{v'} = \frac{Z}{\sqrt{2N}}$$

where V' is the true rms velocity and V'_m is the measured value. Note that the confidence intervals are inversely proportional to $\sqrt{N}$. One therefore has to increase the number of measurements by a factor of four in order to halve the confidence interval. Also, note that C_v is proportional to the turbulence intensity, V'/V, while C'_v is independent of V'/V. Since V'/V is typically on the order of 0.1 or less, a given number of measurements always yields a much better estimate of the mean than of the rms velocity. These facts are illustrated in Table I which shows the number of measurements required to establish a confidence level of 95 percent for various values of V'/V.

An important point addressed in Refs. 11 and 12 is that the statistical error in calculating velocity components increases when using uncorrelated data acquired at different fringe orientations. Data is uncorrelated in a multichannel LA system if signal processor logic is not used to enforce simultaneity of measurements from each channel. Uncorrelated data always occurs when using a single channel LA system to acquire data at multiple fringe orientations. The magnitude of the increased statistical error can be illustrated by considering how a single channel LA system is used to determine orthogonal velocity components.

Figure 6 illustrates the calculation procedure by which velocity and flow angle are obtained with a single channel system. Measurement directions 1 and 2 shown in the figure are the directions normal to the probe volume fringes. Measured velocities V_1 and V_2, acquired at the known angles θ_1 and θ_2, are used to solve for the unknown velocity magnitude, V, and flow angle α. Orthogonal velocity components V_u and V_v can then be determined from V and α. The analysis of Ref. 11 indicates that the confidence levels in V_u and V_v are given by the expressions

$$C_u = M_u \cdot \frac{Z}{\sqrt{N}} \cdot \frac{V'}{V} \qquad C_v = M_v \cdot \frac{Z}{\sqrt{N}} \cdot \frac{V'}{V}$$

M_u and M_v are multipliers which indicate the increase in statistical error over the case in which V_1 and V_2 are acquired simultaneously, i.e., $M_1 = M_2 = 1$ when V_1 and V_2 are acquired simultaneously. If we assume isotropic turbulence, the expressions for M_u and M_v in terms of the geometry of Fig. 5 are

$$M_u = \left[\frac{\sin^2\theta_1 + \sin^2\theta_2}{\sin^2(\theta_2 - \theta_1)}\right]^{1/2} \qquad M_v = \left[\frac{\cos^2\theta_1 + \cos^2\theta_2}{\sin^2(\theta_2 - \theta_1)}\right]^{1/2}$$

Figure 7 is a plot of these multipliers as a function of the mean fringe orientation angle and the magnitude of the fringe angle difference, $\theta_2 - \theta_1$. These results indicate, for example, that for the case of $\theta_1 = 10°$, $\theta_2 = 70°$, the statistical errors in determining V_u and V_v are increased by factors of 1.217 and 1.449, respectively when using data which is not simultaneously acquired. The impact of this increased statistical error must be weighed against the increased system complexity when deciding whether to use a single or multichannel LA system in a given application.

Seed Particle Considerations

The tradeoffs between seeding the entire flowfield or using a point source of seed are briefly discussed below. In addition, the properties of a unique fluorescent seed material are described. General methods used to generate and size particles and considerations related to the particle size required to accurately follow the fluctuations in a given flowfield will be addressed in detail in this symposium by Melling (Ref. 13).

When performing laser fringe anemometer measurements in a gas it is usually necessary to introduce seed particles into the flowfield for two reasons. First, the number of particles which are naturally present in atmospheric air in the 0.5 to 1.0 μm range is generally not sufficient to yield adequate data rates. Second, by generating and injecting seed particles into the flow one can control the size distribution of the scattering particles and can therefore control to some degree the accuracy with which the seed particles follow the flow.

When designing an LA experiment one must decide whether to seed the entire flowfield (full coverage) or to seed only the stream tube which passes through the measurement volume (point injection). Both methods are used in practice and the method chosen is dependent on the particle generation rate of the seeder and on the flowfield characteristics. As an example analysis of particle generation needs, let us consider an LA application which involves flowfield measurements in the turbomachinery environment summarized below:

turbomachine diameter = 1 m
hub/tip radius ratio = 0.7

through flow velocity = 200 m/sec
volume airflow rate = 80 M³/sec

The rate at which particles will cross the LA probe volume is given by

$$R = d \cdot L \cdot V \cdot c$$

where L and d are the probe volume length and diameter, c is the particle concentration in the flow, and V is the flow velocity.

Commercially available seeders are capable of maximum particle generation rates of 10^{11} particles/min. Coupling this rate with the volume flow rate of air through the machine yields a particle density of 2×10^7 particles/M³ if full coverage seeding is employed. If typical probe volume dimensions of d = 100 μm, L = 1 mm are used, we arrive at a particle rate through the probe volume of

$$R = d \ L \ V \ c = (10^{-4} \text{ m})(10^{-3} \text{ m})(200 \text{ m/sec})(2 \times 10^7/\text{m}^3) = 400 \text{ particles/sec.}$$

The actual LA data rate will be less than this number since particles which cross the probe volume outer edges usually do not scatter enough light or cross enough fringes to yield a valid velocity measurement. The conclusion to be drawn from this particular example is that point injection of seed should probably be used.

Point injection of seed is most easily accomplished through a tube placed upstream of the measurement volume as shown in Fig. 8. This tube must be placed far enough upstream to enable decay of the wake shed from the tube before the measurement point is reached. In addition, the seed injection tube is usually carried in a radial and/or circumferential actuator to enable seed injection of the stream tube which passes through the probe volume for arbitrary positions of the probe volume.

A unique seed material which has specific advantages for turbomachinery LA applications is the liquid fluorescing seed described in Ref. 14. This seed material is formed by dissolving an organic dye, rhodamine 6G, in a mixture of benzyl alcohol and ethylene glycol. When irradiated with light from the blue or green lines of an argon-ion laser, seed particles composed of this dye solution fluoresce in the orange band of the spectrum, as shown by the absorption and emission spectra shown in Fig. 9(a). By placing a narrow band orange-pass filter in the LA collection optics in front of the PMT, one can optically stop light reflected from solid surfaces at the incident light wavelength from entering the PMT. This enables one to make measurements near hub and endwall surfaces and within rotating blade rows. When not using fluorescent seed, the light reflected from solid surfaces, which is orders of magnitude higher in intensity than the light scattered by the seed particles, dominates the PMT signal as the surface is approached, i.e., the signal to noise ratio of the PMT signal drops to zero. When fluorescent seed is used, the signal to noise ratio remains constant as a solid surface is approached. In addition, since the light from the seed particles is emitted due to fluorescence rather than scattered, the Mie scattering phenomena does not apply and the intensity of light emitted by the particles is independent of direction. The penalty associated with the use of this technique is that the light-emitting efficiency of the rhodamine dye for a given size particle is generally an order of magnitude lower than the backscattering efficiency of conventional (i.e., nonfluorescing) seed particles of the same size, as shown in Fig. 9(b). In addition, both blue and green wavelengths lie in the absorption band of rhodamine as shown in Fig. 9(a). This technique therefore cannot be used with two-color LA systems.

Alternate Laser Anemometer Methods

In addition to laser fringe anemometry there are several alternate laser anemometry methods which can be used to obtain quantitative flowfield measurements in turbomachinery. These methods are Fabry-Perot interferometry; laser transit anemometry (LTA), (also referred to as the laser two focus (L2F) technique, the time-of-flight technique, and as the two-spot technique); and a hybrid method which combines features of both laser fringe and laser transit anemometers.

The LFA technique measures the frequency difference between the light scattered from each incident laser beam by a seed particle. In contrast, the Fabry-Perot technique directly measures the frequency of the scattered light by using a Fabry-Perot interferometer as a scanning optical spectrum analyzer. Development of the Fabry-Perot technique for measurements of the line-of-sight radial velocity components in a turbine cascade has been reported in Refs. 15 and 16 and will be covered in this symposium by Seasholtz (Ref. 17).

The laser transit anemometer (LTA) will be covered in detail in this symposium by Schodl (Ref. 3). The principal advantages of the LTA technique over the LFA technique are:

(1) the light intensity in the probe volume is higher than in a laser fringe anemometer which enables detection of smaller particles,

(2) the sensitive length of the measurement volume in the line-of-sight direction is much shorter than in an LFA system which enables the acquisition of measurements near solid surfaces,

(3) the LTA provides a high degree of sensitivity in flow angle measurements.

The principle disadvantage of the LTA technique is that it yields a low data rate due to the fact that the LTA measurement volume presents a much smaller "target" which a particle must hit in order to yield a velocity measurement (see Fig. 10). LTA data rates diminish rapidly as the turbulence level increases in a flowfield because the flow angle fluctuations generated by turbulence levels of 10 percent or more are large enough to prevent most particles from crossing both spots.

A hybrid technique currently under development is aimed at removing this limitation by expanding the circular LTA spots into elliptic-shaped spots. The technique represents a trade-off between power density

in the probe volume and probe volume target area. One approach to this technique is described in Ref. 18. This technique will also be discussed in this symposium by Boutier (Ref. 8).

APPLICATION OF LASER ANEMOMETRY TO MEASUREMENTS IN TURBOMACHINERY

There are three major features of the turbomachinery environment which make the application of laser anemometry more difficult in turbomachinery experiments than in external aerodynamic experiments:

(1) the close proximity of highly reflective surfaces (i.e., hub and shroud endwalls and blades),

(2) flowpath geometry (curved endwalls and complex blade shapes),

(3) the rotation of rotor blade rows.

Each of these issues will be addressed in this section. In addition, various data acquisition schemes will be compared and the advantages and limitations of each scheme will be discussed. Finally, the need to provide near real-time data reduction to support intelligent execution of experiments will be discussed.

Reflected Light Problems in Turbomachinery Applications

Two separate problems related to reflected incident light radiation arise in LFA turbomachinery applications. The first of these problems is caused by reflections from window and hub surfaces when making measurements in the flowpath inner and outer endwall regions. Reflections from the window surfaces can be reduced by using antireflection coatings on the window. Fluorescent seeding is an effective means of eliminating the problem of poor signal-to-noise ratio caused by reflection of the incident laser beams from blade and endwall surfaces.

While fluorescent seeding enables one to make measurements directly down to both the hub and shroud endwall surfaces, the proximity to a solid surface which one can achieve with nonfluorescent seeding before reflected light becomes a problem is highly dependent on the type of surface in question and on the design of the optical system. It has been the author's experience that for optical systems with beam crossing angles on the order of 5° or less employing f/4 collection optics and no special stops in the collection optics, the closest approach to a hub endwall or a window in the shroud endwall is on the order of 1 cm. For a machine with a diameter of 1 m and a hub/tip radius ratio of 0.8, a distance of 1 cm corresponds to 10 percent of the blade span.

The second source of reflected light in turbomachinery applications is "blade flash" caused by passage of the rotor blades through the incident laser beams. The severity of the blade flash problem is dependent mainly on the rotational speed of the blade row. The incident laser beams "walk" up the surface of the blade as the blade rotates through them as shown in Fig. 11. As discussed in the next section, the blades appear to be "bent" in this figure due to spanwise twist. The blade surface is in the probe volume itself for a very short time, near $t = 0$. However light can be reflected from the surface into the collection optics at any point between time $t = 0$ when the probe volume first intersects the blade surface and time $t = t_b$ when the beams are no longer blocked by the blade surface. Reflected light entering the collection optics during time $0 < t < t_b$ can cause saturation of the photomultiplier tube (PMT). If this occurs the PMT requires a finite amount of time to recover and measurements which occur during the recovery time will be lost. For rotors operating at tip speeds on the order of 400 to 500 m/sec, blade passing frequencies are on the order of 5 to 15 Khz, and time t_b is on the order of 7 to 20 µsec. However for low speed machines this time can be at least an order of magnitude greater. It has been the author's experience that reflected light from blade surfaces does not cause PMT saturation in high speed machines but can cause problems in low speed applications. Fluorescent seeding therefore appears to be necessary in high speed applications only when measurements in the proximity of the hub or shroud endwalls are desired.

Blade Geometry

One feature of turbomachinery geometry which impacts optical access to the flowfield is spanwise twist of the blading as shown in Fig. 12. This twist leads to the "bent" appearance of hub-to-tip blade sections such as AA and BB when viewed in a streamwise direction. For blades which are radially stacked about the c.g. of each section this bending is worst near the leading and trailing edges. If the incident laser beams are constrained to enter the flowpath in the radial direction, shadowed regions occur as shown in which the tip blade section prevents optical access to the hub section. The extent of the shadowed region can be as great as 20 to 30 percent of the blade pitch at the hub. This shadowing can be eliminated if the LA optical system is capable of orienting the incident laser beams away from the radial direction as shown in Fig. 12.

When acquiring measurements at design speed operating conditions, use of the blade design geometry is generally an accurate method of calculating the information required to relate the axial and circumferential measurement location to the blade surface location. However, at part speed conditions the blade geometry will vary from the design geometry due to deflections caused by reduced mechanical stresses. The principal deflection in axial-type blading is an untwist or change in the blade stagger angle as shown schematically in Fig. 13(a). The amount of untwist varies from zero at the hub to a maximum at the tip. Axial blading also experiences some axial deflection due to thrust loading. In radial-type blading the primary deflection due to mechanical stress is a "flowering" of the rotor disk, which causes a shift in the axial location near the rotor exit. These deflections can be accounted for by measuring the actual location of the rotor during data acquisition and correcting the design blade geometry as required.

The blade geometry at the tip can be measured during data acquisition by positioning the probe volume at the tip radius. If seed injection is turned off, the fringes are oriented to measure the circumferential velocity component, and the laser power is reduced, then the LA signal processor will perceive the

blades passing through the probe volume as seed particles. Since velocity measurements will only occur
over the blade tip, the blade circumferential location can be determined from the location at which mea-
surements have occurred. The sensitivity of such a procedure to changes in the blade stagger angle can
be controlled by the circumferential resolution of the LA measurements. Results obtained from an axial-
flow fan using the above procedure are presented in Fig. 13(b). As described in Ref. 19 the measurements
were acquired in a 51.3 cm diameter rotor using a resolution of 1000 measurement locations per blade
pitch. The rotor has 22 blades which yields a circumferential resolution of 0.008 mm. The measured
untwist was 1.96±0.04° compared to a finite element analysis prediction of 2.02°. These measurements also
indicated that the blade spacing around the wheel was uniform to within 2 percent.

Window Design Considerations

Optical access to wind tunnel models used in external aerodynamics experiments is usually provided
through flat windows mounted in the tunnel walls. The use of flat windows in turbomachinery applications
leads to distortions in the outer flowpath due to shroud curvature in both the circumferential and stream-
wise directions, as shown in Fig. 14 for an axial-type blade. This flowpath distortion is often greatest
in the rotor tip region and can significantly alter the local tip clearance. This problem is particularly
acute in radial turbomachinery applications, where the shroud radius of curvature is small in both the
circumferential and the streamwise direction.

Flat windows are required for laser transit anemometer applications, since the highly focussed
"spots" of a transit anemometer become highly defocussed if the window is not flat. This defocussing
reduces the power density in each spot to levels which are unuseable. Flat windows are not required for
laser fringe anemometers.

One solution to the need for flat windows in curved flowpaths is the use of many small windows, as
shown at stations 5 to 14 in Fig. 15. Such an approach is the only one practical for radial-type turbo-
machines if one desires to maintain proper tip clearances or to use laser transit anemometry. However,
as seen in Fig. 15, the use of many small flat windows limits one's ability to acquire measurements at
arbitrary streamwise locations.

For axial-flow configurations, in which streamwise radii of curvatures are relatively large, curved
windows can be easily fabricated by heating flat glass plates to the yield temperature of the glass and
forming the glass over a mold. Such windows follow both the circumferential and streamwise curvature of
the flowpath and offer unlimited access to arbitrary axial and circumferential measurement points within
the window boundary.

Refraction at the air-glass interface on window inner and outer surfaces causes the following
phenomena which impact measurement accuracy:

(1) The actual probe volume location is translated relative to the location which would have occurred
without refraction effects,

(2) The incident laser beams which generate the probe volume may uncross - i.e., the two beams will
no longer lie in the same plane,

(3) The beam crossing angle, which affects the calibration factor between fringe crossing frequency
and seed particle velocity may change.

Probe volume translation will always occur for both flat and curved windows, while changes in beam
crossing angle only occur for curved windows. Beam uncrossing occurs when the solid angle between the
incident laser beam and the window surface is not equal for each beam in a fringe anemometer. Beam
uncrossing thus generally occurs for curved windows but can occur for flat windows when the beam bisector
is not perpendicular to the window surface. If the uncrossing distance at the probe volume location is
comparable to the beam diameter, the beams will no longer intersect one another and the probe volume will
be destroyed. A change in beam crossing angle can occur only across a curved window. The crossing angle
changes when the change in surface normal orientations between the window outer and inner surfaces are not
the same for both laser beams.

The magnitude of window refraction effects is dependent on the beam crossing angle, the probe volume
immersion into the flow, the window thickness and radius of curvature, and the orientation of the incident
laser beams relative to the window. These effects have been recently studied in detail for flat and
cylindrical windows using an optical ray tracing technique which is applicable to totally general window
shapes (Ref. 20). The impact of typical values of these parameters on the uncrossing problem is shown in
Table II. The conclusion which one draws from this example is that relatively thin windows are required
when curved windows are used. We generally use a window thickness of 3 mm in our research rigs, which
have a diameter of 0.51 m.

One very promising solution to the uncrossing problem is presented in Ref. 21. The procedure
involves making an interference hologram between a reference beam and a laser beam which passes through
the window after passing through the desired measurement point as shown in Fig. 16. The hologram can then
be used to introduce an exact refraction-error correction into an incident laser beam which follows the
path of the reference beam used to create the hologram. The hologram deflects the beam onto the path
required to pass through the window and the measurement point. The technique is suitable for high laser
power levels (on the order of 2 W) due to the high transmission efficiency of the hologram. The only
disadvantage of this technique is the need to make a hologram for each different location at which one
wishes to pass through the window.

Window Cleaning

The use of seed injection into the flowfield in order to enable LA measurements can result in the
accumulation of seed particles on window inner surfaces. This deposition is due to large particles which

do not follow the flow and are therefore centrifuged out toward the shroud. In addition, turbomachinery component research rigs usually have lower quality oil seals than flight-certified engines, which can cause window contamination due to oil leakage even when seed material is not used. An effective method of removing deposits from windows is the injection of a liquid solvent into the flow through small holes located in the shroud upstream of the window. Window cleaning by this method is especially effective in the region over the rotor tip, where the liquid is scraped across the window by the rotating blades. The author has been able to wash windows in single-stage axial compressor applications for rotors with tip speeds on the order of 425 m/sec without reducing the rotor speed, which allows the operating point to remain unchanged during window washing. The use of liquids for on-line window washing may not be practical for applications in higher pressure ratio centrifugal compressors and multistage axial compressors. In such machines the flowfield temperature rise may be so high that window washing liquids would evaporate or cause high thermal stresses when they coat a hot window.

Measurement of Blade Rotational Position

A laser anemometer measurement is a random event triggered by the presence of a seed particle in the probe volume. When acquiring measurements in rotating blade rows one must therefore measure the blade row rotational position every time a velocity measurement occurs. There are four measurement methods which can be used to provide this rotational position:

(1) Enable a measurement window once-per-rotor revolution during data acquisition.

(2) Enable a measurement window once-per-blade passing during data acquisition.

(3) Enable continuous measurement windows during data acquisition.

(4) Record the time between measurements and assign measurement windows after data acquisition.

Methods (1), (3), and (4) require a once-per-rev (OPR) timing signal from the rotor while method (2) requires a once-per-blade (OPB) timing signal.

The generation of measurement windows for the first three methods is shown schematically in Fig. 17. By definition a measurement window is a time interval used to classify velocity measurements according to the rotational position at which they occurred. All velocity measurements which occur within a given window are spatially averaged across the width of the window. It is therefore advantageous to keep the measurement windows narrow. Since LA measurements are usually displayed graphically as discrete measurement points across the blade pitch, it is important to remember that each point represents a spatial average across the window width.

Implementation of methods (2) and (3) for generating measurement windows requires the ability to subdivide the time between once-per-blade (OPB) and once-per-rev (OPR) signals respectively. This requirement is met by generating pulse trains at frequencies which are integral multiples of the OPB or OPR signal frequencies. These pulses are accumulated in a counter which is initialized by each G B or OPR signal. Whenever an LA velocity measurement occurs, the current counter contents are recorded with the LA measurement as a (velocity, clock count) data word pair. The clock count is then used to determine the measurement window in which the velocity measurement occurred.

Note that a variable delay after the once-per-rev signal is needed in order to align the measurement windows with the blade passage. This effect is illustrated in Fig. 17 by delays D_1 and D_2 which are required for measurement axial locations ZM_1 and ZM_2, respectively. Successful implementation of methods (2) and (3) also requires the use of fairly high frequency pulse generators, as shown in the table below for two typical high speed compressor applications.

FREQUENCY REQUIREMENTS FOR WINDOW-GENERATING
PULSE TRAIN

[NB - number of rotor blades; BPF - blade passing frequency; NWP - number of windows per blade passage; F - pulse train frequency; WW - window width in microseconds]

Machine type	rpm	NB	BPF, Khz	NWP	F, Khz	WW
Centrifugal Main blade	36 000	?0	12	16	192	5.2
Main and splitter blade		40	24	16	384	2.6
Axial	20 000	40	13.3	50	665	1.5

Use of constant frequency pulse generators will result in changes in the number of measurement windows between OPB or OPR signals due to rotor speed variations. One must therefore use a phase-locked loop or a tracking shaft angle encoder (Ref. 22) which is capable of rapidly varying the pulse generation frequency in response to rotor speed variations. For high speed applications a digital shaft angle encoder is preferred over a phase-locked loop, since the response lag in phase-locked loops is generally too large to enable accurate tracking of rev-to-rev variations in rotor speed.

The first method listed above is the simplest, and involves enabling a measurement window after a known time delay τ has elapsed after occurrence of the OPR signal. A blade-to-blade velocity profile can be achieved by collecting measurements for various delay times τ. This method allows one to obtain measurements in different blade passages around the wheel. It is the simplest of the four methods and was

therefore used in early applications of LA to turbomachinery (see Ref. 23 for example). While it is simple to implement this method is also inefficient since the measurement window is only opened once per rotor revolution.

In method (2) a fixed number of measurement windows are generated between adjacent once-per-blade (OPB) signals. Since the OPB signals from each blade are all identical, measurements which occur within a measurement window can come from any blade passage on the wheel. This method is more efficient than method (1) since it opens a measurement window at all times. However, in order to measure the flowfield in an individual blade passage, the windows must be enabled for only the passage of interest. In this case data can only be acquired during a time corresponding to (1/NB) of each revolution, where NB is the number of blades. Reference 24 describes the use of this method in a laser transit anemometer system.

Method (3) essentially opens measurement windows at all times and assigns a unique set of measurement windows to each blade passage. This technique therefore allows maximum data acquisition efficiency when one is interested in obtaining measurements in individual blade passages. Use of this technique in a laser fringe anemometer system is described in Ref. 22.

The fourth data acquisition method is similar to the method (3) in that it assigns a unique set of measurement windows to each blade passage. This method, which is described in Ref. 25 for a two-bladed propeller, is shown schematically in Fig. 18. During data acquisition, a trigger signal is recorded once-per-rev along with the elapsed time between each LA measurement. The pitchwise location of each measurement is then determined after data acquisition is complete by using the time-between-measurement data and the triggering pulse (or OPR) data. After the pitchwise measurement location is determined, the measurement is assigned to the appropriate window. Since measurement windows are defined by the user during post-run data processing, this method allows the user the freedom of changing the width and number of the measurement windows without rerunning the experiment. In contrast to methods (1) to (3), this method also enables the user to determine the circumferential location of each LA measurement within the measurement window. This information can be used to assess the degree of spatial averaging which occurs when all measurements within a window are averaged together.

The four approaches discussed above are by no means the only methods which can be used to determine the blade row rotational position for each LA measurement. An approach which is a hybrid of the third and fourth approaches discussed above is described in Ref. 26. This method is similar to method (4) in that it determines the rotational position from the time-between-measurements and a triggering pulse. However, in this method the triggering pulses are generated by an encoder which generates up to 1000 pulses/rev (similar to method (3)), while in method (4) the triggering pulses are generated once-per-rev.

Data Acquisition Methods

The various methods of recording rotational position discussed above allow one to implement several different data acquisition methods. The method which one chooses to use is dependent on the level of information which one is trying to extract from the measured flowfield and on the level of flowfield periodicity.

Averaging Methods

The simplest data acquisition method which enables one to determine the blade-to-blade distribution of velocity and flow angle within a rotating blade row can be referred to as a "blade average" mode of data acquisition. This data acquisition method can be implemented using method (2) discussed above for recording the blade rotational position. When performing blade average data acquisition one generates measurement windows between successive once-per-blade signals. Measurements which are assigned to a given measurement window can originate from any blade passage around the rotor. When using this method one is therefore averaging together the flowfields which occur in each individual passage, and all information concerning passage-to-passage flowfield variations is lost.

A second, more complex method of acquiring data can be referred to as a "window average" mode of data acquisition. This method can be implemented using method (3) discussed above for recording the blade rotational position. All measurements which occur within a measurement window are known to originate from the particular blade passage in which the window lies. Window-average data acquisition therefore allows measurement of the blade-to-blade distribution of velocity and flow angle in individual blade passages, which in turn allows one to assess the level of passage-to-passage flowfield variations around the rotor. Although window average data acquisition provides more information than blade average methods, information concerning the distribution of the individual velocity measurements which occur within a measurement window is still lost during data acquisition. Blade and window averaging methods average together all measurements which occur within a given measurement window. As shown in Ref. 9, if one records the number of measurements, N, which occur within each window, the sum of the measured velocities, ΣV_i, $i = 1, N$, and the sum of the squares of the measured velocities, $\Sigma(V_i)^2$, then one can calculate the mean and standard deviation of the measurements which occurred within the window using the following:

$$\bar{V} = \sum_{i=1}^{N} \frac{V_i}{N}$$

$$V' = \left[\sum_{i=1}^{N} \frac{\left(\bar{V} - V_i \right)^2}{(N - 1)} \right]^{1/2} = \left[\frac{\left(\sum_{i=1}^{N} V_i^2 - N\bar{V}^2 \right)}{(N - 1)} \right]^{1/2}$$

Note that only five words of information, N, ΣV, ΣV^2, need to be recorded for each measurement window (one word for N which is an integer and two words each for ΣV and ΣV^2 which are real numbers).

In addition, the number of words stored is independent of the total number of measurements acquired during a run.

As shown in Refs. 9 and 22, the window average mode of data acquisition can be an efficient method of obtaining good blade-to-blade spatial resolution while minimizing computer storage requirements. The LA system described in these references generates 50 measurement windows across 20 consecutive blade passages. The system therefore records velocity measurements in 1000 measurement windows while using only 5000 words of computer storage. As discussed in Ref. 22 and shown in Fig. 19, the window number (referred to as "shaft position" in Ref. 22) is used as an address in a stored data array. This scheme enables efficient real-time processing and graphical display of the measured data because the data is assigned its proper place in the data array as part of the measurement process.

Data Capture Method

The most complete method of data acquisition can be referred to as a "data capture" method. In the data capture method, each individual velocity measurement which occurs within a window is individually recorded, and the velocities are not summed during data acquisition. This data acquisition mode therefore allows the user to examine the probability density distribution of the measurements which occurred within each window.

There are several advantages and disadvantages to be considered when deciding which data acquisition mode to implement. The data capture method lends itself to direct memory access (DMA) transfer of data from LA counter processors to computer core memory since all measurements are recorded without any averaging or summing. However, this method can require large amounts of computer core memory and archival storage relative to the blade and window average methods since two words of information (integer representation of measured velocity, window number) must be recorded for each measurement.

Consider for example a situation in which one wishes to record velocity measurements in 25 windows from blade-to-blade across 40 individual blade passages. In addition, assume that one wishes to record 100 measurements in each window and that the data is uniformly distributed among the windows. Window average data acquisition in this case would require (25 windows/blade) by (40 blades) by (5 data words/window), or 5000 words of storage. In contrast, data capture acquisition would require (25 windows) by (40 blades) by (100 meas./window) by (2 words/meas.), or 200 000 words of storage.

If DMA data transfer is used, sorting of velocity measurements into a data array which is addressed according to window number cannot be done in real time, but must be performed either after data acquisition is complete or in parallel with data acquisition. Implementation of real-time data display when using data capture methods therefore requires use of a multitasking computer operating system or an interruption of data acquisition for calculation of real-time displays. These issues are becoming less important as the cost of computer hardware and software capability continues to fall.

The ultimate acquisition approach would be to implement data acquisition algorithms which can automatically screen the probability density distribution acquired in each window during capture mode acquisition. If the distribution is well-behaved (i.e., nearly Gaussian), little information is lost by simply recording the distribution mean and standard deviation. The output of such an intelligent data capture method would therefore consist of probability density distributions for those measurement windows in which nonGaussian distributions were detected.

Total Number of Measurements Required

Two data acquisition issues which remain to be addressed are:

(1) how many measurement windows are required across a blade passage,

(2) how many measurements are needed to establish statistical confidence in the data.

The number of measurement windows required for accurate definition of the flowfield is dependent on the magnitude of the velocity gradients in the blade-to-blade direction. These gradients are averaged out across a measurement window during data acquisition since measurements which occur anywhere within a window are effectively assigned to the center of the window. Figure 20 shows a blade-to-blade Mach number distribution measured near the tip of a transonic fan blade in which a two-shock passage shock system is present. The measurements were acquired using 50 measurement windows across the passage. The Mach number distribution shown is the average of the distributions which exist in each of the 17 blade passages in which measurements were acquired. In Fig. 20 the second shock is clearly defined when $N_{window} = 50$. Also shown in Fig. 20 are the Mach number distributions which would result from using 25 and 12 windows across the blade pitch. Although the impact of reducing N_{window} to 25 is minimal, a value of N_{window} of 12 leads to an almost total smearing of the second shock and does not show the Mach number increase near the pressure surface. Note that method (4) discussed in the previous section concerning measurement of blade rotational position allows one to refine window resolution during post processing of the data. The other methods of measuring blade position require the user to fix the window resolution during the measurement process.

As discussed in the section on statistical measurement errors above, the number of measurements required to establish a given level of statistical confidence in the mean velocity, V, is related to the turbulence intensity. The number of measurements required as a function of turbulence intensity was summarized in Table I for various values of turbulence intensity at the 95 percent confidence level.

While a turbulence level of 5 percent is not uncommon in the core flow regions of turbomachinery blade flowfields, the turbulence intensity level within wakes can rise as high as 20 percent. If one desires to establish a 1 percent confidence interval in the mean velocity in a flow with a 5 percent turbulence level, then 100 measurements are required for each window. Acquisition of data across 1000 win-

dows would therefore require a total number of 100 000 measurements to achieve the desired accuracy in each window if the number of measurements were uniformly distributed across all of the measurement windows. In reality the measurements are not uniformly distributed, as shown in Fig. 21 which shows the distribution of the number of measurements which occurred during the measurement of the Mach number distribution previously shown in Fig. 20. One is therefore left with one of two choices:

(1) Collect data until the desired number of measurements are achieved in each window.

(2) Collect the desired total number of measurements and accept an increase in statistical error in those windows which have less than the desired number of measurements.

For typical applications, in which the time for data acquisition is of concern, the second choice is more practical than the first.

On-Line Data Monitoring

The use of on-line data reduction and display can greatly increase the effective use of an LA system in any application even if the data acquisition process is not totally automated. On-line feedback from the measurement process can indicate the presence of poor quality data and can also be used to ensure the capture of relevant flow features.

Figure 22, adapted from Ref. 22, shows one possible real-time display. This display is generated during a data acquisition process which uses 50 windows per blade passage across 20 blade passages. The display is updated every 10 to 15 sec during a run and is based on the data acquired up to that point in the run. The actual real-time display is shown in the center of Fig. 22 and is composed of the upper and lower plots shown in the figure. The upper plot is a plot of the velocity profile averaged across a blade pitch, i.e., it is calculated by averaging together measurements made in all of the individual blade passages. The blade suction surface is on the left side of the plot and the blade itself appears as the cross-hatched region on the right side of the plot. The lower plot in Fig. 22 is a bar graph which shows the number of measurements acquired in each of the 1000 measurement windows. The 20 gaps in the plot are caused by the 20 blades since no measurements are acquired as the blade passes through the incident laser beams. The accumulation of dirt and fluorescent seed material on the surface of the ninth blade passage is causing a large number of measurements due to light scattering from the blade surface.

While a real-time data display can be used to assess the quality of the data at individual survey locations, a rapid analysis of survey results is needed to ensure the capture of relevant global flow features. Use of on-line data analysis can reveal important data points which may have been missed during a survey. These data points can then be acquired while the research rig is still operating under the same conditions during which the survey was performed. An example of a case in which such a procedure would be useful is shown in Fig. 23 for a test run in which the objective is to map out the shock location in a transonic compressor rotor. The plot shown in the figure is a streamwise plot of relative Mach number created by plotting data acquired from several axial locations along line S-S during a flowfield survey. Results from the initial survey, shown on the left, indicate that the front passage shock lies somewhere between 10 and 20 percent chord and that the rear passage shock lies somewhere between 30 and 40 percent chord. If such a plot is available during the research run, the LA operator can make additional surveys in these regions in order to more accurately determine the shock location. The results of such additional surveys, shown on the right in Fig. 23, indicate that the actual front passage shock location is at 15 percent chord.

Sophisticated data acquisition methods which feature automated data acquisition and on-line data analysis require relatively sophisticated minicomputers for successful implementation. Use of 32-bit minicomputers with multitasking operating systems enables large data preparation, data acquisition, and data reduction programs to be core-resident at the same time, enables sharing of data between such programs, and enables concurrent execution of such programs. Large minicomputers also provide the speed required to implement on-line analysis of data acquired in a "data capture" mode. This analysis can provide on-line indication of flow features such as shock unsteadiness and wake vortex streets. Use of 16-bit minicomputers requires that large data acquisition programs be subdivided and "overlayed" in memory due to core storage addressing limitations. The slower execution speed of these smaller computers also limits the researcher to the use of the more efficient averaging methods of data acquisition discussed above which are not capable of resolving certain flow features. Successful LA measurements can also be acquired in turbomachines using 8-bit microcomputers. The type of hardware and software required between these two extremes depends on the level of information and the amount of information which one wishes to extract from the LA measurements.

ANALYSIS OF TURBOMACHINERY FLOWFIELDS USING LASER ANEMOMETER MEASUREMENTS

A number of different data acquisition methods of varying levels of complexity were discussed above. It was shown that data acquisition schemes can be simplified by employing some level of data averaging during the measurement process. However, such averaging prevents the extraction of certain levels of information from the flowfield. In this section an analogous situation will be shown to exist for both data analysis and graphical data display methods. A variety of methods will be presented and illustrated using examples from published results on laser anemometer applications to turbomachinery experiments.

The Hierarchy of Information Obtainable from LA Data

The process of analyzing LA data can be schematically represented by the informational pyramid shown in Fig. 24. The greatest amount of information is at the base of the pyramid. Successive application of averaging operators leads one to the peak of the pyramid. However, detailed information on flow features is lost as one moves to higher levels of the pyramid.

When performing an analysis of the variance in LA measurements acquired from flowfields generated within rotating turbomachinery one must be mindful of the periodicity present in the flowfield. In sta-

tionary, ergodic flows, one usually equates the level of measurement variance with the level of random flow fluctuations due to turbulence. As will be shown below, there is at least one contribution to the measurement variance which is not related to turbulence at each level of the pyramid.

The principles discussed above will be illustrated by analyzing an actual LA data set. This data set was acquired one-half chord downstream of an axial flow fan with a one-component LA system using 50 measurement windows between each blade. Measurements were recorded in 17 of the 22 fan blade passages. The total number of measurements recorded was 30 000, which yielded an average of about 40 measurements in each window. The velocity component measured is that which is in the streamwise direction outside of the blade wakes.

Analysis of Measurement Mean and Variance

The base of the informational pyramid contains the individual velocity measurements acquired in a capture mode of data acquisition. This data can be visualized as a two dimensional array $V(i,j)$. The measurement window number, i, ranges between 1 and $NW = NWP*NB$, where NW is the total number of measurement windows, NWP is the number of windows per blade passage, and NB is the number of blade passages surveyed. In the example data set being used here, $NW = 50$, $NB = 17$ and $NWP = 850$. The index j ranges between 1 and $N(i)$, the total number of measurements in window number i. As shown in Fig. 25, this data can be presented in the form of a velocity probability density distribution (p.d.d.) for each measurement window by classifying the $N(i)$ velocity measurements into velocity bins of fixed width. Although p.d.d.'s can be generated for each measurement window, there are not enough measurements in an individual window in this data set to given an accurate description of the bimodal character of the p.d.d.'s which lie in the blade wake (point A). The p.d.d.'s shown in Fig. 25 therefore contain measurements acquired within the measurement windows located at points A and B in all 17 measured blade passages, and are therefore "blade average" p.d.d.'s. As shown in Ref. 27, the bimodal character of the p.d.d. at point A indicates that a vortex street is present in the blade wake.

Time averaging of the data acquired in each window leads to the second level of the informational pyramid, which contains the time-average circumferential velocity distribution between individual rotor blades, $\overline{V}(i)$. This velocity distribution can be directly acquired using a "window average" data acquisition technique or can be calculated from capture mode data using the averaging operation

$$\overline{V}(i) = \frac{1}{N(i)} \sum_{j=1}^{N(i)} V(i,j) \quad i = 1,\ldots, NW \tag{1}$$

Note that $\overline{V}(i)$ is the statistical mean of the probability density distribution of the measurements from window number i.

The time-averaging operation also allows one to calculate the standard deviation, $\sigma_r(i)$, of the probability density distribution in window number i. This standard deviation is the lowest level of rms velocity information available (see Fig. 24) and can be calculated using the formula

$$\sigma_r^2(i) = \frac{1}{N(i) - 1} \sum_{j=1}^{N(i)} [\overline{V}(i) - V(i,j)]^2 \quad i=1,\ldots,NW \tag{2}$$

Once the data is time-averaged, detailed information concerning the p.d.d. of the individual measurements which occurred in the measurement window is lost. However, the general level of broadening in the p.d.d. is indicated by the magnitude of $\sigma_r(i)$. In addition, information on passage-to-passage variation in the flowfield is still present in the data. Examples of the circumferential velocity distribution given by Equation (1) are shown in Fig. 26 across 2 of the 17 measured passages. The flags at selected points indicate the magnitude of the standard deviation σ_r. Note that the standard deviation rises in the wake as one would expect due to viscous mixing. However, the standard deviation alone does not indicate the vortical nature of the wake flow as inferred by the p.d.d. shown in Fig. 25. This information, which was contained in the p.d.d.'s has been lost due to averaging.

Now let us consider the factors which contribute to the variance σ_r. In a steady, laminar flow, all measurements in a probability density distribution would fall into the same velocity bin. In reality, the p.d.d. is broadened by the following mechanisms:

(1) Random turbulent fluctuations in the flow,

(2) Flow unsteadiness which occurs at frequencies which are not integral multiples of the rotor rotational frequency (such as rotor shock oscillations and trailing edge vortex shedding),

(3) Averaging of velocity gradients across the width of the measurement window,

(4) Flow variations caused by rotor speed drift during data acquisition,

(5) Individual LA measurement errors.

The contributions of items (2) to (5) must be subtracted from the standard deviation $\sigma_r(i)$ calculated from the p.d.d. in order to obtain the level of turbulent flow fluctuations. The LA user can control or can estimate the magnitude of some of the elements in items (2) to (5) above.

The contribution of item (3) can be minimized by reducing the physical size of the measurement window. The contribution of item (5) can be controlled by selecting the fringe orientation angles and the number of measurements so as to minimize the statistical measurement error. Individual LA measurement

errors arising from particle tracking errors can be minimized by generating uniformly small seed parti-
cles. As discussed in Ref. 9, the combined contributions of items (3) and (4) are on the order of 1 to 2
percent for a practical application.

Application of a spatial ensemble averaging process to the circumferential velocity distribution
$\bar{V}(1)$ leads to the third level of the informational pyramid, which contains the ensemble-averaged velocity
distribution $\tilde{V}(k)$. The ensemble averaging operation is given by

$$\tilde{V}(k) = \frac{1}{NB} \sum_{m=0}^{NB-1} \bar{V}(k + m \cdot NWP) \quad k=1,\ldots,NWP \tag{3}$$

This ensemble averaged velocity distribution can be directly acquired using a "blade average" data
acquisition technique in which NWP windows are generated between successive blade passing signals. The
$\tilde{V}(k)$ velocity distribution contains information on the circumferential variation in the flowfield across
an "average" blade passage. Detailed information on the variation of the flowfield between individual
blade passages is lost. This information is lumped into the standard deviation $\sigma_g(k)$ at each point
in the ensemble-averaged velocity distribution, given by

$$\sigma_g^2(k) = \frac{1}{NB - 1} \sum_{m=0}^{NB-1} [\tilde{V}(k) - \bar{V}(k + m \cdot NWP)]^2 \quad k=1,\ldots,NWP \tag{4}$$

Fig. 27 is an illustration of the ensemble-averaged velocity distribution calculated from the example
data set by averaging across the 17 measured blade passages. The flags shown on selected points indicate
the magnitude of the rms velocity σ_g.

This rms velocity arises from passage-to-passage flow variations. This geometric contribution to rms
velocity fluctuations can be seen in Fig. 28, where the individual velocity distributions across the 17
measured blade passages are plotted to the same scale.

The fourth level of the informational pyramid contains the pitchwise-averaged velocity $\bar{\bar{V}}$. This
velocity can be obtained from the spatially ensemble-averaged velocity using the averaging operation

$$\bar{\bar{V}} = \frac{1}{NWP} \sum_{k=1}^{NWP} \tilde{V}(k) \tag{5}$$

The standard deviation of $\bar{\bar{V}}$ is calculated using

$$\sigma_p^2 = \frac{1}{NWP - 1} \sum_{k=1}^{NWP} [\bar{\bar{V}} - \tilde{V}(k)]^2 \tag{6}$$

The values of $\bar{\bar{V}}$ and σ_p calculated from the ensemble-averaged velocity distribution are included
in Fig. 27. This information can be directly acquired by a simple LA system which contains no capability
for measuring rotational position of moving blade rows. All details concerning the blade-to-blade flow-
field are lost at this level of averaging. Data of this type is of interest when comparing LA measure-
ments to those obtained with aerodynamic instrumentation such as total and static pressure probes and
thermocouples whose frequency response is well below the blade passing frequency. The time-average
velocity at the measurement point is also used when measuring the steady state flowfield in stationary
blade rows.

At the top of the informational pyramid, the variance in the pitchwise-average velocity, σ_t, con-
tains contributions from all lower levels of the pyramid. Several authors (Refs. 28 to 30) have addressed
this issue in the past using a model similar to that shown in Fig. 29. These investigators have shown
that the total rms velocity at the measurement point, σ_t, is related to the random fluctuation level and
the periodic fluctuation level σ_p by the relation

$$\sigma_t^2 = \sigma_r^2 + \sigma_p^2$$

These investigators have assumed that the flowfield is the same in each blade passage. If however,
there are flowfield variations from passage-to-passage, such that the velocity distribution $\bar{V}(1)$ in each
passage is not identical to the ensemble-averaged distribution $\tilde{V}(k)$, an additional contribution σ_g
must be included:

$$\sigma_t^2 = \sigma_r^2 + \sigma_p^2 + \sigma_g^2$$

It should be noted that calculation of the ensemble-averaged profile, $\tilde{V}(k)$, can be performed directly
from the individual velocity measurement array $V(1,j)$. It should also be noted that the pitchwise-
averaged velocity, $\bar{\bar{V}}$, is identical to the arithmetic average of all measurements in the $V(1,j)$ array.
The calculation of $\tilde{V}(k)$ in terms of $\bar{V}(1)$ shown in equation (3) and the calculation of $\bar{\bar{V}}$ in terms of
$\tilde{V}(k)$ shown in equation (5) was done in order to more clearly show how information is lost during each
averaging operation. The following formulas can be used for direct calculation of $\tilde{V}(k)$ and $\bar{\bar{V}}$:

$$\tilde{V}(k) = \frac{\left[\sum_{m=0}^{NB-1} \sum_{i=1}^{N(k+m \cdot NWP)} V(k + m \cdot NWP, j)\right]}{\left[\sum_{m=0}^{NB-1} N(k + m \cdot NWP)\right]} \quad k=1,\ldots,NWP$$

$$\bar{V} = \frac{\left[\sum\limits_{i=1}^{NW} \sum\limits_{j=1}^{N(i)} V(i,j)\right]}{\left[\sum\limits_{i=1}^{NW} N(i)\right]} \qquad NW = NWP.NB$$

Care must be taken when computing all of the averages discussed above, since the velocity is a vector which has both magnitude and direction. This point can be seen more clearly by considering the averaging of the two vectors shown in the diagram below:
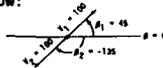
The actual average velocity obtained by vector addition is of course zero. However, if one averages the velocity magnitude and angle separately one gets

$$V_{av} = \frac{(V_1 + V_2)}{2} = 100$$

$$\beta_{av} = \frac{(\beta_1 + \beta_2)}{2} = \frac{(45 - 135)}{2} = -45$$

which is incorrect.

The proper method of calculating average values of any velocity triangle parameter is to average the primary velocity components V_x and V_y first, and then calculate the desired quantity. In the above illustration this would lead to

$$(V_x)_{av} = \frac{(V_{x1} + V_{x2})}{2} = \frac{(71.7 - 71.7)}{2} = 0$$

$$(V_y)_{av} = \frac{(V_{y1} + V_{y2})}{2} = \frac{(71.7 - 71.7)}{2} = 0$$

The proper method of calculating the ensemble-averaged flow angle, $\beta(k)$, for example is therefore:

$$\tilde{V}_z(k) = \sum\limits_{m=0}^{NB-1} \bar{V}_z(k+m.NWP) \qquad \tilde{V}_\theta(k) = \frac{1}{NB} \sum\limits_{m=0}^{NB-1} \bar{V}_\theta(k+m.NWP) \qquad k=1,\ldots,NWP$$

$$\tilde{\beta}(k) = ARCTAN\left[\frac{\tilde{V}_\theta(k)}{\tilde{V}_z(k)}\right] \qquad k=1,\ldots,NWP$$

This same procedure applies to other velocity triangle parameters such as relative and absolute velocity magnitude and relative flow angle.

The preceding discussion indicates that the level of information which one wishes to extract from the flowfield can be used to determine both the type of data acquisition method used and the level of averaging employed during data post-processing. Although information is lost through averaging as one proceeds up the pyramid shown in Fig. 24, substantial savings in data acquisition time, data processing time, and data storage space can be realized at the upper pyramid levels. For example, let NR be the number of measurements required to describe the velocity to a certain level of confidence at each point in the circumferential velocity distribution $\bar{V}(i)$. In keeping with the example used above, let the total number of windows be NW=850, corresponding to 50 windows per blade across 17 blades. The total number of measurements required is therefore NT=NR*NW = 850*NR. If, however, one is only interested in the ensemble averaged velocity $\tilde{V}$ or the time average velocity $\bar{V}$, then the same level of confidence requires only 50*NR and NR measurements respectively.

Continuing with the above example, one cannot hope to assimilate all of the information contained in the p.d.d.'s for each of the 850 measurement windows. Consideration of the circumferential velocity distribution, $\bar{V}(i)$ across 17 blade passages at each axial, radial survey location within the blade row can also be quite tedious. Therefore, in practice one usually resorts to detailed consideration of one of the following:

    (1) The distribution of $\bar{V}(i)$ across a few individual blade passages if passage-to-passage flow variations are large.

    (2) The distribution of $\tilde{V}(k)$ across the ensemble-averaged blade passage if passage-to-passage flow variations are small.

Graphical Methods of Data Presentation

Several different methods of presenting the data accumulated along the circumferential measurement line swept through a rotating blade row at one axial, radial survey location have been presented in the preceding sections. Additional graphical methods are required when attempting to visualize global flow features.

Shock wave locations in transonic blade rows can be determined from a series of blade-to-blade plots of data acquired at different streamwise locations. An independent determination of shock location can also be achieved by streamwise cross-plotting of data obtained at a constant pitchwise distance. These combined procedures are illustrated in Fig. 30. Although the seed particle velocity may lag the gas velocity for a short distance downstream of the shock, the point at which the measured velocity first begins to decrease provides a consistent measure of the shock front location.

In contrast to the one-dimensional slices through the flowfield offered by blade-to-blade and stream-wise plots, contour plots offer the user a two-dimensional view of the flowfield. An example of a contour plot of the Mach number distribution in a transonic axial-flow fan is shown in Fig. 31. Contour plots are often used when comparing LA measurements to results generated by numerical flow analysis codes.

Changes in the magnitude of a flow parameter are more easily discerned from one-dimensional plots such as those in Fig. 30 than from contour plots. This is due to the fact that one must visually inte-grate across contour lines to determine magnitude changes when viewing contour plots. As a result, contour plots tend to be more qualitative than quantitative. This situation can be improved by three-dimensional plotting which adds parameter magnitude to contour plots as a third dimension. The use of varying viewing angles, perspective, and hidden line techniques can greatly enhance the information obtainable from three-dimensional plots, as shown by the examples in Fig. 32. The valley-like features ahead of the blade row represent the Mach number variation caused by bow waves from adjacent blades. The passage shock location is clearly shown in the lower part of Fig. 32.

Example Results from LA Applications in Turbomachinery

Published results from LA investigations will be briefly reviewed below in order to demonstrate the capabilities of the LA technique. The examples will be limited to axial-type turbomachines. A more com-plete list of examples from axial-flow turbomachinery experiments is given in Ref. 31. An excellent sum-mary of LA applications in radial-type machines has recently been given by Krain (Ref. 2). In addition, results obtained in radial-flow turbomachinery will be discussed in this symposium by Schodl and Elder (Refs. 3 and 4).

Passage-To-Passage Flow Variations

An ideal turbomachine would produce an identical flowfield in each blade passage in the blade row. However, manufacturing tolerances limit the degree to which real machines approach this ideal goal. Passage-to-passage flow variations measured in two transonic fan rotors are shown in Fig. 33 in the form of blade-to-blade distributions of relative Mach number in individual blade passages. The blade suction and pressure surfaces are denoted by SS and PS, respectively. The results shown in Fig. 33(a) were obtained in a 550 m/sec tip speed fan with an aspect ratio of 2.87 which had a part-span damper. The results shown in Fig. 33(b) were obtained in an undampered 1.56 aspect ratio fan with a tip speed of 429 m/sec. The Mach number distributions shown in Fig. 33(a) for blade passages 1 and 15 encompass the range of those measured in each of the 38 individual blade passages. Note that the flowfield in passage 15 is representative of an oblique shock while the flowfield in passage 1 indicates the presence of a normal shock. Analysis of data from additional fans has led to the conclusion that the large variations shown in the dampered fan flowfields arise due to variations in blade geometry caused by manufacturing variations in the dampers. Another feature which appears in Fig. 33 is the improved flowfield uniformity at the near stall operating condition shown in Fig. 33(b). This phenomena has also been observed in data from other LA experiments and appears to be a general behavior of transonic fans. Large passage-to-passage flowfield variations have two important impacts:

(1) They generate an increased level of apparent turbulence to downstream blade rows as represented by the rms velocity σ_g discussed in the previous section.

(2) They make numerical flowfield analysis difficult because there is no single blade passage in which the flow can be considered to be representative of the flow throughout the blade row.

Unsteady Flow Features in Isolated Rotors

The capture mode of data acquisition allows detection of flow fluctuations with frequencies which are not integral orders of the once-per-rev frequency. One example of this capability is the detection of vortices in the blade wake as inferred from the double-peaked probability density distribution shown in Fig. 25. Another example of this capability is shown in Fig. 34, which is taken from Ref. 19. The bimodal nature of the probability density functions shown in Fig. 34 indicates an oscillation of the rotor passage shock about the mean location shown in the upper part of the figure. The bimodal p.d.d.'s obtained in windows C and D are due to the fact that these windows lie upstream of the shock part of the time and downstream of the shock part of the time.

Blade Row Interactions

The unsteady flow features just discussed occurred in isolated rotors where the flowfield should nominally be axisymmetric and steady in the rotor relative frame of reference. When a rotor is followed by a stator, the flowfield is unsteady and nonaxisymmetric in both the relative and absolute frames of reference. An investigation of the periodically unsteady flow through a stationary blade row therefore requires a circumferential survey across one blade pitch in the stationary blade row. The array of survey locations used during the experiment reported in Ref. 32 to investigate the flow through a stator located downstream of a compressor rotor is shown in Fig. 35. Note that a total of 128 survey points were used in order to survey the flow at 15 axial locations, which represents an eightfold increase in the number of survey locations which would have been required if the flow was axisymmetric. Data acquired at each pitchwise location must still be tagged with the rotor rotational position. By plotting the velocities measured at each axial and circumferential location for a given rotor rotational position one obtains a snapshot of the periodically unsteady flow through the stator. Figure 36 illustrates this procedure for three different pitchwise locations of the rotor relative to the stator. Turbulence intensity is chosen

as the plotted parameter in this case in order to clearly define the rotor wake location. The rotor wake is sheared as it convects through the stator passage due to the fact that the velocity is higher on the suction side of the passage than on the pressure side of the passage. A similar analysis of turbine vane wakes passing through a turbine rotor has been reported in Refs. 30 and 33.

The above investigations were performed in single stage machines. Measurements acquired within a multistage axial flow compressor using the laser transit technique have been reported in Ref. 34. The application of the LFA technique to a high speed multistage axial compressor will be discussed in this Symposium by Williams (Ref. 35).

CONCLUDING REMARKS

During the last 14 years laser anemometry has been shown to be a viable technique for obtaining detailed internal flow measurements from within the hostile turbomachinery environment. Advances in optics, electronics, and computer technology during this time have led to the availability of commercial, off-the-shelf laser fringe and laser-transit anemometer systems for use in turbomachinery investigations. Future advancements in LA applications will therefore depend on improvements in the following areas:

(1) The efficient acquisition, analysis, and display of the large amount of data which can be produced during LA applications,

(2) Measurement of the radial velocity component which usually lies in the line-of-sight direction of the LA system,

(3) Acquisition and analysis of data from within multistage turbomachines,

(4) Use of flow visualization techniques such as holography and trace gas injection to scope global flow features in order to reduce the number of physical locations at which LA measurements must be acquired,

(5) Accurate measurement of turbulent and periodically unsteady flow fluctuations in turbomachinery in order to accurately assess the relative importance of random and coherent fluctuations,

(6) development of optical techniques for measurement of thermodynamic properties which can be used in conjunction with the LA technique to yield simultaneous measurement of velocity and density, pressure, or temperature.

REFERENCES

1. Wisler, D.C., and Mossey, P.W., "Gas Velocity Measurements Within a Compressor Rotor Passage Using the Laser Doppler Velocimeter," ASME Paper No. 72-WA/GT-2, (1972).

2. Krain, H., "Experimental Observation of the Flow in Impellers and Diffusers," Von Karman Lecture Series No. 7, 1984.

3. Schodl, R., "Laser Two Focus Velocimetry," AGARD CP-399, Advanced Instrumentation for Aero Engine Components, 1986.

4. Elder, R.L., Forster, C.P., and Gill, M.E., "Application of Doppler and Transit Anemometry in Small Turbomachines," AGARD CP-399, Advanced Intrumentation for Aero Engine Components, 19-23, 1986.

5. Seasholtz, R.G., "Laser Doppler Velocimeter System for Turbine Stator Cascade Studies and Analysis of Statistical Biasing Errors," NASA TN D-8297, 1977.

6. Lading, L., "The Time of Flight vs the LDA," Proceedings of the Third International Workshop on Laser Velocimetry, Purdue University, 1978.

7. Boutier, A., D'Humieres, Ch., and Soulevant, D., "Three Dimensional Laser Velocimetry: A Review," Second International Symposium on Applications of Laser Anemometry to Fluid Mechanics, Lisbon, Portugal, July 1984.

8. Boutier, A., "How to Choose a Laser Velocimeter for a Given Application," AGARD CP-399, Advanced Instrumentation for Aero Engine Components, 1986.

9. Strazisar, A.J., and Powell, J.A., "Laser Anemometer Measurements in a Transonic Axial Flow Compressor Rotor," ASME Journal of Engineering for Power, Vol. 103, No. 2 April 1981, pp. 430-437.

10. Larguier, R., "Experimental Analysis Methods for Unsteady FLows in Turbomachines," ASME Journal of Engineering for Power, Vol. 103, April 1981, pp. 415-421.

11. Reinath, M.S., Orloff, K.L., and Snyder, P.S., "A Laser velocimeter System for Large-Scale Aerodynamic Testing," NASA TM-84393, January, 1984.

12. Orloff, K.L., and Snyder, P.K., "Laser Doppler Anemometer Measurements Using Nonorthogonal Velocity Components: Error Estimates," Applied Optics, Vol. 21, January 1982, pp. 339-344.

13. Melling, A., "Seeding Gas Flows for Laser Anemometry," AGARD CP-399, Advanced Instrumentation for Aero Engine Components, 1986.

14. Stevenson, W.H., dos Santos, R., and Mettler, S.C., "Fringe Mode Fluorescence Velocimetry," AGARD CP-193, May 1976, pp. 21.1-21.9.

15. Seasholtz, R.G., and Goldman, L.J., "Three Component Velocity Measurements Using Fabry-Perot Interferometer," Second International Symposium on Applications of Laser Anemometry to Fluid Mechanics, Lisbon, Portugal, July 1984, (NASA TM-83692).

16. Seasholtz, R.G., and Goldman, L.J., "Laser Anemometer Using a Fabry-Perot Interferometer for Measuring Mean Velocity and Turbulence Intensity Along the Optical Axis in Turbomachinery," Engineering Applications of Laser Velocimetry, ASME Book No. H00230.

17. Seasholtz, R.G., and Goldman, L.J., "Combined Fringe and Fabry-Perot Laser Anemometer for Three Component Velocity Measurements in a Turbine Stator Cascade Facility," AGARD CP-399, Advanced Instrumen- tation for Aero Engine Components, 1986.

18. Wernet, M.P., and Edwards, R.V., "Implementation of a New Type of Time-of-Flight Laser Anemometer," Applied Optics, Vol. 25, No. 5, March 1986, pp. 644-648.

19. Strazisar, A.J., "Investigation of Flow Phenomena in a Transonic Fan Rotor Using Laser Anemometry," ASME Journal of Engineering for Power, Vol. 103, No. 2, April 1981, pp. 43-437.

20. Owen, A.K., "A Parametric Study of the Beam Refraction Problems Across Laser Anemometer Windows," Third International Symposium on the Application of Laser Anemometry to Fluid Mechanics, Lisbon, Portugal, July 7-9, 1986.

21. Schock, H.J., Case, S., and Konicek, L., "Window Aberration Correction in Laser Velocimetry Using Multifaceted Holographic Optical Elements," Applied Optics, Vol. 23, No. 5, march 1984, pp. 752-756.

22. Powell, J.A., Strazisar, A.J., and Seasholtz, R.G., "Efficient Laser Anemometer for Intra-Rotor Flow Mapping in Turbomachinery," ASME Journal of Engineering for Power, vol. 103, No. 2, April 1981, pp. 424-429.

23. Walker, D.A., Williams, M.C., and House, R.D., "Intrablade Velocity Measurements in a Transonic Fan Utilizing a Laser Doppler Velocimeter," Minnesota Symposium on Laser Anemometry, University of Minnesota, Minneapolis, October 22-24, 1975.

24. Schodl, R., "A Laser-Two-Focus (L2F) Velocimeter for Automatic Flow Vector Measurements in the Rotat- ing Components of Turbomachines," ASME Journal of Fluids Engineering, Vol. 102, December 1980, pp. 412-419.

25. Lepicovsky, J., and Bell, W.A., "Aerodynamic Measurements About a Rotating Propeller with a Laser Velocimeter," AIAA Journal of Aircraft, Vol. 24, No. 4, April 1984, pp. 264-271.

26. Fraser, S.M., and Carey, C., "Two-Dimensional Laser Doppler Anemometer Measurements in an Axial Flow Fan," presented at the International Symposium on Applications of Laser-Doppler Anemometry to Fluid Mechanics, Lisbon, Portugal, July 5-7, 1982.

27. Hathaway, M.D., Gertz, J., Strazisar, A.J., and Epstein, A.H., "Rotor Wake Characteristics of a Tran- sonic Axial Flow Fan," AIAA Paper 85-1133, 1985 (to be published in the AIAA Journal, 1986).

28. Evans, R.L., "Turbulence and Unsteadiness Measurements Downstream of a Moving Blade Row," ASME Paper No. 74-GT-73 (1975).

29. Joslyn, H.D., Dring, R.P., and Sharma, O.P., "Unsteady Three-Dimensional Turbine Aerodynamics," ASME Journal of Engineering for Power, Vol. 105, No. 2, April 1983, pp. 322-331.

30. Binder, A., Forster, W., Kruse, H., and Rogge, H., "An Experimental Investigation Into the Effect of Wakes on the Unsteady Turbine Rotor Flow," ASME Paper No. 84-GT-178 (1984).

31. Strazisar, A.J., "Application of Laser Anemometry to Turbomachinery Flowfield Measurements, Von Karman Lecture Series No. 3, 1985.

32. Dunker, R.J., "Flow Measurements in the Stator Row of a Single-State Transonic Axial-Flow Compressor with Controlled Diffusion Stator Blades," AGARD CP-351, Viscous Effects in Turbomachines, June 1983.

33. Binder, A., "Turbulence Production Due to Secondary Vortex Cutting in a Turbine Rotor," ASME Paper No. 85-GT-193.

34. Ding, K., "Flow Measurements Using a Laser-Two-Focus Anemometer in a High Speed Centrifugal and a Multistage Axial Compressor," Engineering Applications of Laser Velocimetry, ASME Book NO. H00230.

35. Williams, C., "Laser Velocimetry Study of a Stator-Rotor Interaction in a Multistage Gas Turbine Com- pressor," AGARD CP-399, Advanced Instrumentation for Aero Engine Components, 1986.

Gary Skoch for acquiring and analyzing data. In addition, Carl Williams, Dick Schodl, Tony Smart, David Hobbs, and David C. Prince Jr. have provided many insights over the years into the acquisition and analysis of laser-transit and laser-fringe anemometer data in turbomachinery.

TABLE I. - NUMBER OF MEASURE-
MENTS REQUIRED FOR 95 PERCENT
CONFIDENCE LEVEL IN MEASURED
MEAN VELOCITY AND TURBULENCE
INTENSITY

[N_V = number of measurements
required for 95 percent con-
fidence that the measured
mean velocity is within C_V
percent of the true mean
velocity; $N_{V'}$ = number of
of measurements required for
95 percent confidence that
the measured turbulence
intensity is within $C_{V'}$
percent of the turbulence
intensity; V'/V = turbu-
lence intensity.]

Mean Velocity Estimate

Desired accuracy, C_V, percent	Turbulence level, V'/V, percent			
	1	5	10	20
0.5	16	400	1600	6400
1.0	4	100	400	1600
2.0	1	25	100	400
5.0	--	4	16	64
10.0	--	1	4	16

Turbulence Intensity
Estimate

Desired accuracy, $C_{V'}$, percent	Number of measure- ments, $N_{V'}$
0.5	80 000
1.0	20 000
2.0	5 000
5.0	800
10.0	200

TABLE II. - LASER FRINGE ANEMOMETER BEAM REFRACTION EFFECTS ACROSS
A CYLINDRICAL WINDOW

Window thickness, in.	Beam orientation angle, δ degrees	Beam crossing angle at the probe volume, degrees	Radial shift in p.v. loca- tion, ΔR in.	Beam uncrossing distance		
				Microns	No. of fringes	Percent of probe volume diameter
probe volume radius = 9.5 in.						
0.125	0	1.400	0.043	0	0	0
	45	1.403	.040	2.94	.28	2.4
.250	0	1.400	.086	0	0	0
	45	1.405	.080	6.63	.63	5.3
probe volume radius = 5.0 in.						
0.125	0	1.4000	0.043	0	0	0
	45	1.4015	.027	19.7	1.87	15.8
.250	0	1.4000	.086	0	0	0
	45	1.4025	.053	39.6	3.76	31.7

$$2 \cdot S \cdot \mathrm{SIN}\,\kappa = \lambda$$

$$S = \frac{\lambda}{2 \cdot \mathrm{SIN}\,\kappa}$$

$$f_c = \frac{u_x}{S} = \frac{2\,u_x\,\mathrm{SIN}\,\kappa}{\lambda}$$
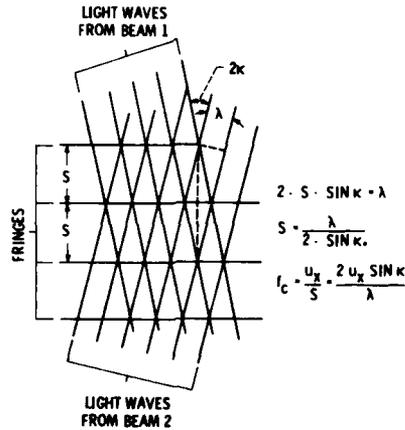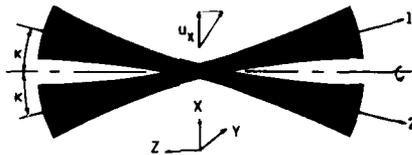
Figure 1. - Fringe model of a laser anemometer.

$d_m \cdot d_e \sim 2/\cos \kappa$

$\ell_m \cdot d_e \sim 2/\sin \kappa$

$V \sim \pi d_e^3 \sim 2/(6 \cos \kappa \sin \kappa)$

$N_{FR} \sim \dfrac{d_m}{d_f} \sim \dfrac{1.27\,d}{D_e\,-2}$
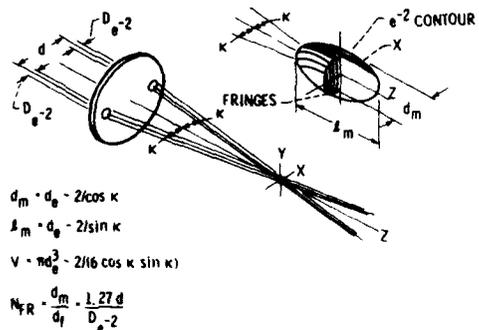
Figure 2. - Geometry of a laser fringe anemometer.

$d_e\,-2 \cdot 4\lambda/\pi D_e\,-2$
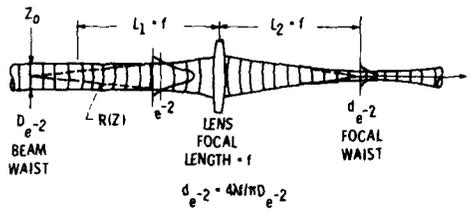
Figure 3. - Properties of a Gaussian beam.
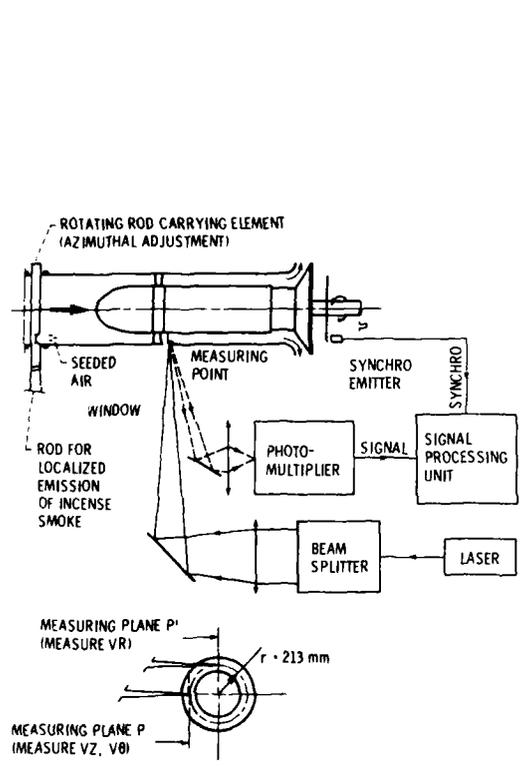
Figure 4. - Measurement of radial velocity components downstream of a compressor blade row. VZ, Vθ measured using window P. VR measured using window P'.

(a) Conventional system.

(b) Radial flow system.
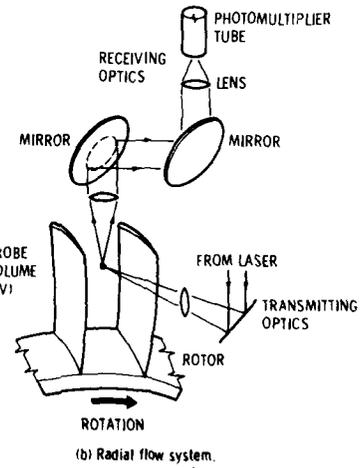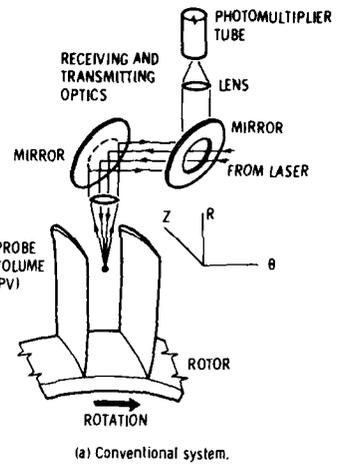
Figure 5. - Measurement of radial velocity components within a blade row using off-axis light collection.
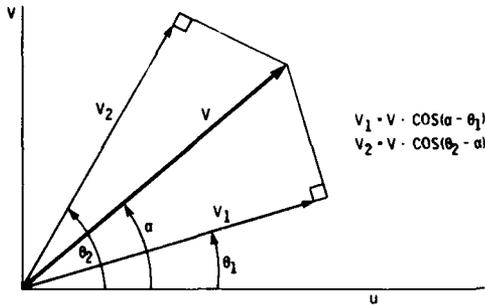
Figure 6. – Determination of unknowns V and α using velocities V_1 and V_2 measured at fringe orientations θ_1 and θ_2.
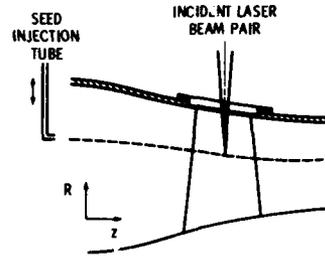
Figure 8. – Point injection of seed into streamtube passing through the measurement point.
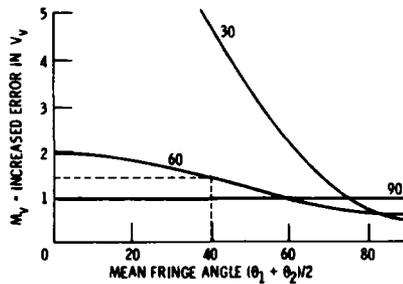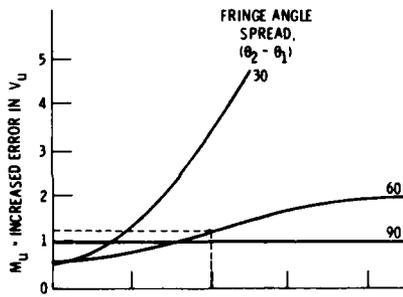
Figure 7. – Increase in statistical error due to use of uncorrelated measurements in calculating velocity components.
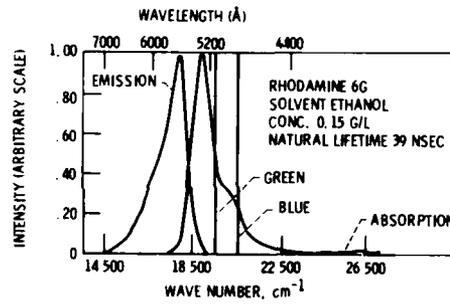
(a) Emission and absorption spectra.
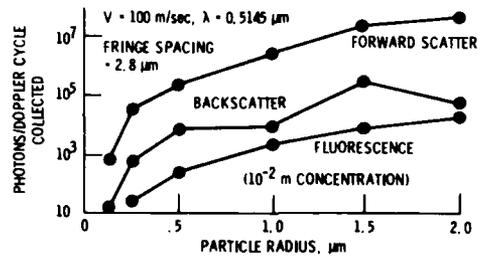
(b) Comparison between fluorescence emission and light scattering versus particle size.

Figure 9. – Characteristics of rhodamine 6G fluorescing dye.
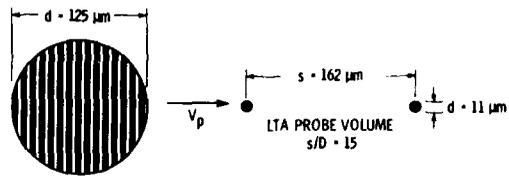
Figure 10. - Comparison of typical laser-fringe and laser-transit anemometer probe volumes.
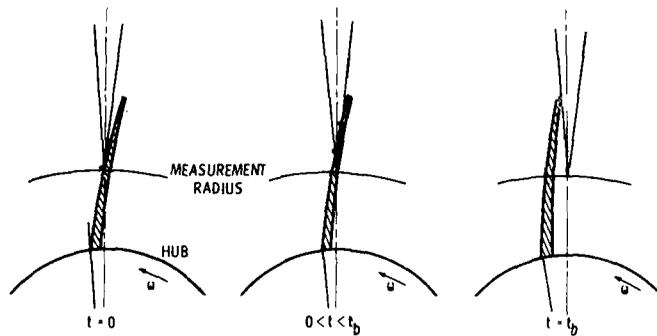
Figure 11. - Incident light reflection from blade surfaces.

(a) Axial view. (b) View looking downstream.
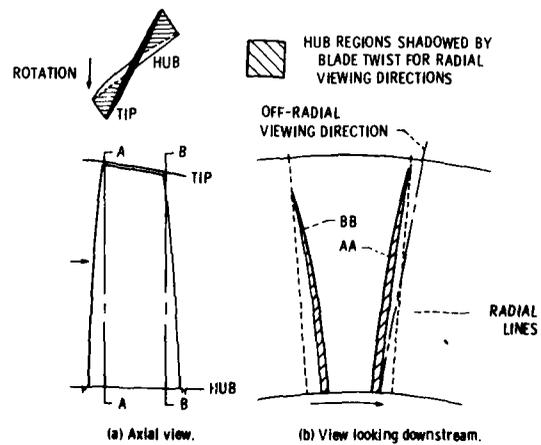
Figure 12. - Existence of shadowed regions caused by blade twist.

STATIC BLADE
GEOMETRY
---- BLADE GEOMETRY
AT DESIGN SPEED

$\Delta(R\theta)$

NASTRAN ANALYSIS
○ MEASURED BLADE
DEFLECTION
BLADE CHORD · 3.66 in.

.4

$\Delta(R\theta)$, in.

.2

0
0   100
CHORD, %
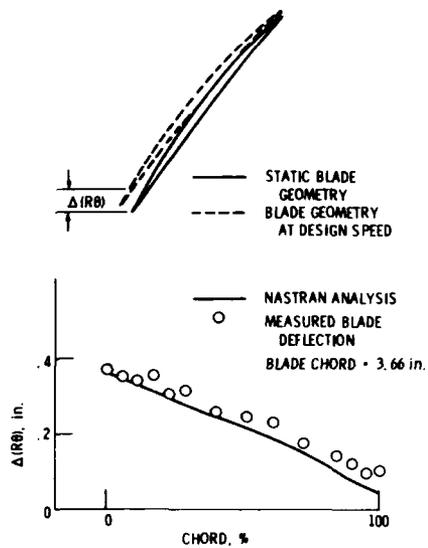
Figure 13. - Comparison of measured and predicted
untwist at the tip of an axial flow fan at a tip speed
of 429 m/sec.

(a) Tip clearance distortion due to casing
curvature.

(b) Tip clearance distortion due to flow-
path convergence.
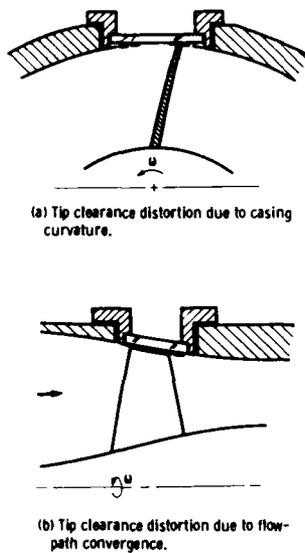
Figure 14. - Flowpath distortions caused by flat
windows.
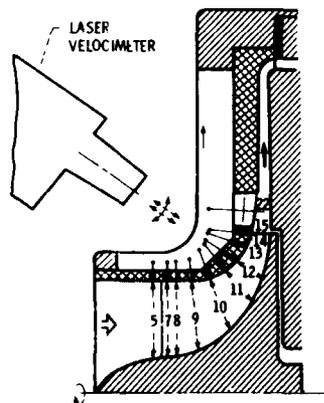
LASER
VELOCIMETER

Figure 15. - Use of small flat windows in radial tur-
bomachines to minimize flowpath distortions.

ARGON-ION LASER

MIRROR

FILM

MASK   PINHOLE   MICROSCOPE
OBJECTIVE

REFERENCE BEAMS

PINHOLE

PLEXIGLAS
CYLINDER

MICROSCOPE
OBJECTIVE   MIRROR
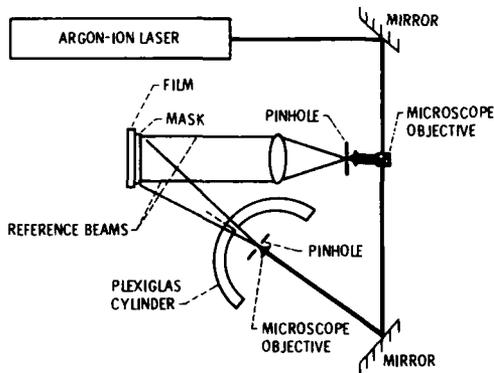
(a) Hologram construction. Pinhole is at the desired probe volume location.

INCIDENT
LASER
BEAMS
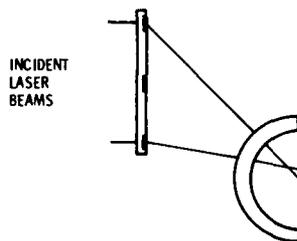
(b) Holographic refraction correction. Incident laser
beams propagate through the hologram in the
direction taken by the reference beam during holo-
gram construction and cross at the desired probe
volume location.

Figure 16. - Holographic correction of window refraction effects.

(a) Generation of one window per revolution.

(b) Generation of windows once per blade passing.

(c) Generation of continuous windows.
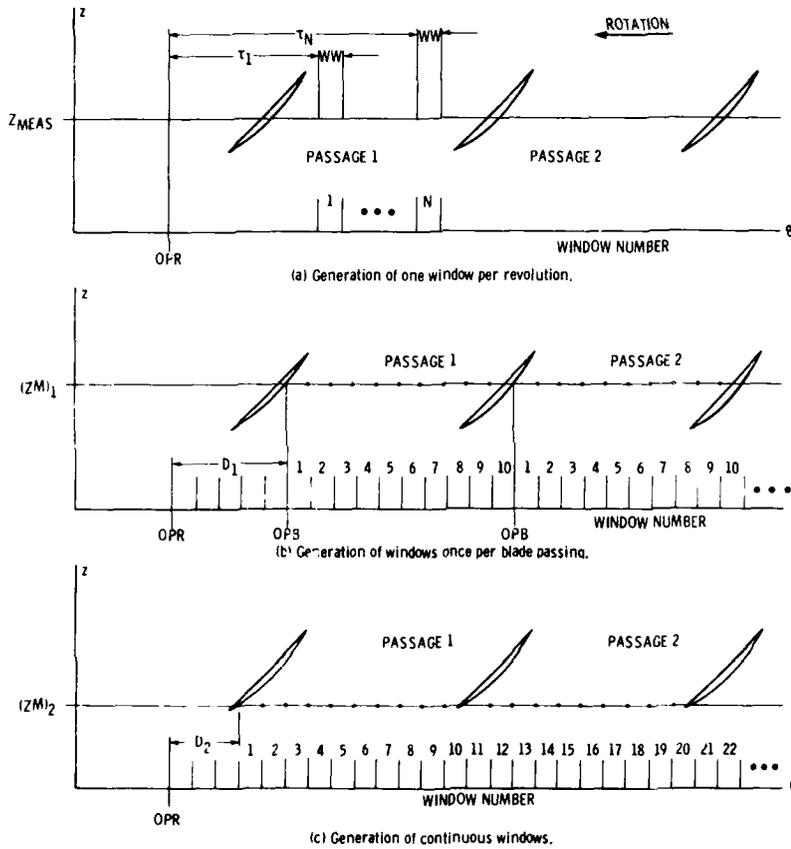
Figure 17. - Three methods of generating measurement windows for LA applications in rotating blade rows.

REVOLUTION 1   REVOLUTION 2   REVOLUTION 3
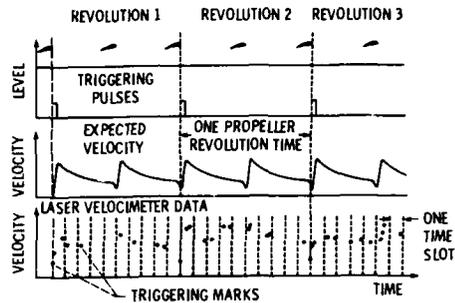
(a) Exact circumferential location of each measurement calculated using elapsed-time-between-measurements data and trigger pulse data.
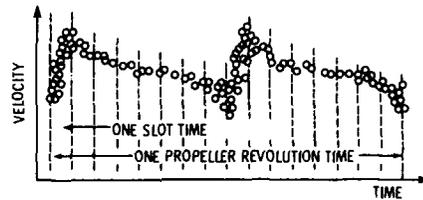
(b) Measurements assigned to proper window during post-run processing.

Figure 18. – Assignment of measurement windows during post-test data reduction.

CIRCUMFERENTIAL PATH

ONE BLADE PASSAGE:
50 SHAFT POSITIONS

ONE MEASUREMENT

N(x) = NUMBER OF MEASUREMENTS AT SHAFT POSITION X
V(x) = ONE VELOCITY MEASUREMENT AT SHAFT POSITION X
SP = SHAFT POSITION
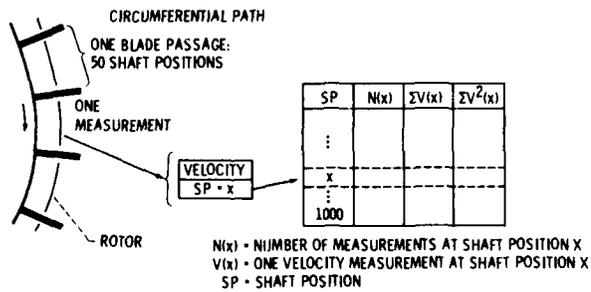
Figure 19. – Data storage scheme used during "window average" mode data acquisition.

1.4
1.3
1.2
1.1
1.0

BLADE

$N_{WINDOW} = 50$

SUCTION
SURFACE

PRESSURE
SURFACE

1.5
1.4
1.3
1.2
1.1
1.0

RELATIVE MACH NUMBER

BLADE

$N_{WINDOW} = 25$

SUCTION
SURFACE

PRESSURE
SURFACE

1.5
1.4
1.3
1.2
1.1
1.0

BLADE

$N_{WINDOW} = 12$

SUCTION
SURFACE

PRESSURE
SURFACE
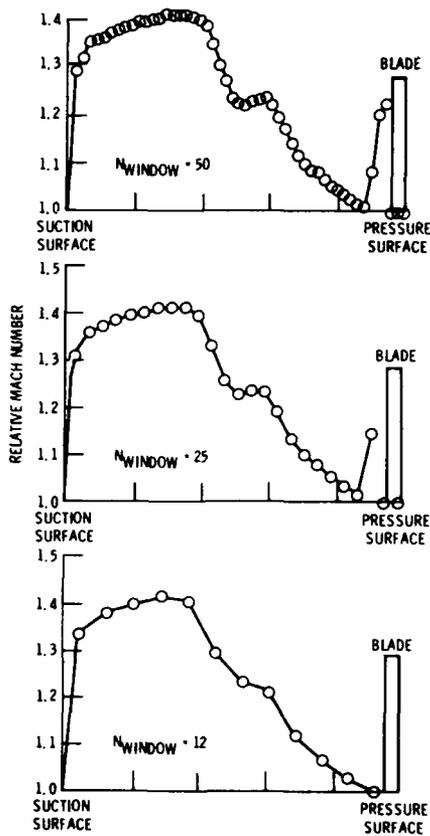
Figure 20. - Effect of window width on resolution of
blade-to-blade velocity gradients.

1.5
1.4
1.3
1.2
1.1
1.0

RELATIVE MACH NUMBER

BLADE

SUCTION
SURFACE

PRESSURE
SURFACE

2000
1600
1200
800
400
0

NMEAS

TOTAL NUMBER MEASURED = 60 000
NUMBER OF WINDOWS = 50
SHOULD HAVE NMEAS = 1200 IN
EACH WINDOW IF DATA IS
UNIFORMLY DISTRIBUTED

BLADE

SUCTION
SURFACE
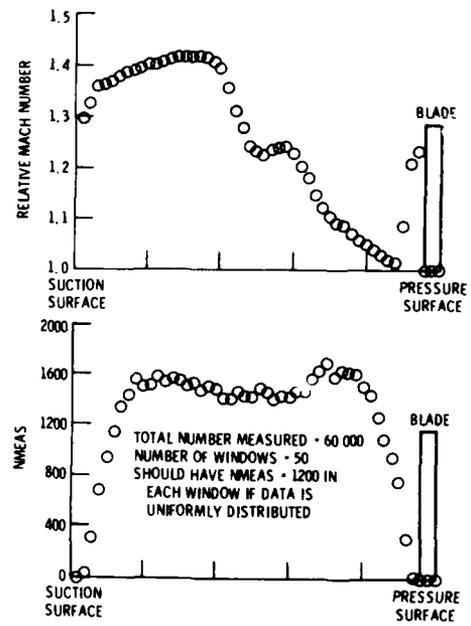
PRESSURE
SURFACE

Figure 21. - Example of nonuniform distribution of the
number of measurements which occur in each mea-
surement window.
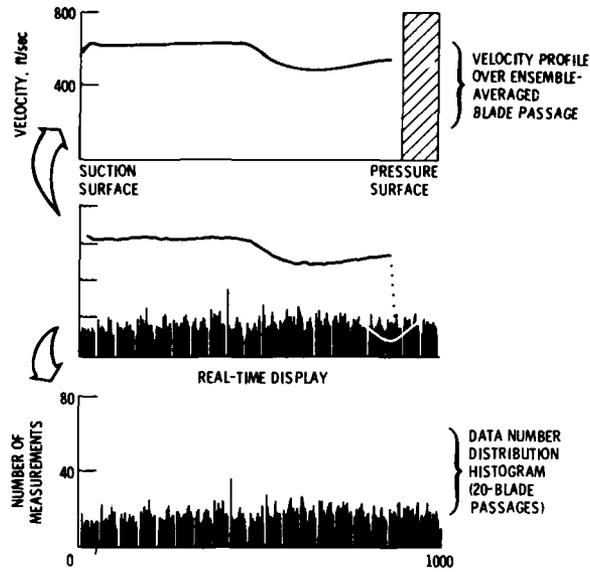
Figure 22. - Real-time display used in the NASA-Lewis LA system during compressor research testing.
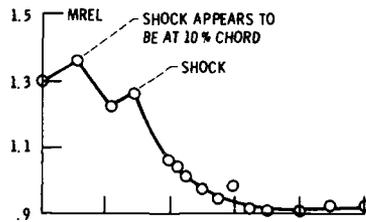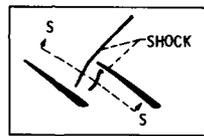
(a) Streamwise distribution (view S-S) of relative Mach number. Initial survey - every 10 % chord over first 40 % chord.
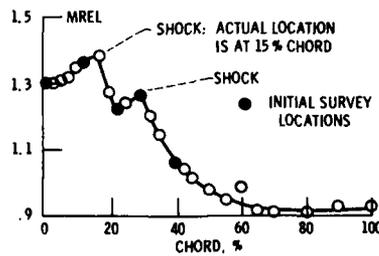
(b) Streamwise distribution (view S-S) of relative Mach number. Refinement of shock location using additional survey locations.

Figure 23. - Use of on-line data analysis to capture shock location in a transonic compressor.
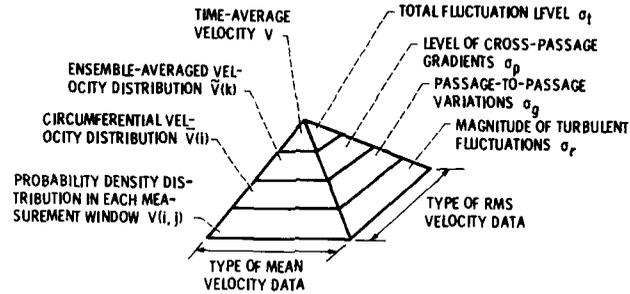
Figure 24. - Schematic representation of information available from LA data.
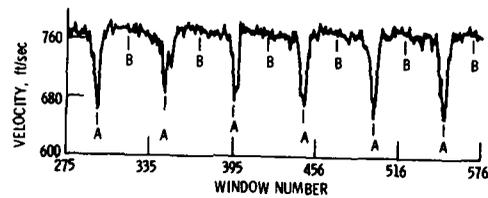
(a) Velocity distribution measured across 6 of the 17 measured blade passages.
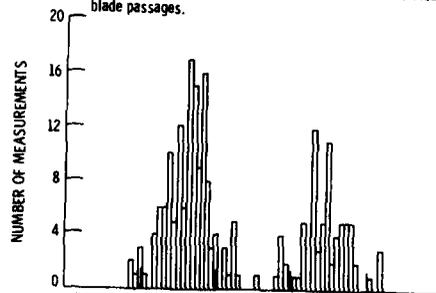
(b) p.d.d. for data acquired at point A in all 17 measured blade passages. Average velocity - 678.2.
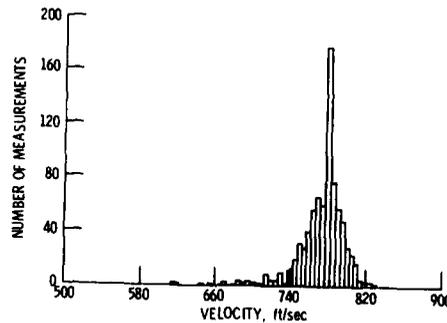
(c) p.d.d. for data acquired at point B in all 17 measured blade passages. Average velocity - 773.0.

Figure 25. - Blade-averaged probability density distributions.
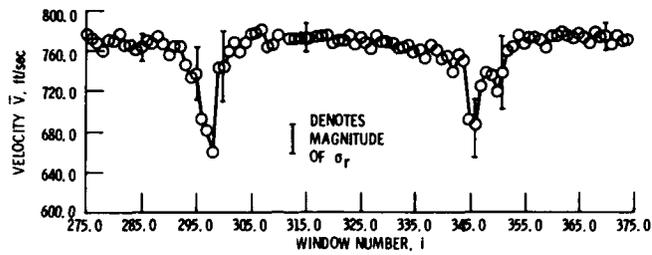
Figure 26. - Circumferential velocity distributions across two of the seventeen measured blade passages.
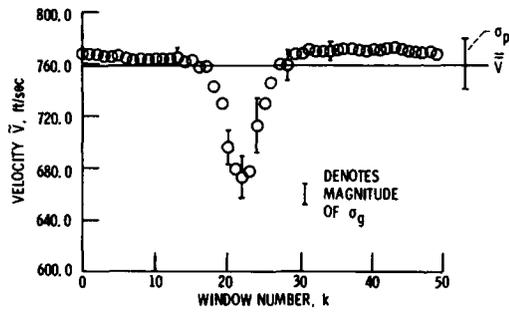
Figure 27. - Ensemble-averaged velocity distribution across the blade pitch.
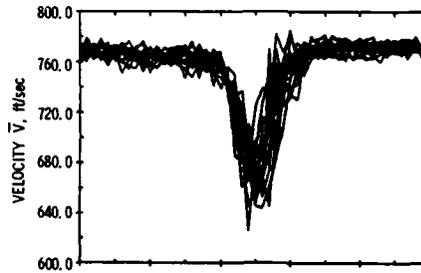
Figure 28. - Contribution of passage-to-passage flow variations to the total rms velocity level. Passage-to-passage flow field variations generate rms velocity σ_g.
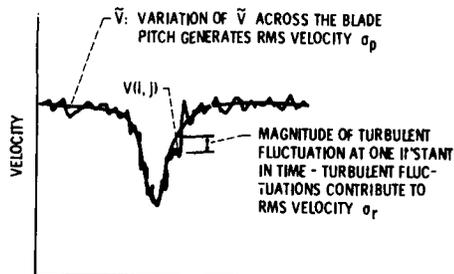
Figure 29. - Model used to illustrate various contributions to the total rms velocity level.
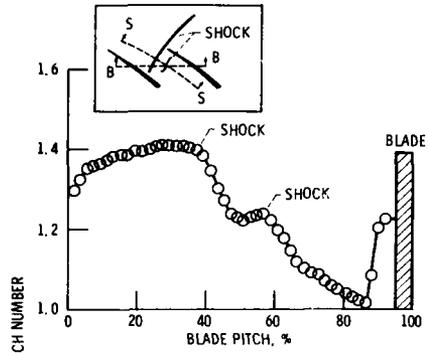
(a) Blade-to-blade distribution (view B-B) of relative Mach number.
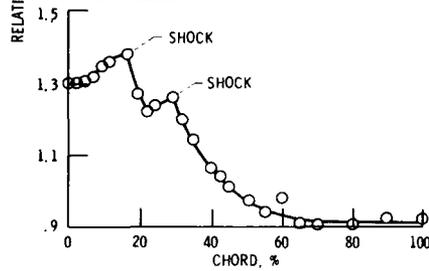
(b) Streamwise distribution (view S-S) of relative Mach number.

Figure 30. - Use of pitchwise and streamwise Mach number distributions to determine shock wave locations.

Figure 31. - Contour plot of relative Mach number distribution in a transonic fan.

(a) Meridional view.

(b) View looking upstream.

Figure 32. - 3D hidden line plot of Mach number data from figure 31 viewed from two different directions.
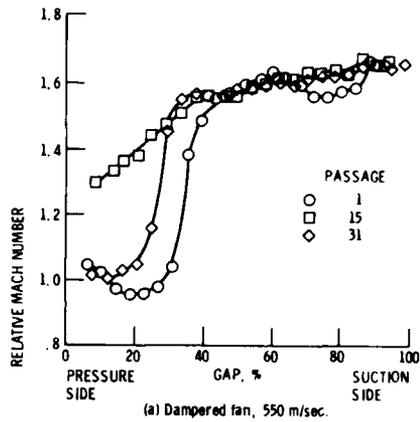
(a) Dampered fan, 550 m/sec.
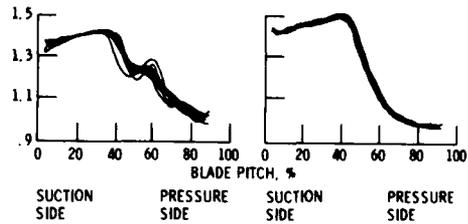
(b) Undampered fan, 429 m/sec.

Figure 33. - Passage-to-passage flow variations in two transonic axial flow fans.
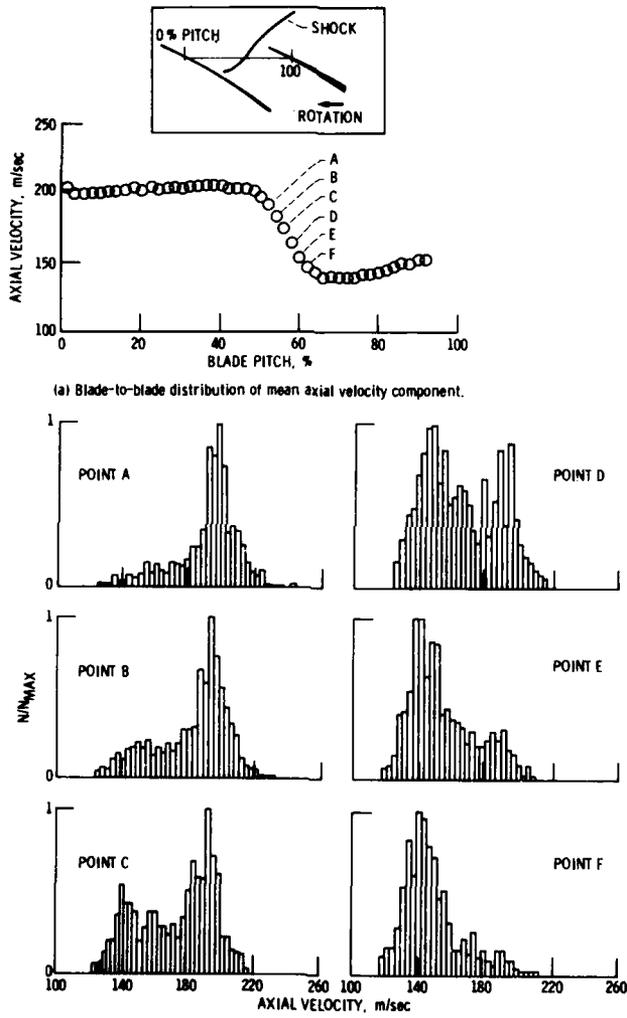
(a) Blade-to-blade distribution of mean axial velocity component.

(b) Velocity probability at points near the passage shock.

Figure 34. – Analysis of rotor passage shock oscillations using velocity probability density distribution.
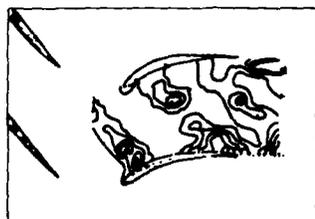
(a) Rotor trailing edge aligned circumferentially with stator leading edge.

(b) Rotor displaced circumferentially by one-third rotor pitch.

Figure 35. - LA survey locations used to investigate the periodically unsteady flow through a compressor stator.

(c) Rotor displaced circumferentially by two-thirds rotor pitch.

Figure 36. - Periodically unsteady stator flow field at three points in the rotor-stator blade passing cycle. Distribution of turbulence intensity parallel to local temporary main flow direction (Tpar) within one stator blade passage.

DISCUSSION

M.G.Alwang, US

Do you make correction for particle lag in plotting velocity distributions through shocks?

Author's Reply

We do not attempt to perform particle lag corrections. In a wind-tunnel application, in which the flow might be steady or nearly two-dimensional, one might entertain the possibility of such a correction. The problem in turbomachinery applications is that once the flow passes through the shock, the flow undergoes additional changes due to the work input of the blade row. It is therefore not possible to separate particle velocity effects due to particle lag from those effects due to the flow itself.

J.Allan. US

My questions are related to the effects of the curved windows which were mentioned as a method of reducing the physical problems associated with flat windows:

(1)   are lens calculations run to evaluate the effects of the window curvature?

(2)   how does the window affect the system calibration?

(3)   how does the window affect the probe volume position?

Author's Reply

(1) The paper presented here by Carl Williams contains reference to a publication which deals with this issue. Richard Seasholtz at NASA Lewis has also done work on the design of window refraction correction lenses.

(2) Flat windows do not affect the systems calibration, in other words the beams crossing angle. However, curved windows can change this angle; a detailed analysis of the magnitude of this effect is reported in reference 20 cited in

my paper.

(3) Both flat and curved windows change the probe volume location. The predominant shift is in the line of sight (or optical axis) direction. For windows on the order of several millimetres thick, this change is on the order of a millimetre. Again reference 20 contains further details on this problem as well.

C.Williams, US

Just as a comment, Paper 11 contains a reference (reference 1) on designing curved windows in which beam steering problems are discussed and partial corrections are suggested.

R.Schodl, GE

You showed a slide where the fluorescent light intensity was plotted against the droplet diameter. Are these theoretical or experimental results?

Author's Reply

The results shown in figure 9 of the paper are taken directly from the paper of Stevenson et al which is reference 14 of the paper. I believe that this is an experimental result, but one should check the original paper to confirm this.

P.J.Bryanston-Cross, UK

Did you explore the relationship on correlation between measured vortex shedding from the compressor blade at its shock movement?

Author's Reply

We did not explore any correlation between shock motion and vortex shedding from the blade trailing edge, both of which we have observed in a transonic fan. Vortex shedding has been observed in both subsonic and supersonic cascades. In subsonic cases, shocks are not present.

Therefore, although vortex shedding may be caused by shock motion, it is not necessarily dependent on shock presence.

LASER-TWO-FOCUS VELOCIMETRY

BY

R. SCHODL

DFVLR-Institut für Antriebstechnik,
Linder Höhe, 5 Köln 90, W. Germany

ABSTRACT

The paper begins with a review of various publications about L2F-velocimetry. Main emphasis is placed upon the important new advances of this technique. The manner of statistical data analysis of turbulent flows including the simplified version which enables a time-saving measuring procedure, is described in some detail. The influence of beam diameter beam separation ratio on the measuring accuracy and on the measuring time is treated. The capability of the L2F-system at close-to-wall measurements could be further improved. Results of measurements in a very small flow channel and in a small turbocharger compressor rotor are presented. The 3-D version of the L2F-system was successfully operated recently. The principle, the optical set-up and the signal processing are described and some first results are presented. At the end a comparison between laser doppler (LD) and laser Two Focus (L2F) velocimeters gives answers about such signal properties as amplitude and rate, the smallest detectable particles and about the measuring time needed, based on the probe volume dimensions.

NOMENCLATURE

a	radius coordinate of laser beams
b	index indicating blue
c_m	meridional component of absolute velocity
d	diameter of the laser beams in the probe volume
d_p	particle diameter
F	velocity function
$\bar{F}$	mean value of velocity function
f	focal length
f	LD-signal frequency
G	two dimensional gaussion probability distribution
$\bar{g}(x)$	mean value of velocity function
g	index indicating green
H_{ij}	corrected value of measured two-dimensional frequency distribution
I,I_o	intensity of light
l	axial length of the L2F-probe-volume
N	number concentration
N_{ij}	value of measured two-dimensional frequency distribution
N_t,N_α	values of measured one-dimensional frequency distributions
$N_{tR},N_{\alpha R},N_{Ri}$	basic level of measured frequency distributions
P,P_Ω,P_o	power of light
P,P_α,P_t	integrated probability density functions
p,p^+,p^{++}	probability density functions
p_I	probability according to probe volume intensity distribution
P_{succ}	probability of a successful two-beam transit
S,S'	separation of the beams in the L2F-probe-volume
T_{ui}	turbulence intensities
t	time coordinate
$\underline{u}$	velocity vector
u_1,u_2,u_3	cartesian components of the velocity vector $\underline{u}$
u_2	circumferential tip speed at impeller outlet
$u_\perp$	amount of velocity vector in the plane perpendicular to the optical axis
$\underline{x}$	local vector
x_1,x_2,x_3	components of the local vector $\underline{x}$
x_{min}	smallest distance of the measurement location from a light scattering wall
α	angle coordinate
α,α_o	angle setting of the L2F beams plane
β	angle of flow vector with the plane normal to the optical axis
γ	angle between the green and blue pairs of laser beams
ε_S	measuring error effecting mean velocity
ε_T	measuring error effecting turbulence intensities
ϕ	angle of rotating of the 3D-L2F-laser beams
ρ	correlation coefficient
$\sigma_i,\sigma_\alpha,\sigma_d$	standard deviations
π_t	total pressure ratio

1. INTRODUCTION

In 1968, very soon after the Laser Doppler (LD) Method became known, an alternative optical flow velocity measuring method was introduced by D.H. Thompson [1]. This method, named "Tracer Particle Fluid Velocity Meter", is the forerunner of the kind of optical measuring devices which are nowadays known as Laser Transit (LT) - or Laser Two Focus (L2F)-Velocimeters. The idea was to measure the time of flight of tracer particles carried with

the fluid passing through two separated, parallel, highly focused laser beams. When he compared his method with the known LD-method, he saw the advantages of a simpler optical set-up, simpler date managing electronics and of lower powered lasers required to detect the scattered light of the small tracer particles.

This system (see fig. 1a and Tab. 1), however, with the fixed orientation of the two beams in the probe volume and the way of measuring the time of flight by averaging a set of oscilloscope traces could only be applied to flows with uniform flow directions and very low turbulence intensities. Therefore, this method did not achieve much importance at that time, but in 1973 three additional papers about the application of Thompson's method were published (ref. [2], [3], [4]). Therein, among others, new ways of processing the time-of-flight data were described by which it became possible to a certain extent to apply Thompson's method also to turbulent flows. This was the main reason that - beginning from that year - a much faster development of this technique was initiated.

In order to give an overview about the first instrumentation used by the authors [1] to [4], the optical arrangements are shown in fig. 1. The other important technical data were collected for comparison and are shown in Table 1.

While the optical arrangements have not been modified very much, considerable development took place on the signal processing electronics. There is one group (ref. [2], [5] - [14]) applying correlators and photo correlators and another group which uses multi channel analysers (MCA) for the statistical analysis of the time of flight measurements (ref. [15] - [29]). From the theoretical point of view there is no question that from its principle the correlation analysis should be superior. However, there are comparisons made (ref. [13], [21], [30], [72]) which demonstrate that only at very high data rates can the correlator prove its superiority in practice. Considering the comparatively low particle rate even in seeded turbomachinery flows the conclusion must be drawn that in most applications the measured cross correlation function equals completely the measured MCA-time of flight histogram (ref. [21]). The data of both types of electronics need a further reduction which is explained in detail in the first part of this paper.

In the past several authors have analysed theoretically the L2F-system (ref. [3], [5], [6], [8], [13], [14], [16], [18], [19], [31], [39]) in more detail. Most of the main error sources are known today and they can be estimated quantitatively. However, there still remains a great deal of research work to be done in order to complete our understanding about this technique.

Nowadays L2F-Velocimetry has achieved importance in the experimental fluid flow analysis comparable to LD-Velocimetry. The L2F specific fields of application are: low turbulent flows, high speed, narrow flow channels.

Several L2F-Systems are on the market today (Malvern, Spectron, Disa, Polytec, TSI, IHI) and some industrial and research organisations have built their own systems for in house use. These systems of sometimes very different design were used e.g. for long range wind speed measurements (ref. [10], [12], [32]), for measurements in heat exchangers (ref. [25]), wet steam flows (ref. [23]) and in water pumps (ref. [35], [36], [37]). There are applications in plasma flows (ref. [34], [38]), in diesel engines (ref. 33) and in wind- and cascade wind tunnels (ref. [40] — [43]). The widest distribution, however, the L2F has achieved is in the field of the experimental investigation of turbomachinery flow. Numerous reports have been published which present results of measurements in centrifugal and axial compressors as well as turbines (ref. [14] - [18], [22], [24], [26] - [29], [44] - [65]).

The detailed laser velocimetry data has contributed a great deal to our improved understanding of turbomachinery internal flow. This is expecially true with regard to rotor flows which are nearly unaccessible for conventional measuring techniques. The comparison with theoretical data has resulted in improved mathematical models and design procedures. Increasing efforts have been made to get more and more information out of the measurements. Recent measurements of turbine and compressor rotor-stator interactions were a high point in the experimental research (ref. [66] - [69]).

Because this measuring technique has been applied to such widespread areas of research, some of its unfavourable properties have been recognized, among which are:

- The limitation to flow turbulence intensities < 30 %

- The unfavourable long measuring time at high turbulence intensities (> 10 %)

Furthermore the experimentalists are now asking for more detailed results, such as:

- 3D-information about the flow vectors,

- closer wall proximity for measurement in small turbo-chargers or for tip clearance flow research.

This demonstrates that a further development of the L2F-technique is required. There are some new ideas and some new improvements in the context of this technique which can help in the future to overcome the mentioned problems and to further extend the range of applicability. In a main part of this paper an overview about this new developments will be given. Another part will deal with a comparison between LD- and L2F-Velocimetry based on consideration of the probe volume geometry. To complement and complete the publications issued to date, the present report deals with the evaluation of the test data as they are carried out in the Institute of Propulsion Technology.

2. PROCEDURE FOR EVALUATING L2F VELOCIMETER DATA

The mathematical fundamentals as well as methods to evaluate two-dimensional frequency distributions are described. In particular, however, a simplified method is presented for calculating the magnitude and direction of the mean velocity as well as the turbulence intensities, which, though mathematically not exact, supplies results which are in general sufficiently accurate for practical applications. This simplified method uses two marginal distributions (integrated two-dimensional frequency distributions), which can be determined by a special, time-saving measuring procedure. Both L2F-systems with correlators and L2F-systems with multi channel analysers can generally be operated as required by this procedure. Then the evaluation procedure is valid for both systems.

2.1 Mathematical fundamentals

A turbulent flow field is described by means of statistics by the probability density

$$p \; (u_1, \; u_2, \; u_3, \; x_1, \; x_2, \; x_3, \; t) \tag{1}$$

where the velocity vector $\underline{u}$ $(\underline{x}, t)$ is considered as a random variable (ref. [70]). u_1, u_2, u_3 are the velocity components in Cartesian coordinates and x_1, x_2, x_3 the Cartesian coordinates of the position vector $\underline{x}$.

If considerations are limited to constant, turbulent flows, the time-independent probability density:

$$p \; (\underline{u}, \; \underline{x}) \; du_1 \; du_2 \; du_3 \tag{2}$$

then indicates the probability that at a fixed position $\underline{x}$ the components of the velocity vector are within the range $u_1 + du_1$, $u_2 + du_2$ and $u_3 + du_3$.

The position-dependent mean values $\overline{F}(x)$ for any arbitrary velocity function $F(\underline{u})$ are calculated according to

$$\overline{F} \; (\underline{x}) = \int\limits_{-\infty}^{+\infty}\!\!\int\int F \; (\underline{u}) \; p \; (\underline{u}, \; \underline{x}) \; du_1 \; du_2 \; du_3 \tag{3}$$

it being understood that the normalization condition

$$\int\limits_{-\infty}^{+\infty}\!\!\int\int \; p \; (\underline{u}, \; \underline{x}) \; du_1 \; du_2 \; du_3 = 1 \tag{4}$$

is valid.

Using the L2F velocimeter, the components of arbitrary velocity vectors $\underline{u}$ lying in the x_1, x_2 plane can be measured for direction α and magnitude $u_\perp$ (see fig. 3). So, for example, the mean value and/or the expected value of the velocity component u_i is obtained from

$$\overline{u}_i = \int\limits_{-\infty}^{+\infty}\!\!\int\int u_i \; p \; (\underline{u}, \; \underline{x}) \; du_1 \; du_2 \; du_3; \; \text{etc.} \tag{5}$$

For two-dimensional velocity functions, e.g.

$$F(\underline{u}) = F(u_1, \; u_2), \tag{6}$$

eq. (3) can be transformed to read

$$\overline{F}(\underline{x}) = \int\limits_{-\infty}^{+\infty}\!\!\int F(u_1, \; u_2) \; [\int\limits_{-\infty}^{+\infty} p(\underline{u}, \; \underline{x})du_3] \; du_1 \; du_2 \tag{7}$$

By means of this equation it is possible to show an essential requirement imposed on two-dimensional velocity measuring methods. Complete information about all velocity functions, e.g. those defined in the u_1, u_2 plane, will only be obtained if a measured two-dimensional probability density function $p^+(u_1, u_2, \underline{x})$ fulfills the condition

$$p^+(u_1, \; u_2, \; \underline{x}) = \int\limits_{-\infty}^{+\infty} p(\underline{u}, \; \underline{x})du_3 \tag{8}$$

This means in practice that the u_1 and u_2 components of all velocity vectors $\underline{u}$ that occur must be taken into account, even for large u_3 components. Hence the axial length "l" of the probe volume measured in the direction of the radiated laser beam (x_3 direction) must be selected to be sufficiently large. In the L2F system, the length of the probe ($\pm l$) is selected to be approximately equal to the separation of the two beams (l $*$ s) so that eq. (8) is satisfied up to turbulence intensities of ≤ 30 % (see fig. 2).

There applies

$$u_\perp \; \cos \alpha \; = u_1$$
$$u_\perp \; \sin \alpha \; = u_2 \tag{9}$$

Transforming eq. (7) into polar coordinates and using eq. (8) and eq. (9), gives

$$\overline{F}(x) = \int\limits_{0}^{2\pi}\!\!\int\limits_{0}^{+\infty} F(\alpha, u_\perp) p^+(\alpha, \; u_\perp, \; \underline{x}) \; u_\perp \; du_\perp \; d\alpha \tag{10}$$

Furthermore, the L2F process does not record the velocity magnitude $u_\perp$, but the time t which a particle takes to cover the distance between the start and stop laser beams namely:

$$t = \frac{s}{u_\perp} \qquad (11)$$

where s is the spacing of the two beams in the probe volume. Transformation of eq. (10) using eq. (11) leads to

$$\bar{F}(x) = \int_0^{2\pi} \int_0^{+\infty} F(\alpha,\,t)\,p^+(\alpha,\,t,\,\underline{x})\frac{s^2}{t^3}\,dt\,d\alpha \qquad (12)$$

Eq. (12) is the basic equation for evaluating the L2F test data; here, also the normalization condition

$$\int_0^{2\pi} \int_0^{+\infty} p^+(\alpha,\,t,\,\underline{x})\frac{s^2}{t^3}\,dt\,d\alpha = 1 \qquad (13)$$

must be satisfied.

At a fixed position $\underline{x}$ the expression $p^+(\alpha,t,\underline{x})\,\frac{s^2}{t^3}\,dt\,d$ indicates the probability that the direction of the flow velocity lies in the angular range α to $\alpha + d\alpha$, and its magnitude $u_\perp$ in the assigned time window t to t + dt.

Now the test data H_{ij} supplied by a L2F system must also be assigned to this probability. For time measurements to be assigned to a test point of the flow velocity, the values are stored and ordered in the time window t_j to $t_j + \Delta t$. Such frequency distributions are obtained for different angles i of the plane of the beams. Those velocity vectors are covered whose directions α are within an angular range α_i to $\alpha_i + \Delta\alpha$. This angular range $\Delta\alpha$ is defined by the geometry of the probe volume (ratio of beam diameter d to the beam spacing s). Hence the frequency H_{ij} is a measure of the probability of the velocity within the time window t_j to $t_j + \Delta t$ and angular range α_i to $\alpha_i + \Delta\alpha$. There applies:

$$H_{ij} \doteq p^+(\alpha_i,\,t_j,\,\underline{x})\frac{s^2}{t^3}\,\Delta t\,\Delta\alpha \qquad (14)$$

Taking into account the normalization condition, for sufficiently small Δt and $\Delta\alpha$.

$$\frac{H_{ij}}{\sum\limits_{i=1}^{m}\sum\limits_{j=1}^{n}H_{ij}} = p^+(\alpha_i,t_j,\,\underline{x})\frac{s^2}{t^3}\,\Delta t\,\Delta\alpha \qquad (15)$$

If the integration in eq. (12) is replaced by a summation, we get by using eq. (15):

$$\bar{F}(\underline{x}) = \frac{\sum\limits_{i=1}^{m}\sum\limits_{j=1}^{n}F(\alpha,\,t)H_{ij}}{\sum\limits_{i=1}^{m}\sum\limits_{j=1}^{n}H_{ij}} \qquad (16)$$

Due to two errors, the frequency distributions N_{ij} measured in practice initially are not equal to the distributions H_{ij}. First, as a result of uncorrelated time measurements, a basic level N_{Ri} occurs which is constant against the time axis (see fig. 4) and second, the distributions are distorted by the fact that high-velocity particles are recorded in greater number than particles of lower velocity. The two errors are corrected by the relation

$$H_{ij} = \frac{N_{ij} - N_{Ri}}{s/t_j} \qquad (17)$$

Thus the final formula for evaluating the L2F data reads:

$$\bar{F}(\underline{x}) = \frac{\sum\limits_{i=1}^{m}\sum\limits_{j=1}^{n}F(\alpha_i,\,tj)\dfrac{N_{ij} - N_{Ri}}{s/t_j}}{\sum\limits_{i=1}^{m}\sum\limits_{j=1}^{n}\dfrac{N_{ij} - N_{Ri}}{s/t_j}} \qquad (18)$$

As examples, the velocity functions for various mean velocity values are listed in Table 2.

The magnitude of the mean velocity is calculated using

$$u_\perp = \sqrt{\bar{u}_1^2 + \bar{u}_2^2} \qquad (19)$$

and the angle of the mean velocity with:

$$\bar{\alpha} = \text{arctg} \frac{\bar{u}_2}{\bar{u}_1}$$

(20)

the turbulence intensity with:

$$Tu_i = \frac{\sqrt{\overline{(u_i - \bar{u}_i)^2}}}{u_i}$$

(21)

Reynolds' shear stresses with:

$$\frac{\overline{(u_1 - \bar{u}_1)(u_2 - \bar{u}_2)}}{u_i^2}$$

(22)

skewness of the distribution with:

$$\frac{\overline{(u_i - \bar{u}_i)^3}}{[\overline{(u_i - \bar{u}_i)}]^{3/2}}$$

(23)

and the degree of flatness with:

$$\frac{\overline{(u_i - \bar{u}_i)^4}}{[\overline{(u_i - \bar{u}_i)^2}]^2}$$

(24)

2.2 The evaluation of two-dimensional frequency distribution

Evaluation of the test data by means of the formulas derived in chapter 2 proves to be particularly easy if the test data is very large in quantity and if the selected time and angle intervals for the discrete frequencies N_{ij} are very small. The summation formulas can be directly applied to the test data without any noticeable errors. Only the summation limits have to be determined.

When there is need to measure the mean velocity vector and also the moments of the velocity distribution function with great accuracy a large quantity of test data is required. It can be shown by statistical theory that, if the same accuracy is required, the quantity of test data must increase if the moments order is increased.

In practice, however, because of restricted measuring periods the test data, especially the number of angle settings of the beams plane, is limited and the summation formulas can not directly be applied. By means of two-dimensional interpolation procedures, the test data can be approximated quite well, and sufficient support points can be established for the summation. In this way additional summation error can be avoided.

The reliability of these approximation methods is only assured if the frequency distributions have only small statistical fluctuations, i.e. if the frequency distributions are mostly continous against the time axis and if the frequency distributions per angle setting do not fall below a minimum number: If the accuracy requirements are not too high, especially if the moments are of no higher order than 2nd, 6 - 8 frequency distributions measured at different angle settings with 500 - 2000 test data points each are needed in practice.

If measurements remain below these values, the statistical uncertainities of the individual test data N_{ij} increase and approximation of the frequency distributions by means of two-dimensional, often very complicated, interpolation procedures becomes more unreliable. Then the errors due to the approximation exceed to a no longer negligible extent the accuracy which is determined by the quantity of test data.

Improving the approximation of the two-dimensional test data and hence reducing the necessary test data quantity is only possible if the characteristic two-dimensional shape of the velocity distributions in a flow is known. In this case, by approximating the test data with known functions, it is possible to increase the accuracy of the calculated mean values compared with the one given by the test data. In practice, such detailed information about the flow to be investigated is usually not available.

3. NEW DEVELOPMENTS OF THE L2F - TECHNIQUE

Measuring-time-reducing computer-controlled-processing of the LD- as well as the L2F-technique is nowadays used with all turbomachinery applications. By applying the so-called "Multi window operation", that is the quasi simultaneous measurement at multiple circumferential locations, an additional reduction of measuring time could be achieved (ref. [18]). This main part of the paper will give an overview of other developments for time saving methods to achieve closer wall proximity and the extension of the L2F-technique to 3D-velocity measurements.

3.1 Determination of the components of the mean velocity and the turbulence intensities based on marginal distributions

In numerous flow investigations, and this applies particularly to turbomachinery, the variables required are the components of the mean velocity vector and, possibly, also the turbulence intensities. Further information on the flow which is included in the two-dimensional frequency distribution - e.g. Reynolds' shear stresses, skewness and distribution excesses - often is of little interest in these investigations.

In such cases it seems to be inefficient to provide two-dimensional velocity distributions whose measurement involves considerable effort and then to use only a fraction of this information content. It seems sensible to see whether the mean velocity values of interest can be determined using far less complex test data than two-dimensional frequency distributions.

Based on the two-dimensional probability density, the mean velocity values are calculated in Cartesian coordinates $p^+(u_1, u_2, x)$ according to eq. (3) and eq. (8).

$$\bar{F}(\underline{x}) = \int\limits_{-\infty}^{+\infty} \int F(u_1, u_2) p^+(u_1, u_2, \underline{x}) du_1 \, du_2 \tag{25}$$

The component u_1 of the mean velocity vector is e.g. obtained from

$$u_1(\underline{x}) = \int\limits_{-\infty}^{+\infty} \int u_1 \, p^+(u_1, u_2, \underline{x}) du_1 \, du_2 \tag{26}$$

If $p^+(u_1, u_2, \underline{x})$ is integrated to each of the two velocity components, we get two one-dimensional distributions which in statistics (ref. [71]/pp. 119 ff.) are known as marginal distributions, namely:

$$P_1(u_1, \underline{x}) = \int\limits_{-\infty}^{+\infty} p^+(u_1, u_2, \underline{x}) du_2 \tag{27}$$

and

$$P_2(u_2, \underline{x}) = \int\limits_{-\infty}^{+\infty} p^+(u_1, u_2, \underline{x}) du_1 \tag{28}$$

As will be shown later, these two one-dimensional marginal distributions contain sufficient information for determining some selected mean velocity values.

If - e.g. in eq. (26) - the two-dimensional probability density in the double integral is replaced by the product of the two marginal distributions and if we put

$$\bar{g}(x) = \int\limits_{-\infty}^{+\infty} \int u_1 \, P_1(u_1, \underline{x}) P_2(u_2, \underline{x}) du_1 \, du_2 \tag{29}$$

it follows:

$$\bar{g}(x) = \int\limits_{-\infty}^{+\infty} P_2(u_2, \underline{x}) \int\limits_{-\infty}^{+\infty} u_1 \, P_1(u_1, \underline{x}) du_2 \, du_1 \tag{30}$$

Using eq. (27) we get

$$\bar{g}(x) = \int\limits_{-\infty}^{+\infty} P_2(u_2, \underline{x}) \int\limits_{-\infty}^{+\infty} \int u_1 p^+(u_1, u_2, \underline{x}) du_1 \, du_2 \, du_2$$

and eq. (26) gives

$$\bar{g}(x) = \int\limits_{-\infty}^{+\infty} P_2(u_2, \underline{x}) \bar{u}_1(\underline{x}) \, du_2$$

$$= \bar{u}_1(\underline{x}) \int\limits_{-\infty}^{+\infty} P_2(u_2, \underline{x}) \, du_2$$

Taking into account eq. (28) and the normalization condition

$$\int\limits_{-\infty}^{+\infty} \int p^+(u_1, u_2, \underline{x}) \, du_1 \, du_2 = 1$$

it follows that:

$$\bar{g}(x) = \bar{u}_1(x) \tag{31}$$

In the same way it can be shown that to determine the mean value of the velocity component u_2 and for the moments of second order $\overline{(u_1 - \bar{u}_1)^2}$ and $\overline{(u_2 - \bar{u}_2)^2}$ necessary for turbulence intensity calculations, the two-dimensional probability density can be replaced by the product of the two marginal distributions. This does not, however, apply to Reynolds' shear stresses, the excess, and the skewness of the distribution, but as mentioned above, these mean values are not of interest in most applications.

It is sufficient if we have two one-dimensional frequency distributions as test data. These can be provided with substantially less measurement efforts (see below).

With L2F, the time of flight "t" and the flow angle "α" are measured, and not the Cartesian components u_1, u_2 of the velocity vector. For the α,t coordinate system, the above considerations cannot be verified with mathematical exactness and errors must be anticipated if calculation of the mean velocity values is not based on the two-dimensional frequency distribution (see eq. 12)

$$p^{++} (\alpha,\ t,\ \underline{x}) = p^{+} (\alpha,\ t,\ \underline{x})\ \frac{s^2}{t^3} \tag{32}$$

but on the marginal distribution

$$P_\alpha (\alpha,\ \underline{x}) = \int_0^{+\infty} p^{++} (\alpha,\ t,\ \underline{x}) dt \tag{33}$$

$$P_t (t,\ \underline{x}) = \int_0^{2\pi} p^{++} (\alpha,\ t,\ \underline{x}) d\alpha \tag{34}$$

To estimate the error, a model calculation was performed. The theoretical frequency distribution was assumed to be the two-dimensional Gaussian distribution:

$$G(u_1, u_2, \underline{x}) = \frac{1}{2\pi\sigma_1\sigma_2\sqrt{1-\rho^2}} \cdot \exp. \left[-\frac{1}{2(1-\rho^2)} \cdot \right.$$

$$\left. \cdot \ < (\frac{u_1-\bar{u}_1}{\sigma_1})^2 - 2\rho\frac{u_1-\bar{u}_1}{\sigma_1}\frac{u_2-\bar{u}_2}{\sigma_2} + (\frac{u_2-\bar{u}_2}{\sigma_2})^2 > \right] \tag{35}$$

by which, as is shown by experiment, most of the frequency distributions measured in real flows can be approximated. The components of the mean velocity vector $\bar{u}_1$ and $\bar{u}_2$ and the turbulence intensities:

$$Tu_1 = \sigma_1 / \sqrt{\bar{u}_1^2 + \bar{u}_2^2} \quad \text{and} \quad Tu_2 = \sigma_2 / \sqrt{\bar{u}_2^2 + \bar{u}_1^2}$$

are exactly known, as is Reynolds' shear stress, which is determined with ρ as the correlation coefficient according to

$$\sigma_1 \cdot \sigma_2 \cdot \rho / (\bar{u}_1^2 + \bar{u}_2^2)$$

The function G (u_1, u_2, $\underline{x}$) can be transformed into the function G (α, t, $\underline{x}$) by substituting the relations $u_1 = \frac{s}{t} \cos \alpha$ and $u_2 = \frac{s}{t} \sin \alpha$.

Taking account of the factor s^2/t^3 which is obtained due to the coordinate transformation in the double integration, we get the frequency distribution

$$p^{++}(\alpha,\ t,\ \underline{x}) = \frac{s^2}{t^3}\ G(u_1 = \frac{s}{t} \cos \alpha,\ u_2 = \frac{s}{t} \sin \alpha,\ \underline{x}) \tag{36}$$

which is recorded by a L2F velocimeter if a velocity distribution according to eq. (35) exists in the flow.

The mean velocity values (see Table 2) calculated with eq. (36) according to

$$\bar{F}(\underline{x}) = \int_0^{2\pi}\int_0^{\infty} F(\alpha,\ t)\ p^{++}(\alpha,\ t,\ \underline{x})\ d\alpha\ dt \tag{37}$$

are of course in agreement with the mean values already known.

Integration of $p^{++}(\alpha,\ t,\ \underline{x})$ according to eq.'s (33) and (34) gives the two marginal distributions which were used for calculating new mean values according to:

$$\bar{F}_R(\underline{x}) = \int_0^{2\pi}\int_0^{\infty} F(\alpha,\ t) P_\alpha(\alpha,\ \underline{x}) P_t(t,\ \underline{x}) d\alpha\ dt \tag{38}$$

As anticipated, the mean velocity values $\bar{F}_R(\underline{x})$ calculated in accordance with eq. (38) differ from the exact values calculated using eq. (37).

The relative error of the components of the mean velocity and the turbulence intensities is plotted for various turbulence intensities and correlation factors in fig. 5. Up to turbulence intensities of 20 %, the relative error of the velocity components is less than 1 % and of the turbulence intensities less than 5 %.

Errors in agreement with these theoretical results occur if, using frequency distributions measured by experimentation, the mean velocity values are calculated in accordance with two different methods. Such small test errors can be tolerated in most applications and particularly in turbomachinery investigations, where the application specific test errors are of the same order of magnitude. This shows that the marginal distributions in α, t coordinates are also sufficient for determining the components of the mean velocity and the turbulence intensities with an accuracy satisfying pracitcal requirements.

Experimental determination of the marginal distributions is as follows:

From a preset (estimated) angle setting α_1, of the plane of the beams, velocity and or time-of-flight measurements are made and the test results $N_{i=1,j}$ stored in the multi-channel analyzer (see fig. 6). Measurement is completed as soon as the particle counter has recorded a preselected number of start events (particles which have passed through the start beam). The angle of the plane of beams is now set to $\alpha_2 = \alpha_1 + \Delta\alpha$ and measurement is continued, with the new measurements $N_{i=2,j}$ being added to the stored data within the multi-channel analyzer. Hence curve 2. At the third angle setting $\alpha_3 = \alpha_1 + 2\Delta\alpha$ and all further $\alpha_m = \alpha_1 + (m-1)\,\Delta\alpha$, the measurements are performed in the same way. After completion at the final angle setting, the distribution N_{tj} is obtained which corresponds to the marginal distribution $P_t(t,\underline{x})$:

$$N_{tj} = \sum_{i=1}^{m} N_{ij} \tag{39}$$

i.e. the *two-dimensional frequency distribution integrated over the angle.*

The areas beneath the individual distributions represent the total number of events recorded per angle setting. These are recorded by means of an additional counter. Now:

$$N_{\alpha i} = \sum_{j=1}^{n} N_{ij} \tag{40}$$

The distribution $N_{\alpha i}$ is the two-dimensional frequency distribution integrated with time and corresponds to the marginal distribution $P_\alpha(\alpha,\underline{x})$ (Representation see fig. 7).

This measurement takes considerably less time than the basically similar measurement process used for determining two-dimensional distributions. The reason is that a very small number of measuring events are sufficient per angle setting. The strong statistical noise of the individual distributions is largely reduced by the integration and even 30 to 50 measured events per angle setting provide very distinct marginal distributions.

In order to get the same accuracy, we need for the representation of a two-dimensional frequency distribution 6 to 8 one-dimensional distributions of the same quality measured at different angle settings, with 500 to 2000 test points within each. Practically, the time for measuring a single one of these distributions is about equal to the time required *for determining the marginal distributions.*

A particular advantage is that during this time for measuring the marginal distribution, which is substantially shorter compared to the total measuring time for two-dimensional distributions, about 20 - 30 different angle settings can be realized. The result - as already mentioned in chapter 2 - is that not only the number of the support points for the time range, but also that for the angular range is sufficiently large to replace by a summation the integration necessary for determining the mean velocity values. Hence interpolation functions are not required in general.

From the test data $N_{\alpha i}$ and N_{tj} we get the marginal distributions necessary for determining the mean velocity, values taking into account the noise level N_{tR}, $N_{\alpha R}$, the error due to the particle integration, and the normalization condition according to:

$$P_t(t_j,\underline{x}) = \frac{N_{tj} - N_{tR}}{s/t} \Big/ \sum_{j=1}^{n} \frac{N_{tj} - N_{tR}}{s/t} \tag{41}$$

and

$$P_\alpha(\alpha_i,\underline{x}) = (N_{\alpha i} - N_{\alpha R}) \Big/ \sum_{i=1}^{m} (N_{\alpha i} - N_{\alpha\cdot}) \tag{42}$$

Both the components of the mean velocity vector and the turbulence intensities are calculated in accordance with:

$$\bar{F}(\underline{x}) = \sum_{i=1}^{m} \sum_{j=1}^{n} F(\alpha_i,t_j)\,P_t(t_j,\underline{x})\,P_\alpha(\alpha_i,\underline{x}) \tag{43}$$

3.2 Influence of flow turbulence on the L2F data rate

The L2F-Velocimeter can only be applied to flows with turbulence levels smaller than 30 %. The reason is that at high turbulence intensities the varying velocities approach to a non negligible extent zero velocity, which can not be measured. Therefore error will occur when mean values have to be evaluated on the basis of an incomplete histogram.

Another, more practical, reason is that the measuring time increases with increasing turbulence intensities and becomes remarkable long at turbulence intensities exceeding 25 %.

The relation between measuring time, flow turbulence and probe volume geometry has been derived by some authors (eg. ref. [13], [65]); however, the gaussian intensity

distribution was not taken into account.

Due to the ratio of beam diameter and beam separation in the L2F probe volume, a certain angle interval is determined within which particles moving in different directions can intercept both laser beams and contribute to the time of flight histogram positively. The probability for successful interception of both beams is not equally distributed within this angle range. Because of the gaussion intensity distribution the signals from particles passing through the centers of the beams have a much higher amplitude than those from particles passing through the margins of the beams (see fis. 8). The intensity distribution described by

$$\frac{I}{I_0} = \frac{4}{\sqrt{2\pi}\,d}\ e^{-\frac{a^2}{2\,(\frac{d}{4})^2}} \tag{44}$$

is a measure of the probability of successful crossings. With the assumption

$$\alpha - \alpha_0 = \text{arc tan } \frac{2a}{S} \approx \frac{2a}{S} \tag{45}$$

and the fact that for flow direction $\alpha = \alpha_0$ the probability must be 1, we can write

$$\frac{I}{I_0} \sim P_I = e^{-\frac{(\alpha - \alpha_0)^2}{2\,\sigma_d^2}} \tag{46}$$

with

$$\sigma_d = \frac{d}{2S} \tag{47}$$

Eq. (33) describes the probability that a turbulent flow has a certain flow direction. In good agreement with real measurement we can assume that this distribution has a gaussian shape. Then the normalized relation is

$$p_\alpha(\alpha) = \frac{1}{\sqrt{2\pi}} \cdot \frac{1}{\sigma_\alpha}\ e^{-\frac{(\alpha - \alpha_0)^2}{2\,\sigma_\alpha^2}} \tag{48}$$

with

$$\sigma_\alpha \approx \text{arc tan } \frac{\sqrt{u_2'^2}}{u_1} \approx \text{arc tan } Tu_2 \approx Tu_2 \approx Tu_1 \approx Tu \tag{49}$$

assuming isentropic turbulence.

Let us assume that the beams plane is just oriented in the direction α_0. Then we get the probability of successful time of flight measurement by

$$P_{succ} = \int_{-\infty}^{+\infty} P_\alpha(\alpha) \cdot P_I\ d\alpha$$

$$= \int_{-\infty}^{+\infty} \frac{1}{\sqrt{2\pi}}\ \frac{1}{\sigma\alpha}\ e^{-\frac{(\alpha - \alpha_0)^2\,(\sigma d^2 + \sigma\alpha^2)}{2 \cdot \sigma\alpha^2 \cdot \sigma d^2}}\ d\alpha$$

$$P_{succ} = \frac{\sigma d}{\sqrt{\sigma d^2 + \sigma\alpha^2}} = (1 + (\frac{2}{d}\ Tu)^2)^{-\frac{1}{2}} \tag{50}$$

The results are shown in fig. 9. The typical L2F probe volume has a beam diameter to beam separation ratio of about 10/350. In this case at 10 % turbulence intensity the probability of successful interception of both beams is only 13 %. When increasing the $\frac{d}{s}$ ratio this value can considerably be improved. However, simultaneously one systematical error does increase which effects the beam spacing. In fig. 10 this situation is shown. A particle passing the beams' centers travels a distance S. But if it tangentially touches the beams as illustrated in the figure the distance travelled is S'. These two distances are related by the equation

$$S' = S \cdot \cos \text{ arc sin } \frac{d}{S} \tag{51}$$

Substituting the beam dimensions the error ε_S was calculated:

$$\varepsilon_S = \frac{S - S'}{S} = 1 - \cos \text{ arc sin } \frac{d}{S} \tag{52}$$

For an error < 1 % the d/s ratio must be smaller than 0.14 ≈ 10/70.

Another limiting condition for the d/s ratio is the lowest measurable turbulence intensity. This effect can be explained with the help of fig. 11. If a laminar flow with no flow angle variations is assumed, the orientation of the beams plane can be selected within a certain angle range which depends on the d/s ratio and measurements can then be taken. A P_α distribution with a certain variance $\sigma d = \frac{d}{2S}$ results indicating a turbulence which does not exist in the flow.

If eq. (45) describes the real p_α distribution which exists in the turbulent flow, then the distribution measured with a L2F-system is:

$$P_{\alpha_i meas} \sim \int_{-\infty}^{+\infty} \frac{1}{\sqrt{2\pi}} \frac{1}{\sigma\alpha} \, e^{-\frac{(\alpha - \alpha_0)^2}{2\sigma\alpha^2}} \cdot e^{-\frac{(\alpha - \alpha_i)}{2\,\sigma d^2}} \, d\alpha \qquad (53)$$

It can be shown that the variance $\sigma_{\alpha\ meas}$ of this new $P_{\alpha_i\ meas}$ distribution is

$$\sigma_{\alpha\ meas} = \sqrt{\sigma_\alpha^2 + \sigma d^2} \qquad (54)$$

From eq. (46) it follows that

$$Tu\ meas = \sqrt{Tu^2 + \left(\frac{d}{2S}\right)^2} \qquad (55)$$

The error ε_T of turbulence measurements is determined by

$$\varepsilon_T = \frac{T\ meas - Tu}{Tu} = \left(1 + \left(\frac{d}{2S\ Tu}\right)^2\right)^{1/2} - 1 \qquad (56)$$

Since the geometrical properties of the probe volume (d/s ratio) are known, one can reduce the measured turbulence intensities to get the true values by means of eq. (55). This can be done with sufficient confidence as long as $\sigma d \leq Tu$. The maximum d/s ratio then is a function of the lowest turbulence intensity to be measured, i.e.

$$\frac{d}{S} \leq 2\ Tu \qquad (57)$$

One gets: $d/S \leq 0.03 \approx \frac{10}{330}$ for $Tu = 1,5\ \%$

and $d/s \leq 0.14 \approx \frac{10}{70}$ for $Tu = 7\ \%$.

When the maximum d/s-values are inserted in eq. (50), the successful two-beam transit reaches

$$P_{succ} = 71\ \%$$

independent of the flow turbulence. From this result, it can be seen that the L2F-measuring time can be minimized when the probe volume geometry is adapted to the flow turbulence (in LD velocimetry the probe volume must be adapted to the maximum mean flow velocity).

3.3 A L2F-System for near-wall application

Due to the high intensity concentration in the probe volume, the L2F-technique is known to be a very powerful tool when applied to near-wall measurements. The minimum distance from a scattering surface perpendicular to the beam axis depends on the system design and is typically about 1 mm.

In the high pressure components of turbomachines the flow channels become very narrow. Very small flow channels can be found in small sized turbochargers of automobiles. The diffuser channel depth there is in the range of a few millimeters. Other areas where measurements are required very close to walls are boundary layer research at hub and casing and investigations of tip clearance effects.

For this kind of application an improved system was developed. The parameters determining the wall proximity x_{min} are

1. the diameter of the beams in the probe volume d. From the formulae published in ref. [8] and [17], one can derive:

$$x_{min} = A \cdot d + B \cdot d^2, \qquad (58)$$

2. the aperture of the receiving optics, the separation of the receiving beam path from the laser beam path, and the quality of the optics used,

3. the arrangement of field stops and apertures

4. and the number of optical elements used especially in the receiving beam path.

In fig. 12 the beam path is shown. The diameter of the beams was chosen to be d = 8 μm. The receiver optics F are diffraction limited. The diameter is 110 mm, the focal length 350 mm. By the field stops H the total receiver aperture is reduced to 70 %. The received scattered light beams are enlarged by the lens J in order to allow proper adjustment of a dual aperture K. Polarization elements L together with specially designed field stops H reduce very strongly the so called cross talk (ref. [45]) between the beams.

In fig. 13 the power received by the photodetectors is plotted against the coordinate z which is zero in the probe volume center. An anodized aluminual plate perpendicular to the optical axis is used as a scattering surface and is moved through the probe volume. The photo detector response compared to the laser beam power in the probe volume demonstrates the high spatial resolution of this device.

Tests were carried out within a very small rectangular flow channel as shown in fig. 14. The channel width along the optical axis of the measuring system was only 3,8 mm. The probe volume was traversed in y- and z-directions. The results of these measurements are shown in fig. 15 and 16, demonstrating the typical flat velocity profile and the thin boundary layer which is due to the strongly accelerated flow (area ratio about 10). The results from both the traverses agree very well, indicating that in spite of the very close wall proximity no significant measuring errors were introduced. The smallest achievable distance from the black painted backwall was 0.1 mm, that approaching the inner window surface was 0.2 mm. The windows were clean and not antireflection-coated. The test air was unseeded laboratory air. When approaching the wall closer than 0,6 - 1 mm the threshold level of the signal discrimination had to be increased and bigger particles were selected for the measurements. The detected power level of scattering particles of different diameter is shown in fig. 13 on the right margin of the plot. Particles of about 0,5 μm in diameter might be detectable at 0,3 mm from the wall.

As an example of the applicability of this measuring device, the results of one of the first measurements within a turbocharger centrifugal compressor rotor of 96 mm outer diameter are shown in fig. 17. Measurements were made at 70 % of the meridional length of the rotor flow channel, the rotational speed was 51,500 rpm, the massflow 0.4 kg/s, the pressure ratio π_t = 1.3. The distribution of the meridional components of flow velocities normalized by the outer diameter circumferential speed shows the rather potential theoretical character of the flow. Only in the region of the casing wall can a breakdown, indicating a starting wake region be observed. Near to the hub the measurements could be made down to a distance of 0.3 mm. To approach the casing window closer than 1 mm, however, was not possible. During these tests the window had to be washed after every measuring cycle. By this washing procedure they did not get as clean as they were originally. We believe that small dirt particles disturb the incident laser beams much more at measurements close to the window than close to the hub. Near the window, the diameter of the laser beams at the window inner surface location is very small - only some 10 μm - and therefore the disturbances caused by a small dirt particle is more severe than in the other case. More sophisticated cleaning procedures are necessary to avoid this restriction.

3.4 The three-dimensional-L2F system

Since the L2F velocimeter measures the magnitude and direction of the flow vector component in the plane perpendicular to the vertical axis, it is considered to be a 2d-measuring system. When two 2d-velocimeters, separated from each other by an angle Ω as shown in fig. 18, measure at the same point within a flow, one gets, two different 2d-velocities from which usually all three components of the total velocity vector can be calculated. To get sufficient resolution the angle Ω between the two devices should be not much smaller than 30 deg. This very ususal method of conducting 3d-measurements requires rather large windows which are very difficult to install in the often strongly curved turbomachinery casings.

In 1980 we found a new method for applying the L2F-principle to 3d-flow analysis. The first prototype based on this method was operated successfully in 1981. It is a compact device by which the transmitted laser beams as well as the received light pass through one collimator lens of nearly the same aperture as used in 2d-L2F systems. Therefore this 3d-method does not require larger windows.

The principle of this method can be explained with the help of fig. 19, where the beam path from the collimator lens on the left side up to the probe volume is schematically drawn. The 3d-system consists basically out of two 2d-L2F systems of different color. The upper pair of parallel lines correspond   centerlines of a blue system, the lower ones to a green system. All four beams are strongly expanded at the collimator location and they are focused down to about 10 μm in diameter at the probe volume location. The beams 1g, 1b and 2g, 2b   intersect in the points A and B respectively. The points A and B and the optical axis determine a reference plane by which the intersection angle 2γ of the blue and the green pair of beams is divided into two equal parts. The two pairs of beams and therefore the reference plane can be rotated around the optical axis (angle φ). In this way the intersection point B moves around a circle while A remains fixed.

Now, let us assume an arbitrary flow vector $\underline{u}$. The reference plane is adjusted by turning the blue and green pairs of beams to such an angle ϕm that the vector $\underline{u}$ lies just within this plane. The straight line x_1 connects the two points A and B and is the intersection line between the reference plane and the plane perpendicular to the optical axis. Line x_1 and the velocity vector $\underline{u}$ include the angle β. The component of the $\underline{u}$ in the direction of the optical axis then is $|\underline{u}| \cdot \sin \beta$.

One necessary supposition for successful L2F-measurements is the fact that the flow vector must lie within the plane of the beams, the measuring plane. In the case shown in fig. 19, the planes of the blue and the green pairs of beams intersect in the straight line x_1. The vector $\underline{u}$ which is in the angle bisector plane is neither in the blue nor in the green measuring plane. Therefore $\underline{u}$ cannot be measured at that orientation ϕ_m of the reference plane even if we assume a sufficient long extension of the probe volume in the direction of the respective pair of beams. A small clockwise turning to ϕ_g will bring $\underline{u}$ into the plane of the green beams and successful measurements occur with the green system and none with the blue. A counter clockwise rotation ϕ_b brings the flow vector into the blue measuring plane and now this system operates and the green one does not.

With the green and the blue systems the same velocity component was measured

$$c_b = c_g \tag{59}$$

however, different angles ϕ_g and ϕ_b were detected. The angle difference is positive increasing when β increases and negative for negative angle β. If β equals zero i.e. $\underline{u}$ is in the direction of x_1, then both the blue and the green system detect the same angle. Considering the geometrical situation the following relation can be derivated

$$\beta = \arctan \frac{\sin\left(\frac{\phi_g - \phi_b}{2}\right)}{\tan \gamma} \tag{60}$$

$$|\underline{u}| = \frac{c_b \ (\text{or } c_g)}{\cos\left(\frac{\phi_g - \phi_b}{2}\right) \cdot \cos \beta} \tag{61}$$

$$\phi = \frac{\phi_g + \phi_b}{2} \tag{62}$$

The angle γ formed by each of the pairs of beams 1g, 2g; 1b, 2b with the optical axis is in practice limited. It is possible, by using spherical optics, to obtain an angle γ of approximately 6.50°. Fig. 20 illustrates the change in the angle difference $\phi_g - \phi_b$ as a function of the angle β, given an angle γ of 6.5°. It will be seen that this curve is substantially linear, so that readily measurable differences $\phi_g - \phi_b$ are obtained even when the angles β are small.

The accuracy in the angle measurement by the L2F method depends to a large extent upon the probe volume dimensions (d/s ratio), upon the number of measurement data gathered, and upon the degree of turbulence in the flow. When turbulence is small (< 5 %) uncertainty in measurement is 0.1° to 0.2° and when turbulence is great (> 10 %) it is 0.3° to 0.5°. Thus, uncertainty in determinating the angle β is 0.4° to 0.7° when turbulence is small, and 1° to 2° when turbulence is great.

The relation between the 3d-velocity-fluctuations and the shape of the measured frequency distribution has not been derived till now, since the consequent further development of this 3d-method was interrupted due to other activities. It also seems to be a very complicated relation and it may take some time until it can be completely understood. In order to overcome this situation, tests can be carried out in flows of known turbulence intensities and from the results, empirical correlations can be deduced which might be useful to give a first estimation about the turbulence intensities.

A complete set of electronics is required for only one of the two systems of different color in order to deliver one flow angle α_g and the velocity component c_g, which equals c_b. For the other system, only the second flow angle α_b must be registered and a much simpler set of electronics is sufficient. Since the differences of the measured angles $\alpha_g - \alpha_b$ are very small, the number of various angle positions of the measuring plane need not be increased significantly over the number needed for 2d-measurements. Therefore the measuring time of the 3d-technique will not be significantly longer.

The optical setup used with the first prototype system is shown in fig. 21. The following numbers indicate: 10 and 11 beam expander, 12 dicroitic beam splitter, 13 $\lambda/4$ plates, 14 and 15 laser line filters, 16 double hole mirror, 17 Rochon prism, 18 image rotator prism, 19 collimator lens, 22 dichroic mirror, 23 mirror, 24 lens, 25 microscope objective, 26 pin hole, 27 laser line filter, 28 Rochon prism, 31,32 photomultiplier.

First measurements made in a flow of selectable, known flow direction have proved in general the 3d-measuring principle. However, the theoretical relation between the measured angle difference $\alpha_g - \alpha_b$ and flow angle β (see eq. 60) was not in good agreement with the measured data as shown in fig. 20. Practically the system was somewhat less sensitive to β angle variations than theoretically predicted. The reasons are not fully understood and require additional future research. It is easy to understand that this method is limited

to β angles smaller than 45° because of the limited axial length of the probe volumes.

A short test period in a transonic axial compressor has demonstrated the applicability of the 3d-L2F techniques to turbomachinery flows. However, also a severe limitation of this first 3d-device was discovered: near-wall measurements were possible only down to distances of about 10 mm. The light scattered from the surfaces of the numerous optical components, especially from the inner surfaces of the image rotator prism, was responsible for this limitation although all parts were antireflection-coated.

At the end of the last year, we restarted the 3d-L2F development work and we believe that the capabilities of the first prototype can be improved in the future.

4. LD/L2F COMPARISON

Although the L2F as well as the LD methods have been well established in experimental fluid flow research, the discussion about their applicability range continues. Comparisons have been carried out which were based more on theoretical considerations than on experimental results (see ref. [8], [13], [17], [42], [72]). Agreement exists today that in general the L2F system has important advantages when applied to small flow channels with high speeds and low turbulence intensities and that the LD-system is superior when the application consists of low speed flows of very high turbulence intensities.

In practice, the flow to be analysed cannot always be clearly classified as being one of the two flow situations considered. Both velocity measurement methods can be operated over rather wide ranges which do overlap to a great deal. Therefore it often becomes a problem of weighting the different properties of the systems in order to decide which is better suited. The results from the following comparison can perhaps be used to simplify such decisions. The comparison is related to the probe volume geometries (see fig. 22) and the properties of the data acquisition electronics.

The LD-velocimeter measures the velocity component perpendicular to the plane of the fringes u, which can be calculated from the signal frequency f_D and the fringe distance S_f according to

$$u = f_D \cdot S_f . \tag{63}$$

With the L2F-Velocimeter the velocity component perpendicular to the beam axis and parallel to the respective α-setting of the plane of the beams can be registered by using the time-of-flight measurements t and the known beam separation S according to

$$u = \frac{S}{t} . \tag{64}$$

The numerous data of both systems usually will be arranged as one or even two dimensional velocity histograms which are the basis for further data reduction and statistical mean value calculation procedures.

The electronics used today for the LD signal analysis, i.e. counter, correlator and frequency tracker can only analyze signals with doppler frequencies lower than f_{Dmax} = 50 MHz. When measurements in turbulent flows are considered, the system must be able to measure at least two times the mean velocity. With eq. (63) and a given value of S_f,

$$\bar{u}_{max} = \frac{f_{Dmax}}{2} \cdot S_f . \tag{65}$$

Furthermore, the LD-signal should exceed a certain length or a minimum number of periods of the amplitude variations, N_{min}, which corresponds to the number of fringes in the probe volume. Frequency shifting, not very usual at high speed applications, is not considered. The diameter d of the LD probe volume is then determined by N_{min} and S_f:

$$d_{min} = S_f \cdot N_{min} \tag{66}$$

From eq. 65 follows the relation which determines the probe volume geometry as a function of $\bar{u}_{max}$

$$d_{min} = 2 \frac{N_{min}}{f_{Dmax}} \bar{u}_{max} \tag{67}$$

For the processing of L2F signal correlators, counters and time to amplitude converters (TAC) in connection with multichannel analyzers can be used. Correlators and counters are digital electronic components with time resolution of 10^{-8} seconds. The TAC is an analog device with a time resolution of about 10^{-10} seconds. A time resolution of 10^{-8} seconds is normally sufficient for accurate measurements even at high speeds. At speed of $\bar{u}$ = 500 m/s and beam separation of S = 0.35 mm the possible velocity error ε is smaller 1 %. This error will only increase with higher speeds and smaller beam separations only by

$$\varepsilon = \frac{\Delta u}{u} \approx \text{time res.} \cdot \frac{\bar{u}}{2S} . \tag{68}$$

Therefore the conclusion can be drawn that L2F probe volume geometry need not be adapted to the highest measurable flow speed.

Such other reasons as the laser power required for small particle detection and the necessity of near-wall measurements determine the diameter of the probe volume, for which about 10 μm is recommended. In order to minimize the measuring time, the d/s-ratio should be based on the flow turbulence according to eq. (50)

$$P_{succ} = (1 + (\frac{2S}{d} Tu)^2)^{-1/2} \tag{69}$$

For comparison we have chosen two LD and two L2F systems, the latter optimized for 40 % successful two beam transits

LD	L2F
1) U_{max} = 500 m/s, $T_u \approx$ 30 %	1) $T_u \approx$ 3 %, $U_{max} \approx$ 500 m/s
S_f = 20 μm	d = 10 μm
d = 500 μm	S = 350 μm
2) U_{max} = 100 m/s, T_u = arbitrary	2) $T_u \approx$ 16 %, $U_{max} \approx$ 500 m/s
S_f = 4 μm	d = 10 μm
d = 100 μm	S = 70 μm

The highest intensity in the probe volumes, taking in account the gaussian intensity distribution of the laser beams, was calculated (see ref. [72]) by using

$$I_{max} = \frac{16 \cdot P_O}{\pi d^2} \qquad\qquad I_{max} = \frac{4 \cdot P_O}{\pi d^2}$$

With the power of the laser used P_O of 1 Watt we get I_{max}

1)	20 W/mm²	12,700 W/mm²
2)	510 W/mm²	

The result is: in order to get an equally good signal quality from the same particle, the first LD-system needs 625 times and the second LD-system 25 times more laser power than the L2F systems.

The power P_Ω scattered from particles of diameter d_p scattered in pure backward direction into collecting optics of a f # of 3.7 related to the laser power P_O is calculated by

$$P_\Omega = P_O \cdot A \cdot I_B \cdot d^{-2} . \tag{70}$$

The probe volume diameter d must be inserted in μm. The value of A equals 1 for L2F- and 4 for LD-systems. The magnitude of I_B depends on the particle diameter. It is plotted in fig. 23. With a fixed probe volume geometry, the power P_Ω is proportional to I_B. As the shape of the curve in fig. 23 indicates:

$$I_B \sim d_p^4 \tag{71}$$

The power ratios P/P_O of the different systems were calculated for some selected particle diameters and shown in table 3.

The ratio of the smallest detectable particle diameters was derived by combining equations (70) and (71), i.e.

$$\frac{d_{p\ LD}}{d_{p\ L2F}} = (\frac{1}{4} (\frac{d_{LD}}{d_{L2F}})^2)^{1/4} . \tag{72}$$

If we assume the smallest detectable diameter for L2F systems to be 0.15 μm (compare with fig. 13) the first LD system will recognize particles of 0.75 μm and the second LD system those of 0.35 μm in diameter.

In several applications, the drawback that LD-velocimeter are restricted to bigger particles can be compensated by the use of high power laser. When the L2F-velocimeter is operated with a power of 0.2 W, the smallest detectable particles are about 0.2 μm in diameter. The second LD system requires a power of 5 W for the detection of the same small particles, while the first LD system needs 125 W which is not available in todays lasers. With a 5 W laser the first LD system will detect only particles bigger than 0.5 μm in diameter.

However, in flow situations where background flare is important, the use of high power laser will not improve the situation, since not only the signal amplitude but also the background flare increases.

The calculation of the background flare often is very difficult. Too many parameters

e.g. the quality of optics, position and design of field stops etc. affect the determination of the measuring positions closest to a wall. The most important parameters, however, are the probe volume diameter and the f-number of the receiver lens used. Calculations were carried out on the basis of relations which were published in ref. [8]. A confocal backscatter optical device with a receiver lens of a f-number of 3,5 was considered. For comparison, all other optical components in the systems considered were kept identical, except for the apertures which were adapted to the respective probe volume diameters. The results in fig. 24 show the related received power scatter from a surface which is moved along the optical axis (x-axis) beginning from the probe volume center. A black anodized aluminum plate was considered to be the scatter surface.

At that position on the axis where the received scattered light power becomes zero the closest possible wall position is determined. We find:

$$x_{min} \sim d \ . \tag{73}$$

These theoretical results agree quite well with the experimental results in the case of the L2F system (see fig. 13) and will also predict quite well the x_{min} value for the LD systems. However, in well designed LD systems another kind of field stop design, from which smaller x_{min} values can be expected, can be more efficient than that considered.

In order to estimate the particle rate, we must consider the volume flow through the probe volume, i.e.

$$\dot{V} = d \cdot l \cdot u \tag{74}$$

with l the axial length of the probe volume. If N_d is the number concentration per unit volume of particles with greater diameters than d, the particle rate R_p follows,

$$R_p = \dot{V} \cdot Nd = d \cdot l \cdot u \cdot N_d \tag{75}$$

In the following the axial probe volume extensions of the different systems were assumed to be:

L2F :   l = 0.3 mm   1) LD :   l =   3 mm

                           2) LD :   l = 0.6 mm

As long as the flow is artificially seeded with particles big enough to be detected by all systems, the data rate R_d, which is

$$R_d = R_p \cdot P_{succ} \tag{76}$$

(see fig. 9), depends only on the probe volume dimensions. Results of example calculations are shown in Table 4. P_{succ} was assumed to be 1 for the LD-system, and takes values according to fig. 9 for the L2F-systems. The other parameters were chosen to be u = 300 m/s and N_d = 1000 particles/cm³. The LD-systems show significantly higher data rates in these kind of flows with particles all bigger than about 0.7 µm. In view of their streamline following behavior, such big particles can be tolerated only in weakly accelerated flows.

In highly accelerated flow particles smaller than 0.5 µm are required. These, however cannot be detected by the first LD system, which is designed for high speed application.

When measurements in unseeded flows are considered, the situation is different. From the Junge distribution of particles in atmospheric air follows

$$Nd \sim d_p^{-4} \tag{77}$$

The smallest detectable particle d_p results from eq. 70 and 71 (LD: A = 4; L2F: A = 1)

$$d_p \sim \sqrt[4]{\frac{d^2}{A}} \tag{78}$$

By inserting eq's 77, 78 and 75 into eq. 76 we get:

$$R_d = P_{succ} \cdot d \cdot l \cdot u \cdot \frac{A}{d^2} \cdot N_{do} \cdot do^2 \tag{79}$$

$$R_d \sim 1/d$$

N_{do} is a reference number concentration, d_o the probe volume diameter of a L2F-reference system. With the assumptions d_o = 10 µm, N_{do} = 3000 particles/cm³ and u = 300 m/s, the data rate was also calculated. Equal powers of the laser used were also assumed.

The results shown in table 5 indicate very similar data rates as long as those L2F-systems optimized to the respective turbulence intensities are considered. If the first L2F system for low turbulence application is used in flows of about 15 % turbulence intensity, the L2F data rate is only 1/10 that of the LD-systems. This is equivalent to a 10 times longer measuring time.

In summary the most important factors which influence the applicability of a velocimeter are:

- The __highest acceleration__ within the flow to be measured. The following behaviour of the particles determines __the greatest particle diameter__ which can be tolerated.

- The __smallest distances__ from surfaces where measurements must be taken.

- The flow turbulence intensity.

- The highest velocity to be measured.

- The number distribution of particles in the flow, seeded or unseeded.

5. CONCLUSION

The development of the L2F-velocimetry was described and an overview of the published literature was given. A procedure for evaluating the flow mean values from the measured data was described and a simplified method was introduced which enables a time-saving measuring procedure. The dependency of the measuring time on the d/s ratio of the L2F probe volume was demonstrated. Two newly developed L2F systems were intoduced: a system well suited for measurements in very narrow flow channels and a 3-dimensional L2F-system. On the basis of probe volume geometry considerations, the different characteristics of two LD- and two L2F systems were compared. In general, the paper has described some new development in L2F velocimetry. There are some other very promising ideas for further development of this technique. One is to replace the two spots with two light sheets in order to get higher data rates, especially in turbulent flows. This system is in development at Onera.

Another exiting idea was introduced by L. Lading (ref. [73]). In his system, each spot is replaced by two spots of different linear polarization. The scattered light from the two double spots is detected by four photodiodes. With this configuration quasi time filtered signals can be obtained, which should enable a much better pulsecenter determination and a reduced background noise.

Future developments will deal with the further extension of the range of applicability of the L2F technik in the field of optical velocimetry.

REFERENCES

[1] Thompson, D.H.: "A Tracer Particle Fluid Velocity Meter Incorporating a Laser". J. Scientific Instruments (J. Phys. E.), Series 2, Vol. 1, 1968, pp. 929-932.

[2] Tanner, L.H.: "A Particle Timing Laser Velocity Meter". Optics and Laser Technology, June 1973, pp. 108-110.

[3] Lading, L: "Analysis of a Laser Correlation Anemometer". Proc. of the 3rd Symp. on Turbulence in Liquids, University of Missouri-Rolla, 1973, pp. 205-219.

[4] Schodl, R.: "Ein neues optisches Geschwindigkeitsmeßverfahren: Laser-Zweistrahlverfahren". DFVLR-Nachrichten 12, 1973, pp. 506-508.

[5] Lading, L.: "Comparing a Laser Doppler Anemometer with a Laser Correlation Anemometer". Proc. of "Conf. on the Engineering Uses of Coherent Optics". Glasgow, 1975, pp. 19-36.

[6] Lading, L.: "The Time-of-Flight Laser Anemometer". AGARD CP 193, Paper 23, 1976.

[7] Smart, A.E.: "Special Problems of Laser Anemometry in Difficult Applications". AGARD Lecture Series No. 90, Aug. 25-26, 1977.

[8] Mayo, W.T., Jr. and Smart, A.E.: "Comparison of Data from the Transit Time Velocimeter with Other Systems Now in Use for Velocity Measurements". 1979, AEDC-TR-79-32, (Final Report on Contract F40500-78-C-0002).

[9] Mayo, W.T., Jr.; Smart, A.E. and Hunt, T.E.: "Laser Transit Anemometer with Microcomputer and Special Digital Electronics: Measurements in Supersonic Flows". 8th ICIASF, held at Naval Postgraduate School, Monterey, CA., Sept. 24-26, 1979.

[10] Bartlett, K.G. and She, C.Y.: "Single Particle Correlated Time-of-Flight Velocimeter for Remote Wind Speed Measurement". Optics Letters, Vol. 1, 1977.

[11] Brown, R.G.W. and Pike, E.R.: "A Combined Laser Doppler and Time of Flight Anemometer". Optics and Laser Techn. 1978, pp. 317-319.

[12] She, C.Y. and Kelley, R.F.: "Scaling Law and Photon-Count Distribution of a Laser Time-of-Flight Velocimeter". J. Opt. Soc. Am. 72, 1982, pp. 365-371.

[13] Brown, R.G.W.: "Velocimetry Signals and Data Reduction in Simulation and Practice". Photon Correlation Techniques, E.O.-Schulz-Du Bois, Springer Verlag, New York,

[14] Ross, M.M.: "Transit Laser Anemometry Data Reduction for Flow in Industrial Turbo-machinery". Proc. of the 3th International Conference on Photon Correlation Techniques in Fluid Mechanics, Churchill College, Cambridge, March 21-23, 1979.

[15] Schodl, R.: "A Laser Dual Beam Method for Flow Measurement in Turbomachines". 1974, ASME-Paper No. 74-GT-159.

[16] Schodl, R.: "Laser-Two-Focus Velocimetry for Use in Aero Engines". Laser Optical Measurement Methods for Aero Engine Research and Development, 1977, AGARD-LS-90, pp. 4.1-4.34.

[17] Schodl, R.: "Development of the Laser Two-Focus Method for Nonintrusive Measurement of Flow Vectors, Particularly in Turbomachines". 1979, ESA-TT-528.

[18] Schodl, R.: "A Laser-Two-Focus Velocimeter for Automatic Flow Vector Measurements in the Rotating Components of Turbomachines". Measurement Methods in Rotating Components of Turbomachinery, ASME, 345 East 47th St., New York, NY 10016, 1980.

[19] Lading, L.: "Spatial Filtering in Laser Anemometry", Proc. of the 4th Symp. on Turbulence in Liquids, University of Missouri-Rolla, 1975.

[20] Schricker, U.: "Optimierung der Meßsignalaufbereitung und der Datensammlung für das Laser-Zwei-Fokus-Geschwindigkeitsmeßverfahren". Mitt. Nr. 79-04, Inst. f. Strahl-antriebe und Turboarbeitsmaschinen, Aachen, 1979.

[21] Schodl, R.; Selbach, H. and Lossau, H.G.: "Comparison of Signal Processing by Correlation and by Pulse-Pair Timing in Laser Dual Focus Velocimetry". Proc. of the Symp. on Long Range and Optical Velocity Measurements, ISL German-French Research Institute, St. Louis, France, Sept. 15-18, 1980.

[22] McDonald, P.W.; Bolt, C.R.; Dunker, R.J. and Weyer, H.B.: "A Comparison between Measured and Computed Flow Fields in a Transonic Compressor Rotor". ASME Transact. Series A, J. Engineering for Power, Vol. 102, No. 4, 1980, pp. 883-891.

[23] Maretto, L. and Troilo, M.: "A Dual Focus Fiber Optic Anemometer for Measurements in Wet Steam". In: "Measuring Techniques in Transonic and Supersonic Flows in Cascades and Turbomachines", Ecole Centrale de Lyon, Ecully, France, 1981.

[24] Fister, W.; Zahn, G. und Adrian, F.W.: "Theoretische und experimentelle Untersuchung an Rückführkanälen hydraulischer Strömungsmaschinen". VDI-Bericht Nr. 424, 1981.

[25] Flügge, H.: "Entwicklung und Anwendung eines Laser-Zwei-Fokus-Meßverfahrens zur Untersuchung von Strömungsgeschwindigkeiten in engen Stabgittern". Thesis University of Bochum, Germany, 1982.

[26] Yasu, S.; Tamaki, T. and Nagano, S.: "Measurements of Flow Field within an Axial Flow Fan Using a Laser Two Focus Velocimeter". Int. Gas Turbine Congress, Tokyo, 1983, Paper No. 83-Tokyo-IGTC-49.

[27] Fottner, L.; Lichtfuss, J.: "Design of Transonic Compressor Cascades for Minimal Shock Losses and Comparison with Test Results". In: Viscous Effects in Turboma-chines", 1983, AGARD CP 351.

[28] Janssens, G.; Labbe, J.: "Two Focus Laser Velocimeter Applied to Measurements in an Experimental Centrifugal Compressor". ICIASF '83 Record, 1983, pp. 251-254.

[29] Hayami, H.; Senoo, Y.; Ueki, H.: "Flow in the Inducer of a Centrifugal Compressor Measured With a Laser Velocimeter". 1984, ASME-paper No. 84-GT-74.

[30] Ross, M.M.: "DFVLR/LEICESTER UNIVERSITY/GEC Laser Anemometer Experiments at the High Speed Aerodynamics Laboratory, Leicester University". GEC Technical Memo No. W/M(2.3) u. 9640, Whetstone, Leicester, England, 1978.

[31] Erdmann, J.C.: "Particle Statistics in Transit Velocimetry". Photon Correlation Techniques, E.O. Schulz Du-Bois, Springer Verlag, New York, 1983, pp. 168-191.

[32] Lading, L.; Skov Jensen, A.; Fog, C.; Andersen, H.: "Time-of-Flight Laser Anemometer for Velocity Measurements in the Atmosphere". Applied Optics 17, 1978, pp. 1486-1488.

[33] Errara, M.P.; Janssens, G.: "Ecoulement Autour de la Soupape d'admission et dans la chambre de combustion d'un moteur diesel". Entropie Nr. 122, 1985.

[34] Kugler, H.P.: "Recent Results in Rocket Exhaust Anemometry". Photon Correlation Techniques in Fluid Mechanics - Proc. from the second International Conference Stockholm, Sweden (June 14-16, 1978), Physica Scripta Vol. 19, Stockholm, Sweden, 1979, pp. 447-452.

[35] Brand, F.L.; Selbach, H.: "Laser Measurements for Kaplan Runners". Water Power and Dam Construction, Febr. 1983.

[36] Furtner, N.; Gröde, E.; Jermann, P.; Durrer, H.; Riedler, J.: "Zweidimensionale Messung des Instationären Strömungsfeldes im und am Rotierenden Laufrad einer Horizontalen Axialmaschine mit dem Laser-Zwei-Fokus-Verfahren". 3. Internat. Seminar: Wasserkraftanlagen, TU Wien, E. Bancher, 1985.

[37] Furtner, N.; Gröde, E.; Bachmann, P.: "Laser-2-Fokus Flow Measurements in the Runner of a Bulb Turbine and Comparison with Calculations". Conference on Water-power, Las Vegas, Sept. 1985.

[38] Steffens, H.D.; Busse, K.H.; Selbach, H.: "Measurements of Particle- and Plasma-Velocity in a Low-Pressure Plasma Plasma Jet". Conf. ISPC-7, Eindhoven, July 1985.

[39] Attis, J.B.; Brown, R.G.W.; Pike, E.R.; Sharpe, P.R.: "Statistical Aspects of Signal Processing in Laser Transit Velocimetry". Conference on Photon Correlation Techniques in Fluid Mechanics, Stanford, California, Aug. 1980.

[40] Schreiber, H.A.: "Supersonic Exit Flow Measurements Downstream of a Compressor Cascade by the Laser-Two-Focus Method". In: Measuring Techniques in Transonic and Supersonic Cascade Flows. Central Electricity Research Labs., UK, 1979, Paper 5.2.

[41] Brown, R.G.W.; Richards, P.H.: "Base Flow Measurements in a Transonic Cascade Using a Laser Transit Anemometer." In: Photon Correlation Techniques in Fluid Mechanics. Poc. 5th Int. Conf. Kiel-Damp, May 1982, Berlin, Springer Verlag, 1983, pp. 192-196.

[42] Brown, R.G.W.; Inman, P.N.: "Direct Comparisons of Laser Doppler, Transit, Hot-Wire Anemometer Measurements in an Axi-Symmetric Jet". In: Tenth Int. Congress on Instrumentation in Aerospace Simulation Facilities. German-French Research Institute (ISL), Saint Louis, France, Sept. 1983, ICIASF '83 Record, pp. 158-164.

[43] Wittig, S.; Eriksen, S.; Schulz, A.; Hassa, C.: "Laser-Doppler- und Laser-Zwei-Focus Messungen in Laminaren und Turbulenten Wandgrenzschichten". VDI-Berichte Nr. 487, 1983, pp. 181-189.

[44] Gill, M.E.; Forster, C.; Elder, R.L.: "Initial Findings During Studies of the Flow within a High Speed Impeller Using a Transit Anemometer". In: Measurement Techniques in Turbomachines, VKI LS 1981-7, 1981.

[45] Smart, A.E.; Wisler, D.C.; Mayo, W.T.,Jr.: "Optical Advances in Laser Transit Anemometry", published by ASME 1980, Measurement Methods in Rotating Components of Turbomachinery, presented at Joint Fluids Engineering Gas Turbine Conference and Products Show, New Orleans, Louisiana, March 10-13, 1980, pp. 149-156.

[46] Smart, A.E.: "Measurements of Velocity Fields within Rotating Blades with a Photon Corre'ator". Proc. Conf. on Photon Correlation Techniques and Fluid Mechanics, Cambridge, England, 1977.

[47] Vouillarmet, A.; Bois, G.: "Comparison between Probe and Laser Measurements at the Outlet of a Centrifugal Impeller". In: Measuring Techniques in Transonic and Supersonic Flows in Cascades and Turbomachines, Ecole Centrale de Lyon, Ecully, France, 1981.

[48] Labbe, J.; Janssens, G.; Avram, F.: "Preliminary Experiments on a Centrifugal Research Compressor Using a Laser-Two-Focus Velocimeter". In: Int. Symp. on Application of Laser Doppler Anemometry to Fluid Mechanics, Lisbon, Portugal, 1982.

[49] Eckardt, D.; Schuster, P.; Schmidt-Eisenlohr, U.: "Flow Field Analysis of Radial and Backswept Centrifugal Compressor Impellers". In: Performance Prediction of Centrifugal Pumps and Compressors, New York, The Americal Society of Mechanical Engineers, 1980, pp. 77-96.

[50] Eckard, D.: "Flow Field Analysis of Radial and Backswept Centrifugal Compressor Impellers". Part 1: Flow Measurements Using a Laser Velocimeter. ASME-Paper 1980 in: Performance Prediction of Centrifugal Pumps and Compressors, 1980.

[51] Eckard, D.: "Detailed Flow Investigations Within a High-Speed Centrifugal Com-pressor Impeller". ASME, J. of Fluids Engineering, Vol. 98, 1976, pp. 390-402.

[52] Dunker, R.J.; Strinning, P.E.; Weyer, H.B.: "Experimental Study of the Flow Field within a Transonic Axial Compressor Rotor by Laser Velocimeter and Comparison with Through Flow Calculations". ASME-paper No. 77-GT-28, 1977.

[53] Dunker, R.; Rechter, H.; Starken, H.; Weyer, H.: "Redesign and Performance Analysis of a Transonic Axial Compressor Stator and Equivalent Plane Cascades with Subsonic Controlled Diffusion Blades". ASME-Journal of Eng. for Gas Turbines and Power, Vol. 106, 1984, pp. 279-287.

[54] Schodl, R.: "Optical Techniques for Turbomachinery Flow Analysis". Nato Institute, Izmir, 1984.

[55]   Krain, H.: "A C D Method for Centrifugal Compressor Impellers". ASME Journal of
        Engineering for Gas Trubines and Power, Vol. 106, 1984, pp. 482-488.

[56]   Krain, H.: "Interdependence of Centrifugal Compressor Blade Geometry and Relative
        Flow Field". ASME-Paper 85-GT-85, 1985.

[57]   Binder, A.; Romey, R.: "Secondary Flow Effects and Mixing of the Wake Behind a
        Turbine Stator". ASME-Journal of Eng. for Power, Vol. 105, No. 1, 1983.

[58]   Binder, A.; Kruse, H.: "Optical Flow Measurements in a Transonic Turbine Stage".
        In: Sixth Int. Symp. on Air Breathing Engines, Paris, June 6-10, 1983,
        Paper 83-7066, New York, AIAA, 1983, pp. 579-584.

[59]   Binder, A.: "Turbulence Production Due to Secondary Vortex Cutting in a Turbine
        Rotor". ASME-Paper 85-GT-584, 1985.

[60]   Janssens, G.; Labbe, J.: "Two Focus Laser Velocimeter Applied to Measurements in
        an Experimental Centrifugal Compressor". Congress on: Instrumentation in Aero-
        space Simulation, ISL/St. Louis, Sep. 1983.

[61]   Kirk, J.A.: "A Dual-Focus Laser Anemometry System For Use on Turbomachinery Test
        Rigs". Royal Aircraft Establishment Technical Report 85001, 1985.

[62]   Fister, W.; Zahn, G.; Tasche, J.: "Theoretical and Experimental Investigations
        About Vaneless Return Channels of Multi-Stage Radial Flow Turbomachines".
        ASME-paper No. 82-GT-209, 1982.

[63]   Miles, J.: "L ser Anemometer Measurements of the Airflow Through a Cascade of
        Steam Turbine Lades". GEC Techn. Memo No W/M(2.2) u. 9661, Whetstone, Leicester,
        1979.

[64]   Fister, W.; Adrian, F.W.: "Experimental Research of Flow in Unbladed and Bladed
        Return Channels of Radial Fluidmachines". 1985, VDI-Report 572.2, Bochum.

[65]   Hayami, H.; Ueki, H.; Senoo, Y.: "Flow Measurement Using a Laser-2-Focus Veloci-
        meter in a High-Pressure Ratio Centrifugal Impeller". Engineering Applications
        of Laser Velocimetry, W.A.M. ASME, Phoenix, 1982.

[66]   Dunker, R.J.: "Flow Measurements in the Stator Row of a Single-Stage Transonic
        Axial Flow Compressor with Controlled Diffusion Stator Blades". In: Viscous
        Effects in Turbomachines, AGARD CP 351, Paper 23, 1983.

[67]   Binder, A.; Förster, W.; Kruse, H.; Rogge, H.: "An Experimental Investigation
        into the Effects of Wakes on the Unsteady Turbine Rotor Flow". ASME-paper No.
        84-GT-178.

[68]   Evans, R.L.: "Turbulence and Unsteadyness Measurements Downstream of a Moving
        Blade Row". ASME Journal of Engineering for Power, Vol. 97, 1974, pp. 131-139.

[69]   Krain, H.: "A Study on Centrifugal Impeller and Diffuser Flow". ASME Jounal of
        Engineering for Power, Vol. 103, No. 4, 1981, pp. 688-697.

[70]   Rotta, J.C.: "Turbulente Strömungen". Teubner, Stuttgart, 1972, pp. 15-25.

[71]   Rasch, D.: "Einführung in die mathematische Statistik". Band 1, VEB, Berlin,
        1976, pp. 147-152.

[72]   Kiok, R.: "Comparative Review of Laser Doppler and Laser-Two-Focus Anemometry
        in View of Turbomachinery Applications". VKI Techn. Memorandum 34, 1984.

[73]   Lading, L.: "Estimating Time and Time-Lag in Time-of-Flight Velocimetry."
        Applied Optics, Vol. 22, No. 22, Nov. 1983, pp. 3637-3643.

	1968	1973		
ref	D.H.Thompson [1]	L.H.Tanner [2]	L.Lading [3]	R.Schodl [4]
Title of the first publication	Tracer Particle Timing Veloc - meter	Particle Timing Laser Veloc - metry	Correlation Anemometry	Laser Dual Beam Method
spot size	40 μm	5 μm	100 μm	12 μm
beam separation	5 mm	1 mm	10 mm	0,4 mm
laser power	He Ne 0,5 mw	He Ne 0,5 and 10 mw	He Ne	Ar and He Ne 100 and 5 mw
optical arrangement	Fig. 1a forward	Fig. 1b forward + backward	Fig. 1c forward	Fig. 1d backward
	no angle turning capability			with angle turning capa- bility
velocity range	20 m/s	> 200 m/s	0 - 5 m/s	$\sim$ 50 m/s
Application	Windtunnel	Windtunnel	two phase flow in simu- lated fluel rod	tube flow Axial com- pressor mentioned
electronics	Oscilloscope	Oscilloscope or Counter	Correlator	statistical data analysis (TAC, MCA)
theoretical considerations	none	none	in much detail	none
angle setting	fixed	fixed	fixed	several angle settings
kind of data	multiple Oscilloscope traces	multiple Oscilloscope traces	one dimensional correlation function	two dimensional probability histogram
results	$\bar{u}$	$\bar{u}$	$\bar{u}$	$\bar{u}, \bar{v}$ Tu, Tv

Table 1: Characteristical data of the first L2F-Velocimeters

$\bar{F}(x)$	$F(\alpha, t)$
$\bar{u}_1$	$\frac{s}{t} \cos \alpha$
$\bar{u}_2$	$\frac{s}{t} \sin \alpha$
$\overline{(u_1 - \bar{u}_1)}^n$	$(\frac{s}{t} \cos \alpha - \bar{u}_1)^n$
$\overline{(u_2 - \bar{u}_2)}^n$	$(\frac{s}{t} \sin \alpha - \bar{u}_2)^n$
$\overline{(u_1 - \bar{u}_1) \cdot (u_2 - \bar{u}_2)}$	$(\frac{s}{t} \cos \alpha - \bar{u}_1)(\frac{s}{t} \sin \alpha - \bar{u}_2)$

Table 2: Velocity functions F(α,t) for various mean velocity values

$P\Omega / Po = A . IB . d^{-2}$					
$dp . (\mu m)^{-1}$	1.0	0.7	0.5	0.3	0.15
LD 1.)	$1,6 . 10^{-7}$	$3,8 . 10^{-8}$	$1,0 . 10^{-8}$	$1,3 . 15^{-9}$	$8,0 . 15^{-11}$
LD 2.)	$4,0 . 10^{-6}$	$1,0 . 10^{-6}$	$2,5 . 10^{-7}$	$3,2 . 10^{-8}$	$2,0 . 10^{-9}$
L 2 F	$1,0 . 10^{-4}$	$2,4 . 10^{-5}$	$6,3 . 10^{-7}$	$8,1 . 10^{-7}$	$5,0 . 10^{-8}$

Table 3: Power scattered from particles of different diameters related to the laser power.

data rate . s	$u = 300$ m/s	$Nd = 1000$ particle . cm^{-3}		
TU	L 2 F		LD	
	1.)	2.)	1.)	2.)
3%	390	830	$4.5 . 10^5$	$1,8 . 10^4$
15%	90	390	$4.5 . 10^5$	$1,8 . 10^4$

Table 4: Data rate as can be observed in flows which were seeded with particle bigger than 0.7 μm in diameter.

data rate . s	$u = 300$ m/s	$Ndo = 3000$ particle . cm^{-3}		
TU	L 2 F		LD	
	1.)	2.)	1.)	2.)
3%	1160	2500	2200	2200
15%	270	1150	2200	2200

Table 5: Data rate as can be observed in flows of unseeded atmospheric air.
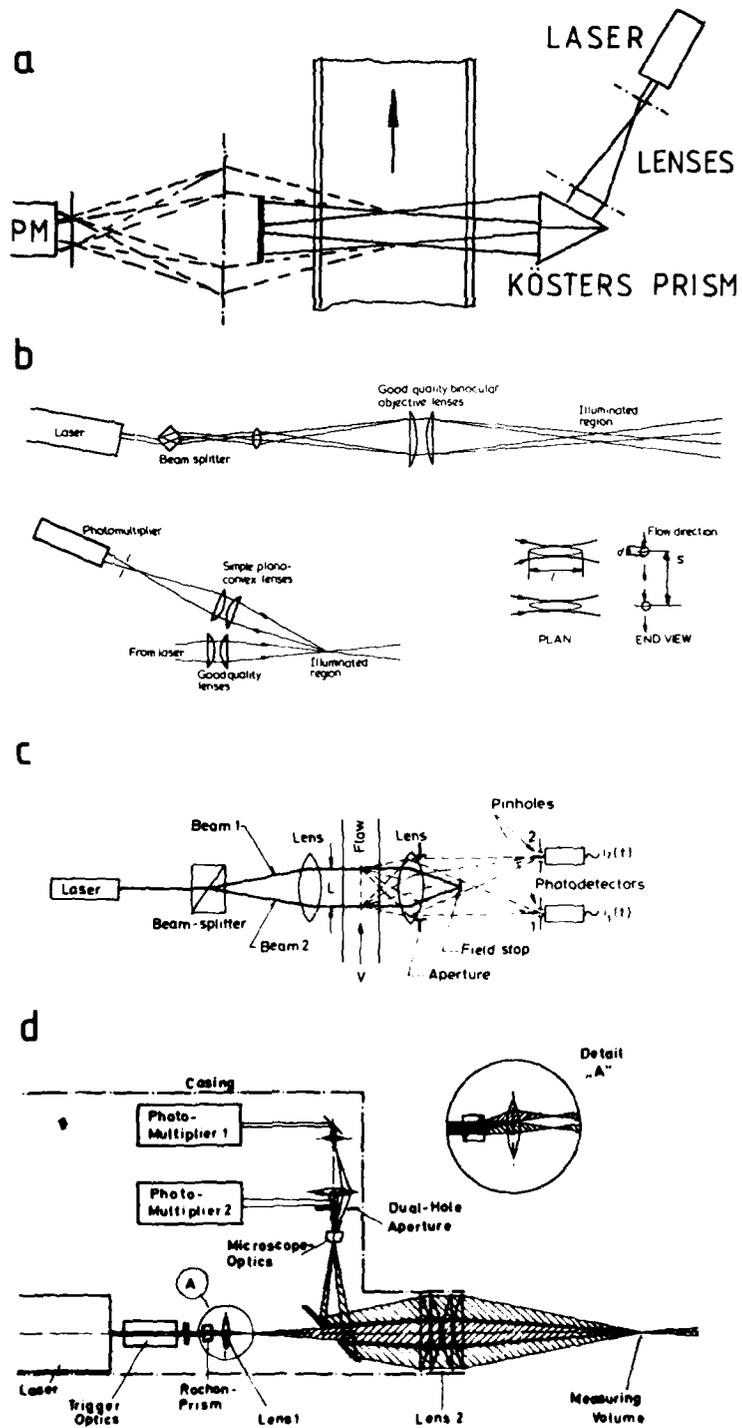
Fig. 1: Schematic layout of various types of L2F-velocimeters
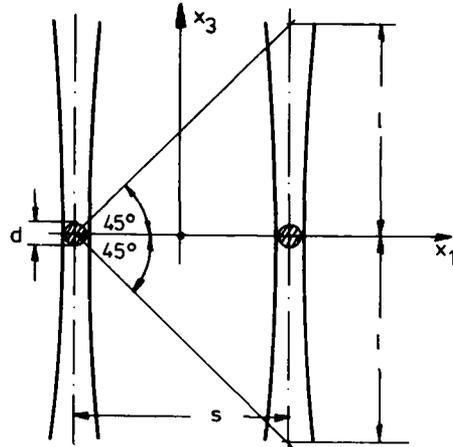
Fig. 2: L2F probe volume (x_1, x_3 plane)
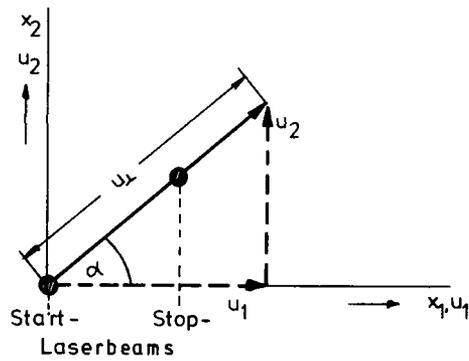
Fig. 3: L2F probe volume (x_1, x_2 plane)
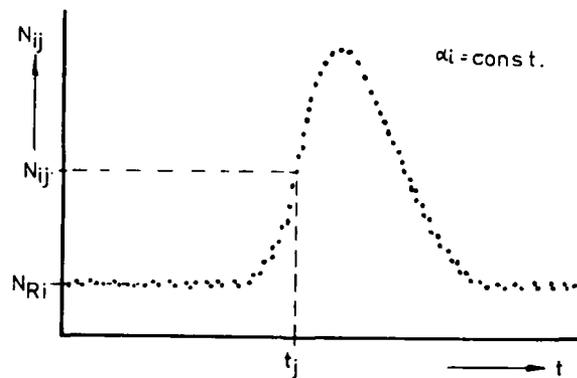
Fig. 4: L2F frequency distribution, measured at an angle setting α_i of the plane of beams.
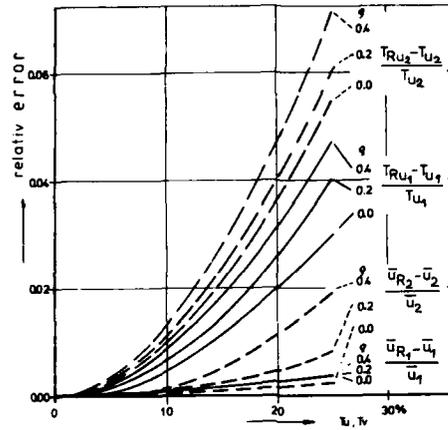
Fig. 5: Relative error of velocity mean values $\overline{F}_R(\underline{x})$ calculated from marginal distributions, plotted against correct mean values $\overline{F}(\underline{x})$
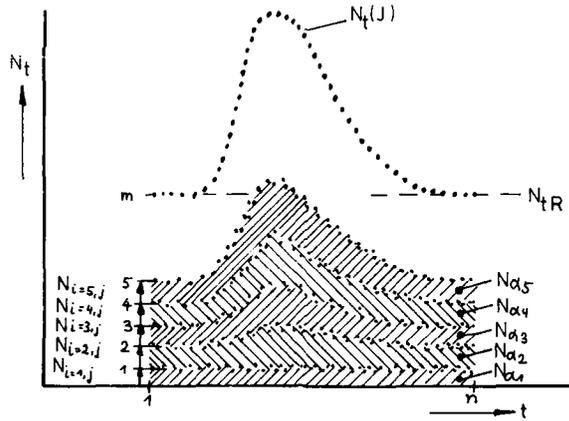
Fig. 6: Measured marginal distribution N_{tj}
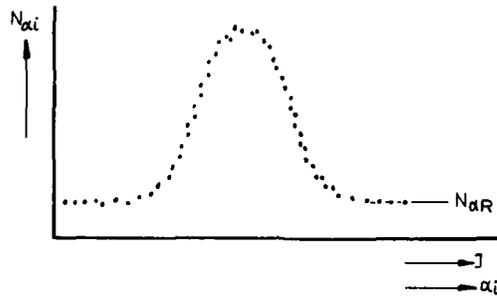
Fig. 7: Measured marginal distribution $N_{\alpha i}$
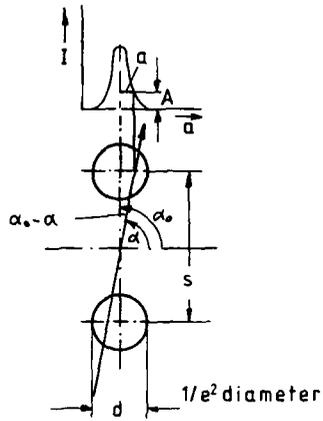
Fig. 8:   Intensity distribution within
           the L2F-probe volume
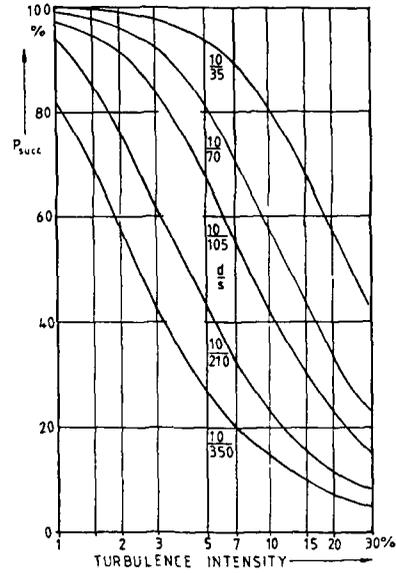
Fig. 9:   Probability of successful
           two beams crossings
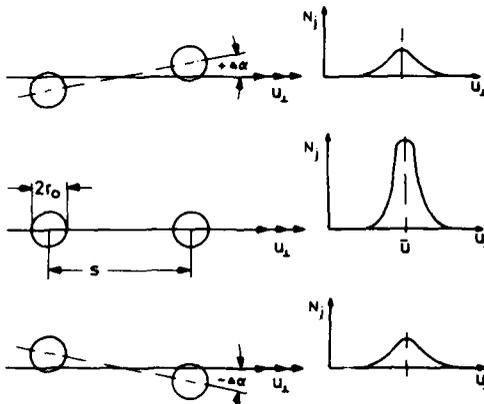
Fig. 11: L2F probe volume (error of turbulence)   Fig. 10: L2F probe volume
                                                              (error of beam separation)
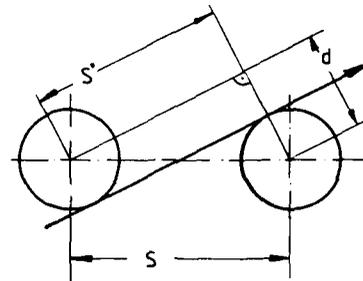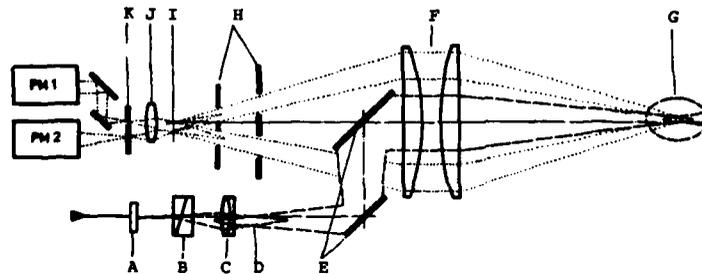
Fig. 12: Beam path of the L2F for close to wall applications
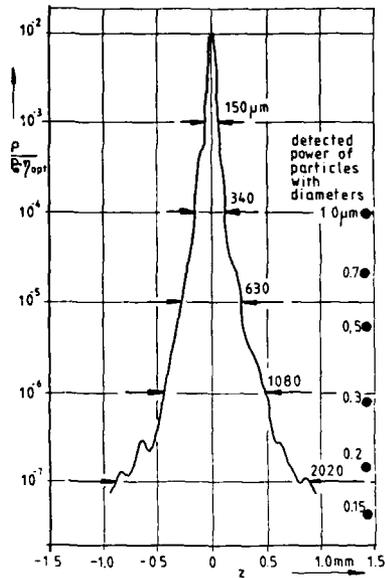
Fig. 13: Intensity detected by the photo
detectors when a scattering
surface was moved about
the axis of the probe volume
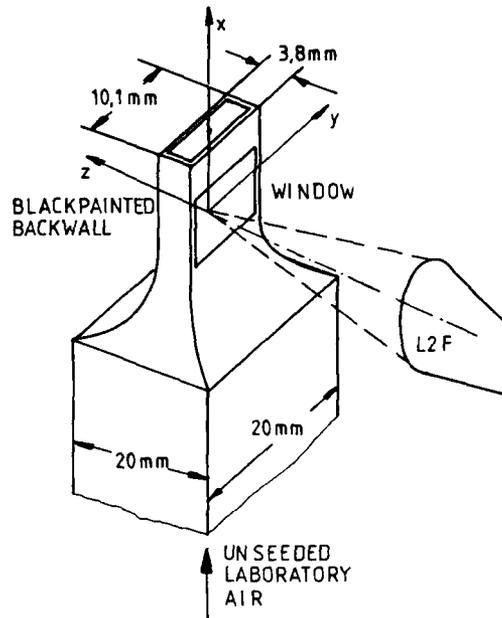
Fig. 14: Test set-up of L2F experiments
in a small flow channel
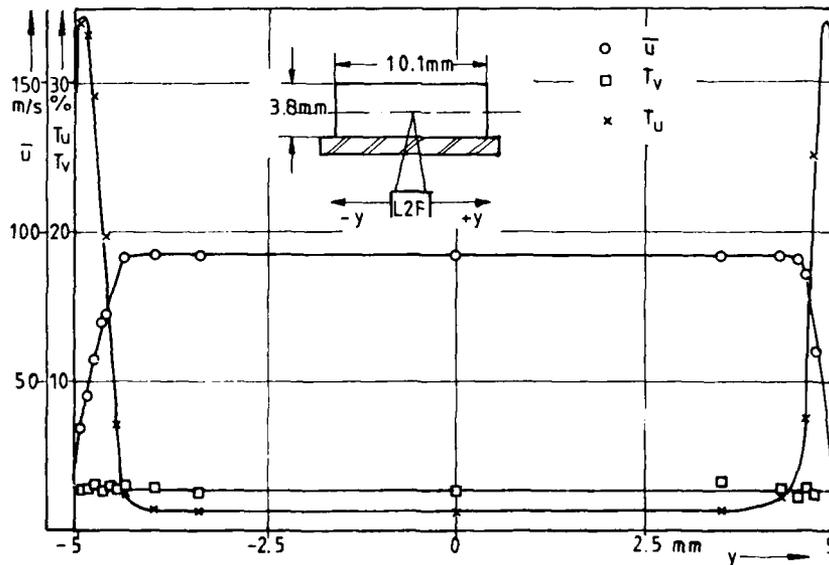
Fig. 15: Results of flow channel measurements (y-traverse)
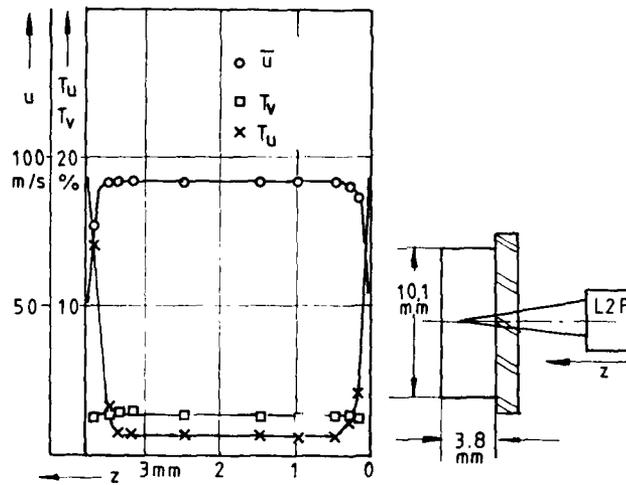
Fig. 16: Results of flow channel measurements (z-traverse)
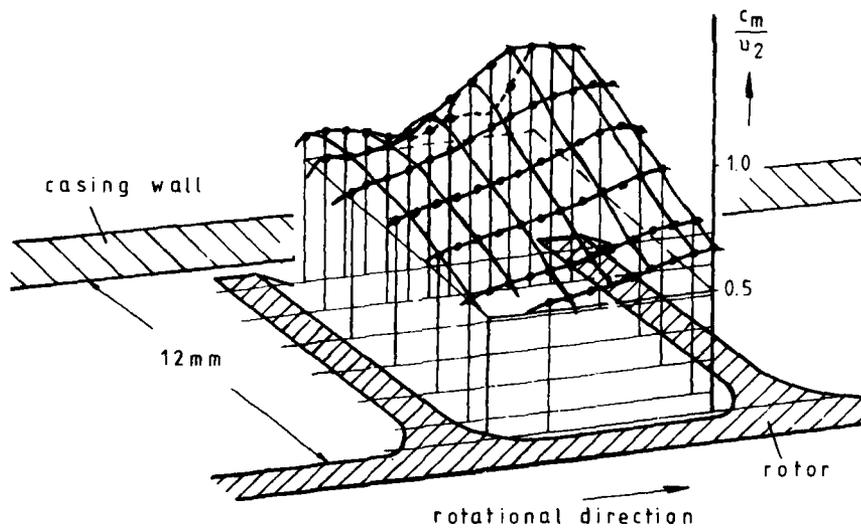
Fig. 17: Results of turbocharger compressor measurements
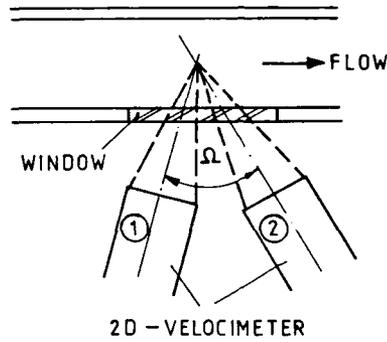
Fig. 18: Usual laser velocimeter arrangement for 3d measurements
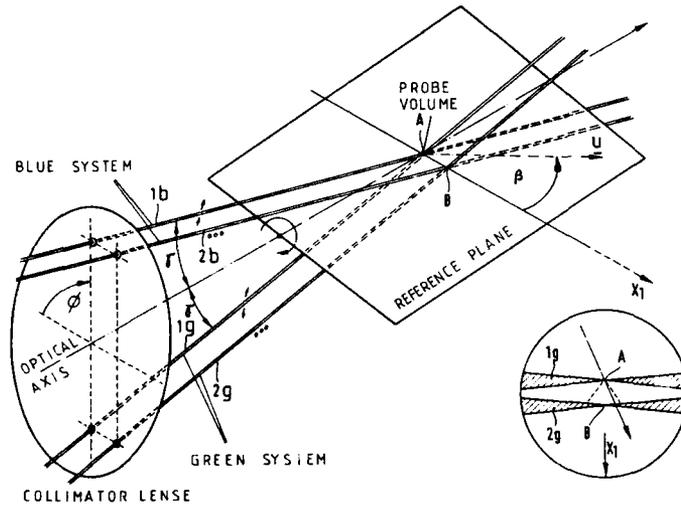
Fig. 19: 3-dimensional L2F principle

Fig. 20: Sensitivy of the 3d-L2F system

Fig. 21: Optical beam path of the 3d-L2F system

Fig. 22: LD- and L2F-probe volume dimensions
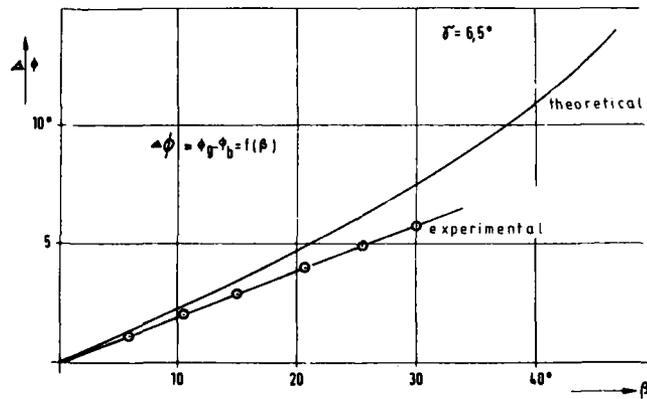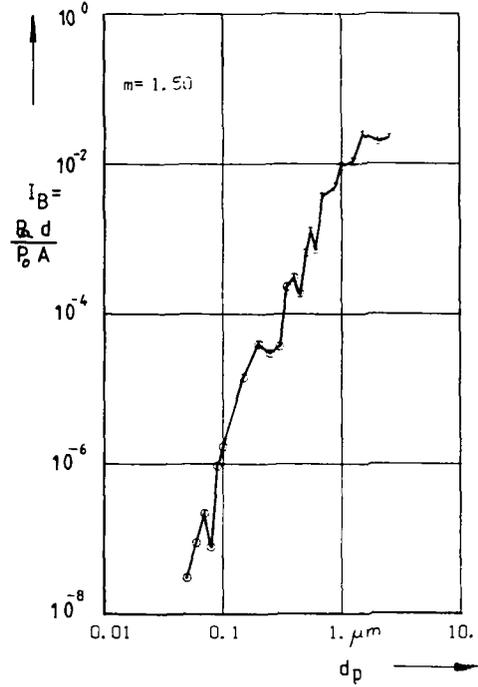
Fig. 23: Scattering intensity as a function of particle diameter (180° backscatter f-number 3.7)
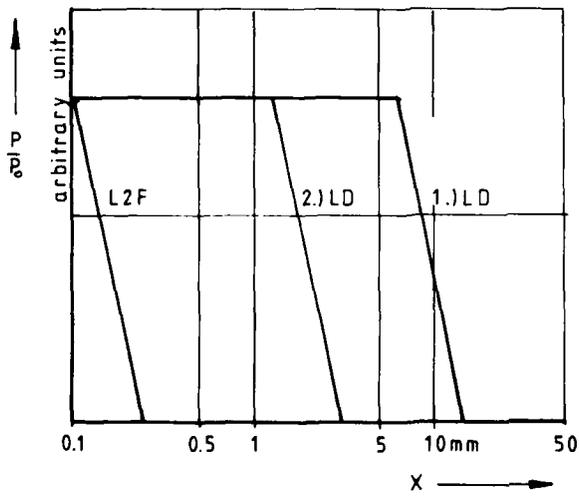
Fig. 24: Received Light power scattered from a surface which was moved along the optical axis

DISCUSSION

R.L.Elder, UK

Would the author like to comment on the various data processors available for Doppler anemometry? Their sensitivity and speed are different, and the choice is important for a particular application.

Author's Reply

The LD-L2F comparison is based on considerations about the probe volume geometry only. If optical systems with equal sensitivity of the receiving optics are considered, the comparative data are related to the signal amplitude of photodetectors of the respective systems. The different SNR (Signal to Noise Ratio) of the different LD electronics used for the signal processing have not been taken into account in this comparison.

P.Hutchinson, UK

What is the dependence and magnitude of the incorrect count number (arising from different particles passing through the two beams) on the turbulence intensity?

Author's Reply

The incorrect count numbers can be identified by a statistical data analysis. By this way of processing, the incorrect count numbers generate a base line in the measured probability histogram. This base line data will be subtracted from the histogram data before the data are used for further reduction. Therefore the incorrect count numbers will not affect the turbulence intensity or any other kind of velocity mean values. The calculation of probability of successful two beams transits does not take into account these incorrect count numbers.

W.G.Alwang, US

How sensitive is the L2F system to the ability to maintain diffraction limited imaging in practical systems, i.e. in the quality of optic, windows, gas density fluctuations, etc...?

Author's Reply

There are no doubts that L2F systems are more sensitive against disturbances in the optical beam path than LD systems. The reason is that the laser beam is focused down in the probe volume to only 10 μm; LD systems have much bigger probe volume diameters. Therefore all optical components including the casing window must be of high quality.

B.Lakshminarayana, US

The 3D system you described is a very exciting system.

(1) Did you take any measurements in an axial or centrifugal flow compressor, including radial velocities?

(2) What is the smallest radial velocity component you can measure?

(3) Did you compare your L2F data with hot-wire data?

Author's Reply

(1) We checked this 3D prototype at first on a free jet, as I told you in my paper. We also did measurements in an axial transonic compressor. The main drawback we found was that we could not approach the window or the hub at a distance less than 10 or 15 mm due to strong background flare problems. Further developments are necessary.

(2) This instrument does not measure a velocity component, but provides data on angles. Depending on the turbulence intensity, for low turbulence levels an uncertainty of 0.2° is obtained and in worse situations 0.5° or 1° which anyway corresponds to low radial components.

(3) We have no experience with hot wires.

A.Eckbreth, US

How serious, typically, are refractive effects which cause steering of the laser beams and result in a variable (and unknown) separation of the laser foci?

Author's Reply

Refractive effects in the beam path will surely have effects on the position of the probe volume. However, the axes of the two converging laser beams are so close together that disturbances do affect both beams in the same way, so that the beams separation is nearly unaffected.

SEEDING GAS FLOWS FOR LASER ANEMOMETRY

A. Melling
School of Mechanical Engineering
Cranfield Institute of Technology
Cranfield, Bedford MK43 0AL, U.K.

SUMMARY

This paper reviews the seeding of gas flows for laser anemometry. The specification and determination of the size of seeding particles to ensure both an adequate response to velocity changes of the flowing medium and a sufficient light scattering capability are examined critically. A compromise between these conflicting criteria is generally given as an upper limit on acceptable particle size, expressed as the diameter of an "equivalent" spherical particle. Problems arise in defining and quantifying this equivalent diameter, generating particles of suitable size from a given material, measuring the particle size distribution at the generator exit, and determining the size distribution actually seen by the laser anemometer. Recommendations are made for particle generators, sizing methods, and interpreting the significance of quoted particle distributions for laser anemometry purposes.

LIST OF SYMBOLS

a	speed of sound	u	velocity fluctuation
d_p	particle diameter	$\hat{v}$	slip velocity
c^p	parameter in Eq.(2.5)	V	visibility
C_D	drag coefficient		
f	focal length	α	scattering parameter in Eq.(4.2)
$E(\omega)$	energy spectrum	λ	wavelength
I, i	intensity	$\lambda*$	fringe spacing
Kn	Knudsen number	μ	viscosity
ℓ	mean free path	ω	turbulence frequency
m	index of refraction	Ω	solid angle
Ma	Mach number	ρ	density
$p(d_p)$	size distribution function	η	scattering angle
r	radius	ϕ	phase angle
Re	Reynolds number		
St	Stokes number	**Subscripts**	
t	time	f	fluid
$\hat{U}$	instantaneous velocity	p	particle
		t	turbulence

1. INTRODUCTION

Satisfactory flow tracking capability of scattering particles is essential for reliable velocity measurements with laser anemometry. The requirements for scattering particles in this respect are more severe for gas flows than for liquid flows, because the density ratio of suspended particles is much higher. Because the concentration of naturally occurring particles of suitable size for adequate scattering intensity is typically very small in gases, seeding of additional scatterers into the flow is almost always essential.

Early work on seeding gas flows for laser anemometry was reviewed in references 1 and 2. Attention was given to the specification of the maximum size of scattering particles as determined by the aerodynamic behaviour of spherical particles, and methods for generating suitable aerosol particles and for determining their size were suggested. Reference 3 took account of improvements in aerosol generators and sizing methods specifically for laser anemometry. Other aerosol generators and sizing techniques with specifications on particle size near those determined by aerodynamic size criteria were also considered, where modification to acceptable specifications appeared possible.

The present paper updates the preceding reviews and considers some remaining deficiencies in the tools available, particularly with regard to non-spherical particles. Section 2 discusses the determination of a limiting size on the basis of the aerodynamic behaviour of aerosol particles. Section 3 deals with methods of particle generation. Section 4 considers sizing techniques. Conclusions are given in Section 5.

2. SPECIFICATION OF SCATTERING PARTICLES

2.1 Introduction

In gases the concentration of naturally occurring particles which are large enough to scatter sufficiently strongly for useful laser anemometry signals is in most cases unacceptably low. It is necessary to seed additional scattering particles into the flow, and for these the question arises, whether they are small enough to follow the gas flow faithfully. The aerodynamic behaviour of a particle depends on its inertia and the drag force; the light scattering behaviour depends on the particle shape, surface area and refractive index. A common parameter determining both the aerodynamic and optical characteristics of the particle is its size or diameter.

A size requirement will be specified according to the maximum diameter of particles which will follow the local, time-varying fluid velocity within a prescribed tolerance. The motion of particles suspended in a moving fluid is influenced by their shape and size, the relative density of particle and fluid, the fluid viscosity, the number of particles per unit volume, and body forces. All analyses of the particle motion assume spherical particles. This is a good assumption for liquid droplets, but poor for most solid particles which tend to be irregular aggregates of smaller particles. Interference between particles is also neglected, thus placing a limit on the maximum concentration to avoid collisions between particles under the influence of aerodynamic or electrostatic forces. The highest scattering particle concentrations achieved by artificial seeding, e.g. 10^{13} to 10^{15} m^{-3}, are, however, too low for such interference effects. Centrifugal body forces may be important, e.g. in turbomachinery.

2.2 Particle Motion Equation

The most important influences on the particle motion are the particle diameter d_p, the particle and fluid densities ρ_p and ρ_f, and the viscosity μ. An analysis of the relative motion of particle and fluid (reference 4) yields the equation

$$\frac{\pi d_p^3}{6} \rho_p \frac{d\hat{U}_p}{dt} = -3\pi\mu d_p \hat{V} + \frac{\pi d_p^3}{6} \rho_f \frac{d\hat{U}_f}{dt} - \frac{1}{2}\frac{\pi d_p^3}{6} \rho_f \frac{d\hat{V}}{dt} - \frac{3}{2} d_p^2 \sqrt{\pi\mu\rho_f} \int_{t_0}^{t} \frac{d\hat{V}}{d\xi} \frac{d\xi}{\sqrt{t-\xi}} \qquad (2.1)$$

where t is the time, $\hat{U}$ and $\hat{U}_f$ are the instantaneous particle and fluid velocities, and $\hat{V} = \hat{U}_p - \hat{U}_f$ is the instantaneous relative velocity. The first two terms represent the force necessary to accelerate the sphere, and the viscous drag force given by Stokes' law. Acceleration of the fluid leads to a pressure gradient force in the third term. The fourth term is the resistance of an inviscid fluid to acceleration of the sphere. The first, third and fourth terms combined give an accelerating force equivalent to that on a sphere whose mass is increased by half the mass of the displaced fluid. The last term represents the drag force arising from non-steady flow. External forces have been neglected.

Stokes' drag law applies to creeping flow past a sphere, when the Reynolds number based on the relative velocity, i.e.

$$Re_p = \frac{\rho_f |\hat{V}| d_p}{\mu} \qquad (2.2)$$

is less than 1. Alternative drag laws are necessary in compressible flows or at low fluid densities, for example. An additional assumption in Eq. (2.1) is the existence of homogeneous, time-invariant turbulence. The particles are supposed also to be smaller than the turbulence microscale and to be surrounded always by the same fluid molecules; a large relative displacement of particles and fluid is thus not admissible as a solution.

For gas flows $\rho_p/\rho_f \gg 1$, so that Eq. (2.1) can be simplified to

$$\frac{dU_p}{dt} = \frac{18\mu}{\rho_p d_p^2} (U_f - U_p). \qquad (2.3)$$

More generally, a vector equation can be written as

$$\frac{d\vec{U}_p}{dt} = \frac{C}{24} Re_p \, C_D \, (\vec{U}_f - \vec{U}_p) \qquad (2.4)$$

where $C = \frac{18\mu}{\rho_p d_p^2}$ \qquad (2.5)

C_D is a drag coefficient which depends on the Reynolds number Re_p, the Mach number $Ma_p = V/a$ and the Knudsen number $Kn_p = \lambda/d_p$; a is the speed of sound and λ is the molecular mean free path.

2.3 Particle Motion in Turbulent Subsonic Flow

Chao (reference 5) solved Eq. (2.1) for turbulent subsonic flow by relating the kinetic energies of particle velocity fluctuations $\overline{u_p^2}$ and fluid velocity fluctuations $\overline{u_f^2}$ with the energy spectrum $E(\omega)$ of turbulent fluid fluctuations of radian frequency ω. When $\rho_p/\rho_f \gg 1$, the relation takes the form

$$\frac{\overline{u_p^2}}{\overline{u_f^2}} = \int_0^\infty \frac{E(\omega)}{1 + \left(\frac{\omega}{C}\right)^2} d\omega \qquad (2.6)$$

Eq. (2.6) indicates that the higher frequencies of the turbulent fluid motion are attenuated in the energy spectrum of the particle motion. In reference 6, this equation was solved for a theoretical turbulent flow with the following energy spectrum:

$$E(\omega) = \frac{2}{\pi\omega_t} \frac{1}{1 + \frac{\omega^2}{\omega_t^2}} \qquad (2.7)$$

which approximates a measured turbulence energy spectrum in pipe flow. Combination of Eq. (2.6) and (2.7) yields the ratio

$$\frac{\overline{u_p^2}}{\overline{u_f^2}} = \frac{1}{1 + \frac{\omega_t}{C}} \qquad (2.8)$$

plotted in figure 1 for various values of C. Small values of C correspond to large particles of high density and are seen to result in poor response to the turbulent fluctuations.

Instead of solving for time-mean quantities, the particle response can be quantified by the instantaneous amplitude ratio $|\hat{U}p/\hat{U}_f|$ and the instantaneous phase angle ϕ of the relative motion of particle and fluid as in reference 7.

By specifying a limit of, say, 0.99 for $\overline{u_p^2}/\overline{u_f^2}$ or $|\theta_p/\theta_f|$, it is possible to determine the maximum allowable particle diameter for a given density ratio ρ_p/ρ_f. Such calculations, e.g. references 1 and 2, indicate an upper limit of 1 μm diameter for seeding particles in gases, when the density ratio is of order 1000. This "rule of thumb" has frequently been accepted without analysing the particle motion in the particular flow under study, although its validity often merits closer examination.

2.4 Particle Motion in Supersonic Flow

In supersonic flow it is important to determine the velocity lag of particles during strong accelerations e.g. through a supersonic nozzle (references 8, 9), a normal shock (reference 10) or an oblique shock (reference 11). The drag coefficient C_D in Eq. (2.4) is specified empirically or semi-empirically, e.g. references 6, 8.

An example of the particle motion across an oblique shock is shown in figure 2 for a 10 degree wedge with an upstream Mach number of 1.5. Eq. (2.4) was solved using the drag law indicated on the figure. Figure 2 shows the distance downstream from the shock necessary for particles of given size to decelerate to the gas velocity. 1 μm particles require a 12 mm relaxation distance. Only particles smaller than about 0.3 μm achieve rapid recovery after the shock.

The rule of thumb for maximum particle diameter in supersonic flow is about 0.3 μm from such calculations. Shock tube experiments (reference 12) support this figure: dust particles were accelerated from rest to nearly 200 m/s in about 4 μs.

2.5 Further Studies of Particle Motion

Calculations of particle dynamics as in sections 2.3 and 2.4 provide guidelines about the size of spherical particles suitable for laser anemometry scatterers. Such calculations could, of course, be made for specific flow configurations and density ratios, e.g. in a cascade of turbine aerofoils (references 13, 14). For more extensive analysis of particle dynamic behaviour, reference should be made to studies of solid particle trajectories through turbomachinery, e.g. references 15 to 17, concerned with erosion by particles impinging on the blades.

Solid particles are generally non-spherical unless formed by freezing, and are often loosely packed agglomerates of smaller grains. A realistic geometrical model for such agglomerates would probably not be feasible, and the formulation of a drag coefficient having general utility is unlikely to be achieved. It would, however, be interesting to see whether trends for the effect of non-sphericity on the drag coefficient could be established from simple cases e.g. two or more spheres of equal diameter rigidly in contact. Estimates of the maximum sphere diameter for velocity tracking of a flow within a given tolerance are in any case conservative when based on Stokes drag. It is thus possible that the rules of thumb of sections 2.3 and 2.4 could be relaxed for highly non-spherical particles.

Two areas of current research interest deserve attention with regard to particles.
● For laser anemometry in two-phase flows, it is necessary to determine the velocity of both the continuous phase and the particulate or bubbly phase. The analysis of deposition or of particle migration in a combined aerodynamic and magnetic field, for example, requires the determination of a size-velocity correlation with the particle shape as a possible additional important factor.
● In mixing studies, both velocity and a scalar property e.g. temperature or species concentration are to be determined, by combining laser anemometry with methods such as Raman spectroscopy (reference 18), Mie scattering (reference 19) or CARS (reference 20).

3. AEROSOL GENERATION

3.1 Introduction

Specifications for aerosol generators for laser anemometry in gases are exacting:
● maximum particle diameter as determined in section 2
● ideally monodisperse aerosol (uniformly sized particles)
● aerosol concentration greater than 10 particle/m^3 for adequate signal rates
● stable delivery rate.

The techniques of air blast atomization (liquids or suspensions) and fluidization (solids in powder form) have proved to be the best (but by no means easy) methods to meet the above requirements. Other methods include condensation generators, ultrasonic atomizers (reference 21) and chemical reactions. Condensation generators such as that of Sinclair and La Mer (see reference 22) produce highly monodisperse aerosols of fine particles, but the rate of particle generation is low. Chemical reactions tend to provide a very unsteady rate of particle generation. The reaction between titanium tetrachloride and water vapour in an air stream has, however, been used with some success (reference 23) to produce titanium dioxide particles in flames. For solid particles, a rotating brush generator is available: a densely packed powder in a cylinder is pushed by a piston steadily towards a rotating brush which scrapes particles off the top of the charge into an air stream blown through the brush.

3.2 Generation of Liquid Aerosol Particles
Simple Air Blast Atomiser

The characteristics of a variety of compressed air nebulizers are compared in reference 24. A

simple design for low velocity LDA experiments is shown in figure 3. A high velocity stream of gas from nozzle B shears a thin liquid film from tube A, causing it to rupture into droplets. The small droplets in the spray follow the gas flow out of the atomizer, but large droplets tend to strike the walls of the atomizer chamber and drain back into the reservoir. Atomizers of this design work satisfactorily with silicone oil, seeding air flows to concentrations of over 10^{10} particles/m^3, with a mean diameter of about 2 µm.

Laskin Atomizer

Detailed constructional and operational information for the Laskin atomizer has been given in reference 25. In this atomizer (figure 4) air is blown through 4 holes in a tube into the liquid to be atomized. These four jets draw liquid through vertical holes drilled in a ring as shown, to produce air bubbles containing finely atomized droplets. As the bubbles rise to the surface, the droplets are released and carried away in the air stream. An impactor downstream of the generator is desirable to remove the larger atomized droplets. The flow rate can be increased by the simple expedient of combining several tubes in the same tank.

Avantages and Disadvantages of Atomized Droplets

Advantages:
- steady rate of production
- spherical particles
- particle diameter can be regulated by driving pressure
- continous atomizer operation for many hours without maintenance

Disadvantages:
- polydisperse aerosol
- droplets not useful at high temperatures
- droplets deposited on test section windows coalesce into films which distort the laser beams.

3.3 Generation of Solid Aerosol Particles
Atomization of Suspensions or Solutions

If solid particles are suspended or dissolved in a liquid they may be dispersed by atomization. Suspensions have been used to seed flows in rotating machines with PVC particles (references 26, 27), flames with aluminium oxide (reference 28) and supersonic flow (reference 29). Atomization of suspensions allows generation of particles at a steady flow rate and concentration. In atomizing a suspension of monodisperse solid particles, the droplets are initially polydisperse; but the aerosol formed after evaporation of the suspending liquid will be monodisperse if no droplet contains more than one particle. To minimize the probability of obtaining two or more particles in one droplet, very dilute suspensions must be used; since most of the resulting droplets are empty, the resulting aerosol concentration is thus very low. If, however, the original solid particles are several times smaller in diameter than the maximum desired particle, higher suspension concentrations may be employed since most coagulates will remain smaller than the limiting diameter.

In generating solid particles from solutions, the particle diameter wi'l depend on the initial droplet diameter and the concentration of the solution. Thus a polydisperse droplet distribution will yield a polydisperse solid particle distribution. Difficulties in atomizing very small droplets are, however, avoided because solid particles smaller than 1 µm may be formed by evaporation of droplets of much greater volume.

Fluidized Beds

Fluidized beds have been used frequently in laser anemometry experiments where solid particles are required. In its basic form (figure 5), a fluidized bed contains a powdered material held in suspension by an upward flow of gas. Some of the smaller particles from the bed are entrained by the gas stream while larger particles which are temporarily ejected from the surface of the bed fall back again under gravitational force. In practice, satisfactory and steady operation of small fluidized beds is very difficult to achieve. The ease of dispersion depends on the particle shape and hardness, and on the humidity of the gas and powder: smooth, hard, dry particles fluidize more easily than rough, soft, moist particles, although extreme dryness can inhibit dispersion because of electrostatic forces. Fluidized beds allow a high production rate and concentration. Particles produced, however, are irregular in shape and size as a result of agglomeration. The resulting mean particle diameter may be much larger than that of the original particles forming the bed. The delivery rate is generally unsteady, especially at low flow rates. Short term unsteadiness arises from air pockets in the bed which rise to the surface and then burst, discharging a high concentration of particles. Long term unsteadiness is caused by intermittent partial blockage of flow passages, or by the formation of large lumps in the bed. The design of fluidized beds tends to be a matter of experience, but reference 30 provides some useful guidance.

In an effort to improve on the conventional fluidized bed, especially with regard to steadiness of operation, a kind of two-phase bed has been developed (references 31, 32), containing a mixture of beads and the powder to be dispersed. The beads, e.g. glass or bronze, have a diameter between 100 and 200 µm, and are much larger than the other particles which distribute themselves over the surface of the beads. Grinding between the beads breaks up agglomerates, and the relatively free air flow in the spaces between the beads minimizes the likelihood of large air bubbles. Fine particles are freed from the bead surfaces in regions where the air velocity is locally high and are carried away by the air stream. The aerosol concentration increases with the air flow and the powder concentration in the bed.

Another alternative to the normal fluidized bed is the cyclone aerosol generator used (reference 33) to seed flames with Al$_2$O$_3$ powder of 0.1 to 1.0 µm basic particle diameter. In this generator a swirling air flow similar to that in a normal cyclone is used to entrain powder from the bottom of the

cyclone cylinder. For concentrations exceeding about 10^9 particles/m^3, the rms unsteadiness in particle concentrations measured over successive 10ms intervals was only 6% of the mean concentration.

Advantages and Disadvantages of Solid Particles

Advantages:
* metal oxides are suitable for seeding high temperature flows
* solid particles deposited on test section windows cause little disturbance until the attenuation becomes excessive.

Disadvantages:
* polydisperse aerosol
* unsteady flow rate and aerosol concentration with most generators
* difficult to seed flows where static pressure exceeds external pressure
* most generators require frequent maintenance.

4. PARTICLE SIZE DETERMINATION

4.1. Introduction

To ensure that the scattering particles present in a flow are small enough to follow the fluid motion using the criteria of section 2, the particle size distribution function $p(d_p)$ should be known. The size distribution should ideally be measured in the flow where the velocity measurements are to be made. Alternatively a sample could be withdrawn from the flow through an isokinetic probe. Size distributions measured at the generator exit will not indicate any changes between the generator and the measurement volume through agglomeration or deposition of particles.

Particle sizing techniques which use properties of the Doppler burst signal are difficult and/or expensive to implement (section 4.5) Alternative methods applicable to the size range 0.1 to 3 μm which is of most interest in laser anemometry include microscopic, aerodynamic and optical techniques (sections 4.2 to 4.4). Particle size normally refers to the diameter of an aerodynamically or optically "equivalent" sphere.

4.2 Particle Sizing by Photomicrogrphy

Since direct photography of particles is limited to diameters exceeding 5 μm, smaller particles must be collected from the flow on to a substrate for photomicrography. To ensure that the method of collection does not bias the size distribution, particles must be sampled from the flow isokinetically. A probe incorporating a removable grid of very fine copper whiskers for collecting sub-micron particles (figure 6) is described in references 6 and 34.

Unlike most other methods, a photographic record provides information on the particle shape as well as its size. Interpretation of such photographs is tedious, however. Manual sizing by comparison with a mask is likely to lead to biased estimates of particle diameter. Even with automatic sizing of spherical particles, several thousand particles must be registered to minimize uncertainty in the size distribution.

4.3 Aerodynamic Particle Sizing
Cascade Impactor

In an impactor, an aerosol is accelerated through a nozzle and impinges on a plate where particles which are too large to follow the sudden change in flow direction are deposited. In a cascade impactor a series of such nozzle-impactor plate pairs is used, with the nozzle size and the distance of the nozzle from the impactor progressively reduced so that the acceleration in each stage is increasingly severe, in order that particles of decreasing diameter are deposited. A wide size range (e.g. 0.05 to 25 μm) is measurable simultaneously and rapidly; but with a practical number of stages, e.g. 10, the size resolution is rather coarse. A mass-weighted rather than number-weighted size distribution is obtained.

Particle Response in Supersonic Flow

The possibility of using particle velocity measurements in supersonic flow, for example, in a nozzle or through an oblique shock, as a means for sizing the particles depends on the analysis of section 2.4. The practical realization of this method was demonstrated in reference 9 using the flow through a Mach 3 conical nozzle, where size distributions based on 20'000 to 50'000 samples could be obtained in runs of under 1 minute duration. A very steady flow whose velocity distribution is accurately specified from thermodynamic relationships is essental, since any variations in particle velocity arising from unsteadiness would be interpreted as particle size variations.

Particle Response in Subsonic Flow

The aerodynamic size distributions of particles in the range 0.5 to 10 μm are obtainable using an aerodynamic particle sizer (reference 35). Using a simple forward-scatter laser Doppler or dual focus anemometer, the velocities of aerosol particles injected through a 0.5 - 1 mm nozzle into a stream of filtered air are measured. According to their size, particles leaving the nozzle require different distances to adjust their velocity to that of the filtered air stream (200 m/s). A particle, therefore, crosses the fixed measuring volume with a velocity depending only on its size. The size-velocity relationship is determined by calibration with monodisperse aerosols of DOP or latex particles between 0.8 and 10.0 μm.

4.4 Particle Sizing from Optical Scattering Properties

The intensity i of light scattered from a beam of intensity I_o and collected through a small solid angle is a function of the refractive index m of the particle relative to the surrounding medium, the scattering parameter $\alpha = \pi d_p / \lambda$ (where λ is the wavelength of the light) and the angle of observation θ relative to the incident beam. Particularly when $d_p \approx \lambda$, i.e. for particle diameters of special interest for laser anemometry, the scattering properties show a very sensitive dependence on the particle diameter. Numerous particle sizing methods have been developed to exploit this dependence, and are based on matching experimental scattered light distributions with theoretical distributions calculated from Mie scattering theory for spherical particles (references 22, 36, 37, 38).

Although these techniques are strictly applicable only to spherical particles of known refractive index, they have been extended to non-spherical particles when the consequent uncertainty of the measurement was acceptable. For example, the use of absolute measurements of low angle scattered light intensity to size spherical transparent particles and irregularly shaped light-absorbing particles in the range 5 to 80 μm diameter is described in reference 39. Since measurement of absolute light intensity is susceptible to errors from background light and instrument drift, a relative measurement may be preferable, as in reference 40 where soot particles (0.08 to 0.38 μm) were sized using the ratio of scattered light intensities at two angles $i_1(\theta_1)/i_1(\theta_2)$. The uncertainty in the diameter for absorbing, non-spherical particles was estimated as 20-30%.

The instrument in figure 7 uses small angle scattering to size particles in a flow which is optically accessible from both sides. Light scattered at an angle θ from any position in the particle stream is imaged by a lens of focal length f at a radius $r = \theta f$ from the axis. Interference between light scattered from particles of different size yields a Fraunhofer diffraction pattern of concentric rings of high and low intensity. Using a suitable multi-element detector the intensity distribution as a function of the scattering angle θ is rapidly scanned to measure the size distribution from a moving stream of particles. Mass- and number-weighted size distributions of solid and liquid particles in the range 1.5 to 500 μm diameter are obtainable. The technique is independent of the refractive index and requires no calibration (at least for spherical particles).

Optical particle counters measure a proportion of the total light energy scattered by aerosol particles passing through a measuring volume formed by a focused light source. In general, the intensity of light scattered at a given angle gives an ambiguous measure of particle size because of the complicated form of the angular scattering functions. However, use of white light and a large solid angle of collection damps out the oscillations of the response function to give an ideally single-valued curve relating intensity to particle size. The geometry of an instrument collecting scattered light over a large solid angle in the near forward direction by means of an elliptic mirror is shown in figure 8. For appropriate instrument design, the response depends only weakly on the refractive index, at least for non-absorbing particles (reference 41). For practical instruments, the response curve is found by calibration against monodisperse spherical particles of known size; a size range from about 0.3 to 5 μm is accessible. The maximum concentration is limited by the requirement that particles cross the measuring volume individually; the error arising from simultaneous detection of two particles can, however, be estimated (reference 42).

4.5 Particle Sizing from Doppler Signal
Signal Visibility

Information about the size of a particle is contained in the visibility of the Doppler signal, defined as

$$V = \frac{I_{max} - I_{min}}{I_{max} + I_{min}},$$ (4.1)

where I_{max} and I_{min} are the maximum and minimum scattered intensities from consecutive bright and dark fringes (figure 9). Farmer (reference 43) considered the case of uniform fringe contrast which holds at or near the geometric centre of the scattering volume for illuminating beams of equal intensity. The visibility of signals from homogeneous spheres is then related to the particle diameter d_p and the fringe spacing λ^* by the equation

$$V = \frac{2 J_1 (\pi d_p/\lambda^*)}{d_p/\lambda^*}$$ (4.2)

where J_1 is a Bessel function of the first kind and order one. Eq. (4.2) indicates that the visibility for spherical particles falls to zero for $d_p / \lambda^* = 1.22, 2.23, 3.24$, etc., as shown in the solid curve of figure 10. The oscillations of the visibility function preclude an unambiguous determination of diameter from V alone, unless $V > 0.15$ corresponding to $d_p < \lambda^*$.

Equation (4.2) represents a limiting case which applies to forward scattering from large spherical particles ($\alpha > 60$), using a very large collecting aperture and incident beams of equal intensity. In references 44 and 45, scalar diffraction theory was used to extend the visibility function to diameters as small as 1 μm, with finite apertures. With a reduction in the collecting aperture the visibility tends to unity, independent of the particle size, as seen in the broken curves of figure 10. To predict visibilities of backscatter signals, the refractive index m and the size parameter α must be considered, in addition to d_p / λ^* and the solid angle of light collection Ω (references 46, 47). Backscatter results shown in figure 11 show qualitative agreement with measured visibilities of 5.1 μm polystyrene spheres. Unlike figure 10, the visbility function shows peaks and troughs, but no zeros.

Advantages:

* Measurements are made within the flow, without disturbance.
* Calibration is unnecessary.

- At least in forward scatter the influence of m is small.

Disadvantages

- Determination of visibility requires a good signal - to - noise ratio and is subject to operator bias in the selection of signals.
- The method has been tested only for monodisperse particles moving at low velocity or held stationary in a moving fringe system.

An instrument based on these principles is described in reference 48.

Signal Phase Differences

For spherical particles of diameter in the approximate range 1 μm to 3 mm, it is possible to obtain size information from the phase difference between the Doppler signals detected by two or more detectors located at different scattering angles but viewing the same particle (references 49 and 50). With two detectors placed at scattering angles near 90°, the phase shift is linearly dependent on particle diameter and relatively insensitive to refractive index variations. The range of particle diameters accessible with this configuration without ambiguity is limited by a maximum phase difference of 360°. By using a third detector the range can, however, be extended unambiguously.

5. CONCLUSIONS

The particle size distribution relevant to laser anemometry is the convolution of the actual size distribution and the probability of detecting a given particle size as determined by the scattering intensity. The resulting distribution will be shifted to a higher mean particle diameter than in the true size distribution.

Except where factors such as evaporation at high temperatures or deposition on windows preclude their use, droplets are preferable to solid seeding particles:
- droplet generators provide steady production rates and require little maintenance
- droplets are spherical and of uniform density, so calculations of aerodynamic behaviour and light scattering are more reliable than for irregularly shaped solid particles.

Although the importance of satisfactory particle motion for correct laser anemometry measurements has been recognized since the introduction of the technique two decades ago, methods of analyzing the particle dynamics and the techniques of aerosol generation and particle sizing remain unsatisfactory compared with the technology of the remainder of the laser anemometer (optics, signal processing). Improvements in all aspects of aerosol technology for laser anemometry remain essential.

REFERENCES

1. Melling, A. & Whitelaw, J. H. Seeding of gas flows for laser anemometry. DISA Information 15, 1973, 5-14.
2. Durst, F., Melling, A. & Whitelaw, J. H. Principles and Practice of Laser-Doppler Anemometry. 2nd edition, London, Academic Press, 1981, chapters 10, 11.
3. Melling, A. Particle behaviour in flows and suitable particles for LDA measurements. Von Karman Institute for Fluid Dynamics, Lecture Series 1981-3 "Laser Velocimetry".
4. Hinze, J. O. Turbulence: An Introduction to its Mechanism and Theory. New York, McGraw Hill, 1959, p. 352.
5. Chao, B. T. Turbulent transport behaviour of small particles in dilute suspension. Oesterreichisches Ingenieur-Archiv. 18, 1964, 7.
6. Haertig, J. Introductory lecture on particle behaviour. ISL/AGARD Workshop on Laser Anemometry, St. Louis, 1976, ISL Report R 117/76.
7. Hjelmfelt, A. T., & Mockros, L. F. Motion of discrete particles in a turbulent fluid. Appl. Sci. Res. 16, 1966, 149.
8. Neilson, J. H. & Gilchrist, A. An analytical and experimental investigation of the trajectories of particles entrained by the gas flow in nozzles. J. Fluid Mech. 35, 1969, 549.
9. Yanta, W. J. & Crapo, B. J. Applications of the laser Doppler velocimeter to measure subsonic and supersonic flows. AGARD-CP-193, 1976, paper no. 2.
10. Cline, V. A. & Lo, C. F. Application of the dual-scatter laser velocimeter in transonic flow research. AGARD-CP-193, 1976, paper no. 4.
11. Yanta, W. J., Gates, D. F. & Brown, F. W. The use of a laser-Doppler velocimeter in supersonic flow. AIAA Paper 71-287, 1971.
12. vom Stein, H. D. & Pfeifer, H. J. Investigation of the velocity relaxation of micron sized particles in shock waves using laser radiation. Appl. Optics 11, 1972, 305-307.
13. Maxwell, B. R. Particle flow in turbomachinery with application to laser-Doppler velocimetry. AIAA J 12, 1974, 1297-1298.
14. Dring, R. P. Sizing criteria for laser anemometry particles. Trans. ASME, J. Fluids Engng. 104, 1982, 15-17.
15. Hussein, M. F. & Tabakoff, W. Computation and plotting of solid particle flow in rotating cascades. Computers and Fluids 2, 1974, 1-15.
16. Dring, R. P., Caspar, J. R. & Suo, M. Particle trajectories in turbine cascades. J. Energy 3, 1979, 161-166.
17. Hamed, A. Solid particle dynamic behaviour through twisted blade rows. Trans. ASME, J. Fluids Engng. 106, 1984, 251-256.
18. Dibble, R. M., Kollmann, W. & Schefer, R. W. Conserved scalar fluxes measured in a turbulent nonpremixed flame by combined laser Doppler velocimetry and laser Raman scattering. Comb. & Flame 55, 1984, 307.
19. Starner, S. H. & Bilger, R. W. Measurements of scalar-velocity correlations in a turbulent diffusion flame. 18th Symposium (International) on Combustion. Pittsburgh, The Combustion Institute, 1980, paper no. 89.

20. Goss, L. P., Trump, D. D. & Roquemore, W. M. Simultaneous CARS and LDA measurements in a turbulent flame. AIAA paper no. 84-1458, 1984.
21. Denton, M. B. & Swartz, D. B. An improved ultrasonic nebulizer system for the generation of high density aerosol dispersions. Rev. Sci. Instrum. 45, 1974, 81-83.
22. Davies, C. N. Aerosol Science. London, Academic Press, 1966.
23. Moss, J. B. Simultaneous measurements of concentration and velocity in an open premixed turbulent flame. Comb. Sci. & Tech. 22, 1980, 115.
24. Raabe, O. G. The generation of aerosols of fine particles. In Liu, B. Y. H. (ed.). Fine Particles. New York, Academic Press, 1976, 57-110.
25. Echols, W. H. & Young, J. A. Studies of portable air-operated aerosol generators. U.S. Naval Research Laboratory, Washington, 1963, NRL report 5929.
26. Wisler, D. C. Shock wave and flow velocity measurements in a high speed fan rotor using the laser velocimeter. Trans. ASME, J. Engng. Power 99, 1977, 181-188.
27. Melling. A. Unpublished work. Brown Boveri & Co. AG. 1983.
28. Ikioka, L. M., Brum, R. D. & Samuelsen, G. S. A laser anemometer seeding technique for combustion flows with multiple stream injection. Comb. & Flame 49, 1983, 155-162.
29. Johnson, D. A., Bachalo, W. D. & Moddaress, D. Laser velocimetry applied to transonic and supersonic aerodynamics. AGARD-CP-1293, 1976, paper no. 3.
30. Kunii, D. & Levenspiel, O. Fluidization Engineering. New York, Wiley, 1969.
31. Willeke, K., Lo, C. S. K. & Whitby, K. T. Dispersion characteristics of a fluidized bed. Aerosol Science 5, 1974, 449-455.
32. Guichard, J. C. Aerosol generation using fluidized beds. In: Liu, B. Y. H. (ed.). Fine Particles. New York, Academic Press, 1976, 173-193.
33. Glass, M. & Kennedy, I. M. An improved seeding method for high temperature laser Doppler velocimetry. Comb. & Flame 29, 1977, 333.
34. Schäfer, H. J. & Pfeifer, H. J. Deduction of aerosol size distribution from particle sampling by whisker collectors. Experiments in Fluids 1, 1983, 185-193.
35. Agarwal, J. K. & Fingerson, L. M. Real-time aerodynamic particle size measurement with a laser velocimeter. TSI Quarterly 5 (1), 1979, 3-6.
36. van de Hulst, H. C. Light Scattering by Small Particles. New York, Wiley, 1957.
37. Kerker, M. The Scattering of Light and other Electromagnetic Radiation. New York, Academic Press, 1969.
38. Azzopardi, B. J. Measurement of drop sizes. Int. J. Heat Mass Transfer, 22, 1979, 1245-1279.
39. Holve, D. J. In situ optical particle sizing technique. J. Energy 4, 1980, 176-183.
40. Wood, C. P. & Samuelsen, G. S. Optical measurements of soot size and number density in a spray-atomized, swirl-stabilized combustor. Trans. ASME, J. Engng. Gas Turbines & Power 107, 1985, 38-47.
41. Cooke, D. D. & Kerker, M. Response calculations for light-scattering aerosol particle counters. Appl. Optics 14, 1975, 734.
42. Willeke, K. & Liu, B. Y. H. Single particle counter: principle and application. In: Liu, B. Y. H. (ed.). Fine Particles. New York, Academic Press, 1976, 697-729.
43. Farmer, W. M. Measurement of particle size, number density, and velocity using a laser interferometer. Appl. Optics 11, 1972, 2603.
44. Robinson, D. M. & Chu, W. P. Diffraction analysis of Doppler signal characteristics for a cross-beam laser Doppler velocimeter. Appl. Optics 14, 1975, 2177.
45. Roberds, D. W. Particle sizing using laser interferometry. Appl. Optics 16, 1977, 1861-1868.
46. Chu, W. P. & Robinson, D. M. Scattering from a moving spherical particle by two crossed coherent plane waves. Appl. Optics 16, 1977, 619.
47. Adrian, R. J. & Orloff, K. L. Laser anemometer signals: visibility characteristics and application to particle sizing. Appl. Optics 16, 1977, 677-684.
48. Bachalo, W. D., Hess, C. F. & Hartwell, C. A. An instrument for spray droplet size and velocity measurements. Trans. ASME, J. Engng. Power 102, 1980, 798-806.
49. Saffman, M., Buchhave, P. & Tanger, H. Simultaneous measurements of size, concentration and velocity of spherical particles by a laser Doppler method. 2nd International Symposium on Applications of Laser Anemometry to Fluid Mechanics. Lisbon, 1984, paper no. 8.1.
50. Bachalo, W. D. & Houser, M. J. Phase/Doppler spray analyzer for simultaneous measurements of drop size and velocity distributions. Optical Engng. 23, 1984, 583-590.
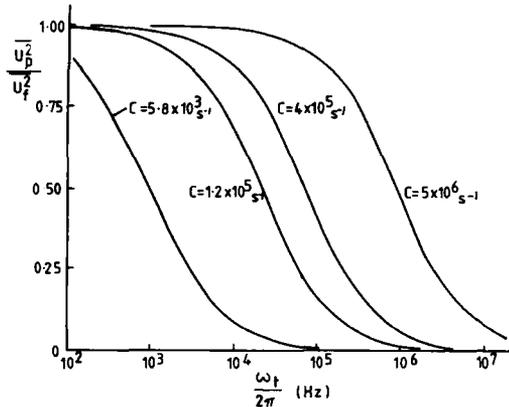
FIG. 1 PARTICLE RESPONSE IN TURBULENT FLOW
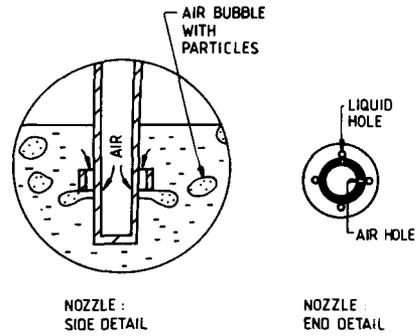
FIG. 4 LASKIN NOZZLE
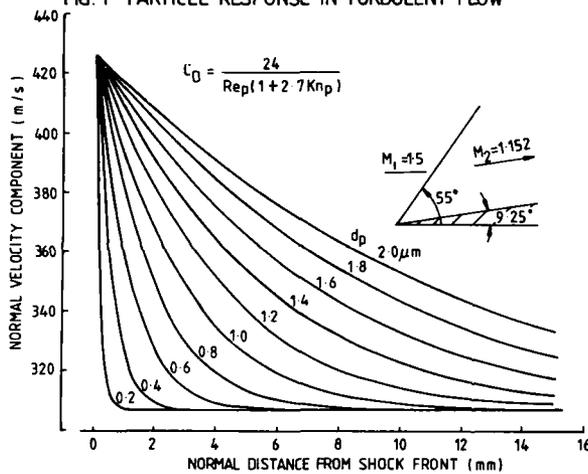
FIG. 2 PARTICLE VELOCITY BEHIND AN OBLIQUE SHOCK
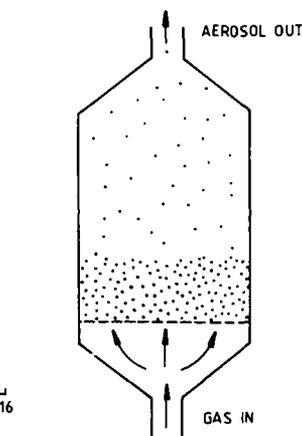
FIG. 5 FLUIDIZED BED
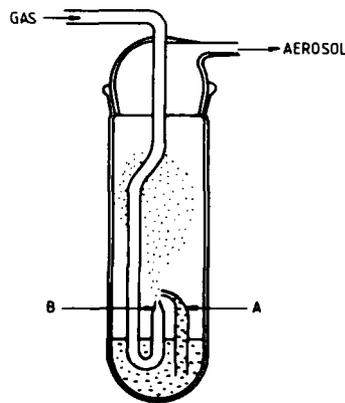
FIG. 3 GLASS ATOMIZER

FIG. 6 PARTICLES COLLECTED WITH
ISOKINETIC PROBE ($0.1 - 5 \mu m$)

FOURIER
TRANSFORM
LENS

MULTI-
ELEMENT
DETECTOR

He-He LASER

BEAM
EXPANDER

PARTICLE
STREAM

θ_1
θ_1
θ_2
r_1
r_2
θ_2

f
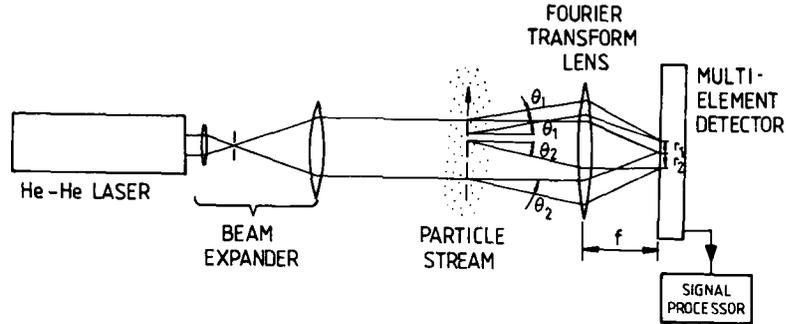
SIGNAL
PROCESSOR

FIG. 7   PARTICLE SIZER USING SMALL ANGLE SCATTERING

FLOW

ISOKINETIC
PROBE

PHOTO-
MULTIPLIER

$I = f(d_p^2)$

REFLECTOR

LAMP
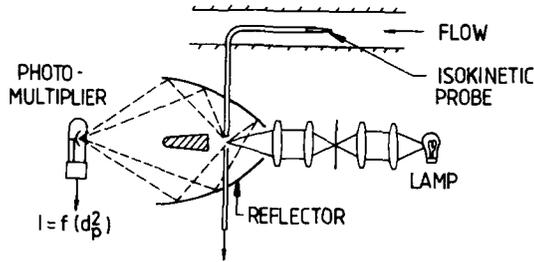
FIG. 8   OPTICAL PARTICLE COUNTER

PEDESTAL
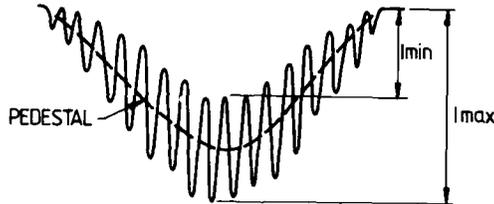
Imin

Imax

FIG. 9   SIGNAL VISIBILITY: $V = \dfrac{Imax - Imin}{Imax + Imin}$

LASER
BEAMS   L
S

COLLECTION
LENS

REF 45

$\dfrac{L}{S}$ { 0·6
1·2
1·8 }

Eq. (4·2)

d_p / λ^*
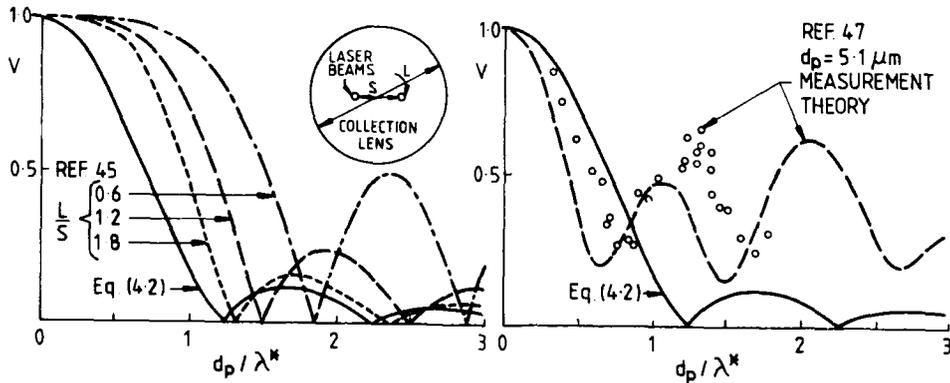
FIG. 10   SIGNAL VISIBILITY FOR DIFFERENT
LENS DIAMETERS AND BEAM
SEPARATIONS

REF 47
$d_p = 5·1\,\mu m$
MEASUREMENT
THEORY

Eq. (4·2)

d_p / λ^*

FIG. 11   SIGNAL VISIBILITY IN BACKSCATTER

DISCUSSION

A.Strazisar, US

Can you comment about point injection for flow seeding?

Author's Reply

I always used point injection in order to have high data rate; I did not try anything else.

P.A.Stewart, UK

Can you give me any references to microballoons, their manufacture and use (particularly metallic microballoons)? I saw microballoons in use at NPL Teddington and believe they are also used in laser fusion studies.

Author's Reply

Cheap microballoons made basically of glass are used, for example, in the manufacture of furniture, by compressing them with an adhesive into a mould. I am unfortunately not aware of any references to the types of microballoons and their potential applications, except for incomplete information given in manufacturer's brochures.

M.L.G.Oldfield, UK

Would you please comment on the fact that although the laser anemometer is by nature non-intrusive, the use of point seeding introduces a flow disturbance upstream of the measurement volume and the spread of this disturbance is similar to the spread of the seeding?

Author's Reply

The introduction of a seeding probe into a flow to provide local seeding at relatively high concentration does indeed detract from the otherwise non-intrusive nature of laser anemometry. The alternative use of uniform seeding can, however, be accompanied by significant disadvantages, e.g. the introduction of more seeding material and more carrier gas into the main flow, or a lower local seeding density and consequently lower data rate. Seeding particles introduced into an internal flow at the walls may not diffuse through the flow within an acceptable distance. So far uniform seeding probes may also be necessary, but they should be inserted into a region of low velocity (e.g. plenum chamber) to minimize the influence of probe wakes.

R.Schodl, GE

I would make a comment on the influence of a seeding probe situated upstream of LV probe volume. In an axial compressor, we put the injection probe at 2 rotor diameters in front of the rotor. We measured velocities with and without seeding (i.e. with atmospheric natural particles). With this local seeding, we found that there are significant deviations especially on the turbulence intensity, but no so serious deviation on mean values (in which we are interested): as a reference we took the data obtained with natural particles. We noticed also the strong influence of additional air when using a point injection. Therefore we decided to install the seeding probe in the settling chamber in order to avoid these disturbances: otherwise, turbulence intensity is increased and we can get wrong data also on mean values.

A.S.Nejad, US

For many years we have used chemical seeders which provide a uniform seeding; very successful.

COMMENT CHOISIR UN VELOCIMETRE LASER POUR UNE APPLICATION DONNEE ?

A. Boutier

Office National d'Etudes et de Recherches Aérospatiales,
BP 72, 92322 Châtillon Cedex, FRANCE

Les différents types de vélocimètres laser sont décrits
avec leurs domaines d'utilisation, leurs qualités et leurs limites.

Les vélocimètres à franges sont aptes à fournir le vecteur
vitesse locale et instantanée, d'où par moyennes statistiques le vec-
teur vitesse moyenne et le tenseur de Reynolds complet. Leur limita-
tion la plus sérieuse est leur inaptitude à mesurer des vitesses près
des parois que les faisceaux heurtent normalement.

C'est pourquoi les vélocimètres deux points ont été dévelop-
pés pour les applications en turbomachines où les écoulements sont
confinés dans des canaux très étroits. Par contre ces vélocimètres
deux points ne peuvent sonder des écoulements dont le taux de turbu-
lence excède 10 à 15 %. Une maquette de vélocimètre deux traits cons-
truite à l'ONERA donne des résultats très prometteurs dans des écoule-
ments plus turbulents.

Un tableau synoptique est proposé dans le but de guider le
choix du vélocimètre laser le plus approprié à des conditions
expérimentales données.

1 - INTRODUCTION

Sous le terme vélocimètre laser, divers types d'appareils fonctionnent sur des
principes différents ; ils peuvent être classés en deux grandes familles : les
vélocimètres à franges et les vélocimètres à barrières optiques. Leur point commun est
de mesurer la vitesse de fines particules servant de traceurs de l'écoulement. Les
capacités et les limitations de ces dispositifs sont répertoriés ; une comparaison de
leur rapport signal sur bruit dans un environnement de lumière parasite forte (mesure
près des parois) est établie. En conclusion un tableau synoptique permet de voir les
propriétés essentielles de chaque type de vélocimètre laser et à quel type
d'information il donne accès dans un écoulement aérodynamique.

Une place particulière est faite au problème de la précision des mesures avec un
vélocimètre à fanges tridimensionnel en fonction de la géométrie des faisceaux laser
accédant au volume de mesure, de la qualité de l'ensemencement, de la procédure
d'étalonnage.

2 - VELOCIMETRIE A FRANGES

2.1 Idée de base

La première famille de vélocimètres laser est issue de l'idée qu'une particule de
vitesse $\vec{V}$, éclairée par un rayonnement de fréquence ν_0, diffuse une lumière de fréquence
ν_d différente de ν_0 par effet Doppler :

$$\nu_d = \nu_0 \left[1 - \frac{\vec{V}.\left(\vec{r_1} - \vec{r_d} \right) n}{c} \right] \qquad (1)$$

$\vec{r_1}$: vecteur unitaire dans la direction d'éclairage

$\vec{r_d}$: "   "   "   "   d'observation

n : indice du milieu où se propage la particule

c : vitesse de la lumière

ν_d(très proche de ν_o) est mesuré directement par analyse spectrale optique dans les vélocimètres "spectromètres" (interféromètres de Michelson ou de Fabry-Pérot). Ce type de vélocimètre est bien adapté pour les mesures de vitesses très élevées et nécessite un ensemencement très important.

Les trois autres types de vélocimètres laser à franges reposent sur l'idée de mesurer une fréquence détectable par des photomultiplicateurs, en réalisant des battements de fréquence (donc des interférences lumineuses) pour éliminer le terme $\nu_o \times 1$ dans l'expression générale de ν_d :

- vélocimètre à faisceau de référence effectuant l'opération $\nu_d - \nu_o$

- vélocimètre à un seul faisceau effectuant l'opération $\nu_d\left(\overrightarrow{r_{d1}}\right) - \nu_d\left(\overrightarrow{r_{d2}}\right)$: observation du signal diffusé dans deux directions différentes.

- vélocimètre à franges effectuant l'opération $\nu_d\left(\overrightarrow{r_1}\right) - \nu_d\left(\overrightarrow{r_2}\right)$: deux faisceaux laser croisés.

Les inconvénients des vélocimètres à faisceau de référence et à un seul faisceau sont bien connus depuis longtemps (difficultés d'alignement, faible rapport signal sur bruit dû à de faibles ouvertures de l'optique de réception). Le vélocimètre à franges est le plus couramment répandu : l'indépendance de sa réponse avec la direction d'observation permet d'utiliser des optiques réceptrices très ouvertes (d'où un meilleur rapport signal sur bruit), et dans des configurations géométriques adaptées à chaque besoin (diffusion avant, rétrodiffusion, etc.). C'est le seul type de vélocimètre laser dont la technologie a été développée au maximum pour mesurer simultanément trois composantes de la vitesse (et très souvent au moins deux).

L'organigramme général d'un vélocimètre laser à franges monodimensionnel est donné sur les figures 1 et 2.

2.2 Vélocimètre tridimensionnel (3D)

Dans un écoulement turbulent, la vitesse locale n'est bien définie que si on a accès à ses trois composantes simultanément sur la même particule. Ensuite les calculs statistiques fournissent les valeurs moyennes et fluctuantes des composantes, ainsi que les contraintes de cisaillement, c'est-à-dire le tenseur de Reynolds complet.

Il faut donc créer localement trois réseaux de franges ayant des directions différentes et des caractéristiques différentes. Pour les vélocimètres bidimensionnels, la distinction des deux réseaux de franges est obtenue soit par des vitesses de défilement des franges différentes (séparation électronique des signaux), soit par des états de polarisation orthogonaux (diaphonie due à des polarisation elliptiques dans le volume de mesure), soit le plus souvent par l'utilisation des deux longueurs d'ondes les plus intenses du laser à argon : la raie verte ($\lambda = 514,5$ nm) et la raie bleue ($\lambda = 488$ nm).

Pour un vélocimètre 3D, compte-tenu de l'expérience acquise avec les vélocimètres 2D, la technique la plus opérationnelle consiste à créer trois réseaux de franges ayant trois couleurs différentes. C'est la technique notamment développée à l'ONERA. En fait seul un vélocimètre 3D permet de caractériser correctement les écoulement complexes turbulents et devant tous être considérés comme tridimensionnels ; néanmoins ce type d'appareillage est plus difficile à mettre en oeuvre qu'un vélocimètre 1D ou 2D pour deux raisons essentielles :

- le coût d'un tel appareillage, utilisant des systèmes optiques, mécaniques et électroniques plus sophistiqués, ainsi qu'un calculateur plus puissant.

- les problèmes géométriques liés à l'accessibilité des faisceaux laser dans la veine d'essai, parfois autour d'une maquette de géométrie élaborée, et généralement à travers des hublots trop petits.

La source laser capable de délivrer trois longueurs d'onde intenses est un laser à argon. En bidimensionnel les raies verte ($\lambda = 514,5$ nm) et bleue ($\lambda = 488$ nm), ont d'abord été utilisés car ce sont les plus intenses et elles ont à peu près la même intensité ; la troisième raie intense est la raie violette ($\lambda = 476,5$nm), mais elle est environ trois fois moins puissante que les raies verte et bleue quand le laser émet simultanément sur toutes les longueurs d'onde. C'est pourquoi dans le vélocimètre 3D conçu à l'ONERA deux lasers à argon de 15 watts, toutes raies sont utilisées comme sources lumineuses : l'un fonctionne à 8 watts toutes raies (3 W pour la composante verte et 3 W pour la composante bleue : vélocimètre 2D initial) et le second fonctionne

en monoraie violette, à son maximum de puissance, c'est-à-dire 2,7 W ; ainsi chaque réseau de franges reçoit la même quantité de lumière.

Le schéma général de ce vélocimètre 3D est donné sur la figure 3 ; trois systèmes de division de faisceau indépendants sont disposés en parallèle sur les trois couleurs. Chacun se compose de :

- un télescope afocal afin que pour chaque composante les faisceaux soient bien focalisés dans V (d'où un interfrange bien constant)
- un diviseur de faisceau (écartement des faisceaux de 30 mm, avec différence de marche nulle),
- deux cellules de Bragg avec prismes et diasporamètres pour remettre les faisceaux émergeant des cellules de Bragg parallèles aux faisceaux incidents;

La lumière diffusée vers l'avant (ou rétrodiffusée pour les basses vitesses) est collectée par deux télescopes Cassegrain travaillant à des distances de 600 mm à 2 m de V (ouverture variant de f/3 à f/10, vu que le miroir primaire a un diamètre de 200 mm) ; l'un est équipé de deux photomultiplicateurs (PM) pour les composantes verte et bleue (le flux est séparé par une lame dichroïque) et l'autre par un troisième PM sensible uniquement à la composante violette ; chaque PM est précédé d'un filtre interférentiel de 4 nm de bande passante. L'angle solide de chaque télescope est toujours disposé de manière à être adjacent au cône défini par les faisceaux laser de la composante concarnée, et ce, afin d'être placé dans la géométrie optimale pour collecter la lumière diffusée selon la théorie de Mie.

Les signaux électriques issus des trois photomultiplicateurs sont traités en parallèle par trois compteurs ; une interface s'assure de la simultanéité des données, de manière à délivrer à l'ordinateur des triplets de valeurs instantanées relatifs à trois composantes de vitesse instantanées de la même particule. L'ordinateur connecté au banc de vélocimètrie laser assure les fonctions suivantes :

- acquisition d'un triplet de données pour chaque particule, ainsi que l'intervalle de temps entre deux triplets successifs, ce qui permet de dater les événements pour des traitements ultérieurs.
- contrôle des déplacements des deux bancs XYZ (un de chaque côté de la soufflerie quand le vélocimètre fonctionne en diffusion avant) : l'ordinateur ordonne aux moteurs pas à pas une certaine amplitude de déplacement, reçoit en retour l'information de position grâce à des codeurs optiques linéaires placés sur chaque axe de translation, ce qui permet un asservissement.
- acquisition des conditions génératrices de l'écoulement (p_i, T_i) pour normaliser les résultats.
- traitement des données de manière à calculer dans un repère trirectangle lié à l'écoulement (ou à la maquette) les vitesses moyennes $\overline{u}$, $\overline{v}$, $\overline{w}$ et le tenseur de Reynolds ($\overline{u'^2}$, $\overline{v'^2}$, $\overline{w'^2}$, $\overline{u'v'}$, $\overline{u'w'}$, $\overline{v'w'}$), ainsi que les ordres supérieurs de la turbulence ($\overline{u'^3}$, $\overline{u'^4}$, $\overline{v'^3}$, $\overline{v'^4}$, $\overline{w'^3}$, $\overline{w'^4}$). Des tracés d'histogrammes sont également possibles, qui peuvent mettre en évidence des phénomènes d'intermittance ou d'instabilité de l'écoulement.

La configuration optique à Chalais-Meudon (cf fig. 4 pour les conventions géométriques) est actuellement la suivante :

- composante verticale w mesurée directement avec la raie bleue (λ = 488 nm)
- deux composantes horizontales R_1 et R_2 mesurées avec les raies verte (λ = 514,5 nm) et violette (λ = 476,5 nm) ; les angles β_1 = (R_1, u) et β_2 = (u, R_2) sont réglables pour chaque type d'écoulement ; (β_1 + β_2) est toujours de l'ordre de 60° pour des questions de précision de mesure exposées dans le § 2.3.1. La flexibilité du choix de β_1 et β_2 est rendue possible par le fait que les optiques émettrices verte-bleue et violette peuvent être glissées indépendamment sur un rail horizontal (cf photo 5).

Les deux bancs de déplacement XYZ (200 mm de course selon chaque axe) supportent les divers corposants optiques : les lasers à argon et le système de division de faisceau 3D se déplacent dans un plan horizontal en X et Y ; les optiques d'émission sont suspendues à un rail mobile selon l'axe vertical de déplacement Z ; de l'autre côté de la soufflerie, en diffusion avant, les deux télescopes Cassegrain sont fixés sur le banc de réception similaire à celui d'émission : chaque banc XYZ possède des degrés de liberté d'orientation (α, β, γ) pour rendre ses axes de déplacements parallèles à ceux de la soufflerie.

2.3 Précision des mesures

L'instrumentation mise en jeu avec un tel vélocimètre 3D est suffisamment coûteuse pour que l'on s'attache à obtenir des résultats de qualité, dans lesquels les utilisateurs puissent avoir confiance. Quatre aspects importants de ce problèmes ont été étudiés : la localisation du volume de mesure, la calibration absolue du vélocimètre, la précision des mesures en tridimensionnel, le comportement des aérosols servant de traceurs de l'écoulement.

2.3.1. Repérage du volume de mesure

Le diamètre du volume de mesure dans le plan XZ est de l'ordre de 400 μm ; le long de l'axe Y, parce que la partie réception a un axe de visée incliné d'une dizaine de degrés par rapport à l'axe de l'optique d'émission, la longueur vue est de l'ordre du millimètre ; ces dimensions caractérisent la résolution spatiale de l'instrument. La robustesse des dispositifs mécaniques de translation fait que l'alignement optique du vélocimètre reste conservé lors des déplacements : la lecture des déplacements est effectuée avec une précision de 0,01 mm ; l'écart de position entre les bancs émission-réception ne dépasse jamais 0,03 mm. Néanmoins il faut localiser ce volume de mesure optique (croisement de 6 faisceaux laser focalisés) par rapport à la maquette présente dans l'écoulement. Généralement on dispose sur la maquette un trou, de la dimension du volume de mesure, dans un plan XZ et dont la position est très précisément connue dans le repère de la maquette.

Les coordonnées du volume de mesure coïncident exactement avec celles du trou de la maquette lorsque les six faisceaux en émergent et qu'ils présentent des anneaux de diffraction par observation visuelle sur un écran : ainsi le volume de mesure est réglé en position par rapport à la maquette avec une incertitude de 0,1 mm dans les trois directions. Autant que possible ce repérage doit être fait en soufflage (trou solidaire de la maquette hors d'une zone à sonder) pour tenir compte des déplacements éventuels de la maquette en cours d'essai.

2.3.2. Etalonnage précis

Pour chaque composante mesurée, il s'agit de déterminer l'interfrange i et la direction de la composante (normale aux plans des franges) dans l'espace.

L'utilisation d'un théodolite installé à proximité du volume de mesure permet d'accéder à tous ces paramètres avec une excellente précision, ce qu'aucune autre des méthodes plus simples, souvent mises en oeuvre pour des vélocimètres 1D ou 2D ne peut réaliser.

Le principe est le suivant : dès qu'un faisceau laser est parallèle à l'axe optique de l'objectif du théodolite, il est focalisé au centre d'une croix placée par construction dans son plan focal image ; cette figure est projetée sur un écran par l'oculaire du théodolite. Les théodolites récents permettent d'adresser directement à un petit calculateur les valeurs angulaires horizontale et verticale (site et azimut de la direction dans l'espace de ce faisceau laser avec une précision élevée. Pour un vélocimètre 3D, il faut pointer ainsi successivement les six faisceaux laser sécants, puis un axe de référence de l'écoulement (autocollimation sur un hublot latéral de la veine, miroir fixé sur la maquette, etc...). Connaissant les trois composantes du vecteur unitaire parallèle à chacun des six faisceaux laser (et de l'axe de référence) dans un repère trirectangle connu (la visée de l'axe de référence sert à déterminer Oy), on peut alors en déduire les trois interfranges et les neuf coefficients de la matrice reliant les composantes mesurées (R_1 R_2 R_3) aux composantes voulues (uvw selon XYZ).

La figure 6 donne la nomenclature des angles et des axes ; de plus, comme la procédure de mesure est rapide, les pointés peuvent être répétés plusieurs fois pour améliorer la précision. Un étalonnage d'un vélocimètre 3D prend ainsi environ une demi-heure pour des incertitudes de mesure de l'ordre de 1 % sur les interfranges et environ 0,1° sur chaque angle.

Une composante de vitesse mesurée R_1 est définie par le vecteur unitaire $\overrightarrow{K_1}$:

$$\overrightarrow{K_1} \begin{cases} K_1 x = \left(A_2^1 - A_1^1\right)\Big/ \ |r_1| \\[2mm] K_1 y = \left(B_2^1 - B_1^1\right)\Big/ \ |r_1| \\[2mm] K_1 z = \left(C_2^1 - C_1^1\right)\Big/ \ |r_1| \end{cases}$$

$$|r_1| = 2 \sin\left(\frac{\theta_1}{2}\right)$$

$$\vartheta_1 = \text{Arc cos} \left[A_1^i \, A_2^i + B_1^i \, B_2^i + C_1^i \, C_2^i \right]$$

L'interfrange est donné par $i_1 = \dfrac{\Lambda_i}{2 \sin \left(\dfrac{\vartheta_1}{2}\right)}$

Alors $R_1 = K_{1x} u + K_{1y} v + K_{1z} w$

Les mêmes équations peuvent être écrites pour les deux autres composantes mesurées R_2 et R_3 (sachant que généralement il est possible de mesurer directement w selon z avec R_3, ce qui conduit à $K_{3x} = K_{3y} = 0$) Alors

$$\begin{pmatrix} R_1 \\ R_2 \\ R_3 \end{pmatrix} = \begin{pmatrix} K_{1x} & K_{1y} & K_{1z} \\ K_{2x} & K_{2y} & K_{2z} \\ K_{3x} & K_{3y} & K_{3z} \end{pmatrix} \begin{pmatrix} u \\ v \\ w \end{pmatrix} = (K) \begin{pmatrix} u \\ v \\ w \end{pmatrix}$$

et $\begin{pmatrix} u \\ v \\ w \end{pmatrix} = \left(K^{-1}\right) \begin{pmatrix} R_1 \\ R_2 \\ R_3 \end{pmatrix}$

2.3.3. Incertitudes de mesure en tridimensionnel

Le montage optique conduisant à la meilleure précision de mesure est assurément celui qui permet la mesure directe des trois composantes u, v et w. Cela nécessite toutefois un accès optique à l'écoulement non seulement par des fenetres latérales (pour u, w cf fig. 4), mais aussi par des hublots au plafond et/ou au plancher de la veine, ce qui est rarement possible hormis à la soufflerie F2 du centre ONERA du Fauga-Mauzac, spécialement conçue à cet effet [2] ou dans des études de jet libres.

Les problemes surgissent quand la composante v le long de l'axe y n'est pas mesurée directement mais par combinaison de deux composantes dans un plan horizontal, par exemple u et R, R faisant un angle β avec u. Cette configuraton est donnée à titre d'exemple car c'était celle des premiers vélocimetres laser 3D exploités aux Etats-Unis à NASA Ames et au NSWC

$$v = \frac{R - u \cos \beta}{\sin \beta} \qquad (2)$$

La difficulté dans cette formule provient de ce que R et $u \cos \beta$ sont généralement deux grands nombres dont la différence est petite, d'où l'incertitude sur v. En développant cette formule avec les notations ci-après, il apparaît qu'en mixant électroniquement les signaux des composantes R et u on peut améliorer la précision de mesure

ν_R frequence mesurée selon R ; ν_{pR} frequence du mouvement des franges selon R

ν_u frequence mesurée selon u ; ν_{pu} fréquence du mouvement des franges selon u

$\nu_v = \nu_R - \nu_u$ frequence mesurée à la sortie d'un mixer

$\nu_{pv} = \nu_{pR} - \nu_{pu}$ frequence apparente du mouvement des franges selon v

i_R interfrange selon R

i_u interfrange selon u

$I = i_R - i_u \cos \beta$

$$v = \frac{(\nu_R - \nu_u) \, i_R - (\nu_{pR} - \nu_{pu}) \, i_R + (\nu_u - \nu_{pu}) \, I}{\sin \beta} = \frac{(\nu_v - \nu_{pv}) + (\nu_u - \nu_{pu}) \, I}{\sin \beta} \qquad (3)$$

La mesure d'une fréquence ν_v plus faible est effectuée plus précisément dans un compteur Malheureusement cette idée se heurte à deux difficultes : à la sortie d'un mixer il faut filtrer le signal pour bien isoler ν_v des fréquences d'entrée ν_R et ν_u ce qui en pratique nécessite d'avoir une idée à priori des valeurs des composantes et de leur turbulence) et d'autre part il faut minimiser ou annuler I, ce qui n'est ni aisé ni precis Les essais effectués à l'ONERA avec des mixers n'ont apporté aucune ameliorat on de la qualité des mesures, mais ont engendré beaucoup plus de complexité instrumentale (apparemment inutile) et une dégradation du rapport signal sur bruit

Par contre un phénomène préoccupant a été mis en évidence pour des faibles valeurs de β (de l'ordre de 20°) Dans un écoulement de turbulence isotrope, c'est à dire par définition $\sqrt{\overline{u^2}} = \sqrt{\overline{v^2}} = \sqrt{\overline{w^2}}$, il a été mesuré $\sqrt{\overline{u^2}}, \sqrt{\overline{w^2}}, \sqrt{\overline{v^2}}$ ...
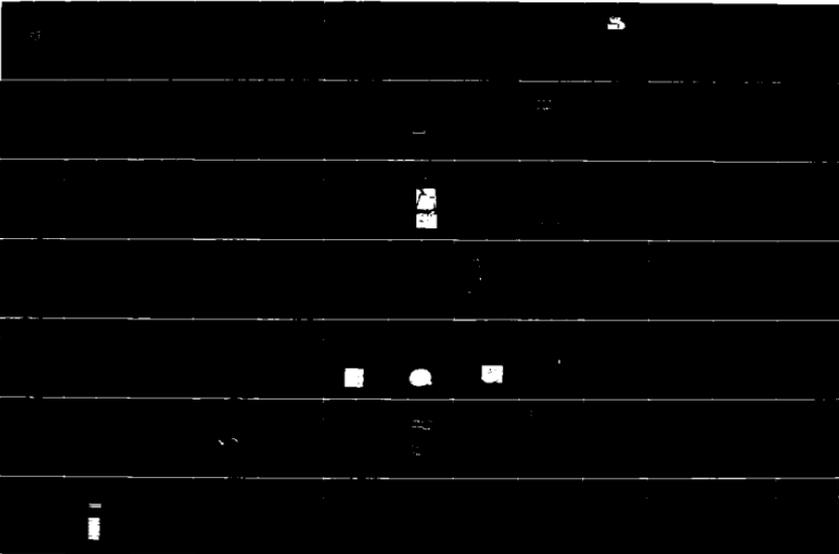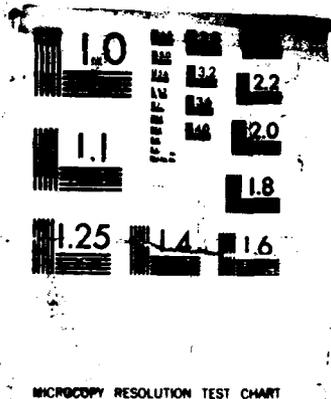
MICROCOPY RESOLUTION TEST CHART

expérimental final $\sqrt{\overline{v'^2}} \simeq 3 \sqrt{\overline{u'^2}}$, aussi bien en subsonique ($V_\infty \simeq$ 50 m/s) qu'à Mach 1. En portant l'angle β entre les deux composantes mesurées dans un plan horizontal à une valeur de l'ordre de 60°, le facteur 3 a été réduit à 1,6 (cf fig. 7). L'explication probable de cet allongement de l'histogramme des vitesses (qui devrait être inclue dans un cercle) est donnée grâce à la figure 8. P_i et P_j sont deux particules réelles, de vitesses différentes (dans le cercle de probabilité de turbulence isotrope), qui délivrent des signaux pendant le critère de simultanéité ; pour la particule P_i le compteur mesurant u_i valide la mesure et pas celui mesurant r_i, pour la particule P_j il se passe le contraire ; le résultat donné par le vélocimètre est une "particule virtuelle" P_v de composantes (u_i, r_j). L'étude détaillée de ce problème est présentée en référence [1] et aboutit aux conclusions suivantes : il faut augmenter β au maximum (60° serait un minimum et 90° l'optimum) et réduire l'ensemencement pour diminuer la probabilité de mesurer ainsi deux particules P_i et P_j. C'est d'ailleurs ce qui se passe dans les écoulements à fort taux de turbulence (tourbillons notamment) où cet effet de l'allongement de l'histogramme s'atténue.

2.3.4. Aérosols utilisés en vélocimétrie laser

Différents types d'aérosols sont utilisés en vélocimétrie laser, issus de divers générateurs de particules. La théorie prévoit que pour suivre de fortes accélérations ou décélérations (traversée d'un choc par exemple) les particules, sur lesquelles repose la mesure du vélocimètre laser, doivent être submicroniques, et même d'autant plus petites que les vitesses à mesurer sont plus grandes.

Une étude comparative du comportement de différents aérosols lors de la traversée d'un choc a été entreprise en collaboration entre l'ONERA et l'IMST en 1985 ; un gros effort de recherche a également été effectué aux Etats-Unis dans ce domaine [3]. Les conclusions essentielles sont résumées ci-dessous :

- les particules de latex calibrées à 0,3 µm par exemple, atomisées à partir d'une solution comprenant 10 ml d'eau + latex (10 % de latex pur) et un litre d'alcool, donnent des résultats conformes à la théorie. Un bon mode d'injection semble être d'atomiser le mélange dans la chambre de tranquillisation, suffisamment loin en amont du point de mesure pour que l'alcool soit totalement évaporé.

- un mélange de 5 % de DOP dans l'alcool (atomisé puis séché dans une colonne chauffante) doit donner une granulométrie de 0,44 µm, alors qu'un mélange de 1 % de DOP dans l'alcool doit donner une granulométrie plus fine de 0,2 µm peu dispersée. Les pentes des courbes u = f(x) au travers d'un choc confirment ces estimations par comparaison avec le latex 0,3 µm.

- un mélange de 20 % d'huile de paraffine (ou de Rhodorsil 710 plus résistant à température élevée jusqu'à 800 K) dans du trichloroéthane, issu d'un atomiseur suivi d'une colonne séchante (système préconisé par le DFVLR en Allemagne) donne également une majorité de petites particules de l'ordre de 0,5 µm, avec l'avantage de ne pas salir rapidement les hublots (notamment en turbomachines).

- les fumées d'encens sont polydispersées ; en diffusion avant à Mach 2, avec une puissance laser de 3 W pour une composante et une optique réceptrice ouverte à f/5, les résultats obtenus sont comparables à ceux dûs aux billes de latex.

Au stade actuel de ces études qui vont se poursuivre on retient les points importants suivants :

- pour qu'un vélocimètre laser, traitant les signaux avec un compteur, soit sensible aux plus petites particules (0,2 à 0,3 µm), à des vitesses de 300 à 500 m/s, il faut disposer d'une puissance laser d'environ 3 W sur chaque composante, et d'une optique de réception ouverte entre f/3 et f/10, suivi d'un photomultiplicateur de gain 10^6, ce qui n'est pas le cas des systèmes commerciaux actuels.

- il semble préférable de s'orienter vers l'utilisation généralisée en écoulement aérodynamique des billes de latex calibrées, qui fournissent un aérosol monodispersé connu, ce qui permettra parfois d'utiliser la rétrodiffusion (en augmentant le gain des amplificateurs électroniques des compteurs) sans détérioration de la qualité des résultats. En effet souvent quand l'aérosol a une granulométrie polydispersée, en rétrodiffusion le vélocimètre laser est systématiquement sensible à la queue de la distribution en taille vers les grosses particules, ce qui ralentit la cadence d'acquisition de données et fausse les résultats de vitesse moyenne et d'écart-type.

- en cas d'utilisation d'une huile, la dilution dans un solvant avant atomisation réduit toujours la granulométrie qui devient souvent à majorité submicronique.

Dans les écoulements à vitesse élevée et haute température, il est préconisé

d'utiliser des particules réfractaires telles que $Ti\ O_2$ jusqu'à 1800 K ou ZrO_2 jusqu'à 2700 K, générées par un lit fluidisé ou un cyclone. Al_2O_3 donne généralement des particules entre 2 et 3 μm.

Pour des essais dans des moteurs à Sandia Laboratories [4], afin d'éviter l'abrasion rapide de la chambre de combustion due aux particules de ZrO_2, un mélange ZrF_4 dans de l'eau est vaporisé : il donne de bons résultats dans la partie froide de l'écoulement, puis se transforme en ZrO_2 uniquement dans la zone de combustion, ce qui limite l'érosion.

2.4. Utilisation de fibres optiques en vélocimétrie laser

Il faut distinguer l'emploi de fibres optiques dans la partie émission et dans la partie réception.

Des fibres optiques multimodes de 600 μm de coeur sont aisément utilisables dans la partie réception pour conduire la lumière diffusée collectée par l'optique réceptrice vers les photomultiplicateurs, qui peuvent ainsi être éloignés de certains environnements hostiles (rayonnement électromagnétique d'un laser, fort niveau de vibration, etc...).

Par contre à l'émisson il s'agit de véhiculer des faisceaux laser (généralement de forte puissance) en conservant leur cohérence spatiale et temporelle afin de créer des interférences de bonne qualité dans le volume de mesure $\mathcal{V}$. Pour éviter des phénomènes de speckle indésirables dans $\mathcal{V}$, ce sont des fibres monomodes qui sont utilisées, avec un coeur de 5 μm environ. Les premiers dispositifs commercialisés ne fonctionnaient qu'avec des laser He-Ne de faibles puissance ; la technologie des fibres optiques évoluant actuellement très rapidement, des systèmes sont maintenant proposés avec des lasers à argon, qui correspondent aux schémas de la figure 9. La puissance laser pouvant entrer dans ces têtes optiques miniaturisées de vélocimètre monodimensionnel, fonctionnant en rétrodiffusion axiale, est encore limitée à 1 watt environ ; la distance de visée est d'une cinquantaine de mm.

Cette technologie va à l'encontre de l'idée fondamentale de la vélocimétrie laser "qui ne perturbe pas l'écoulement", puisqu'il y a introduction de sonde matérielle. Néanmoins cette nouvelle technologie étend le domaine d'application de la vélocimétrie à des écoulements ne possédant pas d'accès optiques latéraux larges, et peut rendre des services quand la chambre d'expérience est entourée par un grand caisson pressurisé (cas de certaines grandes souffleries à caractère industriel).

3 - VELOCIMETRIE LASER A BARRIERE OPTIQUE

Dans le cas où le niveau de lumière parasite est intense, dans les essais en turbomachines par exemple (dans des canaux étroits), les vélocimètres à franges classiques fonctionnent mal : la limite d'approche frontale d'une paroi que les faisceaux laser heurtent est de l'ordre de 5 à 15 mm ; des moyens pour réduire cette limitation sont décrits dans le § 4.2 mais ne sont pas toujours applicables. C'est pourquoi la vélocimétrie à barrière optique s'est développée, avec comme idée fondamentale de plus concentrer l'énergie lumineuse dans le volume de mesure pour améliorer le rapport signal sur bruit. Deux types de vélocimètres sont décrits ci-dessous, l'un disponible commercialement (deux points), l'autre n'étant qu'au stade du laboratoire (deux traits).

3.1 Vélocimètre deux points [5]

Le schéma d'un tel vélocimètre est donné par la figure 10 ; le faisceau laser est focalisé en deux points d'environ 20 μm de diamètre et distants de 400 μm. C'est la lumière rétrodiffusée sur l'axe qui est collectée dans tous les systèmes commerciaux, essentiellement parce que dans les applications en turbomachines l'accès optique est limité à travers de très petites hublots. Les inconvenients de cette technique sont les suivants : les mesures ne peuvent être faites que dans des écoulements faiblement turbulents (moins de 10 à 15 % : une particule traversant le premier point ne doit pas avoir une probabilité trop basse pour traverser le second) et il est impossible d'effectuer des mesures tridimensionnelles simultanées sur la même particule, puisqu'il faut tourner la ligne joignant les deux points pour obtenir localement les variations angulaires de l'écoulement ; la durée des acquisitions pour chaque position du volume de mesure est longue.

Il apparaît donc que ces appareils sont les seuls à pouvoir fournir des mesures très près des parois, mais la durée d'une mesure est longue et on ne peut sonder des

écoulements très turbulents, malheureusement existant souvent près des parois : couches limites, tourbillons, zones de décollement, etc.

Lors de l'étude comparative du rapport signal sur bruit des différents types de vélocimètres, quand nous montrerons quantitativement combien cette configuration optique de vélocimètre laser est avantageuse, il faudra garder en mémoire tous les inconvénients pratiques pour l'exploration des écoulements turbulents.

3.2. Vélocimètre deux traits

A l'ONERA nous avons développé un vélocimètre à barrières optiques monodimensionnel (mesure d'une composante de la vitesse) appelé deux traits (cf fig. 11). Les points (de différentes couleurs : un vert et un bleu issus d'un laser à argon) sont transformés en deux traits en créant de l'astigmatisme dans la partie émission, grâce à des lames à faces parallèles inclinées. Un tel système peut mesurer successivement différentes composantes de la vitesse, par rotation des lames inclinées, ce qui assure une rotation des traits sur eux-mêmes ; la ligne joignant les centres des traits peut être disposée parallèlement à la direction principale de l'écoulement en tournant le prisme séparateur de couleurs. Un tel appareil devient bidimensionnel quand un système de deux croix est créé (cf fig. 11b). Ces vélocimètres à traits sont comparables à des vélocimètres à franges n'ayant que deux franges, mais avec le traitement du signal (convertisseur temps-tension, analyseur multicanaux donnant l'histogramme des temps de transit) et quelques avantages des vélocimètres deux points ; l'étude du rapport signal sur bruit, ainsi que des expériencs de laboratoire, montrent clairement la situation intermédiaire de ce type de vélocimètre laser, capable de travailler dans des écoulements assez turbulents ($\tau_u < 30$ %), mais pas dans des zones de recirculation ; il accepte cependant des variations angualires de l'écoulement jusqu'à $\pm 10°$. Initialement ce vélocimètre laser fut monté en rétrodiffusion co-axiale ; nous montrerons les améliorations obtenues en utilisant une géométrie où l'optique de réception est adjacente à l'optique d'émission (rétrodiffussion hors de l'axe).

4 - RAPPORT SIGNAL SUR BRUIT EN VELOCIMETRIE LASER

Nous considèrerons qu'en raison des flux faibles diffusés par des particules submicroniques le détecteur est un photomultiplicateur. Le rapport signal sur bruit RSB s'écrit alors :

$$RSB = (RSB)_{MAX} \cdot C$$

$$(RSB)_{MAX} = \frac{\sqrt{P_L} \; \alpha_r \; \sqrt{\frac{\Pi}{4}} \; \sqrt{\sigma}}{2 \sqrt{\frac{h \; \nu_o \Delta f}{\eta}} \; \sqrt{S_V}}$$

$$C = \left(1 + \frac{a \; S_V}{\Pi \sigma} K\right)^{-1/2} \qquad K = \frac{S_T}{S_M^{..}}$$

P_L: puissance du laser

α_r : angle du cône de l'angle solide de l'optique réceptrice

σ : section efficace de diffusion d'une particule

($\simeq 10^{-8} mm^2 sr^{-1}$ pour une particule d'eau de 0,8 μm de diamètre)

h : constante de Planck = $6,6 \cdot 10^{14} J.s$

ν_o : fréquence de la lumière laser $\simeq 6 \cdot 10^{14} Hz$

Δf : bande passante de l'électronique (plusieurs MHz)

η : efficacité quantique du PM ($\simeq 0,1$)

S_V : surface éclairée dans le volume de mesure dans un plan x,y

a : albédo d'une paroi ($\simeq 0,1$)

K : caractérise la surface commune au diaphragme placé devant le PM et à l'image $S_M^{..}$ dans le plan du diaphragme, de l'impact des faisceaux laser sur la paroi.

L'évolution de ce rapport signal sur bruit d'après [6] pour des caracéristiques classiques de vélocimètres à franges, deux points, deux traits donne les courbes de la figure 12, mettant en évidence la situation de compromis intéressante dans laquelle se trouve le vélocimètre deux traits.

Mentionnons ici toutefois pour mémoire les diverses façons d'améliorer le RSB dans

un vélocimètre à franges, qui reste la technique la plus opérationnelle car applicable aux écoulements très turbulents, qui se manifestent souvent près des parois :

- réduction de la taille du volume de mesure à 60 μm de diamètre par exemple (ce qui se rapproche de la surface S_v d'un vélocimètre à barrière optique), ce qui entraine des interfranges petits, donc des fréquences élevées à traiter pour des vitesses élevées (limitation en vitesse de l'ordre de 150 m/s dans ce cas).

- utilisation de particules fluorescentes (ce qui annule l'influence de a, car la paroi n'est plus vue par le PM).

- traitement du signal par analyse spectrale, plutôt que par comptage, ce qui réduit Δf d'un facteur 10^3.

Pratiquement il ressort de cette étude les idées fondamentales suivantes :

- pour conserver un RSB > 1 avec un vélocimètre à franges, il faut que le facteur K soit inférieur à 10^{-3}, ce qui signifie que le trou placé devant le photomultiplicateur ne doit quasiment pas "voir" les images défocalisées des impacts des faisceaux laser sur une paroi. C'est ce qui explique l'inefficacité des vélocimètres à franges en rétrodiffusion axiale et la limite d'approche des parois en rétodiffusion hors de l'axe, liée à la géométrie (émission-réception) de l'appareil.

Il est clair qu'une optique de réception placée à 90° de l'axe d'émission permet une approche de paroi à quelques dixièmes de mm, mais se heurte aux problèmes d'accessibilité optique et aux problèmes liés à la diffusion de Mie qui est minimale dans cette direction.

- le vélocimètre deux points a un RSB de 7 dB environ, même sur la paroi.

- le vélocimètre deux traits permet de s'approcher jusqu'à 0,4 mm (théorique), 0,7 mm (pratique) d'une paroi : un RSB supérieur à 1 est obtenu pour K ≤ 13 %. Le fait de se mettre en rétrodiffusion hors de l'axe avec un tel vélocimètre améliore le RSB jusqu'à une distance de 2,7 mm environ ; ensuite le flux parasite sur le détecteur redevient identique à celui reçu en rétrodiffusion axiale.

Le tableau ci-dessous résume cette étude (d : distance de V à la paroi)

	RSB_{MAX}(dB)	RSB	dmm	Commentaires
Vélocimètre à franges rétrodiffusion axiale	22,8	$\dfrac{13,8}{\sqrt{1 + 2.10^5 K}}$	Impossible	Vélocimètre trop sensible à la lumière parasite
Vélocimètre à franges rétrodiffusion hors de l'axe	-	-	5 à 15	Améliorations possibles : traitement du signal par analyse spectrale, plus petit volume de mesure, particules fluorescentes
Vélocimètre deux points rétrodiffusion axiale	40	$\dfrac{102}{\sqrt{1 + 2.10^3 K}}$	0 à 0,5	Approche de paroi optimale, mais en écoulement laminaire
Vélocimètre deux traits rétrodiffusion axiale	32	$\dfrac{40}{\sqrt{1 + 1,27.10^4 K}}$	0,7	Bon compromis en écoulement turbulent près des parois, mais pas dans les zones de recirculation
Vélocimètre deux traits rétrodiffusion hors de l'axe	-	-	-	Amélioration du RSB jusqu'à 2,7 mm de la paroi

5 - SYNTHESE DES CAPACITES DES DIVERS VELOCIMETRES LASER

Type de vélocimètre		Commentaires	Type d'écoulement
Vélocimètre à franges classiques	1 D	Mesure d'1 seule composante ; plusieurs composantes mesurables successivement ; permet de se familiariser avec la technique	Stationnaire $\vec{V}$ approché tangentiellement à quelques 1/10 de mm d'une paroi, mais perpendiculairement entre 5 et 15 mm
	2 D	2 composantes simultanément mesurées : accès optique par hublots latéraux	Turbulent Bidimensionnel (même problème d'approche de paroi que 1 D)
	3 D	3 composantes simultanément mesurées : nécessite larges accès optiques pour avoir une bonne précision	Turbulent Tridimensionnel Tenseur de Reynolds complet mesuré
Vélocimètre à franges spécifiques pour mesures près des parois	Particules fluorescentes	1 seule composante mesurée : plusieurs composantes successivement : particules toxiques de 2 à 3 µm	Turbulent près des parois gradients de vitesse faibles
	Forte résolution spatiale	1, 2 ou 3 composantes simultanément mesurées. Accès optique large	Turbulent près des parois vitesses peu élevées (< à 100 m/s)
	Traitement du signal par analyse spectrale	1, 2 ou 3 composantes mesurées indépendamment ; donc pas accès au tenseur de Reynolds complet. Evolutiontechnologique pour traitement simultané des 3 composantes d'une même particule (numérisation des signaux des PM)	Turbulent près des parois Beaucoup d'avenir dans cette méthode
Vélocimètre 2 points		Mesures bidimensionnelles ; supposent un ensemencement constant	Laminaire (τu < 10 à 15 %) Mesurées très près des parois, quand il y a des particules
Vélocimètre 2 traits, 2 croix		Mesures 1D, 2D ; vélocimètre de compromis entre 2 points et franges ; maquette de laboratoire	Turbulent, mais avec τu < 30 % Mesures à 1 mm environ d'une paroi normale aux faisceaux laser
Vélocimètre à franges avec fibres optiques		Mesures 1D ; technologie en pleine évolution	Turbulent Sonde dans l'écoulement à 50 mm environ du point visé

6 - CONCLUSIONS

La vélocimétrie laser à franges est apte à mesurer simultanément trois composantes du vecteur vitesse locale et instantanée, ce qui permet de sonder de nombreux écoulements turbulents tridimensionnels avec succès. Les seules restrictions à son domaine d'utilisation sont la difficulté d'accès optique au volume de mesure dans

certains cas (sachant qu'il est préférable de se rapprocher d'une configuration où les trois composantes mesurées sont orthogonales) et la dégradation du rapport signal sur bruit près des parois (limite d'approche de 5 à 15 mm quand les faisceaux laser leur sont perpendiculaires, mais quelques dixièmes de mm quand ils leur sont parallèles) ; quelques essais avec un volume de mesure plus petit ou des particules fluorescentes s'avèrent satisfaisants, mais non valables en toute généralité ; une amélioration importante doit apparaître dans un proche avenir grâce à de nouvelles méthodes de traitement du signal par analyse spectrale des signaux issus des photomultiplicateurs que l'on numérise.

Les vélocimètres deux points sont les plus performants près des parois, mais ils sont limités au sondage d'écoulements très faiblement turbulents.

Le vélocimètre deux traits apparaît comme un bon compromis, avec une approche de paroi limitée à 0,7 mm et la possibilité de mesurer des taux de turbulence atteignant 30 % dans des écoulements où la variation angulaire du vecteur vitesse est de l'ordre de $\pm 10°$.

Il faut attacher beaucoup d'importance à la qualité de l'ensemencement de l'écoulement, car cette technique optique dite "non perturbatrice" repose sur la diffusion de la lumière par des aérosols qui doivent être introduits sans perturber l'écoulement, donc suffisamment loin en amont du volume de mesure, ou parfois même en aval de la veine dans une soufflerie à retour. L'utilisation généralisée des billes de latex calibrées submicroniques est hautement recommandée pour l'étude des écoulements aérodynamiques rapides à température ambiante.

En conclusion, le vélocimètre laser idéal et universel capable d'effectuer des mesures près de n'importe quelle paroi, dans un écoulement fortement turbulent, n'existe pas, mais nous sommes capables maintenant de définir les principaux caractères qu'il devrait respecter :

- lumière laser fortement concentrée dans le volume de mesure, ce qui augmente le rapport signal sur bruit avec $S_v^{-1/2}$ et décroît le niveau continu au moins comme S_v^2.
- une géométrie de volume de mesure V et un système de traitement de signal capables de mesurer le vecteur vitesse instantanée d'une particule, quelle que soit sa trajectoire dans V (comme dans les vélocimètres à franges 3D).
- axe de l'optique de réception situé en dehors de l'axe d'émission, car cette géométrie permet de minimiser le paramètre K (lumière parasite reçue par le photomultiplicateur).

Cette évolution de la vélocimétrie laser est demandée par de nombreux utilisateus pour sonder des écoulements autour de maquettes complexes ou dans des régions (entrées d'air par exemple) où l'accès optique est très difficile, dû au manque de hublots.

Ainsi une nouvelle contrainte pour les futurs vélocimètres laser sera l'utilisation de fibres optiques, tant à l'émission qu'à la réception, en vue de miniaturiser les équipements.

REFERENCES

[1] - A. Boutier, D. Pagan, D. Soulevant
Measurements accuracy with 3D laser velocimetry
Int. Conf. on Laser Anemometry Advances and Applications, Manchester, 16-18/12/85

[2] - D. Afchain, P. Broussaud, M. Frugier, G. Rancarani
La soufflerie F2 du Centre du Fauga-Mauzac
20ème Colloque Aérodynamique appliquée AAAF - Toulouse, 8-10/11/1983. TP 1983-139

[3] - *Wind-tunnel seedig systems for laser velocimeters*
Proceedings of a workshop held at NASA Langley - 19-20/03/85 - NASA Conference Publication 2393.

[4] - P.O. Witze, T.A Baritaud
Influence of combustion on laser Doppler velocimeter signal quality in a spark ignition engine.
Int. Symp On Laser Anemometry, Miami, 17-22/11/85 - ASME n° FED, Vol 33

[5] - R.Schodl, H.Selbach, H.G Lossau
Comparison of signal processing by correlation and by pulse pair timing in laser dual focus velocimetry.
Proceedings o the Symp. on long range and short range optical velocity measurements, Saint_Louis, 15-18/09/80.
Rapport ISL 117/80.

[6] - A. Boutier
Laser velocimetry and wall approach limitations
Int. Laser Anemometry Symp, Miami, 17-22/11/85. TP ONERA N° 1985-155.
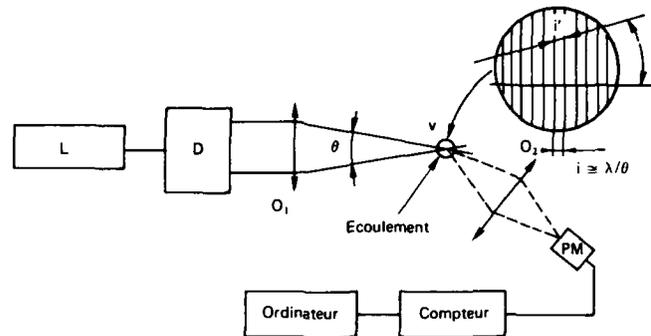
Figure 1 - Schéma de principe d'un vélocimètre laser à franges monodimensionnel (mesure
d'une composante de la vitesse).
L : laser (de longueur d'onde λ)
D : division de faisceaux
O_1: optique d'émission
V : volume de mesure
O_2: optique de réception
PM : photomultiplicateur
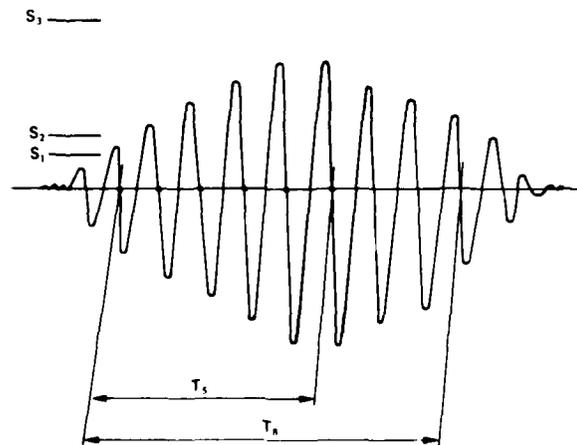
Figure 2 - Traitement du signal par comptage
$\nu = \dfrac{8}{T_8}$: mesure de la fréquence

critère de validation $\dfrac{T_5}{T_8} = \dfrac{5}{8} \pm 1,5$ %

Mesure initialisée si le signal dépasse le seuil S_1
Mesure validée si après T_8 le signal dépasse $S_2 > S_1$: c'est pourquoi
généralement un compteur mesurant sur 8 alternances requiert au moins la
présence de 10 alternances dans le signal.
S_3: seuil haut pour éliminer les grands signaux dûs aux grosses particules
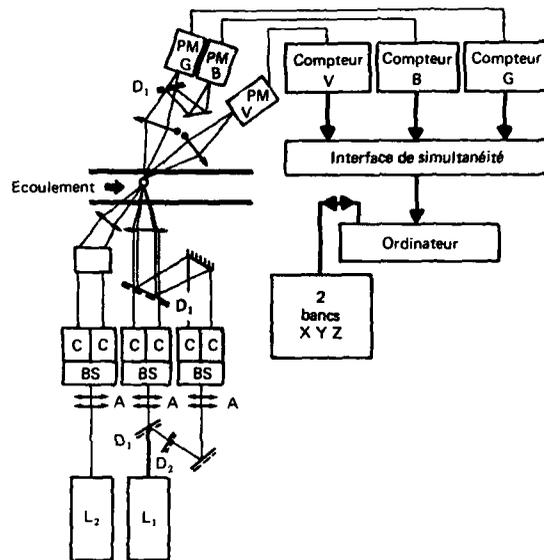
Figure 3 - Schéma du vélocimètre laser tridimensionnel de l'ONERA

L_1: laser à argon 15 W, utilisé à 8 watts toutes raies

L_2: "   "   "   "   " 3 watts sur la raie λ = 476,5 nm (V)

D_1: lame dichroïque transmettant seulement le vert (λ = 514,5 nm) (G)

D_2': lame dichroïque transmettant seulement le bleu (λ = 488 nm) (B)

C : cellule de Bragg + prisme et diasporamètre

BS : séparateur de faisceau

A : télescope afocal
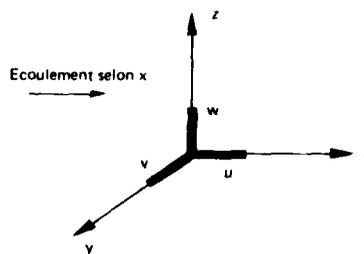
Figure 4 - Géométrie des composantes mesurées en vélocimétrie 2D et 3D
        (x, y : plan horizontal)

Figure 5 - Vélocimétrie tridimensionnel de l'ONERA
D : système de division de faisceaux
R : rail
TA : télescope Cassegrain pour les composantes verte et bleue
TB : " " " la composante violette
A : optique émettrice bidimensionnelle (vert-bleu)
B : optique émettrice violette
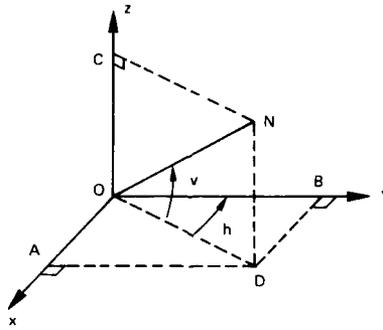
Figure 6 - Détermination des caractéristiques de la direction d'un faisceau laser avec
un théodolite ($\overrightarrow{ON}$: vecteur unitaire parallèle au faisceau laser)
Oy : axe de référence
$v = (OD, ON)$ } mesurés par le théodolite
$h = (OD, OB)$
$\overrightarrow{ON}$ $\begin{cases} A = \cos v \sin h \\ B = \cos v \cos h \\ C = \sin v \end{cases}$
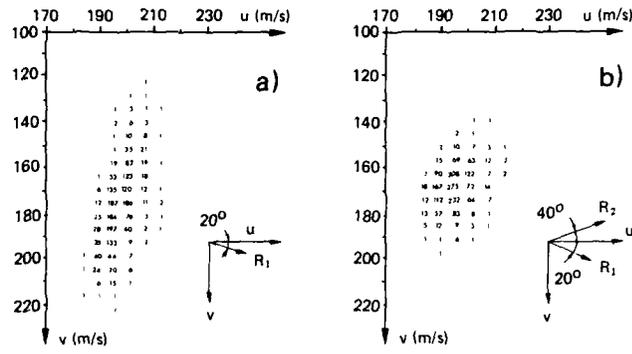
Figure 7 - Histogrammes bidimensionnels dans le plan (u, v) d'un écoulement de turbulence isotrope
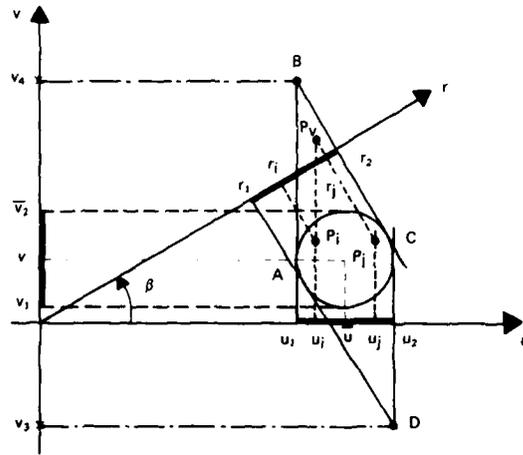
Figure 8 - Intensités de turbulence mesurées dans un écoulement à turbulence isotrope, dues à des "particules virtuelles".
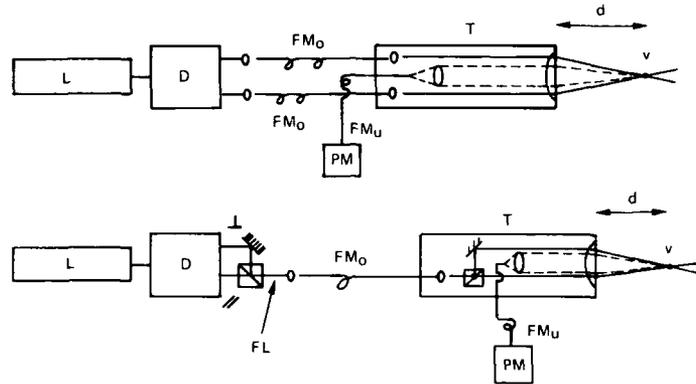
Figure 9 - Schémas de principe de vélocimètres laser utilisant des fibres optiques

L : laser

D : division de faisceau

FM_o: fibre monomode (conservant la polarisation)

FM_u: fibre multimode

T : tube sonde (typiquement 20 mm de diamètre sur 100 m de long)

FL : deux faisceaux laser recombinés, décalés en fréquence par une cellule de Bragg et de polarisations orthogonales

PM : photomultiplicateur

V : volume de mesure

d : distance de visée de l'ordre de 50 mm.
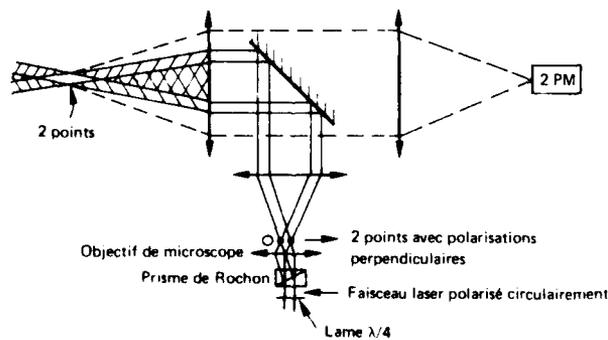
Figure 10 - Schéma de principe d'un vélocimètre deux points

11 a): Deux traits

Point source $\Sigma\lambda$

Lames inclinées e = 20 mm

Bleu

20 μm

100 μm

260 μm — Vert

P.M. bleu

P.M. vert

Lame dichroïque

M_i : miroirs
P : prisme dispersif
O_1 : objectif de microscope
O_2, O_1 : objectifs de 500 mm de focale,
　　　　　ouverts à f/5

11 b): Deux croix

Bleu Vert　　　　Bleu Vert

Ecoulement ►
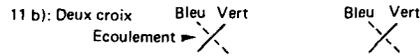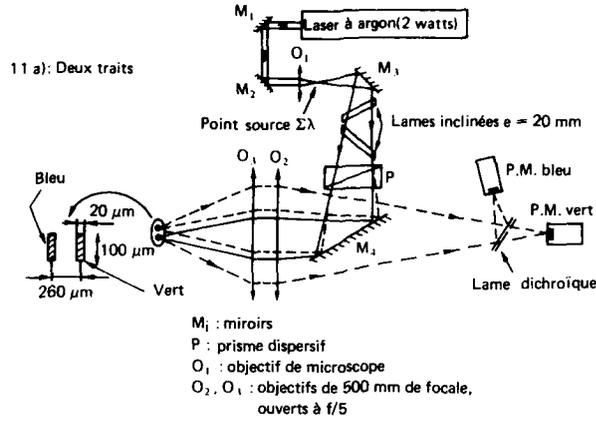
Figure 11 - Schéma du vélocimètre laser deux traits de l'ONERA
　　　　　　11a : deux traits
　　　　　　11b : deux croix
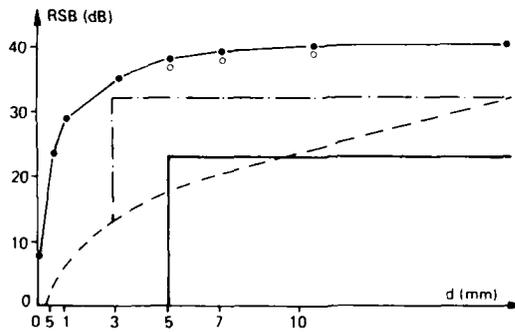
Figure 12 - Evolution du signal sur bruit (RSB) avec la distance d du volume de mesure
　　　　　　à la paroi

-•-•-•— Vélocimètre à franges
————— Vélocimètre 2 points
— — — — Vélocimètre 2 traits (rétrodiffusion axiale)　　　P_1 3w pour les vélocimètres à franges
—·—·—·— Vélocimètre 2 traits (rétrodiffusion hors de l'axe)　　P_1 0,5w dans chaque point ou chaque trait.

DISCUSSION

A.Strazisar, US

Why did you create two dashes of different colours, one green and one blue?

Author's Reply

At first, it was very simple to achieve: a prism disperses the wavelengths to create spots of different colours and independently inclined plates create astigmatism. Moreover this was essentially done to avoid noise cross talk between photodetectors in the receiving part. But this cross talk is only important at a large distance from the wall (about 3 or 5 mm) when the green and blue laser beams impacts on the wall begin to overlap.

J.Fabri, FR

Each type of LV has its advantages and drawbacks; there is not a well defined barrier between their applications domains. I want to emphasize that fact that wall approach limitations are different if the laser beams are parallel or perpendicular to the wall: in the first case LDV probe volume can be approached within 0.5 mm for instance, and in the second case L2F must absolutely be employed for the same approach. The L2F is not able to perform measurements in highly turbulent flows, i.e. recirculation zones for instance: but it allows the determination (even between rotor blades) of the limits of such types of flows; very often it is enough to have this knowledge, without asking for a detailed survey of the flow field inside this turbulent region (where calculation models do not exist). This type of information enables a better understanding of the flow through the machine and does not require further detailed measurements.

APPLICATION OF DOPPLER AND TRANSIT LASER ANEMOMETRY
IN SMALL TURBOMACHINES
BY
R.L. Elder
C.P. Forster
M.E. Gill
School of Mechanical Engineering
Cranfield Institute of Technology
Cranfield
Bedford
MK43 0AL
England

SUMMARY

This paper discusses the selection and application of laser anemometry systems to the particularly hostile environment found in small high speed rotating turbomachines.

There are several different laser anemometry systems which are used in turbomachinery studies and when selecting a system to carry out specific duties it is necessary to have some prior knowledge of the flows to be measured, the spacial resolution required and any limitations on optical access. The optical access will often determine the spatial resolution possible and the quality of the scattered signal will generally determine the type of signal processor which can be used.

The criteria used for the selection of systems at Cranfield are discussed. The arrangements in use include both the Doppler and Transit systems each of which are found to have unique and very distinct advantages. The conclusions of the paper are exemplified by measurements of the flows within small high speed compressors.

1   Introduction

Small turbomachines are being used in an increasingly wide range of applications. Small industrial and aerospace compressors handle all kinds of gases and rotate at up to 200 000 rpm. Of particular interest at Cranfield has been the small centrifugal compressor but studies on various axial machines have also been undertaken. For nearly all systems using these compressors the flow range, efficiency and surge characteristics are of paramount importance and the requirement exists to improve performance and obtain a better understanding of the flow processes involved. There are many design techniques available which attempt to achieve an analytic definition of performance but in order to validate these models it is necessary to be able to measure the flow through actual machines.

In the case of the centrifugal impeller, gas is accepted in an axial direction and expelled at higher temperature, pressure and velocity in a radial direction. There are many complex fluid changes taking place due to rotation, curvature and diffusion processes within the impeller. These complex and interactive fluid processes produce a flow through the impeller and diffuser which is maldistributed and time dependent. Although the flow through axial machines remain in essentially the same plane, the processes in other respects are almost as complex.

The flow structures involved in these processes place high physical demands on any instrumentation used to measure the parameters. The instrument must be sufficiently robust to withstand the unsteady aerodynamic forces, it must not disturb the flow and (especially for the smaller units) it must have good spatial resolution and fast response. Whereas on larger, lower speed units pressure probes and hot wire anemometers may be used, these instruments become unsatisfactory in small high speed machines and it is here that the laser anemometer has been most usefully employed.

This paper attempts to discuss some of the major problems encountered during such laser anemometry studies and how some of these problems have been overcome. The paper exemplifies some of these problems with results from various studies.

2   Experimental Arrangement and Equipment

There are several commercially available laser anemometry systems. These are invariably designed as modular systems so that anemometers can be assembled to suit specific measurement applications. When designing a system it is necessary to have some prior knowledge of the flows expected and also of the practical limitations on optical access.

The optical access will generally determine the optical arrangement of the anemometer. If only one access window is available then only a full backscatter system must be used and if good spatial resolution is required then a Transit anemometer (Schodl (1), Brown and Pike (2)) would normally be chosen in preference to a Doppler system. If two access windows are available, however, then an oblique scatter Doppler anemometer, (LDA) system can overcome the resolution problem, (Elder Forster, Gill(3)).

The quality of the scattered signal will generally determine the processing system used. The choice of signal processor involves a compromise between the ability to operate in a harsh signal-to-noise environment and the speed at which measurements may be taken. Cranfield's choice of processor, a correlator (Abbiss, Chubb and Pike(4)), favoured a system with a very good ability to operate with poor signals. The processor is generally connected to a computer for on-line data reduction or storage.

Design of Current Laser Anemometer Systems

Turbomachinery studies at Cranfield have involved two main types of flow. The first has involved radial flows (ie the flow exiting from a centrifugal impeller) and for these studies it has been possible to incorporate two optical access windows in the available hardware. For these studies therefore, it was decided to use a single axis LDA system working in oblique forward scatter, Figure 1. The exit channel dimensions of 7mm wide were typical and problems were expected with high background flare levels due to the proximity of the wall to the measurement volume. Thus correlation was chosen as a signal processing system trusting this to be the more certain, albeit slower, processing technique. A 35mW HeNe laser and beamsplitter were mounted in a rotation cradle to allow two components of the flow velocity to be measured. These components were arranged so that any small radial inflow on the impeller could be measured. No large flow reversals were expected and frequency shifting was not used. Since a blade to blade flow profile was required the correlator was strobed so that each measurement took data from a similar small time slot between each blade. The correlation data is passed to a DEC PDP11 computer for storage and is processed later using a program based on the work of Abbiss (5) and Sharpe (6). This system has been used extensively to take measurements on a more or less routine basis on a variety of different compressor configurations.

The second major field of study has concerned annular flows (ie axial compressor flows and flows within the inducer of centrifugal compressors). In these studies it is generally only possible to have a single access window and a full backscatter anemometer, the Malvern Instruments 4772 Transit Anemometer, has been used (Brown and Pike (2)). The photomultiplier output was connected to a correlator and the results processed on line by a PDP11 using a program based on the work of Ross (7). Strobing was necessary for these measurements and working in the blade row caused no special problems although the blade shadow prevented measurements in some areas. To provide sufficient particles for scattering, 0.5 micron diameter seed particles (corn oil) were introduced into the flow.

3   Analysis Techniques

The output from the photomultiplier tube consists of a series of digital pulses or an analogue voltage corresponding to the arrival of scattered light on its receiver. Processing of these pulses is carried out by a correlator, the correlation technique being very effective at extracting the required signal from the noise present in the photomultiplier output. The purpose of the data analysis technique to be applied to the correlation function, is to extract from it information about the particles that gave rise to it; usually their mean velocity, and the spread of velocities, or the turbulence of the flow.

The methods of data analysis are quite different for the two arrangements of anemometer, Doppler and Transit, but the purpose of each is usually to determine (from the correlation function) the velocity probability density function of the particles, from which the mean flow velocity and turbulence intensity can be derived. One major difference between the two anemometer arrangements is that the Doppler anemometer measures a component of the flow velocity in the plane of the two beams, and normal to the axis of the anemometer, and it is usual to obtain a second component by rotation of the plane of the beams in order to define the flow vector. Optimum accuracy of the velocity measurements can be obtained by careful selection of the velocity components to be measured. The Transit anemometer, however, measures the magnitude of the velocity of a particle travelling in the plane of the two beams. To define the velocity vector for the Transit arrangement, the plane of the two beams is rotated until it is aligned with the mean flow direction, a condition that can be identified by a correlogram having the maximum peak height to base line ratio, but which is also calculated more accurately by the analysis to be described below.

3.1   Transit Anemometry Data Analysis

The data analysis technique employed when taking measuremnts with the Transit anemometer is based on the theory of Ross (7). It is essential to carry out this analysis on-line to ensure that the mean flow direction has in fact been defined. As the plane of the two beams is rotated, the shape of the correlation function changes, figure 3. Where the plane of the beams is out of alignment with the mean flow, the correlogram will have a small peak, on a high baseline level (caused by particles passing through only one beam). As the plane becomes aligned, (figure 3 again) the peak height increases, while the baseline level decreases.

The Ross analysis relies on assuming a Gaussian model for the flow turbulence, from which it is possible to derive an expression describing the correlation function, $G(\tau,\alpha)$, at a given orientation α. If the expression for $G(\tau,\alpha)$ is integrated over τ, an expression for the integrated counts, or area under the correlogram peak is obtained which depends only on the orientation α, and the mean flow orientation α_0.

The technique proceeds by taking correlograms at different angles and calculating the integrated counts for each correlogram, figure 3. This enables the mean flow direction to be calculated. Taking the correlation function at the orientation closest to the mean flow angle, the mean flow velocity and turbulence intensity can be calculated from the knowledge of the form of $G(\tau,\alpha)$. The details of the analysis are described in Ross (7), and Elder, Forster & Gill (3,8).

3.2   Doppler Anemometry Data Analysis

Several techniques are available for the analysis of the correlation functions arising from a Doppler anemometry experiment, Brown & Gill (9). It has been found, however, that in the generally noisy data obtained when taking measurements in turbomachines, the Fourier transform analysis of Abbiss (5) is the most reliable. The analysis again relies on deriving an analytical expression for the correlation function, in terms of the velocity components of the flow. The Fourier transform technique takes advantage of the fact that the Fourier transform of an autocorrelation function yields the power spectral density of the flow, which in turn is related to the velocity probability distribution. The analysis is complicated by the fact that, superimposed on the oscillatory correlation function, the frequency of which relates to the frequency of particles passing through the fringe pattern, is a decaying baseline, figure 4, the shape of which is due to the Gaussian intensity distribution across the laser beams. Removal of the baseline can result in problems in 'blowing-up' any noise present in the correlogram, and can cause accuracy problems, especially in the turbulence intensity calculation. The analysis technique, therefore, consists of the following steps. A first approximation for the mean flow velocity can be made by assuming a linear base line. Using this approximation, the exact form of the Gaussian baseline can be derived, and removed from the correlation function, taking care that no amplification of unrealistic noise signals takes place. Fourier transform of the modified function now yields the velocity probability density function of the flow, from which the mean velocity and turbulence intensity values can be calculated.

4   A study of Impeller Outlet and Vaned Diffuser Inlet Flows

It has become reasonably well appreciated that the flow within a centrifugal impeller can separate providing a very distorted flow at the impeller outlet with regions of attached and separated flow. The purpose of this investigation was to determine the nature, if any, of the aerodynamic coupling between the impeller and downstream vaned diffuser.

It is important to emphasise that the results shown here are representative only and that the scope of the study was extensive involving more than one impeller and several diffuser arrangements.

The experimental arrangement was generally as illustrated in figure 1 and the oblique forward scatter LDA system described previously was used with a twin window arrangement.

The compressor casing was modified to allow different diffuser inserts to be used for a vaneless and vaned builds. Instrumentation was available to allow standard performance mapping of the compressor and these results were displayed on-line using a microcomputer. The controls for the rig and most of the instrumentation were housed in a control room next to the test house for both safety and comfort of operation.

The measurements were taken on a 100mm diameter impeller of backswept blade design. Speed of rotation was 75 000rpm and measurements were taken at various stations.

Typical laser anemometer results for the vaneless diffuser build are shown in figure 5. These indicate that the flow through the impeller is very complex and it may be expected that there are several different mechanisms at work to account for the flows observed at the tip. Such results are extremely interesting and will be discussed elsewhere.

The radial velocity profiles for both the choke and surge flows are shown in Figure 5. At choke flow there is a wake extending almost all along the shroud surface whereas towards surge the wake is more limited in extent but deeper in the blade passage and situated in the shroud/suction surface corner.

Figure 6 shows typical measurement stations in the vaneless and semi-vaneless space of the vaned diffuser builds. Results for two instances (positions of the impeller) are shown. The flow is clearly unsteady with transient flow at the diffuser inlet and flow switching occurring in the semivaneless space as the rotor blade passes. The quantitative effects of such flows are not usually accommodated in diffuser design and it is difficult to believe that a better understanding and control of this process would not yield worthwhile benefits. The unsteadiness of the flow field is further emphasised in figure 7 where flow angle variation at various points on the pitch diameter of the diffuser vane leading edge show angular fluctuations of nearly $20°$. If any further evidence of the presence of unsteady flows is required these are demonstrated in figure 8 which shows the average velocity at the diffuser inlet throat. The above results are for a vaned diffuser arrangement in which the vane leading edge was at a radius ratio of 1.075 and had 22 vanes.

It is also noteworthy that in addition to the unsteady flow effects there are sizeable differences in the average flow angle across the passage (across the diffuser vane height) for which no account is normally made in the design process.

5   A Study of Stator Outlet Flow in a Small Transonic Fan

As for a centrifugal compressor, the flow in an axial machine operating under reasonable stage loadings and realistic tip clearances is exceedingly complex and this study involved an assessment of the flow conditions at the stator exit of a compressor stage. In this arrangement the blade height was 25mm and the rotational speed 70 000rpm. Figure 9 shows the experimental arrangement with a single access window. In this case the Transit Anemometer described in Section 2 was used. Although measurements were made downstream of a stationary blade row, the results were strobed at

rotor blade passing frequency in order to ascertain the rotor unsteadiness transmitted through the stator. Indeed the degree of unsteadiness transmitted was surprisingly large. Figure 10 shows typical results for design flow conditions. They show considerable distortion and of particular interest is the low velocity region near the stator suction surface/hub corner providing evidence of stall in this region. Similar problems have been reported in low speed compressor studies, Joslyn and Dring (10) which probably arise due to excessive diffusion in the stator tip section and the clearance flow.

6   Problems

Processor speed – In Doppler systems the speed of the processor limits the number of fringes in the control volume, Elder (11), and although analysis is possible (using the correlator) with only three fringes, the analysis is more accurate and the turbulence intensity more easily defined if 10-20 fringes are used. This is not such a problem with counters and trackers (which generally have a higher frequency capability but these tend to increase other problems particularly where the signal is very noisy). Transit anemometers have less exacting processing requirements because the spot spacing is approximately ten times larger than the fringe spacing.

Seeding – Although there is a common requirement to operate with only natural seeding, almost inevitably, additional seed has to be added. For the studies described in this paper great care has to be taken to ensure that seed particles are around 0.5 micron diameter, Elder (11).

For compressor studies where the flows are usually at a temperature of less than 200°C liquid droplet seeding appears to be satisfactory although great care has to be taken when injecting the droplets into the flow to avoid coalescing (the presence of large particles in rotating blade passages becomes immediately apparent because they tend to hit the blade surface and be centrifuged onto the optical access windows). For turbine studies, due to the higher operating temperatures it has been necessary to adopt solid particles (usually titanium dioxide although other substances have been tried). The problem with small solid particles is that, although they may fundamentally of a suitable size (typically 0.2 m) the particles tend to coagulate. The problem is made worse because titanium dioxide is naturally hygroscopic. Indeed these problems may have become insuperable if the plastic industry did not require titanium dioxide particles (of a suitable diameter)treated in a manner preventing the hygroscopic nature and therefore the tendancy to coagulate.

Window Fouling – This a repeating problem and unless windows can be kept reasonably clean for a period of approximately 40 minutes, measurements become increasingly tedious. In-situ window washing arrangements have been used in the past but their general use has been avoided because it has usually proven possible to keep windows clean for longer than the 40 minute period. Instead of these in-situ cleaning arrangements, care has always been taken to ensure the easy removal of windows for cleaning. Excessive window fouling has often been found to be due to the excessive size of oil seeding particles.

Difficulties have also been found with the use of anti-reflection coatings on windows because when they are placed in harsh environments the coatings become damaged by particles in the flow and the damaged coatings give more problems than uncoated surfaces.

Difficult problems have also required drastic and novel remedies. In some cases where windows were observed to suffer from the spluttering of oil particles on the surface which destroyed the wavefronts of the input laser beams it was found beneficial to thinly coat the surface with oil before mounting the window in the rig, figure 11. Window surfaces 'treated' in such a manner tended to reduce the 'spluttering' problem by dissipating the oil globules.

There are significant improvements to be achieved by using a window arrangment where the window is not flush with the flow but displaced with a small apperture, typically 1mm, opening onto the flow as shown in figure 12. The limit here is the acceptability of the small apperture but the method has proven useful for the input of Doppler input beam pairs which can often comfortably be accomodated within 1mm.

Signal Strength – Throughout most turbomachinery studies in which laser anemometry is used, great emphasis is put on methods in which signal strength can be improved relative to background noise. Methods of improving signal strength include using larger seed particles, more laser power (or more appropriate frequencies for optimum PMT response) and fluoresence. Unfortunately these techniques (and others which have been considered) suffer severe problems. For example:

   a) Increased laser power – tests undertaken suggest that using more
      powerful (and expensive) lasers tend to generate almost equal
      increases in signal and noise such that the ratio of signal to
      noise is not noticeably improved. (It usually appears that it is
      the low ratio of signal to noise that creates processing problems
      rather than the lack of signal).

   b) Larger seed particles – undoubtably this makes measurements
      easier (due to their increased scattering capability) but if this
      requires particles greater in diameter than 0.5 m this inevitably
      infers that flow tracking problems emerge in regions of rapidly
      accelerating flow.

c) Fluorescent particles (which have the capability of differencing the noise and signal frequency such that the signals can be preferentially selected by the use of narrow band filters) - again a useful idea but the size of the fluorescent particle is a problem, also the advantages of the technique are overcome as surfaces become coated. A derivative of this technique involves coating surfaces from which flare emerges with fluorescent material. Again the purpose is to difference the flare (noise) and signal frquencies but this has been found to be generally unsatisfactory because better results can usually be obtained with a black surface (matt black or gloss black).

Particle Bunching - Bunching of seed particles can occur due to various factors and need not necessarily infer that, at the place of measurement, the particles do not follow the flow. For example if seed particles are injected locally into the upstream flow of an impeller only a comparatively few of the particles may penetrate the wake flow where measurements are being taken. This can cause scattered light intensity which varies with blade passing frequency. This periodic variation in light intensity can be detected through the correlator (which after all is used because of its inherent sensitivity to embedded frequencies). The tendency is for the correlation function due to this phenomena to become superimposed on that due to the required signal, Brown, Forster and Gill (12). This can occur for either Doppler or Transit systems and its existence tends to complicate the 'baseline' of the correlation function. To overcome this the analysis techniques have to be modified. These procedures generally introduce some doubt in the accuracy of measurements, particularly the definition of turbulence intensity (and especially for the Transit system in highly turbulent regions).

7   Accuracy and Validation

In all studies great effort is undertaken to ensure, as far as possible, that results presented are valid. This commonly involves three separate undertakings:

a) Repeatability - It should be possible to repeat results to within reasonably close tolerances (usually 1%).

b) Local Conservation of Physical Parameters (usually mass and momentum) - This involves repeating measurements in adjacent planes and comparing results for the conservation of mass and angular momentum. Typical results are shown in figure 13 (note that the parameters shown are only constant if density is uniform).

c) Agreement with Bulk Parameters - It should be possible to detine (reasonably accurately) such parameters as overall mass flow and work input across a rotor (using the Euler relation). Typical results are shown in figure 14. It should be noted that the mass flow check can be difficult to satisfy to even a comforting level because of uncertainties in the local density (particularly in high speed machines) and also that local parameters may differ from bulk factors where flow distortion is present (for example due to the collector system).

It is considered that such checks are a important undertaking in laser anemometer studies providing confidence to both the measurement engineer and aerodynamicist.

8   Conclusions

This paper has described some of the approaches and problems encountered during studies in high speed compressor studies in which laser anemometry has been used.

The paper also describes studies undertaken to examine the flow in both centrifugal and axial flow compressors. These studies have shown that the impeller outlet flow and stator outlet flows are very distorted.

In conclusion, it is worth commenting that, despite the high speed flows involved in these and similar high speed compressor stuides, the laser anemometer can be applied and has provided useful results.

References

1. Schodl, R. Laser-Two-Focus Velocimetry (L2F) for use in Aero Engines. AGARD LS90, Laser Optical Measurement Methods for Aero Engine Research and Development, p. 4-1, 1977.

2. Brown, R.G.W., Pike, E.R. A Combined Laser Doppler and Time of Flight Anemometer. Optics and Laser Technology, Dec 1978.

3. Elder, R.L., Forster, C.P., Gill, M.E., Initial Findings During Studies of the Flow Within a High Speed Impeller Using a Transit Anemometer. Fourth International Conference on Photon Correlation Techniques in Fluid Mechanics. Stanford University, California, Aug. 1980.

4. Abbiss, J.B., Chubb, T.W., Pike, E.R., Laser Doppler Anemometry. Optics and Laser Technology, Dec 1974.

5. Abbiss, J.B., Photon Correlation Velocimetry in Aerodynamics. Photon Correlation Spectroscopy and Velocimetry. NATO Advanced Study Institute Series, edited by H.Z. Cummins and E.R. Pike, 1976 (New York: Plenum Press) p.386.

6. Sharpe, P.R. An On-Line Data Reduction System for Photon Correlation Laser Anemometry. Physica Scripta. Vol.19 p411-416 1979.

7. Ross, M.M. Transit Laser Anemometry Data Reduction for Flow in Industrial Turbomachinery Optica Acta, Vol.27, no 4, p511-528, 1980.

8. Gill, M.E., Forster, C.P., and Elder, R.L. Measurements in Turbomachines Using Two Spot Anemometry. Springer Series in Optical Sciences, Vol. 38, ed Schulz - DuBois, 1982.

9. Brown, R.G.W., Gill, M.E. A Comparison of Photon Correlation Laser Doppler Anemometry Data Processing Techniques. Max Born Centenary Conference SPIE, Vol.369, 1982.

10. Joslyn, H.D. And Dring, R.P. Axial Compressor Stator Aerodynamics, ASME Gas Turbine Conference, Amsterdam paper 84-GT-90, 1984.

11. Elder, R.L., Lecture Notes on Laser Anemometry, Course on Measurement Techniques in Turbomachines, V.K.I., May, 1981.

12. Brown, R.G.W., Forster, C.P., Gill, M.E. The Form of Laser Transit Velocimeter Correlograms Obtained in Rotating Machinery. Optical Measurements in Fluid Mechanics 1985, Institute of Physics Conference Series No. 77 Edited P.H. Richards.
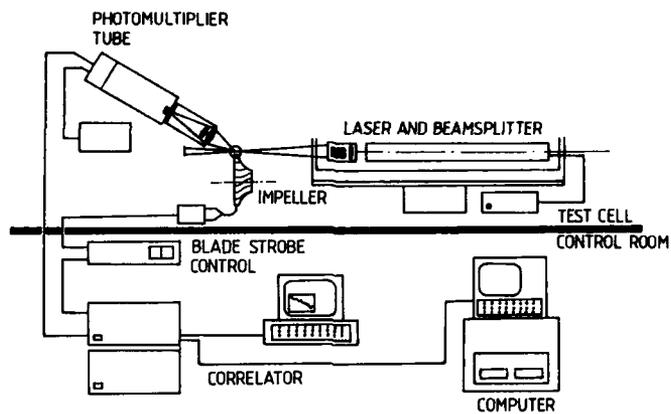
FIG. 1   LDA SYSTEM FOR FLOW MEASUREMENT IN TURBOMACHINES

FIG. 2   MALVERN INSTRUMENTS 4772 TRANSIT ANEMOMETER

CORRELATION

COUNTS

DELAY TIME

APPLY STATISTICAL TECHNIQUE OF CROSS CORRELATION TO INCOMING
SIGNAL BY ELECTRONIC MEANS

ANALYSIS OF CROSS CORRELATION FUNCTION

AS SPOTS ARE ROTATED ABOUT AXIS SIGNAL INTENSITY CHANGES
MAXIMUM SIGNAL OBTAINED WHEN SPOTS ARE IN LINE WITH
MEAN FLOW DIRECTION

COUNTS

θ_1 θ_2 θ_3 θ_4 θ_5

INCREASING ANGLE

INTEGRATED
COUNTS

θ_3
θ_2 θ_4
θ_1 θ_5

α_0

ANGLE

MAIN FLOW
DIRECTION

CALCULATION OF MEAN FLOW VELOCITY AND TURBULENCE INTENSITY

COUNTS

σ

τ_{PEAK} CHANNEL

$$VELOCITY = \frac{SPOT\ SEPARATION}{\tau_{PEAK}} \quad metres/sec$$

$$TURBULENCE\ INTENSITY = \frac{\sigma}{VELOCITY} \times 100\%$$

FIG. 3   SUMMARY OF TRANSIT ANEMOMETER ANALYSIS PROCESS

SIGNAL FROM
PMT

CORRELATOR AND
CORRELATOR STORE

CORRELATOR
CONTROL AND
DISPLAY

COUNTS

A TYPICAL CORRELATOR
RESULT (CORRELOGRAM)

PDP 11 COMPUTER FOR
STORAGE AND ANALYSIS
OF CORRELOGRAMS

CHANNELS

SIGNAL FROM
PMT

CLOCK (WORKING AT SAMPLE TIME)

SHIFT
REGISTER
AND GATES

CORRELATOR
STORES

CHANNELS

THE CORRELATOR

BACKGROUND
PROFILE
+
DOPPLER FREQUENCY
PROFILE

CORRELOGRAM
PROFILE

BACKGROUND PROFILE REMOVED

VELOCITY

VMIN VMAX

FOURIER COSINE TRANSFORM OF
PREVIOUS PROFILE GIVING
VELOCITY DISTRIBUTION

ANALYSIS OF CORRELATOR DATA

FIG. 4   SUMMARY OF DOPPLER ANEMOMETER ANALYSIS PROCESS
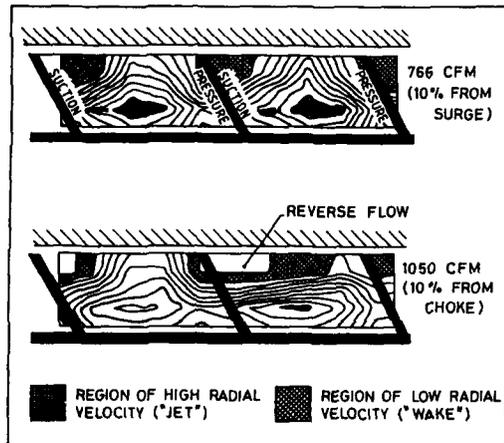
FIG.5 RADIAL VELOCITY PROFILES AT IMPELLER EXIT IN VANELESS DIFFUSER

766 CFM (10% FROM SURGE)

REVERSE FLOW

1050 CFM (10% FROM CHOKE)

REGION OF HIGH RADIAL VELOCITY ("JET")

REGION OF LOW RADIAL VELOCITY ("WAKE")

---- FLOW FROM BLADE POSITION 1
—— FLOW FROM BLADE POSITION 2

MID CHANNEL AND PEAK EFFICIENCY

FLOW TRAJECTORIES IN THE SVS

VELOCITY VECTORS IN THE SVS REGION AT TWO ROTOR POSITIONS

+ MEASUREMENT STATION
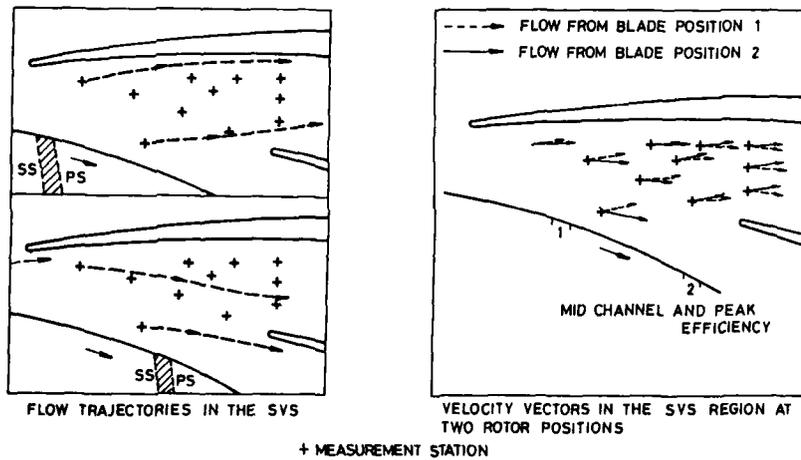
FIG.6 TYPICAL RESULTS FROM THE DIFFUSER INLET REGION OF A CENTRIFUGAL COMPRESSOR
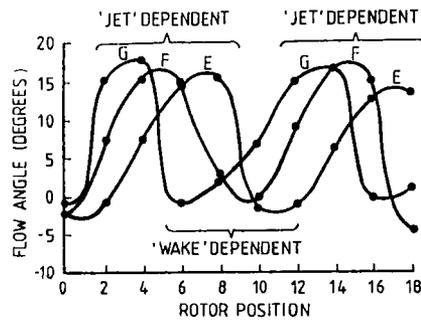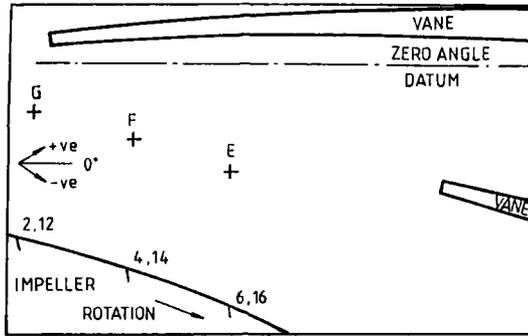
FIG. 7   FLOW DIRECTION AT VARIOUS POSITIONS IN
THE SEMI-VANELESS SPACE
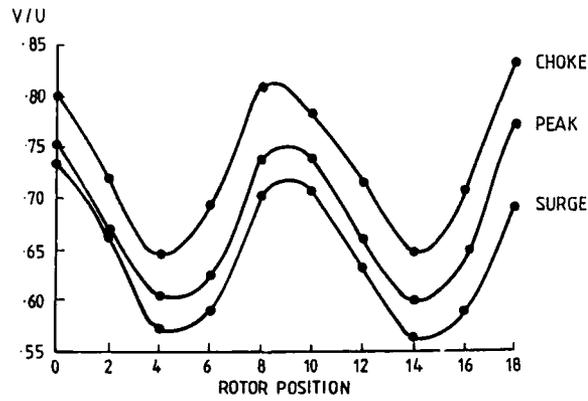
FIG. 8   VARIATION OF THROAT VELOCITY WITH ROTATION
OF THE IMPELLER (VARIATION FOR ONE BLADE
AND ONE SPLITTER PASSAGE SHOWN)
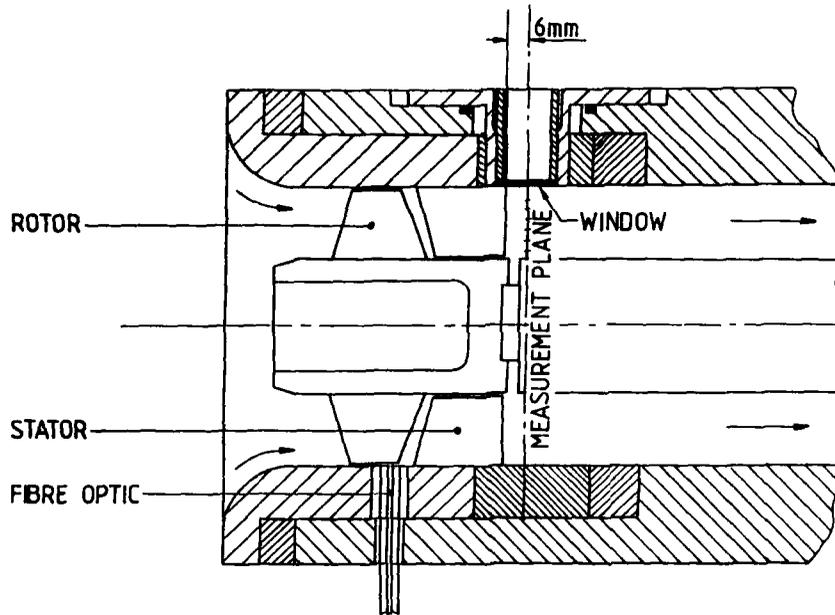
FIG 9 GENERAL ARRANGEMENT FOR THE SMALL AXIAL FLOW
COMPRESSOR STUDY
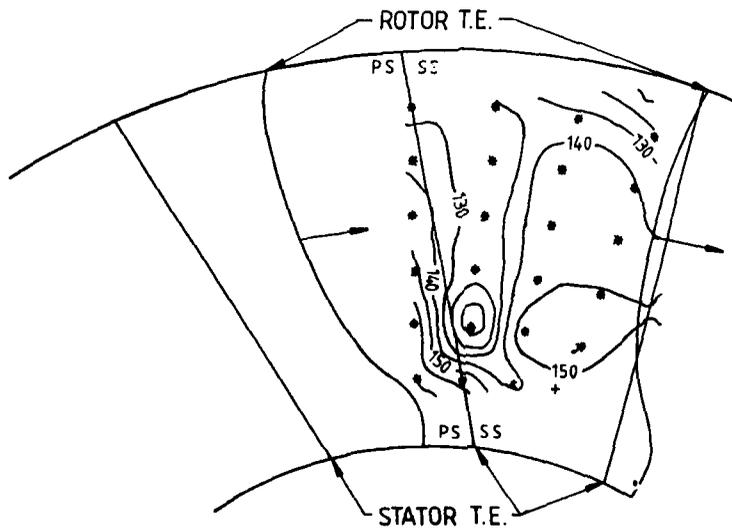
FIG 10 TYPICAL RESULTS SHOWING THE INSTANTANEOUS
FLOW DOWNSTREAM OF THE STATOR
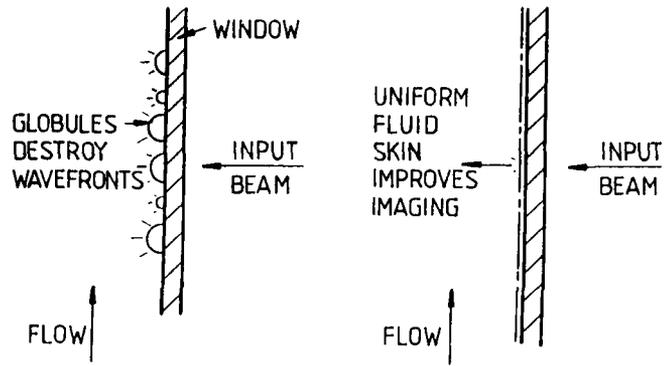
FIG. 11   IMPROVEMENT TO TRANSMISSION QUALITY
           USING OIL FILM
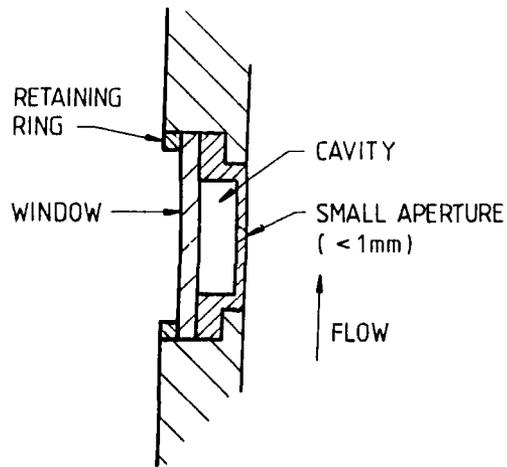
FIG. 12   SIMPLE ARRANGEMENT FOR A WINDOW WITH
           SMALL APERTURE AND CAVITY
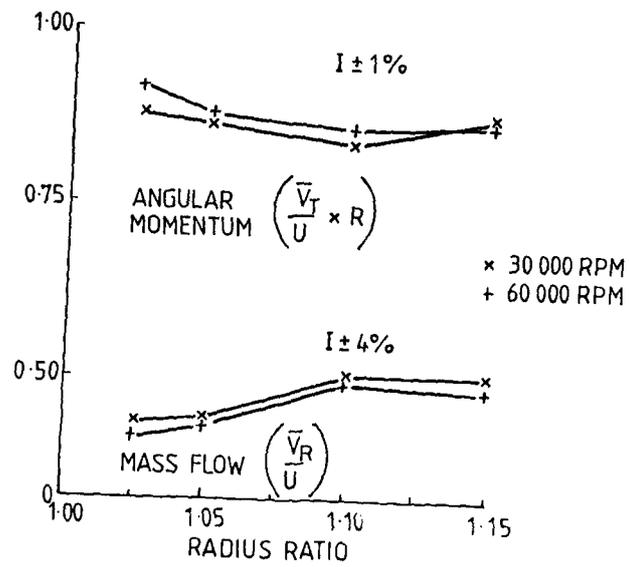
FIG.13 CONTINUITY CHECKS ON L.A. DATA

(a) MASS FLOW

(b) WORK DONE FACTOR
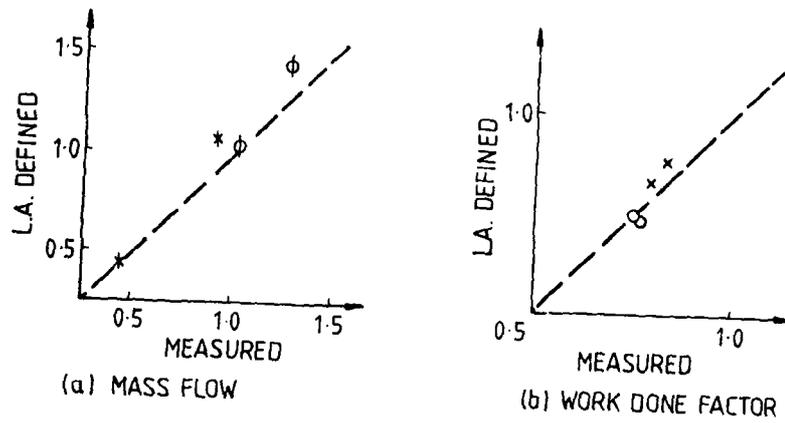
FIG.14 COMPARISON OF BULK PARAMETERS WITH INTEGRATED LOCAL PARAMETERS

DISCUSSION

A.Boutier, FR

First a comment: at ONERA we found an oil (Rhodorsil) which allows measurements with a L2F until 700 K.

Secondly, I want to mention works done on data processing of the autocorrelation function by Dr Staas (Philips Research Lab.) and Dr Tiemersma — Thoone in Netherlands: they tend to point out that the best way is to use a linear transform to obtain $(\bar{u}, \overline{u'^2})$ instead of Fourier or cosine Fourier transform, especially for turbulence rates not too low (cf. Proceedings of ASME Meeting in Miami, November 1985 and LDA Symposium in Manchester, December 1985). What is your opinion?

Author's Reply

The temperature limits for seeding presented in our paper are only intended to be indicative of those for materials we have used. They are not absolute limits and the substance you have mentioned will add a useful extension to the temperature range for liquid seed, although not satisfying our current temperature requirements.

Referring to your question about data analysis techniques, although we have no direct experience of the technique you refer to, we have undertaken quite detailed comparisons of correlator data reduction techniques (reference 9 of our paper) and these have demonstrated the ability of cosine transform techniques to extract the required information from the correlation function. These techniques, however, are computationally cumbersome and in low noise situations there are several other equally adequate and simpler techniques.

A.Ederhof, Switzerland

There are discrepancies in locally measured and integrated and overall data in mass flow (about 10%) and work. Do you think these deviations are caused by LA inaccuracies or mainly by integrating locally achieved data and comparing them with bulk data?

A.Melling, UK

The checks on mass flow and work done indicated on figure 14 are difficult to perform because of uncertainty in the determination of local density and possible deviation from axisymmetry of the flow.

In addition, it is not clear a priori that the product (mean density) × (mean velocity) is the same as the mean of (density) × (velocity). In my experience, the mean flow found by integrating the velocity profile from laser anemometer measurements is invariably higher than that found from, say, a nozzle flowmeter, as your results also show. A systematic discrepancy arising from particle lag would require that the work done factor be lower than that deduced from the enthalpy rise of the fluid, although this is not consistent with figure 14b. Would you be able to comment whether the deviations are systematic or random?

Author's Reply

You are of course correct in suggesting the difficulties associated with simple minded averaging; however, such checks remain an essential confidence building feature, not to be dismissed lightly, although comparisons should be qualified.

The largest areas of uncertainties appear to be associated with the averaging process which is based on inadequate numbers of data points and inadequate knowledge of the density field. Another problem is the possibility of circumferential distortion. Bearing in mind these uncertainties, the agreement shown (on average much less than Dr Ederhof suggests) was considered to be realistic. There appears to be little reason to attribute any disagreement to the basic accuracy of the laser anemometer.

The disagreement observed was not attributed to systematic errors because, considering both these and other results, I find no systematic trend and all discrepancies are within the uncertainties described above. Maybe the problems you refer to can less easily be dismissed during studies on larger machines where more detailed flow mapping is possible. I would also add that the photon correlation process (used here) is less susceptible to biasing results to larger seed particles than other systems where some analog threshold is used.

J.Fabri, FR

I would make a comment on this discussion, I think it is better to make a check even if it is not perfectly correct than not to make any checking.

A.S.Nejad, US

We worked in a compressible highly turbulent flow (hundred feet/s). The mass flow deduced from LV velocity measurements is always higher than the measured mass flow. The local mean velocity value is always higher than expected due to the higher probability for measuring high velocities and to the coincidence bias when using 2D LV; this induces also incorrect measurements of the turbulence intensity.

When you try to make velocity measurements very correlated on two components, you introduce a very small window (i.e. 10 to 20 μs) and you systematically record only the very fast particles that meet your criterion of small window. So your local is always higher than the true velocity. Many methods of velocity weighting may be used; high data rates are necessary. All these problems are not easily solved.

A.Boutier, FR

I do not want to initiate a debate on velocity bias, because it will last all the day; but I want to make some comments. Importance of velocity bias can only be shown at high values of the turbulence rate, not at low values. The criterion of MacLaughlin-Tiederman which says that you measure more higher velocities than lower velocities is completely false: in practical cases you must not apply this correction. You have to verify the physics of your flow, i.e. to calculate the correlation coefficient between the data rate and the velocity.

There is no significant velocity bias in the low turbulent flows described in the paper.

LASER VELOCIMETRY STUDY OF STATOR/ROTOR INTERACTIONS

IN A MULTI-STAGE GAS TURBINE COMPRESSOR

M. Carlson Williams
United Technologies/Pratt & Whitney
400 Main Street
East Hartford, CT 06108

Summary

The measurement of airflow through multi-stage compressor rigs has generally been
limited to the use of flow perturbing pressure and temperature probes. Although
limited studies of the dynamics of these flows have been obtained with hot wire and
hot film probes, the advent of the laser doppler velocimeter with its non-
perturbing nature is expected to develop into the preferred instrumental method.

To assess the feasibility of utilizing an LDV in these flows, an exploratory program
sponsored under the NASA Energy Efficient Engine Contract, NAS 220646, was recently
undertaken at Pratt & Whitney. A multi-stage compressor rig, the Energy Efficient
Engine high pressure compressor consisting of 6th through 15th compressor stages, was
outfitted with windows between the 6th stator-7th rotor, 9th stator-10th rotor, and
13th stator-14th rotor. The windows, extending circumferentially one stator gap
wide, permitted hub to tip traversing midway between the stator trailing edge and the
rotor leading edge both in and out of the stator wakes. A confocal two color,
two component back scatter LDV system developed for use in gas turbine
environs was employed to obtain detailed mappings of velocity magnitude and
air angle as a function of rotor position ($\approx$1000 angular increments were
resolved) at several spanwise and gapwise positions downstream of the 6th
and 9th compressor stators. Although a complete mapping was not obtained,
sufficient data was acquired behind the 13th stator to identify the flow's
character there as well.

The equipment employed in this study and the difficulties encountered will be de-
scribed. Data typical of the findings will be presented. Unexpected modulations in
the data have led to the application of spectral analysis techniques to identify and
characterize the periodic fluctuations. Emphasis will be placed on these data
analysis techniques and the insight gained from their application on the data.

Introduction

Laser doppler velocimetry (LDV) techniques have advanced considerably since their
introduction in the late 1960's; matched with improved data acquisition systems, the
LDV has become a cost effective tool for the study of aerodynamics and hydrodynamics
in many fields. Use of the LDV at Pratt & Whitney got underway in 1969 and evolved
in the direction of operating in harsh environments. Primary goals
included high sensitivity to accommodate relatively small windows for
on-axis backscatter gas turbine studies and rapid data acquisition rates to
minimize test times.

Initial studies at Pratt & Whitney were directed at jet flows and intrablade fan
flows where the relatively large working distances, although presenting numerous
problems, did not require the instrument to focus close to window surfaces or rotor
hubs where substantial quantities of flare light originate. Following the successful
application of Pratt & Whitney's LDV in a number of engine intrablade fan studies, it
was felt that the next significant flow to address was the interrotor
passages of a high pressure compressor. A NASA funded study was planned in
which a detailed mapping of the stator/rotor interactions would be
attempted with this nonintrusive device. In addition to demonstrating the
capabilities and (or) problems associated with this technique, the
availability of data from a non-perturbing instrument would help assess the
relative value of LDV and conventional pressure and temperature probe data
normally utilized in interrotor studies.

Optical Instrument

A two color, two component LDV system operating in a confocal backscatter
configuration has been developed at Pratt & Whitney, Figure 1. A Spectra
Physics Model 164 argon ion laser operating in "all lines mode" supplied
approximately 800 milliwatts to the head. Divergence of the incident laser

beam was reduced in the LDV by first passing the beam through a galilean telescope type assembly to adjust the beam diameter to tailor its size to the number of fringes and fringe spacing required by the flow to be studied and to materially reduce the beam divergence from the laser to minimize the generation of false turbulence signals (better then 95% divergence reduction is normally achieved). This instrument incorporates path length compensation to permit laser operation without an etalon, dichroic beam splitters for color separation during beam splitting, and remotely positionable sensitivity vector beam orientation (resolvable to ±0.05 degrees). This assembly is coupled to a half wave plate which is configured to rotate at one half of the beam splitters' rate to maintain the proper light polarization for the beam splitters' coatings. The beam splitters in this assembly were placed at 56° included angle rather than the 90° orientation frequently utilized. Although a 90° orientation could have been employed, the narrower 56° included angle is generally employed since it permits the two axes to nominally be within 28° of the anticipated flow direction. This orientation substantially increases the effective swept area of the probe volume while concurrently decreasing the effect of angular fluctuations on angle bias generation. In this study although substantial velocity fluctuations were anticipated, angular fluctuations were expected to be small enough that only one orientation of the beamsplitters would be needed for all testing (this proved to be the case).

Backscattered light from the instrument's probe volume was collected by a 3.158 inch diameter trepanned multiple element achromat which incorporated a large, 2.125 inch diameter center stop for flare light control. The control stop served to limit the probe volume length viewed by the collection lens. In addition this stop serves to increase the signal to noise ratio by preventing scattered light from regions some- what outside of the probe volume from entering the annular collection lens. The 7.48 inch focal length collection lens' effective focal length was F3.80. Light collected from the probe volume was brought to focus on a field stop who's size determined the field of view available to the photomultipliers (PMT). Separation of the signals from the two fringe volumes was accomplished with color separating beamsplitters in the PMT housing.

Test Vehicle & Modifications For LDV Testing

A full scale experimental multi-stage compressor comprising rotors 6 thru 15 developed for the NASA Energy Efficient Engine was powered by a 40,000 horsepower steam turbine for this study. To evaluate the potential difficulties associated with making LDV interrotor velocity measurements, three axial locations were selected for study.

The first window location, aft of the 6th stator and forward of the 7th rotor, was chosen to serve as a benchmark since the seed would have passed thru only one rotating stage and particle migration would not be severe enough to significantly restrict measurements throughout the passage. Based on earlier transonic engine fan tests, it was anticipated that data acquisition at this location could be routinely accomplished. The window, 3½ inches in the circumferential direction by 1 inch axially permitted a radial traverse from hub to tip behind approximately 4 inch span stators. In the circumferential direction the window permitted probing from midway between the stators thru a stator wake to the corresponding location in the next passage.

The second window was located in the 9th stator-10th rotor region and was also placed to permit hub to tip and 50% stator gap to 150% stator gap traversing. This location, following four rotor/stator stages, was expected to delineate any problems with seeding loss to the airfoils and walls. In addition the passage height had shrunk to 1.85 inches increasing the likelihood that window and hub flare would make measurements near these surfaces difficult.

The third window in the 13th stator/14th rotor region was chosen to maximize the difficulties faced by the LDV, passage height was reduced to 1.05 inches and the seed would have to survive the passage thru 8 stages of compression and an air temperature rise of several hundred degrees F which was anticipated to promote seed evaporation. Whether the material as a liquid would survive depended somewhat on the increased pressure, roughly eight times atmospheric which might somewhat compensate for the 600+°F rise in gas temperature.

The inner surface of the windows were ground to a cylindrical contour chosen to closely approximate the curvature of the rig's outer flow path. In a window of this type, traversing the LDV vertically (circumferentially) from the normal to the rig axis results in the two incident laser beams for each LDV axis being refracted by

differing amounts for all beam orientations except when the plane of the two incident beams is parallel to the rig axis. This variability introduced into the calibration constants of the 0.488 and 0.5145 micron sensitivity vectors can be somewhat controlled by proper choice of the window's outer surface contour. An analysis was performed at Pratt to select outer contours in an effort to control this effect[1]. Although a complex figure for the window would have permitted better control of the optical distortions, a cylindrical grind was chosen to keep fabrications costs to a reasonable value. Following polishing, the windows were anti-reflection coated on both surfaces.

The windows, formed of approximately 0.25 inch fused silica were fitted into metal frames. The frames were fabricated with approximately 2 mil wide slots upstream of the window's inner surface. These slots were used to conduct washing fluid via an internal channel from either of the remotely located reservoirs. During testing when data rates and (or) signal quality degraded (suggesting that the window had become fouled), either or both of the supplies would be momentarily pressurized to introduce acetone and(or) demineralized water into the airstream immediately upstream of the window. Generally a 1 to 2 second wash (approximately 1 to 2 cubic centimeters) of each fluid would restore the system's performance.

Di(2-ethylhexyl) phthalate (DOP), atomized by four Laskin nozzles was introduced into the ducting one hundred feet upstream of the test rig. A lower vapor pressure oil, Dow Corning's DC704 diffusion pump fluid, was obtained as an alternate seed in the event that evaporation of the DOP occurred. A second backup material, nominal 1.0 micron diameter ziconium dioxide injected by a fluidized bed seeder was also prepared in case the DOP and DC704 were both unsatisfactory.

Test Program

Initial testing was performed in the 9th stator/10th rotor region with the single component LDV utilized previously in a number of transonic fan studies. These efforts demonstrated the viability of getting good measurements at this location. Using these data as a bench mark, the optical head was converted to the recently completed two component mode in order to ascertain whether the more efficient two component mode of operation could be effectively utilized in this study[2]. A series of repeat points were acquired that demonstrated that the two component system's performance was comparable. All remaining data were obtained with the two component optics. Circumferential traverses were made at each of five spanwise locations, 20% span intervals separated the traverses radially while circumferential spacing varied with the finest spacing used to define the stator wake regions; generally approximately 10 circumferentially spaced locations were probed at each spanwise location. The LDV head can be seen in Figure 2 operating at the 9th stator/10th rotor window locations, the 6th stator/7th rotor window is visible to the right. No difficulty was experienced in obtaining data at all locations probed in this region of the compressor. Seed migration effects were not found to be an obstacle to data acquisition, data was obtained everywhere that the instrument probed, and measurements were obtained as close as 0.06 inches from the rig's hub. Once the 5 radial by 10 circumferential point matrix has been completed, a similar set of traverses were performed thru the upstream window. A similar matrix was then attempted at the 13th stator/14th rotor window. At this location data rates dropped to unacceptably low values due to seed loss thru evaporation and window contamination. A lower vapor pressure oil, DC704 diffusion pump oil, was substituted for the DOP and testing resumed. Although an increase in data rate was obtained, the increase was not sufficient to permit a detailed mapping in this region. Despite this difficulty a few representative data sets were obtained which showed the flow structure at this location. Additional seeding experiments utilizing 1-nominal 1.0 micron zirconia suspended in DOP and dispersed via the Laskin nozzle seeder and 2- dispersing dried 1.0 micron zirconia from a fluidized bed were attempted but also met with limited success. In addition to not obtaining adequate seed at the 13th stator/14th rotor location, a significant problem was encountered in keeping the window's inner surface clear of contaminants. Fluids used to periodically wash the upstream windows during

1 An analysis of this aberration and window/lens designs to control the problem can be found in International Symposium On Laser Anemometry, FED Vol. 33, Winter Annual ASME Meeting, Nov. 17-22, 1985, see pages 293 to 298, "LDV Measurements In Pipe Flow Problems and Experiments", by H. Els & G. Rouve.

2 Optical performance of the new two component system was expected to be comparable to the single component design but this had not been established in an engine test environment. Consequently a demonstration of the two component head's capabilities was needed before undertaking a program of this scope.

testing vaporized at this test location. The only way the windows could be cleaned was to reduce the rig operating speed, wash the windows, reset the test condition, and try to obtain a data point before window contamination again excessively degraded the LDV signals. At this point the program goals to obtain data wherever possible and to identify potential problems with LDV testing in multi-stage compressors had been met and testing was terminated. One hundred and thirty-six data points had been obtained with complete mappings at the 6th stator/7th rotor and 9th stator/10th rotor locations and   20% of the matrix completed at the 13th stator/14th rotor locations.

Data Reduction

Each of the data points consisted of 2 velocity components with 100,000 to 300,000 measurements per velocity component. During the acquisition phase each velocity measurement was assigned a rotor position value indicating which of approximately 1000 angular positions of the rotor that the measurement occurred in. Acquisition times of 3 to 10 minutes per data point were typical. The data acquisition system employed in this study is shown in Figure 3. The first step in data reduction was to order the data by angular position (hereafter referred to as click position), review the resulting histograms for possible editing[3], and obtain the mean of each histogram. Figures 4 & 5 shows typical low and high turbulence level histograms obtained. Figure 6 displays the results of analyzing all 1000 positions and plotting in the upper graph the number of velocity data per click, the middle graph displays the histogram's turbulence intensity per click, and the lower graph the mean velocity per click. These data were placed in a data base accessible by the Compressor Aerodynamics Group for review and analysis[4]. These data were then vectorially added to the second velocity component data to produce the resultant velocity vector and air angle data displayed in Figure 7.

Fourier Analysis

An unusual aspect of many of the data sets obtained is the beat like behavior found in the component velocity and resultant velocity mappings. The strength of these features was found to be a strong function of location within the passage with periodic high frequency wave forms becoming strongest in the stator wake regions.

A 4 cycle per revolution beat frequency was observed in the 9th stator/10th rotor location for many of the data sets, see Figure 8. This suggested that the periodicities observed were being caused by the 66 bladed rotor 9's blade wakes interacting with the forward propagating back pressure field from rotor 10's 62 blades. Bear in mind that what is being displayed is spatially separated velocity anomalies not temporally distinct periodicities. For example Figure 5 shows a distinctly bimodal distribution indicating that a periodic oscillation was probably occurring at this click location yet the periodicity of the oscillation was not recorded in the acquisicion process. In the following displays only the mean value of the distribution is used, i.e. all time information has been ignored.

To investigate this beat phenomenon further a Fourier transform (FT) routine was developed to transform the wave form, either Figure 6's velocity component wave, Figure 7 or 8's resultant velocity vector or air angle curve from the spatial into the frequency domain. Figures 9 and 10 display the result of transforming Figure 8's velocity and air angle curves with the spatially discrete periodicities that contributed to the measured waveform clearly observable. In analyzing these results it quickly became evident that many more rotors than the immediate upstream and downstream rotors were contributing to the velocity fluctuations observed. In fact in some data sets periodic contributions from as far forward as rotor 6 were clearly discerned aft of stator 9, Figure 10 displays such a data set with the fundamentals and harmonics from the various rotors identified.

Wave Form Enhancement

With the contributing components' frequency and amplitude levels clearly identified, the possibility of manipulating the data to enhance wave forms

---

3   No data editing was found to be necessary for the bulk of the data. At the 13th stator/14th rotor location noise began to appear due to window contamination. All data is presented with no editing.

4   Results of the aerodynamic analysis will be released in the NASA Contract Final Report, "E3 High Pressure Compressor, Rig #70749-03 LDV Data Assessment".

of specific interest suggested itself. One approach investigated involved extracting only the wake wave form created by one rotor, ignoring all interactions with other rotors. First an FT was performed on the velocity or air angle curve, then the real and imaginary components of the fundamental and harmonics associated with the rotor of interest were extracted, and finally an inverse Fourier transform was performed on these data. Figure 11 displays velocity and air angle data from a 9th stator/10th rotor location where the 9th rotor's 66 blades wakes were severely distorted by the presence of a strong bow wave propagating forward from the 62 blades of rotor 10. The average or mean rotor 9 blade wake shown in Figure 12 was extracted from Figure 11's velocity curve in the manner described above. In a multi-stage compressor with windows located between every stage, this method could be employed to track the distortions introduced and decay produced by passage of a specific rotor's wake thru successive stages.

A second method employed was to subtract out only the contribution of one rotor by similarly performing the FT, identifying and removing the real and imaginary terms of the wave form to be deleted, and performing an inverse Fourier transformation (IFT) on the remaining data. In this fashion, a particularly strong perturbation created by a nearby rotor can be removed allowing weaker fluctuations to be more clearly observed. The upper graph of Figure 13 shows a portion of an air angle wave form from the 50% gap/50% span location of the 6th rotor (26 blades)/7th rotor (50 blades) data set in which the 50E (times engine order) signals from the downstream rotor clearly dominates the data. The fundamental and 2nd thru 4th harmonics of rotor 7 were deleted from the transform and the IFT performed, the lower portion of the figure shows the resulting wave form with the 26E blade wakes now clearly visible.

Conclusions

The initial thrust of the program, identify the viability of using an LDV to obtain nonperturbing measurements of air velocity and angle in the stator/rotor interaction region of a multi-stage compressor, was clearly demonstrated to be practical.

o   Initial concerns with the possibility of locally unseeded regions developing after passage of the seeded flow thru several stages of a compressor was not found to be a problem. No seed level degradation was observed after four stages of compression. After eight stages, unrelated seeding difficulties arose but no locally unseeded regions developed.

o   The additional pressure created in higher stages of compression is not sufficient to offset the increasing volatility of DOP seed produced by the rising temperature. Lower vapor pressure oils or solid particulates will be needed for future testing in these regions.

o   Either methods of cleaning windows during high temperature rig operation will have to be developed which remain effective at the highest stages of compression or possibly methods of supplying a continuous gas purge could be developed.

o   Turbulence introduced by rotor wakes persist in terms of identifiable velocity fluctuations for several stages before mixing reduces the rotor's contributions to unidentifiable random fluctuations.

o   Although the data was not recorded in a fashion that preserved the temporal aspects of the measurement, Fourier transform techniques could be usefully applied. The spatial wave forms obtained could also be manipulated with FT techniques to extract additional information about hardware related periodicities present in the flow.

FIGURE 1
OPTICAL CONFIGURATION OF
TWO-COMPONENT CONFOCAL
BACKSCATTER LASER DOPPLER
VELOCIMETER
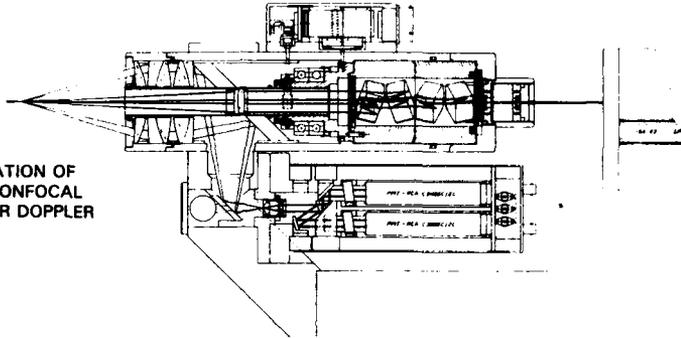
FIGURE 2
COMPRESSOR-LDV TEST
CONFIGURATION, 6TH
STATOR/7TH ROTOR AND 9TH
STATOR/10TH ROTOR
WINDOWS VISIBLE
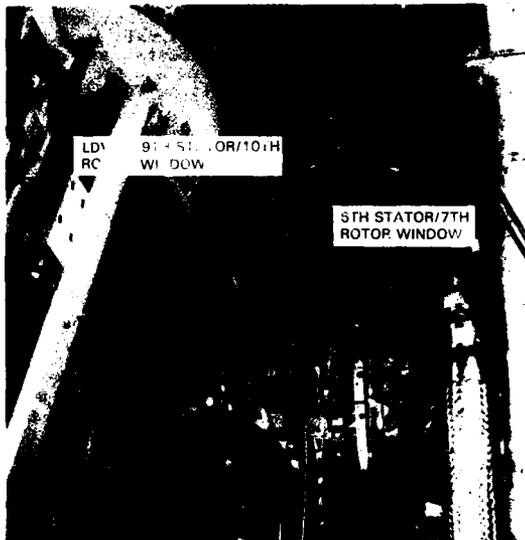
FIGURE 3
TWO-COMPONENT LDV DATA
ACQUISITION SYSTEM UTILIZED
IN E^3 HIGH PRESSURE
COMPRESSOR STUDY

E³ COMPRESSOR   63.4% SPAN   101.3% GAP
9TH STATOR/10TH ROTOR WINDOW   100% SPEED

VELOCITY IN FT/SEC

MEAN VELOCITY — 598.6 FT/SEC   TURBULENCE INTENSITY 0.052
POSITION NO. 24   NO. OF VELOCITY MEASUREMENTS 208

FIGURE 4
LOW TURBULENCE, σ/v = 0.052, MONOMODAL HISTOGRAM

E³ COMPRESSOR   63.4% SPAN   101.3% GAP
9TH STATOR/10TH ROTOR WINDOW   100% SPEED

VELOCITY IN FT/SEC

MEAN VELOCITY — 527.2 FT/SEC   TURBULENCE INTENSITY — 0.178
POSITION NO. 5   NO. OF VELOCITY MEASUREMENTS 89
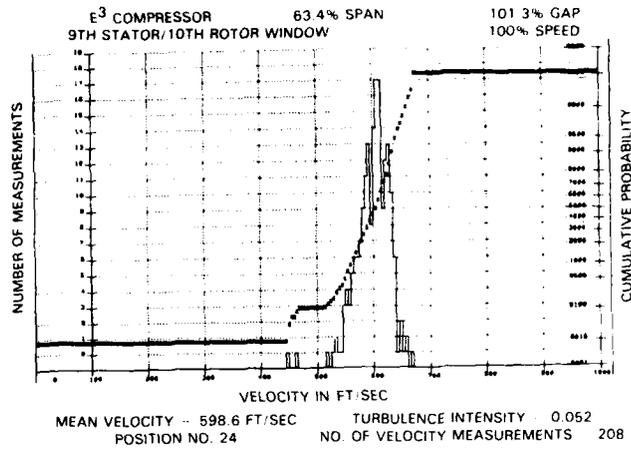
FIGURE 5
HIGH TURBULENCE, σ/v = 0.178, BIMODAL HISTOGRAM INDICATES PRESENCE OF FLOW INSTABILITY

E³ COMPRESSOR   63.4% SPAN   101.3% GAP
9TH STATOR/10TH ROTOR WINDOW   100% SPEED

ANGULAR POSITION OF ROTOR IN CLICKS
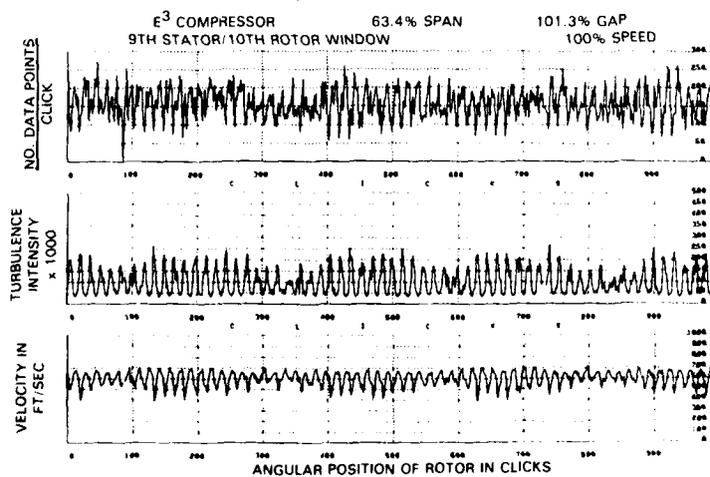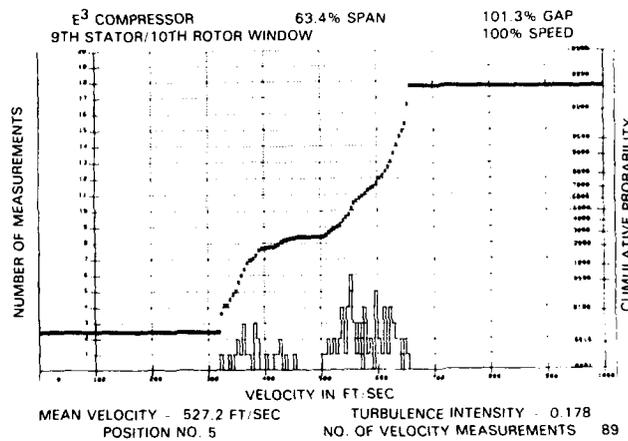
FIGURE 6
ONE VELOCITY COMPONENT, TYPICAL DATA SET SHOWING THE MEAN VELOCITY VALUES
AT APPROXIMATELY 1000 ANGULAR POSITIONS OF THE COMPRESSOR

FIGURE 7
VECTOR ADDITION OF TWO
VELOCITY COMPONENTS AT
9TH STATOR/10TH ROTOR

E³ COMPRESSOR   63.4% SPAN   101.3% GAP
9TH STATOR/10TH ROTOR WINDOW   100% SPEED

ANGULAR POSITION OF ROTOR IN CLICKS
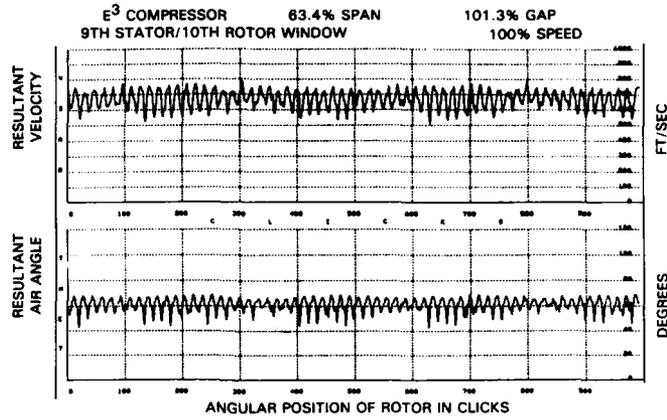
FIGURE 8
RESULTANT VELOCITY AND AIR
ANGLE DATA SHOW PERIODIC
(4E) BEAT AT THIS 9TH
STATOR/10TH ROTOR
LOCATION

E³ COMPRESSOR   70% SPAN   50% GAP
9TH STATOR/10TH ROTOR WINDOW   100% SPEED

ANGULAR POSITION OF ROTOR IN CLICKS

VELOCITY SPECTRA
70% SPAN   50% SPAN

AIR ANGLE SPECTRA
70% SPAN   50% GAP

ROTOR NO.	NO. OF BLADES
6	26
7	50
8	60
9	66
10	62
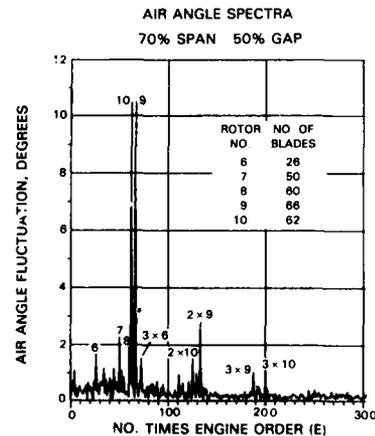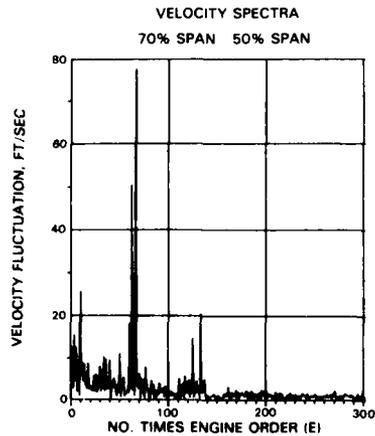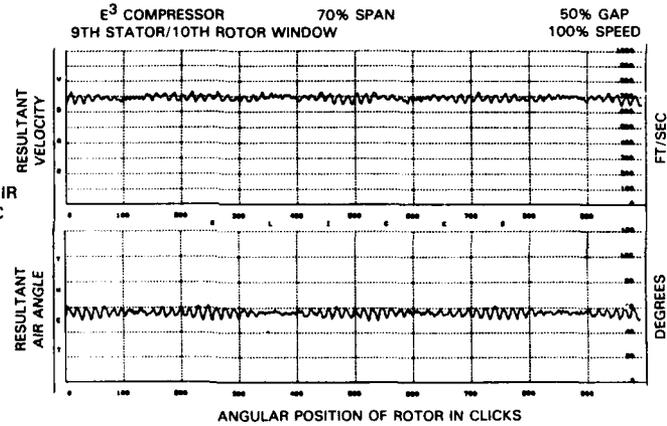
FIGURES 9 AND 10
FOURIER TRANSFORMS OF FIGURE 8'S VELOCITY AND AIR ANGLE WAVEFORMS,
SEVERAL OF FIGURE 10'S PEAKS ARE LABELED BY THE ROTOR NUMBER OF THE SOURCE
AND THE HARMONICS

E³ COMPRESSOR   83.5% SPAN   91.7% GAP
9TH STATOR/10TH ROTOR WINDOW   100% SPEED

FIGURE 11
RESULTANT WAVEFORMS
IN WHICH UPSTREAM
ROTOR WAKE (66E)
IS DIFFICULT TO
DETECT BECAUSE OF THE
PRESENCE OF THE
DOWNSTREAM ROTOR'S
(62E) BOW WAVE

RESULTANT VELOCITY   FT/SEC

RESULTANT AIR ANGLE   DEGREES

ANGULAR POSITION OF ROTOR IN CLICKS

91.7% GAP/80.5% SPAN 9TH WINDOW 9TH ROTOR UBAR
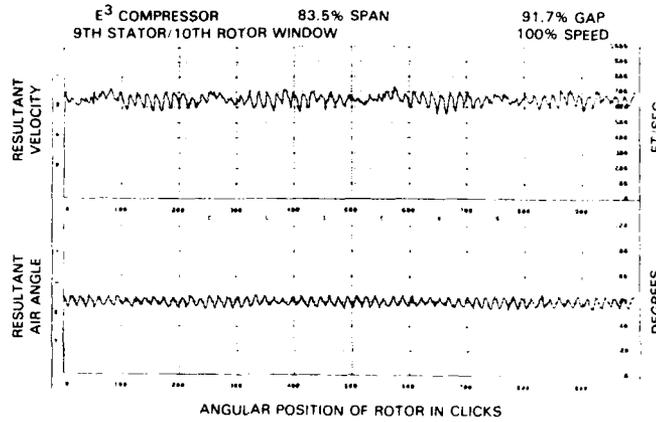
FIGURE 12
FOURIER TRANSFORMATION
AND INVERSE TRANSFORMATION
TO RETRIEVE AVERAGE UPSTREAM
ROTOR BLADE WAKE PROFILE
FROM FIGURE 11'S
RESULTANT VELOCITY WAVEFORM

VELOCITY FLUCTUATION, FT/SEC

UPSTREAM ROTOR'S BLADE SPACING

E³ COMPRESSOR   50% SPAN   50% GAP
6TH STATOR/7TH ROTOR WINDOW   100% SPEED
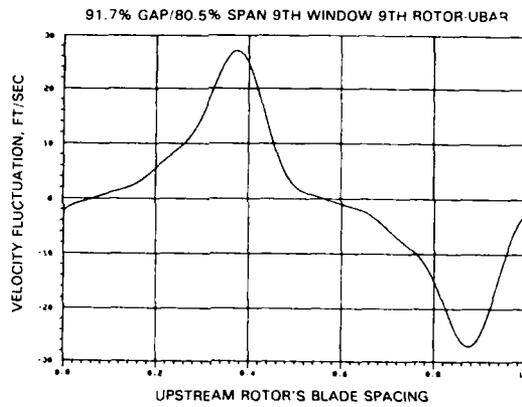
FIGURE 13
DOWNSTREAM ROTOR EFFECTS
DOMINATE AIR ANGLE DATA
FROM THIS DATA SET,
APPLICATION OF FT AND IFT
TECHNIQUES TO REMOVE
FREQUENCY COMPONENTS
FROM DOWNSTREAM ROTOR;
PERMITS UPSTREAM ROTOR
WAKES TO BE SEEN

RESULTANT AIR ANGLE IN DEGREES

ORIGINAL WAVEFORM

ROTOR 7 SPACING

RESULT AFTER REMOVAL OF
DOWNSTREAM ROTOR 7

ROTOR 6
SPACING

ANGULAR POSITION OF ROTOR IN CLICKS
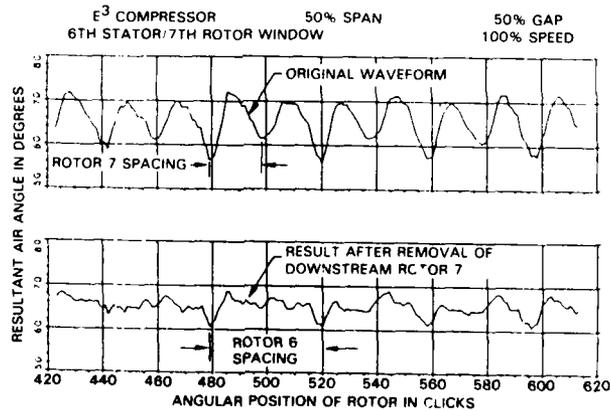
DISCUSSION

A.Strazisar, US

You mentioned that your windows were not constant thickness in an attempt to correct for refraction effects. Was this correction sufficient to bring all 4 beams of your 2-colours system to a common focal point?

Author's Reply

Yes, at all window locations, both beam crossing (4 beams) and the coannular collection optics were brought to a common enough focus so that data acquisition on both channels was not impaired.

R.Schodl, GE

What is the size of the probe volume?

Author's Reply

We have about 30 fringes inside the probe volume; its diameter is 80 μm, and its length 350 μm.

R.L.Elder, UK

In the afterburner tests you have discussed, what do you believe were the seeding particles?

Author's Reply

Our experience indicated that the non augmented flow produced considerably higher data rates than augmented. As the various stages of augmentation were introduced, there was no significant change in turbulence levels, suggesting that beam steering by hot gas cells was not significant. Consequently, I feel the reduction in data rates was due to a reduction in the number of particles present. From this I concluded that the LDV was detecting carbon particles formed in the engine combustor and that many of these particles were combusted in the augmentor during augmentation.

R.B.Price, UK

(1) What is the minimum particle size that your system is able to detect?
   (a) theoretical design value
   (b) that you achieve practically in the multi-stage compressor tests.

(2) What is the size distribution of the seed particles in the multi-stage compressor experiments?

Author's Reply

(1a) We have not performed a theoretical calculation on the minimum particle size that the instrument would be capable of sensing.

(1b) In jet flows, with no intervening windows or far wall light scatterers that could degrade the signal to noise ratio, experiments have suggested that the 183 mm focal length optical configuration (as used in this study) can detect approximately 0.2 μm diameter particles. However in the normal gas turbine environment, where optimum signal to noise ratios are not achieved, a minimum particle diameter detected of 1 μm is more realistic. It is our intent to perform an experiment in a three stage compressor shortly, which will provide a more exact answer to your question.

(2) The size distribution of the seeded used to disperse the DOP seed used in this study was recently measured. I have not had an opportunity to review these data as yet but have been informed that "distribution peaks at 0.6 μm with very few particles larger than 1 μm". I am afraid that I cannot be more definitive.

B.Lakshminarayana, US

Where did you inject the particles? Upstream of the blade or upstream of the stage? Did you have trouble getting enough particles?

Author's Reply

We introduced the seed at the roof of the building, 30 m upstream of the probe volume locations; the particles had to pass through two or three elbows and a plenum chamber.

At the last measurement location, we had difficulties getting the data. We used DOP: we were hoping that the increasing pressure on the seed will compensate the temperature elevation, so that the particles may stay around; unfortunately this seed evaporated. Then we went to Dow Corning 704, which is a vacuum pump oil, with a lower vapour pressure, but not successfully. DOP and ZrO_2 were mixed: this seed slightly improved the data rate; but the window was rapidly getting dirty. Because of elevated temperature we could not wash the window (no success with alcohol, acetone, etc...).

EVALUATION OF L2F-MEASUREMENTS IN UNSTEADY TURBINE FLOW

W. Förster, R. Schodl, H. Kruse
Institut für Antriebstechnik
DFVLR, 5000 Köln 90
Germany

SUMMARY

The L2F-velocimeter is a suitable device with which to perform experimental studies on instationary effects in turbomachines. This report describes the execution and the evaluation of L2F-measurements within and near the rotor blade channel of a single-stage, cold air test turbine.
The measurements provide information on instantaneous distribution of the 2-D flow vector as well as the components of random fluctuating velocity. The turbine rotor flow is periodically unsteady, because of the upstream inlet guide vanes. In order to ensure the almost complete reconstruction of all possible rotor-to-stator orientations, the discrete measurements are evaluated by combining a local and chronological interpolation procedure. A discussion of experimental uncertainties in this application of the L2F-technique is included.

LIST OF SYMBOLS

B   number of rotor blades

c   flow velocity in the absolute frame

M   number of measuring segments within one blade period

n   rotational speed

PS pressure-side

s   separation of beams

SS suction-side

t   time

w   flow velocity in the relative frame

x   coordinate

y   "

α flow direction in the absolute frame

β "   "   "   "   relative   "

φ circumferential angle

SUBSCRIPTS:

1   stator outlet

2   rotor outlet

fl flying particle

l   longitudinal

ms measuring segment

rel relative

R   rotor

tr transversal

SUPERSCRIPTS:

,   random fluctuation

–   ensemble averaged

INTRODUCTION

In order to determine the overall performance of a turbomachine the flow is assumed to be stationary and in most cases the subsequent detailed design of an engine is based upon stationary measurements. In a real engine, however, the flow is unsteady because of the interaction between blade rows; therefore the reliable performance prediction and optimization of modern engines requires more and more the consideration of unsteady effects, especially with respect to loss production, heat transfer, noise generation and the aerodynamic stability of compressors.

The interaction of adjacent blade rows causes periodically fluctuating flow conditions in the downstream as well as in the upstream direction. The potential flow effects act in both directions, whereas the more powerful wake and secondary flow effects lead to inhomogenous distributions of flow parameters downstream of the generating blade row.

Some investigations are known in which attempts to compute the unsteady inviscid flow-field by modelling the wakes of an upstream blade row were made [6].In other investigations, measurement and/or calculation of unsteady boundary layers was attempted [7].But calculation without comprehensive test data for verification is only speculation. Further progress in this field requires detailed measurements of the unsteady flow effects throughout the flow field. Because of the lack of a suitable measuring technique for the unsteady interaction, wall-pressure measurements and in some cases hot wire or hot film probes (even rotating) have been the only source of information until the development of the laser measurement technique.

During the last 10 years the Laser-2-Focus velocimeter has proved to be an extremly useful tool for investigating the unsteady flow in rotating turbomachinery components. The L2F velocimeter makes it possible to collect such two-dimensional data as the velocity, the direction and the turbulence energy even in the periodically unsteady flow field near and within rotating passages. By using small windows and a special traverse mechanism it is possible to examine most of the flow regions of interest, even near the walls.

Distinctive advantages of the L2F method developed at DFVLR with special regard to turbomachinery application are the high sensitivity, which enables in back scattering even the detection of about 0.1 mm particles, and the possibility to automate the time-consuming measuring procedure.

This report contains the description of the unsteady flow phenomena occuring in a turbine, the measurement technique, and the evaluation of data from the unsteady rotor flow, including a discussion of measurement uncertainties. In conclusion, the test apparatus and some results from our turbine experiments are depicted.

UNSTEADY FLOW EFFECTS IN A TURBINE DUE TO THE INTERACTION OF ADJACENT BLADE ROWS

The reason for periodically unsteady flow effects in turbomachines is the relative rotational velocity of two adjacent blade rows. In the vicinity of each blade row there is an inhomogenous flow field which is periodical in the pitchwise direction except for manufacturing inaccuracies. A blade passing any kind of gradient in the flow field causes unsteadiness.

In principle, there are two different kinds of aerodynamic rotor-stator interaction, the first being potential flow or inviscid effects and the second wake and secondary flow or viscous effects. The gradients due to the potential flow are periodic pressure, velocity and direction distributions extending upstream and downstream of an airfoil, the upstream potential effects being stronger because most profiles have their largest loading in the leading edge region. These gradients decay exponentially with increasing axial gap. The potential aerodynamic interaction is therefore important only when the axial gap is small.

The interaction caused by a wake is possible only downstream of the wake-generating blade row. The gradients convected downstream are periodic distributions of aerodynamic losses and therefore of the velocity including radial components as well as a periodic distribution of turbulence intensity. The complete mixing of a wake needs several chord lengths downstream, thus wake interaction cannot be avoided even when the following blade row is distantly spaced. These interactions are of the most serious consequence.

Similar to the wake interaction is the downstream interaction caused by secondary vortices. Secondary vortices near the casing and the hub may cause local differences in the static pressure and in the velocity vector. Moreover the vortex can accumulate flow material with high losses and turbulence energy [10].The mixing of the vortices usually takes place farther downstream than that of the wakes, thus this kind of interaction may be present even with extremly large axial gaps.

Other possible kinds of interaction between blade rows with relative rotational velocity may be due to shock propagation, tip clearance flow and coolant jets.

In principle, it does not matter which blade row rotates; consequently there is no fundamental difference between compressors and turbines. The real effects of both kinds of interactions, however, are different. Looking at the rotor blade row of a single stage compressor,the relative flow field of the rotor is almost stationary because of the homogenous inlet flow conditions and the weak upstream potential effects of the stator blades whereas the stronger downstream effects of the rotor blades cause the fluctuating flow field near and within the stationary blade row. Looking at a single stage turbine, the stator flow is almost stationary except for weak upstream effects of the rotor, whereas the rotor blades chop the stationary periodical stator wakes, causing the strong unsteady effects near and within the rotor blade passages.

In both cases, the entire internal flow field is more or less instationary and the instantaneous flow pattern differs from passage to passage in the circumferential direction as a consequence of different relative positions of the interacting blade rows. In multistage turbomachines, the situation is more complicated because wakes and vortices persist for considerable distances downstream. If more than two

blade rows with different blade numbers are involved, the experimental investigation of the superimposed effects would be difficult.

All the above-mentioned interactions between adjacent blade rows are periodic with the frequency of the passing blades or passages which generate the disturbance. In a detailed investigation of unsteady turbomachinery flow, these periodic fluctuating flow quantities must be recorded as a function of space and time. In general the internal flow of a turbomachine is turbulent, and this superimposed random fluctuation should be recorded as well. Consider, for instance, the phase locked flow field in a turbine rotor. Each rotor fixed point will feel a velocity distribution similar to that shown in Fig. 1. The velocity history shown in the figure looks like the record of a hot wire anemometer rotating with the rotor. The periodic decay of the velocity corresponds to the wakes of the stator vanes and the disturbances with higher frequencies are the turbulent random velocity fluctuations which are higher near the center of the wakes. The periodically fluctuating velocity $\bar{c}(t)$ is the phase locked average of the real velocity $\bar{c}(t)$; $c'(t)$ is the turbulent fluctuating component. Using a hot wire anemometer it is complicated to separate the periodic and the random fluctuating component, but with an L2F device, the instantaneous measuring technique and the statistical evaluation of the data, discussed later, directly lead to the mean velocity $\bar{c}(t)$ and the standard deviation $\sqrt{\overline{c'^2}}$ as well as to the fluctuating flow direction $\bar{\alpha}(t)$.

L2F MEASUREMENT TECHNIQUE IN PERIODIC UNSTEADY FLOW

The Laser-Two-Focus (L2F) velocimeter, which was used to carry out the flow velocity measurements in the rotating blade channels of the turbine rotor, had the following characteristics:

laser power	500 mW
diameter of focused beams	10 μm
separation of beams	350 μm
axial lenght of the probe volume	600 μm
f-number of the receiver optics	3.7
focal length of the receiver optics	350 mm
signal processing	time-to-pulse-height converter plus multichannel analyser

The L2F system was mounted on a x-y-coordinate table. The laser beams were transmitted through a casing window to the probe volume in the rotor flow channel and aligned so that the optical axis of the L2F system intersected the turbine rotor axis at a right angle. By controlling the x-y-table, the probe volume could be positioned along the axial and radial coordinate of the turbine. In order to define the measuring point in the circumferential direction, electronics providing "Multi Window Operation", i.e. offering the possibility of measuring the velocity distribution at different locations between the blades simultaneously, were used. The method of operation can be explained with the help of the timing diagram in Fig. 2. A signal from the rotor (upper trace) is required. The periodically generated bipolar pulses correspond to the blade frequency. A control signal is generated which reduces the laser power periodically for an adjustable time period T just at that moment when the blade passes the probe volume - see P.M.-signals. The delay time T_1 compensates the pace difference between the rotor signal and the passing signals (P.M.-signal). T_1 is also adjustable.
(The strong reduction of the laser power during the blade passages is necessary in order to protect the photomultipliers from becoming saturated by the strong reflection from the blade. The saturation renders measurement impossible for a certain time, which often is not small compared to the blade period.)
Immediately after the blade passes, the laser is switched to full power again - control signal at high level - and an internal timing/routing signal divides the blade period into 16 different circumferential positions. Just at the moment when a stop signal appears - generated by a particle passing the stop beam - the routing value (in this example 10) is stored. The measured time interval is then stored into that part of a group of memories which corresponds to the indicated routine value.

The phase difference between the rotor signal zero crossing and the blade passages is determined by the different circumferential positions of the rotor signal pick up and the L2F system (these were not changed during measurement period) and by the axial changes in position of the probe volume. At a fixed radial position the known blade profile contour has a fixed phase relation to the rotor signal. This relation must either be known or be determined by measurement. For this purpose the photomultiplier blade surface signals can be used as shown in Fig.2. In order to get this blade signal, the laser was not switched off completly during blade passages. Since the axial position of the probe volume is known, the blade contour can be established relative to the measuring windows. The velocity mean values were reduced from the time-of-flight data of each memory group. They belong to the center position of each window.

The L2F-velocimeter was operated in the simplified version, i.e. the two-dimensional frequency distribution of the fluctuation velocity vector was not measured but rather the two one-dimensional marginal distributions. By this method, which is described in ref. [5], measuring time is saved. The data evaluation procedure is explained in ref. [9]. The results of the calculation are such velocity mean values as magnitude and direction of the absolute mean flow vector component in the circumferential plane and the turbulence intensities of the absolute velocity in directions of, and perpendicular to, the measured mean flow vector. The measurement accuracy of the L2F device was determined to be better than 1% for the velocity components and better than 5% for the turbulence intensities, when the level of turbulence was less than 20% [8]. In measuring turbine rotor flows, additional sources of uncertainty are possible.

As it was mentioned already, the L2F technique cannot determine the distribution of the unsteady flow velocity from blade to blade as a continous trace, but rather, uses a finite number of storage segments. Depending on the rotor position, each measurement event is collected in the corresponding segment. The mean values of velocity, angle and turbulence intensities of each segment can be related to a certain circumferential position within the rotor pitch, e.g. the middle of the measurement segment. To achieve a good resolution of the flow field, it is desirable to have as large a number of segments as possible. However, if the number of segments is increased, the measuring time also increases, because it is necessary to collect a sufficient number of data in each segment to allow a statistical evaluation. Also, if the number of segments becomes too great, the time of flight of a particle between the two focal points

approaches the order of magnitude of the traverse time of the measurement volume through one segment. In other words, the segments become narrower with increasing number and eventually would be narrow enough to pass through the measurement volume before a particle could travel from focal point to focal point. This would mean that the measured flight time was only an average over the segment width and thus no better accuracy could be obtained. The ratio of the segment traverse time to the particle flight time is determined by

$$\frac{t_{ms}}{t_{fl}} = \frac{c}{n \, M \, B \, s}$$

In the present application, the ratio t_{ms}/t_{fl} was greater than 5 at the worst ($\bar{c}$ = 100 m/sec).

Another error due to the finite width of the measurement segments occurs when there is a gradient of the flow velocity or angle. If it is assumed that the collected L2F events are uniformly distributed from side to side, i.e. circumferentially within the segment, a linear gradient of the velocity does not alter the computed mean values, but it does lead to an apparent increase of the turbulence intensities. An assessment of the order of magnitude showed that in most cases the apparent turbulence level was in the uncertainty region of the measured turbulence intensities. However, in flow regions with high periodic fluctuations and low turbulence intensities, e.g. in front of the rotor blade leading edge, a correction of the measured turbulence intensities seems necessary.

In an axial turbine the largest velocity components can be expected in the axial and circumferential direction, but actually also radial velocity components occur. These are caused by three-dimensional flow effects, e.g. by secondary flows or tip clearance influence. Due to the lower velocity in the sta-tor vane wakes a radial movement towards the hub occurs as a consequence of the reduced radial pressure gradient [1]. By means of five-hole probe measurements, the radial flow angles behind the stator of the turbine stage were found to be less than ± 10°. However, if the velocity in the mean flow direction is decelerated by an adverse pressure gradient, e.g. in the vicinity of the blades or by secondary-flow-induced separation, significantly greater radial flow angles can be expected. Additionally, in a turbu-lent flow, radial velocity fluctuations occur. The axial length of the measurement volume, which was roughly twice the distance between the measuring foci, assured that the present configuration of the L2F velocimeter could be applied up to radial flow angles of ± 30°. This was sufficient for most of the measuring locations investigated. In some locations, however, even with very long collecting times, no useful results could be obtained. This happened mainly very close to the side walls and in the vicinity of the trailing edges, where boundary layer separations may have occured. One way to conduct measurements in locations with high radial components would be to reduce the distance between the local points while keeping the axial measurement volume length constant.

To improve the signal rate and thus to reduce measuring time, additional seeding was introduced into the test air. The seeding particles were oil droplets (mean diameter about 0,07 μm, see [4]), which had an ex-cellent flow-following behaviour. They were injected into the flow through a seeding probe. The positio-ning of the seeding probe was sometimes a difficult problem. As shown in Fig.3 the position of the seed-ing probe depends on the measuring location (e.g. A or B) according to the flow path in the absolute frame. Problems occur due to the different stator positions established. The seeded flow path often in-teracts with the stator blades and is thus destroyed. A two-axis positioning of the probe was required in order to optimize the signal rate at each measuring location. Certainly, there was not the same im-provement of the signal rate at all measuring locations. Close to the walls and especially in separation zones only a reduced seeding particle rate was obtained because of the lower mass entrainment from the main flow. In such flow regions the measuring time increased significantly.

DATA EVALUATION IN UNSTEADY ROTOR FLOW

The unsteady distribution of the flow quantities in or near a rotor blade channel is determined by the circumferential position of the rotor wheel relative to the stator vanes. Therefore, in a turbine rotor with a number of blades which is not an integer multiple of the stator vane count, we have a different flow in each rotor channel at each instant in time. An observer moving with the rotor wheel would see this in any particular channel as an unsteady flow which is periodic with stator vane frequency. However, the L2F system is an observer who is looking from the absolute (stator) reference system and a special procedure is necessary to transform the measured data into the rotor reference system.

In the case of rotor flow analysis, it is generally necessary to transform the measured flow quantities from the absolute to the relative frame of reference. For mean velocity and flow angle this can be easily done by use of velocity triangles with the assumption of constant rotor speed. The mean squares of ran-dom velocity fluctuations, which are a measure of turbulence intensity, are determined parallel and per-pendicular to the mean (absolute) flow direction. The derivation in the appendix shows, however, that to compute the mean squares of the random velocity fluctuations in any other direction, e.g. in the relative frame of reference, it is necessary to know the mean square of the mixed product of the velocity fluctu-aties $\overline{c_1' c_{tr}'}$, i.e. the shear component of the Reynold s stress tensor.

Generally it is possible to determine $\overline{c_1' c_{tr}'}$ by evaluation of the complete two-dimensional probabili-ty density function of c_1 and c_{tr} in each measurement segment, but actually this means an increase of the measuring time by at least a factor of 10 [8]. A complete mapping of a turbine rotor would become an expensive venture in this case. However, as it is shown in the appendix, the sum of the mean squares of random fluctuating velocity, which is a measure of total (2D) turbulent kinetic energy, is invariant for arbitrary rotations of the reference system:

$$\overline{w_1'^2} + \overline{w_{tr}'^2} = \overline{c_1'^2} + \overline{c_{tr}'^2}$$

Schodl showed in [8] that the mean square of the random velocity fluctuations parallel to the mean (absolute) flow direction is determined with greater accuracy than the mean square of the perpendicular fluctuations for high values of turbulence intensity. For this reason it is often sufficient to assume isotropic turbulence and to use $c_1'^2$ as a measure of it.

By circumferentially rotating the stator vane row with respect to the laser measuring volume, the non-uniform stator exit flow can be examined (Fig. 4 left). Due to the fact that for constant stator position φ_S, the measured data for each of the 16 segments corresponds to another stator-rotor position $\varphi = \varphi_R - \varphi_S$, extensive interpolation is necessary to evaluate the complete momentary distribution of the flow quantities for an arbitrary stator-rotor position.

In Fig. 4 right the magnitude of the stator-rotor angle φ is plotted as a function of stator circumferential position and measurement segment number (segment number 1 here corresponds to the pressure side of the blade or the design rotor inlet or exit stagnation streamline, and the higher numbers move to the suction side). In this figure each segment was replaced by its central circumferential angle φ_R (e.g. stator position A was highlighted.) Stator-rotor angles φ of magnitude greater than the stator pitch can be considered, from periodicty, as coming from the adjacent channel. By this arrangement all measurement positions can be treated as belonging to a single stator channel and the individual stator positions fall on lines with an angle of 45° upward and to the right, when the scales of φ and φ_R are chosen equal. Each measurement location corresponds to a group of measured or derived flow quantities, e.g. the magnitude of the relative velocity. Thus it is possible to define a two-dimensional discrete function for each flow quantity. To obtain an image of a momentary flow situation it is necessary to extract the respective values for constant stator-rotor angle φ. As can be seen in Fig. 4, right, a maximum of 4 measurement locations would be available in this arrangement (6 stator positions) without further interpolation. Moreover, only in some discrete stator-rotor position would an evaluation be possible. However, it is known that the flow development in each of the 16 segments proceeds periodically with the stator pitch. Therefore, in each segment, the data from all stator positions can be used for an interpolation algorithm with periodical end conditions, which delivers an approximation of the desired flow quantity for arbitrary stator-rotor angle φ. Thus for all possible stator-rotor positions a fine grid of base points for spatial interpolation in the circumferential direction becomes available. If the laser measurement volume was positioned within the rotor blade channel, the evaluation procedure is identical except that the number of measurement segments is reduced by the blade thickness in the circumferential direction (Fig. 2).

Fig. 5 shows the history of the relative velocity at a measurement point 25% of axial chord in front of the rotor at midspan as a contour plot. The diagram was developed from the arrangement of measuring points in Fig. 4, right, by the described interpolation procedure. The velocity defect within the vane wake is felt in only some of the stator positions and thus appears on a strip with 45° angle. [5]. The rotor potential influence which in contrast to the vane wakes also acts upstream, is already weak at this axial location. Only a slight broadening of the wake is noticable in the measurement segments which are influenced by the rotor leading edge pressure field.

Many of the experimental techniques used up to now in turbomachinery are based on procedures with high time constants, so the data must be treated as mean values. This is especially true when measurements are executed with such difficult experimental conditions as high rotor speed, high temperature etc. Also most of the available methods for flow field computations produce steady state solutions. For comparison with such data, averaging of the L2F results can be performed in two different ways.

Low response data obtained in the absolute frame of reference neglect the unsteady influence of the rotor. Comparable L2F data are computed by averaging over all measurement segments for constant stator to laser volume position φ_S. (In the diagram Fig. 4, right, this means averaging along the 45°-lines).

Recently, more and more data have been published, which were obtained with rotor-fixed probes or are computational results for a rotor flow field in steady state condition. Here the unsteady effects of the stator vane row (wake or potential influence) has to be dropped. This can be achieved by averaging the laser data in each individual segment for all stator circumferential positions (this means moving along the horizontal lines, i.e. φ_R = const., in the diagram Fig. 4, right).

EXPERIMENTAL APPARATUS AND PRESENTATION OF TYPICAL RESULTS

The description of the experimental apparatus and the presentation of results from a test turbine are repeated in part from previous papers [2,3,5], but it is useful here to show some typical results of the unsteady turbine flow (to illustrate the evaluation procedure just described).

The experiments which are part of the DFVLR turbine research work were carried out with a single stage cold air test turbine whose blading is a scaled version of a projected gasgenerator turbine from MTU-Munich. The outer diameter is 0,45 m, the hub-to-tip-ratio 0.756. The aspect ratio of the vane is 0.564, that of the rotor 0.811; the corresponding blade numbers are 20 and 31. The axial gap is 54 mm at midspan so that as a consequence of the large gap upstream potential flow effects in the vane are negligable. The turbine was run at a speed of n = 7800 rpm, yielding high subsonic maximum flow velocity. L2F measurements were conducted near and within the rotor. The position of the L2F velocimeter itself can be adjusted in the radial and axial direction as previously described. In order to cover the section of interest, seven small plane windows in the casing are staggered in the axial direction (Fig. 6). The casing of the turbine is split in a plane between stator and rotor; both parts of the casing can rotate. By rotating the part with the windows and displacing the L2F-velocimeter in the axial direction into the plane of the respective window, each position of the rotor flow field can be reached except those which are shadowed by the twisted and slightly leaned rotor blade. For each fixed position of the optical axis of the velocimeter, each position in the absolute frame of reference can be reached by rotating the upstream part of the casing together with the stator vanes. For the measurements reported here the stator vane is divided into 6 elements (Fig. 7). In the axial direction 7 measuring planes were chosen, of which two are in front of the rotor blades and one downstream. There were 9 to 11 radial positions. Considering

the 16 time-dependent storage segments along one rotor pitch, 6x7x10x16 = 6720 items of information on a single flow property at a given operating point of the turbine are necessary to take an almost complete map of the rotor flow field, provided that the chosen spacing of the measurement locations is sufficient for a reliable interpolation.

The laser beams and the electronics recording the signals as described above are controlled by 31 trigger signals per revolution (corresponding to the rotor blades) from a disk mounted on the shaft.

Following are some typical results of L2F-measurements from the above described test turbine. Fig. 8 depicts a typical instantaneous turbine situation between stator and rotor. In an axial position 6% axial chord in front of the rotor blades at midspan both the downstream wake effects of the stator vanes and the upstream potential flow effects of the rotor blades are visible. In the circumferential turbulence distribution the frequency of the stator vanes is predominant; the maximum values of the dotted line characterize the stator vanes. The corresponding velocity distribution (solid line) shows that the pressure field in this axial position is governed by the rotating blades. The inhomogeneity of the stator outlet flow only causes weak differences in the periodic velocity distribution near the rotor blades but these differences significantly depend upon the instantaneous relative position of rotor to stator.

The fact that the circumferential distribution of turbulence near and within the rotor is mainly governed by the frequency of the stator vanes makes the measured turbulent kinetic energy a suitable parameter with which to follow different flow material from specific locations in the stator passages. Fig. 9 demonstrates the possibility of following the stator wakes passing the rotor. The figure depicts the midspan pattern of the component of turbulent kinetic energy $\overline{c_1'^2}$ in three neighbouring rotor blade passages for an arbitrary instant situation. The high energy values typify the wake material. The distribution shows the chopping of the wake by the rotor blades and the deformation and turning of the wake segments passing through the rotor channels. Overlaid on this distribution are the fluid filaments which separate the wake from the undisturbed flow [5]. The solid and dotted lines reconstruct the movement of the stator wake by determining the path of the individual fluid particles. The solid lines reconstruct the movement of the undisturbed flow whereas the dotted lines reconstruct the wake. The motion of a fluid particle which enters the measurement region is described by a step-by-step application of the correlated data $w(t)$ and $\beta(t)$. If one determines the angular position of the rotor at which the particles of a certain filament from the absolute system first reach the measurement area, then the subsegment particles enter the first axial measuring plane later at other positions because of rotation and can be followed from there along their paths. As seen by an observer in the relative system, the filament enters the rotor region with the absolute inflow angle α_1 and strikes first on the forward part of the blade pressure side where it is chopped off. Because it is in the stagnation region of the blade, the newly created end of the filament moves more slowly than the following particles and thus the filament begins to take on the form of a bow. Within the entrance part of the rotor the 2-dimensional convective deformation of the fluid filaments agrees amazingly well with the distribution of fluctuation energy; the increasing divergence further downstream is due to 3-dimensional effects which cannot be detected by the L2F-velocimeter.

Another impressive result gives the idea of the rotor secondary flow. Fig. 10 depicts the instantaneous distribution of the absolute flow angle in a plane perpendicular to the axis downstream of the rotor. The rotor blade trailing edges are extrapolated along the mean design direction to characterize three adjacent rotor blade passages. The regions with the strongest deviation gradients typify secondary vortices arising in the rotor blade passages.

Apart from these different instantaneous plots it may be useful to evaluate mean values. Fig. 11 e.g. depicts contours of time-integrated fluctuation energy $\overline{c_1'^2}$ at midspan. The dotted lines characterize the axial rotor section from leading to trailing edge. The identical contours of the averaged fluctuation energy are repeated in the absolute frame in the circumferential direction in order to improve the visual impression. Individual instantaneous effects of the rotor blades disappear. The outstanding result shown in this graph is the strong turbulence increase in the entrance region of the rotor within the stator wake material.

The possibility of time averaging in the relative frame of reference is demonstrated in Fig. 12. Here the individual effects of the stator vanes disappear. The graph depicts contours of "relative" degree of turbulence, that is, the results are calculated by referring the measured random fluctuation energy to the locally measured relative flow velocity. The high turbulence at the pressure side near the leading edge may be of interest for quasi stationary treatment of the rotor blade boundary layer.

CONCLUSION

This report has described the execution and evaluation of Laser-Two-Focus (L2F) measurements within and near the rotor blade row of a single-stage, cold-air test turbine. By application of the L2F "Multi-Window" procedure, each rotor blade pitch is circumferentially divided into 16 segments. In each segment the ensemble averaged 2-D flow vector as well as the mean squares of the random velocity fluctuation parallel and perpendicular to the mean flow direction can be determined by statistical evaluation. (The arrangement used here can not measure the radial components.)

The turbine rotor flow is periodically unsteady, even in the relative frame of reference, because of the upstream inlet guide vanes. To record the unsteady rotor flow, the measuring procedure was repeated for different circumferential positions of the laser measuring volume relative to the stator vane row. The description of the unsteady flow field requires a sufficient local density of measuring points as well as an adequate chronological resolution in order to ensure the accurate reconstruction of all possible rotor-to-stator orientations. The discrete measurements are evaluated by combining chronological and spatial interpolation procedures.

Possible presentations of the results include instantaneous plots of the complete flow field in different planes of the rotor blade channel as well as local distributions of time-averaged results in the

absolute and relative frame of reference. By integration of instationary pathlines the convective deformation of fluid filaments from the stator vane exit flow within the rotor blade channel was evaluated and compared with the instantaneous distribution of turbulence intensity.

REFERENCES

1. Binder, A.   Secondary Flow Effects and Mixing of the Wake
    Romey, R.   Behind a Turbine Stator
                       J. Eng. Pow. 105, No.1, Jan. 1983

2. Binder, A.   An Experimental Investigation into the Effect of Wakes
    Förster, W.   on the Unsteady Rotor Flow
    Kruse, H.   J. Eng. Pow. 107, No.2, April 1985, pp. 458-466
    Rogge, H.

3. Binder, A.   Instationäre Strömungsvorgänge im Laufrad einer Turbine
                       Dissertation Th Aachen, Dez. 1985
                       DFVLR - FB 85 - 66

4. Binder, A.   Anwendung der Laseranemometrie in Turbomaschinen
                       DFVLR, IB 325/85 - 5, Köln, 1985

5. Förster, W.   Instationäre Strömung in einem Turbinenlaufrad
    Mach, K.   VDI Berichte 572.2
                       Thermische Strömungsmaschinen '85
                       Bochum, Sept. 1985, pp. 273-292

6. Hodson, H.P.   An Inviscid Blade-to-Blade Prediction of Wake-
                       Generated Unsteady Flow
                       J. Eng. Pow. 107, No.2, April 1985, pp. 337-344

7. Pfeil, H.   Grenzschichtentwicklung bei instationärer
    Herbst, R.   Zuströmung
                       VDI - Berichte 361, Thermische Strömungsmaschinen '80,
                       Stuttgart, 1980

8. Schodl, R.   A Laser-Two-Focus Velocimeter for Automatic Flow
                       Vector Measurements in the Rotating Components of
                       Turbomachines,
                       J. Fluid. Eng. 102, Dec. 1980, pp. 412-419

9. Schodl, R.   Laser Two Focus Velocimetry
                       AGARD PEP, 67th Symposium on "Advanced Instrumentation
                       for Aero Engine Components",
                       Philadelphia, May 1986

10. Sieverding, C.H. Recent Progress in the Understanding of Basic Aspects
                       of Secondary Flows in Turbine Blade Passages
                       J. Eng. Pow. 107, No.2, April 1985, pp. 248-257

APPENDIX

The mean squares of the random velocity fluctuation parallel and perpendicular to the mean (relative) velocity are defined as

$$\overline{w_1'^2} = \overline{(w_1 - \bar{w}_1)^2} \qquad (A.1)$$

$$\overline{w_{tr}'^2} = \overline{(w_{tr} - \bar{w}_{tr})^2}$$

From Fig. 13,

$$w_1' = c_1' \cos(\bar{\beta} - \bar{\alpha}) - c_{tr}' \sin(\bar{\beta} - \bar{\alpha}) \qquad (A.2)$$

$$w_{tr}' = c_1' \sin(\bar{\beta} - \bar{\alpha}) + c_{tr}' \cos(\bar{\beta} - \bar{\alpha})$$

Then follows

$$w_1'^2 = c_1'^2 \cos^2(\bar{\beta} - \bar{\alpha}) - c_1' c_{tr}' \sin[2(\bar{\beta} - \bar{\alpha})] + c_{tr}'^2 \sin^2(\bar{\beta} - \bar{\alpha}) \qquad (A.3)$$

$$w_{tr}'^2 = c_1'^2 \sin^2(\bar{\beta} - \bar{\alpha}) + c_1' c_{tr}' \sin[2(\bar{\beta} - \bar{\alpha})] + c_{tr}'^2 \cos^2(\bar{\beta} - \bar{\alpha})$$

and because $\bar{\alpha}$, $\bar{\beta}$ = constant (mean values)

$$\overline{w_1'^2} = \overline{c_1'^2} \cos^2(\bar{\beta} - \bar{\alpha}) - \overline{c_1' c_{tr}'} \sin[2(\bar{\beta} - \bar{\alpha})] + \overline{c_{tr}'^2} \sin^2(\bar{\beta} - \bar{\alpha}) \qquad (A.4)$$

$$\overline{w_{tr}'^2} = \overline{c_1'^2} \sin^2(\bar{\beta} - \bar{\alpha}) + \overline{c_1' c_{tr}'} \sin[2(\bar{\beta} - \bar{\alpha})] + \overline{c_{tr}'^2} \cos^2(\bar{\beta} - \bar{\alpha})$$

Eg. A. 4 shows that to derive the desired mean squares it is necessary to know the mean square of the mixed product of c_1' and c_{tr}', i.e. the tangential component of the Reynolds stress tensor.

However, since

$$\overline{w_1'^2} + \overline{w_{tr}'^2} = \overline{c_1'^2} (\sin^2(\bar{\beta} - \bar{\alpha}) + \cos^2(\bar{\beta} - \bar{\alpha}))$$

$$+ \overline{c_1' c_{tr}'} (\sin[2(\bar{\beta} - \bar{\alpha})] - \sin 2(\bar{\beta} - \bar{\alpha}))$$

$$+ c_{tr}'^2 (\sin^2(\bar{\beta} - \bar{\alpha}) + \cos^2(\bar{\beta} - \bar{\alpha}))$$

$$= \overline{c_1'^2} + \overline{c_{tr}'^2} \qquad (A.5)$$

it follows that the sum of the mean squares of random velocity fluctuations parallel and perpendicular to any arbitrary direction is invariant.
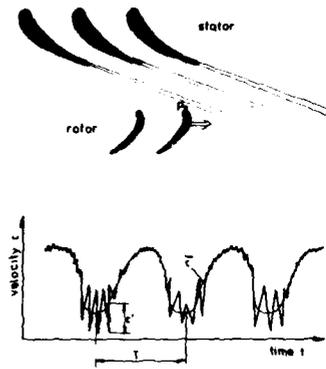
Fig.1: Velocity record as seen by a
rotor blade
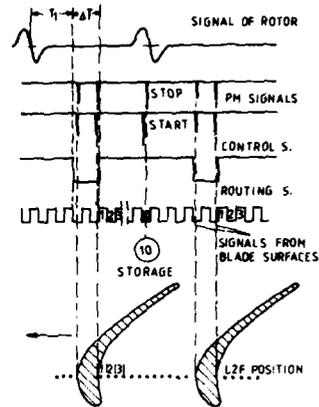
Fig.2: Timing diagram of the multi
window controller
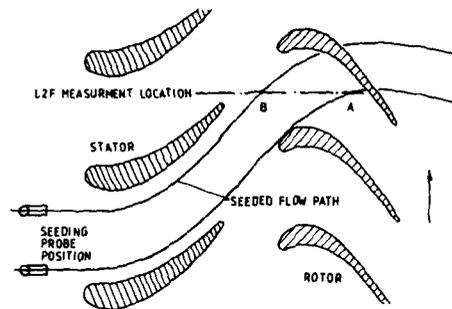
Fig.3: Seeding probe position
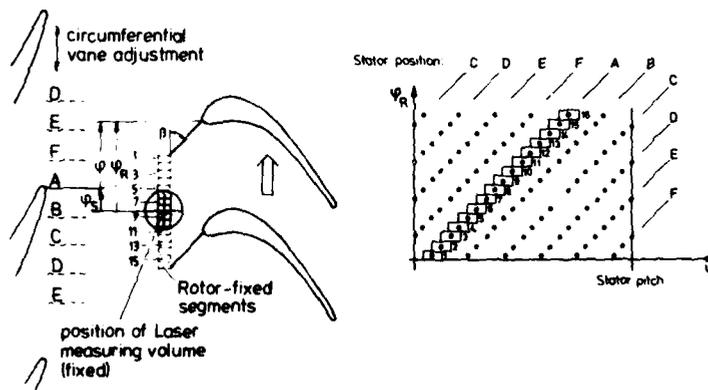
Fig.4:
Circumferential arrangement of Laser measuring positions
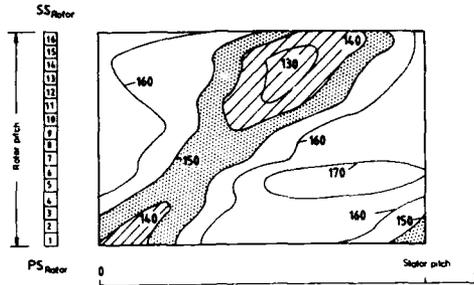
Fig.5: Time slope of relative velocity w [m/s] in front of
the rotor (midspan)
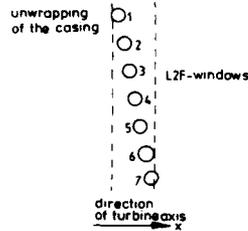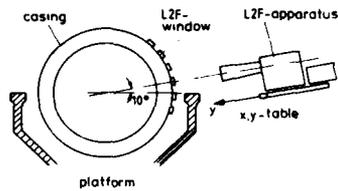
Fig.6: Positioning of the
L2F-velocimeter
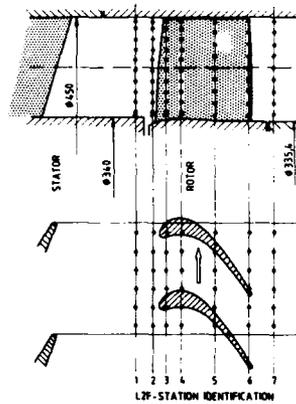
Fig.7: L2F-measurement locations
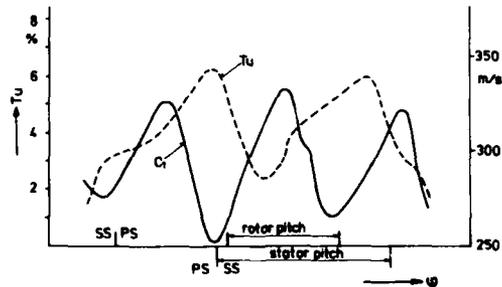
Fig.8: Instantaneous circumferential distribution of
absolute velocity c and turbulence Tu in front
of the rotor

rotor

stator

SS

PS

wake

SS

☐ < 150m²/s²
☐ 150-250m²/s²
▨ 250-350m²/s²
▩ > 350m²/s²

1 2 3 4 5 6 7

measuring plane
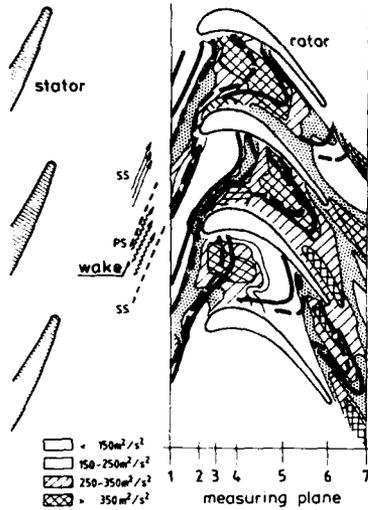
Fig.9: Comparison of convective deformation
with instantaneous distribution of
fluctuation energy $\overline{c_i'^2}$ at midspan

STATOR

150   200

250

300

350

ROTOR SECTION
STATION
1   [m²/s²]   STATION
7
(midspan)
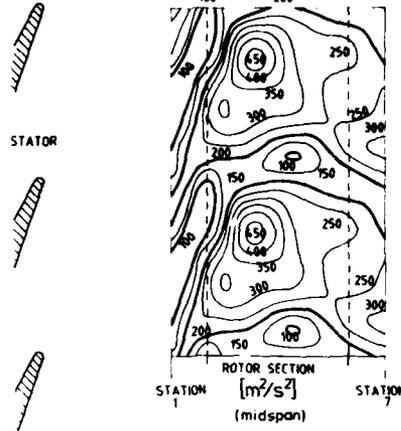
Fig.11: Contours of time averaged
fluctuation energy $\overline{c_i'^2}$ in the
absolute frame (steady state)

direction
of rotation

$\Delta\alpha_2 = 5°$
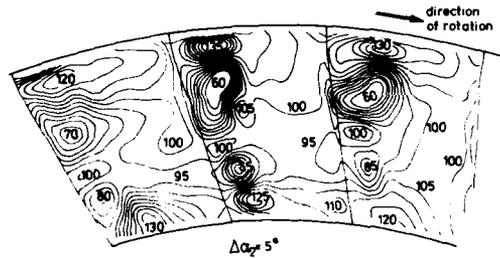
Fig.10: Instantaneous pattern of absolute flow dir ction α_2
at rotor outlet (L2F-plane 7)

rotor

$$Tu_{rel} = \frac{\sqrt{\tfrac{1}{2}(\overline{c_i'^2} + \overline{c_{tr}'^2})}}{W} \times 100$$

(midspan)
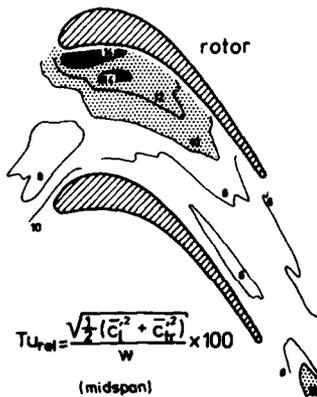
Fig.12: Time averaged relative
turbulence level in the
relative frame (steady
state)

$W \approx C'$

C'_{tr}

α

W C C' W'_{tr}

β

$\overline{W}$ W'_i

$\overline{U}$ $\overline{C}$
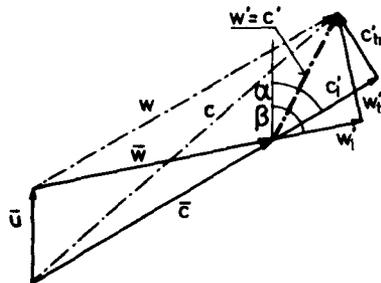
Fig.13: Velocity triangle

DISCUSSION

M.L.G.Oldfield, UK

The acceleration through the passage should change the relative magnitude of the streamwise and transverse components of the turbulent energy. Did you see this in your results?

Author's Reply

Analysis and reduction of our test data is still under way and we have not yet addressed this aspect, although we certainly intend to. One should remember also in regard to our measurements that the streamwise components are determined with greater precision than the transverse ones, and that both components of fluctuating energy are measured in the absolute frame. As explained in the paper, there is no way to transform them to the relative frame knowing the shear components of the Reynolds stress tensor.

R.E.York, US

Do you monitor turbulent intensity or turbulent energy?

Author's Reply

The movie presents the two components of kinetic energy.

COMBINED FRINGE AND FABRY-PEROT LASER ANEMOMETER FOR THREE COMPONENT VELOCITY MEASUREMENTS IN TURBINE STATOR CASCADE FACILITY

Richard G. Seasholtz and Louis J. Goldman
National Aeronautics and Space Administration
Lewis Research Center
Cleveland, Ohio 44135, U.S.A.

SUMMARY

A laser anemometer is described that was developed for use in a 508 mm diameter annular turbine stator cascade facility. All three velocity components are measured through a single restricted optical port, both within the stator vane row and downstream of the vanes. The measurements are made through a cylindrical window in the casing that matches the tip radius of the cascade. The stator tested has a contoured hub endwall that results in a large radial flow near the hub. The anemometer uses a standard fringe configuration (LFA) with a fluorescent aerosol seed to measure the axial and circumferential velocity components. The radial component is measured with a confocal Fabry-Perot interferometer. The two configurations are combined in a single optical system and can operate simultaneously. Data are presented to illustrate the capabilities of the system.

SYMBOLS

$\hat{a}_x, \hat{a}_y, \hat{a}_z$	unit vectors in Cartesian coordinate system
CFPI	confocal Fabry-Perot interferometer
d_o	diameter of probe volume between $1/e^2$ intensity points
FWHM	full-width half-maximum instrumental bandwidth of CFPI
f	focal length
f_D	Doppler shift frequency
$f_{D1,2}$	Doppler shift frequencies of light scattered from beams 1 and 2
$\vec{k}_{1,2}$	wave vectors of incident beams
k_o	wave number $(2\pi/\lambda)$
$\vec{k}_s$	wave vector of scattered light
LFA	laser fringe anemometer (AKA dual-beam laser anemometer)
P_0	inlet total pressure
$P_{h,M}$	hub static pressure at station M
$R_{1,2}$	inner and outer radii of annular clear aperture
T_o	maximum transmittance of CFPI
$\vec{V}$	velocity vector
V_{cr}	critical velocity (fluid velocity at Mach 1)
V_o	velocity magnitude
V_r	radial velocity component
V_{t_j}	measured transverse velocity magnitude
V_x	axial velocity component
V_θ	circumferential velocity component
α_j	angle between fringe normals and cascade axis (x axis)
β	one-half beam crossing angle
Δf_B	standard deviation of angular spectrum of incident beams (Eq. (15))
Δf_F	standard deviation of Fabry-Perot bandwidth
Δf_L	standard deviation of laser frequency jitter
Δf_M	standard deviation of Doppler shifted spectral peak

Δf_R standard deviation of receiver aperture broadening (Eq. (10))

Δf_S standard deviation of sum of broadening effects (Eq. (17))

Δf_T standard deviation of turbulence broadening (Eq. (16))

ΔV_r standard deviation of fluctuations of radial velocity

ϵ deviation of mean Doppler shift from true backscatter shift (Eq. (8))

θ angle between optical axis and flow velocity

θ_s angle between optical axis and scattered light vector

λ laser wavelength

σ one standard deviation

ϕ angle between cascade axis (x axis) and transverse velocity vector

ϕ_s angular coordinate of scattered light vector

ψ angular width of clear aperture in mask used to reduce spectral broadening

Ω solid angle of collected light

$< \, >$ expected value operator

INTRODUCTION

Modern turbine engine designs incorporate geometries that generate highly three-dimensional flow. The accurate measurement of all three velocity components in turbo-machinery research facilities is required for validation of new three-dimensional computer codes under development at the NASA Lewis Research Center and elsewhere for modeling internal flow. The well-known advantages of laser anemometry often make it the best method for obtaining these detailed measurements of internal flow fields.

The preferable approach to three-dimensional laser anemometry is to measure the three orthogonal velocity components directly (Refs. 1 and 2). This generally requires optical access from two orthogonal directions if a fringe (LFA) or two-spot anemometer is employed. Turbomachinery research facilities rarely permit more than a single (usually small) viewing port. With this typical restricted optical access, three-dimensional measurements become much more difficult (see Ref. 3 for a discussion of the problem).

The most common approach to three-dimensional measurements through a single port is to measure nonorthogonal velocity components with an LFA (or a two-spot system) (Refs. 4 to 6). However, the error of the velocity component along the optical axis obtained from this approach becomes large when the window size is small compared to the distance from the window to the measurement region. In general, it is desirable to have an angle between the axes of the LFA components of 30° or more (Ref. 7), although measurements with angles as small as 17° have been reported (Ref. 8). Thus, in spite of the advan-tages of the LFA technique, its limitation to the measurement of transverse components has led to the investigation of other approaches for the measurement of the on-axis component.

One approach to measuring the component along the optical axis is the reference-beam heterodyne technique. Used in a backscatter configuration, a reference-beam system directly measures the on-axis component. This method has been combined with an LFA (Ref. 9) to obtain three-dimensional measurements in a low velocity jet. However, one difficulty with using the reference-beam method in high speed flows is that the Doppler shift is about 4 MHz/m/sec for visible laser light. This results in Doppler shift fre-quencies that can easily exceed the frequency response of most common photomultiplier tubes. Another fundamental limitation of the reference-beam technique is expressed by the Antenna Theorem (Ref. 10), which states that the maximum effective aperture area is limited to about λ^2/Ω where Ω is the solid angle subtended by the probe volume at the receiver aperture.

Another approach for measurement of the on-axis component is the use of a high resolution optical interferometer to directly measure the Doppler shift. One example is the measurement of the optical-axis velocity component in rocket exhausts (Refs. 11 and 12). We have previously shown the feasibility of using a confocal Fabry-Perot inter-ferometer to measure the optical-axis (radial) component in a 508 mm diameter turbine stator (Ref. 13). Also, we have described three-dimensional velocity measurements in a free jet with the Fabry-Perot in a backscatter optical configuration (Ref. 14). Other reported applications of laser anemometry with interferometers include wind tunnels (Refs. 15 to 18), an MHD generator (Ref. 19), and a plasma torch (Ref. 20).

Interferometric measurement of the Doppler shift shares with the reference-beam heterodyne technique the characteristic of providing a direct measurement of the on-axis velocity component in a backscatter optical configuration. It offers the advantage of

having essentially no upper frequency limit, which is important in high speed flows. (Actually, the use of an interferometer for low speed flows is much more difficult than for high speed flows because of the requirements of an interferometer with extremely high resolution and a laser with very good frequency stability.) Another advantage of a confocal Fabry-Perot interferometer is that the amount of usable scattered light is not limited by the Antenna Theorem, but instead by its light-gathering power (etendue). This advantage, however, tends to be offset by its relatively low transmission.

The subject of this paper is a new three-dimensional laser anemometer developed for use in the Lewis 508 mm diameter annular turbine stator cascade facility. The requirements for the anemometer were to measure the three velocity components through a single relatively small viewing port with accuracy of 1 percent of velocity magnitude and 1° of flow angles. The flow in the cascade is in the high subsonic regime with a significant radial component produced by a contoured hub endwall. (Tip endwall contouring was not used because of the difficulty of obtaining optical access for the laser system.) Furthermore, it is necessary to measure small radial velocity components in the presence of large axial and circumferential components.

Conventional fringe-type optics using fluorescent seed were selected for measurement of the transverse velocity components. This technique has previously been used at NASA Lewis for measurements in compressor rotor and turbine stator test facilities (Refs. 21 and 22). After an evaluation of the various techniques discussed above for measuring the third component (the component along the optical axis), a scanning confocal Fabry-Perot Interferometer (CFPI) was chosen.

In this paper, the Lewis turbine stator facility is briefly described. An analysis of scattering theory as it pertains to velocity measurements with an interferometer is presented followed by a description of the optical configuration of the three-dimensional anemometer. Data acquisition and processing are discussed, and some results are presented to illustrate the capability of the anemometer in the cascade facility.

EXPERIMENTAL FACILITY

Stator Cascade

The core turbine stator, full-annular cascade included an inlet section, a test section, and an exit section. A photograph and a cross-sectional view of the facility are shown in Figs. 1 and 2. In operation, atmospheric air was drawn through the inlet section, the blading, and the exit section and then exhausted through the laboratory altitude exhaust system. The cascade is described completely in Ref. 23 and briefly below.

The inlet section, consisting of a bellmouth and a short straight section, was designed to accelerate the flow to uniform axial-flow conditions at the vane inlet.

The test section, for this investigation, consisted of a sector of four vanes that were part of a full-annular ring of 36 vanes. The annular ring is shown in Fig. 3 and a schematic cross-sectional view is shown in Fig. 4. The untwisted vanes, of constant profile from hub to tip had a height of 47.625 mm at the leading edge and 38.10 mm at the trailing edge. The vane axial chord was 38.23 mm and the vane stacking axis was located at the center of the trailing-edge circle. The hub endwall contour was "s" shaped and the coordinates are shown in Fig. 4. The tip endwall had a constant diameter of 508 mm and was not contoured, as explained in the Introduction.

Cascade Flow Conditions

The test conditions in the cascade were set by controlling the pressure ratio across the vane row with two throttle valves located in the exhaust system. A hub static tap located downstream of the test section, where the flow was assumed to be nearly circumferentially uniform (station M, Fig.2), was used to set this pressure ratio. For this investigation the hub-static to inlet-total pressure ratio $P_{h,M}/P_0$ was maintained at a value of 0.724. This prevented the flow from becoming supersonic within the cascade. The design pressure ratio for the previously tested (Ref. 22) cylindrical hub endwall configuration (no contour) was 0.65 and would have produced supersonic flow within the vane passage had it been used.

Windows

A cutout in the test-section outer vane ring (Fig. 3) provided optical access. A second cutout was located downstream of the vane row. The windows were made from 3.175 mm thick window glass. They were formed into a cylindrical shape that matched the tip radius by sagging them, in a vacuum furnace, onto a machined graphite form. The vanes at the window were machined to the tip radius. A silicone rubber sealing material was used to seal both windows to the cascade housing and to seal the vane tips to the window. At the vane row, the window covered about 39° in the circumferential direction and was 4 cm high.

ON-AXIS VELOCITY COMPONENT MEASUREMENT

Scattering Theory

This section presents the theory of using the two beams of a conventional fringe-type anemometer with an interferometer to measure the on-axis velocity component.

Consider two beams with wave vectors $\vec{k}_1$ and $\vec{k}_2$ incident on a particle moving with velocity $\vec{V}$ as shown in Fig. 5. For simplicity, the beams are assumed to lie in the x-z plane and have an included angle 2β. (The fringes formed by the beams thus have normals in the x-direction as shown in Fig. 6.) The receiving optics aperture is assumed to be an annulus centered on the bisector of the beams with outer radius R_2 and inner radius R_1 and is located a distance f (the lens focal length) from the beam crossing position. The wave vector of the scattered light is $\vec{k}_s$. Thus, in Cartesian coordinates with the optical axis along the z-direction

$$\vec{k}_{1,2} = k_o \ (\pm \sin \beta \ \hat{a}_x + \cos \beta \ \hat{a}_z) \tag{1}$$

$$\vec{k}_s = k_o \ (\sin \theta_s \cos \phi_s \ \hat{a}_x + \sin \theta_s \sin \phi_s \ \hat{a}_y + \cos \theta_s \ \hat{a}_z) \tag{2}$$

$$\vec{V} = V_o \ (\sin \theta \cos \phi \ \hat{a}_x + \sin \theta \sin \phi \ \hat{a}_y + \cos \theta \ \hat{a}_z) \tag{3}$$

where $\hat{a}_i$ denotes the unit vector in the i direction and the wave number $k_o = 2\pi/\lambda$. The subscripts 1 and 2 refer to the two incident beams, and the first subscript corresponds to the upper sign.

The Doppler shifts of the light scattered in direction $\vec{k}_s$ are

$$f_{D1,2} \ (\theta_s, \phi_s) = \frac{1}{2\pi} \ (\vec{k}_s - \vec{k}_{1,2}) \ \cdot \ \vec{V}$$

$$= \frac{1}{\lambda} \ \left[V_t [\sin \theta_s \cos(\phi_s - \phi) \mp \sin \beta \cos \phi] + V_r \ (\cos \theta_s - \cos \beta) \right] \tag{4}$$

where $V_t = V_o \sin \theta$ is the transverse velocity component and $V_r = V_o \cos \theta$ is the component along the optical axis (the radial component in the cascade). Note that the scattered light is spread over a range of frequencies because of the finite extent of the light collecting aperture.

The mean values of the Doppler shift frequencies of the scattered light collected over the full annulus are

$$\langle f_{D1,2} \rangle = \frac{1}{\Omega} \int_{\theta_2}^{\theta_1} \int_0^{2\pi} f_{D1,2}(\theta_s, \phi_s) \ \sin \theta_s \ d\phi_s \ d\theta_s \tag{5}$$

where $\langle \ \rangle$ denotes the expected value, and

$$\Omega = \int_{\theta_2}^{\theta_1} \int_0^{2\pi} \sin \theta_s \ d\phi_s \ d\theta_s \tag{6}$$

is the solid angle of collected light. The limits on the integration over θ_s are given by

$$\theta_{1,2} = 180° - \tan^{-1}(R_{1,2}/f) \tag{7}$$

Carrying out the integrations, Eq. (5) becomes

$$\langle f_{D1,2} \rangle = - \frac{1}{\lambda} \ \left[\pm V_t \sin \beta \cos \phi + 2(1 - \epsilon) \ V_r \right] \tag{8}$$

where

$$\epsilon = 1 - \frac{1}{2} \left[\frac{\sin^2 \theta_1 - \sin^2 \theta_2}{2(\cos \theta_1 - \cos \theta_2)} + \cos \beta \right]$$

represents the deviation from pure backscatter and is generally $\langle\langle$ 1. If the scattered light from the two beams is of equal intensity, then the mean value of the frequency of the light scattered from both beams integrated over the annulus is

$$\langle f_D \rangle = \frac{1}{2} \ \left(\langle f_{D1} \rangle + \langle f_{D2} \rangle \right) = - \frac{2}{\lambda} \ (1 - \epsilon) \ V_r \tag{9}$$

Thus, the mean Doppler shift is proportional to the optical-axis velocity component.

The standard deviation of the Doppler shift frequency of the scattered light is, in general, given by

$$\Delta f_R = \left\langle (f_D - \langle f_D \rangle)^2 \right\rangle^{1/2} \tag{10}$$

If the light scattered from the two beams is not of equal intensity, the terms in Eq. (8) proportional to V_t will not cancel, and $\langle f_D \rangle$ will not, in general, be proportional to V_r. However, note that if the velocity is in the y-z plane (i.e., perpendicular to the fringe normals as shown in Fig. 6), $\phi = 90°$ and the Doppler shifts of light scattered from the two beams are equal for any scattering direction. Equation (8) in this case reduces to

$$\langle f_{D1} \rangle = \langle f_{D2} \rangle = -\frac{2}{\lambda}(1 - \epsilon) \quad V_r, \phi = 90° \tag{11}$$

Example

For the annular aperture described in the Optical Layout section,

$$\theta_1 = 176.3°$$

$$\theta_2 = 174.7°$$

$$\beta = 1.134°$$

$$\epsilon = 0.00169$$

To estimate the spectrum of the scattered light, we can let $\theta_s = 175.5°$ (since θ_s only varies over a small range) and assume that the velocity is in the y-z plane ($\phi = 90°$). Then the Doppler shift frequency given by Eq. (4) becomes

$$f_D(\phi_s) = \frac{1}{\lambda}\left[0.0785 \sin \phi_s V_t - 1.9967 V_r \right] \tag{12}$$

The mean value of the Doppler shift is (Eq. (11))

$$\langle f_D \rangle = -\frac{1.9967}{\lambda} V_r \tag{13}$$

and the spectral width due to the receiving optics is (Eq. (10))

$$\Delta f_R = \frac{0.0785}{\lambda} \left\langle \sin^2 \phi_s \right\rangle^{1/2} V_t \tag{14}$$

For light collected over the full annular aperture, $\left\langle \sin^2 \phi_s \right\rangle^{1/2} = 1/\sqrt{2}$. For example, if $V_t = 250$ m/sec and $\lambda = 514.5$ nm, then $\Delta f_R = 27$ MHz.

Mask for Reduction of Spectral Width

A technique for reducing the spectral width caused by aperture broadening is to introduce a mask having a clear aperture angular width 2ψ as shown in Fig. 6. The mask must be oriented as shown to ensure that the mean radial velocity measurement is unbiased. An example of the spectral broadening for a transverse velocity $V_t = 250$ m/sec is shown in the following table for several masks.

ψ, deg	$\left\langle \sin^2 \phi_s \right\rangle^{1/2}$	Δf_R, MHz
30	0.294	11
45	.426	16
60	.542	21
90	.707	27

If the flow angle $\phi \neq 90°$, then the spectrum will be somewhat broader than these values.

One word of caution should be mentioned: if an angular mask is used which is not properly oriented, then the mean Doppler shift frequency will be biased. But, if no angular mask is used, the mean Doppler shift will be correct, although the spectral width will be greater.

Other Causes of Spectral Broadening

In addition to the spectral broadening discussed above caused by the spread in the wave vector of the scattered light, four other factors cause broadening. One is the

inherent instrumental broadening Δf_p. For the purposes of this paper, Δf_p is approximated by one-half of the FWHM bandwidth. (The FWHM bandwidth is given by the FSR divided by the finesse, so $\Delta f_p \cong 30$ MHz).

Another factor is jitter in the laser frequency (Δf_L), which is typically about 10 MHz in a low-noise, low-vibration environment. In a noisy environment, such as a test cell, the jitter will be greater. This jitter, of course, likewise affects the unshifted peak and the Bragg peak. A third cause of broadening is the angular spectrum of the incident beams, which is given by (Ref. 24)

$$\Delta f_B = V_t/(\pi d_o) \tag{15}$$

where V_t is the transverse velocity and d_o is the diameter of the probe volume. For this application, $\Delta f_B < 1$ MHz and therefore can be neglected.

Finally, fluctuations in the flow velocity (i.e., turbulence) cause broadening of the measured spectrum. If turbulence broadening is greater than broadening from all other effects, then the spectral width can be used as a measure of the intensity of the radial turbulence. An estimate of the intensity of the turbulence fluctuations of the on-axis velocity component is then given by

$$\Delta f_T = (\Delta f_M^2 - \Delta f_S^2)^{1/2} \tag{16}$$

where Δf_M is the measured width (1σ), and Δf_S is the sum of all other broadening mechanisms except turbulence. The various broadening mechanisms are assumed to be independent so Δf_S is given by the root-sum-square

$$\Delta f_S = (\Delta f_L^2 + \Delta f_B^2 + \Delta f_R^2 + \Delta f_F^2)^{1/2} \tag{17}$$

If, for example, the turbulence is isotropic with 10 percent intensity, the mean radial velocity is zero, and the transverse velocity is 250 m/sec, then the turbulence fluctuations of the radial velocity $\Delta V_r \approx 25$ m/sec and $\Delta f_T = \Delta V_r/(\lambda/2) \approx 100$ MHz. This is larger than the broadening usually observed due to other causes; and, for this case, the measured width could be used as a measure of the turbulence intensity. In practice, the broadening due to the laser jitter and the instrumental bandwidth can be determined from the width of the spectral peak of the laser light scattered from the walls.

LASER ANEMOMETER SYSTEM

Optical Layout

A photograph of the optical system and the layout are shown in Figs. 7 and 8. The argon-ion laser was equipped with a temperature controlled etalon and had a maximum output power of 0.8 W at a 514.5 nm wavelength with a vertically polarized TEM$_{oo}$ transverse mode and single axial mode.

Lenses L1 and L2 (focal lengths 80 and 100 mm, respectively) function as mode-matching lenses to position the beam waists at the focal plane of lens L3. The beam divider (constructed from two appropriately coated 6.35 mm thick glass plates) split the single beam into two equal intensity parallel beams (approximately 10 mm separation). The divider was mounted in a motor driven rotary mount, so the orientation of the fringes could be set at any desired angle. A half-wave retardation plate (gear driven by the mount at one-half the angle of rotation of the divider) was located at the input of the beam divider to maintain the proper linear polarization at the input of the beam divider.

The two parallel beams from the beam divider were turned by mirrors M3, M4, and M5. Mirror M4 was elliptical with a minor axis of 15.2 mm and major axis of 21.6 mm. The parallel beams were focused by lens L3 (250 mm focal length, 46 mm clear aperture) to cross at the probe volume after being reflected by mirror M5. Mirror M5 was mounted on a motor driven goniometer stage with axis perpendicular to the plane of the optical table. This enabled the optical axis to be positioned along the radial direction in the stator cascade.

The diameter ($1/e^2$ intensity) of the probe volume was about 100 μm and the fringe spacing was 13 μm (about 8 fringes). Light scattered from particles passing through the probe volume (after reflection by M5) was collimated by lens L3. An aperture mask with a central circular stop (diameter 32 mm) was used to reduce the effective length of the probe volume. This mask blocked 50 percent of the full clear aperture of the collection lens L3, which means the receiving optics had an effective f-number for light collection of f/6. The pair of lenses L4 and L5 (focal lengths 160 and 60 mm, respectively) is used to reduce the diameter of the collimated scattered light beam to 17 mm. The beam is then split with a dichroic beam splitter, which reflects 514.5 nm wavelength light and passes the longer wavelength fluorescence orange light.

After passing through a long wavelength pass filter LWP (to remove any residual 514.5 nm light), the fluorescent beam is focused by lens L6 (100 mm focal length) through a 100 μm diameter pinhole (PH) located in front of photomultiplier PMT1 (RCA

4526). The signal from this PMT is processed by a counter-type processor to provide velocity components transverse to the optical axis.

The light reflected by the dichroic beamsplitter is light elastically scattered by seed particles (i.e., not fluorescence). This 514.5 nm wavelength light is focused by lens L7 (100 mm focal length) through another 100 μm pinhole and a 16 mm focal length lens (L8, a 10X microscope objective). A narrow band laser line filter (LLF) removes any residual fluorescence and background light before the light enters the confocal Fabry-Perot interferometer (CFPI).

The CFPI has a free spectral range of 3 GHz and a maximum transmission of about 10 percent. The measured finesse (ratio of free spectral range to instrumental band-width) was about 50. The light exiting the CFPI was detected by photomultiplier PMT2 (RCA 8850). Photon counting electronics provided a digital count rate corresponding to the light intensity passed by the CFPI. (Additional factors to be considered in the use of a CFPI for laser anemometry are discussed in Ref. 13.)

An acoustic-optic modulator (Bragg cell) was included to generate a reference signal offset from the laser frequency by 400 MHz. The 200 MHz Bragg cell frequency was crystal controlled (the second order diffracted beam was used). This signal was used to provide a calibration signal for each sweep of the interferometer. A lens (L9) was used to collimate the beam before the Bragg cell.

Acoustic shielding was necessary to reduce vibration of the laser, which would cause a large jitter in the laser frequency. (The acoustic noise level near the cascade was measured at 105 dB.) The optics and laser were mounted in a wood box covered with a layer of an acoustical foam and lead composite. The weight of the lead shielding used was about 10 kg/m^2.

Positioning System

The laser and optics were mounted on a 610 mm by 1524 mm by 64 mm thick aluminum optical breadboard, which was mounted on a 3 axis positioning system with a 12 μm positioning accuracy and 1 μm resolution. The positioning system controller was locaated in the test cell near the cascade with an RS-232 serial communications link to the minicomputer located in the control room. In addition to the three linear stages, the beam divider and goniometer mounted mirror were also controlled with this system. This provided a sufficient number of degrees of freedom to allow the optical axis to be directed along a radial line throughout the test region.

Calibration Procedures

A critical requirement for obtaining laser anemometer data for computer code veri-fication is the accurate determination of the probe volume location relative to the experimental hardware. For the stator cascade described in this paper, location accu-racies of +25 μm are desired. A complicating factor in achieving this accuracy is that the stator cascade hardware moves relative to the laser anemometer when going from no-flow to flow conditions and when the ambient temperature changes. Because of these reasons, position calibration must be done under test conditions. The needed parameters are the coordinates of the cascade axis, the axial position of the leading edge of the vane row, and the circumferential location of the suction and pressure surfaces of the vanes at a given axial position.

These parameters are determined after the flow has been set to the test operation condition and has stabilized. The location of a surface is determined by scanning the probe volume through the surface and recording the intensity of the collected light. The peak in the measured intensity corresponds to the center of the probe volume being at the surface. An example of such a scan is shown in Fig. 9 for determination of the hub location. The actual peak location is estimated using a least squares fit of the data to a Gaussian as shown in the figure. By making several radial scans through the hub at different circumferential positions, sufficient data is acquired to calculate the coordinates of the cascade axis. The other parameters are determined similarly. These procedures are automatically executed to minimize the loss of test time.

A scan through a normal surface, as shown in Fig. 9, also shows the length of the probe volume. At the 1/e^2 intensity points, the probe volume length is thus about 2.2 mm. Of course, the effective length of the measurement region can be less than this due to the signal processor threshold and the size distribution of the seed particles. In addition, the scattered light was simultaneously measured in both optical paths to verify that the probe volumes defined by the fringe and the Fabry-Perot receiving optics were located at the same position. The peak locations were within 0.25 mm.

The following procedure was used to calibrate the fringe orientation relative to the vertical axis of the positioning system. A 50 μm by 3 mm air slit was aligned parallel to the positioning system vertical axis and located about 140 mm from the probe volume. The positioning system was used to twice scan the beams horizontally across the slit. The transmitted light was recorded for each beam, and the optical system was moved vertically between the two scans so that the beams were at the same position on the slit. When the maximum light transmitted by the slit for both scans occurred at the same indicated horizontal position, the beams lay on a vertical line (fringe normals

vertical). By rotating the beams 180°, the angular rotation could also be calibrated. The goniometer stage was calibrated in a similar manner. The fringe spacing (13.0 µm) was determined from the beam crossing angle measured by scanning the two beams across the air slit with the probe volume at several distances from the slit.

Seeding

A fluorescent dye aerosol was used as the seed material for these tests. This material allowed measurements (using the technique described by Ref. 25) to be made by the LFA part of the system close to the hub, the vanes, and the windows. A liquid dye solution (0.02 molar solution of rhodamine 6G in a 50-50 mixture, by volume, of benzyl alcohol and ethylene glycol) was atomized with a commercial aerosol generator. The aerosol was injected through a 6 mm diameter tube into the flow at the entrance of the bellmouth.

The fluorescence, because it is broadband, is only usable for the fringe measurements and not for the Fabry-Perot measurements. As a consequence, transverse component measurements could be made closer to surfaces than could radial component measurements. The Fabry-Perot measurements could be made to within 3 mm of the hub. Previous work (Ref. 23) in a turbine stator cascade with a similar optical system using fluorescence allowed fringe measurements within 1 mm of the hub. Of course, it is also possible to use elastically scattered light for both the LFA and Fabry-Perot measurements. One would just substitute an ordinary beamsplitter for the dichroic beam splitter and use nonfluorescent seed.

DATA ACQUISITION

A minicomputer was used for experiment control and data acquisition. It was also used to generate on-line displays of the data so that the system could be monitored for proper operation.

Fringe Signal

The fringe signal from PMT1 was processed with a counter-type processor using four cycles of the Doppler burst. The counter output data, consisting of Doppler frequency and time-between-measurements, were transferred to the minicomputer via a DMA interface having a maximum transfer rate of about 200 kHz. Data were taken at several fringe orientations at each measurement position. For this experiment, the maximum number of fringe orientations was limited to seven by the available minicomputer memory. The fringe orientations were selected at 10° intervals and bracketed the predicted flow angle. At each fringe orientation, 1000 data pairs were taken. The frequency data (corresponding to velocity components) were stored in 256 bin histograms for later off-line processing. Typical data rates ranged from 1 to 5 kHz.

Fabry-Perot

Data from the Fabry-Perot interferometer were obtained by scanning the passband over a frequency range that included the laser frequency, the Doppler shifted frequency of light scattered from seed particles, and the Bragg shifted reference frequency. A linear ramp generator, which produced a sawtooth waveform with adjustable period, amplitude, and DC offset, was used to scan the interferometer. The data from the photon counting electronics were stored in 256 bin histograms; each bin contained the number of counts in 1/256 of the sweep duration. An adjustable number of repetitive sweeps was used to build a composite histogram. Typically, 20 sweeps of 1 sec duration were used. Each sweep was examined by the computer to determine the bin number of the peak corresponding to the Bragg reference peak. The data were then offset to place the Bragg peak at a predetermined bin. This technique was used to eliminate the effect of drift in the laser frequency for data taken over long time intervals. It was found to be desirable to take data over several seconds to reduce biasing caused by short term variations in the rate of seed particles passing through the probe volume. (The observed variation in the data rate was believed to be caused by random cross-flow at the entrance of the bellmouth where the seed was injected.)

If the radial velocity is near zero, the above technique is not applicable, but the following previously reported (Ref. 14) technique can be used. In that situation, the signal from the seed particles overlaps the zero-shift signal from the laser light scattered from the cascade walls. To extract the desired signal, two histograms are constructed: one with the seeding turned on and one with the seeding off. The histograms are subtracted during the data processing to give a difference histogram that contains only the desired signal. (Of course, the noise from the removed peaks remains.) For the result presented in this paper, this technique was not used. It would be necessary for surveys taken farther from the contoured hub.

EXPERIMENTAL RESULTS

Fringe Data

The fringe data were stored in histogram form - one 256 bin histogram for each fringe orientation at each probe volume position. A typical histogram is shown in Fig. 10. The mean velocity and flow angle of the projection of the velocity in the axial-circumferential plane were obtained using a two-step procedure. First, each of the histograms was least-squares fit to a Gaussian function to get estimates of the mean transverse velocity components V_{t_j} as a function of the fringe orientation α_j.

These Gaussian histogram fits also provided estimates of the standard deviations of the flow fluctuations as a function of angle.

The second step was to determine the transverse velocity magnitude V_t and flow angle ϕ. These were found using the procedure described in Ref. 22, where V_t and ϕ are found using a least squares fit to (Fig. 11).

$$V_{t_j} = V_t \cos(\phi - \alpha_j) \tag{18}$$

The axial and circumferential components are then given by

$$V_x = V_t \cos \phi, \qquad V_\theta = V_t \sin \phi \tag{19}$$

Deviation of the data from the cosine model function provides an indication of angle biasing errors. Angle biasing is caused by a variation of data rate with flow angle, which causes the components at large angles from the mean flow direction to be biased high (Ref. 26).

In addition to the Gaussian fit, the velocity components and standard deviations were directly calculated from the histograms. The direct calculation usually gave velocity components very close (within 0.5 percent) to those obtained from the Gaussian fit, but the standard deviations tended to be larger (typically 5 to 10 percent larger). This was probably a result of stray data on the tails of the histograms. Hence, the results obtained from the Gaussian fit were used.

Fabry-Perot Data

For simplicity, no angular mask was used in the Fabry-Perot receiving optics (i.e., $\psi = 90°$), so light was collected over the full annulus. The spectral broadening due the receiver aperture is thus given by Eq. 14. Data was taken at each of the fringe orientations used for the fringe measurement; no appreciable differences was noticed in the spectral widths.

The Fabry-Perot histograms consisted of three spectral peaks (Fig. 12). The right peak is a result of unshifted laser light scattered from surfaces near the probe volume; its amplitude is a function of position of the probe volume. The left peak is the reference peak from the Bragg cell; it is shifted 400 MHz from the right peak and its amplitude could be controlled by the drive voltage on the Bragg cell. The center peak corresponds to the Doppler shifted light scattered from the seed particles. Estimates of the frequencies of the three peaks were obtained by a least-squares fit of the data to a three peak Gaussian function. The Doppler-shift frequency of the light scattered from the seed particles is thus proportional to the separation between the center and right peaks, and the mean radial velocity is then given by Eq. 9.

It is also possible to obtain an estimate of the intensity of the radial velocity fluctuations as discussed in the section Other Causes of Spectral Broadening. For this test, the width (1σ) of the non-Doppler shifted peak was about 40 MHz, which included broadening due to laser jitter and the instrumental bandwidth of the Fabry-Perot. The receiving aperture broadening Δf_R, which depends on the transverse velocity, was less than 30 MHz. Thus, the sum of all broadening effects except turbulence was less than about 50 MHz. This is less than the observed width of the Doppler-shifted peak, so an estimate of the radial component fluctuations can be calculated using Eq. 16. For the histogram shown in Fig. 12, the rms radial velocity fluctuations were approximately 7 percent of the velocity magnitude.

Survey Data

An example of the measurement of the three velocity components is shown in Fig. 13. These data show a circumferential scan between the suction and pressure surfaces of the vanes at 80 percent axial chord and 10 percent span; this location is close to the center of the contoured section of the hub where a relatively large radial velocity component exists. The figure shows data taken on two dates as well as the results of a three-dimensional inviscid computer code (Ref. 27). The DENTON computer program is a time marching finite volume solution of the Euler equations. Shown are the axial component V_x, the circumferential component V_θ, and the radial component V_r. Also shown is the velocity magnitude V_0. These are normalized with respect to the critical velocity V_{cr} to eliminate differences due to am'ient temperature changes between the measurements performed on different days.

The trends in the experimental measurements and the agreement with the theoretical calculations are quite reasonable and encouraging. However, these preliminary results are only intended to illustrate the capability of the anemometer and are not meant for code verification purposes.

CONCLUDING REMARKS

The laser anemometer described in this paper is shown as a viable means of measuring the three mean velocity components in an annular turbine stator facility. The addition of a confocal Fabry-Perot interferometer to a conventional fringe-type anemometer allowed the measurement of the radial velocity component with a backscatter configuration. The advantage of this technique compared with other methods of measuring the radial component is that it does not require a large optical access port. An important feature of the anemometer is its ability to measure a small radial velocity component when the transverse component is much larger.

The scanning Fabry-Perot interferometer used in this work for measurement of the radial (optical-axis) component does, however, have some limitations compared with fringe and two-spot anemometers used for measurement of the transverse components. These include an increased data acquisition time, an inability to measure time history data, the need for an acoustic enclosure to protect the laser from the high acoustic noise levels, and poorer performance near walls. Other applications having more generous optical access may be better served by other techniques.

REFERENCES

1. Meyers, J.F., and Wilkinson, S.P., "A Comparison of Turbulence Intensity Measurements Using a Laser Velocimeter and a Hot Wire in a Low Speed Jet Flow," International Symposium on Applications of Laser-Doppler Anemometry to Fluid Mechanics, D.F.G. Durao, ed., 1982, pp. 17.4-1 to 17.4-14.

2. Pfeifer, H.J., "A New Optical System for Three-Dimensional Laser Doppler-Anemometry Using an Argon-Ion and a Dye Laser," International Congress on Instrumentation in Aerospace Facilities, IEEE, 1985, pp. 56-62.

3. Meyers, J.F., "The Elusive Third Component," International Symposium on Laser Anemometry," A. Dybbs and P.A. Pfund, eds., ASME, 1985, pp. 247-254.

4. Johansson, T.G., et al, "A Three-Component Laser-Doppler Velocimeter," Applications of Non-Intrusive Instrumentation in Fluid Flow Research, AGARD CP-193, 1976, pp. 28-1 to 28-4.

5. Neti, S., and Clark, W., "On-Axis Velocity Component Measurement with Laser Velocimeters," AIAA J., Vol. 17, No. 9, Sept. 1979, pp. 1013-1015.

6. Sathyakumar, R., "LDV System for Three Component Measurement," U.S. Patent No. 4,263,002, Apr. 21, 1981. (Thermal Systems Inc.)

7. Orloff, K.L., and Snyder, P.K., "Laser Doppler Anemometer Measurements Using Nonorthogonal Velocity Components: Error Estimates," Appl. Opt., Vol. 21, No. 2, Jan. 15, 1982, pp. 339-344.

8. Snyder, P.K., Orloff, K.L., and Reinath, M.S., "Reduction of Flow-Measurement Uncertainties in Laser Velocimeters with Nonorthogonal Channels," AIAA J., Vol. 22, No. 8, Aug. 1984, pp. 1115-1123.

9. Orloff, K.L., and Logan, S.E., "Confocal Backscatter Laser Velocimeter with On-Axis Sensitivity," Appl. Opt., Vol. 12, No. 10, Oct. 1973, pp. 2477-2481.

10. Siegman, A.E., "The Antenna Properties of Optical Heterodyne Receivers," Proc. IEEE, Vol. 54, No. 10, Oct. 1966, pp. 1350-1356.

11. James, R.N., Babcock, W.R., and Seifert, J.S., "A Laser-Doppler Technique for the Measurement of Particle Velocity," AIAA J., Vol. 6, No. 1, Jan. 1968, pp. 160-162.

12. Morse, H.L., et al, "Development of a Laser-Doppler Particle Sensor for the Measurement of Velocities in Rocket Exhausts," J. Spacecr. Rockets, Vol. 6, No. 3, Mar. 1969, pp. 264-272.

13. Seasholtz, R.G., and Goldman, L.J., "Laser Anemometer Using A Fabry-Perot Interferometer for Measuring Mean Velocity and Turbulence Intensity along the Optical Axis in Turbomachinery," Engineering Applications of Laser Velocimetry, (H.W. Coleman and P.A. Pfund eds., ASME, 1982, pp. 93-101.

14. Seasholtz, R.G., and Goldman, L.J., "Three Component Velocity Measurements Using Fabry-Perot Interferometer," Second International Symposium on Applications of Laser Anemometry to Fluid Mechanics, 1984, pp. 8.6 to 8.12.

15. Jackson, D.A., and Paul, D.M., "Measurement of Hypersonic Velocities and Turbulence by Direct Spectral Analysis of Doppler Shifted Laser Light," Phys. Lett., A, Vol. 32, No. 2, June 15, 1970, pp. 77-78.

16. Jackson, D.A., and Paul, D.M., "Measurement of Supersonic Velocity and Turbulence by Laser Anemometry," J. Phys. E., Vol. 4, No. 3, Mar. 1971, pp. 173-177.

17. Eggins, P.L., and Jackson, D.A., "Laser Doppler Velocity Measurements in Supersonic Flow without Artificial Seeding," Phys. Lett. A, Vol. 42, No. 2, Nov. 20, 1972, pp. 122-124.

18. Jackson, D.A., and Eggins, P.L., "Supersonic Velocity and Turbule..ce Measurements Using a Fabry-Perot Interferometer," Applications of Non-Intrusive Instrumentation in Fluid Flow Research, AGARD CP-193, 1976, pp. 6-1 to 6-13.

19. Self, S.A., "Laser Doppler Anemometer for Boundary Layer Measurements in High Velocity, High Temperature MHD Channel Flows," Proceedings of the Second International Workshop on Laser Velocimetry, H.D. Thompson and W.H. Stevenson, eds., Purdue University, 1974, pp. 44-67.

20. Mannik, L., and Brown, S.K., "Laser Doppler Velocimetry of Particles in a Plasma Torch," Appl. Opt., Vol. 25, No. 5, Mar. 1, 1986, pp. 649-652

21. Powell, J.A., Strazisar, A.J., and Seasholtz, R.G., "Efficient Laser Anemometer for Intra-Rotor Flow Mapping in Turbomachinery," J. Eng. Power, Vol. 103, No. 2, Apr. 1981, pp. 424-429.

22. Goldman, L.J., and Seasholtz, R.G., "Comparison of Laser Anemometer Measurements and Theory in an Annular Turbine Cascade with Experimental Accuracy Determined by Parameter Estimation," Engineering Applications of Laser Velocimetry, H.W. Coleman and P.A. Pfund, eds., ASME, 1982, pp. 83-92.

23. Goldman, L.J., and Seasholtz, R.G., "Laser Anemometer Me surements in an Annular Cascade of Core Turbine Vanes and Comparison With Theory," NASA TP-2018, 1982.

24. Edwards, R.V., et al., "Spectral Analysis of the Signal from the Laser Doppler Flowmeter: Time-Independent Systems," J. Appl. Phys., Vol. 42, No. 2, Feb. 1971, pp. 837-850.

25. Stevenson, W.H., dos Santos, R., and Mettler, S.C., "Fringe Mode Fluorescence Velocimetry," Applications of Non-Intrusive Instrumentation in Fluid Flow Research, AGARD CP-193, 1976, pp. 20-1 to 20-9.

26. Seasholtz, R.G., "Laser Doppler Velocimeter System for Turbine Stator Cascade Studies and Analysis of Statistical Biasing Errors," NASA TN D-8297, 1977.

27. Denton, J.D., "An Improved Time Marching Method for Turbomachinery Flow Calculation," J. Eng. Power, Vol. 105, No. 3, July 1983, pp. 514-524.

Figure 1. - Stator cascade facility.
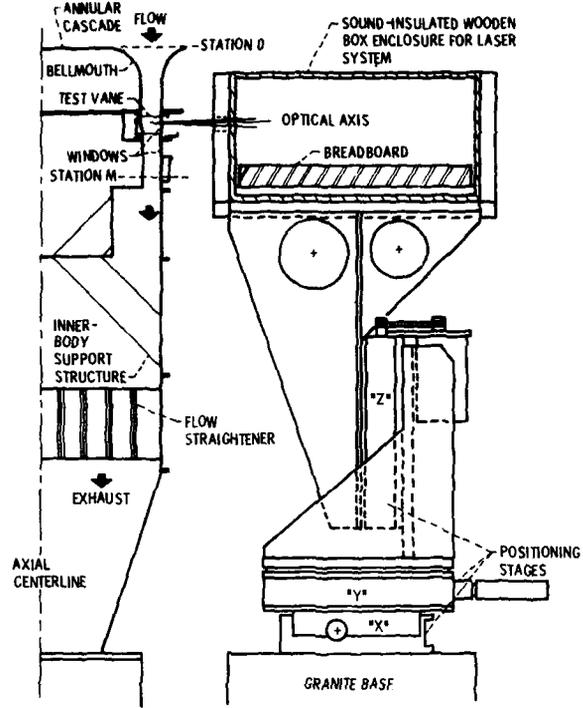
Figure 2. – Schematic cross-sectional view of core turbine stator cascade and laser positioning system.
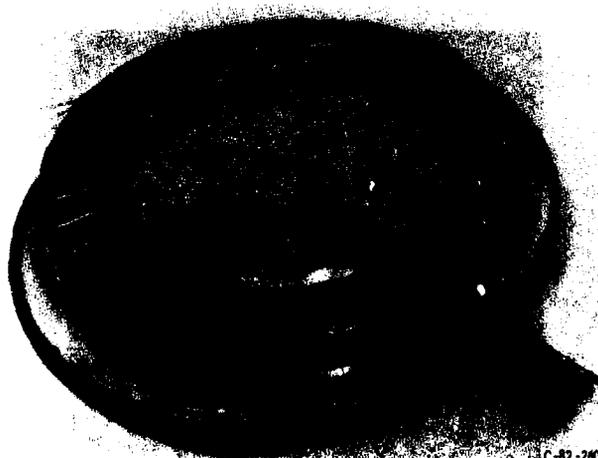
Figure 3. – Annular vane ring.

"X", mm	"Y" DIAM, mm
0. 0	412. 750
↓	↓
19. 177	412. 750
21. 463	412. 953
23. 749	414. 274
25. 654	416. 662
27. 178	419. 278
28. 702	422. 275
30. 226	425. 272
31. 750	427. 888
33. 655	430. 276
35. 941	431. 597
38. 227	431. 800
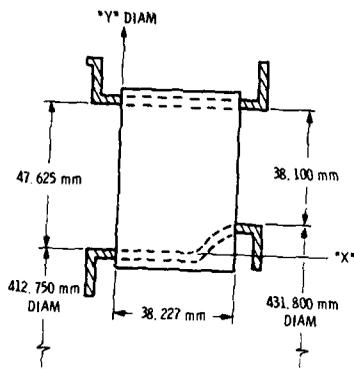
Figure 4. - Schematic cross-sectional view of contoured hub endwall vane ring.
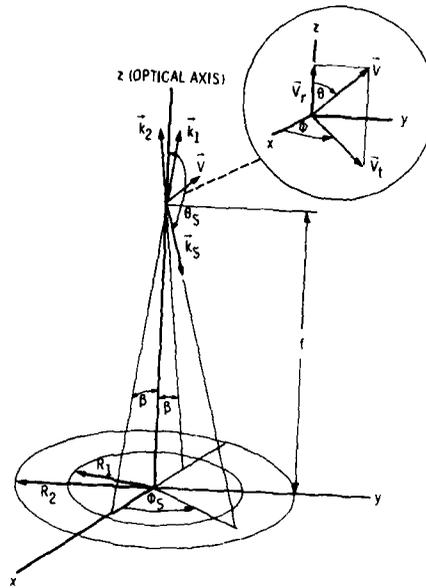
Figure 5. - Scattering geometry.
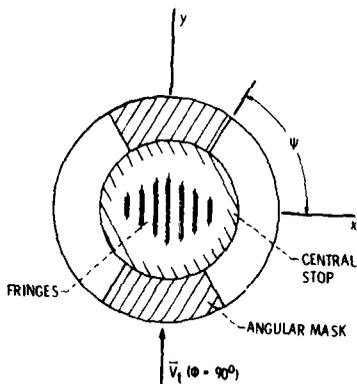
Figure 6. - Aperture mask.

Figure 7. - Three component laser anemometer.

Figure 8. - Optical layout.

Figure 9. - Radial scan of probe volume through hub.

Figure 10. - Fringe data histogram.

Figure 11. - Least squares fit of velocity components to cosine.

Figure 12. - Fabry-Perot spectrum.
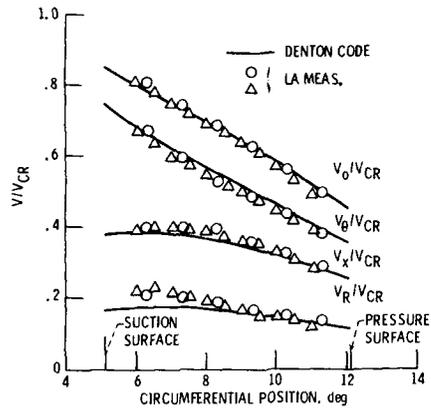
Figure 13. - Experimental survey data and Denton code results.

DISCUSSION

R.Schodl, GE

(1) What is the velocity resolution in the low speed range of the Fabry-Pérot system?

(2) What are the smallest particles which can be detected by this system?

Author's Reply

(1) The resolution of the radial velocity component measurement depends on several factors including the transverse velocity (which broadens the spectrum), the turbulence intensity, and the amount of wall-scattered light that is detected. For low turbulence, the resolution should be 1 or 2 m/s. Note that for small radial velocities (where the spectral peak of the light scattered from the seed particles overlaps the spectral peak of the wall scatter) the seed rate modulation techniques described in reference 13 must be used.

(2) Unlike the fringe and two-spot systems, the Fabry-Pérot signal is due to all particles passing through the probe volume. The effective size is thus given by the particle size distribution weighted by the scattering cross section. The size can be very small for a large volume of small particles.

R.Elder, UK

What is the measurement volume size and can it be readily reduced?

Author's Reply

The probe volume diameter is 100 μm and the length is 2.2 mm. The length is given by the distance between the e^{-2} detected light power points as the probe volume is scanned through a surface normal to the optical axis (figure 9). The probe volume size could be reduced by any of the following: either a smaller probe volume diameter (and corresponding field stop), or a larger lens aperture (i.e. a faster lens), or a larger central aperture stop.

AD-P005 535

VELOCITY AND TEMPERATURE MEASUREMENTS IN

A CAN-TYPE GAS-TURBINE COMBUSTOR

by

A F BICEN, M V HEITOR* & J H WHITELAW
Imperial College of Science & Technology
Department of Mechanical Engineering
Fluids Section, London SW7 2BX

* Instituto Superior Technico,
Mechanical Engineering Department,
Lisbon, Portugal

SUMMARY

Velocity and temperature measurements have been obtained in a can-type combustor operating at near atmospheric pressure. Velocity characteristics were determined with a laser Doppler velocimeter and a digitally compensated fine bare-wire thermocouple was used to measure the mean and rms values of temperature fluctuations. This paper emphasises the experimental methods, identifies the main sources of imprecision, evaluates the estimate of the related errors and presents sample results so as to demonstrate the effect of air-fuel ratio on the velocity and temperature characteristics of the combustor.

The imprecision in velocity measurements was mainly associated with statistical errors and velocity gradient broadening effects due to the finite size of the measurement volume. The maximum statistical errors were of the order of 2 and 3% for the mean and rms values and the broadening effects can lead to overestimation by up to 25% in the rms values of the swirl velocity component near the swirl centre.

The error in the mean temperature was mainly due to radiation losses which monotonically increased with temperature and were less than 8%. The catalytic effects were small and limited to regions close to the fuel injector, causing a maximum increase in the mean temperature by no more than 70 K. The uncertainties in the time constant resulted in a maximum error in the rms values of the order of 7%.

The effect of AFR on the velocity and temperature characteristics was relatively weak in the primary zone of the combustor. The effect became progressively more pronounced at downstream locations with increased temperatures, thus reduced densities, associated with lower air-fuel ratios resulting in higher mean and rms velocities.

1. INTRODUCTION

The experimental investigations of references 1 to 4 focussed attention on flows in idealised axisymmetric combustors and provided important information. Isolation of a certain part of the combustor field does not, however, allow representation of the links between the fuel, primary jet, dilution jet and exit flows of a real combustor and there is growing evidence, for example reference 5, that slight changes in combustor geometry can alter combustor performance. Although the calculation method of reference 6 provides the foundation for interpolating and extrapolating the experimentally acquired information, they embody approximations which have to be tested against measurements. References 7, 8 and 9 provided experimental information in a can-type combustor configuration of immediate practical relevance and, by so doing, increased understanding of the salient processes and at the same time assisted the development of calculations methods for predicting the flow in complex combustor geometries. Reference 7 reports on the temperature and composition measurements in the present can-type combustor and references 8 and 9 provide more detailed information on the velocity, temperature and species characteristics of the combustor for a w.de range of air-fuel ratios with and without preheat. The water model of reference 10 allows detailed information, through increased optical access, on the isothermal velocity field of the present combustor.

The main purpose of this work is to describe in more detail the experimental methods previously used to measure the velocity and temperature characteristics, to identify the main sources of imprecision associated with the techniques, to evaluate the estimates of the related errors and finally to present some sample results so as to demonstrate the effect of air-fuel ratio on the velocity and temperature field of the combustor.

The following section provides a brief description of the combustor geometry and gives a detailed account on the experimental methods and their accuracy. The third section presents and discusses the results and Section 4 summarises the main conclusions of the work.

2. EXPERIMENTAL SYSTEM

2.1 Flow Configuration

The combustor used in the present study is shown in Figure 1 and is a model of the low-emission can-type combustors described in reference 5. It is identical to that of references 7, 8 and 9, is fabricated from a laminated porous sheet metal, known as "Transply", and consists of a hemispherical head followed by a circular barrel of 74 mm diameter which contains the rows of 6 primary and 12 secondary dilution holes. The barrel is terminated by a circular-to-rectangular nozzle as shown in Figure 1. The combustor is housed in a plenum to provide as near as possible a uniform flow through the dilution holes. The swirler, which is fitted to the head, comprises 18 curved vanes oriented at 45 degrees and the resulting swirl number, according to the definition of reference 11, is 0.73. The fuelling device used for the injection of gaseous propane is mounted in the hub of the swirler and contains ten 1.7 mm diameter holes located in a 4.5 mm radius and with their axes at 45 degrees to the axis of the combustor.

The combustor was operated at near atmospheric pressure and with an inlet air temperature of 312 K. The inlet air flow rate used was 0.085 kg/s which resulted in a Reynolds number of around 8 10^4, based on the combustor diameter. Various air-fuel ratios (AFR) were used, covering a range from 40 to 70 which, typically, encompasses full-power to ground-idle conditions in real combustion chambers. The fuel used was high grade gaseous propane.

2.2 Velocity Measurements

Velocity measurements were obtained by a dual-beam laser Doppler velocimeter operated in forward-scatter mode as schematically shown in Figure 2. The transmitting optics comprised an Argon-Ion laser operated at a wavelength of 514.5 nm and at a power ranging from 50 mW to 1 W depending on flow conditions and location, a beam splitter, a Bragg cell unit which provided an optical frequency shift of 40 MHz, a beam displacer, a mirror and a focussing lens of 500 mm local length. The collecting optics consisted of a lens which focussed the forward-scattered light on the pinhole of a photomultiplier. The main optical characteristics of the laser Doppler velocimeter are summarised in Table 1.

Table 1   Main Optical Characteristics of Laser Doppler Velocimeter

Half angle of beam intersection	3.85 degrees
Fringe spacing	3.83 µm
Length of measuring volume at $1/e^2$ intensity	3.67 mm
Diameter of measuring volume at $1/e^2$ intensity	0.25 mm
Number of fringes in measuring volume at $1/e^2$ intensity	65

Optical access was provided by quartz windows on each side of the plenum chamber and through the primary and dilution holes as depicted in Figure 2. The comparatively large dimensions of the measuring volume are a consequence of the need for a small intersection angle to allow the beams to pass through the primary and dilution holes of the combustor.

The flow was seeded with fine alumina particles with a nominal diameter less than 1.0 µm, dispersed in a purpose built spark discharge particle generator , reference 12. When the optical shift was employed, the Doppler signals from the photomultiplier were downmixed with a signal from an electronic frequency shifter and resulted in an effectively lower frequency shift, variable in the range from 1 to 9 MHz to resolve the directional ambiguity of the velocity vector. The output from the frequency shifter was band-pass filtered and amplified prior to its input to a frequency counter. At the combustor exit Doppler frequencies encountered were sometimes higher than the maximum cut-off frequency of the frequency shifter (about 30 MHz). When this has occurred, both the Bragg cell and the shifter were circumvented, and the output of the photo-multiplier was directly input to the counter via the filter. The counter was inter-faced with a microcomputer which performed the statistical calculations to plot velocity pdf's and obtain mean and rms values of velocity samples of typically 3000. The sampling rate was software controlled with a maximum value of around 20 KHz. For the measurements presented here, however, a lower value of 0.1 KHz was used to mini-mize the bias effects.

Errors incurred in the measurements of velocity arise mainly from two sources associated with: 1) finite sample statistics and 2) velocity gradient broadening effects due to the finite measuring volume size. The effect of the refractive index gradients associated with combustion is negligible over the small diameter of the present combustor (cf. reference 13) and seeding bias effects, reference 14, were minimized by using similar seeding particle densities in the fuel and air lines as suggested in reference 15. Velocity bias effects, see for example reference 16, were

also minimized by employing the relatively slow sampling rate of 0.1 KHz (cf. reference 17); in general, the turbulence intensities were lower than 15% in most regions and the sampling interval was longer than both the expected turbulence time scale and the particle arrival time.

The statistical error in the mean velocity value associated with a finite sample size (N) is dependent on the local turbulence intensity and can be estimated, within a certain confidence limit, according to reference 18, by:

$$(error)_{\bar{U}} = \frac{Z_c}{\sqrt{N}} \frac{\sqrt{\bar{u}^2}}{\bar{U}} \tag{1}$$

where Z_c is equal to 2.0 for a 95% confidence limit.

For example, the minimum sample size of 2000 used during the measurements results in a statistical error in the mean value of less than 2% in the regions where turbulence intensity is 30%.

The corresponding error in the rms value is independent of the local turbulence intensity and can be estimated from:

$$(error)_{\sqrt{\bar{u}^2}} = \frac{Z_c}{\sqrt{2N}} \tag{2}$$

which indicates, with the 95% confidence limit, an error of about 3% for the minimum sample size used in the measurements.

The error associated with velocity gradient broadening effects is of main concern in the measurements of the rms value. The measured rms value contains contributions from both the turbulence and the spatial variation of the mean velocity across the finite length (L) of the measuring volume. The contribution associated with the mean velocity gradient is given, from reference 13, by:

$$\sqrt{\bar{u}^2}_g = \frac{L}{4} \frac{d\bar{U}}{dr} \tag{3}$$

and the associated error can be deduced from:

$$(error)_{\sqrt{\bar{u}^2}} = (1 + \frac{\bar{u}^2_g}{\bar{u}^2})^{1/2} - 1 \tag{4}$$

According to equation 4, non-turbulent broadening effects can lead to over-estimation by up to 25% in the rms values of the swirl velocity component in regions close to the swirl centre. In most parts of the combustor, however, the maximum error in the rms value is less than 8%.

With the assumption of insignificant seeding and velocity bias effects, it is expected, reference 14, that the measured velocity averages should be close to density weighted averages. In reference 19, for example, the temperature measurements obtained in a premixed flame and conditioned with velocity measured by a laser Doppler velocimeter are closer to density weighted averages and thus suggest that velocity averages should also be closer to density weighted.

2.3 Temperature Measurements

Temperature measurements were obtained with an uncoated thermocouple fabricated from 40 μm diameter platinum, 13% rhodium-platinum wire and digitally compensated. The thermocouple wire was supported on 500 μm diameter wires of the same material cemented in alumina (2.5 mm O.D. tube) which in turn was placed in a stainless steel tube of 4 mm O.D.. The output of the thermocouple was differentially amplified by a low noise, low drift amplifier and digitised. The samples were stored in the memory of a microprocessor at a rate varying between 5 and 13 KHz. The important features of the electronic circuit are shown in Figure 3.

Details of the compensation arrangement have been described in reference 19 for premixed flames with the following differences. In this case with a non-premixed type flame, the variation of the time constant (τ) was considered to be dependent only on the fluctuating temperature and the variations with velocity and mixture fraction were not considered. A preliminary investigation in non-premixed propane bunsen-flames indicated that the variation of the time constant with the mixture fraction was unimportant and together with the relatively high velocities observed in the regions downstream of the primary zone justified the above simplification in most parts of the combustor. A linear variation of the time constant between 6 and 2 msec was adequate for temperatures from 300 to 2000 K respectively.

The accuracy of the compensation procedure can be determined with reference to Figure 4 which shows the frequency analysis of the thermocouple response. Figure 4(a)

shows that frequencies up to 2 KHz in the measured signal are still distinguishable from the noise level of the system and Figure 4(b) shows the compensated spectrum associated with that of the measured signal of Figure 4(a). The shape of the cumulative energy distribution for $\tau = \tau(T)$, Figure 4(c), indicates that the frequency spectrum up to about 1.8 KHz contains 95% of the total energy, which is within the frequency response of the system. The uncertainty in the time constant reflects primarily in an error in the rms of the temperature fluctuations and this can be estimated by calculating the consequences of a systematic error of 10% in the instantaneous value of the time constant on the cumulative energy. In addition to the curve obtained with the normal compensation procedure (that is $\tau = \tau(T)$), the cumulative energies associated with a fixed mean time constant of 4 msec and for variations of ±10% of this value (i.e. $\tau = 3.6$ and 4.4 msec) are also shown in Figure 4(c) and indicate a 15% variation in total energy which corresponds to a maximum error of around 7% to be associated with the rms of the temperature fluctuations. In common with reference 2 any tolerance in τ was found to be unimportant as far as the mean temperature is concerned. Preliminary measurements obtained with 15, 40 and 80 μm wires indicated almost identical mean temperature values therefore suggesting that the averages are unweighted and support the analyses reported in references 20 and 21.

The results presented in the following section are not corrected for radiation losses or catalytic activity on the thermocouple surface, but the effects on the mean temperature were quantified. The magnitude of the heat losses from the thermocouple wire by radiation was determined by vacuum calibration in a vacuum chamber of about 10^{-4} torr (see reference 22 for further details). A ceramic coating was used to evaluate the catalytic effects, and the absolute errors could be estimated by comparing the radiation losses of uncoated and coated thermocouple wires.

Figure 5(a) shows the radiation losses associated with the coated and uncoated 40 μm wire and also includes those associated with a larger diameter wire of 80 μm for comparison purposes. The figure shows a monotonic increase of the losses with temperature and that the values with the uncoated wires are all less than 8% for the measured temperatures. The radiation losses in Figure 5(a) are calculated on the assumptions that the radiation heat transfer between the wire and the gases of the flame is negligible and that the average radiation temperature $(\overline{T+t})^4$ is equal to $\overline{T}^4$. The first assumption is not likely to lead to significant errors in the present flame and the effect of the second assumption depends on the magnitude of the temperature fluctuations. The present results, however, indicate that the maximum intensity of temperature fluctuations observed (around 13%) are likely to affect the radiation losses indicated in Figure 5(a) by no more than 10%.

Figure 5(b) shows the radial profiles of mean temperature obtained at two axial locations within the combustor with coated and uncoated wires of 40 and 80 μm diameter. In general, the discrepancies between measurements obtained with coated and uncoated wires are accounted for by the differences in the radiative emissivites of the two surfaces, except for z < 90 mm where catalytic effects may increase the measured mean temperature by up to 70 K. This is due to the comparatively high concentrations of unburned fuel that exist near the fuel injector, reference 8. The effects on the rms of the temperature fluctuations are of secondary importance.

3. RESULTS AND DISCUSSION

The axial and swirl components of velocity were measured with various AFR's from 40 to 70 and the corresponding mean and rms values ($\overline{U}$, $\overline{W}$ and $\sqrt{\overline{u^2}}$, $\sqrt{\overline{w^2}}$) are presented in radial profile forms for an axial location inside the combustor, corresponding to the plane of the primary holes. Similar profiles are also presented at the combustor exit plane but here care must be taken in interpreting the results due to the change from cylindrical polar velocity components inside the combustor to Cartesian components at the exit plane. The contours of the rms temperature ($\sqrt{\overline{t^2}}$) are plotted for the same plane as intensity contours ($\sqrt{\overline{t^2}}/\overline{T}$) to allow an easier comparison between one AFR case and another.

3.1 Velocity Characteristics

Figures 6 and 7 show the influence of AFR on the mean flow field prevailing in the primary and exit zone of the combustor, respectively. Figure 8 shows the corresponding effect on the turbulence field of the combustor. In these figures, profiles associated with the isothermal flow are also included for comparison purposes and since they represent the flow in one of the limiting cases.

The axial velocity profiles of Figure 6 indicate that the primary zone recirculation has increased in strength and decreased in width compared to that with isothermal flow. The combustion also results in more uniform velocity profiles at the exit, Figure 7. The axial velocity profiles with different AFR's and in the primary zone, Figure 6(a), are of similar shape and the maximum positive velocity observed close to the wall is essentially independent of AFR. The velocities near the centreline, however, are influenced. For example, the centreline value increases as the AFR is increased from a value of around -7 m/s at AFR of 40 to about +8 m/s at AFR of 70. The trend here is practically identical to that observed with increasing fuel injector flow in the isothermal case and reported in reference 9. The primary zone

flow thus appears to be only weakly dependent on mixture strength. This feature is also evident in the temperature measurements presented in the following subsection. In contrast, the velocities at the exit plane, Figure 7, are strongly affected by AFR. The higher temperatures and thus lower densities associated with the lower value of AFR result in higher velocities.

The profiles of turbulent kinetic energy (k) shown in Figure 8 are calculated on the basis of local isotropy (i.e. $k = (3/4)(\bar{u}^2 + \bar{w}^2)$) and the higher centreline peaks observed particularly in the primary zone, Figure 8(a), suggest a possibility of precession of the swirl core, so that they may not be representative of turbulence. In parallel to the trends observed in the mean flow, the effect of AFR on turbulence is relatively weak in the primary zone, but a decrease in AFR from 70 to 40 causes a significant increase in turbulent kinetic energy (around 2.5 times) at the combustor exit. Local turbulence intensity values at the exit, however, remain independent of AFR with maximum values around 13%.

3.2 Temperature Characteristics

The effect of AFR on the combustor mean temperature field is shown in Figure 9 corresponding to the mid-vertical plane of the combustor. Both AFR's (52 and 70) result in temperatures in excess of 1900 K in the primary zone. Measurements could not be obtained near the axis and upstream of the primary holes and this suggests temperatures above 2050 K and close to the adiabatic values. An increase in AFR to 70, Figure 9(b), reduces, as expected, the temperature particularly in regions down-stream of the primary holes. The maximum exit value is less than 1300 K in contrast to that of above 1600 K with AFR of 52. In the primary zone, however, the temperatures are very similar for the two AFR cases and confirm the observed trends in the primary zone velocity field (see Figure 6); similar observations were also made for the species concentrations of the primary zone, reference 8.

The corresponding contours of the intensity of temperature fluctuations are shown in Figure 10. Although the rms values of temperature fluctuations are similar for the two AFR's and are below 160 K, the lower mean temperatures associated with the higher AFR result in higher intensities inside the combustor. The intensities near the exit, in common with the velocity fluctuations, range to around 13%, tend to decrease with temperature and have maximum values in the regions of maximum mean temperature gradient. With the increase in AFR the highest values remain at around 13%, but the relatively stronger influence of the secondary dilution jets with AFR of 70 causes the peak values to move towards the centre of the exit plane.

4. CONCLUSIONS

The following are the main conclusions of this work:

1. The velocity characteristics of the combustor were determined with a laser Doppler velocimeter. The errors incurred in the measurements were mainly due to finite sample statistics and velocity gradient broadening effects, with overall maximum uncertainties in the mean and rms values of around 2 and 10% respectively in most parts of the combustor.

2. The mean and rms values of temperature fluctuations were measured by a digitally compensated fine bare-wire thermocouple. The errors in the mean values were mainly due to radiation losses which have monotonically increased with temperature and were less than 8%. The catalytic effects were small and occurred in the primary zone, increasing the mean temperature by up to 70 K. The maximum uncertainties in the rms values were of the order of 7% and were due to uncertainties in the time constant.

3. The effect of AFR on velocity and temprature characteristics was relatively weak in the primary zone of the combustor, but became progressively more pronounced at downstream locations. Independent of AFR, the maximum intensities of velocity and temperature fluctuations were around 13% at the combustor exit.

REFERENCES

1.   Owen F K "Measurements of Instantaneous Velocity and Concentration in Complex Mixing Flows", AIAA Progress in Astronautics and Aeronautics, v.53, p.293, 1978

2.   LaRue J C, Samuelsen G S & Seiler E T "Momentum and Heat Flux in a Swirl-Stabilised Combustor", Proc. 20th Int. Symp. on Combustion, The Combustion Institute, 1984

3.   Altgeld H, Jones W P & Wilhelmi J "Velocity Measurements in a Confined Swirl Driven Recirculating Flow", Exp. in Fluids, v.1, p.73, 1983

4.   Gouldin F C, Depsky J S & Lee S L "Velocity Field Characteristics of a Swirling Flow Combustor", AIAA, v.23, p.95, 1985

5.   Bhangu J K, Snape D M & Eardley B R "The Design and Development of a Low Emissions Transply Combustor for the Civil Spey Engine", AGARD-CP353, Paper No.23, 1983

6.   Jones W P & Whitelaw J H "Calculation Methods for Reacting Turbulent Flows: A Review", Comb. and Flame, v.48, p.1, 1982

7.   Jones W P & Toral H "Temperature and Composition Measurements in a Research Gas Turbine Combustion Chamber", Comb. Sci. and Tech., v.31, p.249, 1983

8.   Heitor M V & Whitelaw J H "Velocity, Temperature and Species Characteristics of the Flow in a Gas-Turbine Combustor", Comb. and Flame, to appear, 1986

9.   Bicen A F & Jones W P "Velocity Characteristics of Isothermal and Combusting Flows in a Model Combustor", Comb. Sci. and Tech., to appear, 1986

10.   Koutmos P & McGuirk J J "Investigation of Inlet Swirl-Level Variations on Primary Zone Flow Patterns in a Water Model Can-Type Combustor", Imperial College, Mech. Eng. Dept. Report No.FS/84/28, 1984

11.   Beer J M & Chigier N A "Combustion Aerodynamics", Appl. Science Publ., London, 1972

12.   Altgeld H, Schnettler A & Stehmeir D "Spark Discharge Particle Generator for Laser Doppler Anemometry", J. Phys. E.: Sci. Instrum., v.13, p.437, 1980

13.   Durst F, Melling A & Whitelaw J H "Principles and Practice of Laser-Doppler Anemometry", 2nd Edition, Academic Press, New York, 1981

14.   Glass M & Bilger R W "The Turbulent Jet Diffusion Flame in a Co-Flowing Stream - Some Velocity Measurements", Comb. Sci. and Tech., v.18, p.165, 1978

15.   Dibble R W, Hartman V, Schefer R W & Kollmann W "Conditional Sampling of Velocity and Scalars in Turbulent Flames Using Simultaneous LDV-Raman Scattering", Proc. ASME 105th Winter Annual Meeting, New Orleans, Louisianna, Dec. 9-13, 1984

16.   McLaughlin D K & Tiederman W G "Biasing Correction for Individual Realisation of Laser Anemometer Measurements in Turbulent Flows", Physics of Fluids, v.16, p.2082, 1973

17.   Durao D F G, Laker J & Whitelaw J H "Bias Effects in Laser Doppler Anemometry", J. Phys. E.: Sci. Instrum., v.13, p.442, 1980

18.   Yanta W J & Smith R A "Measurements of Turbulent-Transport Properties with a Laser Doppler Velocimeter", AIAA Paper 73-169, 11th Aerospace Science Meeting, Washington, 1978

19.   Heitor M V, Taylor A M K P & Whitelaw J H "Simultaneous Velocity and Temperature Measurements in a Disk-Stabilised Premixed Flame", Exp. in Fluids, v.3, p.323, 1985

20.   Toral H & Whitelaw J H "Velocity and Scalar Characteristics of the Isothermal and Combusting Flows in a Combustor Sector Rig", Comb. and Flame, v.45, p.251, 1982

21.   Attya A M & Whitelaw J H "Velocity, Temperature and Species Concentration in Unconfined Kerosene Spray Flames", ASME Paper 81-WA/HT-6, 1981

22.   Heitor M V "Experiments in Turbulent Reacting Flows", Ph.D. Thesis, University of London, 1985
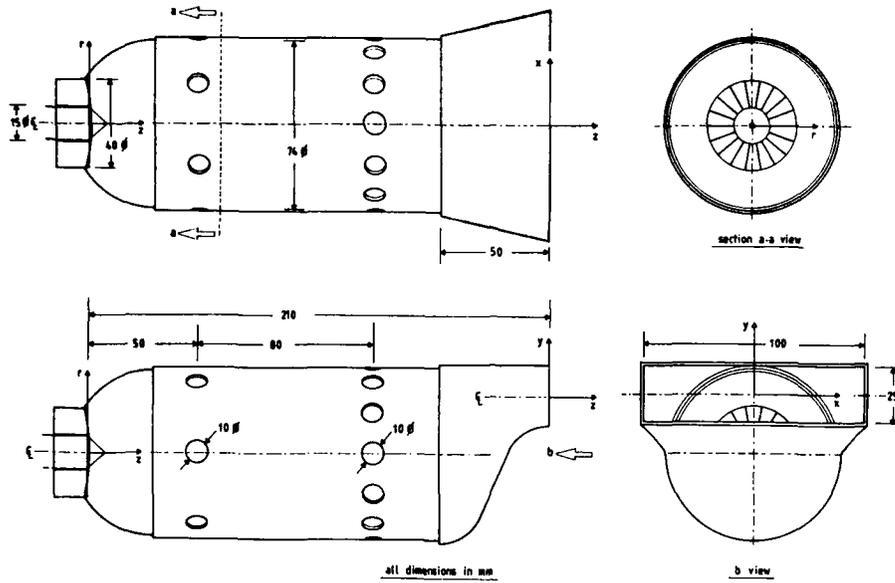
Figure 1 Model can-type combustor
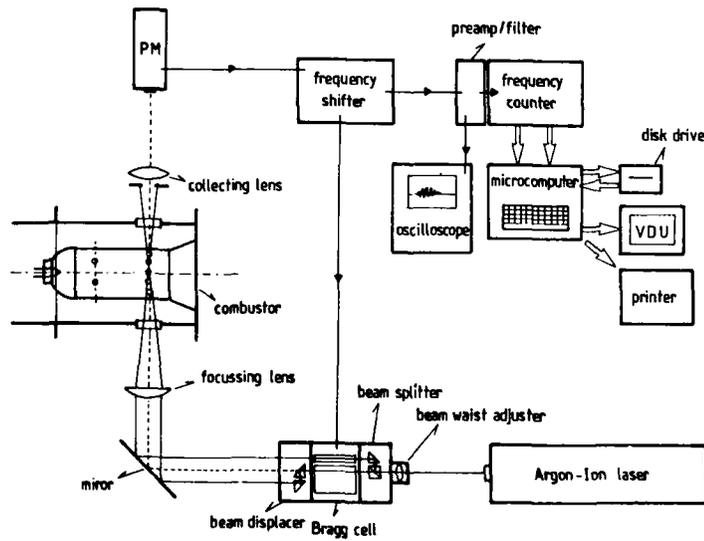
Figure 2 Schematic diagram of laser Doppler anemometer
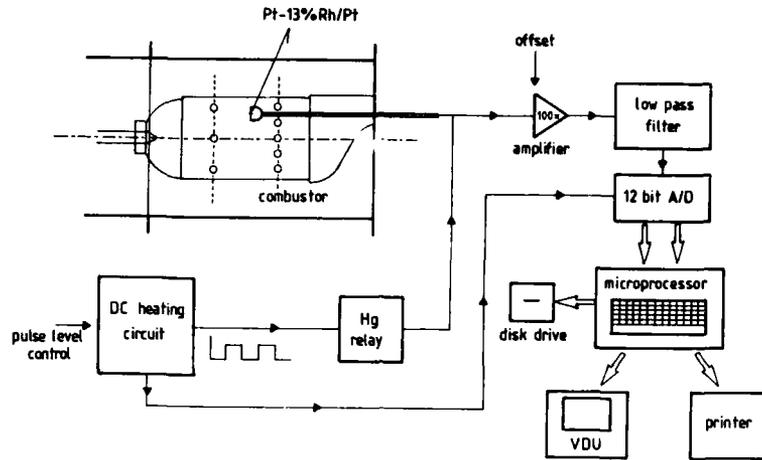
Figure 3   Schematic diagram of thermocouple system
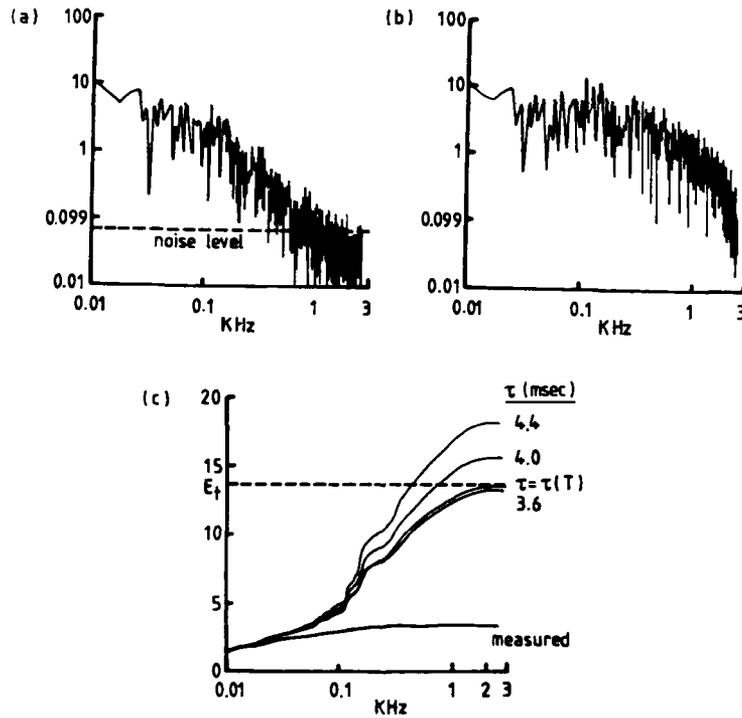
Figure 4   Frequency analysis of thermocouple response; AFR=52,
exit plane, z=20mm, y=2.5mm

(a) Power spectrum of measured signal
(b) Power spectrum of compensated signal: $\tau = \tau(T)$
(c) Cumulative energy of measured & compensated spectra

(a)

(b)

Figure 5 (a) Radiation losses from uncoated and coated
wires of 40 and 80 μm diameter; AFR = 52

(b) Radial profiles of mean temperature obtained
with uncoated and coated wires of 40 and
80 μm diameter; AFR = 52

(a)

(b)

Figure 6 Effect of AFR on primary zone
flow pattern

(a) Axial component of mean
velocity

(b) Swirl component of mean
velocity
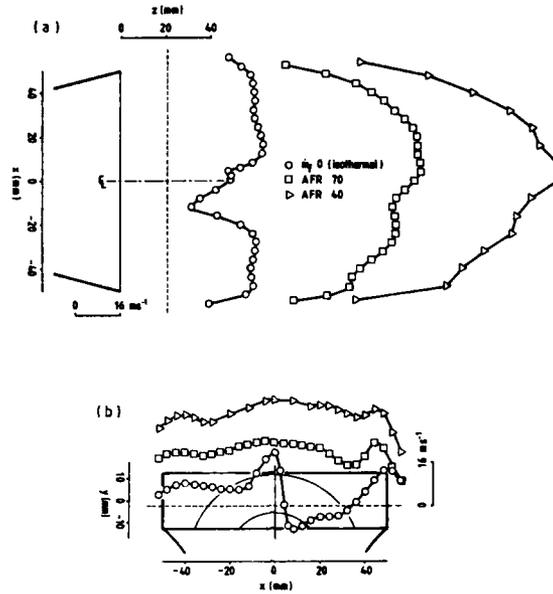
Figure 7 Effect of AFR on exit flow pattern

(a) Axial component of mean velocity
(b) Normal component of mean velocity
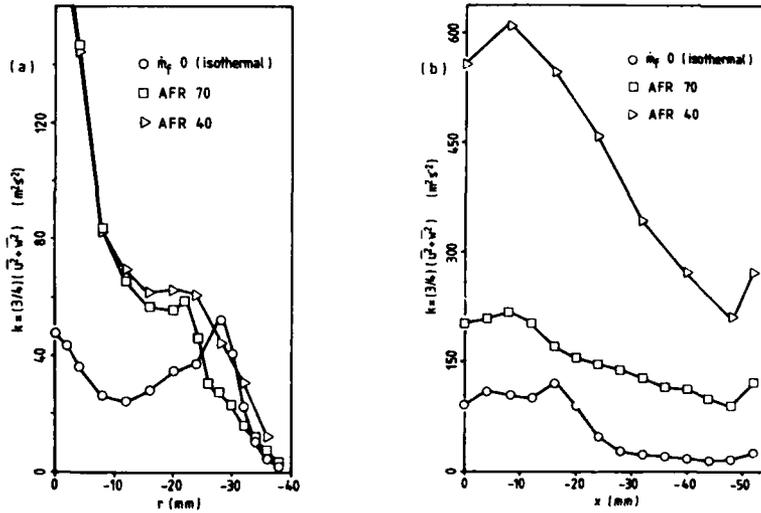
Figure 8 Effect of AFR on combustor turbulence

(a) Primary zone turbulent kinetic energy
(b) Exit turbulent kinetic energy
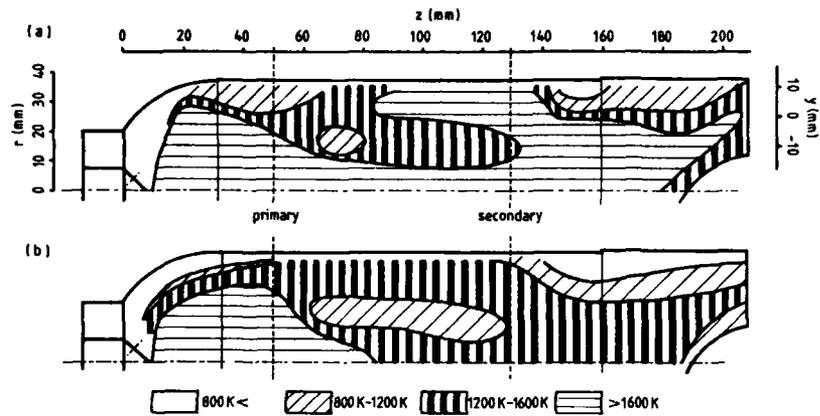
Figure 9   Effect of AFR on combustor mean temperature field

(a)   With AFR of 52
(b)   With AFR of 70
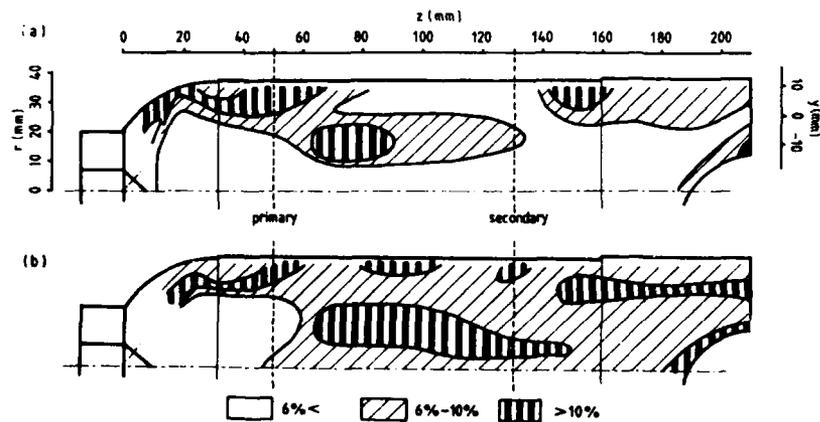
Figure 10   Effect of AFR on intensity of temperature fluctuations
inside combustor

(a)   With AFR of 52
(b)   With AFR of 70

DISCUSSION

A.Melling, UK

In figure 9 showing the effect of air-fuel ratio on the mean temperature, an increase in AFR from 52 to 70 led to a particularly marked temperature reduction in the secondary zone. Was the AFR increased by increasing the secondary dilution air while keeping the primary air flow rate constant?

Author's Reply

No, the AFR was increased by decreasing the fuel flow rate while keeping the total air flow rate constant. The temperature reduction in the secondary zone is thus associated with the local increases in AFR and stronger quenching effects of the dilution jets, particularly on the CO to CO_2 reaction.

W.O'Brien, US

Please give more data on the method of production and introduction of the alumina particle seed in the burner. Were the particles sizes measured, and if so, how?

Author's Reply

We generated alumina particle from a spark generator; a monodisperse aerosol was obtained with reduced agglomeration. The particles are introduced upstream of the combustor in both air and fuel streams. We thought it was necessary to seed the fuel as well, particularly for the measurements in the primary zone, in order to reduce the particles biasing effect.

We did not do any detailed analysis with regard to the size of the particles, but we have looked at some of the particles on the microscope, and they are about 1 μm (± 10%).

W.A.Alwang, US

Did you measure the time scale or frequency content of the temperature or velocity fluctuations?

Author's Reply

The normal data acquisition rate was about 3 to 4 KHz; we deliberately lower the sampling rate down to 0.5 to 1 KHz, in order to reduce the biasing effects.

We did not look at the time scales, both for velocity and temperature fluctuations.

We did some spectrum analysis of the temperature fluctuations, but not of the velocity ones.

J.A.Nabity, US

Could you describe briefly the method used to compensate the fine wire thermocouple?

What is the maximum frequency response of the thermocouple?

Author's Reply

Compensation was performed only on the basis of measured instantaneous temperature and the effects of mixture fraction and velocity fluctuations were not considered. Preliminary measurements with non-premixed flames indicated insignificant effects of mixture fraction on time constant and relatively high velocities, particularly at the secondary and exit zones of the combustor, did not justify the consideration of velocity effects. The frequency response of the system was around 2 KHz and frequencies up to 1.8 KHz represented 95% of the total energy.

THE FLOW AROUND A SQUARED OBSTACLE

by

D.F.G. Durão, M.V. Heitor and J.C.F. Pereira
Department of Mechanical Engineering
Instituto Superior Técnico
1096 Lisboa Codex
Portugal

ABSTRACT

Laser-Doppler measurements of the velocity distribution around and in the wake of a two-dimensional squared obstacle for Re=14000 are reported. The results were measured with a counter interfaced with a microprocessor. The counter was built based on a specific design to quantify and diminish errors resulting from bias sources. In addition the periodic character of the flow in the wake was characterised by measurements of turbulence spectra with FFT instrumentation. The values of the predominant frequencies were correlated with the flow Reynolds number.

1. INTRODUCTION

Laser-Doppler velocimetry with its non-perturbing nature is very often the only instrumental method available for research of the local velocity characteristics in flows with recirculating zones. Althought it has been used for many years, questions still remain regarding the accuracy of LDV measurements. These questions are mainly associated with the precision of the individual measurements and with the choice and number of the population elements from which the statistical results are calculated. The non uniformity of the density of particles in the flow, the presence of velocity gradients in the control volume or the different sizes of particles are examples of bias sources. Several bias corrections have been proposed and at the same time new instruments were designed (e.g. counters) to improve the accuracy of the measurements, see e.g. Durão et al (1982), Durst et al (1984) and Heitor et al (1984).

In this paper measurements of velocity and power spectra are reported using two counters that were built based on a specific design to avoid errors usually associated with counting systems.

The concentration of the naturally-occuring scattering centers in water, which give rise to Doppler signals, is such that the probability of finding more than one particle in the measuring volume of the anemometer is negligiby small: hence the occurrence of Doppler signals is a discrete, rather than continuous process. This fact limits the spectral analysis of the velocity characteristics, once fast Fourier transform methods cannot be directly used. Several methods have been proposed for spectral estimation of LDV information (see, for example, Srikantaiah and Coleman, 1985; Loding, 1985; Saxena 1985) and the procedure adopted here has consisted in frequency analysing the analogue output of a purpose-built counter described by Durão et al (1982) in which the LDV velocity signal at each Doppler burst is sampled and held until another valid signal arrives.

The LDV equipment was used to study the flow around a squared obstacle. Flow around two-dimensional bluff bodies, particularilly circular cylinders and two-dimensional sharp-edged bodies, had received particular interest for decades, as the article reviews of e.g. Mair (1971), Bearman and Graham (1980), and Griffin (1985). The quasi-periodic nature of the fluctuations existing on the wake region, which occur as the result of the alternate shedding of vortices from each side of the body, is a Reynolds number and geometrical dependent phenomena. The flow conditions in which they occur are presented in many engineering situations, for example bluff-body stabilized flames in high-velocity reactant streams, vehicle aerodynamics, industrial pipe flows and wind effects on buildings. Their study is relevant for many design purposes, since their understanding is still an open subject of research.

The purpose of the present study it is the use of LDV to obtain accurate measurements, in order to bring new physical understanding of the flow.

Next section presents the flow configuration and the following section describes the measurement technique including the characteristics of the counter used and the accuracy to be expected; section 4 discusses the experimental results and the paper ends with a summary of the conclusions.

2. FLOW CONFIGURATION

The experiments were performed on an horizontal, 120x152 mm, water tunnel made of perspex with a 20x20 mm or 8x8 mm obstacle, H, set accross the narrow dimension, W, and completely spanning the duct as schematically shown in figure 1. The duct extended for 1.56 m upstream and for 0.44 m downstream of the obstacle. The water flow was driven by the pressure difference between a constant head and a discharge tank and was passed through straightners upstream of the duct inlet.

Most of the results were obtained with the obstacle centered between the top and the bottom of the duct, for a reference velocity of U_o=0.68 m/s and a freestream turbulence intensity of 6%. However, the effects of the proximity of the wall and of the Reynolds number on the wake-flow are also presented. Measurements obtained in the tunnel without the obstacle have shown that the flow was symmetric and that the wall boundary layer around the region where the obstacle was located, was 15 mm thick.

The origin of the axial, X, and vertical, Y, coordinates in the duct is taken at the centre of the upstream face of the obstacle.

3. MEASUREMENT TECHNIQUE

Velocity was measured by a laser-Doppler velocimeter operated in the dual-beam, forward-scatter mode with sensitivity to the flow direction provided by light-frequency shifting from acousto-optic modulation (Bragg cells). The resulting frequency shift was normaly set at 700 KHz. The principal characteristics of the laser-Doppler velocimeter, in particular those of the transmitting optics, are summarized in Table 1.

TABLE 1

PRINCIPAL CHARACTERISTICS OF THE LASER-DOPPLER VELOCIMETER

- 15 mW (nominal) He-Ne laser; wavelength:	632.8 nm
- focal length of focussing lens	300 mm
- beam diameter, at e^{-2} intensity, of laser	1.1 mm
- measured half-angle of beam intersection (in air)	4.81^0
- calculated half-angle of beam intersection (in water)	3.61^0
- fringe separation (line pair spacing)	3.77 μm
- calculated dimensions of measuring volume, at e^{-2} intensity, (major and minor axis of ellipsoid in water)	3.489; 0.220 mm
- velocimeter transfer constant	0.2650 MHz/(ms^{-1})

The light scattered by naturally-occuring centres in the water was collected by a lens (focal length of 200 mm) and focussed onto the pinhole aperture (0.3 mm) of a photomultiplier (OEI, type LD-0-810) with a magnification of 1.55. The output of the photomultiplier was band-pass filtered and the resulting signal processed by a laboratory-built frequency counter. Two counters were used and one of them have the necessary information for the use of FFT instrumentation to obtain the turbulence spectra and energy on predominant frequencies.

3.1 Characterization of the Counters

The counters used allowed the knowledge and control of measuring parameters such as the actual and the minimum possible time intervals between two consecutive valid burst, which permit to satisfy the best experimental conditions according to the analysis referred by Durão, Velho and Whitelaw (1984) and Durão, Laker and Velho (1985). The frequency of Doppler signals is evaluated by the counter through gating a 250 MHz clock (100 MHz clock for the second counter used with the FFT instrumentation) over a preset number of 8 or 16 Doppler cycles (only 16 for the second counter), with only one measurement being performed for every Doppler "burst". Each measurement is subject to preset validations in the amplitude and time domains and, if valid, is digitised as a floating point number and transferred to the microcomputer. The amplitude-domain validation is based on two trigger levels and the counting circuity is activated only if both of them have been crossed in the correct sequence: the beginning of a Doppler burst is detected by the first correctly sequenced crossing of the higher threshold; the end of a Doppler burst is deemed to have occurred at the first absence of higher threshold crossing. The time-domain validation procedure accepts or rejects the measurement depending on wether the difference between the frequencies of the first 5 and 8 (or 10 and 16) cycles of the burst is within a pre-selected tolerance, up to 0.19%. The sampling frequency is limited to around 25 KHz due to the time taken for data validation and data transfer, but lower values were used to reduce velocity-bias effects on the data processing. Figure 2 shows the timing sequencies of the counter and further information can be found in Heitor et al (1984).

3.2 Accuracy of the Measurements

Errors incurred in the measurement of velocity by displacement and distortion of the measuring volume due to refraction on the duct walls and the change in refractive index were found to be negligibly small and within the accuracy of the measuring equipment. The tolerance on the output of the counter derives from the error in the clock count and from the resolution of the floating point format of the data: the maximum error is always less than 1%. Non-turbulent Doppler broadening errors due to gradients of mean velocity across the measuring volume (e.g., Durst et al, 1981), may affect essentially the variance of the velocity fluctuations, but for the present experimental conditions are of the order of 3×10^{-3} U_0^2 and, therefore, sufficiently small for their effect to be neglected. Other sources of errors, such as those due to finite sample size and velocity bias effects are considered in the following paragraph. It is noted that the positioning of the measuring volume inside the duct was precise to within ± 0.5 mm.

In the experiments the number of individual velocity values used to form the averages was always above 7000 and reached 60000 in the near-wake region, where the highest flow oscillations were found. As a result the largest statistical (random) errors were of 0.5 and 3%, respectively for the mean and variance values, according to the analysis referred by Yanta and Smith (1978) for a 95% confidence interval. No corrections were made for sampling bias, and the systematic errors that could have arised were minimised by using high seed rates in relation to the fundamental velocity fluctuation rate, as suggested for example by Dimotakis (1978), Erdmann and Tropea (1981) and Erdmann et al (1984) for both random and periodic flows. In addition, no correlations were found between Doppler frequencies and time interval between consecutive bursts, suggesting that such bias effects are unimportant for the present 'low conditions (see Durão, Laker and Velho, 1985). It is also noted that the zone of the flow characterized by the highest amplitude of the flow oscillations (which are essentially non-turbulent and occur for the vertical velocity component, as discussed below) is also that where the mean velocity is close to zero and the probability density distributions is near bimodal, such that the bias of the negative velocities

offset that of the positive velocities, as shown by Erdmann et al (1984).

The counter used to measure power spectra with FFT instrumentation is described in detail by Durão et al (1982) and although with slightly lower accuracy of the absolute measurements (due to the use of a slower clock of 100 MHz and measuring only over 16 Doppler cycles), it allows to obtain the power spectrum of the LDV velocity signal by sampling and holding the velocity at each new Doppler burst until another valid signal arrives. The condition under which the output of the counter yields a satisfactory spectral analysis has been discussed by, for example, Dimotakis (1978), Edwards and Jensen (1983) and Adrian and Yao (1985) and was satisfied in the present experiments. A high mean sampling frequency up to 2 KHz was used, suggesting that structures of the order of 0.35 mm and above can be resolved. This is about two orders of magnitude smaller than the smallest length scale in the duct, which implies that the energy containing motions are resolved by the counter. In addition, the power spectral density can be reconstructed up to about 1 KHz.

4. EXPERIMENTAL RESULTS AND DISCUSSION

The results presented in figures 4 to 9 were extracted from a detailed set of measurements to characterize the flow around the two-dimensional obstacle described previously. The measurements include mean and variance values of axial, U, and normal, V, components of velocity and spectral analysis of the velocity fluctuations.

Prior to the detailed measurements, visualization of air bubbles, as shown in figure 3, was used to guide the choice of measurement locations and to observe the mechanism of vortex shedding, which was confirmed to exist by the subsequent spectral analysis presented in sub-section 4.2.

4.1 Flow Pattern

The distribution of the time-averaged axial velocity component, U (paralell to the channel walls), along the centreline of the channel is shown in figure 4. The measured time-averaged length of the recirculation region behind the obstacle and the maximum negative velocity were respectively 1.825 H and 20% of the reference velocity U_0=0.68 m/s. The figure also shows that at X/H=-2 the mean flow was basically undisturbed; on the contrary at X/H=5 the value of U/U_0 was 0.75.

Figure 5 shows values of mean and variance of U and V obtained at X/H=-1.0, 1.5 and 3.0 respectively upstream the obstacle, in the recirculation zone and in the near-wake. Figure 5(a) presents the profiles of the mean axial velocity which clearly show that the flow is symmetric. The profile at X/H=-1.0 indicates a large influence of the obstacle having its maximum velocity away from the centreline; at X/H=1.5 the maximum axial velocity is 1.465 U_0 and occurs at Y/H= ± 1.325; far downstream, at X/H=3, the profile is characteristic of a developing wake region. The location of U-maximum is consistent with the V-profiles shown in figure 5(b). It can be seen that in agreement with the flow visualization of figure 3, upstream of the obstacle the flow moves away from the centreline while downstream, in the wake, the opposed movement occurs.

The distribution of the variance of the axial velocity fluctuations upstream of the obstacle has a minimum value on the centreline but the local turbulence intensities remains near constant and between 6.5 and 8.0%. Figure 5(d) shows the variances of the normal velocity fluctuations and indicates that upstream of the obstacle the turbulent flow is near isotropic. At X/H=1.5 the $\overline{u'^2}/U_0^2$ profile shows two symmetric peaks located around the separation streamline and the $\overline{v'^2}/U_0^2$ profile, shown in figure 5(d), presents a peak on the centreline, which could be respectively associated with the maximum gradients of the axial and radial mean velocity. These profiles are qualitatively similar to those reported in non-periodic turbulent wake flows, e.g., in the near-wake of the axisymmetric bluff bodies of Taylor and Whitelaw (1984), but the magnitude of the peaks is comparatively higher ($\sqrt{\overline{u'^2}}/U_0$=0.654 at Y/H= ± 0.55 and $\sqrt{\overline{v'^2}}/U_0^2$=0.647 at Y/H=0 compared with 0.35 and 0.42 respectively, for the 25% area blockage disc of Taylor and Whitelaw, 1984). On the other hand, these maximum values and the high degree of turbulence anisotropy found in the near wake are similar to those reported by Bradbury (1976) in the wake of a 10% area blockage flat plate and explained as the result of vortex shedding. The present flow is also periodic, as further analysed in the next sub-section, such that the values of figures 5(c) and (d) are result of the time averaging measuring process in which the turbulent and the periodic, non-turbulent, contributions to the total variance are not decomposed.

Downstream of the obstacle, at X/H=3.0, the $\overline{u'^2}$ and the $\overline{v'^2}$ profiles are qualitatively similar to those at X/H=1.5 but with comparatively lower values, suggesting the attenuation of the magnitude of the local periodic oscillations with the development of the wake flow.

4.2 Spectrum of Velocity Fluctuations

Spectral analysis of Doppler signals was conducted to characterize the oscillating nature of the present flow as a function of the Reynolds number, the dimension of the obstacle and of its distance to the wall of the channel.

Figure 6 shows the characteristic digital and analogue time-resolved output of the two counters used for the normal velocity fluctuations in the centreline of the wake of the squared obstacle, for Re=14000. The signal follows a fairly sinusoidal wave with a corresponding bimodal probability density function, figure 6(c), and a single spectral peak at the predominant frequency of 4.7 Hz, as shown in figure 7(a).

The dependence of the power spectrum on the Reynolds number for values less than 14000 can be identified in figures 7(a) to (f), which indicate a linear variation of the spectral peak with Re. These results refer to the normal component of velocity but a similar behaviour was observed for the axial velocity, although with lower intensity peaks in the power spectrum.

Figure 8 summarizes the variation of the Strouhal number (S=f.H/U) with the Reynolds number obtained in the water channel. The figure also shows a good agreement with measurements obtained by Okajima (1982) for different squared obstacles using hot film or hot-wire anemometry. The Strouhal number is approximately constant and close to 0.133 for all the heights (H) of the obstacles investigated in the range $10^3 \leqslant Re \leqslant 2 \times 10^4$.

Measurements of the vortex shedding frequencies obtained with the 20x20 mm obstacle located at five different distances from the wall are shown in figure 9 for $10^3 \leqslant Re \leqslant 1.7 \times 10^4$. The predominant shedding frequencies do not vary with the proximity of the wall up to Y/H=0.375, but have not been found for smaller values of Y/H. Experiments are being carried out to map in detail the time-averaged flow properties of the near-wake region of the obstacle placed at Y/H=0.25 and 0.375 in order to explain the absence of flow orcillations.

5. CONCLUSIONS

LDV measurements have provided information of the velocity characteristics of the flow around squared obstacles in the range $10^3 \leqslant Re \leqslant 1.7 \times 10^4$. The following is a summary of the more important findings and conclusion of this work.

● The velocity information was quantified using two purpose built counters in which the Doppler signals were subject to validation in the amplitude and time domains. Information of the time interval between valid bursts has also been provided and has allowed to conclude that errors in the velocity measurement due to bias effects are significantly small for their effect to be neglected, because of the high seed rates used. Spectral analysis has been sucessfully conducted by sampling and holding the velocity signal at each new Doppler burst until another valid signal arrives.

● The measurements have shown that the flow field includes regions of near-uniform, recirculating and accelerating velocity, which are qualitatively similar to those reported in non-periodic turbulent wake flows. Nevertheless the shear layer surrounding the recirculation bubble, for Re=14000, is a region of intense velocity fluctuations with unusually high values of the velocity variances, explained as the result of vortex shedding.

● The vortex shedding frequency vary linearly with the Reynolds number, with a value of 4.7 Hz at Re=14000. These frequencies are independent of the vertical position of the obstacle in the water channel up to Y/H=0.375, but the oscillation are tottaly supressed for smaller values of Y/H. The Strouhal number is approximately constant and equal to 0.133 for obstacle heights between 8 and 20 mm in the range $10^3 \leqslant Re \leqslant 2 \times 10^4$.

ACKNOWLEDGEMENT

REFERENCES

Adrian, R.J. and Yao, C.S. (1985). Power spectra of fluid velocities measured by laser Doppler velocimetry. ASME, Winter Annual Meeting, Miami Beach, Florida, November 17-22, 1985.

Bearman, P.W. and Graham, J.M.R. (1980). Vortex shedding from bluff bodies in oscillatory flow: A report on Euromech 119. J. Fluid Mech., 99, part 2, pp.225-245.

Bradbury, L.J.S. (1976). Measurements with a pulsed-wire and a hot-wire anemometer in the highly turbulent wake of a normal flat plate. J. Fluid Mech., 77, pp.473-497.

Dimotakis, F. (1978). Single scattering particle laser Doppler measurements of turbulence. AGARD CP 193, paper 10.7.

Durão, D.F.G., Laker, J.R., Taylor, A.M.K.P. and Yanneskis, M. (1982). Operation and performance of the Fluids Section FS02 Frequency Counter. Imperial College, Mech. Eng. Dept. Report.

Durão, D.F.G., Velho, A. and Whitelaw, J.H. (1984). The study of bias in turbulent flows. Proc. of 2nd Int. Symp. on Appl. of LA to Fluid Mechanics, July 2-4, Lisbon, Portugal, Paper 2.3.

Durão, D.F.G., Laker, J.R. and Velho, A. (1985). Velocity and amplitude bias and the development of laser anemometry counters. ASME Winter Annual Meeting, Miami Beach, Florida, November 17-22.

Durst, F., Ernst, F. and Founti, M. (1984). A new counter signal processor for true time-averaged fluid velocity measurements. Proc. of 2nd Int. Symp. on Appl. of LA to Fluid Mech., July 2-4, Lisbon, Portugal.

Durst, F., Melling, A. and Whitelaw, J.H. (1981). Principles and Practice of Laser-Doppler Anemometry, 2nd ed., Academic Press, New York.

Edwards, R.V. and Jensen, A.S. (1983). Particle-sampling statistics in laser anemometer: sample-and-hold and saturable systems. J. Fluid Mech., 133, pp.397-411.

Erdmann, J.C., Lehmann, B. and Tropea, C.D. (1984). The statistical bias of laser anemometry applied in sinusoidal flowfields. Proc. 2nd Int. Symp. on Appl. of LA to Fluid Mech., July 2-4, Lisbon, Portugal, Paper 2.4.

Erdmann, J.C. and Tropea, C.D. (1981). Turbulence-induced statistical bias in laser anemometry. Proc. 7th Biennal Symp. – Turbulence. Rolla. Missouri.

Griffin, O. (1985). Vortex shedding from bluff bodies in a shear flow: A review. J. of Fluids Engineering, 107, pp.258-306.

Heitor, M.V., Laker, J.R., Taylor, A.M.K.P. and Vafidis, C. (1984). Instruction Manual for the FS "model 2" Doppler-Frequency Counter. Imperial College, Mech. Eng. Dept., Report FS/84/10.

Lading, L. (1985). Spectral analysis versus counting. ASME, Winter Annual Meeting, Miami Beach, Florida, November 17-22.

Mair, W.A. (1971). Bluff bodies and vortex shedding - a report on Euromech 17. J. Fluid Mech., 45, part 2, pp.209-224.

Okajima, A. (1982). Strouhal numbers of rectangular cylinders. J. Fluid Mech., 123, pp.379-398.

Saxena, V. (1985). Power spectrum estimation from randomly sampled velocity data. ASME Winter Annual Meeting, Miami Beach, Florida, November 17-22.

Srikantaiah, D.V. and Coleman, H.W. (1985). Turbulence spectra from individual realization laser velocimetry data. Exp. in Fluids, 3, pp.35-44.

Taylor, A.M.K.P. and Whitelaw, J.H. (1984). Velocity characteristics in the turbulent near wakes of confined axisymmetric bluff bodies. J. Fluid Mech., 139, pp.391-416.

Yanta, W.J. and Smith, R.A. (1978). Measurements of turbulent-transport properties with a laser Doppler velocimeter. AIAA paper 73-169, 11th Aerospace Science Meeting, Washington.
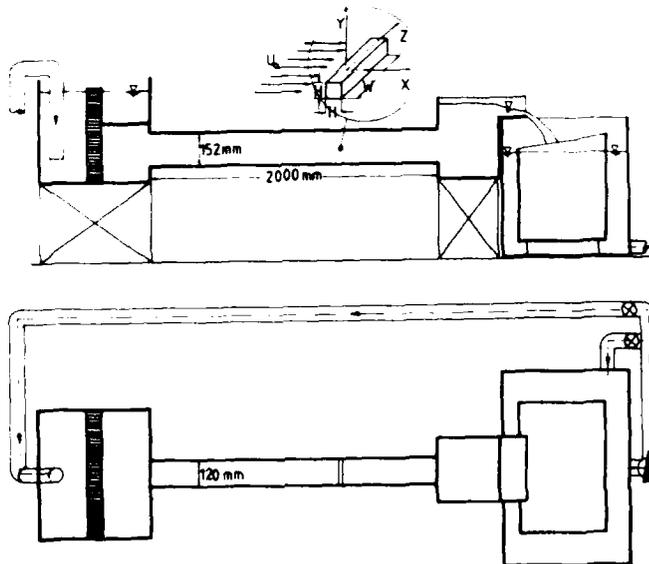
Fig. 1 - View of water tunnel and test section.
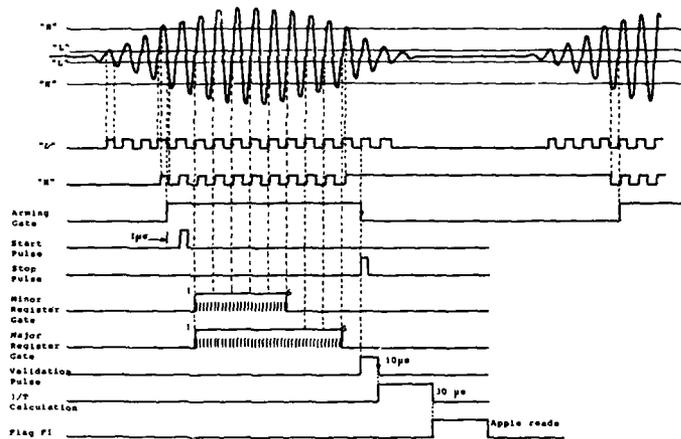
Fig. 2 - Timing diagram of the operation mode of the counter.

Fig. 3 - Flow visualization of air bubbles.
Reference velocity: $U_o = 0.68$ m/s; Re ≈ 14000
Exposure time of the photo: 67 ms
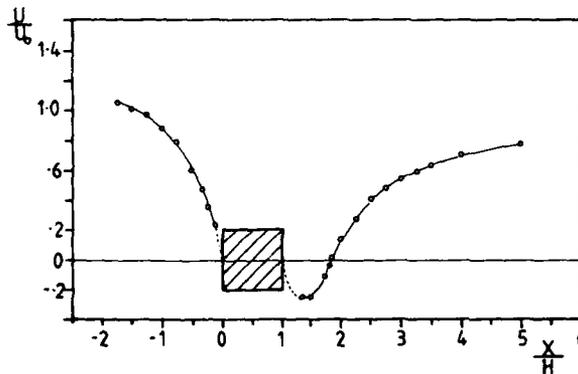
Fig. 4 - Centreline profile of the mean axial velocity component $\bar{U}/U_o$, upstream and downstream of the obstacle.
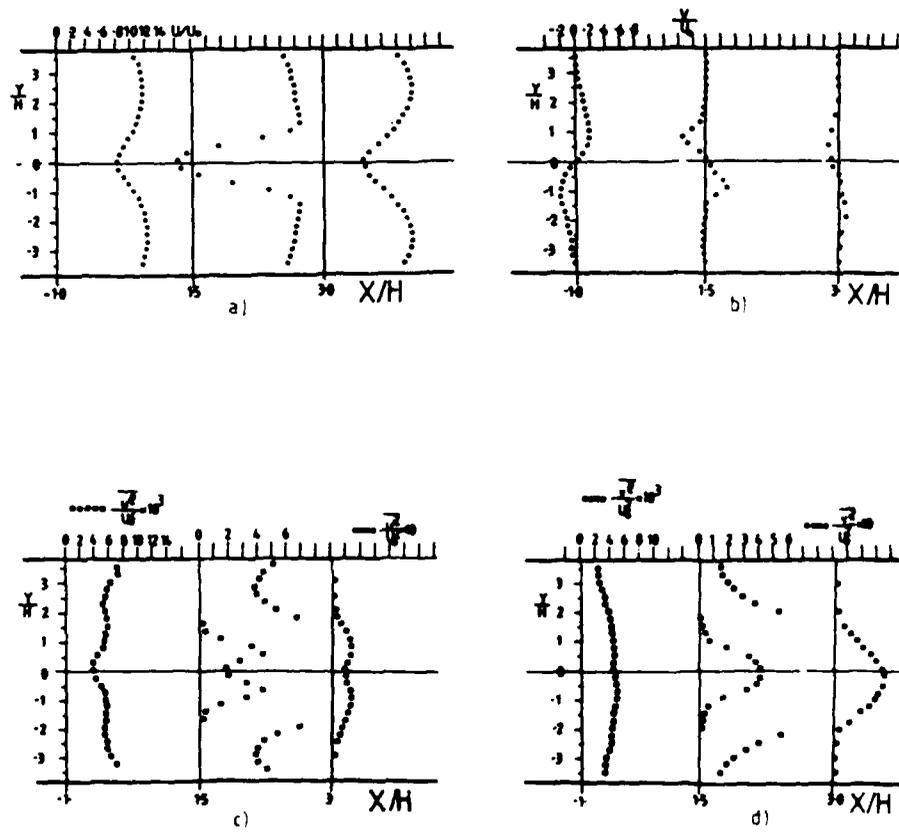
Fig. 5 - Mean and variance profiles of the axial and normal velocity components.

a) mean axial velocity, $\bar{U}/U_o$

b) mean normal velocity, $\bar{V}/U_o$

c) variance of axial velocity,

open symbols: $\overline{u'^2}/U_o^2 \times 10^3$

closed symbols: $\overline{u'^2}/U_o^2 \times 10$

d) variance of normal velocity,

open symbols: $\overline{v'^2}/U_o^2 \times 10^3$

closed symbols: $\overline{v'^2}/U_o^2 \times 10$
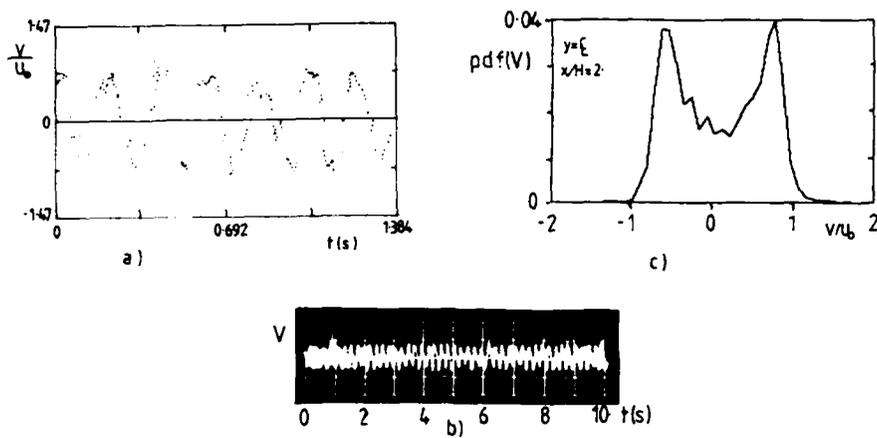
Fig. 6 - Signal traces of normal velocity fluctuations and their measured probability density function on the centreline of the near-wake flow.

$\bar{V}/U_o = 0.$; $f = 4.7$ Hz (figure 7a)

a) digital output of the counter at each Doppler burst

b) analogue output of the counter used with the FFT instrumentation

c) P.d.f. of measured normal velocity fluctuations.
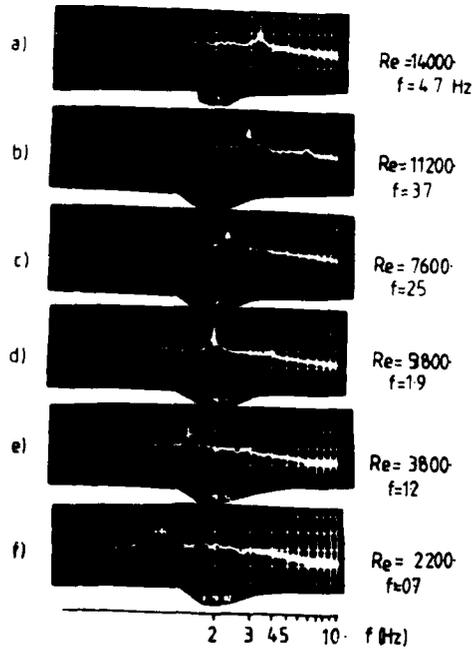
Fig. 7 - Power spectra of normal velocity fluctuations in the centreline of the wake flow for different Reynolds numbers.
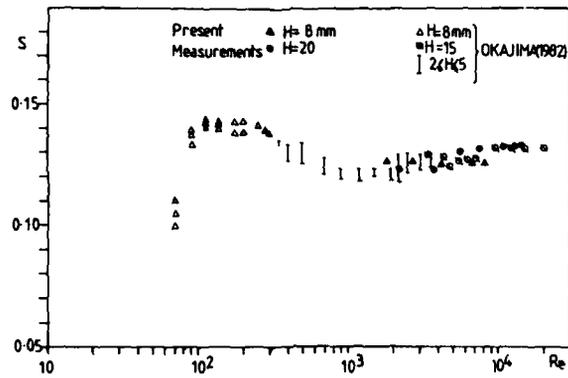
Fig. 8 - Variation of the Strouhal number, $S = fH/U_o$, with the Reynolds number $Re = U_o H/\nu$, for a squared obstacle.
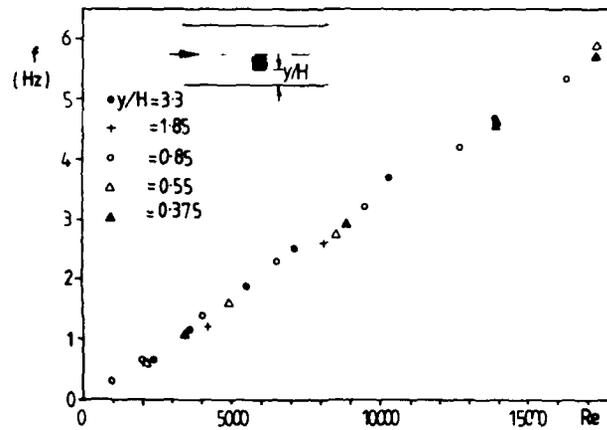
Fig. 9 - Variation of the vortex shedding frequency with the Reynolds number and the vertical position of the obstacle within the water channel.

ROUND TABLE DISCUSSION
SESSION II

M.Carlson Williams, US

A benchmark of instrument performance is being utilized at Pratt & Whitney for comparison of laser velocimetry instruments before and after incorporating optical revisions as well as for comparisons of our LDV with commercially available instruments. Perhaps others will find the method useful in establishing benchmarks in their laboratories. The technique does not require concurrent testing of instruments and comparisons can be performed between instruments operating at different test sites, if necessary.

In our tests, the technique utilized the ambient aerosol as seed in the flow discharging from a small electricity driven fan and an aerosol analyzer capable of characterizing the ambient aerosol size distribution. The range covered by the aerosol sizing instrument must span the range of particle sizes capable of being detected by the velocimeters. In our studies, the TSI 3030 Electrical Aerosol Analyzer with a range of 0.003 to 1.0 microns was employed. Using this method, a laser doppler velocimeter designed at Pratt & Whitney Aircraft was compared with comercially available Laser-Two-Focus and Laser Transit Anemometers.

The benchmark is obtained by measuring the velocity of the flow from a small fan or jet[1], noting the validated data rate, and measuring the turbulence intensity level. The ambient aerosol size distribution should be continuously sampled during testing.

(1) Using the particle sizing data, produce a log-log plot of cumulative number of particles/cm^3 $\geq$ a specified diameter versus particle diameter. See Figure 1.
(2) Either calculate or experimentally determine the swept area of the probe volume thru which particles of sufficient diameter could be expected to produce a valid signal. Typically $1/e^2$ points are used to define probe volume dimensions.
(3) Using the swept area and flow velocity, calculate the volume per unit time (cm^3/sec) being sampled by the laser velocimeter.
(4a) For fringe systems, calculate the number of particles/cm^3 being detected by dividing the measured data rate by the volume swept per unit time. From the aerosol distribution curve generated during the test, read on the abscissa the minimum particle diameter which corresponds to the detector particle concentration.
(4b) Two spot systems are handled similarly except that the probability of a two spot transit is inversely related to the turbulence level. To obtain a realistic result, the data rate must be adjusted upward by a suitable factor to compensate for this effect as the probability of two spot transits occurring is considerably less than unity in most flows[2].

Figure 1 includes calculations for two data points from an LDV/LTA comparison. Note the wide discrepancies in the data rates that were observed during testing. Although the two spot system is sensitive to somewhat smaller particles, the factor of 20 increase in data acquisition time eliminates any incentive to use the two spot system unless extreme flow accelerations preclude the use of the somewhat larger particles which the LDV detects. A second factor which also favors the use of LDV for our gas turbine studies is the ability to readily provide detailed mappings of the entire rotor (typically data is stored as a function of approximately 1000 angular position of the rotor) thereby permitting detailed examination of all blade gaps individually. Conversely two spot systems are generally limited to storing data at 16 angular positions which forces one to examine a composite of all blade gaps or to repeat the measurement for each gap of interest if individual passages are being examined.

The benchmark technique previously described has been used to evaluate instrument performance characteristics for several instruments in a variety of test configurations. Figure 2 is an example of one such test in which the minimum particle size sensitivity of three instruments were determined as a function of laser power in the instruments' probe volumes. It should be noted that the particle size distributions obtained by P & W's aerosol analyzer is based on electrical mobility of the particles while the instruments under test are sensing the ability of the particles to backscatter incident laser light. As the two characteristics may not be linearly related for all aerosols, some scatter and imprecision in results may occur depending on the nature of the constituents of the ambient aerosol. The three curves of Figure 2 represent two different test sites, East Hartford, CT and West Palm Beach, FL, and three different test dates, yet the results clearly delineate the trend in the data and the relative performance of the instruments.

---

1 We often employ a converging nozzle supplied by two vacuum cleaner blowers connected in tandem. This arrangement provides velocities up to 700 ft/sec at the nozzle discharge.

2 Figure 9 of Dr Schodl's paper Laser-Two-Focus Velocimetry (found elsewhere in this volume) displays the probability of a two spot transit as a function of turbulence for several two spot instrument geometries.

COMPARISON OF LASER DOPPLER
& TWO SPOT VELOCIMETER
PARTICLE SIZE SENSITIVITY vs LASER POWER
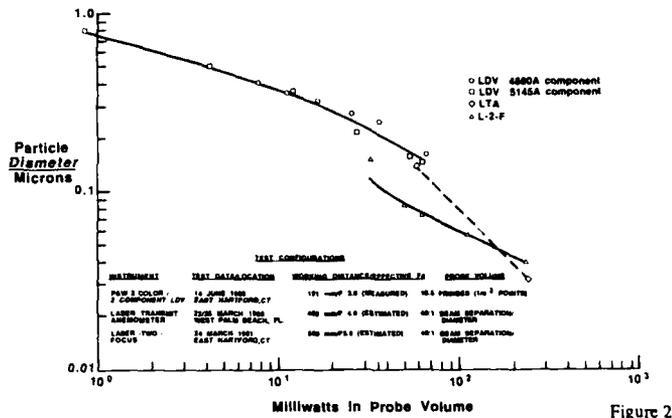
Figure 2

METHOD FOR ESTABLISHING SENSITIVITY
OF LASER DOPPLER and (or)
LASER TRANSIT VELOCIMETERS
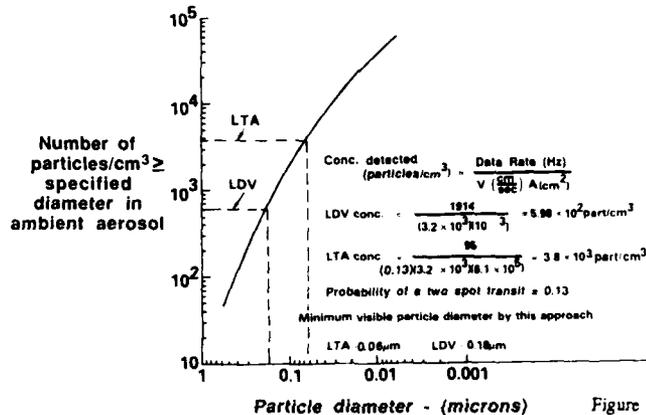
Figure 1

R.Elder, UK

What were the different focal lengths and F #'s for the various instruments compared?

M.C.Williams, US

The LDV had the advantage here, using a 191 mm focal length, 80 mm diameter lens. Accounting for internal blockages produces an effective F # of 3.8. The LTA system originally employed in the comparative study contained a 400 mm focal length, 100 mm diameter lens. Our measurements indicated an effective F # of 7.4 (this was the lowest F # lens available for the instrument at the time of the first test). This data is shown in Figure 1. The manufacturer has since made some internal changes which have improved the effective F #. I am not aware of the current F #, but the performance of the upgraded system has been evaluated and is shown in Figure 2. The L-2-F/LDV comparison study was performed in conjunction with the instrument's manufacturer, so I assume that the lowest F # lens normally utilized was supplied. The lens has a 500 mm focal length and a diameter of 104 mm. I do not know the effective F #.

R.Elder, UK

Would you like to comment on how these differences might influence such a comparison?

M.C.Williams, US

Yes, our LDV is equipped with four interchangable 80 mm diameter collection lenses of 127, 191, 318, and 345 mm focal length. Consequently, the longer focal length lenses have higher F #'s and to maximize performance we select the shortest focal length lens consistent with our needs. The LDV lens selected for the comparison was not the lowest F # lens available, but rather the lens most frequently used in our studies. I believe that there are areas other than F # which also contribute to a sensitive measuring system. For example, we introduce a fairly large central stop in our collection lens which cuts collection efficiency nearly 50%. The positive benefits of doing this include restricting the effective probe volume length and preventing much of the stray reflections from neighbouring surface from impinging on the photomultipliers. This design may, in part, explain why despite having a less sensitive collection system, the L-2-F Laser had to be turned off during the passage of blades in an intrablade turbocharger comparison test to prevent momentarily blinding the instrument's PMTs. The LDV operating at the same intrablade location required no gating.

W.G.Alwang, US

For those testing large scale turbomachinery, it seems necessary to have both L2F and laser Doppler (fringe) systems. The fringe systems have much higher data rates and therefore test costs are greatly reduced, if they are used whenever appropriate. Then you may also need a transit anemometer for working near walls or if very small (less than 0.5 μm) particles sizes are needed.

M.L.G.Oldfield, UK

Short duration wind tunnels may run for only 0.3 seconds. How will it be possible to obtain mean velocity, turbulence level and turbulence spectrum to 50 KHz in less than 1 second at one position per run?

A.Boutier, FR

During such very short runs, it is very difficult to use classical fringe or 2 focus laser velocimeters. One way may consist to use transient recorders to digitize all photomultipliers signals and process them quietly after the run. Another way is to use the spectrometer laser velocimeter developed at ISL (St Louis, France) by Dr Smeets and using the same principle as the Fabry-Pérot LV of Dr Seasholtz (NASA Lewis): but in this spectrometer velocimeter the Doppler shifted light is very quickly analyzed by a Michelson interferometer. This technique proved its feasibility to characterize the rapid flow variations issuing from a shock tube, but with a high seeding of tobacco smoke. This apparatus would provide mean velocity as well as velocity fluctuations.

The turbulence spectrum analysis of the velocity fluctuations is not widely spread in laser velocimetry. In fact, with current data acquisition rate of 10 KHz, when applying the Shanon criterion one cannot expect higher frequencies than 5 KHz. But a way to overcome this limitation is to calculate the autocorrelation function of the signal V(t) and then its Fourier transform: nevertheless this procedure necessitates long time data recordings. Many papers begin to be published on this subject, essentially at the ASME meeting held in Miami (17−22/11 '85). Anyway, in the type of flow you mentioned, to obtain the velocity fluctuations spectrum seems presently very difficult.

T.Wychers, NE

As Dr Melling explained, solid particles are, at least, less sufficient for LDA measurements. However, solid particles are naturally present in certain flows, such as sooting flames. Is it possible (avoiding seeding equipment) to use soot particles for LDA measurements in such flames, eventually by cancelling out the strong signals from big particles?

A.Melling, UK

To my knowledge, successful LDA measurements in flames have to date always required seeding scattering particles. I see no reason why soot particles should not be used as scatterers, although the signal strength for a given particle size is likely to be reduced relative to seeded refractory particles, because of the absorptivity of carbon. Whether the soot particles would follow the gas flow is, of course, a matter which can be decided only with knowledge of the particle size distribution. Soot agglomerates are likely to have a higher drag coefficient and lower effective density than carbon spheres, so particles of "equivalent" diameter exceeding the commonly quoted 1 μm guideline may be acceptable as tracers at the prevailing conditions of gas density and viscosity.

Electronic amplitude discrimination is a feasible technique to suppress the signal from particles which are significantly larger than the rest, by lowering the discrimination level until the measured velocity becomes independent of the threshold. Its application to continuous size distributions is less satisfactory: the technique will not distinguish between small particles crossing near the central high intensity region of the LDA measuring volume and large particles crossing near the edge of the volume. The end result may be only a sharp reduction in the data rate.

A.Straziaar, US

Is it possible to construct a system which adapts from 2-spots to 2 dashes? What is optimum geometry of 2 dashes system?

A.Boutier, FR

The two dashes LV we built at ONERA was in fact very flexible; when considering fig.11 of paper 9 (A.Boutier) when the inclined plates are removed and the rectangular apertures in front of the photomultipliers replaced by circular holes, the 2 dashes LV has become a 2-spots LV, with 2 spots of different colours. Therefore in commercial 2 spots LV, there are two simple modifications to operate: to include inclined plates in the emitting part (in order to create astigmatism on spots, the inclined plates rotation inducing dashes orientation) and to change circular holes in front of detectors in order to install rotating rectangular aperture (matched to the dashes size image).

The optimum geometry for a 2 dashes system has to be checked; in the ONERA system of fig.11, when varying the thickness of inclined plates, the height of the dashes varies; when changing the angle between the two stuck prisms, the distance between the two dashes is adjustable; notice that rotation of the dispersing prism induces rotation of the line joining the 2 dashes centre, which enables one to optimize the measurement probability because this line may be this way aligned along the main flow direction.

D.A.Greenhalgh, UK

Does the two bars system perform as well as the two spots system near walls? In particular, I would expect the two bars system to have a lower beam divergence for one plane and this will reduce signal to flare ratios.

A.Boutier, FR

As I showed in my paper no.9, and in more details in reference 6 of this paper, the two dashes LV is a compromise between 2 spots and fringe LV; it is practically able to perform measurements up to 0.7 mm from a wall. Certainly the SNR is not as good on the wall with a 2 dashes LV as compared to a 2 spots LV; figure 12 of paper 5 shows the phenomenon very well. But we can consider that it is still a good compromise and may have further developments, as it is done at NASA Lewis by M.P.Wernet.

R.Seasholtz, US

This is a comment on discussion of ability of elliptical spot anemometer to match circular spot anemometer in measuring close to walls.

The ability of an elliptical spot time-of-flight anemometer to measure close to walls can approach that of a circular spot system if the proper aperture stop is used. Roughly speaking, the aperture stop should be designed to block light along the major axis of the elliptical spots and pass light along their minor axes.

P.Ramette, FR

Can we expect limitations of laser velocimetry at very high temperatures, over 2000 K, due to the seeding in particular? I am thinking about measurements inside or at the exhaust of rockets for example.

A.Boutier, FR

The limitation for using any laser velocimeter (working on light scattered by aerosols present in the flow) comes from the fact that at temperatures higher than about 3000 K all refractory powders burn. The most refractory and fine powder is ZrO_2 which resists until 2700 K. Beyond this temperature other materials, which are heavy and with an unknown size distribution, may resist but without oxygen in the fluid flow (which must be either argon or nitrogen). We looked at these problems for plasma jets investigation at 5000 K, but we did not succeed.

So the present limitation in temperature to use laser velocimetry is given by ZrO_2 and is 2700 K.

In high temperatures flow, depending on the turbulence level and the flow thickness, the importance of wandering laser beams due to variations of the refraction index must be studied.

P.J.Bryanston-Cross, UK

Does anybody have knowledge of the use of laser diodes in laser velocimetry?

A.Boutier, FR

J.Meyers at NASA Langley constructed a laser anemometer 6 or 7 years ago using a laser diode. The system was about the size of a match box and was embedded inside a wind-tunnel model to study a shock-wave boundary layer interaction. However, we are not aware of any continuing effort in this area.

TECHNICAL EVALUATION REPORT
SESSION III — PYROMETRY

by

J.Swithenbank
Department of Chemical Engineering
University of Sheffield
Sheffield, S10 2TN, UK

Fibre optics have moved from the situation where they were a solution looking for a problem to being an important new diagnostic technique for propulsion applications. The particular feature in common between the papers presented this morning was the use of fibre optics.

The papers that we have just heard have analysed very thoroughly the state of the art presented by experts in the technology, and the audience has contributed some very important points to the discussion. This really makes my task particularly easy and there is little point in repeating what the authors have already said with more authority and skill that I can put over. However, I think there are a few key points that have emerged quite clearly.

For example, if we consider the first paper by Dan Tichener which presented a novel and powerful diagnostic technique for measuring temperature with very high accuracy and very high frequency response, I would like to remind you of some of the potential of the applications. In particular, this technique when used to measure steady temperature could determine the efficiency of combustion and could even be used to determine the efficiency of the compressor provided we can extend the measurement temperature down low enough. Certainly the efficiency of the turbine system could be assessed and conceivably it could be used for assessing the dissociation effects in combustors. Thus, in terms of steady state, I believe that it has a very wide range of application.

If we now look at the high frequency capabilities of the system we realise that the fluctuating temperature emerging from the combustor and the fluctuating temperature within the combustor are both very important parameters related to one of the unresolved problems of the present time; that is the interaction between mixing and kinetics in combustion systems. The modelling of such systems is not yet at a completely satisfactory state and we urgently need experimental data. I believe that this instrument is one of the tools that we could use to address this problem.

Furthermore, we heard of the novel application of the fibre optic device for studying transients within pyrotechnic systems. This leads me to wonder a little about the spatial resolution, since composite pyrotechnic propellants are not uniform materials. There are inhomogeneities consisting, for example, of discrete aluminium and ammonium perchlorate crystals and I suggest that we must look into the local structures within these systems in addition to the one-dimensional movement of heat and flame fronts.

The problems which arise in many of these instruments are due to the very rapid change in output with temperature; caused by the T^4 relationship. This means that at 2000 degrees, we get approximately 1 per cent change in output per degree centrifuged. Clearly this gives us the source of our high accuracy but also gives us the source of difficulty in that we need a very wide dynamic range of the amplifiers. All the speakers have addressed this problem of the dynamic range of the sensing systems.

Now we look at one or two detailed problems in fibre optic temperature measuring probes, in particular, the problem of relating the true stagnation temperature of the gas to the output from the probe. This involves the radiation correction, and clearly much more work is necessary in this area. Progress may be either by radiation shield development or some other technique such as the use of variable size probes. In this latter technique, correction for the effects of radiation may be made by using the signals from two different sizes of probes for which the radiation correction would be different, and therefore correctable.

A further factor which I believe should be addressed is the coating of the sapphire fibres. If dirt is accumulated on the surface of the sapphire fibre, some signal can be lost, however, if the fibre of sapphire has a surface layer of lower refractive index, then we can eliminate this particular loss. Clearly, development in this area is necessary if fibres are to be used in dirty environments.

Another area needing attention is the stability of the material of the fibre tip coating. So far, experience indicates that many of us have had problems in obtaining stability of the material of the tip coating and whilst it was indicated that solutions are perhaps possible, we need them documenting and thoroughly testing, both in oxidising environments and in reducing environments. For example, the standard Dills probe that any of us use already is recommended for use in inert atmosphere

above about 1500°C. This is a severe restriction when we wish to use the probe for advanced gas turbines, where temperatures are approaching stoichiometric flame temperatures.

We also need to address in more detail the problem of the cavity design. The cavity at the end of the fibre optic either needs to be a black body (or a very close approximation) or to be such that we know exactly what its radiation characteristics are. This leads us to the question of calibration. The discussion this morning emphasized the difficulty of calibration especially at high frequency.

Thus we see a number of interesting questions emerging from the particular area of technology of the first paper.

Moving on to the other two papers; these are both concerned with the infra-red pyrometry of turbine blades. Clearly, these two papers have a great deal in common but they also address two different areas to which I would like to draw your attention. The paper by Dr Kirby discussed the problem of installing fibre optic diagnostics systems on production engines, and to a lesser extent on research engines. The other paper, by Koschel et al, was concerned very specifically with a water-cooled probe-design, which would be unsuitable for flight but ideal for test facility installation.

Lens purge design was emphasized by Dr Kirby and I would like to return to this subject later.

The advantages and limitations of the two colour pyrometry were discussed; however when we actually try exploiting this attractive technique we discover its limitations. These limitations emanate not only from the properties of the source; that is the turbine blade with all the reflections of unwanted signals, but extend through the design of the sensor, the pre-amplifiers and the signal processing systems.

It has been particularly interesting to consider the use of pyrometry for control purposes and we have had some useful contributions here from the control engineers. Clearly this is a developing area of pyrometry since, if we can control the engines directly from blade temperature, it will give us a sensitive and precise way of optimizing the control. As we increase the gas temperatures and hence the role of blade cooling, so the blade temperature as a direct control signal becomes more and more attractive. The problems arising from control are quite different from those arising from diagnostics on test rigs. In the latter case, we require the temperature distribution over the blades and hence want a high frequency signal. On the other hand, for control we have two aspects to consider. Firstly, the air/fuel ratio control, and here the important factor is the drift. The long term drift is due to either the electronics or possibly the window fogging. Long term fogging of the window can be a problem on flight engines, much more so than on rig engines. On a rig engine, the provision of lens purge is relatively easy because we can take a clean purge gas supply. On a flight engine the purge gas has to be taken from the compressor delivery air and this inevitably contains a variety of contaminants. Oil is a common contaminant, and if guns are fired on military aircraft, there is also the possibility of ingestion of material from the guns. So clearly we have to address the purge problem quite differently in the case of flight engines. The other 'control' information that is required is the identification of faulty blades. We have seen how the diagnostic systems can very easily resolve individual blades that are overheating and one could envisage a monitoring system whereby an engine is taken out of service in preventive maintenance when difficulties are first detected, rather than depend on periodic static inspection and replacement.

The electronic analysis of results during flight to pick out *peak* blade temperatures and to pick out *mean* blade temperatures, whilst eliminating the effects of carbon particles, is clearly important and feasible.

I now wish to refer briefly to the installation of fibre optic probes. The installation has led to a fair amount of discussion and is clearly not an easy task. If optical pyrometers are to become an integral part of the engine system they must be designed into the engine right from the beginning. It is not always easy to retrofit them if some provision was not made originally.

There are a few areas that do give us cause for thought for the future:—

(a) Firstly, one would like to know temperatures at more than one line at one radius around the turbine and multi-installations are therefore required. Should this be done by scanning a single pyrometer or should it be done by multiple installations?

(b) How many units are needed for reliability, since if this device is a major element of the control loop then reliability is very important.

(c) I would also like to mention other diagnostic procedures that one can use once the pyrometer is installed. For example, a pyrometer can be used not only for engine control but also for diagnostics of light-up behaviour and conceivably even for surge control etc.

Clearly we have many potential applications of optical pyrometer systems and there is considerable scope for further research and development of these devices.

I will now discuss the problem of lens purge design by the computation of purge flow, based on our experience at Sheffield University. Purge flow is particularly relevant to the flight engine rather than the ground based engine. The basis of a purge system is essentially that one has to keep a clean flow *over* the surface of a lens. That is, one must try to avoid the deposit of dirt which can come from the engine, particularly during a shut down period. The feature of a purge system is that you must *not* blow small jets at the lens. If you do, they will entrain dirt which will be thrown at the window and will stick there and give trouble. The correct approach is much more akin to the combustor film cooling design problem where you try

to put a film of clean gas over the surface. If we represent the purge flow situation (or the film cooling flow) in terms of the length of the potential core of the film over the surface as a ratio to the height of the slot blowing the film over the surface, and plot this ratio against the velocity ratio of the jet flow, (that is the ratio of the flow velocity through the slot to the external flow velocity), then you find that at matching velocities there is a relatively long distance protected. At a high jet flow velocity protection is achieved for a length corresponding to approximately 8 jet heights. At low purge flows, a length corresponding to approximately 5 jet heights can be protected. This then is the crude basis of a purge flow design, but one has to analyse the actual design in more detail. We have carried out some design computations using the FLUENT code. The first case consists of a window located with a purge flow coming down a relatively large annular passage behind the lens, then accelerating the flow through a narrow radial slot around the lens. The slot should protect to approximately 5 slot heights in other words the slot height needs to be about a tenth of the diameter of the lens. The results of the computations show that the jet flows in radially and protects the lens fairly well. However, there is a large recirculation region in the centre of the lens and an annular recirculation zone downstream of the purge slot. The recirculation in the centre of the lens is of the order of one fifth of the diameter, and there is the possibility that some material will be deposited in this region. If you have initially picked up fuel on the lens surface then the jet coming across, (if its velocity is about 50 metres per second), will remove the particles from the surface unless they are very tightly bonded or burnt on. This criterion corresponds to the saltation velocity, which varies from about 20—50 metres a second. However you cannot easily remove the material from the centre of the lens. Using the capability of particle tracking which is built into the FLUENT code, particles may be introduced at different points to ensure that they follow a path which leaves the lens fairly clear. Such particles may arise if there is oil contaminating the purge flow. The capability of FLUENT to calculate the paths of the particles *including the effects of turbulence* on the particle trajectories is also useful. For example 5 micron particles introduced as a group spread somewhat, but still keep away from the lens. When we go down to one micron particles there is significant turbulent diffusion of the particles. Some of them are carried back into the central recirculation eddy.

Clearly, if we have a very short duct between the lens and the turbine flow then it is possible to get external flow into the central recirculation region. If there are particles present of certain critical sizes they can be deposited on the lens.

In an axisymmetric design, the size of that recirculation eddy in the centre of the lens is due to the fact the flow is coming *radially* inwards, hence a lot of flow is trying to get towards the centre of the lens resulting in a large separation effect. In our next study, we took a 2-dimensional purge flow rather than an annular situation, with purge gas velocity coming past the surface of the lens of the same order as the turbine entry velocities. In this case there is an extremely small separation region because of the 2-dimensionality of the flow, rather than the 3-dimensionality discussed above. Particle paths of one micron introduced at different regions keep relatively clear of the lens. Ten micron particles do not follow the flow but hit the wall, bounce off, and then are entrained into the purge flow. When we decreased the width of the slot we observed strong vortices and higher velocity vectors which purged the lens rather better. However, one must not of course, reduce the slit too small otherwise there will be entrainment of particles into the mixing layer which will actually get through to the surface of the lens. Following particles of one micron through the narrow slit is interesting since their trajectories almost coalesce independent of where the particles are introduced. Thus following the particle path throws quite a lot of light on what is happening in these systems, especially if we include the effects of particle diffusion due to the turbulence in the gas.

These systematic studies illustrate the phenomena that are occurring in purge systems and clearly we need a great deal more analysis before we can evolve a reliable design procedure for production type applications.

Finally, we conclude that we have a rapidly evolving area within the technology of the application of fibre optics to pyrometry, which may be applied to propulsion systems.

The three papers presented in session III all used a fibre optic element in their construction together with a sensor and electronic signal processing to translate the radiation measurement to temperature.

The first paper described a temperature probe which used a coating on the end of the probe or a surface adjacent to the end of the sapphire probe as a grey/black body cavity. The other two papers both used a lens located beyond the end of the fibre optic rod, focused on a remote point on the turbine blade, to indicate blade temperature. These two papers presented pyrometer systems suitable for application to flight engines and research turbines, respectively.

In all cases the high frequency response and good potential accuracy of the devices were demonstrated. The value of the pyrometers for diagnosing faulty blades was also notable.

During the presentation, and the discussion period, problems requiring further research and development were identified due to:

(1) the lower temperature limit of the sytems

(2) the survival of the 'black body' film on the surface of the sapphire temperature probe

(3) the coating of the sapphire with low refractive index material to prevent the loss of radiation due to surface contaminants

(4) the precise calibration of the temperature probe, particularly during rapid transients. Both the relationship between the probe tip temperature and the required gas temperature must be clarified

(5) the increase in signal noise which occurs at low temperature and with low spot size when using the remote pyrometers

(6) the sensitivity of the pyrometers to scattered radiation and changes in surface emissivity was indicated

(7) the importance of making provision for installation of the pyrometers at the initial engine design stage was emphasized

(8) the problems and advantages associated with two colour pyrometry were both highlighted

(9) the problems associated with window purging for flight applications require further study since the available purge flow may contain oil and other contaminants

As a result of this session, *priority* items for further R & D work are:— (a) temperature probe tip designs to achieve good life and accuracy, and (b) design of lens purge systems for flight installations of the turbine blade pyrometer.

Sapphire Fiber Optic Temperature Probe *

D. A. Tichenor, K. R. Hencken and R. W. Bickes, Jr.
Sandia National Laboratories

ABSTRACT

A sapphire fiber optic pyrometer, has been developed for use in combustion environments. Two configurations of the device are described. One is designed to measure rapid gas temperature fluctuations and the other is designed to measure the rapid temperature rise in a confined pyrotechnic prior to ignition. The key element in the device is a high temperature optical fiber made of single-crystal alumina (sapphire) with a thin film of platinum deposited on one end. Temperature is derived from the intensity of thermal radiation emitted by the platinum and collected by the fiber. The device is capable of measuring rapid gas temperature fluctuations, in excess of 10kHz, in harsh environments where thermocouple life is severely limited by oxidation, corrosion, or erosion. A second configuration of the device collects infrared radiation directly from a solid object and operates in the mid-infrared to detect lower temperatures. The temperature of a confined pyrotechnic has been measured in the range from 370 K to 1100 K at heating rates greater than 100 K per microsecond.

INTRODUCTION

The requirements for temperature measurements in industrial research and development are numerous and widely varied. To meet these needs new methods of temperature measurement using fiberoptics have been developed.[1,2] Some of the advantages offered by fiberoptic sensors are immunity to RF noise, low thermal conductivity, fast response time and resistance to harsh chemical environments. These capabilities can be extended in some applications by using sapphire optical fibers. Sapphire fibers are available only in short lengths sufficient for use as sensing elements but not for transmission over long distances. Several properties of sapphire are useful in temperature measuring applications. First, sapphire remains transparent in the optical and near infrared at elevated temperatures. Second, at room temperature the transmission band extends to 4 microns. Finally, the melting point of sapphire is higher than that of conventional silica fibers and platinum-rhodium thermocouples.

In this paper, two applications of sapphire fiberoptic sensors are described. The applications are very different, and the devices are configured accordingly. The first device was developed and demonstrated by R. R. Dils of the National Bureau of Standards, now with Accufiber Company in Vancouver, Washington, and one of us (DAT) to measure rapid temperature fluctuations in combustion gases.[3] The second is being used to measure the rapid heat-up of a confined pyrotechnic prior to ignition.

MEASUREMENTS OF RAPID GAS TEMPERATURE FLUCTUATIONS

Temperature fluctuations in combustor exhaust gases are of practical interest because downstream components, such as turbine blades, can suffer fatigue of protective metal-oxide surface layers and accelerated oxidation and corrosion due to the temperature fluctuations. Gas temperature fluctuations have been measured in combustion environments using fine-wire thermocouples with a bandwidth of 1 kHz.[4]

A sapphire fiberoptic temperature probe was developed to increase the bandwidth, the maximum operating temperature and the lifetime in harsh environments. The key element in this device is a high temperature optical fiber made of sapphire (see Figure 1), which remains transparent and non-emitting in the optical and near infrared at temperatures up to its melting point, 2345 K. On one end of the fiber a thin film of platinum or other high temperature alloy serves as a thermal radiator. The other end of the high temperature fiber is connected to a photodetector through a conventional fused silica fiber. In operation, thermal radiation from the metallic thin film is collected by the high-temperature fiber and transmitted through the conventional optical fiber to a detector assembly. The radiation is then transmitted through a band pass filter, and the intensity is measured using a photodetector. The system is calibrated to account for the emissivity of the thin-film tip, the responsivity of the detector and the gain of the amplifier.

Figure 1. High-Temperature Fiberoptic Thermometer

The frequency of response of the fiberoptic probe is inherently superior to that of fine-wire thermocouples because the output of the fiberoptic device depends only on the surface temperature of the probe. The output of a thermocouple depends on the internal temperature of the wire. As a result, the transfer function that relates gas temperature to probe temperature decreases at a rate of 3 db per octave at high frequency rather than the 6 db per octave characteristic of thermocouples.

The high frequency performance of the fiberoptic optic probe was demonstrated using a laboratory combustor which creates a thermodynamic and aerodynamic environment similar to that produced by gas turbine main burners. The fuel is injected through a pressure atomizing nozzle at the front of the combustor, which has an exit nozzle 5 cm in diameter. Primary and secondary air is supplied independently to permit external adjustment of the air flow within the combustor. By adjusting the flow of primary and secondary air it is possible to vary the power spectral density function of gas temperature within the combustor exhaust from

broad band (near random) to narrow band (near harmonic) profiles.

A prototype fiberoptic pyrometer was constructed using a sapphire fiber 1.25 mm in diameter and 50 mm in length. A thin film of platinum, about 2000 Angstroms in thickness, was sputtered on one end and along the sides of the fiber for a distance of 1.5 mm. The other end of the sapphire fiber was optically coupled to a conventional plastic-clad-silica fiberoptic having a core diameter of 400 microns. The silica fiber was protected from the combustion temperatures using a water cooled jacket that exposed a 2 cm length of the sapphire fiber to the exhaust gases. Thermal radiation transmitted through the silica fiber was collected by a lens at the receiving end, filtered at a center wavelength of 800 nanometers with a bandwidth of 10 nanometers, and detected using a silicon photodiode. The photocurrent was amplified using a two-stage solid state amplifier having a current to voltage gain of 10^7 volts/amp.

The primary and secondary air supplies to the combustor were adjusted to yield a relatively flat spectrum with maximum high frequency content. The power spectrum of the emitted radiation was measured out to a frequency of 14 kHz and divided by the squared modulus of the system transfer function to yield the power spectrum of the gas temperature. The resulting power spectrum (Figure 2) is almost flat out to 1 kHz and contains significant components beyond that frequency. The amplifier noise power spectrum (with the light to the photodiode blocked) is also shown. At 14 kHz the signal spectrum is greater than the amplifier noise spectrum. This is a significant extension beyond the frequency range covered by fine-wire thermocouples.
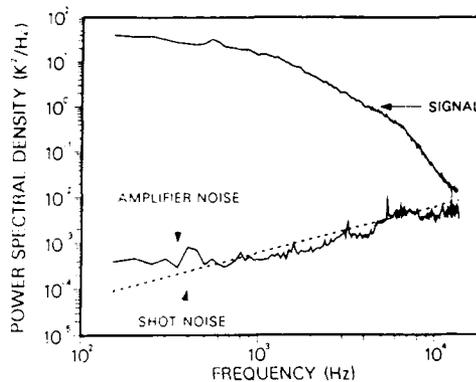
Figure 2.

HIGH-SPEED TEMPERATURE MEASUREMENTS IN A CONFINED PYROTECHNIC

A sapphire fiberoptic temperature probe, significantly different from the device described above, has been developed to measure the rapid temperature rise in a confined pyrotechnic prior to ignition. This data is useful in developing a better understanding of the ignition process, which is known to depend on temperature, heating rate and the degree of compaction.[5] The details of this dependence are not well understood.

In this application the device must measure temperatures well below that of combustion processes with a bandwidth much higher than that observed in the above experiment. To achieve lower temperature capability, the system is operated at in the mid-infrared. Higher bandwidth is achieved by omitting the thin-film thermal radiator and collecting thermal radiation directly from the surface of the pyrotechnic.

The instrument is comprised of a 1 mm sapphire optical fiber, one end of which is pressed against the pyrotechnic so that the charge is completely confined (Figure 3). Thermal radiation is collected directly from the pyrotechnic and guided to a set of calcium fluoride lenses. The lenses focus the radiation onto a liquid-nitrogen-cooled, indium arsenide detector which has a peak sensitivity at 3 microns. Conventional optical fibers become opaque above 2 microns, making them unsuitable for this application, however, sapphire fibers transmit wavelengths up to 4 microns. Temperatures in the range 370 K to 1100 K can be measured with a rise time less than the time required to observe the rapid heat up of a given point in the pyrotechnic wave.
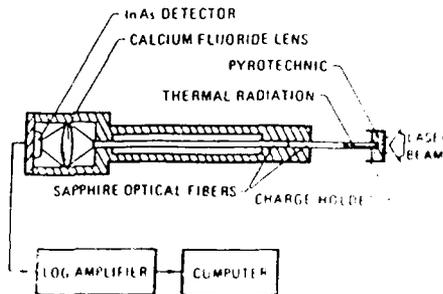
To derive temperature from the measurements of thermal radiation, calculations were performed and used in the calibration. The integrated radiance was measured experimentally at 3 microns to determine whether radiation from the interior reached the far surface and invalidate the temperature measurement. The pyrotechnic was composed of titanium subhydride and potassium perchlorate. The ignition of a 20 milligram charge was observed. The purpose of this experiment was to determine whether the instrument had adequate response time. An approximate calibration yielded a temperature profile of the pyrotechnic shown in the figure. At the start of the measurement, the heating rate was very high with a heating rate of about 670 K, followed by a plateau in the temperature profile due to melting of the potassium perchlorate.
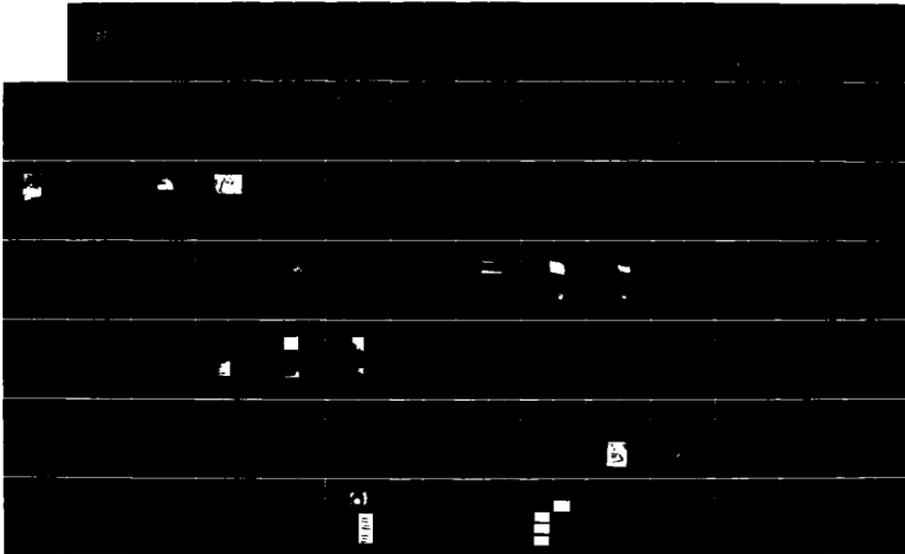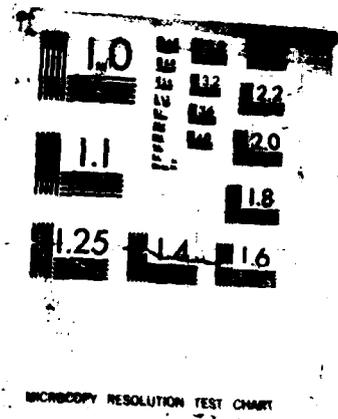
MICROCOPY RESOLUTION TEST CHART

a more careful calibration should reduce this discrepancy. In any case, the melting of potassium perchlorate in this mixture cannot be observed at low heating rates where the pyrotechnic ignites below the melting point of potassium perchlorate. In a subsequent experiment the endothermic process was observed at heating rates on the order of 100 Kelvins per microsecond. At higher heating rates the endothermic reaction is not as well delineated as in Figure 4, perhaps due to a slight tilt of the deflagration wavefront relative to the plane containing the end of the fiber.

A two-color version of the instrument is being built so that accurate temperature measurements can be made without precise knowledge of the emissivity.

Figure 4.

TIME (MICROSECONDS)
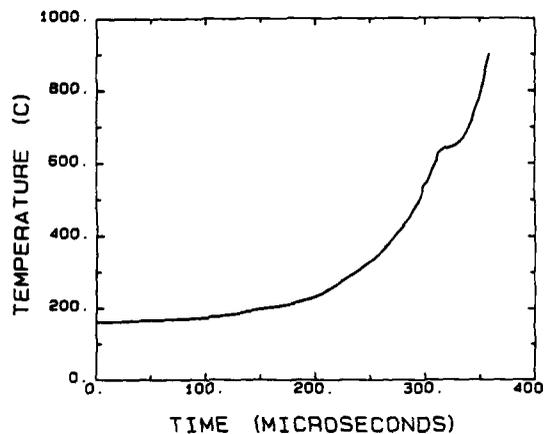
CONCLUSIONS

Dynamic temperature measurments in a laboratory combustor demonstrate the capability of measuring temperature fluctuations at frequencies up to 14 kHz using a sapphire fiber optic pyrometer. These measurements extend the frequency range previously covered using fine-wire thermocouples by more than an order of magnitude.

A sapphire fiber optic pyrometer operating in the mid-infrared can be used to measure the rapid heating in a confined pyrotechnic. Heating rates as high as 100 K per microsecond can be observed with sufficient response time to resolve endothermic reactions prior to ignition.

REFERENCES

1. A. F. Cheng, "Fluoroptic Thermometry," Measurements and Control, p 115, April (1981).

2. M. Gottlieb and G. B. Brandt, "Fiber-Optic Temperature Sensor Based on Internally Generated Thermal Radiation," Applied Physics, Vol. 20, No. 19, p 3408, (1981).

3. R. R. Dils and D. A. Tichenor, A Fiberoptic Probe for Measuring High Frequency Temperature Fluctuations in Combustion Gases, Sandia National Laboratories, SAND83-8871, (1984). Also submitted to the ASME Journal of Engineering for Gas Turbines and Power.

4. R. R. Dils, "Dynamic Gas Temperature Measurements in Gas Turbine Transition Duct Exit," Journal of Engineering for Power, Trans, ASME, Vol. 95, Series A, No. 3, p 265 (1973).

5. J. H. McLain, Pyrotechnics, Franklin Institute Press, Philadelphia, PA (1980).

FIGURE CAPTIONS

Figure 1. High-Temperature fiberoptic pyrometer

Figure 2. Power spectral density function of exhaust gas temperature for case 4, Figure 4 measured by the fiberoptic probe to a frequency of 14 kHz.

Figure 3. Infrared fiberoptic pyrometer for measuring temperature of a confined pyrotechnic.

Figure 4. Temperature of pyrotechnic PA-29 during ignition as measured by a sapphire fiber optic temperature probe.

16-4

DISCUSSION

A.Ederhof, Switzerland
  (1) What is the lowest temperature that can be detected with the high-temperature fibre optic thermometer and how does it influence the maximum achievable frequency?

  (2) What is the influence of contaminants such as soot on the behaviour (frequency response) of the high-temperature thermometer?

Author's Reply
  (1) The practical lower temperature for this device is 5500 degrees C. To operate at a given signal-to-noise ratio the integration time must be increased as the temperature (and therefore the signal level) decreases. As a result the maximum achievable frequency will decrease at lower temperatures.

  (2) Contaminants deposited on the probe will have no effect on the frequency response as long as the thickness of the deposited layer is thin compared to the thermal wavelength corresponding to the highest frequency of interest.

T.Wychers, NE
  You stated that the temperature measurement is not affected by radiation loss, due to the high gas velocities. Can you give an estimated gas speed, where the drop of temperature measured (due to radiation loss) is 10 degrees? At low speeds the drop can be several hundreds of K (as you and I measured).

Author's Reply
  At low gas velocities the radiation correction for the fibre optic probe is similar to that for thermocouples. The temperature correction, which may be several hundred Kelvin, depends on several parameters, including gas velocity, probe diameter and emissivity. The error in the correction is typically dominated by uncertainty in the probe emissivity.

W.G.Alwang, US
  (1) Have you attempted to confirm experimentally the transfer function derived theoretically? In particular, the point where transition from 6dB per octave to 3dB per octave occurred? (In my opinion, experimental confirmation is needed).

  (2) Have you had any problems with survival of the film?

Author's Reply
  (1) We have not attempted to verify the transfer function experimentally. I agree that experimental verification is needed.

  (2) We did have some problem with adhesion of the platinum film to the sapphire. The platinum appeared to adhere better to the end of the fibre, which had been polished with an abrasive, than to the side, which was formed in the edge-defined-growth process.

M.L.G.Oldfield, UK
  (1) Would it be possible to use the step rise in temperature from a shock tube to calibrate the probe?

  (2) Is not the main problem of high frequency calibration that of knowing the heat transfer coefficient between the flow and the probe tip, as, at high frequencies, the probe effectively measures heat transfer rates?

  (3) Would a coating with zero emissivity on the outside and an emissivity of one on the film-sapphire interface remove the necessity of radiation correction?

Author's Reply
  (1) The impulse response of the probe could be measured using a shock tube if the gas velocity and gas temperature are accurately known.

  (2) I agree that the gas temperature measurements are limited mainly by the uncertainty in the heat transfer coefficient.

  (3) A low emissivity (high reflectivity) coating would reduce the radiation correction for both the fibre optic probe and thermocouples. However, it is difficult to maintain such a surface in a high temperature environment. In any case some thermal radiation must be emitted to provide the pyrometry signal.

M.Misrahi, FR
  In order to know the heat transfer to the back of our rockets, we do tests at a reduced scale. During these tests we measure the convective flux and also the temperature of gas at the back. Presently, the measurement of temperature has been done by thermocouple but we do not get a good measurement because during the short time of the propulsion (<0.5s) the response of the thermocouple is not very quick. With a range of temperature of gas of 1000 K to 2000 K and this short time of the test, do you think your thermometer is suitable?

Author's Reply

The task of measuring gas temperature in a transient event with the fibre optic probe is more difficult than that of measuring the power spectral density of a random process as demonstrated in this paper. In a transient even we must know the correction for both the amplitude and phase of the transfer function, while the power spectral density function depends only on the squared modulus of the transfer function.

I understand that Accufiber Company, Vancouver, Washington is in the process of applying a fibre optic probe to the measurement of gas temperature in a reciprocating engine. Your requirements (0.5 s) would be less demanding in terms of frequency correction than in the engine application.

D.A.Greenhalgh, UK

Would it be possible to check your high frequency response experimentally in a clean tailored, turbulent flame by comparison with Rayleigh scattering?

Author's Reply

Yes, it should be possible to measure the transfer function of the fibre optic probe by simultaneously measuring the temperature in a turbulent flow using Rayleigh scattering and comparing it to the probe response. If the measurement volume for the Rayleigh system is located a small, known distance upstream of the probe tip, both the amplitude and phase of the transfer function can be measured.

SOME CONSIDERATIONS RELATING TO AERO ENGINE PYROMETRY

P. J. Kirby
Vice President
Land Turbine Sensors Inc.
P.O. Box 1623
Fox Drive/Main Street
Tullytown, PA 19007, USA

SUMMARY

With turbine blade optical pyrometry rapidly becoming accepted by the aerospace community as a viable flight control technique, some of the traditional and emerging demands are described, with examples of how they are being addressed.

Many of these demands are now being met by skilful application of materials technology, electronic engineering, signal processing and fluid flow techniques, but it is probable that flight conditions will impose a more pragmatic approach than customarily adopted towards test bed installations.

NOMENCLATURE

λ	wavelength
A, B, C	constants
C_d	detector shunt capacitance
C_2	second radiation constant
D	lens stop diameter
d	target spot diameter
ε	emissivity
f	frequency
$F(\lambda,T,Ta)$	pyrometer signal, blackbody source
G	amplifier gain-bandwidth product
I	photocurrent
$J(\lambda,T)$	spectral intensity of emitted radiation, Wien approximation
k	calibration scaling constant
L	pyrometer focus distance
N	noise equivalent temperature (Kelvin)
R	feedback resistance
s	velocity of target spot on rotor
$S(\lambda)$	detector spectral response
T	temperature (Kelvin)
U	view factor
V_n	noise voltage
V(T)	pyrometer output radiance voltage
w	viewable blade width
subscript a	ambient
b	blade
m	maximum photocurrent response
r	ratio
s	system
t	target
1	short waveband channel
2	long waveband channel

INTRODUCTION

Since its introduction in the mid-1960's, optical pyrometry has gained widespread acceptance as an invaluable technique for turbine blade temperature measurement in engine research and development programs. However, since the Turbo-Union RB199 turbofan was first instrumented with flight pyrometers in the early 1970's, acceptance of the technique in flight has been slow, the only other known example being the General Electric F110 turbofan.

The purpose of this paper is to highlight some of the more important aspects of turbine pyrometry in relation to its acceptability for flight usage. Difficulties still remain, however there are clear signs not only that flight pyrometry will very probably be employed in the next generation of high performance combat aircraft engines, but also that successful deployment of the technique may well be a prerequisite to effective management of the high operating temperatures planned for such engines.

discussed include:

INTERCHANGEABILITY; Peak blade temperature measurement; Radiation interferences; optics contamination, and Measuring ratios

There are obvious logistical needs for pyrometers to be interchangeable, particularly in military applications. Optical and mechanical features present no severe problems in this regard, but pyrometer output signal characteristics can vary markedly from one instrument to another.

The silicon photodiode is widely accepted as the optimum detector for turbine blade pyrometry, and produces a photocurrent which is a function of both target temperature and ambient temperature. The ranges pertinent to aero applications are approximately 870-1450 K and 220-400 K.

The characteristic $I \propto F(T,Ta)$, from which temperature is inferred, is extremely stable and reproducible for a single detector, but differs between detectors. One standardization approach is to adopt an average characteristic, based upon a large sample, and control detector reproducibility. This requires rigid specification of the starting silicon crystal and its subsequent processing. The approach is limited in effectiveness by the need for reasonable device yield, with a realistic reproducibility corresponding to measurement error of 5-10 K of target temperature. The attendant problems of device supply reliability and cost are severe.

An alternative approach obviating the need for detector reproducibility may be formulated as follows. Spectral sensitivity typical of a silicon detector at room temperature is shown in Fig.1. Blackbody radiation illumination produces a photocurrent according to the product $S(\lambda)J(\lambda,T)$, that is

$$dI \propto S(\lambda)\lambda^{-5}\exp(-C_2/\lambda T)d\lambda \qquad (1)$$

The result is a spectrally sharp spike, with peak photocurrent occurring at approximately 1 μm for the entire target temperature range of interest. This suggests approximating to monochromatic response at approximately 1 μm, thus

$$I \propto \lambda_m^{-5}\exp(-C_2/\lambda_m T) \qquad (2)$$

Fig.2 shows typical deviation between the approximation and numerical integration of the product $S(\lambda)J(\lambda,T)$. Over the range 870-1450 K, the maximum error is less than 3 K.

The ambient temperature dependence may be incorporated as follows. The intrinsic energy gap for silicon can be approximated with very little error by a linear dependence (Ref.1), therefore $1/\lambda_m$ would be expected to show a similar dependence. In addition, the variation of I with ambient temperature is invested predominantly in the exponential term of Eq.(2), suggesting a further approximation

$$I \propto \exp-[(A+BTa)/T] \qquad (3)$$

or

$$T = (A+BTa)/(C-\ln I) \qquad (4)$$

The set of values A, B, C is determined empirically and is unique to a particular detector. By providing read-out of A, B, C and Ta from each pyrometer, T can be determined from Eq.(4) using a standard software routine in the engine control computer, and complete interchangeability of pyrometers is achieved. Typical accuracy for the technique is ±5 K for all ambient and target temperature combinations.

PEAK BLADE TEMPERATURE MEASUREMENT

While average rotor temperature can be obtained comparatively easily, peak (hottest blade) temperature measurement is more difficult. The latter is nevertheless a natural refinement of turbine pyrometry and would enable further gains in engine performance as well as providing valuable diagnostic information.

This has resulted in requests for smaller target spot sizes and increased system bandwidth. Fig.3 is an example of the fidelity that can be achieved with a correctly specified pyrometer system. Alumina-coated blades, and a single overheated blade, are clearly distinguishable. The following comments are intended to highlight the more important effects that must be considered when individual blade resolution is important.

Direct measurement of true peak temperature is prevented by finite electronic bandwidth and finite viewed area on the blade. However, peak reading error can be expressed in terms of the dimensionless parameters f_s/f_b and w/d (Ref.2) and appropriate corrections applied to indicated values. For high resolution pyrometry, matching of spatial resolution and electronic bandwidth may be expressed as (ibid)

$$f_s/f_b = w/d \qquad (5)$$

or

$$d = s/f_s \qquad (6)$$

It may be shown that, for a photodiode/transimpedance amplifier combination

$$f_s = (G/2\pi C_d R)^{\frac{1}{2}} \qquad (7)$$

Thus

$$d = s(2\pi C_d R/G)^{\frac{1}{2}} \qquad (8)$$

The photocurrent produced by the detector can be approximated to

$$I = k(dD/L)^2\exp(-B/T) \qquad (9)$$

and it follows that

$$V(T) = \frac{RA(dD/L)^2}{\exp(B/T)} \qquad (10)$$

Eliminating R between Eq.(8) and Eq.(10) gives

$$d = \left[\frac{sL}{D}\right]^{\frac{1}{2}} \left[\frac{2\pi C_d V(T)\exp(B/T)}{GA}\right]^{\frac{1}{4}} \qquad (11)$$

System noise may be defined

$$N = V_n/(dV/dT) \qquad (12)$$

which, from Eq.(10) may be written

$$N = V_n T^2 / BV(T) \tag{13}$$

Comparison with Eq.(11) reveals that

$$N \propto 1/d^4 \tag{14}$$

Thus, for matched conditions, halving the spot size increases noise by a factor 16.

Eq.(10) in Eq.(13) gives

$$N = \left[\frac{V_n}{ARB(dD/L)^2} \right] T^2 \exp(B/T) \tag{15}$$

Therefore, for a given application,

$$N \propto T^2 \exp(B/T) \tag{16}$$

Fig.4 illustrates the rapid increase in noise with decreasing target temperature for a typical pyrometer. It is evident from the foregoing that choice of target spot size and minimum measuring temperature is of great importance. Overspecification of either parameter will severely compromise system performance.

The effects of defocus upon spatial fidelity are small and can usually be ignored. For moderate departures from focus, spatial sensitivity becomes weighted towards the view axis, which tends to offset loss of fidelity associated with larger viewed area on the target surface. See Fig.5 for a typical example, and the Appendix for a simplified treatment of defocus.

Peak temperature measurement is highly susceptible to errors due to hot particle interference, necessitating the application of statistical sampling (Ref.3) or dual spectral (Ref.4) techniques. The advent of digital engine control units can be expected to make practical the use of such techniques in flight.

In applications where the pyrometer scan is from the leading edge towards the trailing edge, peak temperature usually occurs at the leading edge. For average rotor temperature measurement, an effective emissivity of unity can be assumed with an error unlikely to exceed 5%. However, the emissivity at the leading edge will, in general, not be unity and its value must be known if true peak temperature is required. For engine development this is of great importance, but for flight control an observed temperature difference, peak-average, is usually accepted as adequate. While the difference will not be correct in an absolute sense, an increase from normal values is a clear indication of blade overheating and once it has exceeded acceptable levels an appropriate allowance can be made in the control signal, or control can be switched from average reading to peak reading.

RADIATION INTERFERENCE

A single waveband pyrometer measures the spectrally-integrated radiation field at its collection lens. In the absence of polarization effects, the instrument cannot distinguish between emitted and reflected radiation. Consequently, the intense radiation associated with hydrocarbon combustion can cause serious positive errors in indicated blade temperature, especially when straight-through burner geometry is employed.

Accurate calculation of the errors is made difficult by the complex internal geometry of a turbine engine and by fluctuations in flame size, position, temperature and emissivity. Measurements based upon dual spectral pyrometry reported by Atkinson and Guenard (Ref.4) indicated maximum errors of 50-100 K with first stage blade pressure surface viewing. Other view positions were not reported. Their results agree with those reported by Douglas (Ref.3), who compared single waveband measurements with a discrete burner switched on and off, again viewing first stage pressure surface.

Flame radiation reflected from first stage suction surface will be diluted in intensity by the view factor between this surface and the adjacent pressure surface of the neighboring blade, and by the reflectivity of the suction surface. A simple model in which the blades are represented by parallel plane surfaces yields view factors typically in the range 0.21 to 0.07 corresponding to a midspan position, and trailing edge view position (the latter is an over-estimate due to blade curvature). If blade reflectivity is assumed to be perfectly diffuse, with typical value 0.15, the product of view factor and reflectivity becomes $3.2 \times 10^{-2} - 1.1 \times 10^{-2}$, that is, a worst case result for suction surface viewing of about 3% of the effect at the pressure surface. Measurements (Fig.6) carried out on used blades and vanes from a high performance fighter engine indicate that worst case radiation interference at first stage suction surface is approximately 1/30 that at first stage pressure surface, which compares well with the calculated estimate.

While these results should be regarded as only approximate, and are dependent upon specific turbine geometry, it appears reasonable to conclude that even under steady engine conditions first stage pressure surface pyrometry is not a practical proposition unless flame radiation correction methods can be employed. Conversely, first stage suction surface viewing may be considered free of serious errors under steady engine running and it follows that second stage viewing will similarly not be subject to significant errors.

Concern about aftward movement of the flame front during rapid throttle maneuvers has spurred development of dual spectral techniques for flame correction. Such difficulties with second stage viewing have not been reported, and the need for corrections will probably be restricted to first stage pyrometry. The principle of the dual spectral correction method is as follows.

A pyrometer operating at wavelength λ produces a signal

$$V = \epsilon F(\lambda, T) \tag{17}$$

Radiation leaving the surface of a turbine blade comprises emitted radiation due to the blade surface temperature plus radiation originating from other hot components and reflecting off the blade. Reflectivity is the complement of emissivity and the observed signal is

$$V = \epsilon_b F(\lambda,T_b) + (1-\epsilon_b) \sum_i \epsilon_i U_i F(\lambda,T_i) \tag{18}$$

Thus large reflected contributions give large positive errors in indicated temperature.

In a gas turbine there are five major sources of radiation:-

(i)   the target blade
(ii)   the neighboring blade
(iii)   static vanes
(iv)   combustor wall
(v)   flame

Sources (ii)-(iv) involve temperatures similar to the target blade, giving only moderate reproducible positiv errors that can be evaluated and allowances made. The flame, being considerably hotter than the blade, is a source of intense radiation, and fluctuates in position, shape, size and temperature. By employing two thermometer channels operating at different wavelengths the following relations are obtained

$$V_1 = \epsilon_b F_1(T_b) + (1-\epsilon_b)\epsilon_f U F_1(T_f) \tag{19}$$

$$V_2 = \epsilon_b F_2(T_b) + (1-\epsilon_b)\epsilon_f U F_2(T_f) \tag{20}$$

The view factor U between flame and blade is not predictable due to flame fluctuations. Eliminating U and rearranging gives

$$V_1 - QV_2 = \epsilon_b [F_1(T_b) - QF_2(T_b)] \tag{21}$$

where

$$Q = F_1(T_f)/F_2(T_f) \tag{22}$$

By assuming values for ϵ_b and Q (i.e. flame temperature) this relation can be solved for T_b by generating the calibration

$$F(T_b) = \epsilon_b [F_1(T_b) - QF_2(T_b)] \tag{23}$$

and using $V_1 - QV_2$ as the signal.

Alternatively, the relation may be rearranged as

$$V_1 - QV_2 - \epsilon_b [F_1(T_b) - QF_2(T_b)] = 0 \tag{24}$$

and solved by iteration.

A third method is to use look-up tables stored in the engine control computer, relating the difference between indicated temperatures T_1 and T_2 to the appropriate correction.

All these methods rely upon the flame creating different errors in the two channels. It is important to note that if the flame contribution becomes a large fraction of the total signal, the method becomes less effective. For example, if in Eq.(19) and Eq.(20) the contributions are

$$V_1 = 1 \text{ (blade)} + 1 \text{ (flame)}$$

$$V_2 = 1 \text{ (blade)} + 1.3 \text{ (flame)}$$

and if

$$Q = 0.75 \text{ (a typical value)}$$

then $V_1 - QV_2 = 0.275$, and the method becomes one of small differences between large signals.

The choice of viewing position is critical. Serious loss in correction accuracy occurs when the reflected energy results in more than about a 50 K error, which may restrict first stage flight pyrometry to blade suction surface. The need for correction techniques will depend upon flame movement during flight maneuvers and this is yet to be determined. Finally, it is to be noted that flame radiation effects are far more severe for ratio thermometry (typically six times worse) than for single waveband thermometry. The ratio technique is therefore restricted to second or lower stage viewing.

OPTICS CONTAMINATION

A turbine pyrometer is designed such that only one optical surface, the outer surface of the collection lens, is exposed to the turbine environment. This surface must be maintained deposit-free, or correction methods employed, if accurate temperature readings are to be maintained. Typical requirements for time between overhaul are several hundred hours (military applications) and several thousand hours (civil). Lens contamination is of crucial importance since it constitutes a fail-dangerous (low reading) error mode. Three candidate approaches are being evaluated; air purging, ratio correction and hot lens.

The air purge approach utilizes the Coanda layer attachment effect whereby compressor air is directed over the lens surface to prevent particulate matter in the turbine main flow from coming into contact with the lens. An important feature of the purge is its scrubbing action for removal of ignition phase deposits which may form during engine start-up. The purge flow is directed via a sight tube through a continuous annular slit coincident with the edge of the lens surface as shown in Fig.7. Consequently a layer of high velocity gas is formed across the lens domed surface, separating near the center of the lens. This geometry may be considered as constituting a 3-dimensional curved wall jet. Provided the potential core extends to the center of the lens, surrounding gases in the sight tube cannot make contact with the lens. Further, in the potential core, the finite entrainment capacity of the jet does not result in mixing with the ambient gas.

Results to date have been very encouraging on engine test beds but no more than adequate on flight applications. A purge improvement program utilizing computer modelling of particle trajectories is planned and includes a study of the effects of contaminants in the purge flow itself.

The ratio correction method (Ref.5) utilizes two different wavebands and relies upon lens contamination being spectrally gray and therefore attenuating both spectral signals equally. A ratio of the signals is then unaffected by contamination, and may be used as a reference against which the individual spectral signals can be compared. If blade temperature measurement is carried out by one of the spectral channels, with a correction applied according to the result of the reference comparison, the high speed and sensitivity of single waveband temperature measurement can be exploited. The reference comparison may be carried out at a fixed indicated ratio temperature, preferably high in the measuring range where signal strengths permit better accuracy in the ratio signal. Fig.8 illustrates the technique.

Peak to peak modulation is relatively unaffected except under very extreme lens contamination, thus the method preserves individual blade information. It should be noted that the ratio reference method is not suitable when flame radiation is present in the pyrometer signal, consequently it is likely to be restricted to second stage measurements. Ratio pyrometry has been successfully demonstrated on industrial power generation turbines (Ref.6).

By operating the pyrometer lens at a sufficiently high temperature it is possible to burn off carbonaceous deposits. This self-cleaning action is an attractive proposition but places severe thermal demands upon pyrometer design. Carbon oxidation rate is insufficient at 750 K (that is, the arrival rate exceeds the oxidation rate), but laboratory tests at 1000 K have shown rapid and complete cleaning of engine-contaminated lenses. An existing study program is expected to result in a successful design but this is yet to be proved. In addition, long term build up of contaminants not removed by oxidation will need to be assessed.

MEASURING RANGE

If it were possible to extend reliable temperature measurement down to perhaps 400 K, important gains such as hot start detection and removal of thermocouple sensors could be realized. However, silicon photodiodes have spectral response (~1 μm) far removed from the radiation emission peak for such low target temperatures (~8 μm) and give insufficient signal below about 900 K.

A complete review of alternative detectors is beyond the scope of this paper, but mention of several important limitations will be made.

The military electronics component operating range of 218 to 398 K restricts the choice of detector, and is a major factor in the selection of the silicon photodiode. Vibration levels (typically DC-20 kHz, 20 g) demand rugged detector construction. Conventional glass fiber optics with good transmission up to 1.2 μm have proved to be extremely reliable under the vibration levels and 580 K operating temperature typically encountered in flight. There are reasonable prospects for suitable silica fiber light guides, extending transmission to 2 μm, and with about twice the transmissivity of glass at 1 μm. However, beyond 2 μm, it appears unlikely that in the near future suitable light guides will become available. Above 1 μm, H_2O, CO and CO_2 absorption bands must be taken into account. By way of example, Fig.9 shows H_2O absorption for the second stage power turbine of an advanced technology fighter engine, calculated from the data of Ref.7.

In summary, it appears that the silicon photodiode will remain the optimum choice for the foreseeable future, but possibly with silica displacing glass as a light guide material. Using the best available silicon photodiodes (0.6 amps/watt response at 0.95 μm) a reasonable expectation would be an extension of measurement down to about 800 K, at least for rate of temperature change measurement.

CONCLUSION

Pyrometer interchangeability requirements can be met by reference to the fundamental properties of silicon photodetectors, and the use of algorithms. This approach is applicable to filtered or unfiltered detectors. The need to match spatial and electronic resolution should be recognized. Selection of target spot size is extremely important in relation to signal noise. If peak blade temperature is required only in the higher portion of the measuring range, signal fidelity will be limited by achievable amplification bandwidth.

Dual spectral pyrometry is effective for removal of flame radiation effects at first stage blade pressure surfaces on engine development test beds, provided corrections do not exceed about 50 K. If the technique cannot be successfully deployed in flight on the next generation of fighter engines, pyrometry will very probably be restricted to first stage suction surface or second stage viewing.

Ratio pyrometry is restricted to second stage viewing but offers the prospect of lens contamination tolerant operation, and may gain favor for this reason.

The silicon photodiode is unlikely to be displaced as the optimum detector in the near future. Continuing improvements in radiation energy collection efficiency and photosignal amplification offer prospects of a moderate extension of the lower temperature measuring limit down to about 800 K.

17-6

REFERENCES

1   Blakemore, J.S., Solid State Physics, 2nd edition, W.B. Saunders & Co., 1974, p.306.

2   Stones, R.H., The Fidelity of Turbine Blade Profiles Achieved by Infrared Pyrometry, Tempcon, London, June 1983.

3   Douglas, J., High Speed Turbine Blade Pyrometry in Extreme Environments, ASME Measurement Methods in Rotating Components in Turbomachinery, 1980.

4   Atkinson, W.H. and Guenard, R.N., Turbine Pyrometry in Aircraft Engines, Electro '78, Boston, May 23-25, 1978.

5   Beynon, T.G.R. and Kirby, P.J., British Patent Specification No. 8505631, Improvements Relating to Radiation Thermometers: Monochromatic/Ratio Thermometer, March 1985.

6   Kirby, P.J., Zachary, R.E. and Ruiz, F., Infrared Thermometry for Control and Monitoring of Industrial Gas Turbines, ASME 86-GT-267, to be presented at ASME Gas Turbine Conference and Exhibit, Dusseldorf, June 8-12, 1986.

7   NASA Handbook of Infrared Radiation from Combustion Gases, NASA SP-3080, Marshall Space Flight Center, 1973.

Fig.1   Spectral Distribution of Silicon Detector Photocurrent
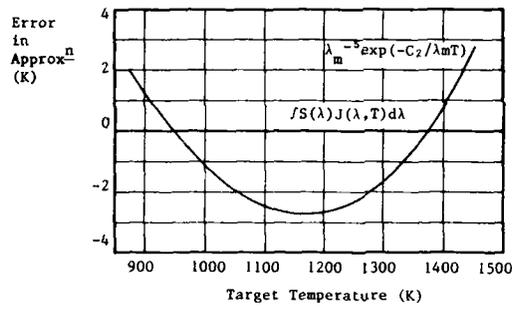
Fig.2   Monochromatic Approximation of
Pyrometer Response
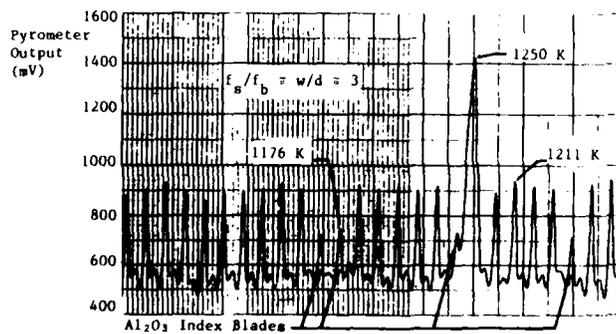
Fig.3   Individual Blade Resolution
(Courtesy Garrett Turbine Engine Company)
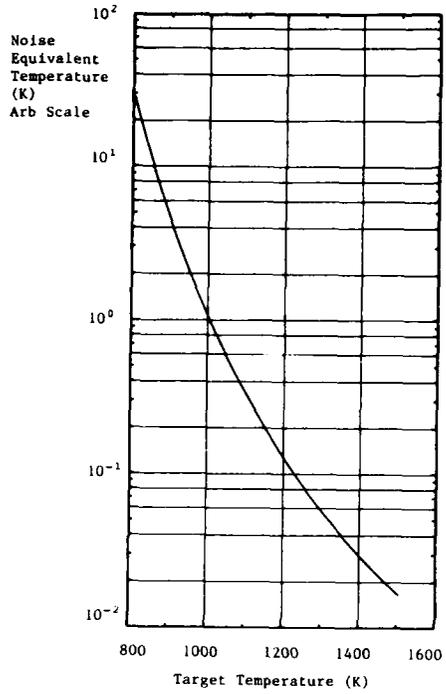
Fig.4 Pyrometer Noise as a Function
of Target Temperature
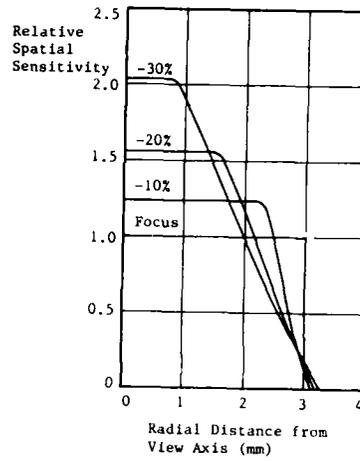
Fig.5 Pyrometer Defocus
Effect
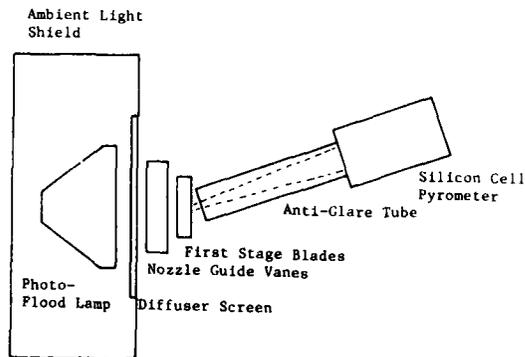
Fig.6 Schematic of Radiation Interference Measurement
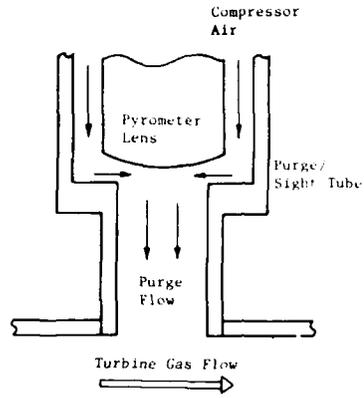
Fig.7 Sectional Schematic of Coanda Purge
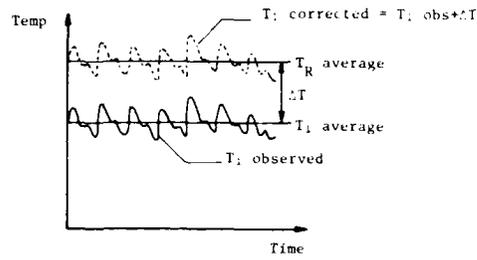
Fig.8 Ratio Reference Method for
Overcoming Lens Contamination
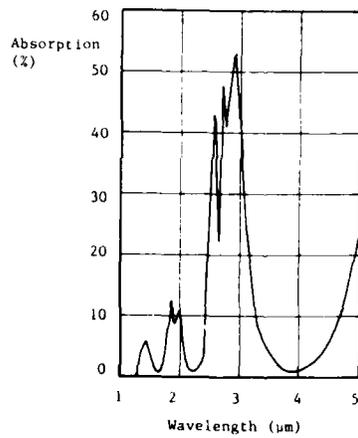
Fig.9 Typical Water Vapor
Absorption for an
Aerospace Turbine

APPENDIX

THE EFFECT OF DEFOCUS ON PYROMETER SPATIAL SENSITIVITY

Nomenclature

A_1	lens stop area
A_2	focused target spot area
J	radiative flux
r_1	lens stop radius
r_2	focused target spot radius
S(r)	spatial sensitivity

The following analytical model enables changes in spatial sensitivity to be determined for view distances less than the focus distance. The target surface is assumed to be a uniformly bright Lambertian radiator. Cosine effects, lens aberrations and wide angle response are ignored.

Target at Focus Distance

The flux collected by any elemental area of the lens from any elemental area of the target is JdA_1dA_2/L^2. The total flux collected from any dA_2 is therefore JdA_2A_1/L^2, giving a top-hat spatial sensitivity profile. See Fig.A1 and A2.

Target at Less Than Focus Distance

The limits over which the lens collects flux from any point can be visualized by noting that only rays passing through the point, the lens stop and the focused target area will be collected. Refer to Fig.A3.

From postion P_1 flux is collected over the entire lens. From P_3 no flux is collected. At P_2 the portion of the lens stop collecting flux is defined by the area of intersection of two circles; the lens stop, and a circle (radius r) formed by the locus in the lens stop plane of a line pivoted at P_2 and moved around the circumference of the focused target spot. See Fig.A4.

Spatial sensitivity is proportional to A/ℓ^2, thus A requires defining as a function of ℓ and z, (Fig.A5).

From Fig. A5 it can be seen that

$$r = r_2\ell/(L-\ell)$$

and from Fig.A3

$$\Delta = r_1 - z + \ell(r_2-z)/(L-\ell)$$

Note that z_{max} occurs when $\Delta = 0$,

that is,

$$z_{max} = [\ell r_2 + r_1(L-\ell)]/L$$

Case I, $r \geqslant r_1$

If the intersecting circles are represented as in Fig.A6, then intersection occurs when $x = x_i$, that is when

$$(|r_1^2 - x_i^2|)^{\frac{1}{2}} - (|r_1^2 + \beta^2|)^{\frac{1}{2}} = 0$$

where

$$\beta = r - \Delta + r_1 - x_i$$

which is solved by iteration.

The area of intersection is then given by

$$A = \int_{x_i}^{r} (r^2-x^2)^{\frac{1}{2}}dx + \int_{\beta}^{r_1} (r_1^2-x^2)^{\frac{1}{2}}dx$$

Note that when $\Delta \geqslant 2r_1$ the complete lens stop is illuminated. Note also that the above expression is valid only when A does not include more than half the lens stop area, i.e. the limiting condition is given by Fig.A7, and by

$$r + r_1 - \Delta \geqslant (r^2 - r_1^2)^{\frac{1}{2}}.$$

When

$$r + r_1 - \Delta < (r^2 - r_1^2)^{\frac{1}{2}}$$

we have the condition shown in Fig.A8 and the area of intersection is given by

$$A = \int_{x_i}^{r} (r^2-x^2)^{\frac{1}{2}}dx + \frac{1}{2}\pi r_1^2 + \int_{0}^{-\beta} (r_1^2-x^2)^{\frac{1}{2}}dx$$

Performing the integrations gives,

$$A = \begin{cases} [(r^2+r_1{}^2)\arcsin 1]-\alpha, & r-\Delta+r_1 \ge (r^2-r_1{}^2)^{\frac{1}{2}} \\ [\frac{1}{2}\pi r_1{}^2-r^2\arcsin 1]-\alpha, & r-\Delta+r_1 < (r^2-r_1{}^2)^{\frac{1}{2}} \end{cases}$$

where

$$\alpha = r^2\arcsin(x_i/r)+x_i r(1-x_i{}^2/r^2)^{\frac{1}{2}}+r_1{}^2\arcsin(\beta/r_1)+r_1\beta(1-\beta^2/r_1{}^2)^{\frac{1}{2}}$$

Case II, $r < r_1$

This condition is dealt with by interchanging r and r_1 in the above expressions, noting that when $\Delta \ge 2r$, the lens area illuminated is πr^2.

Fig.A1

Fig.A2

Fig.A3

Fig.A4

Fig.A5

Fig.A6

$$y = (r^2 - x^2)^{\frac{1}{2}}$$

$$y_1 = [r_1^2 - (x - r - r_1 + \Delta)^2]^{\frac{1}{2}}$$
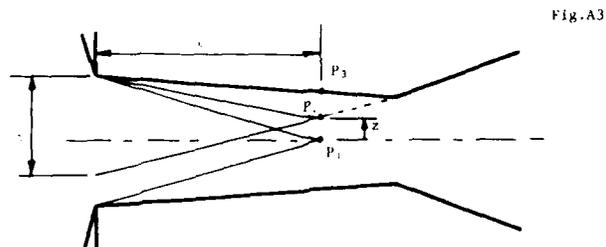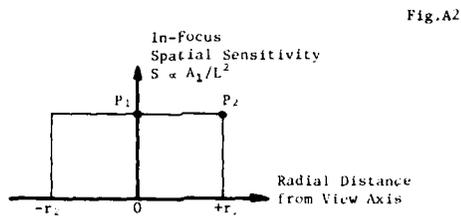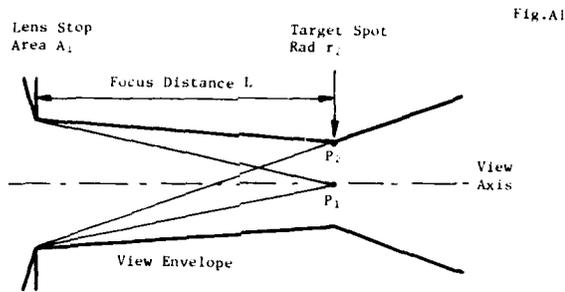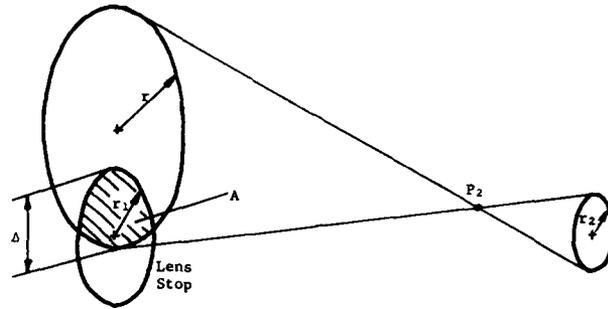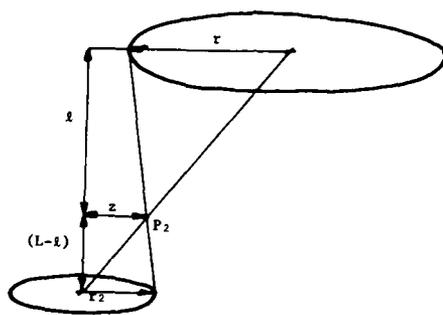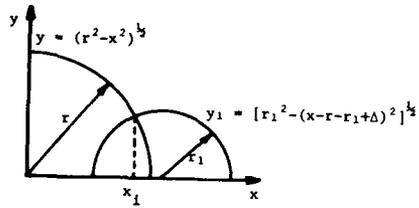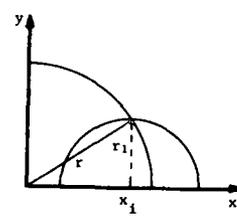
Fig.A7
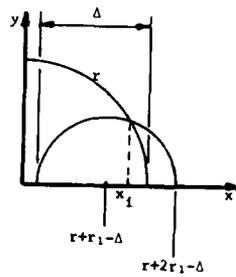
Fig.A8

DISCUSSION

E.A.Pinsley, US
Have you observed variations in temperature readings over long periods of time due to accumulation of deposits causing emissivity variations?

Author's Reply
During engine burn-in, an oxide layer forms on the turbine blades, increasing in thickness with time. This increases the blade emissivity to an asymptotic value, for which the oxide layer is sufficiently thick to be opaque to the pyrometer. Since the pyrometer operates at 1 µm, a very thin oxide layer is sufficient to be opaque, and forms very quickly at the turbine operating temperature. Deposits from external sources (sodium for example) have been reported, but this type of problem with regard to pyrometry appears to be restricted to marine and industrial applications. No difficulties with aero engines have been reported so far, but recognition of possible difficulties is important. Work on industrial turbines suggests that there are good and bad blade viewing positions with regard to deposits — this iis mentioned in ref. 6.

J.Chivers, UK
With the increase in popularity of the use of thermal barrier coating on the surfaces of first stage turbine blades, what effect is this likely to have on future applications?

Author's Reply
Conventional thermal barrier coatings are polycrystalline and are dielectrics and therefore exhibit emissivity as a volumetric effect, as opposed to metals for which it is a *surface* effect. Coating emissivity therefore depends not upon surface finish, but upon grain boundary, impurity and bulk absorption effects. There are three cases:—

(a) Coating completely transparent at 1 µm wavelength — this has no effect upon pyrometer readings.

(b) Coating sufficiently thick to be considered opaque — the pyrometer will collect radiation from within a volume of the coating and transpose this into a bulk averaged temperature.

(c) Coating partially transparent — the pyrometer temperature reading will be intermediate between the coating surface temperature and the temperature of the coating/blade interface.

In terms of *reproducibility*, pyrometry is not likely to be degraded in quality as a control technique by the application of thermal barrier coatings.

D.Davidson, UK
Do you have any evidence from engine companies that they are using the 'hot blade' detection capability of pyrometers to remove substandard blades from the engine on production pass-off?

Author's Reply
Only for industrial gas turbine production. I believe that Ruston Gas Turbines, UK, are using pyrometry for this purpose. Reference to validation of pyrometry for detecting partially blocked or undersize cooling channels can be found in: 'Radiation Thermometry Applied to the Development and Control of Gas Turbine Engines'; T.G.R.Beynon, in Temperature, Its Measurement and Control in Science and Industry, 5, Part 1, pp 471—477, Amer. Inst. Physics, 1982.

D.Davidson, UK
What measures do you take to minimise the effects of hot particle radiation from the signals?

Author's Reply
I know of two techniques:—

(a) Application of slew rate limiting (SRL) to the pyrometer output signal. This is effective for average rotor output signal. This is effective for average rotor blade temperature, but individual blade information is lost. We have provided systems to several aero engine manufacturers with SRL incorporated into the pyrometer detector/amplifier module.

(b) Multiple sampling followed by statistical processing. This more sophisticated method, enables blade profiles to be recovered in the presence of hot carbon particle interference, but requires accurate (1) timing of the sampling relative to the rotational speed of the rotor. An example of this approach is given in ref.3. The sampling and processing can be readily carried out by digital engine control units — there appears to be no advantage in incorporating it into a pyrometer.

H.May, GE
In what range lie the values of the average emissivity of the blade?

Author's Reply
New unused blades of high nickel alloy have emissivity at 1 µm wavelength of typically 0.7. During initial engine

running, an oxide layer forms on the blades, rapidly reaching sufficient thickness to be opaque at 1 μm wavelength. The emissivity is then approximately 0.85

Thermal radiation collected by a pyrometer consists of two components:—

(a)   Radiation emitted by the target blade plus radiation originating from other sources and *reflecting* off the target blade.

(b)   The neighbouring blade is a significant source of reflected radiation, and results in an *effective* emissivity for the target blade of about 0.85 at the leading edge, increasing to about 1.15 as the pyrometer scans towards the trailing edge. For average rotor temperature, a value of unity can be assumed, with an error unlikely to exceed 5%. However, for thermal mapping, allowance must be made for the variation of effective emissivity along the pyrometer scan. For a detailed discussion of this, see ref.3.

TURBINE ROTOR BLADE MEASUREMENTS USING INFRARED PYROMETRY

BY

W. Koschel, D. Salden and T. Hoch
Institute for Jet Propulsusion and Turbomachinery
Technical University of Aachen
Templergraben 55, D-5100 Aachen

SUMMARY

An infrared pyrometer system has been developed for the noncontacting measurement of metal temperatures on turbine rotor blades. The system with a high bandwidth ratio, a small target size and a high signal-to-noise ratio meets the requirements for the accuracy of temperature measurements to be performed on small gas turbines running at high speeds. The system set-up is described and special features of the probe head design, the lay-out of the detector/amplifier unit and the signal processing are discussed in detail. Results of the automated calibration of an infrared pyrometer system concerning the influence of variations in the target-to-lens distance, in the lens stop diameter and in the observation angle on the detector signal output will be reported herein. Finally some results of temperature measurements obtained for the cooled rotor blades of a small research turbine are presented.

NOMENCLATURE

a	sighting distance	x	target diameter
a_o	nominal target-to-lens distance	α	observation angle
f^o	focal distance	λ	wave length
K	Kelvin	ϕ	focussing lens diameter
LE	leading edge		
R	resistance		Subscripts
t	time		
T	temperature	K	calibration
TE	trailing edge	L_o	lens aperture
U	detector output voltage	0°	at zero observation angle
		i,j,k	numbering of variables

1. INTRODUCTION

The determination of the thermal loading of gas turbine blades implies the accurate knowledge of the actual temperatures in the vane and blade material. During research and development work thermocouples are often used on turbine or engine test rigs to get the necessary information. But there are some shortcomings, if thermocouples are applied especially to rotor blades:

- limited number of measuring positions within the blade,
- reduced mechanical strength of the blades due to the inserted thermocouples wires,
- inaccessibility of the critical locations like the trailing edge region,
- insufficient time response and
- difficulties concerning the signal transmission from the rotating system.

The concept of the noncontacting opto-electronical temperature measuring system based on the infrared pyrometry avoids a lot of these disadvantages.

A strong effort has been made in the development of infrared pyrometers for jet engine applications starting in the late sixties [1], [2], [3]. Since then they have become a reliable tool for the inflight blade temperature monitoring [4] and even for diagnostic purposes during the experimental evaluation of blade cooling designs [5],[6]. Though the principle of measuring the emitted radiation of a hot spot by means of a photovoltaic detector seams to be rather simple, there are many problem areas associated with the application of an infrared pyrometer system to the temperature measurements of rotating turbine blades. The system design must satisfy the needs for a fast time response at high blade passing frequencies and sufficient spatial resolution of the observed target spot in relationship to the viewed blade width in order to make it to an accurate instrument in the turbine research. A high bandwidth ratio which is defined as the ratio of the amplifier bandwidth to the blade passing frequency must be accomplished to record the actual signal rise [7]. Due to the physical limitations of silicon type detectors which are commonly used for turbine blade pyrometer systems there are some difficulties to fulfil these requirements especially in the case where rotor blade temperatures have to be measured in small turbines at a low temperature range.

The present paper reports on an infrared pyrometer system which has been developed for the purpose of scanning rotor blade temperatures in small research turbine stages running at high speeds. Special emphasis has been laid upon the following aspects

- miniaturisation of the probe head,

- high bandwidth ratio
- good signal-to-noise performance at target temperatures below 600° C for a silicon type detector/amplifier unit and
- automated calibration of the lense/detector system.

Some details of the work carried out to fulfil these requirements are presented and discussed. A lot of experience has been gained with this infrared system during the last years applying it to temperature measurements on a cooled rotor blade of a model turbine. Some of these results are reported herein.

2. DESCRIPTION OF EQUIPMENT

2.1 SYSTEM

The infrared pyrometer system consists of
- the optical probe head,
- the detector/amplifier unit and
- the signal processor.

Fig. 1 shows the block diagram of the system set-up. The thermal radiance of the target spot, which has typical diameters ranging from 1.0 to 1.5 mm, is received by a focussing lens in the probe head. In most of the applications the housing with the detector/amplifier unit is placed far from the test engine environment. The signal between the probe and the detector is then transmitted by a fibre optic light guide. A correction amplifier and a magnetic shutter controlled diaphragm are used for the zero adjustment of the signal. Further system components are the target positioner with a light source, the temperature control unit for the detector cooling and the blade selector unit, which allows the scanning of the individual rotor blades of the test turbine. The signal processing is performed by means of a transients recorder linked to a computer.

2.2 PROBE DESIGN

The design of an infrared pyrometer probe for gas turbine applications includes the following items:

- design of the optical lens system and the deviation mirror if needed,
- cooling of the probe and its support and
- air purging to avoid fouling of the observation window.

These problems must be solved individually for each test case accounting for the possibilities of accessibility in the turbine stage. In Fig. 2 two different designs of probe heads are shown. The first type, which has been used in engine tests, has a water-cooled probe shaft with an outer diameter of 9 mm. The second probe with a head diameter of 7 mm has been designed for small turbine applications. This probe is additionally equipped with an air purge for the observation window. These probes can be positioned by means of steppermotor controlled supports.

2.3 DETECTOR/AMPLIFIER UNIT

If it is supposed that the analog to digital signal conversion does not account for invalidations, the system accuracy is determined by the performance of the analog component i.e. the detector/amplifier unit. A maximum signal-to-noise ratio at the photo current conversion, a fast time response, small linear and nonlinear distortions and a sufficient slew rate reserve in order to exclude transient intermodulations at high signal dynamics are the objectives of the detector system design.

The temperature resolution, the measuring accuracy and the lower limit of measurable temperatures depend on the maximum attainable signal-to-noise ratio. Therefore a lot of effort has been made to optimize the detector system.

Silicon type photodiodes are usually applied in turbine infrared pyrometer systems. Fig. 4 shows black body radiant emittance at different temperatures and the spectral sensivity range of silicon diodes. The silicon-PIN-photodiode, which is used in the presented system, has the following advantages over the PN-type diodes:

- faster time response
- higher quantum efficiency,
- smaller junction capacitance,
- smaller back conductance and
- a higher possible reverse voltage resulting in a lower capacitance modulation.

Typical properties of a silicon PIN-photodiode with an integrated infrared filter can be drawn from table I.

The quality of the signal-to-noise ratio and the dynamic sensor performance depend strongly on the detector operating mode and the detector circuit. Comparison has been made between conventional photoamplifier circuits and the transimpedance amplification (see Fig. 5). It can be stated that the best results concerning the noise and distortion reduction have been obtained by the choice of a transimpedance photoamplifier. Using this PIN-type diode the dominant noise is produced by the amplifier elements, whereas

Table I

Properties of the used silicon-PIN-photodiode
BP 104, Siemens, with built-in IR-filter

Semiconductor	:	silicon
Type	:	PIN-photodiode
Quantum efficiency	:	92 %
Responsivity	:	0.71 A/W
Peak-wavelength	:	950 nm
Cut-off-wavelength	:	830 nm, 1080 nm
Dark current	:	2 nA (10 V, 25 C)
Rise time	:	10 ns (10 V)
Detector capacitance:		10.8 pF (10 V)
Detectivity	:	5.4×10^{12} cm $\sqrt{Hz}$ /W

the dark current noise is of a minor importance. By a proper selection of low noise ampli-
fiers a high signal-to-noise ratio can be achieved. Fig. 6 shows the detector/amplifier
circuit used in the actual pyrometer system design. A dark current compensation has been
added in order to allow the operation of diodes with a higher dark current in the system
or without cooling. The compensation does not affect the signal-to-noise ratio. This was
achieved by using an extreme high impedance input stage with an effective bandwidth re-
duction and by applying a low noise FET current source. Then the signal is fed to a line
driver buffer amplifier for preserving the dynamic accuracy and the signal-to-noise ratio
at transmission.

The overall system performance can be specified by the following data based on a target
diameter of 1.5 mm:

- noise equivalent temperature: 525 C
- 3 dB bandwidth   : 300 kHz
- rise time   : 1.15 µs
- system detectivity   : $4.7 \cdot 10^{11}$ cm $\sqrt{Hz/W}$

2.4 SIGNAL PROCESSOR AND READOUT UNIT

The subsequent signal evaluation is performed on-line by means of a data processor. The
schematic set-up of the signal processor is shown in Fig. 6. In the first step the analog
detector signal is converted into 512 digital points/curve by a Nicolet transients recorder.

The time window, which is derived from the turbine rotor trigger, can be preselected by
a link between the transients recorder and the data processor. Linearisation and the con-
version of the detector signal output voltages into temperatures based on the calibration
data are performed by the computer. A smoothening of the raw detector signals can be
achieved by applying a sampling method and by using low pass filtering. High sample rates
and a sufficient quantization are needed for minimizing aliasing errors and quantization
noise. The evaluated temperature data can be displayed on a terminal screen or edited by
a printer or a plotter.

3. PYROMETER CALIBRATION

3.1 CALIBRATION PARAMETERS

One of the major problems in the design of the optical system of infrared pyrometers for
turbine blade applications is due to the fact that the sighting distance i.e. the target-
to-lens distance varies while the blade passes in front of the probe head. Variations in
the sighting distance result in changes of the target spot diameter and geometry correspon-
ding to the blade profile shape and in changes of the observation angle. Since these geo-
metrical parameters influence the received radiant energy at a given temperature level
and in consequence the detector output voltage, it is necessary to carry out a calibration
of the infrared pyrometer system.

Fig. 7 shows schematically the interdependencies between the detector output voltage U
and the calibration parameters:

- calibration temperature level T
- measuring distance a and
- observation angle α.

3.2 CALIBRATION SYSTEM

An automated calibration procedure was developed to determine the relationship between
the detector output and the geometrical parameters like the target-to-lens distance, the
observation angle and the target spot diameter at varying temperatures for a given probe
construction. The calibration method is based on a comparative temperature measurement
of an electrically heated strip target equipped with 2 thermocouples. Since the strip
target is made of the same material as the turbine blade the influence of the temperature-
dependent emissivity changes can be eliminated.

Fig. 8 shows the block diagram of the automated calibration system with its main functions.
The probe with the optical system, which has to be calibrated, is mounted on an optical
support which allows a stepper-motor-controlled shifting of the target-to-lens distance

as well as turning the target. The minimum step width is 0.005 mm in the distance variation and 0.02 degrees in the observation angle variation. A microprocessor controls the whole calibration procedure and the acquisition of the geometrical data, of the detector output and of the thermocouple readings. The multiparameter approximation of the measured calibration data is carried out on a central computer. A set of polynominal coefficients is obtained as a result of the calibration, which allows the calculation of temperatures as a function of the measured detector output voltages and of a known target geometry. This approximation method was adopted from the calibration of multi-hole-pressure probes [8].

A view of the calibration place consisting of the measurement console and the stepper motor controlled optical support unit in front of it is shown in Fig. 9.

3.3 PROBE CALIBRATION RESULTS

In Fig. 10 the deviation of the measured temperature indication is plotted as a function of the sighting distance related to the nominal target-to-lens distance at the calibration temperature of 1210 K. The focussing length of the lens amounts to 30 mm and the inlet slot diaphragm has a width of 1 mm. This result indicates that an optical probe design which is relatively insensitive to target-to-lens distance variations can be realized.

The influence of the sighting distance on the geometry change of the viewed target spot is shown in Fig. 11. Though the target diameter increases with the greater sighting distance the sensed radiant intensity remains nearly constant due to the compensating effect of the increasing solid angle.

The calibration system turned out to be a very useful tool in the design process of the pyrometer lens system especially with regard to the selection of the optimum lens aperture. Fig. 12 shows an example of the influence of the lens aperture diameter on the detector output signal. The lens diameter was in that case $\emptyset = 17$ mm. The best signal shape has been obtained by the choice of an aperture diameter of $\emptyset_L = 5$ mm.

A typical result of the observation angle calibration is shown in Fig. 13.

In Fig. 14 the detector output signal is plotted versus the calibration temperature at 3 different amplification ratios for an infrared pyrometer system. The amplification ratio is chosen according to the blade temperature range to be measured.

4. TURBINE BLADE TEMPERATURE MEASUREMENTS

A lot of experience with the infrared pyrometer system has been gained by applying it to a research turbine. The rotor blades of the one-stage axial turbine were equipped with 80 imbedded thermocouples. Thus an excellent comparison could be made between the thermocouple readings and the infrared pyrometer measurements on the blade surface. Fig. 15 shows a view of the turbine rotor from the rear side. Two different types of probes were used in order to measure blade surface temperatures viewing from the front side and the rear side of the rotor.

A typical plot of the blade surface temperature distribution over two blade spacings taken by the rear pyrometer probe is shown in Fig. 16. A sawtooth shape is obtained, which is typical for cooled turbine blades, when looking from the rear onto the profile suction sides. The peak values belong to the trailing edges of two neighbouring blades. By applying the above mentioned smoothening techniques the signal quality can be improved as can be seen from the plotted temperature distribution in Fig. 17.

Finally, a comparison of the blade temperature distributions obtained by the thermocouple measurements and by the infrared pyrometer readings has been made [9]. The temperatures from the infrared pyrometer measurements are slightly higher, which may be explained by the fact that the thermocouples are imbedded below the blade surface. Therefore they must indicate lower temperatures, if the temperature gradient in the material of the cooled blade is taken into account. Hence the agreement between the results of the two different measurement methods can be regarded as excellent.

5. CONCLUSION

Infrared pyrometry has proven its ability to measure blade temperatures on high speed turbines with a high degree of accuracy. During the development work carried out in the last years good progress has been attained concerning the dynamic performance of the detector/amplifier system characterised by high bandwidth ratios and high signal-to-noise ratios in the low temperature range. Improvements have been also achieved in the lens design, in automated calibration methods and last but not least in the signal processing. There are still problems left associated with radiation from combustor liners or from glowing particles in the gas path. In some cases these effects may contribute to considerable errors in the infrared pyrometer readings. Further research work is therefore dedicated to these problem areas in order to establish suitable methods allowing for corrections of these influences.

REFERENCES

[1] Barber, R.: A Radiation Pyrometer Designed for Inflight Measurement of Turbine Blade Temperatures.
SAE-Paper No. 690432, 1969

[2] Mossey, P.W.: Experimental Pyrometer for Turbine Blade Temperature Measurement.
SAE-Paper No. 690431, 1969

[3] Rohy, D.A., T.E. Duffy and W.A. Compton: Radiation Pyrometer for Gas Turbine Blades,
SAE-Paper No. 720159

[4] Beynon, T.G.R.: Turbine Pyrometry - an Equipment Manufacturer's View.
ASME-Paper No. 81-GT-136

[5] H.W. Atkinson and R.N. Guenard: Turbine Pyrometry in Aircraft Engines.
IEEE Convention - "Electro '78".
Boston, USA, 1978

[6] Charpenel, M. and Wilhem, J.: Pyromètre Optique Infrarouge pour la Mèsure des Températures d'Aubes de Turbine.
AGARD-CP 390 on Heat Transfer and Cooling of Gas Turbines, Bergen, Norway, 1985, p. 29-1/29-9

[7] Douglas, J.: High Speed Turbine Blade Pyrometry in Extreme Environments.
in "Measurement Methods in Rotating Turbomachinery",
ADME 1980, p. 335-343

[8] Gallus, H.E. and D. Bohn: Multi-Parameter Approximation of Calibrating Values for Multi-Hole-Probes.
"Measuring Techniques in Transsonic and Supersonic Cascade Flow",
Communication de l'Institut de Thermique Appliquée, Lausanne, 1976

[9] Kühl, W. and U. Stöcker: Temperature Measurement Techniques and their Application on Gas Turbine Rotor Heat Transfer Research,
Heat and Mass Transfer in Rotating Machinery. Proceedings of the International Centre for Heat and Mass Transfer No. 16, 1984, p. 337-350
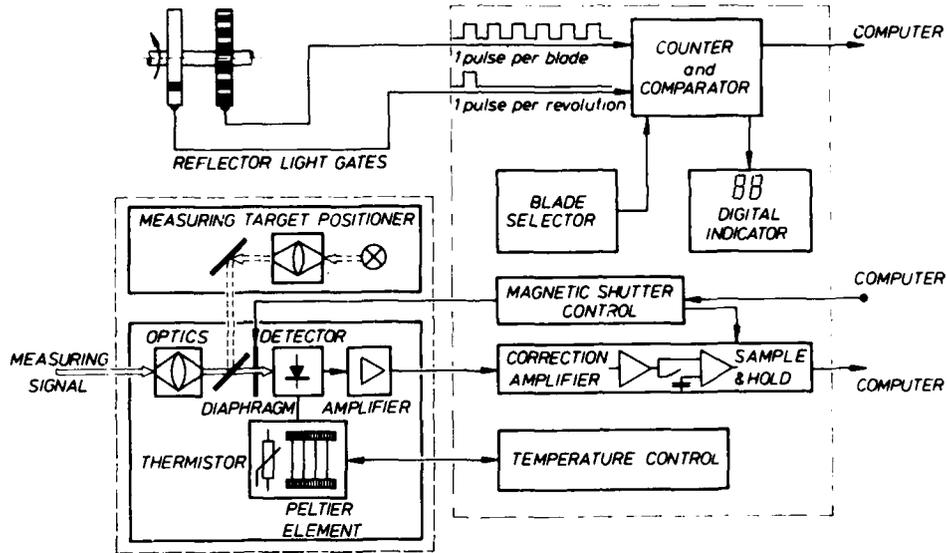
Fig. 1: Block diagram of the infrared pyrometer system
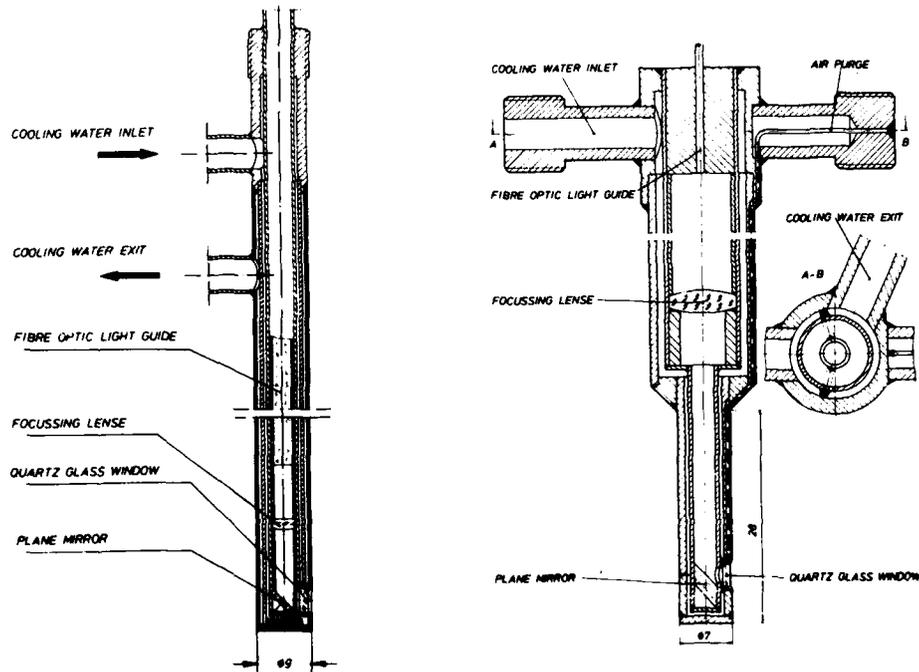
Fig. 2: Examples of probe head designs used for turbine blade
       measurements

SPECTRAL RADIANT
EMITTANCE
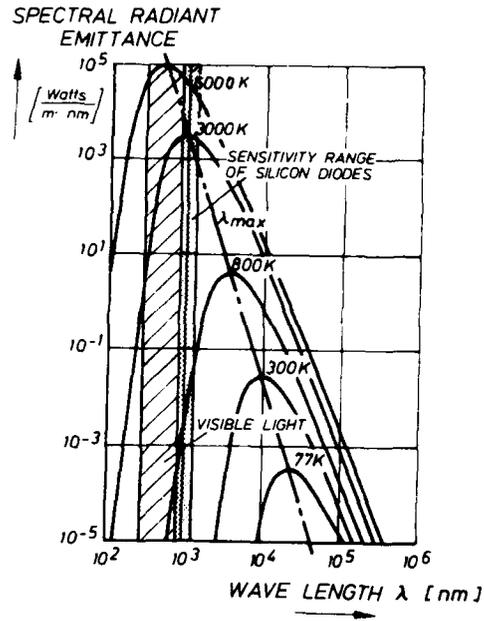
Fig. 3: Spectral radiant emittance from a blackbody source
at different temperatures and spectral response of
silicon diodes
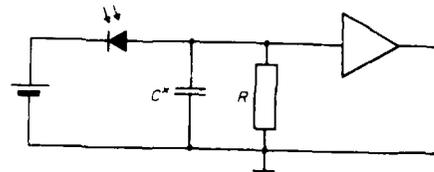
CONVENTIONAL PHOTOAMPLIFIER
(SIMPLE RESISTOR LOAD CIRCUIT)
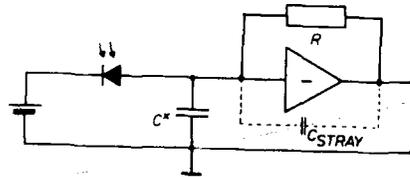
TRANSIMPEDANCE PHOTOAMPLIFIER
(CURRENT CONVERTER CIRCUIT)

Fig. 4: Photoamplifier circuits
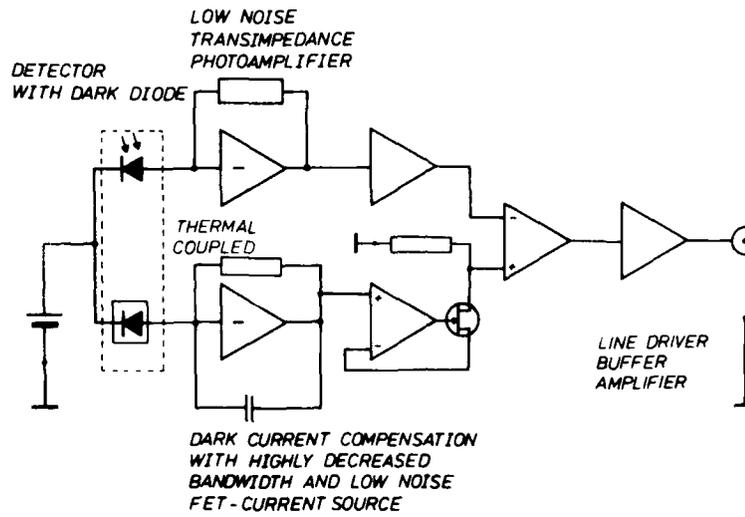
Fig. 5: Block wiring diagram of the detector/amplifier unit
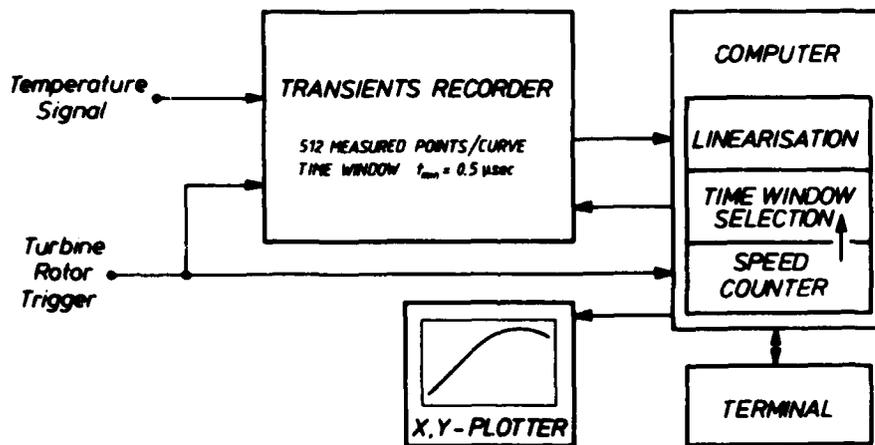
Fig. 6: Schematic signal processing
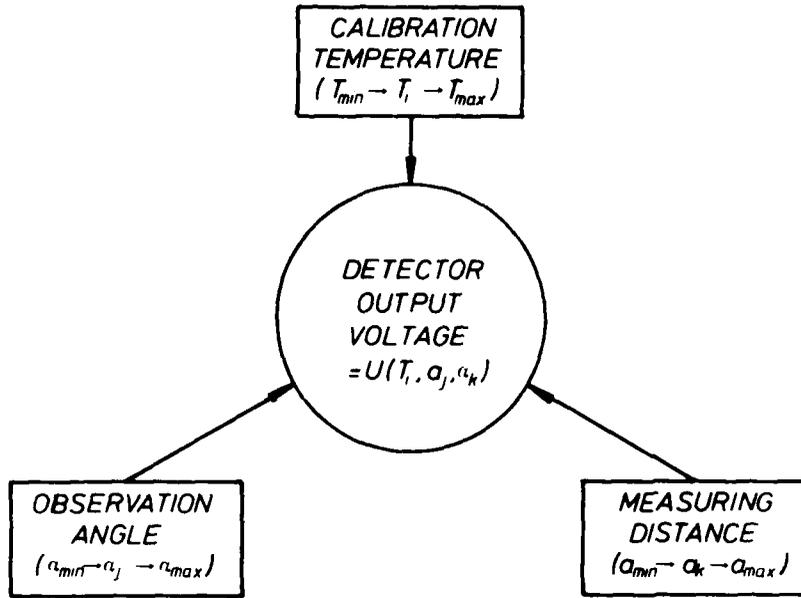
Fig. 7: Interdependencies of the calibration parameters
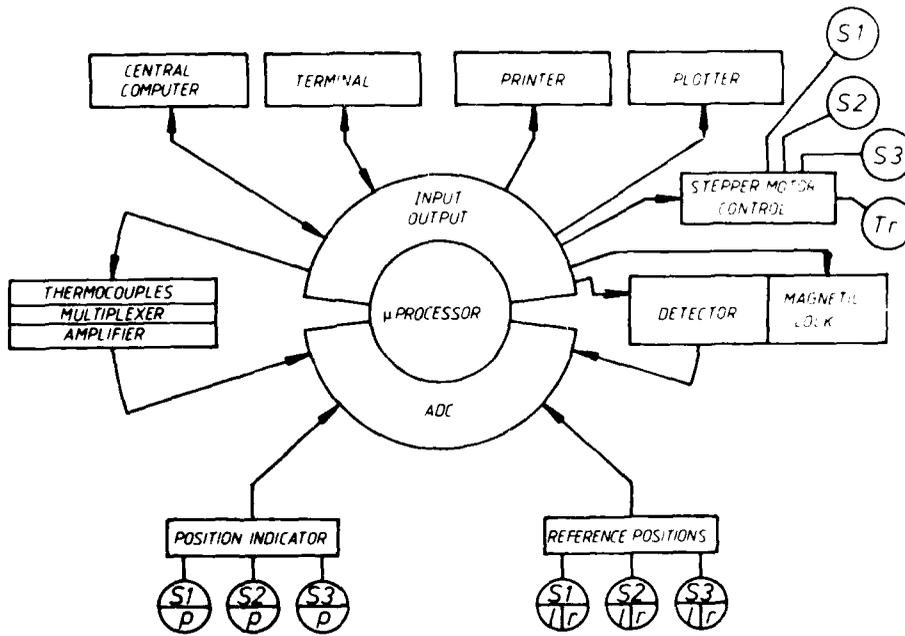
Fig. 8: Build-up of the automated calibration system
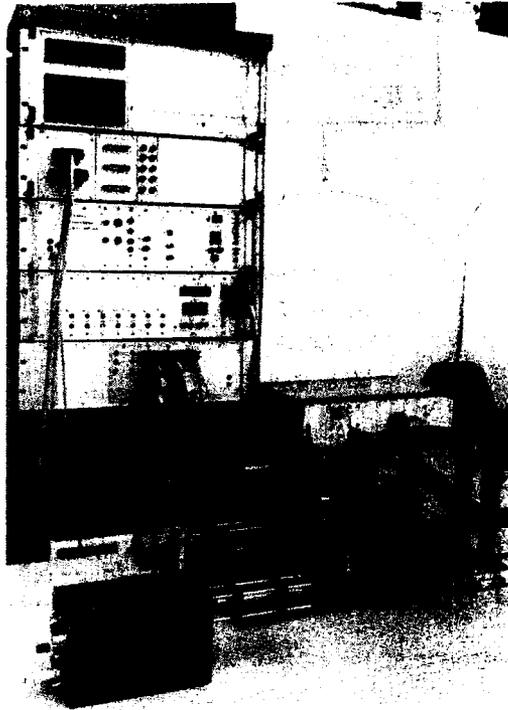
Fig. 9: View of the calibration system

DIFFERENCE IN TEMPERATURE

MEASURING DISTANCE a/a_0
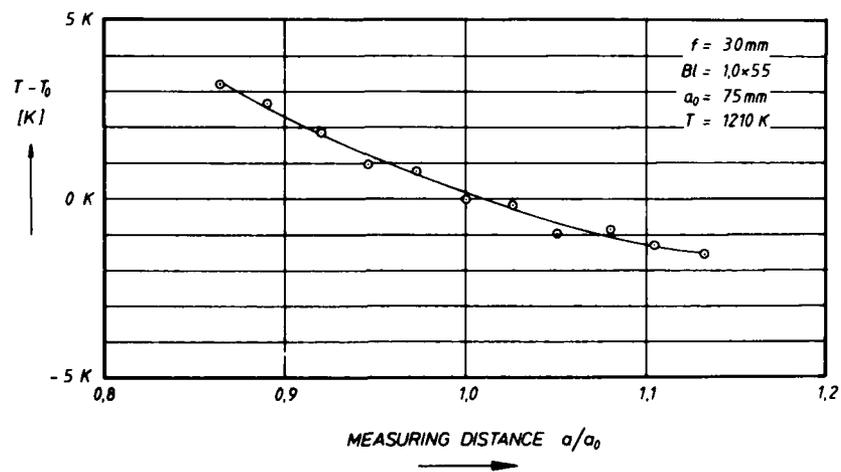
Fig. 10: Influence of sighting distance variations on
temperature indication

DETECTOR OUTPUT SIGNAL

MEASURING TARGET DIAMETER x [mm]
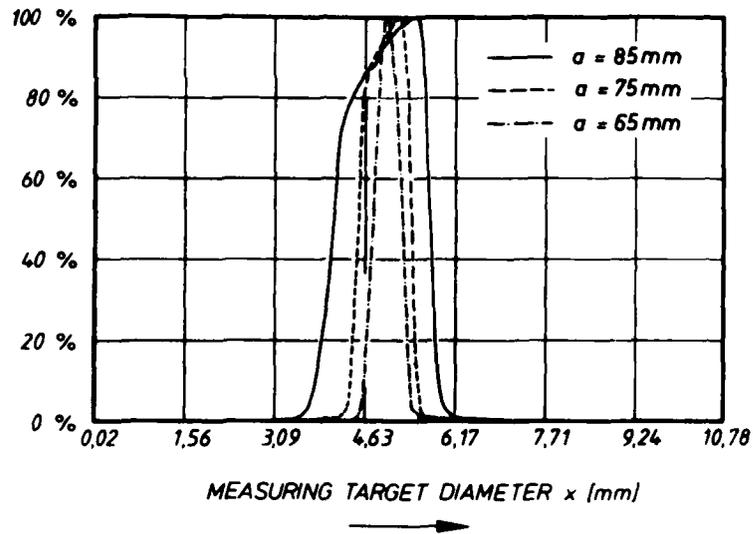
Fig. 11: Influence of sighting distance variations on the
detector output signal

DETECTOR OUTPUT SIGNAL

MEASURING TARGET DIAMETER x [mm]
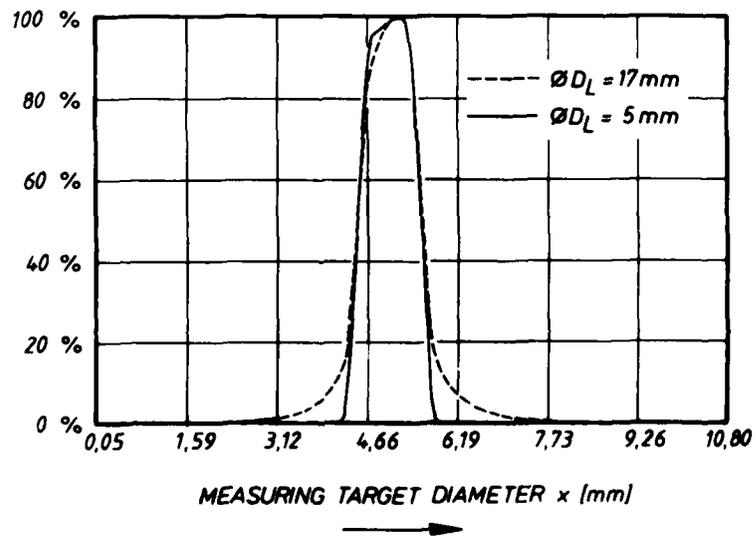
Fig. 12: Influence of the lens aperture on the detector
output signal
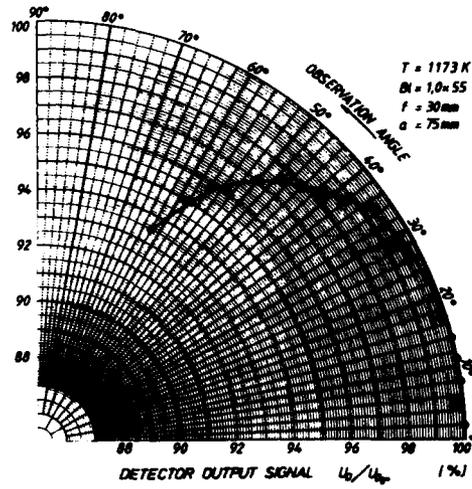
Fig. 13: Influence of the observation angle on the detector
output signal
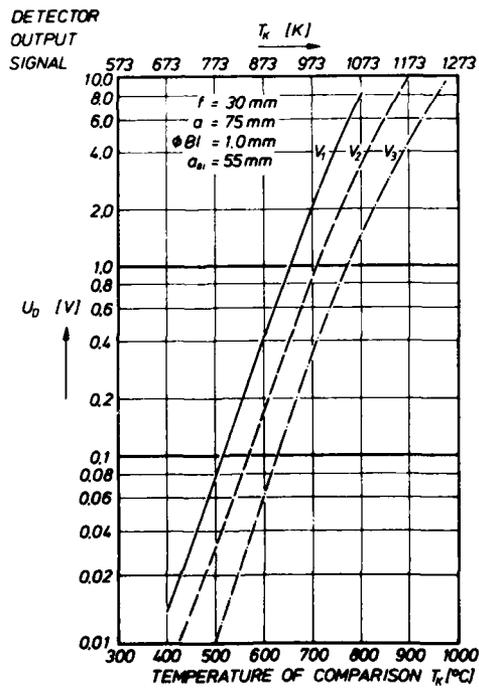
Fig. 14: Typical calibration curves for an infrared pyrometer
system at different amplification ratios
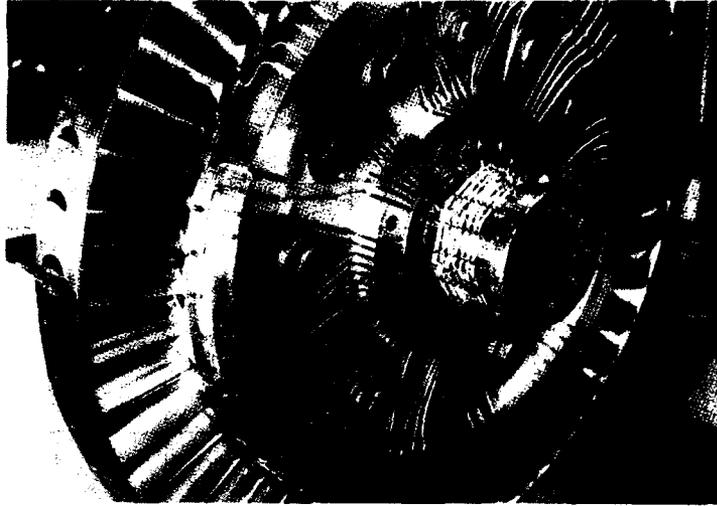
Fig. 15: View of the turbine rotor from the rear side
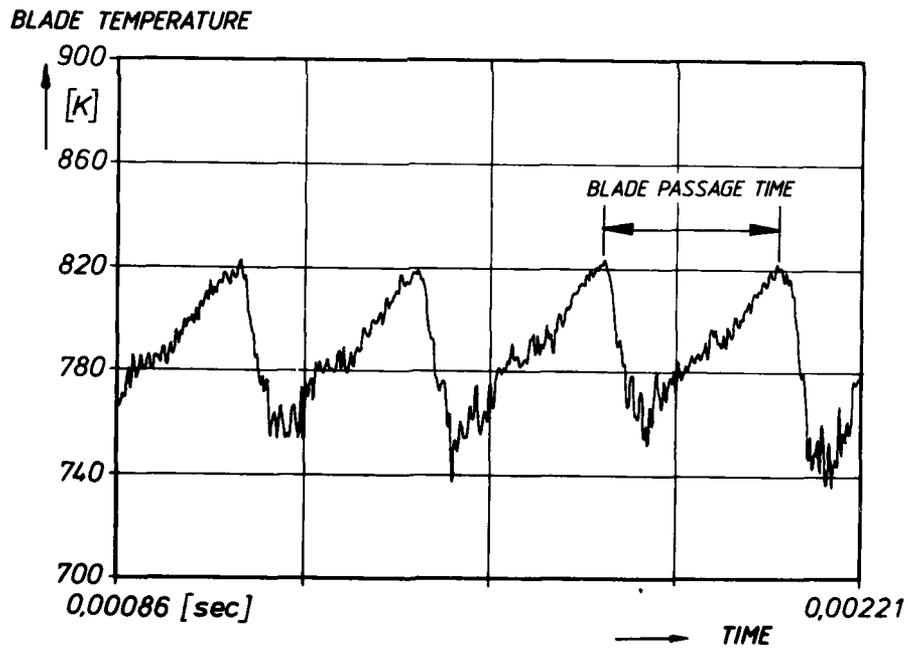
BLADE TEMPERATURE

Fig. 16: Raw temperature signals from a cooled turbine blade
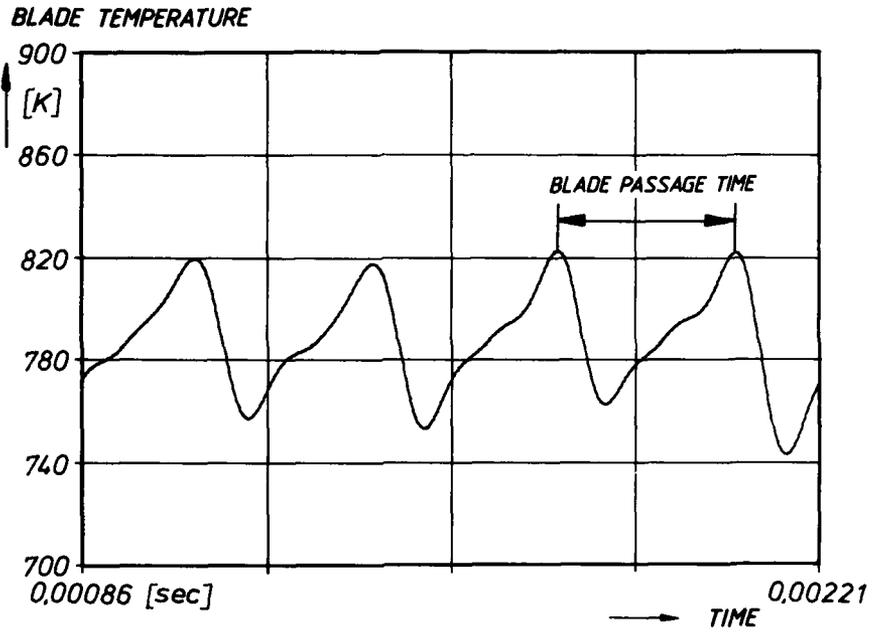
BLADE TEMPERATURE

Fig. 17: Smoothened blade temperature signal
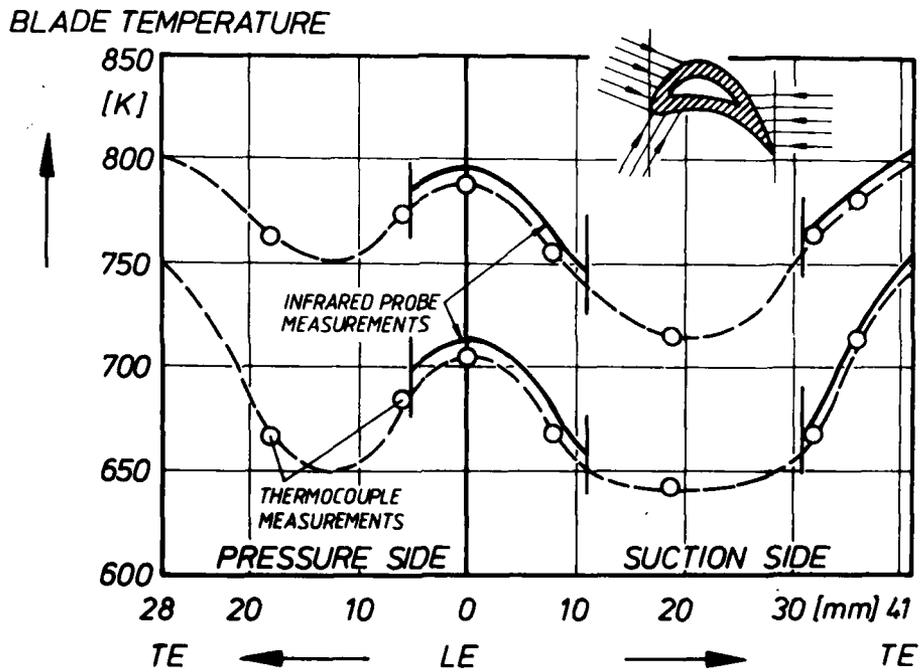
BLADE TEMPERATURE

Fig. 18: Comparison of blade temperature distributions obtained
by thermocouple measurements and from infrared pyrometer
readings

DISCUSSION

P.Kirby, UK

Did you measure effective emissivity which arises from the influence of adjacent blades?

Author's Reply

I try to evaluate it by my numerical methods not by experimental methods.

P.Kirby, UK

How isothermal was the test strip used to check the sensitivity of the pyrometer to the focusing?

Author's Reply

Uniformity of temperature — it has a special shape first. We put on it several thermocouples, then looked at the uniformity of the temperature distribution.

G.Alwang, US

You made corrections for temperature on neighbouring blades by modifying the emissivity on these surfaces, (re: question (1) by P.Kirby), is that correct?

Author's Reply

That case is a residue which has been gained three years ago. At that time we did no corrections but now we have a 2-dimensional model in order to correct for the reflection of the neighbouring blades for a given geometry.

P.Kirby, UK

Did you account for possible effects of surface finish upon the value of emissivity?

Author's Reply

This is a test turbine which has a good surface quality, the same as the heated strip. Later on, we did some measurements using, for example, two colour pyrometry, and so on.

D.Davidson, UK

How much air cooling was applied to your test turbine?

Author's Reply

I must point out that this turbine was only used for basic research. It was not used to develop a higher degree of cooling effectiveness. We looked at the influence of external heat transfer on the rotor blades. Therefore you must consider the cool blade only has a heat 'string'.

E.Pinsley, US

What was the upstream temperature of gas, i.e. was it near the combustor?

Author's Reply

There is a combustor supplied with natural gas upstream, but it is far from the turbine, thus they are separated. There is a chamber between the turbine and the combustion chamber. Therefore the turbine is shielded from radiation coming from the combustion.

J.Allan, US

Was probe looking upstream or downstream?

Author's Reply

The first one looked downstream. For upstream looking probes we use air purging.

J.Allan, US

Did you have trouble with purge?

Author's Reply

No, not at all.

R.E.York, US

The following comments are offered as an aid to the chairman in forming his own summary and I will not feel slighted if

you choose not to include these remarks directly. They are based on my dual experience as a heat transfer research engineer and as head of a controls R & D department. They represent an interesting contrast in how 'temperature' is viewed.

We must be careful to distinguish between the requirements of temperature measuring systems for research and engine development with those for engine control systems. Both the thermal sciences research scientist and the engine development engineers place a high value on temperature accuracy. Accuracy in this context means both absolute levels in mean values of either the gas or blade surfaces, and sufficiently high response to capture temperature variations. However, the controls system engineer does not usually share this concern for either ultimate accuracy or very high response. He needs only a signal related to temperature that has a response rate comparable to engine transients. He is totally comfortable with applying empirical correction factors and lead/lag constants determined during iterative engine development testing. The controls engineer places a higher value on durability, stability over long operating times, reliability, and cost of the 'temperature measurement' system.

These two different requirements should therefore result in quite different system designs. For example, a cryogenically -cooled detector, needed to meet the high sensitivity requirements for R & D, would be ill-suited to the high-temperature environment of a high flight Mach number advanced fighter.

Hopefully, the further development of advanced temperature measurement technology, of either the fibre optic sensor or pyrometry-type, or yet another principle, will allow us to design affordable systems optimized to each application. Such advances are a critical technology need for the high temperature engine cycles of the next-generation of gas turbines.

TECHNICAL EVALUATION REPORT
SESSION IV – HIGH SPEED DATA ACQUISITION AND PROCESSING

by

F.Auzolle
SNECMA
Centre de Villaroche
775500 Moissy Cramayel
France

1. SOMMAIRE

Les présentations qui ont fait l'objet de la 4ème Session du 67ème Symposium ont permis d'illustier de nombreux aspects des techniques d'acquisition et de traitement des données à haute vitesse. Elles ont en particulier mis en évidence l'importance du traitement numérique de l'information et en conséquence sa dépendence des progrès faits dans le domaine informatique.

Des progrès considérables sont encore envisageables et concerneront surtout les vitesses de transfert d'information, les capacités de stockage, les possibilités de calcul temps réel, la souplesse d'utilisation et d'une façon générale, une meilleure ergonomie des moyens. Toute cette évolution devra sa faire de telle sorte que la mise en oeuvre de ces techniques se fasse sans nécessiter de formation trop spécifique du physicien à celles-ci.

2. INTRODUCTION

L'acquisition et le traitement des données à haute vitesse sont devenues deux clefs essentielles du développement des méthodes de mesures les plus évoluées. Ils ne constituent pas une fin en soi pour le physicien mais des moyens indispensables qui, comme le montrent nombre d'exposés, peuvent contribuer à freiner l'efficacité des expérimentations si ils sont insuffisamment pris en compte. Les présentations faites au cours de cette session ont cherché à en montrer de nombreux aspects: quelles fonctions recouvrent ces techniques, quelles en sont les particularités et les limitations, quel gain opérationnel on doit en attendre? Nous sommes en effet dans un contexte où le facteur temps a une très grande valeur: tout progrès fait dans le cycle de traitement des informations sera un atout essentiel pour celui qui aura su l'obtenir.

3. EVALUATION

Sous l'appellation "acquisition et traitement des données à haute vitesse", de nombreuses fonctions sont à considérer. Elles touchent aussi bien au pur traitement des données qu'en l'automatisation des expérimentations, tâches qui contribuent toutes deux à améliorer les qualités opérationnelles des essais de recherche et développement.

3.1 Acquisition/Traitement des données

Pour ce qui concerne cette première tâche, on peut distinguer les fonctions suivantes:

— acquisition des signaux (qui reste encore analogique dans la majorité des cas),

— filtrage puis numérisation,

— stockage-mémorisation,

— traitement avec possibilité de dialogue avec l'expérimentateur. Cette phase peut elle-même être divisée en 2 classes: les traitements qui sont faits alors que l'expérience se poursuit, généralement appelés "temps réel" ou "temps quasi réel" et ceux effectués en temps différé, hors essais,

— présentation des résultats (en recherchant la forme la plus explicite possible d'illustration de phénomènes complexes).

Aucune des fonctions exposées ci-dessus n'est en fait indépendante des autres et la totalité du processus doit être pensée globalement pour arriver à un résultat performant. Il faut souligner que les moyens analogiques ont pratiquement disparu pour laisser la place aux numériques avec la mise en oeuvre, au coeur des systèmes de mesure, de moyens informatiques de puissance croissante: mesure — acquisition — numérisation — traitement sur ordinateurs sont devenus indissociables. Grâce à cette démarche, les méthodes développées peuvent plus facilement passer du stade laboratoire à celui de la Recherche/Développement et enfin à celui de la mise en oeuvre courante, ce qui doit être notre souci permanent.

Plusieurs techniques de mesure peuvent conduire à des situations où l'acquisition et le traitement doivent être effectués à haute vitesse et ceci pour deux raisons principales qui agissent dans le même sens:

— le nombre de capteurs nécessaires à une même expérience va en croissant,

— l'approche "dynamique" des phénomènes physiques est devenue essentielle.

En pratique, la multiplication du nombre de capteurs par la fréquence d'échantillonnage (fonction de la bande passante utile) conduit à des situations difficiles. Les exemples présentés illustrent bien les ordres de grandeur des besoins: 50 000 échantillons par seconde pour le suivi du fonctionnement transitoire d'une turbomachine, 1 million d'échantillons par seconde en aérodynamique non stationnaire des entrées d'air, 300 000 à 2 millions d'échantillons par seconde pour le suivi vibratoire complet d'une machine.

Il faut remarquer également qu'il est de plus en plus rare que les valeurs mesurées soient utilisables telles quelles. Soit elles ne sont qu'une image très indirecte du phénomène physique, soit elles nécessitent pour le moins des corrections et un traitement, souvent statistique, pour être rendues exploitables. L'expérimentateur doit donc posséder une puissance de calcul disponible qui lui permettra non seulement de ne pas travailler en aveugle mais de pouvoir piloter son essai, orienter le programme... Ceci est indispensable vu le coût d'exploitation des lourdes installations d'essais dans lequelles les expériences sont conduites et explique donc l'importance qu'il faut accorder aux possibilités de calcul "temps réel ou quasi réel".

Dans de nombreux cas, un archivage des informations brutes est malgré tout nécessaire et doit être fait sans dégradation ni en amplitude, ni en phase relative. Les raisons principales peuvent être très diverses:

— sécurité (possibilité de rejouer un essai qui ne peut être recommencé),

— impossibilité de transmettre les informations en cours d'essai,

— besoin de faire des traitements paramétriques avec des réglages différents,

— nécessité de pouvoir reprendre un essai bien plus tard à des fins de comparaisons ou avec un nouveau modèle d'exploitation.

Pendant longtemps, pour les types d'acquisition qui nous préoccupent, l'enregistrement magnétique FM a été généralisé (soit IRIG large bande Groupe 1 puis 2, soit FM multiplex). Mais cette méthode limite la précision au mieux à 1% et peut induire des déphasages entre signaux. Aujourd'hui, suivant les cas d'application, des évolutions sont prévisibles, soit vers des solutions purement informatiques avec les progrès faits en matière de mémoires de masse, soit vers le principe de l'enregistrement numérique haute densité. Cette dernière technique mérite une fiabilité de l'enregistrement magnétique classique avec de nombreux avantages liés au numérique dont en particulier la précision, le bon rapport signal/bruit, l'absence de déphasage... Il existe un besoin pour des machines ayant une capacité de plusieurs Mmots/seconde avec des autonomies de l'ordre de 30 min à 1 h. Par contre, une difficulté de taille subsiste et devrait être traitée en priorité: il s'agit de l'absence de standard universellement adopté en la matière. Si en enregistrement magnétique classique, le standard IRIG est remarquablement bien appliqué, en numérique haute densité, les technologies des constructeurs sont différentes, ce qui rend les échanges entre organismes quasiment impossibles à moins de choisir rigoureusement les mêmes matériels. On peut également noter que cette technique présente l'intérêt de pouvoir exister en technologie embarquable, ce qui étend son champ d'application à la totalité des conditions expérimentales.

Une autre voie est celle des enregistreurs de transitoires. Très intéressants car ils combinent en un seul appareil facile d'emploi toutes les fonctions; ils sont cependant souvent limités par le volume total d'information qu'ils peuvent stocker sur chaque voie de mesure. Ils sont très performants sur le plan de la vitesse de transfert et de mémorisation et sous cet aspect dépassent ce qu'on peut attendre du couplage classique d'un ordinateur associé à un disque dur (dans une gamme de prix raisonnable).

Certaines applications du traitement du signal et en particulier le traitement d'images devraient pouvoir trouver des possibilités d'extension avec le développement des disques optiques qui pourront se substituer aux mémoires tampons. Hormis leur avantage sur le plan de la capacité, il faudra ici aussi que des progrès soient réalisés en ce qui concerne la vitesse d'accès.

Les installations de mesure spéciales à hautes performances resteront vraisemblablement en nombre limité dans chaque organisme alors que les sites d'essais sur lesquelles elles doivent être mises en oeuvre sont beaucoup plus nombreux. En conséquence, la puissance d'acquisition et de traitement doit être mobile, disponible et doit suivre les équipements de mesure. Cela signifie qu'il ne faut souvent pas compter sur la puissance d'un gros calculateur central comme il en existe dans tous les Centres d'Etudes. C'est à ce niveau que les progrès faits en matière d'ordinateur et tout particulièrement de processeurs vectoriels devraient ouvrir des horizons nouveaux. Quelques applications sont désormais opérationnelles y compris en utilisant les machines sans faire appel à la bibliothèque standard de traitement du signal. Mais de telles applications sont encore lourdes à développer et des progrès sont indepensables dans la programmation de tels systèmes pour en tirer le meilleur parti sans avoir à utiliser des méthodes de programmation spécifiques et très délicates.

3.2 Automatisation des expérimentations

Dans le cadre de cette deuxième tâche, on peut distinguer les fonctions suivantes:

— pilotage de la machine en essai,

— ajustement des conditions de fonctionnement du banc d'essai et des servitudes,

— télécommande des divers dispositifs de mesure,

— surveillance/alarme et automatisation des procédures,

— et bien entendu, tout ceci étroitement combiné avec l'acquisition de toutes les mesures associées et leur traitement continu.

Sur les moyens complexes, toutes ces fonctions autrefois dévolues à des instruments analogiques et à des techniciens sont désormais gérées par un ou plusieurs ordinateurs. Une des conséquences essentielles est le besoin croissant de traitement temps réel de toutes ces informations. Ceci ne peut être accompli que si les systèmes informatiques ont la capacité de traiter des acquisitions ou rafales d'acquisition prioritaires tout en pouvant imbriquer les autres fonctions de calcul et en particulier celles qui relèvent du temps partagé. Il faut aussi traiter avec un soin particulier la qualité et l'efficacité de la sortie des résultats:

— au niveau des moyens d'essai. Le pilote et l'expérimentateur doivent pouvoir disposer très rapidement (parfois quasi-instantanément) d'éléments clairs et synthétiques permettant de travailler efficacement en toute sécurité.

En plus des moyens alphanumériques, les systèmes graphiques peuvent apporter une aide considérable: pour aider à la conduite du banc en présentant des synoptiques continuellement mis à jour en fonction des conditions d'essais mais aussi en affichant une représentation souvent en couleur des phénomènes physiques étudiés (écoulements, cartes, traitement d'images).

— au niveau de la connexion avec des moyens extérieurs. Il est rare en effet qu'une installation d'essais soit isolée et il faut pouvoir transférer facilement les résultats expérimentaux pour pouvoir les confronter ou le utiliser dans de gros modèles de calcul qui ne peuvent opérer que sur des calculateurs très puissants. Si la bande magnétique numérique est et restera un moyen très utilisé, il y aura de plus en plus de besoins de mise en place de lignes spécialisées à plusieurs Mbits/seconde donc à des cadences du même ordre que celles qui existent en acquisition pure.

4. CONCLUSIONS

La mise au point des turbomachines implique le développement de méthodes de mesures très sophistiquées. Aujourd'hui, pratiquement aucune ne peut être conçue sans prendre en compte dès le début de la conception les possibilités d'acquisition et de traitement des données à haute vitesse. On peut même penser que les progrès en matière de mesure passent dans de nombreux cas par ceux faits en matière en traitement des données. Si les méthodes analogiques ont été largement employées par le passé, elles tendent aujourd'hui à céder le pas aux moyens numériques.

Ces derniers apportent de grands avantages en matière de coût, de souplesse, de qualité des informations, ils posent cependant certains problèmes dont ceux correspondant à la vitesse de calcul et à tout ce qui touche à ce que l'on appelle couramment le temps réel ne sont pas des moindres. Ces techniques étant relativement récentes et fortement dépendantes des progrès faits en informatique, il faudra prendre soin à rechercher des solutions qui permettent une bonne compatibilité, que ce soit au sein d'un organisme ou entre les laboratoires qui sont amenés à travailler ensemble.

Il faut enfin souligner que le développement d'une nouvelle méthode de mesure complexe ne peut être fait qu'au sein d'une équipe pluridisciplinaire qui doit inclure pour le moins avec le physicien, le spécialiste de mesures et l'informaticien qui devront coordonner leurs efforts pour utiliser au mieux les progrès techniques.

5. RECOMMANDATIONS

L'acquisition et le traitement des données à haute vitesse sont des outils essentiels qui peuvent contribuer à réduire la durée des cycles de développement des turbomachines. Afin de les rendre plus performants et d'en étendre le champ d'application, les recommandations ci-dessous peuvent être formulées:

5.1 La numérisation de l'information doit être pratiquée aussitôt que possible. Les capteurs à sortie numérique seront donc très intéressants dans ce but.

5.2 Il est nécessaire de disposer de moyens de stockage puissants, conservant la précision et de vitesse d'accès très élevée. Trois voies doivent être développées:
   — l'enregistrement numérique haute densité,
   — les enregistreurs de transitoires,
   — les disques optiques.

5.3 Dans le domaine de l'enregistrement numérique haute-densité, il est nécessaire qu'un standard soit fixé afin d'assurer une compatibilité entre les divers équipements.

5.4 Il faut pouvoir disposer de moyens de calculs puissants, y compris sur des installations mobiles de taille modeste. Le processeur vectoriel associé à un miniordinateur hote peut constituer une excellente solution. Des progrès restent cependent à faire en matière de facilité de programmation de tels outils.

5.5 Dans de nombreux cas, des calculs relativement complexes sont souhaitables sur le système informatique dédié à l'application expérimentale. Il faut alors que les ordinateurs utilisés permettent l'acquisition et le calcul temps

réel associé de façon prioritaire mais aussi puissent servir simulanément divers autres utilisateurs en temps partagé.

5.6   Il faut développer toutes les méthodes graphiques et d'imagerie qui peuvent permettre d'illustrer et mieux faire comprendre les phénomènes physiques mis en jeu.

5.7   Il faut développer les liaisons numériques à très haut débit, soit pour connecter entre eux les équipements d'une même installation, soit pour pouvoir les relier de façon performante à un système informatique centralisé puissant sur lequel peuvent être implantées des bases de données.

HIGH RESPONSE DATA ACQUISITION SYSTEM

Mark K. Fall, Senior Project Engineer
Henry P. Dress, Senior Mathematician
Naval Air Propulsion Center
P.O. Box 7176
Trenton, New Jersey 08628-0176

SUMMARY

High response instrumentation is used frequently in gas turbine engine testing to determine the transient and dynamic behavior of various engine and component parameters. The Naval Air Propulsion Center (NAPC) enhanced its data acquisition and analysis capability in April 1983 with a new digital high response data acquisition system which eliminated many of the problems inherent with older analog data acquisition and analytical methods. This system has the capability of acquiring multiple parameters simultaneously at an aggregate sampling rate of up to 48,000 samples per second with on-line digitization and real time recording on a private data disk. The NAPC offline data analysis system provides same-day access to the data with the capability to display the data in various tabular and graphical formats. Analytical techniques available include time zero analysis, high pass, low pass, and band pass digital filtering, and power spectral density analysis using fast fourier transformations.

INTRODUCTION

The testing of gas turbine engines often requires determination of the transient and dynamic behavior of various engine component parameters using high response instrumentation. Earlier methods of displaying and analyzing high response data at NAPC were complicated by throughput and accuracy problems. The only available techniques to obtain data were to display analog signals on paper traces in the test cell control room and/or to record the data in analog format on magnetic tape for post-test analysis. The paper traces provided only limited data and analysis entailed the time-consuming study of hundreds of feet of traces. While the analog magnetic tape provided more data channels, the digitization of the analog recording was also a tedious and time-consuming process. Both methods were also beset with many inherent sources of inaccuracy which significantly detracted from the quality of the results obtained.

In order to overcome the deficiencies of these early high response data systems, NAPC developed in April of 1983 a fully digital high response data acquisition and processing system for the engine test cell environment. This state-of-the-art system gives NAPC an accurate and efficient method of acquisition and analysis of high response engine test data. This paper presents information on the background that led to the development of the present system, the capabilities of the system including examples of an actual application, and future directions of high response data acquisition at NAPC.

PREVIOUS HIGH RESPONSE DATA ACQUISITION SYSTEMS

During the investigation of engine stall characteristics or operation with distorted inlet conditions, a limited number of parameters were displayed on paper traces in the control room for immediate cursory analysis, and the primary medium for recording high response data was on an analog FM tape data system. This type of system had been utilized at NAPC, at the Arnold Engineering Development Center in Tullahoma, TN, and at other test centers throughout the aerospace industry.

The procedure to acquire and process data was very complex and had many limitations. As shown in Figure 1, data was recorded on analog tape at the test site for up to 144 data channels, with six to eight hours of data on a tape. The procedure for setting up and calibrating the equipment required one full day of preparation time by skilled operators and project engineers before data acquisition could begin. The data acquired was a merge of high frequency, high response (AC) information from Kulite semiconductor transducers and low response (DC to 0.25 Hz) data from strain gage transducers, combined together to provide the value for each parameter.

After the data was recorded, the tape was carried to the playback device attached to the DEC PDP-11/70 central computer where the data would be digitized. Six channels at a time for a total of 60 channels were read from the analog tape, digitized, and converted to engineering units and stored at 2,500 samples per second on a digital tape for a one second time frame. The data was then read from the digital tape, one frame at a time, and put on a computer disk for analysis. A massive fixed calculation package was used for data interrogation, editing and analysis. Data was adjusted to reference using manually input values. Results available to the project engineer were in the form of graphs, contour plots, and detailed and summary printouts.

The data quality was questionable (about 5 percent full scale) because of the analog taping methods. Most of the final processing and analysis occurred three to six months after the completion of the test, eliminating the capability to reacquire lost or erroneous data. Data on the analog tape contained tape noise, which could not be

effectively eliminated. Data analysis for each frame was limited to a one second time period with no optional calculations and no frame-to-frame comparison.

EVOLUTION OF THE CURRENT DIGITAL HIGH RESPONSE COMPUTER SYSTEMS

A high response data system was required for the Pratt and Whitney (P&W) TF30 Engine Stall Recovery Test that was conducted from May through September of 1983. The TF30 engine was equipped with twelve (12) Kulite transducers to detect instantaneous airflow reversals during an engine stall. Requirements for this test were to acquire data for up to 48 channels at 1,000 samples per second, process data for five to ten second time windows, analyze data with a set of P&W-provided calculations and digital signal analysis software, plot data on an individual and multiple run basis, and accomplish all processing between weekly scheduled test periods. Because of the limitations of the existing analog system, a new system was necessary to meet these specific requirements.

Because of a short lead time, NAPC made use of existing or similar hardware and software whenever possible to eliminate long purchase and development lead times. It was also necessary to utilize key personnel who were most familiar with the standard hardware and software to facilitate the transition to the new equipment and to incorporate required software enhancements.

HIGH RESPONSE DATA ACQUISITION COMPUTER SYSTEM

As shown in Figure 2, the TF30 test program would be able to use the standard NAPC test cell data system to monitor and record most of the engine parameters required for controlling the test conditions. However, the standard system could not take the additional job of acquiring high response data. Therefore, a second data system was developed to run in parallel with the standard system to provide high response capabilities. At first, the data system utilized the computer (DEC PDP-11/55) of the adjacent test cell, but later used its own dedicated computer (DEC PDP-11/70). Three significant modifications were made to accommodate the special high response requirements. First, data was acquired using a newly-purchased NEFF 100 analog to digital converter capable of acquiring up to 50,000 samples per second (five times the rate of the standard NEFF 400), meeting the TF30 requirement 48 data channels each at 1,000 samples per second. Second, this data was digitally written to a dedicated RK07 disk drive instead of the existing magnetic tape drive to meet the required data transfer rates. Each removable RK07 disk pack could hold more than four minutes of data at the required acquisition rate. Third, a specially-modified subset of the standard test cell software was installed on the second computer system utilizing the NEFF 100 and RK07 data disk but retaining as many standard features as possible. Several standard test cell functions were therefore available on the high response data system. Automatic calibration of all high response data channels was completed at the beginning of each test period and periodically during the day as necessary. A real time monitor was available for displaying up to 60 high response converted parameters including calculations. High response steady-state data was acquired using the same parameters acquired on the transient system, averaging 2.4 seconds of converted data and stored on a magnetic tape.

HIGH RESPONSE DATA REPROCESSING COMPUTER SYSTEM

Up to 1983, the central computer system for NAPC was a DEC PDP-11/70. Because of the TF30 reprocessing requirements for special software and multiple run comparison capability, the standard reprocessing programs on the central computer were unable to handle all of the needs of NAPC and P&W project engineers. The hardware and disk space were inadequate for the amount of data required. The program size limitations would have caused the time for processing transient data to increase dramatically. Additionally, the standard software did not support multiple run capability or any of the special P&W required software. Since NAPC had already recognized the deficiencies of the PDP-11/70 as a central computer, a VAX-11/780 central computer was already in place to replace the PDP-11/70. The TF30 project was the first application to be installed on the new central computer. As shown in Figure 3, the only additional requirement was to add an RK07 disk drive on the VAX for high response transient data processing.

Standard steady-state and transient processing programs were first converted to the VAX-11/780 computer. High response processing was developed using the standard system as a guideline, adding improvements and other required capabilities. Steady-state data was read from tape and reprocessed as necessary. Data outputs were printouts, plots, and customer tape copies. Transient data was read from the storage media (magnetic tape for standard transient, and RK07 disk for high response), converted to engineering units, and stored on the system. Up to 20 regular transient and 10 high response transient runs could be saved on the system at the same time, although this could be expanded or decreased if necessary for specific test requirements (the TF30 test required 50 regular runs and 20 high response runs). This data was immediately available to the project engineer and could be printed, plotted (single and multiple runs), filtered, analyzed, and copied to another magnetic tape for the engine manufacturer. Interactive, multiple-user capability was also added to improve engineer and operator efficiency (normally, five terminals can be processing data at the same time).

ADDITIONAL CURRENT HARDWARE FEATURES

Digital high response data acquisition requires high response pressure transducers, signal conditioning, filtering, very fast analog-to-digital conversion and multiplexing, and a digital computer to record all of the data.

Most typically, subminiature Kulite pressure transducers are used as high response total pressure probes. Each Kulite is paired with an accurate pressure transducer such as a Statham or scanivalve channel to measure the absolute pressure at the same station. Signal conditioning for the Kulite transducers is accomplished with Vishay System 2300 signal conditioner and amplifier modules. Additional instrumentation such as speeds, positions or flows are recorded with the high response data system to provide independent analysis capability without reference to the standard data system, as well as providing a synchronization capability with the standard data system if needed.

The effective maximum aggregate sampling rate of the NEFF 100 as controlled by the NEFF 500 microprocessor is approximately 48,000 samples per second after systematic overheads are taken into consideration. For the TF30, the system was configured for 48 data channels at 1,000 samples per second per channel. At this sampling rate, the maximum frequency which can be recorded without aliased signals is just below 500 Hz. To obtain alias-free signals from the Kulite transducers, but still maintain the highest possible frequency response, a 64 channel Precision Filters programmable low pass filter is used. The anti-aliasing filters were set at 300 Hz for the TF30. Other tests have acquired 16 data channels at 2,500 samples per second with the anti-aliasing filters set to 1,000 Hz. The low pass filtered Kulite signals are then input to the NEFF 100 analog-to-digital converter and multiplexer. The digitized signals are transferred directly to the memory of the on-line PDP-11/70 computer by the NEFF 500.

ADDITIONAL CURRENT SOFTWARE FEATURES

Data acquisition capabilities can vary with the requirements for each engine test. High response transient data has been acquired at varying rates - the two presently in use being 1,000 time slices per second for 48 channels, and 2,500 time slices per second for 16 channels. The transient rate can vary from engine test to engine test, but not from day-to-day within an engine test.

Another system capability is a choice of continuously running or circular buffer data storage. This capability allows data to be either continuously acquired until the data run is terminated (capturing all data from the start of the run), or saved only for a fixed period (e.g., the last 10 seconds) of data for every run, no matter how long the run (done with a circular buffer). At the beginning of an engine test, the project engineer can choose which acquisition style and rate is needed to acquire the high response transient data, and these capabilities will be incorporated throughout the entire test.

The high response steady-state data is processed on the VAX-11/780 with all standard reprocessing capabilities. The data is read from the magnetic tape, processed, and recalculated as necessary. The data is then printed in a predesigned format, stored on disk for plotting, screen design analysis, or production of customer tape copies. The data stored in the plotting files is curve fit, and is used for data comparison against new data.

All high response transient data is processed on the VAX-11/780, using the RK07 disk drive for data retrieval. A subset of the raw data is read from the RK07, converted to engineering units, and stored on larger project disks. At this time, data modifications are included in the data stored on disk. More than one run is stored on the disk at the same time, providing a base of transient runs for analysis. Most tests have 10 high response runs of five-to-ten seconds' duration available at any time.

The plotting program for the high response system includes all standard graphics capabilities. Up to six "Y" parameters are plotted against one or two "X" parameters. Predefined page designs, sets, and titles are set up for batch plots for single or multiple runs. Up to five runs can be overlayed on the same graph at the same time, as shown in Figure 4. A time zero offset can be input to the program for each run to allow direct run-to-run comparisons. Scale modification for plot sets is available for easier plot set design.

For data analysis purposes, two software packages have been incorporated into the standard transient plotting programs on the VAX 11/780. The first is a filtering program using a digital approximation of a Butterworth filter. The filtering package produced low-pass and high-pass data using selectable pole and cutoff frequency values for a time range (up to five seconds for high response transient data). This package separated high frequency (high-pass) information from the low frequency (low-pass) data. Both the high-pass and low-pass information are available for analysis. Multiple pass capability through the filtering program is implemented to allow for low-pass filtering at various cutoff frequencies at different time intervals, or band-pass filtering. Band-pass filtering is first filtering with a low-pass filter and then with a high-pass filter at a different cutoff frequency, allowing a limited frequency range to affect the data. In addition, a recalculation option is available to recalculate any parameter which is a function of any filtered parameter.

The other software package is a Fast Fourier Transform (FFT), used to determine spectral characteristics of the data. Data for two parameters for a selected time range (two seconds for high response transient data) are processed and plotted. Calculations available for plotting are power spectral magnitude, cross spectral density, cross spectral phase, and coherence, all at a function of frequency. The frequency range is from zero to half of the data acquisition rate. The density of the resulting plotting points and the magnitude of the spectral densities are dependent on the variables used to run the fast fourier transform software, the number of segments and number of points per segment. This software is used not only to identify the dominant frequency but also to compare two pressure spectral densities.

SOFTWARE DATA CORRECTION METHODS

Various data correction methods for the high response Kulite transducers are incorporated for different engine tests. The TF30 engine test used a combination of Kulite, Statham, and scanivalve pressures. Though the Kulite pressures are very accurate at recognizing high response pressure changes, they drift over time and temperature. To guarantee the most accurate pressure for high response data, corrections for the Kulites are calculated from both the scanivalve pressures and the Statham pressures acquired at the same location in the engine. Curve fits are generated from the steady-state scanivalve data and Kulite pressures. Results of these curve fits are compared to the curves generated from Statham pressures versus Kulite pressures (both acquired on the high response system). There was a negligible difference between the two curves. These curve fits are updated every test period to correct the Kulites to the more accurate scanivalve pressures. These curves stabilize after a few test periods and updates are no longer necessary. When the high response data is processed for the on-line high response real time monitor and for plotting on the central computer, the Kulites are adjusted by these curve fits to correct the absolute pressure characteristics. Also, another correction is calculated to adjust for temperature shifts at the time the data is acquired. During reprocessing on the VAX-11/780, for each Kulite/Statham pressure pair acquired on the high response system, a one-half second average of static data prior to the start of the dynamic condition is calculated. The averages of the Kulites and Stathams are compared and the delta is added to all Kulite samples for that run. This corrects the Kulite for temperature shifts that may have occurred since the last calibration.

TF30 ENGINE STALL RECOVERY TEST

The first use of the new high response system was for the TF30 engine stall recovery test program, conducted at NAPC from May through September of 1983. The purpose of this test was to develop a method for the TF30 engine to self-recovery from what would be otherwise non-recoverable stalls. The goals of this test program were to first determine the pre- and post-stall characteristics of the TF30 engine, and then using this knowledge to develop stall recovery techniques.

The engine used for this test was a P&W TF30-P-414 engine. The TF30-P-414 engine is an afterburning turbofan used in the F-14A aircraft. The compression system consists of a combination three-stage fan and a six-stage low-pressure compressor (LPC) on the low-speed rotor and a seven-stage high-pressure compressor (HPC) on the high-speed rotor. The engine was specially instrumented with six high-response rakes with two rakes each installed at the fan discharge/LPC entry (station 2.4), at the LPC discharge/HPC entry (station 3.0), and at the HPC discharge (station 4.0) as shown in Figure 5.

The high response rakes used for this test were each instrumented with two high response absolute pressure transducers, two low response absolute pressure transducers, and one fast response thermocouple. A sketch of a typical high response rake is shown in Figure 6. The forward and aft facing probes on each high response rake are used for dynamic mass flow measurement. The dynamic mass flow is calculated based on the relationship between the forward pressure (Pf), and the aft pressure (Pa). An example of this relationship, which was formed from steady-state data, is shown in Figure 7.

Using the high response rakes, it was now possible to determine in which component of the engine compression system the stall originates. An example of engine stall where the HPC surges first is shown in Figure 8. As can be seen in the figure, there is an abrupt decrease in pressure at the HPC discharge followed three msec later by an increase in the pressure at the HPC entry. The decrease in HPC discharge pressure and corresponding rise in HPC entry pressure shows that the HPC has surged and stopped pumping. The LPC surge is indicated by a pressure rise at the LPC entry approximately six msec after the HPC surged.

The next part of the analysis is concerned with when and where the rotating stall cell originates. A compressor stall typically starts with a planar axial pressure oscillation of low frequency (2-20 Hz). The compressor therefore experiences a series of rapid flow reversals and recoveries. As the stall continues, a rotating stall cell will form and the planar oscillation will damp out leaving only the rotating stall cell present and the compressor will then be operating at a stall operating point, at which time the compressor is in what is usually termed a non-recoverable stall condition.

Figure 9 is a plot of the two forward facing high response pressures at the discharge of the HPC for the first 0.50 second after the stall has occurred. The traces show that the pressure oscillations for both the pressures are in phase for

approximately the first 0.10 second, therefore indicating that the pressure oscillations were planar. After the initial 0.10 second, the pressure oscillations then are out of phase indicating that a rotating stall cell has developed. The development of the rotating stall cell can be further confirmed by using the fast fourier transform (FFT) routine. The FFT routine is used to determine the phase shift of the pressure oscillations seen by the two pressure rakes. Figure 10 is a plot of the phase shift and power spectral density versus frequency for the portion of the stall in which a rotating stall cell is believed to be present. The phase shift at the 40 Hz frequency is approximately equal to the angular displacement between the two station 3.0 pressure rakes, therefore confirming that a rotating stall cell is present.

It is also possible to determine when the planar pressure oscillations are damped out, leaving only the rotating stall cell. This is done by use of the filtering function. Figure 11 is a HPC entry forward facing pressure comparison of unfiltered, 20 Hz low-pass filtered and 20 Hz high-pass filtered data. The low-pass filtered data shows the low-frequency planar pressure oscillations and the 20 Hz high-pass filtered data shows the higher frequency planar oscillations and the rotating stall. The low-pass filtered data shows that the planar oscillations have damped out completely by 1.3 seconds after the surge occurred.

By using the FFT routine for different time intervals of the stall, it is possible to determine the rotational speed of the rotational stall cell and by comparing this speed to the LPC rotor and HPC rotor speeds, it is possible to determine in which component of the compression system that the stall is generated by. The results of this are plotted in Figure 12, which shows that the rotating stall cell speed is consistently 47 percent of the LPC rotor speed. Therefore, the rotating stall cell is generated by the LPC.

The final part of the analysis of the characteristics of the compression system is the determination of the post-stall operating lines of the LPC and HPC. Figure 13 is a plot of the LPC pressure ratio versus corrected LPC entry mass flow during a stall with no filtering. By using the digital filtering routine to remove the rotating stall cell frequencies, it is possible to then determine the average compressor operating line as is shown in Figure 14. Using the same procedure for the HPC, the results are shown in Figures 15 and 16.

FUTURE CONSIDERATIONS

The future enhancements to the high response data system consist of completing the conversion of the remaining features of the standard test cell data system to the high response system. This would add a failure monitor feature, a real time diagnostic capability and several on-line processing options that would provide more immediate analysis results while still in the test cell. Also, as NAPC remote computers are in a network with our central VAX-11/780 computer system, methods are being investigated to transfer the test cell data to the central computer immediately after each run to perform more complex analysis and send the results back to the test cell.

CONCLUSIONS

In summary, the high response data acquisition system has proven to be highly reliable and has provided quality data for analysis for all engines tested. With the computing power of the VAX-11/780 available for post-processing data analysis, the enhanced analysis capabilities and availability of information for the project engineer after a test period has been significantly improved. The quicker turn around of the data allows timely data analysis of the test results enabling the test program to be conducted in a more efficient manner.
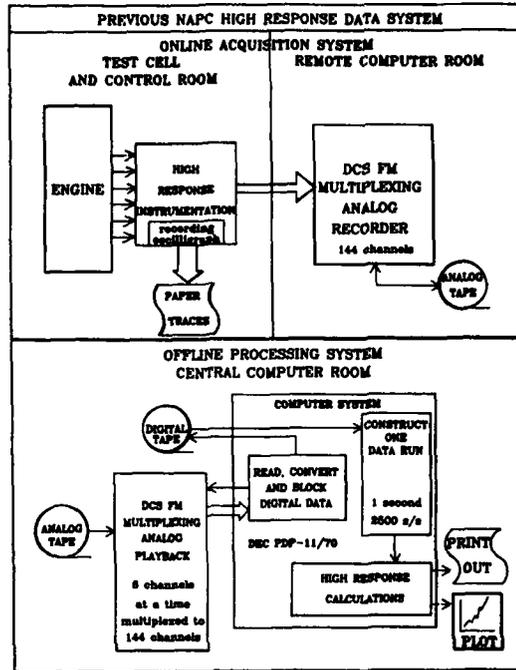
FIGURE 1
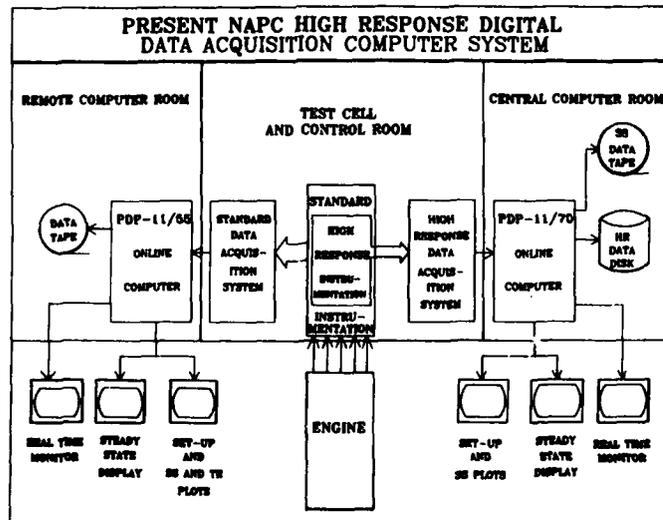
FIGURE 2
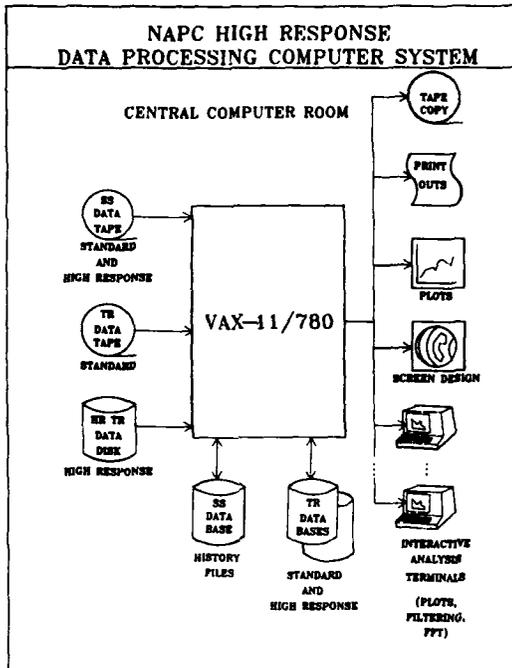
FIGURE 3

FIGURE 4: Comparison of 5 Surges

RUN 1166(□),1167(▲) .1168(+) .1169(x) .1170(◇)

FIGURE 5: TF30 Compression System High Response
Instrumentation Locations
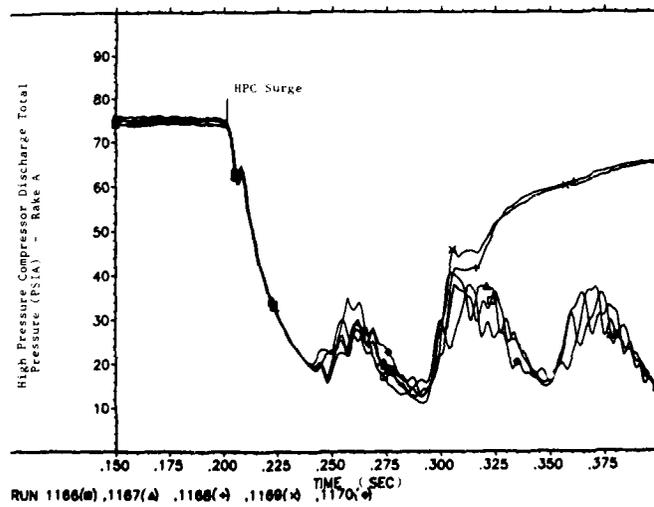
FIGURE 5: TF30 Compression System High Response
Instrumentation Locations
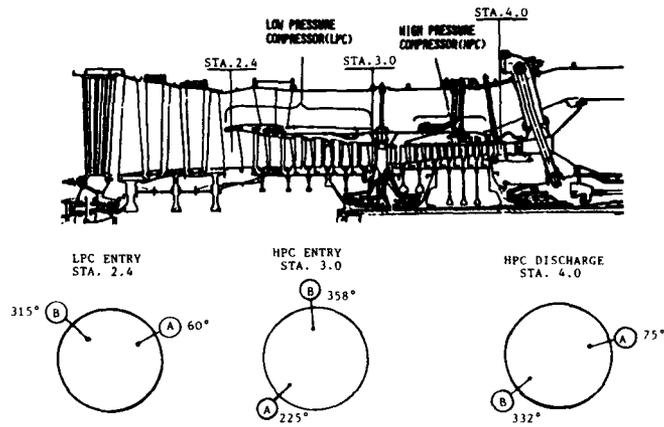
Figure 6: Sketch of a Typical High Response Rake
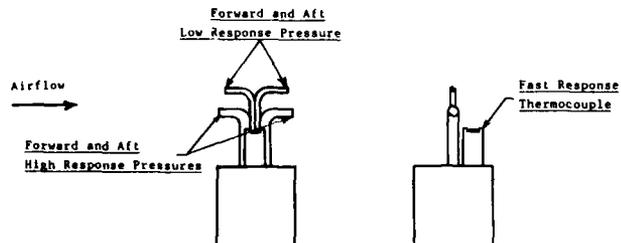
FIGURE 7: Typical High Response Rake
Mass Flow Calibration

$$\sqrt{\frac{P_f - P_a}{P_f}}$$
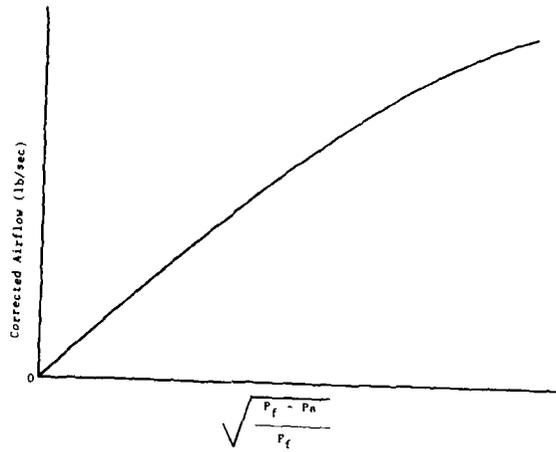
Figure 8: TF30 Compression System
Characteristics at Surge Initiation
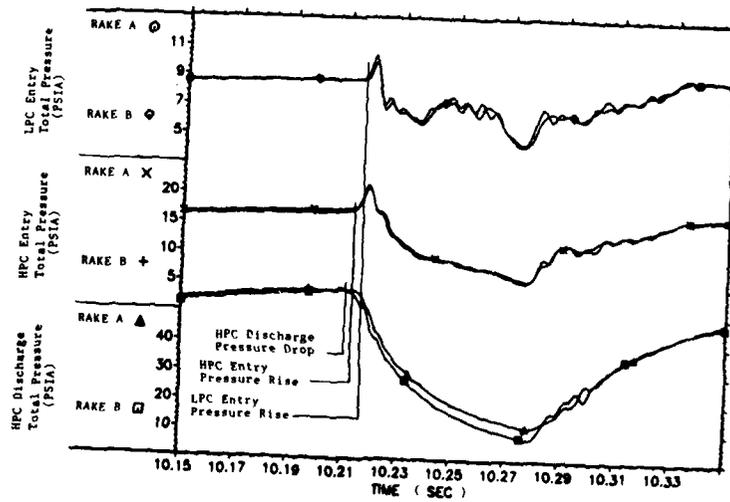
FIGURE 9: High Pressure Compressor Discharge
Pressure During First 0.5 sec of Surge
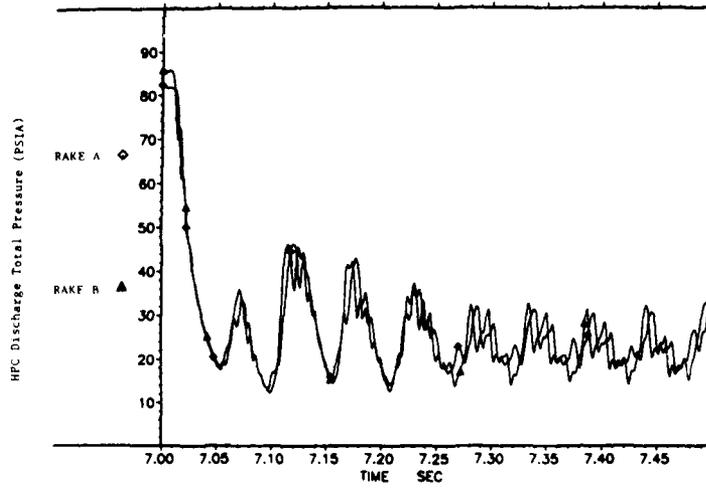
FIGURE 10: Typical Power Spectral Density and
Phase Shift Comparison of Two Pressures
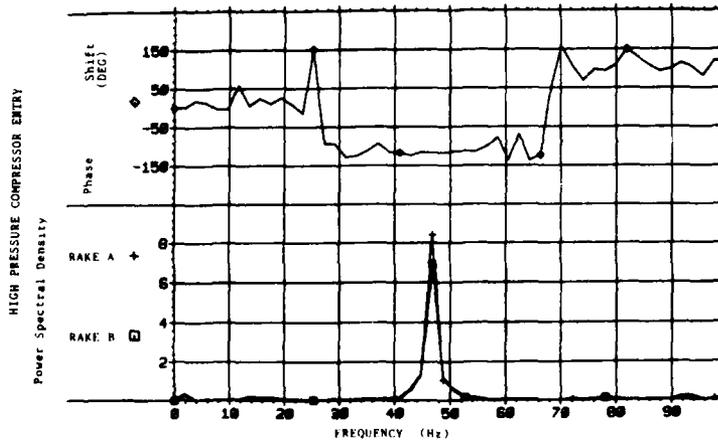
FIGURE 11: Comparison of Unfiltered, Low-Pass Filtered
and High-Pass Filtered Data
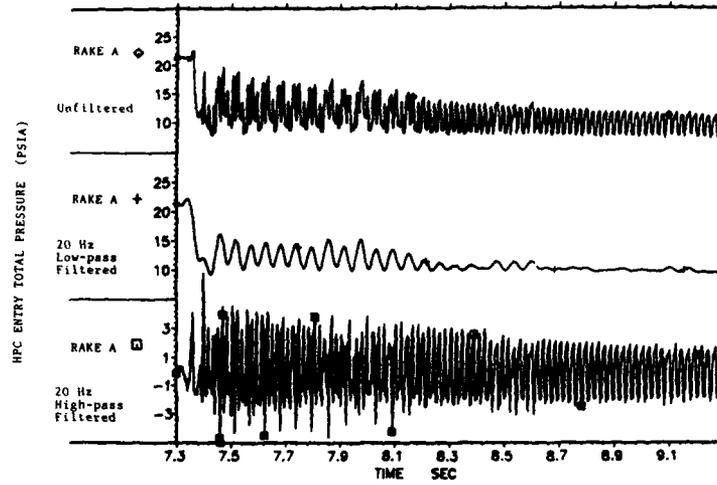
FIGURE 12: Rotating Stall Frequency Versus
Low Pressure Compressor Speed
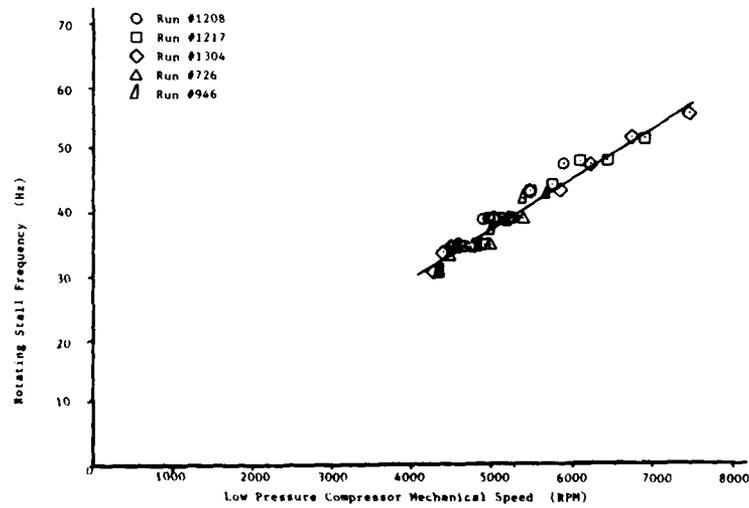
FIGURE 13: Low Pressure Compressor Operation During Surge,
Unfiltered Data
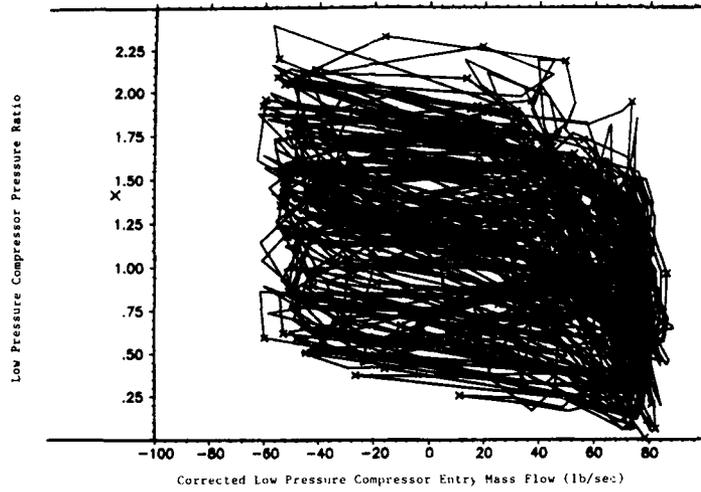
FIGURE 14: Low Pressure Compressor Operation During Surge,
Low-Pass Filtered at 20 Hz.
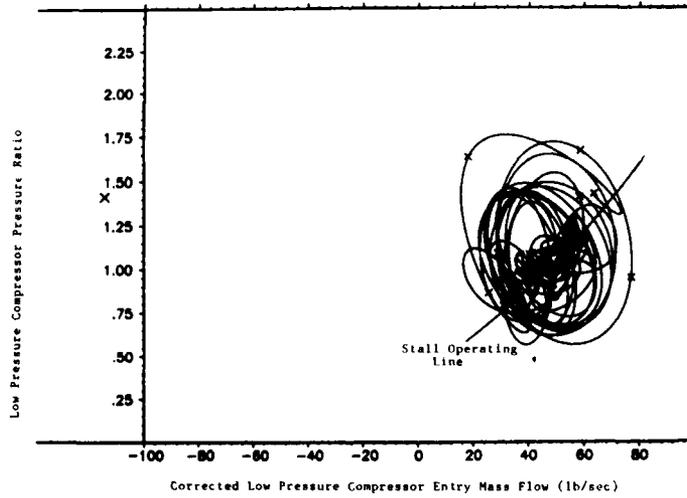
FIGURE 15: High Pressure Compressor Operation During Surge,
Unfiltered Data
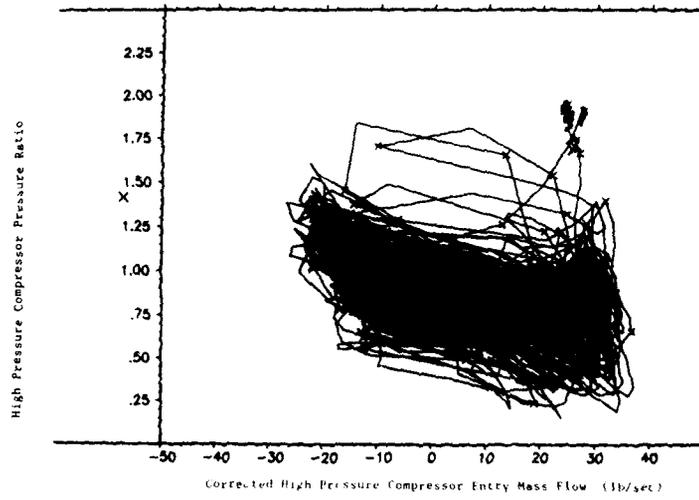
FIGURE 16: High Pressure Compressor Operation During
Surge, Low-pass Filtered at 20 Hz
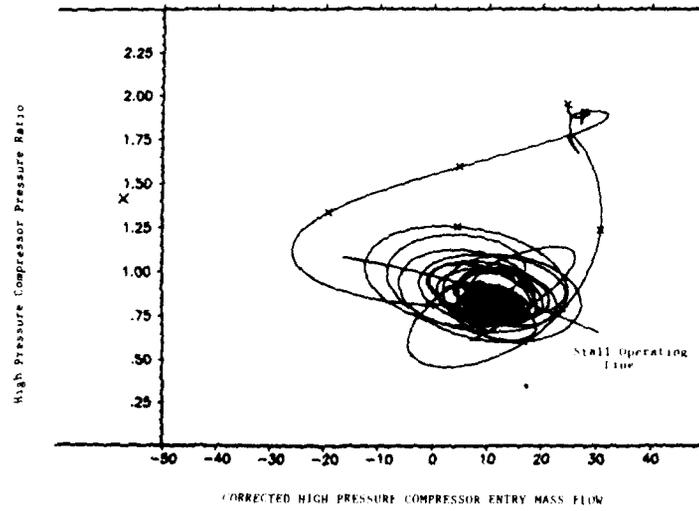
DISCUSSION

D.Davidson, UK

What was the frequency response of the stall probe that you used and how did this compare with the engine stall frequencies?

Author's Reply

The high response probes had frequency response greater than 500 Hz and the engine stall frequencies were less than 300 Hz.

R.Demers, US

What did you do to take into consideration the time skew of your data?

Author's Reply

The analog to digital processing utilised a parallel sample and hold technique to eliminate time skewing concerns.

R.Wallace, UK

How do you transfer data from the PDP to the VAX system?

Author's Reply

The disk RKO2 on the PDP-11 is used to store the primary data. After the test, the data is transfered on a magnetic tape over the VAX system.

ACQUISITION AND ANALYSIS OF DYNAMIC ROTATING MACHINERY DATA

by

R. Wallace
Signal Processing and Applications Group,
Cranfield Institute of Technology,
Cranfield, Bedford MK43 0AL, England.

SUMMARY

During the development and design of new engines, vast quantities of vibration data are acquired. An efficient analysis system designed to analyse dynamic rotating machinery data (accels, decels, etc.) is described. The system is built round a general purpose multi-tasking computer which not only analyses the data directly from pre-recorded tapes or rigs but allows engineers to post-analyse data at the same time. Examples of different types of presentation are given which enable easy interpretation of measured data. Comments of general acquisition rates and methods are also given.

1.0 INTRODUCTION

Data which is to be acquired from rotating machinery experiments can be characterised into three types:

(a) static or slow moving data where the requirement is to monitor lots of parameters at sampling rates of up to 10 or 20 samples per second.

(b) transient or surge type data where relatively quick changes in a selection of parameters have to be monitored at sampling rates of up to 500 or 1000 samples per second.

(c) dynamic data where a few parameters have to be sampled at rates of up to 50000 or 100000 samples per second.

This paper deals with the latter case - the acquisition and analysis of dynamic data. Using this dynamic data the engineer will investigate in detail frequency and time domain functions. A typical requirement is to measure 50 or 100 channels at a frequency bandwidth of 20KHz giving a sampling rate of 50000 samples per second per channel. The needs of a computer based system to handle this work is discussed. A working system for off-line analysis is given with details of the configuration and the procedures used. There are many advantages of having a true on-line system to investigate the dynamical behaviour of experiments. An example is given, from a related field, of how on-line acquisition and analysis of dynamic data gave significant cost and technical advantages. The paper concludes with current progress towards a powerful on-line system to handle dynamic data from rotating machinery where artificial intelligence techniques can be used to assist the engineer in the understanding of these complex problems.

2.0 COMPUTER SYSTEM REQUIREMENTS

The basic requirement is that of all high speed Signal Processing systems - the ability to handle large volumes of data at high data rates and the ability to organise comprehensive, yet efficient, analysis easily. What is meant by Signal Processing? - What tasks have to be done?

Signal Processing can be divided into four stages - acquisition, analysis, output and application. Acquisition involves the measurement of a phenomena and the process of being able to describe this in a numerical form in a digital computer. Analysis is the operations on the data to produce meaningful quantities for the engineer. Output is the media from which the engineer can easily understand the information. It is from these three stages that the engineer can understand what is happening on the application and therefore make decisions.

2.1 Acquisition

The engineer wants to gain knowledge of motion (or some other parameter) of the machinery so a transducer is placed on the machinery to measure that motion. This transducer provides an electrical signal - a voltage - which is proportional to the movement. This signal is then converted into digital data using an analogue to digital convertor (ADC) and transmitted to the computer for analysis. In some instances this
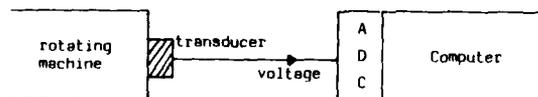
conversion is done within the transducer and related signal conditioning itself and digital data is trans-
mitted directly from the transducer to the computer. In other cases the analogue signals are first record-
ed on an analogue tape recorder, then off-line analysis is done using a similar ADC and computer arrange-
ment. The techniques described in this paper are the same for all methods of measurement.

2.2 Analysis System
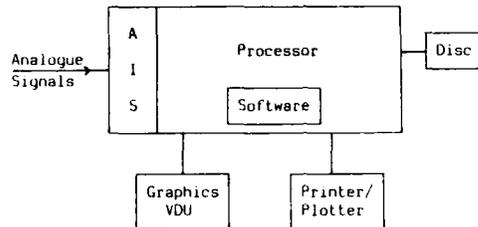
The basic components required for a Signal Processing System to acquire and analyse data are:

(a) computer processor to run the software which analyses the data and controls the
    peripherals.
(b) an analogue input system to acquire the data.
(c) graphics display units to output the analysed data.
(d) disc backing store to store programs and analysed data.
(e) printer or plotter to get a permanent copy of results.

Processor

The trend in computing over the last few years has been to 32-bit multi-tasking mini computers because of
their cost effectiveness, ease of use and power. Are these mini computers suitable for handling the 'real
time task' of acquiring and analysing 'dynamic data'? First of all 'What is meant by real time?'

'Real time' are words just like 'data processing' - they have lost their meaning. Depending on context it
means either 'time sharing' or 'true real time'. How can the difference be defined and is it indeed a
true difference?

'Time sharing systems' are normally associated with commercial type systems e.g. transaction processing,
banking with many terminals connected to a computer. They are also present in engineering/scientific multi-
user, multi-terminal large number crunching systems. Response must be quick - the quicker the better.
However, the over-riding feature of time sharing is that time does not actually effect the process. If the
interrupt does take a long time occasionally, it does not matter since the next interrupt will not occur
until the first one is serviced.

'True real time' systems are those which give response to happenings extremely quickly. For on-line
processing the response must be quicker than the time interval between data samples. If the interrupt is
not serviced quickly enough by the computer, data or other important information is lost and can never be
recovered. Therefore, with the information lost, the whole process fails.

Thus, in a multi-user system used for real time work the system must appear, whenever necessary, to have
the ability to handle the real time response very quickly and the other tasks running in the system must
not interfere with this process; in this manner no experimental data will get lost.

To take an example, Cranfield use the Perkin-Elmer 3200 series computers for this type of work. On these
computers the operating system OS32 is the true real time operating system and the time sharing require-
ments are handled by a monitor program called MTM. As with most similar systems the priority system used
within the multi-tasking system ensures fair use of resources by all users. Hence, to ensure the highest
priority for real time work, the real time task can be run on a special terminal outside the time sharing
system at a priority greater than any of other tasks.

This has two distinct disadvantages:

(a) it is inconvenient to run from a special terminal and some features of the time sharing
    system are not available.

(b) in general, the real time task will consist of pre-processing of data, real time work
    (when high priority is really necessary) and then post-processing. In an ideal situation
    (fair to all users) the pre- and post-processing stages should time share with all other
    tasks. If the task has high priority all of the time while it is being run, the pre- and
    post-processing stages may result in poor response to other users.

To solve this problem a small resident 'Assist task' has been developed which is kept in memory to control
priority levels when, and only when, real time work is taking place. For example, when a user who is run-
ning at an MTM terminal wishes to do a multiple buffer (continuous) data acquisition, the priority of his
task is automatically changed. The subroutine, when called, communicates with its 'Assist task' so when
real time work is taking place the task remains at the highest priority and reverts back to its original
priority after the data transfer has finished.

It has been found that there is a distinct advantage of using these type of systems for handling real time
applications because other tasks and users not only can coexist with data acquisition but can work rela-
tively unaffected and efficiently. As is shown later, current acquired data can be processed and previously
acquired data can be post-processed while acquisition is taking place.

A lot of the analysis process can involve the calculation of Fast Fourier Transforms and related block
arithmetic. Typically, a 2048 real point FFT may take 300 milliseconds to calculate on a medium sized mini
computer. To speed this up an array processor can be used which not only calculates the FFT but can
speedily de-multiplex the data and do other necessary block type calculations such as calibrating, scaling
for plotting, square rooting, etc. As an example, Cranfield use a Masscomp system with an array processor
for general signal processing work. With this system two channels of data can be continuously acquired at
20000 samples per second per channel (i.e. no data missed), all power and cross spectra are calculated, and
the current spectral values of a selected channel are drawn on a screen. Without the array processor the
continuous acquisition speed would drop by a factor of 10.

For off-line work, as is shown in a case history later, an array processor is not essential but in an on-
line situation it is highly recommended.

Analogue Input System
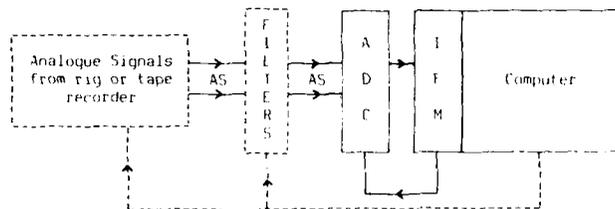
Analogue signals from the experiment or tape recorder are fed through anti-aliasing filters into the
Analogue to Digital Converter. The ADC is controlled by and feeds data through an interface module using
software drivers and subroutines so that digital information (i.e. a replica in digital format of the
measured signals) can be stored in the computer.

When signals come from a tape recorder, automatic control of the recorder from the computer can be benefi-
cial. The example given later shows how automatic running of a system overnight can reduce the man power
effort required to run the system - this could not be done without computer control of the tape recorder.
Anti-aliasing filters are almost essential when acquiring data. Cranfield usually use 48dB Butterworth
filters or 135dB Cauer (elliptic) filters from Kemo or Precision Filters. Normally the filters are under
computer control.

Cranfield use a range of analogue input equipment from Micro Consultants, Preston Scientific, Phoenix Data
and Tustin. Standard systems available can acquire data at 15-bit resolution at total throughput rates of
up to one million samples per second.

Peripherals

A disc driver is a fundamental part of the system. Apart from storing programs, the disc is used to save
a replica of the analogue data in digital format and to save analysed data. Continous throughput rates of
up to 350K samples per second from the ADC to the disc are currently achieved - the limiting factor is the
disc. With modern discs this rate can now reach nearly 500K samples per second. Using two discs it is
therefore now possible to acquire on-line continuously a manoeuvre of 16 channels with a frequency band-
width of 20KHz.

Graphics is a very important part of all Signal Processing. For most work, standard graphics terminals
such as Tektronix (or compatible) units are ideal. However, for on-line display of data from experiments,
special high speed display units are used; referring to the Masscomp example given above, a 512 line
spectra can be updated on a screen at least 5 times per second in on-line work. A system always has to
have the means of getting the hard copies of the graphs shown on the terminals - usually on a pen plotter
or printer/plotter.

3.0 **ANALYSIS AND OUTPUT**

Cranfield have worked with several engine manufacturers and related organisations in the handling of dynamic rotating machinery data. A typical test which has to be analysed is an 'accel' or 'decel' where the engine is run from one speed to another over a period of time which can vary from 30 seconds to 4 minutes or more. The engineer wants to examine, often in detail, the vibration or dynamic behaviour of components during the manoeuvre.

The basic analysis strategy in a series of programs called ROMAS - Rotating Machinery Analysis System. The aim is a complete system to acquire, analyse and then output results in a readily understandable form for the engineer. The principle components are:

(a) the input and set up o' data files using parameters logged on the engine test bed.
(b) acquiring and interpreting calibration signals.
(c) acquiring and analysing data whether it comes for accels, decels or steady state running.
(d) plotting graphs and displaying summary tables.

Input of Data

Data which is normally put down on the log sheets of the test is requested by the system. This includes:

(i)   details about the group of tests being conducted such as engine type, build, test location, test title and engine shaft speeds (tachos).
(ii) details about the parameters of the transducers such as name, calibration, gain etc.
(iii) details of the calibration test runs.
(iv) details of individual test runs such as configuration, manoeuvre and which transducers are being used.

There are two important reasons for inputting this data - to have a permanent record of the test (as on a log sheet) and to ensure that all graphs presented have the correct labelling. Once data has been entered automatic labelling of all outputs is ensured.

Calibration

Two types of calibration procedures are used:

(a) a series of dc levels representing known calibration points - these are acquired and a least squares fit method calculates the calibration factors.
(b) a series of sine waves over the frequency range of interest where the rms of the sine wave represents known calibration levels. It has been found useful to have calibration points over the whole frequency range because the system can then compensate for signal conditioning characteristics - particularly at higher frequencies.

Acquisition and Analysis

The basic parameters required to acquire and analyse the data, apart from the transducer channels themselves, are:

(a) frequency - the range to be investigated (which determines the sampling rate), the filter settings and if zoom analysis is required.
(b) reference signal - which tacho and the speed range required; a speed (tacho) signal or time can be used as the reference base.

The normal procedure when off-line analysis is being done is to position the recorded tape to the correct position, either manually or under program control, and continuously acquire and store on disc the required channels of data and tacho signals. If the required throughput rate of acquisition is greater than the overall system capability then the replay tape recorder can be slowed down. While acquisition is taking place a trace of the tacho speed is shown on the screen.

The tacho signal is often recorded as a sine wave whose frequency is proportional to the shaft speed. There are three choices of how to decode this - to use an ac to dc converter and digitise this converted signal, to use an external counter and read in the output, or, to accept the sine wave type signal into the system and let the computer do the counting. This latter method has been found to be the most accurate. At high speeds there is little difference in the methods but at low speeds the ability of the computer system count method allows interpolation between crossing points giving greater accuracy.

At the end of the acquisition stage continuous blocks of digital data are held on disc backing store and the speed associated with each block is known. This data has then to be analysed and displayed. The density graphical form of the Cambell diagram provides, perhaps, the most effective summary presentation for this type of data. For the convenience of output devices used the presentation allows 360 spectra taken at different speeds during the accel to be displayed with 320 frequency points in each spectrum. The tacho speeds calculated during acquisition are inspected, the requested range is split into 360 and using a block of data associated with each required speed the spectra are calculated. This has the advantage over the conventional method in selecting blocks at equal time intervals because engine order lines shown are now

straight, aiding interpretation of the data. During an accel a request to the driver is made to make a steady speed increase - however, in practice this is not often possible to do; the method described counteracts this problem.

In displaying this type of data there are three variables; variation in speed (x axis), variation in frequency (y axis) and variation in intensity of vibration. The display shown (Figure 1) uses intensity as this third variable. In the example given an 8 level grey scale of intensity is used - the amplitude being shown as a logarithmic scale. Colours replace greyness when displayed on an on-line terminal.

The density plot gives a qualitative initial description of the overall vibration content. To give more detail an initial supplementary plot is produced of 'peak hold', the highest amplitude in the frequency bandwidth, 'rms', giving c erall vibration content at a given speed and 'density magnitude'; in this latter plot the greyness indicates frequency range. Hence, from comparing the two graphs the engineer gets an immediate approximate appreciation of the distribution of areas of major vibration levels. Figures 2 and 3 show a pair of typical outputs.

Once the spectra have been calculated they are stored on the disc backing store and these outputs can be re-displayed in different ways using other tachos (in a multi-tacho system) as reference, if needed, without having to re-acquire the data. To investigate different frequency ranges more accurately, the axes can be expanded. The resolution in Figure 4 is poor so if more detail is required the analysis has to be repeated using zoom techniques where, in Figure 5, all the frequency points are packed into the range 12K to 15KHz. The zoom method preferred is to use a large point FFT transform (up to 32K spectral lines). Technically this gives better spectral estimates than the usual signal processing zoom techniques of frequency translation or bandpass filtering because the results are not contaminated by any pre-processing calculations.

The plots described are used to give an overall summary of the manoeuvre. Once the data has been acquired, analysed and stored on disc the data is available to be processed in detail in many ways so that 'a complete picture' can be built up by the engineer. Typical analyses include:

(a) amplitude along engine order lines, or modes (Figure 6); in general a track across a com-
     bination of multiple shafts and frequency, such as, $aN1 + bN2 + cN3 + d$, is done where N1,
     N2, N3 represent the engine shaft speeds and a, b, c, d are selectable variables.

(b) average amplitude against frequency or engine order (Figure 7).

(c) phase difference and cross amplitude levels between pairs of channels (Figure 8). Since
     the acquisition method is multi-channel it is no more difficult to calculate cross spectral
     terms as auto spectral terms - hence phase relationships between channels are available.
     One point to note is that the coherence function is also given. The coherence function
     measures the linear dependence or correlation between the two parameter channels in the
     frequency domain. If the coherence value is not close to unity then the two parameters
     could be not mutually dependent, the system relating the two could be non-linear or the two
     signals could be contaminated by a lot of measurement noise; hence the value of modulus
     and phase angle should be qualified if the coherence value is low.

(d) waterfall diagram (Figure 9); there is a limit in the number of spectral lines that can be
     displayed on one plot so the density plot is usually preferred.

(e) engine speeds against time plot (Figure 10).

In addition, time amplitude statistics such as time history display (Figure 11), probability values, rain-flow counts etc., can be calculated. One interesting technique used when investigating time history data is how to overcome the problem of display of large amounts of data. On a screen it is usually only realis-tically possible to show about 2000 points in one line. With, say, tens of thousands of points to display the technique of 'block presentation' is used. The total number of points to be displayed is broken down into about 2000 blocks. For each block either a single point, an averaged value or more generally the maximum and minimum point is displayed. The engineer can thus see where the activity he is interested occurs and interactively expand the timescale of that portion of the data record by re-displaying over the true period of interest.

4.0 **CASE HISTORY**

Figure A shows an actual configuration of a system which acquires and analyses dynamic rotating machinery data. The ROMAS system described is used.

An automatic tape control system was designed utilising one track of the tape recorder. A request to analyse a particular test is fed into the computer with the time of the test and under computer control the test item is found, acquired and analysed. This system, and the architecture of the program suite, allows automatic running overnight thereby ensuring quick turn round of the analysis and also reducing the man power required to run the system. The system can display the 'density type' graphs either on the Versatec V80 plotter or the colour Ramtek display units. The actual real time continuous throughput rate of acquisition normally required ranges from 500 to 800000 samples per second. The tape control system automatically selects the optimum tape replay speed for the analysis system - usually between 150000 and 300000 samples per second; speeding up of the tape results in quicker analysis and slowing down achieves very high real time acquisition rates. At the same time as the main stream acquisition and analysis is being performed engineers can carry out exhaustive post analysis work on data already analysed. This facility demonstrates the ability of these systems to mix high speed data acquisition with post analysis work.

5.0 ON-LINE DYNAMIC DATA COLLECTION

The advantages of extending this off-line system work to on-line analysis are illustrated in the case history of acquisition and analysis of dynamic aerodynamic data from models mounted in a high speed wind tunnel at the Royal Aircraft Establishment in Bedford, England.

Modern experimental techniques for the testing of all prototype structures require that an ever increasing number of data channels be measured. Although sample rates of only 5000 per second are required, 64 channels of data have to be monitored and analysed for continuous periods of up to 2 minutes; this gives a total throughput rate of 320000 samples per second. Much less than some rotating machinery requirements but still high.

A system called PRESTO was installed to do this work. Before the PRESTO system was installed tests were performed by pre-defining conditions, running the tests and recording the data on analogue tape. Minimal on-line single channel analysis was carried out using an FFT analyser. After completion of the tests the data was comprehensively analysed over the following few weeks.

With the multi-tasking system these tasks are now performed simultaneously:

(a) high speed data acquisition and test data storage.
(b) analysis of data using parallel processing techniques.
(c) post-processing of data (e.g. aerodynamic analysis).

The processes are completely independent providing the following advantages:

acquisition

After data acquisition corresponding to one test condition, data may be acquired for subsequent tests as soon as the tunnel conditions are ready. This process may be carried out even if the previous data run has not been completely analysed. This 'independent' acquisition approach means that less electrical power is used since the tunnel is operated for the shortest possible time. Also, the life of the model within the tunnel is extended because of reduced fatigue damage.

analysis

the analysis required is divided into several segments based on the SPAG programs which can run in parallel. Although PRESTO starts as a single-tasking job run from a time sharing terminal it invokes multi-tasking by creating parallel processing tasks.

post-processing

aerodynamic results can be displayed on-line enabling the test engineer to re-design the test schedule as he progresses. Thus, irrelevant tests can be eliminated and unexpected results may be immediately investigated in greater depth. This process allows a more efficient use of the test schedule.

The above advantages have led to the hardware cost of PRESTO being recovered on each tunnel entry by the savings in electricity alone, hence showing the power of an on-line multi-tasking system.

6.0 ON-LINE DYNAMIC ACQUISITION OF ROTATING MACHINERY DATA

A typical current requirement is to acquire 200 channels of dynamic data at 20KHz bandwidth giving a total throughput of 10 million samples per second. Realistically, there is no way that a system can acquire and usefully deal with that amount of data truly on-line. What can be done is to take 16 of those channels (about one million samples per second acquisition rate) into the system recording all channels onto tape recorders at the same time. With an array processor based system some of the data can be analysed truly on-line with the rest of the analysis being done just after the manoeuvre has finished. With a high speed output display 'density or campbell type' data may be displayed on-line. Because of the ability of the coexistence of other software tasks, specialised programs may be run to detect known occurrences such as engine order peaks, flutter mode maxima etc. Indeed, special artificial intelligence type programs may be run to deduce trends and unexpected happenings during manoeuvres. Using this approach only a few channels are analysed truly on-line or nearly on-line - the rest of the channels may be analysed immediately after completion of the manoeuvre by replaying, under computer control, the other data channels recorded during the test in an off-line manner as described earlier.

7.0 CONCLUSION

This paper has attempted to show how dynamic data from rotating machinery can be acquired and analysed in an efficient manner. The extension of the system described to on-line work has extreme technological advantages since this will speed up development time and hence save substantial amounts of money. The major current problem is the interpretation of the data and the development of the algorithms to filter the analysed data so that quicker development decisions may be taken. The ability of acquisition and analysis techniques to produce the data is now available.
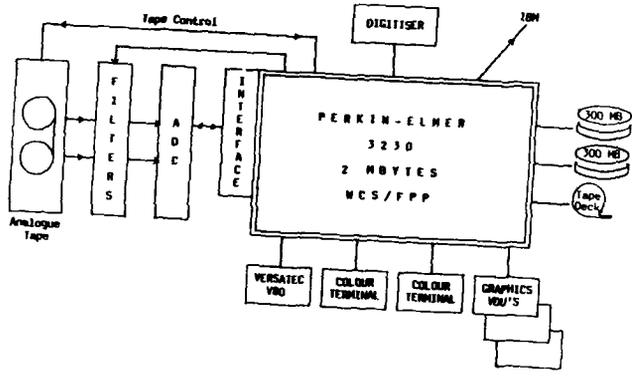
Figure A
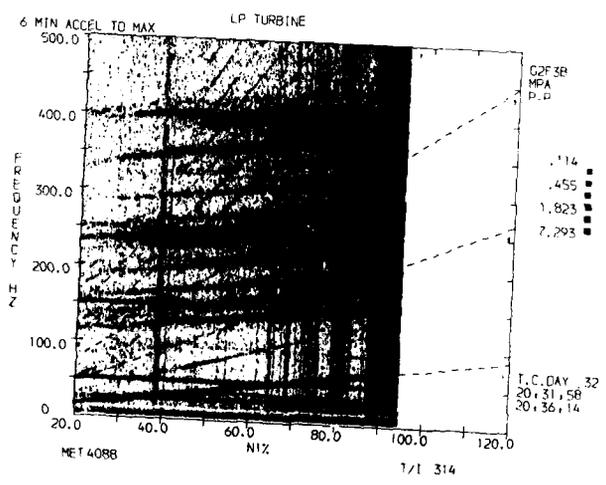
Figure 1
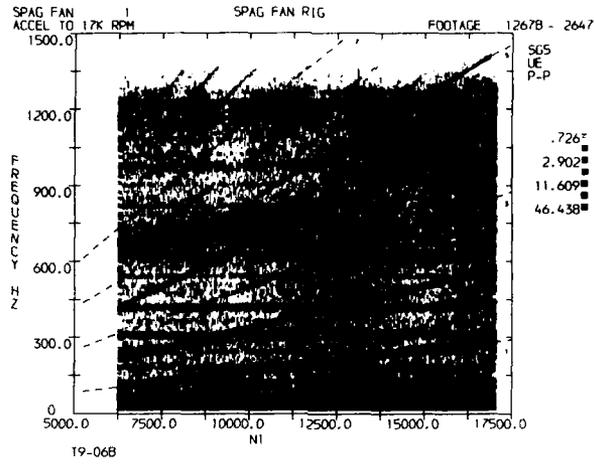
Figure 2
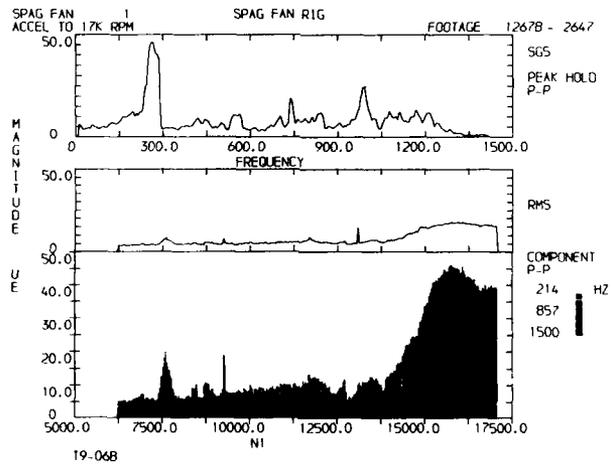
Figure 3
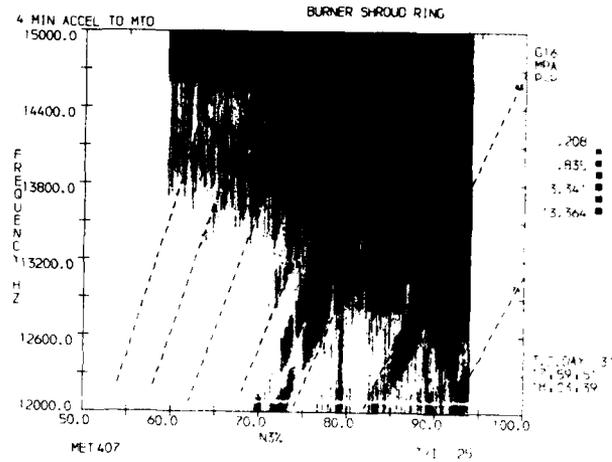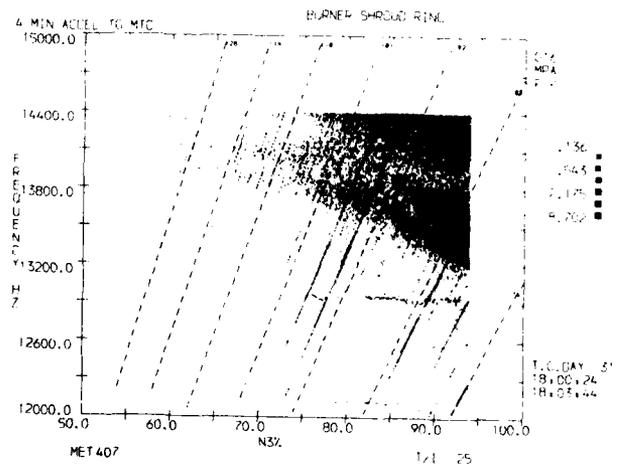
Figure 4

Figure 5
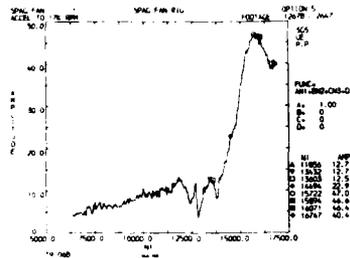
Figure 6
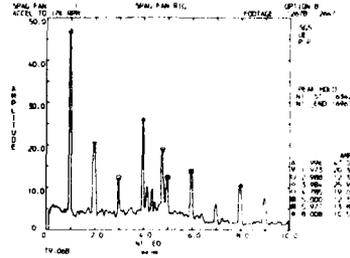
Figure 7
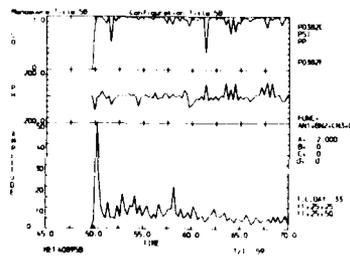
Figure 8
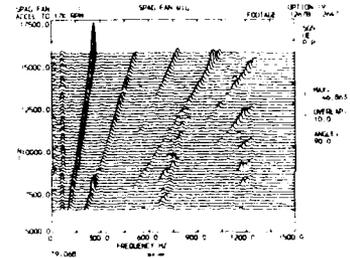
Figure 9
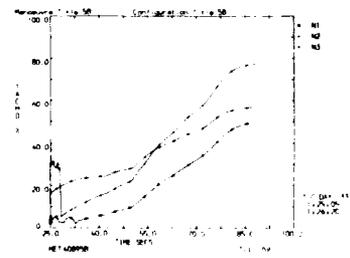
Figure 10
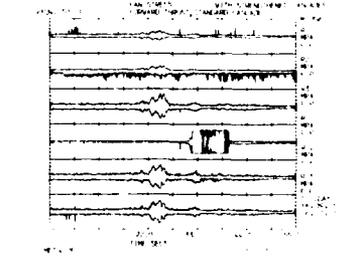
Figure 11

DISCUSSION

D.Davidson, UK

I am concerned that with such powerful spectral analysis techniques that the dangers are increasing of parasitic inputs being interpreted as real data.

While the types of analysis and display that you have shown can be a great help to the engineer, I feel that even greater care must be exercised in designing the experiment so that these parasitic effects can be evaluated.

Author's Reply

It is very important for the engineer to quantify any features he sees from his results, thereby identifying such parasitic items. In general, we calibrate our systems to check that the acquisition and analysis process does not introduce such parasitic effects.

After this stage, the engineer must inspect his results and determine what is real and what has been introduced by his measurement process.

M.L.G.Oldfield, UK

As microprocessors and memory are now very inexpensive, surely the best system is to separate the A/D conversion and real-time storage functions from the time-sharing or multi-tasking computer used for processing and display. An example of this would be the use of intelligent transient recorder types of system which communicate to the computer through a high speed parallel bus. Such systems solve the problems of high data rates into the computer by allowing asynchronous transfer of the data, while still providing reasonably prompt response to the user at a terminal.

Do you agree?

Author's Reply

Individual systems have individual requirements. The sheer bulk of data which we usually deal with makes your approach often ineffective.

However, in some cases, particularly at throughput rates of over one million per second and shortish periods of time, your approach is probably the only feasible way.

J.Chivers, UK

We recently had a problem to collect data from 10 channels at a 10 MHz/channel sampling rate. We adopted a very similar approach with individual ADC and Buffers before sending the data to a minicomputer. We found it was a very effective approach.

ACQUISITION ET TRAITEMENT DES MESURES

DE PRESSIONS NON STATIONNAIRES DANS LE CADRE

DES ETUDES DE DISTORSION D'ENTREES D'AIR

par

JL. EYRAUD et F. AUZOLLE - SNECMA
Centre de Villaroche - 77550 MOISSY-CRAMAYEL FRANCE -
et M. WAGNER - ONERA
Centre de Modane Avrieux - 73500 MODANE FRANCE -

SOMMAIRE

Les études de compatibilité entre l'entrée d'air d'un avion et le moteur constituent une étape essentielle de la mise au point d'un nouveau matériel.
Ces travaux s'appuient entre autres sur une activité expérimentale qui, pour être exploitée dans les meilleures conditions, impose la mise en oeuvre de moyens très complets d'acquisition et surtout de traitement des mesures. L'ensemble des moyens décrits ici illustre la panoplie des systèmes analogiques et numériques qui sont désormais opérationnels. L'accent est mis en particulier sur l'importance du suivi temps réel de l'essai qui conditionne dans une large part l'architecture des moyens originaux qui ont dû être développés.

1 - INTRODUCTION

Les constructeurs d'avion et les motoristes qui cherchent à établir le bilan propulsif et la meilleure intégration de l'ensemble prise d'air-moteur dans toutes les conditions de vol sont désormais conduits nécessairement à s'intéresser aux caractéristiques non stationnaires de l'écoulement à l'entrée du compresseur. Les études correspondantes s'appuient sur une recherche expérimentale très importante qui couvre tous les domaines allant de l'essai sur maquette en soufflerie à l'essai final sur avion en vol. Dans tous les cas les expérimentateurs ont dû faire évoluer leurs moyens d'essais en adaptant les outils de mesure, d'acquisition et de traitement au nouveau problème posé : celui de l'analyse des phénomènes non stationnaires. Cet article présente donc les moyens étudiés et réalisés par l'ONERA (essais soufflerie) et la SNECMA (essais sur machines à l'échelle 1) pour couvrir totalement le champ de ces études expérimentales. Ces développements effectués en liaison très étroite garantissent une compatibilité et une complémentarité excellente des équipements. Typiquement le problème posé consiste à traiter à une fréquence de l'ordre de 4 à 8 KHz 40 signaux aléatoires de façon à en extraire un certain nombre de paramètres (indices de distorsion) qui peuvent ensuite être corrélés avec le comportement de la machine, c'est à dire avec sa réponse à une alimentation en air hétérogène mais connue.

2 - OBJECTIFS GENERAUX D'UN SYSTEME DE MESURE ET DE TRAITEMENT

Une des principales difficultés rencontrées lors des essais réside dans le caractère aléatoire des phénomènes observés et en conséquence dans le ratio très faible entre la durée des phénomènes utiles sur le plan "aérodynamique" et la durée totale de l'essai. Il est également connu que dans ce type d'essais le volume global d'informations est tel qu'il rend l'exploitation extrêmement lourde et longue par les moyens traditionnels. L'objectif final recherché a donc été de localiser et d'analyser en détails les seules tranches de temps susceptibles de présenter un intérêt sur le plan aérodynamique. En plus de cet objectif général nous nous sommes imposés des spécifications complémentaires contribuant à garantir une grande souplesse expérimentale :

a) pouvoir effectuer la sélection des informations sur la base de critères évolutifs.

   Par exemple :

   - utiliser divers indices de distorsion,
   - choisir différentes bandes passantes utiles,
   - utiliser certains "évènements" sur des grandeurs mesurées avec d'une façon générale la possibilité de changer individuellement tous ces paramètres dans le but d'avoir l'étude la plus complète possible sur la base d'un même essai. Il est clair par exemple que les tranches de temps sélectionnées ne seront pas les mêmes suivant la formulation de l'indice de distorsion choisi.

b) pouvoir rejouer la totalité de l'essai afin de mettre à profit les facilités offertes par les possibilités exposées ci-dessus et donc disposer d'un support fiable couvrant largement la gamme de fréquence choisie avec un volume de stockage suffisant (autonomie) et une précision correcte.

c) donner à l'Ingénieur d'essai des moyens performants de conduite de l'essai permettant d'une part d'économiser les durées d'essai en ne testant en détails que les configurations intéressantes sur le plan aérodynamique et d'autre part en évitant de maintenir longtemps la machine dans des conditions expérimentales généralement difficiles sur le plan de sa tenue mécanique. Ceci nous a amené à mettre un accent très particulier sur les moyens de traitement en temps réel en recherchant de plus pour ceux-ci une qualité identique à celle des dépouillements complets qui peuvent être faits en temps différé. Une retombée importante de ces choix se retrouve dans l'efficacité accrue qu'ils entraînent lors de la phase dépouillement complet.

d) être capable d'assurer tous les types d'essais qui peuvent être rencontrés dans la mise au point d'un matériel :

- essais d'entrée d'air en soufflerie (essais maquettes)
- essais compresseurs puis moteurs complets (en conditions sol ou altitude)
- essais sur avions en vol

Dans ce cadre, sous l'égide du STPA et en liaison étroite avec la Société AMD-BA, la SNECMA et l'ONERA ont développé des systèmes compatibles et complémentaires. Il s'agit d'une part d'un système mobile capable de couvrir l'éventail des besoins et conçu uniquement pour cette application et d'autre part de systèmes dédiés aux souffleries. Ceux-ci viennent compléter les chaînes d'acquisition traditionnelles et permettent d'assurer un service efficace lorsque le système mobile est utilisé par ailleurs (cf fig.1).
Il faut dès à présent insister sur le fait que tous ces dispositifs font largement appel aux techniques numériques.

3 - MESURES

3.1 Paramètres à mesurer

Il s'agit de caractériser l'évolution temporelle et spatiale du champ de pression totale dans le plan frontière qui sépare la manche d'entrée d'air du compresseur. La durée de vie des phénomènes aérodynamiques à étudier, c'est-à-dire ceux qui sont susceptibles d'entraîner des variations de la stabilité de fonctionnement de la machine est de l'ordre d'une fraction de révolution du compresseur. Pratiquement le diagnostic est fait à partir de l'étude de la variation temporelle de coefficients dits "coefficients de distorsion" qui sont calculés à partir de l'ensemble des mesures élémentaires de pression totale. Certains coefficients intéressent des fractions de tour (par ex DC60, Kθ) aussi avons nous choisi de faire des acquisitions jusqu'à une fréquence utile correspondant à 4 fois la vitesse de rotation du moteur.
Afin de mieux comprendre la réponse de la machine aux fluctuations d'écoulement il faut également acquérir les signaux provenant d'un certain nombre de capteurs dynamiques disposés judicieusement à certains emplacements dans le moteur.

3.2 Peignes de mesure

Les signaux à traiter sont issus de capteurs de pression miniatures montés sur des peignes radiaux comportant chacun plusieurs capteurs ainsi que les équipements annexes (câblages, tubes amortisseurs ...). Les mesures ont été standardisées à 8 peignes de 5 capteurs donc 40 signaux élémentaires distincts.
Ce montage garantit, à l'heure actuelle, un bon compromis entre la facilité de mesure, une obstruction limitée de l'écoulement et une description correcte des distorsions de pression totale radiales et circonférentielles.
Suivant les applications les capteurs sont montés soit directement "en pitots" soit intégrés à l'intérieur du peigne en montage à membrane affleurante avec dispositif antirésonnant.

3.3 Capteurs

Tous les calculs à effectuer portent sur les valeurs globales de pression : valeur moyenne et valeur fluctuantes incluses. Les conditions d'environnement (température) pouvant être très variables selon les types d'essai trois systèmes de capteurs sont utilisés pour acquérir en particulier la composante continue. Ceci conduit donc à des principes d'acquisition légèrement différents suivant les cas d'essais.

3.3.1 Essais en soufflerie (échelle maquette)

L'ONERA effectue des mesures de pressions instationnaires à l'aide de peignes équipés de capteurs différentiels KULITE XQL093-5 de diamètre 2 mm montés en pitot. Ces capteurs initialement destinés à des mesures de fréquences et d'amplitude crête-crête présentaient des dérives de zéro et de sensibilité qui interdisaient de faire des mesures absolues. Une amélioration des caractéristiques mécaniques des capteurs par la Société KULITE ainsi que le développement par L'ONERA de méthodes de compensation des effets de dérive thermique ont permis de créer une génération de capteurs permettant de mesurer la valeur absolue de la pression avec une bande passante de 10 KHz.

3.3.2 Essais au sol ou en condition d'altitude (compresseur ou moteur - échelle 1)

Les composantes moyennes et fluctuantes de la pression sont mesurées par des capteurs distincts comptetenu de la très grande dynamique qui peut être rencontrée sur le plan thermique. Les capteurs non stationnaires de type ENDEVCO 8507-B ou 8537-20 (Ø membrane 2 mm) sont montés en membrane affleurante avec un système antirésonnant. Rappelons que dans tous les cas les capteurs sont du type à membrane silicium à jauges diffusées. Pour ce qui concerne la composante continue et vu que les essais sont toujours pratiqués en conditions de fonctionnement stabilisées (point de fonctionnement et configuration) les valeurs moyennes de pression sont acquises par un capteur unique commuté pneumatiquement (SCANIVALVE).

3.3.3 Essais en vol

Bien que les peignes soient identiques à ceux du cas précédent la mesure de la pression moyenne est faite ici par un ensemble de 40 capteurs spécifiques montés à l'extrémité d'un tube d'amortissement de telle façon que la bande passante soit limitée à 10 Hz pour cette mesure. Les capteurs de pression non stationnaires sont les mêmes que dans le cas précédent.
En conséquence pour tous les essais à l'échelle 1 il faut, au niveau calcul, procéder pour chaque capteur et à la fréquence d'acquisition à la composition des deux valeurs moyenne et fluctuante.

4 - MOYEN SPECIFIQUE POUR ESSAI EN SOUFFLERIE

4.1 Acquisition et enregistrement PCM (Pulsed Coded Modulation) (cf fig.2)

Compte tenu de l'échelle des maquettes d'entrée d'air (de l'ordre du 1/4) et de la durée des phénomènes utiles qui comme nous l'avons vu est une fraction de révolution du compresseur, la fréquence maximale d'intérêt pour ce type d'essai est de l'ordre de 2 KHz. Ceci conduit, vu la dynamique recherchée et la pente des filtres utilisés à une fréquence d'échantillonnage de 8 KHz. Dans ces conditions, les 64 mesures acquises en synchronisme représentent un flux d'information de 512 000 mots par seconde avec des points d'essai dont la durée est supérieure à 30 secondes. Cette durée est justifiée par la necessité de bien acquérir des distorsions aléatoires d'amplitude maximale.
Dans ces conditions seul l'enregistrement numérique haute densité (PCM) autorise tout à la fois la précision recherchée et la capacité de stockage. Telles quelles les informations stockées sur la bande PCM ne sont pas exploitables instantanément par l'expérimentateur par contre le suivi de certains paramètres calculés à partir de la totalité des valeurs acquises peut permettre une conduite efficace de l'essai.
L'ONERA a donc développé des systèmes originaux de traitement en temps quasi-réel qui ont complété les chaînes d'acquisition des souffleries pour optimiser le déroulement de ce type d'essais. Comme parallèlement la totalité de l'information est enregistrée sur PCM le dépouillement complet et plus détaillé peut-être réalisé en différé sur la chaîne décrite au paragraphe suivant.

4.2 Suivi en temps réel des distorsions non stationnaires (cf fig.3)

Les essais en soufflerie sont des essais importants, longs et coûteux et les combinaisons possibles de configurations à essayer peuvent être innombrables. Il est donc tout à fait impensable de conduire un tel essai sans disposer de résultats en temps réel pour valider les mesures faites et orienter la suite du programme. L'ONERA a donc développé trois outils qui, bien que fournissant des informations partielles mais travaillant en temps quasi réel sont essentielles pour la conduite des essais.

4.2.1 "Système d'acquisition rapide" (SAR) (cf fig. 4)

Développé en premier le SAR permet d'acquérir 64 voies analogiques indépendantes en synchronisme à une fréquence d'échantillonnage de 20 KHz par voie mais pendant un temps relativement court. Pratiquement, chaque voie dispose d'un convertisseur analogique numérique 12 bits et d'une mémoire tampon pouvant contenir un maximum de 256 valeurs par voie. Lorsque la mémoire tampon est pleine, l'acquisition s'arrête et la mémoire est transférée vers l'ordinateur principal de la soufflerie (VAX 782).
Chaque acquisition simultanée des 40 pressions issues du peigne constitue une "carte" instantanée. L'ordinateur VAX 782 calcule ensuite la valeur maximale de chacun des coefficients de distorsion intéressant le motoriste sur les 256 cartes acquises. La cadence d'acquisition choisie dans de nombreux cas est de 4 KHz, les mémoires tampons sont donc remplies au bout de 64 ms et il faut 1 seconde pour effectuer le transfert vers le VAX 782 et autoriser de nouveau le SAR à faire des acquisitions. Il en résulte que le temps d'observation du signal est faible par rapport au temps total or des analyses statistiques ont montré que plusieurs milliers de cartes seraient nécessaires pour décrire le phénomène de distorsion instationnaire (figures 5 et 6).Il est donc envisageable d'opérer ainsi uniquement lors d'essais de recherche limités en durée mais c'est tout à fait exclu pour explorer tout le domaine de vol d'un avion. Le SAR permet en fait d'obtenir en temps réel une information condensée sur les phénomènes non stationnaires mais le caractère aléatoire des prélèvements fait que cette information est insuffisante pour opérer un tri rapide parmi des configurations différentes présentant des caractéristiques assez proches. C'est pourquoi l'ONERA a développé un nouveau système qui associé au SAR répond au problème posé de façon plus complète.

4.2.2 Le calculateur analogique Kθ (cf fig.7)

Le problème à résoudre était de trouver un système de tri sélectionnant les signaux à des fréquences très élevées. Comme à cette époque seul le coefficient de distorsion Kθ était d'un intérêt majeur, la solution analogique est apparue la mieux adaptée. Le calculateur étudié comprend deux parties :

- un châssis conditionneur qui convertit les signaux issus des capteurs en tensions directement représentatives des pressions mesurées. Le réglage de ce châssis et les vérifications sont automatiques et sont gérés par une logique à microprocesseurs.
- un châssis de calcul qui admet à son entrée 40 signaux calibrés et délivre en sortie une tension proportionnelle au coefficient Kθ. La bande passante du calculateur est de 10 KHz avec une précision meilleure que 1 %. Cette sortie est généralement connectée à une entrée du SAR.

Deux dispositifs annexes ont été associés au calculateur Kθ :

- un comparateur à seuil qui génère un topage, lorsque la tension de sortie du calculateur devient supérieure à une tension prédéterminée. La tension de seuil peut-être réglée de diverses façons ; soit fixée soit élaborée par un ordinateur, soit incrémentée automatiquement en fonction de la valeur du Kθ analogique.
- un châssis de détermination du Kθ maximum. Ce dispositif conserve en mémoire la valeur maximale du Kθ jusqu'à ce qu'un ordre de remise à zéro provienne de l'ordinateur de la soufflerie.

Cet ensemble a donné toute satisfaction mais à la suite du développement du calculateur Kθ de nouveaux besoins sont apparus : en particulier la nécessité de calculer d'autres coefficients de distorsion (IDC, IDR, ΔP/P ...). C'est pourquoi L'ONERA a développé un calculateur de distorsions appelé "calculateur CTR".

4.2.3 Le calculateur "CTR" (cf fig.8)

Contrairement au calculateur précédent et afin de posséder une grande souplesse de programmation une solution à base de microprocesseurs a été retenue. Le calculateur "CTR" travaille à partir des tensions normalisées issues du châssis conditionneur décrit au paragraphe précédent et est composé :

- d'un châssis de filtrage numérique par moyenne glissante.
- d'un châssis d'acquisition composé de plusieurs microprocesseurs travaillant en parallèle. Les calculs de différents coefficients y sont réalisés (IDC, IDR ...), le débit dans la manche est également calculé. Ce châssis possède une mémoire circulante et sur un top de déclenchement il est possible de conserver dans cette mémoire les cartes entourant l'instant choisi. Deux mémoires travaillant alternativement permettent de prendre en compte plusieurs tops successifs.
- d'un châssis de contrôle qui assure les fonctions suivantes : prise en compte des coefficients issus du châssis d'acquisition ; une visualisation sur écran graphique de coefficients ; gestion du blocage de la mémoire circulante ; détection de maximum de certains coefficients avec génération de tops ; pilotage du châssis de filtrage ; liaison avec l'ordinateur VAX 782. De plus ce châssis peut être connecté avec l'enregistreur PCM en mode relecture.

La bande passante de ce calculateur est de 4 KHz avec sa précision de $\pm$ 1 %.

4.3 Procédure d'essai

Afin d'utiliser au mieux le temps de fonctionnement de la soufflerie deux procédures sont utilisées :

4.3.1 Balayage d'un paramètre

Lors de la variation continue d'un paramètre (incidence de la maquette, dérapage, débit etc ...), les acquisitions sont faites suivant deux méthodes :

- déclenchement en parallèle du SAR et du calculateur $K\theta$ par une horloge.
- déclenchement du SAR par le signal dépassement de seuil du calculateur $K\theta$.

Ces balayages permettent d'explorer rapidement une configuration.

4.3.2 Points stabilisés

Tous les paramètres d'essais étant fixes, des enregistrements PCM de 30 s environ sont effectués. En parallèle le SAR et le calculateur $K\theta$ sont utilisés pour obtenir en temps quasi réel les maxima de distorsion rencontrés.

De plus pour accélérer encore les procédures d'essai la SNECMA peut venir connecter le système CATI qui sera présenté au chapitre 5 sur les chaînes d'acquisition soufflerie. Cette procédure permet alors l'analyse rapide la plus détaillée des résultats concernant chaque configuration testée.

4.4 Présentation de quelques résultats

4.4.1 Déclenchement du SAR sur dépassement du seuil

La figure 9 présente les résultats d'une succession de déclenchements SAR lors d'un point stabilisé. Les déclenchements sont obtenus par dépassement d'un seuil asservi à la valeur issue du calculateur $K\theta$ analogique. On constate le bon accord entre les valeurs de l'indice $K\theta$ calculé à partir des acquisitions SAR et celles fournies par le calculateur analogique.

4.4.2 Comparaison des valeurs de coefficients de distorsions obtenues par différents procédés

Sur la figure 9 sont représentées les valeurs $K\theta$ en fonction de l'incidence aérodynamique de la maquette :

- la valeur stationnaire de $K\theta$ acquise par la chaîne standard de la soufflerie (fréquence de coupure 1 Hz).
- la valeur maximale de chaque paquet 256 cartes SAR, celui-ci étant déclenché par une horloge chaque seconde.
- la valeur maximale enregistrée par le châssis "$K\theta$ maximum" pendant un temps d'une seconde.
- pour une incidence la valeur maximale enregistrée par le châssis "$K\theta$ maximum" au cours d'un point stabilisé de 30 s.
- pour cette même incidence la valeur maximale enregistrée lors de 20 déclenchements SAR de 40 cartes, les déclenchements étant manuels c'est à dire aléatoires.

On constate que le SAR utilisé seul au cours d'une polaire donne un résultat assez éloigné de ce que donne le calculateur $K\theta$ analogique. Par contre l'observation pendant 30 s avec des conditions stables est ici tout à fait justifiée et ne fournit pas des valeurs trop éloignées de la valeur $K\theta$ analogique obtenue en polaire (cf fig.10). On montre également ici que des déclenchements aléatoires du SAR sur 800 cartes donnent un niveau de distorsion assez éloigné de la valeur obtenue sur 30 s par le calculateur analogique. Cet ensemble d'observations confirme bien qu'il faut procéder à un examen complet des signaux et que le traitement ne doit négliger aucun échantillon si l'on ne veut pas courir le risque de ne pas détecter les distorsions extrêmes qui sont finalement les seules aérodynamiquement utiles.

5 - MOYEN DE TRAITEMENT GENERAL

Ce système appelé CATI pour Chaîne d'Analyse et de Traitement de l'Instationnaire couvre la totalité du domaine expérimental cité ci-dessus. Cette chaîne développée par la SNECMA depuis 1979 est pleinement opérationnelle depuis 1982.

5.1 Architecture et possibilité (cf fig.11)

La chaîne s'articule autour de deux grands ensembles :

- un système d'acquisition-numérisation et stockage des données utilisant la technique d'enregistrement PCM.
- une unité de calcul et de visualisation des résultats dont le coeur est un calculateur vectoriel.

L'ensemble est installé dans une remorque routière climatisée qui assure toutes les servitudes nécessaires et permet le raccordement sur tout site d'essai. De plus la partie acquisition et stockage, réalisée en version embarquable, peut être dissociée et embarquée sur un avion d'armes.

5.1.1 Acquisition et sotckage (cf fig.12)

Cet ensemble comprend :

a) Un petit calculateur d'acquisition qui permet l'entrée des données générales de l'essai et l'ensemble du paramètrage. Ce calculateur gère aussi l'acquisition des données dites lentes : composantes moyennes des pressions relevées sur Scanivalve en particulier ainsi que les liaisons avec des systèmes extérieurs de relevé des paramètres aérothermodynamiques de fonctionnement de la machine. Finalement ce calculateur assure la transmission de toutes ces données à la cadence nécessitée par le dispositif d'enregistrement PCM.
b) Un générateur de temps IRIG synchronisable sur un signal extérieur qui permettra :
   - de mélanger des informations de temps (sous forme numérique) avec des valeurs mesurées.
   - d'enregistrer le temps sous forme analogique pour rechercher par la suite automatiquement les points à analyser.
c) Un groupe de 64 conditionneurs embarquables permettant d'alimenter les capteurs et d'amplifier les signaux issus des capteurs dynamiques.

   Ces conditionneurs comportent également :
   . des filtres antirepliements pilotés
   . des échantillonneurs-bloqueurs sur chaque voie.
d) Un ensemble KAYSER de numérisation et de mise en forme PCM.
   Ce système assure la numérisation sur 10 bits de 64 canaux, en fonction d'une horloge extérieure dérivée de la vitesse de rotation de la machine. Il assure le pilotage correct des filtres antirepliements, le mélange des informations de temps et des mesures stationnaires.
e) Un enregistreur embarquable 14 pistes utilisé en mode direct à une vitesse comprise entre 30 et 120 ips suivant la bande passante souhaitée.
f) Un système de surveillance pouvant se connecter avant ou après l'enregistrement afin de visualiser rapidement le comportement des signaux de tous les capteurs et de valider globalement les signaux mesurés.

5.1.2 Calcul et visualisation

Cette partie se compose principalement d'un calculateur vectoriel (AP120B de la Société FPS - puissance 12 Mflops équipé de 32 K mémoire) dont le rôle en temps réel est :

- de transformer les valeurs mesurées en unités physiques,
- de remplacer les valeurs délivrées par des capteurs identifiés comme défectueux par des mesures extrapolées de celles fournies par les capteurs adjacents,
- d'effectuer un filtrage numérique à la fréquence désirée sur tous les capteurs.
- de faire tous les calculs d'indices de distorsion,
- de relever les maxima d'indices dépassant un seuil fixé et leur instant d'occurrence.

Ce calculateur vectoriel est géré par un calculateur d'usage général (HP-16 bits) doté d'un système d'exploitation temps réel. Ce dernier permet d'assurer le dialogue avec l'opérateur et les sorties de résultats sur :

- écran à balayage cavalier ou vidéo couleur
- tracé sur papier par traceur électrostatique
- dérouleur de bande numérique pour envoi des résultats à un gros centre de calculs (constitution d'une base de données)
   Ceci permet en particulier d'entrer des données expérimentales dans des modèles de calculs théoriques développés par ailleurs à la SNECMA.
Il gère également une unité de recherche automatique de temps au standard IRIG A ouB qui permet de retrouver commodément, en temps différé, les instants intéressants relevés en temps réel.

5.2 Performances et résultats

5.2.1 Le système d'enregistrement PCM haute densité est capable de traiter 64 voies dynamiques (il peut être étendu jusqu'à 128).
La numérisation se fait sur 10 bits avec une extension possible à 12 bits. La cadence d'enregistrement maximale est de 10 Mbits/s ou 1 M mots/sec, avec une autonomie de 20 minutes. Ceci représente une capacité d'environ 1,2 G mots ou 2,4 G octets.
Les cadences de numérisation par voie généralement utilisées par la SNECMA sont :

- pour les essais en soufflerie (maquette) de 8 à 16 KHz par voie (64 voies)
- pour les essais au sol (échelle 1) de 2 à 4 Khz par voie (64 voies)

Cette valeur correspond à 16 fois la vitesse de rotation de la machine en essai mais il ne faut pas oublier que les bandes passantes mesurées sont 4 fois plus faibles.

5.2.2 Le système de calcul et de visualisation nous permet de plus à la SNECMA :

a) le filtrage et la réévaluation des capteurs défectueux,
b) le calcul simultané de 6 indices de distorsion en temps réel pour les essais au sol (à 4 KHz par voie) IDC - IDR - Kθ ... (cf par ex fig.13 le calcul de l'indice Kθ),
c) le calcul en temps réels en soufflerie (8 KHz) de deux indices avec présentation immédiate des résultats sous forme de nuages dans un diagramme caractéristique (cf fig. 14),
d) la possibilité de changer plusieurs fois par jour le jeu d'indices calculés sans nécessiter de nouvel investissement.

Ces performances ont été atteintes car le logiciel temps réel ainsi qu'une grande partie du logiciel temps différé ont été écrits en langages machine et ont permis de profiter de la pleine puissance du processeur vectoriel (12 Mflops). Il faut souligner que ce logiciel développé par LEUVEN MEASUREMENT SYSTEM représente environ 4 000 lignes de langage assembleur.
Il est ainsi possible de présenter les résultats sous des formes extrêmement diverses et ceci à volonté uniquement dans les périodes aérodynamiquement intéressantes (cf fig.15 à 18) :

- cartes temporelles d'indices ou de pressions individuelles,
- cartes isopressions moyennes ou non stationnaires,
- cartes d'isoturbulence,
- analyses spectrales,
- statistiques d'extremums...

En pratique la variété des résultats n'est plus limitée par le logiciel développé en langage de haut niveau. C'est aussi ici, que le choix par la SNECMA, d'un processeur vectoriel s'avère judicieux lorsque l'on sait la performance de ce type de calculateur pour tout ce qui touche au traitement du signal.

6 - CONCLUSION

Cette présentation avait pour but de montrer l'importance et la variété des moyens qui doivent être mis en oeuvre pour traiter les études expérimentales en matière d'aérodynamique non-stationnaire. Elle a permis de voir comment les techniques les plus évoluées de codage-enregistrement (numérique haute densité) et de traitement (calculs numériques - processeurs vectoriels) pouvaient être associés pour arriver à l'objectif : faire et exploiter des campagnes d'essais complexes dans des délais très courts. Il ressort également que l'adaptabilité des moyens doit être une préoccupation essentielle : il faut que l'activité expérimentale puisse suivre en permanence l'évolution de la formulation théorique des phénomènes. Dans ce but l'expérimentateur utilisant des technologies numériques aura la possibilité de pouvoir faire évoluer ses moyens au moindre coût. Sur un plan plus général, nous pensons aussi que l'architecture choisie préfigure celle des systèmes d'acquisition et traitement qui seront couramment nécessaires à l'avenir pour la gestion des informations dynamiques de toutes natures.

DISCUSSION

G.C.Oates, US

(1) On the case of the coefficient Kθ, data processing is aided greatly when the rakes are distributed equally. Does the use of equally spaced rakes in flight hardware lead to compromizes regarding upstream wakes...

(2) In the same way, when a probe is damaged, is its "effective" signal reconstructed from the readings of adjacent probes?

Author's Reply

(1) Our software is designed to handle the case of equally spaced rakes by reconstructing signals at the positions the rakes should be. This achieved by the same re-evaluation method used to replace false sensor during normal test.

Our experience is that we never had problems with equally spaced probes in flight conditions.

(2) The re-evaluation of false transducers is effectively done by interpolation from values given at the same instant by adjacent sensors.

D.Davidson, UK

Were the plots of fig.15 & 16 obtained on line or off-line please?

Réponse d'Auteur

Ces tracés sont effectués en temps différé car ils sont relativement longs. En temps réel, on cherche surtout, par le calcul des coefficients, à trouver les instants où les cartes tracées seront les plus intéressantes sur le plan aérodynamique.

D.Davidson, UK

Could you please elaborate on the slide that you showed of the sensor array. What is its size and physical arrangement?

Author's Reply

The diameter of the sensor array is under 10 cm. It is located on the scale model of the aircraft at the end of air inlet, at the place the engine should be.

J.Fabri, FR

Vous avez montré le point de vue de l'expérimenteur qui met en évidence l'existence de pointes de distorsion de très court durée. Est-ce que de telles pointes ont un effet sur le fonctionnement du compresseur?

Réponse d'Auteur

De telles pointes peuvent avoir un effet sur le compresseur, leur durée étant en relation avec une fraction de rotation de celui-ci.

Lors des études sur maquettes, les durées significatives sont également à l'échelle de la maquette.

AD-P005 542

DEVELOPMENTS IN DATA ACQUISITION AND PROCESSING USING AN
ADVANCED COMBUSTION RESEARCH FACILITY

by

J. B. Bullard, F. S. E. Whitcher and R. V. Steeden
Royal Aircraft Establishment, Pyestock, Farnborough, Hants GU14 OLS UK

SUMMARY

A new combustion rig is described which is designed to acquire rapid and detailed information on the combustion processes occurring within a sector of large annular gas turbine combustors operating over a range of inlet pressures and temperatures representative of engine conditions. Gas samples are extracted using a probe positioned within the volume under examination and transferred to a system designed to perform analyses with a point-to-point cycle time of less than 30 seconds. A computer is used to control and synchronise the probe positioning and gas analysis function and to present co-ordinated results to rig controllers. The system is capable of automatic traversing within a prescribed volume or of control by a dummy traverse gear which permits tracing of air and fuel flows.

The Paper outlines the main features of the rig, together with the types of instrumentation, the methods and range of operation used and anticipated. Some of the more unusual items are highlighted.

1 INTRODUCTION

The military and commercial operational pressures to advance gas turbine technology continue unabated. The demand for increased thrust output while striving for economies in fuel consumption is steadily pushing up engine cycle pressures and temperatures. The resulting conflict with the need to achieve improved reliability and longer life is obvious. Careful design and persistent development are therefore necessary to evolve engine components that together attempt to satify these requirements.

The need to advance combustion technology is no exception. A combustion chamber must control the passage of high pressure air from the compressor to the turbine with minimum pressure loss, inject, vaporise and mix varying quantities of fuel with part of the air and then burn the resulting fuel/air mixture efficiently and cleanly over a wide range of pressure and temperatures, presenting to the turbine hot gas having an acceptable temperature distribution. Such air that is not used in the combustion process is crucial for maintaining the metal walls at acceptable temperatures to achieve adequate life and mechanical integrity.

Current designs of combustion chambers for gas turbine engines are based mainly on a combination of experiment and experience using well established empirical correlations and design rules. A new design is constructed and tested, but invariably shortfalls in performance or other problems are encountered and a period of dedicated development is necessary. Development generally proceeds on a test/observation/modification basis, often referred to as 'cut and try', ie the combustion chamber shape is altered or the air entry holes are moved or varied in size, and then the chamber is retested. In this cycle observations of combustion chamber characteristics and performance are usually based on turbine entry plane measurements. The exception is, of course, the thermal integrity of the chamber itself which is assessed using thermally sensitive paints to identify hot spots.

A major shortcoming of this approach is that diagnosis of aerodynamic and combustion problems occurring within the primary zone of the combustor is dependent upon analysis and interpretation of data measured some 30 to 40 cm downstream of the event. Not surprisingly, the process of development using these techniques is slow and expensive and a better method of diagnosing the cause of performance shortfalls and problems is required.

In recent years research programmes at Royal Aircraft Establishment (RAE), Pyestock have developed and refined techniques for exploring in detail the internal characteristics of combustion chambers. So far the work has concentrated on model chambers[1] but the principles are applicable to full-scale research and development combustors. The time is right for this to be put into practice and this Paper describes a rig (known as the Sector Combustion Rig (SCR)), which is to play a vital role in the contribution being made by the RAE to the advancement of aero engine combustion technology.

2 THE RAE SECTOR COMBUSTION RIG

The main feature of the rig is its versatile, internal traversing probe. This enables detailed measurements of the composition of the reacting gases to be made throughout the volume defined by a sector of a fully annular combustion chamber from the primary zone to its exit plane. A comprehensive, computer-controlled gas analysis system permits measurement of local fuel/air ratio, carbon monoxide, carbon dioxide, oxides of nitrogen, total hydrocarbon, oxgen, hydrogen and smoke. It also has the facility for monitoring tracer gases such as helium.

The rig has been installed and is currently being commissioned. Assembly of the computer-controlled data acquisition and analysis system is complete and commissioning is proceeding on a phased basis.

2.1 Range of operation

The first build of the SCR is capable of operating with air inlet temperatures up to 920 K and at pressures up to 10 atm. Experience has shown that full pressure engine conditions can be sensibly and economically simulated by testing at the true air temperature but at a lower rig pressure providing the mass flow is adjusted accordingly to maintain the correct inlet Mach number and providing the pressure level is high enough to ensure a fully developed spray pattern and representative combustion chemistry. Pressures of at least 10 atm have been shown to be adequate for most research and development purposes.

The maximum air mass flow (AMF) was determined from considerations of entry Mach number and the largest size of combustion chamber to be tested in the rig; the value is 11.4 kg/s (25 lb/s). This value approximates to that required by an 80° sector of a modern large civil turbofan engine and typically allows four complete burner sectors to be tested.

Bleed flows to simulate turbine cooling flows, etc may also be necessary if airflow distribution around the combustor flame tube is to correctly simulate an engine installation and allow examination of their influence on combustor exit conditions. Four separate bleed lines (inner and outer diameter at entry and exit) have been installed, each capable of taking a flow of up to 10% of the main stream AMF.

The exhaust system is designed to withstand gas temperatures up to 1750 K at the maximum operating condition without using water injection sprays.

2.2 Mechanical arrangement

The main features of the SCR are shown in Figs 1 and 2. Air is supplied from a plant compressor via a non-vitiating heater to the SCR. The hot pressurised air enters from the plant pipework through a circular inlet section which contains a honeycomb flow straightener and a water-cooled bursting disc; this protects the rig against accidental over-pressurisation as the plant air supply is capable of 16 atm compared with the present 10 atm capability of the rig. An entry section converts the flow from circular to a sector cross-section to suit the combustion chamber sector on test. The pressure profiles expected at compressor exit can be simulated by means of profile generators thus ensuring that diffuser operation, bleed flows and wall cooling are correctly simulated.

The combustor sector on test is contained within a pressure casing and the four bleed flows are removed through this casing. An adaptor plate with a sector-shaped exit is used to direct the hot exhaust gases through a dummy nozzle into the exhaust drum (Fig 3). The exhaust drum carries a mounting plate which in turn carries the traverse gear, used to position the sampling probe within the combustor sector. The main exhaust (Fig 1) then passes from the bottom of the exhaust drum via ducting containing averaging sampling rakes to the back pressurising exhaust valve. A water spray ring and thrust diffuser cone lead to the main exhaust system and extraction fan. Flows through the four bleed lines pass through separate control valves before being manifolded and dumped into the main exhaust system.

Provision has been made to remove a section of horizontal main exhaust duct to permit the exhaust drum to be moved rearwards. This will allow the insertion of a flange carrying special instrumentation immediately downstream of the adaptor plate.

Detailed mechanical design and manufacture followed by proof build and test of the rig was undertaken by Lucas Aerospace Ltd, Fabrications Division to RAE specifications. Gas analysis instrumentation was designed in-house or modified from commercial apparatus to handle samples ranging from '100%' air to '100%' fuel.

2.3 Rig measurements

The main air supply to the rig is measured after compression, but before heating, by a vortex-shedding meter. This type of meter is able to measure a much wider range of flows than an orifice plate, but this device cannot withstand the high air temperatures downstream of the heater. The bleed lines, however, use orifice plates for AMF measurement since they are passing hot air.

Two small (less than 0.5% of the main stream flow) air supplies are used for cooling and sealing of the traverse gear ball pivot (section 3.2). These supplies are taken from the main air supply before the metering section, controlled, measured and then fed to the traverse gear.

Fuel is supplied to the test combustor through two systems nominally pilot and main. The two systems can be used separately or in parallel, thus covering a wide range of fuel flows from 0.0005 to 0.27 l/s (0.36 to 210 gal/h). Fuel flows are measured using Pelton wheel type meters. A range of fuel types can be supplied by the plant system, enabling combustion of alternative fuels to be evaluated.

The air and fuel pressures and temperatures are measured by transducers and thermocouples positioned at appropriate points in the pipework.

3 INSTRUMENTATION

3.1 General description

A key feature of the SCR is the use of wide ranging gas analysis equipment to study the mixing and combustion of fuel and air within the combustion chamber. A continuous flow of sample can be extracted from any part of the combustor volume through a single point probe and transferred through stainless steel tubing to the remote gas analysis system.

The probe is positioned by the traverse gear (Fig 3) and its temperature controlled by the use of a high pressure hot water system capable of operating up to 463 K (190°C).

The traverse gear is part of an integrated probe positioning and gas analysis system designed to minimise the time spent obtaining and analysing the necessary information.

An Intercole Compulog 3 computer system monitors rig parameters, drives the gas sampling probe and sample acquisition system, and outputs results from the gas analysis instrumentation in both tabular and graphical form. Initially the computer system will be used to present results and provide the operators with rig status information. Ultimately it is intended that the installation will be able to perform limited control functions such as maintaining the SCR on condition thus relieving the rig controller of the more tedious parts of the test runs.

Experience on model combustor rigs has shown that detailed traversing of a volume requires gas samples from discrete points spaced no more than 10 mm apart. Applying this requirement to the full-scale combustors to be examined on the SCR means that up to 1000 points may need to be sampled at a test condition. In order to minimise acquisition time, a target gas analysis cycle time of 30 s has been set. The gas analysis cycle includes automatic purging of the sample line, acquisition of the sample, gas analysis and movement of the probe to its next position.

3.2 Traverse gear

Probe access to the chamber is from the downstream combustor exit plane (Figs 3 and 4). Thus in order to extract samples throughout the volume of interest a cranked probe capable of movement in four dimensions is required (Fig 4). As the traverse gear must be able to investigate different sizes of combustion chamber with various internal features, limit switches cannot easily be used to protect components. Instead a system using computer control (for speed, accuracy and the avoidance of protrusions) together with slipping clutches (to prevent damage should the probe contact any surface) was chosen.

The traverse ball pivot acts as the fulcrum for all the movements and also provides the simple seal between the hot internal pressurised gas and atmosphere. A supply of sealing air is used to balance the internal pressure but another supply is required to ensure integrity of the ball pivot system. This second air supply is routed to the front of the ball pivot to provide a protective film; this small quantity of air must therefore be taken into account when using the averaging outlet rakes.

The probe which acquires the gas samples is mounted in the traverse gear but must be easy to remove since it is very vulnerable to damage by overheating and may need to be changed. Also different shapes and types of probe may be required for different purposes. A setting gauge can be mounted on the front of the traverse gear to locate the probe and establish a datum set of co-ordinates which can be held in the computer. High pressure hot water and gas sample transfer connections are attached at the rear (cold) end of the probe after the complete traverse system has been fitted into the rig. The flexible sample transfer and water lines are carried on a support arm which moves in the horizontal plane to minimise side loads on the traverse gear (Fig 1).

In addition to forming part of the integrated probe positioning and analysis system, the traverse gear can also be driven manually using its control box or by means of a dummy traverse gear. The control box provides a separate control for each of the four movements. The dummy traverse gear is a replica of the actual traverse gear. A dummy probe can be manipulated within a model of the actual combustor on test - the movements of this probe are translated into electrical signals by the dummy traverse gear thus providing command signals to the real traverse gear fitted on the SCR. The synchronised position of both probes is also relayed to the computer and can be displayed or printed along with the appropriate gas analysis results.

3.3 Gas sampling probes

It is essential that the composition of the gas sample should not alter during its transfer from the sampling point to the gas analysis instruments. This requires that the composition should be 'frozen' by rapid cooling within the probe. The sample should subsequently be maintained at a temperature low enough to inhibit further reaction and high enough to prevent deposition of condensable constituents. This temperature has been set at 453 K (180°C) to cover all the types of fuel anticipated.

In addition to the above conditioning duties the pressurised hot water system is also used for probe cooling.

The design of the traversing probes is such that the hot water passing up the inner annulus (Fig 5) conditions the gas temperature to that of the water before the sample reaches the probe outlet. The return flow through the outer annulus provides cooling, and hence protection, for the probe against the very hostile flame environment of the combustor primary zone (T >2000 K).

The gas analysis equipment requires approximately 20 litres of gas sample per minute if it is to perform the analysis cycle at the required 30 second intervals. The bore of the probe must be large enough to permit this flow at all operating conditions but the outside diameter must be as small as possible (10 mm) to minimise any interference with the flow patterns being sampled. At high rig pressures a blow-off system is used to remove excess sample flow.

All the above remarks refer to the small 'minimum disturbance' probes designed for use in the primary zones of combustion chambers. The outlet rakes contain a number of sampling holes spaced on an area weighted basis to measure an average gas sample leaving the combustion chamber. They are sited downstream of the chamber exit (Fig 1) where the environment is less hostile.

A third probe of simple uncooled design and situated upstream of the rig is used to obtain a sample of the air supplied to the combustor.

3.4   Gas sample transfer system

Each of the three systems (Fig 6), for intra combustor, combustor outlet and air sample transfer, consists of a short section of high pressure hot water conditioning line followed by approximately 20 metres of 8 mm bore stainless steel tubing heated by electrical heating tape.

A separate line is used to transfer smoke samples directly to a smoke meter (section 3.5.2(i)); this line is configured to minimise any degradation of the sample.

Pressure in the sample line is controlled by remotely operated relief valves in bleed lines connected close to the probe outlets. Reduction of pressure lowers both sample residence time (for a given atmospheric pressure flow rate) and dewpoint. Thus the operating level is set only to that necessary to produce the required flow rate in the instruments.

An upper temperature limit (453 K) is imposed by those instruments which operate on the raw sample, ie as captured by the sampling probe. Continuing reactions are not likely to be serious during the short residence time (<2 seconds) at this temperature chosen for the transfer system but deposition from the complex primary zone products is difficult to predict; any potential contamination of subsequent samples must be detected and remedied. This is done by using the level of the computer monitored signal from one of the flame ionisation detectors (FID) as a measure of the acceptability of the sample. If a threshold value of hydrocarbon is exceeded the computer will operate zero gas selectors in the filter oven (Fig 6) and will then inhibit further analysis until an acceptable level is attained.

3.5   Gas analysis instrumentation

   3.5.1 Design considerations

In aero engine emissions measurement, a comprehensive description of hydro-carbon/air combustion product composition can be achieved by the measurement of only a small number of key chemical species provided a number of assumptions are made. The calculations require a knowledge of the chemical composition of the fuel and air and the application of conditional equations involving reactant and product atomic balances.

The measuring systems used for the SCR system are based on relatively fast commercial on-line analysers. It was decided that such instruments afforded the best means of achieving the target analysis time of 30 seconds per point albeit with an increase in the number of instruments used to meet the wider range of constituent measurement required.

None of these instruments respond only to their designated constituent; corrections for interference effects are therefore necessary. The procedures used, familiar in emissions measurement, become more significant in the presence of potentially greater 'contaminant' concentrations in the SCR. The interferences are of two types (a) those where the instrument responds directly to the 'contaminant' and (b) those where the 'contaminant' modifies the response to the measured constituent. Direct measurement of additional species simplifies the computer calculated correction procedure and also eliminates some of the assumptions made in the calculation of composition. A list of instruments used is given in Table 1.

In section 3.4 reference was made to instruments which operate on the raw sample. Others, whose operating temperature would result in deposition of condensable constituents, must be protected by a combination of coolers and driers. There is thus a need to relate measurements made on raw and processed samples. The correlations are made by the assumptions of (a) removal or non-removal of organic matter in the drying process and (b) the molecular state of the organic matter. In the system described here use is made of a recently developed commercial non-dispersive infra-red instrument capable of operation at

453 K. Carbon dioxide is measured on both raw and processed samples thus providing a factor for the conversion of all constituent concentration between these two samples.

In the following section (3.5.2) a knowledge of current gas analysis instrument fundamentals[2,3] is assumed and only special features are detailed.

3.5.2 Instrument description

(a)   Gas analysis console

The analysers are housed in a console (Fig 7) together with ancillary apparatus including pen recorders, temperature and flow control systems and span and zero solenoid valves. Local manual control of all instrument operating functions is available at the console and an interface provides access for computer control and data gathering.

(b)   Carbon dioxide and carbon monoxide

Both of these constituents are measured in the processed sample using non dispersive infra-red (NDIR) analysers, although additional measurements of carbon dioxide are made of the raw sample (section 3.5.1). To obviate delays arising from range changing within instruments, the SCR system uses five separate single range instruments operating in parallel, all outputs are logged and the most appropriately ranged instrument result is selected by the computer.

(c)   Oxygen

The instrument used for the measurement of oxygen is of the paramagnetic type. This depends for its response on the large difference in magnetic susceptibility between oxgyen and other gases. Most combustion product gases other than nitrogen have small direct interference effects which become more significant in low oxygen concentration samples from the primary zone.

(d)   Hydrogen

In the absence of any known suitable on line method of hydrogen measurement, a gas chromatographic method is used.

To provide the required dynamic range with good resolution at low concentration a dual analysis system is operated using one katharometer detector (Fig 8). Sample flow is alternated between the two loops and swept through the appropriate column system by a carrier gas. Unwanted components are removed by the backflush gas.

If tracing of air flows is required, this system can be used for the detection of tracer gases such as helium.

(e)   Total hydrocarbon (THC)

In the method used here a sample valve isolates a discrete small volume sample. This 'slug' is introduced into a carrier stream and is carried to the flame ionisation detector (FID). The detector output is integrated with respect to time and the peak area obtained is related to the hydrocarbon concentration. An additional, very basic FID system was designed and used in the continuous sample mode to monitor the primary THC analyser sampling inlet. The magnitude of this response during purging is used by the computer to decide and preset the optimum gain setting of the primary unit. The basic FID also provides the sample monitoring facility (section 3.4).

(f)   Water vapour

A high temperature NDIR analyser is used to measure the water vapour concentration in the raw sample. A conventional (ie low temperature) NDIR analyser is also used in the system to measure the water vapour in the processed sample, primarily to monitor the performance of the drying system.

(g)   Oxides of nitrogen

In common with current practice the measurement of oxides of nitrogen is based on the principle of chemiluminescence. The instrument is twin channelled, one channel containing a thermal converter for the conversion of nitrogen dioxide to nitric oxide, and each channel contains a reactor cell monitored by a photomultiplier. Thus nitric oxide and nitric oxide plus nitrogen dioxide are measured concurrently. There is limited cross-sensitivity to other combustion products.

(h)   Fuel/air ratio (FAR) tracer measurement

A mass spectrometer is used for the rapid measurement of all species required to determine the carbon dioxide/nitrogen ratio (a simple function of FAR) in a completely burnt sample. This instrument also permits simultaneous tracing of component airflows by monitoring through the chamber changes in concentration of inert gases injected into the component (eg from a selected combustor air dilution hole). The usual tracer gas is helium but argon may be used (instead or as a second tracer) with lower accuracy and sensitivity since nearly 1% is already present in the air.

(i) Smoke

Initially, measurements are to be made on the sample from the exhaust averaging rakes. The SAE technique is used whereby a predefined volume of sample is filtered and the optical attenuation of the filter medium is calculated.

3.5.3 Calibration

Since all the analysers used are essentially comparators, the accuracy of any measurement depends on the calibration procedure. Basic calibration of each instrument depends on the preparation of a suitable number of mixtures of the constituent to be measured, to cover each range. These mixtures are generated in a suitable mixing device, usually a precision gas mixing pump fed with a primary mixture equivalent to about 90% of range, and the diluent gas, usually nitrogen. A careful audit of all primary field mixtures is carried out periodically to compare them with the high quality National Bureau of Standards related reference mixtures in the RAE gas standards laboratory[4].

The undiluted field mixtures are used routinely to 'span' each instrument during use. Computer control of solenoid selector valves provides frequent interleaving of zero and span readings with sample readings during a combustion run.

One calibration procedure which falls outside normal practice is that for water vapour. Since storage of vapour mixtures up to 15% by volume is impractical, their on-line generation is necessary. The water concentration of the mix produced by a vapour generator is measured by a cooled mirror dewpoint meter.

4   COMPUTER AND PERIPHERALS

The computer and its peripherals have functions which fall into two main categories - (a) monitoring and control and (b) data logging. The monitoring and control function includes provision for rig driving aids in the control room, raising alarms to warn of rig malfunctions and, in due course, will permit certain rig control operations to be undertaken. The data logging function includes driving the traversing probe and all instrumentation and recording all readings either periodically or on demand (Fig 9).

4.1   Computer system

A programmable logic controller (PLC) was chosen to provide routine safety monitoring and display, to inhibit rig start-up unless performed in a safe sequence and to provide automatic shut-down in the event of an emergency.

Control of the mass spectrometer requires detailed interfacing to its control electronics so a dedicated microcomputer is used. Both the microcomputer and the PLC are linked to the main computer.

4.1.1 Hardware

Fig 10 outlines the main features of the computer system. An Intercole Systems Ltd Compulog 3 data logger was used as the basis of the system. An extra 196 kbytes of memory, a programmable clock and a high speed direct memory access serial line interface have been incorporated. High speed disc storage media is by way of a removable disc cartridge with a fixed lower platter - the drive emulates four standard 10 Mbyte discs. A further 2 x 5 Mbyte capacity disc drive is used for transferring updates to system software. A small, 0.6 Mbyte capacity disc drive is used for archiving test results - results from one full day of running can be stored on a single 3½ inch flexible disc.

Three 16 bit ADCs are used for analogue voltage sampling and multiplexers allow up to 300 readings/second to be taken. Status channels are used to provide switching, either at TTL logic levels or of other voltages via internal relays. Paper tape is used for permanent archiving of programs and a line printer and printing terminal are used for obtaining hard copy.

4.1.2 Software

The RSX11-M operating system, a multi-user, multi-tasking facility allows each computer function to be implemented by a discrete program unit. Each program unit is ascribed a frequency of operation and a priority level. A high priority task, eg traverse control, can therefore gain maximum use of system resources if it requires them. A scheduler has been incorporated to ensure that even the lowest priority tasks are not locked out indefinitely.

The main memory includes a common block which contains all lookup tables (eg amplifier gain settings to voltage conversions), calibration coefficients and updated results. The rest of main memory is used by the operating system Executive and allocated to tasks as demand dictates. A commercial plotting package (Simpleplot) is used for on-line graphic presentations. Languages used are Fortran IV and the machine's assembler language, Macro-11.

4.2   Rig control, monitoring and displays

The computer is equipped with interface equipment for performing rig control functions. Currently, the rig is driven in a semi-manual fashion but computer control will be

gradually introduced as experience is gained. However, rig monitoring by the computer has been required from the outset. Two banks of 16 digital displays and seven analogue displays are used to provide monitoring information in engineering units. Thumbwheel switches are used to display the result of particular calculations. An alarm buzzer and warning lights draw attention to readings that transgress pre-defined limits and a VDU screen gives detailed information on the offending item. The computer also drives panel illumination to indicate when the combustor is alight and when flameout has occurred by a simple comparison between combustor inlet and outlet temperatures. The rig monitoring program runs on a cyclic basis, updating each display once every 3 seconds.

4.3   Probe control

Fig 11 shows the main components of one axis of the traversing probe control system. The control system is a hybrid computer/servo amplifier system with DC servo motors. The computer outputs a desired positional value for a specified axis down a serial line to a D to A converter. The analogue output from this converter feeds into a DC servo amplifier. The servo amplifier contains the necessary proportional, integral and derivative elements to drive the servo motor so that the desired position is reached and stabilised in the minimum timescale.

Independent feedback of probe position is supplied to the computer so that checks can be made on desired and achieved positions. This feature is used to avoid striking the chamber wall with the probe, an event which is more likely to happen whilst entering or withdrawing from the combustor.

The dummy traverse gear is similar to the rig traverser, but contains only positional feedback potentiometers with no drive motors. The dummy traverser can be moved manually whilst the potentiometers are being read by the computer. A control button is pressed to signal the computer at positions where a gas analysis sample is required.

In order to collect samples from discrete positions within the combustor, an alternate sequence of positioning the probe and collecting and analysing the sample is followed. At each position, time is allowed for the sampled gas to reach the analysers and for the analysers to stabilise. The entire system is designed to run automatically at a rate of 120 probe positions per hour with a positional resolution better than 1 mm. Sample line pressures and temperatures are continuously monitored and warnings are raised if a malfunction occurs.

4.4   Sample analysis

When the probe is at a sampling position and sample is reaching the instruments, the computer initiates an analysis cycle. The continuous readout instruments are sampled 10 times per position and the readings are averaged by the program. 'Slug' analysis instruments and the mass spectrometer are cycled by the program and the readings, taken periodically during 'slug' transfer, are integrated through the cycle.

4.4.1 Chromatographic instruments

The program firstly reads THC with the wide band, low accuracy FID instrument. This reading enables the program to calculate and set the gain range for the narrow band high accuracy FID, and to initiate 'slug' transfer. The hydrogen gas chromatograph is also started at this stage. Finally the mass spectrometer analysis cycle is inititated. The probe is moved to the next sampling position before all analysis cycles are complete to take advantage of the delay during chromatograph analysis times.

The instruments use a 10 volt full scale analogue output signal which is read by the computer using common mode rejection techniques to minimise noise.

4.4.2 Mass spectrometer

The mass numbers of the gas constituents to be measured by the mass spectrometer are held in a lookup table in the microcomputer. This lookup table and the program software are loaded from the main computer at the start of a run. On initiation of an analysis cycle by the main computer, the microcomputer drives the mass spectrometer to the first mass number in the table. It then scans the peak, averaging many readings to produce an accurate result, and passes the averaged result to the main computer. The process is repeated for all masses in the table. The mass spectrometer has the slowest sample transfer time of all the instruments and so, in real time, readings are being taken after the discrete instruments.

4.5   Processing and presentation of results

During a run, results can be plotted on a graphic display terminal and hard copy may be taken as required, as well as being stored in a file on a 3½ inch flexible disc. This disc can be replayed into an off-line computer system where data from selected runs can be analysed.

A remote workstation is used to process the data and present results. This workstation contains 3/4 Mbyte desk top computer, two printers and a colour graphics display terminal with colour hardcopy unit. A commercial database system is used to collate the data items of interest and produce a file for further processing. This file is read by programs which calculate derived results and present them either printed out as tables or

plotted in colour as two- or three-dimensional contours using the commercial Simpleplot plotting package. A complete picture can be formed from the data points, thus illustrating the combustion process within the test chamber.

5 DISCUSSION

As pressures and temperatures of advanced aero gas turbine engines rise to meet the demands of the military and civil operators the problems of ensuring that the combustion chamber can satisfy the new performance requirements without compromising durability become increasingly severe. New combustors face diminishing design margins and the combustion engineer now requires much greater information about the processes which influence wall temperatures and outlet temperature distributions. Mathematical modelling of the relevant processes is advancing but is not yet able to provide all the assurances required at the research or development stages. Invariably these methods require some input from experimentation and high quality data concerning the internal flow structure or fuel/air distribution, for example, are often lacking.

New instrumentation methods are being actively sought and developed. Many of these rely on non-intrusive techniques which require optical access to the flow within the chamber. Whilst these have many advantages they are not yet widely available and suffer many disadvantages in their application to full scale practical combustors. The Pyestock system offers a practical method of meeting the demands for more information about the internal processes both quickly and cheaply. Whilst intrusive probe techniques invariably cause some distortion of the absolute values of the information sought, experience has shown that the single point probe is an effective compromise and can satisfy many of the needs outlined above.

The Pyestock rig is seen to have very good prospects of answering many of the questions facing combustion researchers both quickly and economically. Having been fully tested in the burning mode before delivery the mechanical parts of the rig are in final stages of installation and commissioning is well advanced with the expectation of full operational status by mid 1986.

6 ACKNOWLEDGMENTS

The authors wish to gratefully acknowledge the contributions made by their colleagues and associates in the development of this Sector Combustion Rig.

Acknowledgement is also made of the valuable contributions which were made by Lucas Aerospace during the design and procurement stages of the rig.

Table 1

Measured constituent	Instrument type	Range	Sample type
Carbon dioxide	NDIR	0-15%	Processed
Carbon dioxide	NDIR	0-2%	Processed
Carbon monoxide	NDIR	0-15%	Processed
Carbon monoxide	NDIR	0-1%	Processed
Carbon monoxide	NDIR	0-0.05%	Processed
Oxygen	Paramagnetic	0-25%	Processed
Hydrogen	Chromatograph	$\left\{\begin{array}{l}0-0.1\% \\ 0-10\%\end{array}\right.$	Processed
Water vapour	NDIR	0-15%	Raw
Water vapour	NDIR	0-5%	Raw
Carbon dioxide	NDIR	0-15%	Raw
Carbon dioxide	NDIR	0-2%	Raw
THC	Flame ionisation	0-10%	Raw
NO_x	Chemiluminescence	0-0.1%	Raw
NO	Chemiluminescence	0-0.1%	Raw
FAR	Mass spectrometer		Burnt
Tracer	Mass spectrometer		Burnt

REFERENCES

1 Jones, W.P., Clifford, W.C., Priddin, C.H. and deChair, R., "A comparison between predicted and measured species concentrations and velocities in a research combustor", AGARD, CP-229, 1977

2 Lefebvre, A.H., "Gas turbine combustion", Hemisphere Publishing Corporation, 1983, pp 463-514

3 "Procedure for the continuous sampling and measurement of gaseous emissions from aircraft turbine engines", Aerospace recommended practice 1256, Society of Automotive Engineers, 1980

4 Murrell, R.J., "The RAE Pyestock Gas Analysis Standards Laboratory", RAE TM-P1019, 1984
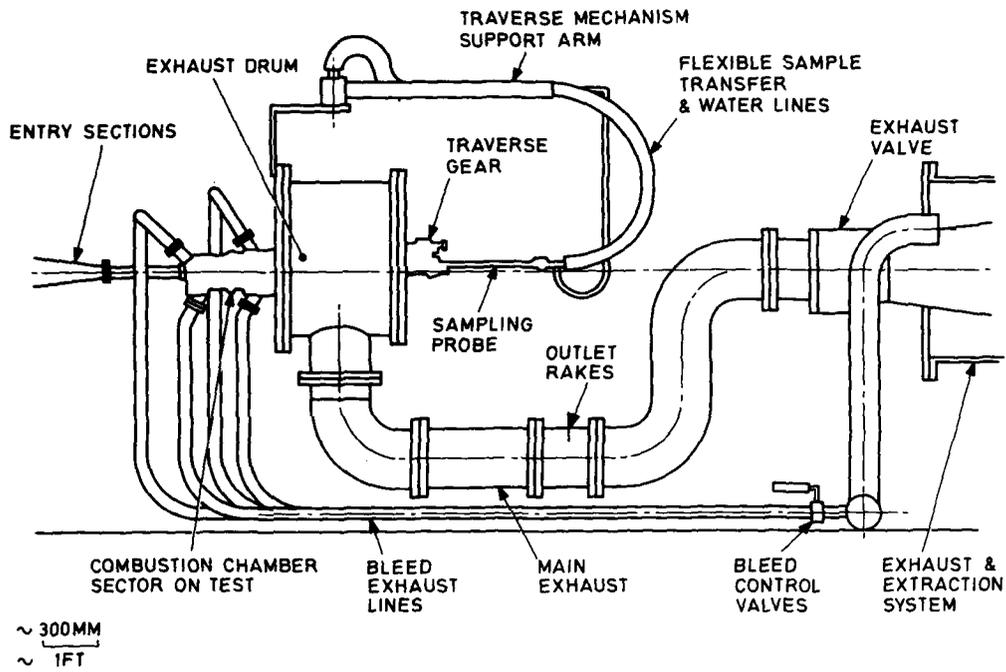
Fig 1   General arrangement of sector combustion rig

Fig 2   Sector combustion rig
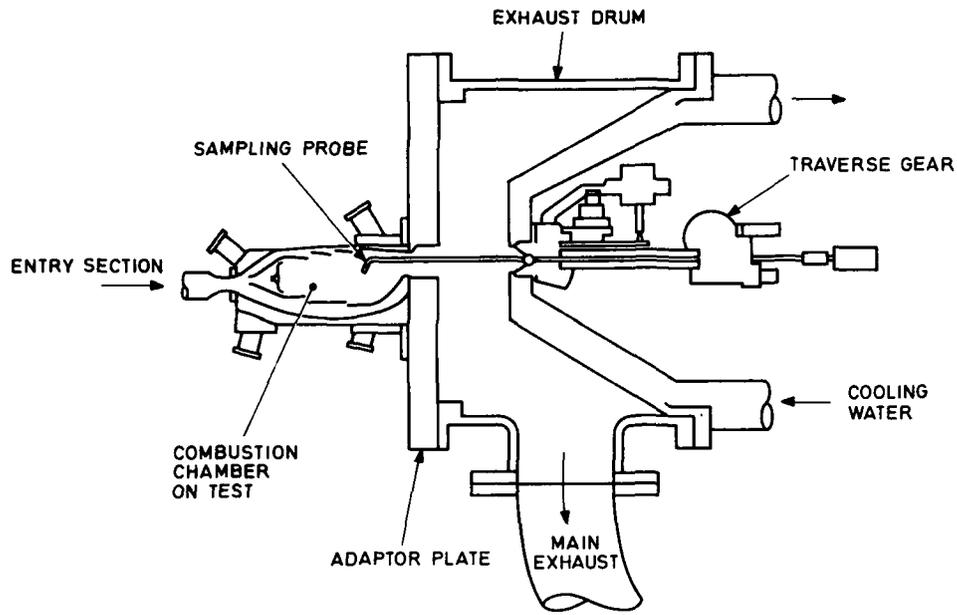
Fig 3 Working section of sector combustion rig
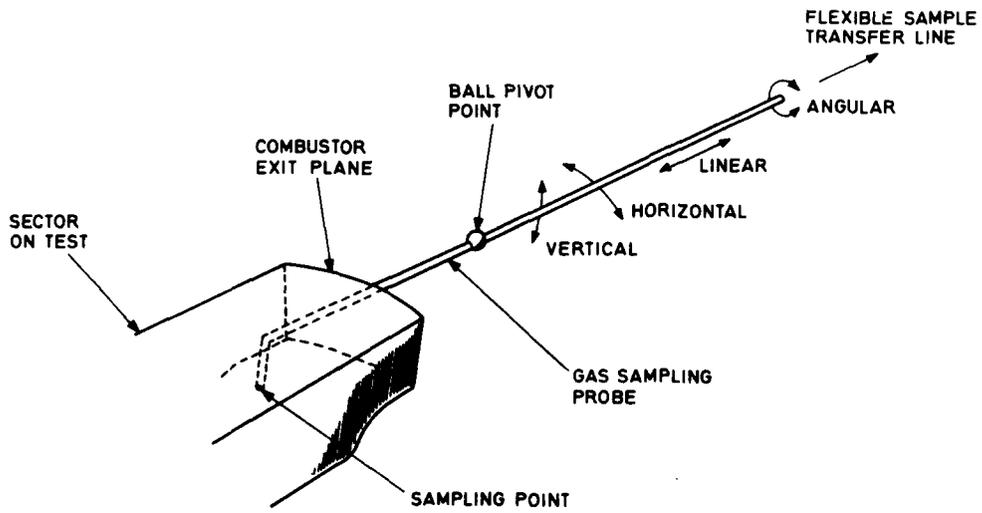
Fig 4 Traverse gear movements
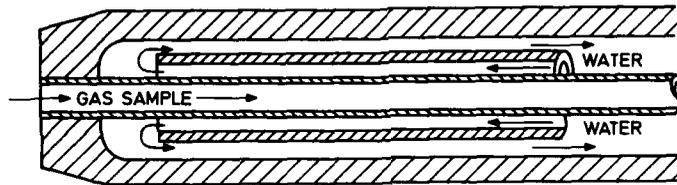
Fig 5   Sampling probe
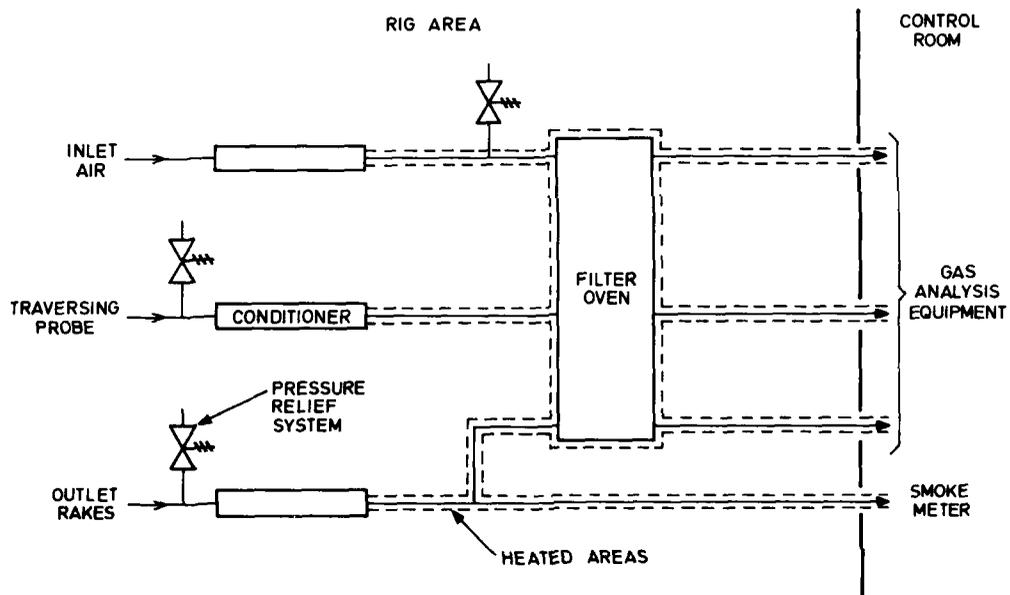
Fig 6   Sampling and transfer system - rig area
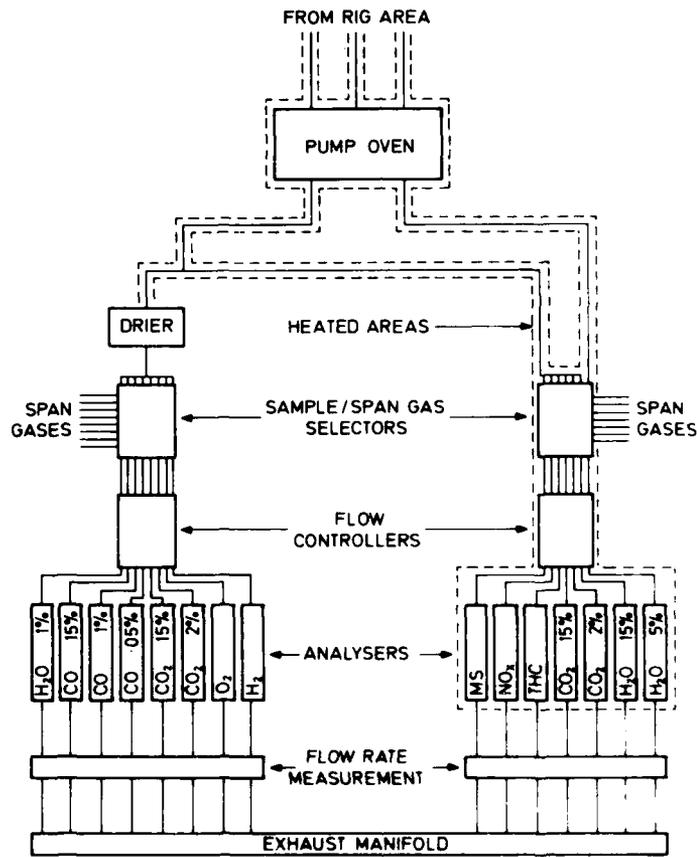
Fig 7 Gas analysis console - control room
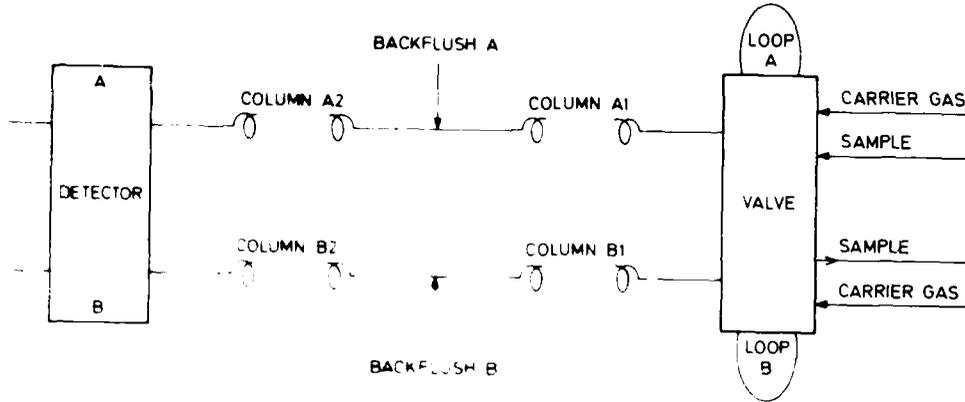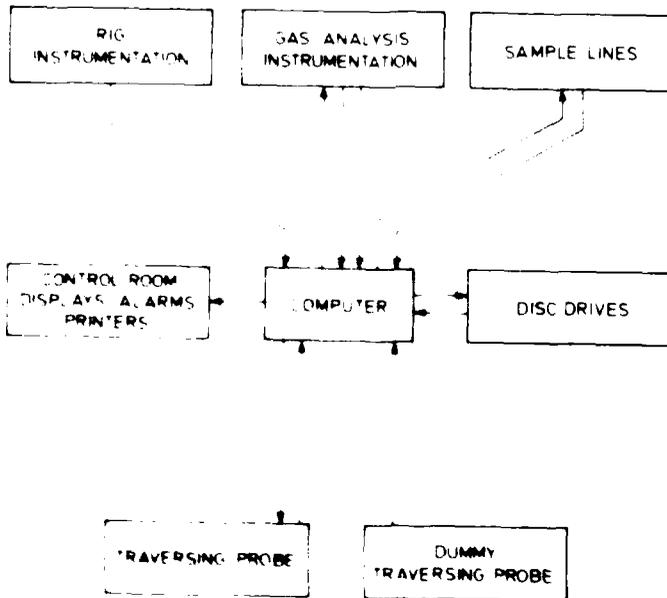
A sampling and detection system for hydrogen
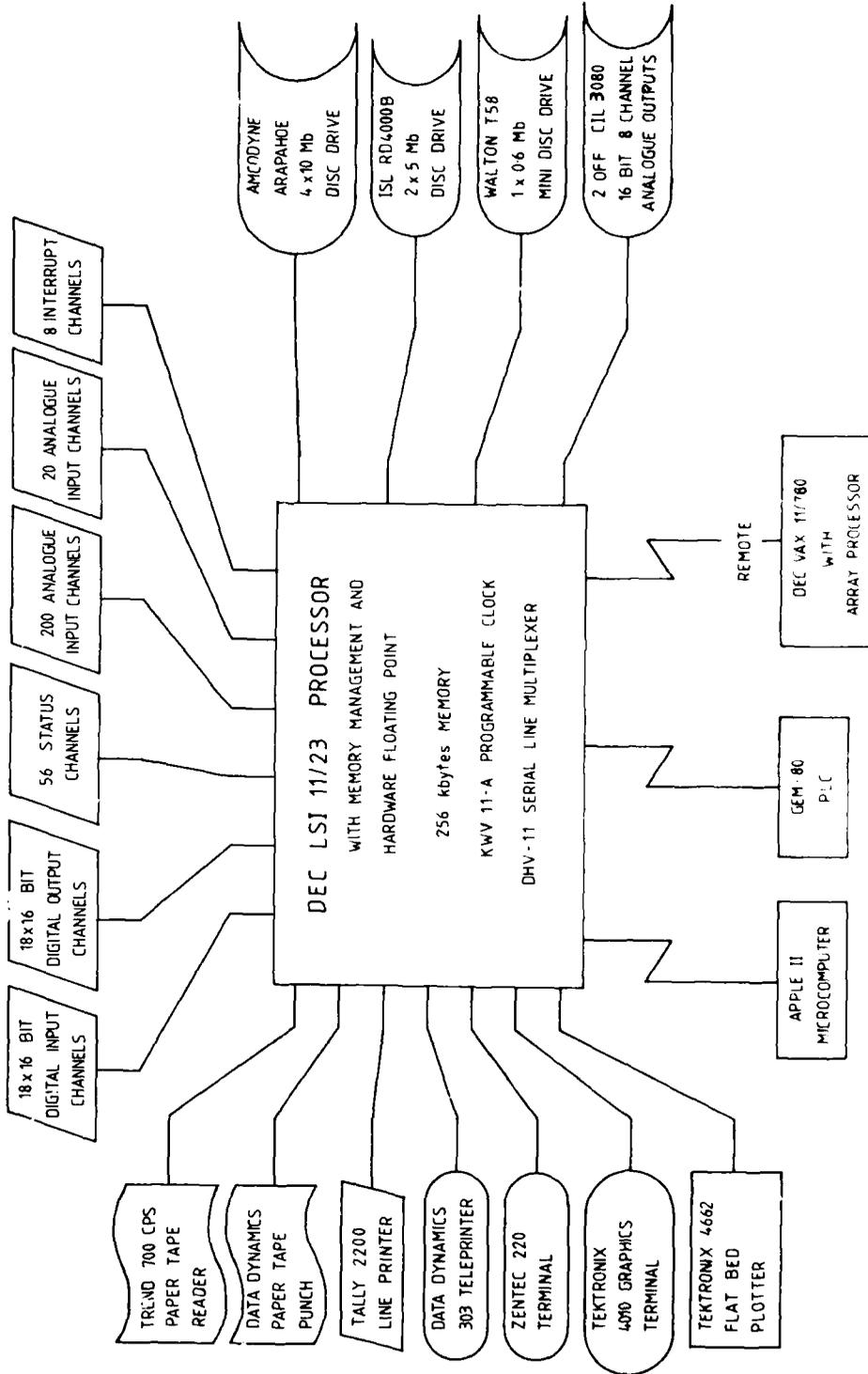
Fig 10 DCH data acquisition and processing system
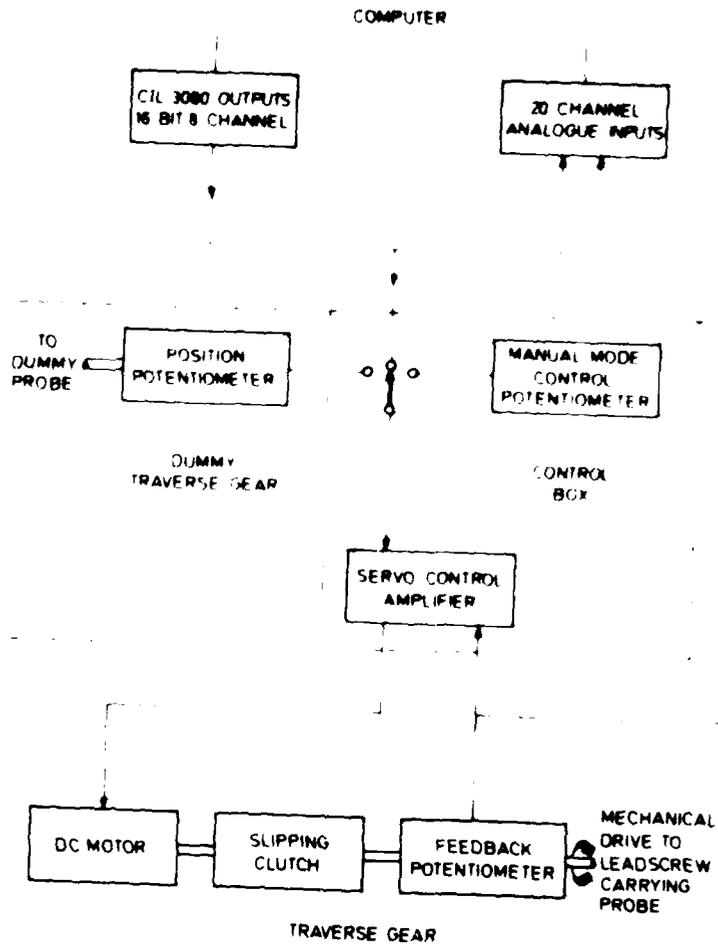
Fig 11   Probe control system

DISCUSSION

T.A.Jackson, US

(1) What is your target temperature and the target time to achieve this temperature in order to quench primary zone reactions?

(2) Without supersonic quench or diluent by inert gas addition, how do you achieve a sufficiently rapid quench of reactions which occur on the order of milliseconds?

Author's Reply

Our target in order to quench primary zone reactions is to reduce the temperature to less than 1600 K in less than 300 microseconds. Bench tests and a computer model of the convective system described in the paper indicate that the probe will reduce the sample temperature from 2500 K to 1500 K in 180 to 250 microseconds depending on the probe bore diameter.

J.Allen, US

How many spatial locations are typically used in a complete combustor survey? Is the rig set point stability sufficient over this extended period of time?

Author's Reply

During general surveys we expect to take samples at 10 mm spacings. This can lead to a large number of points (say 1000) and corresponding long run times. After some initial problems with the compressor pressure controller we now achieve remarkable stability, eg. pressure and inlet temperature maintained within 0.02 atm and 3 K respectively for extended periods of operation.

P.A.Pheeley, US

(1) Have you made any comparisons between rig and engine operation?

(2) Have you made any high frequency comparisons?

Author's Reply

(1) Comparisons have been made in the UK and shown satisfactory agreement.

(2) Present instrumentation is not capable of making high frequency measurements. The ability to make such measurements is dependent on the availability of suitable instruments.

R.York, US

(1) It appears that the rig has a universal pressure plenum instead of an actual engine combustor case. Our experience is that there is often a strong interaction between the combustor liner and the case which affects the air flow distribution. How do you assure inclusion of engine installation effects in your setup?

(2) I second the concern over the design of your sampling probe, relative to the ability to adequately quench the sample. The key element of your system, the probe, does not appear to represent the same level of investment and sophistication as the traverse, analysers, computers, etc.

Author's Reply

(1) The pressure plenum is designed to suit the particular installation.

The example included in the paper (Fig 3) uses an engine casing inside the pressure casing on the inner diameter and the outer diameter pressure casing replicates the engine scantlings.

Compressor delivery profiles can be simulated using grids, trips, etc.

(2) On the basis of earlier experience (Ref.1) we consider that the final design will provide adequate quenching without causing excessive interference with the flows and reactions we are measuring.

DIGITAL IMAGE PROCESSING APPLIED TO FLUID DYNAMIC PROBLEMS

J.M. Buchlin

von Karman Institute for Fluid Dynamics
Chausée de Waterloo, 72
B - 1640 Rhode Saint Genèse - Belgium

SUMMARY

The present paper deals with applications of visualization techniques associated with Digital Image Processing in fluid dynamics. Two typical fluid flow problems of interest for propulsion are selected to illustrate the purpose.
- The mixing properties of the jet. Laser tomography and light scattering from micro-droplets of oil lead to the quantification of the three dimensional concentration field.
- The local heat transfer distribution on a heated surface from oblique and co-linear impinging jets. Thermographic imaging system is used. Digitized infrared pictures are processed to provide local and average values of the heat transfer coefficients.

INTRODUCTION

Digital Image Processing (DIP) is a new branch of signal processing which becomes increasingly important with the improvement of digital computer capabilities. Digital image processing has already many applications in industry, biomedicine and space exploration. One recent application of DIP which is developing rapidly is in the field of fluid mechanics where flow visualization plays a predominant role. When integrated together computer image analysis and flow visualization techniques become powerful tools available to scientists for the extraction of quantitative information from pictures. In addition such an approach has the advantage common to purely optical probes of causing minimal disturbance in the flow.

The present paper deals with applications of DIP to fluid dynamic problems. Two typical fluid flow problems of interest for propulsion are selected to illustrate the purpose. The first example concerns the mixing process of a gas jet in a coflowing air stream. The second example considers the determination of the local heat transfer coefficient at the impaction of gas jets onto heated flat plate. For both the purposes selected the potential and the actual limitations of the DIP technique are emphasized.

1. MIXING PROPERTIES IN A JET

1.1 Introduction

The development of techniques for the measurement of concentration of a tracer or gas species in a flow field is of particular interest for improving the knowledge of mechanisms of mixing processes. Average concentration measurement can be performed by isokinetic sampling technique (Ref. 1). A more involved technique to determine the concentration has been developed at VKI in using wire principles to measure the thermal conductivity of the gas mixture (Ref. 2). At the same time non-intrusive techniques have been proposed (Refs. 3, 4). They are mainly based on the light scattering phenomena. The concentration is inferred from the intensity of the Lorentz-Mie scattered radiation from the flow which is seeded by small particles. In the first technique the measuring volume is formed by the intersection of two laser beams. A proper optical system collects and focusses the light scattered onto a multiplier tube. The second non-intrusive technique allows the spatial determination of the concentration in two dimensions using the digital image of the flow when illuminated by laser sheet. Its development at VKI has been initiated by Lourenço (Ref. 5) and continued by Borleteau & Buchlin (Ref. 6). A similar experimental procedure is also followed by Schon (Ref. 7). The main features of this technique are presented on the basis of the study carried out at VKI and dealing with the mixing properties of a gas jet coflowing within an air stream which is also regarded as an interesting test exercise by other researchers (Refs. 7, 8).

1.2 Measurement technique

The measurement technique lies on optical detection of the light scattered by particles in suspension in a fluid. It is shown by Becker et al. (Ref. 9) that light scattered is a linear measure of marker concentration when the concentration profile does not exhibit important curvature within the control volume. In the study of the mixing of the two gases, one of the species is seeded with particles which are used as markers. In the present technique the seeding selected is formed by small oil droplets of about 1.5 micrometers of diameter (Ref. 10). They have small inertia; their velocity response is better than 90% up to frequency of 10 kHz (Ref. 9). In addition because they have small residence time, the effects of evaporation and coagulation due to collision and diffusion by Brownian are negligible. The density of these tracers in the measuring volume has to be sufficiently low to ensure independent scattering. After Van der Hulst (Ref. 11), oil droplets of 1.5 micrometer have not to exceed 3% in volume fraction which corresponds to a tracer concentration of 2.10^{15} per m^3. A more restrictive condition on the sol particles concentration is necessary to minimize the attenuation of the light scattered from the measuring volume and traversing the mixing field. It turns out that an upper limit of 10^{12} particles per m^3 must be ascertained. In addition, according to Rosenweig (Ref. 12) the marker shot noise is negligible if the number of tracers in the measuring volume is larger than 1000.

The incident light is formed by a laser plane projected in the flow field. The optical signal produced by the light scattered from the markers is detected by video camera. The video signal is sampled to obtain a digital image which is a bounded two dimensional space discrete distribution of light intensity. The actual scattered light in the laser sheet is reconstructed from the digital image of the detected light by using DIP techniques, including noise spikes removal, low pass filtering, and correction for the non-uniform distribution of the incident light in the laser sheet and for optical defects. The points of measurements

are the resolvable points of reconstructed digital image which involves reasonably small volume of gas satisfying all requirements. The value of the scattered light intensity at a point of measurement is displayed on the image as one of the possible intensity levels. Calibration of data in the digital image is done by measuring the concentration of the seeded species with a single point measurement technique at a few points in the flow. Another possibility is to take advantage of a priori knowledge of data displayed on the digital image. For example, in the study of the mixing process of jet, the concentration level is 100% just at the exhaust of the nozzle and 0% at the outside of the jet. Then, provided the linearity of the measurement technique could be checked, no calibration would be required to determine the concentration level from the reconstructed digital image. It is now worth quoting that this technique differs slightly from that used by Schon which involves the counting of the tracing particles (Ref. 7).

1.3 Application to the mixing properties of gas jets

1.3.1 Test facility and instrumentation

The application of the aforepresented non-intrusive technique is illustrated by the measurement of concentration field of a freon 12 jet discharging at 1.65 m/s into a co-flowing air stream at 0.6 m/s. The experimental setup is sketched in figure 1. The jet nozzle of 4.25 mm in diameter is located on the axis
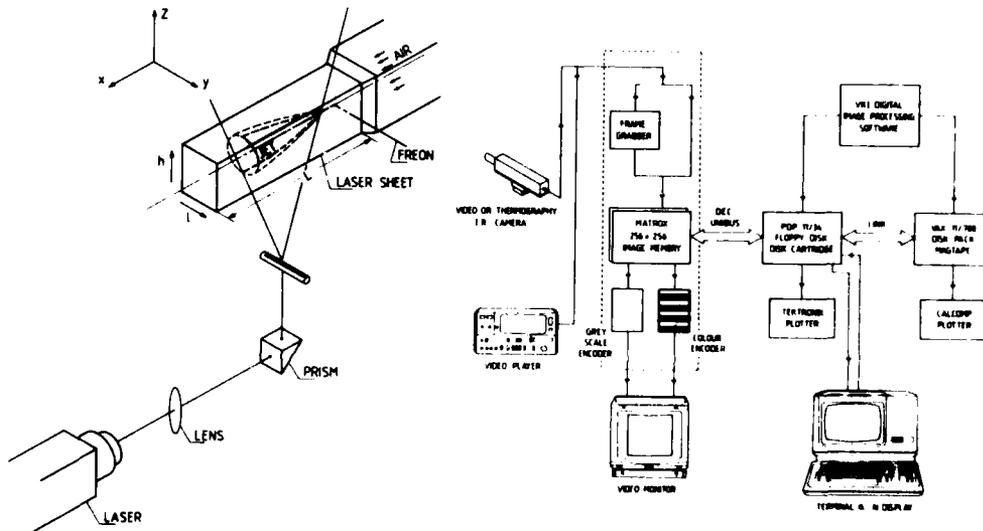
FIG. 1 - SKETCH OF THE TEST SETUP FOR JET MIXING   FIG. 2 - VKI DIGITAL IMAGE PROCESSING SYSTEM

of symmetry of the test section of a wind tunnel with a transparent square cross section of 0.20×0.20 m and 2 m long. The freon jet is seeded with oil smoke.

The incident light plane is produced by passing an argon laser beam (≈ 5145 Å) of 2 W continuous power through a cylindrical lens. The light scattered from the laser sheet is detected by a video camera and recorded by video tape of U-matic format which is later analyzed frame by frame by means of the VKI DIP system the general structure of which is shown in figure 2. A frame grabber with a resolution of 8 bits/pixel converts each frame in digital form updating continuously two memory boards with a spatial resolution of 256×256 pixels. The combination of these two boards provides a quantization level of 8 bits/pixel allowing up to 256 gray level scales or false colour variations. For gray level to colour conversion and monitoring purposes a high speed 8-bit D/A converter and a two 8-bit gray scale/colour encoders are also built in the system. The false colour output is displayed on a Barco monitor. The assembly is mounted on the unibus of a PDP 11/34 which is the host computer controlling the DIP system. In addition the PDP 11/34 is linked to a VAX 11/780 to handle heavy processing of large matrices involed by image analysis. A software package specially developed in Marco II assembly language permits the access of the DIP system by Fortran programs.

1.3.2 Typical results

The optical response of the whole imaging system is accounted for by recording before each test a suitable illumination reference obtained by flooding the test section with oil smoke such that the marker density is uniformly distributed. Figure 3 shows a typical digitized reference image displayed with 16 pseudo-colours with increasing gray levels from left to right. Such final reference image has been obtained after using a one dimensional FIR low pass filter based on 51 points with a Hamming window function. This image reflects firstly the effect of the Gaussian distribution of the incident light (horizontal variations) and secondly the focussing effect of the spherical lens used in the optical setup (vertical profile). It is worth noting that all the useful numerical pictures are processed with the same digital filter, the modular transfer and the impulse response functiond of whichare plotted in figure 4 and corrected by the corresponding reference image.

FILTERED IMAGE

FIG. 3 - RESPONSE OF IMAGING SYSTEM

The laser sheet is moved transversely along the y-direction to scan the jet according to nine different vertical longitudinal cuts. The nine resulting digitized images shown in figure 5 portray the spreading of the mixing field; each colour is assigned to an isoconcentration contour. A first feature of interest is the concentration in the plane of symmetry (y=0). The centerline concentration profile in this plane is plotted in normalized form in figure 6. The measurements from the optical technique are compared to the
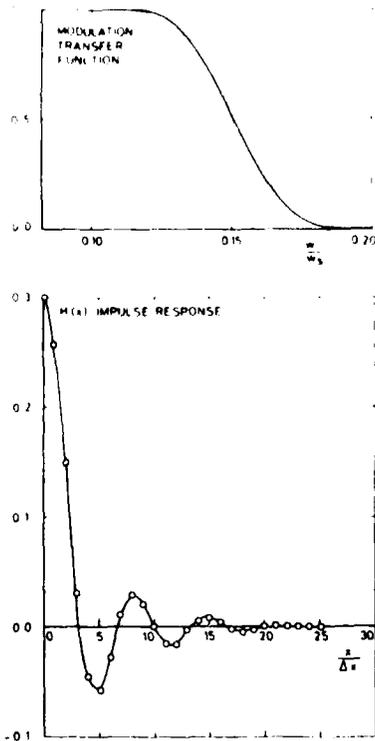
FIG. 4 - ONE DIMENSIONAL FIR FILTER (51 POINTS)   FIG. 5 - DIGITAL IMAGES OF THE FREON JET (256 GREY LEVELS)

measurements performed with a single point hot wire sensor (Ref. 2) in the range of distance 20-35 nozzle diameters. Good agreement is observed. However, poor repeatability is found in the initial region of the jet. The reason invoked emphasizes the eventual too high tracer density which leads to partial extinguishment
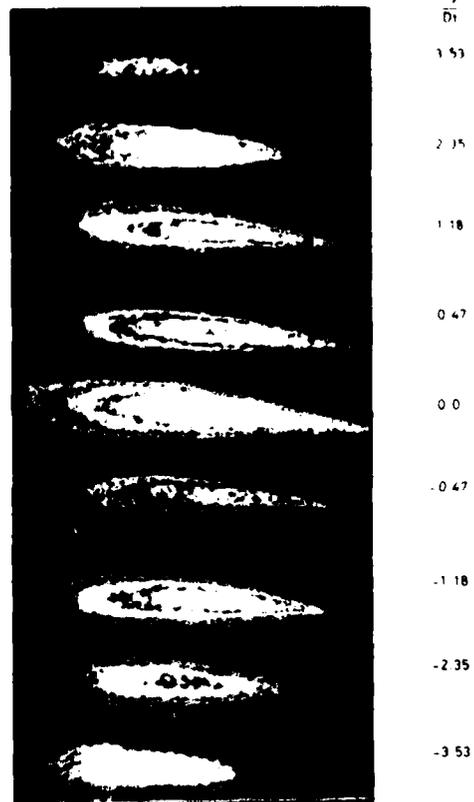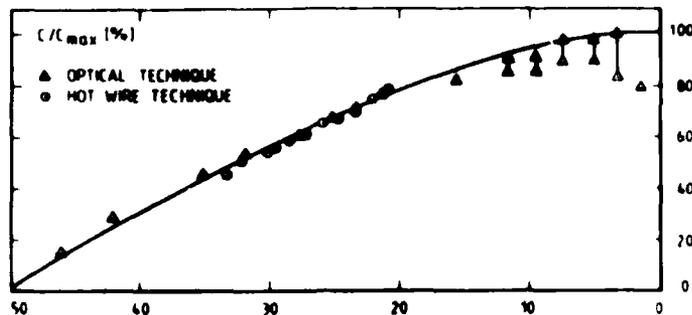
FIG. 6 - CENTERLINE CONCENTRATION PROFILE. PLANE (x.0)

of the laser sheet as well as the breaking conditions
of the independent scattering. The nine pictures
presented in figure 5 are grouped in a tri-dimensional
matrix which is scanned to afford isoconcentration
lines in the section normal to the flow. Typical map
of isoplets is shown in figure 7, emphasis is again
placed on the comparison between the two measurement
techniques. In the center or core of the jet the
agreement between the optical and hot wire measure-
ments is satisfactory. Moving towards the periphery
of the jet, the results become slightly different.
Presumably in this region the probe affects the mix-
ing process because the aspirating velocity of the
concentration sensor is larger than the actual velo-
city, in the mixing field. The extra amount of air
added to the actual mixture leads to measure lower
concentration at the edges of the jet with the hot
wire sensor.

1.4 Conclusions

An optical technique to measure the two dimen-
sional concentration field is presented. The prin-
ciples of the technique rely on the measurement of
the light scattered by markers seeding the flow
field. The illuminating plane is produced by laser
tomography. The optical two dimensional signal is
sampled to reconstruct digitized pictures of the
flow field which are analyzed by using DIP. This

FIG. 7 - COMPARISON OF ISOCONCENTRATION LINES AT
x/D = 32.5 (— AFTER OPTICAL TECHNIQUE,
-- AFTER SINGLE POINT MEASUREMENTS)

non-intrusive technique is compared to a single
point measurement technique based on the hot wire principle in the case of mixing properties of a freon jet
in a co-flowing air stream. Good agreement is observed between the two types of measurements in the center of
the jet. However, the results describing the initial region of the jet show that the optical method is
sensitive to density of the tracers at the source, that is, to independent scattering conditions and partial
extinguishment of the incident light.

2. HEAT TRANSFER CHARACTERISTICS OF IMPINGING JETS

2.1 Introduction

Impinging jets are often encountered in processes where heat and/or mass transfer prevail because of
their ability to produce high local transport coefficients.

Some of their more important applications are the annealing of metals, the tempering of glass sheets,
the drying of paper and textiles and the cooling of turbine blades. A problem of interest is also the
direct interaction of the propulsion jet with the flaps in the case of STOL aircraft.

The basic configuration generally investigated is the single jet impacting normally on a flat plate
(Refs. 13-23). In some applications the jet may be oblique either because of constraint on the nozzle
position or deflection by cross flow before the impingement (Refs. 31, 49). However, practical considera-
tions lead to study array of jets emphasizing the effect of the mutual interference of the nearby jets
(Refs. 32-38, 50).

Different experimental techniques have been processed to determine the local and the average heat trans-
fer coefficients on the target surface. Most of the experimental procedures are based on the use of heated
or cooled flat plate instrumented with temperature sensors and/or calorimeters (Refs. 13, 14, 20, 21, 24
32, 34, 37, 49, 50). Mass transfer analogy involving water evaporation (as Schlunder & Krotzschref reported
in Ref. 36) or naphtalene sublimation (Refs. 31, 35) or diffusion controlled electrolysis (Ref. 19) is also
adopted. The technique which is presented in this paper belongs to the visualization class as that developed
by Goldstein & Timmers who utilized heated plate covered by liquid crystals substance (Ref. 38). It mainly
relies on the utilization of constant emissivity heat flat foil the temperature of which is measured

with a thermographic system. The recent progress made in infrared imaging systems commercially available (Refs. 39-44) has significantly initiated the development of thermographic techniques for dealing with fluid flow problems (see for instance 44-47). One of its advantages apart from the non-intrusive character that it owns,is that the resulting thermograms can be fruitfully analyzed by means of digital image processing. The method is exemplified through revised experimental result. of investigations of single oblique jet (Ref. 49) and array of collinear jets (Ref. 50) carried out at VKI.

2.2 Test apparatus and experimental procedure

A sketch of the experimental setup is shown in figure 8. Compressed air is supplied from a regulated 7 bar line. The air flow rate is measured by means of a rotameter before it enters in a plenum chamber
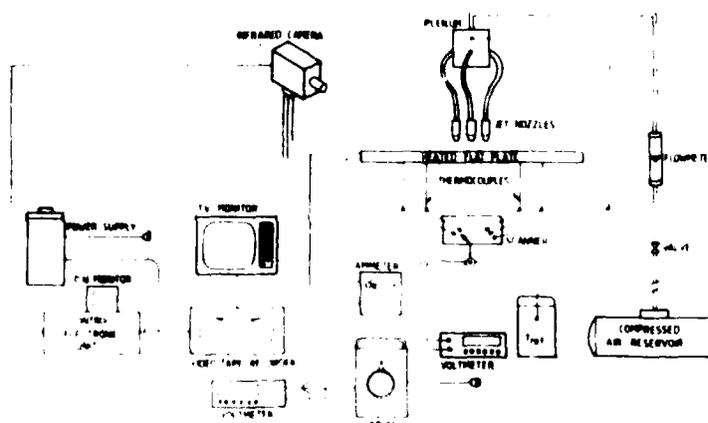
FIG. 8 - SKETCH OF THE EXPERIMENTAL SETUP FOR IMPINGING TESTS

where fluid temperature is measured. The air jets are issued from convergent type brass nozzles with 0.01 m (single jet tests) or 0.008 m (co-linear jet tests) exit diameter. The quality of the velocity profile produced by the nozzles can be appreciated in figure 9.

A constant heat flux flat plate of 0.56-0.51 m is constructed from a circuit board - EGS 102 type GE - made of 35 micrometers copper foil coated by an epoxy FR-4 sheet of 0.0015 m thick. The insulating face of the plate is painted black uniformly and exposed to the impinging flow. The copper face of the plate is machined to cut lengthwise grooves of 0.003 m forming a rectangular wavy continuous strip which is connected to an AC power source controlled by variac and measured by ammeter and voltmeter. Back and edge conduction losse; are minimized by embedding the heating surface in a styrofoam packed pine wood allowing for lateral thermal expansion.

FIG. 9 - VELOCITY PROFILE IN AIR JETS

The black heated plate is sampled by a video infrared camera of Intrametrics 525 type which allows only relative temperature measurement (the minimum detectable temperature difference provided by this imaging radiometer system is 0.3°C). Thus, some copper-constantan junctions are mounted flush and uniformly distributed in the epoxy jet facing layer to provide information for the determination of the absolute temperature-intensity calibration curve of the thermograms. The infrared pictures are recorded on video tape replayed frame by frame for analysis by the aforepresented DIP system (cfr. § 1.3.1).

The principle of the technique demands to adjust a constant energy dissipation per unit area, q_w, from Joule heating and to measure the local distribution of the surface temperature impacted by the air jets. The local heat transfer coefficient, h_w, is calculated from the conventional relationship :

$$h_w(x) = \frac{q_w - q_{loss}}{T_w(x) - T_{jr}} \tag{1}$$

where q_{loss} represents the heat loss including conduction and radiation effects. It turns out that q_{loss} is generally less than 3% of the total heat flux. Tjr is the air recovery temperature which, for most of the present experimental tests, does not differ significantly from the temperature measured in the plenum temperature.

2.3 Typical results

For each test, a time of about 10 min is allocated to ensure the steady state conditions be reached before recording the infrared image and the camera is tilted (see Fig. 8) in order to visualize all the target without being masked by the jet nozzle system.

Figure 10 shows a typical unprocessed digitized infrared picture (displayed in pseudo colours) of the impaction area of a normal single jet onto the heated flat plate. The analog signal is digitized in 64 discrete intensity levels since the IR camera output is presently a 6-bit signal. In a first step a spatial warping technique for image restoration is applied to correct the distortion effect due to camera tilting angle (Ref. 51). In a second step the redressed image is enhanced; a digital noise cleaning algorithm based on a low pass convolution masked is adopted (Ref. 52).

The convolution 3 by 3 array H of low-pass form utilized is :
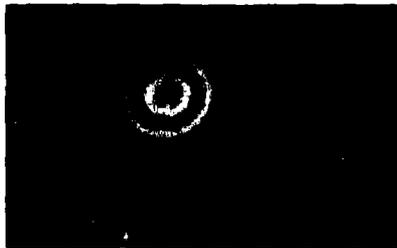
FIG. 10 - DIGITIZED NO-RESTORED THERMOGRAM
FOR NORMAL IMPINGING JET

$$H = \frac{1}{10} \begin{vmatrix} 1 & 1 & 1 \\ 1 & 2 & 1 \\ 1 & 1 & 1 \end{vmatrix} \qquad (2)$$

$$OUT(m1,m2) = \sum_{n1, n2} \sum INP(n1,n2)H(m1-n1+1,m2-n2+1) \qquad (3)$$

In a third step the grey intensity distribution of the noise smoothed images are calibrated. The average intensity of a small 4 by 4 pixel area centered on the position of selected thermocouples is calculated by the DIP system and related to the corresponding temperature through a polynomial curve fitting procedure.

FIG. 11a

Typical restored and calibrated digital images are shown in figure 11. They afford quantitative visualization of the thermal field of the heated flat plate for the single normal jet (Fig. 11a), a 30 degree inclined jet (Fig. 11b), and three co-linear jets (Fig. 11c). Note in figure 11c only a view of the center and outer jet is presented.

FIG. 11b

The wall temperature contours so determined from infrared pictures are reduced in terms of the local Nusselt number distributions. A typical spanwise Nu-profile for normal round jet is plotted in figure 12; the nozzle-plate spacing is two orifice diameters ($z/d = 2$) and the Reynolds number Re_d is 40000. Figure 12 compares the present measurements to the data obtained by means of the liquid crystal technique (Ref. 38) which appear to be 30% lower. In spite of this ascertainment it can be concluded that similar trends are observed. In particular the minimum local heat transfer coefficient ocrurring at the stagnation point is a characteristic of this flow configuration ($z/d = 2$).

It indicates that the mixing-induced turbulence has not penetrated to the center of the jet. Only the potential core of the jet impacts onto the stagnation region because of the small nozzle-to-target spacing. However, it is remarked that more informations are available on the thermographic Nu-profile. The set of distinct humps symmetrically shared on the profiles are noteworthy and in full agreement with the mass transfer data produced by Koopman & Sparrow (Ref. 35) and the results obtained by Gordon & Akfirat with a two dimensional air jet (Ref. 33). On the other hand they corroborate the shear stress measurements performed by Kamoi & Tanaka (Ref. 27) and support the numerical

FIG. 11c

FIG. 11 - TYPICAL RESTORED & FILTERED THERMOGRAMS

simulations achieved by Amano (Ref. 22).
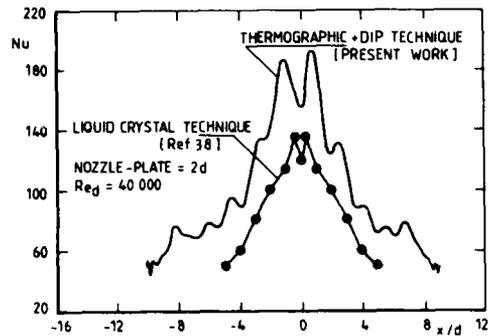
FIG. 12 - SPANWISE Nu-PROFILE FOR NORMAL ROUND JET
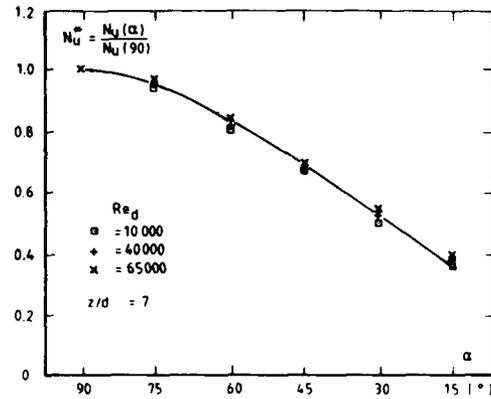
FIG. 13 - EFFECT OF THE INCLINATION ANGLE α ON THE MAXIMUM NUSSELT NUMBER

Figure 13 deals with the effect of the jet inclination on the maximum value of the heat transfer coefficient. The ratio Nu* of the Nusselt number of oblique jet, $Nu(\alpha, Re_d)$, to the Nusselt number of a normal jet, $Nu(90, Re_d)$, determined for the same flow conditions, is plotted versus the tilt angle of the nozzle, α, counted with respect to the plate. The modest data scatter observed in figure 13 enables to presume that Nu* does not depend on the Reynolds number in the range investigated ($10000 \cdot Re_d \cdot 65000$). The <Nu*> values calculated on averaging areas are compared well to the Sparrow & Lovell mass transfer data (Ref. 31) as shown in figure 14 which in addition emphasizes the net effect of the z/d parameter on the heat transfer coefficient.
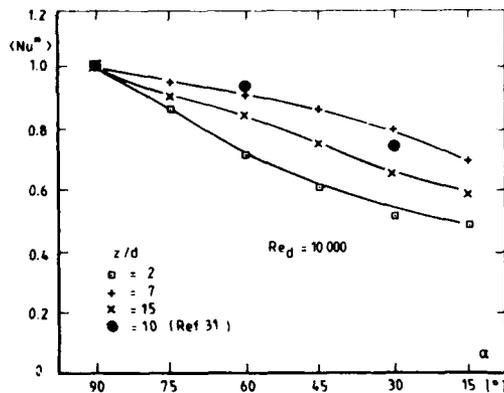
FIG. 14 - EFFECT OF THE INCLINATION ANGLE α ON THE AREA AVERAGED NUSSELT NUMBER
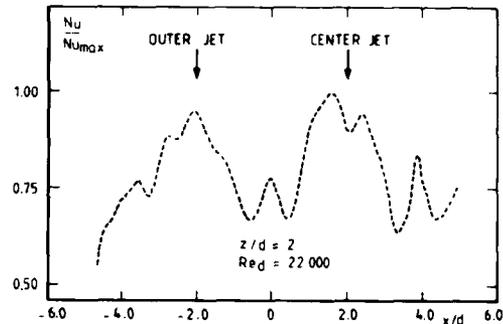
FIG. 15 - LOCAL Nu DISTRIBUTION ALONG THE CENTER-LINE OF CO-LINEAR JETS

Figure 15 gives a typical Nu number distribution in the case of three co-linear jets produced by nozzles distant by four orifice diameters and located at two diameters from the plate. The flow conditions are characterized by a Reynolds number of each jet equal to 22000. The Nu-profile plotted along the central impingement line is limited to the region including the inner and one of the outer jets (as seen in Fig. 11c). Again in full agreement with published data (Refs. 33, 35, 38), a secondary maximum of Nu number occurs midway between the two adjacent vertical jets due to the collision of the two wall spreading flows. This thermal behaviour is corroborated by static pressure measurements (Ref. 50) suggesting that even in this type of complicated flow interaction a possible analogy between momentum and heat transfer could hold. It is also worth noting that local minimum of the heat transfer persists anew at the stagnation point with more predominance for the center jet as observed by Sparrow & Timmers (Ref. 38). However, when the nozzle-to-plate distance is increased the secondary Nu maxima and minima vanish and each jet tends to form rather a bell shaped Nu-distribution as depicted in figure 16.

2.4 Conclusions

A thermographic technique to determine the local heat transfer coefficient from impinging jets on to a flat plate is presented and illustrated by typical results of single round oblique jets and array of three co-linear jets.

The experimental procedure relies on the digital processing of the infrared pictures of the uniformly heated target. This non-intrusive visualization technique allows to reproduce and quantify all the effects of the flow parameters on the heat transfer coefficient.

Associated with information recording and processing systems the infrared imaging system appears to be a powerful tool for research in fluid dynamic problems.

FIG. 16 - LOCAL Nu DISTRIBUTION ALONG THE CENTERLINE
OF CO-LINEAR JETS

3. GENERAL CONCLUSIONS

The present paper emphasizes the potential of flow visualization techniques when associated with digital image processing. The non-intrusive nature and the possibility of two dimensional instantaneous measurements offered by such an experimental approach are illustrated by applications to the study of the mixing properties of a gas jet and the heat transfer characteristics of impinging jets.

In both of these examples, the DIP data compare well with results obtained by means of conventional measurement methods. The limits of the "imaging" techniques are generally fixed by the quality of the flow picture. A promising future of this measurement technique in the field of fluid dynamics is foreseen.

REFERENCES

1. BOOTHROYD, R.G.: Flow gas solid suspensions.
   Chapman & Hall, 1971.

2. OLIVARI, D.: VKI gas concentration meter. Probe series 5.
   von Karman Institute ID-1, 1979.

3. BORREGO, C. & OLIVARI, D.: A method for the measurement of mixing properties in a turbulent jet flow.
   AGARD CP 281 "Testing and Measurement Techniques in Heat Transfer and Combustion", 1980, paper 23;
   also von Karman Institute Preprint 1980-07.

4. LONG, M.B.; CHU, B.T.; CHANG; R.K.: Instantaneous two dimensional gas concentration measurement by
   light scattering.
   AIAA Journal, Vol. 19, No. 9, September 1981, pp 1151-1157.

5. LOURENCO, L.: It is possible to obtain a gas concentration field using digital image processing of
   images, acquired by means of a laser sheet technique.
   Thèse Annexe, Université Libre de Bruxelles, 1982.

6. BORLETEAU, J.P. & BUCHLIN, J.M.: Study of the mixing in a jet with digital image processing.
   von Karman Institute IN 75, 1983.

7. SCHON, J.P.: Instantaneous concentration and velocity measurements through laser visualization
   associated with a digital processing system. In "Digital Image Processing in Fluid Dynamics",
   von Karman Institute LS 1984-03.

8. LONG, M.B. & CHU, B.T.: Mixing mechanism and structure of an axisymmetric turbulent mixing layer.
   AIAA Journal, Vol. 19, No. 9, September 1981, pp 1158-1163.

9. BECKER, H.A.; HOTTEL, H.C.; WILLIAMS, G.C.: On the light scatter technique for the study of turbulence
   and mixing.
   Journal of Fluid Mechanics, Vol. 30, Part 2, November 1967, pp 259-284.

10. ANDERS, K.: Measurement of velocity distributions in delta wing vortices using laser doppler velocimetry.
    von Karman Institute PR 1981-03, 1981.

11. VAN DER HULST, H.C.: Light scattering by small particles.
    Chapman & Hall, 1957.

12. ROSENWEIG, R.E.: Smoke scattered light measurement of turbulent concentration fluctuations.
    Chem. Eng. Science, Vol. 15, 1961, p 111.

13. SMIRNOV, V.A.; VEREVOCHKIN, G.E.; BRDLICK, P.M.: Heat transfer between a jet and a held plate normal
    to flow.
    Int. J. Heat & Mass Transfer, Vol. 2, Nos. 1-2, March 1961, pp 1-7.
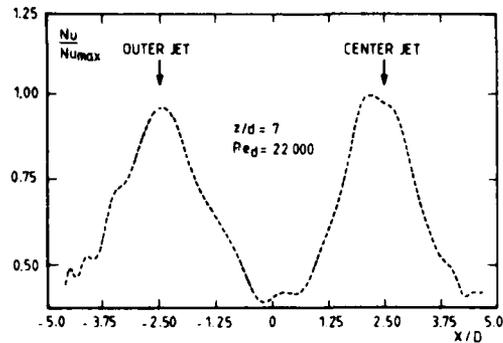
14. HUANG, G.C.: Investigations of heat transfer coefficients for air flow through round jets impinging normal to a heated-transfer surface.
ASME Trans., Series C : Journal of Heat Transfer, Vol. 85, No. 3, August 1963, pp 237-245.

15. GARDON, R. & AKFIRAT, J.C.: The role of turbulence in determining the heat-transfer characteristics of impinging jets.
Int. J. Heat & Mass Transfer, Vol. 8, No. 10, October 1965, pp 1261-1272.

16. NAKATOGAWA, T. et al.: Heat transfer of round turbulent jet impinging normally on flat plate.
Fourth Int. Heat Transfer Conf., Versailles, 1970, Vol. II, Paper FC 5.2.

17. HRYCAK, P.; LEE, D.T.; GAUNTER, J.W.; LIVINGOOD, J.N.B.: Experimental flow characteristics of a single turbulent jet impinging on a flat plate.
NASA TN-D 5690, 1970.

18. BECKO, Y.: Étude de la liaison entre le refroidissement d'une paroi par l'effet d'impact d'un jet axisymérique et les phenomenes de turbulence qui y sont associes.
Ph.D. Thesis, Universite Libre de Bruxelles, 1975.

19. VALLIS, E.A.; PATRICK, M.A.; WRAGG, A.A.: Radial distribution on convective heat transfer coefficient between axisymmetric turbulent jet and a flat plate held normal to the flow.
Proc. 6th Int. Heat Transfer Conf., Toronto, 1978, Vol. 5, pp 297-303.

20. DYBAN, Y.P. & MAZUR, A.I.: Heat transfer in the vicinity of the stagnation point produced by impingement of a turbulized jet onto a baffle.
Heat Transfer-Soviet Research, Vol. 11, No. 1, 1979.

21. HRYCAK, P.: Heat transfer from round impinging jets to a flat plate.
Int. J. Heat & Mass Transfer, Vol. 26, No. 12, December 1983, pp 1857-1865.

22. AMANO, R.S.: Turbulence effect on the impinging jet on a flat plate.
Bulletin of the JSME, Vol. 26, No. 221, 1983, pp 1891-1899.

23. STRIEGEL, S.A. & DILLER, T.E.: An analysis of the effect of entrainment temperature on jet impingement heat transfer.
ASME Trans., Series C : Journal of Heat Transfer, Vol. 106, No. 4, November 1984, pp 804-810.

24. HOLLWORTH, B.R. & WILSON, S.I.: Entrainment effects on impingement heat transfer : Part I - Measurement of a heated jet velocity and temperature distributions and recovery temperatures of target surface.
ASME Trans., Series C : Journal of Heat Transfer, Vol. 106, No. 4, November 1984, pp 797-803.

25. MATHIEU, J.: Contribution a l'etude aerothermique d'un jet plan evoluant en presence d'une paroi.
Publications Scientifiques et Techniques du Ministere de l'Air, 1961.

26. SCHAUER, J.J. & EUSTIS, R.H.: The flow development and heat transfer characteristics of plane turbulent impinging jets.
Stanford University, Technical Report No. 3, 1963.

27. KAMOI, A. & TANAKA, H.: Measurement of wall shear stress, wall pressure and fluctuations in the stagnation region produced by oblique jet impingement.
Fluid Dynamic Measurement Conference Papers, Vol. 1, 1972.

28. FOSS, J.F. & KLEIS, S.J.: The oblique impingement of an axisymmetric jet.
NASA CR 134 961, 1972.

29. FOSS, J.F. & KLEIS, S.J.: Preliminary results for a large angle oblique jet impingement and flow for the effect of initial conditions on the near field of an axisymmetric jet.
NASA CR 121 257, 1973.

30. BOUCHEZ, J-P. & GOLDSTEIN, R.J.: Impingement cooling from a circular jet in a cross flow.
Int. J. Heat & Mass Transfer, Vol. 18, No. 6, June 1975, pp 719-730.

31. SPARROW, E.M. & LOVELL, B.J.: Heat transfer characteristics of an obliquely impinging circular jet.
ASME Trans., Series C : Journal of Heat Transfer, Vol. 102, No. 1, February 1980, pp 64-70.

32. GOLDSTEIN, R.J. & BEHBAHANI, A.I.: Impingement of a circular jet with and without cross flow.
Int. J. Heat & Mass Transfer, Vol. 25, No. 9, September 1982, pp 1377-1382.

33. GARDON, R. & AKFIRAT, J.C.: Heat transfer characteristics of impinging two-dimensional air jets.
ASME Trans., Series C : Journal of Heat Transfer, Vol. 88, No. 1, February 1966, pp 101-108.

34. KERCHER, D.M. & TABAKOFF, W.: Heat transfer by a square array of round air jets impinging perpendicular to a flat surface including the effect of spent air.
ASME Trans., Series A : Journal of Engineering for Power, Vol. 92, No. 1, January 1970, pp 73-82.

35. KOOPMAN, R.N. & SPARROW, E.M.: Local and average transfer coefficients due to an impinging row of jets.
Int. J. Heat & Mass Transfer, Vol. 19, No. 6, June 1976, pp 673-683.

36. MARTIN, H.: Heat and mass transfer between impinging gas jets and solid surfaces.
Advances in Heat Transfer, Vol. 13, 1977, pp 1-60.

METZGER, ... for ... and staggered ...
ASME Trans. Series ...

GOLDSTEIN, ...
Int. J. Heat & Mass Transfer ...

MEASURING TECHNIQUES FOR CORRELATION
OF LDA AND THERMOCOUPLE SIGNALS
by
M.N.R. Nina and M.R.A. Pita
Department of Mechanical Engineering
Instituto Superior Tecnico
1096 Lisbon Portugal

SUMMARY

A technique was developed to enable the evaluation of the correlation between velocity and temperature fluctuations as the nature of velocity signals and fine wire thermocouple as that of flow temperature.

The discontinuous nature of LDA signal require a special technique for the correlation, in case that only the seeding particles are present in the flow.

The thermocouple signal was analog compensated in frequency and the effect of the value of time constant in the velocity temperature correlation was studied.

NOMENCLATURE

C$_{uT}$

R$_{uT}$ velocity temperature cross correlation coefficient
T' temperature fluctuation
u' axial velocity fluctuation
u axial velocity
v' radial velocity fluctuation
x axial distance
r radial displacement
t time interval
τ thermocouple time constant
t sampling time

INTRODUCTION

Measurement of the properties of reacting flows, in simple geometries as well as in gas turbines combustors, have been performed by several authors using different techniques, the common goal beeing the detailed knowledge of the turbulent transport mechanisms.

The present program of work includes the study of turbulent reacting internal flows, directly related to gas turbine combustors, the work reported here concentrates on a simpler flow, a hot air jet, in order that the technique under study be first tested without the interference of errors and problems that are associated with a reacting flow measurement, namely those originated by the presence of radiation and catalytic effects, probe life and minimum wire diameter, deposition of seeding particles on the thermocouple.

There are a number of questions to be clarified with the help of experiments in a hot air jet that will set the basis for the work on the second phase involving combustion.

The two different fluids, hot air and cold air, identified by their temperature signature in association with conditional sampling can be studied.

The time constant of the thermocouple is a function of pressure, local temperature and velocity and to a lesser extent, composition.

The testing of the technique of correlation of a continuous and a discontinuous signal, the effect of separation of the two measuring volumes, LDA and thermocouple, on the values of correlation was studied.

EXPERIMENTAL SET UP

The velocity measurements were made with a laser doppler velocimeter and the temperature was evaluated with fine wire thermocouples. The arrangement of the experimental apparatus is shown in Fig.

The LDA system used was of the forward scatter light type, comprising a 2 watt Spectra Physics argon Laser, an OEI optical unit with two Bragg cells to frequency shift the beams and a 310mm focal length lens.

The photomultiplier signal was band pass filtered and subsequently analysed by a frequency counter interfaced to an Apple II microcomputer. The counter allowed frequency comparison between 5 and 1/6 cycles within each burst and the frequency comparator circuit was used with the narrowest validation criteria guaranteeing the absence of significant errors in the measurement of frequency. The counter has two outputs: a digital and an analogue one.

The digital output was in fluctuating point form of two eigth bit words. A flag into the microcomputer when a new valid velocity measurement has been made. This value is converted to
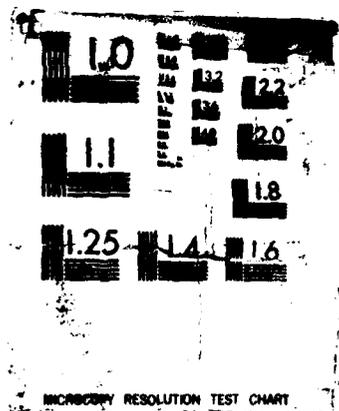
MICROCOPY RESOLUTION TEST CHART

memory and the micro waits for a new measurement. This output was used to built the velocity histogram that was the base to evaluate the mean, the r.m.s. and the p.d.f. (no time information was obtained).

The voltage from the analog output was proportional to the frequency of the doppler signal . This voltage value was kept constant until a new valid measurement has been made. This output was analised by the microcomputer throught an analog/digital converter and used to evaluate the velocity power spectra and autocorrelation. Fig. 2 shows two curves of velocity versus time obtained from the analog output in two different situations, curve (a) with a high number of valid signals and curve (b) when a few seeding particles are present in the flow.

The temperature measurements were obtained with a 5 μm diameter thermocouple Platinum versus Platinum + 13% Rhodium. The output voltage was amplified 100 times, analogue compensated and digitalised by an analogue/digital converter interfaced with the microcomputer.

The A/D converter allows a maximum sampling rate of 12 kHz. The input signal is transformed into a 12 bit word.

As the voltage-temperature relation of the thermocouple was non linear some care was needed in building the temperature histogram. A table of voltages corresponding to equal temperature intervals was built and used to make the temperature histogram.

To store the data two 140Kb diskettes were available as well as Racal 7700 magnetic tape unit, which allowed the storage of significative amounts of data also used to interface with other computers in other to get shorter processing times of the recorded data.

MEASUREMENTS

When measuring the velocity with an LDA system the sampling rate will depend usualy on the number of valid doppler signals detected by frequency counter as was shown in Fig. 2 .

When the time interval between the arrival of two consecutive particles to the LDA control volume was small compared with the velocity fluctuations caracteristic time, the analog output from the counter allows the evaluation of velocity power spectra and autocorrelations. Fig. 3 shows the evaluation of the velocity power spectra measured in the center line of a hot air jet where velocity oscilations at frequencies greater than 100 Hz are present.

When the arrival time between particles is greater than 0.8 ms this frequencies are not detected in the velocity spectra.

The number of valid velocity signals is also important when measuring the velocity temperature correlations. Two different conditions can happen in this case:

If the number of velocity signals is high then the usual method to evalute the correlation coefficient can be used.

$$R_{uT} (\delta, \Delta t) = \frac{\overline{u'(r,t).T'(r+\delta, t + \Delta t)}}{\sqrt{\overline{u'^2(r,t). T'^2(r+\delta,t)}}} \qquad (1)$$

$$-\infty < \Delta t < +\infty$$

in this case a record of simultaneous temperature and velocity measurements is necessary. This is obtained using two sample and hold modules, one to the temperature and another to the velocity. Fig. 4 shows measurements made in a hot air jet, 470 C outlet temperature and 14m/s outlet velocity. The velocity is measured at the centre line, one diameter from the outlet and the temperature is measured at the same axial distance but at r/D = 0.5.

This record allows also the evaluation of the temperature and velocity spectra that are shown in Fig. 5 . This curves are the mean of 10 sets of 1024 values each measured with a 5kHz sampling rate.

Figure 6 shows the Rut coefficient. The common frequency to both signals is 240Hz as it has been previously detected in the U and T spectra, with a fase difference of almost 90 degrees.

These records allow also the evaluation of the velocity temperature joint probability distribution. This curve is shown in Fig. 7.

The same results, measured at X/D=2, are shown in Fig. 8, 9, 10. The results are equally good, i.e., the time description of the velocity signal is also good.

When the velocity is measured in a region where the number of particles is not enough to describe the flow oscilations, another method must be used to evaluated the Rut coefficient. This method will be described now.

When a valid velocity measurement is detected by the microcomputer, i.e., the flag is turned on, then the sampling of temperature values begins and is stored in the Apple memory. When the buffer is full the velocity and temperature values are recorded in the Racal magnetic tape and a new cicle begins. This procedure is repeated 800 times.

The correlation coefficient is evaluated according to expression 2

$$R_{uT}(\delta, \Delta t) = \frac{\overline{u'(r,t).T'(r+\delta, t+\Delta t)}}{\sqrt{\overline{u'^2(r,t).T'^2(r+\delta, t+\Delta t)}}} \qquad (2)$$

$\Delta t \geqslant 0$

To compare these two methods of evaluating the velocity temperature cross correlation coeficient, the Rut value was measured at the same conditions of Fig. 6, 10, based on this new method. Fig. 11,12 shows the new curves. As the temperatures are measured after the measurement of a velocity value, only for positive time delays is possible to calculate the curve. They agree quite well with the previous ones evaluated according to expression 1.

As the number of particles in the outer region of the jet is small, the usual method used to evaluate the Rut coefficient will not be recomended. The method based on expression 2 will be better and with this method a radial displacement of the velocity control volume is possible. Fig. 13 shows the variation of Rut when the velocity control volume is displaced along the jet radius (X/D=1).

Due to the physical limitation of having a solid probe (the thermocouple) that would interfier with the laser beams, it is impossible to measure the velocity and temperature at the same spacial position and then evaluate the cross correlation coeficient at this conditions. The minimum distance between control volumes is about 1 mm.

To make the correct positionement of both control volumes, the laser beams are focused on the thermocouple junction. This corresponds to a high temperature reading that confirms the coincidence of both control volumes. Then the laser is displaced to the measuring position.

THERMOCOUPLE TIME CONSTANT

The temperature was measured with a 15μm thermocouple. This thermocouple diameter is adequate to measure in the air jet temperatures because it has a long life time and has also the advantage of having a small time constant, i.e., the thermocouple time lag is quite small, around 5ms which allows the detection of temperature fluctuations up to 1 kHz.

The thermocouple time constant was evaluated with a heating step method described in Nina and Pita (1985). As it has been then noted the analogue compensation will impose a mean time constant to be used with the consequences that have been also pointed out there.

The influence of the thermocouple time constant on the Ru,t coefficient curve is shown in Fig. 14 . Measurements are made at X/D=1, radial velocity at R=5mm and temperature at R=15mm. The measured time constant using the D.C. heating technique was 5.3ms.

The Rut values obtained without compensation of the thermocouple output signal are small, less than 0.2 and are always positive. Also the measured fase difference between the velocity and temperature oscilations is larger than that measured with the compensated signals. In this case the different time constants used do not alter the measured fase difference between the two signals. The Rut values suffer significative changes only when the value of varies between 2.3 and 7.3ms. For greater values of the main differences in Rut curves appears only for time delays greater than 3ms.

CONCLUSIONS

For low seeding rate situations, a method was devised to correlate the discontinuous signal from LDA and the continuous thermocouple output.

The results of correlation of velocity and temperature by this method were found to be in good agreement with those obtained by current methods when applied in highly seeded flow regions.

The fluctuating flow temperature was evaluated by analogue compensated thermocouples and the effect of the magnitude of this compensation was observed both on phase and amplitude of $R_{u,T}$.

ACKNOWLEDGEMENTS

REFERENCES

Heitor, M.V., Taylor, A.M.K.P. and Whitelm, J.H.(1985)
Simultaneous velocity and temperature measurements in a premixed flame
Experiments in Fluids 3, pp323

Nina, M.N.R. and Pita, G.P. (1985)
Measurements of fluctuating temperatures using compensated fine wire thermocouples.
AGARD Conference Proceeding N.390, Paper 32

24-4

Starner, S.H. and Bilger, R.W. (1981)
Measurement of scalar velocity correlations in a turbulent diffusion flame.
Eighteenth Symposium (International) on Combustion, pp921

Yanagi, Tetsui and Mimura, Yoichi (1981)
Velocity temperature correlation in premixed flame
Eighteenth Symposium (International) on Combustion, pp 2031

Fig. 1 -Experimental set up

HIGH PARTICLE
CONCENTRATION
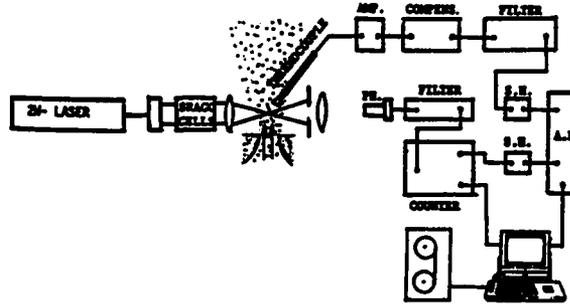
LOW PARTICLE
CONCENTRATION
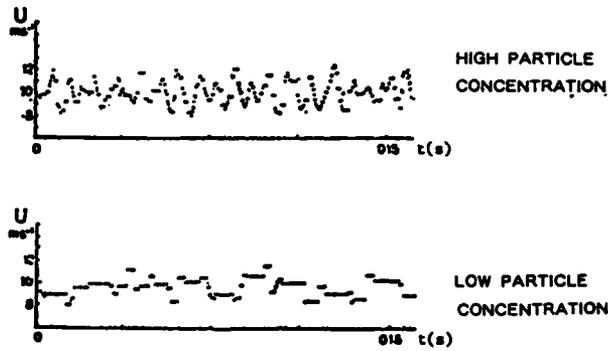
Fig. 2 - Counter analogue output for different particle concentrations

τ_s= 0,8 ms

τ_s= 0,25 ms

τ_s= 0,12 ms
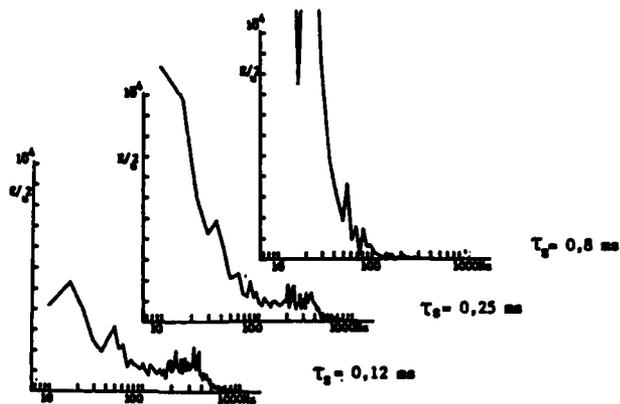
Fig. 3 - Velocity power spectra, with varying particle
concentration in the flow

U-x/D=1 , r/D=0 ; T- x/D=1 , r/D=0.5
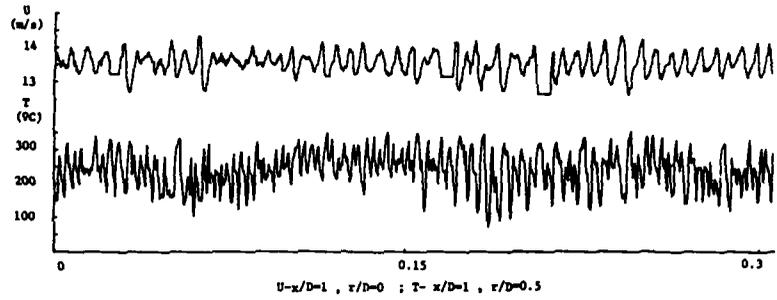
Fig. 4 -Simultaneous temperature and velocity measurements
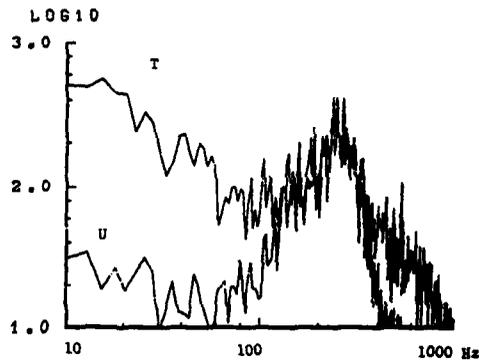
Fig. 5 - Velocity and temperature spectra from signals plotted in Fig. 4
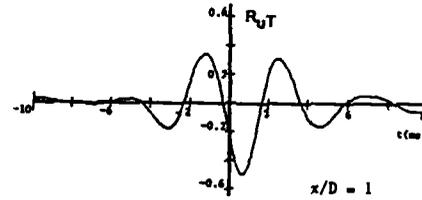
Fig. 6 - Cross correlation coefficient from signals plotted in Fig. 4
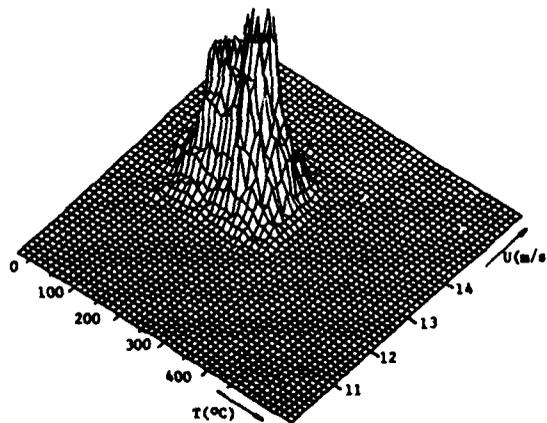
Fig. 7 - Joint probability distribution from u and T plotted in Fig. 4
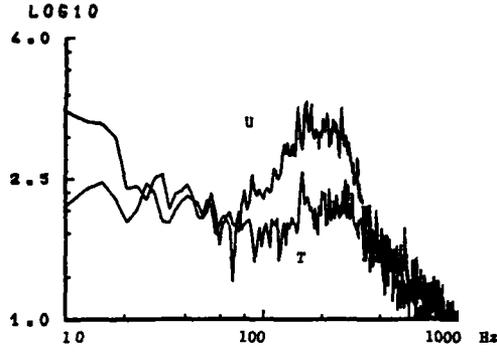
Fig. 8 – Velocity and temperature spectra at
x/D=2, u r/D=0, T r/D=0.5
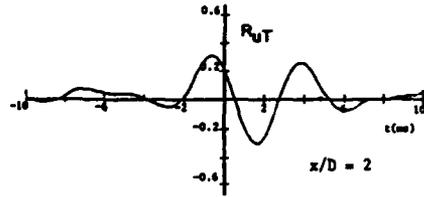
Fig. 9 – Cross correlation coefficient. R_{uT}
x/D=2, u r/D=0, T r/D=0.5
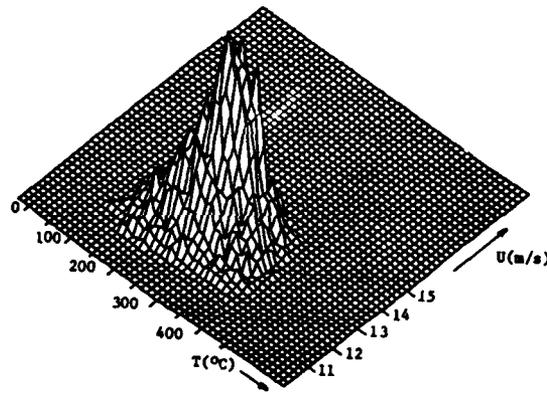
Fig. 10 – Velocity temperature joint probability distribution
x/ D=2, u r/D=0, T r/D=0.5
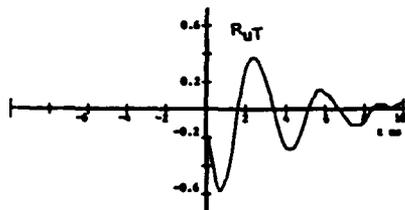
Fig. 11 – R_{uT}, x/D=1
u r/D=0
T r/D=0.5
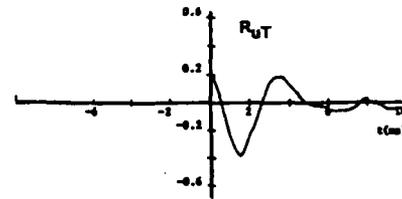
Fig. 12 – R_{uT}, x/D=2
u r/D=0
T r/D=0.5
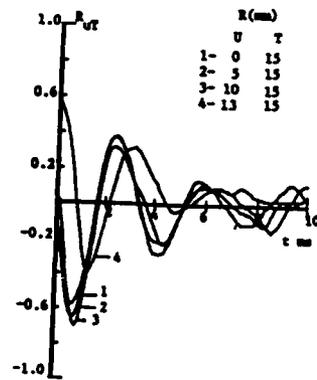
Fig. 13 - R_{uT}, x/D=1

Displacement of the
velocity control volume
along the radius
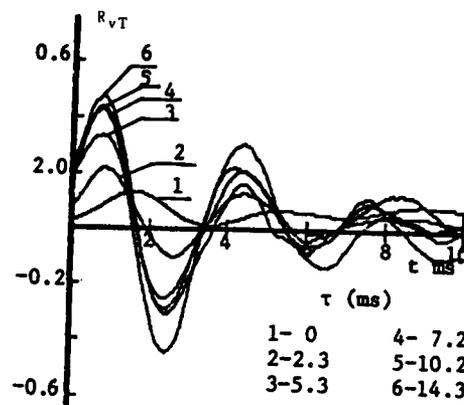
Fig. 14 - R_{vT}, x/D=0, T r/D=0.5

Variation of the R_{vT} coefficient with the thermocouple
compensation

DISCUSSION

A.Melling, UK

Considering that the velocity and temperature are not measured at the position, what is the significance of your velocity-temperature correlations R_{UT}?

Author's Reply

The significance and interest of a velocity-temperature correlation depend on the type and region of flow under study. In our case we were looking at temperature fluctuations due to jet entrainment and velocity fluctuations in the jet potential core. Comparison between R_{UT} obtained at different locations in the flow gave information about phase differences and correlations intensities.

Comment

We have used here a rather abnormal jet. The jet has, as we have seen, a frequency of around 250 Hz and if we use two thermocouples, the inner thermocouple would not tell anything because the temperature incoming from the jet potential core is uniform. So, what we are looking at is some structures, located outside of the jet and in fact who are making the turbulence or the fluctuating temperature driving because it was the mixing structures between the inner jet and the outside atmosphere.

TECHNICAL EVALUATION REPORT
SESSION V — VIBRATION, THIN LAYER AND TIP CLEARANCE MEASUREMENTS

by

D.P.Davidson
Rotadata Ltd
Liversage Street
Derby DE1 2LD, UK

I would like to thank Mr Stewart for inviting me to sum up this very interesting session on tip clearance measurement.

This forum of AGARD has seen and indeed stimulated the development of a number of new measurement techniques. The examples of optical thermometry and optical velocimetry come particularly to mind. There is now an extensive corpus of information which allows us to judge the capabilities, limitations and applicability of these techniques. The techniques have given rise to a complete new philosophy of measurement which is being well researched and documented.

The presentations we have heard today form a welcome addition to the record of development of methods for measuring the physical behaviour of the mechanical elements that form the turbomachine.

The excellent paper from Dr Knoell has shown the systematic approach that must be taken in applying such techniques and in their calibration. His charge coupled system has been shown to give excellent results for temperature ranges in the compressor region of the machine.

Dr Demers, by contrast has chosen a frequency modulation phase detection system that has the potential to operate in more severe environments with inherent noise rejection advantages. Variants of this system have been adopted by several companies, including Rolls Royce, and we look forward to hearing of his experiences.

Tip clearance measurement has now grown through the four phases of application maturity: research, design, diagnosis and is moving towards control.

At the research level we are investigating the causes and effects of varying aerofoil to end-wall clearances (both static and rotating). We are evolving new design codes to minimise and accommodate tip clearance effects leading to such innovations as non-circular casings. Tools for diagnosis are becoming more and more complex as we start to understand some of the dynamic influences at play. We are also moving towards active control with clearance measurement transducers in closed loop systems.

Much attention must also be paid to the ways in which information is analysed and displayed in much the same way as we heard yesterday in the data acquisition papers. I hope that we are not seeing a division between the transducer engine and the data acquisition engineer. I for one would welcome an authoritative view of the techniques currently in use for examining the steady state and transient output from such systems.

In designing our measurement system, we have seen that we must be prepared to make compromises according to the system priorities. We cannot necessarily have low complexity (and hence high reliability) at the same time as high accuracy and high bandwidth. Mr Stewart's own fascinating presentation has shown us that the achievement of results as remarkable as his may require capital facilities that would fall off the end of a performance/cost graph, even on a logarithmic scale.

In particular, it is our duty, as measurement engineers, to concentrate on justifying the confidence or "plausibility" levels of our measurements. We must develop a rigorous methodology and start to consider the need for agreed practices that are exemplified by the measurement panel activities that have been taking place behind the scenes here this week.

I would like to encourage bodies like AGARD to stimulate more activity in the areas of evaluation, calibration and assurance, What, for example, are we to take as a standard reference for our clearance measurements? How are we to provide the absolute traceability of measurement that marks a mature measurement system.

I look forward to future AGARD meetings when we can hear more about the actual results obtained by these interesting techniques and perhaps eventually even a report on active closed-loop-in-flight clearance systems.

UTILISATION DES CAPTEURS PELLICULAIRES
POUR LA MESURE SUR TURBOMACHINES
par

A. Bruère, M. Portat, J.C. Godefroy et F. Hélias

Office National d'Etudes et de Recherches Aérospatiales,
BP 72, 92322 Châtillon Cedex, FRANCE.

INTRODUCTION

Dans le but d'accroître le rendement et de réduire les nuisances acoustiques des turbomachines, il est nécessaire, parmi d'autres possibilités, d'accéder à la connaissance des phénomènes physiques qui se développent à l'interface des aubes fixes ou tournantes, avec le milieu gazeux. Cette connaissance s'appuie sur des mesures diverses : pression, température, flux thermique, turbulence, contrainte, etc.

Les laboratoires et les constructeurs ont montré la nécessité de mesurer les grandeurs physiques directement sur les profils, par intégration de capteurs à leur surface.

Les capteurs traditionnels, même miniatures, nécessitent un usinage des parois du profil pour permettre leur intégration. Cet usinage s'avère toujours délicat, voire impossible. Il modifie les caractéristiques du profil du point de vue mécanique, thermique et quelquefois du point de vue aérodynamique, ce qui entraîne d'importantes perturbations dans les mesures [1].

Pour toutes ces raisons, l'ONERA soutenu par la DRET (Direction des Recherches, Etudes et Techniques), a étudié une nouvelle famille de capteurs, appelés "pelliculaires".

1. GENERALITES

Quatre types de capteurs pelliculaires ont été développés :
- les capteurs de pression à détection capacitive,
- les thermomètres à température de surface et,
- les fluxmètres thermiques de convection, utilisant l'effet thermoélectrique qui prend naissance à la jonction de deux métaux ou alliages déposés en couches minces,
- les capteurs d'analyse de la couche limite d'un écoulement aérodynamique, utilisant la variation de la résistivité d'un métal en fonction de la température.

Les propriétés communes à tous ces capteurs sont les suivantes :
- épaisseur maximale hors tout 80 µm,
- intégration sur les parois à instrumenter par collage, sans nécessiter d'usinage,
- possibilité de réalisation de plusieurs capteurs sur un même substrat, évitant ainsi, lors d'essais aérodynamiques, les perturbations de l'écoulement provoquées par des sur-épaisseurs locales, liées à l'implantation de plusieurs capteurs distincts le long du profil,
- dimensions, géométrie des éléments sensibles et répartition de ceux-ci sur le substrat, adaptés aux besoins métrologiques.

La possibilité de réaliser ces différents types de capteurs pelliculaires résulte de :
- l'existence de diélectrique en feuille souple de Kapton (Dupont de Nemours), choisi pour sa disponibilité en faible épaisseur (6 à 100 µm) et pour sa bonne tenue en température (300°C),
- la mise en oeuvre des techniques d'évaporation sous vide, ou de pulvérisation cathodique, pour réaliser en couches minces (épaisseur 0,2 µm), les parties métalliques des éléments sensibles et les conducteurs acheminant le signal,
- la possibilité d'obtenir des films de colle de très faible épaisseur (2 à 4 µm) pour assembler plusieurs feuilles de Kapton.

2. CAPTEURS PELLICULAIRES DE PRESSION

Deux types de capteur pelliculaire de pression, qui utilisent une variation de capacité, ont été développés.

Le premier type utilise, comme élément sensible, une feuille de diélectrique en Kapton. Ce matériau permet de fonctionner sous très fortes pressions statiques.

Le second type utilise, comme élement sensible, l'air emprisonné dans des micro-cavités ; ce transducteur procure une plus grande sensibilité que le précédent

2.1 Principe

Ce capteur est un détecteur de type capacitif, dont l'élément sensible est constitué d'une feuille de diélectrique souple, métallisée sur ses deux faces, formant ainsi un condensateur de capacité C (fig. 1). Sous l'action d'une variation de pression Δp, l'épaisseur *e* de cette feuille diminue d'une valeur Δe. Il en résulte une variation relative de la capacité C proportionnelle à la variation de pression [2].

$$\frac{\Delta c}{c} = - \frac{\Delta e}{e} = \frac{\Delta p}{K} \tag{1}$$

K étant le module de compression uniaxial.

La capacité est polarisée par une source de tension continue V, a travers une très haute impédance, et sous l'action d'une variation de pression une différence de potentiel ΔV apparait entre les extrémités de cette impédance.

$$\frac{\Delta V}{V} = \frac{\Delta c}{c} = \frac{\Delta p}{K} \tag{2}$$

En pratique, des circuits de garde sont disposés de chaque côté de la connexion "point chaud" qui relie l'élément sensible à l'entrée d'un circuit de mesure constitué par un adaptateur d'impédance. Ce dernier polarise également les circuits de garde.

2.2 Description des capteurs
2.2.1. *Capteur à diélectrique solide*

La structure de ce type de capteur correspond à la représentation de la figure 2. La valeur de la sensibilité à l'écrasement peut être explicitée sous la forme :

$$\frac{\dfrac{\Delta C}{C}}{\Delta p} = \frac{1}{K} = \frac{(1 + \sigma)(1 - 2\sigma)}{E(1 - \sigma)} \tag{3}$$

avec :
E : module élastique du matériau,
σ : coefficient de Poisson du matériau.

En fait en milieu gazeux, en régime adiabatique, à la réponse à l'écrasement due aux fluctuations de pression s'ajoute, dans le domaine basse fréquence, une réponse aux fluctuations de température du gaz induites par la pression. Cet effet secondaire rend difficilement exploitable la phase du signal délivré par le capteur. De ce fait ce type de capteur est principalement utilisé pour connaître la répartition spectrale des raies de fluctuation de la pression.

2.2.2. *Capteur à diélectrique gazeux*

Ce capteur est formé par des alvéoles multiples découpées dans une feuille de Kapton (fig. 3 et 4). Ces alvéoles, remplies d'air, sont fermées par deux autres feuilles de Kapton portant les électrodes qui constituent ainsi l'élément sensible capacitif. La feuille supérieure est utilisée comme membrane déformable.

Pour chaque alvéole, la sensibilité à la pression a pour expression :

$$\frac{\dfrac{\Delta c}{c}}{\Delta p} \simeq \frac{\left(1 - \sigma^2\right) a^4}{16\ Eh^3 \ell} \tag{4}$$

a : rayon de l'alvéole,
h : épaisseur de la membrane
ℓ : hauteur de l'alvéole,
c = capacité d'une alvéole.

Pour évaluer la sensibilité globale de l'élément sensible, il faut tenir compte de la capacité C_K due à la présence de murs en Kapton autour de n alvéoles.
D'où

$$\frac{\frac{\Delta c}{c}}{\Delta p} = \frac{\left(1 - \sigma^2\right) a^4}{16 \, e \, h^3 \ell} \times \frac{nC}{C_K + nC} \qquad (5)$$

La sensibilité du capteur peut être adaptée au besoin en choisissant l'épaisseur de la feuille de Kapton constituant la membrane déformable.

Ce type de capteur permet la mesure de l'amplitude et de la phase de la fluctuation de pression.

2.3 Caractéristiques des capteurs de pression

Ces capteurs ne deviennent fonctionnels qu'après implantation sur le profil à instrumenter. Leurs étalonnages doivent donc être effectués après intégration à l'aide, par exemple, d'une petite cavité, équipée d'un capteur de référence, de forme adaptée au profil et alimentée pneumatiquement de façon convenable.

Caractéristiques	Capteurs à diélectrique solide	Capteurs a diélectrique gazeux	
		Membrane Epaisseur 12 μm	Membrane Epaisseur 25 μm
Sensibilité en $\frac{\Delta c}{c}/Pa$	Variable de 2.10^{-9} à 2.10^{-10}	3.10^{-7}	4.10^{-8}
Bande passante (Hz)	1 à 10^5	1 à 10^5	1 à 10^5
Détectivité à 1 kHz (Pa. Hz$^{-1/2}$)	2 (polarisé sous 100 V)	10^{-1} (polarisé sous 10 V)	6.10^{-1}
Epaisseur du capteur (μm)	50	80	92
Température d'utilisation ($^{\circ}$C)	0 à 60	0 à 60	0 à 60

2.4 Exemples d'utilisation

Les capteurs pelliculaires de pression à diélectrique solide ont déjà été utilisés dans plusieurs expériences de type industriel.

L'équipement d'une grille d'aubes fixe supersonique avec ces capteurs a permis de mettre en évidence les instabilités de l'écoulement en fonction de la valeur de la contre-pression en aval des canaux inter-aubes [3].

L'intégration de capteurs pelliculaires sur des aubes mobiles d'un compresseur SNECMA (fig. 5 et 6) a permis d'en caractériser les sources de bruit [4]. Dans cette expérience les signaux délivrés par les capteurs étaient amplifiés dans des chaînes de mesure à grand gain, logés dans la partie tournante du compresseur, avant d'être transmis par un collecteur tournant vers les systèmes d'acquisition. A la vitesse maximale de rotation, les accélérations centrifuges subies par les chaînes de mesure embarquées et par les capteurs étaient respectivement de 20 000 g et 48 000 g. La figure 7 montre le spectre des fluctuations de pression calculé à partir du signal délivré par un capteur situé sur l'extrados du profil, au voisinage du bord d'attaque.

Un autre profil de grille d'aubes a été équipé de capteurs pelliculaires à diélectrique gazeux (fig. 8). Il a subi des essais en soufflerie transsonique, un mouvement de tangage sinusoïdal lui étant appliqué pendant l'écoulement. Les mesures recueillies dans ces conditions doivent permettre de calculer la valeur du moment de tangage instationnaire de ce profil.

3. CAPTEURS DE TEMPERATURE, DE FLUX THERMIQUE ET D'ANALYSE DE LA COUCHE LIMITE

Tous ces capteurs sont des détecteurs de phénomènes thermiques. Ils utilisent deux principes différents

3.1 Principes
3.1.1. *Température et flux*

Les capteurs de température et de flux thermique (fig. 9a et 9b) utilisent tous deux l'effet thermoélectrique existant à la jonction de deux métaux ou alliages A et B [5] montés en circuit fermé. La force électromotrice ξ apparaissant dans le circuit est liée aux températures de la soudure chaude T_c et de la soudure froide T_f par la relation polynomiale suivante :

$$\xi = a(T_c - T_f) + \frac{1}{2} \, b \left(T_c^2 - T_f^2\right) + \ldots \tag{6}$$

En ce qui concerne le flux thermique statique Φ, celui-ci se déduit de la mesure de la différence des températures T_s et T_i présentes de part et d'autre d'un élément calorimétrique constitué par une feuille de Kapton d'épaisseur e et de conductibilité thermique λ :

$$\Phi = \frac{\lambda}{e} \, (T_s - T_i) \tag{7}$$

T_s et T_i sont mesurées à l'aide de deux thermocouples, dont la différence des forces électromotrices est $\Delta\xi$.

Avec les couples Cuivre-Nickel la sensibilité obtenue pour les thermomètres est de 18.10^{-6} V. K^{-1} à température ambiante et de $2,7.10^{-6}$ V. kw^{-1}. m^2 pour les fluxmètres de 25 µm d'épaisseur. La gamme de température s'étend de 0 à 200°C.

3.1.2 *Analyse de la couche limite*

Les capteurs analysant la couche limite d'un écoulement aérodynamique sont constitués d'un film métallique résistant, déposé sur une feuille en diélectrique Kapton dont la résistance R varie avec la température T à laquelle il est soumis (fig. 9c) :

$$R = R_0(1 + \alpha T) \tag{8}$$

α étant le coefficient de température de la résistance du film.

Le film est chauffé par effet Joule et stabilisé à une température choisie T.

En présence d'écoulement, ce film se refroidit par convection et l'échange convectif diminue lorsque l'épaisseur ϵ de la couche limite augmente. La valeur de la puissance P_c, qui doit être appliquée au film pour le maintenir à la température constante T, renseigne donc sur l'épaisseur de la couche limite au-dessus du film :

$$P_c = f(\epsilon) = P_v - P_o \tag{9}$$

avec P_v puissance appliquée au film en présence d'écoulement,
et P_o puissance appliquée au film sans écoulement.

D'autre part, le rapport de la puissance efficace de fluctuation P_f appliquée au film, sur la puissance moyenne $\overline{PV}$, permet d'évaluer le taux de turbulence τ de la couche limite.

Pour analyser la couche limite présente autour d'un profil un ensemble multicapteurs, constitué de films chauds, réalisé sur un support unique, est intégré le long de la corde de ce profil.

La valeur de la sensibilité thermique α des films de Nickel réalisés est de $2,9.10^{-3}$ exprimé en $\frac{\Delta R}{R}$. K^{-1}.

3.2. Exemples d'utilisation

Un des premières applications des capteurs thermiques a consisté à équiper un profil symétrique *NACA 65-012* de 28 fluxmètres pelliculaires cuivre-nickel (fig. 10) pour connaître l'évolution, le long de la corde, du coefficient d'échange gaz-profil h ou du nombre de Stanton qui y est lié (fig. 11). La même évaluation a été effectué sur un autre profil, lequel était soumis à un refroidissement par film gazeux (fig. 12).

Pour mieux connaître les caractéristiques de la couche limite le long d'un profil de grille d'aubes, un ensemble de 20 capteurs film chaud, déposés sur une même feuille de Kapton et répartis le long de la corde, a été collé sur un profil [6] (fig. 13). La figure 14 présente l'évolution, le long de la corde, de la puissance convectée et du taux de turbulence.

4. CONCLUSION

Les études menées à l'ONERA ont permis le développement de capteurs pelliculaires de pression, de température, de flux thermique et d'analyse de la couche limite. Ces capteurs, dont la technologie est acquise, permettent de répondre aux besoins métrologiques dans différents domaines.

Les capteurs pelliculaires de pression ont été développés à l'ONERA pour répondre aux besoins en aérodynamique, mais également pour permettre d'améliorer les connaissances sur les sources de bruit qui prennent naissance dans les turbomachines.

Une nouvelle version de ces capteurs est actuellement disponible. Elle est particulièrement bien adaptée aux applications en hydrodynamique.

Les capteurs de température et de flux thermique sont parfaitement adaptés aux études sur turbomachines, pour la mesure des températures à la surface des profils et pour l'évaluation des coefficients d'échange gaz-profil.

. Des études sont actuellement en cours dans le but de développer des capteurs thermiques haute température (1400 K) en couche mince. La mise en oeuvre de tels capteurs est primordiale pour caractériser les conditions thermiques de fonctionnement des étages de turbines et évaluer en particulier les conditions de refroidissement des aubes.

Les capteurs d'analyse de la couche limite répondent aux besoins spécifiques du domaine aérodynamique :

- caractérisation de la nature de la couche limite et plus particulièrement détermination de la zone de transition le long du profil,
- étude des interactions onde de choc-couche limite présentes en régime supersonique dans les empilages de profils : grille d'aubes, zone de compresseur,...

REFERENCES

[1] - J. Paulon, M. Portat, J.C. Godefroy, E. Szechenyi
Measurement techniques in turbomachines, ultrathin transducers applied to measurements in turbomachines.
Institut Von Karman 1981, Tiré à Part ONERA 1981-38.

[2] - M. Portat
Les capteurs pelliculaires et leurs applications
La Recherche Aérospatiale n° 1982-3.

[3] - M. Chatanier et Y. Le Bot
Utilisation des capteurs pelliculaires pour la mesure des pressions instationnaires dans les turbomachines.
Symposium IUTAM, Paris, 1976, Tiré à Part ONERA 1976-73.

[4] - P. Raffy, S. Léwy, J. Lambourion et M. Chatanier.
Investigation of Subsonic fan noise sources by fluctuating pressure measurements on rotating blades.
AIAA Paper n° 77-1321, Tiré à Part ONERA 1977-95.

[5] - J.C. Godefroy
Thin film transducers for temperature and heat flux measurements.
La Recherche Aérospatiale, 1981-2.

[6] - A. Fourmaux
Recherches sur l'Aérodynamique des turbomachines.
Rapport Technique n° 34/7079 AY, ONERA 1979 .
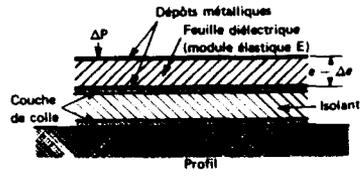
Fig. 1 — *Représentation simplifiée d'un capteur pelliculaire de pression, vue en coupe.*

$$\Delta V = V \frac{\Delta C_p}{C}$$
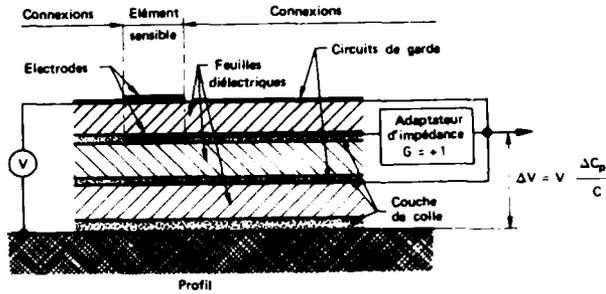
Fig. 2 — *Représentation schématique, vue en coupe, d'un élément de capteur équipé de ses connexions, de ses circuits de garde et associé à un adaptateur d'impédance.*
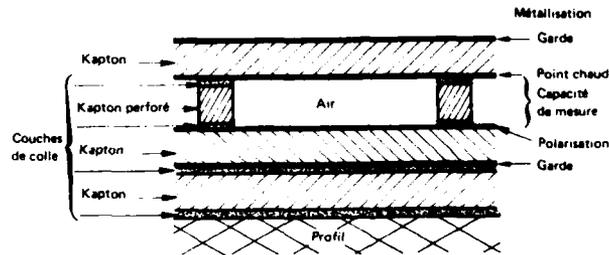
Fig. 3 — *Principe du capteur pelliculaire à diélectrique gazeux.*

Fig. 4 — *Exemple de réalisation de capteur alvéolé avec murs isolants (trous de φ 700 μm)*

Fig. 5 — *Aube équipée de capteurs de pression pelliculaires.*
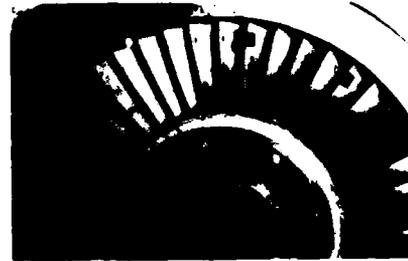
Fig. 6 — *Roue mobile avec ses équipements. (Document SNECMA).*
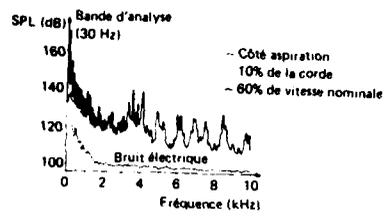
Fig. 7 – Spectre déduit des mesures de pression instationnaires.

SPL (dB)
Bande d'analyse
(30 Hz)
160
140
120
100
~ Côté aspiration
10% de la corde
~ 60% de vitesse nominale
Bruit électrique
0 2 4 6 8 10
Fréquence (kHz)
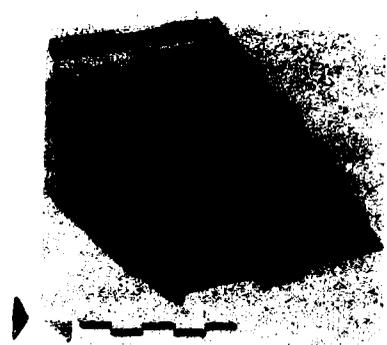
Fig. 8 – Aube équipée avec capteurs à diélectrique gazeux,
en vue de mesures en aéroélasticité.
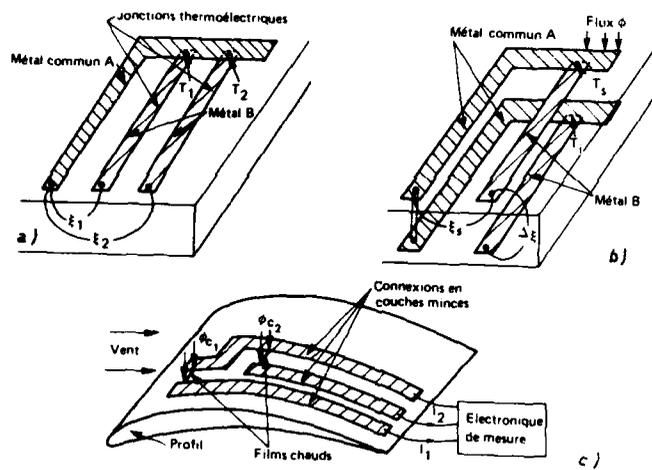
Fig. 9 – Représentation schématique des capteurs thermiques.
a) Thermomètre ; b) fluxmètre ; c) détecteur d'analyse de la couche limite.

Fig. 10 – Profil NACA 65-012 équipé de fluxmètres.

Nombre de Stanton
6 10⁻¹
Calcul de la couche limite
Modèle (Ke) Tu : 5%
M 0,50
M 0,22
4 10⁻¹
2 10⁻¹

	Mach	P, (bar)	T, (K)
●	0,22	2,26	550
▲	0,50	1,64	600

Laminaire Transition Turbulent
BA 0,2 0,4 0,6 0,8 BF
Abscisses curvilignes réduites
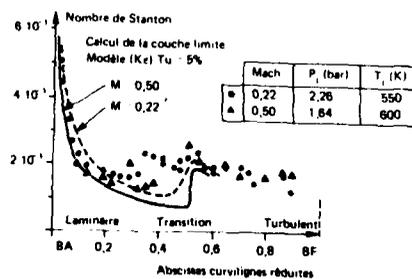
Fig. 11 – Mesure du coefficient de transfert thermique
sur profil symétrique.
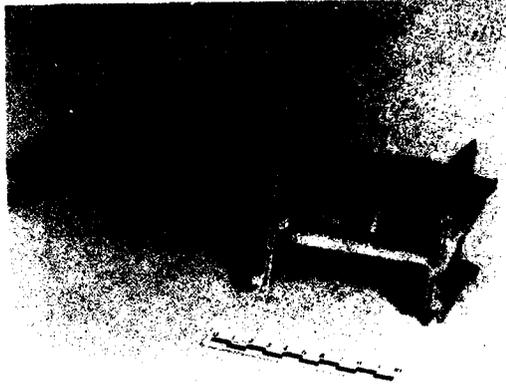
Fig. 12 – Mesure du coefficient d'échange thermique
sur une aube MINOS.
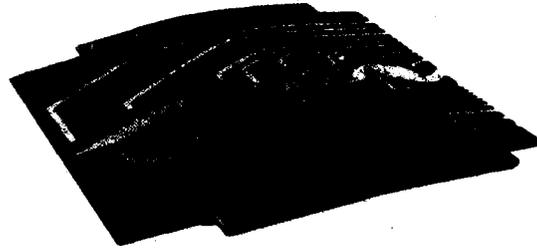
Fig. 13 – Aube MAC équipée de 20 films chauds
déposés sur un même substrat.
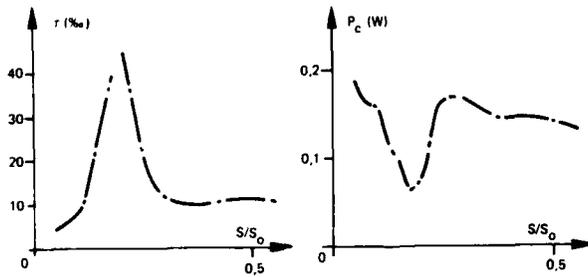
Fig. 14 – Evolution de la puissance convectile P_C et du taux de turbulence τ le long du profil.

DISCUSSION

R.Elder, UK

Would the author please comment on the thermal sensitivity of the pressure transducers?

Réponse d'Auteur

En milieu gazeux, en régime adiabatique, à une fluctuation de pression est associée une fluctuation température. Pour les capteurs massifs, la fluctuation de pression entraîne une variation de capacité par modification de l'épaisseur du diélectrique, alors que la fluctuation de température induite dans le diélectrique modifie la capacité par variation de sa permittivité. Cet effet associé explique la plus grande sensibilité de ce type de capteur au dessous de 2000 Hz.

L'ajout d'une protection thermique de 50 microns d'épaisseur réduit le domaine de fréquence de cette influence à 10 Hz environ.

Les capteurs à diélectrique gazeux présentent une évolution de sensibilité 'S' de $1.1 \ 10^{-3} \ \Delta S/S.K^{-1}$ entre 0 et 40°C.

J.Chivers, UK

Please could you tell me whether or not you have experience of operating your thin film transducers above 400°C and if not do you intend to explore temperatures above 400°C?

Please could you tell me what insulator you have used for sensors to be used at 400°C if not Kapton?

Rèponse d'Auteur

La température maximale d'utilization des capteurs pelliculaires de température et de flux est de 200°C. La tenue de métallisations et des colles employées ne permet pas d'aller au-delà.

Pour les températures supérieures les isolants utilisés sont l'alumine et le zircone-yttrium, déposés directement sur les profils.

A.Buggele, US

Please comment on the effect of strain on the pressure transducer....... causing drift due to leakage of the cavity pressure, temperature changes due to dynamic working, when this system is used as a dynamic pressure measurement system.

(1) I did not see any evidence of a strain isolation system on this transducer;

(2) Was a simple deflection test performed on the pressure transducer on a flat plate or aerofoil..... static deflection and dynamic reflection over a range of 15 Hz to 2000 Hz?

(3) I worry about you measuring strain (dynamic) and not pressure with this pressure transducer system as presently mounted on the airfoil;

(4) If strain (dynamic) cancellation system was used did it automatically compensate for the temperature and pressure drift...... and how was this achieved?

Réponse d'Auteur

La réponse extensométrique exprimée sous forme de signal de pression équivalent s'etablit à:

— 50 mb/10^{-6} Δ L/L pour les capteurs de pr..)n à diélectrique solide.

— 30 μb/10^{-6} L/L pour les capteurs de pression à diclectrique gazeux.

G.Santo, US

Would you like to comment on the effects of length of connecting wires between pressure transducer and signal conditioning?

Réponse d'Auteur

Une microélectronique d'adaptation d'impédance de gain unité, permet de:

— fournir une signal de même amplitude et phase que celui issu du capteur dans le but de porter au même potentiel les connexions de garde du capteur.

— delivra un signal utile sous basse impédance (impédance de charge $\geqslant 2$ KΩ)

De ce fait l'information désponsible en sortie de l'adaptateur d'impédance est pratiquement indépendante de la longueur des connexions.

INTERFEROMETRIC MEASUREMENT OF STRAINS AND
DISPLACEMENTS IN ENGINE COMPONENTS

by

C. Ruiz, P.H. Webb
Oxford University
Department of Engineering Science
Oxford
OX1 3PJ
England

and

D. Post
Virginia Polytechnic Institute
and State University
Blacksburg
VA 24061
USA

SUMMARY

The strains and displacements in engine components, and in particular in inter-locking joints, have been measured by means of two interferometric methods:

1) high sensitivity Moire interferometry, using gratings with 1200 lines/mm,
2) a coarser grating of 40 lines/mm.

The two methods are described in this paper and the results compared to the predictions of a finite element program for a typical dovetail joint. The application of the technique to the assessment of fretting damage and to the lifing of dovetail joints is discussed.

INTRODUCTION

The application of Moire techniques to the determination of the state of strain over a whole field is particularly attractive when compared to point-by-point measurements such as resistance strain gauges. In essence, the Moire pattern is a contour map of the displacement field, from which it is possible to obtain extensional and shear strains. How the pattern is formed in the case of coarse gratings is illustrated in Fig. 1(a), where dark bands are formed whenever a bar in grating 1 ocludes a slit in grating 2. If the pitch of grating 1 is p and that of grating 2 is p', the distance between the centre lines of any two adjoining bands or fringes is

$$\ell = n\,p = (n-1)\,p' \qquad (1)$$

where n is the number of lines in the grating. If the difference in pitch results from a uniform extensional strain, where AB stretches to AB', the displacement of point B, BB' is one pitch,

$$u = p' - p \qquad (2)$$

and the strain is

$$\epsilon = \frac{u}{\ell} = \frac{p}{\ell} \qquad (3)$$

Fringes are also formed when one grating rotates with respect to another grating of equal pitch, Fig. 1(b). The displacements of points such as B on the first order fringe with respect to points A on the reference is also one pitch, the angle of rotation of the grating is,

$$\alpha = \frac{p}{\ell} \qquad (4)$$

and, as before, fringes may be interpreted as loci of equal displacement points.

The grating frequency, F, is normally limited to 40 lines/mm (1000 lines/inch) corresponding to p = 25 μm (1 thou) thus limiting the sensitivity of the method which is applicable to the measurement of relatively large displacements (1). It is only as a result of recent developments that it has been possible to increase the sensitivity of Moire measurement by more than an order of magnitude. In the high sensitivity Moire interferometry a grating of, typically, 1200 lines/mm is transferred to the surface of the object under study following a simple process described elsewhere (3) although other methods have been used (4). When illuminated by a ray of monochromatic light, a diffracted ray of order m emerges with an orientation θ_m in accordance with the law,

$$\sin \theta_m = m\lambda F + \sin \phi \qquad (5)$$

See Fig. 2(a) Taking $\phi = \sin^{-1} (\pm \lambda F)$, gives a ± 1 order diffracted ray normal to the plane of the grating. Thus, when the grating is illuminated by two rays, at angles

$\pm \sin^{-1} (\lambda F)$, two first order diffracted rays emerge along the normal to the grating. If the frequency changes to F' $(F' \gtrsim F)$, Fig. 2(b), the two diffracted rays diverge from the normal and their wave fronts produce dark fringes as a result of destructive interference. It follows from equation 5 and the normality condition that

$$\theta_{+1} = - \lambda F' + \lambda F \qquad \theta_{-1} = \lambda F' - \lambda F$$

and

$$\ell \cong \left| \frac{\lambda}{\theta_{+1} - \theta_{-1}} \right| \cong \left| \frac{1}{2(F-F')} \right| \qquad (6)$$

Since $\frac{F-F'}{F} = \epsilon$, $\ell = \frac{1}{2F\epsilon}$ and the fringes may be interpreted as loci if equal displacement $N/2F$ where N is the fringe order. The grating, of frequency F or F', illuminated by the two symmetrical rays therefore acts as a pair of gratings of pitch $p = 1/2F$ or p'. The similarity can be extended to in-plane rotation, Fig. 2(c). In that case, a rotation by α of the grating of frequency F causes the diffracted first order rays to diverge from the normal by angles $\theta_{+1} \theta_{-1}$ on the vertical plane. Interference fringes then appear

every $\ell = 1/2F\alpha$.

When using 1200 lines/mm, the fringes are contours of equal displacement at 0.4 μm (0.013 thou) steps. Rotations of the object about the y and z axis (Fig. 2(c)) are not detected. The gratings have bars along the x and y directions: illumination on the xz plane yields displacements u in the x direction, illumination on the yz plane yields displacements v in the y direction.

APPLICATION TO THE STUDY OF A DOVETAIL JOINT

a - Low-frequency gratings

Gratings with a frequency of 40 lines/mm on photographic stripping film (5) were transferred onto the dovetail joint shown in Fig.3. For a nominal strain of 10^{-3}, the relative displacement between two points 25 mm apart - the maximum distance in 'blade' or 'sheet' - is only one pitch and therefore only one fringe would appear under load. A number of methods have been proposed to increase the sensitivity of the Moiré, one of the simplest consisting in introducing an initial pattern by viewing the grating on the specimen through a reference grating with a slight rotational mismatch (5). Referring to Fig. 1(b), it is easy to see (Fig. 4) that a change of pitch of the deformed grating causes a rotation of the fringes, such that

$$\tan \gamma = \frac{BD - AB}{p'} = \frac{1}{\sin \alpha} \frac{p - p' \cos \alpha}{p'} \cong \frac{1}{\alpha} \frac{p - p'}{p'} = \frac{\epsilon}{\alpha} \qquad (7)$$

for small angles. It is therefore possible to obtain the strain by measuring the angle of rotation of the fringes, although the presence of shear strains makes the interpretation of the fringe pattern rather difficult. Fig. 5 shows the fringe patterns obtained when the model grating is viewed through a reference grating in the unloaded model and in the loaded model, and the calculated strains along the centre line of the blade, the free face of the sheet and at the most highly strained point. The results are compared with the theoretical prediction of a computer program (6).

An alternative method of transferring the grating has been found preferable in that it avoids the glare produced by unwanted light reflections on the model and reference gratings, facilitates photography and permits measurement at elevated temperatures. In this method, developed by Burch and Forno (7), a matrix of dots is painted by spraying with an air brush a fine suspension of titanium dioxide through a stencil held in contact with the surface of the model. In Forno's method the grating is photographed using a specially modified 35 mm camera with the appropriate demagnification to give a frequency of about 300 lines/mm in the negative, which is then analysed to provide contour maps of displacement in the x and y directions. With a small field this is not necessary. The model grating is viewed through a lens with a 1 to 1 magnification in the arrangement of Fig. 6. Interference fringes are produced on the image plane where a linear grating is placed on a rotatable frame. The fringes are photographed with a conventional 35 mm camera. The sensitivity depends solely on the pitch of the model grating, any mismatch method may be used and, since this is a non-contacting method and the titanium pigment remains white at very high temperatures, it may be used in aggresive environments.

b - Diffraction gratings

The use of 1200 lines/mm diffraction gratings for the study of dovetail joints has been described in detail elsewhere (8). The model tested is the same as in Fig. 3, and the experimental set up is shown in Fig. 7. The process of replication of the grating onto the model consists of the following steps:-

    i - a mold is prepared by exposing a photographic plate to two beams of laser light
         at an angle such as to produce interference fringes at the required frequency.
         A square grating of hollows and ridges is formed by taking two exposures at
         right angles.

ii - the mold is aluminised
iii - a pool of epoxy cement is deposited on the model and the aluminised face of the mold is pressed against it until the cement sets.
iv - the backing glass is lifted off taking with it the photographic emulsion and leaving, as an imprint, the aluminized square grating.

Typical results are shown in Fig. 8, which illustrates contour lines of u and v displacement fields with a 0.417 μm step. It will be observed that two 'bridges' have been established between the blade and the sheet. These bridges are made of a low modulus plastic and have no effect on the stiffness of the model. Their purpose is to provide continuity between the two elements so as to define an absolute fringe order in both. This facilitates the determination of the relative displacement at the interface which is simply equal to the difference between the fringe orders on the blade-side and on the sheet-side times 0.417 μm. For example, the gap opening at the bottom of the joint is 34 μm for the load corresponding to Fig. 8, 4.5 kN. (Nominal stress in the blade 250 MPa).

APPLICATION TO BIAXIAL TESTS OF DOVETAIL JOINTS

The high sensitivity Moire technique, as described, is limited to static testing, due to the long exposure times required when a conventional laser is used. A pulsed laser, capable of giving a short, higher energy pulse - typically 300 mJ in 10 or 20 ns - makes it possible to apply the same technique to the study of moving parts, objects under cyclic loading, etc. A long term investigation into the behaviour of dovetail joints between blades and disks has offered an opportunity to test the technique. The joints are modelled by a sheet with three pairs of blades, loaded under biaxial tension in a special fatigue testing machine with a capacity of 250 kN in both axes (9,10,11). It has been shown that the state of stress is the same as the one in a rotating disk with blades, that the test reproduces the significant features of the more expensive spinning disk test and that the fatigue and fretting depend of the peak stress, the shear stress at the interface and the relative displacement between blade and disk.

While the correct alignment of the experimental set-up of Fig. 7 does not present any serious difficulties when using, for example, a He-Ne laser, the same is not the case if a pulsed ruby laser is used due to the short duration of the pulse. Referring to equation 5, the angles of incidence for the He-Ne light (λ = 633 nm) and ruby (λ = 694 nm) are 49.4° and 56.4° respectively. It is therefore not possible to adjust the relative positions of all the optical components with a continuous He-Ne laser since the alignment would be quite wrong when the pulsed ruby laser is used during the actual test. To overcome this difficulty a 'white light' interferometer has been designed. The principle of this instrument is illustrated in Fig. 9. Light from a laser illuminates the transmission diffraction grating of frequency F, producing the two first order rays OA, OB that, after reflection on the two mirrors illuminate the model grating with the correct incidence to be diffracted along the normal to the grating, regardless of the wavelength. The only condition is that the model and window gratings should be of the same frequency and parallel and that the two mirrors should be normal to both gratings. A misalignment due to a rotation about the 2 axis has the effect already described. An error in the alignment of mirrors must also be considered. Assume that the angles of incidence are $(\phi + \Delta_1)$ and $-(\phi + \Delta_2)$ (Fig. 10). Then the first order diffracted rays have the direction,

$$\sin \theta_{+1} = \lambda F + \sin (-(\phi + \Delta_2)) = - \Delta_2 \cos \phi \quad \text{where} \quad \phi = \sin^{-1} (\lambda F)$$

$$\sin \theta_{-1} = \lambda F \cdot \sin (\phi + \Delta_1) = \Delta_1 \cos \phi$$

fringes, parallel to the lines of the grating, appear every

$$\ell_0 = \frac{\lambda}{(\Delta_1 + \Delta_2) \cos \phi}$$

giving a pattern equivalent to the one corresponding to an initial strain

$$\epsilon_0 = \frac{(\Delta_1 + \Delta_2) \cos \phi}{2\lambda F} \qquad .$$

For example, with $\Delta_1 = \Delta_2 = 10^{-3}$ radians, λ = 694 nm and F = 1200 lines/mm, ℓ_0 is 0.62 mm and ϵ_0 = 0.660 x 10^{-4} approximately. Adding a rotation α = 10^{-3} radians about the z axis and an extensional strain of 10^{-3} would tilt the fringe and reduce their distance, as shown in Fig. 10 (b), where,

$$\epsilon_x = \frac{1}{2\ell_{xx}F} - \frac{1}{2\ell_{ox}F} \qquad (8)$$

$$\alpha = \frac{1}{2\ell_{xy}F} \qquad (9)$$

Similarly, when the grating is along the y axis,

$$\epsilon_y = \frac{1}{2\ell_{yy}F} - \frac{1}{2\ell_{oy}F} \qquad (10)$$

$$\alpha' = \frac{1}{2\ell_{yx}F} \qquad (11)$$

The shear stress strain is $\alpha + \alpha'$, the difference $\alpha - \alpha'$ being the rigid body rotation.

The presence of a zero-load fringe pattern is not necessarily undesirable. Indeed, it becomes a necessity when using low-frequency gratings.

To apply this technique to the study of the dovetail joint under cyclic loading, the interferometer described schematically in Fig. 11 was designed and built around the biaxial fatigue testing machine. Light from either the He-Ne alignment laser or the pulsed ruby lever is expanded, collimated and directed to illuminate the two window gratings, to provide contour maps of both u and v displacements simultaneously. The rays diffracted from the model grating produce fringe patterns that are clearly visible on the screens of the two camera backs. The whole instrument is first adjusted, using the He-Ne illumination, until only a few fringes are observed under zero load. This operation is fairly tedious due to the number of inter-related adjustments needed and to the fact that the slightest vibration or movement of the model or testing machine shakes and blurs the fringe pattern. When the adjustment is completed, the He-Ne laser is switched off, the model is loaded and the pulsed laser is triggered to provide a flash at the required level in the load cycle. Fig. 12 shows typical photographs obtained with the instrument. For the interpretation of the patterns in terms of strains, equations 8 to 11 are applied, measuring ℓ_{xx}, ℓ_{yy}, etc, from the enlarged photographs with an X-Y coordinate measuring machine. The values obtained along the interface are compared to those predicted by numerical analysis in Fig. 13. It must be noted that the numerical analysis depends on the knowledge of the friction coefficient between the surfaces in contact. Since this depends on the surface roughness, which varies throughout the test due to the damage caused by fretting, its exact value is not known a priori and has to be deduced by reference to the experiment. The procedure consists in repeat the analysis for various values of the friction coefficient, comparing the results to those of the experiment. This comparison is facilitated by choosing, as a characteristic parameter, the gap opening.

DISCUSSION

As new materials are developed and the severity of the demands placed on aero-engines increases, it becomes apparent that a single figure of merit such as the peak elastic stress is inadequate to characterise the strength of a component. Fretting damage between contacting parts has been recognised as a possible cause of premature fatigue failure that is clearly dependant on the energy dissipated as the two parts rub together rather than on the peak principal stress. To characterise fretting damage a parameter, defined as the product of the shear stress - or the normal stress times the friction coefficient - times the relative displacement has been defined and shown to be in good agreement with experimental data. When this parameter is itself multiplied by the maximum principal stress, required to open up the small surface cracks resulting from fretting, it yields a combined fretting fatigue damage parameter that can be used in design to complement the traditional peak elastic stress (10,11). Numerical analysis by finite elements permits the calculation of these parameters once the contact conditions are clearly To do so it is necessary to recur to an experiment. It is possible to verify the numerical analysis indirectly, by reference to the back gap opening, that can be measured with an extensometer or a coarse Moire grating. The coarse Moire grating stencilled on the model with titanium dioxide pigment has the advantage over the extensometer of providing a general qualitative impression of the whole displacement/strain field, revealing regions of strain concentration, plastic deformation and creep. The diffraction grating, so far limited to room temperature testing, gives a whole field picture of the same field with sensitivity similar to that of conventional resistance strain gauges but iwth a gauge length that may be taken to be infinitely short. Like all other methods, Moire is limited to surface measurements.

The transferred grating provides a permanent record. In this investigation, it was interrogated after 5000 cycles, thus providing an indication of early fretting damage as evidenced by an increase in the friction coefficient.

CONCLUSIONS

The value of Moire interferometry in combination with numerical stress analysis has been proved (8-11). The two techniques described here may be regarded as complementary. Although further developments of the high sensitivity Moire interferometry using diffraction gratings may extend its application to high temperature measurements, at present these are only possible using coarse gratings. The white light interferometer has made it possible to measure displacements of the order of one-tenth of a μm on moving objects, taking the technique out of the specialised optical metrology laboratory and into the testing laboratory or even into the workshop.

REFERENCES

1- A.J. Durelli and V.J. Parks, Moire Analysis of Strain Prentice-Hall, Englewood Cliffs, New Jersey, 1970.

2- D. Post, 'Moire interferometry at VPI and SU', Experimental Mechanics, 23(2) 203-210, 1983.

3- M.L. bashore and D. Post, 'High-frequency, high-reflectance transferable Moire gratings', Experimental Techniques,8 (5), 29-31, 1984.

4- D. Post, 'Moire Interferometry', Ch.7 in SESA Handbook or Experimental Mechanics, A.S. Kobayashi, ed., to be published.

5- F.P. Chiang, 'Moire Methods of Strain Analysis', Ch. 6 in SESA Manual on Experimental Stress Analysis, Experimental Mechanics, 19(8), 290-308, 1979.

6- C. Ruiz, K. Chen and P.H. Boddington, 'The numerical analysis of dovetail joints', Computers and Structures, 20(6) 731-735, 1985.

7- J.M. Burch and C. Forno, 'High resolution Moire photography', Optical Engineering 21, (4), 602-614, 1982.

8- C. Ruiz, D. Post and R. Czarnek, 'Moire interferometric study of dovetail joints', J. Appl. Mechanics, 52(1), 109-114, 1985

9- P.H. Boddington and C. Ruiz, 'A biaxial fatigue test for dovetail joints' Proc. ASME Int. Conf. Advances in Life Prediction Methods, ASME, Albany, April 1983.

10- C. Ruiz, P.H. Boddington and K. Chen, 'An investigation of fatigue and fretting in a dovetail joint', Experimental Mechanics, 24(3), 208-217, 1984.

11- C. Ruiz and K. Chen, 'Fatigue life assessment of turbine blade-disk joints', Proc. Int. Conf. Fatigue of Eng. Matls. and Structures, I. Mech. E., Sheffield, September 1986.
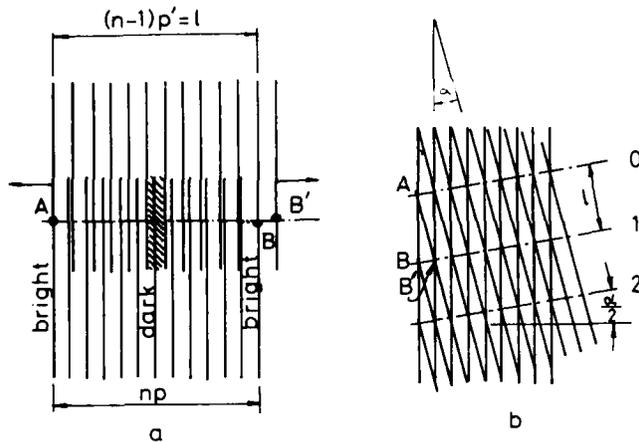
Fig. 1 — (a) Formation of fringes by superposition of two coarse gratings with a slightly different pitch. (b) Formation of fringes by the rotations of one grating with respect to another of equal pitch.
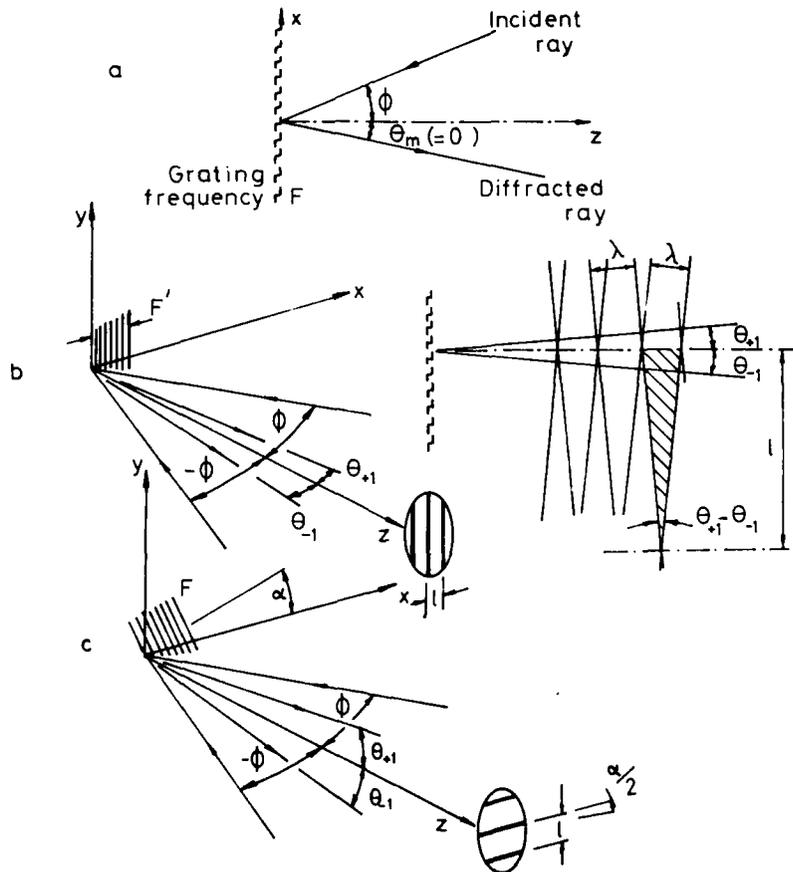
Fig. 2 — (a) A diffraction grating illuminated by a monochromatic ray (b) Interference between two diffracted rays nearly normal to the grating. (c) Effect of in-plane rotation.
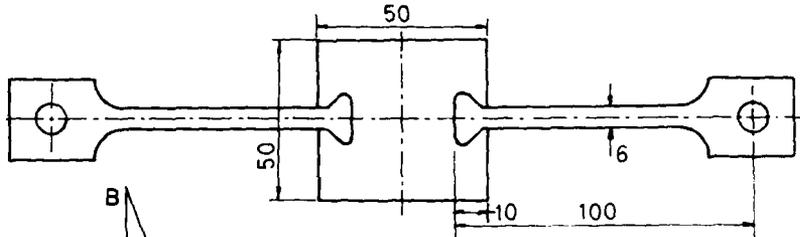
Fig. 3   -   Model of a dovetail joint between a
             blade and a disk, loaded along one axis.

Reference
grating

$$\overline{AB} = p\frac{1}{\sin\alpha}$$

$$BD = p'\frac{1}{\tan\alpha}$$
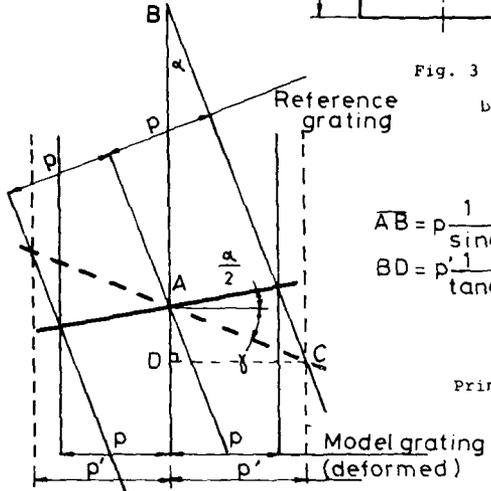
Fig. 4   -

Principle of the rotational mismatch method.

Model grating
(deformed)

$2.5\ \varepsilon_{nom.}$

$\varepsilon_{nom.} = 1$
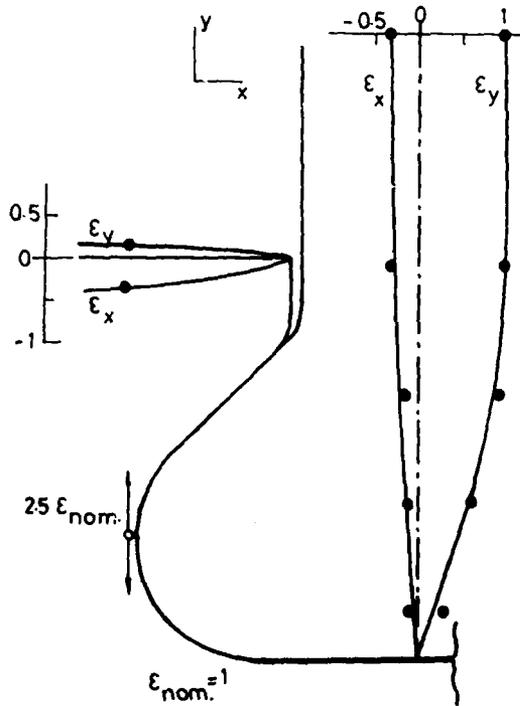
Fig. 5   -   Application of rotational mismatch to the measurement of strains in the model
              of Fig. 3.
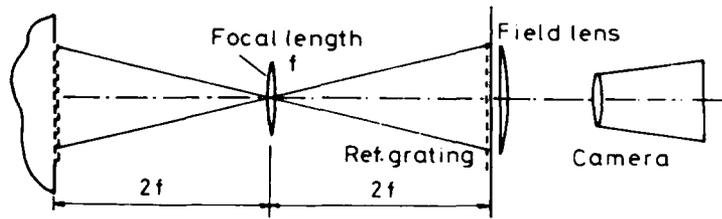
Fig. 6 — System for the photography of fringes produced by two low-frequency gratings.
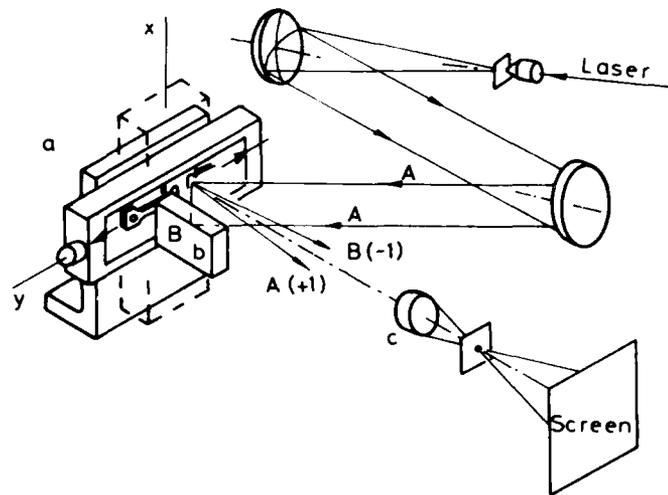
Experimental set-up for the study of a dovetail joint by high-sensitivity Moiré interferometry (8).
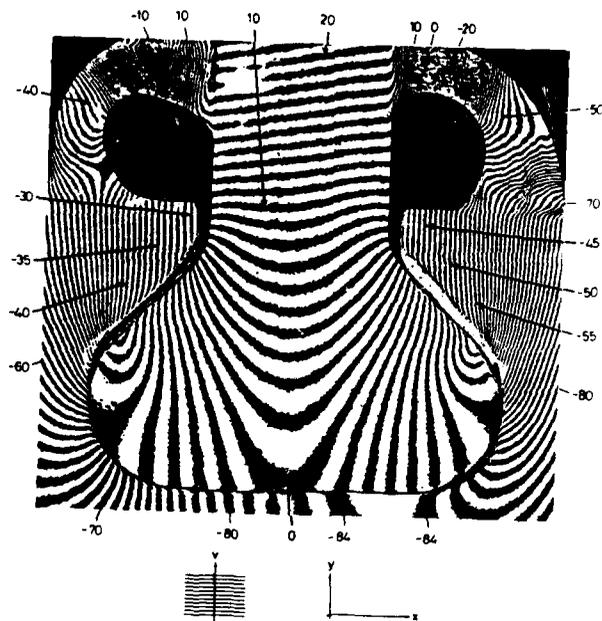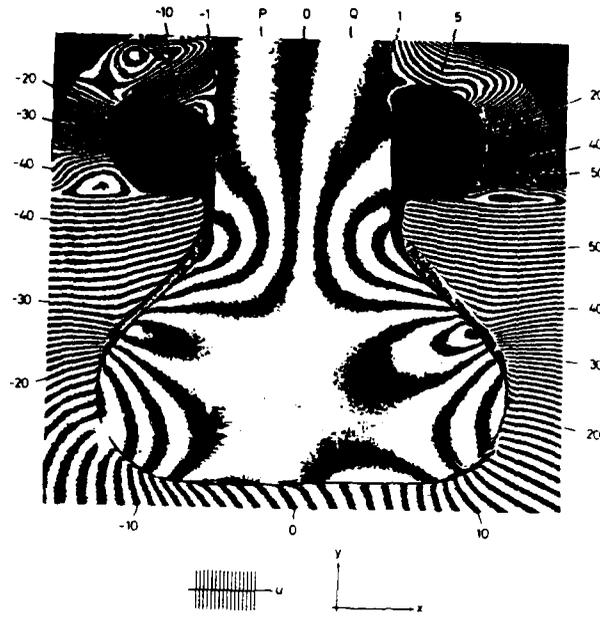
Fig. 8 — Typical fringes obtained from a 1200 lines/mm grating. (8).
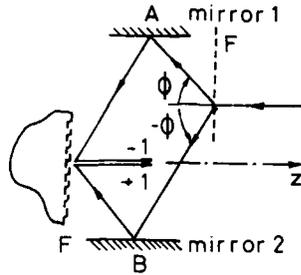
Fig. 9 — Principle of the white light interferometer.
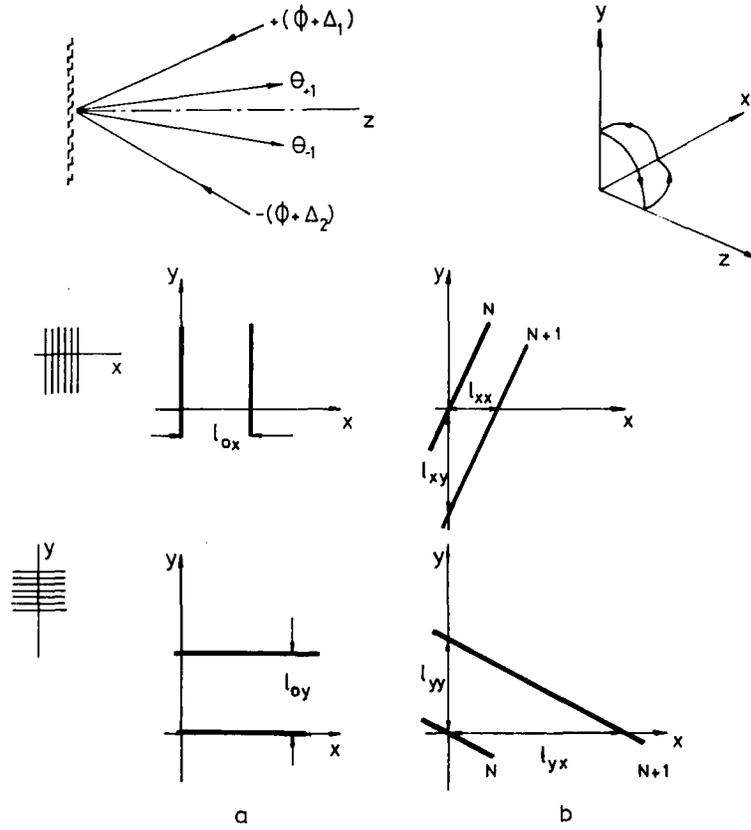
Fig. 10 — Effect of an error in the alignment of the interferometer mirrors, (a) initial fringes, (b) additional rotation about the 2 axis and extensional strain ϵ_x.
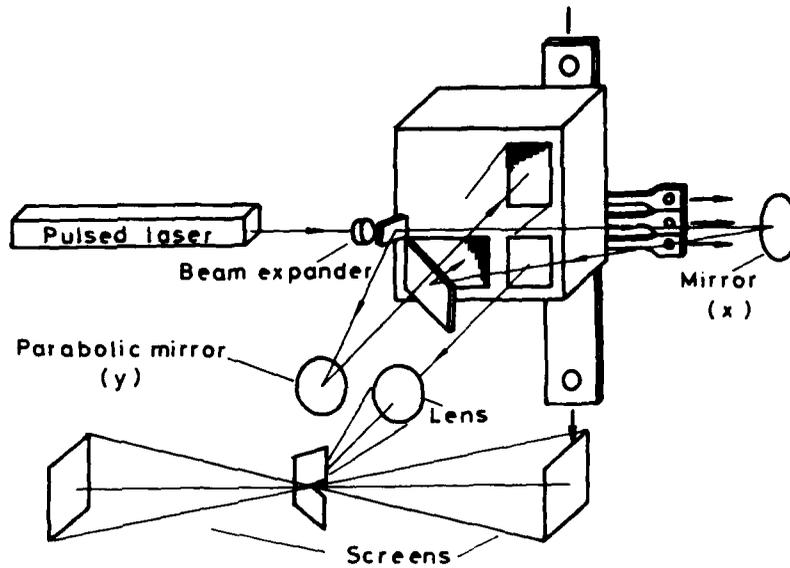
Fig. 11 - White light interferometer instrument adapted to a biaxial fatigue testing
machine: general arrangement.
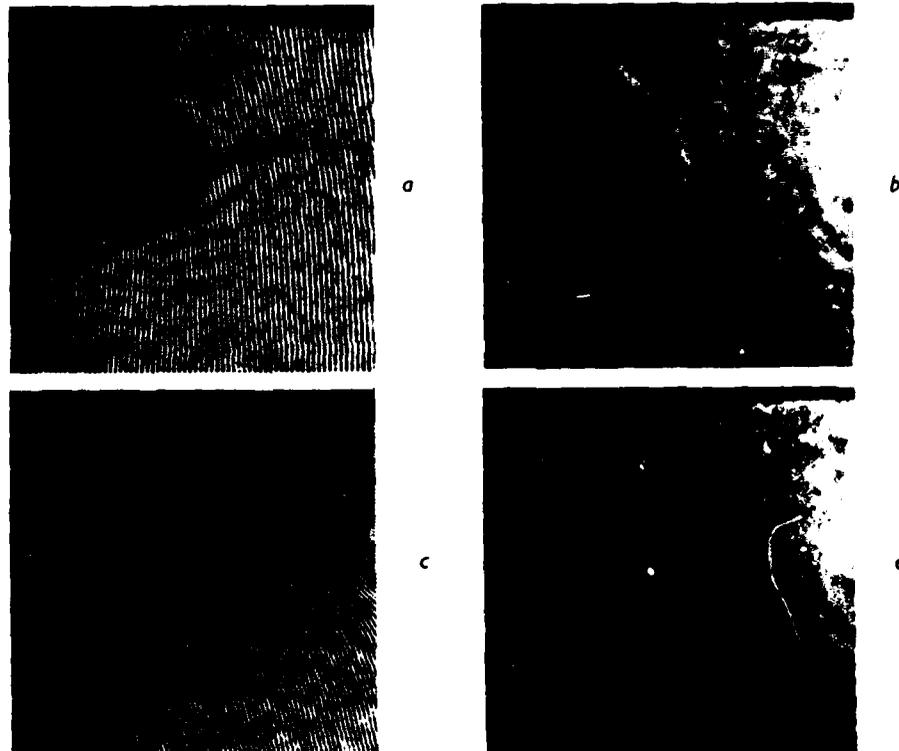
Fig. 12 - Typical photographs obtained with the white light interferometer, (a) zero load,
u displacement, (b) zero load, v displacement, (c) 10 kN, u displacement,
(d) 10 kN, v displacement.
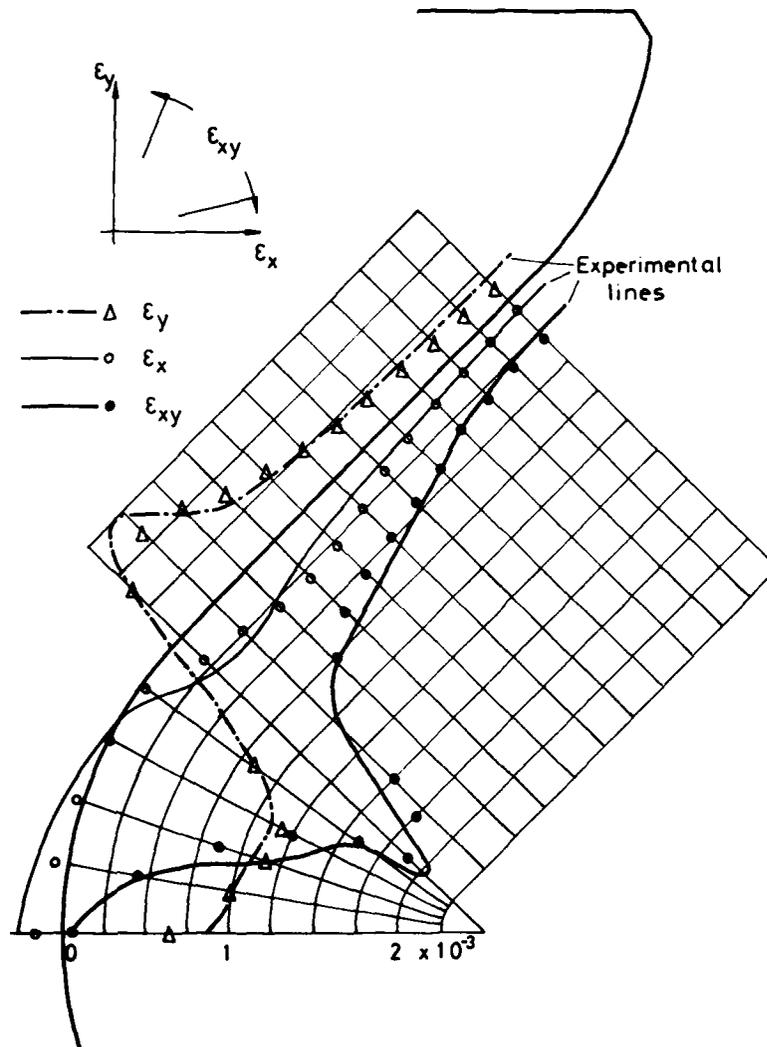
Fig. 13 — Comparison between predicted and experimental values of strain along dovetail interface for a load of 10 kN.

DISCUSSION

P.Stewart, UK

Do you see any future possibility of carrying out measurements on dynamically rotating specimens?

Author's Reply

Well, I think that there are a number of problems with this technique. The first one is that you have to operate on flat surfaces and this means that it cannot be applied directly to a rotating machine. One would first have to produce a flat surface there to apply to the grating. With this proviso I see no reason why one shouldn't be able to use it on rotating specimens because after all, provided you can synchronise the laser to trigger at the time when you are looking at the actual grating, you can do it. The laser would give you a picture over a period of say 20—40 nanoseconds which is more than sufficient for very high velocity applications.

VIBRATION ANALYSIS BY SPECKLE INTERFEROMETRY

Hartwig Knoell
MTU MOTOREN- UND TURBINEN-UNION MÜNCHEN GMBH
Dachauer Str. 665, 8000 Munich 50
Federal Republic of Germany

ABSTRACT

The vibrational modes of complex systems can be visualized with high sensitivity by laser light speckle interferometry. Electronic speckle pattern interferometry (ESPI), in contrast to holography, does not use photo-chemical storage media but shows a live image of the vibrational modes created by the time-average method directly on a monitor screen. The particular advantage of this very useful and now almost conventional procedure of vibration analysis is demonstrated by two applications to aero-engine parts: an IPC blade and an impeller of a small centrifugal compressor.
(Intermediate pressure compressor)

1. INTRODUCTION

The life of highly-stressed engine components such as blades and discs is governed primarily by static, dynamic and thermal loading. The object of modern engine development is the further improvement of efficiency with a higher power-to-weight ratio. With the decreasing amount of material used, the mechanical stress on the components is increased. Similarly, the tendency to vibrate is increased by the decreasing wall thicknesses and more intricate profiles, in blades for example. This can shorten the life of the part considerably. If critical component resonances are excited to high amplitudes of vibration within the operating speed range of the machine, material fatigue can arise prematurely.

Estimation of the stress distribution and thus the assessment of the material loading is made easier if the vibrational behaviour at the various resonance points is known. Finite element methods are now capable of calculating the resonance frequency and vibrational mode, even of complex structures. However, with thin, curved and twisted blades especially, deviations, which can be considerable in the elevated frequency range (10kHz), occur between the arithmetical prognosis and reality. Experimental vibration analysis on the actual object, therefore, still gives the most reliable information about its vibrational behaviour.

The positive experiences made by MTU with optical vibration analysis and the trouble-free handling of the equipment, even under industrial routine operating conditions, will be demonstrated using two practical examples following a brief commentary on the technique and a description of the equipment.

Optical Elements

BS : Beam splitter
M : Mirror
VA : Variable attenuator
L : Lens
PH : Pinhole
VO : Variable objective
P : Prism
SM : Stripe mirror
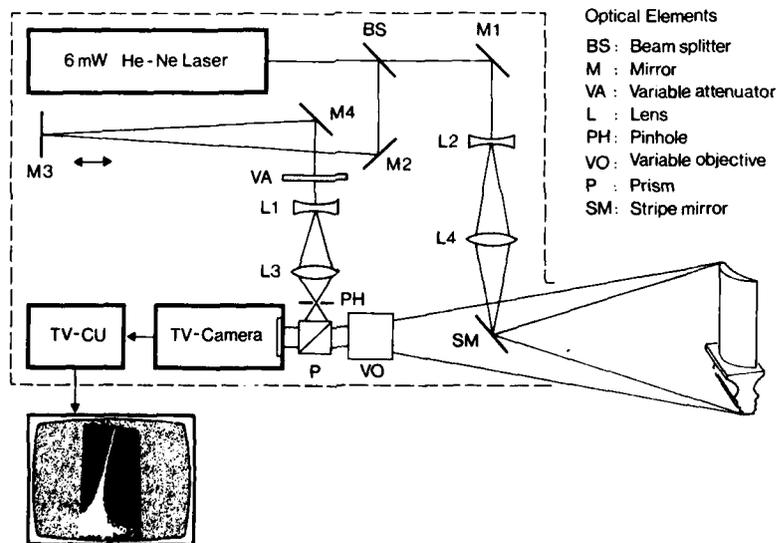
Fig. 1   Optical arrangement of the MTU electronic speckle pattern interferometer (ESPI)
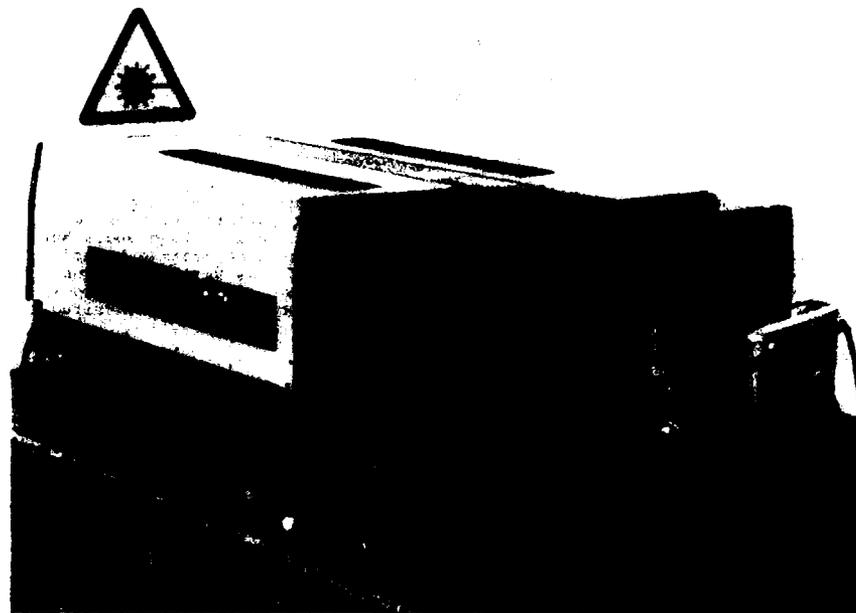
Fig. 2   ESPI vibration analysis set-up (without the TV monitor).
          Assembly located on a heavy granite table with shock dampers.

2.   SOME BASIC COMMENTS ON THE MEASUREMENT TECHNIQUE

Using former mechanical tracing inspection techniques, the acoustic figures of delicate blades could not be analysed without the resonance of the object under inspection being de-tuned by the extra mass of the probe. Only with the advent of modern optical methods of holography and its related techniques was it possible to visualize vibrational modes even with very small amplitudes, without affecting the object under inspection in any way. However, holography could not be applied in industry for routine inspection until an electronic storage medium was found to replace the complicated and time-consuming photographic storage of interference patterns and reconstruction of the holograms. The speckle effect was first used about 15 years ago by Leendertz /1/ to measure surface movement. Speckles /2/ are visible as a granular, statistical dot pattern when an optically rough surface illuminated with laser light is imaged through a lens or even simply observed with the naked eye. The size of the speckles depends on the aperture of the viewing lens. Each individual speckle is already a separate interferogram whose phase and amplitude define the position in space of the scattering surface. The speckle effect can be exploited to determine the position, or relative displacement, of the surface if the phase and amplitude information contained in the speckles can be successfully extracted.

The phase information can be extracted by superimposing a coherent reference beam. If the object surface is moved, and thus the speckle phase position is varied in relation to that of the reference beam, this becomes apparent in the interference pattern with the reference beam as a variation of the speckle brightness. The variation in brightness of the speckle interference pattern, which is coarsely rastered in comparison to the light wavelength, can be registered electronically with a TV camera, i.e. converted into an equivalent electrical signal. As with the classical time-average method of holography, this so-called electronic speckle pattern interferometry (ESPI) can be used to produce an interference fringe pattern which represents the acoustic figure of a resonating object. With ESPI, this fringe pattern is visualized on the monitor in real time, without any intermediate stages.

As early as 1975, MTU took a commercial ESPI system, made by the no longer existent Austrian company EUMIG, into service for routine inspection of blades and discs. The system is only suitable for vibrational analysis of a stationary, restrained object at room temperature. This so-called stationary vibration measurement (SVM) gives a realistic image of vibration behaviour in the range up to 80kHz. The sum of the opposing effects of centrifugal force and temperature on the vibrational behaviour of rotating components in the engine is small and can be corrected arithmetically with sufficient accuracy using the results of the SVM.
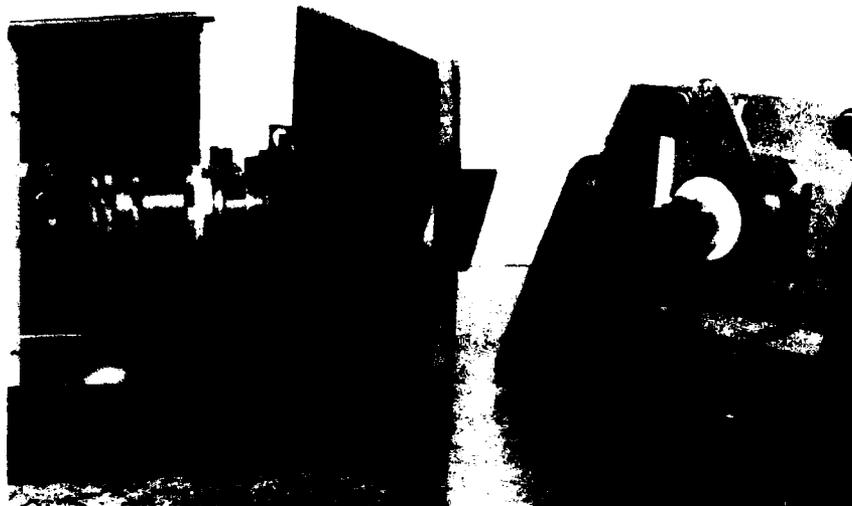
Fig. 3   Detail view of the ESPI optical components (dust cover removed).
           Piezo exciter with white painted compressor blade is shown on the right.

3   DESCRIPTION OF TEST EQUIMPMENT

The ESPI system HT 10 (HOLOTEST) was developed at the beginning of the seventies by EUMIG, Austria, and was originally intended for inspection of car tyres. The system used by MTU today is now more than 10 years old. However, its optical and electronic set-up differs only insignificantly from modern systems. Fig. 1 shows the major components of the MTU unit, of which the layout and function will be described briefly. Speckle interferometry is dealt with thoroughly by R. Jones and C. Wykes with a detailed description of the technical possibilites and equipment designs /3/. The work done at Loughborough University of Technology in Great Britain, which forms the basis of the book, has also brought about the development of a modern, commercial ESPI unit which is marketed by EALING under the designation VIDISPEC.

With the MTU unit (Fig. 1), the beam of a 6mW He-Ne laser is divided at the beam splitter (BS) into the approximately 90% intensity object illumination beam and the approximately 10% intensity reference beam. After 90° deflection at mirror M1, the object beam is expanded by lens L2 and then focused through microscope objective L4 onto a narrow stripe mirror (SM) which is suspended on a thin holding strap in the observation cone of variable objective VO, and which deflects the object beam through 90° onto the object in a conical shape. The laser light which is scattered at the rough object surface is captured by objective VO and imaged as the characteristic speckle pattern on the target of the TV camera via prism P. The object image must be greatly reduced because of the smallness of the camera's target.

In crder to maintain its coherence, the reference beam is directed via mirrors M2, M3 and M4 in the unit along a compensatior. path whose length can be adjusted to that of the object beam path by displacement of mirror M3. After slight expanding by lens L1, the reference beam is focused through microscope objective L3 in a space filter arrangement onto aperture PH. The homogenized reference beam is superimposed onto the object beam via prism P to create interference with the speckle pattern in the target plane of the TV camera tube. With a suitable speckle size, which is governed by the aperture of the viewing lens, the geometric resolution of the camera is sufficient to generate an exact image of the interference intensity profile, i.e. convert it into an equivalent electrical signal, in spite of the reduction. With ESPI, the desired information is contained solely in the statistical part of the speckle pattern, and therefore in the alternating component of the electrical video signal. The homogeneous intrinsic intensities contain no useful information. There-fore, in the signal conditioning unit (TV-CU, Fig. 1), the alternating component is separated from the direct component by a high-pass filter and directed to the monitor after suitable amplification and rectification.

With the system operating in time-average mode, the natural modes of the re-sonated object can be observed directly, in real time on the monitor. The vibrational nodes in the figure show up as bold bright lines along the object surface. Inter-ference fringes of decreasing brightness indicate the amplitudes of the individual

oscillating areas by the density of the fringes. The phase relationship of the oscillation in these areas is not given by ESPI. Other techniques known from holography can also be realized with an ESPI system using the appropriate accessories. The MTU system is used exclusively in the time-average mode for vibration analysis.

The quality of the speckle interferograms on the monitor can be improved decisively by giving the object a thin coating of a paint which increases its reflectiveness. White paints containing minute glass beads are particularly suitable. Beside the marked improvement in fringe pattern contrast, these paints have the additional advantage that objects up to a diameter of 0.8 m are sufficiently illuminated by the low-powered 6 mW laser.

A good base for the ESPI system and the objects has proved to be a 1 x 2 m², 1.3t granite table which is mounted on dampers, since uncontrolled mechanical vibration and airborne sound can greatly impair the quality of the interferograms. Figure 2 shows the inspection set-up with a compressor blade restrained at the root as the object. The blade is excited using the piezoelectric exciter recognizable in Figure 3.
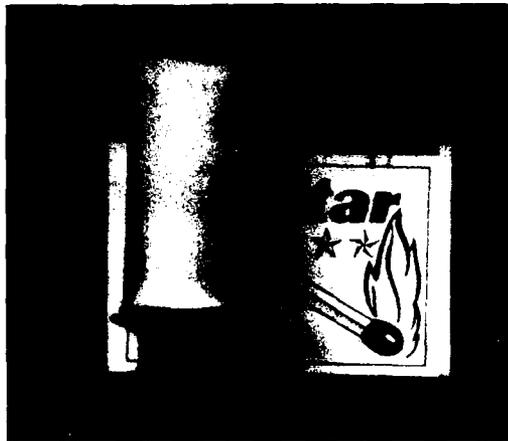
Fig. 4   The item analysed:
          An IP-compressor blade with 38mm maximum airfoil height (suction side).

4   EXPERIMENTAL RESULTS

The capabilities of the ESPI system are demonstrated on two representative examples.

The first example, shown in Figure 4, is an intermediate-pressure compressor rotor blade with a maximum airfoil height of 38mm. The natural frequencies and vibratory modes of this blade were determined with the ESPI unit /4/. Because of the high operating speed of the intermediate-pressure compressor and the large number of stator vanes in the upstream and downstream cascades, excitation frequencies of over 40 kHz can be expected within the operating speed range of the engine. An appropriately high frequency range was selected for the vibration test. Figures 5 and 6 show a few of the characteristic bending, torsion and plate-type vibrational modes of this small blade. The natural frequency found, i.e. the excitation frequency during the take, and, as far as possible, the interpretation of the vibration mode are indicated for each picture. All interferograms are taken from the suction side. The classic acoustic figures of the cantilevered airfoil in fundamental and harmonic vibration are distinct in the lower frequency range and are reproducible at a defined frequency. In the excitation frequency region above 24 kHz, the thin-walled blade profile tested shows plate-type vibrations whose lack of symmetry indicates that the oscillating object does not have a geometrically simple profile. This means that the arithmetical prognosis is also indefinite.

Selected results of stationary vibration measurement (SVM) of a centrifugal compressor impeller are shown in Figures 7 and 8. All interferograms were taken from the plane rear side of the impeller disc which is shown from the front, bladed side in Figure 9. The impeller is 240 mm in diameter. It can be clamped without difficulty at the shaft stub end and excited with the piezoelectric exciter. The photographs taken from the screen clearly show that the vibrational behaviour of the rotor is determined mainly by the geometry of the disc. As shown in Fig. 10, a detail taken from the front of the impeller, the vibrational behaviour of the individual blades is distinctly present and can be observed well with the ESPI unit. It has, however, no

recognizable effect on the vibrational mode of the centrally restrained disc, in the
lower frequency range (12kHz) at least. It is notable that the natural frequencies
of completely different types of vibration modes vary only slightly (Fig. 7): the
two-nodal-diameter mode at 5507 Hz is only 10 Hz below the distinct umbrella mode at
5517 Hz. Furthermore, identical vibrational modes, such as the two-nodal-diameter
mode mentioned, occur with different phase at clearly different excitation fre-
quencies: at 5507 Hz and also at 5557 Hz.
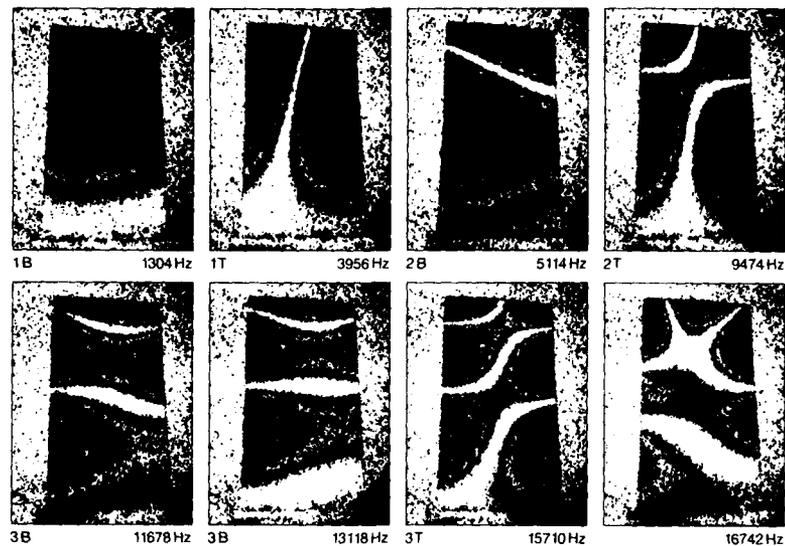
Fig. 5   Photographs of selected IPC blade vibration modes as taken from the
screen: B = bending mode, T = torsion mode. The natural frequency of each
mode is given on the lower right-hand side.
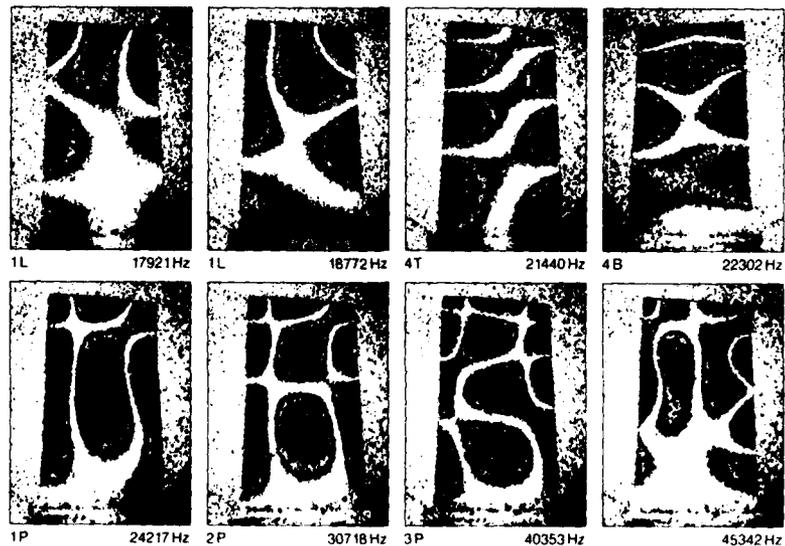
Fig. 6   Selected high-frequency vibration modes of the blade shown in fig. 5:
L = lyra mode, T = torsion mode, B = bending mode, P = plate mode.
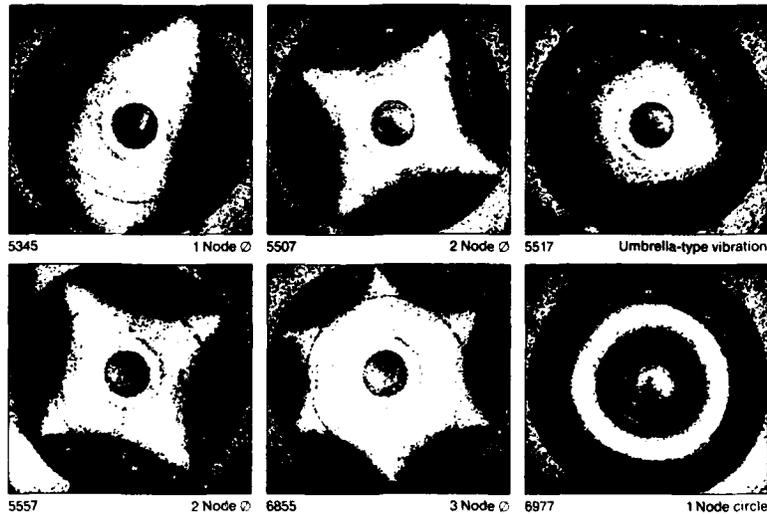
Fig. 7   Selected vibration modes of an impeller. The natural frequency and an
          interpretation of the type of vibration is given at the bottom of each
          photograph. All pictures show the plane rear of the rotor disc.
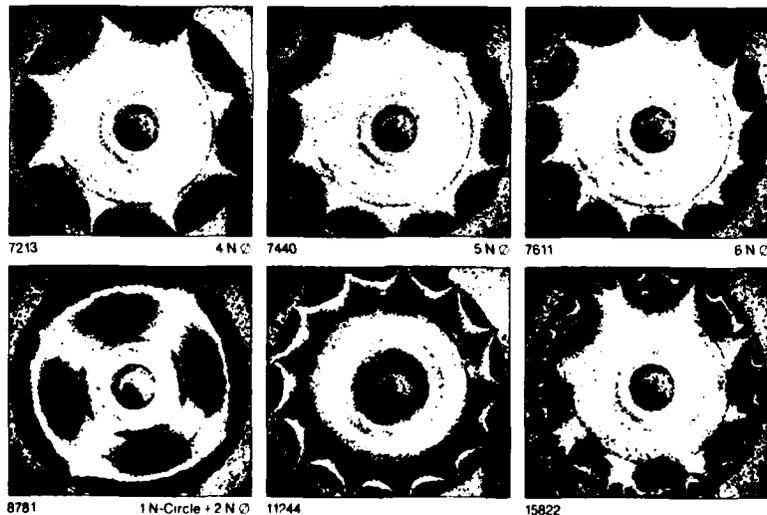
Fig. 8   Selected high-order vibration modes of the impeller disc.

5   CONCLUSION

Operation and handling of the ESPI system at MTU present no difficulties. The
extremely low power of the laser beam, which only leaves the housing in an expanded
state, greatly reduces the number of requirements on safety. During the ten years of
operation with an average utilization of 60%, four laser tubes were consumed, and the
TV system was renewed about a year ago.

The results of stationary vibration measurement (SVM) with ESPI are significant
for the early evaluation of engine components as regards shape and stress. Vibration
analysis with the ESPI system performs five tasks with very little experimental
effort:
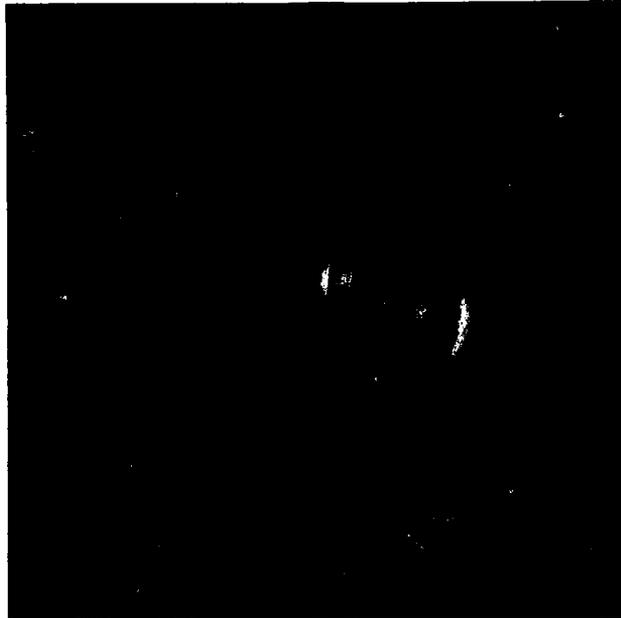
Fig. 9   Bladed side of the impeller tested. Outer diameter is 240 mm.

8809 Hz   10822 Hz
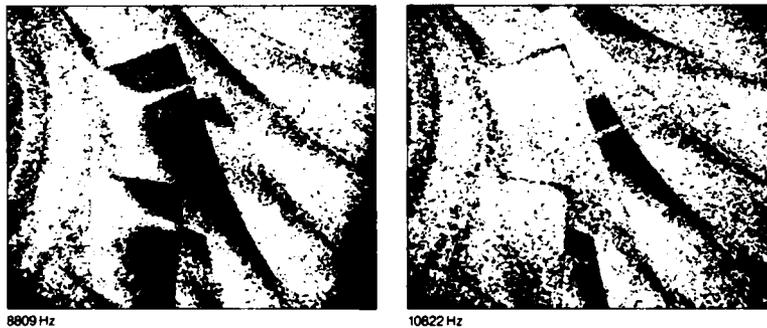
Fig. 10   Typical natural vibration modes of the differently shaped impeller
          blades as observed on the front of the rotor. Vibration of the longer
          blades is shown on the left, that of the shorter, and therefore stiffer,
          blades on the right ESPI photograph.

a)   The calculated natural frequencies and vibrational modes are checked on the
actual object. In the frequency range above 10 kHz, reliable information about vibra-
tional behaviour can only be obtained by SVM.

b)   The effects of restraint on vibrational behaviour can be considerable, es-
pecially in the case of blades. The various restraining methods can be simulated with
SVM and the changes in vibration behaviour analysed. In this way, ESPI analysis
provides, simultaneously, exact marginal conditions for the finite element cal-
culation.

c)   Critical components are monitored with strain gauges during the first test runs
of a module or engine. In Figure 11, the signals from a strain gauge sensor mounted
on a compressor vane with a supercritical profile are plotted versus frequency and
engine speed. By comparison of the resonant frequencies measured during the test run
with those of the SVM, the resonances observed in operation can be allocated to de-
finite vibrational modes, since the vibrational mode for each natural frequency is
known from the ESPI analysis

d)   If, on a component such as a particular blade type, critical resonances repre-
senting a hazard for the component, or drastically reducing its life, are excited
within the operating range, an attempt can be made at remedial action by specific
form changes. By trimming the trailing edge of the blade, the natural frequency can
be offset, ideally right out of the excitation range of the machine. The success of a
particular form change can be demonstrated directly on the object by SVM.

e)   The sensitive dependence of the natural frequencies of complex components on the
accurate reproduction of shape makes it possible to monitor, for example, the casting
quality of blades using ESPI.

ESPI analysis is, therefore, a versatile and important tool for engine develop-
ment, whose operation requires very little specialist knowledge of optics beyond the
necessary care.
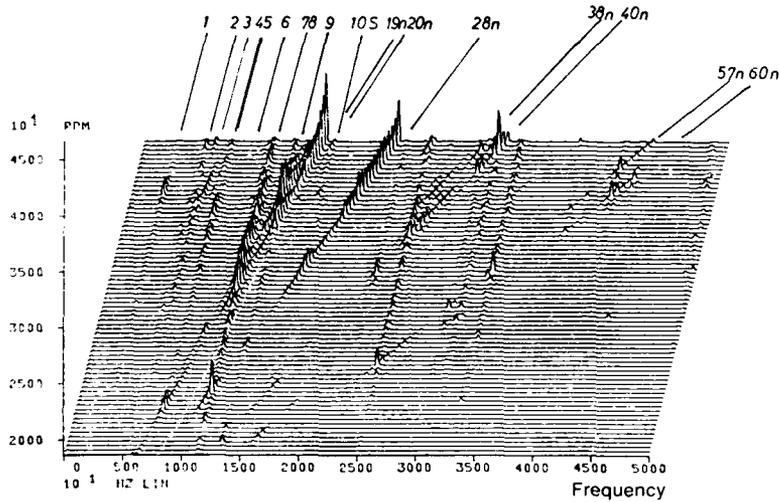
Fig. 11   Strain gauge measurement of a 2nd stage guide vane with supercritical
profile. The observed natural frequencies are sequentially numbered (1S to
10S) together with harmonic multiples of the rotational speed, e.g. 38n.
Obviously, there is an excitation due to the aerodynamic coupling between
the stator and the upstream and the downstream rotor.

6   REFERENCES

/1/   Leendertz J.A., Interferometric displacement measurement on scattering surfaces
utilising speckle effect; J.Phys.E., 3, 1970, p. 214-218

/2/   Butters J.N., Optical transducers and techniques in engineering measurement;
London, New York, Applied Science Publishers, 1983, p. 205-238

/3/   Jones R. and Wykes C., Holographic and Speckle Interferometry; Cambridge,
Cambridge University Press, 1983, p. 198-239

/4/   MTU-Technical Note, Standschwingungsmessung an MDV-Schaufeln alternativer Vor-
materiallieferanten, EV2-Notiz 97/84 M, 1984

/5/   MTU-Technical Note, Standschwingungsmessung am Radial-erdichter-Laufrad S/N 1,
EV2-Notiz 21/85 M, 1985

7   ACKNOWLEDGEMENTS

DISCUSSION

C.Reames, US

What is the sensitivity of the ESPI instrument — can the sensitivity be varied by varying the optical geometry of the instrument and if so through what range?

Author's Reply

The sensitivity is within the wavelength of the laser system used and in our case its about 0.5 micron or so.

With regard to the second part of the question — the sensitivity, which means the means to measure amplitudes, is given by this fringe density but we use it to see where are the nodal lines — not the amplitude. In any case, one is interested to see whether the amplitude is higher in this edge rather than in this edge; this is important but not quantitatively.

C.Reames, US

The reason for my question was that with holography being a very sensitive instrument you often cannot vibrate thing at an amplitude corresponding to what happens in an engine and I was wondering if the speckle technique perhaps could be made less sensitive so that it would more nearly approach an engine environment.

Author's Reply

That's not possible.

R.B.Price, UK

I would like to comment on the sensitivity of the ESPI system. Inherently of lower signal to noise ratio than holographic fringes would be, unless you are able to do some signal processing on the fringes technique it isn't going to be possible to get the detailed amplitude information out of these types of fringes.

Author's Reply

That is completely right, Dr Price, our main goal is to use this system in an industrial environment. It's a tool for routine application and not for the sophisticated analysis of details.

All we do is put a blade in — put a disk in — switch it on and it works. That is the main goal of such a system. It's rather more sensitive to use normal holography; that's right.

R.B.Price, UK

Might I go on to ask you "are you intending to capture the ESPI fringe pattern and do signal processing on it?"

Author's Reply

No, we won't do that.

R.B.Price, UK

Just one last comment — I wasn't too sure what you meant by your earlier comment that holography can not be a routine industrial tool. I think this is not the case — I can assure you that it is so used at Rolls Royce.

AD-P005 547

"THE APPLICATION OF RADIATION PHYSICS AND PHOTOGRAMMETRIC TECHNIQUES FOR THE DIAGNOSIS AND SOLUTION OF MECHANICAL ENGINEERING PROBLEMS AND PERFORMANCE IMPROVEMENTS IN THE DEVELOPMENT OF AERO GAS TURBINE ENGINES AT ROLLS ROYCE"

P A E STEWART
Chief - Advanced Projects Department
Corporate Engineering, Rolls Royce Limited, Bristol

SUMMARY

"Research into the applications of penetrating radiations or particles for the non-invasive imaging and measurement of events within aero gas turbines on dynamic test at Rolls Royce are discussed.

High Energy (8 MeV) X-rays are used to determine metal component movements for engine performance improvements and integrity confirmation, using film. Real time video is used for transient events. Low energy x-rays with high speed cine fluoroscopy have been used to analyse molten metal flows in the turbine blade casting process.

'Cold' neutrons and low energy x-rays have been used to analyse two phase flows and oil distribution in the 'Gem' engine oil scavenge system.

Positron emitting isotope techniques are being developed to determine fuel and lubrication system dynamics.

The images captured by these systems are then processed by digital techniques and pattern recognition and crosscorrelation is carried out. Measurements are made from the film and video images using two and three dimensional photogrammetric methods".

INTRODUCTION

In the development of an aero gas turbine engine, a mechanical engineer requires answers to questions in two major areas:

. What is the behaviour of the metal components?
. What is the behaviour of the engine fuel and lubrication systems?

In considering metal component movements, the engineer needs to know:

. Which components move?
. When do they move?
. How do they move? In what direction do they move and by how much?

In considering engine lubrication systems behaviour, he needs to know:

. How the lubrication system primes itself on engine start?
. How long it takes for critical parts to be lubricated?

With the engine running, he needs to know:

. The efficiency of oil management in the lubrication system - the supply and removal of oil from key areas.
. The general distribution of the lubricating fluid throughout the system - oil hiding problems - and how this distribution varies with engine power level settings.
. The fluid flow rates at critical points in the system for cooling and lubrication.
. If two phase flow is present, the liquid and gas fractions and the pressure drop in the section under examination.
. The behaviour and distribution of the lubricating fluid in engine gearboxes both qualitatively and quantitatively.
. The efficiency of lubrication of gears and gear teeth and the distribution and retention of lubricating fluid on the faces of gear teeth in operation.

To provide answers to these questions, three separate imaging techniques using penetrating radiations, each with specific characteristics and application areas, have been identified and developed at the Advanced Projects Department of Rolls Royce, Corporate Engineering at Bristol.

These systems are non-invasive and require little or no modification to the engine under examination. They may be used to visualise directly, in real time, areas of the engine and to determine inter-related component or fluid movements. Measurements may be made using two or three dimensional photogrammetric methods.

Through the use of these techniques, solutions may be provided to the questions discussed in the introduction. The three techniques are:-

- High Energy X-ray Imaging (8 MeV) to visualise and measure metal component movements.
- "Cold" Neutron Imaging (0.004 ev) to visualise and quantify lubricating fluid movements and distribution, particularly during engine priming.
- Positron Emission Tomography for the location of fluid masses within engines and characterisation of the behaviour of jets, fluid annuli etc. General imaging of fluid movements.

1.0 High Energy X-ray Imaging of Metal Component Movements

High Energy X-rays were chosen in 1970 for their ability to penetrate the chordal thicknesses of steel (up to 10") found in large gas turbine engines. Fig 1 shows the curve for steel penetration versus x-ray energy and it can be seen that penetration increases sharply up to 8 MeV but flattens out thereafter. Above a threshold of about 12-14 MeV, activation of materials within engines occurs with neutron production and subsequent handling problems. The useful energy range for an x or gamma ray source would appear to be in the 4 to 10 MeV range depending on engine size. Such energies may be provided by a radiographic electron linear accelerator or "linac". - To optimise the application some linacs have switchable energy ranges (fig 2).

In order to image the transient movements of engine components such as high pressure turbine blades, in 'accel' or 'decel' conditions a high x-ray dose is required in a brief time - say a few seconds, or parts of a second, depending on whether it is a 'slow' or 'fast' transient. This requires a high dose rate from the linac which may be, if necessary, accommodated in the "burst mode".

The original RDL 'Super X' linear accelerator was delivered in 1971 and had an output of 1500 rads/min measured at 1 metre from the source, at a fixed x-ray energy level of 8 MeV. Because of the heavy x-ray programme a second RDL 'Super X' 3000 linac is to be delivered in early 1986 and will have a capability of 3-4000 RMM with switchable energies of 6 to 10 MeV. This will provide a capability for the recording of transients on high resolution film, for normal and high speed x-ray video and for high speed cine fluorography. These two linacs are mounted to traverse along the length of the engine, they may be raised and lowered and angled to suit the application. They have adjustable x-ray beam collimators to reduce the scatter and improve the images. Radiographic film images are captured by film change systems developed by Rolls Royce and CGR. Real time surveillance of the engine during a test is provided by a range of high energy x-ray video systems designed by RR APD for which world patents are held - The Queens Award for Technological Achievement was given for this development in 1978 (fig 3). They are now commercially available from Rolls Royce.

It is desirable to be able to arrest the motion of a single blade and to index individual blades on a turbine to check variations, blade to blade, whilst the engine is running. Similarly it is useful to image within an engine, the centre shaft, and to search for suspected shaft "whirling", a source of shaft vibration, and to look at spacer bounce in compressor or turbine packs. A linac such as the 'Super X' may be remotely pulsed from an engine mounted inductive pick-off at harmonics of the engine turbine rotational frequencies to act as a high energy x-ray stroboscope in conjunction with the video system. The 'Super X' pulse repetition frequency is 500 to 750 pulses per second.

In certain types of test such as engine surge margin determination, vibration surveys, foreign object ingestion or "blade off" and engine destruction tests, a high speed imaging capability is required. This may be provided by the linac running at its maximum pulse repetition frequency, or in the "burst mode" for a short period. The images are captured by an x-ray intensifier with 'fast decay' phosphors, lens coupled, to a high speed cine camera such as the LOCAM, or to a high speed video system such as the SPIN PHYSICS SP2000.

Using the high speed x-ray cine fluoroscopy expertise developed with the linac, an application was made to improve foundry work. The flow pattern or distribution of molten metal into a turbine blade multi-casting mould was uneven, leading to a cooling of the surface of the metal in one partially filled blade and producing a 'cold shut' in the cast blade. The Thomson-CSF X-ray Intensifier and LOCAM cine camera were used at 300 frames/second with a 300 KVCP X-ray source. The cine film clearly showed the metal distribution, and highlighted the problem. A solution was obtained by changing the design of the mould.

The Linear Accelerator is transported by and operated from a Linac Control and Transit Vehicle or LCTV, fig 4, which has been designed by, and custom built for, Rolls Royce. The High Energy X-ray video and Image Processing System is transported in a separate vehicle and comprises Thomson CSF High Energy X-ray Intensifiers and special video cameras, configured to Rolls Royce design, incorporating low light level SIT Tubes with specialised phosphors. Digital image processing of the x-ray video and radiographic images is carried out.

Cross-correlation techniques are used including template matching and pattern recognition and the standard 'enhancement', integration, noise reduction and other processing routines. The image processors used range from Quantel Intellect 1 and 100 through to the VICOM 1850. Image recording is currently analogue, using Grundig 10 MHZ reel to reel recorders.

X-ray images of high spatial resolution are provided by radiographs. These are analysed on Packman X-Y coordinate tables by skilled photogrammetrists (fig 5). Average accuracies are around 0.006" but on good edges 0.004" can be achieved. These are based on a 95% confidence of repeatability. Ellipsing of the disk images limits measurement in the axial direction. Radial measurement can be made over a broader field. Semi-automated measurement systems are being developed. Examples of applications are as follows:-

. Performance improvements by profiling of tip seals for turbines to reduce energy losses over the range of engine operating conditions leading to improvements in SFC.
. Understanding of thermal growths in casings and differential expansions between blades, disks and casings for instance, on 'scramble' situations on the one hand or descent from cruise altitude on the other. The RB199 compensating casing was designed using x-ray data.
. Engine air system optimisation from a knowledge of the behaviour of internal labyrinth seals and compressor and turbine root seals. An understanding of the performance of all seals is necessary to maintain air pressure balances throughout the engine.
. Engine integrity investigations ranging from static assembly checks before test - seal incorrectly fitted-to "in service" problems such as spacer bounce on TF41 and VIPER in flight.

The HEDR system has 3 prepared sites at RR Bristol, 1 at Dowty at Cheltenham, 1 at RR Ansty and 1 at RR Hucknall. The 'Super-X' linac is also now routinely used at the Cell 3 High Altitude Facility at RAE Pyestock. The years programme may cover activity at most of these sites and the linac system moves to provide service. To date 40,000 radiographs have been taken and analysed on a total of 130 engines of 23 different engine types.

50 High Energy X-ray video tests have been carried out and Rolls Royce have invested £3/4 million in new equipment in 1985/6 for the project.

For this work, Rolls Royce APD were given the MacRobert Award of the Fellowship of Engineering, November 1985. This is the premier UK engineering award. References (1) to (18) describe the work in more detail as do Patents 1 and 2.

2.0 'Cold' Neutron imaging of lubricating fluid movements

Following the success of the High Energy X-ray programme in defining the metal component movements within running engines, in 1975 an initiative was developed to similarly visualise and measure lubricating fluid movements.

In any "penetrating radiation" imaging system, the image quality parameters of importance are the Modulation Transfer Function, Contrast Transfer Function and signal to noise ratio.

The MTF is a measure of the fidelity by which the image represents the original - frequency for frequency. In any image it is also important that the Contrast between objects in the image which it is required to differentiate, are at a maximum. Thus one of the objectives in specifying this system was to differentiate images of the oil from images of the steel components. In other words to see the lubricating oil behaviour through the steel walls of the engine casings. To render the steel casings transparent.

Now if one examines the combined scattering and absorption cross-sections of steel and hydrogen, one may plot these on a graph as a function of neutron energy (fig 6). Lubricating fluid is of course largely hydrogenous. It will be seen that with decreasing neutron energy (temperature) the absorption and scattering cross section of hydrogen increases virtually exponentially, whilst, the cross section of steel increases slowly and then drops dramatically at the 'Bragg' cut-off. Thus a neutron energy level of 4 milli-electron volts (0.004 ev) at the Bragg cut-off in the sub-thermal or 'cold' neutron range was chosen for the work.

The 'Herald' Research reactor (fig 7) at AWRE Aldermaston with an energy level of 5 Megawatts had a 'cold hole' and was chosen for preliminary work. It had a cold neutron beam flux of 2×10^6 cold neutrons $cm^{-2} sec^{-1}$. In the initial experiments (1975), quantitative tests showed that it was possible to visualise small oil galleries through 3" of steel. A 'Viper' gas turbine was also mounted alongside the reactor and used as a static test object. Oil was pumped into the centre of the engine from an auxiliary rig and was imaged in real time video. The flow of oil into the centre bearings could be clearly seen and from thence down into the gearbox. This showed that oil could be imaged and seen at the centre of a static aero gas turbine engine. World Patents were taken out on the technique (Patent 3).

Later, in 1976, a problem arose concerning oil leakage on the 'Gem' engine in the 'Lynx' helicopter (fig 8). This problem provided a unique opportunity to apply the technique to a real problem within a running engine.

It was not possible to run an engine in the 'Herald' reactor hall and therefore the work was carried out at the more powerful 'DIDO' reactor at Harwell. This reactor has an output of 25 Megawatts and an external cold neutron beam tube. A suitable experimental station existed at 25m on the beam tube where the 'Gem' engine could be installed (fig 9). At DIDO the flux at the 25m station was 5 x 10^3 cold neutrons cm^{-2} sec^{-1}. Thus an improved imaging system performance was required. Due to the lower flux the signal to noise ratio was worse and quantum mottle was evident on the images.

The 'Gem' engine (fig 10) was installed and run at various engine operating conditions for neutron radiography and for neutron video using a specially modified Oude Delft 'Delcalix' image intensifier with Gadolinium Oxysulphide phosphor screen. The location and distribution of the oil with the engine static was clearly visible (fig 11) and when the engine ran up to 'ground idle' the priming sequence was also clearly seen (fig 12).

The engine was then run up to 'Flight Idle' conditions and a number of features of engineering interest were visible:

.   The time to prime and fill the centre shaft from engine start and the time for the gear lubricating jet to commence operation could be recorded.
.   The quantity of oil in the scavenge sump could be measured precisely for each engine operating condition.
.   The efficiency of lubrication of the gear wheels could be observed. The air currents created by the rotating gears could be seen to create a depression on the surface of the scavenge pool. The lubricating jet was deflected by the air currents with the result that the gear teeth were not lubricated by the jet.
.   Due to the lack of an air deflector in the scavenge system, as it entered the rear bearing housing, the rear air passed down the rear scavenge return pipe preferentially to the oil. A constriction occurred in the return pipe at a union joint and it appeared that little oil was passing the union and returning to the oil tank. As a result the bearing housing overfilled and leakage occurred.

Thus, in the first experimental work, using Neutron Radiography, significant information was obtained on the behaviour of lubrication systems. Indeed the sensitivity of the real time imaging system was such that oil mist droplets estimated at 20 microns diameter could be seen in the centre of a running aero gas turbine.

In other parts of the engine, problems were encountered due to films of oil trapped within external heat shields which obscured the internal images. Similarly, when oil was thrown onto the walls of the bearing housing by the rotating gear wheels, then all internal imagery was lost and the casings became opaque. Thus the technique has great value in priming sequences. Image blur was encountered due to small angle scattering in the JETHETE material.

In 1977 a specialised Thomson-CSF Neutron Intensifier was obtained and used to examine oil and fuel pumps.

A useful technique used in the cold neutron imaging project was to image an engine "dry" with no fuel and to store this image digitally in a frame store. The engine was then filled with oil, the engine started, and the priming and running sequences were imaged. The original engine image was continually subtracted in live time from the incoming running engine image leaving on the monitor screen only the lubricating oil image. This could be clearly seen and its distribution determined. By this means cold engines and cold fuel at various temperatures could be tested to determine the way in which temperature/viscosity relationships affect the lubrication distribution patterns.

The main problem besetting Neutron Radiography as a technique at present is the fixed nature of the neutron source. This requires that all engine or rig testing should be carried out at Harwell. As pumping rigs are not always transportable, this limits the test programme. The size of the experimental station in the 20 metre blockhouse limits engine installations and engine noise was a problem. The limitation on the thickness of steel which may be penetrated, to 3", also reduced the application.

It would now appear that a portable, superconducting magnet, cyclotron, neutron source may become available from Oxford Instruments within the next 5 years. This would remove some of the basic problems which have limited Neutron radiography and permit its use in gas turbine engine test beds in the same manner as the 'Super X' linac is applied.

References (19) to (22) describe the work in more detail as does Patent 3.

3. **Positron Emission Tomography imaging of lubricating fluid behaviour**

This describes a collaborative programme between Rolls Royce, Castrol, Rutherford Appleton Laboratory and Birmingham University (ref the NIM paper). Following the cold neutron radiography work which commenced in 1975-6 and covered aero gas turbines, Ramjet fuel metering systems, Fuel Vapour Core pumping systems and Automotive engines, it was realised that neutron techniques were good for certain subjects but not for others. A portable technique was required which could be taken to engine test beds. Then, as now, no such portable neutron source exists and so other alternative imaging possibilities were explored.

In 1980, following a year of cooperative investigation into a range of techniques including gamma cameras, it was concluded that the medical technique of Positron Emission Tomography had application to mechanical engineering problems. In particular that it may be possible to image and locate in 3 dimensions the lubricating oil within the engine and to identify oil management problems. It was also realised that engineering has an advantage over medicine. The internal distribution of mechanical components in the engine lubrication system is well known and relatively static and of course they can withstand higher radiation doses.

The heart of the industrial PET system is the two multi-wire proportional counters which were developed for medical appli ations by the Rutherford Appleton Laboratory of the SERC. For the Industrial Positron Emission Tomography (Patent 4) project new larger format MWPC's were devel ped by R.A.L. with 200mm x 400mm effective active area and delivered to Birmin nam University in May 1984.

An MWPC is placed on either side of the test object and a positron emitting isotope is injected into the lubricating oil or fluid flow within the test object.

A positron is an anti-matter particle - a positive electron. When emitted from an isotope it travels a short distance and encounters an electron, in this encounter, annihilation occurs. Two gamma rays at a precise energy level of 511 KeV are generated at the annihilation site and are virtually co-linear travelling in opposite directions.

Due to the construction of the multi-wire counter - it has a number of wire matrices assembled together in a block - it can detect the X-Y co-ordinate locations of the incident gamma rays. A coincidence counter ensures that each gamma pair incident in the two detectors is identified as originating from the same annihilation site. This information is stored in computer memory. Thus a three dimensional image is maintained defining the distribution of radio-labelled lubricating oil in the system.

Similarly, a three dimensional volume graphical image may be constructed within the computer simulating the engine or test object. The axes of the graphical and isotope images are then superimposed and an engineer may sit at a terminal and call up any of 16 or 32 vertical planes or tomes distributed across the test object. He may view a desired graphical section through the test object and the location of the oil may be superimposed. In order to obtain information contained within a number of planes, oblique or other inclined sections may be accessed. A three dimensional graphical image may be constructed of the engine lubrication system.

With known volumes of oil and the system geometry - quantitative data on fluid volumes may be derived. Thus the distribution of the lubricating fluid throughout the system may be defined and the way in which this varies with engine power level setting.

Work has been carried out using the PET system on a bearing rig which was designed to incorporate the three major methods of lubrication, fig 13, these being: a flood feed and two types of jet pressure feed. The liquid was Turbine Engine Lubricating Fluid doped with the positron emitting isotope - Gallium 68. The bearing was driven at 1500 rpm and the efficiency of the feed methods were examined in turn.

Flood feed 'A' demonstrated the simplest form of lubrication. Oil is supplied to one side of the bearing and the sealing system is so arranged that the only exit is across the bearing into a drain on the opposite side. A more refined system is jet feed 'B' in which oil is directed at the gap between the cage and the races - scavenge ports are provided on both sides of the bearing. Jet feed 'C' represented an under race oil feed.

Sixteen tomogram planes were taken across the bearing rig with 5mm separation. The images were provided in five colours to show the intensity variation within a particular image to aid interpretation.

(Fig 14) Flood feed 'A' could be seen to provide saturation lubrication, with large quantities of oil moving around the bearing race during operation. Jet feed 'B' (fig 15) was shown to provide adequate lubrication of the bearing with most of the oil being forced into and across it. Jet Feed 'C' (fig 16) was examined and the results were totally unexpected. Close inspection of the isotope imagery revealed an oil injection vector opposite to that intended. It was concluded that the rig was mis-assembled. On strip it was found that the feed pipe had rotated approximately 135° from design position. Thus the capability of the technique in imaging oil jets and flow behaviour was clearly proven and its value in fault diagnosis was unintentionally shown in the first experiment.

The next step in he programme was to apply the PET system to a real engine situation. The 'Gem' engine was selected due to its small size and because it exhibits an interesting oil system behaviour. A module was made available (fig 17) and doped oil was fed and imaged within the module to calibrate the system and determine appropriate activity levels, absorptions and scattering. A full engine was then supplied and placed between the MWPC's in the laboratory (fig 18) and point and line sources were placed in selected fluid annuli with good results.

It is intended to carry out a full test in late 1986 with a running engine and a programme is currently proceeding to prepare for this test. The MWPC's have been checked for integrity and performance in the noise field of a simulated running engine and the on-site isotope production and handling facilities are currently being prepared.

In the future the collaboration expects to extend the work to characterise the behaviour and distribution of lubricating fluid in engine gearboxes at varying power level settings.

Reference (23) (24) and Patent 4 describes the work in more detail.

4. Conclusions

It can be seen that non-invasive techniques using penetrating radiations for the visualisation and measurement of events in gas turbine engines represents a new generation of diagnostic methods.

Conventional instrumentation, often requires extensive modification to the engine to sample and lead out the data. Radiation techniques need little if any modification and can examine any engine exhibiting a problem as supplied without expensive and time consuming strip and rebuild.

Radiation imaging methods can provide area scans across an engine - this is not usually possible with point instrumentation. Local relationships between for instance, adjacent seals can be easily seen with x-rays.

Summing up, metal component behaviour can be seen with high energy x-rays. Lubricating fluid and fuel behaviour can be seen with 'Cold' Neutron imaging and Positron Emission tomography. At the present time, it has not been possible to characterise the behaviour of air and combustion gas flows using radiation based non-invasive techniques but this remains a distinct possibility for the future.

REFERENCES

General Papers

1. Stewart P A E, "Radiography of Gas Turbines in Motion", Chartered Mechanical Engineer, Vol 19, No 5, May 1972, Pp 65-67

2. Stewart PAE, "Engine Testing using Advanced Techniques", Aeronautical Journal, Vol 79, No 776, Aug 1975, Pp 331-343

3. Stewart P A E & Brasnett K A, "The contribution of dynamic x-rays to gas turbine air-sealing technology", AGARD Conference Proceedings - 'Seal Technology in Gas Turbine Engines' CP-237, Pp 10.1-10.13, 1978

4. Stewart P A E, "Transparent Engines at Rolls Royce" Rolls Royce Magazine, No 2, Sept-Nov 1979, Pp 28-33.

5. Stewart P A E, "Development of a real time high energy x-ray imaging system for use in dynamic fluoroscopy of aero gas turbines", ASME Paper 75-GT-117, March 1975

6. Stewart P A E, "High Energy X-ray TV of Gas Turbines on Test", Chartered Mechanical Engineer, Vol 25, No 4, April 1978, Pp 65-67.

7. Stewart P A E, "Advances in Radiography and Fluoroscopy" British Journal of NDT, January 1982, Pp 27-32.

8. Stewart P A E & Cox N P G, "Progress Report on High Speed Cine Fluorography research for Foreign Object Tracking" RR Publication TRH 150, June 1975.

9. Stewart P A E & Huston A, "Cine Radiography with continuous X-ray sources", SPIE, VOL 97, 1976, Pp 140-145.

10. Stewart P A E & Adams T S, "An investigation into the feasibility of dynamic fluoroscopy and cine-radiography in the CRDF at Bristol", RR Publication TRH 155, 9th August 1976.

11. Stewart P A E & Adams T S "Report of Fluoroscopy and Cine-Radiography undertaken at Derby PCF", RR Publication TRH 155, June 1977

12. Stewart P A E & Pullen D A W P, "Some applications of cine radiography to gas turbines", SPIE, Vol 312, 1983, Pp 40-49

13. Stewart P A E, "An investigation of an 8 MeV Linear Accelerator to determine system parameters and sensitivities affecting radiographic quality", RR Publication TRH 184, February 1980.

14. Stewart P A E, "Close range x-ray and neutron photogrammetry at Rolls Royce" Phil. Trans. R.Soc. London A, Vol 292, No 1390, Pp 175-176 (1979)

15. Stewart P A E, "X-ray photogrammetry of Gas Turbine Engines at Rolls Royce", Photogrammetric Record, Vol 9, No 54, October 1979, Pp 813-821.

16. Stewart P A E, "Photogrammetry for the non-invasive measurement of void fraction and velocity in two phase flow" Int Archives of Photogrammetry and Remote Sensing, Vol XXV, Part A5, Commission V, Pp 657-666.

17. Stewart P A E, "Photogrammetry for Engineering Research and Development using High Speed Photography and Video", SPIE Volume 491, Part 1, Pp 494-501.

18. Stewart P A E, "Photogrammetry for the non-invasive measurement of void fraction and velocity in two phase flow", Photogrammetric Record, Vol 12, No 67, April 1986, Pp 5-25

19. Stewart P A E, "Cold Neutron imaging for gas turbine inspection", ASTM STP716, 'Real Time Radiologic Imaging' - Ed D A Garrett & D A Bracher, 1980, Pp 180-198.

20. Stewart P A E, "The application of dynamic cold neutron fluoroscopy for the visualisation of fuel and oil system operating characteristics in gas turbine development", 'The Aeronautical Journal', January 1982, Pp 23-28.

21. Stewart P A E, "Aero engine applications of cold neutron fluoroscopy at Rolls Royce", in "Neutron Radiography", Ed, John P Barton and P von der Hardt, D Reidel Publishing Co (1983) Pp 625-633.

22. Stewart P A E & Heritage J, "Cold Neutron Fluoroscopy of Operating Automotive Engines", in 'Neutron Radiography', Ed John P Barton and P von der Hardt, D Reidel Publishing Co (1983), Pp 635-642.

23. J Heritage, T Hoyes, P A E Stewart, R Witcomb, Prof Walker, Dr M Hawkesworth et al "An imaging system for the radioactive tracing of lubricants in automotive components" - 'Combustion Engines - reduction of friction and wear', Inst of Mech Engr, Conference Publication 1985-3 (1985), Paper C71/85, Pp 111-119

24. M R Hawkesworth, M A O'Dwyer, J Walker et al "A Positron Camera for Industrial Application" - (to be submitted for publication).

PATENTS

1. Stewart P A E, 'Improvements in Diagnostic Apparatus for, and Method of, investigating the movement of the internal parts of an operating rotating turbine engine' (High Energy x-ray TV of Gas Turbines on Test).
    British Patent No: 1,458,013   Application Filed - 6th January 1973
    Complete Specification published - 9th Dec 1976
    US Patent No: 3,992,627   Japanese Patent No: 7617/74
    German Patent No: 2,400,013   US Patent No: 4,092,537
    French Patent No: 7,400,288   Italian Patent No: 1,008,104

2. Stewart P A E, 'Diagnostic Apparatus and method for Gas Turbines' (High energy x-ray and High Speed cine for tracking foreign objects in gas turbines under operating conditions).
    British Patent: 6,040/75 (12th February 1975)
                    38311/75 (18th September 1975)

US Patent No: 4,092,537   (30th May 1978)   (Filed 4th February 1976)

3.   Stewart P A E, 'Improvements in Equipment and Method for diagnosing fluid
      movements within Engines'. (Uses 'cold' neutrons with neutron video to image and
      measure oil and fuel flows inside running gas turbine and automotive engines)
      British Patent No: 1,542,860
        Application filed - 23rd December 1975
        Complete Specification filed - 16th December 1976
        Complete Specification published - 28th March 1979
      US Patent No: 4,152,598
      French Patent No: 7,638,875
      German Patent No: 2,658,286

4.   P A E Stewart, M R Hawkesworth and R C Witcomb, 'Method of, and apparatus for,
      analysing fluid flows within hollow bodies' (Uses Positron emitting isotopes to
      trace fluid flows in Gas Turbines - Isotope Tracing 1).
      British Patent No: 2,087,685 - 13th November 1981
      US Patent Application No: 318,939 - Filed 6th November 1983 (In final stages
                                 15th May 1985)
      Patents Pending in France, Germany and Japan
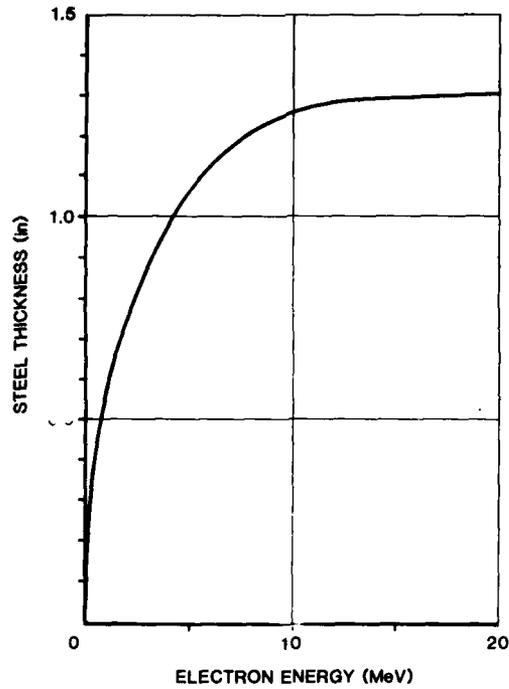
Fig 1 - X-ray penetration of steel versus x-ray energy
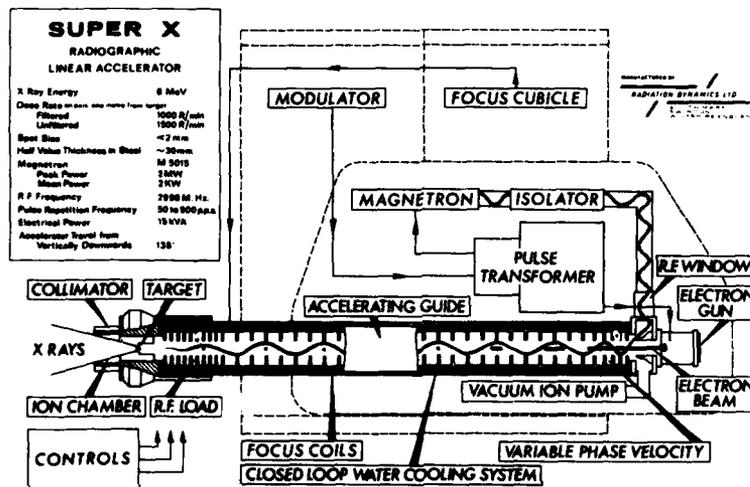
Fig 2 - Block diagram of RDL 'Super X' linear accelerator
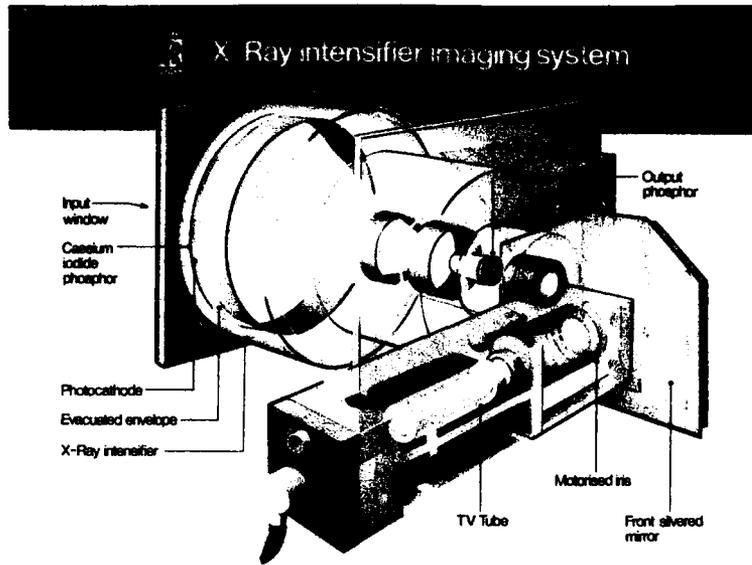
Fig 3 - Rolls Royce High Energy X-ray imaging system

LINAC CONTROL AND TRANSIT VEHICLE (L.C.T.V.)
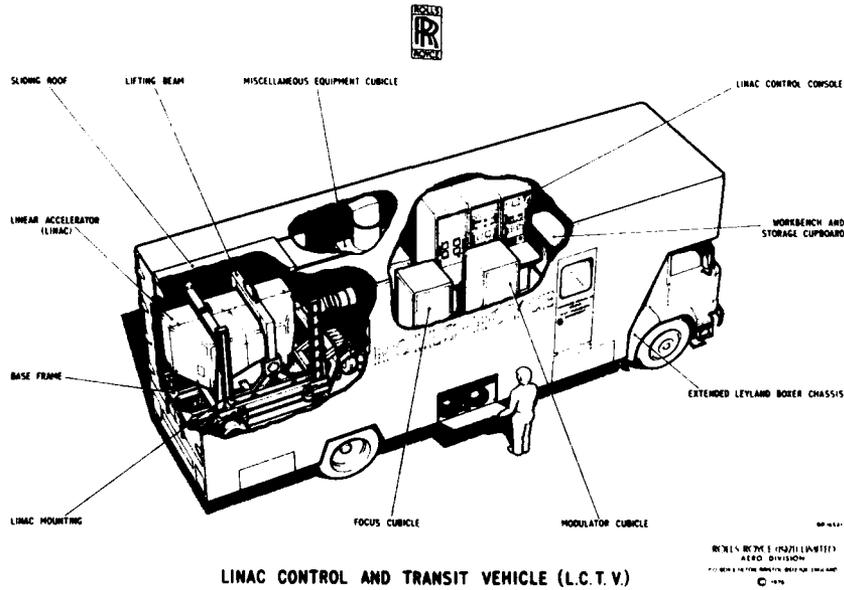
Fig 4 - Linear Accelerator Control and Transit Vehicle (LCTV)
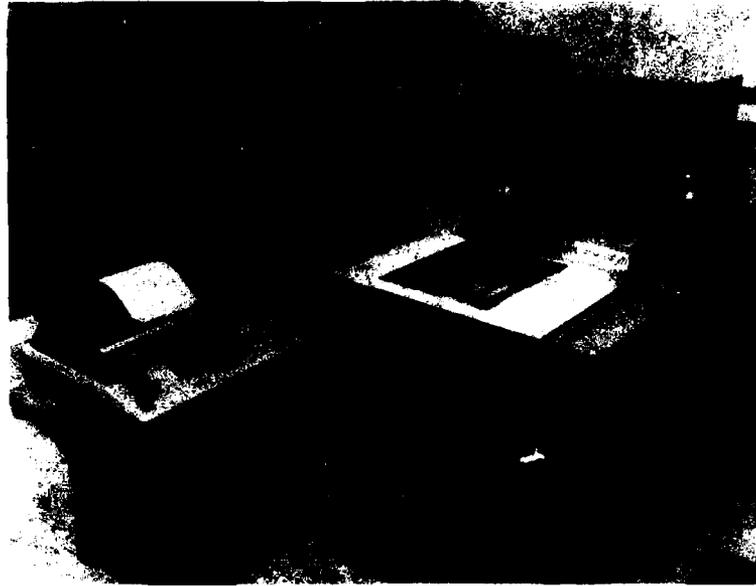
Fig 5 - Rolls Royce X-ray Photogrammetry system
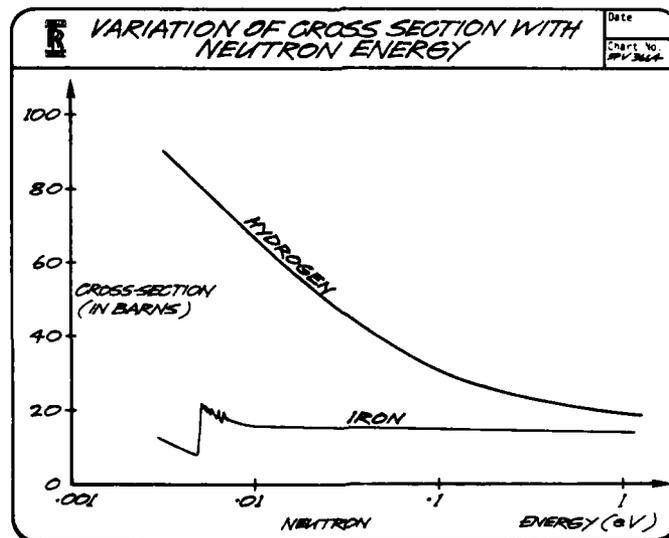
Fig 6 - Differential absorption and scattering neutron cross-sections for hydrogen
(oil) and iron versus neutron energy
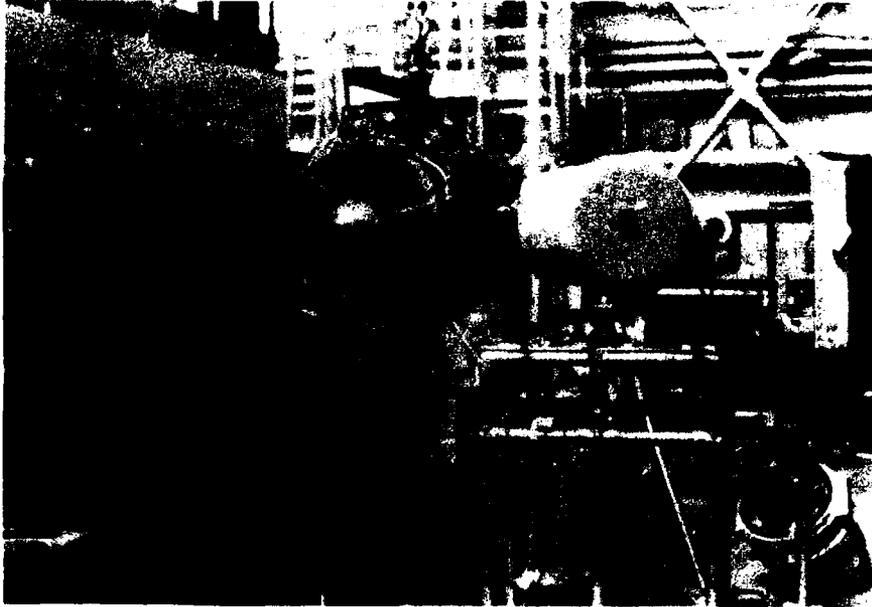
Fig 7 - Installation of RR 'Viper' engine and 'Delcalix' real-time neutron imaging
system on C1 residual cold beam - 'HERALD' reactor AWRE Aldermaston

ROLLS-ROYCE RS 360
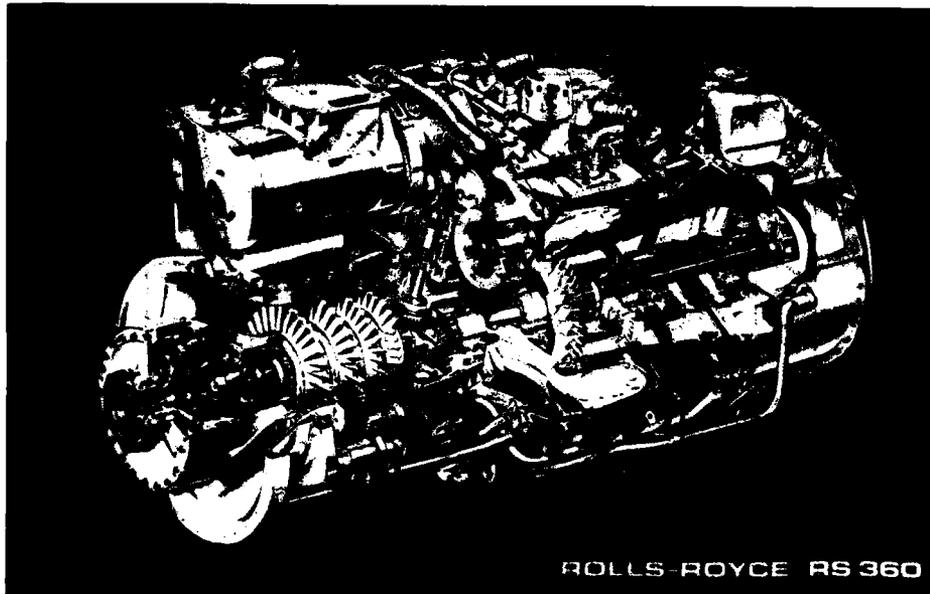
Fig 8 - Cutaway view of Rolls Royce 'Gem' helicopter engine
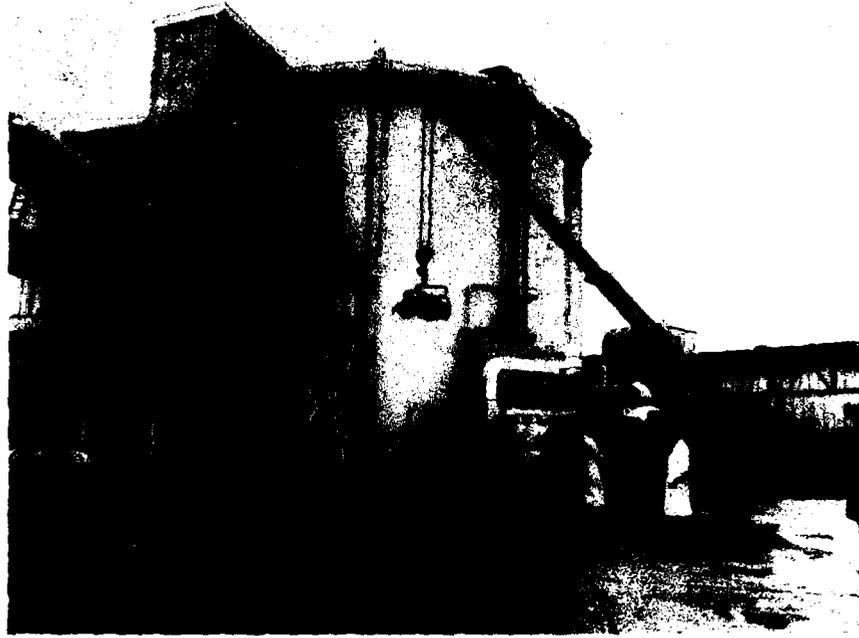
Fig 9 - Installation of RR 'Gem' engine on 6H cold beam, 30M station, 'DIDO' reactor
AERE - Harwell

'GEM' ENGINE OIL SYSTEM - PRESSURE SCAVENGE

BEVEL REDUCTION
GEAR

PRESSURE OIL FEED
TO CENTRE SHAFT

PRESSURE SCAVENGE
AIR INLET

REAR BEARING
HOUSING

OIL SCAVENGE
RETURN PIPE

OIL SCAVENGE
SYSTEM SUMP
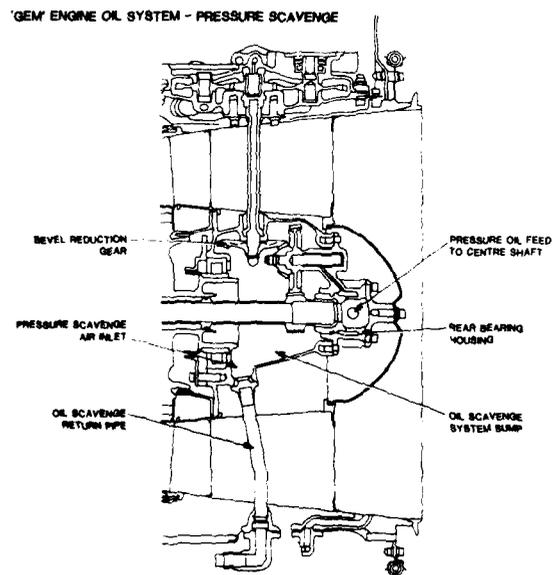
Fig 10 - General arrangement of RR 'Gem' engine oil pressure - scavenge system

Fig 11 - RR 'Gem' engine oil pressure scavenge system. Neutron radiograph of engine-
static (Harwell - NDT Centre)

Fig 12 - RR 'Gem' engine oil pressure - scavenge system. Neutron radiograph of engine
        - ground idle (Harwell NDT Centre)
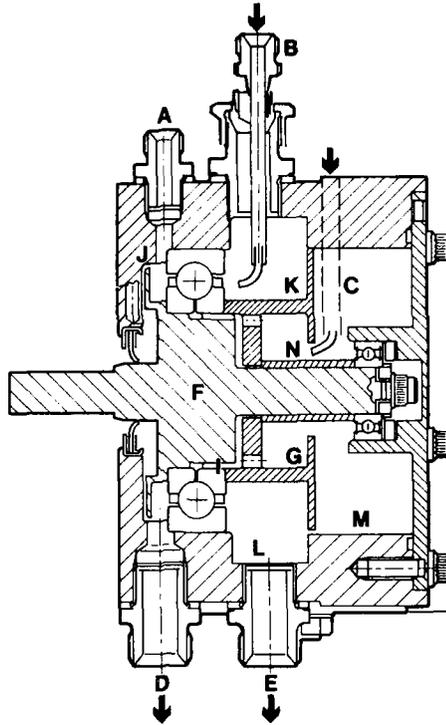
Fig 13 - Sectional view through bearing rig

Fig 14 - Radioisotope and computer model overlay images - Flood feed 'A'
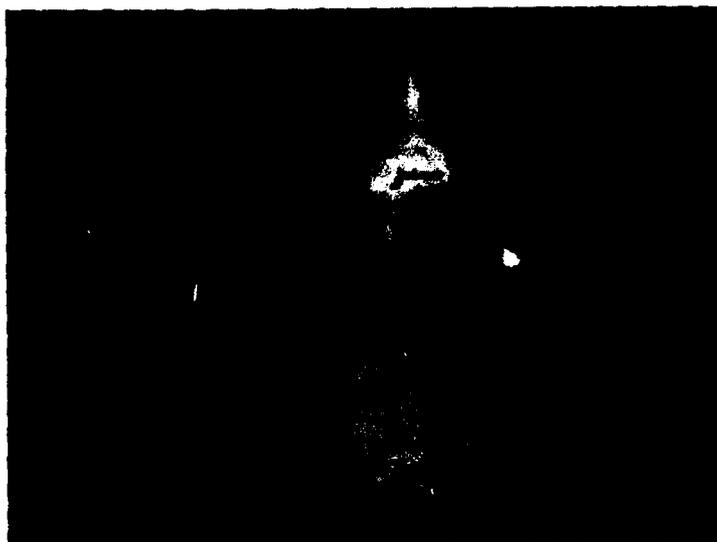
Fig 15 - Radioisotope and computer model overlay images - Jet Feed 'B'

Fig 16 - Radioisotope and computer model overlay images - Jet Feed 'C'
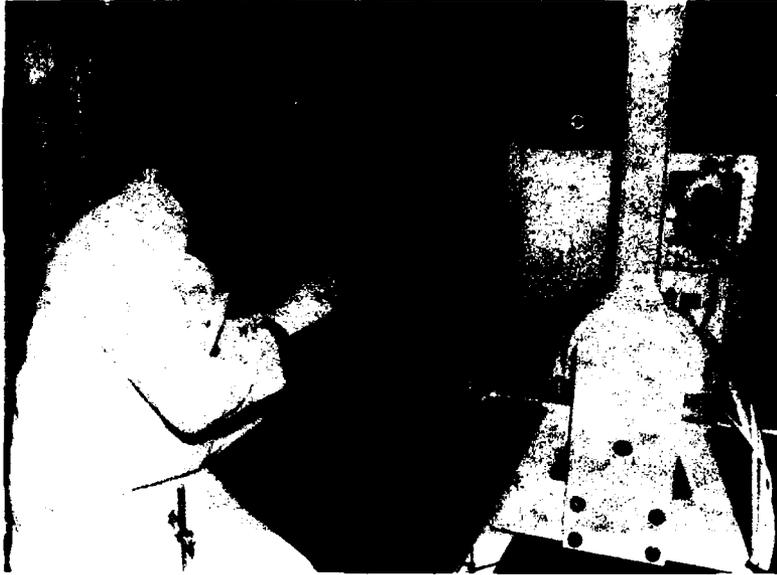
Fig 17 - Positron emitting line source inserted in centre shaft of 'Gem' engine with multiwire proportional counters at Birmingham University.

Fig 18 - Radioisotope and computer model overlay images of 8, 9 & 10 bearings and centre shaft of RR Gem engine at Birmingham University (COI photo)

DISCUSSION

G.Alwang, US

Do you hold any hope that Neutron radiography of that type could be done with sources other than reactor neutrons?

Author's Reply

Yes. At the present moment we are working on exactly such a source; there are some new advances. The NMR scanner utilises superconducting magnets; we are working with Oxford Instruments in the UK who produce most of the superconducting magnets. We are looking at a superconducting cyclotron; I have to do some studies when I get back but we are hoping that it might be available within then next 5 years and that does three things. It has an output of 10^{14} cold neutrons/sec and it will do neutron radiography both Epithermal, thermal and Cold. We think that probably the flux will be about 10^6 cold neutrons per cm^2 per second. It is also a source of position emitting isotopes of high energy and short duration, rather than the gallium 68 techniques we have been using, and finally with storage rings it should be suitable for non-invasive remote temperature measurement to an accuracy of about 5°C in 1000°C of metal temperature non-invasively.

G.Alwang, US

In the X-ray example that you used you say the trailer was up to 200 ft away from the source of x-rays. Do you have to eliminate people from an area of 200 ft to protect them from radiation?

Author's Reply

We tend to operate in the same way that you do at Pratts with test sites which are enclosed in test beds, but the one I was showing was an open air site at Rolls Royce at Hucknall and we define a zone which is unsafe and then beyond that it is safe. 200 ft just happens to be a distance.

W.Stange, US

Have you given any thought to or looked into using neutron diffraction for measuring strains in an operating engine?

Author's Reply

Neutron diffraction has in fact been studied quite extensively at Harwell and we are hoping to go onto a very intense beam at the ISIS accelerator at the Rutherford-Appleton Laboratories in the UK. I think that trying to measure strain by neutron diffraction is possible but in an operating engine it would be very difficult because of the vibration. However, using a pulsed neutron source, this may be possible. One could use it for looking into turbine disks deeper than one could with x-rays.

TIP CLEARANCE MEASUREMENT IN MODERN
COMPRESSOR COMPONENTS

Hartwig Knoell, Kurt Ding
MTU MOTOREN- UND TURBINEN-UNION MÜNCHEN GMBH
Dachauer Str. 665, 8000 Munich 50
West Germany

ABSTRACT

    With regard to maximum efficiency of gas turbine compressors, small blade tip
clearances during all engine operating conditions should be achieved. In order to
determine the tip clearance during compressor tests, a reliable measuring technique
has been developed at MTU. Using this temperature-insensitive capacitive probe system
(Coulomb system), tip clearance can be monitored even during fast transient con-
ditions. The sensors of the multichannel equipment can operate up to high tempera-
tures without cooling. Application to compressor testing is described in two
examples; a high-speed centrifugal compressor rig and the intermediate-pressure
compressor of a jet engine.

1.   INTRODUCTION

    The efficiency of a compressor depends not only on the aerodynamic configuration
of the rotor and stator blades, but also on the clearance between the rotor blade
tips and the casing, which varies for each operating point. Different effects cause
the clearance to change depending on the operating condition of the machine. During
speed increase extension of the rotor as a result of increasing centrifugal force
reduces the clearance. In contrast, heating of the casing by the compressed, and
thereby warmed-up, working medium (air) increases the clearance. These two phenomena
act on the clearance with different time constants, meaning that a statement con-
cerning the actual clearance during transient conditions can be made only if the
clearance is measured continously by a reliable means.

To be suitable the measuring procedure must satisfy a number of requirements; namely,
it must be capable of measuring the clearance and registering rapid changes up to
high rotor speeds, i.e. at high blade cycle frequency (max. 50 kHz), with sufficient
accuracy (error less than 0.01 mm). The measurement result must not be influenced by
the temperature at the probe and along the connecting lead or by the way it changes.
Furthermore, the probes must be capable of operating without cooling throughout the
working temperature range of the compressor, because any form of probe cooling
disturbs the thermal profile of the test item locally, consequently changing the
geometry at the measuring point, i.e. causes distortion of the clearance measurement.

A suitable commercial measuring system that met all these requirements did not exist,
so one has been developed at MTU München over the last 10 years. The operating prin-
ciple of the so-called Coulomb system /1/ and of the equipment, which has now been
developed into a mulitchannel test set, is explained briefly below. Then the effi-
ciency of the system is demonstrated by two examples of application taken from prac-
tice.
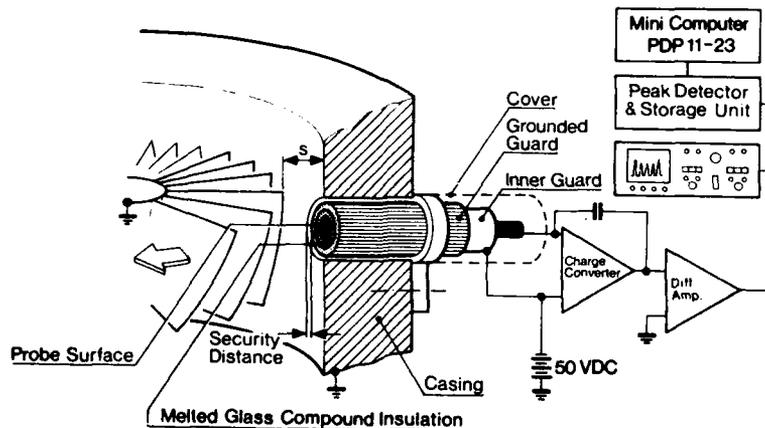
Fig. 1   Coulomb system tip clearance measurement set-up

2. MEASURING TECHNIQUE

The measuring probe of the Coulomb system is a capacitive sensing element of triaxial construction, firmly installed in the test item casing (Fig. 1). The metallic sensing surface of the probe, which is surrounded by two mutually insulated concentric screens, in conjunction with the blade surface forms a plate capacitor. The capacitance of the latter depends on the spacing between the plates, i.e. on the gap between the probe and blade tip. The capacitance increases when the gap decreases.

Contrary to usual capacitance measuring devices, the MTU Coulomb system does not measure the overall capacitance including that of the probe itself and of the wiring, but only that of the clearance capacitor between the blade tip and probe. This is achieved by measuring the electrical load required for charging and discharging the clearance capacitor when a blade moves past the probe. With constant initial voltage between the blade and probe, each blade charges the probe again individually, since the capacitor is totally free of charge within the spaces between the blades. The amount of the charge varies according to the individual blade to probe distance.

A charge converter with bias connected to the probe transforms the charge pulses to voltage pulses. Each of these pulses represents the charge of the clearance capacitor with one blade. The pulse height is approximately inversely proportional to the tip clearance. Therefore the output signal of the charge converter is fed to a peak reader to measure and digitise the height of each pulse. A minicomputer calculates the tip clearance on the basis of calibration data.

In calibration, the influence of the active area of the probe and blade is determined directly at the point of measurement, and the nonlinear relationship between the clearance and measurement voltage, which deviates slightly from the physical law of a plate capacitor, is also determined. This relationship, which is different for each measuring position, then forms the basis for converting the measured peak voltages into clearance values with the minicomputer.

For system calibration the rotor is fixed with a blade tip opposite to the centre of the probe. During calibration the distance of the probe to the fixed blade is varied. Using an AC voltage instead of a DC bias at the probe, a clearance-dependent charge is induced, which is precisely as great as that with a blade passing at the same distance with DC bias. This has the decisive advantage that calibration with the machine at standstill *directly provides the parameters for measurement on the machine in operation.*
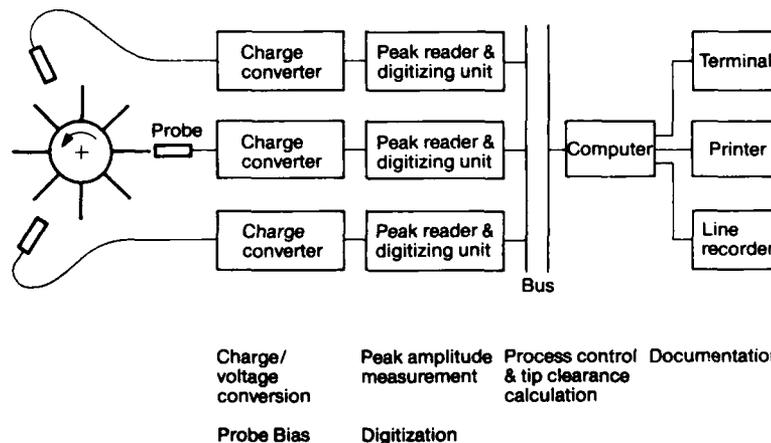
Fig. 2   Main components of the 3-channel Coulomb system

3. MEASURING EQUIPMENT

Apart from the accompanying minicomputer, the whole test set was developed at MTU to suit the special requirements. A schematic of a 3-channel Coulomb system is shown in figure 2.
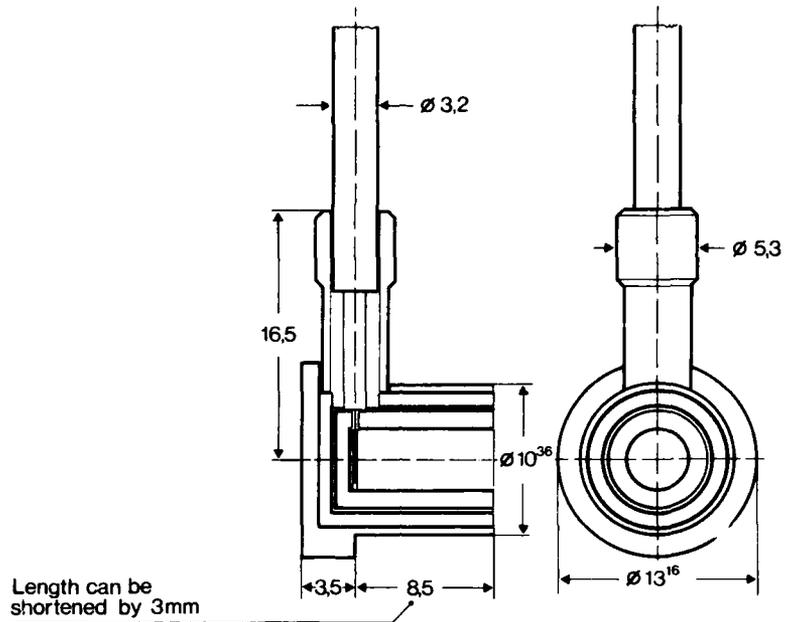
Fig. 3   Dimensions of the Coulomb probe for core engine application
         (IP compressor, 1st stage) with rigid cable connexion
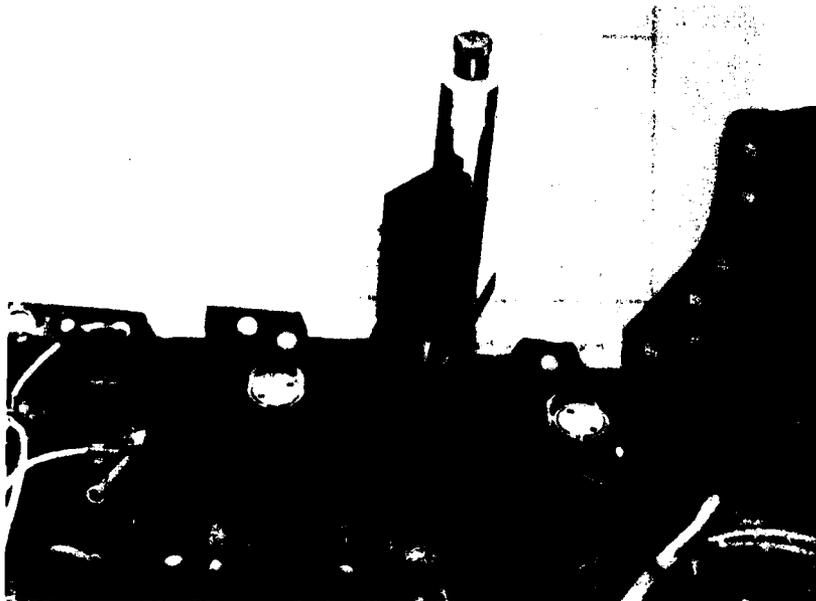
Fig. 4   Three Coulomb probes installed in the 3-stage axial section of an
         axial-centrifugal compressor. The detachable calibration slide, consisting
         of a micrometer screw with digital displacement transducer, can be seen in
         position at the middle probe

The triaxial probe is made with specific dimensions for each test point. A method of manufacture has now been standardised which guarantees the necessary high insulation resistance between the electrodes throughout the service temperature range, although - as shown in figure 3 - the outer dimensions of the probes are relatively small. Figure 4 represents an axial-centrifugal compressor with Coulomb probes for clearance measurement fitted to the three axial-flow stages. The removable calibrating slide, consisting of micrometer and digital linear transducer, is still attached to the middle probe.

A charge amplifier is used to transform the pulse-type changes in the charge of the probe into equivalent voltage signals with high sensitivity (50 mV/pC). The required maximum blade cycle frequency of 50 kHz means that the band-width of the amplifier must be in the region of 500 kHz to make certain that the amplitude of every pulse is reproduced faithfully, even with steep forward edges, i.e. with high frequency-content of the signals. The amplifier unit, which is installed in the test chamber about 2 m from the probe during measurement, is fitted with three other elements; the power pack for the whole unit, a stabilisation stage for the 50 V DC initial probe voltage and a differential amplifier, which refers the floating output signal of the charge amplifier stage to the mass potential again with slight reamplification (see Fig. 1).

The amplitudes of all blade pulses are determined and digitised by the conditioning electronics. In addition to the digital measured values, an incorporated interface also passes various error codes on to the computer. The computer is thus able to recognise if the charge amplifier or the conditioning electronics is/are overloaded, or if the probe initial voltage has failed or differs too much from the specified value.
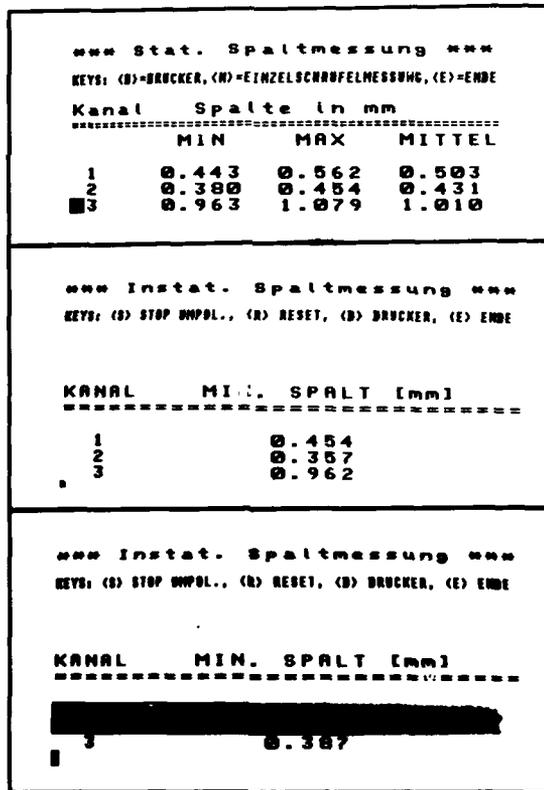
Fig. 5   VDU read-out of the 3-channel Coulomb system running in the steady-state measuring mode (top), transient measuring mode (middle), and in the case of an error occurring in channel 1 and channel 2 (bottom)

Up to 6 special channels can be connected to the computer, type PDP 11-23 with standard periphery. All channels are scanned sequentially and the results are processed in accordance with the operating mode selected; where the maximum, minimum and mean clearance can be shown by the VDU for each channel in steady-state measurement mode (Fig. 5, top), but only the minimum clearance at increased speed of measurement in the transient measurement mode (Fig. 5, middle). The error signals are also shown on the VDU (Fig. 5, bottom). Another mode, that of individual blade measurement, is not illustrated in figure 5. In this mode, a clearance value is printed out for every blade of the rotor.

The accuracy of the Coulomb system depends decisively on the range of measurement, which is about 0-2 mm for the usual blade geometry at MTU. Best accuracy of $\pm$ 5μm is attained in the range of 0-1 mm, whereas the error increases to about $\pm$ 12μm toward the range limit of 2 mm. The maximum permissible operating temperature of the Coulomb probes is about 1000 K without additional cooling.

4.   EXPERIMENTAL RESUTLS

Two examples of application to compressors under development demonstrate the variety of the system: a high-speed centrifugal compressor and an IP compressor in an engine.

Because of the extremely compact size of the centrifugal compressor, the probes have to be very small for measurement of the axial clearance. The positions of probe installation are shown in figure 6. Three probes are arranged at 120° intervals around the circumference. The minimum clearance values of the three probes are available on-line during the test. A section from an UV recorder plot for the take-off phase is represented in figure 7, showing the probe signals, speed and exhaust temperature. The signals from the three probes reveal identical clearance characteristics throughout the operating range. In other words, no asymmetrical deformation of the casing or uncontrolled axial movement of the rotor occurred.
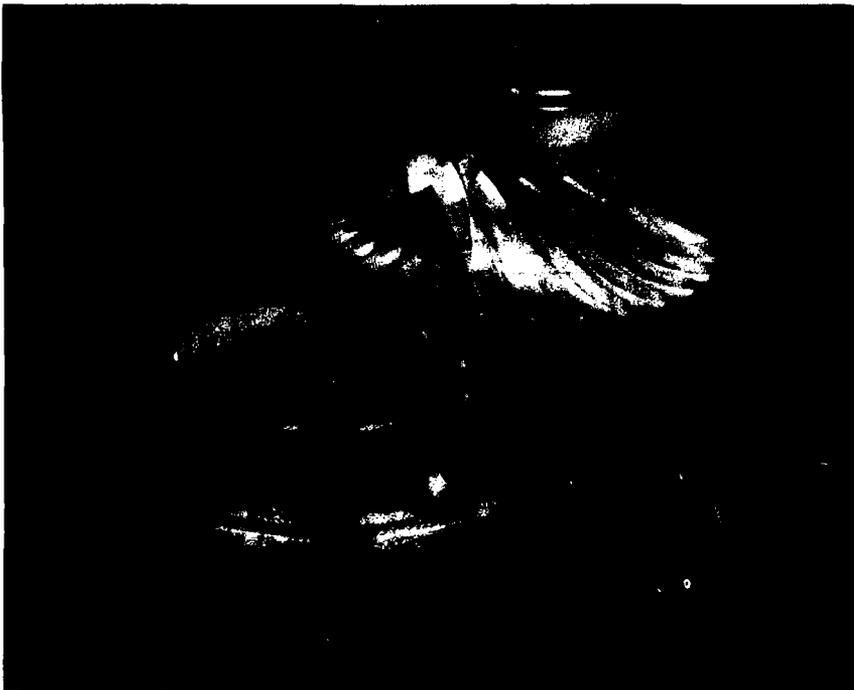
Fig. 6   Stator and rotor of the centrifugal compressor removed for probe installation and calibration. Two of the three mounting positions provided on the casing for the axial clearance measuring probes can be seen, as well as one of the probes with two components of the calibration device on the right (diameter of the impeller is about 240 mm)

Vertical scale: AC-Probes: 0.05/DIV   Temperature: 50°C/DIV   Speed: 5%/DIV
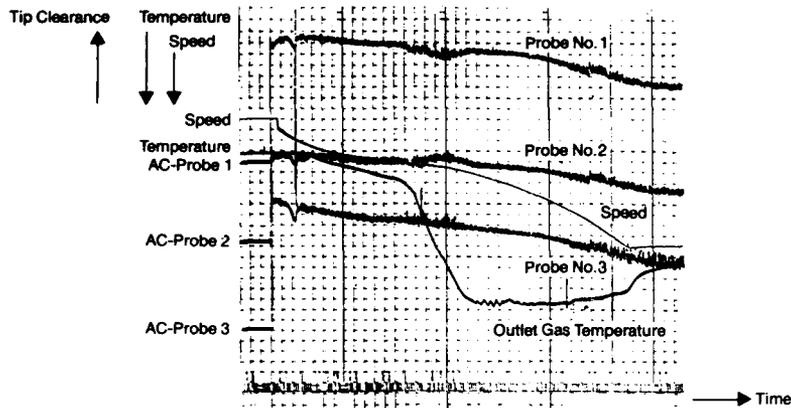
Fig. 7   UV recorder plot of axial clearance (AC) behaviour during starting phase of
the centrifugal compressor
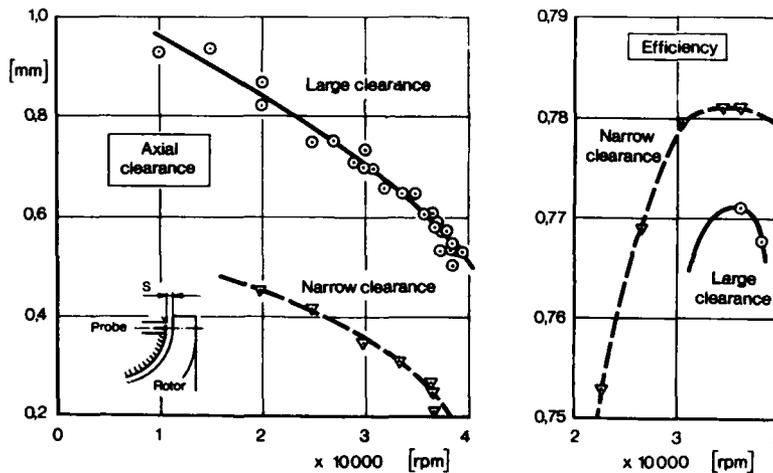
Fig. 8   Relation between efficiency and axial clearance of a centrifugal compressor

This compressor was provided with the possibility of running the rotor in two
axial positions about 0.2 mm in difference. The axial clearance measurements for the
two positions are compared with the efficiency, measured at the same time over the
full speed range of the rig (Fig. 8). The results show that an increase of 0.2 mm in
the clearance is enough to reduce the efficiency of the centrifugal stage by 1%.

Because of the light construction of modern jet engine casings, it is advisable
to have simultaneous tip clearance measurement at more than one circumferential
position per plane. Three Coulomb probes were mounted in the first stage of an IP
compressor, and connected to the multichannel Coulomb system for simultaneous measure-
ment of the transient behaviour of the tip clearance (Fig. 9). Figure 10 shows the
face of an installed probe looking towards the casing inner contour. The triaxial
arrangement of the electrodes is clearly visible. The high dynamic variation in the
radial clearance, resulting from acceleration or deceleration, is illustrated in
figure 11. The influence of centrifugal force during acceleration makes itself felt
by simultaneous narrowing of the clearance (Fig. 11, left). The delayed heating of

the casing then increases the clearance somewhat, before heating of the rotor disc
with still longer time constant narrows the clearance again. A brief speed reduction
is followed accordingly by the clearance in the opposite direction (Fig. 11, right).

Fig. 9   One of three Coulomb probes
          mounted in the inner casing of
          an IP compressor, 1st stage

Fig. 10   Face of an installed Coulomb
          probe looking towards the
          casing inner contour
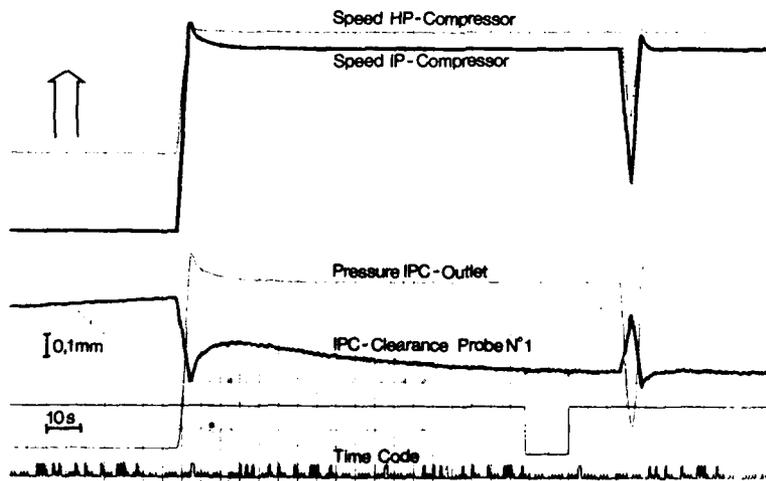
Fig. 11   Real-time read-out of radial tip clearance variation during fast
          acceleration and short deceleration

5. CONCLUSION

In the meantime it has been possible to demonstrate the reliability of the Coulomb system in a large number of applications. Because of the complicated manufacturing procedure of the probes and the individual manufacture of the special electronics, the financial outlay for the test set is very high. In contrast, the expenditure on installing the probes in the test item is very low, because the probes are easy to install thanks to their small dimensions. The laying of the electrical leads is also simple, even when the probes are installed in areas that do not give easy access.

The simultaneous clearance measurement at several circumferential positions in one plane provides a comprehensive picture of the clearance behaviour. It also makes it possible to clearly distinguish between rotationally-symmetric clearance changes and asymmetric casing deformations or the effects of shaft displacement. Since the Coulomb probe measures each blade individually, its signal can be used also for triggering other processes (e.g. Laser-two-focus velocity measurement) at the blade passage by means of simplified electronic cicuitry, or it can be used for verifying blade fracture.

At present, active closed-loop clearance control by Coulomb probes is still hampered by the required complexity of the electronics, but this represents a worthwhile challenge for further development of the system.

6. REFERENCE

/1/ Knoell H., Schedl K., Kappler G., Two Advanced Measuring Techniques for the Determination of Rotor Tip Clearance During Transient Operation; Fifth International Symposium on Airbreathing Engines, Bangalore, India, February 16-21, 1981

DISCUSSION

J.Chivers, UK

Can you indicate the level of noise you experience on both rig and engine testing as your circuits do not show any filters and using peak detectors I would expect noise problems.

Author's Reply

Signal to noise ratio is about 40 dB of the measured value. The uncertainty in the peak detector signal caused by noise effects is additionally reduced by multiple measurement and averaging of the results in the computer.

J.Chivers, UK

How would you expect the system to perform in the presence of gas turbine combustion products which could:—

(a)   contaminate the insulators and lead to a loss of probe insulation resistance to earth and

(b)   may have a high ionic content.

Author's Reply

Up to now we don't have any experience in measuring tip clearance in the tough environment of the turbine. We do know the influences of temperature and of contamination on the insulation resistance of the probe material separately but we do not know the result when all these hostile effects are in play together.

J.Allan, US

I understand your system is a DC excitation system; do you experience at the higher temperatures any type of a microphonics problem with the actual cable that comes out of the engine?

Author's Reply

Yes — there were microphonic problems which we have now solved in the case of insufficient fixture of the cable and high vibrational 'g'-load. Success is particularly a question of the proper selection of a suitable cable from the market. The voltage we use is about 50 volts DC its a bias at the probe and we didn't see any problems by resonance or effects like that.

J.Allan, US

Do you mean to imply an absolute accuracy of ±5 micron for your system, or a resolution of this value? I feel that the major difficulty in overall accuracy is position measurement.

Author's Reply

±5 micron is the absolute accuracy of the measurement of the probe-blade distance. Another question is the accuracy of the probe position with respect to the inner contour of the casing within the whole range of temperature.

The measurement method that we use to check this accuracy is another electromechanical system that we use in our laboratory. It's described in this paper of 1981; its called EMAG and this has an accuracy of about 2 microns — this is the borderline for control of accuracy, but we can't say so. ±5 is the most accurate system that we have to check the accuracy within the Industrial Environment, not within the Laboratory.

A.Ederhof, Switzerland

Is there any dependency between the detector signal and the rotor speed? In other words, do you have to make any corrections due to rotor speed?

Author's Reply

Not at all, within the limit of the maximum detector blade passing frequency and this is 50 kHz. If you operate below this there is no correction at all. There is no physical dependency, provided the freqency band width of the acquisition electronics is adequate.

A.Ederhof, Switzerland

Sometimes, especially in larger engines, it can be difficult to calibrate these systems. Do you have any experience with absolute devices for detecting tip clearances of around 2 mm or less?

Author's Reply

If there is no mechanical access to the probe position for probe calibration — not even during the phase of engine assembly — I guess there will be no chance to install an absolute electro-mechanical sensing device like our EMAG on the Rotadata equipment. But if there is access, our EMAG is the most accurate instrument we have and a proper reference for the Coulomb probe.

Unidentified Speaker

Could you discuss the limiting aspects or conditions of your clearance probe — specifically concerned with the following:

(1) Long lead lengths of 100 ft or so in a high RF or noise environment in a test cell.

(2) Wide range of clearance measurement 0.001 inch to 0.25 inch.

(3) Wide range of ambient temperature to several hundred degrees F or C.

(4) Wide range of contamination — lube oil or vapour — coupled with various vibrating mechanical systems.

(5) Reliability and durability for the system when subjected to all the above conditions simultaneously.

Author's Reply

(1) Maximum distance between the probe and the first electronic component (charge amplifier) should be about 2 m (7 ft). This low level signal connection cable should be laid out and fixed very carefully. The long distance lead from the charge converter to the peak reader unit (about 30 m = 100 ft) which carries the amplified signal can be shielded sufficiently not to cause noise induction by the test bed environment.

(2) With respect to the blade geometry and the adequately sized dimensions of our probes the measuring range is 0—2 mm (see p.29—5). The most accurate part of this range is from 0—1 mm due to the fact, that the probe signal is inversely proportional to tip clearance.

For security reasons we usually work in the range above 0.2 mm because of the displacement of the probe behind the contour of about 0.2 mm.

(3) There are no limitations for the application of the Coulomb system at high temperature due to temperature induced drift of probe or cable capacity, however due to the variation in electrical resistance of the insulating probe material. The particular high temperature limit stated by the input circuitry of the charge amplifier is its minimum input resistance of 100 k Ω.

(4) Contamination is a limit as far as clearance capacity itself is concerned by variation of the dielectric properties. Lube oil and other dirty deposits on the probe surface will limit its usability only if the overall resistance of insulation drops below 100 Ω. This was observed in one single case, when the blades worked in the abrasive layer inside the casing and spread this material over the face of the probe.

(5) Practice told in a large number of applications that real limitations and restrictions on reliability and durability are only given by extraordinary contamination (see pt 4) e.g. due to unreasonably heavy seeding with aerosol particles during laser-two-focus measurement.

A.Bruere, FR

Have you observed some effect of dielectric polarisation of the probe insulator on the sensitivity of the system?

Author's Reply

We have observed polarisation effects, but up to now we are not able to trace these effects to their origin. They may be caused by dielectric polarisation of the probe insulation material but also by insufficient grounding of the rotor blade tips. Nevertheless we overcome this problem by measuring the clearance capacity with both directions of the DC-bias voltage and by calculating the mean values of these two measuring results. We overcome the problem.

A.Bruere, FR

How do you take into consideration the effect on signal of thickness disparity between blades?

Author's Reply

Thickness disparity can only be taken into account by the calibration of each blade or by an independent mechanical measurement of blade tip thickness prior to the coulomb application.

A.Bruere, FR

What is the size of the smallest measuring electrode you have developed or checked?

Author's Reply

The smallest outer probe diameter is 10 mm (see figure 3 of my paper). The diameter of the sensitive face-area (of the core electrode) usually is 4.0 mm in accordance with blade geometry of the test item. The height of the probe is only about 10 mm.

COMPRESSOR BLADE CLEARANCE MEASUREMENT USING CAPACITANCE AND PHASE LOCK TECHNIQUES

ROSARIO N. DEMERS

ELECTRONICS ENGINEER

AFWAL/POTX, WRIGHT-PATTERSON AFB OH 45433-6563

The clearance measurement system described in this paper has several unique features which minimize problems plaguing earlier systems. These include tuning stability and sensitivity drift. Both these problems are intensified by the environmental factors present on compressors i.e., wide temperature fluctuations, vibrations, conductive contamination of probe tips and others. The circuitry in this new system provides phase lock feedback to control tuning and shunt calibration to measure sensitivity. The use of high frequency excitation lowers the probe tip impedance thus minimizing the effects of contamination. A prototype has been built and tested. The ability to control tuning and to calibrate has been demonstrated. An eight channel system is now being constructed for use in the Compressor Research Facility at Wright-Patterson AFB OH.

The efficiency of a turbine engine is to a large extent dependent upon the mechanical tolerances maintained between its moving parts. One critical tolerance is the compressor blade tip to case clearance. For some machines this clearance can exceed 2% of the blade span. Although this tolerance may not appear severe, the impact on compressor efficiency is dramatic. The penalty in percent efficiency has been shown to be three times the percent clearance to blade span ratio[1]. In addition, each percent loss in compressor efficiency represents one half percent loss in specific fuel consumption. However, reducing the blade tip clearance or predicting it analytically within certain accuracies is difficult to achieve.

There are many factors which affect blade tip clearance. Some of these are listed as follows:

1. Machining tolerances

2. Mechanical dynamics (e.g. shaft vibrations)

3. Thermal growth

    a. Differences in thermal growth of the case versus the growth of the rotor and blades.

    b. Dynamics of thermal growth due to the rate of change of case growth versus rotor growth during a change in operating condition.

    c. Case distortion due to thermal conditions.

Many of these factors cannot be predicted accurately through analytical models. Better insight, therefore, can only be achieved through actual measurements.

Of the many techniques available to measure clearance through non-contact methods only a few are capable of such measurements on an operating machine. These approaches include, capacitance, optical and traverse probe techniques. This paper is limited to one of the several capacitance techniques generally used.

The criteria used to develop the capacitance clearance measurement system was derived in part from our experience with the J85 jet engine. The 7th and 8th stage of this engine's compressor has 140 blades each which are approximately 0.5mm thick at the tips. At 100% speed the blade passage rate exceeds 37,000 per second which allows only a 1.8 microsecond exposure to the capacitor sensor. It is this time window which determines the minimum bandwidth necessary. The highest temperature for the eighth stage is approximately 300°C which although not very high does present problems to the capacitance clearance measurement system. This problem is due to the effect of temperature on the dielectric properties of the ceramic used in the construction of the probe. A change in probe temperature causes a change in capacitance and this effect must be accounted for. In addition, the probe tips are exposed to contaminants such as oil and water which are sometimes ingested into the engine. These contaminants adversely affect the probe sensitivity and calibration by shunting the probe tip with an electrical resistance.

Based on the conditions described above, the following criteria was established for the development of a new capacitive clearance measurement system.

1. Accuracy of .025mm with a 0.5mm thick airfoil at 0.5mm distance from sensor using a 3mm sensing element.

2. Frequency response of 1MHZ.

3. High tolerance to probe contamination (i.e. 10K ohms across the sensing element and ground).

4. Low offset drift under all operating conditions.

5. Useful temperature range to 800°C

[1]Charles W. Elrod, "Advances in Gas Turbine Engine Sealing," 9th International Conference on Fluid Sealing (April 1981): 299-312

6. On-line sensitivity calibration

7. Simple probe design

Keeping in mind the criteria established above, the basic system consists of a 10MHZ tuned circuit in which the blade to sensor capacitance changes the circuit phase response. It is this phase change which is detected and processed. The circuit can be configured in either series or parallel resonance. In addition, the component electronics are removed from the probe assembly and are included in the exciter/detector electronics a short distance away from the probe. The probe itself is connected to the exciter/detector via a short low capacitance low noise cable. The advantages of this configuration are many. The probes are simple enough to be designed and built to accommodate any machine and environment. The 10MHZ excitation frequency provides for a relatively low sensor impedance of 100 to 400 ohms and is high enough to insure adequate response bandwidth. The probes can be calibrated at very low speeds and by utilizing precision variable capacitors with very low temperature coefficients the sensitivity can be calibrated during operation. By using a varactor diode and feedback circuit the base line tuning can be kept constant.

The series configuration as shown on Figure #1 and its' analytical model as show in Figure #2 and #3 is the simplest. The phase shift at resonance is already 90° and further phase shift prior to the phase detector is unnecessary. If R_s is assumed to be infinite the sensitivity is $d\theta_{1,2}/dC = -1/wR$ C^2 Note the sensitivity is inversely proportional to the frequency, series resistance and the square of the total capacitance. The reduction of total capacitance has the greatest effect on the increase of sensitivity and every effort is made to minimize this parameter. Although it is desirable to obtain a high Q for this circuit, there are practical limitations which must be considered. First, the voltage ratio between point #1 and point #2 should be kept reasonable due to the limitations of the electronics involved (i.e. the voltage at point #2 can cause amplifier overload). Second, the effects of contamination of the probe tip would greatly exaggerate the changes in sensitivity. A good compromise has been found through experimentation on a prototype system. In this system, R_s = 5 ohms and R_p = 50K ohms. Figure #4 illustrates the effect R_s on the sensitivity. By changing the shunt resistance from 100K ohm to 10K ohm the sensitivity reduced by a factor of 2/3. This reduction is unacceptable unless some provisions are made to measure the change in sensitivity. The technique used will be described in a later paragraph.

Using the parallel configuration as described in Figures' #5, #6, and #7 provides similar results to the series configuration. The advantage of this circuit is the near unity voltage ratio which reduces the burden on the limited amplifier. The disadvantage of this configuration is the necessity to establish a 90° phase shift in the reference signal input to the phase detector. The phase shift is created by two R.C. networks which are adjusted to provide 45° of phase shift each. Figure #8 provides some insight to the effect of shunt resistance on sensitivity.

Because of the problems associated with drift an automatic tune control is used. Tuning is accomplished by a feedback voltage circuit Figure #9. The necessary feedback error signal is provided by a negative peak detector which is connected to the phase detector output. This negative peak detector discriminates between the baseline and signal. Although analog circuitry could be used for the feedback signal conditioning, a digital technique was chosen. The digital approach allows the feedback voltage to the varactor diode to be held constant while a sensitivity calibration is being done. Since this calibration requires less than a few seconds, the amount of drift in the baseline due to temperature is not anticipated to be significant.

The sensitivity calibration set-up is accomplished via a SPDT relay and a pair of very stable variable air capacitors (Figure #1). One of the capacitors is adjusted to fine tune the cable probe assembly, whereas the second capacitor when selected by the relay is adjusted to a predetermined baseline shift. The varactor control voltage is held at a nominal value during these procedures. The probe to blade calibration must then be done while there is assurance that the sensitivity of the system has not changed. From then on during any test operation, the calibration relay can be energized and the baseline shift noted (feedback to varactor diode held constant when the relay is energized). Any change in baseline value from that taken during bench calibration is used to adjust the data accordingly.

Although the techniques described above eliminates some of the problems related to capacitance clearance measurement systems, other problems persist. One major problem of capacitance systems is the electric field fringing effects associated with the sensor probe. The assumption of using the capacitance model of two flat plates is invalid insofar as small probe sensors are concern. Therefore, physical calibrations rather than analytical predictions must be made. In addition, if the blade tips are closely spaced as in the J85 compressor the actual calibration becomes even more complex (Figure #10). The only recourse now is to obtain as much information as possible on bench calibration prior to test. An alternative is to redesign the probe and some of the circuitry in a way to reduce the fringing effects (Figure #11). The use of a driven guard can be used to reduce the fringing effects. Two advantages come about from such a configuration. First the blade to blade spacing is not as critical because of the reduced fringing and second the apparent total capacitance to the tuned circuit is reduced thus improving sensitivity significantly. The disadvantage is the requirements placed on the guard driver amplifier which must drive a higher capacitance load. The capacitance on the guard to ground shield on triax cable is in the order of 120 pf/ft and the capacitance of the probe guard to probe ground is anticipated to be in excess of 100pf depending on design. Obviously, this approach, is not a panacea because of added complexity to the circuit and probe design.

As of this writing a prototype exciter/detector circuit and probe assembly has been built (Figure #12). However, the testing of the prototype has been limited to the verification of all of the concept described above. The sensitivity measured during this verification process was well within the value predicted analytically; the operation of the varactor diode and the calibration circuits have performed without problems using manual control. The feedback control circuitry and computer interface electronics have been designed but not built. Our present effort is to finish the fabrication of six channels for use on the F100 engine compressor which is to be tested during July 1986 at the Compressor Research Facility at Wright-Patterson AFB OH. Manual control and analog recording will be used on these channels

since the fabrication of the control and computer interface circuits will not be completed in time. Future efforts will include some modification of the exciter/detector circuit and probe assemblies to include the driven guard design as described earlier.
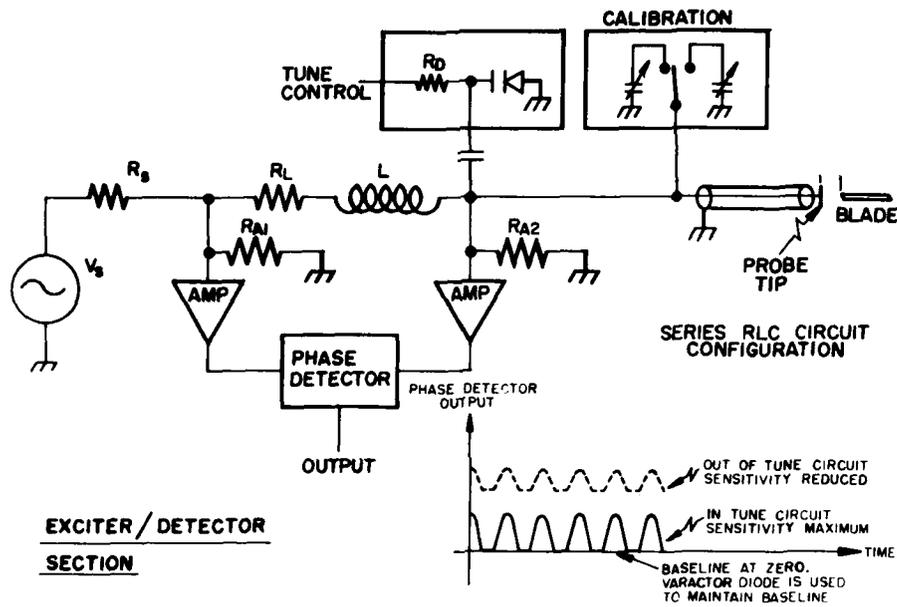
FIG. I   EXCITER / DETECTOR   SECTION   SERIES CIRCUIT

$$\frac{V_0}{V_i} = \frac{R_2}{R_L + R_2(1-\omega^2 LC) + j\omega(R_L R_2 C + L)}$$

$$\phi_{1,2} = -\tan^{-1}\left[\frac{\omega(R_L R_2 C + L)}{R_L + R_2(1-\omega^2 LC)}\right]$$
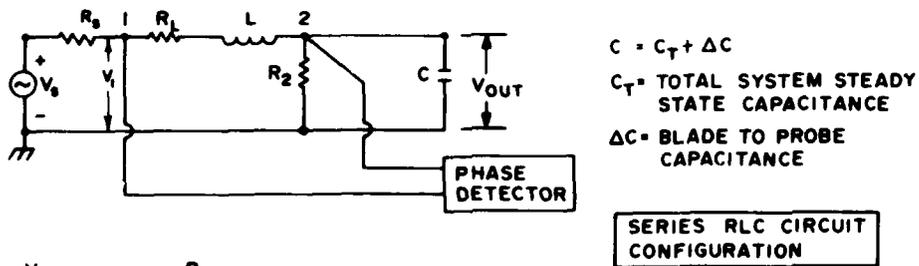
$$U = \frac{\omega(R_L R_2 C + L)}{R_L + R_2(1-\omega^2 LC)}$$

$$\frac{d\phi_{1,2}}{dC} = \frac{-U^2}{U^2+1}\left[\frac{\omega R_L^2 R_2 + \omega R_L R_2^2 + \omega^3 R_2 L^2}{\omega^2 R_L^2 R_2^2 C^2 + 2\omega^2 R_L R_2 LC + \omega^2 L^2}\right]$$

FIG. 2   SERIES RLC CIRCUIT CONFIGURATION
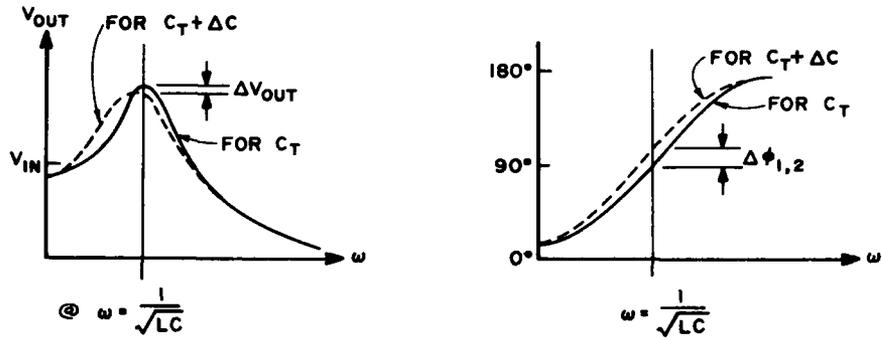
FOR $R_2 \gg \omega L$

$U \gg 1 \quad \therefore \quad \dfrac{U^2}{U^2+1} \approx 1$

$\dfrac{d\phi_{1,2}}{dC} \approx \dfrac{-1}{\omega R_1 C^2}$

EFFECT OF PERTURBING
C IN THE SERIES RLC
CIRCUIT CONFIGURATION

FIG. 3   EFFECT OF PERTURBING C IN THE SERIES RLC
         CIRCUIT CONFIGURATION

$C_T = 50\,pf$

$L = 5.07\,\mu h$

$R_L = 5\,\Omega$

PHASE DETECTOR
SENSITIVITY = 8 mV / DEGREE

PHASE DETECTOR
OUTPUT FOR SERIES
RLC CIRCUIT
CONFIGURATION

FIG. 4   PHASE DETECTOR OUTPUT FOR SERIES RLC
         CIRCUIT CONFIGURATION

TUNE CONTROL CALIBRATION

BLADE

PROBE TIP

PARALLEL RLC CIRCUIT CONFIGURATION

PHASE DETECTOR

OUTPUT

OUT OF TUNE CIRCUIT SENSITIVITY REDUCED

90° SHIFT

EXCITER / DETECTOR SECTION

IN TUNE CIRCUIT SENSITIVITY MAXIMUM

TIME

BASELINE AT ZERO VARACTOR DIODE IS USED TO MAINTAIN BASELINE
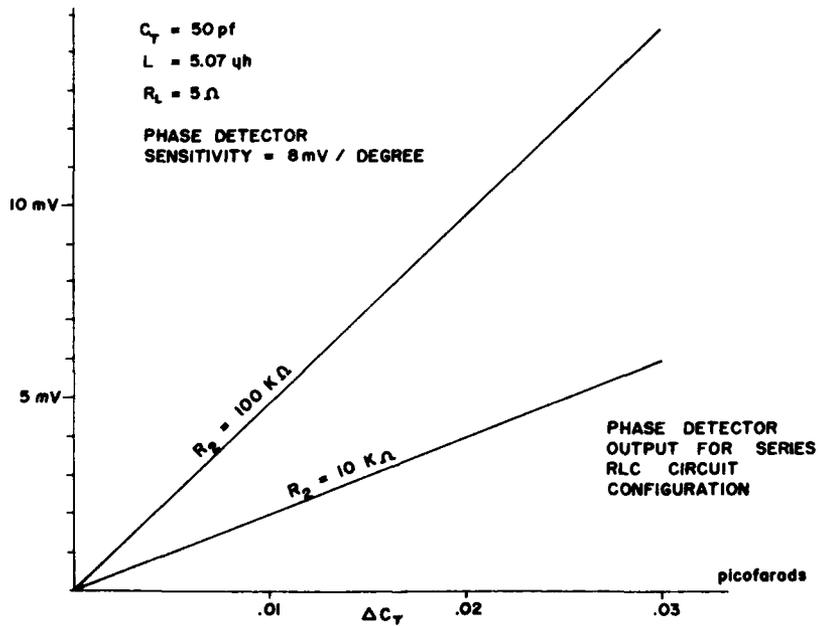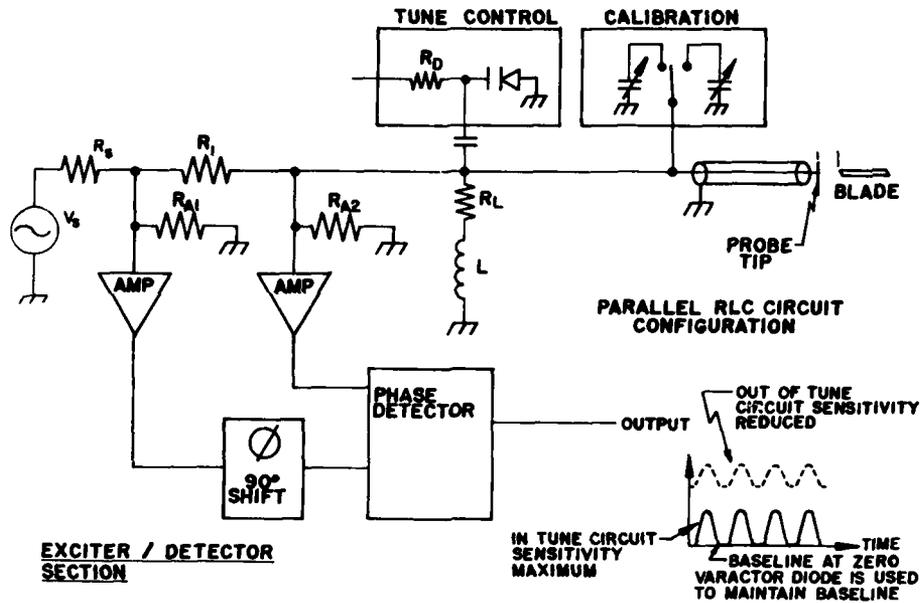
FIG. 5   EXCITER / DETECTOR SECTION   PARALLEL CIRCUIT

PHASE DETECTOR

$C = C_T + \Delta C$

$C_T =$ TOTAL SYSTEM STEADY STATE CAPACITANCE

$\Delta C =$ BLADE TO PROBE CAPACITANCE

PARALLEL RLC CIRCUIT CONFIGURATION

$$\frac{V_{OUT}}{V_I} = \frac{R_L^2 R_2^2 + R_1 R_L R_2 (R_L + R_2) + \omega^2 R_L^2 (R_1 + R_2) + j\left[\omega R_1 R_L^2 (1-\omega^2 LC) - \omega R_1 R_L^2 R_2^2 C\right]}{(R_1 R_L + R_1 R_2 (1-\omega^2 LC) + R_L R_2)^2 + \omega (R_1 R_L R_2 C + R_1 L + R_2 L)^2}$$

$$\phi_{1,2} = \tan^{-1}\left[\frac{\omega R_1 R_L (1-\omega^2 LC) - \omega R_1 R_2 R_L^2 C}{R_L^2 R_2 + R_1 R_L (R_L + R_2) + \omega^2 L^2 (R_1 + R_2)}\right]$$

$$U = \frac{\omega R_1 R_2 L (1-\omega^2 LC) - \omega R_1 R_L^2 R_2 C}{R_L^2 R_2 + R_1 R_L (R_L + R_2) + \omega^2 L^2 (R_1 + R_2)}$$

$$\frac{d\phi_{1,2}}{dC} = \frac{-1}{1+U^2}\left[\frac{+\omega^3 R_1 R_2 L^2 + \omega R_1 R_L^2 R_2}{R_L^2 R_2 + R_1 R_L (R_L + R_2) + \omega^2 L^2 (R_1 + R_2)}\right]$$

FIG. 6   PARALLEL RLC CIRCUIT CONFIGURATION

FOR $R_2 \gg R_1 \gg \omega L \gg R_L$

THEN $\quad U \simeq 0$

EFFECT OF PERTURBING
C IN THE PARALLEL
RLC CIRCUIT
CONFIGURATION

$$\frac{d\phi_{1,2}}{dC} \approx \frac{-\omega^3 L^2 R_1}{\omega^2 L^2 + R_1 R_L}$$

FIG. 7   EFFECT OF PERTURBING C IN THE RLC PARALLEL
CIRCUIT CONFIGURATION

C_T = 50 pf

L = 5.07 μh

R_L = 5 Ω

R_1 = 100 KΩ

PHASE DETECTOR
SENSITIVITY = 8mV / DEGREE

PHASE DETECTOR
OUTPUT FOR
PARALLEL RLC
CIRCUIT CONFIGURATION

R_2 = 100 KΩ

R_2 = 10 KΩ
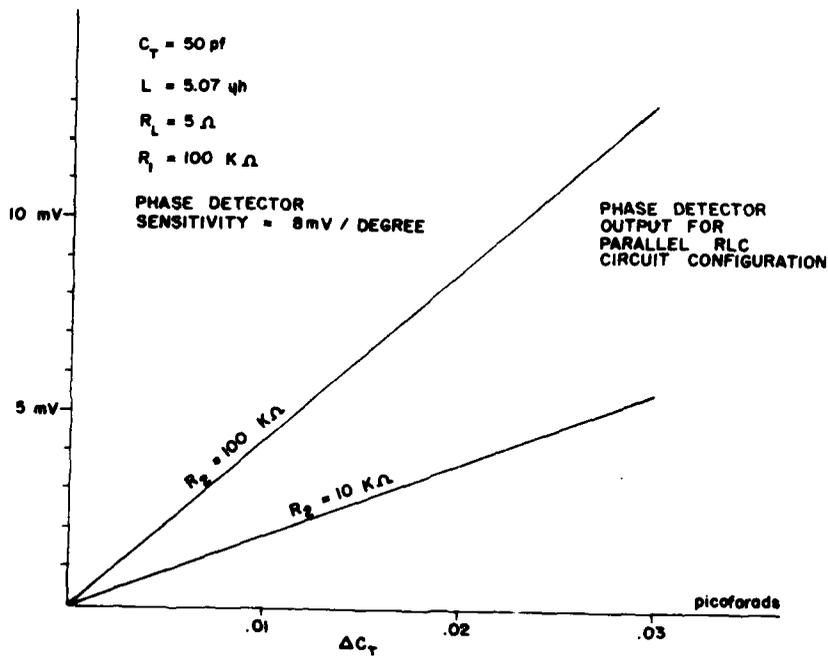
FIG. 8   PHASE DETECTOR OUTPUT FOR PARALLEL RLC
CIRCUIT CONFIGURATION
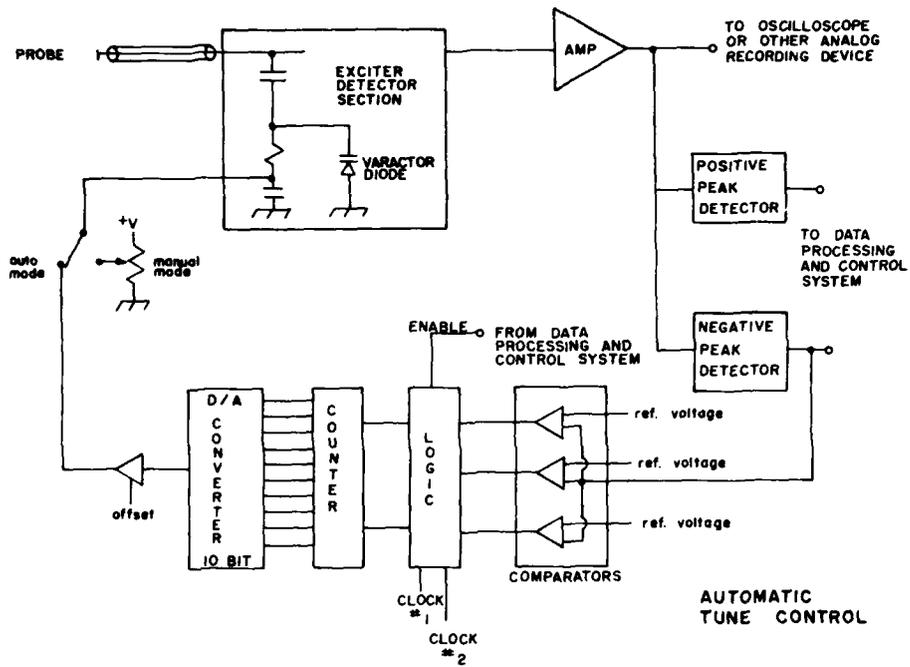
FIG. 9   AUTOMATIC   TUNE   CONTROL
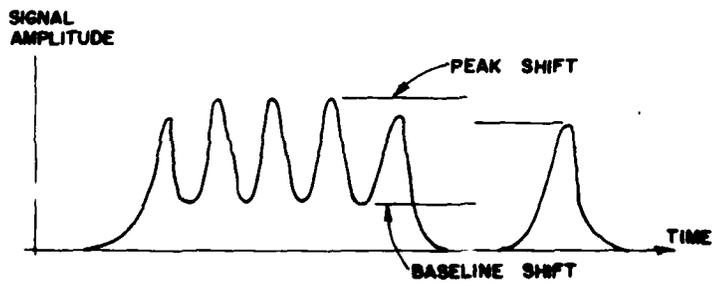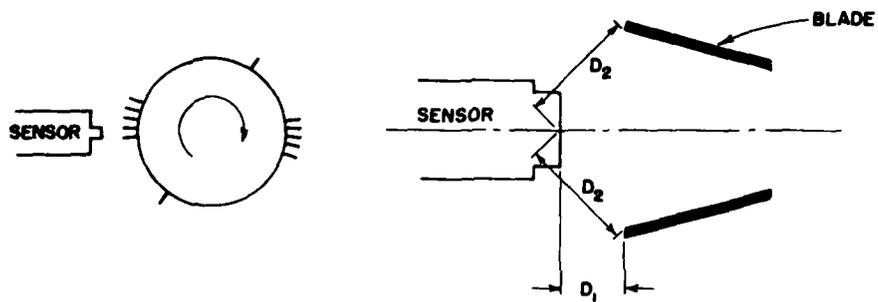
FIG. 10   EFFECT   OF   CLOSE   BLADE   SPACING
ON   SIGNAL
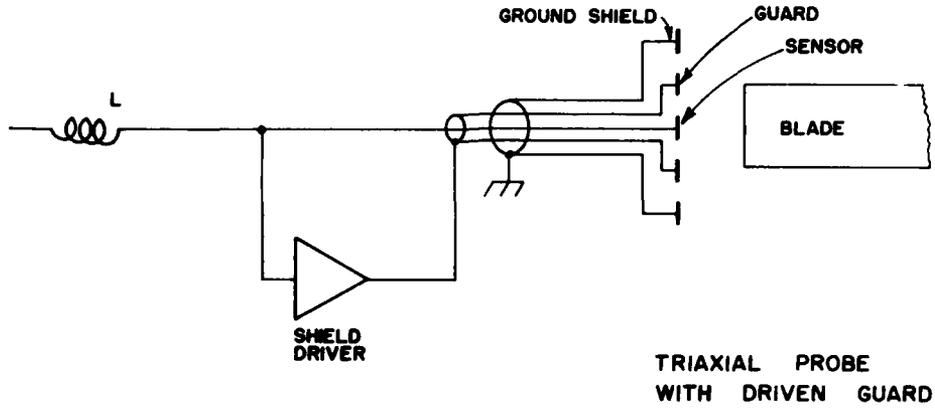
FIG. II   TRIAXIAL PROBE WITH DRIVEN GUARD

FIG. 12   CLEARANCE MEASUREMENT EXCITER / DETECTOR
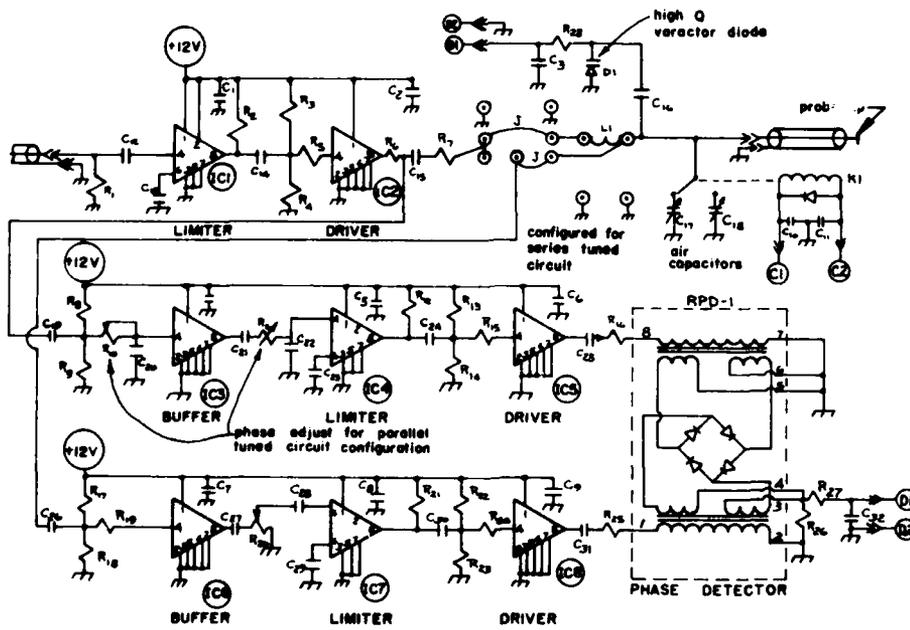
DISCUSSION

J.Chivers, UK

Will the clearance system stability be improved sufficiently by the possible incorporation of the driven guard electrode to avoid the need for constant recalibration to correct for temperature induced sensitivity changes?

Author's Reply

The feed back circuit (variacter diode) keeps the circuit tuned. The cable capacitance is expected to change with temperature and thus the sensitivity is expected to do likewise. The sensitivity change will be twice the present change in total capacitance. However the change in total capacitance is expected to be slow, therefore recalibration via the sensitivity calibration circuit need not be accomplished often. Even so, the calibration need only take a few seconds.

J.Chivers, UK

There is, in fact, a capacitance carrier based guarded clearance system which is commercially available in the UK from one or possibly (in the near future) two manufacturers. This system has had operational experience on engine and rig fans, high pressure compressors and also engine high pressure turbines.

Author's Reply

I talked to Davidson and I understand that system is and FM system. One of the advantages of the system I have is that I use one frequency. I can go to as many probes as I want using the same frequency and I tune to that frequency. I don't have to worry about beat frequencies and that is an important consideration.

J.Chivers, UK

Yes, I agree that is an important consideration but in fact there is operational experience of running 18 of these probes simultaneously — it has been a problem but it has been overcome.

J.Allan, US

The size of the probe was not mentioned in your paper. What is the probe size — what is its diameter?

Author's Reply

The probes can be made of any size. The one that I am using on the F-100 is 6 mm in diameter — it is threaded — the sensing element is 3 mm in diameter. The length is approximately 75 mm. However the sensors are very simple in construction and can be made to accommodate any components. They should be good from about zero to 40 mils in terms of sensitivity — I have had no problem in getting a good signal at 40 mils.

J.Allan, US

It seems to me that using the tuned circuit that you have you are going to have a change with resistance — this is going to be changing throughout the operating range of the engine because your temperatures are varying. Are you going to be able to compensate for operational changes in temperature?

Author's Reply

That is the beauty of the whole thing. I have those calibration capacitors — I have a vari-actor diode which always keeps it in tune through the feedback and it's doing that continually — every few minutes the calibration is accomplished in a few seconds.

A.Bruere, FR

How do you take into consideration the effect on signal of thickness disparity between blades?

Author's Reply

In terms of the thickness, one would have to do a calibration, blade by blade. It is a little tedious — you will find that the variations from blade to blade are not all that great — although it will affect your accuracy if you don't do it.

A.Bruere, FR

How do you calibrate your probe versus the distance between blade and case?

Author's Reply

.... in other words — try to duplicate what you would have on the machine that you are going to put the probes on — now admittedly you will probably have a loss in accuracy. That way there are always undefined areas — differences which you can't always take into account — but you try to minimize those when you do the actual calibration. The other thing too is that we have planned to use this system and complement it with the ROTADATA system, using the capacitance to look at the dynamic conditions or the changes in the machine and to use the ROTADATA system almost right next to it to take care of the steady state measurement. That way we will get the best of both worlds.

A.Bruere, FR

What is the size of the smallest measuring electrode that you have developed or checked?

Author's Reply

The smallest one that I have made — the sensing element is approximately 3 mm and the diameter is approximately 5 mm of the stem. There is no reason why they cannot be made a little bit smaller but you must remember that as you go down in size then sensitivity is reduced to a considerable extent and it cannot be as effective as for larger gaps.

C.Veret, FR

My question is a little outside the framework of the two presentations but does deal with clearances in turbo engines. Some years ago, work was published on obstacle methods used for measuring the clearances in gearboxes and housings. This work was done by Pratt and Whitney — I wonder if this work has been updated? The work is concerned with optical measurements of clearances in gearboxes and housings.

Author's Reply

Pratt and Whitney and General Electric both have had optical systems for measurement of clearance — I have seen a variety of diagrams. One of the problems that I see with using optical techniques is the contamination of the optics and the complexity is also a problem with optical techniques.

C.Veret, FR

I conclude then that these techniques are no longer in use and no additional studies are being conducted with them.

J.Chivers, UK

As far as clearance measurements in gearboxes are concerned which if I understood the question correctly is what it was about — our experience is that we would tend to go away from a capacitance based technique or an optical based technique for the very reasons that were given — because of the contamination — and we would tend to be looking for an eddy current-inductive technique. We have used these in a gearbox environment with a fair degree of success.

G.Alwang, US

To respond to the specific question of optical proximity probes and assuming that we are talking about turbine blade tips and compressor blade tips — they are still very much in use and they have the advantage of course that you can use them at extremely high temperatures so they are being used routinely — nevertheless we are also quite interested in the simpler capacitive probes for the regions in which they are applicable.

I.Namer, US

Probably this is somewhat of an unfair question since you are talking about capacitance measurements but could you comment on the possibility of using an ultrasonic transducer to try and determine the tip clearances?

Author's Reply

When you are looking at a working machine and you are taking a look at ultrasonics let's consider some of the problems that you are dealing with. You are dealing with blade no 5 passing frequencies in the order for the JT-5 of 37, — 38,000 blades per second. The JT-5 for example has a tip thickness of approximately 0.5 mm its in front of any type of a probe for example in the case of the JT-5 for 1.8 microseconds — in other words, you are dealing with a phenomenon for example that is already in the ultrasonic region. The other thing is how are you going to use the ultrasonics — are you looking at the wave propagation from an emitter and then you are looking at the delay time? Well, the blades are not there long enough for that to happen unless you have some other phenomenon that you are using the ultrasonics which I don't know anything about.

Unidentified Speaker

An experience that we had at MTU with ultrasonics was that we were not able to detect the tip of the blade: all that we got was information about the hub of the system.

TECHNICAL EVALUATION REPORT
SESSION VI — FUTURE PROSPECTS

by

C. Veret
ONERA
29 Avenue de la Division Leclerc
92320 Châtillon sous Bagneux
France

Les techniques nouvelles qui viennent d'être présentées se rattachent aux trois thèmes suivants :
- Mesure des températures et concentrations dans des mélanges gazeux s'appliquant particulièrement aux milieux en cours de réaction et en combustion.
- Développement des méthodes d'interférométrie holographique pour conduire à leur exploitation quantitative.
- Mise en oeuvre d'une méthode de vélocimétrie laser fournissant des résultats simultanés dans tout un champ.

1 - MESURE DES TEMPERATURES ET CONCENTRATIONS DANS LES MELANGES GAZEUX

En ce qui concerne la première de ces techniques, Monsieur Rosier nous a montré les résultats qu'il a obtenus à l ONERA lors de l'étude d'une flamme.

La technique à laquelle il est fait appel, de spectrométrie par absorption n'est pas nouvelle en elle-même, mais ce qui est nouveau, c'est la manière de la mettre en oeuvre grâce à l'emploi de diodes laser.

Jusqu'à présent, la source lumineuse utilisée en spectrométrie d'absorption était une source à spectre large dont le rayonnement, après traversée du milieu absorbant était analysé au moyen d'un spectromètre avant d'être reçu sur un photodétecteur ou un ensemble de photodétecteurs juxtaposés.

Par contre, les diodes laser ont pour propriété d'émettre un rayonnement spectralement très étroit dont on peut changer la longueur d'onde d'émission en faisant varier sa température. Un photodétecteur reçoit ce rayonnement après qu'il ait traversé le milieu absorbant. La présence d'un monochromateur n'a pour rôle que d'éliminer des rayonnements parasites et non de déterminer la largeur de la bande spectrale analysée.

Le balayage spectral obtenu en faisant varier la température de la diode peut être très rapide ce qui permet d'analyser périodiquement un petit intervalle spectral correspondant à l'une des bandes d'absorption d'un composant donné, à une fréquence qui peut atteindre le kilohertz.

Ainsi, cette technique se révèle prometteuse pour mesurer les concentrations de composants donnés dans des milieux en réaction, des flammes fluctuantes ou tout mélange gazeux instable pour étudier les évolutions de ces concentrations avec une bonne résolution temporelle. Il est à noter, toutefois, que, spatialement, la mesure porte sur la totalité du composant rencontré sur le trajet du rayonnement, comme pour toutes les méthodes d'absorption.

Il est envisageable aussi, dans certaines conditions, de déterminer la température moyenne du composant sur le trajet suivi par le rayonnement absorbé.

2 - DEVELOPPEMENT DES METHODES D'INTERFEROMETRIE HOLOGRAPHIQUE

Sur le thème de l'interférométrie holographique, Monsieur Bryanston-Cross de l'Université de Warwick nous a d'abord rappelé les avantages de cette technique sur l'interféromètre classique, par exemple du type Mach-Zehnder. Ces avantages se résument en une plus grande facilité de réalisation et d'exploitation ainsi qu'en la possibilité d'utiliser comme source lumineuse des lasers impulsionnnels à durées très brèves permettant l'étude de phénomènes, même rapidement évolutifs. Les travaux en cours dans le domaine de l'interférométrie holographie tendent, d'une part, à examiner des écoulements tridimensionnels pour y localiser les phénomènes observés (c'est le cas pour des grilles d'aubes annulaires ou des compresseurs axiaux) et, d'autre part, à quantifier les images enregistrées pour les comparer aux résultats obtenus par calcul à l'aide de modèles. Dans les deux cas, des difficultés à la fois pratiques et théoriques restent à résoudre avant que l'emploi de la méthode puisse s'étendre.

Un bel exemple d'application à l'étude d'une grille d'aube de turbine a ensuite été présenté. La grille d'aube est placée entre deux hublots perpendiculaires à la direction du faisceau d'étude du dispositif holographique de manière que les phénomènes aérodynamiques entre les aubes puissent être considérés comme bidimensionnels.

La technique est utilisée soit en hologramme absolu, soit en hologramme différentiel. Dans le premier cas, la pose de référence est effectuée avant la mise en marche de la soufflerie et la seconde pose pendant l'essai de sorte que l'interférogramme montre des franges qui représentent les lignes de densité constante dans l'écoulement.

En hologramme différentiel, les deux poses successives sont séparées de 100 µs pendant le fonctionnement de la soufflerie et les franges représentent alors les lignes d'égal changement de densité en 100 µs.

Les résultats des mesures de densité obtenues à partir des hologrammes sont en bon accord avec ceux fournis par des mesures de pression à la surface des aubes et à ceux obtenus à l'aide d'un modèle de calcul.

Dans le but d'étudier des écoulements fluctuants dans le temps, comme dans une grille d'aube dont les aubes sont agitées en oscillation pour simuler le flutter, ainsi que pour faciliter la quantification des données contenues dans un hologramme, Arthur Decker nous a présenté les travaux qu'il a entrepris sur les méthodes d'interférométrie holographique à modulation de faisceau.

La technique nécessite l'emploi de deux sources de références distinctes lors de l'enregistrement des deux hologrammes superposés. De plus, si, lors de la restitution, les deux sources de référence ont des longueurs d'onde légèrement différentes, il devient possible d'effectuer des mesures sur l'interférogramme par des techniques de mesures de phase sur les signaux d'un photodétecteur explorant l'interférogramme point par point. Ceci donne accès, non seulement à une amélioration de la précision de mesure des densités gazeuses liées aux positions dans les franges, mais encore à une automatisation du dépouillement des hologrammes conduisant à leur quantificaiton et à leur comparaison à des résultats de calcul sur modèles.

Des résultats encourageants ont déjà été obtenus sur la mise en oeuvre de cette technique, mais il reste encore des améliorations à apporter aux montages optiques et un nouveau laser à colorant pompé par flash, mieux adapté à l'emploi de la technique que ceux utilisés jusqu'à présent est attendu prochainement.

3 - MISE EN OEUVRE D'UNE METHODE DE VELOCIMETRIE LASER

Le troisième thème, développé dans le dernier exposé présenté par J. Kompenhaus de la DFVLR à Göttingen concerne la mesure simultanée des vitesses d'un écoulement dans tout un champ.

Cette technique récente vient compléter celle de la vélocimétie laser à franges ou à deux points qui ne fournissent, à un instant donné, que des mesures ponctuelles. Le champ d'écoulement observé simultanément est celui éclairé par une nappe lumineuse mince obtenu par élargissement d'un faisceau laser dans une direction au moyen de lentilles cylindriques.

Le laser fournit deux impulsions lumineuses brèves à des intervalles de temps connus. Des particules contenues dans l'écoulement deviennent ainsi, à la traversée de la nappe lumineuse des points brillants doubles dont les images sont enregistrables au moyen d'un appareil photographique.

Différentes techniques sont étudiées pour effectuer, le plus automatiquement possible, les dépouillements des images enregistrées. Elles conduisent toutes à l'établissement au moins d'une carte des vitesses projetées dans le champ d'éclairage, déterminée d'après les écarts et les directions des couples de points obtenus. La limitation actuelle pour des écoulements rapides, à fortes accélérations est due à ce qu'il n'est possible d'enregistrer que des particules ayant quelques microns de diamètre.

Les travaux actuels portent sur la mise en oeuvre opérationnelle de cette technique sur des cas déterminés (jets libres ou chambre fermée par des hublots) et sur les moyens d'améliorer la sensibilité pour enregistrer des particules plus fines, en utilisant des lasers plus puissants, des optiques de meilleure qualité et des supports de plus grande sensibilité.

CONCLUSION

Chacun des trois thèmes présentés contribue ainsi à apporter des informations quantifiées sur les caractéristiques des gaz en mouvement à l'intérieur d'un moteur. La poursuite des travaux entrepris est donc vivement souhaitable afin qu'ils aboutissent à des méthodes de mesure opérationnelles sur les composants du moteur, chambres de combustion et turbines, sans perdre de vue que, pour atteindre ce stade, les résultats de mesure doivent être fournis en temps quasi-réel, ce qui devient possible à l'aide des moyens informatiques modernes.

ETUDE DE LA COMBUSTION PAR SPECTROSCOPIE DIODE LASER

par B. Rosier, P. Gicquel et D. Henry
Office National d'Etudes et de Recherches Aérospatiales
BP 72, 92322 Châtillon Cedex, France

RESUME

Nous avons appliqué la spectrométrie d'absorption infrarouge par diode laser à l'étude des gaz de combustion.

Cette méthode présente les avantages des mesures in-situ non intrusives. Elle permet des mesures de concentration alliant précision, spécificité et résolution temporelle (1 ms).

Nous présentons des mesures de concentrations du monoxyde de carbone et de la vapeur d'eau dans un foyer méthane-air à pression atmosphérique.

Nous avons étudié l'évolution de ces concentrations en fonction de la richesse du mélange.

Ces gaz ont également été observés dans un brûleur basse pression (20-25 Torr). Deux types de flammes ont été utilisés : CH_4-O_2, $CH_4-NH_3-O_2$. Nous avons relevé les profils de concentration de CO et H_2O le long de l'axe de la flamme. Ces résultats sont comparés avec des mesures publiées antérieurement et effectuées à l'aide d'une sonde couplée à un spectrographe de masse.

1. INTRODUCTION

L'étude des phénomènes de combustion nécessite des mesures de concentrations et de températures. Parmi les nouvelles méthodes de mesure in-situ, la spectroscopie d'absorption, utilisant les diodes laser accordables[1,2], offre d'intéressantes possibilités. On peut l'utiliser pour mesurer les concentrations de la plupart des substances actives en infrarouge. Comme toutes les méthodes de mesure du coefficient d'absorption, elle conduit à une mesure intégrée sur le trajet optique. Cette technique, non-intrusive et sensible, permet une mesure très spécifique de la concentration. De plus, sa bonne résolution temporelle (de l'ordre de 1 ms à 100 µs selon le matériel employé) offre la possibilité d'étudier des phénomènes transitoires et/ou des éventuelles fluctuations de température et concentrations du milieu observé.

Depuis 1983, nous avons employé cette technique pour mesurer les absorptions de gaz en cuve chauffante et dans diverses flammes. Nous avons, en particulier, mesuré les concentrations de CO et H_2O dans un foyer méthane-air à pression atmosphérique ainsi que dans un brûleur sous pression réduite.

2. MONTAGE ET PROCEDURES EXPERIMENTALES

Le montage (fig. 1) se compose du brûleur équipé des mesures de débit, du bâti d'optique de laser et de l'électronique associée, du système optique et des appareils de détection et de traitement du signal. Nous utilisons un système diode laser fourni par laser analytics inc., équipé d'un système de refroidissement en circuit fermé. Un équipement associé permet d'ajuster et de stabiliser la température de fonctionnement de la diode. Pour obtenir un spectre d'absorption, la fréquence du mode d'émission doit balayer un petit intervalle spectral (1 à 1.5 cm⁻¹). Ce balayage résulte de la modulation du courant traversant la diode. Nous utilisons un courant en dent de scie d'amplitude adaptée à l'intervalle spectral balayé. Nous pouvons ajuster sa fréquence de 50 Hz à 1 kHz. Nous obtenons ainsi, à cette fréquence, un spectre d'absorption du milieu en combustion qui présente la caractéristique intéressante de respecter la forme des raies déterminée par le phénomène étudié : en effet, la largeur du mode d'émission de la diode (10⁻⁴ cm⁻¹) peut être négligée devant la largeur Doppler des raies.

La diode, à base de sels de plomb, présente des modes d'émission autour de 1900 cm^{-1}. Un système de deux lentilles L_1L_2 en fluorine focalise le faisceau, issu de la diode, au centre du foyer. Une autre lentille L_3 en forme l'image sur la fente d'entrée d'un monochromateur à réseau. Ce monochromateur filtre d'éventuels modes d'émission indésirables, lorsque le fonctionnement de la diode n'est pas monomode. Il élimine aussi le rayonnement parasite provenant des gaz de combustion. A la sortie du monochromateur, une lame en ZnSe répartit le faisceau sur deux voies. Sur l'une des voies se trouve une cuve de référence contenant du monoxyde d'azote NO sous basse pression (0,1 à 1 Torr) et à température ambiante. Sur l'autre voie, nous disposons d'un étalon Fabry-Perot en germanium de 2,54 cm d'épaisseur (interfrange $\simeq$ 0,0489 cm^{-1} à λ = 5,2 µm). Le système de franges sert à l'étalonnage spectral. Enfin, chaque faisceau est focalisé sur un détecteur InSb refroidi à l'azote liquide (77 K). Un oscilloscope numérise et visualise les signaux amplifiés, à la fréquence de balayage de l'intervalle spectral.

L'origine de l'échelle de numérisation des spectres correspond au niveau nul (absorption totale) de la transmission. Un micro-ordinateur HP gère l'acquisition et le stockage des signaux. Si nécessaire, nous pouvons moyenner jusqu'à 256 spectres.

Ce montage expérimental permet l'acquisition d'un spectre en un temps bref (30 à 1 ms). Lorsque des flammes instables (et/ou très turbulentes) sont étudiées, cette réduction du temps d'acquisition diminue très nettement les fluctuations, de l'intensité transmise, sur la durée du spectre. De plus, il devient possible d'observer des phénomènes transitoires avec une résolution de 1 ms.

Le traitement des spectres s'effectue en temps différé sur un ordinateur HP 1000.

La cuve de référence (Fig 1) contient un gaz dont le spectre est bien connu. Nous avons utilisé le monoxyde d'azote dont les positions des raies, contenues dans la banque de données spectrales AFGL 82[3,4], sont fournies avec une précision de 5.10^{-4} cm^{-1}. L'intervalle spectral balayé contient toujours une et, si possible, plusieurs raies de NO. Nous effectuons ensuite une modélisation des franges de Fabry-Pérot, par une méthode des moindres carrés. Chaque fois que possible, nous déterminons l'interfrange à l'aide d'une deuxième raie de NO de référence, éloignée de la première. Ceci permet de s'affranchir des problèmes tels que la variation de l'interfrange avec la température. Par cette méthode, la valeur du nombre d'onde est déterminée, avec une précision absolue de 3 10^{-3} cm^{-1}, en tout point de l'intervalle spectral.

Nous calculons ensuite les pressions partielles des espèces étudiées à l'aide de la loi de Beer I_σ/I_σ^0 = exp $(-\alpha_\sigma \ell)$

avec I_σ, I_σ^0 intensité transmise avec et en l'absence d'absorption, au nombre d'onde σ,

ℓ trajet dans la flamme (en cm),

α_σ coefficient d'absorption au nombre d'onde σ

Dans le cas d'un milieu homogène

$$\alpha_\sigma = \sum_{i \in G} \sum_{j \in R_i} S_{ij}(T) \ f_{ij}(\sigma, T, P_{i \in G}) \ P_i$$

avec   G   ensemble des gaz.

R_i ensemble des raies du i^{ème} gaz.

S_{ij} force de la raie fonction de la température (cm^{-2} Atm^{-1}).

f_{ij} profil de la raie, dépendant de la température et des pressions partielles des divers gaz, élargissement Lorentz.

P_i pression partielle du i^{ème} gaz (Atm)

En pratique, il suffit de prendre en compte un nombre très limité de raies pour retrouver convenablement le spectre d'absorption sur un petit intervalle. Les données nécessaires au calcul de S(T) (force de raie à une température de référence, énergie du niveau de base de la transition, position de la raie) proviennent de la compilation AFGL 82[3,4] en ce qui concerne NO et H_2O. Pour CO nous avons utilisé les données de A Goldmann (communication privée)

Le tableau 1 donne les paramètres des principales raies observées. Nous avons utilisé pour f_{ij} un profil de Voigt, calculé par l'approximation de Humlicek[5]. La température provient de mesures indépendantes. A partir de ce qui précède, les concentrations ont été déduites du spectre étudié, en utilisant une méthode de meilleure approximation au sens des moindres carrés.

3. RESULTATS EXPERIMENTAUX

3.1. Brûleur à pression atmosphérique

Description - Le brûleur (fig. 2) fonctionne à pression atmosphérique. Il utilise un prémélange méthane-air de richesse ϕ ajustable entre 0,7 et 1,2. Une enveloppe interne en silice permet de limiter les échanges thermiques avec l'extérieur afin de s'approcher des conditions adiabatiques. Nous avons utilisé un thermocouple (Pt/Pt - 10 % Rh corrigé des transferts radiatifs et convectifs) pour mesurer le profil de température le long du trajet optique dans le foyer. Nous avons relevé l'évolution de ce profil en fonction de la richesse. Ces valeurs des températures (1700 à 1900 K) concordent avec des mesures précédentes obtenues par pyrométrie[6] et par la méthode de Diffusion Raman Anti Stokes Cohérente (DRASC[7]).

Mesures par diode laser - Des hublots de mica, refroidis par un jet d'azote, limitent les interactions entre les gaz de combustion et l'air ambiant. Ils définissent un trajet optique de 9,5 cm, dont 5,5 cm dans la flamme. On peut voir, figure 3, un exemple de spectre obtenu. Les fluctuations de l'intensité transmise au travers des flammes peu stables ($\phi = 0,7$ à 0,8) nous ont conduit à opérer sur des moyennes de 20 acquisitions consécutives.

Nous avons mesuré l'évolution des concentrations de CO et H_2O en fonction de la richesse. Nous avons, aussi, pu détecter la présence de méthane dans les flammes riches ($\phi \simeq 1,2$), à l'aide d'une diode centrée sur 2900 cm^{-1}. Les paramètres des raies observées sont regroupés dans le tableau 1. Les concentrations ont été déterminées en utilisant les mesures de température par thermocouple.

La figure 4 présente les concentrations obtenues ainsi que des résultats de calculs théoriques. Un premier calcul correspond à une combustion adiabatique. Le deuxième évalue les concentrations à l'équilibre, à la température mesurée dans la flamme.

Discussion -
Pour le méthane, la concentration mesurée (environ 2 % en volume) dans une flamme de richesse $\phi \simeq 1,2$, présente une grande imprécision. Nous estimons en effet la limite de détection de ce corps à 1 % en volume (dans les conditions expérimentales).

Cette sensibilité paraît limitée, principalement, par la précision de la détermination du niveau zéro d'absorption (enveloppe du mode). Le méthane n'a pas été détecté dans les flammes de richesse inférieure à 1,1.

Les mesures de concentration en vapeur d'eau ont été corrigées de l'absorption par la vapeur d'eau atmosphérique le long du trajet optique. Dans ce but, nous avons enregistré un spectre avant chaque allumage du foyer. La principale source d'incertitude de ces mesures provient de la présence de couches "froides" (~ 1200 K) entre la flamme et les hublots. Nous estimons à 20 % l'erreur relative sur les concentrations.

Dans le cas de CO, cette erreur se limite à 10 %. En effet, l'énergie élevée du niveau de base des transitions observées, rend négligeable l'influence des couches "froides".

On constate un accord satisfaisant entre nos mesures et le calcul à l'équilibre à la température mesurée pour les richesses supérieures à 1. L'excès de CO, détecté dans les flammes saturées indique sans doute, une condition de non équilibre chimique (comme précédemment par Hanson[8]).

3.2. Brûleur à pression réduite
Ce brûleur (fig. 5) se compose d'un disque poreux en bronze fritté, alimenté en méthane enfermé dans une enceinte à vide. Nous avons étudié une

flamme 6.5 % NH_3-31.5 % CH_4-62 % O_2, de 25 Torr de pression Puechberty[9] a caractérisé ce foyer en température et concentration, en fonction de la hauteur dans la flamme (distance au plan de sortie du poreux). Les températures résultent de mesures par spectroscopie d'absorption en ultraviolet sur le radical OH[10]. Les concentrations proviennent de mesures effectuées par prélèvement à l'aide d'une sonde couplée à un spectromètre de masse. Ces mesures s'étendent de 0 à 20 mm du plan de sortie du diffuseur par pas de 1 mm. La précision des mesures varie de 10 à 20 % suivant la concentration.

Nous avons également étudié une flamme CH_4-O_2 de richesse 1 de 20 Torr de pression.

Mesures par diode laser - Nous avons adapté le montage optique de façon à obtenir sur tout le trajet dans la flamme, une limite de résolution spatiale meilleure que 1.0 mm. Les mesures ont porté sur l'évolution des concentrations de CO et H_2O en fonction de la distance de l'axe de visée au plan du diffuseur ; nous avons fait varier cette distance entre 0 et 20 mm par pas de 1 mm.

La figure 6 montre un exemple de spectre obtenu dans ces conditions. La figure 7 permet de comparer nos résultats aux valeurs mesurées par Puechberty. Nous estimons l'erreur relative sur les concentrations à 20 % pour l'eau et 10 % pour CO. Dans le cas de l'eau, ainsi que pour CO de 5 à 20 mm, les résultats obtenus par les deux méthodes concordent (aux incertitudes près). Par contre, il existe une nette divergence des résultats entre 0 et 4 mm, c'est-à-dire dans la région proche du front de flamme.

La figure 8 regroupe les résultats des mesures par diode laser sur la flamme CH_4-O_2.

Correction des incertitudes - Cette méthode de mesure peut s'étendre à l'étude d'autres espèces jouant un rôle important dans la combustion CH_4, NO, HCHO etc.

Nous avons observé des raies de NO et CH_4 dans les flammes précédentes, mais la sensibilité de notre montage doit être améliorée. Dans le cas des mesures effectuées sur le foyer à pression atmosphérique, on peut répertorier quatre principales sources d'incertitude:
- l'évaluation de la température,
- la détermination de l'enveloppe du mode (I_v^0),
- les données spectroscopiques,
- la présence de couches froides

● **Mesure de la température**

La technique diode laser permet de mesurer directement la température par la méthode des deux raies. Hanson[11] a obtenu une précision de 40 K autour de 2100 K, en utilisant la paire de raies de CO 2105.2564-2105.1254 cm^{-1}.

● **Enveloppe du mode**

Le niveau zéro d'absorption varie sur l'intervalle spectral balayé. Nous modélisons l'enveloppe par une expression polynomiale. Les paramètres de cette expression et les concentrations sont déterminés simultanément par une méthode des moindres carrés. Nous pourrions, sans doute, améliorer la restitution de l'enveloppe du mode, en utilisant un montage à double faisceaux.

● **Données spectrales**

Les données tabulées dans l'AFGL 82 manquent parfois de précision à haute température. Ce problème se pose nettement dans le cas du méthane. Nous avons dû mesurer les forces et les positions relatives de plusieurs raies de ce corps. D'une façon générale, une incertitude sur la force de référence utilisée détermine une incertitude du même ordre sur la concentration.

● **Couches "froides"**

La présence de ces couches, situées entre la zone homogène de la flamme et les hublots, entraîne une incertitude importante lorsque les raies observées ont une faible énergie du niveau de base. Quand le milieu présente une symétrie axiale, une inversion d'Abbel permet de retrouver les profils des divers paramètres. Mais dans le cas où une telle méthode n'est pas utilisable, on doit extraire le maximum d'information d'un

spectre unique Si l'on considère un milieu inhomogène, il est possible de le découper, le long du trajet optique, en couches sensiblement homogènes en température et concentrations

On montre alors que ces paramètres peuvent être restitués par inversion numérique du spectre observé Le caractère univoque et la précision de la restitution dépendent du nombre de raies observées, de leurs paramètres spectroscopiques, du nombre de couches considérées, du rapport signal/bruit Il est évidemment nécessaire de connaître les paramètres des raies utilisées (force, paramètres d'élargissement, dépendance de ces paramètres en fonction de la température,) avec une très bonne précision Nous avons développé un code d'inversion utilisant une méthode de type Marquardt[12] Nous l'appliquons actuellement à des spectres synthétiques afin d'évaluer l'influence des divers paramètres sur la restitution des températures et des concentrations

CONCLUSION

La spectroscopie d'absorption par diode laser accordable nous a permis de mesurer les concentrations de CO et H_2O dans une flamme à pression atmosphérique Ces résultats concordent avec les valeurs à l'équilibre, pour les richesses supérieures à 1

Des mesures similaires sur une flamme NH_3-CH_4 O_2 sous basse pression ont été comparées à des résultats obtenus par prélèvement grâce à une sonde couplée à un spectromètre de masse Les profils de concentration sont relevés le long de l'axe de la flamme Les valeurs données par les deux méthodes concordent au delà de la région du front de flamme Comparée à cette dernière technique la spectroscopie d'absorption par diode laser présente l'avantage d'être non intrusive et permet une bonne résolution temporelle

REMERCIEMENTS

REFERENCES

[1] J C Hill G P Montgomery. Diode lasers for gas analysis. Applied Optics, 15, 3, March 1976, 748-755

[2] R S Eng, J F Butler, K J Linden. Tunable diode laser spectroscopy an invited review. Optical Engineering, 19, 6 Nov 1980, 945-960

[3] L S Rothmann et al. AFGL trace gas compilation 1982 version, Applied Optics, 22, 11, June 1983, 1616

[4] L S Rothmann et al. AFGL atmospheric absorption line parameters compilation 1982 edition, Applied Optics, 22, 15, August 1983, 2247

[5] J Humlicek, An efficient method for evaluation of the complex probability function the Voigt function and its derivatives, J. Qu. Spec Rad. Trans., 21, 1979, 309-313

[6] M Charpenel, Mesures instantanées par pyrométrie infrarouge de températures de gaz de combustion. Application à la turbulence thermique, Rev. Phys. Appl., Tome 14, mars 1979, 491

[7] M Péalat, S. Druet, B Attal, J.P. Taran, Temperature and concentration measurements in a reactif media by Coherent Anti-Stokes Raman Scattering, 16th Internal Symposium of Combustion, MIT Cambridge, Mass., 1976.

[8] R.K Hanson, S.M. Shoenung, CO and temperature measurements in a flat flame by laser absorption spectroscopy and probe techniques, Combustion Science and Technology, 24, 1981, 227-237.

[9] D. Puechberty, Thèse de Docteur ès Sciences, Université de Rouen, 1980.

[10] D. Puechberty and J.M. Cotterreau, Nitric oxyde formation in an amonia doped methane-oxygene low pressure flame, Combustion and Flame, n° 51, 1983, 299-311.

[11] R.K. Hanson, P.K. Falcone, Temperature measurement technique for high-temperature gases using a tunable diode laser, Applied Optics, 17, 16, August 1978, 2477-2480.

[12] D.W. Marquardt, R.G. Bennett, E.J. Burrel, Least square analysis of electron paramagnetic resonance spectra, J. Mol. Spect., 7, 1961, 269-279.

Posi... cm^{-1}	Corps	Niveau de base cm^{-1}	Force° mol^{-1} cm	Transition				Raies observées dans le foyer		
								Foyer basse pression		Foyer atmos pherique
								CH_4-O_2	NH_3-CH_4-O_2	CH_4-O_2
1920,913	H_2O	2129,600	$0,197.10^{-22}$	020	550	010	441	X	X	X
1921,922	CO	4488,002	$0,145.10^{-19}$	1	47	0	48			
1932,545	CO	4127,955	$0,158.10^{-19}$	1	45	0	46	X	X	X
1933,167	H_2O	1060,156	$0,741.10^{-21}$	010	946	000	835			
1933,641	H_2O	2631,272	$0,664.10^{-21}$	010	16215	000	15114			
1937,465	H_2O	2904,872	$0,851.10^{-24}$	020	1047	010	936		X	X
1937,814	CO	3954,458	$0,164.10^{-19}$	1	44	0	45			
1937,947	H_2O	2246,888	$0,339.10^{-22}$	010	14312	000	13211			
1953,449	CO	3452,157	$0,181.10^{-19}$						X	
1953,745	CO	4809,655	$0,207.10^{-19}$							
1957,656	H_2O	1613,224	$0,112.10^{-21}$	010	1249	000	1138	X		
1958,604	CO	3292,475	$0,167.10^{-19}$	1	40	0	41			
1958,718	CO	4669,921	$0,212.10^{-19}$	2	35	1	36			
2945,885	CH_4	1562,858	$0,960.10^{-22}$	$\nu_3 + \nu_4 - \nu_4$						
2945,898	CH_4	1562,790	$0,104.10^{-21}$	"						X
2945,932	CH_4	1562,574	$0,200.10^{-21}$	"						

°CO à 4500 K ; H_2O et CO à 296 K

Tableau 1 - Raies observées dans le foyer.
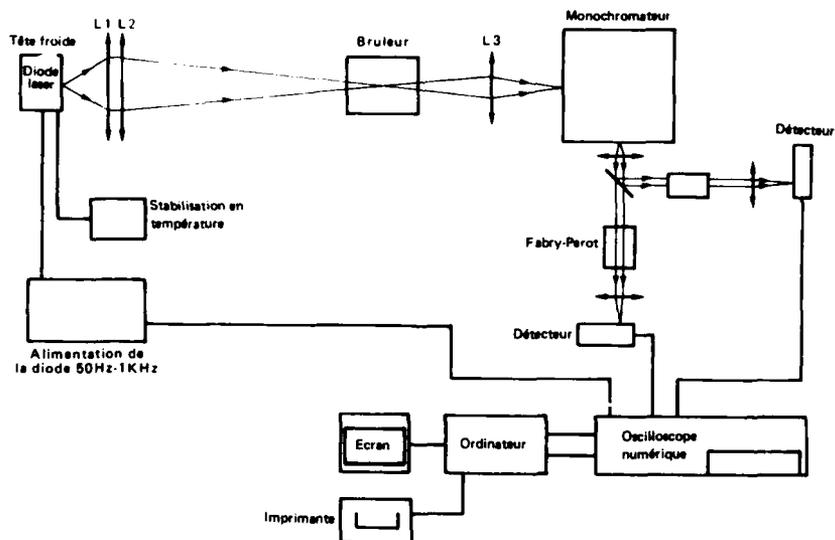
Fig. 1 - Montage expérimental.
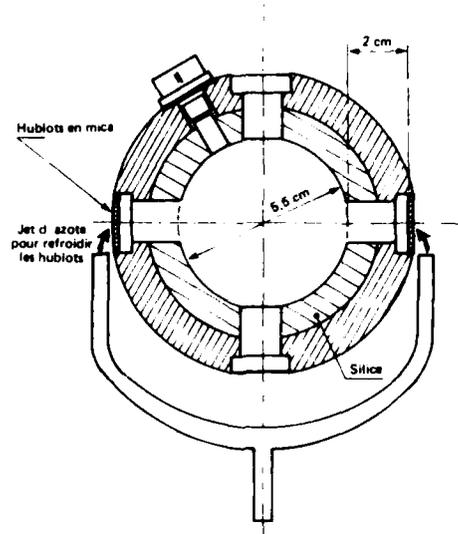
Fig 2 - Coupe horizontale du foyer homogène
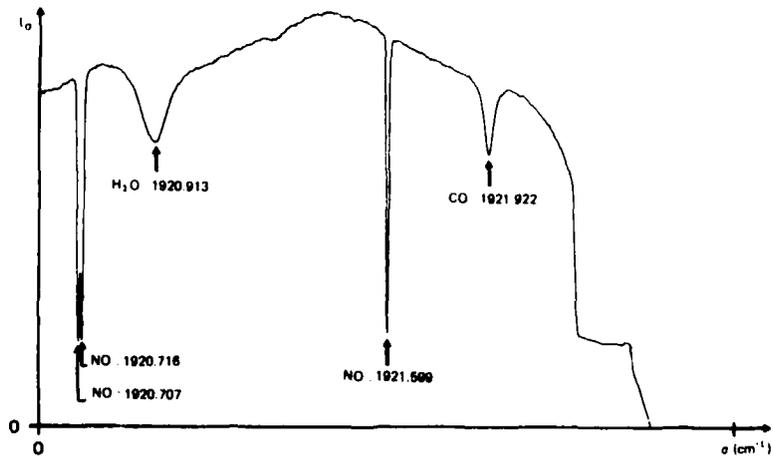
Fig. 3 - Foyer homogène
Intervalle spectral 1920,6-1922 cm^{-1}.
Temps d'acquisition 3 ms,
Moyenne de 20 spectres.
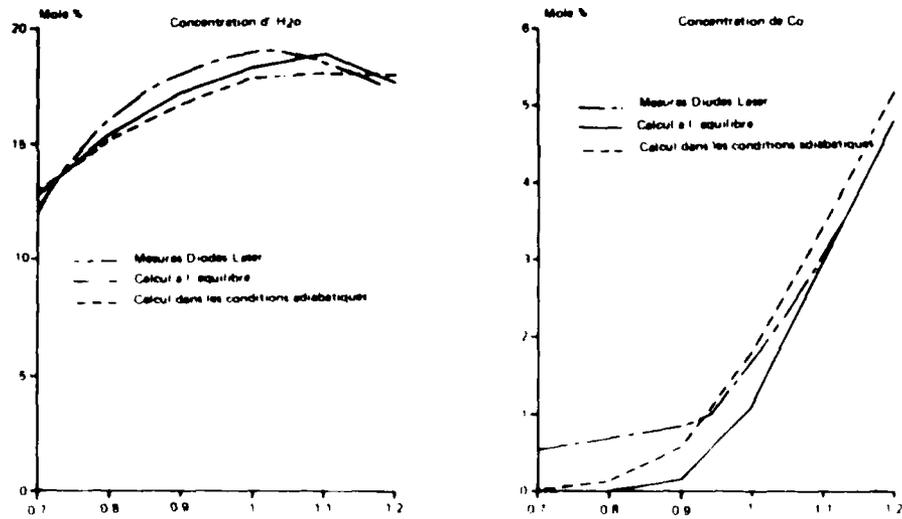
Fig 4   CH$_4$-O$_2$ flamme à pression atmospherique
Evolution des concentrations de H$_2$O et de CO en fonction de la richesse
mesures diode laser
calcul à l'équilibre (temperature mesurée)
calcul à l'équilibre (combustion adiabatique)
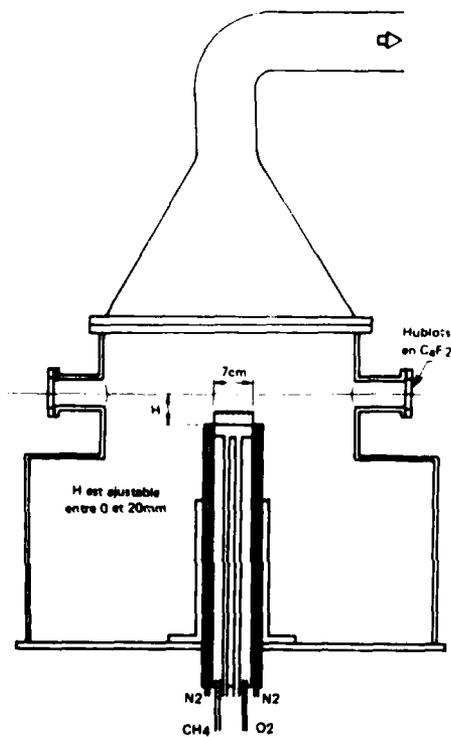
Fig 5 - Foyer basse pression.
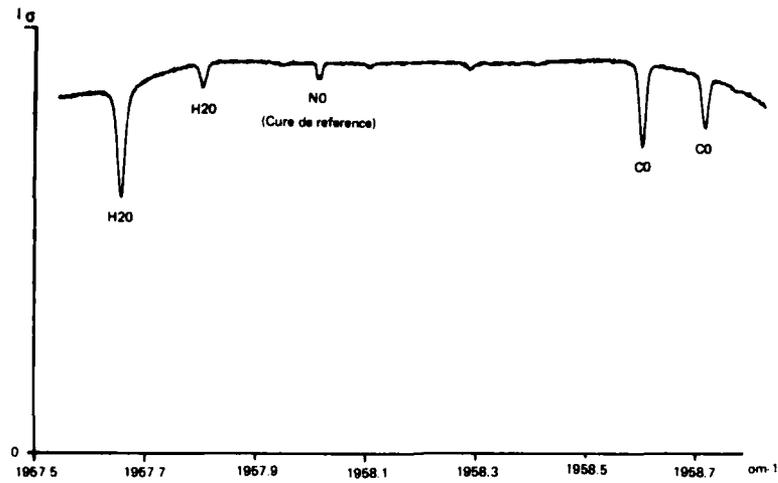
Fig. 6 - Foyer basse pression (20 Torr).
Distance 4 mm, flamme CH_4-O_2, temps d'acquisition : 5 ms
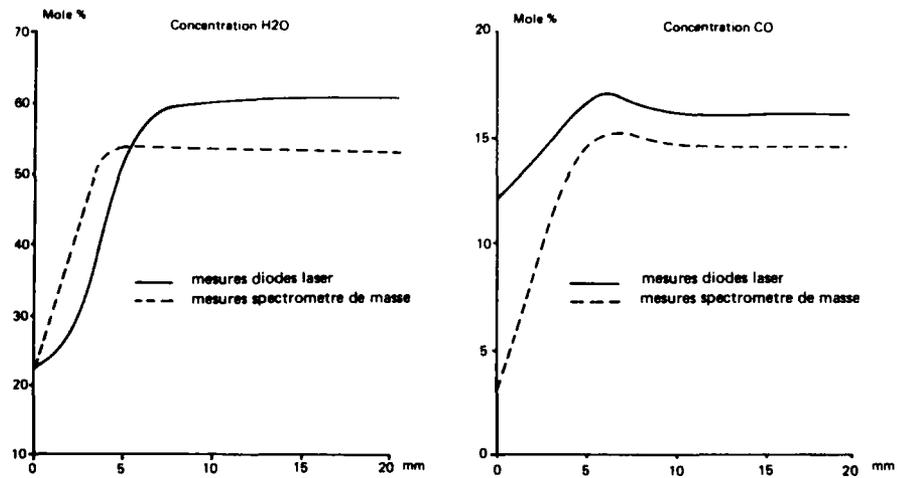
Fig. 7 - Evolution des concentrations de H_2O et CO le long de l'axe de la flamme.
CH_4 = 31,5 %, NH_3 = 6,5 %, O_2 = 62 %, flamme à 25 Torr.
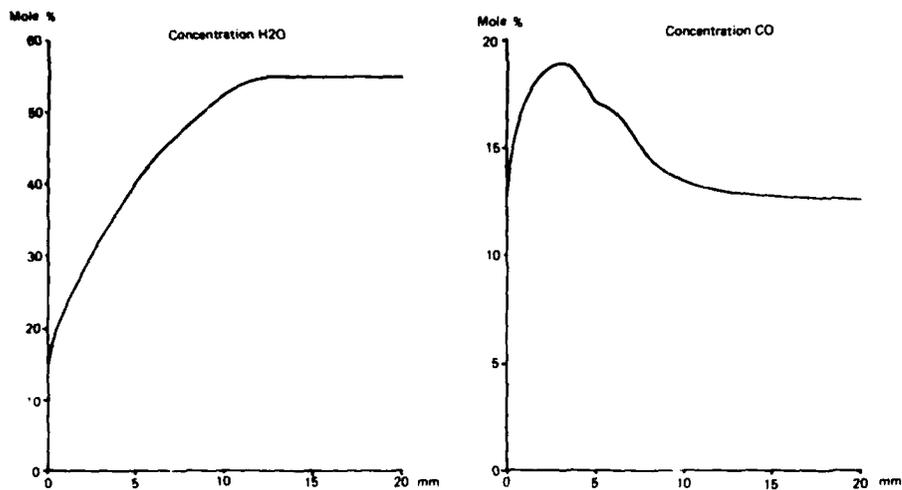
Fig 8 - Evolution des concentrations de H_2O et CO le long de l'axe de la flamme.
Flamme CH_4-O_2 à 20 Torr

DISCUSSION

R.B.Price, UK

Did you correct for the effects of mixing at the edge of the flame?

What are the errors that arise in the measurements from this source?

Author's Reply

We took into account infrared absorption at the air-flame interface, and in the "cold" layers along the optical path. Nevertheless important uncertainties remain in the modelisation of this interface.

Their influence on concentration determination varies with the lower state energy of the observed line. The relative uncertainty from this source is about 15% for H_2O and less than 5% for CO.

D.A.Greenhalgh, UK

Could you comment on the discrepancy in your residuals for the spectral you have fitted? Perhaps the Galatry profile, such as described by Varghese, would give a better fit?

Author's Reply

The residual error of the least squares best fit for H_2O lines, indeed looks like the difference between a Voight and a Galatry function. The collisional narrowing effect on Doppler linewidth is large for H_2O molecules. However, in our experimental conditions, the discrepancy between observed and calculated line shape may come from several other error sources. Until we have a better precision, the Voight profile, which save computer time, seems a sufficient line shape approximation.

The Application of Holography as a Transonic Flow Diagnostic to Rotating Components in Turbomachinery.

P J Bryanston-Cross
Department of Engineering
Warwick University
Coventry CV4 7AL, UK

Abstract.

This paper presents a review of the application of holography as as a whole field flow visualisation diagnostic in turbomachinery. Starting with two dimensional cascade testing, which required wavelength toleranced optical tables, it has now been found possible to obtain results with bolt-on optical components. In order to achieve this, compromises have been made in optical quality and attention has been given to the nature of the data required. Holographic systems are shown which have been applied to visualise the flow in a linear cascade, an annular cascade, a three dimensional compressor shock in a rotating flow and a diffuser blockage observed in a rotating turbocharger.

Nomenclature

C	Dale-Gladstone constant	D	Area of coherent illumination
L	Optical path-length	Ma	Mach Number
n	Fringe order	R	Radius of rotation
V	velocity	t	Time sec.
W	Angular velocity	Z	Length
λ	Wavelength of light	ρ	Density of air
σ	Speckle size	μ	Refractive index of air

Introduction

In the design of turbomachinery the ability to make accurate measurements in transonic flows is essential both as a diagnostic and as a test to numerical prediction. With the current progress of prediction methods and the efficiency gains availble using advanced designs, the demand from such measurements have increased.

The ideal requirements now asked of a flow visualisation diagnostic are:- A non-disturbing real time diagnostic tool which can produce a three dimensional qualitative picture of the flow. The diagnostic tool should be able, with good resolution, to visualise both steady and unsteady, rotating and non-rotating flows at transonic speeds. It should also have the facility to make direct comparisons with theory. The measurement data should further be able to give a quantitative description of the density, velocity and temperature of the fluid in three dimensions.

These requirements cannot as yet be met by any single diagnostic. This paper will make a critical review of what has been achieved and possible with holographic interferometry.

Of the techniques available conventional pressure probe measurements though widely used, suffer from the well known problems of interference and calibration, as described in (1). They also suffer from the difficulties of discrete sampling, as discussed in detail in (2).

Several optical methods are now being used, the most established methods being those of two-spot (L2f) and doppler anemometry (LDA) (3&4). However unless fluorescent seeding is used in the flow, (5), the time required to accumulate a quantitative picture of the flow can be of the order of 2 minutes per point in transonic flows. Both methods are highly dependent of the size of the seeding particles used and the position at which they are introduced into the flow (6). Point measurements also can only discretely sample unsteady flows, making the interpretation of data uncertain.

More recent optical methods are now capable of producing a whole field
visualisation of the flow-field. Laser fluorescence, as developed by A
Epstein at MIT, has within a dedicated environment produced results of
rotating transonic flows. (7,8&9). It requires that a molecularly diffusing
gas diacetyl, is mixed with air. A plane of light is then formed using a
ultraviolet pulse laser. Ultraviolet light causes the diacetyl to fluoresce,
the density of the gas being proportional to the intensity of the light
emitted from the fluorescent material. In transonic flows where the density
of the air is related to Mach number, the intensity of the emitted light is a
measure of the flow speed. The technique has the potential, with the
development of fast data transmitting, high resolution, photon counting
cameras, to provide a direct whole field high resolution visualisation of the
three dimensional density distribution within the fluid.

Pulse Laser Velocimetry is also a recent measurement method, developed
at the Von Karman Institute by R Meynart (10). It requires the creation of a
plane of light by a pulse laser and seeding of the air. The light plane is
imaged directly onto a photographic film and two flashes of a pulse laser are
used to form a double image of the seeding particle distribution on a
photographic film. An unexpanded laser beam is projected through the
photographic negative and when a pair of particle images are detected they
form Youngs fringes. The interferometric fringe spacing is directly related
to the speed of the flow and the orientation of the fringes to the flow
direction. The system has been demonstrated for low speed flows, ie 2 to 30
metres per second, its application being limited by the power and quality of
the lasers used, and the flow following ability of the seeding particles.
Both Lockheed-Georgia in the USA (11) and DFVLR in Germany (12) are
evaluating this approach. The method ,at present, can be used with flow in a
defined plane, cut of plane movement being difficult to evaluate.

Holographic Interferometry

Holographic interferometry is very similar to its predecessor Mach Zehnder
interferometry, but more robust, simpler to use and can be used to produce a
three dimensional representation of the flow field.

Interferometric fringes are produced by the phase change of a ray passing
through a fluid. Changes in refractive index can be related to density for
gases by the Dale Gladstone expression.

$$(\mu-1)/\rho = \text{Gladston-Dale constant} \quad C=2.24E-4 \ m^3 /Kg \ (for \ air)$$

where μ is the refractive index of the gas
ρ is the density of gas

In the classical Mach Zehnder approach a collimated optical beam is divided
into two parts. One beam travels through the test section the other through
an alternative path-matched route. Fig(1) A recent example of this method has
been completed at the Max-Planck Institut Gottingen. Where the interaction
between the vortex shed from a bluff body and an aerofoil at incidence is
being studied. Measurements have been made of the dynamic response of the
blade to a 10KHz vortex passing event using a flash light and Fastex camera
(13).

The technique is limited in its application. The polychromatic light source
used has a very short coherence length makeing the optical system difficult
to set up. To produce an interferometric result the route taken by the two
light paths have to be matched to less than a millimetre. There is a loss
in optical resolution resulting from the low light levels and high
speed films needed to record the interferometric data. It is also not
possible to locate the flow disturbance spatially.

In most situations replacing the noncoherent light source with a reliable
coherent pulse laser has several advantages:-

The long optical coherence length of the laser allows the two optical paths
up to 1 metre miss-match between them. They beams can if required be
carried within a fibre optic (14), it is also possible to use the Smartt
interferometric approach (15), which requires that only one beam need pass
through the flow . When a high power pulse laser is used, because of its
light intensity (MW) and short flash duration (30 nsec.) high speed flow
occurrences can be visualised with good resolution in three dimensions.
This has lead to greater understanding of the flow, in particular, in the
visualistion of turbulent structures within shear and boundary layers and
in the shed vortex interaction behind a turbine rotor (16).

Holographic data has been extracted in environments unsuitable for classical
interferometry and in some cases anemometry. For example in the very large 4
m wind tunnels at NASA Ames (17), in annular rotating and non-rotating
cascades (18&19) and within the gas turbine engine itself (20). This has been
posssible for two reasons, firstly the speed at which data can be captured.
Secondly many of the surface and internal imperfections   of the optical
components used, such as found for example in   perspex, which would
randomise the pictures obtained by a classical interferometer, are encoded
into the hologram and do not distort the flow field data.

Three dimensional data using holographic interferometry has been extracted by
two approaches. When a collimated beam is passed perpendicular to the flow
direction of interest, the density change within the fluid is observed
as an integrated line of sight across the test section.   Three dimensional
data has been extracted from flow fields by taking many different collimated
ray paths through the flow and then using an inverse solution to extract
localised flow features. Tne early work using this method (21&22) was
limited by the then available computer storage. Recently NASA has yielded
several successful solutions using this technique to solve the absolute
density field around a helicopter rotor blade (23).

An alternative holographic approach, was to illuminate a diffuse backgroud
to form a scattering surface. The human eye, and the camera lens both use
scattered light to localise objects in three dimensions. In this manner
sharp discontinuities in the fluid such as shock waves or periodic even*s, as
found with shed vorticity and flow separation, can be localised. The sharper
or more discontinuous the flow the more accurately it can be localised. A
resolution of 10 microns is possible in the case of a solid surface, such as
a nuclear fuel rod (24). A millimetre in the case of a shock wave, and a few
millimetres for a shed vortex structure in the wake of a turbine blade. The
spatial definition possible with a smoothly changing absolute density field
is much lower and better approached by the previously described multi-view
technique. The application of the scatter plate method is also dependent on
tne quality of the optical processing applied ie a high diffraction
efficiency holographic image is essential to the extraction of the three
dimensional flow field data.

Applications of Holographic Interferometry.

 Two Dimensional Holographic Visualisation of Transonic Flows.

A situation has arisen in the development of complicated numerical prediction
codes where there are few well documented test cases against which they can
be critically tested. Interferometric data has sufficient resolution to
test these codes at the points where they are most sensitive.

This is illustrated in the two dimensional approach developed at EPFL (Ecole
Polytecnique Federale de Lausanne), for visualising the trailing edge shock
structure around the trailing edge of a 30 times scaled model of a steam
turbine, figure 3, (18). The boundary layers on the object can clearly be
seen followed by an isentropic Prandtl-Meyer expansion where the flow
accelerates from M=1.3 upto M=1.9 figure 4. The shear flow converging to form
the confluence region and boundary layer seperation at the end of the
trailing edge can also be seen in detail . Figure 5, made using two
holographic pulses 3 microseconds apart, shows the unsteady component of the
fully developed flow of figure 4. For the first time and as a consequence of
the scale of this trailing edge it is possible to observe the vortex
structure present in the shear layer directly after the separation point. The
size and strength of this vortex structure can be seen to increase at the end
of the confluence region with the influence of the downstream compression
shock. The Lavel nozzle can also be configured operate as a with subsonic
exit conditions as shown in figure 6.

EPFL are now in the process of evaluating this interferometric data against
their numerical prediction methods (25).

Two dimensional high resolution inteferometry has also been used to visualise
the blade leading edge, where a comparison with an inviscid code has been
made, figure 7 (26). In the trailing edge of the blade, figure 8 (27),
it led to improvements in the Navier Stokes numerical solver applied   and
contributed to the understanding of the turbulence modelling (28). The
simplest method of evaluating and interpreting data in these cases has been
to scale the output contour plots of the numerically generated data to match
in size the photographic reconstructions made from two dimensional
interferograms (29). The contour´s heights, which then match the optically
generated isodensity fringe spacings, give a sharp test of the ability of the
code to model the flow, as illustrated in figure 9.

484

Three dimensional flow visualisation applied t ar annular turbine as the of EPFL.

Holography has been used to visualise the shock str ... in annular turbine cascade ... In this case a Reynolds number s ... turbine intra-passage flow has been visualised. The flow sp ... 100mm making the shock visualisation more difficult. From the experiment carried out the following observations can be made. That the si ... unless deliberatly vibrated has a natural oscilatin frequen ... KHz region and requires a laser pulse separatio of ... 100millisecs to visualise it. The incoming sample beam w ... reflected off the innerwall of the cascade, fi ... entering the ... ahead of the blade row. It was found that when the beam wa ... downstream of the of the blade the trailing edge tur ... the phase of the incoming light beam. It has now been shown that th ... structure can be visualised in three dimensions over the wi ...
cascade, shown in figure 13.

Following the tests on the annular cascade a number o ... made holograms which could be viewed with a white light s ...
illumination. During the copying it became necessar ...
position of the holograms to a point much closer t the ...
several features became apparent. The view of the sho ...
exhibited a greater paralax to the eye making it easier t ...
position. Secondly, in making the holograms white light ...
brighter to see, with no risk to the eye, as wi ...
Finally it is possible to choose where in the volume of the ...
hologram is to be formed. It has been found that it ...
of the hologram is defocused, making it possible ...
within the flow and blurr out unwanted noise such a ...
turbulent tunnel sidewall flow effects.

Three dimensional rotating flows.

Large axial Rotating Compressor.

Laser holography is used on a regular basis for the three dimensional visualisation of the leading edge shock of a the first stag engine ... holographic system for this application is considered a routine diag ... for engine testing, (6). The technique uses two closely separated holographic exposures reflected of a diffusely painted backgroun t localise spatialy the three dimensional shock structure. This is an approach also well matched to the visualisation of the tip vortex structure of interest in the development of unducted fans.

The first stage transonic compressor fan is typically up to 2m in diameter, figure 14, with the shock structure existing over two thirds of the blade height. The virtue of this method over the alternative approaches is speed. The holographic system uses a high power ruby pulse laser to give an intantaneous whole field viualisation of the flow. In no more than 4hrs of rig running for 4 characteristic points on a performance curve every blade can be mapped. Approximately 200 holograms are made for each test. They are examined and used to select particular blade passages for more detailed quantitative study with L2F. Normally, the detailed L2F measurements take a further 10 to 40hrs of engine running.

The output beam from a pulse laser is divided into two parts. One forms the reference beam the other the object beam, figure (15). The coherence length of the ruby pulse laser is of the order of 1 metre, making it possible to form holograms without contour fringes of objects up to 3 metres across. As a result it is possible to expand a laser beam to reflect from the inside surface of a gas turbine of 4 square metres. This illuminated area forms the background against which the shock structure can then be viewed. The sample beam illuminates the inside of the casing of the engine directly ahead of the rotor. From a view point just over the rotor it is possible to see between the passing blades the upstream illuminated area.

The air just ahead of the shock has a density lower than that just after the shock. If two holographic exposures are made (approximately 2 microseconds apart) then two holograms are made on the same piece of film. The only difference between the holograms being the movement of the shock as it passes the viewing window, figure 16. It is this difference in shock position and its overlap between the two exposures in the hologram, which is visualised as an optical phase shift. Such a shift makes the position of the shock apparent as a dark or bright area in the reconstructed hologram as shown in figure 17.

Optical Turbomachinery

... last year in holographic experiments had been peformed on small (100mm
diameter) radial turbochargers. These machines, which are used to boost the
compression power of large truck engines rotate at upto 80,000 revs. They can
reach transonic speeds at the blade tip, and generate loss through shock
waves. Using a holographic system, developed from that used previously on
a radial axial fans, it has been possible to produce visual evidence of this
shock structure and trailing edge wake structure from the turbine exit of the
wheel figure (18), reference (33). As with the data from EPFL, the pulse
laser had holograms were copied, firstly to make them white viewable for
display but and also to move the observer closer to the plane of interest.

Quantitative holographic interferometry.

Although holographic interferometry has been used regularly to produce
qualitative flow information, two dimensional and particularly three
dimensional quantitative data has been harder to achieve. The amount of data
stored in any one hologram is very large and complicated. It is not until
recently, that the numerical computing power and control over scanning systems
has been available to reduce it to manageable levels.

As an example, consider the unsteady flow conditions when a transonic stator
and rotor pass each other. It is possible, using a pulse laser, to form
a train of holograms of this event (34), with a time duration of 5 microsec
between each pulses. This would be a hologram for every 0.2mm movement of the
rotor. The problem is how can each hologram being interpreted automatically
without error to an optical resolution of 100 microns and also give some
indication of the three dimensional flow field.

In previous approaches to holographic flow visualisation, two separate
exposures of a holographic plate were made using the beam from a
ruby pulse laser. The time between these exposures has been varied from
microsec to seconds in order to visualise, as interferometric fringes, a
change in the flow field density. Examples are given where the flow-off
condition is compared to the flow-on and of how flow unsteadiness can be
visualised, also where the density change due to rotation of the flow is
visualised. The technique is sensitive to movement between the two
exposures, a physical vibration or rotation can either create spurious
fringe data or at worst prevent the formation of the hologram. Although this
sensitivity can be optically minimised it can leave uncertainty in the
analysis in the flow field.

It has been shown by Bachelo (15), working at NASA Ames in California,
that two dimensional data can be extracted from a hologram in one single
exposure. In Bachelo s case a collimated optical beam was passed through the
NASA 4ft span wind tunnel. Then using a beamsplitter divided into two, one
beam was spatially filtered. By spatially filtering the optical phase
component of the light which carries the information of the flow is filtered
out. The two beams were then recombined to produce isodensity interferometric
data. It has thus been shown possible to strip the phase or flow data from
one half of the beam and compare it directly with the other.

Bachelo's flow was two dimensional, however it is possible to extend this
approach to a three dimensional flow by processing the hologram in two
separate steps. A hologram can be made with a single 30nsec. exposure of a
ruby pulse laser. Interferometric stability being maintained over the
duration of the pulse. The extraction of data can be carried out at a
later time on a optical table designed for the purpose.
Holograms visualising the absolute flow could thus be made of ...
that would normally vibrate or decorrelate the data during the time
between two holographic exposures. In particular ...
using a rotating background, or the inside wall ...

Post processing of the data in this manner would ...
interagation methods developed by Bachelo for ...
measurement of the interferometric data ...
fringe. Without some optical processing of the data ...
resolution to within a 1 ... fringe in the ...
turbine stage of span. In this way ...
to the Mach number. A Mach ...
any pair of holographic fringes ...

AD-A182 954   ADVANCED INSTRUMENTATION FOR AERO ENGINE COMPONENTS: 6/6
               CONFERENCE PROCEEDIN..(U) ADVISORY GROUP FOR AEROSPACE
               RESEARCH AND DEVELOPMENT NEUILLY..   NOV 86 AGARD-CP-399

UNCLASSIFIED   F/G 14/2   NL

MICROCOPY RESOLUTION TEST CHART

A futher difficulty which has limited the application of holography to rotating turbomachinery is that of decorrelation of phase information. To form a conventional hologram of a flow field the illumination of the background required to have a stable specular nature.   Speckle size is defined in two ways:- Objective speckle, which defines the limit of resolution through a lens system (36), and is expressed as

$$\sigma = 1.21 * F * \lambda$$

where   is the wavelength of light and F=the F number of the imaging lens, F = (focal length of lens/diameter of lens).
Subjective speckle, which is the speckle size recorded on a photographic plate by an unfocused beam which has been scattered by a lambertian surface.

$$\sigma = 1.21 * \lambda * (Z/D)$$

where D is the diameter of the object illumination on the scatter surface and Z is the distance from the suface to the holographic plate.

In the case of a rotating surface, the specular pattern may also be rotating. If the rotation of the specular pattern is grater than   /10 during the holographic exposure, then decorrelation will occur. Even with short duration (30 nsecs) high intensity pulse lasers if the surfase moves buy more than 1/10   it is not possible to form holographic information. For the example of a turbine rotor, the speed of the speckle on the surface would be of the order of,

$$v = 2*pi*r*w$$

where v is the velocity of the surface, r is the radius of the cascade and w is the angular velocity of the cascade.

$$v = 120m/sec$$

The speed of the speckle patten at a distance 0.4m from the axis of rotation of the cascade

$$v(s) = 400m/sec.$$

and the size of the speckle pattern would be,

$$\sigma = 1.21 \quad Z/D$$

$$= 4 \text{ microns.}$$

For the data to avoid decorrelation then the holographic exposure should occur with a duration.

$$t = 4*E-6/400 \text{ secs}$$

$$= 10 \text{ nsecs.}$$

Thus in order to form holographic data from a single laser pulse there are two possible solutions. To reduce the pulse duration of the laser or to make the inner hub of the rotating cascade with a mirror finish and refect a static specular pattern form outside the cascade onto it.

The last part of the approach describes how three dimensional data can be extracted from hologram and the accuracy and resolution likely to be obtained. This can be achieved by discretly sample the hologram and which reduces the data field at a pre-digitisation stage of the problem. The alternative approach would be to digitise each separate view and recombine them numerically using a tomographic solution, examples of which can be found in references (21)&(32).

A selective scanning process would reduce the time and complexity of the numerical problem. By using a scanning beam of 2 to 5mm in diameter a small part of the hologram is illuminated. The image which this scanned area of the hologram projects is equivalent to viewing the original flow through a small aperture. Previously such projected images have suffered from high noise levels generated in part by the high monochromaticity of the laser source. By averaging several areas of the plate the sharpness of the interferometric fringes can be retained and the speckle noise recursively averaged out. In using this approach it will also be possible to make only small changes from one view to the next, which is preferential to solving large numbers of linear equations, both in terms of data storage and speed.

Finally the data at each point can be found by weighting a large number of ray paths through co-incident points in the fluid. This is a technique which has be used successfully in X-ray analysis for producing 'cat-scans' of the brain and other organs(22). It will also be possible to produce in specified areas of sudden flow acceleration, ie at the leading and trailing edges, the equivalent high resolution isodensity mach lines possible with the previously used two dimensional systems.

Conclusions

There is now a strong drive to produce quantitative instantaneous three dimensional data of transonic flows. Methods which employ discrete sampling techniques such as laser anemometry are limited to the assumption that the flow field is steady or periodic over relatively long sampling periods.

Alternative optical whole field flow three dimensional diagnostics are now being developed, one of which, holographic interferometry has been discussed in depth in this paper.

Several applications of holographic interferometry to two and three dimensional transonic flows have been presented. It has beeen shown that for two dimensional flow fields the method for extracting quantitative data is well established. Whereas, with limited exception, the results obtained from three dimensional flows have been qualitative.

The limitations of holographic interferometry to three dimensional flow visualisation have been described and solutions by which quantitative data can be obtained, presented.

References.

1. 'Probe Calibration Workshop'. edited by T Fransson. 7th Symposium on Measuring Techniques and Supersonic Flow in Cascade and Turbomachines, held at the Institute fur Strahlantriebe and Turoarbeitsmascinen, Rheinisch-Westfalische Technische Hochschule Aachen. Dec 1984.

2. Bubeck H. 'Measuring Errors of Pneumatic Multi-Hole-Probes.' 7th Symposium on Measuring Techniques and Supersonic Flow in Cascade Turbomachines, Technishe Hochschule Aachen. Dec 1984.

3. Schodal R. 'A Laser Two Focus (L2F) Velocimeter for Automatic Flow Measurements in the Rotating Components of Turbomachines' ASME Journal of Fluids Engineering. Vol102,Dec1980 pp412-419.

4. Strazisar A. 'Investigations of Flow Phenomena in a Transonic Fan Rotor Using Laser Anemometry'. Journal of Engineering for Gas Turbines and Power. April 1985. Vol107. pp427-435.

5. Strazisar A J and Powell J A, ' Laser Anemometry Measurementsin a Transonic Axial Flow Compressor Rotor', ASME Journal of Engineering for Power, Vol103, April 1981, pp430-437.

6. Moore C, Jones D, Haxel C, Bryanston-Cross P and Parker R. 'Optical Methods of Flow Diagnostics in Turbomachinery'. ICJASF 81. IEE 81 CHI 712/9/8/40000-0244

7. Epstein A. 'Fluorescent Gaseous Tracers for 3D Flow Visualization. 'GTL report No117 Jan1974 M.I.T.

8. Haymer-Harber G and Tompkins W. 'Comparison of Experimental and Computational Shock Structure in a Transonic Compressor Rotor'. Journal of Engineering for Power. Jan 1981.

9. Epstein A. 'Quantitative Density Visualisation in a Transonic Compressor Rotor.' GTL Report No.124 Sept 1975.

10. Meyart R. 'Laser Speckle Velocimetry in Fluid Dynamic Appications'. paper presented as part of the von Karman Institute for Fluid Dynamics course on Digital Image Processing in Fluid Mechanics March 5-9 1984.

11. G A Reynolds, M Short and M C Wiffen. 'Automatic Reduction of Instantaneous Flow Field Images' Optical Engineering, May 1985, Vol24 No.3, pp475-479.

12. J Kompenhans. 'Data Reduction of Images in Fluid Dynamics at DFVLR'. Presented at the workshop on Automated Data Reduction of Images and Holograms, NASA Ames Research Centre, Jan 1985.

13. Meier G, Timm R & Becker. 'Initial Experiments on Profile Vortex Interaction.' internal report ISSN 0436-1199 Max-Planck-Institute Fur Strmungsforschung, Gottingen. June 1983.

14. Sharma A, Halme S & Bustusov M. 'Optical Fibre Systems and Their Components.' No 24 Springer Series in Optical Sciences. Published by Springer-Verlag 1981. pp220.

15. W Bachelo and M Houser. 'Optical Interferometry in Fluid Dynamics Research'. Optical Engineering. May 1985. Vol24 No.3, pp455-461.

16. Bryanston-Cross P, Edwards J and Squire L. 'Measurements in an Unsteady Two Dimensional Shock/Boundary Layer Interaction.' presented at the IUTAM Unsteady Aerodynamics Conference, Jesus College Cambridge Sept. 1984

17. J Craig, G Lee and W Bachalo. 'Nd:YAG Holographic Interferometer for Areodynamic Research.'presented at the SPIE conference on Industrial and Commercial Applications of Holography, August 24-25 1982 San Diego, California

18. Bryanston-Cross P J, Beretta-Piccoli F and Ott P. 'Implementation of the Ruby Pulse Laser Holography System at the LTT/EPFL.' Internal report LTT-TM-16-84. Ecole Polytechnique Federale de Lausanne Sept 1984.

19. RF Wuerker, RJ Kobayashi, LD Hejlinger and TC Ware 'Applications of Holography to flow Visualization within Rotating Compressor Blade Rows.' NASA CR 121264 1974

20. Bryanston-Cross P J. 'Three dimensional Holographic Flow Visualisation'. Presented Sept 1981 at the Symposium on Measuring Techniques in Transonic and Supersonic Cascade Flow. Lyon.

21. Sweeney D and Vest C. 'Reconstruction of the Three Dimensional Refractive Index Fields from Multi-directional Interferometric Information'. Applied Optics. vol 12 1973.

22. Bracewell R and Werneckle. 'Image Reconstruction over a Finite Field'. Journal of the Optical Society of America Vol 54. 1976.

23. F Becker and Yung H Yu. 'Digital Fringe Reduction Techniques Applied to the Measurement of Three Dimensional Transonic Flow Fields', Optical Engineering, May 1985. Vol24 No.3, pp429-434.

24. Tozer B & Webster J. 'Engineering Applications of High Resolution Holography of Large Volumes.' Electo Optics and Laser International, 1980, April Brighton.

25. Bolcs A & Sari O. 'Unsteady Measurements in a Turbine Cascade in Stalled Transonic Flow' presented at the IUTAM Unsteady Aerodynamics Conference, Jesus College Cambridge Sept. 1984

26. Bryanston-Cross and Denton J. 'Comparison of a Measured and Predicted Flow around the Leading Edge of an Aerofoil'. AIAA Vol22 pp 1025-1026 1984

27. Dawes W.N and Bryanston-Cross. 'A Numerical and Experimental Study of the Loss Generation in a Transonic Rotor Blade'. to be published, International Journal of Heat and Fluid Flow.' late 1985.

28. Bryanston-Cross P J and Dawes W N. 'Comparison of Inviscid and Viscous Computations with an Interferometrically Measured Transonic Flow.' AIAA June 1985 Vol23, No6 pp834.

29. Bryanston-Cross P J Lang T Oldfield M and Norton R. 'Interferometric Measurements in a Turbine Cascade using Image Plane Holography'. Journal of Engineering for Power Jan 1981.

30. Craig J. 'Laser Interferomentry for an unsteady airfoil undergoing dynamic stall', Spectron Developments Lab. AIAA vol22 1984.

31. Johnson D. & Bachelo W. 'Transonic flow past a symmetrical airfoil, invicid and some turbulent properties' NASA Ames research center Moffett Field AIAA vol 18 No 1 1980

32. Hesselink L. 'Quantitative Three-dimensional Flow Visualization'.
Presented at the third Symposium on Flow Visualization, Ann Arbor, Michigan,
Sept 1983 pp375-380.

33. Bryanston-Cross P. 'A Holographic System for Visualising a Vortex
Structure in a Turbocharger', Presented at the meeting of Holographic
Measurement, Speckle and Allied Phenomena at the CEGB Headquarters London
April 16th to 17th 1985.

34. Ebeling K. 'high speed holocinematography using spatial multiplexingfor
image separation'. Optics Communications April 1977.

35. Dandliker R. 'Strain and Stress Analysis Through HeterodyneHolographic
Interferometry', Brown Boveri Report No KLR77-107C. 1977

36. Born M. & Wolf E. 'Principles of Optics', Pergamon Press Ltd 1959.

_Figures

Fig 1

Mach Zehnder
Interferometer

Mach-Zehnder
Interferometer

B1 beamsplitter
M1 Mirror

Fig 2
Bachelo's Smartt
Single beam interferometer
M1 mirror
B1 beam splitter
H1 holographic plate
L1 positive lens
S1 spatial filter

1	Sidewalls of the Laval Nozzle	8	Negative lenses
2	Trailing edge model	9	Large aperture collimating lens
3	Perspex vindows	10	Large aperture plano-convex lenses
4	Pulse Laser (J.K.)	11	Collimating lens
5	Dielectrically coated mirrors	12	Mirrors
6	50% beam splitter	13	Holographic plate
7	Microscope objective x5	14	EPFL optical table

3. Diagramatic layout of the EPFL image plane rugby pulse interferometric system as applied to a two dimensional Laval Nozzle.

4. Supersonic trailing edge flow showing the Prandtl-Mayer expansion of the flow from a Mach number of Ma= 1.3 to Ma= 1.9
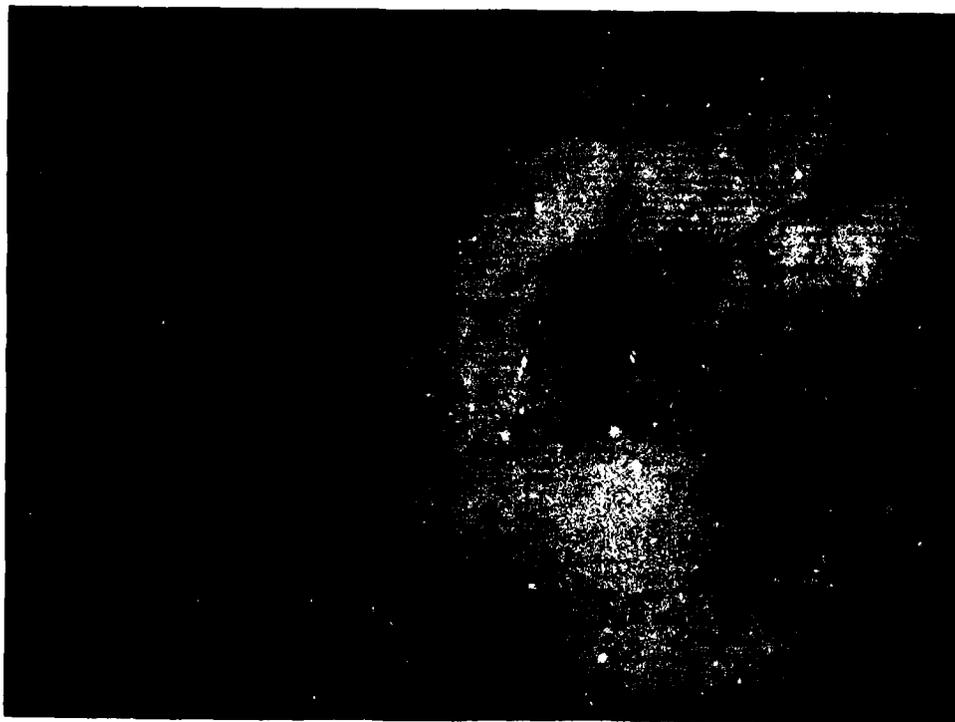
5. Unsteady components of the stable exit flow shown in figure (4).

6. Laval nozzle now adjusted to operate in the subsonic region. Ma= 0.6
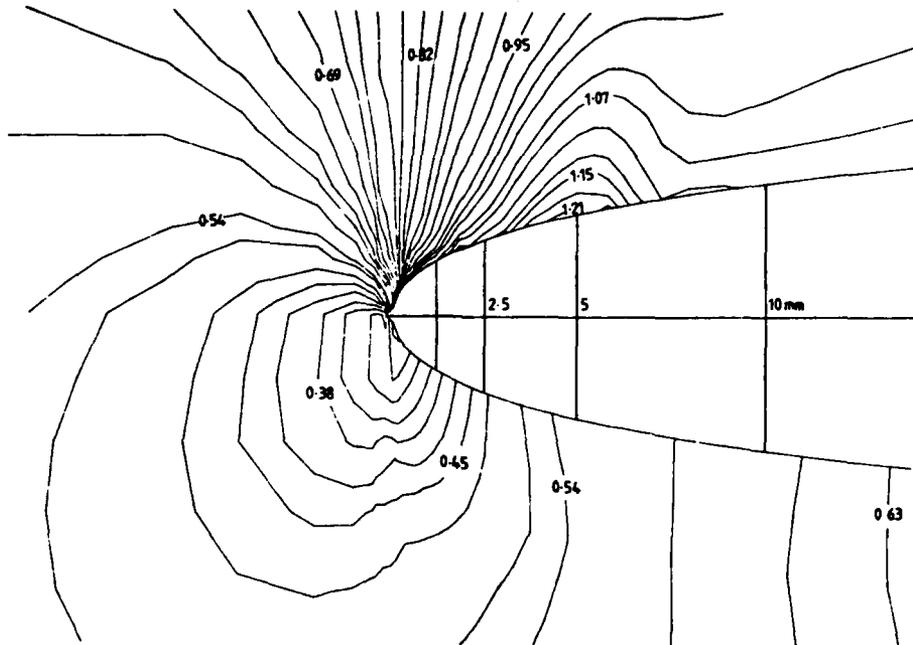
7. Comparison between an interferometric measurement made of the transonic flow around an isolated aerofoil and its numerical prediction using a time marching solution.
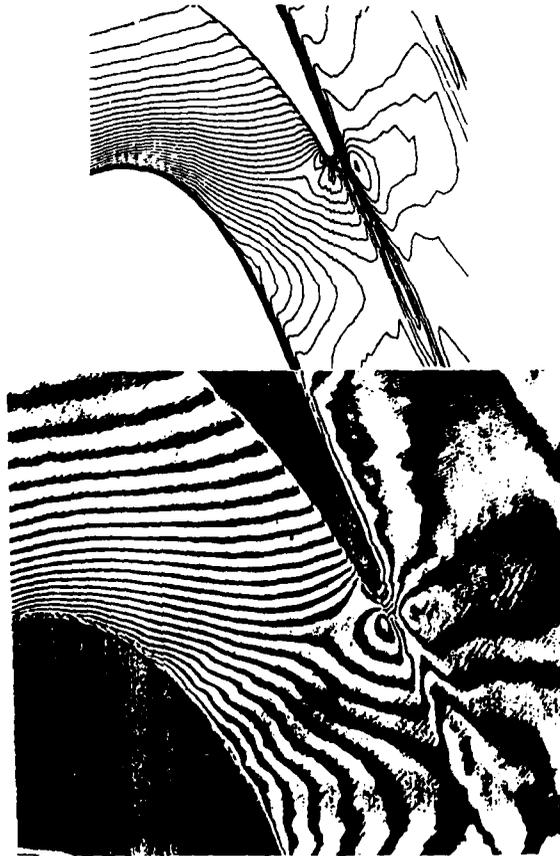
8.   Comparison between the trailing edge flow in a linear cascade measured
interferometrically and a loss predicting Navier-Stokes solver computed
solution.
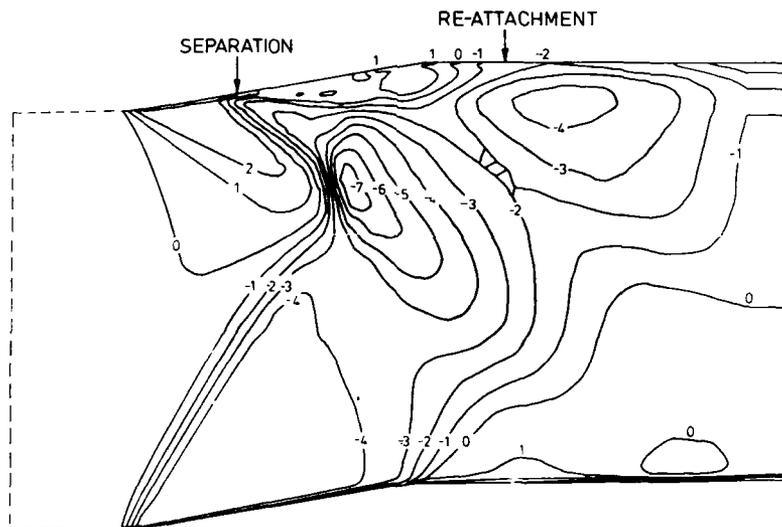
9. Comparison of a transonic wedge profile with side
   wall boundary layer separation and a viscous numerical
   solution.
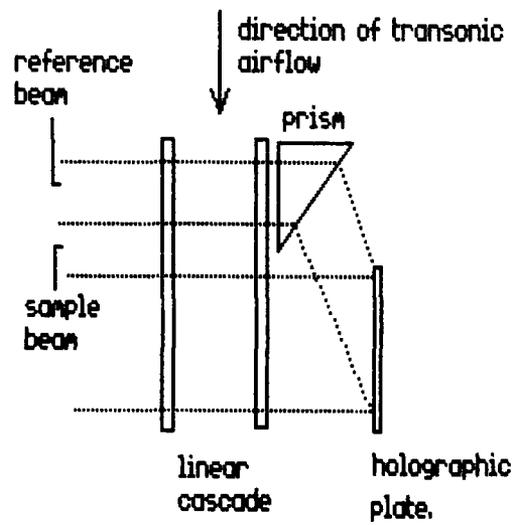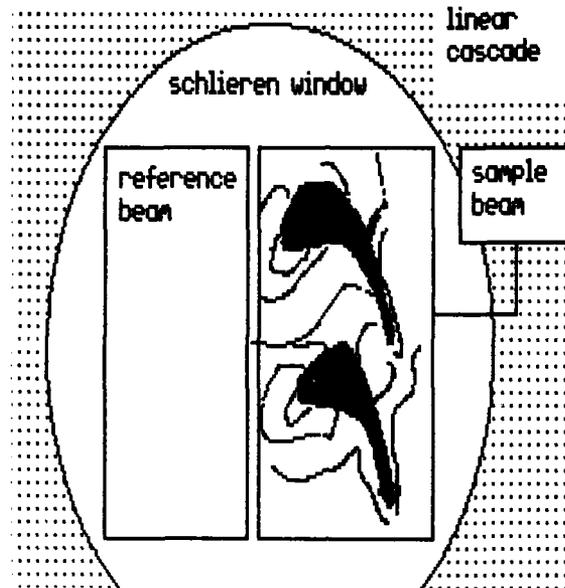
10.   Optical approach applied at the Whittle Laboratory.

11.   Interferometric reconstructions made from the Whittle Lab
experiment. Both the leading edge and trailing edge flows can clearly be
seen, the confluence region has been enlarged to show the formation of
the trailing edge vortex structure.

ANNULAR CASCADE
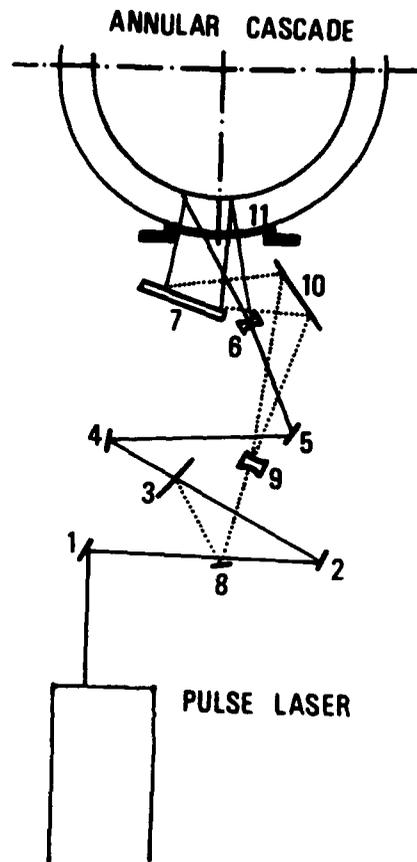
Fig 12

<u>Diagram of the EPFL three dimensional
holographic flow visualisation optical
system</u>

(1,2,4,5 & 8)
    Small front silvered mirrors
(3) 50% Beam splitter
(6 & 9) Negative lenes
(7) Holographic plate
(10) Large front silvered mirror
(11) Anti-reflection coated window

PULSE LASER
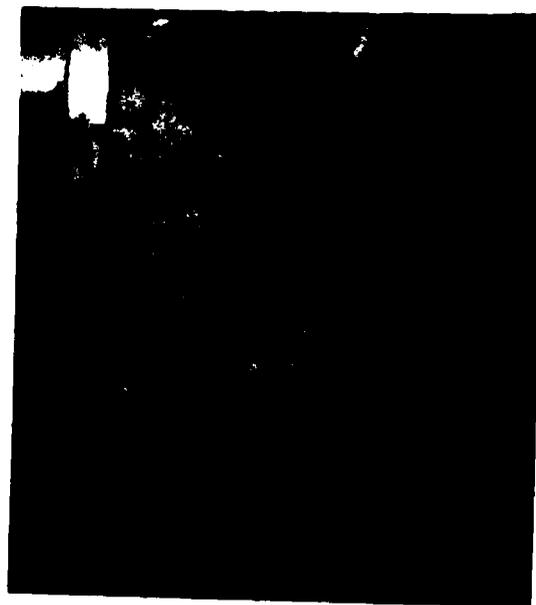
13.   A photographic reconstruction
made from a hologram of the shock
structure   within the EPFL Reynolds
number scaled annular steam turbine
cascade.
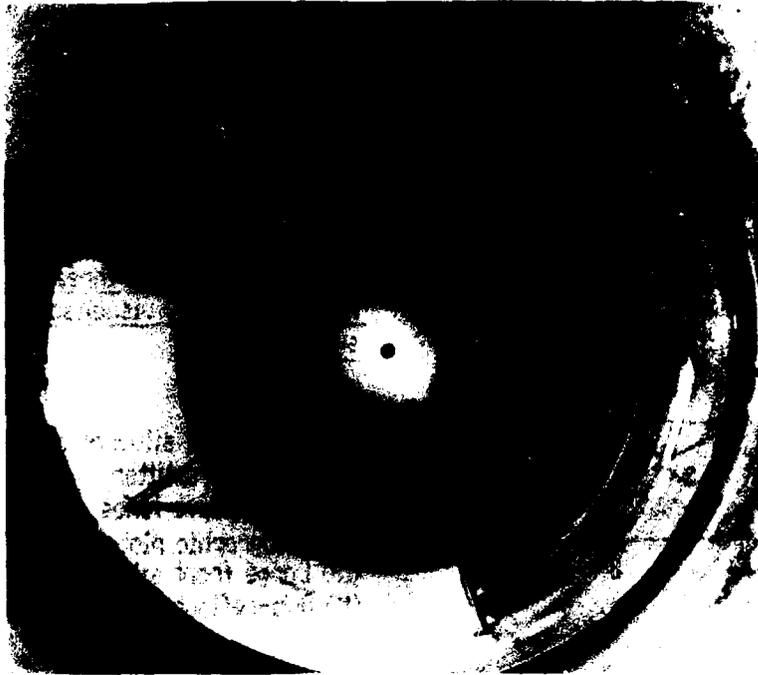
14.   Axial gas turbine first stage compressor fan as used in a holography test. The arrow points to the 19mm diameter negative lens through which the sample beam of the ruby pulse laser was expanded. The opposite side of the casing has been painted white to diffuse and reflect the laser light.
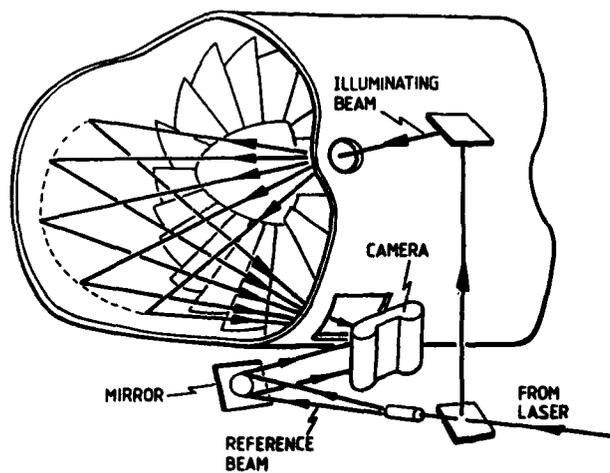
15.   Diagram showing the method by which the holographic system was applied to the first stage compressor fan.
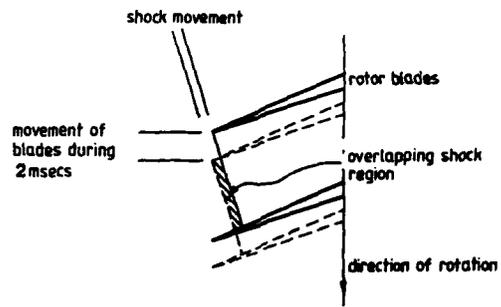
Movement of a normal shock between two pulses with a 2msecs separation.

16.   Diagram showing the movement of the compressor blade fan assembly between two holographic exposures.

17.   Photographic reconstruction showing the shock structure at the tip of the compressor fan as visualised using holography.
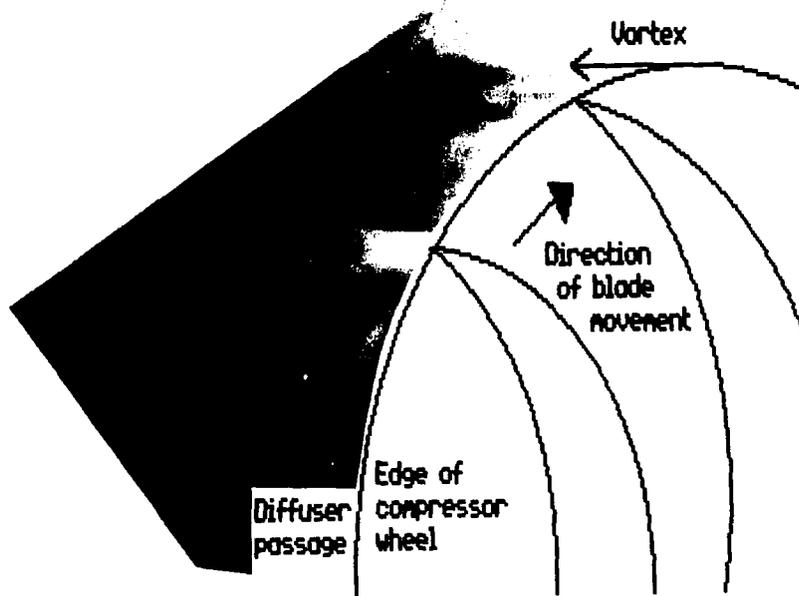
18. Vortex structure as visualised holographically in the diffuser section of a turbocharger rotating at 80,000 revs.

A STUDY OF PASSAGE FLOW THROUGH A CASCADE OF TURBINE BLADES USING IMAGE PLANE HOLOGRAPHIC INTERFEROMETRY

M.L.G. OLDFIELD
        Dept. of Engineering Science, University of Oxford, Parks Road, Oxford OX1 3PJ, UK

P.J. BRYANSTON-CROSS[1]   J.H. NICHOLSON[2]   C.T.J. SCRIVENER
        Rolls Royce plc, PO Box 31, Derby DE2 8BJ, UK

[1] Now at: Department of Engineering, Warwick University, Coventry CV4 7AL, UK
[2] Now at: Caledonian Air Motive, Prestwick International Airport, Prestwick, Scotland, UK

ABSTRACT

A series of holographic interferograms is presented, showing the flow through two passages of a cascade of turbine rotor blades in the Oxford Isentropic Light Piston Tunnel with full-scale Reynolds numbers, Mach numbers and gas-to-wall temperature ratios. Using a previously described technique, double exposure absolute and differential image plane holograms were obtained of the complete flowfield under a range of conditions. The isodensity contours predicted by a timemarching throughflow calculation compare well with the positions of the interference fringe on the holograms. The intersections of these fringes with the blade surfaces give blade surface Mach numbers which agree well with those from surface pressure measurements. Wakes, shock waves, and the presence of upstream and side wall turbulence are all evident in the holograms.

NOMENCLATURE

C	Dale-Gladstone coefficient	T	Temperature
Cax	Blade axial chord	Tg	Gas total temperature
L	Optical path length (blade span)	Tw	Wall temperature on blade
M	Mach Number	Tu	Turbulence level u/U
Me	Isentropic exit Mach number	X/Cax	Proportion of axial chord
N	Fringe number from stagnation point	γ	Ratio of specific heats
Re	Reynold's number based on exit isentropic conditions and blade tangential chord	λ	Wavelength of illuminating laser
		ρ	Gas density
		ρ_t	Upstream total density

INTRODUCTION

Flow visualisation techniques are powerful tools in helping to understand the complex flows in gas turbine blade passages. This is especially true when testing turbine blade profiles in two-dimensional cascade tunnels, where the blades can be mounted between optically high quality windows, giving optical access far superior to that available in a rotating turbine.

Although schlieren and shadowgraph techniques can be used to locate flow features such as shock waves and blade wakes, it is desirable to have quantitative measurements of the passage flow which can be compared with those predicted by the methods of computational fluid dynamics (CFD).

Laser doppler or laser 2-spot anemometry can determine the local velocity at a point in the flow, but to build up a complete flowfield takes considerable time and effort as the anemometer has to be scanned over the area of interest. This technique is also better suited to continuously running tunnels than it is to the short duration cascade tunnel used for this paper.

Two-dimensional image plane holography, as used in the work described here, can give a flow density map at a given instant of time, which can be easily compared with CFD predictions. It is ideally suited to short duration wind tunnels, as reference exposures can be made just before a tunnel run, and high quality interferograms can be obtained.

In this paper, holography is used to study the flowfield in a cascade of turbine blade profiles typical of those in modern single stage, high efficiency, high pressure turbine stages used in high bypass ratio civil engines. The holographic technique used is a refinement of that described in [1].

CASCADE TUNNEL

The Oxford Isentropic Light Piston Cascade Tunnel[2,3], employed in the work described in [1], was again used to provide a flow over a cascade of turbine blades at full-scale Reynolds and exit Mach numbers. Temperature ratios (Tg/Tw = upstream total temperature/blade surface temperature) of 1.5 and

1.0 were used with Tw at room temperature (approx. 288 K), giving tunnel runs lasting 0.4 sec. and 1.0 sec. respectively. Tunnel movements during the run were again, at most, $\pm$ 0.16 mm in any direction.

TEST CASCADE

The 7 passage linear cascade of turbine blade profiles used is shown in Fig. 1. The cascade geometry and nominal test conditions are shown in Table 1. The holographic work described here was part of a larger programme described by Nicholson [4] encompassing aerodynamic, CFD, and heat transfer studies as well as flow visualisation.

TABLE 1 CASCADE GEOMETRY and NOMINAL TEST CONDITIONS

Blade tangential chord	43.8 mm
Blade axial chord	33.7 mm
Blade span in cascade	50.0 mm
Cascade pitch	36.8 mm
Measured throat	13.92 mm
Inlet angle	42.75 $^{\circ}$
Inlet Mach number (measured)	0.31
Exit Mach number (based on inlet total and exit static pressure measured behind downstream expansion step)	
Design: Me =	0.96
M+ condition: Me =	1.20
Reynolds number (tangential chord, and isentropic exit conditions)	
Re =	2.0×10^{6}
Blade temperature Tw =	288 K
Upstream Total Temperature	
Hot flow:	Tg/Tw = 1.5
Tg =	432 K
Cold flow	Tg/Tw = 1.05
Tg =	303 K
Upstream total Pressure	
Hot flow: Pt =	510 kPa
Cold flow: Pt =	325 kPa
Upstream turbulence level	
Grid in Tu =	4.1%
Grid out Tu =	<0.2%
Stagnation density	
Hot flow ρ_t =	4.11 kg/m^3
cold flow ρ_t =	3.74 kg/m^3

The turbine blade profile used is a high efficiency single-stage high pressure turbine profile, designed using aerodynamic criteria alone. The same profile has been used in other studies [5,6,7,8] at a larger scale in a 5 passage cascade.

This profile performs best with a just subsonic exit Mach number, although results at a supersonic Mach number are also given here. Dimensions and nominal running conditions are given in Table 1.

The upstream turbulence experienced by a turbine rotor was simulated in some of the runs by placing a turbulence grid of circular bars upstream of the cascade, as shown in Fig. 1. Hot wire measurements, using the technique described in [3] measured the rms upstream turbulence level to be Tu = 4.1% with the grid in place and Tu < 0.2% with it removed. Temperature fluctuations with the grid in were < 0.2% rms even with hot flow passing over a cold turbulence grid.

HOLOGRAPHIC SYSTEM

The optical system used in these experiments was similar to the two-dimensional, image plane system previously described in [1], and shown in Fig. 2.

Image plane holography dispenses with the inherently three-dimensional nature of holograms in order to yield high resolution two-dimensional images with minimum aberrations due to diffraction and refraction of the light rays as they pass through the test section.

White light reconstruction was again used (Fig. 3) in order to avoid the speckle pattern normally associated with holographic images.

Two types of holograms were taken:

(a) Absolute Holograms.
A reference exposure is made by firing the laser just before the tunnel run, and a second exposure is taken during the run. The interference fringes on the image reconstructed from the hologram can be interpreted as contours of constant density in the cascade passage.

In [1] it is shown that, if fringes are counted from a stagnation point with stagnation density ρ_t, the local density at fringe number N is given by

$$\frac{\rho}{\rho_t} = 1 - \frac{N\lambda}{\rho_t LC} \qquad (1)$$

and the local isentropic Mach number by

$$M^2 = \frac{2}{\gamma-1}((1 - \frac{N\lambda}{\rho_t LC})^{-(\gamma-1)} - 1) \qquad (2)$$

here the Dale-Gladstone coefficient $C = 2.25 \times 10^{-4}$ m^3/kg for air at the wavelength $\lambda = 694.3$ nm used.

(b) Differential Holograms.
The two exposures (or laser pulses) are separated by 100μs and the interference fringes represent contours of constant density change in 100 μs. This type of hologram proved useful in locating freestream turbulent features, unsteady wakes and shock waves.

The image plane holographic techniques described in [1] have been used to study transonic flow around an airfoil [9] and a wedge [10]. Similar techniques have been used by Lee et al.[11] .

A number of steps were taken to improve the quality of the reconstructed holographic interferograms compared with those shown in [1]:

(a)   the blades were more rigidly mounted to prevent blade movement due to flow forces between the reference (no flow) and second (with flow) exposures.

(b)   experiments showed that the effects of refraction in the density gradients associated with the blade surface boundary layers could be minimised by focussing the optical system on the mid-span plane of the cascade, as would normally be done with a schlieren system. The blades were painted matt black to minimise the effects of surface reflection. Diffraction from the blade edges was considered secondary to the above effects and no direct attempts were made to minimise its effect.

(c)   The viewing area was increased by using larger windows showing two complete passages, and care was taken to ensure uniform laser illumination.

(d)   Spurious fringe shifts across the image were significantly reduced by using a more rigid optical bench, and great care was taken to isolate the bench from sources of movement.

SCHLIEREN FLOW VISUALISATION

Figs. 4 and 5 show conventional spark schlieren images of the cascade flowfield with hot turbulent upstream conditions at Me = 0.96 and Me = 1.2. Sharp flow features such as shock waves and wakes are readily apparent, as schlieren detects density gradients, but the Mach number variation through the passage cannot easily be determined.

It must be noted that Figs. 4 and 5 indicate excellent periodicity in this 7 passage cascade, even at the design exit Mach number, where there are multiple moving shock waves in the transonic region, adjacent to the suction surface.

ABSOLUTE HOLOGRAMS OF THE FLOW

Initially, absolute holograms were taken of the flow with the (4.1%) turbulence grid in place and with hot upstream flow, conditions which are normally considered to best model the turbine flow. When interpreted as lines of constant density, the fringes shown in Fig.6 (Me = 0.96) and Fig.7 (Me = 1.20) clearly show the density changes due to the acceleration of the flow through the passage. the leading edge stagnation points are encircled by small fringes, and the shock wave structure, weak in Fig.6, coalesces at the higher exit Mach Number in Fig.7 to a well defined trailing edge shock system. Evidence of the presence of a regular Karman vortex street in the blade wake flow is stronger in Fig.6.

There are, however, two features apparent in Figs. 6 and 7 which required further investigation:

(i) The fringes are rough in shape, and exhibit random kinks. the supposedly uniform upstream flowfield is filled with a random fringe pattern.

(ii) A careful count of fringes from one blade leading edge to the next shows that there are overall fringe number shifts of one or more between the same points on different blades.

The roughness (i) was found to be due to random turbulent density fluctuations in the flow. This arose from two sources:

Firstly, there is the 4.1% level of freestream turbulence created by the upstream grid (Fig.1), which would be expected to generate random fringe shifts. However, a hot (Tg/Tw = 1.5) run (Fig.8) with the turbulence grid removed still showed considerable random fringe structure.

It was then realised that the turbulent boundary layers on the tunnel windows, normal to the line of sight, contain random density fluctuations due to the temperature difference between the cold (288K) windows and the hot (432K) flow. Although the analysis given in [1] shows that the time averaged change in optical path length due to the temperature gradients in both window boundary layers was only 0.8 mm in a 50 mm blade span (1.4%), the random density structures in these turbulent boundary layers can easily generate the observed fringe shifts.

This source of fringe randomness was removed by running the tunnel cold, with the flow total temperature just above that of the windows, in order to have insignificant turbulent temperature fluctuations in the window boundary layers. Fig.9 shows the flowfield with cold flow (Tg/Tw = 1.05) with the turbulence grid in place. It is noticeable that the random fringe fluctuations due to grid turbulence in this figure are of a longer length scale, or a lower spatial frequency, than those due to the window boundary layers in Fig.8. Although this is partially due to the greater low frequency energy content of the grid produced turbulence, the main contributing factor is the integration of the density field over the 50 mm optical path corresponding to the blade span. This will reduce the visibility of turbulent structures having a length scale of less than 50 mm. For a typical cascade inlet velocity of 100 m/s, this corresponds to a low pass filter with an upper frequency cut off starting at 2 kHz. This implies that much of the 300 Hz - 100 kHz measured turbulence spectrum upstream of the cascade, reported in [4], will not be seen in Fig.9. In Fig.8 the effective integration length for the window boundary layers is much smaller, of the order of 2 mm, and so smaller scale structures are evident.

the overall fringe shifts between blades are evident with the grid in (Figs. 6,7, and 9), but not with the grid out (Fig.8), which indicates that they arise from the presence of low frequency, large scale, turbulent structures in the grid produced turbulence which are missing in the window boundary layers.

To obtain Holograms yielding interferograms which may usefully be compared with CFD two-dimensional flowfield predictions, it is necessary to run the tunnel both with cold flow and without the turbulence grid. Fig.10 shows a hologram taken with Tg/Tw = 1.05 and Tu < 0.2%. In this case density fluctuations caused by temperature or velocity fluctuations, and the window boundary layer density fluctuations, are minimised. The interferogram shows excellent passage to passage repeatability, and the region upstream of the blade row is of constant density. The fringes have smooth profiles except in regions of secondary corner flow on the latter half of the suction surface, and where the horseshoe vortex can be seen as a kink in the fringes.

The density changes in the blade wakes can be clearly seen, with a periodic vortex structure. the multiple shock waves on the suction surface seen previously in Figs. 4 and 6 are evident as kinks in the fringes.

It had initially been hoped that holographic interferograms, such as Fig.10, would have yielded useful quantitative information in the blade surface boundary layers. Unfortunately, in practice, the fringes due to the boundary layer density gradients are distorted by refraction and diffraction effects and accurate measurements are difficult to obtain. Qualitatively, however, it is readily apparent that the boundary layer on the latter part of the suction surface is, as expected, thicker than that of the pressure surface. The increase of density approaching the blade surface is visible as a distinct kink in the fringes.

It is important to emphasise that these holograms portray the flow at an instant in time, and do not show a time averaged view.

DIFFERENTIAL HOLOGRAMS OF THE FLOW

Differential holograms, taken with both hot and cold flow, and with and with the turbulence grid in, confirm the overall picture shown in the absolute holograms. Being sensitive to changes of density with time, they highlight unsteady features in the flowfield. the 100 μs pulse separation used corresponds to a convective displacement of about 10 mm in the upstream flow and thus will emphasise structures smaller than this.

Following the sequence of the absolute holograms, fig. 11 shows the flow for Tg/Tw = 1.5 and Tu = 4.1%. Although the suction surface shock waves and the wakes can be discerned, the image is dominated by the random fluctuations in the turbulent mainstream and in the window boundary layers.

Removing the turbulence grid, but leaving the flow hot (Fig.12) again demonstrates that the high frequency fluctuations are due to the window boundary layers.

Running the tunnel cold, but with the grid in (Fig.13) confirms that integration along the optical path over the cascade span shows only the lower frequency components of the upstream turbulence.

Fig.14 shows the cascade with cold low-turbulence flow. Except for slight spurious fringing not related to the flow, the upstream flow is steady. The moving suction surface shock waves are evident, together with Mach waves generated by the periodic wake shedding at the trailing edge. The vortex street in the wake is also clearly seen.

The high frequency disturbances in the region adjacent to the latter part of the suction surface are due to the local turbulent secondary flow region on the corner between the blade and the window side wall. Oil dot surface flow visualisation results, shown in [4], confirm the existence of this region, which by the trailing edge, extends over about 12% of the blade span on the suction surface.

By chance, an overall shift of half a fringe between exposures in the differential hologram shown in Fig.15 highlights a not often seen feature of the flow. If the background of spurious closely spaced fringes is ignored, the core of the horseshoe vortex can be clearly seen as a long kinked line stretching from near the leading edge into the passage on the pressure surface side. It is interesting to note that the position of this core is unsteady both in position and in time. Careful subsequent examination of other schlieren and holographic images have confirmed the existence of these unsteady vortex cores which are apparently unstable even with steady, low-turbulence flow upstream of the cascade. Can present CFD techniques predict this?

COMPARISON WITH BLADE SURFACE PRESSURE MEASUREMENTS

By locating the position of the intersection of the free stream fringes with the blade surface in an absolute hologram, the blade surface Mach number distribution can be computed. this was done by extrapolating the fringe normal to the blade surface at the point where the fringes change direction suddenly because of the density gradients in the boundary layer. The surface isentropic Mach number was then calculated at the edge of the boundary layer, with the standard assumption of constant static pressure across the boundary layer, by using Equation (2).

Fig.16 compares the surface Mach number distribution obtained from the cold flow, low-turbulence hologram in Fig.10 with that deduced from static pressure measurements at the blade surface. The error bars on the holographic data represent an error of 1/2 a fringe, arising mainly from the uncertainty of locating the stagnation fringe, and they show that the errors become large for regions where M < 0.2 .

With care, the hot turbulent flow holograms can also be used. Fig.17 shows a similar comparison obtained from Fig.7 .

In both cases the agreement is good, particularly over the suction surface. The differences in the region where the shock wave meets the suction surface arise from the hologram accurately locating shock at one instant of time in the run, whereas the time averaged surface pressure measurements broaden the apparent location of the shock, which moves slightly during the run.

COMPARISON WITH TIMEMARCHING CFD PREDICTION

The absolute holograms provide useful experimental data with which to compare CFD flowfield predictions. Nicholson [4] describes the use of the timemarching techniques developed by Denton [12] to predict the two-dimensional passage flowfield in the cascade described in this paper.

Comparisons between the isodensity contours obtained from the absolute holograms in Figs. 10 and 7 and from the timemarching program are shown in Figs. 18 and 19 . Generally, the agreement between the prediction and the experiment is good, except where 3-dimensional secondary flow features affect the hologram, and in the region of shock waves, which are broadened by the prediction technique. Certainly, absolute holograms provide an excellent experimental check on the accuracy and assumptions of CFD techniques.

CONCLUSIONS

Two dimensional image plane holography with white light reconstruction has been used to obtain absolute interferograms showing two passages of the flowfield in a two dimensional cascade of high efficiency turbine blades. Results obtained from these holograms compare well with those obtained from blade surface pressure measurements and from timemarching CFD predictions.

Differential holograms were used to study unsteady flow features, such as shock waves, wakes and secondary flow. It was found that the observed pattern of isodensity interference fringes could be corrupted by turbulence in the freestream and by turbulent temperature variations in the window boundary layers. the most suitable holograms for comparison with other flowfield measurements and predictions are obtained by using and ambient total temperature, low turbulence flow though the test cascade.

ACKNOWLEDGEMENTS

REFERENCES

1. P.J. Bryanston-Cross, T. Lang, M.L.G. Oldfield and R.J.G. Norton. Interferometric Measurements in a Turbine Cascade using Image-Plane Holography. Journal of Engineering for Power, Vol. 103, 124-130, Jan 1981.

2. D.L. Schultz, T.V. Jones, M.L.G. Oldfield and L.C. Daniels. A New Transient Cascade Facility for the Measurement of Heat Transfer Rates. AGARD-CP-229, 1977 .

3. M.L.G. Oldfield, T.V. Jones and D.L. Schultz. On-line Computer for Transient Turbine Cascade Instrumentation. IEEE Transactions on Aerospace and Electronic Systems, Vol. AES-14, 738-749, Sept. 1978.

4.   J.H. Nicholson. Experimental and Theoretical Studies of the Aerodynamic and Thermal Performance of Modern Gas Turbine blades. D.Phil. Thesis, Oxford University, 1981.

5.   F.G. Horton, D.L. Schults, and A.E. Forest. Heat transfer Measurements with film Cooling on a Turbine Blade Profile in Cascade. Paper 85-GT-117 presented at ASME Gas Turbine Conference, Houston, March 1985 .

6.   D.J. Doorly and M.L.G. Oldfield. Simulation of Wake-Passing in a Stationary Turbine Rotor Cascade. AIAA Journal of Propulsion and Power, Vol.1, 316-318, July-Aug 1985 .

7.   D.J. Doorly, M.L.G. Oldfield and C.T.J. Scrivener.   Wake Passing in a Turbine Rotor Cascade. AGARD-CP-390, 1985.

8.   D.J. Doorly and M.L.G. Oldfield.   Simulation of the effects of shock Wave Passing on a turbine Rotor Blade. Journal of Engineering for Gas Turbines and Power, Vol. 107, 998-1006, Oct. 1985 .

9.   P.J. Bryanston-Cross and J.D. Denton. Comparison of Measured and Predicted Transonic Flow around an Airfoil, AIAA Journal Vol. 22, 1025-1026, Aug. 1984 .

10.   P.J. Bryanston-Cross and W.N. Dawes.   Comparison of Inviscid and Viscous Computations with an Interferometrically Measured Transonic Flow. AIAA Journal Vol. 23, 834-839, June 1985 .

11.   G. Lee, D.A. Buell, J.P. Licursi and J.E. Craig. Laser Holographic Interferometry for an Unsteady Airfoil Undergoing Dynamic Stall, AIAA Journal Vol. 22, 504-511, April 1985 .

12.   J.D. Denton.   A Timemarching Method for Two and Three dimensional Blade to Blade Flows. ARC R M 3775, 1975 .
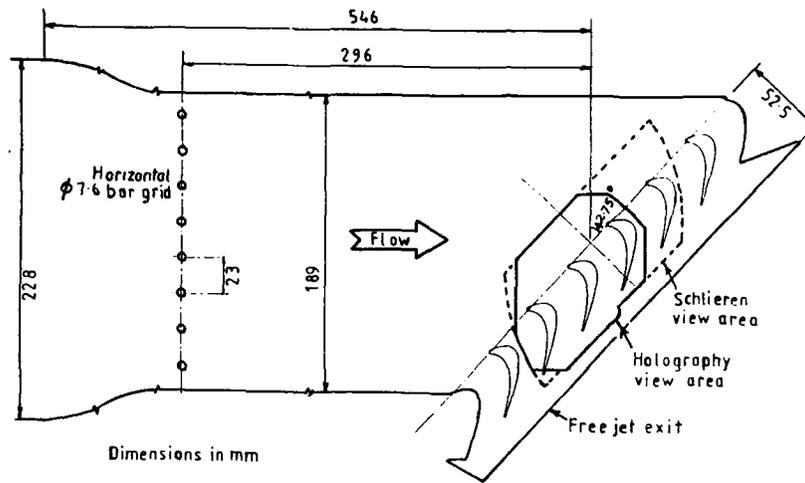
Fig 1. General arrangement of Test cascade.
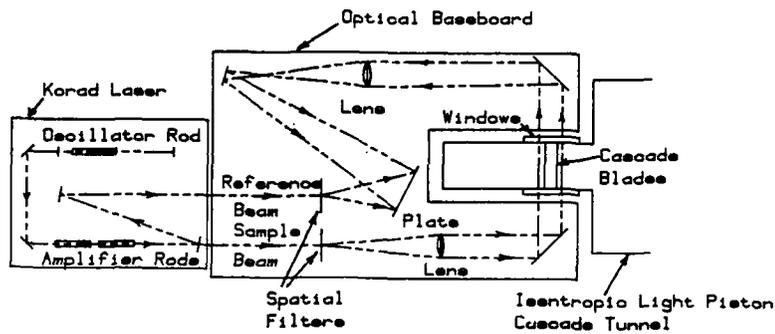
Fig 2. Optical System used to obtain image plane
holograms of the cascade flow (from [1]).
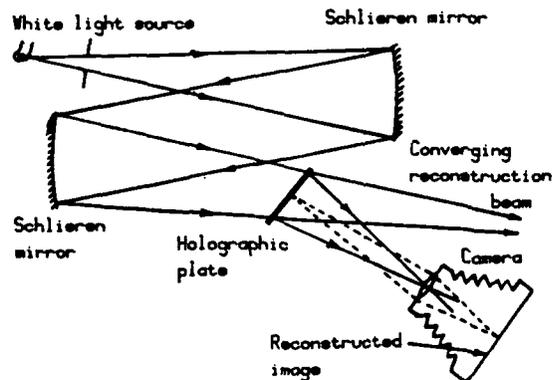
Fig 3. White light reconstruction system (from [1]).

Fig 4. Spark schlieren photograph of cascade flow
Re = 2.0x10^6, Me = 0.96, Tu = 4.1%, Tg/Tw = 1.5

Fig 5. Spark schlieren photograph of cascade flow
at M=+ conditions.
Re = 2.0x10^6, Me = 1.20, Tu = 4.1%, Tg/Tw = 1.5

Fig 6. Absolute hologram of cascade
with hot turbulent upstream flow.
Re = 2.0x10^6, Me = 0.96, Tu = 4.1%, Tg/Tw = 1.5

Fig 7. Absolute hologram of cascade at M+
with hot turbulent upstream flow.
Re = 2.0x10^6, Me = 1.18, Tu = 4.1%, Tg/Tw = 1.5

Fig 8.   Absolute hologram of cascade
      with hot low-turbulence upstream flow.

Re = 2.0x10^6, Me = 0.96, Tu < 0.2%, Tg/Tw = 1.5

Fig 9.   Absolute hologram of cascade
      with cold turbulent upstream flow.

Re = 2.0x10^6, Me = 0.96, Tu = 4.1%, Tg/Tw = 1.05

Fig 10.   Absolute hologram of cascade
      with cold low-turbulence upstream flow.

Re = 2.0x10^6, Me = 0.96, Tu < 0.2%, Tg/Tw = 1.05

Fig 11.   Differential hologram (100μs separation)
      with hot turbulent upstream flow.

Re = 2.0x10^6, Me = 0.96, Tu = 4.1%, Tg/Tw = 1.5

Fig 12.   Differential hologram (100μs separation)
with hot low-turbulence upstream flow.

Re = 2.0x10^6, Me = 0.96, Tu < 0.2%, Tg/Tw = 1.5
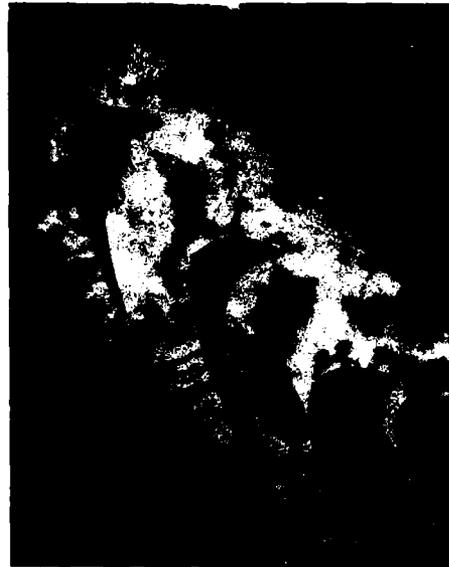
Fig 13.   Differential hologram (100μs separation)
with cold turbulent upstream flow.

Re = 2.0x10^6, Me = 0.96, Tu = 4.1%, Tg/Tw = 1.05

Fig 14.   Differential hologram (100μs separation)
with cold low-turbulence upstream flow.

Re = 2.0x10^6, Me = 0.96, Tu < 0.2%, Tg/Tw = 1.05

Fig 15.   Differential hologram (100μs separation)
with cold low-turbulence upstream flow,
showing horseshoe vortex.

Re = 2.0x10^6, Me = 0.96, Tu < 0.2%, Tg/Tw = 1.05
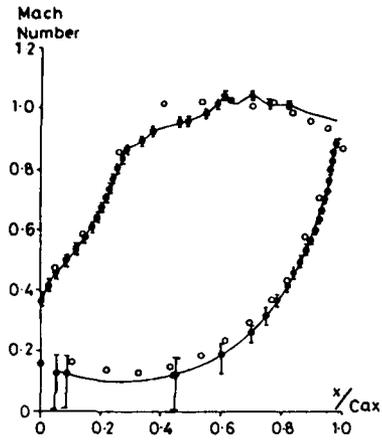
Fig 16. Comparison of blade surface Mach number distribution from Fig 10 hologram with that from blade surface static pressure tappings. Me = 0.96.
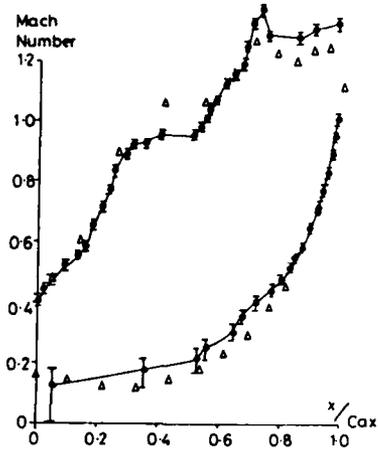
Fig 17. Comparison of blade surface Mach number distribution from Fig 7 hologram with that from blade surface static pressure tappings. Me = 1.18.

Isodensities from Timemarching Prediction

Isodensities from Hologram

Isodensities from Timemarching Prediction
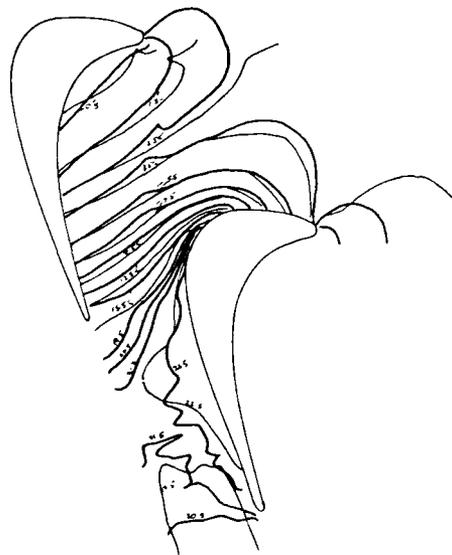
Isodensities from Hologram

Shock wave pattern from hologram

Fig 18. Comparison of isodensity contours from Fig 10 hologram with timemarching predictions. Me = 0.96.

Fig 19. Comparison of isodensity contours from Fig 7 hologram with timemarching predictions. Me = 1.18.

DISCUSSION

H.J.Lichtfuss, GE

Your Schlieren pictures clearly show side wall effects as horse-shoe vortices and secondary flows and you clearly indicated that your Schlieren figures are averages over the profile span. On the other hand, the comparison of profile pressure distribution at mid span, between Schlieren and pressure top results does not show such discrepancies to be associated to side wall effects. Could you please explain this?

Author's Reply

Schlieren photography is sensitive to the spatial derivative of the flowfield in a direction perpendicular to the optical path. Hence it emphasizes sharp discontinuities in the flow, such as shock waves, wakes and secondary flow vortices, and is insensitive to the background passage density field. On the other hand absolute holograms, such as in fig.10 are directly sensitive to the absolute density field, and secondary flow features represent only small perturbations of the fringe pattern of the two dimensional field integrated over the 50 mm span.

For example, in fig.10, the horse-shoe vortex causes a fringe shift of less than half a fringe, which is within the accuracy assumed when making the comparisons in figs 16—19.

However, we agree that care must be taken to ensure that the holograms are sufficiently representative of two dimensional flow before comparing them with other 2D measurements and predictions.

W.G.Alwang, US

(1) What part of the horse-shoe vortex are you seeing?

(2) Do you think that diffuse illumination would allow better definition of the 3D nature of the vortex? i.e. localization of the density variations.

Author's Reply

(1) We think they are the corner secondary flow vortex cores and that they are close to the ends of the blade.

(2) It should be possible to visualize the vortex by the manner you describe. In a similar situation [10], the vortex structure within a supersonic boundary layer was visualized.

BEAM-MODULATION METHODS IN QUANTITATIVE AND FLOW-VISUALIZATION HOLOGRAPHIC INTERFEROMETRY

Arthur J. Decker
National Aeronautics and Space Administration
Lewis Research Center
Cleveland, Ohio 44135

SUMMARY

This report discusses heterodyne holographic interferometry and time-average holography with a frequency shifted reference beam. Both methods will be used for the measurement and visualization of internal transonic flows, where the target facility is a flutter cascade. The background and experimental requirements for both methods are reviewed. Measurements using heterodyne holographic interferometry are presented. The performance of the laser required for time-average holography of time-varying transonic flows is discussed.

INTRODUCTION

Among the beam-modulation methods described in the literature are diffuse-illumination heterodyne holographic interfereometry[1-4] and diffuse-illumination time-average holography with frequency modulation of the reference wave.[5-7] A goal at NASA Lewis Research Center is to implement both methods in a test-cell environment as well as in the laboratory. The intended applications are structural analysis, flow visualization, and flow-properties measurements.

The technological problems and details that must be attended to for these methods are similar for structural analysis and for the measurement or visualization of internal transonic flows. This paper, then, centers on internal transonic flows, although we are by no means exclusively or even primarily interested in this flow region. A major factor is that a number of transonic-flow facilities have been constructed in the past decade.[8-12] Some of these facilities are available for evaluating heterodyne and time-average holography. The degree of difficulty is realistic: techniques which have some successes in the internal transonic environment are likely to be transferable to other applications in the field. One particular facility, a flutter cascade of blades vibrating in a pitching motion, has been tested with schlieren,[11] rainbow schlieren,[13] and holographic flow visualization,[14] and is convenient for a test of the beam modulation methods.

Some difficulties in implementing diffuse-illumination, heterodyne, holographic interferometry for flow measurements are generation of the two reference beams required and transference of alignment from the test-cell to the hologram readout station. Other difficulties are the generation of a fringe pattern with enough contrast or signal-to-noise, and the avoidance of time-varying fringe patterns produced by components other than the flow.

A major incentive for overcoming these difficulties is that the necessary hardware for both methods is available off-the-shelf, with minimal modifications. For the heterodyne techniques, this hardware includes pulsed lasers with interpulse beam-switching capability, stable continuous wave lasers, acoustooptic frequency shifters, and inexpensive computers and computer controlled accessories.

The major difficulty in implementing time-average holography for flow visualization is the acquisition of a suitable laser system. For time-average holography, there is at least one long-pulse flashlamp-pumped dye laser with good beam uniformity, which requires some modifications for the holographic application. This laser is being acquired for evaluation, since it offers the combination of energy and pulse length required for transonic flow visualization.

The available hardware makes it possible and desirable to take advantage of some well known properties of heterodyne and time-average holographic interferometry. Included are the high precision, the continuous fringe interpolation capability, and the computer compatibility of heterodyne interferometry, and the fringe-contrast control capability of time-average holography. These properties are combined with the advantages and disadvantages of diffuse-illumination interferometry, including the fringe-localization effect, three-dimensional measurements and visualization, and the noise of the laser speckle effect.

This paper summarizes some steps taken and conclusions arrived at in the NASA Lewis program. A general background for beam modulation methods is presented: diffuse-illumination heterodyne and time-average holography are two special cases. Then the quantitative fundamentals of these two special cases are reviewed, and the status of the implementation of these cases is discussed in terms of hardware, tests, experimental results, and future potential.

BACKGROUND

Most of the concepts of holographic optical processing of the past 24 years can be represented by two equations. At the recording plane H of a two-dimensional hologram, the reconstructed wave satisfies the proportionality

$$O_R(r_H,t) \propto \int S(r_H,t')O(r_H,t')R^*(r_H,t')R_R(r_H,t) \, dt' \tag{1}$$

where

$O(r_H,t)$ is the object wave,

$R(r_H,t)$ is the reference wave,

$R_R(r_H,t)$ is the reconstruction wave,

and $S(r_H,t)$ is the shutter function, which can be absorbed mathematically in the reference wave. The position on the hologram is denoted by r_H, and all functions potentially have a relative time dependence denoted by t.

A second equation is obtained by including linear operations preceding and following the hologram recording step. If an object wave $O_0(r_0,t)$ originates at positions r_0 and a reconstructed wave $O_R(r_D,t)$ is subsequently detected at positions r_D, then

$$O_R(r_D,t) \propto \int\int\int\int\int \quad h_R(r_D;r_H;t;t_H)h(r_H;r_0;t_H';t_0)O_0(r_0,t_0)$$
$$R^*(r_H,t_H')R_R(r_H,t_H) \, dt_H \, dr_H \, dt_H' \, dt_0 \, dr_0 \tag{2}$$

where h_R and h are impulse response functions connecting the detection (r_D,t), the reconstruction (r_H,t_H), the recording (r_H,t_H'), and the object (r_0,t_0) coordinates and times.

The selections of R and R_R can be used to enhance the visualization of the object wave O_0, or to condition the object wave for measurements and analysis.

For methods discussed in this paper, R and R_R are carefully matched geometrically, so as to faithfully reconstruct the object wave fronts. The form of the output wave O_R is determined by time modulation of R and R_R. Diffuse-illumination holography is used exclusively, and the usual geometrical optics viewpoint is adopted. The consequences of these choices are summarized next.

Diffuse-Illumination Interferometry[15]

In diffuse-illumination holography, light rays arrive at each point r_H at the hologram recording plane from all parts of the fluid. For linear recording, the light rays are treated independently. Associated with the direction of polarization of the reference wave, each light ray has a magnitude and a phase, where the phase has both a random and a deterministic part. For a time-varying fluid, the deterministic part has a time variation apart from the variation at the frequency of light. The impulse-response functions in Eq. (2) are associated with the propagation and imaging of light rays, and need not be mentioned again. Where different light rays intersect, the random component of phase leads to a high frequency interference effect called the laser speckle effect. Within a given light ray, the time variation of phase is given by a familiar expression

$$\phi(t) = \frac{2\pi}{\lambda} G \int_{S_1}^{S_2} \rho(r,t) \, dS \tag{3}$$

where λ is the wavelength of the laser beam, G is the Gladstone-Dale coefficient ($G = 0.227 \times 10^{-3}$ m³/kg for air at $\lambda = 532$ nm), $\rho(r,t)$ is the density as a function of position on the light ray r and the time t, and S is the distance along the light ray.

The light rays themselves are generally curved lines, but, for the internal-flow facilities treated herein, it is reasonable to assume that the rays are straight lines (refractionless limit).[16,17] A fringe pattern is formed as in Fig. 1, when the light rays are superimposed by imaging. Except for explaining the speckle effect, the intensities of the individual light rays add independently, so that the interference pattern I is given by the proportionality.

$$I \propto \sum_i I_{1i} + \sum_i I_{2i} \cos(\Delta\phi_i) \tag{4}$$

where i is a ray-to-ray summation index, carried over an imaging pencil, and $\Delta\phi_i$ is the phase relative to a reference.

The fringe pattern will have high contrast only for those images of points where the variation of $\Delta\phi_i$ is negligible within the imaging pencil. Then, a first-order criterion for high contrast is the fringe localization condition

$$\partial\Delta\phi/\partial\theta_{ix} = 0 \qquad \partial\Delta\phi/\partial\theta_{iy} = 0 \tag{5}$$

where θ_{ix} and θ_{iy} are angles about the central ray z in the xz and yz planes, respectively (Fig. 1). When θ_{ix} and θ_{iy} are not independent as in slit viewing, a single localization equation applies.

Equations (4) and (5) imply that each point in a high-contrast fringe pattern can be associated with the central ray of the imaging pencil. The intensity is determined by the interferometric phase for that ray as given by Eq. (3). For some flow features such as shock-wave surfaces,[14,18-19] Eq. (5) predicts that localization will occur nearby, on, or within the flow feature, thereby providing three-dimensional visualization of the flow feature.

Double-exposure techniques for performing measurements or visualization based on Eqs. (1) to (5) are reviewed next.

Double-Exposure Techniques

Ordinary double-exposure holographic interferometry, heterodyne holographic interferometry, and quasi-heterodyne holographic interferometry are derivable from Eq. (1). In all cases, individual exposures are short when compared with the time variation of $\Delta\phi$. Then the shutter function is represented by the proportionality

$$S(r_H, t) \propto \delta(t) + \delta(t-T) \tag{6}$$

where T is the time between exposures, and the reconstructed ray is represented by the proportionality

$$O_R(r_H, t) \propto O(r_H, 0)R^*(r_H, 0)R_R(r_H, t) + O(r_H, T)R^*(r_H, T)R_R(r_H, t) \tag{7}$$

In Eq. (7), the phase difference between exposures (interference phase) is given by

$$\Delta\phi = \frac{2\pi}{\lambda} G \int [\rho(r_H, T) - \rho(r_H, 0)] \, dS \tag{8}$$

and the interference pattern is of course proportional to

$$/O_R(r_H, t)/^2$$

For a faithful reconstruction of the geometry of a light ray, the reconstruction wave has the form

$$R_R(r_H, T) = \mathcal{A}(r_H, 0) \exp [j(\gamma_0(r_H) + \omega_0 t)] + R(r_H, T) \exp [j(\gamma_T(r_H) + \omega_T t)] \tag{9}$$

where the γ's are phase shifts and the ω's are circular light frequencies. That is, the reference wave at each of the two exposures is matched by one term of the reconstruction wave, except possibly for a small phase shift and a frequency offset.

For ordinary double-exposure holography, the geometry and time-independent phase of the reference do not change between exposures and are matched during reconstruction.

$$R(r_H, 0) = R(r_H, T)$$

$$\gamma_0(r_H) = \gamma_T(r_H)$$

$$\omega_T = \omega_0$$

The interference pattern has the general form

$$I = I_1 + I_2 \cos(\Delta\phi) \tag{10}$$

where the interference phase is given by Eq. (8).

For the heterodyne techniques, the reference beams are geometrically distinct at the two exposures.

Then, for heterodyne holographic interferometry,

$$R(r_H, 0) \neq R(r_H, T)$$

$$\gamma_0(r_H) = \gamma_T(r_H)$$

$$\omega_0 \neq \omega_T$$

and the interference pattern assumes the time varying form

$$I = I_1 + I_2 \cos[\Delta\phi + (\omega_T - \omega_0)t] \qquad (11)$$

The interference phase can be measured relative to a reference by using a phase sensitive detector.

For quasi-heterodyne holographic interferometry,

$$R(r_H, 0) \neq R(r_H, T)$$

$$\gamma_0(r_H) \neq \gamma_T(r_H)$$

$$\omega_0 = \omega_T$$

and the interference pattern has the form

$$I = I_1 + I_2 \cos[\Delta\phi + \gamma_T(r_H) - \gamma_0(r_H)] \qquad (12)$$

If $\Delta\gamma(r_H)$ is given three different values, typically 0, 120, and 240°, and if I is measured at each value, then the interference phase is given by

$$\Delta\phi = \tan^{-1}\left[\frac{\sqrt{3}\,(I_{240} - I_{120})}{(2I_0 - I_{120} - I_{240})}\right] \qquad (13)$$

It is also to be noted that the choice of $\Delta\gamma(r_H)$ can be used to modify or control fringe contrast and fringe localization. Equation (5) assumes the modified form

$$\partial[\Delta\phi(r_H) + \Delta\gamma(r_H)]/\partial\theta_{ix} = 0$$
$$\partial[\Delta\phi(r_H) + \Delta\gamma(r_H)]/\partial\theta_{iy} = 0 \qquad (14)$$

In this paper, the modification of fringe contrast is left to time-average holography, the next topic for review.

Time-Average Holography[20]

For time-average holography, the reference and reconstruction beams are geometrically identical. The reference wave may have a relative time dependence. For an exposure time T, the reconstructed wave from Eq. (1) is given by the proportionality

$$O_R(r_H) \propto \int_0^T O(r_H, t')/R(r_H)/^2 \exp[-j\gamma(r_H, t')]\, dt' \qquad (15)$$

where $\gamma(r_H, t)$ represents the relative time dependence of the phase of the reference wave. In terms of the time varying phases of the reference and object waves, the reconstructed wave satisfies the proportionally

$$O_R(r_H) \propto \int_0^T \exp[j(\Delta\phi(r_H, t') - \gamma(r_H, t'))]\, dt' \qquad (16)$$

Time-average analysis is easiest when the time and position dependences of the phases can be separated.[20] To first order for a flow, that separation assumes the form

$$\Delta\phi(r_H, t) = t\phi_r(r_H) \qquad (17)$$

If the time dependence of the reference wave is chosen to have the same form, then

$$\gamma(r_H, t) = t\gamma_r(r_H) \qquad (18)$$

For these time dependences, Eq. (16) reduces to

$$O_R \propto \frac{T\sin[(\phi_r(r_H) - \gamma_r(r_H))T/2]}{[(\phi_r(r_H) - \gamma_r(r_H))T/2]} \qquad (19)$$

A brightest fringe will occur when $\phi_r - \gamma_r = 0$, where $\gamma_r(r_H)$ is a simple shift in the circular frequency of the reference wave. Hence, for flow visualization, the highest contrast can be chosen for the flow-feature of interest, by the correct choice of a frequency offset of the reference wave.

IMPLEMENTATION OF HETERODYNE HOLOGRAPHIC INTERFEROMETRY

Objective and Requirements

The eventual objective is to perform heterodyne diffuse-illumination holographic interferometry in a nine-blade transonic flutter cascade. The blades in this machine are vibrated about their midchord axes to simulate aeroelastic instability or flutter.[11] The density field is time dependent as a result of this motion. Holographic flow visualization has been performed in this cascade, and its performance for holography has been well documented.[14]

The flutter cascade is a fairly difficult test rig for performing holographic interferometry, and any positive results would be encouraging. Diffuse-illumination holographic interferometry is performed by shining a laser beam through a window in the front side-wall of the cascade, by reflecting it from the diffusely reflecting back side-wall, and by recording the reflected light after it has passed between the blades and back out the window. Because of the blades and other restrictions on access, there is a narrow angle for shadow-free illumination of the interblade passages. It is difficult to avoid recording holograms of the reflections from the window and blades. These reflections may be particularly destructive to heterodyne holography, since their spurious signals can cause systematic phase errors.

Holographic interferometry in wind tunnels such as the flutter cascade requires a double-pulse, Q-switched laser. The laser available for implementing holography in the nine-blade flutter cascade at NASA Lewis is a frequency-doubled Nd:YAG laser, which is optimized to operate at 20 double exposures/sec. The exposure separation can be varied from about 3 to 100 μs. Other suitable lasers would be the ruby laser and possibly the alexandrite laser.

An additional requirement of the heterodyne techniques is the ability to change reference beams between exposures. Ruby lasers, intended for combining holographic interferometry with moire, are available commercially with beam-direction switching capability. For an existing laser such as the Nd:YAG laser in the flutter cascade, a beam switch can be constructed from a Pockels cell and a polarization sensitive beam splitter. A half-wave plate is used after the beam splitter to rotate the polarization of one of the two beams by 90°, so that the speckel patterns of the two holograms are correlated.

A requirement for successful use of diffuse-illumination heterodyne holographic interferometry is to be aware of its systematic and random sources of error. These errors are determined by alignment, by spurious time-varying fringe patterns, by differences in wavelength between the lasers used for recording and reconstruction, and by the electronics used for detection and measurement of the time-varying fringe pattern. There is an additional requirement for a good reference for measuring the relative interferometric phase of the fringe pattern. The random and systematic sources of error are reviewed next. These errors can easily reduce the accuracy of heterodyne holographic interferometry by a factor of 2 to 10.

ERRORS IN DIFFUSE-ILLUMINATION HETERODYNE INTERFEROMETRY

Dändliker and his colleagues have outlined the requirements for dual-reference beam, diffuse-illumination holographic interferometry in several publications.[1-3,21] These papers cover structural analysis, but they are equally applicable to fluid density measurements. The most important points based on our experience are summarized below. Good discussions, with a few errors, are found in Dändliker's publications.

There are two distinct reference waves R_1 and R_2 and two distinct object waves O_1 and O_2 corresponding to the two exposures of the double-exposure hologram. During reconstruction, the frequency of R_1 is shifter relative to the frequency of R_2. Even for linear recording, there is a multitude of time varying interference patterns. To avoid detecting interferences due to the zero-order terms of the hologram, it is essential to satisfy the off-axis-reference-wave criterion, as in Fig. 2. This criterion must be satisfied for any object which is recorded, and every practical effort should be made to avoid illuminating extraneous objects. Even then, care should be exercised to assure that the detectors doe not see reflected zero-order light. Very small spurious signals will cause significant periodic phase errors.

If detection of the zero-order terms is avoided, then the remaining reconstructed waves that can be detected are:

$$R_1R_1{}^*O_1 \ \exp(j\omega_1 t) \qquad R_2R_2{}^*O_2 \ \exp(j\omega_2 t)$$

$$R_1R_2{}^*O_1 \ \exp(j\omega_2 t) \qquad R_1R_2{}^*O_2 \ \exp(j\omega_1 t)$$

$$R_1R_2O_2{}^* \ \exp(j\omega_1 t) \qquad R_1R_2O_1{}^* \ \exp(j\omega_2 t)$$

The waves in the first row are the reconstructions of interest, and do not overlap the reconstructions in the third row, if the reference beams originate from the same side of the diffuser. Overlap with the waves in the second row is avoided by choosing an angle between the reference beams greater than the angular diameter of the diffuser

(Fig. 2), where the diffuser is assumed to be the only object recorded. However, as discussed later, said overlap can be tolerated. The consequences of overlap with these cross reconstructions are a loss of accuracy, but an increase in the tolerance to misalignment.

If the time-varying interference between the waves in the first row is the only signal detected, then that signal is proportional to

$$2\text{Re}[R_1 R_1{}^* R_2 R_2{}^* O_1{}^* O_2 \exp(j\omega t)]$$

where $\omega = \omega_2 - \omega_1$. If $\Delta\phi$ is the phase difference or interference phase between the two object waves, then the signal varies as $\cos(\Delta\phi + \omega t)$.

If there is a negligible decorrelation between the speckle patterns of the two exposures, and if the above signal can be reconstructed exactly, then the accuracy depends only on the electronics for measuring the interference phase. But any misalignment of the hologram relative to the reference beams, any change in the wavelength of the laser beam, or any misalignment of the reference beams themselves introduces both random and systematic phase errors. The nonlinear nature of the hologram recording process also introduces systematic phase errors.

The proper geometry for imaging the fringe pattern is shown in Fig. 3. The imaging lens is shown placed directly against the hologram. This choice of the lens position eliminates systematic errors, assuming no overlap of the cross reconstructions and neglecting the contributions of the nonlinear terms in the hologram. But the random phase error remains.

If the alignment of the reference beams for reconstruction is perfect, and if the fluid-induced interexposure decorrelation of diffuser speckel patterns is negligible, then each light ray can be treated as unchanged between the two exposures. If the reference beams are misaligned prior to reconstruction, each ray from the reconstructed image from the double-exposure hologram of the diffuser is split into a diverging pair of rays at the hologram as shown in Fig. 4. This divergence results in a lateral shift of the two reconstructions of the diffuser and decorrelation of their speckle patterns. The diverging rays also produce misalignment fringes on the hologram, and the elimination of these fringes can be used for realignment.

If the angle between the diverging rays is α, then the lateral shift of the speckle patterns in the image plane of the lens in the paraxial approximation is given by

$$u = \alpha d \tag{20}$$

where d is the distance of the image of the fringe pattern. If the diameter of the lens used to image the fringe pattern is D, then the fringe contrast is multiplied by a factor

$$\gamma = \frac{2J_1[\pi\alpha D/\lambda]}{\pi\alpha D/\lambda} = \frac{2J_1[\pi Du/(\lambda d)]}{\pi Du/(\lambda d)} \tag{21}$$

The number of misalignment fringes within the aperture of the lens is given by

$$n = \alpha D/\lambda \tag{22}$$

A more serious effect of decorrelation is a random phase error given by the expression

$$\delta\phi = \left[\frac{(1 - \gamma^2)}{2\gamma^2(N + 1)}\right]^{1/2} \tag{23}$$

where N is the number of speckles within the aperture of the detector used to make the phase measurment. For perfect alignment ($\gamma = 1$), there is no phase error. But, a small amount of speckle pattern decorrelation requires a large number of speckles and a correspondingly large detector to compensate.

The above error is reduced by minimizing the number of misalignment fringes in the lens aperture or by minimizing the frequency of those fringes. The spatial frequencies of the misalignment fringes at the hologram are given by

$$f_x = (1/2\pi)[\Delta k_{2x} - \Delta k_{1x}] \tag{24}$$

$$f_y = (1/2\pi)[\Delta k_{2y} - \Delta k_{1y}] \tag{25}$$

where the reference beams are misaligned by Δk_1 and Δk_2, respectively. Misalignment occurs because of a difference in wavelength between the recording and reconstruction beams, because of a change in the included angle between the reference sources, and because of rotation of the hologram about its x_H, y_H, and z_H axes.

If the reference sources are in the x_H, z_H plane, if the reference beams are approximately collimated, and if the hologram is in the x_H, y_H plane, the various sources of misalignment result in the following fringe frequencies:

change $\Delta\lambda$ in wavelength

$$f_y = 0 \quad f_x = (\Delta\lambda/\lambda^2) \ [\cos \theta_{x1} - \cos \theta_{x2}] \tag{26}$$

Symmetrical change $\Delta\theta$ in included angle

$$f_y = 0 \quad f_x = (\Delta\theta/\lambda) \ \sin\left[\frac{\theta_{x1} + \theta_{x2}}{2}\right] \cos\left[\frac{\theta_{x1} - \theta_{x2}}{2}\right] \tag{27}$$

rotation $\Delta\alpha$ about the x-axis

$$f_y = (1/\lambda)[\cos \theta_{z2} - \cos \theta_{z1}] \ \Delta\alpha \quad f_x = 0 \tag{28}$$

rotation $\Delta\beta$ about the y-axis

$$f_y = 0 \quad f_x = (1/\lambda)[\cos \theta_{z1} - \cos \theta_{z2}] \ \Delta\beta \tag{29}$$

rotation $\Delta\gamma$ about the z-axis

$$f_y = (1/\lambda)[\cos \theta_{x1} - \cos \theta_{x2}] \ \Delta\gamma \quad f_x = 0 \tag{30}$$

where $\cos \theta_{x1,2}$, $\cos \theta_{y1,2}$, $\cos \theta_{z1,2}$ are direction cosines of the reconstruction rays relative to the hologram coordinate axes.

A change in wavelength can be compensated by a change in included angle or by rotation about the y-axis.

If there is a large angle between the two reference beams, the required alignment accuracy is high. The best results are achieved when the included angle is large enough to prevent overlap with the cross reconstructions. But the required alignment accuracy may be impractical for transferring the hologram from a test cell to a readout station.

The sensitivity to misalignment can be reduced substantially for Eqs. (26) and (28) to (30) by choosing a very small angle between the reference beams. For a small enough angle, the interference between the reference beams can be viewed and used to set the included angle precisely. The sensitivity to misalignment is reduced enough that film can be used rather than glass plates to record the hologram.

The costs of overlapping the cross reconstructions with the reconstructions of interest are increased systematic and random errors. To avoid a periodic systemmatic error, pairs such as

$$R_1^*R_2O_1 \ \exp[j\omega_2 t] \quad \text{and} \quad R_1^*R_1O_1 \ \exp[j\omega_1 t]$$

must be decorrelated. The magnitude of decorrelation is determined by Eq. (21), where α is now the angle between the two reference beams, and $\alpha D/\lambda$ is the number of reference-beam fringes in the lens aperture. It is desirable to have the voltage produced by any signal at the heterodyne frequency at least 20 dB less than that contributed by the direct interference of O_1 and O_2.

Even if the above decorrelation is adequate, the overlapping speckel patterns contribute an additional random phase error given by

$$\delta\phi = \left[\frac{5}{2(N + 1)}\right]^{1/2} \tag{31}$$

where N is the number of speckles in the detector aperture. More than 10^4 speckles are required for a phase error less than 1°. Also, the overlapping reconstructions reduce the fringe contrast.

Another possible source of error, discussed thoroughly by Dändliker,[3] is the nonlinear response of the hologram recording medium. The periodic error produced by this effect is minimized by controlling the parameters that affect linearity (beam ratio, exposure, processing) and by eliminating from the hologram all object waves that do not originate from the changing part of the object.

The implementation of time-average holography for flow visualization involves fewer considerations as discussed in the next section.

IMPLEMENTATION OF TIME-AVERAGE HOLOGRAPHY FOR FLOW VISUALIZATION

Objective

The main objective is to use time-average holography to improve the three-dimensional flow-visualization effect associated with fringe localization. A second objective is to increase the quantitative capabilities of flow visualization based on diffuse-illumination holographic interferometry over those available from the double-exposure method.

One goal eventually is to evaluate time-average holography in the nine-blade flutter cascade mentioned previously. The double exposure holograms recorded of the flows in that cascade show so many flow features that it is at times difficult to isolate them. It is expected that time-average holography with frequency modulation of the reference-beam will allow the fringe contrast of a flow-feature of interest to be enhanced relative to that of other flow features.

PROPERTIES AND REQUIREMENTS

Time-average, diffuse-illumination, holographic interferometry for flow visualization does not differ significantly from time-average holography for the visualization of vibrational modes.[5,15] Furthermore, the flow-visualization effect depends on fringe localization, just as it does for double-exposure, diffuse-illumination, holographic interferometry.

When the time and spatial dependences of the variation of phase can be separated as in Eq. (17), the fringe contrast and fringe localization depend on the spatial part $\phi_\zeta(r_H)$. If the reference beam is modulated as given by Eq. (18), then localization is given by Eqs. (14) and (15), with ϕ_r and γ_r substituted for $\Delta\phi$ and $\Delta\gamma$, respectively. The fringe contrast is determined by the so-called characteristic function, which for separable flows is proportional to Eq. (19). For comparison, the characteristic function for vibrational analysis is proportional to the familiar zero-order Bessel function of the first kind.

For $\gamma_r = 0$ the characteristic function and fringe contrast depend on $\phi_r T/2$. For example, for a two-dimensional flow field, which varies with x,y in a test section of length L along the z-axis, the argument of the characteristic function is given by

$$\phi_r T/2 = \frac{\pi}{\lambda} \, GLT \, \frac{\partial \rho}{\partial t} \, (x,y,t) \tag{32}$$

for rays parallel to the z-axis.

As stated, the potential advantage of time-average holography over double-exposure holography is the ability to use frequency shifts of the reference beams to transfer the highest contrast (brightest) fringe to the flow feature of interest. For Eq. (32), the required circular frequency shift for such a transfer is given by.

$$\omega = \gamma_r = \frac{2\pi}{\lambda} \, GL \, \frac{\partial \rho}{\partial t} \, (x,y,t) \tag{33}$$

A map of the required ω versus position is of course a map of $\partial \rho(x,y,t)/\partial t$.

The only other significant point to note in implementing time-average holography is that its sensitivity, in a certain sense, is one half that of double-exposure holography. For double-exposure holography and the two-dimensional flow of Eqs. (32) and (33), the first fringe minimum (dark fringe) occurs for

$$\frac{2\pi}{\lambda} \, GLT \, \frac{\partial \rho}{\partial t} = \pi \tag{34}$$

whereas the first fringe minimum in time-average holography requires that Eq. (34) equal 2π.

The major difficulty in implementing time-average holography for internal transonic flow visualization is to acquire a suitable laser system. Double-exposure holography in the above-mentioned transonic flutter cascade has required exposure separations ranging from 15 to 100 μs. Time-average exposures ranging from 30 to 200 μs would be required for the same sensitivity, assuming no frequency shift of the reference beam.

The long-pulse, flashlamp-pumped, dye laser seems to be the best choice. This laser produces smooth pulses having good beam quality and adequate energy in the required pulse-length range. The major remaining problem is to achieve a narrow enough spectroscopic line-width for adequate temporal coherence and convenient holography.

The actual execution of the beam modulation techniques involves a number of experimental steps, test, evaluations, and preliminary results. These are discussed in the next sections.

EXPERIMENTAL AND DEVELOPMENTAL RESULTS

Expectations and Approach

Dändliker has claimed accuracies for diffuse-illumination heterodyne interferometry of 1/1000 fringe, which corresponds to a phase-measurement accuracy of better than 0.4°. With great care, this accuracy can be achieved in a laboratory. Light must be detected from the primary reconstructions O_1 and O_2 only. The images must be bright, the fringe contrast high, and the alignment for reconstruction very good. The effects of path fluctuations between the reference beams must be minimized, so the reference signal is derived from the fringe pattern itself.

A more realistic expectation is 1/300 fringe, particularly if overlapping cross reconstructions are to be tolerated for ease of alignment and reduced alignment sensitivity.

If the reconstructed images are not bright, if alignment and fringe contrast are poor, or if there are extraneous signals at the frequency offset, then the accuracy can easily drop to 1/100 fringe.

Because of the multiple random and systematic errors that affect accuracy, our approach is to evaluate a heterodyne holography setup in the test cell, but with a flow field or phase object that is both known and repeatable. We use a so-called gas-flow simulator.[22]

Flow Simulator

The flow simulator is a large crystal of KD*P. The crystal, Fig. 5, has 50 by 50 mm faces, which are perpendicular to the optic axis and are separated by 30 mm. Electrodes, 10 mm wide and 50 mm long, are attached to the 50 by 50 mm faces at 4 parallel edges. The actual crystal is held in a mount, where it is submerged in Pockels cell fluid. The two parallel 30 by 50 mm faces are accessible through windows for allowing light to pass through the crystal. Light polarized perpendicular to the optic axis experiences refractive index changes when voltages are applied to the electrodes. The double-exposure holograms compare voltage and no-voltage conditions.

Figure 6 shows the infinite-fringe patterns which result when voltage is applied to electrodes 2 and 4 with electrodes 1 and 3 grounded. The fringe pattern is quite sparse, and its accurate measurement is a good test of the fringe interpolation capability of heterodyne interferometry. The laser illumination has passed through a diffuser before entering the flow simulator.

The flow simulator has been used by Decker and Stricker to compare heterodyne holographic interferometry with conventional finite-fringe holographic interferometry and with heterodyne moire deflectometry.[4] Data from the report is shown in Fig. 7, together with predicted error ranges corresponding to various random fringe-measurement errors. The ordinate of Fig. 7 is the numerically evaluated first derivative of the interference phase, converted to a refractive index derivative by assuming a two-dimensional refractive-index field. It is appropriate to display the derivative of the measurements, since derivatives and differences of the interference phase are required for three-dimensional flow analysis. The graph represents a horizontal scan midway between the 50 by 50 mm faces. The derivatives are determined with central differences with data points separated by 1 mm, and with a 2 mm optical gauge length. That is

$$\Delta\phi_i' = \frac{\Delta\phi_{i+g/2} - \Delta\phi_{i-g/2}}{g} \tag{35}$$

where g = 2mm.

The optical setup used to record, reconstruct, and read out the hologram is shown schematically in Fig. 8. Except to remove the hologram and process it, the setup was not disturbed. The 514.5 nm line of the argon-ion laser was used for recording and for reconstruction. The frequency offset was produced with an acoustooptic frequency shifter. The time-varying fringe pattern was detected using two 0.75 mm diameter optical fibers routed to photomultiplier tubes. The phase was measured using a dual-phase lock-in amplifier, with the amplified output of one photomultiplier used as a reference. The other fiber was translated, and its position measured using a laser interferometer. The lens diameter D was 5.1 cm, and the fringe pattern was imaged at a distance d of 48.3 cm.

The predicted error ranges, shown superimposed on Fig. 7 are of interest in the next section of this report. The ranges show the predicted scatter of the data, should various random fringe-measurement errors occur. Each range is associated with plus or minus a particular value of the fringe interpolation accuracy, and it is seen that the scatter is 50 percent of the general level of the gradient of the refractive index at 1/100 fringe.

As summarized next, the flow simulator was used to investigate possible reference-beam geometries for heterodyne holographic interferometry in the flutter cascade.

Reference-Beam Geometry for a Flutter Cascade

The reference-beam optics were placed together with the flow simulator on a vibration isolation table. The optics consisted of a polarization sensitive beam splitter, a half-wave plate in one beam, an acoustooptic frequency shifter in the other beam, various alignment pinholes and spatial filter assemblies, and a glass-plate holder with precision x,y and y-axis rotation adjustments.

The more desirable wide-angle separation between reference beams was tested first, where the mutual angle was about 7°, and the mean angle was about 45°. The holograms were all recorded at the same flow-simulator settings: 5 kV on electrodes 2 and 4 with electrodes 1 and 3 grounded. The holograms were recorded at 496.5 nm and reconstructed at 514.5 nm, a difference of 18.0 nm. Unless an argon-ion pumped dye laser is used for readout of the holograms recorded with the Nd:YAG laser, those holograms will be recorded at 532 nm and reconstructed at 514.5 nm, a difference of 17.5 nm.

The reference beams were collimated to maintain a constant angle across the hologram. The change in wavelength was compensated for by rotating the hologram about the y (vertical) axis (see Eqs. (26) and (29)). This rotation and the xy adjustments were used to eliminate the misalignment fringes and to maximize the fringe contrast. The fringe pattern was formed at a distance of 48 cm from a 2 cm diameter lens, placed in contact with the hologram. The electronic reference was derived from the fringe pattern itself.

The change in wavelength from recording to reconstruction resulted in a small but noticeable difference. The tolerance of this setup to misalignment followed by realignment was also tested.

A general conclusion is that the wide-angle geometry is feasible, but probably practical only if the holograms are recorded and reconstructed in the test cell. Another possibility is to design and construct identical hardware for the test cell and the readout station, or to construct a portable reference-beam, glass-plate magazine to be transported back and forth. Attempts to use the wide-angle geometry with film were not successful.

The small-angle geometry with overlapping reconstructions was tested next. The same beam switch was used as before, but the reference beams were made nearly coaxial after passing through the half-wave plate and frequency shifter, respectively. The beams were then diverged through a single microscope objective. The mutual angle was set by measuring the separation of the fringes produced by the interference of the two reference beams. Holograms were recorded for various mutual angles varying from 25 to 250 μrad. The only other change in technique was to derive the electronic reference from the interference pattern formed between the two reference beams; the overlapping cross-reconstructions reduce the contrast of the measured fringe pattern and the quality of the electronic reference derived from it.

Vivid examples of the random and systematic phase errors discussed above were easy to generate with this geometry, although the errors were never worse than 1/100 fringe. Results of 1/300 fringe or better required the cross-reconstruction decorrelation associated with at least 10 reference-beam fringes in the lens aperture. The full 5 cm diameter of the imaging lens was used to minimize the random phase error of Eq. (31). Holograms were recorded at 514.5 nm and reconstructed at both 488 nm and 514.5 nm, a difference of 26.5 nm. Fortunately, only minor alignment was required, even after the wavelength change: the reference-beam fringes made it difficult to observe misalignment fringes.

For comparison with Fig. 7, Fig. 9 presents measurements made at 488 nm. The included angle was 100 μrad. Figure 10 presents data measured at 514.5 nm for an included angle of 250 μrad. The lens was close to, but not in contact with, the hologram when these measurements were made.

Film was also used successfully at the small mutual angles, although the best accuracy was only 1/150 fringe. The emulsions used, however, were not the optimum emulsions for the argon-ion laser or for the large average reference-beam angle. Film offers the possibility of higher hologram recording rates or fast processing in the test cell.

The narrow-angle geometry proved fairly easy to use and will be selected at least for the initial work in the flutter cascade. The flow simulator will be built into the measurement system, so that the performance of the system can be tested and checked periodically.

The status of the time-average-holography project is summarized next.

LASER SYSTEM FOR TIME-AVERAGE HOLOGRAPHY

Figure 11 shows the fringe pattern associated with a time-average hologram of a flame induced flow over a blade. The hologram was recorded with an argon-ion laser. The exposure times required for such holograms are 10's to 100's of milliseconds. The internal flows in a flutter cascade by contrast change significantly in 10's of microseconds.

The specification of a suitable laser for transonic flow visualization in the presence of windows using a reflective diffuser has been discussed in another paper.[14] There is no off-the-shelf laser available for time-average holography in such an environment. The general specifications for such a laser are easy enough to state. There should be at least 50 mJ of polarized light per pulse with a spectroscopic full line-width at half maximum power around 0.03 cm^{-1}. To make good use of higher energies, narrower linewidths are required. The pulses should be smooth and repeatable from shot to shot. Pulse repetition rates at motion-picture frequencies are desirable to increase data rates. As explained previously, pulse lengths up to 200 μs can be used. The beam should have a smooth profile and a small enough diameter and divergence angle to be controlled conveniently. A wavelength that can make use of the most sensitive photographic emulsions is desirable (610 nm to 650 nm for the KODAK SO 253 emulsion).

Commercially available flashlamp-pumped dye lasers are available with pulse widths out to 400 μs. But, the simultaneous narrowing of linewidth, maintenance of pulse width, and control of beam profile have proven difficult. Still, a laser with adequate properties appears to have been constructed and will be tested.

The test of the performance of such a laser is not difficult. For example, if the laser produces pulses having a full length at half maximum power of 50 μs, then a hologram can be recorded of a structure vibrating in a 20 kHz resonant mode. The results can be compared with those recorded with an argon-ion or helium-neon laser. The linewidth can be measured using an interferometer, or better yet by recording a hologram of a scene with a large scene depth.

CONCLUDING REMARKS

It should be convenient to use heterodyne holographic interferometry to measure the relative flow-density field or properties related to it, if the mutual angle between reference beams is small. At least 10 reference-beam fringes are required in the aperture of the imaging lens and more than 10^4 speckles are required in the detector aperture. The flow simulator can be used to determine the error level of the measurement and to assure that systematic errors do not lead to erroneous conclusions concerning complex flows. It is realistic to expect an accuracy of about 1/300 fringe. Higher accuracies are possible with a large mutual angle, but on-site recording, processing, and readout probably are required. Spurious reflections from windows or blades may have a larger effect on accuracy than some of the error sources discussed in this report. It is possible to use film when the angle between reference beams is small.

Heterodyne holographic interferometry is excellent for automated fringe measurements. An automated fringe measurement laboratory is being constructed at NASA Lewis for structural analysis, and will also be used for flow analysis.

It is expected that the flashlamp-pumped dye laser for time-average holography will be available for evaluation very soon.

REFERENCES

1. Dändliker, R., Eliasson, D., Ineichen, D., and Mottier, F.M. (1976). "Quantitative determination of bending and torsion through holographic interferometry," in The Engineering Uses of Coherent Optics, edited by R. Robertson, Cambridge University Press, Cambridge, England, pp. 99-117.

2. Dändliker, R., Ineichen, D., Eliasson, B., and Mastner, J. (1977). "Quantitative Strain and Stress Determination from Holographic Interferograms," (AD-A048640.)

3. Dändliker, R., (1980). "Heterodyne Holographic Interferometry," in Progress in Optics, Volume 17, edited by E. Wolf, North Holland Publishing Co., New York, pp. 1-84.

4. Decker, A.J., and Stricker, J., (1985). "A Comparison of Electronic Heterodyne Moire Deflectometry and Electronic Heterodyne Holographic Interferometry for Flow Measurements," SAE Paper 851896.

5. Stetson, K.A., (1970). "Effects of Beam Modulation on Fringe Loci and Localization in Time-Average Hologram Interferometry," Journal of the Optical Society of America, Vol. 60, No. 10, pp. 1378-1388.

6. Wilson, A.D., (1970). "Characteristic Functions for Time-Average Holography," *Journal of the Optical Society of America*, Vol. 60, No. 8, pp. 1068-1071.

7. Stetson, K.D., (1976). "The Use of Characteristic Functions in Concomitant Holographic Vibration Analysis," in *The Engineering Uses of Coherent Optics*, edited by R. Robertson, Cambridge University Press, Cambridge, England, pp. 123-131.

8. Boldman, D.R., and Buggele, A.E., (1978). "Wind Tunnel Tests of a Blade Subjected to Midchord Torsional Oscillation at High Subsonic Stall Flutter Conditions," NASA TM-78998.

9. Strazisar, A.J., and Powell, J.A., (1980). "Laser Anemometer Measurements in a Transonic Axial Flow Compressor Rotor," in *Measurement Methods in Rotating Components of Turbomachinery*, edited by B. Lakshminarayana and P.W. Runstadler, ASME, New York, pp. 165-176.

10. Strazisar, A.J., and Chima, R.V., (1980). "Comparison Between Optical Measurements and a Numerical Solution of the Flow Field in a Transonic Axial-Flow Compressor Rotor," AIAA Paper 80-1078.

11. Boldman, D.R., Buggele, A.E., and Michalson, G.M., (1981). "Stall Flutter Experiment in a Transonic Oscillation Linear Cascade," NASA TM-82655.

12. Boldman, D.R., Buggele, A.E., and Decker, A.J., (1982). "Three-Dimensional Shock Structure in a Transonic Flutter Cascade," *AIAA Journal,* Vol. 20, No. 8, pp. 1146-1148.

13. Howes, W.L., (1984). "Rainbow schlieren and its applications," *Applied Optics*. Vol. 23, No. 14, pp. 2449-2460.

14. Decker, A.J., (1986). "Evaluation of Diffuse-Illumination Holographic Cinematography in a Flutter Cascade," NASA TP-2593 (to be published).

15. Vest, C.M., (1979). *Holographic Interferometry*," Wiley, New York.

16. Howes, W.L., and Buchele, D.R., (1952). "A Theory and Method for Applying Interferometry to the Measurement of Certain Two-Dimensional Gaseous Density Fields," NACA TN-2693.

17. Howes, W.L., (1985). "Rainbow schlieren vs Mach-Zehnder interferometer: a comparison," *Applied Optics*, Vol. 24, No. 6, pp. 816-822.

18. Decker, A.J., (1982). "Fringe Localization Requirements for Three-Dimensional Flow Visualization of Shock Waves in Diffuse-Illumination Double-Pulse Holographic Interferometry," NASA TP-1868.

19. Decker, A.J., (1981). "Holographic Flow Visualization of Time-Varying Shock Waves," *Applied Optics*, Vol. 20, No. 18, pp. 3120-3127.

20. Decker, A.J., (1984). "Measurement of Fluid Properties Using Rapid-Double-Exposure and Time-Average Holographic Interferometry," AIAA Paper 84-1461.

21. Dändliker, R, and Thalmann, R., (1985). "Heterodyne and quasiheterodyne holographic interferometry," *Optical Engineering*, Vol, 24, No. 5, pp. 824-831.

22. Weimer, D., (1982). "Pockels-Effect Cell for Gas-flow Simulation" NASA TP-2007.
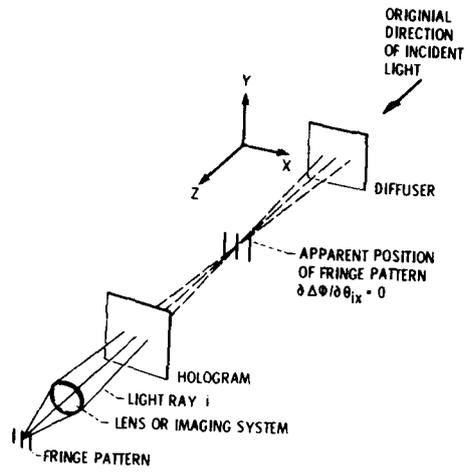
Figure 1. - Imaging a localized interference fringe pattern.
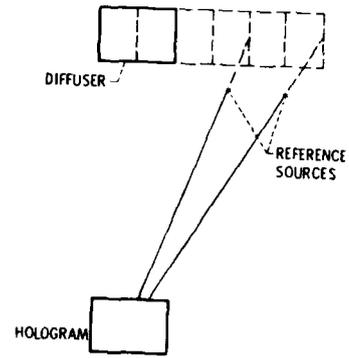
Figure 2. - Minimum reference angles for non-overlapping cross reconstructions and zero-order waves.
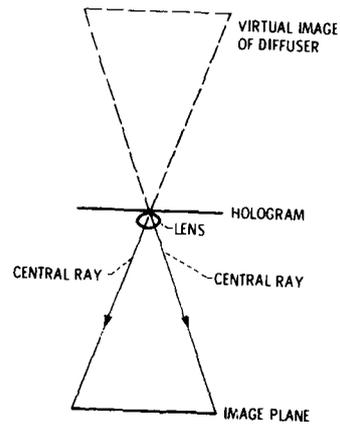
Figure 3. - Proper geometry for imaging fringe pattern in dual reference-beam holography.
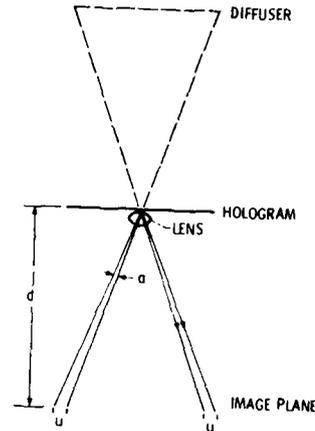
Figure 4. - Splitting of reconstructed rays due to misalignment of reference beams in dual reference-beam holography.
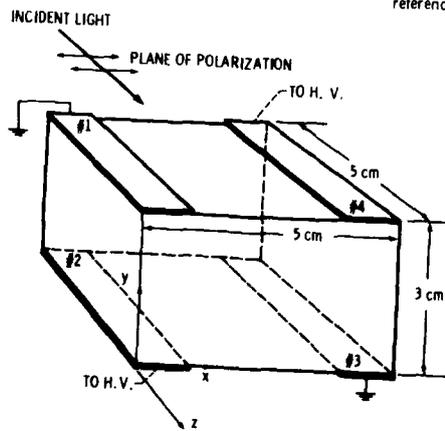
Figure 5. - Flow simulator-crystal of KD•P.

ELECTRODE 1   ELECTRODE 4

ELECTRODE 2   ELECTRODE 3

(a) Potential of 7 kV.   (b) Potential of 6 kV.

(c) Potential of 5 kV.   (d) Potential of 4 kV.

(e) Potential of 3 kV.   (f) Potential of 2 kV.

Figure 6. - Infinite fringe patterns--Pockels flow simulator.

ERROR 1/50   1/100   1/300   1/600 FRINGE

EXPECTED SCATTER FROM
RANDOM ERRORS ILLUSTRATED
FOR COMPARISON WITH DATA

$-\frac{\Delta n}{\Delta x} \times 10^6$, cm^{-1}

X, mm

Figure 7. - X-derivative of refractive index of flow simulator,
together with expected scatter from various random fringe-
measurement errors.

MIRROR   MIRROR   MIRROR

MIRROR

BEAM
EXPANDER

BEAM
SPLITTER

ACOUSTIC
FREQUENCY
SHIFTER

MIRROR

LASER

MIRROR

DIFFUSER

FLOW
SIMULATOR

REFERENCE

REFERENCE

MIRROR

HOLOGRAM   IMAGING LENS

MIRROR   BEAM   MIRROR
          SPLITTER

FRINGE PATTERN

FIBERS

TO PHOTOMULTIPLIERS
AND PHASE DETECTOR

(a) Schematic.

Figure 8. - Electronic heterodyne holographic interferometer.

Figure 9. - Flow simulator results: recording wavelength 514.5 nm; reconstruction wavelength, 488 nm, included reference-beam angle 100 μ rad.
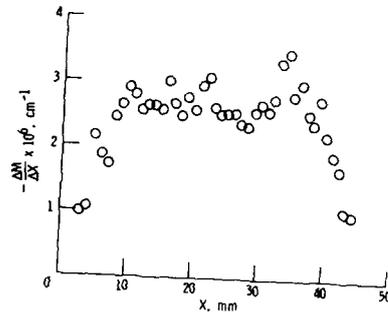
Figure 10. - Flow simulator results: recording wavelength 514.5 nm; reconstruction wavelength 514.5 nm; included reference-beam angle 250 μ rad.

Figure 11. - From time - average hologram of flame - induced flow over blade.

DISCUSSION

P.Bryanston-Cross, UK

(1) What length of time is required to form a "time-average" hologram?

(2) In the frequency shifting approach, does the reconstruction lens quality provide any limitation to the fringe resolution found?

Author's Reply

The pulse length is about twice that required for the equivalent double-exposure hologram. For our transonic work, pulse separations in double-exposure holography have ranged from 5 to 100 μsec. Hence pulse lengths for time-average holography should range from 10 to 200 μsec. The flashlamp pumped dye laser is being tested at 50 μsec.

The two fundamental limitations on precision and sensitivity are speckle-pattern decorrelation and the non linear response of the silver halide emulsion used to record the hologram. These will always be present. It also should be pointed out that off-the-shelf phase meters are not reliable to better than 1/100 fringe. Some should be believed to no better than 1/360 fringe. The lens quality should have some effects, but I would be surprised to find that its effect is a major limitation.

PARTICLE IMAGING VELOCIMETRY IN A LOW TURBULENT WINDTUNNEL AND OTHER FLOW FACILITIES

by J. Kompenhans and J. Reichmuth

Deutsche Forschungs- und Versuchsanstalt für Luft- und Raumfahrt

Bunsenstrasse 10, D-3400 Göttingen, Germany

SUMMARY

Particle imaging velocimetry (PIV) is a new technique to measure flow velocity and flow direction at one instant in time within a large area of the flow field. For that purpose PIV utilizes the light scattered by small particles in the flow, which are illuminated by two short laser pulses. This paper is intended to report on the experience we gained with this method. In a first part our special PIV system will be described, thereby explaining the principle of PIV. The requirements which have to be fulfilled when applying PIV in windtunnels will be kept in mind, as well. Young's fringes method to evaluate the velocity data is discussed. Examples of our first experimental results are given.

INTRODUCTION

Due to the progress in modern optical methods and the development of advanced image processing systems it is now possible to obtain quantitative data on a flow field with reasonable effort by means of visualization techniques.

Thus, in aerodynamics the interest in optical methods - even in those whose basic ideas have been known for a long time - has been renewed because of their main advantages: non-intrusiveness, very fast data acquisition and an instantaneous survey of the flow field.

One of these methods is 'laser particle imaging velocimetry' (PIV), or as it is sometimes called '(double) pulsed laser velocimetry' or -somewhat incorrectly- 'laser speckle velocimetry'. PIV has been developed in the last five years by several investigators ([1-3], summary and references cited in [4]) in different laboratories to a stage where one can think of its application to flow fields in windtunnels.

To illustrate the principle of PIV it can be best compared with the classical method of flow visualization by means of tracer particles [5]. The flow field, seeded with particles, is two or more times exposed to a light pulse. At PIV a cylindrical lens is used to illuminate only a thin sheet of the flow field (see Fig. 1). The light scattered by the particles is imaged on a photographic plate. In a later evaluation process the local flow velocity vector (2-dimensional) at different positions within the flow field can be calculated from the distance between the particle images due to the first and second light pulse and the time difference between the two light pulses. The advantage of PIV over classical methods - as, for example, image streaks of particles - is, that coherent optics provides methods which allow fast evaluation of the flow velocity at a great number of points in the flow.

The aim of our research project is to find out whether PIV could be a useful tool for the investigation of flow fields in our windtunnels. In the last months we carried out a feasibility study, designed an optical system for

imaging and evaluation - thereby taking into account the knowledge already published in literature - developed image processing software, and performed some experiments in test flows.

EXPERIMENTAL SET-UP FOR PARTICLE IMAGING VELOCIMETRY

Light source

As already explained, a thin sheet of the flow field is illuminated by a light pulse. The use of coherent light is not necessary [3], but for convenience lasers are mostly used as light sources. The following requirements have to be fulfilled:

(i) The laser has to be able to produce two or more short light pulses within a selectable time interval.

(ii) The energy of the pulsed laser light, scattered by the particles and collected and focused by the camera lens, must exceed the level necessary to expose the photographic material.

(iii) The wavelength should be in the visible range because of safety and alignment purposes.

(iv) The laser should be continuous or nearly continuous to be able to align the transmitting optics within reasonable time.

Most researchers use giant pulse ruby lasers which fulfil condition (ii). Sometimes a continuous Argon ion laser is used (iii), the output of which is modulated to obtain light pulses. In a feasibility study, carried out in our low turbulence windtunnel, the performance of two lasers was compared:

(i) A giant pulse ruby laser (5 Joule/pulse) with a wavelength of $\lambda = 694$ nm (in cooperation with Prof. Hinsch of University of Oldenburg).

(ii) A 70 mJoule, frequency doubled Nd:YAG laser($\lambda = 532$ nm).

The comparison showed that - under the same experimental conditions - the energy of both lasers was sufficient for photographic recording due to the fact that different photographic materials with different sensitivity at different wavelengths are available. A comparison of those photographic materials mostly used in PIV is given in [2].

However, much more time and skill of the experimentator was necessary to align the optics if a ruby laser (typ. one pulse per minute, red light) was used. Position of the focus and of the light sheet could only be obtained using burn paper, which was a time consuming exercise.

On the other hand, the Nd:YAG laser with a repetition rate of 10 Hz allowed very efficient alignment of the optics. The green light is best suited for visual inspection of the light sheet by the experimentator.

But one drawback of a Nd:YAG system had still to be overcome. Usually, a double pulse is produced by two times switching the Pockels cell, located in the resonator, during the short time interval when the energy is pumped into the laser rod by the light of the flashlamp. With a Nd:YAG system the maximum time difference achievable is only about 150 - 200 µsec. In cooperation with the German representative of JK Lasers we decided to have a two oscillator system. Both oscillators can be triggered independently. Thus, it is now possible to

have a time interval between the two laser pulses in the range of 3 μsec to
10 ms. The output energy of both pulses is excellently controllable and sta-
ble. The final set-up of our laser system (JK model HY 200 Special) is shown
in Fig. 2. The light of the two Nd:YAG oscillators (λ = 1064 nm), differently
polarized at an angle of 90°, is combined by means of different polarizing
prisms. The light passes through a rotator plate to give the same linear
polarization for both pulses. Afterwards the frequency of the light is doubled
(λ = 532 nm). Components at 1064 nm are blocked off in a wavelength separator.

The length of an individual laser pulse is 16 nsec. The output of the system
is 2 × 70 mJ; an additional laser amplifier may be included later on. The
repetition rate of double pulses is 10 Hz; it may be increased up to 50 Hz.
In our first experiments the single shot option was used.

Transmitting optics

The transmitting optics is needed to transform the circular, pulsed laser beam
into a thin light sheet. The specification of the transmitting optics depends
on the diameter and divergence of the laser beam, the measuring distance and
the thickness and width of the laser light sheet, as required for the exper-
iment. Some configurations have been discussed in the literature [2,6]. Our
solution is sketched in Fig. 3. First, the laser beam is expanded to a diameter
of appr. 50 mm. A combination of different cylindrical lenses is used to shape
a thin light sheet with an almost uniform thickness at the location of the flow
field under investigation. The resulting light sheet is appr. 70 mm wide and
0.5 mm thick; the distance between laser and flow is about 2-3 m.

Flow facility

The feasibility study was carried out in a low turbulence windtunnel with a
test section of 0.3 × 1.5 m². Here, problems as 'seeding the flow in a wind-
tunnel' or 'aligning the optics in a noisy environment' could be studied. The
result of this part of the investigation was, that it is possible with our
laser system to use PIV in the low turbulence windtunnel for recording of a
flow field of appr. 30 × 7 cm² at flow velocities up to 20 m/s.

In a second step further testing and optimization of the experimental set-up
(transmitting optics, imaging system, photographic material and development
process, reconstruction optics, image processing algorithms) was necessary
This could be also done, utilizing a smaller flow facility which would be
always available to us, in contrast to the windtunnel. Therefore, we used a
jet flow facility with different nozzles in front of a plenum chamber with
anti-turbulence grids and flow silencers, supplied with pressurized air.
Three important flow types can be studied simultaneously: laminar flow in the
potential core, wave like motion in the mixing region of the jet, where the
shear layer rolls up, and turbulent flow at a distance several diameters
downstream of the nozzle.

Tracer particles

It must be emphasized that for all measuring techniques using tracer particles
(e.g. LDA or L2F) it is difficult to seed the flow properly. This is supported
by the fact that one complete paper at this meeting is related to this topic
[7].

For PIV experiments we could rely on the experience made in our group when
using a laser Doppler anemometer.

The aerodynamic diameter of a particle determines how accurately a particle
can follow an abrupt change of fluid motion. Large particles need some dis-
tance to reach again the velocity of the fluid. Therefore small particles are
desirable. However, a compromise has to be found because smaller particles

scatter less light. Our particles are produced in a Laskin nozzle [8].
Pressurized air, injected in corn oil, leads to the formation of small oil
droplets. The diameter of the droplets had been measured in an aerodynamic
particle sizer and was found to be of the order of 1 μm. Such particles were
thought to be sufficient for our PIV experiments.

Another important problem is to find a location in the windtunnel where par-
ticles can be inserted in the flow without disturbing the flow. In the case
of the nozzle experiment the particles are inserted in the settling chamber.
The jet is completely seeded with particles (see Fig. 4a). It is also neces-
sary to seed the air surrounding the jet, in order to have enough particles
in the entrainment region of the jet (Fig. 4b).

For large windtunnels it was found necessary to insert the particles in the
settling chamber upstream of the grids in order not to disturb the flow. As
the particle generator does not deliver enough particles to seed the flow
completely, one has to traverse the particle generator in the settling chamber
to seed only those streak lines which - later on in the test section - will
pass through the measuring plane. This is not a simple task, because due to
low frequency disturbances in the windtunnel the streak lines are not constant
in time.

Imaging system

The light scattered by the particles is recorded in a plane parallel to the
light sheet. For the recording of the scattered light we use - as it was
available in our laboratory - a 35 mm camera with a f/2.8 - 60 mm lens with
Kodak Technical Pan 2415 film. A typical value of the diameter of a particle
image measured on the photographic plate is 15 μm (i.e. diffraction limited).

With a flow velocity of about 100 m/s, a magnification of the camera of 1:3,
and a time delay between the two laser pulses of 4 μsec the distance between
the two images of an particle on the negative is about 130 μm. As an example
Fig. 4a and b show two different PIV recordings. The nozzle can be seen on
the left side of the photograph. The external seeding (Fig. 4b) in the
entrainment region of the jet was carried out by injecting the particles
through borings in a small tube. This process is not optimized, as still
clusters of particles can be seen in the entrainment region.

Depending on the number of particles within a unit area on the photographic
plate, different density regimes are distinguished [2'

(i)   At a very high density of particles one observes speckle patterns
instead of individual particle images. Laser speckle photography is
extensively used in solid mechanics.

(ii)   For fluid mechanics problems a medium density of particles is
desired, where the image of an individual particle can be detected on the
photographic plate. Correlation or Fourier methods are used to evaluate
the flow velocity. This will be described later.

(iii) In the low density case the average distance between the particles
is greater than the distance the two particles travel between the two
pulses. It is possible to identify the particle image pairs and to measure
the distance between the two particle images by means of image processing
methods. However, this type of evaluation requires a high computer capac-
ity.

DATA REDUCTION

Before starting with data reduction, it proved to be advantageous to reduce the film noise of our double exposed photography (high transmittance). Thus, a contact copy was produced on high contrast photographic material. This process is explained e.g. in [9].

The particle concentration in our experiment was in the medium density range (see Fig. 4a and b). Therefore the Young's fringes method was chosen for data reduction. The beam of a He-Ne laser is focused on the contact copy of the double exposed photographic plate (see Fig. 5). Each combination of particle images within the interrogation spot of the laser beam forms a system of interference fringes. As the particles are distributed randomly in the flow, most interference fringes will be averaged and contribute to a constant noise level. However, those image pairs which are due to the first and second exposure of particles which all propagated the same distance and in the same direction during exposure will result in interference fringes of the same fringe spacing and fringe orientation. These fringes will add up and produce a fringe pattern from which the displacement vector can be calculated. The fringe spacing is inversely proportional to the distance between the two images of each particle. The orientation of the fringes is perpendicular to the direction of the movement of the particles.

Examples of fringe patterns are given in Fig. 6a and b. These patterns were obtained by interrogating image pairs shown in Fig. 4b. Different flow velocities and flow directions at two different interrogation spots in Fig. 4b yield different fringe spacing and orientation in Fig. 6a and b. It is obvious that - when using Young's fringes method - the flow velocity is averaged within the area illuminated by the He-Ne laser. If all particles move with the same speed in the same direction a rather sharp fringe system with high contrast is expected. In the case of turbulent flow where flow velocity and direction are not constant within the interrogated area, it is possible to get information on the turbulence level by evaluating the local visibility of the fringe pattern [10].

The remaining problem is to obtain quantitative values for the spacing and orientation of the fringes. This can be either done by measuring the density profile along a line across the fringe system by means e.g of a photodiode or by digitizing the whole fringe pattern with a video camera and an analog-digital converter and then feeding the grey values into a computer.

Several evaluation methods are discussed in literature (e.g 1-D averaging, averaged autocorrelation technique in [11], spatial correlation in [2]). In our first experiments the time necessary to evaluate the velocity at a single point was not the most important parameter. Thus, we decided to take the full information delivered by the fringe pattern and perform a rather time consuming digital 2-D Fourier transform to obtain distance and orientation of the fringes.

An image processing system IPS by KONTRON was at our disposal. 16 image memories, 512 × 512 pixel each, with 8 bit resolution (256 grey levels) and an additional overlay bit were available. Image processing was done in an array processor. The host computer was also able to control the x-y translation stage on the optical bench where the double exposed negative had been mounted.

Image processing was done in the usual manner. A kind of shading correction was carried out and the contrast of the images was enhanced. The 2-D spectra of the fringe systems of Fig. 6a and b are calculated. Three peaks (bright spots) are found in the spectrum. These three peaks have to be discriminated by image processing (see Fig. 7a and b) and their position has to be found.

The central peak is due to the mean grey level of the image. The two other anti-symmetric peaks are related to the spatial frequency of the fringe pattern. Now flow velocity and direction can be calculated from the position of these two peaks with respect to the centre. If e.g. a reference pattern in the plane of the light sheet (without flow) has also been registered on the film and is processed in the same manner as the double exposed photograph, a geometrical calibration factor (magnification ratio of the imaging system) is obtained. Knowing the exact time delay between the two pulses, absolute values of flow velocity and flow direction in the plane of the light sheet can be calculated.

It should be noticed, that because one does not know which particle image is related to the first and which to the second light pulse, the sign of the velocity vector cannot be determined. One possible solution of this problem (i.e. translation of the photographic material between the two exposures) is indicated in [4].

The parameters of the recording and the evaluation process must be carefully selected:

- The time between exposures is given by the maximum permissible displacement of the particles.

- The particle displacement on the photographic material must be less than the diameter of the interrogating beam.

- The particle concentration in the flow must be small enough to avoid speckle patterns.

- The number of particles within the interrogated area must be high enough to yield evaluable Young's fringes.

- The particles must not leave the light sheet between the two exposures. (This would lead to a higher noise level when using the Young's fringes method.)

Details for those considerations are given in [1,2 and 6].

EXPERIMENTAL RESULTS

The final result of the evaluation of a PIV recording should be a plot of the two dimensional velocity field where at each interrogation spot a small arrow indicates magnitude and direction of the 2-D velocity vector, e.g. in [1,3].

As the development of our PIV system is still in progress, up to now no recordings have been completely evaluated quantitatively.

For the experiment with the nozzle, the jet exit velocity is well known. Thus, the flow velocity measured close to the nozzle and the calculated velocity can be compared. Good agreement was found for jet exit velocities up to 100 to 200 m/s. It was even possible to obtain evaluable recordings at a Mach number of 1. However, the aerodynamic behaviour of the particles has to be checked prior to presenting flow velocity data in this velocity range. Therefore we will give some results obtained at lower flow velocities. Fig. 8 shows the variation of the magnitude of the instantaneous velocity on the jet center line with increasing axial distance from the nozzle for three different nozzles. For small distances from the nozzle (up to 1 or 2 diameters) a nearly constant

flow velocity is found. For greater distances from the nozzle exit ($x/D \geq 8$) the flow velocity decreases due to the spreading of the jet. In the range $2 \leq x/D \leq 8$ fluctuations of the instantaneous velocity are found. This is related to the rolling up of the shear layer and the on-set of turbulent motion at the end of the potential core at $x/D = 5$.

Figures 9a and b show the x-and y-component of the instantaneous velocity vector on the center line of the 7 mm nozzle as a function of the axial distance. The corresponding PIV recording was shown in Fig. 4b.

The y-component (perpendicular to the jet axis) fluctuates around zero with a maximum velocity of 15 m/s to either side. The x-component shows - as a function of the distance from the nozzle - a similar behaviour as the magnitude of the velocity vector (Fig. 8).

Fig. 8 and 9 can only give an impression of the kind of results which can be expected when using PIV. The quantitative correctness and the significance of the data has to be proven in near future when a larger number of recordings have been evaluated.

The fluctuations of the velocity vector do not seem to be related to a lack of accuracy but rather to the fact that only a short time interval of the history of the flow field (4 µsec) is observed. Exact values for the error of our velocity data cannot yet be given. Some considerations on this topic have been discussed in [12].

OPERATION OF PARTICLE IMAGING VELOCIMETRY IN WINDTUNNELS

From the experience we gained by our experiments and from the information given in literature we see the following main problems for the operation of PIV in windtunnels:

- Particle size. For higher flow velocities or abrupt changes of flow direction (e.g. vortex core) even smaller particles are necessary. However, less light is scattered by smaller particles.

- Seeding. Disturbance of the flow by the seeding apparatus must be avoided. A location within the flow for the insertion of the particles must be found which ensures that the particles pass through the measuring area. It is very difficult to bring particles in flow regions with high accelerations (e.g. vortex cores).

- A homogeneous distribution of the particles within the flow field would be desirable. However, due to the fluid mechanics of the object which is under investigation (eg. vortex core, boundary layer) this is not always possible.

- The velocity range is limited by the time interval between the two exposures (small velocities need large time delays to obtain high accuracy; high flow velocities need short time delays). If the velocity range is very large, one observes areas on the recorded image where the displacement of the particle images is too large or too small for evaluation with the Young's fringes method.

- Accessibility of the windtunnel. The windtunnel must have windows for the light sheet. It must be possible to transmit the laser light sheet to that plane where the measurements shall take place. (Fiber optics would help to overcome these difficulties). The recording plane (camera) has to be parallel to the light sheet.

- To enlarge the width of the light sheet a more powerful laser would be necessary. The development of more sensitive photographic materials or e.g. more sensitive video cameras would be a possibility to have a larger light sheet with the present laser power.

- To obtain sharp images of the particles on the film the distance from the camera to the light sheet has to be adjusted in the order of half a millimeter. This cannot be done by visual inspection at the view finder of the camera. An automatic alignment procedure would be less time consuming.

- Whereas the time needed for recording the flow field is in the order of microseconds the time necessary to compute the 2-D velocity vector at a single point is of the order of a minute with our system. For standard use faster computers would be necessary.

- When comparing results obtained by PIV with velocity data obtained with hot-wires, pressure transducers or laser Doppler anemometers, it has to be considered that PIV measures the instantaneous flow velocity within a very short time interval of some microseconds, whereas the other methods - the flow velocity (at a single point) is averaged for at least some seconds. This explains why e.g. in turbulent flows a single PIV recording cannot provide data on mean velocity or higher order moments with the same accuracy as known from the other methods.

However, PIV is to our knowledge so far the only method with which it is possible to obtain data on the 2-D velocity vector within a complete flow field. Short comings as mentioned in this chapter must be tolerated.

In our feeling, PIV is a new technique, which has enough possibilities for further development. In future, PIV will give a helpful contribution at the investigation of a great number of fluid mechanics problems.

REFERENCES

[1] Meynart, R., "Speckle Velocimetry Study of Vortex Pairing in a Low-Re Unexcited Jet", Phys. Fluids, Vol. 26, 1983, pp. 2074-2079.

[2] Adrian, R.J.; Yao, C.-S., "Development of Pulsed Laser Velocimetry (PLV) for Measurement of Turbulent Flow", in Proc. of Eighth Biennial Symposium on Turbulence, University of Missouri, Rolla, Missouri, 1983, ed. G. Patterson and J. L. Zakin.

[3] Ferrari, T., et al. "Instantaneous Velocity Fluid Measurement in a Sheet of Fluid by means of Chronophotography in Coherent Light: Improvement of the Method", International Congress on Instrumentation in Aerospace Simulation Facilities, St. Louis, France, Sept. 20, 1983, ICIASF '83 Record, pp. 23-29.

[4] Lauterborn, W.; Vogel, A., "Modern Optical Techniques in Fluid Mechanics", Ann. Rev. Fluid Mech., Vol. 16, 1984, pp. 223-244.

[5] Merzkirch, W., "Flow Visualization", New York, Academic Press, 1974.

[6] Meynart, R., "Mesure de champs de vitesse d'ecoulements fluides par analyse de suites d'images obtenues par diffusion d'un feuillet lumineux", Ph.D. thesis, Universite Libre de Bruxelles, October 1983.

[7] Melling, A., "Seeding Gas Flows for Laser Anemometry", AGARD Conference Advanced Instrumentation for Aero Engine Components, Philadelphia, 19.-23. May, 1986, AGARD-CP 399, paper no. 8.

[8] Echols, W.H.; Young, J.A., "Studies of Portable Air-Operated Aerosol Generators", U.S. Naval Research Laboratory, NRL Report 5929, Washington, July 1963.

[9] Pickering, C.J.D.; Halliwell, N.A., "Speckle Photography in Fluid Flows: Signal Recovery with Two-Step Processing", Appl. Opt., Vol. 23, 1984, pp. 1128-1129.

[10] Arnold, W.; Hinsch, K.; Mach, D., "Turbulence Level Measurements by Speckle Velocimetry" (Letter), Appl. Opt., Vol. 25, 1986, pp. 330-331.

[11] Meynart, R., "Convective Flow Field Measurement by Speckle Velocimetry", Rev. Phys. Appl., Vol 17, 1982, pp. 301-305.

[12] Meynart, R., "Instantaneous Velocity Field Measurements in Unsteady Gas Flow by Speckle Velocimetry", Appl. Opt., Vol 22, 1983, pp. 535-540.
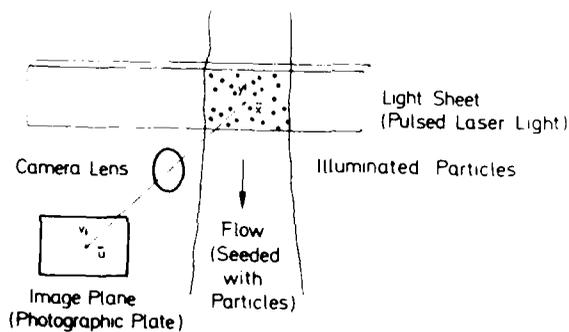
Fig. 1 Principle of Particle Imaging Velocimetry
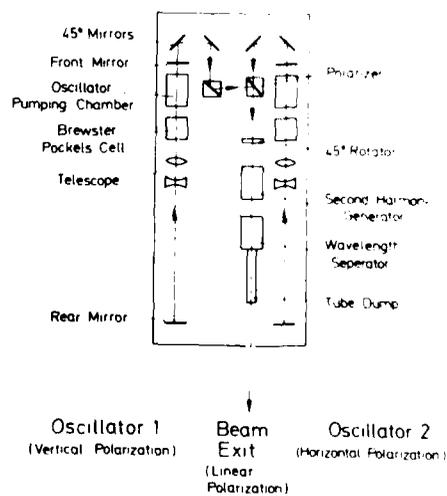
Fig. 2 General lay out of the double pulse Nd:YAG laser system
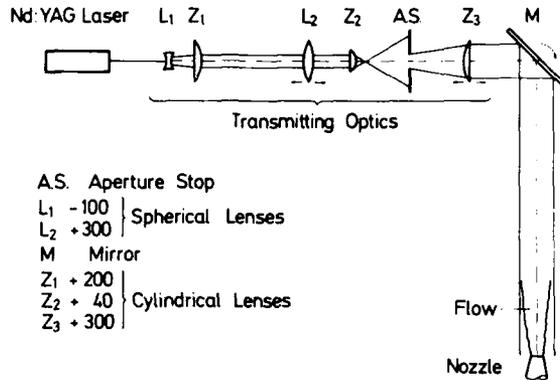
Fig. 3   Experimental set-up of the tramsmitting optics

4 a)
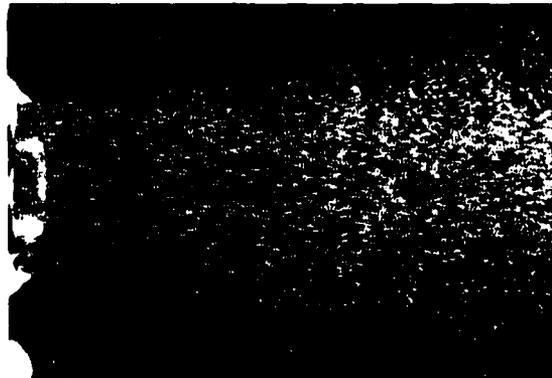
4 b)

Fig. 4   Particle images recorded in a jet flow
a) Nozzle diameter: 15 mm; flow velocity : 90 m/s;
   time between pulses: 4 µs, internal seeding.

b) Nozzle diameter : 7 mm; flow velocity: 90 m/s;
   time between pulses: 4 µs, external and
   internal seeding.

He - Ne Laser Spatial Converging Beam Recorded Fourier TV Camera Image
Filter   Image   Plane   Processing
                                                                       Computer

Young's Fringe Method
For Data Reduction

Optical   Digital
2D-Fourier   Fast Fourier
Transform   Transform
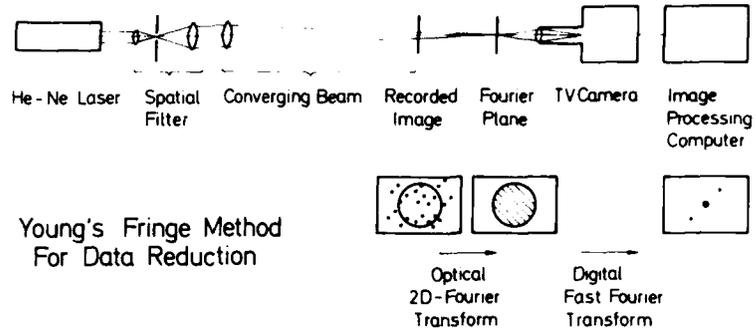
Fig. 5   Experimental set-up for data reduction
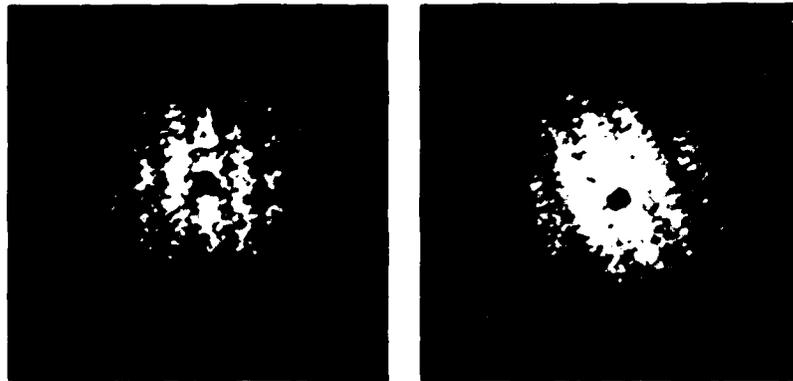
Fig. 6   Intensity distribution of Young's fringes related to a flow with
          a) Flow velocity : 80.8 m/s;   b) Flow velocity: 67.1 m/s
             flow angle : -1.2 deg.   flow angle: -38.2 deg.
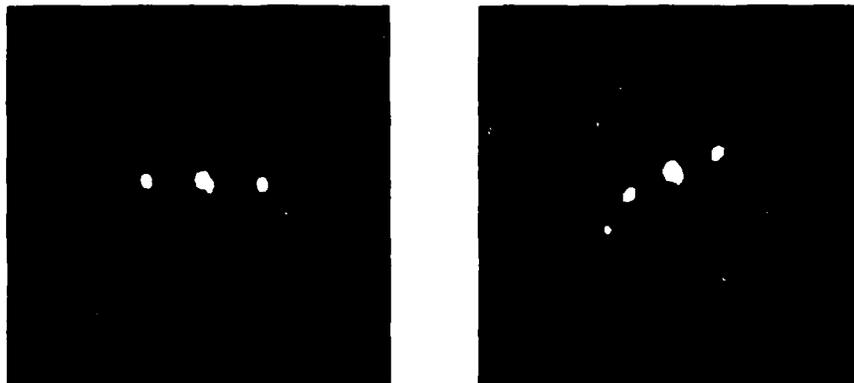
Fig. 7   Discriminated peaks of 2-D Fourier spectrum of the fringe pattern of
a) Fig. 6a   b) Fig. 6 b
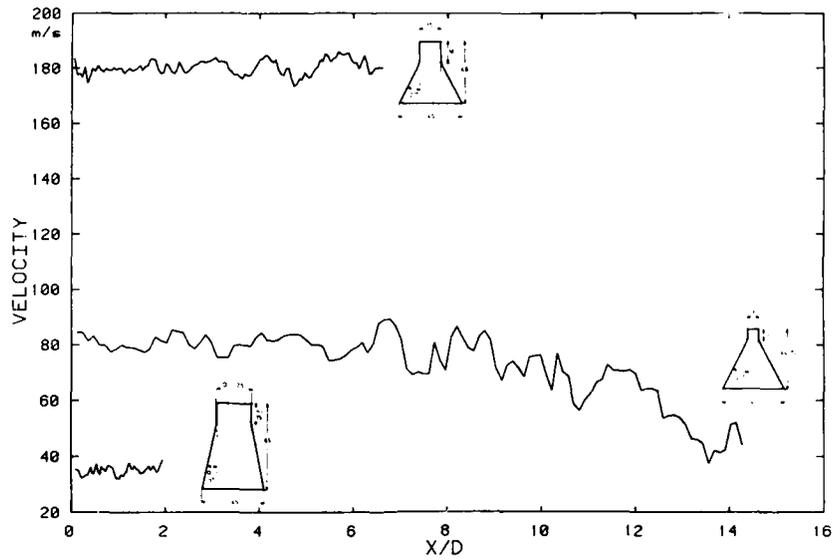
Fig. 8   Example for the evaluation of PIV recordings.
Instantaneous flow velocity on the jet center line for three different nozzles
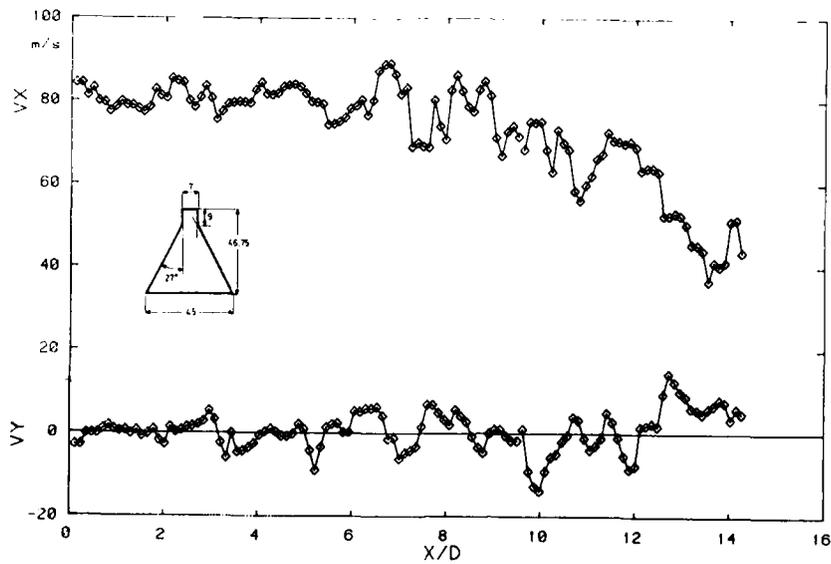
Fig. 9   Evaluation of the PIV recording, shown in Fig. 4b.
X- and Y-component of the instantaneous velocity vector on the jet center line
(nozzle diameter : 7 mm)

DISCUSSION

M.L.G.Oldfield, UK

According to your process, you take the Fourier transform of the particle field to get a fringe pattern and, then, the Fourier transform of the Fourier Transform to get the three dots figure. What would happen if you would examine the original particle pair images to get the velocity directly without processing by a double Fourier transform?

Author's Reply

You could do it if the particle density is low because in this case the particle pair identification is easy. But, for higher particle density, you cannot easily distinguish between particle pairs. Processing by optical Fourier Transforms allows, in this case, to get a mean value of the velocity vector in a measuring volume corresponding to the diameter of the illuminating beam, even including a certain number of the particle pairs.

M.L.G.Oldfield, UK

When I look at your image of the particle field, I see a number of three point systems. Are they different particle pairs or are they false image of one particle pair?

Author's Reply

I am not quite sure. You must attentively examine the particle field in order to identify, surely, particle pairs and false images.

P.Bryanston-Cross, UK

What is the limit for high speed with this technique?

Author's Reply

I think that it is only a problem of time interval between laser pulses. As example, for a recording at Mach number 1.1, we had pulse separation of about 3 or 4 μs. It is, for the moment, our lower limit due to electronics. but, as we have two separate laser oscillators, I don't see a problem to have a shorter time interval between pulses. Of course, if the pulse length of an individual laser pulse is 60 ns, it corresponds to a lower limit.

REPORT DOCUMENTATION PAGE

1. Recipient's Reference	2. Originator's Reference	3. Further Reference	4. Security Classification of Document
	AGARD-CP-399	ISBN 92-835-0401-1	UNCLASSIFIED

5. Originator	Advisory Group for Aerospace Research and Development North Atlantic Treaty Organization 7 rue Ancelle, 92200 Neuilly sur Seine, France

6. Title	ADVANCED INSTRUMENTATION FOR AERO ENGINE COMPONENTS

7. Presented at	the Propulsion and Energetics Panel 67th Symposium, held in Philadelphia, Pennsylvania, USA, 19—23 May 1986.

8. Author(s)/Editor(s)	9. Date
Various	November 1986

10. Author's/Editor's Address	11. Pages
Various	556

12. Distribution Statement	This document is distributed in accordance with AGARD policies and regulations, which are outlined on the Outside Back Covers of all AGARD publications.

13. Keywords/Descriptors

Instrumentation	Components of aero engines
Raman spectroscopy	CARS
Laser anemometry	Pyrometry
Data acquisition	Vibration measurements
Thin layer measurements	Tip clearance measurements

14. Abstract

The Conference Proceedings contains 35 papers presented at the Propulsion and Energetics Panel 67th Symposium on Advanced Instrumentation for Aero Engine Components which was held 19—23 May 1986 in Philadelphia, USA.

The Symposium was arranged in the following sessions: Coherent Anti-Stokes Raman Spectroscopy (5); Laser Anemometry (10); Pyrometry (3); High Speed Data Acquisition and Processing (6); Vibration, Thin Layer and Tip Clearance Measurements (6); and Future Prospects (5). The Technical Evaluation Reports were separately prepared for each session and are included in the Conference Proceedings at the beginning of each session. Questions and answers follow each paper, and a Round Table Discussion follows each session.

The Symposium was addressed to research scientists and development engineers for aero engines in order to discuss the state-of-the-art and to be informed on new measurement possibilities. The achievements of the Symposium were discussed in the Technical Evaluation Reports of each session.

AGARD-CP-399

AGARD Conference Proceedings No.399
Advisory Group for Aerospace Research and Development, NATO
ADVANCED INSTRUMENTATION FOR AERO ENGINE COMPONENTS
Published November 1986
556 pages

The Conference Proceedings contains 35 papers presented at the Propulsion and Energetics Panel 67th Symposium on Advanced Instrumentation for Aero Engine Components which was held 19—23 May 1986 in Philadelphia, USA.

The Symposium was arranged in the following sessions: Coherent Anti-Stokes Raman Spectroscopy (5); Laser

Instrumentation
Raman spectroscopy
Laser anemometry
Data acquisition
Thin layer measurements
Components of aero engines
CARS
Pyrometry
Vibration measurements
Tip clearance measurements

P.T.O

AGARD-CP-399

AGARD Conference Proceedings No.399
Advisory Group for Aerospace Research and Development, NATO
ADVANCED INSTRUMENTATION FOR AERO ENGINE COMPONENTS
Published November 1986
556 pages

The Conference Proceedings contains 35 papers presented at the Propulsion and Energetics Panel 67th Symposium on Advanced Instrumentation for Aero Engine Components which was held 19—23 May 1986 in Philadelphia, USA.

The Symposium was arranged in the following sessions: Coherent Anti-Stokes Raman Spectroscopy (5); Laser

Instrumentation
Raman spectroscopy
Laser anemometry
Data acquisition
Thin layer measurements
Components of aero engines
CARS
Pyrometry
Vibration measurements
Tip clearance measurements

P.T.O

AGARD-CP-399

AGARD Conference Proceedings No.399
Advisory Group for Aerospace Research and Development, NATO
ADVANCED INSTRUMENTATION FOR AERO ENGINE COMPONENTS
Published November 1986
556 pages

The Conference Proceedings contains 35 papers presented at the Propulsion and Energetics Panel 67th Symposium on Advanced Instrumentation for Aero Engine Components which was held 19—23 May 1986 in Philadelphia, USA.

The Symposium was arranged in the following sessions: Coherent Anti-Stokes Raman Spectroscopy (5); Laser

Instrumentation
Raman spectroscopy
Laser anemometry
Data acquisition
Thin layer measurements
Components of aero engines
CARS
Pyrometry
Vibration measurements
Tip clearance measurements

P.T.O

AGARD-CP-399

AGARD Conference Proceedings No.399
Advisory Group for Aerospace Research and Development, NATO
ADVANCED INSTRUMENTATION FOR AERO ENGINE COMPONENTS
Published November 1986
556 pages

The Conference Proceedings contains 35 papers presented at the Propulsion and Energetics Panel 67th Symposium on Advanced Instrumentation for Aero Engine Components which was held 19—23 May 1986 in Philadelphia, USA.

The Symposium was arranged in the following sessions: Coherent Anti-Stokes Raman Spectroscopy (5); Laser

Instrumentation
Raman spectroscopy
Laser anemometry
Data acquisition
Thin layer measurements
Components of aero engines
CARS
Pyrometry
Vibration measurements
Tip clearance measurements

P.T.O

Anemometry (10); Pyrometry (3); High Speed Data Acquisition and Processing (6); Vibration, Thin Layer and Tip Clearance Measurements (6); and Future Prospects (5). The Technical Evaluation Reports were separately prepared for each session and are included in the Conference Proceedings at the beginning of each session. Questions and answers follow each paper, and a Round Table Discussion follows each session. The Symposium was addressed to research scientists and development engineers for aero engines in order to discuss the state-of-the-art and to be informed on new measurement possibilities. The achievements of the Symposium were discussed in the Technical Evaluation Reports of each session. Papers to be presented at the Propulsion and Energetics Panel 67th Symposium, held in Philadelphia, Pennsylvania, USA, 19—23 May 1986. ISBN 92-835-0401-1	Anemometry (10); Pyrometry (3); High Speed Data Acquisition and Processing (6); Vibration, Thin Layer and Tip Clearance Measurements (6); and Future Prospects (5). The Technical Evaluation Reports were separately prepared for each session and are included in the Conference Proceedings at the beginning of each session. Questions and answers follow each paper, and a Round Table Discussion follows each session. The Symposium was addressed to research scientists and development engineers for aero engines in order to discuss the state-of-the-art and to be informed on new measurement possibilities. The achievements of the Symposium were discussed in the Technical Evaluation Reports of each session. Papers to be presented at the Propulsion and Energetics Panel 67th Symposium, held in Philadelphia, Pennsylvania, USA, 19—23 May 1986. ISBN 92-835-0401-1
Anemometry (10); Pyrometry (3); High Speed Data Acquisition and Processing (6); Vibration, Thin Layer and Tip Clearance Measurements (6); and Future Prospects (5). The Technical Evaluation Reports were separately prepared for each session and are included in the Conference Proceedings at the beginning of each session. Questions and answers follow each paper, and a Round Table Discussion follows each session. The Symposium was addressed to research scientists and development engineers for aero engines in order to discuss the state-of-the-art and to be informed on new measurement possibilities. The achievements of the Symposium were discussed in the Technical Evaluation Reports of each session. Papers to be presented at the Propulsion and Energetics Panel 67th Symposium, held in Philadelphia, Pennsylvania, USA, 19—23 May 1986. ISBN 92-835-0401-1	Anemometry (10); Pyrometry (3); High Speed Data Acquisition and Processing (6); Vibration, Thin Layer and Tip Clearance Measurements (6); and Future Prospects (5). The Technical Evaluation Reports were separately prepared for each session and are included in the Conference Proceedings at the beginning of each session. Questions and answers follow each paper, and a Round Table Discussion follows each session. The Symposium was addressed to research scientists and development engineers for aero engines in order to discuss the state-of-the-art and to be informed on new measurement possibilities. The achievements of the Symposium were discussed in the Technical Evaluation Reports of each session. Papers to be presented at the Propulsion and Energetics Panel 67th Symposium, held in Philadelphia, Pennsylvania, USA, 19—23 May 1986. ISBN 92-835-0401-1

AGARD

NATO ⊕ OTAN

7 rue Ancelle · 92200 NEUILLY-SUR-SEINE

FRANCE

Telephone (1)47.38.57.00 · Telex 610 176

DISTRIBUTION OF UNCLASSIFIED

AGARD PUBLICATIONS

AGARD does NOT hold stocks of AGARD publications at the above address for general distribution. Initial distribution of AGARD publications is made to AGARD Member Nations through the following National Distribution Centres.Further copies are sometimes available from these Centres, but if not may be purchased in Microfiche or Photocopy form from the Purchase Agencies listed below.

NATIONAL DISTRIBUTION CENTRES

BELGIUM
Coordonnateur AGARD — VSL
Etat-Major de la Force Aérienne
Quartier Reine Elisabeth
Rue d'Evere, 1140 Bruxelles

CANADA
Defence Scientific Information Services
Dept of National Defence
Ottawa, Ontario K1A 0K2

DENMARK
Danish Defence Research Board
Ved Idraetsparken 4
2100 Copenhagen Ø

FRANCE
O.N.E.R.A. (Direction)
29 Avenue de la Division Leclerc
92320 Châtillon

GERMANY
Fachinformationszentrum Energie,
Physik, Mathematik GmbH
Kernforschungszentrum
D-7514 Eggenstein-Leopoldshafen

GREECE
Hellenic Air Force General Staff
Research and Development Directorate
Holargos, Athens

ICELAND
Director of Aviation
c/o Flugrad
Reyjavik

ITALY
Aeronautica Militare
Ufficio del Delegato Nazionale all'AGARD
3 Piazzale Adenauer
00144 Roma/EUR

LUXEMBOURG
See Belgium

NETHERLANDS
Netherlands Delegation to AGARD
National Aerospace Laboratory, NLR
P.O. Box 126
2600 AC Delft

NORWAY
Norwegian Defence Research Establishment
Attn: Biblioteket
P.O. Box 25
N-2007 Kjeller

PORTUGAL
Portuguese National Coordinator to AGARD
Gabinete de Estudos e Programas
CLAFA
Base de Alfragide
Alfragide
2700 Amadora

TURKEY
Millî Savunma Başkanlığı (MSB)
ARGE Daire Başkanlığı (ARGE)
Ankara

UNITED KINGDOM
Defence Research Information Centre
Kentigern House
65 Brown Street
Glasgow G2 8EX

UNITED STATES
National Aeronautics and Space Administration (NASA)
Langley Research Center
M/S 180
Hampton, Virginia 23665

THE UNITED STATES NATIONAL DISTRIBUTION CENTRE (NASA) DOES NOT HOLD
STOCKS OF AGARD PUBLICATIONS, AND APPLICATIONS FOR COPIES SHOULD BE MADE
DIRECT TO THE NATIONAL TECHNICAL INFORMATION SERVICE (NTIS) AT THE ADDRESS BELOW.

PURCHASE AGENCIES

National Technical
Information Service (NTIS)
5285 Port Royal Road
Springfield
Virginia 22161, USA

ESA/Information Retrieval Service
European Space Agency
10, rue Mario Nikis
75015 Paris, France

The British Library
Document Supply Division
Boston Spa, Wetherby
West Yorkshire LS23 7BQ
England

Requests for microfiche or photocopies of AGARD documents should include the AGARD serial number, title, author or editor, and publication date. Requests to NTIS should include the NASA accession report number. Full bibliographical references and abstracts of AGARD publications are given in the following journals:

Scientific and Technical Aerospace Reports (STAR)
published by NASA Scientific and Technical
Information Branch
NASA Headquarters (NIT-40)
Washington D.C. 20546, USA

Government Reports Announcements (GRA)
published by the National Technical
Information Services, Springfield
Virginia 22161, USA

END

DATE
FILMED

9-87